Title
Engineering Evaluation of Post-Liquefaction Strength

Author
Weber, Joseph Patrick

Publication Date
2015

Peer reviewed|Thesis/dissertation

Engineering Evaluation of Post-Liquefaction Strength

By

Joseph Patrick Weber

A dissertation submitted in partial satisfaction of the

requirements for the degree of

Doctor of Philosophy

In

Engineering – Civil and Environmental Engineering

in the

Graduate Division

of the

University of California, Berkeley

Committee in charge:

Professor Raymond B. Seed, Chair
Professor Juan M. Pestana
Professor Douglas S. Dreger

Summer 2015

Engineering Evaluation of Post-Liquefaction Strength

By

Joseph Patrick Weber

Abstract

Engineering Evaluation of Post-Liquefaction Strength

by

Joseph Patrick Weber

Doctor of Philosophy in Engineering – Civil and Environmental Engineering

University of California, Berkeley

Professor Raymond B. Seed, Chair

Over the past three decades, engineers working in the area of soil liquefaction engineering have been called upon to develop increasingly well-refined evaluations of expected performance of structures and of critical infrastructure in the event of potential soil liquefaction. A critical element in such evaluations is the engineering assessment of post-liquefaction strengths of in situ materials. Prior to the past three decades, it was common practice to ascribe assumed negligible strengths and stiffnesses to liquefied soils for engineering analyses. Today, increasingly higher-order analyses are performed involving either simplified seismic deformation or seismic displacement analysis methods, or fully nonlinear analyses implemented in a finite element or finite difference framework. In all of these analyses, the evaluation and modeling of post-liquefaction strengths is typically a critical issue.

This has led to a surge of interest, and to a significant amount of research involving laboratory, centrifuge, and analytical studies. The focus for engineering analysis and design efforts for actual projects is often on the use of empirical relationships for engineering evaluation of in situ post-liquefaction strengths. This is due, in large part, to complications and challenges inherent in the use of laboratory-scale physical testing for development of estimates of post-liquefaction strengths at full field scale. These challenges are generally well understood, but some of them (e.g. localized void redistribution under globally "undrained" shearing) continue to confound reliable assessment by means of laboratory testing for most projects. As a result, empirical relationships, established based on back-analyses of full-scale field liquefaction failure case histories, are the common approach for most projects. These current efforts have been focused on this approach.

These current studies began with a technical review of previous efforts. That proved to be a valuable exercise. Evaluation of previous work, and recommendations, with emphasis on strengths and drawbacks of prior efforts, led to some important insights. It turns out that a number of previous efforts had developed important lessons, and in some cases important pieces of the overall puzzle. They also served to provide ideas and to inspire elements of these current studies, and they provided lessons with regard to mistakes to avoid.

A suite of full-scale liquefaction failure case histories were then reviewed, vetted and selected for back-analyses. New methods were developed for performing these back-analyses, including methods that more accurately and reliably deal with momentum effects in liquefaction failures that experience large displacements. A suite of additional empirical relationships were

developed specifically for cross-comparison of the results of back-analyses of large deformation liquefaction failures. In the end, a suite of back-analysis results of unprecedented reliability were developed, based on (1) improved back-analysis procedures, (2) internal cross-checking within the framework of the empirical relationships developed, and (3) external cross-checking against the results obtained by previous investigations, with an informed understanding of the strengths and drawbacks of the back-analysis methods and assumptions employed in those previous studies.

The resulting hard-earned back-analysis case history database was then used, in the context of probabilistic regressions that incorporated the best obtainable evaluations of uncertainties, to perform probabilistic regressions by the maximum likelihood method in order to develop new predictive relationships for engineering evaluation of post-liquefaction strength as a function of both (1) corrected SPT penetration resistance, and (2) initial in situ effective vertical stress.

These new relationships were then compared with previous relationships and recommendations. Here, again, with understanding of the strengths and drawbacks of the procedures by which the previous relationships were developed, and of the back-analyses that often provided the parameters for the earlier efforts, a coherent overall pattern emerged and the relative juxtaposition of values of post-liquefaction strengths provided by different relationships can now be better understood.

The new predictive relationships developed in these current studies agree surprisingly well with the recent recommendations of Wang (2003) and Kramer (2008) who executed a similar overall effort, but with significant differences in approaches, and judgments, at essentially every step of the way. This level of agreement occurs when adjustments are made for apparent errors in development of a number of their model input parameters, and so the work to develop better understandings of strengths and weaknesses of various case history back-analysis approaches was particularly important here. Similarly, the results and recommendations from these current studies can also be shown to provide fairly good agreement with earlier recommendations of (1) Seed and Harder (1990), (2) Olson and Stark (2002) and (3) Idriss and Boulanger (2008), but only over specific ranges of (1) initial in situ effective vertical stress, and (2) corrected SPT penetration resistance. In other ranges, these previous relationships can now be shown to be either conservative, or unconservative, and the reasons for this can now be understood.

The new predictive relationships for engineering evaluation of post-liquefaction strength are presented in a fully probabilistic form, and can be used for probabilistic risk studies and design of high-level projects. They are then recast in a simplified deterministic relationship likely to be more widely applicable to more routine projects.

These new relationships offer potentially significant advantages over previously available recommendations and relationships. They are based on back-analyses, and regressions, which provide insight into the underlying forms of the relationships between post-liquefaction strengths and both (1) penetration resistance and (2) effective vertical stress, over the ranges of conditions well-represented in the 30 full-scale field liquefaction case histories back-analyzed. Because they provide insight as to the underlying forms of these relationships, they provide a better basis for extrapolation to higher ranges of penetration resistance, and to higher ranges of effective stress, than do previous recommendations. The back-analyzed field case history database

provides fair to good coverage for values of $N_{1,60,CS}$ up to approximately 14 blows/ft, and for representative effective overburden stresses of up to approximately 4 atmospheres. The range of principal engineering interest is usually $N_{1,60,CS} \approx 10$ to 22 blows/ft., however, as it is over that range that field behavior, and project performance, often transitions from unacceptable to acceptable. Similarly, for major earth and rockfill dams (and their foundations), ranges of effective overburden stress considerably larger than 4 atmospheres are often of critical importance.

In addition to the development of improved relationships for engineering evaluation of post-liquefactions strengths, the suite of new empirical relationships developed for use in cross-checking of back-analyses of liquefaction failure case histories will likely also have applications with regard to checking of engineering analyses of expected performance for forward analyses of actual engineering projects, including high-level analyses involving fully nonlinear finite element or finite difference analyses for critical and/or high risk projects.

To my wife, Madison,
without your constant support,
this accomplishment would not be possible.

TABLE OF CONTENTS

ACKNOWLEDGEMENTS

I would first like to thank Professor Raymond B. Seed. I will always be grateful for your inspiration, mentorship and assistance over the years. I would also like to thank his wife, Professor Mary Seed; you were so kind and patient as to allow me to steal time with your husband while completing this endeavor.

To my entire family, especially my wife, Madison, my parents, John and Mary, my brother Thomas, and Phyllis, Christopher, Christine, Mariea and Sean Byrne, thank you all for the unwavering love and support you have always provided.

I would also like to thank the other members of my doctoral committee, Professors Juan Pestana and Douglas Dreger. Professor Pestana, you have always been a great source of guidance and inspiration. Professor Dreger, thank you for your insight and direction throughout this process.

Professor Robb Moss, thank you for your assistance in developing the correlation contained herein. Professor Reichenberger, thank you for your mentorship throughout my collegiate years. Professors Sitar, Bray and Reimer, thank you for your instruction and guidance. You have all helped guide me on this path and for that I am ever appreciative.

To the advisory panel for this work: Dr. Les Harder, Dr. David Gillette, Dr. Peter Robertson, Professor Les Youd and Professor Kyle Rollins. Thank you all for your discussion and insight on this subject, which helped steer the direction of the research. I especially want to thank Dr. Les Harder for providing key background data.

Thank you to my fellow UC Berkeley GeoEngineering colleagues and friends, Dr. Tonguc Deger, Dr. Hamed Hamedifar, Garrett Harris, Dr. Justin Hollenback, Debra Murphy, Chukwuebuka Nweke, Khaled Chowdhury, Brandon Kluzniak, Jeff Braun, Eileen Test, Julien Cohen-Waeber, Dr. Joshua Zupan, Dr. Roozbeh Geraili, Professor Ben Mason and others with whom I have had the honor to work alongside.

To my friends James Braga, Patrick and Eric Larsen, Fr. Stephen Barber, S.J., Manny and Trudi Hurtado, Dr. Eric Keldrauk, Dr. Matthew and Mal Over, Dr. Will and Kati Trono, Jose Beristain, Dr. Robert Jaeger, John Roveda, Brandon Romo and others, thank you for your patience and understanding in my lack of presence while completing this work. Your support has always been appreciated.

To my colleagues at HDR, Inc., especially Mark Stanley, thank you for your flexibility, understanding and support during this time.

Lastly, I would like to thanks the U. S. Nuclear Regulatory Commission for funding this research effort. This support is gratefully acknowledged. The contents of this report reflect the views of the authors, who are responsible for the accuracy of the information and data presented. The contents do not reflect the official position or policy of the U.S. Nuclear Regulatory Commission.

Chapter One

Introduction and Overview

1.1 Introduction

Soil liquefaction came prominently to the attention of the geotechnical engineering profession in the mid-1960's, largely due to the widespread and severe liquefaction-induced damages wrought by the 1964 Great Alaskan Earthquake (M_W = 9.2) and by the 1964 Niigata Earthquake (M_W = 7.7). The phenomenon of soil liquefaction was, of course, already known but prior to these two events there were no well-established engineering methods for dealing with soil liquefaction and its consequences.

In the wake of these two events, the first engineering investigation and analysis methods were developed for evaluation of the risk of triggering, or initiation, of soil liquefaction due to seismic loading (e.g.: Kawasumi, 1968; Seed and Idriss, 1971; etc.). Methods for evaluation of seismic soil liquefaction potential, or likelihood of triggering, under both static and cyclic loading have continued to evolve, and today there are a wide variety of well-established methods that range from simplified empirical methods based on in situ testing through laboratory-based methods and also increasingly advanced, fully nonlinear constitutive analysis models and methods implemented in either finite element or finite difference computer analysis frameworks.

The liquefaction-induced failure of the upstream side of the earthen embankment of the Lower San Fernando Dam during the 1971 San Fernando Earthquake (M_W = 6.6) nearly resulted in uncontrolled release of the Van Norman Reservoir, which would have had catastrophic consequences for the large urban population immediately downstream. This embankment failure was followed a year later (1972) by the non-seismically induced liquefaction failure of the Buffalo Creek mine tailings dam in West Virginia. The Buffalo Creek Dam failure resulted in uncontrolled release of the reservoir impoundment, and devastated the community immediately downstream. One hundred and twenty five lives were lost. These two events led to a surge of interest in liquefaction-related risks associated with dams, and helped to lead to the eventual creation of the U.S. National Dam Safety Program in 1986. This program has contributed considerably to the further development of improved methods for engineering treatment of soil liquefaction issues.

Additional impetus for advancement of liquefaction-related engineering analysis methods, and for corollary liquefaction risk mitigation measures, has come from interest and research associated with other critical infrastructure, and more recently the focus has continued to broaden to include more routine projects and structures.

Both in the U.S. and abroad, much of the focus of the rapidly evolving field of soil liquefaction engineering practice in the 1970's and 1980's was initially on dams and other critical facilities and infrastructure. Over the five decades that have now passed since the mid-1960's, attention has progressively extended to also consider and deal with liquefaction risk for an increasingly broad range of facilities and structures, including ports and harbors, transportation

facilities (bridges, roads, embankments, tunnels, airports, etc.), in-ground lifelines (power, gas water, telecommunications, etc,.), critical structures (power plants, industrial facilities, waste impoundments, etc.), more routine structures (e.g. homes and businesses), and more.

As the breadth of applications has increased, so has the development of increasingly accurate and reliable methods for evaluation not only of the risk of triggering or initiation of soil liquefaction, but also for evaluation of the expected resulting performance or consequences for a given site or facility. Increasingly, engineers are being called upon to assess the expected consequences of potential liquefaction in terms of deformations, displacements, and damages to the structures or systems of concern.

Over the first 10 to 15 years after the two 1964 earthquakes in Alaska and Niigata, most liquefaction-related engineering was focused primarily on evaluation of the risk, or likelihood, of "triggering" or initiation of liquefaction. If liquefaction was considered likely to be triggered, either statically or cyclically, then negligible post-liquefaction strengths and stiffnesses were commonly assigned to the materials judged likely to liquefy for the next (subsequent) steps involved in evaluation of expected consequences.

That was a very conservative approach, and it was clear early on that post-liquefaction strengths were not necessarily equal to zero; certainly not in all cases. The evolving understanding of the mechanics of soil liquefaction, and of critical state soil mechanics (e.g. Casagrande, 1940; Schofield and Wroth, 1968; etc.), and progressively advancing laboratory testing capabilities and also analytical capabilities, led to the continuing development of improved analytical tools for dealing not just with triggering of soil liquefaction, but also with the engineering assessment of resulting deformations and displacements of both the ground and the structures and systems affected.

This, in turn, has led to a need for better assessments of post-liquefaction strengths so that more accurate (and less over-conservative) engineering assessments of expected performance and consequences can be made.

It is here that these current studies are focused.

1.2 Overview of These Current Studies

Chapter 2 presents a brief history of the development of approaches for evaluation of post-liquefaction soil strengths, and a review of important methods, including an assessment of the advantages and drawbacks of the main approaches available for engineering evaluation of in situ post-liquefaction strengths. In most research investigations, this type of review is presented as a bit of a formality. For this current study, however, this close review and re-evaluation of previous efforts was a key element in the development of the findings eventually produced here. Armed with the advantage of hindsight, it turns out that multiple previous investigation efforts, and researchers, had developed important insights and/or elements of work that end up contributing to the overall solutions and findings of these current studies. In some interesting cases, the previous

investigators did not (at the time) recognize the eventual importance of some of those pieces of the puzzle.

Chapter two discusses methods for evaluation of post-liquefaction strengths based on laboratory testing, as well as methods for assessment of post-liquefaction strengths using empirical relationships developed based on back-analyses of full-scale field failures. The main emphasis in Chapter 2 is on empirical methods, because a number of difficulties can arise with regard to the direct use of laboratory-based methods for project-specific applications, as is also discussed in this chapter. The development of improved empirical methods is the principal focus of these current studies. Advantages and disadvantages, as well as strengths and weaknesses, in previous approaches are examined. A number of errors by previous investigators and/or studies are also examined and explained. Some of these issues will be addressed again in Chapters 5 and 6, as the results of these current studies are compared against the results of previous efforts.

Chapter 3 presents an explanation of the review and selection of liquefaction field performance case histories for back-analyses in these current studies. A significant number of previous investigators have now worked on this problem, and a large number of potential case histories have been collected and analyzed by various investigators. The quality of case histories available spans a considerable range, both with regard to the quality of data available for each case, and also the caliber of the documentation available regarding those data. In addition, some of the cases represent situations in which the nature of the field performance observed permits reasonably well-defined or well-constrained back-analyses for evaluation of post-liquefaction strengths. In other cases, the nature of the failure mechanism involved simply does not permit such an accurate assessment of post-liquefaction strengths. Selection of cases to be considered, and of cases to be back-analyzed and included in the development of the resulting probabilistic and deterministic relationships for evaluation of post-liquefaction strength, is thus an important issue.

Chapter 4 then presents an explanation of the back-analyses of field failure case histories performed for these current studies. The chapter begins with an overview of significant back-analysis approaches taken in these current studies, as well as in previous studies, with an assessment of strengths and drawbacks of each. This is important because the eventual predictive relationships developed will be cross-compared with existing relationships in Chapter 5, and it is thus important to understand the relative advantages and drawbacks of some of the back-analysis approaches taken in previous studies.

Chapter 4 then goes on to present and describe the development of a number of new back-analysis methods, and new empirical tools, and their application to the back-analyses of the case histories selected in Chapter 3. Many previous studies have not fully documented, or provided sufficient details, of back-analyses performed for purposes of assessing post-liquefaction strengths, and that has made it difficult to check and verify the general validity and reliability of the resulting recommended approaches for assessment of in situ post-liquefaction strengths for application to engineering analysis and design of real projects. One of the objectives of this current investigation is to break this trend, and to suitably document both the methods employed, and also the details of the analyses as these methods are applied to each individual case history. Methods and assumptions, cross-sections, modeling details and parameters, etc. involved in performing these back-analyses are presented and discussed. Detailed summaries of the back-analyses

performed for each of the individual cases selected and analyzed are presented in Appendices A and B.

Chapter 4 also presents a series of cross-checks of the values and parameters back-calculated from the liquefaction failure case histories. A series of empirical relationships developed in these current studies are used to check the internal consistency of the results of the 30 case histories back-analyzed in these current studies, based on a number of criteria. These cases are then further cross-checked against the values back-calculated by previous investigators, with an understanding of the likely errors and systematic biases involved in some of those previous analyses.

Chapter 5 then presents and describes the use of the results of the back-analyses performed in Chapter 4 to develop recommended probabilistic and deterministic relationships for engineering evaluation of post-liquefaction strengths. The initial emphasis is on development of fully probabilistic empirical relationships for assessment of in situ post-liquefaction strengths based on engineering evaluations of in situ penetration resistance and of initial in situ vertical effective stresses. These methods are expected to be employed mainly for important projects that warrant a probabilistic or risk-based approach. The probabilistic methods are then used to develop recommended deterministic methods, with likely applications to more routine engineering analysis and design.

Comparisons are then made between the probabilistic and deterministic tools and methods developed in these current studies, and a suite of other empirical approaches and relationships previously developed by other investigators. In the end, a coherent picture emerges and it now appears that the efforts of a number of previous investigations can be fit together, much like assembling a puzzle, and that a relatively coherent overall understanding of methods suitable for engineering evaluation of post-liquefaction strengths is achieved.

Chapter 6 presents an overall summary of the findings and recommendations from these studies.

Chapter Two

Previous Studies

2.1 Introduction

This chapter presents a review of existing methods for engineering evaluation of post-liquefaction strengths. This includes an overview of the historical progression of such methods, and an assessment of the strengths and shortcomings of each of these methods, and of the investigations performed to develop them.

2.1.1 Key Principles and Definitions

The term "soil liquefaction" has had many meanings ascribed to it by a large number of engineers and researchers. In these current studies, soil liquefaction will be taken as being: a significant reduction in strength and stiffness of a soil, primarily as a result of reduction in effective normal stresses due to pore pressure increase. This does not mean that pore pressure increase is the only cause of reduction in effective stress, or of reduction in strength and stiffness.

The term "flow failure" has also had multiple meanings. In these current studies, flow failure will refer to very large ground deformations and displacements that occur primarily because the static (gravity induced, non-seismic) "driving" shear stresses exceed the available shear strengths during some significant portion of the period over which displacements occur.

"Statically-induced liquefaction" will be taken as soil liquefaction that occurs in the absence of cyclic loading, either as a result of (1) monotonic increase in driving shear stresses, (2) decrease in effective stress due to non-cyclically induced increases in pore pressure, or (3) contractive behavior of the liquefying soil in the face of imposed deformations from moving boundary conditions (see the Fort Peck Dam failure).

"Seismically-induced liquefaction" will be taken as liquefaction triggered in some part by cyclic stresses, which may occur in combination with gravity-induced static driving shear stresses already in place. Seismically-induced liquefaction will generally include liquefaction resulting from seismic loading, and also vibrations from explosions, vibro-densification, passing trains, etc. In these current studies it will also include vibrations from large vibro-seis trucks used to generate controlled vibrations for deep geophysical studies (see the Lake Ackerman embankment failure).

"Post-liquefaction strength" has a very broad range of meanings and definitions to various engineers and researchers. In these current studies, the definition of this term will be a matter of context. When referring to post-liquefaction strength as deliberatively determined by others, their definition will generally be employed. When referring to post-liquefaction strength assessed in these current studies, the symbol used will be S_r and it will refer to the post-liquefaction shear strength that can be mobilized at non-insignificant strains to resist deformations and displacements.

Two additional terms warrant definition here as well. The first of these is "post-liquefaction initial yield stress" ($S_{r,yield}$). This is not an actual "strength", but rather the value of shear stress calculated to be needed within liquefied soils to provide an overall (theoretical) static Factor of Safety equal to 1.0 for conditions after (assumed) triggering of liquefaction and before significant resulting displacements begin to occur. This would, of course, over-estimate the actual value of available post-liquefaction strength (S_r) for cases in which significant displacements then do occur. If the value of S_r had actually been equal to $S_{r,yield}$, then large displacements would not have resulted.

An additional term is "post-liquefaction residual strength based on residual geometry" ($S_{r,resid/geom}$), which is also not an actual "strength". Instead, it is the value of S_r back-calculated to provide a static Factor of Safety equal to 1.0 based on post-failure residual geometry. This is an over-conservative basis for estimation of actual post-liquefaction strength, as it neglects momentum effects as the moving slide mass has to be decelerated back to a stable and stationary residual condition. $S_{r,resid/geom}$ will therefore significantly underestimate the actual value of S_r during failure for most cases.

2.2 Laboratory Based Methods

2.2.1 Poulos, Castro and France (1985)

Poulos et al. (1985) proposed a laboratory based method for engineering assessment of in situ post-liquefaction strengths. This method was generally based upon principles of critical state soil mechanics (Casagrande, 1940; Schofield and Wroth, 1968; etc.), and it involved very carefully performed field sampling efforts as well as high quality laboratory testing.

The basic underlying principal of critical state soil mechanics is illustrated schematically in Figure 2.1. This principle asserts that soils, when sheared, will seek to either dilate or contract depending on whether their current "state" (their current combination of void ratio and effective confining stress) is located above or below a locus of points known as the Critical State Line (CSL) in void ratio (e) vs. effective confining stress (σ_3') space. Soils above the CSL are "loose" and will exhibit contractive behavior when sheared, and soils below the CSL are "dense" and will exhibit dilatant behavior when sheared. Soils will dilate or contract until they reach a new state on the CSL, at which point further changes in void ratio and effective confining stress will cease to occur, and the soil will continue to shear at constant void ratio, constant effective confining stress, and constant shear strength. Soils that have reached the CSL, and that exhibit constant shear strength, void ratio, and effective stress are defined as having reached "critical state". Under drained shearing conditions, soils will change volume (and thus void ratio), moving vertically upwards or downwards in Figure 2.1, in order to proceed towards the CSL. Under undrained shearing conditions, soils instead exhibit either increases in pore pressure (contractive behavior) or decreases in pore pressure (dilatant behavior), resulting in equal and opposite changes in effective confining stress, and thus approach the CSL laterally as shown in Figure 2.1. Eventually all soils, if sheared sufficiently, will theoretically reach a (critical state) condition of constant shearing resistance at some point located on the CSL. The location and shape of the CSL is, of course, different for each individual soil.

Castro and Poulos (1977) and Poulos (1981) define a "steady state" wherein a soil sheared to large enough strains reaches a state of constant shearing resistance, constant effective stress, constant volume and constant strain rate. The main difference between this steady state and the previously defined critical state is the addition of the condition of constant strain rate, and it should be noted that the strain rate part of this definition is often ignored. Accordingly, the steady state and the critical state line are often analogous.

Figure 2.2 then illustrates the laboratory-based steady state method proposed by Poulos et al. (1985) for evaluation of post-liquefaction shear strengths of in situ soils based on sampling and laboratory testing. This illustrative figure shows the application of this approach to a high quality (nearly undisturbed) sample of silty sand hydraulic fill from the downstream shell of the Lower San Fernando Dam.

The first step is to obtain fully disturbed bulk samples of the in situ soils. Samples are then reconstituted in the laboratory, at different void ratios, and these are subjected to isotropically consolidated undrained (IC-U) triaxial compression tests to determine a steady state line (or critical state line) for these reconstituted samples. The resulting steady state line for the Lower San Fernando Dam hydraulic fill is shown by the solid line in Figure 2.2. Critical state lines, and steady state lines, are commonly plotted as void ratio vs. the logarithm of effective confining stress, and in this semi-log space steady state lines are generally approximately log-linear (or nearly so) over the range of principal engineering interest for liquefiable soils, and then they inflect downwards at higher effective stresses. The steady state line developed for these reconstituted samples is not taken directly as a basis for evaluation of in situ steady state strengths. Instead it is then used to "correct" the results of additional IC-U triaxial tests performed on a limited number of higher quality (more nearly undisturbed) samples. This "correction" addresses effects of sampling disturbance, and additional disturbance (and volume changes) that occur during sample transport, extrusion, mounting and reconsolidation prior to undrained shearing in the laboratory.

Higher quality samples are then also obtained, either by advancing sharp-edged and relatively thin-walled samplers, or by excavating a large diameter shaft and then lowering an engineer or technician into the base of the shaft to carefully hand carve a sample while slowly advancing a cylindrical sampling tube (mounted on a tripod) about the sample as it is carved. Advancing sharp-edged samplers is the more common method, and these must be pushed (not driven with hammers) to avoid vibratory densification of the soils being sampled. In either case, as samplers are advanced, the precise depth of penetration or sampler advance is closely measured. Sample recovery is carefully logged. Knowing the length of sampler advance, the radius of the cutting edge, the radius of the inside of the sampler tube, and the length of recovered sample within the tube, a calculation is then made to estimate volume (and thus void ratio) changes during sampling. When the sample is then returned to the laboratory, length is again measured, and any further volume (and void ratio) changes are calculated. When the sample is extruded and trimmed to length, and a confining membrane and top and base caps are applied, the new initial "mounted" sample height and diameter are measured and any further volume (and void ratio) changes are again recorded. Finally, additional volume (and void ratio) changes during reconsolidation are also measured. In this manner, the void ratio of the final, consolidated sample as actually subjected to undrained shearing is "known", and so is the original in situ void ratio prior to sampling.

The undrained shearing portion of the IC-U triaxial test is then performed to measure the undrained steady state strength ($S_{u,s}$) at the sample's final, laboratory consolidated void ratio. This is plotted in the lower right-hand corner of Figure 2.2 (the large, solid "square"), and it is plotted at the laboratory void ratio as tested. This laboratory value of $S_{u,s}$ is then "corrected" back to the initial in situ void ratio by assuming a correction path parallel to the steady state line developed based on testing of reconstituted samples, as shown in Figure 2.2, producing the solid "dot" in the upper left-hand corner of the figure. This assumed parallelism of the correction with the slope of the steady state line previously developed for reconstituted samples represents a major assumption, and there is no good explanation as to (1) why the steady state line for the reconstituted samples is not the same as the steady state line for the higher quality samples, and (2) why the reconstituted and more nearly undisturbed steady state lines would be exactly parallel, justifying this assumption. Corrections in terms of $S_{u,s}$ tend to be very large, and any small change in the slope of the line followed in making this correction can significantly affect the final results.

The upstream slope of the Lower San Fernando Dam failed due to liquefaction that occurred during the 1971 San Fernando Earthquake, and this has been a much-studied case history. A multi-agency effort was formed in the mid-1980's to re-study this case history as one part of a two-part effort to investigate the viability and reliability of the laboratory-based steady state methodology proposed by Poulos et al. for evaluation of in situ post-liquefaction steady state strengths ($S_{u,s}$). The San Fernando Dam studies were overseen primarily by the U.S. Army Corps of Engineers. The other part of this effort was overseen primarily by the U.S. Bureau of Reclamation (USBR), and involved retaining Poulos et al. (GEI Consultants) to employ the steady state method to assess in situ $S_{u,s}$ for a number of soil zones and soil strata for five USBR dams and some of their foundation soils. This second part of the effort will be discussed further at the end of this current Section 2.1.1.

Four teams performed testing on reconstituted samples of the silty sand hydraulic fill materials from the lower portion of the downstream shell of the Lower San Fernando Dam, and one of the questions to be answered was the reliability with which different laboratories could develop similar steady state lines by this approach. Figure 2.3 shows the "consensus" steady state line developed for these studies. The four laboratories were all selected for good reputations with regard to high level testing, and these were (1) GEI Consultants, (2) the U.S. Army Corps of Engineers Waterways Experiment Station (WES), (3) Rensselaer Polytechnic Institute and State University (RPI), and (4) Stanford University working jointly with U.C. Berkeley. As shown in this figure, this was difficult testing and two of the laboratories did not quite develop data that would have usefully defined in good detail the steady state line that was developed by consensus. But this element of the procedure was judged to be at least feasible (Seed, et al., 1989).

A series of IC-U triaxial tests were then performed by both the GEI and Stanford laboratories on higher quality (more nearly undisturbed) samples, and these were then corrected using the steady state procedure (assuming parallelism with the steady state line from Figure 2.3). Figure 2.4 shows the resulting corrected estimates of in situ $S_{u,s}$, and the laboratory $S_{u,s}$ values upon which they are based. This is the interpretation by Seed et al. (1989), and a slightly different interpretation was developed by Castro, et al. (1989), with one of the main differences being the amount of earthquake-induced void ratio change estimated to have occurred due to cyclic pore pressure generation and then subsequent reconsolidation after the 1971 San Fernando earthquake.

Figure 2.4 illustrates several of the challenges involved in this method. The first is the very large correction from laboratory $S_{u,s}$ to the estimated field (in situ) $S_{u,s}$. Correction factors range from approximately 2.5 to more than 20, with 4 out of the 11 samples having corrections factors of greater that one full log-cycle (factors of 10 or greater). These are very large correction factors to be applying to shear strengths, especially given the unconfirmed assumption of parallelism between the steady state lines of (a) reconstituted samples, and (b) the higher quality (more nearly undisturbed) samples tested for Figure 2.4. A second problem is the wide scatter in the resulting corrected values of estimated in situ $S_{u,s}$ (the large dots in Figure 2.4), which range over more than a full log-cycle.

Back-calculated strengths for the upstream side slope failure that actually occurred due to the earthquake fall within the range of "corrected" values of in situ $S_{u,s}$ shown in Figure 2.4, but this is a large range.

A further evaluation of the potential usefulness and reliability of the steady state methodology was provided by the second part of these studies. Figure 2.5 shows the values of estimated in situ $S_{u,s}$ developed for 35 soil layers and strata at five U.S. USBR dams (Von Thun, 1986). These values of $S_{u,s}$ are plotted on the vertical axis, and the horizontal axis is the representative $N_{1,60}$ value ascribed to each of those sandy and silty soil units as a result of SPT investigations. Also shown in this figure is a shaded range proposed by Seed (1987) of $S_{u,s}$ values based on back-analyses of a number of full-scale field liquefaction failure case histories. As shown in Figure 2.5, a strong majority of the estimates of in situ $S_{u,s}$ developed by GEI using this procedure are higher than would be suggested by the empirical range suggested by Seed (1987) based on back-analyses of failure case histories.

Further laboratory investigations, and scale model tests, quickly followed and these would shed further light on some of the key issues affecting not only the original steady state methodology as proposed by Poulos et al. (1985), but also on the use of laboratory testing in broader and more general terms for evaluation of in situ post-liquefaction strength $S_{u,s}$ (or S_r).

2.2.2 Additional Laboratory Investigations and Approaches

The steady state methodology proposed by Poulos et al. (1985) led to significant further laboratory investigations, and some of these helped to clarify the likely causes of the apparently variable and often unconservative $S_{u,s}$ values developed based on the original steady state methodology. They also led to improved understanding of a number of mechanisms and factors affecting post-liquefaction strengths.

A number of investigators (e.g.: Vaid et al., 1990;, Riemer and Seed, 1997; Yoshimini et al., 1999) found that stress path (or method of shearing) affected measured $S_{u,s}$, or S_r, with undrained triaxial compression (TXC) tests developing significantly higher $S_{u,s}$ values than either undrained direct simple shear (DSS) tests or undrained triaxial extension (TXE) tests. Triaxial compression is often a largely suitable mode of shearing for representing conditions at the back heel of a landslide, or the back heel of a bearing capacity failure surface. Triaxial extension generally better represents conditions at the toes of these types of failure surfaces. And conditions

across the base, or belly, of a failure surface are generally better represented by DSS. The use of TXC-based $S_{u,s}$ values (as had been employed in the method of Poulos et al., 1985) can significantly overestimate strengths and introduce systematic unconservatism. This can fixed, and the TXC tests of the original steady state procedure can be replaced with more representative tests providing a DSS-type of shearing, as is now often done.

Castro (1969) performed monotonic IC-U TXC tests on soils formed to a range of densities, and found three different types of resulting behavior based on initial density or relative density. Yoshimine and Ishihara (1998) further investigated this, and formalized a set of useful principles and nomenclature. Figure 2.6 (from Kramer, 2008) provides a simplified illustration of these findings. Sands and low plasticity silts with very low relative densities tend to follow "contractive" type undrained stress paths (and exhibit stress-strain behaviors) that lead to very low undrained residual strengths ($S_{u,s}$) at large strains. Dense soils, at the other extreme, follow "dilatant" type stress paths (and exhibit stress strain behaviors) that lead to high undrained strengths ($S_{u,s}$) at large strains. Soils of "intermediate" relative density can initially exhibit "contractive" type undrained stress paths and stress strain behaviors that consist of initial post-peak strength reduction (strain softening), but then they can experience a phase transformation to dilatant-type behavior and resulting strength increase at larger strains to a final (very large strain) undrained strength higher than the "low point" reached along the way.

The condition at which a locally minimum value of strength is observed at moderate strains (marked with a small "x" in Figure 2.6) in samples of intermediate density is increasingly referred to a "quasi-steady state" (after Alarcon-Guzman, 1988), and the values subsequently reached at very large strains can be referred to as ultimate steady state. Yoshimine and Ishihara (1998) investigated this, based on more extensive laboratory test data for a number of clean sands, and proposed four ranges of behavior based on initial relative densities from very low to high. Their resulting recommendations fit well within the behaviors shown in the simplified illustration of Figure 2.6. As shown in Figure 2.6, quasi-steady state strength can be lower than ultimate steady state strength for soils of intermediate relative density. Multiple additional investigators have now produced similar results (e.g. Yamamuro and Convert, 2001, etc.), and these behaviors are now well established. There is no full consensus as to whether ultimate steady state strength, or quasi-steady state strength, is the better engineering basis for post-liquefaction strength and modeling/analyses. Ishihara (1993) recommends in favor of quasi-steady state strength, and the authors here generally concur.

Another factor investigated by a number of researchers is the effect of the initial level of effective confining stress on post-liquefaction strengths observed. This issue is clouded to some extent by the question as to whether ultimate steady state strength or quasi-steady state strength should be taken as the basis. Based on the quasi-steady state basis, Riemer and Seed (1997) found that samples formed and consolidated to exactly the same post-consolidation void ratios, but at different initial effective confining stresses, and then subjected to undrained triaxial compression shearing produced higher $S_{u,s}$ values if the initial effective confining stresses were higher. This increase in $S_{u,s}$ is not linear with increase in initial confining stress, however, and the ratio of eventual steady state strength vs. initial vertical effective confining stress ($S_{u,s}$ /P) decreases with increasing initial effective confining stress.

Numerous additional laboratory investigations, and scale model experiments (both on shaking tables and on centrifuges), have now been performed and these continue to usefully illuminate many of the basic mechanics and fundamental mechanisms involved in the transition to post-liquefaction residual strengths from initial liquefaction-induced shear failures initiated either by monotonic or cyclic loading conditions.

This has not yet, however, resulted in the development of universally accepted laboratory-based approaches for evaluation of post-liquefaction strengths for in situ soils. There are three sets of additional challenges or issues that arise which continue to complicate this issue, and render the use of laboratory test data potentially unconservative with regard to determination of in situ post-liquefaction strengths for full-scale field applications. These are the phenomena of (1) "void redistribution", and the sometimes related issues of (2) "partial drainage", and (3) potential inter-layer particle mixing effects.

2.2.3 Void Redistribution and Partial Drainage

Void redistribution is the movement of both solid particles and also pore fluids within a soil zone of constant overall volume ("globally undrained") so that the localized void ratio (and relative density) changes occur in some portions of the overall volume of saturated material. This can produce localized changes in void ratio under monotonic and/or cyclic loading conditions thought to represent "globally" undrained shearing.

A good early discussion of this was presented by the National Research Council (1985), and Figure 2.7 shows a simplified illustration of this phenomenon from that report. In this figure, a layer of more pervious cohesionless soil is confined between less pervious overlying and underlying layers. As a result, this pervious stratum will initially behave in an "undrained" manner, with constant overall volume maintained, if loaded rapidly (e.g. by cyclic loading from an earthquake). Although this stratum is "globally" undrained, internally it will experience some rearrangements of both solids and pore fluids as cyclically generated pore pressures cause fluids to seek to escape towards the ground surface, increasing the void ratio near the top of the layer, while solids settle and void ratio decreases in the lower portions of the layer. This results in development of a looser top region up against the interface with the overlying less pervious stratum, and a slightly denser overall condition deeper within the liquefying stratum.

Minor changes in void ratio can produce significant changes in post-liquefaction steady state strength (e.g.: Figures 2.2 through 2.6). The result can therefore be a significant reduction in strength at the top of the confined stratum as void ratio redistribution occurs. In extreme cases, a "blister" of water, or a water film, can develop at the top of a confined stratum, providing a potential shearing zone of essentially negligible post-liquefaction strength.

These phenomena have been observed and demonstrated in numerous laboratory model tests on both centrifuges and on shaking tables (e.g. Liu and Qiao, 1984; Arulanandan et al., 1993; Fiegel and Kutter, 1994; Kokusho, 1999; etc.). The basic mechanics are generally well understood, and the observed effects in some of these model tests have been shown to be very significant. Failure surfaces have the opportunity to seek out the path of least resistance, and when void

redistribution results in a zone or sub-layer of weaker conditions the failure surface will attempt to exploit this zone of weakness.

This is very challenging with regard to the use of laboratory testing, and classical critical state theory (and steady state theory), to predict post-liquefaction behavior in the field. Post-liquefaction behavior will be controlled by the void ratio after void redistribution has occurred, not by the pre-event void ratio in situ. The mechanics of this void redistribution process are understood, and analytical modeling can be performed (e.g. Malvick et al., 2006), but it is not yet possible to reliably predict the actual amounts and rates of void redistribution likely to occur in the field, and it is not yet feasible to reliably predict by analytical methods the resulting effects on post-liquefaction strengths at field scales.

It is difficult to accurately pre-determine for most field situations the localized scale at which void redistribution will occur. This phenomenon occurs primarily within layered soils where some layers are less pervious and thus impede flow to dissipate excess pore pressures. Most liquefaction failures occur within alluvial sediments, hydraulic fills, poorly compacted fills placed in layers, or loess. All of these deposits are commonly layered (or sub-stratified) in a manner that lends itself to potentially adverse void redistribution effects. And these soils often have layering, and sub-layering, at variable scales in a given stratum or deposit. Figure 2.8 shows a photograph of the side of one of the two investigation trenches excavated through the hydraulic fill near the base of the Lower San Fernando Dam after the dam experienced a liquefaction-induced slope failure in 1971. As shown in this photograph, the material is strongly striated (layered) with lighter colored sub-layers of sandier material and darker sub-layers of siltier soil with higher fines content. Closer inspection of any of the lighter sub-strata would reveal even smaller scale sub-layering within these sub-strata, with coarser and finer (lighter and darker) sublayers occurring within the apparent lighter colored larger strata that are not visible at the scale of this photograph.

As explained by Seed (1987), the problem is not that laboratory testing, or critical state (and steady state) theory, do not serve to explain and characterize soil behavior. The problem is that void redistribution occurs in a manner that cannot yet be reliably well predicted, and that it produces changed conditions (that still conform to critical state and steady state theory); and it is these changed conditions that can control the overall behavior in the field. The inability to pre-determine the scale at which these void ratio distribution effects will occur, and the inability to predict the rate and severity with which these effects will occur, continues (so far) to routinely defeat laboratory-based efforts to reliably deal with them for field design and performance assessments.

Void redistribution effects are naturally included in field performance case histories. These likely vary with the relative contrast in permeabilities between layers and strata, and with the scales and geometry at which this redistribution occurs, so no one individual case history can be expected to provide conclusive data regarding likely post-liquefaction strengths that can be mobilized for other sites. Accordingly, it is important to analyze observed full-scale field performance, and to back-analyze field failure case histories, for multiple field cases in order to inform efforts to evaluate likely post-liquefaction strengths for engineering analysis and design.

A second phenomenon that can be closely related is partial drainage. When pore pressure increases occur, either due to cyclic loading or due to contractive behavior under undrained

monotonic loading, the resulting pore pressures begin to dissipate by means of flow away from the area of elevated pore pressure. Intuitively, this dissipation of pore pressures would seem to be a positive thing as it serves to re-establish higher effective stresses and thus higher shear strengths. But as the fluids travel, they can be temporarily impeded at less pervious boundaries, and this can result in a localized build-up in pore pressure, resulting in a second type of void redistribution that can occur over a larger time scale than the more localized type of void redistribution illustrated in Figure 2.7. Partial dissipation of pore pressures, or ongoing dissipation in progress, can thus also potentially serve to locally exacerbate void redistribution effects.

2.2.4 Inter-Layer Particle Mixing

An additional, and related, phenomenon that cannot yet be suitably dealt with either (1) analytically, or (2) by means of direct laboratory testing, is inter-layer particle mixing. When shearing occurs along the interface between two different materials, then the chaotic interactions (rubbing, grinding, etc.) can cause finer particles from one soil to insert themselves between coarser particles of the other soil. This can allow the finer particles and the coarser soil to locally achieve a more efficient "packing" of particles, and it can create a material that occupies less volume than either of the two parent soils per unit weight of solids. In a "globally undrained" shearing situation, this is essentially another form of void (or particle) redistribution, and it can also lead to further reductions in shear strengths along interfaces or boundaries.

Failure mechanisms will tend to seek out and exploit these weaknesses if they are geometrically able to do so. This is thus another mechanism, also favoring failures at and near interface boundaries, that cannot yet be reliably handled either analytically or by means of direct laboratory based testing because it is not generally possible to determine a priori (1) how much mixing may occur, and (2) the extent to which such mixing might degrade "undrained" post-liquefaction strengths.

2.3 Empirical and Semi-Empirical Methods

Because of the currently intractable challenges posed by (1) void redistribution, (2) partial drainage, and (3) inter-layer mixing, it has been necessary to examine full-scale field failures to garner further insight as to likely post-liquefaction strengths that can be mobilized for different sets conditions. This leads to empirical methods for estimation or evaluation of post-liquefaction strength (S_r) based on full-scale field case histories. These case histories, and empirical relationships for evaluation of S_r based upon them, naturally include the effects of all three of these issues or challenges (void redistribution, partial drainage, and interlayer mixing), albeit to varying degrees in any specific case history.

2.3.1 Seed (1987) and Seed and Harder (1990)

The late Prof. H. Bolton Seed developed a suite several successive (evolving) proposed correlations between S_r values back-calculated from liquefaction failure case histories and SPT

penetration resistance during the mid-1980's, and these culminated in the relationship proposed in Seed (1987). This relationship is presented in Figure 2.9.

This 1987 paper presented an excellent overview of many of the challenges in evaluating post-liquefaction strength S_r, and it also presented this proposed empirical relationship which Prof. Seed describes as a "tentative" relationship. Immediately after the paper had been published, it was pointed out that one of the twelve case histories back-analyzed had been plotted with S_r values based on pre-failure geometry, which would have provided an unconservative assessment of the likely actual S_r value. Based on an assumption that momentum effects were relatively minor, the Lower San Fernando Dam case is plotted too high in Figure 2.9; with $S_r \approx 750$ lbs/ft^2 and $N_{1,60,CS}$ = 15 blows/ft. Prof. Seed subsequently determined this to be an error, but was too ill with the cancer that would shortly take his life to repair it. So his son, and a recent former doctoral student, jointly undertook to posthumously correct this error. The resulting modified relationship was published by Seed and Harder (1990), and it was published in an unusual venue; appearing in the Proceedings of the late Prof. Seed's Memorial Symposium rather than in the ASCE geotechnical journal. Both Seed and Harder had previously been involved in earlier stages of development of some of the case histories involved. They re-evaluated the 12 cases originally presented in Seed (1987), and they added five additional cases to bring the total number of cases to seventeen.

Figure 2.10 shows the resulting revised correlation between post-liquefaction strength S_r and corrected $N_{1,60,CS}$ values of Seed and Harder (1990), with a reduced value of S_r for the Lower San Fernando Dam failure case history, and with additional case histories added.

Back-analysis methods were not yet well-established at this time, so a variety of approaches and assumptions were applied to various cases within this limited suite of available case histories. Many of the "smaller" cases involving embankments and slopes of modest height, and with low values of $N_{1,60,CS}$, were analyzed with relatively approximate methods. The Upper San Fernando Dam case history was a "non-failure" case history, and assessment of the likely value of S_r for this case was based on the value having been higher than that for which a major flow-type failure would have occurred, with some additional judgment as to likely cyclic inertial effects.

Three of the largest failures were the Calaveras Dam, the Lower San Fernando Dam and the Fort Peck Dam case histories, and Seed and Harder approximately incorporated "inertial" effects (momentum effects) in the back-analyses of these three cases by selecting S_r values between the values that would have been calculated as $S_{r,yield}$ for pre-failure geometry, and $S_{r,resid/geom}$ for post-failure residual geometry. The "apparent" pre-failure yield stress ($S_{r,yield}$) which is defined as the theoretical strength along liquefied portions of the eventual slide surfaces that would be required to provide a calculated static Factor of Safety equal to 1.0 for pre-failure geometry, and (2) the "apparent" residual stress based on final residual geometry ($S_{r,resid/geom}$) defined as the strength along liquefied portions of the failure surface that would be required to provide a post-failure calculated static Factor of Safety equal to 1.0 for the final, residual post-failure geometry. The actual post-liquefaction strength (S_r) would be less that $S_{r,yield}$; otherwise the post-liquefaction failure mass would be statically stable and would experience only small displacements due to cyclic lurching. Similarly, $S_{r,resid/geom}$ would over-estimate the actual post-liquefaction strength (Sr); as the moving failure mass would accumulate momentum, and would have to be decelerated

and brought back to rest at its final resting position. Neglect of the shear strength needed to decellerate the moving failure mass (to overcome momentum effects) would cause $S_{r,resid/geom}$ to underestimate the actual value of S_r (see Sections 4.3.2 and 4.4.1, and Chapters 5 and 6). Davis et al. (1988) were also performing back-analyses during this same period, and their method for more explicitly incorporating inertial effects also produced values between $S_{r,yield}$ and $S_{r,resid/geom}$. Seed and Harder were aware that their estimates would be reasonable approximations of S_r with inertial effects included, and they adopted values of S_r nearer to $S_{r,resid/geom}$ than to $S_{r,yield}$ for cases in which runout distances of the failure mass had been very large.

For several other cases (the La Marquesa Dam and the La Palma Dam case histories), cyclic inertial effects were approximately accounted for by initially adopting values of S_r nearly intermediate between $S_{r,yield}$ and $S_{r,resid/geom}$, and then adding additional strength to approximately account for cyclic inertial effects due to strong shaking for cases in which (1) overall displacements were somewhat limited, and (2) seismic loading intensity was high; conditions in which cyclic inertial effects were considered to be potentially significant.

The S_r values of Seed (1987) and Seed and Harder (1990) were plotted as a function of procedurally corrected, overburden corrected, and fines adjusted $N_{1,60,CS}$ values.

The fines adjustment proposed by Seed (1987) differed slightly from that of contemporary SPT-based liquefaction triggering correlations, and was as follows:

$$(N_1)_{60\text{-}CS} = (N_1)_{60} + \Delta(N_1)_{60} \qquad \text{[Eq. 2-1]}$$

where $\Delta(N_1)_{60}$ was the fines adjustment, which was a function of fines content as

Fines Content (%)	SPT Correction, $\Delta(N_1)_{60}$ in blows/ft
0	0
10	1
25	2
50	4
75	5

Seed and Harder (1990) employed the same fines adjustment.

Figure 2.11 repeats the base figure of Figure 2.10, but this time adds the result of a least squares regression performed as part of these current studies. The resulting R-square value of $R^2 = 0.64$ indicates a moderately good overall fit.

Seed and Harder (1990) recommended a "one-third" value for simplified, deterministic analyses; a value approximately one-third of the way between the lower bound and the upper bound lines shown in Figure 2.10.

2.3.2 Idriss (1998)

Idriss (1998) would go on to employ the same suite of 17 failure case histories to develop an additional proposed relationship. He "re-interpreted" the case history database of Seed and Harder (1990), but in fact employed the same S_r values as proposed by Seed and Harder for all 17 cases. He did modify selection of "representative" $(N_1)_{60}$ values to formally employ median values, but the values plotted did not visibly change as Seed and Harder had previously done largely the same. He then presented a single central curve fitting the data, as shown in Figure 2.12, rather than the upper and lower bounds as proposed by Seed and Harder (1990), and extended this curve beyond the upper bound of the available data with a dashed line that presumably indicates extrapolation beyond the range of the available data. This curve fits neatly between the upper and lower bounding curves proposed by Seed and Harder (1990) as presented in Figure 2.10, and is largely parallel to these upper and lower bounding curves but at a location slightly below the mid-point between the bounding curves of Seed and Harder. Seed and Harder had recommended approximately "one-third" values as a basis for typical engineering analyses, and the curve proposed by Idriss (1998) was very similar to this.

2.3.3 Stark and Mesri (1992)

Stark and Mesri examined the available data, and concluded that post-liquefaction strength S_r was likely linearly dependent upon initial vertical effective stress ($\sigma_{v,i}'$). They took the S_r values back-calculated for 17 cases by Seed and Harder (1990), and added three additional case histories. They calculated average initial effective vertical stress along the eventual failure surface for each case, and developed ratios of S_r/P where P = initial vertical effective stress within liquefiable materials on the failure plane. Their resulting relationship was the first to express post-liquefaction strength in terms of liquefied "strength ratio" (S_r/P). This relationship is shown in Figure 2.13.

This relationship proposed by Stark and Mesri (1992) established a second "school of thought", and set up a contrast between empirical relationships based (1) on classical critical state theory wherein post-liquefaction strength (S_r) would be expected to be constant for any given relative density, as suggested by the form of the Seed and Harder (1990) relationship, and (2) relationships based on assumed constant strength ratio (S_r/P) in a manner somewhat analogous to the framework of SHANSEP for clays.

This led to some debate within the profession, but it was never a serious issue. It was clear early on that the best answer likely lay between these two points of view. In the end, in these current studies, that turns out to be the case.

A series of nonlinear least squares regressions were performed on the data from Stark and Mesri (1992). A second order polynomial curve was fit to the data, but the inflection was a slight downward curvature with increasing penetration resistance. The resulting R^2 value was $R^2 \approx 0.22$. Because the curvature of the initial regression was slightly downwards, and the associated regressed quadratic coefficient was very close to zero, a linear fit was next investigated. This also resulting in a value of $R^2 \approx 0.22$, as shown in Figure 2.14. Second order polynomial curves with a positive quadratic coefficient (which would produce an upwards inflection) were then also

imposed on the data, but resulting R^2 values were very low. A curve that approximately represented the median line recommended by Stark and Mesri was then imposed, and manual calculations showed that this resulted in a value of $R^2 = 0.12$. These results suggest that the data is poorly behaved (randomly scattered) and that the regression is not well able to provide a good predictive "fit", especially when compared to the correlation bounds proposed in Stark and Mesri (1992).

This does not mean, however, that there is no merit to their suggestion of a relationship between S_r and initial effective stress, and the results of these current studies will in fact result in findings that suggest that initial in situ vertical effective stresses do indeed significantly affect S_r (see Chapter 5). It simply suggests that the data as plotted in Figures 2.13 and 2.14 do not support a well-defined relationship between penetration resistance and post-liquefaction strength as plotted.

2.3.4 Ishihara (1993)

Prof. Ishihara developed a multi-step procedure based on extensive laboratory test data for estimation of post-liquefaction strength (S_r) as a function of SPT penetration resistance. The data were developed for a number of Japanese sands, and were of high quality. As discussed previously in Section 2.2.2, Prof. Ishihara preferred to use quasi-steady state strength rather than ultimate steady state strength, and so targeted this approach accordingly. Prof. Ishihara noted a clear dependence of $S_{u,s}$ on initial effective confining stress. He suggested that while there is a clear dependence here, it is a different relationship for different sands. His approach was based on an assumed log-linear relationship between void ratio (e) and logarithm of effective vertical stress (σ_v') for steady state lines, and he characterized the slopes of the quasi-steady state lines in e vs. log σ' space based on indices derived from the laboratory data for each of several well-characterized clean sands. SPT $(N_1)_{60}$ values were also inferred for each sand as a function of density (void ratio) and effective overburden stress.

He then compared the resulting relationships between quasi-steady state strength against the values of strength ratio calculated by Stark and Mesri (1992), with an adjustment of $(N_1)_{60}$ values to conform with Japanese standards of practice with regard to SPT equipment and procedures. Figure 2.15 shows the proposed relationships for several test sands, and a comparison with the values of strength ratio calculated by Stark and Mesri. As shown in this figure, the relationships developed appear to provide unreasonably steep curves of strength ratio vs. $(N_1)_{60}$, when compared to the relationships developed based on back-analyses of field case histories by most other investigators, including Seed and Harder (1990), Stark and Mesri (1992), Idriss (1998), Olson and Stark (2002), Kramer (2008) and these current studies.

The reasons for this are not fully clear, but it is noted that this procedure assumes a log-linear relationship for the slope of the quasi-steady state line, which may not be valid at the low densities (high void ratios) of principal interest here, and that the high quality laboratory data sets employed did not include potential full scale "field" effects such as void redistribution, partial drainage, and inter-layer mixing as shearing occurs along interfaces between soil layers. It is also interesting to note, however, that Wride et al. (1999) subsequently developed a proposed

relationship between $(N_1)_{60\text{-}CS}$ and S_r based on back-analyses of a selected suite of liquefaction failure case histories, but employing "reasonable lower bound" values of $(N_1)_{60}$ as being "representative" based on the assumption that the weakest strata would control the failures. Their resulting relationship between post-liquefaction strength ratio (S_r/P) and $(N_1)_{60}$ has a form much like that of Ishihara, with steeply rising values of S_r/P at relatively low $(N_1)_{60}$ values (see Section 2.3.5).

2.3.5 Konrad and Watts (1995)

Konrad and Watts proposed a method for estimation of post-liquefaction strength S_r as a function of SPT penetration resistance that was based on a theoretical framework based on critical state soil mechanics. This framework was then calibrated based on a limited number of back-analyzed failure case histories. As with Ishihara (1993), this methodology assumed a series of log-linear relationships, including a log-linear slope of the steady state line, but an additional calibration factor χ was then developed based on back-analyses of five large displacement liquefaction failure case histories. Figure 2.16 shows the estimated relationship between this calibration factor χ and the slope of the steady state line (λ) based on the five field case histories. Three of the five case histories are represented with two points each in this figure, reflecting the ranges of values employed.

This was a "hybrid" method, involving both an empirically-based calibration factor based on S_r values back-calculated from previous field failure case histories, and also laboratory tests for the specific soil of interest for a given project. A four step procedure was employed. Step 1 was site characterization by means of SPT. The fines adjustment of Seed (1987) was employed here. Step 2 was the performance of laboratory tests to ascertain the maximum void ratio (e_{max}) and the slope (λ) of the steady state line. Step 3 was the estimation of χ based on the relationship shown in Figure 2.12. Step 4 was then the estimation of mobilized shear strength (S_r) based on (1) the laboratory determined value of shear strength at e_{max}, (2) the slope (λ) of the laboratory determined steady state line, and (3) the calibration factor χ.

Konrad and Watts reportedly employed this procedure to successfully predict cases of failure and non-failure of artificial sand fills (islands) constructed in the Beaufort Sea for offshore petroleum exploration. This procedure was apparently effective in estimating values of S_r for newly created loose sand fills, but there are a number of important assumptions involved (e.g. a log-linear slope of the steady state line). Additional potential drawbacks of this procedure include the need to accurately determine the slope of the steady state line, the assumption that laboratory-based tests will correctly determine the steady state line for field placement conditions, and the neglect of potential void redistribution effects, etc. in the field.

2.3.6 Wride, McRoberts and Robertson (1999)

Wride et al. (1999) performed a thoughtful review of 20 liquefaction failure case histories that were available and being back-analyzed and used at that time for development of one or more empirical relationships between penetration resistance and either post-liquefaction strength or post-liquefaction strength ratio. This was a paper that warranted more attention than it received.

Wride et al. studied all 20 cases, and eliminated the Lake Merced bank case from their data set. The remaining 19 cases were then examined in a number of ways and were characterized as to mode of failure, method of initiation of failure, and failure mass runout characteristics (various measures of eventual displacement or runout distances, some of them normalized vs. slope height). A number of useful insights were developed as a result of this exercise. Having learned some important lessons from this, indices regarding failure and displacement modes, and runout characteristics, are also developed and employed in these current studies.

Wride et al. then re-evaluated the "representative" $(N_1)_{60}$ values being used to characterize the 19 failure case histories of interest. They took an approach that had been discussed, but not employed, before. It was their view (widely shared) that failure surfaces would tend to seek out and follow weak spots and weak sub-strata, and that it might be more reasonable to use a much lower than mean or median value of penetration resistance to characterize the failure zones controlling displacements and deformations. This was analogous to the "weakest-link-in-the chain" argument of Fear and Robertson (1995) with regard to triggering or initiation of liquefaction for these types of failures. Based on the work of Popescu et al. (1997) regarding effects of spatial variability on soil liquefaction, Yoshimine et al. (1999) had recommended the use of a 20^{th} percentile value (20% of the measured penetration resistances are lower) for CPT tip resistance data for liquefaction studies. Wride et al. took a similar view, and targeted a "reasonable lower bound" which, in practice, was either the lowest value measured for cases where penetration data were sparse, or the near lower bound when more data were available.

There is less explanation and discussion presented regarding selection of representative post-liquefaction strengths for each of the 19 case histories considered. Values of S_r developed by previous investigators were collected and tabulated, and the values then selected as best estimates for each case history are tabulated and presented as well. The most useful comment in the text of the paper regarding the basis for selection of representative S_r values for each case is to note that "When possible, the value of S_u was selected as one which incorporated energy effects (Poulos, 1988; Davis et al. 1988) as this was felt to be closer to the "true" value of S_u". On balance, the values of S_u (or S_r) selected appear generally reasonable.

Figures 2.17 and 2.18 present the resulting data points for the 19 case histories re-evaluated, and also a number of relationships developed by previous investigators for comparison. It should be noted that most previous investigators did not take a near lower bound approach to estimation of $(N_1)_{60\text{-}CS}$.

Figure 2.17 shows data points plotted as post-liquefaction strength (S_u) vs. "reasonable minimum" $(N_1)_{60\text{-}CS}$ as developed by Wride et al. (1999). The range proposed by Seed and Harder (1990) is shown, and so is the additional (more steeply rising) range proposed by Konrad and Watts (1995) for Kogyuk and Erksak sands. Also shown are (1) the lower bound relationship proposed by Ishihara (1993), (2) the relationship proposed by Yoshimine et al. (1999) for triggering of flow slides, and (3) an additional material-specific relationship developed by Wride and Robertson (1995) for Ottawa sand based on laboratory testing and CPT data.

Figure 2.18 shows data points plotted as post-liquefaction strength ratio (S_u/P) vs. minimum $(N_1)_{60\text{-}CS}$ as developed by Wride et al. The range proposed by Stark and Mesri (1992)

is shown, and so is the additional (more steeply rising) range proposed by Konrad and Watts (1995) for Kogyuk and Erksak sands. Also shown are (1) the lower bound relationship proposed by Ishihara (1993), (2) the relationship proposed by Yoshimine et al. (1999) for triggering of flow slides, and (3) an additional material-specific relationship developed by Wride and Robertson (1995) for Ottawa sand based on laboratory testing and CPT data.

In both of these figures, data points for cases where there is especially high uncertainty (or variance) with regard to SPT N-values are highlighted by open symbols around the solid symbols.

In examining these figures, it appears that the available data, as interpreted by Wride et al. (1999), could be construed as supporting, or at least partially supporting, any of the previous relationships shown, especially given that some of the relationships did not employ near lower bound assessments of penetration resistance. This served to illustrate the importance of being clear on the basis for development of empirical relationships for estimation of in situ S_r, and it also suggests the potential validity of near lower bound strengths (and associated penetration resistances) asserting some measure of control over field failure outcomes.

2.3.7 Olson (2001) and Olson and Stark (2002)

Olson and Stark performed studies to develop their own evaluations of post-liquefaction strengths for an expanded suite of 33 field failure case histories. Olson (2001) employed two types of approaches to the back-analyses of the 33 case histories studied. Olson employed an adapted version of the methodology of Davis et al. (1988) to account for the "kinetics" of flow failures (i.e. momentum effects), and applied this to 10 of the field failure case histories for which it was judged that sufficient information and data were available, in order to develop new estimates of S_r that explicitly included consideration of momentum effects. For the remaining 23 cases that he studied, it was judged that the available information and data were insufficient for a full "kinetics" analysis, and these cases were back-analyzed either by directly calculating the theoretical value of $S_{r,resid/geom}$ that would provide a static Factor of Safety equal to 1.0 for the residual geometry, or with a "simplified" back-analysis that was essentially a simplified infinite slope analysis that also targeted an approximate value of $S_{r,resid/geom}$. As discussed previously in Section 2.3.1, and as discussed at more length on Sections 4.3.2 and 4.3.3 and Chapters 5 and 6, these simplified analyses would have been systematically over-conservative due to their failure to include momentum effects. Ordinarily, some measure of conservatism might be appropriate for simplified analyses. Unfortunately, as described in Section 2.3.7.2, and in Chapters 4 through 6, the degree of over-conservatism was significantly larger than Olson and Stark had anticipated, and the use of $S_{r,resid/geom}$ instead of S_r for these 23 of the 33 overall case histories back-analyzed significantly damaged the resulting predictive relationship for post-liquefaction strength (S_r).

2.3.7.1 Kinetics Analyses

The analytical approach employed to incorporate "kinetic" effects (momentum and inertia) in analyses of 10 of the best-documented case histories was adapted, with some modifications, from the approach proposed by Davis et al. (1988) as illustrated schematically in Figure 2.19.

Davis et al, proposed that a displacing failure mass would initially accelerate downslope, accumulating increasing velocity and momentum, and then it would decelerate, with reducing velocity and momentum until it finally came to rest. With simplifying assumptions, it is then possible to track the progressive development and dissipation of acceleration, velocity, displacement, and momentum of the center of gravity.

Davis et al. (1988) also postulated that at some point between start and finish there would be a transition from acceleration to deceleration, and that there would be no net shear force transfer of inertial force to the base of the moving slide mass (which would be at peak displacement velocity) at that moment. That, in turn, means that at this intermediate displacement condition (at the moment of transition from acceleration to deceleration) when there is zero inertial force transfer, that a static stability analysis can be performed to calculate S_r directly, and the resulting value would correctly incorporate inertial (momentum) effects. There is, however, significant difficulty and subjective judgment involved in ascertaining the likely geometry of the failing slope at this moment of transition. As a result, Seed and Harder (1990) preferred to calculate the "apparent" $S_{r,yield}$ for the pre-failure geometry, and the "apparent" $S_{r,resid/geom}$ for the final, residual (post-failure) geometry, and then adopt a value of S_r between these two as the best estimate of S_r with consideration of inertial forces (momentum) being a function of apparent runout of the failure mass. Wang (2003) and Kramer (2008) chose, instead, to attempt to infer the geometry (displaced cross-section) of this intermediate transitional condition with zero inertial force (ZIF), giving rise to their "ZIF method" for back-analyses incorporating inertial effects as will be discussed in Section 2.3.8. In these current studies, a new method is presented that incrementally tracks the evolving displaced geometry and uses this as the basis for a progressive analysis that incorporates inertial effects (momentum) in back-calculation of S_r from failure case histories.

Olson elected to perform a full progressive inertial analysis tracking the evolution of acceleration, velocity and displacement of the center of gravity of the failure mass. Olson's analysis procedure is illustrated schematically (for the Wachusett Dam case history) in Figure 2.20.

The first step, as described by Olson (2001), was to determine the initial and final locations of the center of gravity for the full failure mass, as shown at the top of Figure 2.20.

A third order polynomial function was then fitted to approximate the progressive locus of points through which the center of gravity would then be assumed to travel from inception of failure to post-failure residual geometry. It was stated that it was important that this polynomial function produced a "curve" parallel to the average curvature of the overall sliding surface, or at least with a localized slope parallel to the average slope of the overall sliding surface associated with each successive position of the overall (field) sliding surface, as best this could be estimated.

The preceding conforms to the explanation of this approach as presented by Olson (2001), but it does not appear to quite correctly capture the physics of this approach, and it also appears likely that Olson had actually performed better analyses than the preceding text would suggest.

Driving forces in the downslope direction (tangent to the polynomial curve) at any laterally displaced location (x) of the center of gravity were taken as being equal to the weight of the overall failure mass (W) multiplied by $\sin\Theta$, where Θ is the slope at any point on the polynomial curve.

As a result, it was actually important that this slope of the polynomial curve results in a good approximation of the total downslope driving shear stresses in the field at any laterally displaced location of the center of gravity. It was not important that the polynomial curve approximated the actual loci of points through which the center of mass of the overall failure surface passed; instead it was important that the local slope of the polynomial function defining the "sliding surface" on which the centroid "slid" had a value of Θ such that, at each lateral location (x) the displaced center of mass passes by provides a calculated total driving downslope shear force ($W \bullet \sin \Theta$) approximately equal to the actual total downslope driving shear forces of the overall displaced failure mass at that stage of lateral centroid displacement.

Based on the good matches achieved between the values of S_r calculated by Olson (2001) for nine of the 10 cases that he analyzed by this "kinetics" approach, and values calculated in these current studies using a more rigorous "incremental momentum analysis" approach for these same cases, it appears likely that he realized this and accommodated it with careful selections of at least the initial (zero displacement) and final (ultimate displacement) slopes of the polynomial sliding surface. But this is not documented either in his thesis (Olson, 2001) or in the subsequent paper (Olson and Stark, 2002) and so this must be considered to be a "surmise" here.

The current investigation team have performed a number of these analyses for selected cases to assess this approach. It is a relatively simple matter to determine the initial downslope driving shear forces along the base of the full failure mass, and thus to determine the initial (steepest) "equivalent" slope $\Theta_{initial}$ at null displacement. It is similarly easy to determine the final "equivalent" slope Θ_{final} at full runout that would produce final downslope static driving shear forces equal to those calculated by simple two-dimensional limit equilibrium analyses for the final (residual) displaced geometry.

It is then considerably more difficult to determine "correct" values of Θ at intermediate levels of lateral displacement at all stages from the initial slope (and null displacement) to the final slope (and final, residual displacement). To do that accurately would require the careful inference and drawing of multiple stages of partially-displaced geometries between the initial (pre-failure) and the final (residual) geometry. Olson did not do that. On the other hand, this investigation team has determined that reasonably good calculated values of S_r can be developed so long as (1) the initial slope $\Theta_{initial}$ suitably matches initial driving forces, (2) the final slope Θ_{final} suitably matches residual driving forces, and (3) the instantaneous (local) slope angle Θ transitions smoothly between initial to final slope; ideally with a smooth tapering off of slope severity as movements develop.

A single strength S_r was reportedly assigned by Olson (2001) along the failure surface in the full scale cross-section, and the shear strength along the failure plane multiplied by the length of the failure plane was then calculated and used as the resisting (upslope) force acting on the center of gravity in a direction tangent to the sliding surface of the polynomial curve. Comparing upslope vs. downslope forces at each point in time, any force imbalance was then applied to create acceleration [a] based on Newton's second law [$F = M \bullet a$]. The system was then solved incrementally using a time-step algorithm to calculate progressive changes in accruing and dissipating acceleration, velocity and displacement of the center of gravity.

The value of S_r employed was iteratively adjusted until the calculated final displacement of the center of gravity of the failure mass equaled the observed displacement of this center of gravity in the field failure. At that point, the post-liquefaction strength along the actual lengths of the failure surface controlled by liquefiable materials was reportedly adjusted to account for strengths of non-liquefied materials based on Equation 2-2 as

$$S_u(LIQ)=\frac{S_u-\left(\frac{L_d}{100}\cdot S_d\right)}{\left(1-\frac{L_d}{100}\right)} \qquad \text{[Eq. 2-2]}$$

in which the overall average shear strength along the failure plane is sub-partitioned into (a) S_r for the lengths of the failure plane controlled by post-liquefaction strengths, and (b) drained strength S_d for the portions of the failure plane controlled by non-liquefied materials.

This conforms to the description and explanation presented in Olson (2001), but it appears that Olson actually did a better and more clever job than this with these analyses. Failure plane lengths and geometries, and the sub-sections of the failure plane controlled by liquefied and non-liquefied materials, change progressively as failure displacements accrue. Olson also modeled reduced shear strength at the base of portions of the toe of the failure mass that entered into water to account for potential hydroplaning effects. And Olson also accounted for progressive buoyancy increase as failure masses entered into bodies of water. Each of these effects would likely have been progressively adjusted as failure movements progressed, and that would have involved a far more detailed, tedious, and time consuming analytical effort than is suggested by Equation 2-2. Alternatively, Olson may have exercised judgment in approximately accounting for these progressively changing factors in his more simplified analyses.

Examining a number of the calculated plots of shear strength mobilized along the failure plane (e.g. the one near the top of Figure 2.16) in Olson's dissertation, it is clear that overall shear strength along the failure plane progressively changes as the failure displacements proceed. This suggests that an even more correct analysis was performed which included progressively implementing some level of changes in conditions and geometry as displacements progressed.

Olson assigned reduced shear strengths (50% reduction) for soils that travelled beyond the initial toe of a slope and entered into a reservoir to account for potential hydroplaning effects and what he termed reservoir mixing, and then allowed this to vary from 0% to 100% for subsequent parameter sensitivity studies. He did not explicitly discuss potential sliding along the top of weak reservoir sediments, or weak offshore slope sediments, beneath the advancing toe of the failure, but his approximation of 50% strength reduction is reasonable for both situations. Wang (2003), and these current studies, each take different approaches on these issues (hydroplaning and potentially weak reservoir sediments), but it should be noted that Olson's modeling approach was also reasonable here.

Figure 2.20 shows an example calculation for the Wachusett Dam failure case history. The top of the figure shows the shape of the selected polynomial curve along which the center of gravity of the overall failure mass is assumed to slide. The next four figures below show the evolution (vs. time) of: (1) total shear resistance along the field failure surface, (2) acceleration (and then deceleration) of the center of gravity, (3) velocity of the center of gravity (which initially increases

and then eventually drops back to zero), and (4) accumulated displacements of the center of gravity.

Figure 2.21 shows another illustration of this analytical procedure, this time for the upstream slope failure of the Lower San Fernando Dam. The top figure shows the pre-failure and post failure geometries, and also the pre-failure and post-failure positions of the center of gravity of the overall failure mass, and the shape of the curved (polynomial) curve "surface" along which the sliding of the center of gravity was calculated. The four figures below show (1) total shear strength vs. time along the failure surface, (2) acceleration vs. time of the center of gravity of the overall failure mass, (3) velocity vs. time of the center of gravity, and (4) displacement vs. time of the center of gravity.

There are a number of challenges and drawbacks to this analytical approach by Olson's kinetics method.

One of these is potential sensitivity of the calculations to the selected shape of the polynomial curve along which the center of gravity slides, and the concurrent difficulty of suitably modelling a slope that approximates the overall "driving" shear stresses along the actual (full scale) field failure plane at each successive stage of calculated displacement of the center of gravity. As discussed previously, simply aiming at being largely "parallel" to the overall failure surface is not sufficient here; it is the sum total of driving shear stresses in the field (associated with field conditions and geometry) that should match well with the driving shear stresses resulting from the modeling of the slope of the curved path along which the center of gravity slides, and at each successive step of development of displacements.

Another challenge is the fact that non-liquefied soils routinely had to be modeled with fully drained frictional shear strengths, so that S_d was a function of effective normal stresses on those portions of the field failure plane. This is difficult to implement in the framework as described by Olson (2001) because effective normal stresses (and geometry) would have been changing as movements occurred. Olson does not explain how this was treated.

A similar challenge would have been the modeling of shear strengths along portions of the field failure surface where two different soil materials progressively come into contact as the failure movements progress. Ideally, the weaker of the two materials should control shear strength over portions of the failure surface where two different materials progressively come into contact. Olson does not explain how this was treated.

Another (similar) challenge would have been the modeling of undrained shear strength in cohesive soils, where the large displacements involved in the case histories back-analyzed would have been expected to result in a transition from peak to residual undrained shear strengths as failure movements progressed. Olson does not explain how this was treated.

Finally, it appears that several of the failure case histories may have been incrementally progressive (retrogressive) failures, with initial failures (or failure "slices") initially occurring close to the front of the eventual overall failure mass, followed by retrogressive development of additional slices farther from the front face, with each successive slice sequentially beginning to

initiate its own displacements as it becomes partially unbraced due to movements of the preceding slice(s), until the failure surface eventually reaches the back heel of the final, overall failure. This would be tremendously difficult to model with the simplified kinetics approach that tracks only a monolithic single failure mass or "block".

In the face of all of these challenges, it should also be noted that the overall value of S_r calculated is well "bounded" for these analyses. As observed by Davis et al. (1988), and Seed and Harder (1990), assessment of the initial yield stress ($S_{r,yield}$) required within liquefiable materials to provide a calculated Factor of Safety equal to 1.0 will necessarily overestimate the actual value of S_r, because otherwise large displacements would not have occurred. Similarly, assessment of the "apparent" value of $S_{r,resid/geom}$ required within liquefied soils to provide a calculated Factor of Safety equal to 1.0 for the eventual post-failure residual geometry will significantly underestimate the actual value of S_r as it fails to account for momentum effects as the moving slide mass must be brought to rest. So a finite range of possible values of S_r would be between $S_{r,yield}$ and $S_{r,resid/geom}$. If the initial slope of the polynomial curve along which the center of gravity of the failure mass will slide is "set" so as to provide the correct initial (pre-failure) overall driving shear stresses, and the final slope of the polynomial curve is "set" so as to provide the correct final (post-failure, residual) overall driving shear stresses, then values of S_r calculated by this type of kinetics approach would naturally fall within this finite range. With better modeling, and judgment, significantly better answers could be expected.

And Olson appears to have executed excellent kinetics analyses, and with good judgment. His calculated values of S_r for nine of the ten case histories to which this kinetics analysis method was applied produced values of S_r in generally good agreement with the values subsequently back-calculated employing other methods by (1) Wang and Kramer (2003, 2008) and (2) these current studies. For the other case (Shibecha-Cho Embankment) Olson's back-calculated value of S_r was significantly lower than those subsequently calculated by Wang & Kramer, and by these current studies. Based on the cross-sections and explanations of Olson's analysis for this case, the Shibecha-Cho failure was modeled as a progressively incremental (retrogressive) failure, proceeding in a "slice by slice" fashion from the initial toe failure until the final slice reached the eventual overall back-heel of the failure. But Olson's kinetics analysis method could not handle a progressive (retrogressive) incremental failure. Recognizing this, Olson made a good effort at simplification and analyzed only the movements of the first failure slice (the initial slice nearest the front face of the eventual overall failure); for which acceleration, velocity and displacement were tracked by the kinetics analysis performed. Because only the first (initial) slice was modeled and analyzed, the overall scale of the failure (and failure mass) were underestimated; so that overall driving forces, and momentum, and post-liquefaction strength (S_r), were underestimated. This points up the difficulty of applying the simplified "kinetics" analysis approach to analyses of these types of incrementally progressive failures. This Shibecha-Cho case history, and the challenges of back-analyses of progressively incremental (retrogressive) liquefaction-induced failures in general, will be discussed further in Chapters 4 through 6.

Overall, Olson's back-calculated values of S_r for nine of the ten cases that he analyzed using the kinetics method to account for momentum effects appear to have produced generally good answers. The tenth case history (Shibecha-Cho Embankment) produced a conservative (low) estimate of S_r.

2.3.7.2 Back-Analyses of the 23 Less Well Documented Case Histories

There were then 23 additional (less well documented) case histories for which Olson judged that there were insufficient information and data available as to justify the full incrementally progressive kinetics analysis approach. For 11 of these cases, "simplified" analyses, or estimates, were employed to assess values of S_r. These were approximate approaches, and so they were (appropriately) conservatively implemented and tended to produce conservative estimates of S_r. For the most part, these simplified analyses amounted to essentially back-calculating the values of $S_{r,resid/geom}$ that would be required to produce a "theoretical" static factor of Safety equal to 1.0 for the residual geometry with zero inertial forces (no momentum effects) using an infinite slope analysis to approximate the actual field geometry. For the other 12 cases, the apparent post liquefaction strength ($S_{r,resid/geom}$) required to provide a calculated static Factor of Safety equal to 1.0 for residual post-failure geometry and conditions was directly calculated, using full post-failure geometry (rather than an approximated infinite slope analysis), and this value of $S_{r,resid/geom}$ was then taken as the value of S_r. Accordingly, for all 23 of the less well documented case histories, Olson calculated and employed $S_{r,resid/geom}$ instead of the actual post-liquefaction strength S_r.

As discussed previously, and as demonstrated later in Chapter 4, this use of $S_{r,resid/geom}$ was very conservative and would have significantly underestimated the actual values of S_r because it neglected to account for the effects of momentum as the moving failure masses had to be decelerated back to zero velocity at the end of slide movements. This underestimation would likely have produced values of S_r that would have been low by factors of between approximately 1.2 to 3.4 (see Chapter 4, Section 4.4.1, and Fig. 4.9).

As a result of these over-conservative approaches taken to the back-analyses of these 23 less-well defined and less-well characterized case histories, there was then a disparity between the S_r values calculated for the 23 lesser cases and the remaining 10 cases to which the higher order kinetics analysis approach had been applied. The 23 lesser cases had overly conservative (low) values of S_r, and 9 of the the 10 kinetics cases had what tended to be more accurate (higher) values. One case (Shibecha-Cho Embankment) had a low S_r value as discussed in the previous Section 2.3.7.1 because Olson's kinetics method was not able to correctly handle this strongly incrementally progressive (retrogressive) failure. The two sets of cases (the 10 high quality cases, and the 23 lesser quality cases) were essentially analyzed on very different bases, and the disparity in bias (or level of conservatism) of estimated S_r values served to obscure trends when the data were subsequently plotted jointly as a function of representative penetration resistance.

2.3.7.3 Predictive Relationship

Olson then calculated average values of initial vertical effective stress along portions of the eventual plane occupied by liquefiable materials, and the S_r values determined for the full 33 case histories were divided by the effective vertical stresses to produce back-calculated values of post-liquefaction strength ratio (S_r/P) for each case.

Representative values of $(N_1)_{60}$ were also developed for each case. It was the position of Olson (2001), and of Olson and Stark (2002), that the fines adjustment proposed by Seed (1987)

was not well founded, and they elected to apply no fines adjustment at all, and so the values employed were $(N_1)_{60}$ values rather than $(N_1)_{60,CS}$ values. That was unfortunate, because a significant number of the 33 case histories that they analyzed had liquefiable soils that were comprised mainly of silty sands and sandy silts, and those materials likely warranted significant fines adjustments. So the lack of a fines adjustment may have biased the representations of some of the penetration resistances for this particular data set. That may have also contributed to the lack of a well-defined relationship between S_r and $N_{1,60}$ that was eventually developed.

Figure 2.22 shows the overall relationship recommended by Olson and Stark (2002) for estimation of post-liquefaction strength ratio as a function of $(N_1)_{60}$, along with the data pints from the 33 back-analyzed case histories. The two solid lines show the recommended range, and the heavy dashed line between these is the center of this range.

The recommended range and best estimate relationship proposed represents some degree of engineering judgment, because it does not well match the slope of the overall trend of the data presented. A least squares regression was performed as part of these current studies, and the results are presented with a red line in Figure 2.23. As shown in this figure, the actual slope of the regressed relationship is somewhat flatter than the recommended relationship, and the calculated R-squared value ($R^2 = 0.23$) indicates that the data is poorly behaved (randomly scattered) and that the regression is not well able to provide a good predictive "fit".

The recommended relationship is likely strongly conservatively biased overall, due in large part to the conservative underestimation of S_r for the 23 (out of 33) back-analyzed case histories that were evaluated on an overly conservative basis (as $S_{r,resid/geom}$ instead of S_r), as discussed in the previous Section 2.3.7.2, and the conservatively low value of S_r calculated for one of the 10 high quality cases (Shibecha-Cho Embankment), as discussed in the previous Section 2.3.7.1.

The lack of a clearly discernable strong trend between S_r and $(N_1)_{60}$ in Figures 2.22 and 2.23 appears to have three main causes. The first of these is the disparity in the average level of conservatism between the S_r values calculated for 10 case histories based on the kinetics back-analysis approach, and the far more conservatively biased S_r values calculated for the remaining 23 cases, as discussed previously. A second contributing cause may have been the lack of an applied fines adjustment for the SPT penetration resistances. A third cause was the assumption that ratios of S_r/P would not vary as a function of effective overburden stress (see Chapter 5).

It is interesting to note that Olson had also directly calculated the initial post-liquefaction yield stress ($S_{r,yield}$) for each of his 33 case histories, although he did not employ these back-analysis results in the subsequent development of a predictive relationship for post-liquefaction strength (Sr). Instead, these $S_{r,yield}$ calculations were targeted at development of an un-related liquefaction triggering analysis method.

As a result, Olson had back-calculated both the initial yield strength ($S_{r,yield}$) and also the "apparent" post-liquefaction residual strength based on residual post-failure geometry ($S_{r,resid/geom}$) for all but one of the 33 cases. As demonstrated in Chapters 4 and 5, averaging these two values (simply adding then together and then dividing by two) might have been expected to produce significantly better estimates of the actual S_r values for the 23 case histories that Olson did not

back-analyze by the higher-order kinetics method. Even better estimates of S_r for those 23 cases could have been obtained by adding together $S_{r,yield}$ and $S_{r,resid/geom}$, then dividing by two, and then multiplying that result by a number slightly less than 1 (e.g. multiplying by ~ 0.8 or so), as demonstrated later in Chapters 4 and 5.

Finally, it should be noted that Olson's work was a significant milestone achievement in its day. Those were turbulent times, rife with discussion and debate. Olson made two important contributions that were likely not fully appreciated at the time. The first of these was the level of detail and transparency with which he documented his analyses (the assumptions, procedures, cross-sections, properties, failure surfaces analyzed, etc.) This had no similar precedent, and no subsequent study has (yet) been as well documented either. One of the objectives of these current studies is to set a similarly high standard for documentation and transparency as well.

A second important contribution was that he calculated $S_{r,yield}$ and also $S_{r,resid/geom}$ for all but one of his 33 case histories. Because the analyses were reasonably well documented, the details of these calculations are generally well understood. Now, 14 years later, these values turn out to be an important piece of the overall puzzle, and good use is now made of them in these current studies as they are a very useful basis for comparison with values back-calculated for the same case histories when they are back-analyzed in these current studies.

2.3.8 Wang (2003), Kramer (2008), and Wang and Kramer (2015)

Wang (2003) working on his doctoral research with Kramer examined the case histories that had been used by previous investigators, and developed his own estimates of the key indices (S_r, $N_{1,60,CS}$ and $\sigma'_{v,i}$) that would eventually be employed to develop new probabilistic relationships for SPT-based assessment of in situ post-liquefaction strengths (Kramer, 2008). The regressed relationships developed by Kramer (2008) would subsequently be re-published in an archival journal (Kramer and Wang, 2015).

Wang's initial work had developed values of fines-corrected $N_{1,60,CS}$, but the relationships subsequently developed by Kramer (2008) and published by Kramer and Wang (2015), were based on non-fines-corrected values of $N_{1,60}$. There is some confusion here, because the report by Kramer (2008) inadvertently presents a table of "input" values to the regressions performed, and this table (Table G.4, which is re-produced here as Table 2.4) lists $N_{1,60,CS}$ values. That was essentially a typographical error (Kramer, 2015). The wrong table was inserted in the report; the regressions, and the predictive relationships that resulted, were actually based on non-fines-corrected $N_{1,60}$ values. Kramer and Wang (2015) present a new (and correct) table of input values for their regressions showing the penetration resistances correctly presented in terms of $N_{1,60}$. These corrected values are shown in Table 4.5.

Because these current studies employ $N_{1,60,CS}$ as the penetration resistance measure, values of $N_{1,60,CS}$ developed for each individual case history will be cross-compared with Wang's values of $N_{1,60,CS}$ (rather than the subsequent $N_{1,60}$ values) for cases analyzed by both investigation teams for purposes of cross-checking the results of back-analyses of individual case histories. It will later be necessary, however, to make a modest approximate modification of the predictive relationship developed by Kramer (2008) in order to compare that relationship with the

relationship developed in these current studies; both will be compared on an approximated $N_{1,60,CS}$ basis (see Section 5.4.1).

2.3.8.1 Wang (2003)

Both the 2008 and the 2015 relationships are based on the initial case history evaluations developed by Wang (2003). As a first step, Wang examined and vetted case histories of small to moderate displacement (e.g. most of the lateral spreading case histories) and compared observed displacements against the values that would be predicted by the empirical relationship for lateral spreads developed by Youd et al. (2002). Cases where the observed displacements were not significantly greater than predicted by the relationship of Youd et al. were deleted from further study, because it was assumed that cyclic inertial forces were a significant contributor to observed displacements, and current analytical methods do not yet permit very accurate assessment of S_r based on back-analyses of such cases.

The remaining 31 cases were then examined more closely, and 9 of them were judged to have sufficient data and information as to warrant independent re-analyses. These 9 cases were designated as the Primary case histories, and each was back-analyzed to develop estimates of the three indices (S_r, $N_{1,60,CS}$ and $\sigma'_{v,i}$), and also assessments of uncertainty or variance associated with these estimates. The remaining 22 cases were judged to not have sufficient data and information as to warrant full re-analyses. These were designated as Secondary cases, and the 22 Secondary cases were not back-analyzed; instead values of S_r back-calculated by previous investigators were collected, and then generally averaged together, to develop values of S_r and $\sigma'_{v,i}$ for these remaining 22 case histories. Interestingly, independent values of representative $N_{1,60,CS}$ values appear to have been developed for each of these 22 secondary cases, though documentation of details is poor on this issue.

The details of the implementation of each of these two approaches (for Primary and for Secondary cases) are important, and these will be discussed in Sections 2.3.8.1 (a) and (b) that follow.

The assessments performed for the 9 Primary case histories appear to have been reasonable, and to have produced values in good general agreement with the values produced for these same case histories in these current studies. There were a number of apparent errors and/or shortcomings in the assessments of key parameters for a number of the 22 Secondary case histories, however, and these appear to be the issues principally responsible for the apparent shortcomings in the predictive (regressed) relationship of Kramer (2008) and Kramer and Wang (2015).

2.3.8.1(a) Zero Inertial Factor Back-Analyses of the Nine Primary Case Histories

The 9 highest quality case histories were considered to be "Primary" cases by Wang (2003), and these were back-analyzed using a new methodology that Wang developed that he referred to as the zero inertial factor (or ZIF) method. These were 9 of the same 10 highest quality case histories which Olson (2001) had back-analyzed using his "kinetics" analysis method.

This ZIF method was based on the observation by Davis et al. (1988), as described previously and illustrated in Figure 2.19, that a slide mass moving downslope initially accelerates, and then decelerates and comes to rest. Davis et al. further postulated that at some point between start and finish there would be a transition from acceleration to deceleration, and that there would be no net shear transfer of inertial force to the base of the moving slide mass (which would be at peak displacement velocity) at that moment. That, in turn, means that at this intermediate displacement condition (at the moment of transition from acceleration to deceleration) when there is zero inertial force transfer, a static stability analysis can be performed to calculate S_r directly, and the resulting value would correctly incorporate inertial effects.

Wang elected to attempt to estimate or infer the displaced position and geometry (displaced cross-section) corresponding to this transitional moment of zero inertial force. The fraction of eventual overall (final) displacement required to reach this transitional displaced cross-section geometry was termed the zero inertial factor (or ZIF). Once this fractional ZIF displacement had been estimated, the pre-failure geometry was then judgmentally transitioned part-way towards the final displaced (post-failure) geometry in proportion to this ZIF. Static limit equilibrium stability analyses were then performed using this ZIF cross-section to back-solve for the post-liquefaction strength needed to provide a static Factor of Safety equal to 1.0 at this ZIF displacement geometry.

The estimation or inference of the likely displaced (and deformed) cross-section geometry at this ZIF moment for any given geometry is very challenging. One cannot simply assume a displaced condition exactly mid-way between the initial geometry and location and the final residual geometry and location, in part because the ZIF transition from overall acceleration to overall deceleration appears to usually occur before half of the overall displacements have accrued; due to progressive diminishment of driving static shear stresses as the failure progresses and as the slope "flattens". This is clearly illustrated in the "kinetics" analyses performed by Olson (2001), and also in the incremental inertial analyses performed for these current studies as described in Chapters 3 and 4, and as presented in Appendix A.

The difficulties involved in estimating this displaced geometry at the transitional moment of zero inertial force transfer were recognized by Wang (and Kramer) who explained that the approach taken was to begin by examining the pre-failure and post-failure geometries (cross-sections) for selected, well-characterized case histories. Then the kinetics displacement analyses performed by Olson (2001) for these nine cases were next examined to determine what fraction of overall (final) displacement, or ZIF, appeared to correspond to the point of transition from acceleration to deceleration of the overall failure mass. A number of "points" on the pre-failure cross-section were then selected, and these were partially displaced towards the final (post-failure cross-section) geometry in approximately the estimated proportion required. This was used to create an approximate cross-section, and this was then iteratively refined to develop a cross-section that was reasonable based on considerations of soil mechanics, the materials and geometries involved, the inferred failure mechanism and mechanics, and the observed pre-failure and post-failure cross-sections. This was an iterative process, requiring both art and judgment.

Wang (2003) provided only a single illustration of this process; for the Wachusett Dam failure case history. Figure 2.24(a) shows points selected on the pre-failure cross-section (solid line) and connected locations of the same points on the post-failure cross-section (dashed cross-section). For this case, Olson estimated that the ZIF was 43.3%, so 43.3% of the displacements

from initial to final locations of each of the points selected was targeted, and the resulting initial estimates of the locations of these points on the zero inertial geometry in Figure 2.24(a) were then projected as the initial best estimates of the locations of those points for the ZIF cross-section. This was then artfully modified, allowing for curved paths between initial and ZIF locations of selected points, in a manner judged to be consistent with soil mechanics and the inferred failure mechanism. The resulting eventual ZIF displaced cross-section for the Wachusett Dam that was analyzed by means of static limit equilibrium methods is then shown in Figure 2.24(b).

As Kramer (2008) notes: "The procedure was laborious and is recognized as being approximate, a fact that was accounted for in the Monte Carlo analyses described subsequently."

There are a number of challenges and potential drawbacks to this approach. One is the question as to whether the ZIF calculated by Olson (2001) was fully accurate, so that the correct fractional displacement was modeled for the ZIF cross-section in Wang's subsequent studies. Wang's "ZIF" was dependent upon both the accuracy of Olson's calculations for each case history, and the judgments made with regard to modeling of progressively changing shear strengths as failure masses displaced. Another question is the reliability with which the actual ZIF cross-section details (geometry and stratigraphy, etc.) can be inferred by this approach. Another is the question as to whether the projected ZIF cross-section developed for any specific case history could then be suitably further advanced to eventually produce the post-failure cross-section actually observed. [In the incremental inertial analyses performed for these current studies, incremental displaced/deformed cross-sections are developed progressively from initial to final observed field cross-section geometries; much like an "animation" or progressive simulation of the progressing failure. This turned out to be very useful, providing insights as to progression paths of successive incremental geometries that could successfully finish with the actual observed post-failure cross-section. In some case this helped to shed light on likely failure mechanics details. See Chapter 4 and Appendix A.]

Despite these challenges, it is the opinion of the current investigation team that for well-characterized failure case histories, with well-defined pre-failure and post-failure cross-section geometries, this ZIF approach can (if wielded with suitable engineering judgment) be expected to provide useful back-calculated values of S_r with levels of accuracy and reliability at least compatible with those developed by the kinetics method employed by Olson (2001). Cross-comparisons between S_r values back-calculated (1) by this ZIF method, (2) by the kinetics method of Olson (2001), and (3) by the incremental inertial analysis method employed in these current studies (see Chapters 4 and 5) bear this out.

Wang (2003) developed a simplified approach to estimate the amount of hydroplaning that would occur as the toes of failure masses entered into bodies of water, based on a review of available research. The likelihood and lateral extent of hydroplaning at the toe was taken as a function of displacement velocity of the displacing mass, and the extent over which hydroplaning would occur was limited to a distance beneath the toe of the slide mass extending inboard not more than 10 times the thickness of the toe mass entering the reservoir. This was a rational approach, but the procedure should be considered somewhat speculative, however, as it was constructed based on research that was far from definitive. Wang recognized this, and he took a probabilistic approach to implementation of modeling of hydroplaning effects.

Wang systematically varied a number of parameters and variables for each of the 9 case histories back-analyzed by this ZIF approach. Cross-section details, failure surface locations, phreatic surface locations, unit weights, and soil material strength parameters for soils that did not liquefy were then all systematically varied within estimated reasonable ranges, and 50,000 Monte Carlo simulations representing randomized combination within these ranges were analyzed for each individual case. This was done to provide an assessment of variability in S_r values back-calculated, and also to provide a basis for more formal assessment of both means and variability of means expressed in terms of standard deviation of the means for the three key indices (S_r, $N_{1,60,CS}$ and $\sigma'_{v,i}$). The established ranges of variations of parameters and geometry actually pre-established the variances that would be produced by the Monte Carlo analyses, but this was not a bad overall procedure for development of estimates of standard deviations of mean values of S_r for each case.

Unfortunately, the actual ZIF cross-sections used and other key analysis details (including failure surfaces considered, phreatic surfaces, and soil properties, etc.) were not presented for 8 of the 9 cases histories back-analyzed, so it is not possible to check these analyses, nor to know exactly what was done for each individual case history. The example illustrative ZIF cross-section for the Wachusett Dam case history shown in Figure 2.24 was the only ZIF cross-section presented, and other key details for even this case are not presented.

This lack of documentation and transparency is unfortunate, and it appears to have slowed or partially prevented the overall work (including development of recommended correlations for assessment of in situ S_r) from garnering the attention that it appears to have deserved.

It should be noted that these ZIF analyses were performed before the incremental momentum analyses that were developed and performed for these current studies, and that Wang and Kramer thus did not know what the answers developed by these current studies would be. There is generally good to very good agreement between the results from these nine ZIF back-analyses, and the corresponding results of the incremental inertial back-analyses from these current studies for these same nine cases (see Chapter 4). And so it must be concluded that the judgments required for implementation of the ZIF approach were generally well executed.

One of the nine common cases was the Shibecha-Cho Embankment, which as discussed previously in Section 2.3.7 was an incrementally progressive (retrogressive) failure that Olson's kinetics method could not correctly analyze. Olson settled for analyzing only the first (toe) slice, and so significantly underestimated overall momentum, overall scale, and S_r for this case history. Wang (2003) employed Olson's back-calculated displacement time history to select his "ZIF", and then applied it to the overall cross-section as a monolithically triggered failure. This was clearly an incompatible set of assumptions and analyses. Fortunately, the overall value of S_r back-calculated by Wang (2003) for this case history (S_r = 208.8 lbs/ft^2) agrees very well with the value of S_r back-calculated in these current studies (S_r = 224 lbs/ft^2) using the incremental inertial method.

In the end, Wang's (2003) values of S_r back-calculated by the ZIF method for these 9 cases agreed within a factor of +/- 1.31 or better (often much better) with the values back-calculated for these same 9 cases in these current studies using the more complex and more flexibly adaptable

incremental momentum analysis method. This provides good support for Wang's values, and it also provides good support for the incremental momentum analysis method that will be the primary tool of choice in these current studies.

Wang's values of mean $N_{1,60,CS}$ for these nine Primary case histories generally agree reasonably well, but not perfectly, with the values developed for these same case nine histories in these current studies. Differences appear to be due in large part to differences in the fines adjustments made. The text of Wang (2003) appears to indicate that a fines adjustment approximately compatible with the fines adjustments proposed for post-liquefaction strength by Seed (1987) and by Stark and Mesri (1992) were employed. These two fines adjustments are fairly closely similar, and they both add potentially very large blowcount increases at even very low $N_{1,60}$ values when fines contents are high. Differences between the resulting $N_{1,60,CS}$ values based on variations between these approaches would have been relatively small for most of the cases, and the values developed by Wang (2003) appear to be generally reasonable given these fines corrections. This will be discussed further in Chapters 4 and 5.

Wang's values of standard deviation in mean $N_{1,60,CS}$ were developed by a rigidly formulaic approach, and some of these appear (for some of the case histories) to be excessively large, and this will also be discussed further in Chapters 4 and 5. This does not appear to have had a very significant adverse impact on the predictive correlations and relationships eventually developed.

The approach taken by Wang (2003) to evaluation of $\sigma'_{v,i}$ for his nine "primary" case histories was a bit convoluted, but it appears to have resulted in generally good agreement with values of $\sigma'_{v,i}$ back-calculated by (1) Olson (2001) and (2) these current studies for at least seven of the nine ZIF-analyzed cases, and at least fair agreement for the other two cases (see Table 2.3).

2.3.8.1(b) The Less Well Documented (Secondary) Case Histories

The 22 remaining case histories employed by Wang (2003) and Kramer (2008) were judged to not have sufficient data and information as to warrant or support ZIF-type analyses, and Wang referred to these as the "secondary" cases. Wang was then in the same position as Olson (2001) of having to decide how to develop suitable estimates of his three key sets of indices (S_r, $N_{1,60,CS}$ and $\sigma'_{v,i}$) for these lesser cases.

The approach taken was not to perform independent back-analyses of these cases, but instead to select values of S_r and S_r/P developed by other (previous) investigators, and then use these to develop or infer overall estimates of S_r and $\sigma'_{v,i}$ for each of the secondary cases. A mixed approach was taken to development of $N_{1,60,CS}$ values, as some of these values were developed largely independently by Wang and some were largely developed based on values from previous investigations.

Discussions of Wang's assessments of each of these three indices follow.

(i) Representative Values of $N_{1,60,CS}$

Wang (2003) collected estimates of either $N_{1,60}$ or $N_{1,60,CS}$ from multiple previous investigators, and then selected his own best overall estimates for these 22 cases. Values of $N_{1,60,CS}$ appear to have been judgmentally modified to be compatible with the values from the 9 primary case histories of Section 2.3.8.1(a), but full details are not presented. With only one exception, the values of $N_{1,60,CS}$ selected by Wang (2003) for these 22 cases agree reasonably well with the values developed in these current studies for these same cases. That singular exception was the El Cobre Tailings Dam case history. Wang's value of best-estimated median $N_{1,60,CS}$ was $N_{1,60,CS}$ = 6.8 blows/ft., while the value from these current studies was $N_{1,60,CS}$ = 2 blows/ft. The difference here appears to be due in large part to a very large fines correction made by Wang for these silt-dominated tailings materials; while in these current studies the fines adjustment is applied as a function in part of the un-corrected $N_{1,60}$ value resulting in a smaller fines adjustment for this case. There are several other case histories in which Wang's selected value of mean $N_{1,60,CS}$ differs by as much as 3 to 4 blows/ft from the value used in these current studies; but this is a relatively small level of difference in a large suite of complex case histories requiring significant engineering judgment for development of estimates of equivalent $N_{1,60,CS}$. Overall, the values of $N_{1,60,CS}$ developed or selected by Wang (2003) for most of these case histories agree well with those developed in these current studies.

Wang (2003) assigned standard deviations in $N_{1,60,CS}$ based on the number, and variability, of SPT N-values available in the liquefiable material of interest. For 13 of the 22 Secondary case histories, there were no N-values available (and so "representative" N-values had to be estimated or inferred from other data or information). These cases were with no N-values available were all assigned a maximum coefficient of variation (COV) equal to 1.5. Lesser values of COV, and corresponding values of standard deviation, were assigned to the remaining case histories for which at least some N-values were available. Values of COV for these remaining 9 cases ranged from 0.15 to 0.75.

Some of the values of COV assigned appear to be unreasonably high; those values are significantly higher than were employed in these current studies for those same case histories. It does not appear, however, that this was a major issue, and the overall predictive correlation developed does not appear to have been much adversely affected by choices of COV, or standard deviation, in $N_{1,60,CS}$ for the 22 Secondary case histories.

(ii) Representative Values of S_r

The mean value of S_r for each of these 22 cases was taken as the average of values selected from among available values back-calculated by previous investigators. Only values considered to be applicable were employed here, and the basis for judgment as to applicability was that a preference was made for values that appear to incorporate momentum effects. This was, statistically, likely a better approach than the conservatively biased approach used by Olson (2001) to estimate S_r for his 23 "lesser" cases (see Section 2.3.6) in which he used $S_{r,resid/geom}$ instead of S_r. But it was not an ideal approach, and there appear to have been at least two outright errors, and a number of additional problems or issues.

Table 2.1 presents (1) the collected selected values from previous investigators for each of the 22 Secondary case histories, and (2) the final values selected by Wang (2003). These values are from Table 6-8 from Wang (2003).

There appear to be two significant straightforward errors in this table.

For the El Cobre Tailings Dam case history, Wang lists only a single value of S_r = 195 lbs/ft^2 from Olson (2001), and then selects this value of $\underline{S_r = 195 \text{ lbs/ft}^2}$ as his representative mean value for this case history. But Olson's actual reported value for this case was $\underline{S_r = 40 \text{ lbs/ft}^2}$.

For the Hokkaido Tailings Dam case history, Wang lists two values of S_r from two previous investigations as

$S_r = 408$ lbs/ft^2 (Ishihara, et al., 1990)

and

$S_r = 172$ lbs/ft^2 (Olson, 2001)

The average of these two values would be 290 lbs/ft^2. But Wang's selected representative value is S_r = 251 lbs/ft^2; making this one of only a few case histories for which Wang's selected value is not a straightforward average of the available S_r values listed. More importantly, the value of S_r = 408 lbs/ft^2 attributed to Ishihara et al. (1990) is in error. The actual value developed by Ishihara et al. (1990) for this case history is only $\underline{S_r = 137 \text{ lbs/ft}^2}$. With this correct value of 137 lbs/ft^2, there would be relatively good agreement between the two values and the average of the two values listed for this case would then be a representative overall value of $\underline{S_r = 154.5 \text{ lbs/ft}^2}$, rather than the value of $\underline{S_r = 251 \text{ lbs/ft}^2}$ that Wang (2003) and Kramer (2008) employ in their regressions for development of predictive correlations.

Finally, unbeknownst to Wang at the time, the value of S_r independently developed in these current studies for the Hokkaido Tailings Dam case history is S_r = 131 lbs/ft2 (see Appendix B.8). So the three values available now are: S_r = 137 lbs/ft^2 (Ishihara et al., 1990), S_r = 172 lbs/ft^2 (Olson, 2001) and S_r = 131 lbs/ft^2 (these current studies). The average of these values would then be $\underline{S_r = 146 \text{ lbs/ft}^2}$. Given the excellent agreement between these three independent assessments, this would appear to be a well-supported number.

In addition to these two apparently straightforward errors, there are additional values of representative S_r values that appear to be questionable; often due to failure to fully back-track into the histories of the development of the values listed in Table 2.1 and to understand their origins.

It is interesting to note that Wang's Table 6-8 (presented here as Table 2.1) lists values of S_r from Olson (2001) for all 22 of the cases. The values listed are not Olson's selected values (of $S_{r,resid/geom}$) upon which Olson and Stark (2002) based their eventual predictive relationship for S_r. Instead, Wang noticed that Olson had calculated both $S_{r,yield}$ and $S_{r,resid/geom}$ for each of these case histories (as discussed previously in Section 2.3.7.2), and so Wang (2003) instead adopted a value of S_r that he "attributed" to Olson (2001) that was the average of these two values as

$$S_r = (S_{r,yield} + S_{r,resid/geom}) \times 0.5 \qquad \text{[Eq. 2-3]}$$

As demonstrated later in Chapter 4, this was a generally good idea, but it would have produced slightly biased (high) estimates of S_r. They would have been much better estimates than the $S_{r,resid/geom}$ values that Olson and Stark (2002) used in their development of predictive relationships for S_r, but even better estimates would have been achieved using an equation

$$S_r = (S_{r,yield} + S_{r,resid/geom}) \times 0.5 \times \xi \qquad \text{[Eq. 2-3a]}$$

where ξ is a function of runout distance of the slide mass normalized by initial failure slope height. The parameter ξ has values that range between $\xi \approx 0.4$ to 0.99 for the case histories in these two sets of studies, with an average of approximately 0.8 for the current suite of case histories (see Chapter 4). On average, a simplistic first-order estimate of S_r based on Olson's values of $S_{r,yield}$ and $S_{r,resid/geom}$ can be taken as

$$S_r = (S_{r,yield} + S_{r,resid/geom}) \times 0.5 \times 0.8 \qquad \text{[Eq. 2-3b]}$$

This implies that Wang's values of S_r inferred from Olson's values of $S_{r,yield}$ and $S_{r,resid/geom}$ are, on average, high by approximately 25%. The impact of this is variable from case history to case history, depending on how many other values of S_r from other previous investigations are averaged in with the value of S_r inferred from Olson. As shown in Table 2.1, there are between zero (four cases) to as many as six (one case) other values of S_r to average in with the inferred values from Olson (2001).

Another issue is the apparent failure of Wang (2003) to investigate the origins and backgrounds of many of the individual values of S_r that he collected and compiled from previous investigations. This also had a potentially significant deleterious effect on some of the results.

A good example of the importance of tracking back to understand the history of development of values from previous investigations is the Nerlerk Berm 1 case history. Wang (2003) lists four values for this case history from four sets of previous teams of investigators as:

$S_r = 42$ lbs/ft^2 (Sladen et al., 1985)

$S_r = 308$ lbs/ft^2 (Jeffries et al., 1990)

$S_r = 300$ lbs/ft^2 (Stark and Mesri, 1992)

$S_r = 54$ lbs/ft^2 (Olson, 2001)

and he then averages these for his selected representative value of $S_r = 179$ lbs/ft^2. (The actual average of these would be $S_r = 176$ lbs/ft^2; the slight difference here may be due to units conversions from the original publications cited.)

But a review of the history of development of the four apparently independent values cited for this case history changes the picture significantly. Sladen et al. (1985) were the original investigators, and their value of $S_r = 42$ lbs/ft^2 thus has good credence. Jeffries presented a value

of S_r = 308 lbs/ft^2, but did not present the details (or cross-sections, etc.) of the analyses that produced this value; and so they cannot be properly checked. Stark and Mesri (1992) simply adopted the value of S_r = 308 lbs/ft^2 from Jeffries et al. without independent analyses of their own, and rounded it to S_r = 300 lbs/ft^2. So this is <u>not</u> an additional independent value. Olson (2001) did then, subsequently, perform his own independent analyses to develop the value of S_r = 54 lbs/ft^2. Because he published this as Olson and Stark (2002) it may be concluded that this replaces the judgment of Stark and Mesri that the value of Jeffries (1990) was appropriate. Finally, unbeknownst to Wang at the time (2003), the back-analyses performed for these current studies developed a value of S_r = 68 lbs/ft^2 for this case history. So a better summary would appear to be:

S_r = 42 lbs/ft^2 (Sladen et al., 1985)

S_r = 308 lbs/ft^2 (Jeffries et al., 1990)

~~S_r = 300 lbs/ft^2~~ ~~(Stark and Mesri, 1992)~~ [redundant, from Jeffries et al.]

S_r = 54 lbs/ft^2 (Olson, 2001)

and [S_r = 68 lbs/ft^2] [These current studies.]

The value of Jeffries et al. (1990) is not suitably documented, and it appears to be in error, with three other independent teams of investigators developing values of S_r = 42, 54 and 68 lbs/ft^2 for this case history (in good agreement with each other). Straightforward averaging of these three values would produce a representative value of <u>S_r = 55 lbs/ft^2</u>, a significantly lower value than the <u>S_r = 176 lbs/ft^2</u> adopted by Wang (2003).

Another good pair of examples are the two La Marquesa Dam case histories (Upstream Face and Downstream Face). Considering only the downstream side case history here; Wang's Table 6-8 lists values from four previous investigation teams. These are

S_r = 423 lbs/ft^2 (De Alba et al., 1987)

S_r = 400 lbs/ft^2 (Seed and Harder, 1990)

S_r = 400 lbs/ft^2 (Stark and Mesri, 1992)

S_r = 190 lbs/ft^2 (Olson, 2001)

The first three of these values are redundant; they do not represent three independent evaluations or back-analyses. De Alba et al. (1987) included both Seed and Harder as members of their investigation team. Seed and Harder (1990) simply rounded the value of S_r = 423 lbs/ft^2 to S_r = 400 lbs/ft^2. Stark and Mesri (1992) did not perform any independent back-analyses; instead they simply adopted the value of S_r = 400 lbs/ft^2 from Seed and Harder (1990). The value of S_r = 129 lbs/ft^2 attributed to Olson (2001) is then the second independent value. This is again, of course, not the (lower) value of $S_{r,yield}$ that Olson (2001) and Olson and Stark (2002) employed in development of their predictive relationship. They employed a value of $S_{r,resid/geom}$ = 111 lbs/ft^2;

and Wang (2003) modified this to a value representing instead the average of Olson's values of $S_{r,yield}$ and $S_{r,resid/geom}$ as discussed above to produce the value of S_r = 190 lbs/ft^2. The value of S_r developed by De Alba et al. (1987) probably took excessive account of potential cyclic inertial effects for this case, and it may be somewhat unconservative. Averaging this value three times with only one times the approximate actual S_r value derived (by Wang, 2003) from Olson's analyses of $S_{r,yield}$ and $S_{r,resid/geom}$ would then likely produce an unconservatively biased overall average. Wang's value selected for this case was then S_r = 344 lbs/ft^2.

The value back-calculated in these current studies for this same case is S_r = 214 lbs/ft^2. If only one of the values of approximately $S_r \approx$ 400 lbs/ft^2 was averaged with the other independent value of S_r = 190 lbs/ft^2, then the resulting average would have been S_r = 295 lbs/ft^2, in better agreement with the value back-calculated in these current studies.

The best cross-comparison (now), however, would likely be to use (1) the value of 0.5 times the average of Olson's values of $S_{r,yield}$ and $S_{r,resid/geom}$ multiplied by $\xi \approx 0.8$ (as discussed in Chapter 4) to produce the value of S_r = 152 lbs/ft^2, and (2) the value of S_r = 214 lbs/ft^2 independently back-calculated in these current studies. These two values are in fairly close agreement, and the average of these two independent values would be $\underline{S_r = 183 \text{ lbs/ft}^2}$; a value that is lower than Wang's value of S_r = 344 lbs/ft^2 by a factor of 344/183 = $\underline{1.88}$.

Similar re-evaluation suggests that the value of S_r selected and employed by Wang (2003) for the La Marquesa Dam upstream side case history also significantly over-estimates S_r, and for largely similar reasons.

These same types of issues occur for a number of the other "secondary" case histories as well. Close examination of the values and citations listed in Table 2.1 shows a number of similar issues, though generally of lesser impact on an individual case by case basis. The most common of these issues is that many of the case histories have two sets of S_r values listed as being attributed to Seed and Harder (1990) and to Stark and Mesri (1992). As described previously in Section 2.3.3, Stark and Mesri (1992) simply adopted the values of S_r back-calculated by Seed and Harder (1990), so these are the $\underline{\text{same}}$ numbers (they are redundant) and are not two independent sets of values, and they should not be listed (and used) as two separate sets of independent estimates.

Overall, there are a number of apparent (1) errors and (2) judgments and/or choices made by Wang that appear to produce unconservatively biased (high estimates) of S_r for a significant number of the 22 "secondary" case histories. These appear to be high, on average, by about 10% to 20% (though for some individual cases the degree of bias is greater), and this unconservatism will be more than offset by over-conservatism in many of the values of "representative" values of initial effective vertical stress ($\sigma_{v,i}'$) developed by Wang (2003) and employed by Kramer (2008), as will be discussed in Section 2.3.8.1(b)-(iii) that follows.

Coefficients of variation (COV) for each of the 22 secondary cases were estimated based on (1) the COV's calculated for the nine cases previously back-analyzed using the ZIF-based approach, (2) the perceived quality of data and information available for each case (which was "indexed" to a factor affecting overall COV), and (3) variance or dispersion in available values of S_r from previous studies. The equational relationship inter-relating these factors was designed to

increase overall COV somewhat to account for the increased effects of modeling uncertainty in these less well defined case histories. This was an interesting approach, and it was not without merit. It is interesting to contrast the resulting estimates of variance (expressed as standard deviation in mean value of S_r for each case) against the values of standard deviation of S_r for each of these same cases as developed by very different approaches employed in these current studies.

(iii) Representative Values of $\sigma_{v,i}'$

The eventual regressed predictive relationship developed by Kramer (2008) predicted S_r based on both (1) $N_{1,60,CS}$ and (2) initial effective vertical stress ($\sigma_{v,i}'$). Surprisingly, values of mean $\sigma_{v,i}'$, and of the standard deviations of these means, for the 31 cases analyzed were never explicitly stated; neither in the thesis work of Wang (2003) nor in the subsequent WashDOT report of Kramer (2008) which presented the regressions performed and the resulting development of probabilistic and deterministic correlations for evaluation of S_r. Table 2.3 is from Kramer (2008), and it presents the mean values, and standard deviations in mean values, of both S_r and $N_{1,60,CS}$ for each of the 31 cases, along with weighting factors developed by Kramer for use in performing the regressions which followed. Not listed are the mean values, and standard deviations in mean values, of initial effective vertical stress; despite the fact that initial effective vertical stress turns out to be of essentially co-equal importance along with $N_{1,60,CS}$ for prediction of S_r in the predictive correlations subsequently developed. This was another significant lapse in terms of transparency of documentation.

The eventual journal paper by Kramer and Wang (2015) finally explicitly presented the values of representative initial effective stress ($\sigma_{v,i}'$) used for each case history. These are presented in the column of Table 2.3 labeled "[3]". These values of $\sigma_{v,i}'$ can now be back-tracked and checked in detail. There are some significant problems here.

The process employed by Wang (2003) to develop his estimates of representative values of $\sigma_{v,i}'$ was a very poor one, and it led to a number of significant errors. These errors carried forward into the predictive relationships subsequently developed by Kramer (2008) and published by Kramer and Wang (2015).

In addition to collecting values of S_r from previous investigators for each case history (as presented in Table 2.1), Wang (2003) also collected values of S_r/P from previous investigators, and these are presented in Table 2.2. These values were then averaged to develop estimates of the overall representative values of S_r/P for each case history, as also listed in Table 2.2.

These resulting averaged values of S_r/P were not used to estimate overall values of S_r for any of the cases, but they <u>were</u> used to infer representative values of "P" (or $\sigma_{v,i}'$) for each of the 22 Secondary case histories. Values of S_r (from Table 2.1) were combined with values of S_r/P (from Table 2.2) to derive "representative" values of $\sigma_{v,i}'$ for each of the 22 Secondary case histories. The problem was that the "averaged" evaluations of S_r (Table 2.1) and of S_r/P (Table 2.2) were not developed in a manner intended to be compatible with each other. They were developed by different teams of investigators, and often represented different assumed and/or

back-analyzed failure mechanisms or failure surfaces, as well as other differences in technical opinions and modeling or analysis details.

This led to some clearly unreasonable values of "representative" $\sigma_{v,i}'$, which serve to at least partially undermine the validity of the (regressed) probabilistic predictive relationships subsequently developed.

Table 2.3 lists, and cross-compares, the values of $\sigma_{v,i}'$ developed and used by [1] Olson & Stark (2002), [2] these current studies (see Chapter 4), and [3] Kramer (2008) and Kramer & Wang (2015).

The first two columns of numbers in Table 2.3 present the values of $\sigma_{v,i}'$ employed by [1] Olson & Stark (2002) and [2] these current studies. The third column then presents the ratio of values of $\sigma_{v,i}'$ calculated/selected by each team for each of the case histories. Agreement between these two sets of independently developed values of representative $\sigma_{v,i}'$ is very good for most of the 30 case histories (and sub-case histories) analyzed by both investigation teams. For 14 of the common cases agreement is within +/- 10% or better, and for all but 7 cases and sub-cases agreement is within +/- 25% or better. For two cases (Helsinki Harbor and Lake Merced Bank) the ratios of values between the two studies are 1.62 and 0.61. These differences are the result of different choices of failure planes for these cases by the two different investigation teams. Similarly, for the two sub-cases of the Nerlerk Embankment Slides 1 and 2 (of three Nerlerk Embankment slides analyzed by both teams) the ratios are 1.93 and 1.87, again representing differences in failure planes selected by the two investigation teams. This would appear to indicate that the values are largely "correct", as they are mutually well-supported by the two independent research teams of [1] Olson and Stark(2001, 2002) and [2] these current studies.

Overall, the average of the ratios of $\sigma_{v,i}'$ for the 30 cases and sub-cases analyzed by both teams is 1.11, as shown in Table 2.3, representing an excellent level of agreement for such a complex and judgmental exercise. Most of this difference is associated with differences in the failure planes employed for the four cases discussed in the preceding paragraph, but a bit of this difference is associated with the tendency of Olson (2001) to select slightly shallower "most critical" failure planes for a number of cases while these current studies tended to select most critical potential failure surfaces that plunged a bit more deeply. With the four cases and sub-cases highlighted in yellow deleted (as the failure surfaces used by the two studies differ deliberatively for these four cases), the average of the ratios of $\sigma_{v,i}'$ for the remaining 25 cases is 1.04. That appears to represent a strong level of overall agreement.

The fourth column of values in Table 2.3 (marked with a [3]) presents the values of $\sigma_{v,i}'$ selected and employed by Wang (2003). The final column then compares these with the averages of the two studies of [1] Olson & Stark (2001) and [2] these current studies. Agreement is very poor for many of the 28 cases histories in common among all three investigation teams. Values highlighted in yellow (and shown in rounded parentheses) are values where agreement is not within +/- a factor of 1.5 (ratios of less than 0.67 or greater than 1.5), and values highlighted in green are values where agreement is not within +/- a factor of 2 (ratios of less than 0.5 or greater than 2.0).

The most erroneous value of $\sigma_{v,i}'$ is the value of $\sigma_{v,i}'$ = 9,760 lbs/ft^2 for the El Cobre Tailings Dam failure case history. Olson independently back-calculated a representative (average) value of $\sigma_{v,i}'$ = 1,946 lbs/ft^2 for this case history, and the value independently back-calculated in these current studies if $\sigma_{v,i}'$ = 2,075 lbs/ft^2. It appears that there is good agreement that the appropriate value would be on the order of approximately 2,000 lbs/ft^2, or so. The value developed by Wang by combining his estimated S_r from Table 2.1 with his estimated S_r/P from Table 2.2 is 9,760 lb/ft^2, which is too high by a factor of approximately 4.85. There is some small level of uncertainty in assessment of the unit weight of the tailings in this case history, and also in estimation of the phreatic surface at the time of the failure. And there is also some minor level of uncertainty as to the elevation of the largely horizontal failure surface for this case history. But these are relatively minor issues. The overall height of the tailings impoundment would have to be increased at least four-fold (or more) to generate values of $\sigma_{v,i}'$ in the range of Wang's value. This is clearly a physically impossible value; and it serves as one of the three principal variables representing this case history in the subsequent regressions performed by Kramer (2008) and by Kramer and Wang (2015) to develop predictive correlations for S_r as a function of $N_{1,60,CS}$ and $\sigma_{v,i}'$ or $N_{1,60}$ and $\sigma_{v,i}'$.

There are five additional case histories (highlighted in green) in Table 2.3 for which the values of $\sigma_{v,i}'$ selected by Wang (2003) differ from those of [1] Stark & Olson (2002) and [2] these current studies by factors of more than 2, and there are three additional cases where the factors of difference are greater than 1.8. All of these are associated with cases for which better values appear to be well established by good agreement between the values independently back-calculated by [1] Stark & Olson (2002) and [2] these current studies. Accordingly, these appear to be physically unreasonable values. Nine of the values of $\sigma_{v,i}'$ selected by Wang (2003) appear to be physically unreasonable, and at least six additional values appear to be in at least relatively poor agreement with the values of [1] Stark & Olson (2002) and [2] these current studies.

These errors appear to be mainly the result of the poor procedure of employing incompatible "averaged" values of S_r from Table 2.1 with "averaged" values of S_r/P from Table 2.2 to calculate "P" ($\sigma_{v,i}'$), but two of the cases (highlighted in yellow in Table 2.3) with poor agreement are two of Wang's nine "primary" cases [Uetsu Railway Embankment, and Hachiro-Gata Road Embankment], and it is less clear why these two cases match poorly.

In all but two of the 15 cases for which Wang (2003) appears to have selected either poor or physically unreasonable values of $\sigma_{v,i}'$, the values selected by Wang are far too high. These errors were carried forward into the regressions and resulting predictive correlations subsequently developed by Kramer (2008) and published by Kramer and Wang (2015). As shown in Table 2.3, the overall average ratio of Wang's selected values of $\sigma_{v,i}'$ relative to the values selected by [1] Olson and Stark (2002) and [2] these current studies is approximately 1.57. The effect of these erroneous (high) values of $\sigma_{v,i}'$ would be to "stretch" the $\sigma_{v,i}'$ values to the high side in the regressions performed; resulting in somewhat conservative under-predictions of S_r for any given actual (real) value of $\sigma_{v,i}'$. This conservative bias appears to outweigh the somewhat unconservative bias introduced in some of the evaluations of Sr for some of the Secondary cases, as discussed in the previous Section 2.3.8.1(b)-(ii). This will be discussed further in Chapters 5 and 6.

2.3.8.2 Regressions and Predictive Relationships of Kramer (2008)

Table 2.4 shows the values of the three principle indices, and their modeled variances, as listed in Table G.4 of Kramer (2008). These are the values from Wang's (2003) studies, and they are directly comparable to the values developed in these current studies. Unfortunately, Table G.4 made an error in listing values of $N_{1,60,CS}$, as Kramer (2008) actually elected instead to base his regressions on non-fines-corrected $N_{1,60}$ values instead. He found that variance was little different when using either $N_{1,60}$ or $N_{1,60,CS}$, and he elected to switch to $N_{1,60}$ (Kramer, 2015). The other values in Table 2.4 (penetration resistances and initial effective stresses) are correct, and match those used in the regressions of Kramer (2008). A second error in Table G.4 was the omission of the values of $\sigma_{v,i}'$ and of variance in $\sigma_{v,i}'$ for each case history.

Because of these two errors in Table G.4, the actual values used in the regressions of Kramer (2008) were only eventually published in Kramer and Wang (2015). Table 2.5 shows the values of the three principle indices, as employed in the regressions performed by Kramer (2008) and published by Kramer and Wang (2015).

This table does not show values of variance for the three indices, so there are still no published values available documenting the variances of $N_{1,60}$ and $\sigma_{v,i}'$ for each of the case histories. As a result, in these current studies cross-comparisons will be made using the published values of variances in $N_{1,60,CS}$ from Wang (2003) which should be closely similar to variances in $N_{1,60}$, based on the procedures used to develop them. No published values of variance in $\sigma_{v,i}'$ are available, and so no cross-comparisons or checks can be made for those.

The resulting $N_{1,60}$-based equation is not fully compatible for direct cross-comparison with the relationship developed by these current studies due to the differences between $N_{1,60,CS}$ and $N_{1,60}$. Neglecting fines corrections would intrinsically tend to introduce a potentially conservative bias if the regressed relationship was then subsequently applied to sands with lesser fines contents. The overall relationship was already significantly conservatively biased due to errors in derivation of a number of the representative $\sigma_{v,i}'$ values used to represent 13 of the case histories (as discussed previously in Section 2.8.3.1, Part 3). This bias due to erroneous $\sigma_{v,i}'$ values would significantly outweigh any additional (and much lesser) conservative bias introduced by the use of $N_{1,60}$ instead of $N_{1,60,CS}$. This will be discussed further in Chapter 5.

The weighting factors shown in Tables 2.4 and 2.5 are potentially important. These weighting factors were developed by Kramer (2008) in order to account for the variable quality of information and documentation of data available for the individual case histories. Poorer documentation would be expected to lead to higher levels of uncertainty. Unfortunately, full details involved in development of these weighting factors are not presented. They appear to have been a matter of engineering judgment. That said, they do appear to be generally reasonable in the view of the current investigation team, although any two different investigation teams would likely have differences of opinion as to the details or the relative weighting factor assigned for any specific case history. (In these current studies, it was preferred to incorporate uncertainties associated with poor documentation of information and data, as well as with the variable quality of data, directly in the variances ascribed to the key regression parameters; so no additional weighting factors were applied in these current studies.) Weighting factors in Table 2.4 range

from w = 1.0 for well documented cases, to very low values for poorly documented cases. The two cases with the lowest assigned weighting factors are Asele Road (w = 0.20) and the Soviet Tajik - May 1 Slide (w = 0.22). With these very low weighting factors, these two cases are virtually eliminated.

Kramer (2008) performed a large number of nonlinear least squares regressions to ascertain the forms of useful predictive relationships (general equation forms) that would be well suited to the data set and provide generally good model fit across the domain of the data set. He then performed fully probabilistic Bayesian regressions using the maximum likelihood method to develop a better probabilistically based relationship incorporating all uncertainties. This relationship was what Kramer described as a "hybrid" model, with predicted values of S_r being dependent upon both SPT penetration resistance and initial effective vertical stress.

In examining the resulting predictive correlation, Kramer observed that values of S_r predicted at very low initial effective stresses appeared to be unreasonably low. He reasoned that if such values actually occurred, then larger numbers of very shallow flow slides would be observed. He examined the suite of available field case history data for lateral spreading cases (not flow slides) developed by Youd et al. (2002), and reasoned that the value of S_r within the liquefied materials for each of these lateral spreading cases must have been at least as large as the static driving shear stress; otherwise these would have been flow failure case histories rather than lateral spreads. He made simplified estimates of the static driving stresses at shallow depth for these cases, based on an infinite slope assumption, and in this manner estimated the minimum (lower bound) potential value of S_r for each lateral spreading case at initial vertical effective stresses of less than 0.6 atmospheres. These were plotted vs. effective vertical effective, and the resulting plot is shown in Figure 2.25. Based on this, but without explanation of details, Kramer concluded that one of his model fitting parameters (Θ_4) would be modified to slightly increase the values of S_r predicted at very low confining stresses. This was a "judgmental" manipulation, and it served to correct what appear to have been overly conservative predictions of S_r at low initial effective stresses.

His regressed model, with the parameters developed by the maximum likelihood method, but with variance or uncertainty developed based on First Order Second Moment analyses, and with Θ_4 thus slightly constrained, was then reformulated into a more tractable form for use by engineers. The final proposed relationship was then

$$\overline{\ln S_r} = -8.444+0.109N+5.379S^{0.1} \qquad \text{[Eq. 2-3]}$$

where

$$\sigma_{\ln S_r} = \sqrt{\sigma_m^2+0.00073\overline{N}^2\ COV_N^2+4.935S^{-0.2}\ COV_S^2} \qquad \text{[Eq. 2-3a]}$$

and

$$\sigma_m^2 = 1.627+0.00073N^2+0.0194N-0.27NS^{0.1}-3.099S^{0.1}+1.621S^{0.2} \qquad \text{[Eq. 2-3b]}$$

Figure 2.26 shows the median (50th percentile) values of S_r based on this relationship. A series of curves are shown relating S_r to $\overline{N_{1,60,CS}}$, with each curve labeled with the value of $\overline{\sigma'_{vo}}$ for which that curve would apply. The overall relationship is fully probabilistically based, and similar curves can be developed and plotted for other percentiles or likelihoods of exceedance.

Kramer then went on to further consider appropriate levels of conservatism for "deterministic" values of S_r for engineering applications, and determined that 40th percentile values would be appropriate here. These values, recommended for routine geotechnical design, are shown in Figure 2.27.

2.3.8.3 Predictive Relationship of Kramer & Wang (2015)

The predictive relationship developed by Kramer (2008) was subsequently published by Kramer and Wang (2015). This publication presented the actual values of $N_{1,60}$ and of $\sigma_{N1,60}$ that had been employed in the regressions to develop their predictive relationship.

The form of the equation expressing the regressed relationship as published in Kramer and Wang (2015) is

$$\overline{\ln S_r} = -8.444+0.109N+5.379S^{0.1} \qquad \text{[Eq. 2-4]}$$

where

$$\sigma^2_{\ln S_r} = 1.627 +0.00073N^2+0.0194N-0.027NS^{0.1} -3.099S^{0.1}+1.621S^{0.2}+0.00073\sigma^2_N+4.935S^{-1.8}\sigma^2_S \qquad \text{[Eq. 2-4a]}$$

The best-fit mean value surface (Equation 2-4) is exactly identical to the best-fit mean value surface equation of Equation 2-3 from the previous $N_{1,60,CS}$-based formulation. It is only the error term (Equation 2-4a) that has been reformatted slightly from the original publication by combining Equations 2-3a and 2-3b.

2.3.9 Idriss and Boulanger (2008)

Idriss and Boulanger (2008) considered a subset of 17 of the 33 large-displacement liquefaction failure case histories in the data set complied by Olson and Stark (2002). The basis for selection of each of these was not explicitly explained, but it is understood that they selected the cases that they felt were best characterized and best documented, and deleted the rest. They then categorized each of these 17 case histories into one of three groups; Groups 1, 2, and 3. Group 1 were the cases considered to be those that were best characterized and documented, and Group 3 those that were least well characterized.

They did not perform any of their own independent back-analyses of these 17 case histories. Instead, they next adopted the values developed from back-analyses by (1) Seed (1987), (2) Seed and Harder (1990), and (3) Olson and Stark (2002) for those cases which each of these

previous teams had analyzed. Ten of the cases had been back-analyzed by Seed (1987), 13 by Seed and Harder (1990) and all 18 by Olson and Stark (2002). Values of S_r back-calculated by Seed (1987) and by Seed and Harder (1990) were normalized by dividing by estimated representative values of effective vertical stress to develop post-liquefaction strength ratios for each case.

The resulting values of strength ratio (S_r/P) were then plotted vs. $N_{1,60,CS}$ values developed by each of the three previous investigation teams. Values of $N_{1,60}$ developed by Olson were modified to approximate $N_{1,60,CS}$ values here. The results are shown in Figure 2.28. In this figure, the shapes of the symbols identify the investigation team responsible for the values of S_r and $N_{1,60,CS}$ plotted, and the sizes of the symbols indicate whether the case was considered by Idriss and Boulanger to be a Group 1 (high quality) or Group 2 and 3 (lower quality) case.

A line was drawn through these plotted data (the solid line in the lower left-hand portion of the figure), based on judgment, and this line was then extended as a dashed line to express additional judgment as to the likely extrapolation to higher $N_{1,60,CS}$ values. An equation was then fitted to this proposed relationship for ease of implementation in spreadsheet calculations and similar.

A second dashed line was then added, inflecting steeply upwards, to represent recommended values of S_r as a function of $N_{1,60,CS}$ for situations in which void redistribution effects are expected to be negligible. This upper line is not well explained, but it is independent of the back-analyzed field case history data plotted, and it is reportedly based primarily on laboratory test data.

There are a number of problems and drawbacks in this proposed relationship, and with the figure presented. The first of these is the fact that the large, solid "dot" plotted at $N_{1,60,CS} = 15$ blows/ft and $S_r/P \approx 0.21$ (Point "A" in Figure 2.29) represents the S_r value initially proposed by Seed (1987) for the Lower San Fernando Dam case history. As discussed previously in Section 2.3.1, Prof. H. B. Seed later reconsidered this and concluded that this was an error and that the strength that he had originally proposed was too high. Seed and Harder (1990) and Olson (2001) both back-analyzed this case, and both had developed lower S_r values. The values of Seed and Harder (1990) and Olson and Stark (2002) are in such close agreement that they plot largely over each other in Figure 2.29 (Points B & C in this figure). For clarity, Figure 2.29 repeats Figure 2.28, but this time the erroneous data point for Lower San Fernando Dam is circled with a dashed line (and partly dimmed), and the locations of the (arguably more correct) plots of the data points developed by Seed and Harder, and by Stark and Olson, for the Lower San Fernando Dam are clearly indicated.

This changes the figure significantly, especially on a visceral (graphical) basis. It removes the large "dot" that otherwise appears to "anchor" the upper dashed curve. This dot was never actually part of the upper curve, because all of the back-analyzed field case histories were actually ascribed to situations wherein void redistribution was assumed to have potentially occurred (and so all field cases back-analyzed are associated with the lower curve, not the upper curve). But many engineers do not read text, and simply view the figure and assume that the upper curve is somehow associated with this (very prominent) erroneous data point.

With the erroneous data point thus relocated, Figure 2.29 then shows clearly the very large degree of engineering judgment involved in recommending the upwards bending curve to extrapolate the lower solid line's recommended relationship to values of $N_{1,60,CS}$ greater than about 15 blows/ft. There is nothing obvious in the data, as presented, that supports this interpretation. Neither the slope of the lower portion of the curve, nor the upwards inflection of the upper part of the curve, can be reliably ascribed to the data as plotted.

It should also be noted that six data points plot high in the upper left-hand corners of Figures 2.28 and 2.29. These six high "floating" points are unexplained by this relationship, as presented and described by Idriss and Boulanger, but it turns out that they are actually well-explained by the predictive relationships developed by Wang and Kramer (see Section 2.3.8) and by these current studies (see Chapter 5).

Finally, it should be noted that the "upper" dashed line is intended to be applied only to field cases in which void redistribution will not be significant. It has proven difficult to define such cases in the field. Many engineers are well used to having an upper bound and lower bound relationship proposed (as with Seed and Harder, 1990, Stark and Mesri, 1992, and Olson and Stark, 2002) and so they are used to interpolating between the upper and lower bounds as presented to select values of post-liquefaction strength for actual projects. This is not the apparent intent of Idriss and Boulanger who intend the lower line to represent not a "lower bound" but rather the "recommended" values for field cases wherein void redistribution effects can occur (most field situations), and who intend the upper dashed line (which was based on laboratory test data rather than back-analyzed field case histories) to represent not an "upper bound" but rather a second relationship for situations in which void redistribution effects will not be significant.

Idriss and Boulanger also present their selected data points, and recommended relationships, in the form of S_r (not S_r/P), and these are shown in Figure 2.30. The same issues discussed above apply here as well. This includes the large solid "dot" representing the values initially proposed by Seed (1987) for the Lower San Fernando case history. Relocation of this data point (to the positions determined by Seed and Harder, 1990, and by Olson and Stark, 2002) is illustrated in Figure 2.31.

2.3.10 Olson and Johnson (2008)

Olson and Johnson (2008) recognized the paucity of liquefaction-induced failure case histories for back-analyses of post liquefaction strengths at full field scale. To address this, they collected a large number of available liquefaction-induced lateral spreading case histories (39 cases). Lateral spreading case histories differ from liquefaction flow failure case histories in that they experience more limited displacements, and a large fraction of their displacements are often driven primarily by cyclic inertial lurching during strong earthquake shaking. Lateral spreads tend to be of finite thickness and/or slope (though they can sometimes be very large), and thus the initial (pre-earthquake) gravity-induced static shear stresses tend in most cases to be equaled or overshadowed by the cyclic "lurching" induced stresses during strong shaking.

Accordingly, Olson and Johnson applied various Newmark-type analyses to back-analyze the displacements observed in the field for these cases in order to estimate the post-liquefaction

strengths involved. Newmark-type analyses are not a very precise analysis methodology (e.g. Bray and Rathje, 1998) and this was further exacerbated by the sensitivity of calculated displacements to the intensity and details of actual earthquake shaking at each site, and the lack of site-specific ground motion records for each case. As a result, there was significant scatter (or variance/uncertainty) in the resulting estimates of S_r for each case.

A tentative recommended relationship between strength ratio (S_r/P) and penetration resistance was developed, but the large variance or uncertainty made this of little apparent value relative to relationships already available. In the end, the most important lessons from this study were: (1) the difficulty of assessing S_r based on performing back-analyses of cases with only limited displacements wherein cyclic lurching generates a significant fraction of the overall displacements that accrue, and (2) the difficulty of extracting back-analyzed values of S_r by means of simplified Newmark-type analyses.

2.3.11 Gillette (2010)

Faced with the apparently conflicting views that post-liquefaction strengths might best be evaluated [1] based on a "classical" critical state basis using post-liquefaction strength S_r assumed to be independent of effective overburden stress, or [2] on the basis of post-liquefaction strength ratio (S_r/P) with an assumed linear dependence between S_r and initial effective vertical stress, a number of engineers have recommended a middle position.

Baziar and Dobry (1995) had used back-analysis results from liquefaction case histories developed by previous investigators, and had proposed a predictive relationship for S_r that was a function of both $N_{1,60,CS}$ and also effective vertical stress. Unfortunately, that relationship was posed in the form of a figure that was not intuitively transparent, and their relationship did not receive the attention that it may have warranted.

Seed et al. (2003) had suggested that the best answer likely lay somewhere in between these two extreme views, and that there was likely a significant influence of initial effective stress on S_r, but that it was not likely that S_r was fully linearly correlated with initial effective vertical stress. He recommended evaluating S_r based on each approach (S_r and S_r/P), and then averaging the two results (with weighting factors varying a bit as a function of fines content) to produce values of S_r with some partial dependence on initial effective vertical stress until this could be better resolved. This was an interim suggestion, until better "hybrid" approaches could be developed.

As described in Section 2.3.7, Kramer (and Wang) developed "hybrid" predictive correlations for post-liquefaction strength based on both SPT penetration resistance and effective vertical effective stress, with the influence of vertical effective stress modeled as not being linearly related to S_r.

Gillette (2010) used a selected subset of the back-analyzed data bases of Seed and Harder (1990) and Olson and Stark (2002), and performed least squares regressions implementing a number of relatively simple potential equational forms that allowed for varying levels of partial (or nonlinear) dependence of S_r on initial effective vertical overburden stress. His resulting best

fit relationship employing back-analysis results for S_r from Seed and Harder (1990) with effective vertical stresses estimated by Olson and Stark (2002) was

$$S_{ur}=0.64\ (N_1)_{60\text{-}cs}{}^{1.35}+0.1\ \sigma'_{vo}{}^{0.80}\text{-}2.3\pm6\ \text{kPa} \quad \text{with} \quad R^2 \approx 0.78 \qquad \text{[Eq. 2-5]}$$

This R^2 value of 0.78 is significantly higher than the R^2 values previously calculated for the relationships proposed by Seed and Harder (1990), by Stark and Mesri (1992) and by Olson and Stark (2002) in Sections 2.3.1, 2.3.2 and 2.3.6 respectively, further supporting the merit of a middle position wherein S_r would be taken as being nonlinearly dependent upon both penetration resistance and also initial vertical effective stress.

Table 2.1: Compilation of selected values of post-liquefaction strength (S_r) from previous investigations for the 22 Secondary Case Histories and the representative mean values adopted by Wang (2003) as reported in Table 6.8 from Wang (2003).

Case	References	S_r Values (psf)	Mean S_r (psf)
Asele Road	Konrad and Watts (1995)	11	
	Olson (2001)	241	164
Chonan Middle School	Ishihara et al (1990)	167	
	Ishihara (1993)	194	
	Olson (2001)	178	179
El Cobre	Olson (2001)	195	195
Helsinki Harbor	Olson (2001)	53	53
Hokkaido Tailings	Ishihara et al. (1990a)	408	
	Olson (2001)	172	251
Kawagishi-cho	Seed (1987)	120	
	Seed and Harder (1990)	120	
	Stark and Mesri (1992)	120	120
Koda Numa	Lucia (1981); Lucia et al. (1982)	25	
	Seed (1987)	50	
	Seed (1987)	50	
	Olson (2001)	66	48
La Marquesa Downstream	De Alba et al. (1987)	423	
	Seed and Harder (1990)	400	
	Stark and Mesri (1992)	400	
	Olson (2001)	190	344
La Marquesa Upstream	De Alba et al. (1987)	208	
	Seed and Harder (1990)	200	
	Stark and Mesri (1992)	200	
	Olson (2001)	129	181
Lake Merced	Seed (1987)	100	
	Seed and Harder (1990)	100	
	Stark and Mesri (1992)	100	
	Olson (2001)	257	139
La Palma Dam	De Alba et al. (1987)	210	
	Seed and Harder (1990)	200	
	Stark and Mesri (1992)	200	
	Olson (2001)	156	189

Table 2.1 (Cont'd): Compilation of selected values of post-liquefaction strength (S_r) from previous investigations for the 22 Secondary Case Histories and the representative mean values adopted by Wang (2003) as reported in Table 6.8 from Wang (2003).

Case	References	S_r Values (psf)	Mean S_r (psf)
Metoki Road	Olson (2001)	113	133
Mochi Koshi Dike 1	Poulos (1988)	60	
	Davis et al. (1988)	60	
	Olson (2001)	258	159
Mochi Kosho Dike 2	Lucia (1981); Lucia et al. (1982)	210	
	Seed (1987)	210	
	Seed (1987)	210	
	Poulos (1988)	250	
	Seed and Harder (1990)	250	
	Stark and Mesri (1992)	250	
	Olson (2001)	223	234
Nalband	Yegian et al.(1994)	117	
	Olson (2001)	152	140
Nerlerk Berm 1	Sladen et al (1985a)	42	
	Jeffries et al. (1990)	308	
	Stark and Mesri (1992)	300	
	Olson (2001)	54	179
Sheffield Dam	Seed (1987)	50	
	Seed and Harder (1990)	75	
	Stark and Mesri (1992)	75	
	Olson (2001)	198	100
Snow River	Seed (1987)	50	
	Seed and Harder (1990)	50	
	Stark and Mesri (1992)	50	50
Solfatara Canal	Seed (1987)	130	
	Seed and Harder (1990)	50	
	Stark and Mesri (1992)	50	
	Olson (2001)	88	77
Soviet Tajik - May 1 Slide	Ishihara et al (1990b)	167	
	Olson (2001)	418	334
Tar Island Dike	Plewes et al. (1989)	305	
	Konrad and Watts (1995)	80	
	Olson (2001)	500	346
Zeeland	Olson (2001)	226	226

Table 2.2: Compilation of selected values of post-liquefaction strength ratio (S_r/P) from previous investigations for the 22 Secondary Case Histories and the representative mean values adopted by Wang (2003) as reported in Table 6.8 from Wang (2003)

Case	References	S_r/σ'_{vo} Values	Mean S_r/σ'_{vo}
Asele Road	Olson and Stark (2002)	0.104	0.104
Chonan Middle School	Olson and Stark (2002)	0.091	0.091
El Cobre	Olson and Stark (2002)	0.020	0.020
Helsinki Harbor	Olson and Stark (2002)	0.060	0.060
Hokkaido Tailings	Olson and Stark (2002)	0.074	0.074
Kawagishi-cho	Stark and Mesri (1992) Olson and Stark (2002)	0.098 0.075	0.087
Koda Numa	Stark and Mesri (1992) Wride et al. (1999) Olson and Stark (2002)	0.032 0.032 0.040	0.045
La Marquesa Downstream	Stark and Mesri (1992) Wride et al. (1999) Olson and Stark (2002)	0.224 0.223 0.110	0.186
La Marquesa Upstream	Stark and Mesri (1992) Wride et al. (1999) Olson and Stark (2002)	0.125 0.125 0.070	0.107
Lake Merced	Stark and Mesri (1992) Wride et al. (1999) Olson and Stark (2002)	0.105 0.105 0.108	0.106
La Palma Dam	Stark and Mesri (1992) Olson and Stark (2002)	0.120 0.120	0.120
Metoki Road	Olson and Stark (2002)	0.043	0.043
Mochi Koshi Dike 1	Stark and Mesri (1992) Wride et al. (1999) Olson and Stark (2002)	0.092 0.015 0.060	0.091
Mochi Kosho Dike 2	Stark and Mesri (1992) Wride et al. (1999) Olson and Stark (2002)	0.092 0.048 0.104	0.081
Nalband	Olson and Stark (2002)	0.109	0.109
Nerlerk Berm	Jeffries et al (1990) Stark and Mesri (1992) Olson and Stark (2002)	0.150 0.148 0.086	0.124
Sheffield Dam	Stark and Mesri (1992) Wride et al. (1999) Olson and Stark (2002)	0.038 0.038 0.053	0.043
Snow River	Stark and Mesri (1992)	0.024	0.024
Solfatara Canal	Stark and Mesri (1992) Wride et al. (1999) Olson and Stark (2002)	0.052 0.052 0.080	0.063
Soviet Tajik - May 1 Slide	Olson and Stark (2002)	0.082	0.082
Tar Island Dike	Olson and Stark (2002)	0.058	0.058
Zeeland	Olson and Stark (2002)	0.048	0.048

Table 2.3: Cross-comparison of values of initial effective vertical stress employed by [1] Olson & Stark (2002), [2] These Current Studies, and [3] Kramer and Wang (2015)

Group	Case	[1] Olson & Stark (2002) σ'_{vo} (psf)	[2] Current Studdies σ'_{vo} (psf)	Ratio of [2]/[1]	[3] Kramer and Wang (2015) σ'_{vo} (psf)	Ratio of [3]/(0.5 x ([1]+[2])
A	Wachusett Dam - North Dike	3158	3142	0.99	2558	0.81
	Fort Peck Dam	7341	7258	0.99	7466	1.02
	Uetsu Railway Embankment	1280	1448	1.13	916	(0.67)
	Lower San Fernando Dam - U/S Slope	3482	3174	0.91	3538	1.06
	Hachiro-Gata Road Embankment	670	673	1.00	398	(0.59)
	La Marquesa Dam - U/S Slope	911	981	1.08	1682	(1.78)
	La Marquesa Dam - D/S Slope	1000	1215	1.22	1850	(1.67)
	La Palma Dam	789	767	0.97	1577	[2.03]
	Lake Ackerman Highway Embankment	1076	909	0.84	838	0.84
	Chonan Middle School	1119	1032	0.92	1968	(1.83)
	Soviet Tajik - May 1 Slide	2170	1907	0.88	4122	[2.02]
	Shibecha-Cho Embankement	1351	1416	1.05	1048	0.76
	Route 272 at Higashiarekinai	1030	1285	1.25	1043	0.90
B	Zeeland - Vlietepolder	2396	2488	1.04	4708	(1.93)
	Sheffield Dam	1429	1308	0.92	1389	1.01
	Helsinki Harbor	522	846	(1.62)	887	1.30
	Solfatara Canal Dike	624	669	1.07	1224	(1.89)
	Lake Merced Bank	1372	834	(0.61)	1316	1.19
	El Cobre Tailings Dam	1946	2075	1.07	9760	[4.85]
	Metoki Road Embankment	875	871	1.00	2655	[3.04]
	Hokkaido Tailings Dam	1376	1203	0.87	3386	[2.63]
	Upper San Fernando Dam - D/S Slope		3138	N/A		
	Tar Island Dyke	4300	4197	0.98	6279	1.48
	Mochi-Koshi Tailings Dam, Dikes 1 and 2	1251	1564	1.25	1746	1.24
		1090	1447	1.33	2884	[2.27]
	Nerlerk Embankment, Slides 1 ,2 and 3	616	1186	(1.93)	1440	(1.60)
		650	1215	(1.87)		
		925	1277	1.38		
	Asele Road Embankment	1251	1037	0.83	1573	1.38
	Nalband Railway Embankment	1101	1209	1.10	1283	1.11
	Sullivan Tailings		2422	N/A		
	Jamuna Bridge		1404	N/A		
C	Calaveras Dam	6422	7097	1.11	6850	1.01
				Avg. = 1.11		Avg. = 1.57

Notes : (Round parentheses) = Ratio <0.67 or >1.5
[Square parentheses] = Ratio <0.5 or >2.0

Table 2.4: Component values and final weighting factors for all case histories as presented in Table G.4 (from Kramer, 2008)

Case History	$\overline{N}$	σ_N	$\overline{S_r}$	σ_{S_r}	w_{total}
Asele Road	11.0	10.7	163.6	54.6	0.20
Calaveras Dam	10.5	9.7	636.9	223.1	0.55
Chonan Middle School	6.4	6.9	178.7	32.0	0.74
El Cobre Tailings Dam	6.8	0.9	195.2	64.8	0.60
Fort Peck Dam	15.8	0.9	671.6	130.2	0.85
Hachiro-Gata Roadway	5.7	2.8	65.0	24.7	0.55
Helsinki Harbor	5.9	8.0	53.2	19.0	0.39
Hokkaido Tailings	5.1	1.4	250.6	71.9	0.31
Kawagishi-cho Building	4.3	1.2	123.5	56.7	0.50
Koda Numa Embankment	3.6	4.1	48.0	15.9	0.44
Lake Ackerman Roadway	4.8	1.2	98.0	20.4	1.00
La Marquesa Downstream	9.9	3.0	343.5	113.8	0.72
La Marquesa Upstream	6.5	2.8	185.1	82.1	0.76
La Palma Dam	4.2	1.8	193.3	86.3	0.80
Lake Merced Bank	5.9	8.0	139.5	41.4	0.39
Lower San Fernando Dam	14.5	1.1	484.7	111.0	1.00
Metoki Road	2.0	1.5	116.8	53.7	0.39
Mochi Koshi Tailings Dam 1	8.9	0.6	158.9	47.7	0.34
Mochi Koshi Tainilgs Dam 2	10.0	1.3	233.6	78.0	0.67
Nalband Railway	6.3	5.6	139.9	40.2	0.51
Nerlerk Berm	11.4	7.7	179.1	32.1	0.41
Route 272 Roadway	8.5	2.6	130.5	33.5	0.70
Sheffield Dam	8.2	6.8	100.0	29.8	0.37
Shibecha-Cho Embankment	5.6	2.2	208.9	38.6	0.70
Snow River Bridge Fill	8.5	9.0	50.1	16.6	0.50
Solfatara Canal Dike	4.9	6.9	77.1	25.6	0.42
Soviet Tajik – May 1 Slide	8.9	5.7	334.3	110.9	0.22
Tar Island Dike	8.9	9.7	364.2	115.6	0.32
Uetsu-Line Railway	2.9	4.2	43.7	24.8	0.55
Wachusett Dam	7.3	1.9	348.0	74.8	1.00
Zeeland	8.5	5.5	226.0	75.0	0.39

Table 2.5: Component values and final weighting factors for all case histories as employed in the regressions performed (from Kramer & Wang, 2015)

Case history type	Case history	Weighting factor	SPT resistance	Fines content (%)	Initial vertical effective stress (atm)	Residual strength (atm)
Primary	Calaveras Dam	0.55	7.9	34	3.237	0.311
	Fort Peck Dam	0.85	11.7	54	3.528	0.322
	Hashiro-Gata	0.55	4.4	15	0.188	0.030
	Lake Ackerman	1.00	4.8	0	0.396	0.045
	Lower San Fernando Dam	1.00	12.6	25	1.672	0.240
	Route 272	0.70	6.6	33	0.493	0.061
	Shibeca-Cho	0.70	3.7	20	0.495	0.099
	Uetsu	0.55	3.0	0	0.433	0.021
	Wachusett Dam	1.00	7.3	8	1.209	0.164
Secondary	Asele road	0.20	8.9	32	0.310	0.060
	Chonan	0.74	5.1	18	0.930	0.085
	El Cobre Tailings Dam	0.60	1.2	95	4.608	0.092
	Helsinki Harbor	0.39	6.1	0	0.417	0.025
	Hokkaido	0.31	1.1	50	1.603	0.119
	Kawagishi-cho	0.50	4.3	2	0.646	0.058
	Koda Numa	0.44	3.05	40	0.504	0.023
	La Marquesa D/S	0.72	8.2	20	0.874	0.163
	La Marquesa U/S	0.76	4.1	30	0.795	0.087
	La Palma Dam	0.80	2.9	15	0.745	0.092
	Lake Merced	0.39	6.1	0	0.620	0.066
	Metoki road	0.39	2.1	0	1.246	0.055
	Mochi-Koshi 1	0.34	4	73	0.826	0.075
	Mochi-Koshi 2	0.67	5.2	73	1.365	0.111
	Nalbland	0.51	4	30	0.607	0.066
	Nerlerk Berm	0.41	10.6	10	0.682	0.085
	Sheffield Dam	0.37	5	40	1.099	0.047
	Snow River	0.50	7	20	0.984	0.024
	Solfatara	0.42	5.1	0	0.578	0.036
	Soviet Tajik	0.22	7.6	15	1.948	0.158
	Tar Island	0.32	8.2	13	2.966	0.172
	Zeeland	0.39	7.7	11	2.225	0.107

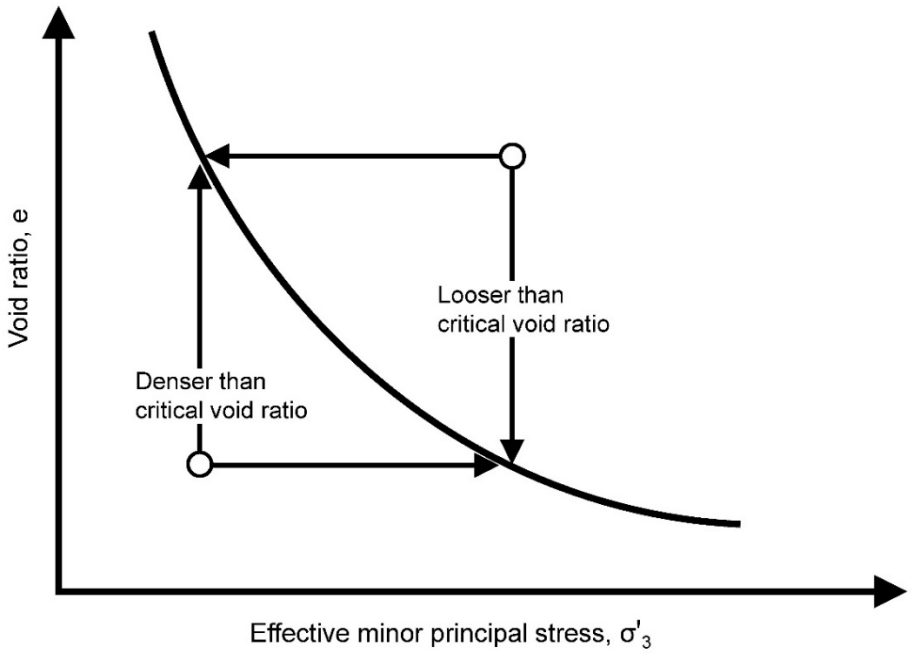

Figure 2.1: Simplified representation of the critical state line.

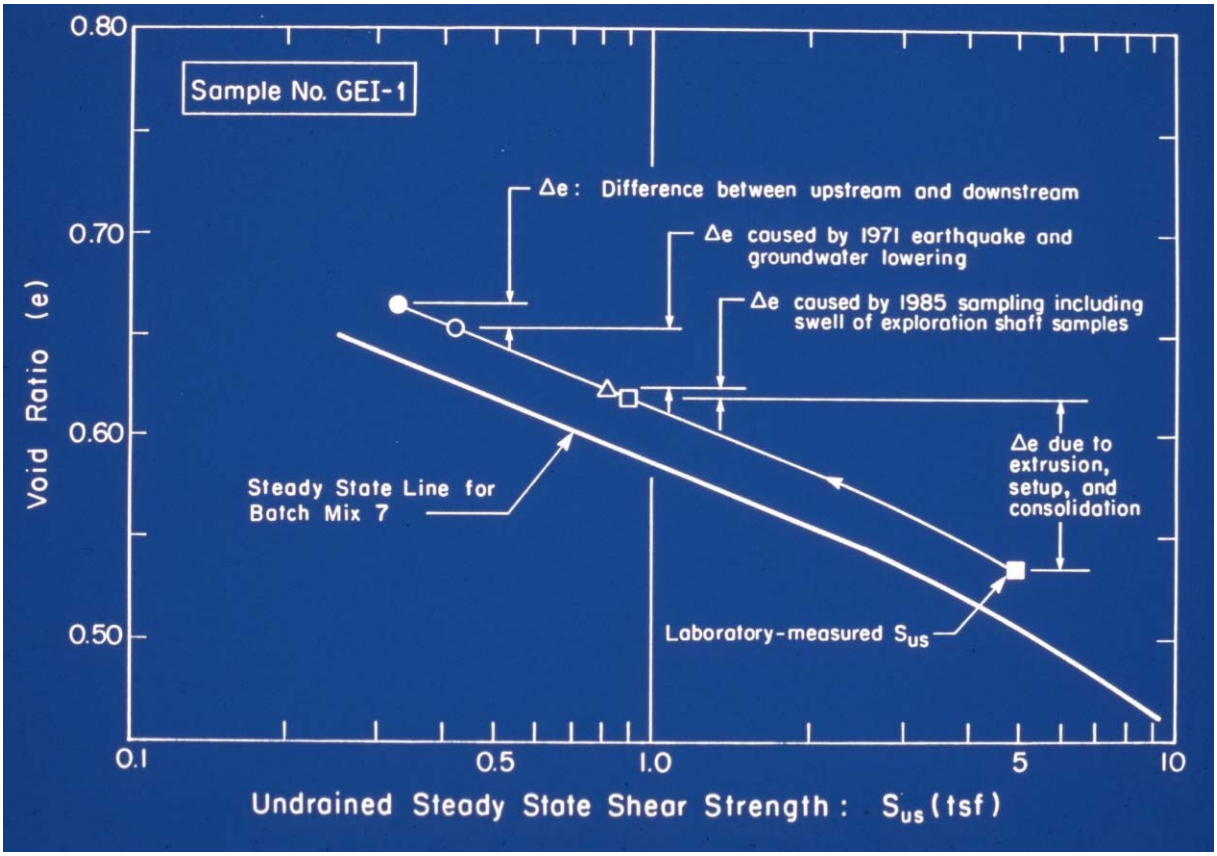

Figure 2.2: Illustration of the Steady State method of Poulos, et al. (1985) for assessing post-liquefaction strength for a sample of silty sand hydraulic fill from the Lower San Fernando Dam (Castro et al., 1992)

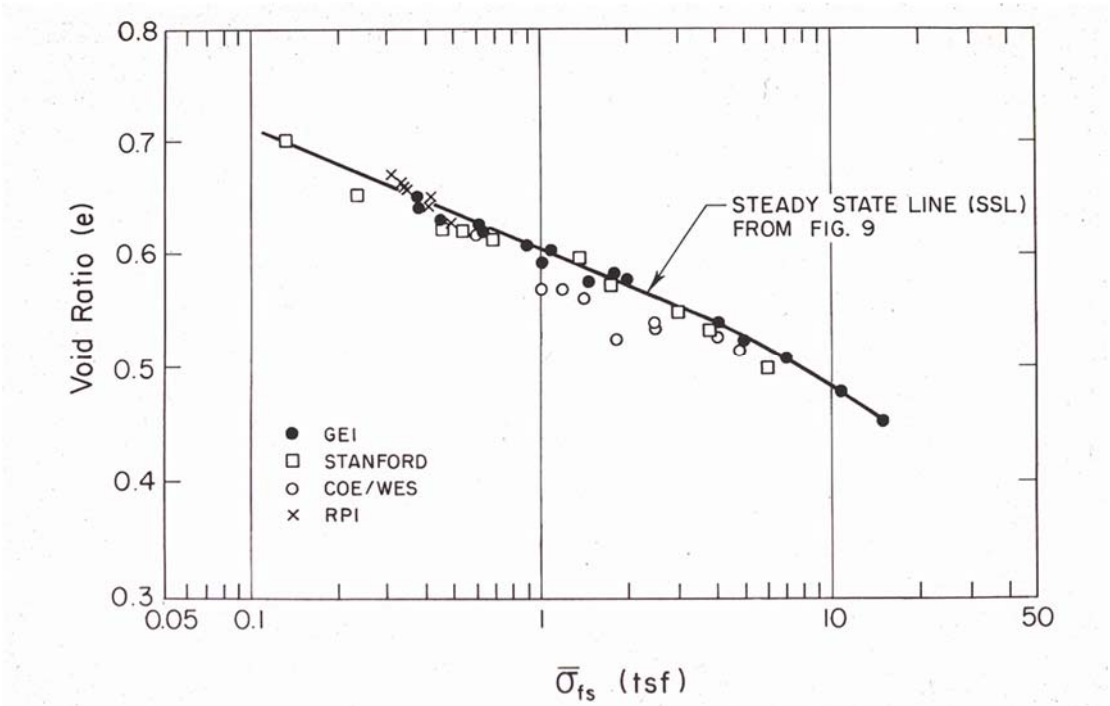

Figure 2.3: Steady state line based on IC-U triaxial tests performed by four laboratories on reconstituted samples of silty sand hydraulic fill from the lower portions of the downstream shell of the Lower San Fernando Dam. (Figure from Castro, et al., 1992)

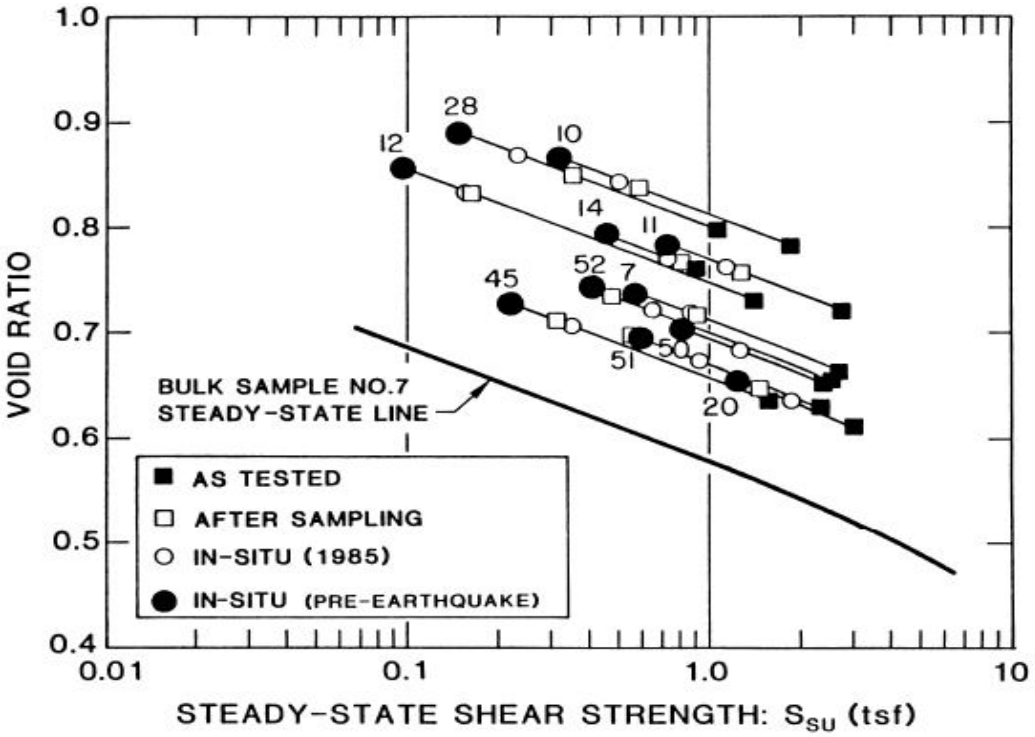

Figure 2.4: Corrections of IC-U triaxial tests of silty sand hydraulic fill from the Lower San Fernando Dam by the steady state method in order to develop estimates of in situ undrained steady state strengths. (Figure from Seed et al., 1988)

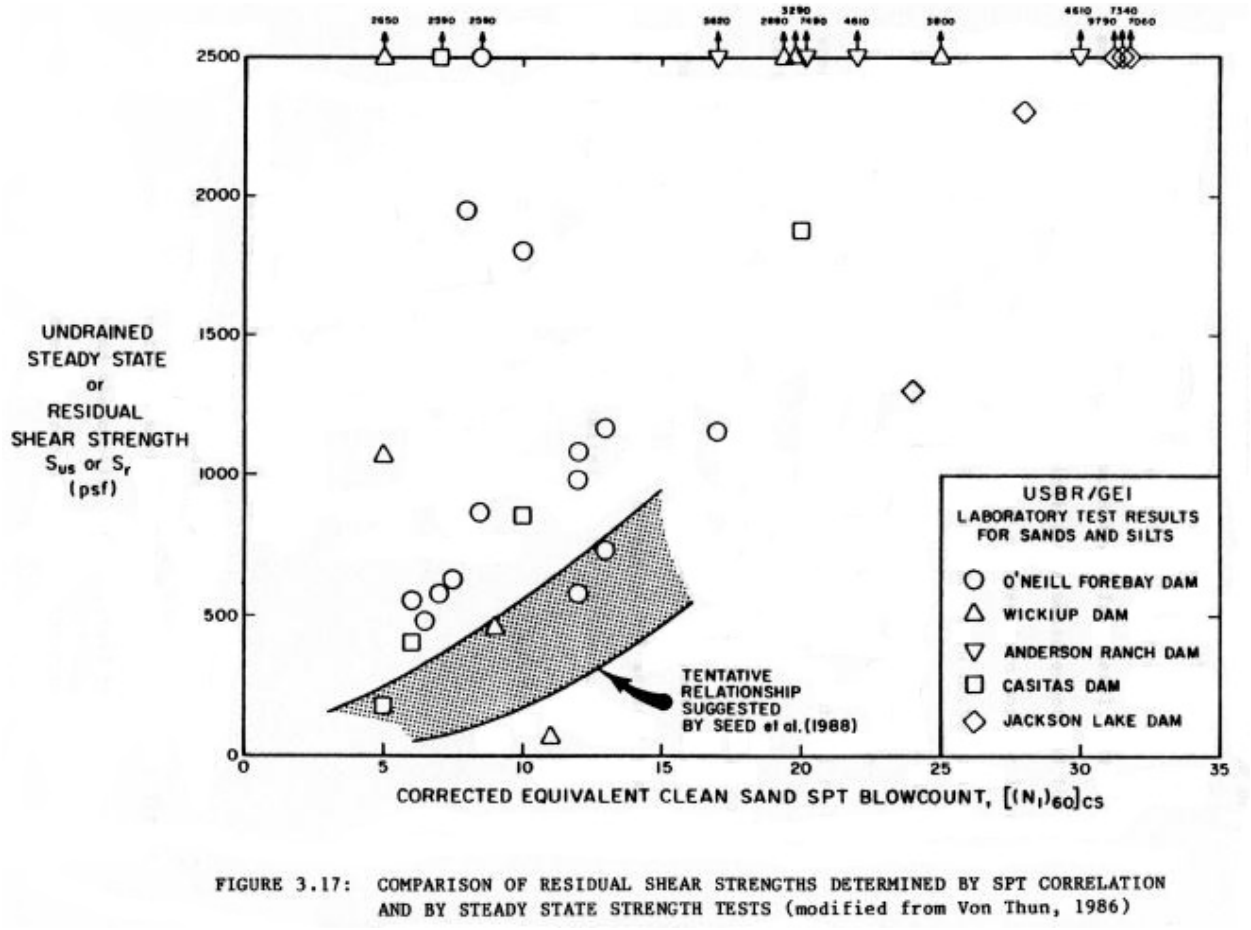

FIGURE 3.17: COMPARISON OF RESIDUAL SHEAR STRENGTHS DETERMINED BY SPT CORRELATION AND BY STEADY STATE STRENGTH TESTS (modified from Von Thun, 1986)

Figure 2.5: Values of estimated in situ steady state strength (S_r) developed by GEI, Inc. based on the laboratory-based steady state method of Poulos et al. (1985) for five U.S. Bureau of Reclamation dams. (Figure from Harder, 1988; modified after Von Thun, 1986)

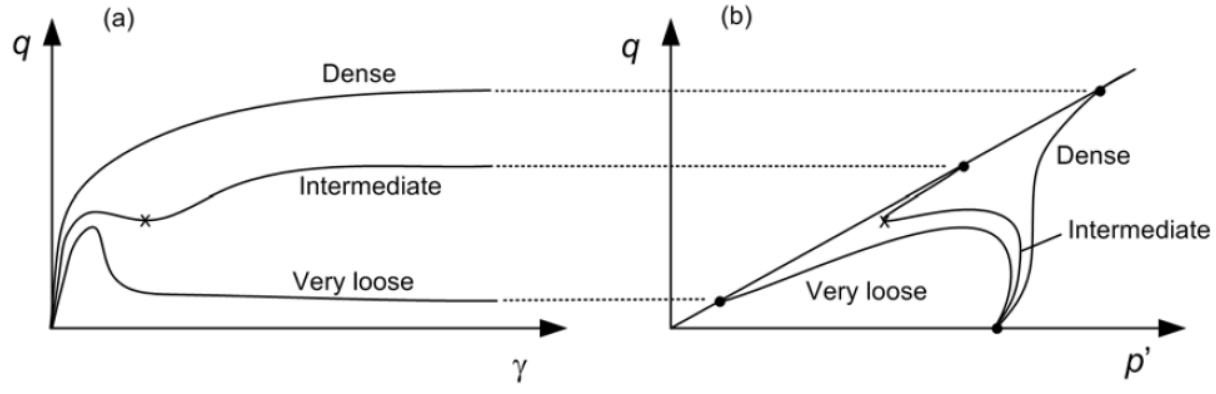

Figure 2.6: Simplified schematic illustration of stress-strain and stress path behaviors of sands of different relative densities under monotonic loading. (Figure from Kramer, 2008)

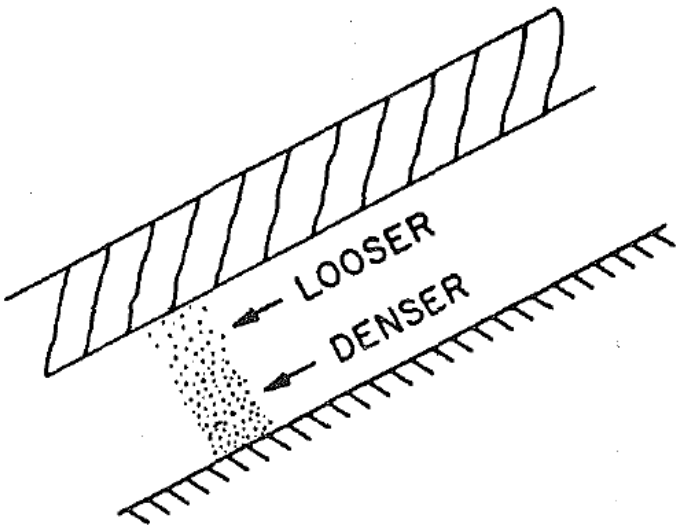

Figure 2.7: Simplified illustration of void redistribution within a confined soil stratum (National Research Council, 1985).

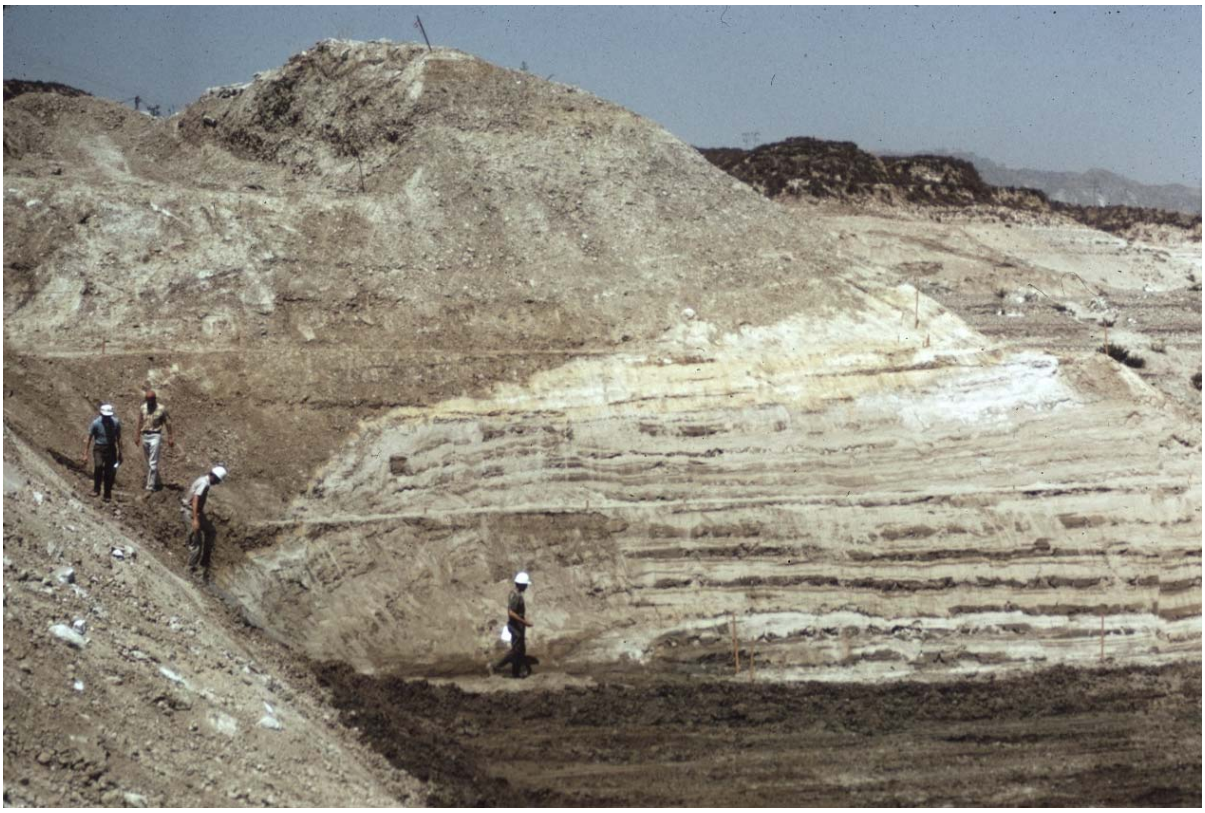

Figure 2.8: Photograph showing layering in the hydraulic fill of the Lower San Fernando Dam (photo by the California Department of Water Resources).

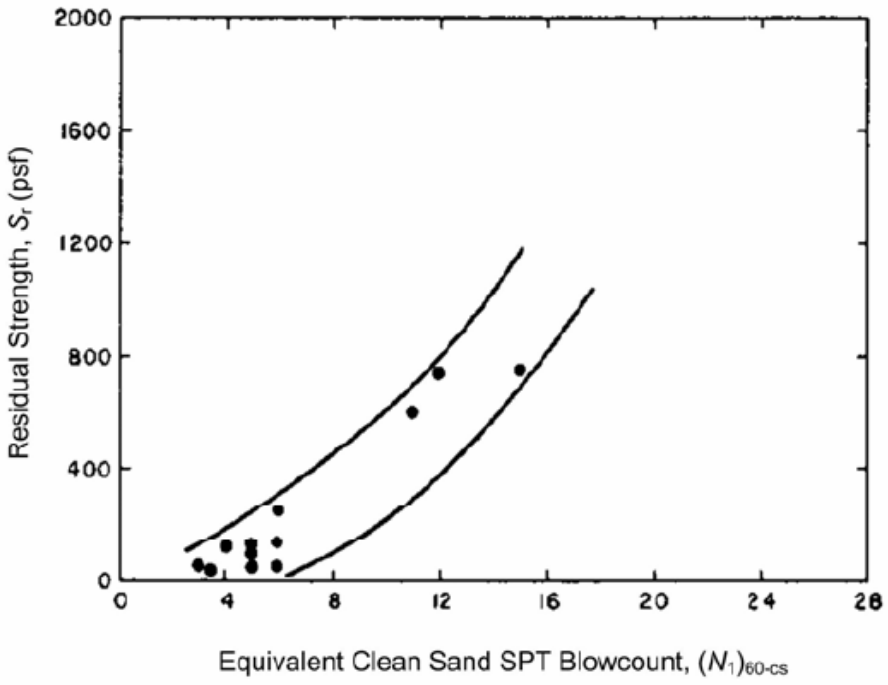

Figure 2.9: Variation of post-liquefaction residual strength Sr as a function of fines adjusted SPT penetration resistance $(N_1)_{60\text{-}CS}$ (Seed, 1987).

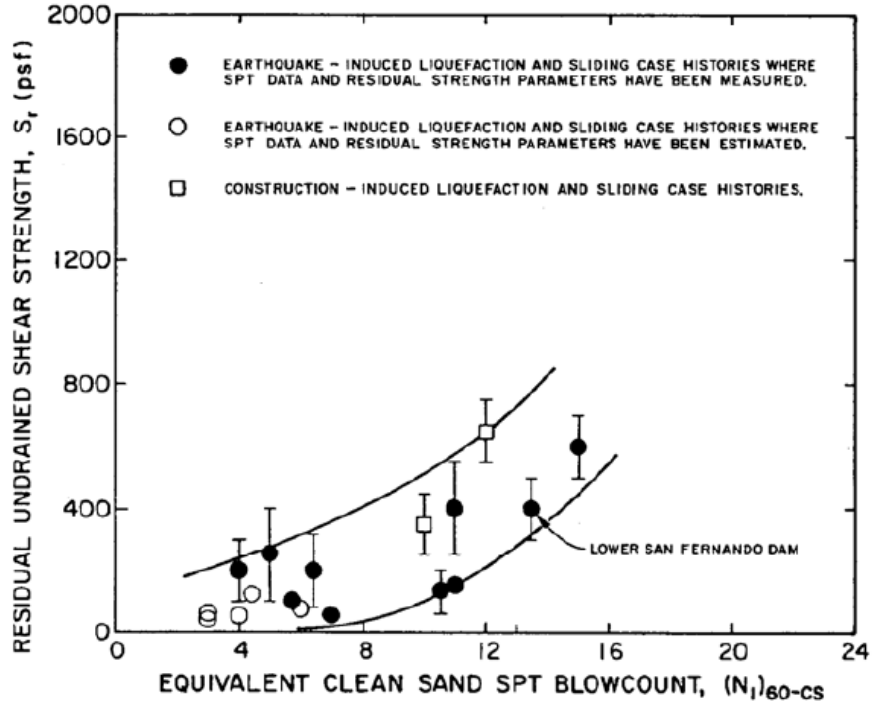

Figure 2.10: Variation of post-liquefaction residual strength S_r as a function of fines adjusted SPT penetration resistance $(N_1)_{60\text{-}CS}$ (Seed and Harder, 1990).

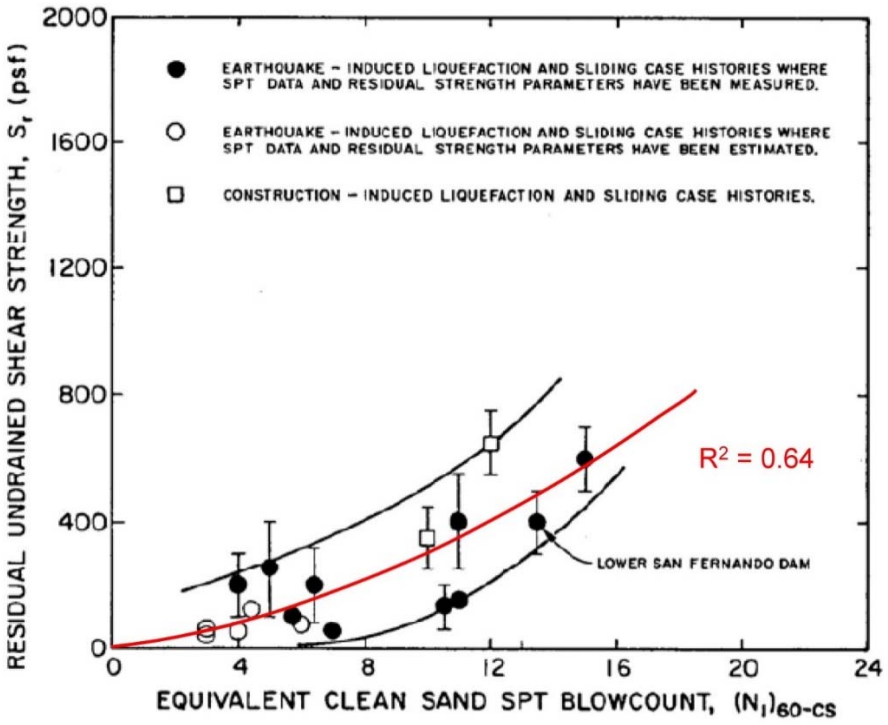

Figure 2.11: Figure 2.10 repeated, this time showing a least squares regression of the data.

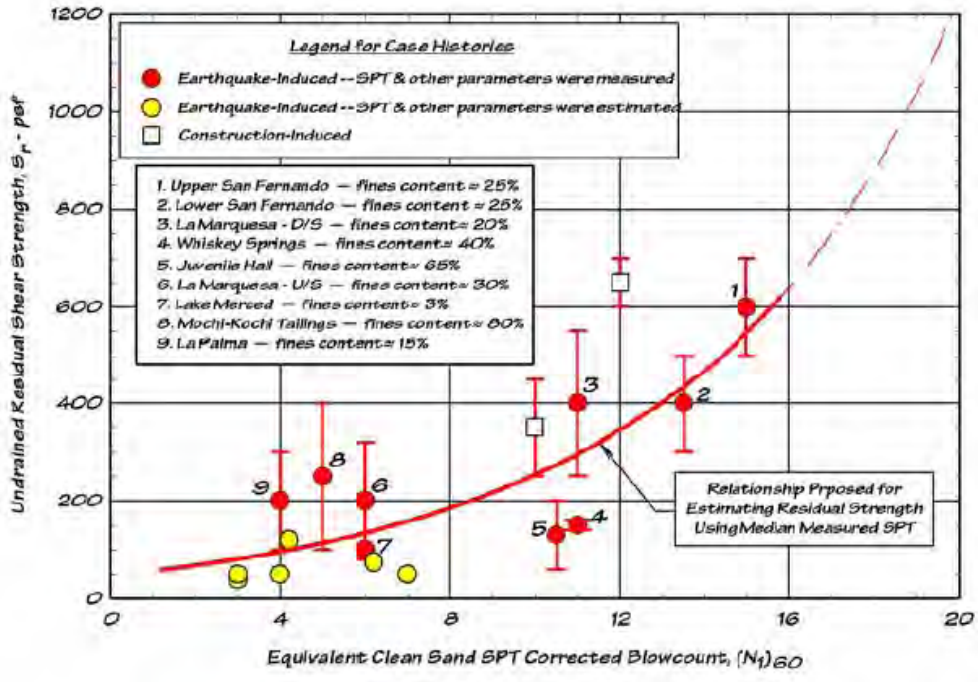

Figure 2.12: Variation of post-liquefaction residual strength S_r as a function of fines adjusted SPT penetration resistance $(N_1)_{60\text{-}CS}$. (Idriss, 1998)

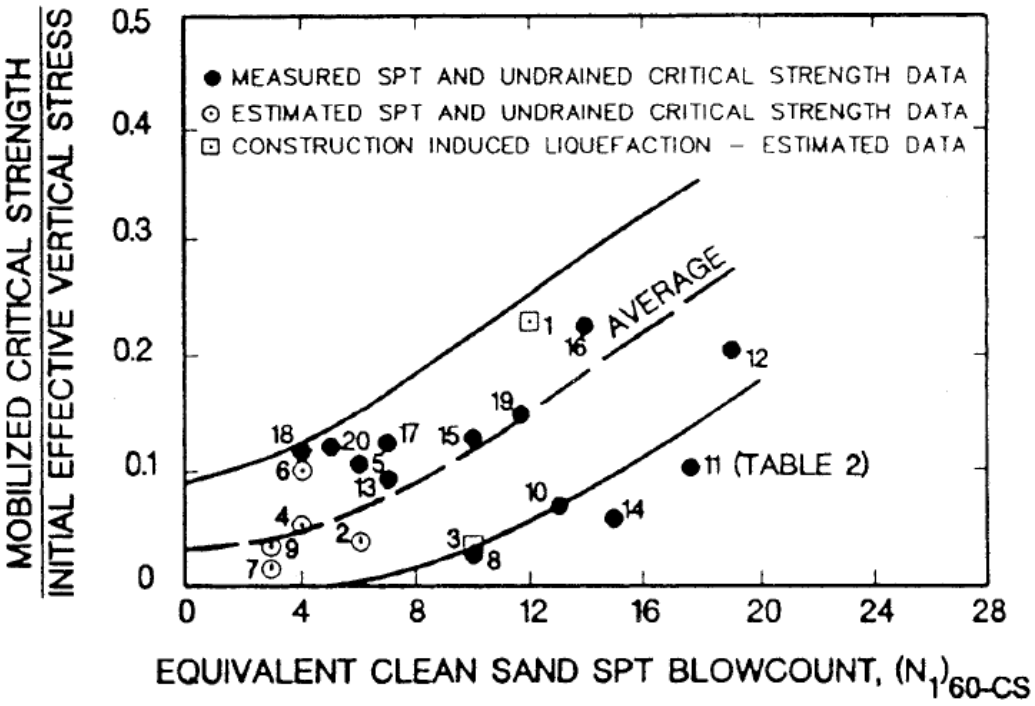

Figure 2.13: Variation of post-liquefaction residual strength ratio (S_r/P) as a function of fines adjusted SPT penetration resistance $(N_1)_{60\text{-}CS}$ (Stark and Mesri, 1992).

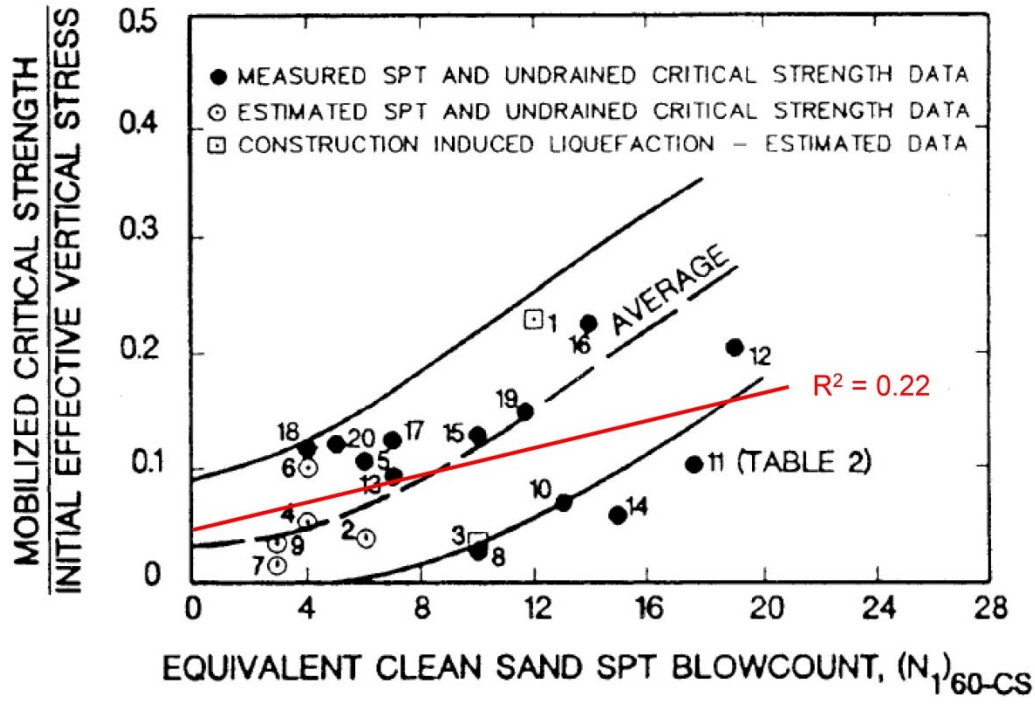

Figure 2.14: Figure 2.13 repeated, this time showing the results of a least squares regression.

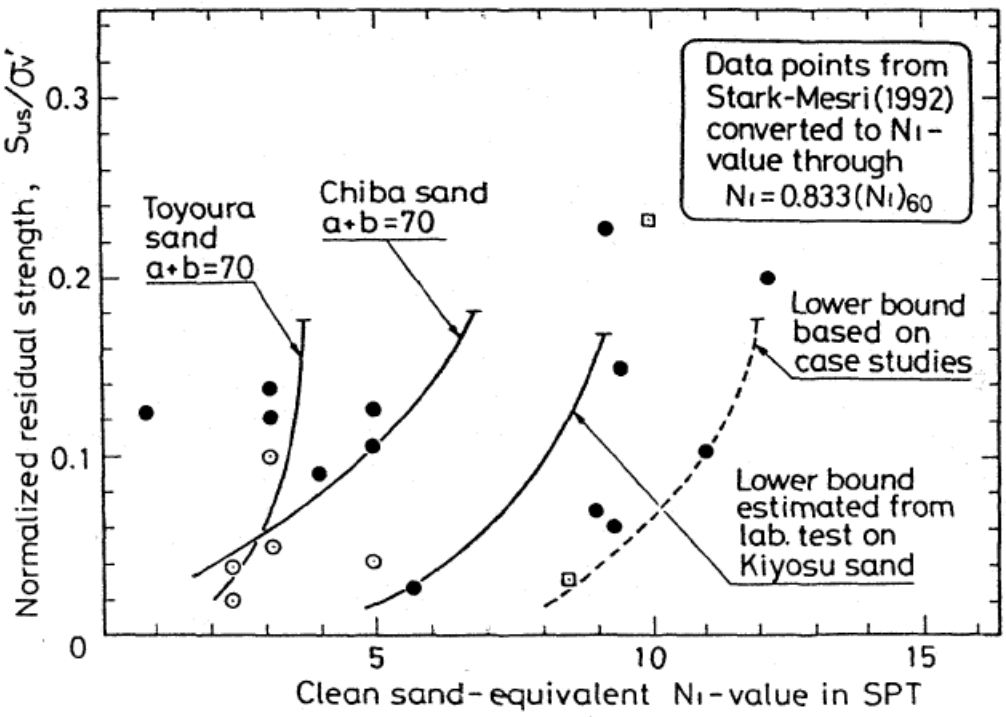

Figure 2.15: Ishihara (1993) relationship between quasi-steady state strength ratio $S_{u,s}/P$ and $(N_1)_{60}$, and comparison with values calculated by Stark and Mesri (1992).

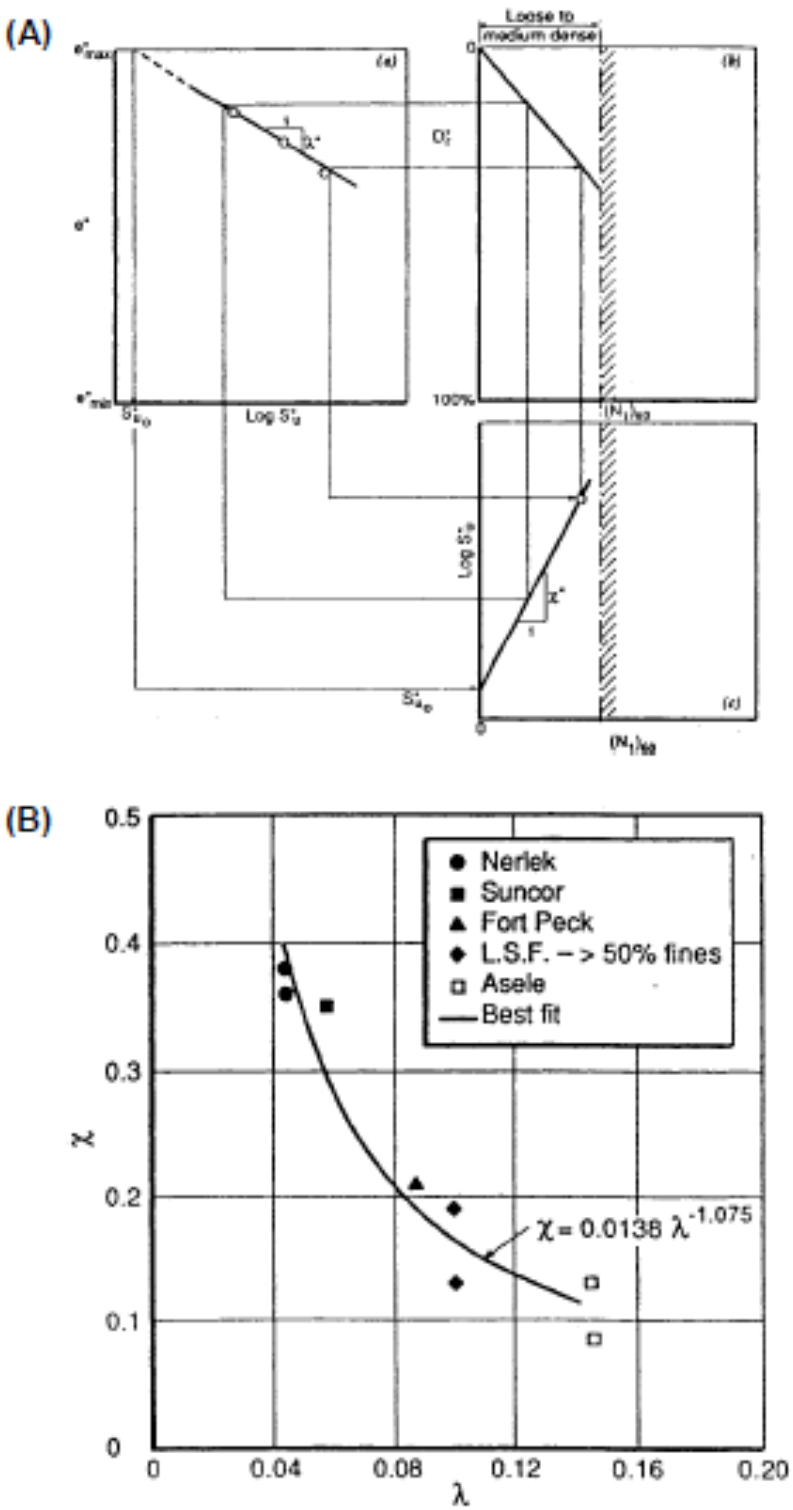

Figure 2.16: Derivation of the calibration factor χ as a function of λ, based on five back-analyzed field failure case histories (Konrad and Watts, 1995).

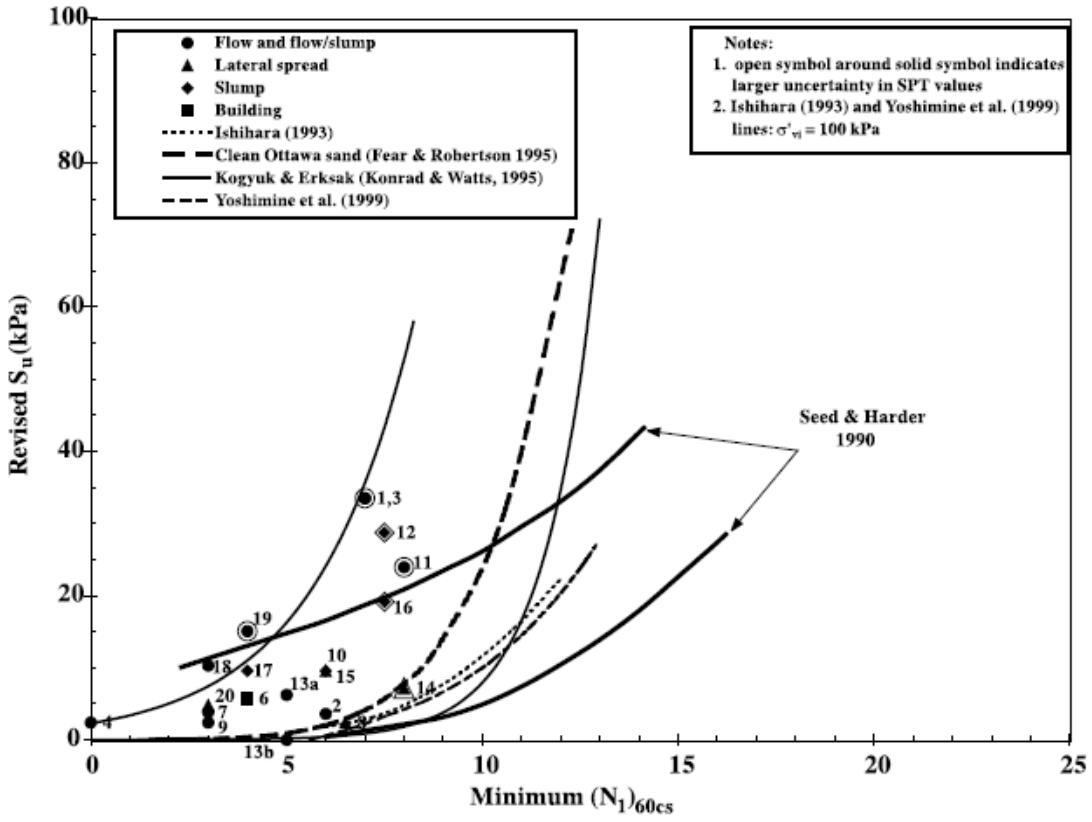

Figure 2.17: Re-evaluated data points (S_u and $N_{1,60,CS}$) for 19 failure case histories, and selected relationships proposed by previous investigators. (Wride et al., 1999)

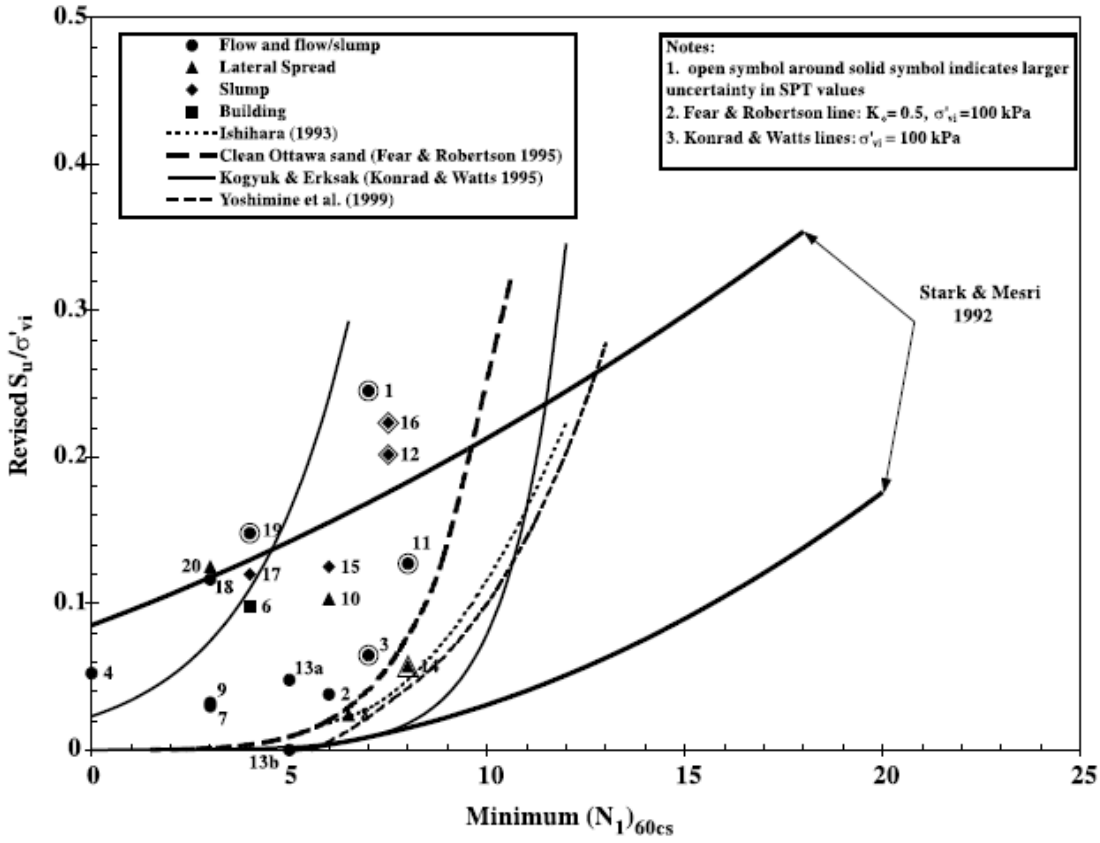

Figure 2.18: Re-evaluated data points (S_u/P and $N_{1,60,CS}$) for 19 failure case histories, and selected relationships proposed by previous investigators (Wride et al., 1999).

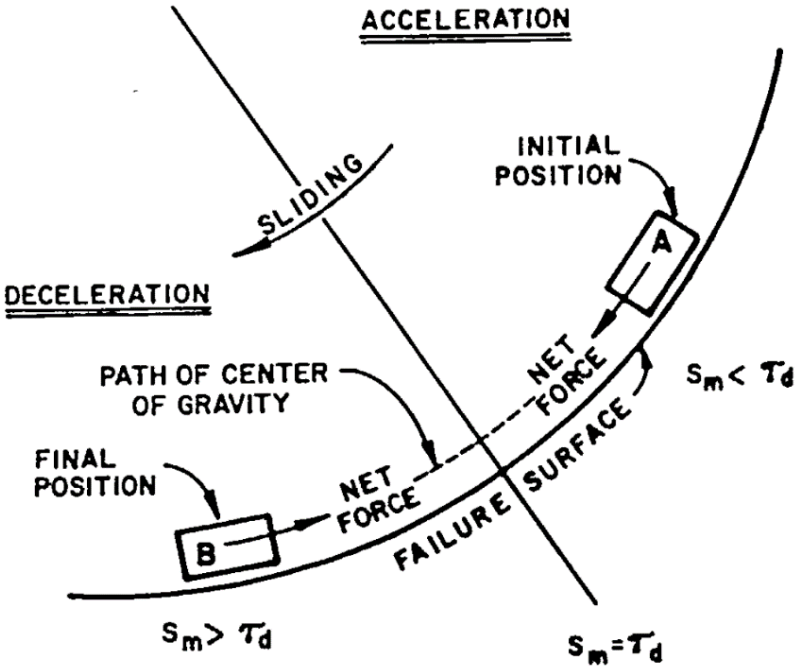

Figure 2.19: Schematic illustration of failure dynamics showing the progression of a mass moving downslope and the net forces on the base shear surface as the mass initially accelerates downslope, and then decelerates and comes to rest (Davis et al. 1988).

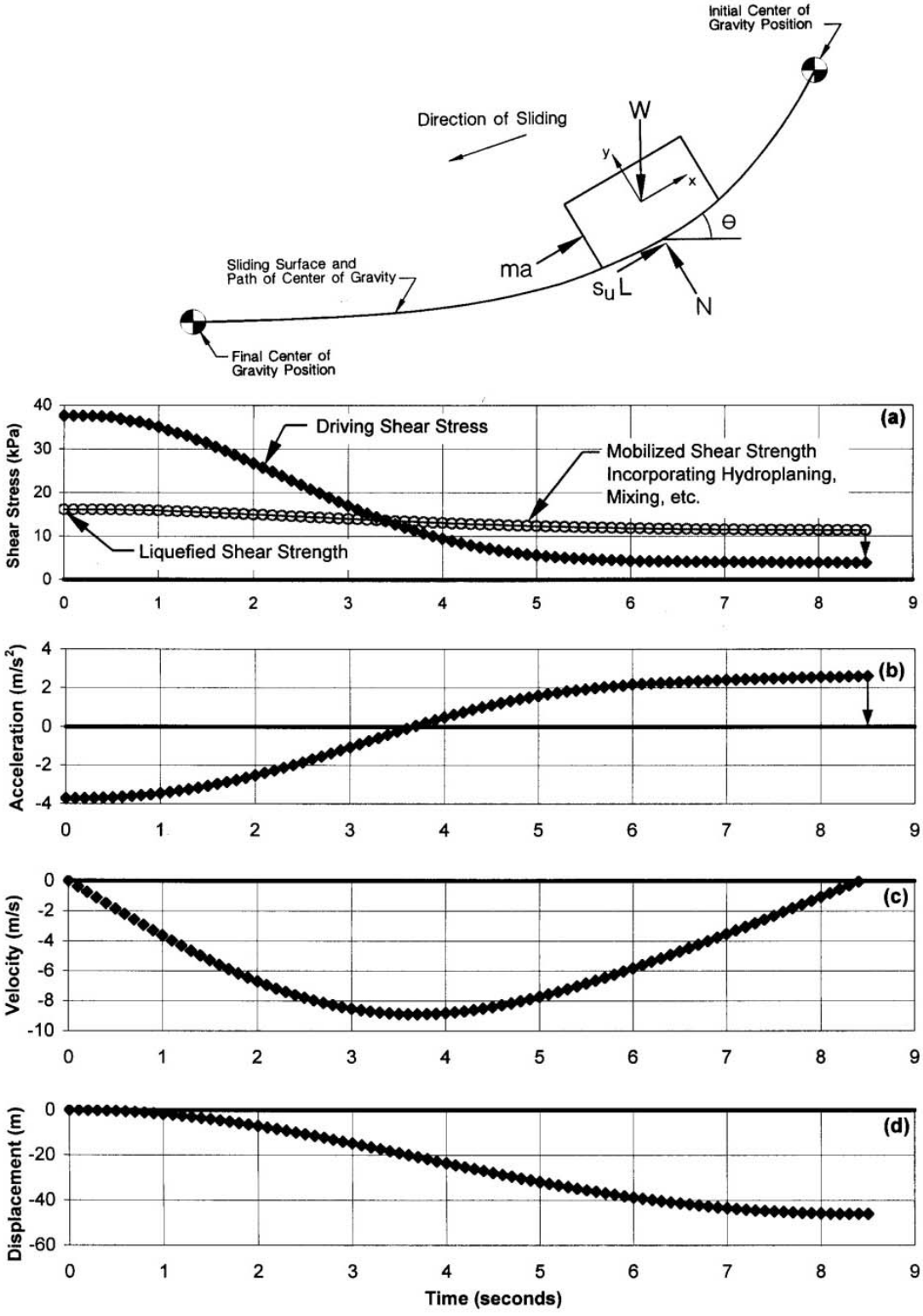

Figure 2.20: Schematic illustration of Olson's "kinetics" analysis of the failure of the upstream slope of Wachusett Dam (Olson, 2001).

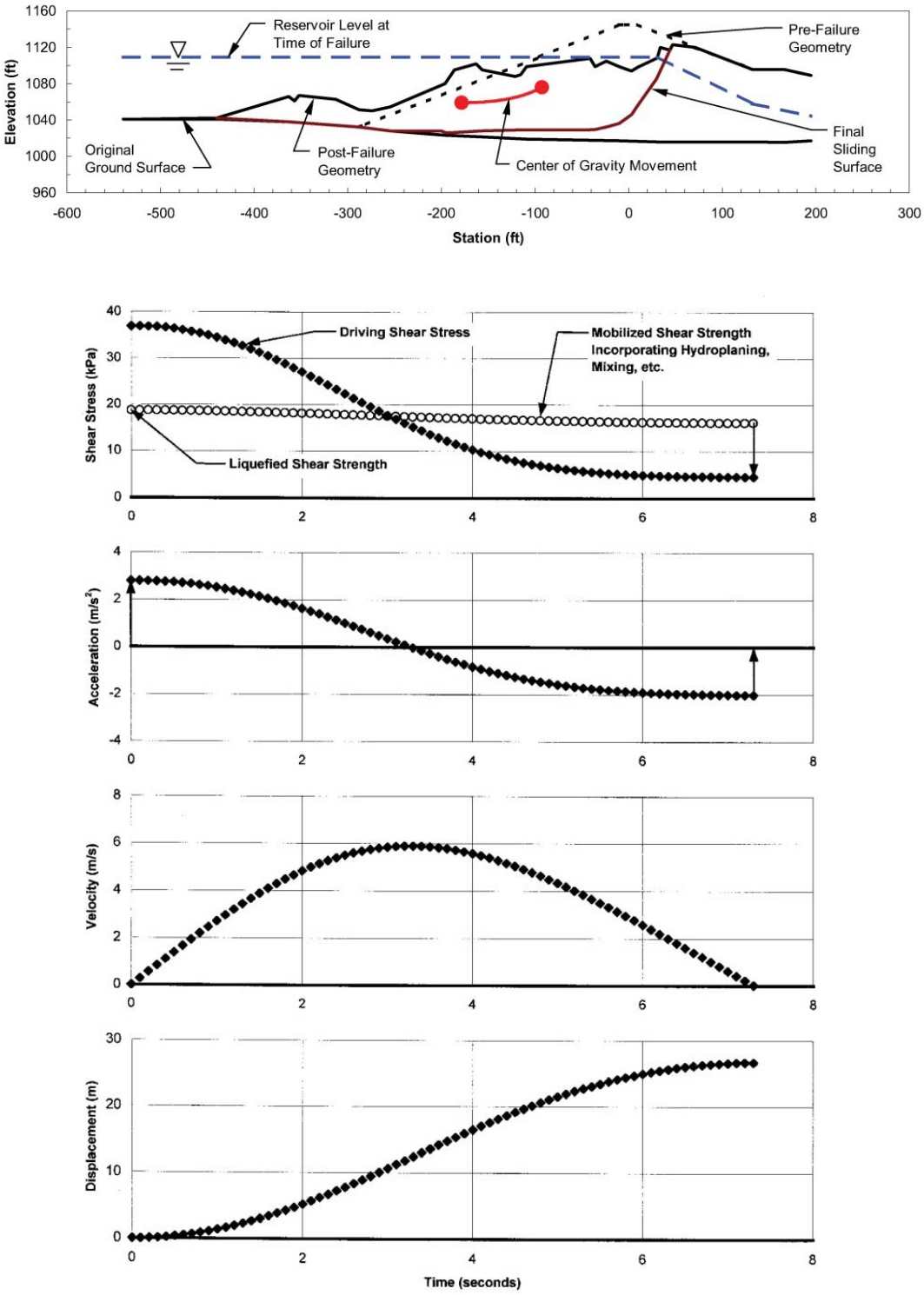

Figure 2.21: Illustration of "kinetics" analysis of the failure of the upstream slope of the Lower San Fernando Dam (Olson, 2001).

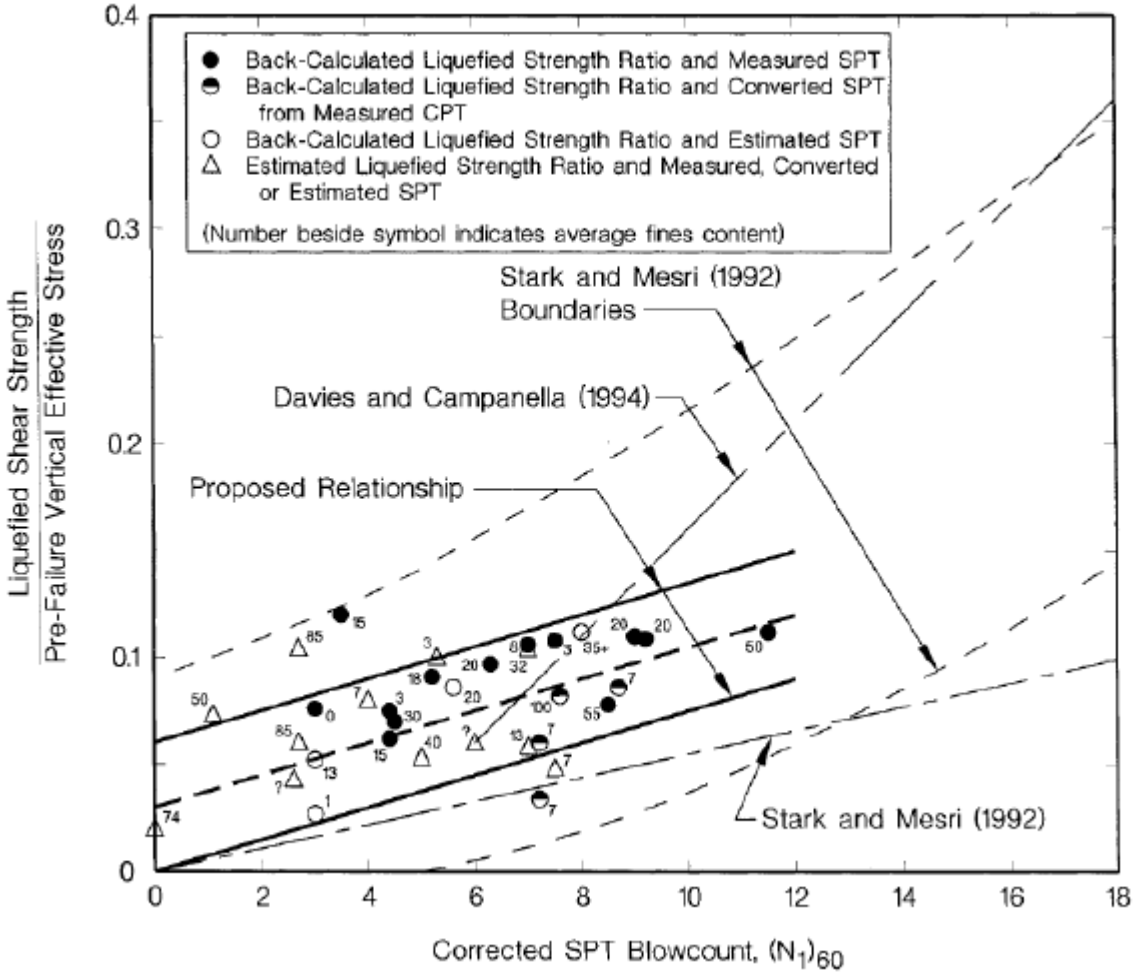

Figure 2.22: Recommended relationship for estimation of normalized residual strength ratio as a function of SPT penetration resistance (Olson and Stark, 2002)

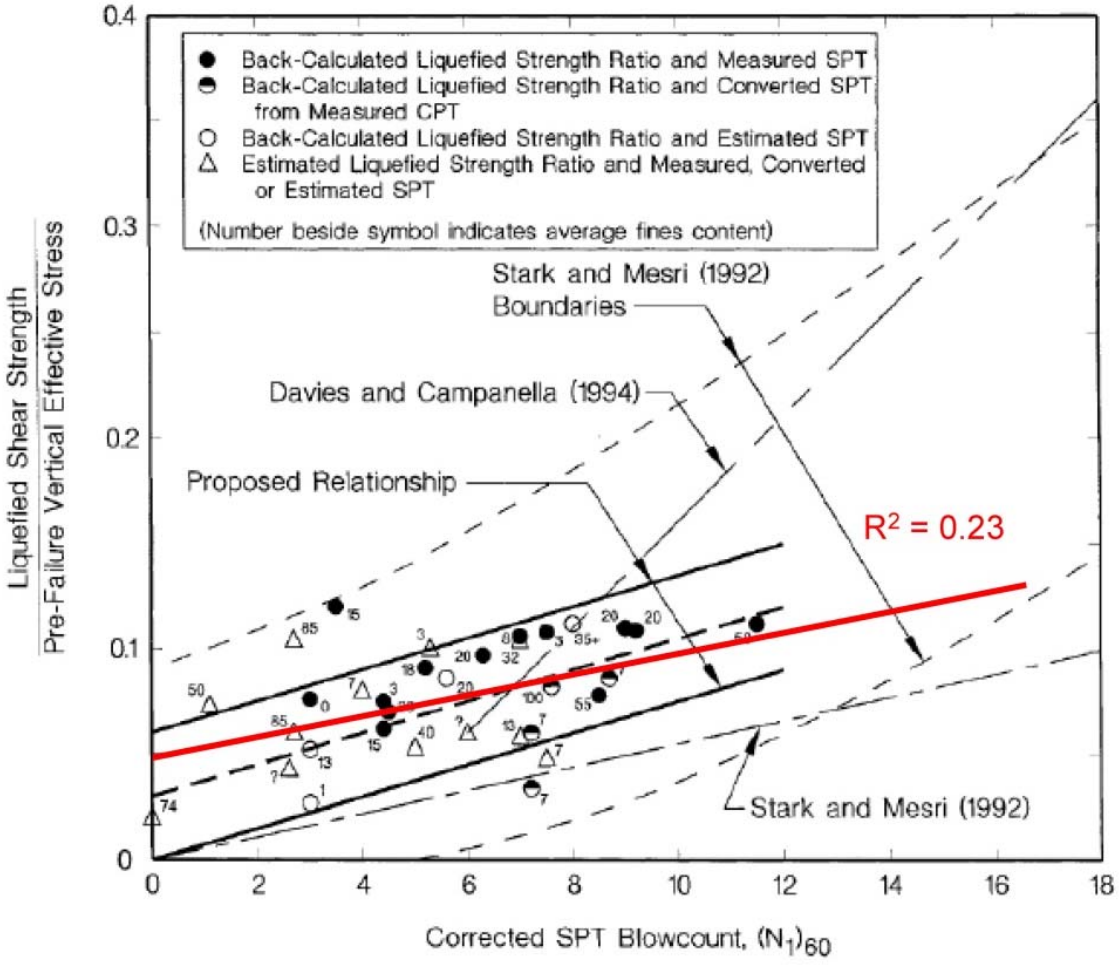

Figure 2.23: Least squares regression of the data set developed by Olson and Stark from Figure 2.22.

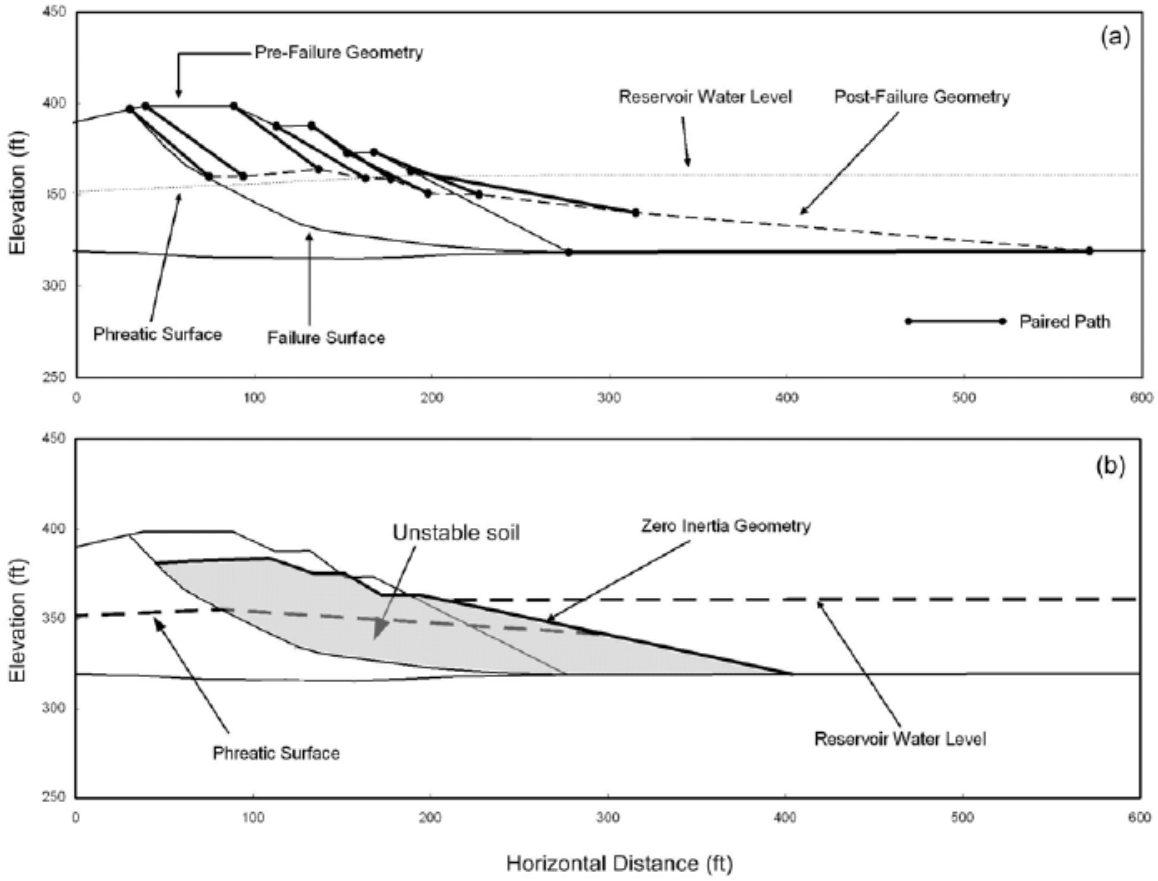

Figure 2.24: Illustration of the procedure employed by Wang (2003) for estimating zero inertial geometry (Figure from Kramer, 2008, after Wang, 2003)

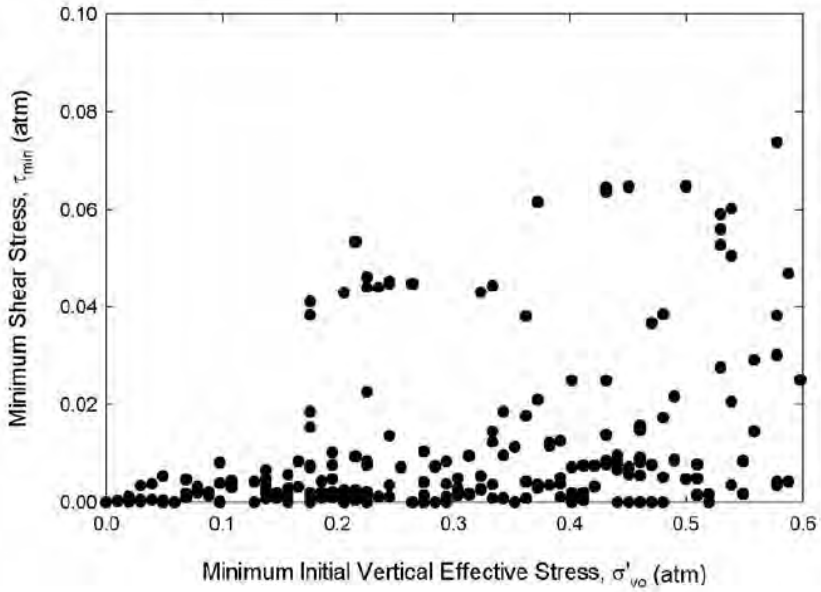

Figure 2.25: Combinations of minimum shear stress and minimum initial vertical effective stress from database of shallow lateral spreading case histories (Kramer, 2008).

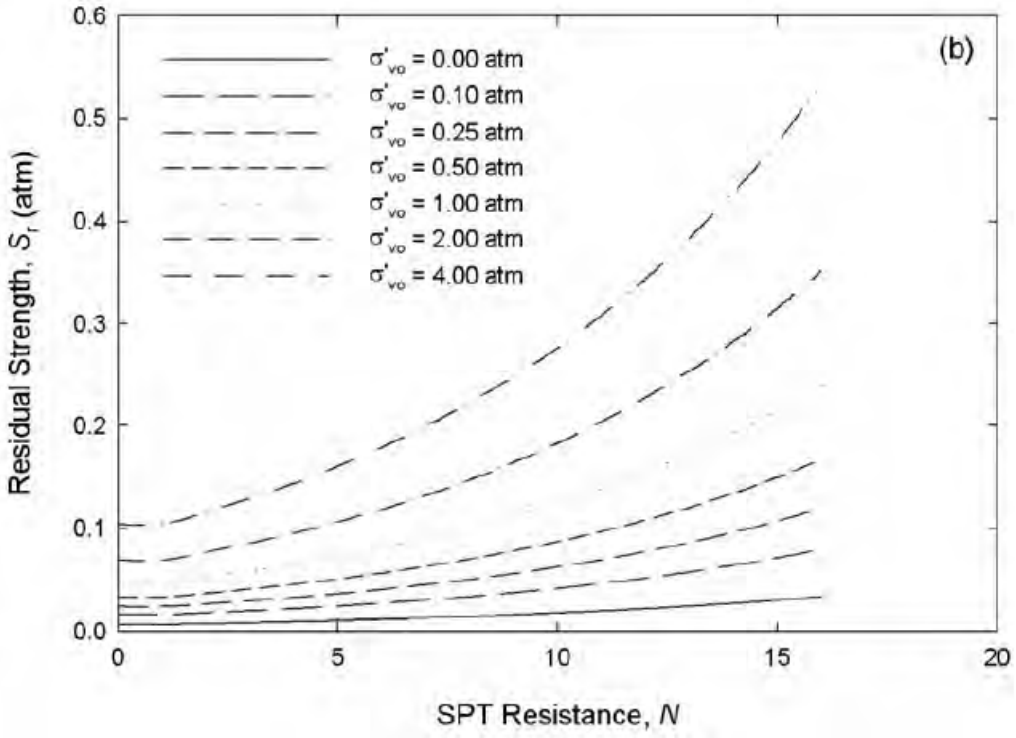

Figure 2.26: Median residual strength curves based on SPT resistance and initial effective vertical stress (Kramer, 2008).

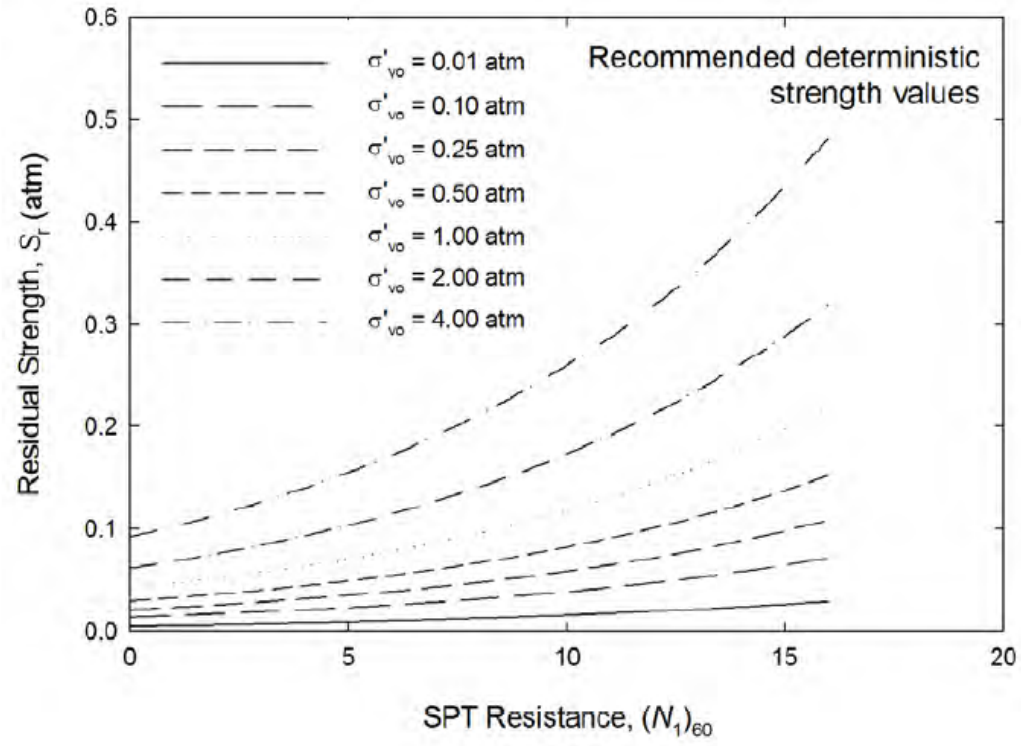

Figure 2.27: Recommended deterministic residual strength curves based on SPT resistance and initial effective vertical stress (Kramer, 2008).

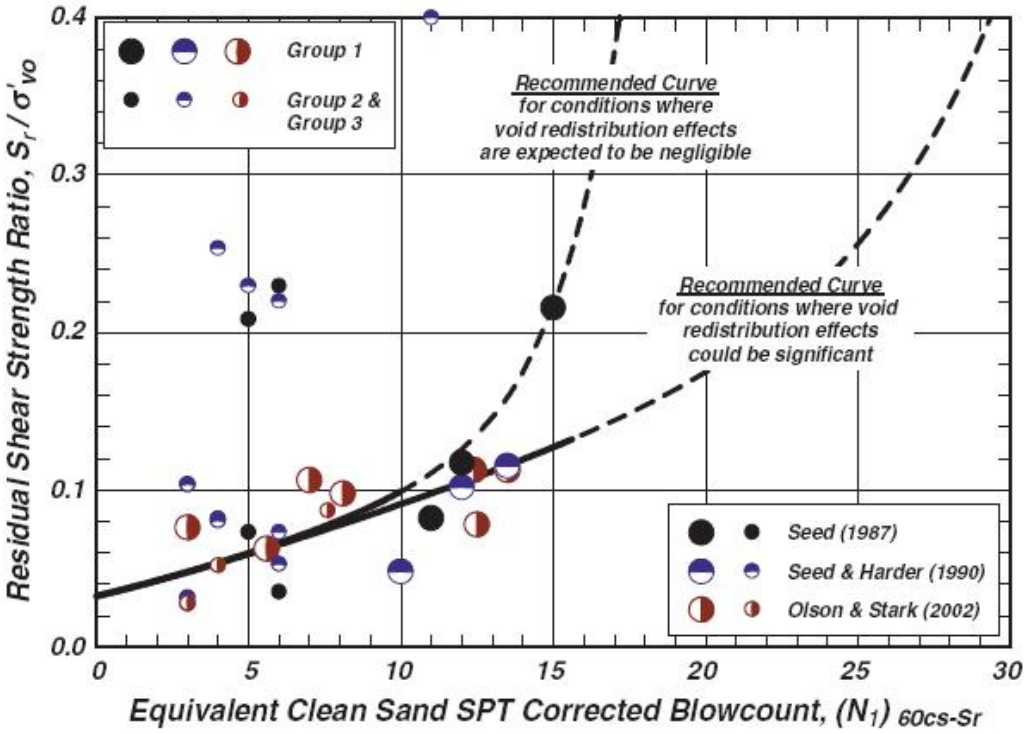

Figure 2.28: Recommended relationship for estimation of normalized residual strength ratio as a function of SPT resistance (Idriss and Boulanger, 2008)

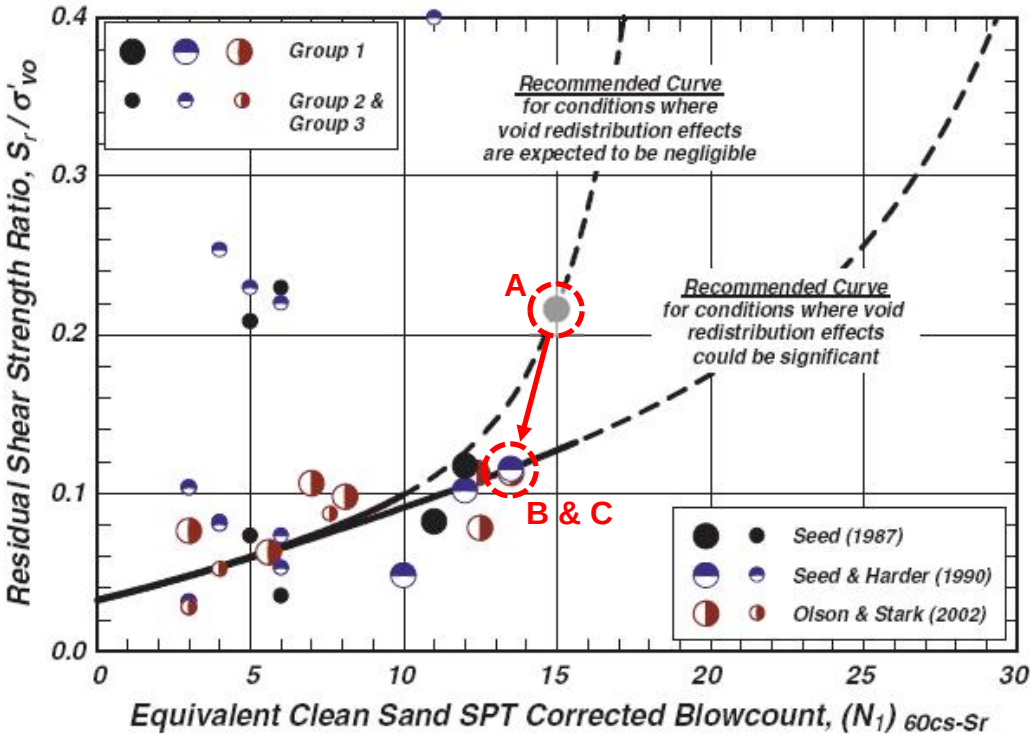

Figure 2.29: Figure 2.28 repeated, showing relocation of the data point for the Lower San Fernando Dam.

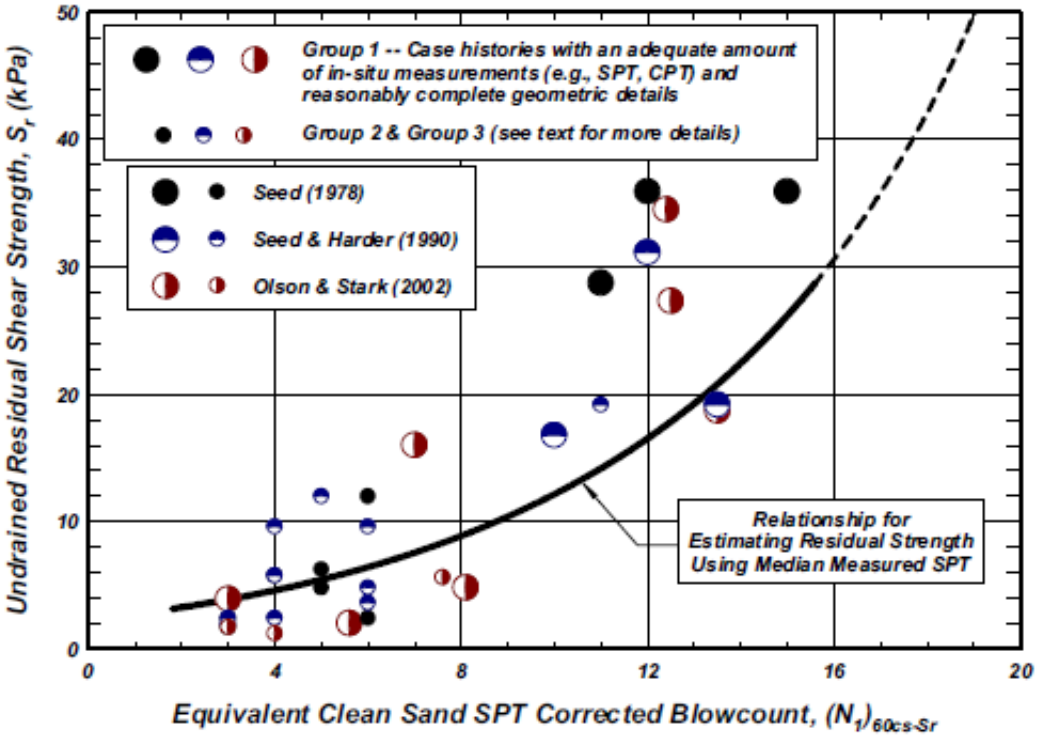

Figure 2.30: Recommended relationship for estimation of residual strength as a function of SPT resistance (Idriss and Boulanger, 2008)

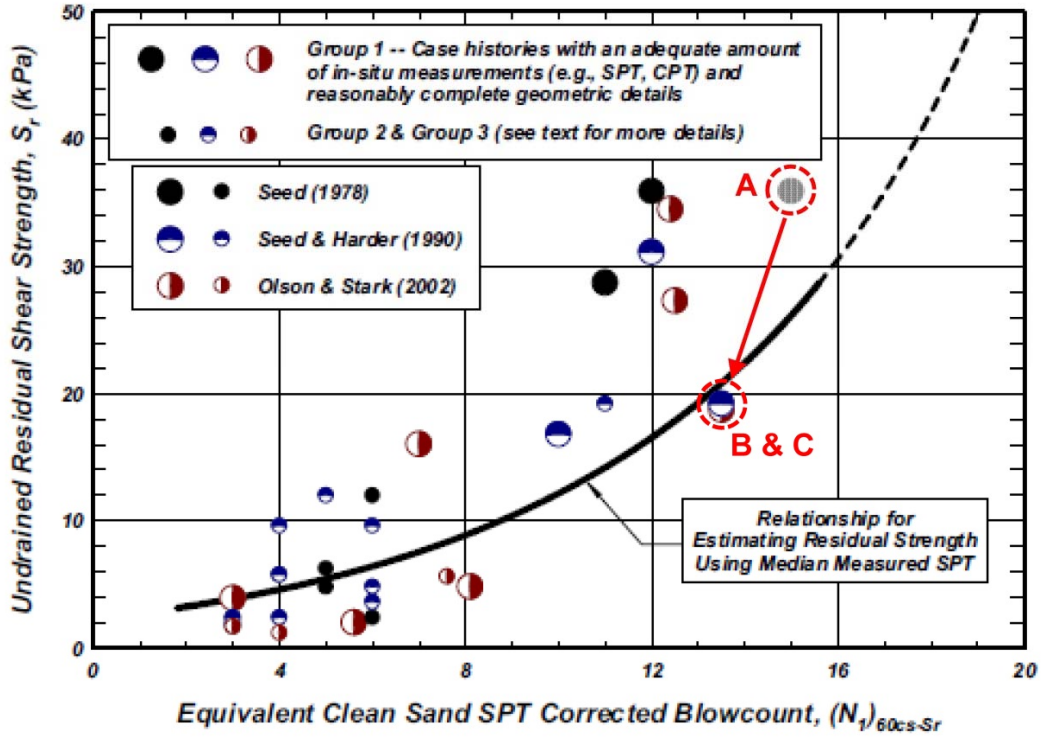

Figure 2.31: Figure 2.30 repeated, showing relocation of the data point for the Lower San Fernando Dam.

Chapter Three

Review and Selection of Liquefaction Case Histories for Back-Analyses

3.1 Introduction

The selection of full-scale liquefaction case histories to be back-analyzed for purposes of development of empirical methods for evaluation of in situ post-liquefaction strengths represents an important set of judgments and decisions.

A large number of previous investigations, and experts, have (a) back-analyzed sub-sets of the available case histories, or (b) employed the results of back-analyses performed by other investigation efforts, in their own development of empirical approaches for evaluation of post-liquefaction strengths. Different decisions, and different selections, were made by various investigators. In some cases (early efforts) there were only a limited number of potential field case histories available, so selections were often made on the basis of attempting to optimize use of these limited opportunities.

In more recent investigations (after about the mid-1990's), selection or de-selection of cases for back-analyses or for inclusion in development of empirical relationships were more often made on the basis of one or more of the following considerations:

1. Perceived availability, quality and documentation of information regarding pre-failure and post-failure geometry and conditions. In addition to basic geometry and stratigraphy, this also includes information constraining the location of the phreatic surface at the time the failure occurred.
2. Perceived quality and/or availability of information or data available for characterization of the soil units suspected of having liquefied. Highest quality data here were generally considered to be well-documented SPT or CPT data. Lesser quality data were sparse penetration data, non-standard penetration data, and cases in which penetration resistance had to be inferred more qualitatively from apparent relative density, soil placement history, etc.
3. Additional data and information, including witness accounts, information and data regarding soil properties (unit weights, strength parameters, etc.) for both liquefied and non-liquefied soils, etc.
4. Tractability of the observed (or suspected) failure mechanism with regard to relatively accurate and reliable back-analysis for the specific purpose of assessment of post-liquefaction strength S_r.
5. Personal preferences. For example some previous efforts preferred to consider only cases in which CPT data were available.

Not all previous studies presented clear explanations as to the reasons for selection and de-selection of case histories considered and/or back-analyzed.

Some level of general consensus can be inferred by the common choices made by a significant number of previous investigators with regard to a number of the available case histories. But as new information has developed, some of these choices now appear less attractive (e.g. the Calaveras Dam case history).

In these current studies, the full suite of case histories considered to date were fully re-considered, with (1) understanding of the decisions and selections made by previous investigation teams, (2) the benefits of examination and review of previous back-analysis efforts and of previously developed approaches for assessment of in situ post-liquefaction strength (see Chapter 2), and (3) new information that appears to have been developed recently and that was therefore not available to a number of investigation teams (e.g. the Calaveras Dam case history).

Table 3.1 presents a listing of the field liquefaction case histories back-analyzed, or included in empirical correlations, by a select sub-set of six previous investigation efforts. These six previous efforts were selected for presentation in this table because (1) they were notably comprehensive efforts with regard to inclusion of case histories at their time, and (2) between them they comprise a list of essentially all potentially useful cases currently available for purposes of back-analyses to evaluate in situ S_r.

3.2 Lateral Spreading Case Histories

Having noted the relative paucity of available case histories of large-displacement liquefaction failures, Olson and Johnson (2008) back-analyzed a significant number of lateral spreading case histories, many of them from the lateral spreading case history database assembled by Youd et al. (2002), as discussed previously in Section 2.3.9. Youd et al. had compiled this database for purposes of developing empirical methods for prediction of lateral spreading displacements. Olson and Johnson employed simplified Newmark-type methods to attempt to back-analyze the lateral spreading case histories to extract estimates of post-liquefaction strength. One of the principal findings was the difficulty of extracting reliable estimates of back-calculated S_r for cases (lateral spreads) wherein the overall movements included a strong contribution from transient cyclic lurching forces.

Lateral spreads are differentiated from the other (and generally larger displacement) cases in these current studies as being cases in which relatively moderate levels of gravity-induced static "driving" shear stresses do not, by themselves, generate a large majority of the observed movements and displacements. Instead, transient cyclic seismic loading, and resulting "cyclic lurching" forces, are also an important contributor. These cyclic forces are difficult to accurately back-analyze for several reasons. One reason is that simplified Newmark-type analysis methods do not provide a high degree of precision here. Another difficulty is the importance of details of the transient seismic loads (e.g. acceleration time histories) that actually occurred at the site in question. A potentially high degree of sensitivity of calculated displacements to these details contributes significantly to the uncertainties involved in back-analyses of these lateral spread case histories for purposes of back-estimation of S_r.

Accordingly, it was determined in these current studies that cases wherein transient cyclic lurching forces appear to be of sufficient importance as to potentially obscure, or prevent reliable assessment of, post-liquefaction strengths would not be included in the data set.

In addition to the lateral spreading cases added by Olson and Johnson (2008), a number of additional lateral spreading cases collected and processed by Faris (2004) specifically for the purpose of developing relationships for prediction of lateral spreading displacements were also examined.

The semi-empirical method for prediction of lateral spreading displacements developed by Faris (2004) was developed specifically for use with cases of limited "lateral spreading-type" displacements in which cyclic lurching forces contributed significantly to overall deformations and displacements. These are cases in which post-liquefaction overall stability has a Factor of Safety greater than 1.0 in the absence of cyclic lurching forces, so that it is primarily cyclic lurching forces (which produce transient periods of time during which the Factor of Safety is temporarily less than 1.0; during which displacements occur) that "drive" observed displacements.

The Faris (2004) semi-analytical method was inverted, and was used as a preliminary screening process to assess the potential usefulness of these lateral spreading cases for purposes of back-evaluation of S_r. If observed field displacements did not significantly exceed those predicted by the Faris (2004) method, then that would represent a situation in which cyclic lurching forces contributed a significant portion of the overall observed displacements. For cases in which observed field displacements were not at least two times greater than those predicted by the Faris (2004) method, the case histories were deleted from the database for these current studies. For cases in which the observed field displacements were more than twice those predicted, but less than about three times greater, the cases were examined on an individual basis to determine whether or not they would be carried forward and included in these current studies.

Figure 3.1 illustrates the use of the Faris (2004) procedure for a typical case; the Shonan-Cho lateral spread which occurred during the 1983 Nihonkai-Chubu earthquake. As shown in the top left figure, a liquefaction triggering evaluation was made for each SPT $N_{1,60,CS}$ value measured within materials considered potentially liquefiable. Those judged likely to liquefy were then re-plotted in the upper right-hand figure on a plot showing shear strain potential as a function of (1) $N_{1,60,CS}$ and (2) equivalent uniform cyclic stress ratio (CSR_{eq}) for a causative event of $M_W = 7.5$. These shear strain potentials are based on laboratory isotropically consolidated and then undrained cyclic triaxial testing, and do not (yet) include effects of initial "driving" shear stresses. The resulting estimates of strain potential are then ascribed to the interval in each boring represented by the individuals $N_{1,60,CS}$ values, and accumulated displacement potential from bottom to top of the boring (up to the ground surface) is then calculated as shown in the plot of the right-hand middle figure. In this figure, depth ranges over which liquefaction strain potential are summed vary due to changes in overall thickness of the potentially liquefiable materials at different borehole locations within the overall lateral spreading feature. This results in an estimated "displacement potential index" (DPI) at the location of each SPT boring.

These estimated DPI values are not direct estimates of expected displacements; they are only indices of stiffness or deformability. Faris compiled these indices for a large number of field case histories, and then performed regressions to develop empirical correlations for prediction of

expected lateral spreading displacements as a function of (1) DPI, (2) initial static driving shear stresses (estimated in a simplified manner based on slope and/or free face height at the toe of a lateral spreading feature, and (3) earthquake magnitude (serving as an approximation of duration or number of cycles). Each value of DPI, for each boring, is then transformed using the regressed relationship, to develop values of predicted actual displacements at each boring location. This is shown in the bottom left-hand corner of the figure. The resulting calculated "predictions" of expected displacement are then averaged together to develop an average calculated displacement (or predicted displacement). The displacements actually observed in the field (ideally at the boring locations) are then also averaged to produce the average observed displacement. These averaged calculated and observed displacements are plotted in the figure in the bottom left-hand corner. The resulting overall average ratio of predicted vs. observed displacements is then calculated.

For this screening level exercise, it was determined that cases in which either (1) observed displacements were less than 3 feet, or (2) the ratio of observed vs. predicted displacements was less than a factor of 2, would be assumed to have had sufficiently significant cyclic lurching effects that it would not be appropriate to attempt to back-analyze them for purposes of trying to accurately discern post-liquefaction strength S_r. Cases only marginally exceeding these two limits would be more closely examined on an individual basis.

This screening level analysis was applied to all of the cases compiled by Olson and Johnson (2008), and to the cases compiled by Faris (2004), for purposes of development of empirical relationships for prediction of lateral spreading displacements. Of the few cases where the ratio of displacements observed vs. those predicted was greater than 2, most had overall (average) displacements of less than 3 feet.

One case that came close to being carried forward for further back-analysis was the Shitayama School lateral spread from the 1964 Niigata earthquake. This case had an observed average displacement of 12.2 feet, and an average calculated (predicted) displacement of 5.4 feet based on Faris' semi-empirical method. The resulting ratio was then 12.7 ft. / 5.4 ft. ≈ 2.4. This case was then examined further, and the engineering team determined that we would not be confident that cyclic inertial effects did not contribute significantly to observed displacements at this site due to (1) the relatively moderate pre-earthquake static driving shear stresses, and (2) the estimated intensity and duration of strong shaking at this site.

In the end, only two of the "lateral spreading" case histories from either the Youd et al. (2002) database examined by Olson and Johnson (2008) or from the additional cases developed by Faris (2004) were carried forward for further consideration in these current studies of post-liquefaction S_r. These were the San Fernando Valley Juvenile Hall lateral spread case history, and the Whiskey Springs Fan case history, and these will be discussed further in Sections 3.3.3.4 and 3.3.3.5, respectively.

3.3 Remaining Potential Candidate Liquefaction Case Histories

3.3.1 Separation of Case Histories into Groups Based on Assessed Quality and Reliability

With most of the lateral spreading case histories thus eliminated, 36 potential candidate cases remained. These are listed in Table 3.2. When available, the results of back-analyzed values

of post-liquefaction strength, or post-liquefaction strength ratio, as well as representative vertical effective stress and SPT penetration resistance are presented, as developed by (1) Seed and Harder (1990), (2) Olson and Stark (2002), and (3) Wang and Kramer (2003 and 2008).

After studying these cases, they were sub-divided into four groups: Groups A, B, C and D, as shown in Table 3.2.

Group A case histories were judged to be generally of the highest quality with regard to well-documented data and information regarding (1) pre-failure and post-failure geometry, (2) penetration resistance within the critical liquefiable materials, and (3) other details including phreatic surface at the time of failure, shear strengths of non-liquefied soils, etc. These 13 case histories were judged to warrant the application of the incremental momentum back-analysis methods described in Chapter 4, Section 4.2, to develop best possible estimates of post-liquefaction strengths.

The 16 case histories of Group B were judged to have lesser quality data, or less well-documented data, than the Group A cases, leading to greater uncertainties. These cases were judged not to warrant the performance of full incremental momentum analyses, but it was judged that useful estimates of post-liquefaction strength could be made, and useful estimates of representative penetration resistance and of representative vertical effective stress as well. Uncertainties associated with these values would generally be expected to be higher than for Group A cases.

The single Group C case history (Calaveras Dam) was also judged to have high quality data and information regarding geometries, etc., needed for high-level back-analyses to evaluate post-liquefaction strength, and so it was also back-analyzed using the incremental momentum methodology. But this case was <u>not</u> then subsequently used to help to develop empirical relationships for evaluation of in situ post-liquefaction strength, as will be explained further in Section 3.3.2.

The six cases of Group D had all been used in one or more previous studies, but upon detailed review and assessment these were deleted from further consideration as explained in Section 3.3.3.

3.3.2 The Calaveras Dam Case History

This case had been a prominent case history in the works of multiple previous investigation teams. But information developed in the late 1990's as part of seismic investigations of the repaired dam showed clearly that many of the embankment's hydraulic fill materials had a significant clay content. The main (pre-failure) dam was being constructed by the hydraulic fill method, with hydraulic deposition of fill materials simultaneously from the upstream and downstream sides, and was nearing completion when the failure occurred in 1918. These fill materials were sourced form weathered colluvium on the local hillsides, and from weathered alluvium deposits also derived largely from the weathered colluvium. As shown in Figure 3.3 (and additional Figures in Appendix A, Section A.14), and Table 3.3, the resulting hydraulic fill

zones were complex in terms of the nature and distribution of materials (Olivia Chen Consultants, 2003).

The massive failure of 1918 occurred on the downstream side, and so the materials shown in Figure 3.3 on the downstream side of the dam represent the "post-repair" section, and not the original materials that controlled the failure.

In the current cross-section, the materials of Zones V and VI best represent (by approximate symmetry) the materials that would have principally controlled the 1918 failure. Materials in these zones are highly variable, and consist of broadly well-graded mixes of gravels, sands and clayey fines. Gravel contents vary greatly, and are often high enough as to warrant the use of Becker Penetrometer testing (BPT) as well as short-interval SPT (SPT performed with 1-inch blowcounts and then adjusted for apparent gravel effects, as described in Seed et al. (2003)), as part of the 1990's seismic investigations. Gravel contents generally ranged between approximately 20% to 55%, but variability was high enough that some portions of these same hydraulic fill zones were judged to be clearly "cohesive fines dominated". Fines contents also varied greatly, from very low to as high as 70% or more in some zones. The fines were mainly low to moderate plasticity clays (CL), with PI generally between approximately 15% to 25%.

The dam failed in 1918 as initial construction was nearing completion. As a result, these materials, and especially those comprised of sufficient clay as to be subject to significant consolidation, were still consolidating under the rising fill loads. These soils were likely variably underconsolidated, and conditions at the time of failure are not likely to be well-represented by the modern SPT or BPT penetration resistances obtained eight decades later. It is difficult to reliably predict the effects of (1) additional consolidation over the past eight decades for these hydraulic fill materials, some of which were cohesive fines-dominated materials subject to potentially significant consolidation strength gains, and (2) ageing effects over eight decades in these highly variable and challenging mixed soils. As a result, it was the reluctant conclusion of this current investigation team, and with the unanimous concurrence of the informal advisory group of experts that assisted on this overall investigation, that it is not reasonable to attempt to correlate back-calculated strengths from this failure with available penetration resistance data.

This does not mean that this is a poor case for back-analyses. On the contrary, this is an excellent case of liquefaction-induced failure, and it was back-analyzed with the best available methods (including the incremental momentum method) to study the mechanics of this type of failure. The results of these back-analyses were then used, along with the results of back-analyses of the 13 case histories from Group A, to develop empirical correlations for estimation of post-liquefactions strengths as a function of runout characteristics, etc. These, in turn, were then used (1) to internally cross-check the back-analysis results of the case histories in Group A, and (2) to assist in development of assessments of post-liquefaction strengths from the case histories of Group B, and for cross-checking some of the back-analysis results for group B cases.

But the SPT and BPT penetration resistance values cannot be directly correlated with the back-analyzed estimates of post-liquefaction strength (S_r) for this otherwise important case history, and so this case history was not employed in the empirical regressions performed to develop new predictive models for assessment of S_r.

It should be noted that most previous efforts to develop relationships for estimation of post-liquefaction strengths did employ the Calaveras Dam case history, and that it was one of a limited number of cases providing high S_r values at relatively high penetration resistances. The information regarding materials character developed by the studies of Olivia Chen Consultants (2003) was not available to most of these previous investigators. Because this case was one of only a few case histories with (1) large effective overburden stresses, and (2) relatively large $N_{1,60,CS}$ values, the deletion of this case history from relationships and correlations based on the new information and data from the recent 1997 - 2002 seismic studies would be expected to result in potential changes in these previous relationships.

3.3.3 Group D Cases

The six Group D cases in Table 3.2 were deleted, and were not formally back-analyzed nor used to develop predictive relationships in these current studies.

3.3.3.1 Kawagishi-Cho Building

The Kawagishi-Cho apartment building suffered a liquefaction-induced bearing capacity failure and toppled over during the 1964 Niigata earthquake (M_W = 7.5). This was a well-documented case history, but it is a difficult one to back-analyze. The bearing capacity failure does not appear to have been symmetric and the building toppled as it failed. Cyclic inertial forces are unknown, and difficult to estimate, and the cyclic overturning moments exerted on the structure, and the resulting non-uniform bearing pressures at the base of the structure that contributed to the failure, cannot be reliably estimated. This case was eliminated from further analysis or use in these current studies.

3.3.3.2 Snow River Bridge Fill

The Snow River bridge fill suffered a liquefaction-induced failure during the 1964 Alaskan earthquake (M_W = 9.3). This liquefaction-induced failure has also been employed in multiple previous studies. This case was eliminated from further consideration in these current studies because of (1) uncertainties with regard to pre-failure geometries, (2) uncertainties with regard to actual failure mode (e.g. depth of failure), and (3) uncertainties associated with soil-structure interaction effects associated with the piles supporting the bridge.

3.3.3.3 Koda Numa Railway Embankment

The Koda Numa railway embankment suffered a liquefaction-induced stability failure with large displacements during the 1968 Tokachi-Oki earthquake (M_W = 7.9). This case had also been used in multiple previous studies. This case was eliminated for further back-analyses in these current studies because of lack of confidence in the information and documentation available regarding the post-failure geometry and runout characteristics. The mass of the post-failure "displaced" material appears to be more than twice the mass that this same material occupied in the pre-failure geometry, and this discrepancy could not be resolved.

3.3.3.4 San Fernando Valley Juvenile Hall

The large hill slope adjacent to the San Fernando Valley Juvenile Hall facility suffered a liquefaction-induced downslope movement during the 1971 San Fernando earthquake (Mw = 6.6). This case had been employed in the previous studies, and relationships, of Seed (1987), Seed and Harder (1990) and Idriss (1998). This was a lateral spreading case history, and it was judged by the current engineering team (1) that the combination of relatively moderate static driving shear stresses and the significant cyclic lurching forces led to a situation in which cyclic lurching forces likely contributed significantly to the observed displacements, and (2) that the difficulties of dealing analytically with these cyclic forces would render accurate assessment of post-liquefaction S_r challenging. This case was therefore deleted from further consideration.

3.3.3.5 Whisky Springs Fan

The Whiskey Springs Fan was essentially another lateral spreading case, and it occurred during the 1983 Borah Peak earthquake (M_W = 7.3). This case had also been employed in the previous studies, and relationships, of Seed (1987), Seed and Harder (1990) and Idriss (1998). It was judged by the current engineering team that cyclic lurching forces likely contributed significantly to the observed displacements, and that the difficulty of having to analytically deal with these cyclic lurching forces would render accurate assessment of post-liquefaction strength challenging at best. This case was also deleted from further consideration.

3.3.3.6 Fraser River Delta

The Fraser River Delta case history involved a static liquefaction flow failure in the Fraser River Delta that occurred in 1985. It was employed in relationships developed by Olson and Stark (2002) and by Robertson (2010). This case was eliminated from further consideration in these current studies (1) because of lack of reliable pre-failure and post-failure geometries, and (2) because the post-liquefaction strength ratio had therefore been estimated only on the basis of laboratory tests performed on reconstituted samples of Fraser River Delta sands; tests that would not have included potential effects of field-scale void redistribution and/or inter-layer mixing.

3.4 Case Histories Selected for Formal Back-Analyses

Table 3.3 lists the 30 full-scale liquefaction field case histories back-analyzed in these current studies. These are divided into three Groups (Groups A, B and C) as described previously. The date of the observed field performance event, and the principal cause or mechanism, is also listed for each case history.

Table 3.1: Candidate Liquefaction Case Histories Considered

Case History	Apparent Cause of Sliding	Seed and Harder (1990)	Stark and Mesri (1992)	Olson and Stark (2002)	Robertson (2010)	Faris (2004)	Olson and Johnson (2008)
Zeeland - Vlietepolder	1889 High Tide	--	--	X	X	--	--
Coyote Creek	1906 San Francisco, California	--	--	--	--	X	--
Salinas River	1906 San Francisco, California	--	--	--	--	X	--
Sullivan Marsh	1906 San Francisco, California	--	--	--	--	X	--
Mission Creek	1906 San Francisco, California	--	--	--	--	X	--
Wachusett Dam - North Dike	1907 Reservior Filling	--	--	X	X	--	--
Calaveras Dam	1918 Construciton	X	X	X	X	--	--
Sheffield Dam	1925 Santa Barbara Eq. (M_L = 6.3)	X	X	X	X	--	--
Helsinki Harbor	1936 Construction	--	--	X	X	--	--
Fort Preck Dam	1938 Construction	X	X	X	X	--	--
Solfatara Canal Dike	1940 El Centro Eq. (M = 7.2)	X	X	X	X	--	--
Lake Merced Bank	1957 San Francisco Eq. (M = 5.7)	X	X	X	X	--	--
Snow River Bridge	1964 Alaska Eq. (M = 8.5)	X	X	--	--	--	--
Kawagishi-Cho Building	1964 Niigata Eq (M = 7.5)	X	X	X	X	X	--
Uetsu Railway Embankment	1964 Niigata Eq (M = 7.5)	X	X	X	X	--	--
North of Bandai Bridge	1964 Niigata, Japan	--	--	--	--	X	--
Echigo Railway	1964 Niigata, Japan	--	--	--	--	X	--
Hokuriku Building	1964 Niigata, Japan	--	--	--	--	X	--
Hotel Niigata	1964 Niigata, Japan	--	--	--	--	X	--
NHK Building	1964 Niigata, Japan	--	--	--	--	X	--
South of Niigata Station	1964 Niigata, Japan	--	--	--	--	X	--
North of Niigata Station	1964 Niigata, Japan	--	--	--	--	X	--
North of Route 345	1964 Niigata, Japan	--	--	--	--	X	--
Shitayama Shool	1964 Niigata, Japan	--	--	--	--	X	--
Showa Bridge	1964 Niigata, Japan	--	--	--	--	X	--
Portage Creek	1964 Prince William Sound, Alaska	--	--	--	--	X	--
Twentymile River	1964 Prince William Sound, Alaska	--	--	--	--	X	--

Table 3.1: Candidate Liquefaction Case Histories Considered (Continued)

Case History	Apparent Cause of Sliding	Seed and Harder (1990)	Stark and Mesri (1992)	Olson and Stark (2002)	Robertson (2010)	Faris (2004)	Olson and Johnson (2008)
Hokkaido Tailings Dam	1968 Tokachi-Oki Eq. (M = 7.9)	--	--	X	X	--	--
San Fernando Valley Juvenile Hall	1971 San Fernando Eq. (M_W = 6.6)	X	X	--	--	X	X
Lower San Fernando Dam U/S	1971 San Fernando Eq. (M_W = 6.6)	X	X	X	X	--	--
Lower San Fernando Dam D/S	1971 San Fernando Eq. (M_W = 6.6)	--	--	--	--	--	--
Upper San Fernando Dam	1971 San Fernando Eq. (M_W = 6.6)	X	X	--	--	--	--
Jensen Filtration Plant	1971 San Fernando, California	--	--	--	--	X	--
Tar Island Dyke	1974 Construction	--	--	X	X	--	--
Mochi-Koshi Tailings Dams	1978 Izu-Oshima Eq. (M = 7.0)	X	X	--	--	--	--
- Dike 1	1978 Izu-Oshima Eq. (M = 7.0)	--	--	X	X	--	--
- Dike 2	1978 Izu-Oshima Eq. (M = 7.0)	--	--	X	X	--	--
Heber Road	1979 Imperial Valley Eq. (M_W = 6.5)	--	X	--	--	X	X
Whiskey Springs Fan	1983 Borah Peak Eq. (M = 7.3)	X	X	--	--	X	X
Pence Ranch	1983 Borah Peak, Idaho	--	--	--	--	X	--
Hachiro-Gata Road Embankment	1983 Nihon-Kai-Chubu Eq. (M = 7.7)	--	--	X	X	--	--
East Slope of Maeyama	1983 Nihonkai-Chubu, Japan	--	--	--	--	X	--
South Slope of Maeyama	1983 Nihonkai-Chubu, Japan	--	--	--	--	X	--
Adjacent to Road No. 7	1983 Nihonkai-Chubu, Japan	--	--	--	--	X	--
Shonan-Cho	1983 Nihonkai-Chubu, Japan	--	--	--	--	X	--
Yoneshiro River	1983 Nihonkai-Chubu, Japan	--	--	--	--	X	--
Asele Raod Embankment	1983 Pavement Repairs	--	--	X	X	--	--
La Marquesa Dam - U/S Slope	1985 Chilean Eq. (M_S = 7.8)	X	X	X	X	--	--
La Marquesa Dam - D/S Slope	1985 Chilean Eq. (M_S = 7.8)	X	X	X	X	--	--
La Palma Dam	1985 Chilean Eq. (M_S = 7.8)	X	X	X	X	--	--
Fraser River Delta	1985 Gas Desaturation and Low Tide	--	--	X	X	--	--
Chonan Middle School	1987 Chiba-Toho-Oki Eq. (M = 6.7)	--	--	X	X	--	--
Landing Road Bridge	1987 Edgecumbe, New Zealand (M_W = 6.5)	--	--	--	--	--	X
James Street Loop	1987 Edgecumbe, New Zealand (M_W = 6.5)	--	--	--	--	--	X

Table 3.1: Candidate Liquefaction Case Histories Considered (Continued)

Case History	Apparent Cause of Sliding	Seed and Harder (1990)	Stark and Mesri (1992)	Olson and Stark (2002)	Robertson (2010)	Faris (2004)	Olson and Johnson (2008)
Nalband Railway Embankment	1988 Armenian Eq. (M_S = 6.8)	--	--	**X**	**X**	--	--
Moss Landing MBARI Bldg 4	1989 Loma Prieta (M_W = 7.0)	--	--	--	--	--	**X**
Moss Landing MBARI Bldg 3	1989 Loma Prieta (M_W = 7.0)	--	--	--	--	--	**X**
Moss Landing MLML Bldg Eastward Spread	1989 Loma Prieta (M_W = 7.0)	--	--	--	--	--	**X**
Moss Landing MLML Bldg Westward Spread	1989 Loma Prieta (M_W = 7.0)	--	--	--	--	--	**X**
Miller Farm	1989 Loma Prieta (M_W = 7.0)	--	--	--	--	**X**	**X**
Farris Farm	1989 Loma Prieta (M_W = 7.0)	--	--	--	--	**X**	**X**
Leonardini Farm	1989 Loma Prieta (M_W = 7.0)	--	--	--	--	--	**X**
Sea Mist Farm	1989 Loma Prieta (M_W = 7.0)	--	--	--	--	--	**X**
Marina District, St. Francis Yacht Club	1989 Loma Prieta (M_W = 7.0)	--	--	--	--	--	**X**
Treasure Island	1989 Loma Prieta (M_W = 7.0)	--	--	--	--	--	**X**
MBARI	1989 Loma Prieta, California	--	--	--	--	**X**	--
MLML	1989 Loma Prieta, California	--	--	--	--	**X**	--
Leonardini Farm	1989 Loma Prieta, California	--	--	--	--	**X**	--
Soviet Tajik - May 1 Slide	1989 Tajik, Sovit Union Eq. (M_L = 5.5)	--	--	**X**	**X**	--	--
Nerlerk Embankment	1990 Construction	--	**X**	--	**X**	--	--
Eastbank	1990 Luzon, Phillippines	--	--	--	--	**X**	--
Southbank	1990 Luzon, Phillippines	--	--	--	--	**X**	--
Perez Blvd	1990 Luzon, Phillippines	--	--	--	--	**X**	--
Magsaysay Bridge, E. bank, d/s	1990 Luzon, Phillippines (M_W = 7.6)	--	--	--	--	--	**X**
Nable Street West	1990 Luzon, Phillippines (M_W = 7.6)	--	--	--	--	--	**X**
Nable Street East	1990 Luzon, Phillippines (M_W = 7.6)	--	--	--	--	--	**X**
Magsaysay Bridge, E. bank, u/s	1990 Luzon, Phillippines (M_W = 7.6)	--	--	--	--	--	**X**
Magsaysay Bridge, W. bank, u/s	1990 Luzon, Phillippines (M_W = 7.6)	--	--	--	--	--	**X**
Pogo Chico W. bank	1990 Luzon, Phillippines (M_W = 7.6)	--	--	--	--	--	**X**
Rudbaneh Town Canal	1990 Manjil, Iran (M_W = 7.4)	--	--	--	--	--	**X**
Sullivan Tailings	1991 Dyke Rising, British Columbia	--	--	--	**X**	--	--

Table 3.1: Candidate Liquefaction Case Histories Considered (Continued)

Case History	Apparent Cause of Sliding	Seed and Harder (1990)	Stark and Mesri (1992)	Olson and Stark (2002)	Robertson (2010)	Faris (2004)	Olson and Johnson (2008)
Aichi West	1993 Nansei-oki, Japan	--	--	--	--	X	--
Jamuna Bridge	1994 Construction, Bangladesh	--	--	--	X	--	--
Balboa Blvd.	1994 Northridge (M_W = 6.7)	--	--	--	--	X	X
Wynne Ave.	1994 Northridge (M_W = 6.7)	--	--	--	--	--	X
Potrero Canyon	1994 Northridge (M_W = 6.7)	--	--	--	--	--	X
Wufeng Site C (A-A')	1999 Chi-Chi, Taiwan (M_W = 7.6)	--	--	--	--	--	X
Wufeng Site C (B-B')	1999 Chi-Chi, Taiwan (M_W = 7.6)	--	--	--	--	--	X
Wufeng Site C1	1999 Chi-Chi, Taiwan (M_W = 7.6)	--	--	--	--	--	X
Wufeng Site B	1999 Chi-Chi, Taiwan (M_W = 7.6)	--	--	--	--	X	X
Wufeng Site M	1999 Chi-Chi, Taiwan (M_W = 7.6)	--	--	--	--	--	X
Nantou Site N	1999 Chi-Chi, Taiwan (M_W = 7.6)	--	--	--	--	--	X
Hotel Sapanca	1999 Kocaeli, Turkey (M_W = 7.4)	--	--	--	--	X	X
Police Station	1999 Kocaeli, Turkey (M_W = 7.4)	--	--	--	--	--	X
Soccer Field	1999 Kocaeli, Turkey (M_W = 7.4)	--	--	--	--	X	X
Yalova Harbor	1999 Kocaeli, Turkey (M_W = 7.4)	--	--	--	--	--	X
Norswing Drive	2003 San Simeon (M_W = 6.5)	--	--	--	--	--	X
Juanita Ave.	2003 San Simeon (M_W = 6.5)	--	--	--	--	--	X
Canadian Mine	(See Robertson (2010))	--	--	--	X	--	--

Table 3.2: Case Histories More Closely Considered for Potential Back-Analyses for Evaluation of Post-Liquefaction Strength (S_r)

Group	Case	Failure Date	Seed and Harder (1990)		Olson and Stark (2002)				Wang (2003) + Kramer (2008)			This Study
			S_r	$N_{1,60,CS}$	S_u(Liq)	S_u(Liq)/σ'_{vo}	σ'_{vo}	$N_{1,60}$ (1)	$\bar{S}_r$ (2)	S_r/σ_{vo}'	$\bar{N}_{1,60,CS}$	
A	Wachusett Dam - North Dike	1907 Reservior Filling			334	0.106	3158	7	348	0.136	7.3(3)	Analyzed
	Fort Peck Dam	1938 Construction	350	10	570	0.078	7341	8.5	671.5	0.091	15.8	Analyzed
	Uetsu Railway Embankment	1964 Niigata Eq (M = 7.5)	40	3	36	0.027	1280	3	43.5	0.048	2.9	Analyzed
	Lower San Fernando Dam - U/S Slope	1971 San Fernando Eq. (M_W = 6.6)	400	13.5	390	0.120	3482	11.5	484.7	0.133	14.5	Analyzed
	Hachiro-Gata Road Embankment	1983 Nihon-Kai-Chubu Eq. (M = 7.7)			42	0.062	670	4.4	65	0.164	5.7	Analyzed
	La Marquesa Dam - U/S Slope	1985 Chilean Eq. (M_S = 7.8)	200	6	65	0.07	911	4.5	(185.2)	0.110	6.5(3)	Analyzed
	La Marquesa Dam - D/S Slope	1985 Chilean Eq. (M_S = 7.8)	400	11	111	0.11	1000	9	(343.5)	0.186	9.9(3)	Analyzed
	La Palma Dam	1985 Chilean Eq. (M_S = 7.8)	200	4	100	0.12	789	3.5	(193.3)	0.123	4.2	Analyzed
	Lake Ackerman Highway Embankment	1987 Seismic Survey			82	0.076	1076	3	98	0.114	4.8	Analyzed
	Chonan Middle School	1987 Chiba-Toho-Oki Eq. (M = 6.7)			100	0.09	1119	5.2	(178.7)	0.091	6.4(3)	Analyzed
	Soviet Tajik - May 1 Slide	1989 Tajik, Sovit Union Eq. (M_L = 5.5)			175	0.08	2170	7.6	(334)	0.082	8.9(3)	Analyzed
	Shibecha-Cho Embankement	1993 Kushiro-Oki Eq.(M_L = 7.8)			117	0.086	1351	5.6	208.9	0.200	5.6	Analyzed
	Route 272 at Higashiarekinai	1993 Kushiro-Oki Eq.(M_L = 7.8)			100	0.097	1030	6.3	130.5	0.125	8.5	Analyzed
B	Zeeland - Vlietepolder	1889 High Tide			115	0.05	2396	7.5	(226.1)	0.048	8.5(3)	Analyzed
	Sheffield Dam	1925 Santa Barbara Eq. (M_L = 6.3)	75	6	75	0.05	1429	5	(99.8)	0.043	8.2(3)	Analyzed
	Helsinki Harbor	1936 Construction			32	0.06	522	6	(52.4)	0.067	5.9(3)	Analyzed
	Solfatara Canal Dike	1940 El Centro Eq. (M = 7.2)	50	4	50	0.08	624	4	(77.1)	0.063	4.9(3)	Analyzed
	Lake Merced Bank	1957 San Francisco Eq. (M = 5.7)	100	6	144	0.11	1372	7.5	(139.5)	0.106	5.9(3)	Analyzed
	El Cobre Tailings Dam	1965 Chilean Eq. (M_L = 7 to 7.25)			40	0.020	1946	0	(195.2)	0.020	6.8	Analyzed
	Metoki Road Embankment	1968 Tokachi-Oki Eq. (M = 7.9)			38	0.04	875	2.6	(116.8)	0.044	2.0	Analyzed
	Hokkaido Tailings Dam	1968 Tokachi-Oki Eq. (M = 7.9)			100	0.07	1376	1.1	(250.6)	0.074	5.1	Analyzed
	Upper San Fernando Dam - D/S Slope	1971 San Fernando Eq. (M_W = 6.6)	600	15								Analyzed
	Tar Island Dyke	1974 Construction			251	0.06	4300	7	(364.2)	0.058	8.9(3)	Analyzed
	Mochi-Koshi Tailings Dam, Dikes 1 and 2	1978 Izu-Oshima Eq. (M = 7.0)	250	5	75	0.06	1251	2.7	(158.9)	0.091	8.9	Analyzed
					113	0.10	1090	2.7	(233.6)	0.081	10.0	
	Nerlerk Embankment, Slides 1, 2 and 3	1983 Construction			52	0.09	616	8.7	(178.5)	0.124	11.4(3)	Analyzed
					36	0.06	650	7.2				
					31	0.03	925	7.2				
	Asele Road Embankment	1983 Pavement Repairs			132	0.10	1251	7	(163.7)	0.104	11.0(3)	Analyzed
	Nalband Railway Embankment	1988 Armenian Eq. (M_S = 6.8)			119	0.11	1101	9.2	(139.9)	0.109	6.3(3)	Analyzed
	Sullivan Tailings	1991 Dyke Rising, British Columbia										Analyzed
	Jamuna Bridge	1994 Construction, Bangladesh										Analyzed
C	Calaveras Dam	1918 Construction	650	12	721	0.112	6422	8	632.7	0.099	10.5(3)	Analyzed
D	Kawagishi-Cho Building	1964 Niigata, Japan (M = 7.5)	120	4	111	0.08	1474	4.4	(123.5)	0.089	4.3	Not Analyzed
	Snow River Bridge Fill	1964 Alaskan Eq. (M = 8.5)	50	7					(50)	0.025	8.5(3)	Not Analyzed
	Koda Numa Railway Embankment	1968 Tokachi-Oki Eq. (M = 7.9)	50	3	25	0.05	485	3	(48)	0.045	3.6	Not Analyzed
	San Fernando Valley Juvenile Hall	1971 San Fernando Eq. (M_W = 6.6)	130	10.5								Not Analyzed
	Whiskey Springs Fan	1983 Borah Peak Eq. (M = 7.3)	150	11								Not Analyzed
	Frasier River Delta	1985 Low Tide			N/A	0.100	N/A	5.3				Not Analyzed

Notes : (1) No fines content correction utilized in Olson and Stark (2002).
(2) Where noted in parentheses, $S_{u,r}$ values shown are for secondary cases in Wang (2003) and were not fully reanalyzed.
(3) $N_{1,60,CS}$ values were changed in Kramer (2008) from the values reported in Wang (2003). The updated values are shown.

Table 3.3: Case Histories Back-Analyzed for Evaluation of Post-Liquefaction Strength (S_r)

Group	Case Number	Case	Failure Date
A	1	Wachusett Dam - North Dike	1907 Reservior Filling
	2	Fort Peck Dam	1938 Construction
	3	Uetsu Railway Embankment	1964 Niigata Eq (M = 7.5)
	4	Lower San Fernando Dam - U/S Slope	1971 San Fernando Eq. (M_W = 6.6)
	5	Hachiro-Gata Road Embankment	1983 Nihon-Kai-Chubu Eq. (M = 7.7)
	6	La Marquesa Dam - U/S Slope	1985 Chilean Eq. (M_S = 7.8)
	7	La Marquesa Dam - D/S Slope	1985 Chilean Eq. (M_S = 7.8)
	8	La Palma Dam	1985 Chilean Eq. (M_S = 7.8)
	9	Lake Ackerman Highway Embankment	1987 Seismic Survey
	10	Chonan Middle School	1987 Chiba-Toho-Oki Eq. (M = 6.7)
	11	Soviet Tajik - May 1 Slide	1989 Tajik, Sovit Union Eq. (M_L = 5.5)
	12	Shibecha-Cho Embankement	1993 Kushiro-Oki Eq.(M_L = 7.8)
	13	Route 272 at Higashiarekinai	1993 Kushiro-Oki Eq.(M_L = 7.8)
B	15	Zeeland - Vlietepolder	1889 High Tide
	16	Sheffield Dam	1925 Santa Barbara Eq. (M_L = 6.3)
	17	Helsinki Harbor	1936 Construction
	18	Solfatara Canal Dike	1940 El Centro Eq. (M = 7.2)
	19	Lake Merced Bank	1957 San Francisco Eq. (M = 5.7)
	20	El Cobre Tailings Dam	1965 Chilean Eq. (M_L = 7 to 7.25)
	21	Metoki Road Embankment	1968 Tokachi-Oki Eq. (M = 7.9)
	22	Hokkaido Tailings Dam	1968 Tokachi-Oki Eq. (M = 7.9)
	23	Upper San Fernando Dam - D/S Slope	1971 San Fernando Eq. (M_W = 6.6)
	24	Tar Island Dyke	1974 Construction
	25	Mochi-Koshi Tailings Dam, Dikes 1 and 2	1978 Izu-Oshima Eq. (M = 7.0)
	26	Nerlerk Embankment, Slides 1, 2 and 3	1983 Construction
	27	Asele Road Embankment	1983 Pavement Repairs
	28	Nalband Railway Embankment	1988 Armenian Eq. (M_S = 6.8)
	29	Sullivan Tailings	1991 Dyke Rising, British Columbia
	30	Jamuna Bridge	1994 Construction, Bangladesh
C	14	Calaveras Dam	1918 Construction

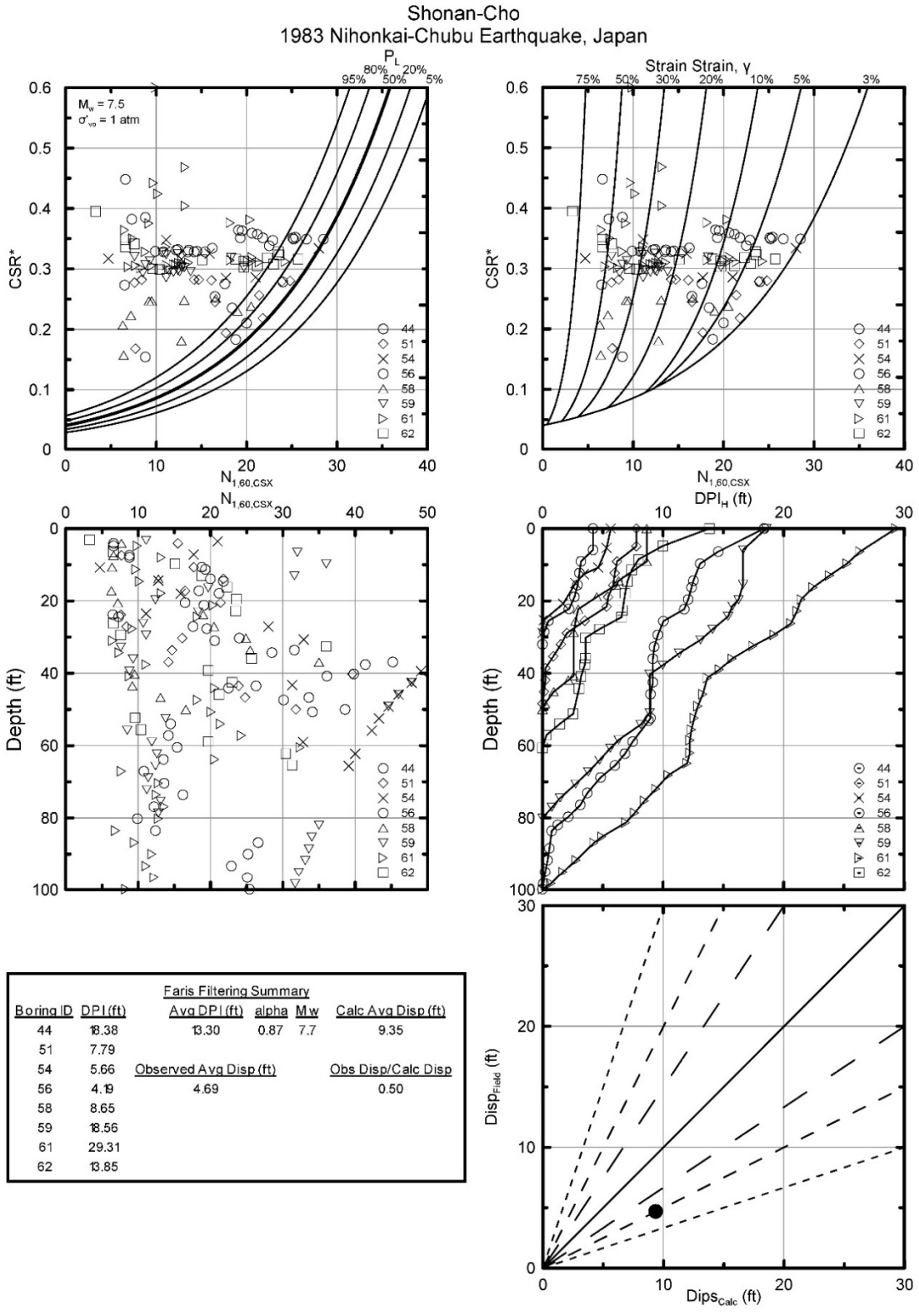

Figure 3.1: Illustration of the methodology developed by Faris (2004) for prediction of lateral spreading displacements; example analysis applied to the Shonan-Cho case history.

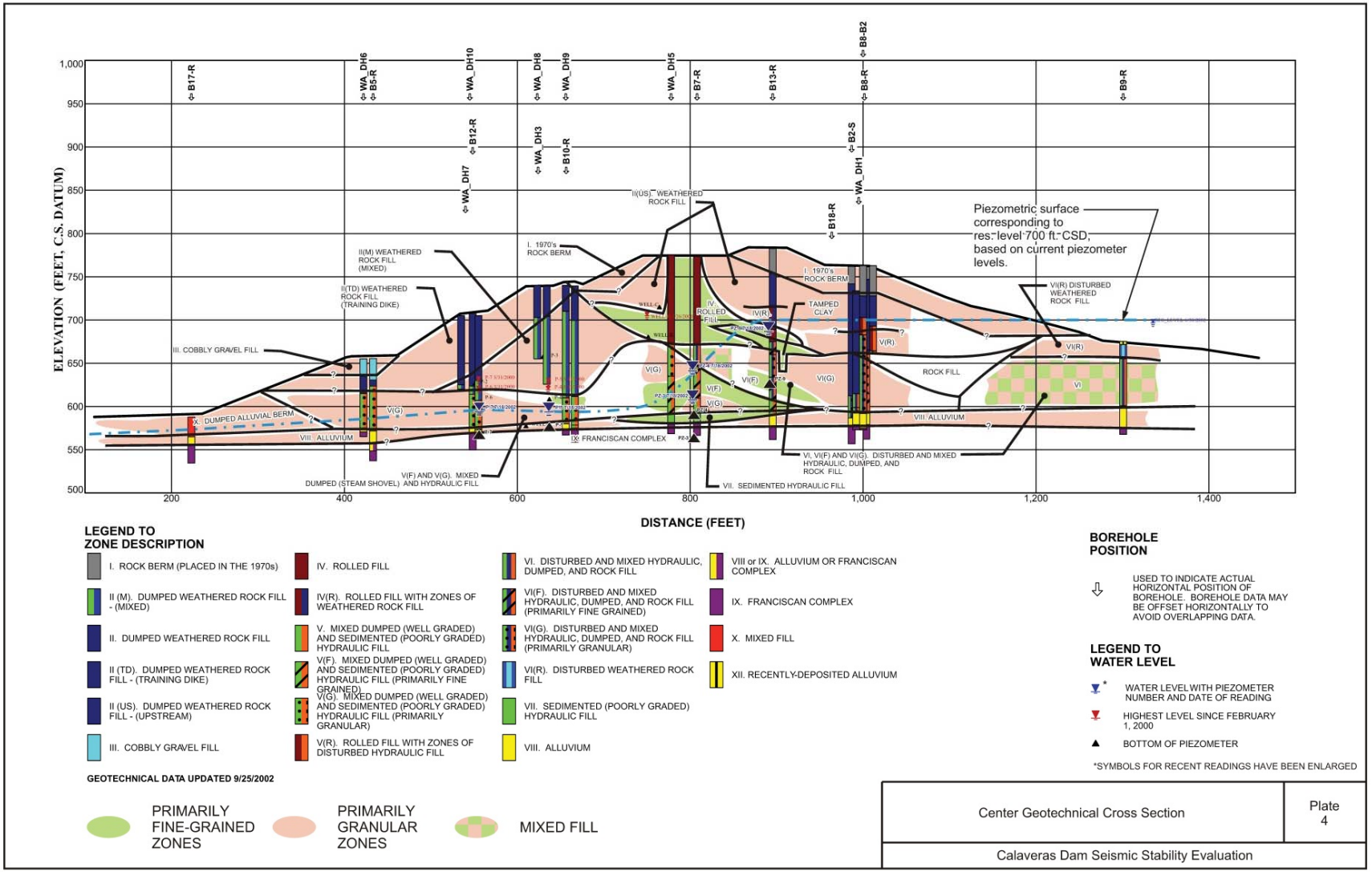

Figure 3.2: Cross-section of the reconstructed Calaveras dam showing general soil material zones as developed based on recent Seismic investigations (Olivia Chen Consultants, 2003).

Chapter Four

Back-Analyses of Liquefaction Failure Case Histories

4.1 Introduction

The 30 liquefaction failure case histories selected for inclusion in these studies (see Table 3.2) were subjected to back-analyses and back-assessments by a variety of methods, depending upon the amounts and quality of data available for each of these cases. Cross-comparisons were made with other case histories back-analyzed in these current studies, and cross-comparisons were also made with the results and findings from previous investigations.

A number of new methods were developed in these current studies for improved back-analyses and assessments of post-liquefaction strengths, and these will be presented and explained as this chapter proceeds. It is also important to understand the approaches and procedures used by a number of previous investigators for similar back-analyses or back-assessments of post-liquefaction strengths in order to understand the juxtaposition of the results of those previous studies with the new results presented herein. Accordingly, this chapter will also discuss a number of previous back-analysis methods, and their strengths and drawbacks.

Table 4.1 presents a list of the principal methods of interest for these current studies. These include methods employed by previous investigators, and also new methods developed for these current studies. This list provides a useful template for some of the discussions that will follow. Methods listed towards the top of the list tend to provide the highest levels of accuracy and reliability with regard to back-analyzed values of post-liquefaction strengths for cases to which they can be applied. But they tend to require good quality data and information, and cannot be applied to all case histories. Methods listed lower on the table tend to provide intermediate to lower levels of accuracy and reliability, but can more readily be applied to cases with lesser levels of information and data available.

4.2 The Incremental Momentum Method

4.2.1 General Overview

A new method has been developed to provide a more accurate and reliable means of incorporating momentum effects in back-analyses of large displacement liquefaction failures performed for purposes of assessment of post-liquefaction strength (S_r). This new method will be referred to as the incremental momentum analysis method.

This method is illustrated in Figures 4.1 through 4.3, for the case of the liquefaction-induced slope failure that occurred on the upstream side of the Lower San Fernando Dam as a result of the 1971 San Fernando earthquake. A full explanation of this failure case history, and a more complete exposition of all back-analyses performed for this case history, are presented in Appendix A, Section A.5.

As shown in Figure 4.1, the upstream slope failure of the Lower San Fernando Dam was the result of liquefaction of the lower portion of the hydraulic fill materials comprising the upstream shell of the dam during the 1971 San Fernando earthquake. This was an unusually well-investigated failure, and two large trenches were excavated fully through the failed embankment so that a detailed mapping of the displaced locations of recognizable portions of the embankment could be documented. Largely intact portions (or "blocks") of the displaced upstream side of the dam were then mapped back to their initial positions, and it could be seen that the failure involved liquefaction of the lower portion of the hydraulic fill on the upstream side (the "dark" zone in Figures 4.1(a) and (b)), with the overlying embankment sections translating outwards in the upstream direction borne along atop the liquefied materials.

The incremental momentum method involves developing a series of estimated (and feasible) cross-sections incrementally tracking the progression of displaced geometries from inception of movements to the final, residual post-failure geometry. This is more challenging than the approach taken in estimation of the "ZIF" interim cross-section geometry by Wang (2003), as discussed previously in Section 2.3.8, because it requires that all intermediate geometries must provide a reasonable path forward all the way to the observed final residual geometry. It is therefore a very tedious and time-consuming process, involving numerous iterations between analyses and estimation and drawing of cross-sections, and one that requires both engineering judgment and some artistic capability.

Important benefits of this approach, relative to the previous "kinetics" approaches taken by Olson (2001), as discussed in Section 2.3.7, and the previous "ZIF" method of Wang (2003), as discussed in Section 2.3.8, include the following:

1. This process is constrained by the eventual need to converge on the observed final geometry, requiring a more reasonable and reliable path forward at each incremental cross-section.

2. The process lends itself to creating a step-wise "animation" which can be clicked forward and in reverse on a computer screen, much like a step-wise video, and these animations have proven to be useful with regards to enhancing engineering insight and understanding.

3. The series of incremental cross-sections permit updated evaluations of (a) driving shear stresses, (b) failure plane details (e.g. lengths of the failure plane currently controlled by liquefied or non-liquefied materials, overall failure plane lengths, sections of the failure plane where stronger or weaker soils have over-ridden weaker or stronger soils as shearing progressed (weaker soils then control), etc.), and (c) evolving geometries and properties (including strengths) as displacing and deforming embankment toes enter into bodies of water and potentially either hydroplane or ride out atop weaker reservoir or offshore sediments, etc. These are potentially very important benefits, but the ability to "update" the evolving analyses in all of these regards also poses an additional set of analytical judgments and responsibilities, and it also takes further time and effort.

4. The analysis is performed with basic physics (Newton's Second Law) and basic soil mechanics governing the progressive evolution of accelerations, velocities, momentum, and displacements during the slide movements. The analysis proceeds continuously from

inception of movements to completion. There is therefore no need to "estimate" the partial displacement stage that corresponds to the "ZIF" displacement stage of Wang (2003).

5. Driving shear stresses are correctly calculated at each increment, so there is no difficulty or uncertainty with regard to the level of accuracy with which the curvilinear polynomial surface of the "kinetics" analysis method of Olson (2001) suitably approximates the driving shear forces at each stage of partial lateral displacement.

6. The incremental inertial method is the only method among the three that can largely correctly deal with the issues and effects associated with incrementally developing (retrogressive) failures that initiate and fail in a "slice by slice" progression beginning with an initial slice (or wedge) near the front face and then retrogressing (with successive slices) eventually back to the final back heel of the overall failure.

The resulting analysis is thus more accurate, more reliable, more adaptable, and better able to account for evolving details as the failure progresses. The corollary price to be paid is then the additional level of effort, and time, involved in performing these very challenging and tedious analyses.

Figure 4.2 shows the incremental progression of cross-sections judged to represent this current engineering team's "best estimate" of the likely progressive evolution of failure for the case of the Lower San Fernando Dam upstream slope failure. The benefits of this progressive approach, in terms of approximate "animation" and visualization, were of special value here, as it has long been debated whether this failure occurred either (1) as an initially monolithic failure, with subsequent "break-up" and partial separation (or articulation) of individual slices and blocks occurring as the failure progressed, or (2) as an incrementally progressive failure, with the slices nearest the front face of the slide mass moving first, followed by successive slices, in sequence, as each successive slice was partially "unbraced" by the displacement of the slice that preceded it, until the failure eventually retrogressed in incremental fashion back to the eventual final back heel. By creating multiple potential realizations of the failure sequence, it became clear that this particular failure likely initiated relatively monolithically, and then broke up as it traveled, because it was otherwise not feasible to re-produce the observed final positions of some of the more rear-ward slices. This could not be reliably ascertained a priori, and it should be noted that some of the other case histories back-analyzed in these current studies clearly did proceed in an incrementally progressive (retrogressive) manner, and that others did not.

Appendix C, Section C.2, presents a series of composite incremental steps of the analysis of the Lower San Fernando Dam failure, showing (1) the incremental evolution of displaced geometries, (2) the evolution of the displaced location of the center of gravity of the overall failure mass, and (3) incremental evolution of acceleration, velocity and displacement of the center of gravity vs. time. As each sheet shows all of these features on a single page, and as each sheet steps forward through time, these can be put on a screen (either as pdf's, or with PowerPoint), and they can then be "clicked through" like a movie or simulation, giving the viewer a sense of the motions and of the development of forces and displacements, etc. This can be surprisingly useful, and it can enhance understanding and can also serve as a basis for further tuning of the modeled progression of cross-sections.

Figure 4.3 then illustrates the calculated evolution of acceleration, velocity and displacement of the center of gravity of the eventual overall failure mass. At each step in time, the best estimate of (a) driving (downslope) shear forces and (b) resisting (upslope) shear resistance are compared, and any overall force imbalance is then applied to the overall failure mass by Newton's Second Law ($F = m \bullet a$). The resulting acceleration (or deceleration) is then calculated, and so is the corollary resulting increase or decrease in velocity, and the associated incremental accumulation of displacements as well. As shown in Figure 4.3, velocity initially increases as the mass begins to move downslope, and then decreases as the mass eventually comes to rest.

Shear strengths for non-liquefied soils are modeled at each stage based on the best available information and data, and basic principles of soil mechanics. Liquefied zones are assigned a post-liquefaction strength of S_r, and the value of S_r is then iterated until the calculated progression (e.g. Figure 4.3) shows the final displacements to match those observed in the field. This requires another series of iterative adjustments, and analyses, further adding to the effort required. The seven "dots" for small circles on the plots of Figure 4.3 show the situation at time-steps corresponding to the first seven updated (incremental) cross-sections of Figure 4.2. The eighth and final cross-section of Figure 4.2 differs from the seventh only in that the reservoir has eventually seeped through and infilled the "dip" near the top back-heel of the slide mass of the preceding (seventh) incremental cross-section.

Once a best-estimate case had been established and analyzed, parameter (and assumption) sensitivity studies were next performed. Only a few additional fully incremental momentum analyses were usually performed here. Instead a case-specific relationship between pre-failure and post-failure geometries, strengths, and representative S_r was established for each case (see Section 4.4), and then simpler analyses of pre-failure and post-failure geometries were performed to more efficiently evaluate the effects of changes in conditions and parameters over the ranges considered plausible and/or feasible. In some cases, additional full incremental analyses had to be performed to examine modeling of challenging situations such as (1) ranges of potential conditions with regard to monolithic vs. incrementally retrogressive initiations of failures, and (2) ranges of modeling choices for toes of slide masses entering into bodies of water, etc.

In this manner, the effects of variations in properties, assumptions, and modeling details on back-calculated values of S_r were evaluated to inform estimates of uncertainty or variance. Variations that were commonly modeled and analyzed here often included: (1) shape and location of the failure surface, (2) whether or not the failure was incrementally progressive (retrogressive) or monolithically initiated, (3) location of the phreatic surface at the time of the failure, (4) shear strengths of soils judged not to have liquefied, (5) variations in unit weights, and (6) variations in assumptions and modeling of conditions at the bases of toes of failures that enter into bodies of water or that travel outward into areas occupied by weak sediments.

4.2.2 Modeling of Strengths at the Toes of Slide Masses Entering Bodies of Water, and Weak Sediment Effects

A number of the failure case histories involved liquefaction flow slides that either entered into reservoirs, or that progressed underwater in offshore waters. In these cases, the question arises

as to whether hydroplaning occurred, and if so to what extent, and what effect would it have had on shear strengths at the bases of the toes of these masses. Hydroplaning is the entrapment of water beneath the toe of an advancing slide mass, so that the toe section (or some portion of the toe section) rides out atop the entrapped water; with the strength of water rather than of soil (or liquefied soil) then controlling shear strength beneath some portion of the slide toe.

This had been addressed very approximately on a case by case basis by Seed (1987) and by Seed and Harder (1990). Most other previous investigators did not address this issue, or did not discuss it if they did. Olson (2001) discussed this for some specific cases, and appears to have assigned a 50% reduced post-liquefaction strength (0.5 x S_r) at the bases of toes of a number of slides as they entered into bodies of water, and then examined variations of between 0% reduction to 100% reduction in assessing potential parameter sensitivity effects. Wang (2003) [and Kramer, 2008] examined the available literature regarding hydroplaning, and developed a simplified but repeatable, quantitative (and semi-probabilistic) procedure for analysis of the likelihood that hydroplaning would occur, and for the likely resulting effects on strengths at the bases of toes of slide masses entering into water. They allowed a maximum lateral penetration of hydroplaning effects beneath the toes of slide masses of up to 10 times the thickness of the soils entering into water, and the amount of this maximum distance that was specifically assumed (modeled) as being affected by hydroplaning for any given case was then primarily a function of velocity of movements. Higher velocity movements were assumed to over-ride and capture/entrap larger areas of water (hydroplaning).

In these current studies, yet another approach was taken.

Examining the available research, it was our investigation team's conclusion that the available knowledge does not yet support rigorous analytical treatments of potential hydroplaning. Likelihood of hydroplaning is clearly affected by velocities of the traveling soil masses, but this does not yet give rise to fully reliable calculation methods. Wang (2003) addressed this with probabilistic estimates of likelihood and extent of hydroplaning, and with subsequent Monte Carlo simulations of the effects of these variations on back-calculated S_r values. Similarly, available research suggests that hydroplaning would occur only to some limited depth of penetration beneath advancing toes of slopes, but attempting to extrapolate table-top scale experimental physical models to field situations is challenging, and it is further complicated by the tapered shapes of the toes of advancing slide masses making it difficult to select a "representative" thickness of the slope materials entering the water. As a result, the approach taken to hydroplaning was largely judgmental, informed when possible from evidence from each individual case history. For example; if the runout of a slide mass into a body of water results in separation of some portion of the toe if the slide mass from the remainder, then it is concluded that the toe section likely hydroplaned and continued farther than the remainder of the slide mass. In many cases there was no definitive data or evidence as to the occurrence or absence of hydroplaning; in those cases judgments were made by the engineering analysis team, and then averaged and also bounded as sensitivity studies to inform both best estimates as well as variance or uncertainty.

A second issue potentially also affecting a number of the liquefaction failure case histories is the presence of weak reservoir sediments, or the presence of weak offshore slope sediments, or weak soils or sediments in agricultural fields adjacent to roadway or railway embankments. Advancing toes of slide masses traveling out onto such weaker sediments can be partially

"lubricated" at their bases if the advancing slide mass rides atop the weaker sediments, in which case the strengths of the weaker sediments can control. But it is also possible for the toes of slide masses to "plough through" weaker sediments, displacing them, in which case lesser reduction in available strengths beneath the toes would occur. Previous investigations have usually not been clear as to whether, or how, they addressed the effects of potential sliding atop weaker sediments at the advancing toes of failure masses.

In these current studies, it was decided to address these two issues (potential hydroplaning, and potential sliding atop weak sediments) on a case by case basis.

In considering hydroplaning, velocities of the advancing toes would be considered but would only provide some guidance. And some limitations on depths of potential penetration of hydroplaning laterally beneath the toes of advancing slide masses would be imposed, but this would vary over a somewhat broader range than just a maximum of 0 to 10 times the thickness of the advancing soils, in part because selection of a representative thickness was not well-defined. When possible, details of the actual observed eventual runout of the failure flow slide mass were examined for clues as to likely hydroplaning. As an example, for the failure of the Fort Peck Dam (see Appendix A, Section A.2) it appears that a portion of the extreme toe of the failure mass separated itself to some extent from the more intact rest of the failure mass, and extended itself more thinly out into the reservoir. This suggests hydroplaning at the toe of this failure. Similarly, the main "toe" section of the failure mass runout of the upstream side of the Lower San Fernando Dam (as shown in the final three cross-sections of Figure 4.2) appears to continue on with its own momentum in late stages of the slide and separates itself a bit from the rest of the slide mass; suggesting either hydroplaning and/or sliding atop soft reservoir sediments. In other cases, failure masses traveled very large distances and did not really "come to rest" in the classical sense; also suggesting hydroplaning. In many cases, however, this was simply a source of uncertainty, and the full range of possible hydroplaning conditions were included within the parameter sensitivity analyses performed. Similarly, strengths where hydroplaning was modeled were varied from 20% to 80% of the overlying soil (or liquefied soil) strengths.

Weak sediments were handled in a similar manner. Strengths at the bases of slide masses traveling outwards onto likely weak sediments were typically assigned strengths equal to values that varied from 25% to 100% of the overlying soil (or liquefied soil) strengths as part of the parameter sensitivity studies performed.

More detailed explanations of modeling and treatment of hydroplaning, and of weak sediments, are presented for each of the individual case histories in Appendices A and B.

4.2.3 Incrementally Progressive (Retrogressive) Failures

A number of the liquefaction failure case histories were suspected of having possibly proceeded in an incrementally progressive manner, initiating with movements of a smaller "slice" or wedge near the front face, and then retrogressing back towards the eventual rear heel of the overall slide in a sequence of subsequent initiations of movements of additional slices or wedges as each slice becomes partially unbraced by loss of support from the slices that preceded it.

This type of incrementally progressive (retrogressive) failure propagation was not tractable to accurate analyses by previous methods, and so the potential impacts of this (as opposed to assumed monolithic initiation of the entire failure as a single coherent mass right from the start) was unknown. It should be noted that failures can be initiated as largely monolithic failures and can then "break up" (or segment and articulate) as they travel, so it can sometimes be difficult to discern whether a given failure was monolithically initiated, or was incrementally progressive (retrogressive) in its initiation mechanics.

The incremental momentum method developed and employed in these current studies can successfully address both monolithic and incrementally progressive (retrogressive) failures.

This is illustrated in Figures 4.4 and 4.5 for the Shibecha-Cho Embankment failure case history. A more complete exposition of this case history is presented in Appendix A, Section A.2.

The Shibecha-Cho Embankment was a very large side-hill fill that supported a populated development, and it failed during the 1983 Kushiro-Oki earthquake. The failure was known to have been an incrementally progressive (retrogressive) failure, and so it was analyzed as such in these current studies.

Stability analyses performed for the un-displaced (pre-failure) cross-section, assuming that liquefaction has been "triggered", show that a slice near the front face is the most critical (has the lowest factor of safety). This failure case history was modeled (best estimate case) as beginning with the inception of movements of this first slice, and then progressing with successive inceptions of movements of two additional successive "slices", as shown in Figure 4.4. After the first slice had progressed some distance, a second slice began to move, and then eventually a third.

The analyses tracking the incremental development of acceleration, velocity and displacements for this case were performed for two parallel sets of centers of gravity, and the results are shown in Figure 4.5. The incremental values for the center of gravity of the initial slice (the slice closest to the front face) are initially tracked by the dashed lines in Figure 4.5. Simultaneously, the values for the eventual overall failure mass are also calculated (by weighted mass averaging of the moving slice, and of the portions of the eventual failure mass not yet in motion), and these are shown by the solid lines in Figure 4.5. The initial failure slice is thus the "active" element in the opening stages. When the second slice begins to move, the dashed lines then track the evolving values for the center of gravity of the combined first and second slice masses (by weighted mass averaging), while the solid lines continue to track the evolving movements of the center of gravity of the overall eventual slide mass (also by weighted mass averaging). The same is then done when the third and final slide mass begins to move, at which point the entire failure mass is engaged and the overall slide mass center of gravity is tracked by the remainders of the solid lines.

Modeling initiation of successive slices reduced overall peak velocities, and also reduced corollary overall momentum, and thus produced a lower back-calculated value of S_r than would have been produced by a monolithic inception of failure. The value of S_r back-calculated with modeling of incrementally progressive failure for the Shibecha-Cho Embankment case history (as illustrated in Figures 4.4 and 4.5) was $S_r \approx 224$ lbs/ft^2. When this case was modeled instead as a

monolithically initiated failure, the somewhat higher momentum effects produced a higher value of $S_r \approx 263$ lbs/ft^2. The effects of incrementally retrogressive initiation of this failure were thus of moderate magnitude with regard to back-calculated values of S_r for this case; reducing S_r by approximately 15% from the "monolithic inception" failure model for this particular case.

4.2.4 Evaluation of Representative Penetration Resistance

Appendix C, Section C.1, presents an expanded discussion of the basis for evaluations of representative SPT $N_{1,60,CS}$ values in these current studies for each of the case histories back-analyzed. An abridged discussion will be presented here.

For cases where modern, and properly well-documented, SPT data were available, correction of SPT N-values to generate equipment and procedurally corrected N_{60}-values were made using largely the corrections proposed by Cetin et al. (2004), except that (1) a slightly reduced adjustment was made for short rod effects at shallow depths as per Deger (2014), and (2) normalization of N_{60}-values for effective overburden stress effects was performed using the relationships recommended by Deger (2014) The slightly reduced short rod correction had essentially negligible effect in these current studies, as few SPT data were used from the very shallow depths at which this might have produced a noticeable difference. The effective overburden stress normalization relationships of Deger (2014) provide normalization curves somewhat intermediate between those of Cetin et al. (2004) and of Idriss and Boulanger (2008). These relationships are presented in Appendix C, Section C.1.

The procedural and equipment corrections made herein were largely similar to those of Seed et al. (1984), and of Idriss and Boulanger (2008), and would produce largely compatible results for most of the field liquefaction failure case histories.

Fines corrections for this study were made using the fines corrections recommended by Cetin et al. (2004). This is an area where some minor differences occur between various investigation teams working on studies of post-liquefaction S_r. The fines adjustment of Cetin et al. is somewhat intermediate between the fines adjustments of Seed et al. (1984) and the fines adjustment that Seed (1987) suggested specifically for S_r purposes. In the end, the fines corrections of these studies, and (1) those employed by Seed (1987) and (2) those recommended by Idriss and Boulanger (2008) do not produce major differences, but they do vary slightly relative to each other. Olson and Stark (2001, 2002) elected not to employ any fines corrections, so that they used $N_{1,60}$-values rather than $N_{1,60,CS}$-values, and that causes a number of their characterizations of SPT penetration resistance to vary somewhat from the other studies for soils with higher fines contents.

Different investigation teams took different approaches to determining what "representative" penetration resistances were. It is widely understood that lower than median values of penetration resistance will likely control actual field failures because nature (and the laws of physics) will choose to exploit zones of weakness within a zone of heterogeneity of strengths. Wride et al. (1999) specifically developed predictive correlations for estimation of post-liquefaction strength (S_r) based on near lower bound values of penetration resistance, as discussed

in Section 2.3.6. A drawback of that approach is volatility of the near lower bound value, especially for cases with sparse data.

In these current studies, it was decided instead to use slightly "scalped" (or selectively filtered) median values of penetration resistance to characterize the liquefiable soils of interest. Median values have the advantage of providing a more stable characterization when data are sparse, and they can also be approximately correlated with lower-percentile enveloping of corrected N-values (values representing lower probabilities of non-exceedance).

"Scalped" in these current studies means deletion of potentially (or likely) spurious high penetration resistance values, and also examination of penetration resistance values for SPT performed in mixed soils with the fines representing potentially cohesive clayey soils. High individual SPT N-values ("flyers") that separate themselves from the main body of data for a soil zone or stratum are examined, and if this separation is large then these anomalously high values are deleted as likely spurious; up to a few percent of the overall data may be deleted here. These anomalously high values may be the result of potential gravel effects, or their cause may be unknown. In addition, when sufficient data are available, SPT performed in soils classified as SC are also deleted. Currently available fines adjustments do not well handle these materials, and their corrected SPT N-values often tend to be lower than many of the rest of the SPT performed on less cohesive materials, even after fines adjustments, in mixed soil zones of varying fines content and consistency.

"Representative" $N_{1,60,CS}$ values were selected in these current studies by examining the median and mean values from the scalped or slightly filtered data sets, and then selecting a value equal to the median except in cases with significant numbers of data where the mean and median differed greatly; for those cases the selected "representative" value was sometimes closer to the average between these two (mean and median). In most data sets, median values were generally used. $N_{1,60,CS}$ values were assumed to be normally distributed in performing regressions to develop empirical relationships between penetration resistance and post-liquefaction strength. Median and mean values were thus assumed to be essentially the same, and standard deviations <u>of the mean</u> of $N_{1,60,CS}$ were modeled as a measure of estimated variance. This standard deviation of the mean is very different than the standard deviation of the $N_{1,60,CS}$ values, and it exhibits smaller variance. These variances were in many cases controlled more by uncertainties involved with conversion of non-standard penetration resistance data to estimates of equivalent SPT $N_{1,60,CS}$ values, than by variance among the individual penetration resistance values measured for a given soil stratum. When either CPT data, or non-standard penetration data, or lesser quality information regarding placement conditions and history, were used to develop estimates of equivalent SPT $N_{1,60,CS}$ values, the details of ascertaining and/or estimating both mean $N_{1,60,CS}$ values and Standard deviation of the overall mean $N_{1,60,CS}$ values are presented on a case by case basis in Appendices A and B.

For two of the case histories (Wachusset Dam and Fort Peck Dam) additional corrections were required for ageing effects, as multiple decades elapsed between the occurrences of these two failures and the eventual performance of modern SPT investigations. The details of the corrections made for ageing effects in these two cases were case specific, and these details are presented in Appendix A, Sections A.1 and A.2, respectively.

4.2.5 Evaluation of Representative Initial Effective Vertical Effective Stress

Values of "representative" initial effective vertical stress in liquefied materials for each case history were evaluated by averaging the pre-failure effective vertical stresses along the portion of the failure plane that would be controlled by liquefied materials. Approximate calculations were made by summing vertical stresses at the bases of slices in liquefied materials in slope stability calculations for the pre-failure geometries, and averaging these along the liquefied slide plane lengths. These provided adequately close approximations of initial vertical effective stresses, and they also appear to provide good agreement with estimates of initial vertical stresses made by Olson and Stark (2001, 2002) for most cases, especially if Olson's values are adjusted slightly (reduced a bit) to account for the fact that he generally assumed slightly shallower failure surfaces for most of his cases, and (2) Wang (2003) and Kramer (2008) for the nine "primary" case histories for which Wang (2003) performed independent assessments of initial effective vertical stresses.

A more comprehensive discussion and cross-comparisons between values of representative values of initial effective vertical stress for each case history developed and/or employed by different investigation teams is presented in Sections 2.3.8.1(b) – (ii) and at the end of this chapter in Section 4.7.

4.3 Back-Analyses of the 14 Case Histories of Groups A and C

4.3.1 Back-Analyses and Results

The 14 "high quality" case histories of Groups A and C were back-analyzed using the new incremental momentum method, and the details of these analyses are presented in Appendix A. The single Class C case history was also back-analyzed using the new incremental momentum method, but the results were used only to help calibrate and check the other case history back-analyses and not for development of regressed predictive relationships for evaluation of S_r. The main analyses of the Class A and C cases were performed by the incremental momentum method, and additional analyses were also made using simple static limit equilibrium stability analyses to develop back-calculated values of (1) the "apparent" pre-failure yield stress ($S_{r,yield}$) which is defined as the theoretical strength along liquefied portions of the eventual slide surfaces that would be required to provide a calculated static Factor of Safety equal to 1.0 for pre-failure geometry, and (2) the "apparent" residual stress based on final residual geometry ($S_{r,resid/geom}$) defined as the strength along liquefied portions of the failure surface that would be required to provide a post-failure calculated static Factor of Safety equal to 1.0 for the final, residual post-failure geometry. These values of $S_{r,yield}$ and $S_{r,resid/geom}$ would prove useful (1) in evaluating the results of the incremental momentum analyses, (2) in developing empirical methods for checking these types of back-analyses, and (3) for helping to make back-assessments of S_r for some of the case histories in the set of 16 Class B cases, as will be described in Section 4.4.

Table 4.2 shows the results of the back-analyses performed for the 14 Class A and C case histories (in the columns to the far right). Also shown are values developed by the previous investigations of Seed and Harder (1990), Olson and Stark (2001, 2002), and Wang and Kramer (2003, 2008). Values shown are "representative" values developed by each investigation team.

For these current studies these are "best estimate mean values". The values for the other three investigation teams appear to be largely compatible with this basis.

The values of effective vertical overburden stress listed for Wang and Kramer (2003, 2008) in Table 4.2 are inferred from their collection and averaging of multiple values of S_r and S_r/σ'_{vo} for each case, and then using these to infer σ'_{vo}. As discussed previously in Section 2.3.8.1(b), (and shown in Table 2.3) this proved to be a poor process and it resulted in clearly unreasonable values of σ'_{vo} for at least nine of their "secondary" case histories, and poor values for four additional cases. The secondary case histories of Kramer and Wang (2003, 2008) can be identified in this table because their S_r values are enclosed in parentheses.

4.3.2 Comparison with Results from Previous Studies

Table 4.3 shows a modified presentation of the same cases shown in Table 4.1.

Values of S_u(Liq) [S_r in these current studies] for ten of the field failure case histories studies by Olson and Stark (2002) were calculated using their "kinetics" method (see Section 2.3.6), which appears to have largely correctly incorporated momentum effects. These were the ten case histories that Olson and Stark judged to have sufficient quality of data available as to justify this relatively advanced analysis approach. The resulting values of post-liquefaction strength for these ten "high quality" case histories back-analyzed by the "kinetics" method which incorporates momentum effects are listed in Table 4.2 without parentheses. The other 23 cases with lesser quality data or information that Olson analyzed were back-analyzed using what they described as "simplified" methods. This amounted largely to evaluation of the "apparent" post-liquefaction strengths based on the value of S_u(Liq) required to provide a calculated static Factor of Safety equal to 1.0, and those values thus represent values of $S_{r,resid/geom}$. These $S_{r,resid/geom}$ values would significantly underestimate the actual S_r values, as discussed later in Section 4.4, likely by factors of approximately 1.2 to 3.4 (see Figures 4.8 through 4.11), and so they are not directly comparable with the values calculated in these current studies for the Class A and C cases. Fortunately, Olson (2001) had also calculated values of both $S_{r,yield}$ and $S_{r,resid/geom}$ for all but one of the 33 cases which he back-analyzed. The $S_{r,yield}$ values were developed as part of an examination of a potential triggering analysis approach that was not intended to be directly related to back-analyses of S_r, and the $S_{r,resid/geom}$ values were developed as a primary basis for conservative estimation of S_r for the 23 less well-documented case histories. As a result, it is possible to use his values of these two indices to develop better estimates of S_r that would then be more directly comparable with the S_r values back-calculated for the Class A and C cases in these current studies. As will be developed in detail in Section 4.4, reasonably good estimates of the actual S_r values for most cases can be estimated as

$$S_r \approx \xi \bullet (S_{r,yield} + S_{r,resid/geom}) / 2 \qquad \text{[Eq. 4-1]}$$

where ξ can be taken as approximately 0.8.

This produces values of S_r that approximately incorporate momentum effects. Ten of Olson's cases were back-analyzed using his "kinetics" method which incorporates momentum

effects. Given the availability of values of $S_{r,yield}$ and $S_{r,resid/geom}$ back-calculated by Olson (2001), the values of S_u(Liq) not calculated by the "kinetics" method can be replaced with values estimated by Equation 4-1, employing a value of $\xi = 0.8$. For 22 of the 23 cases that were not back-analyzed by Olson's "kinetics' method, and for which Olson's own values of values of $S_{r,yield}$ and $S_{r,resid/geom}$ are available, values of S_r as estimated based on Equation 4-1 have been substituted in Table 4.3. These are shown in Table 4.3 [within square brackets], to provide values of S_r that also (at least approximately) incorporate momentum effects. Several of Olson's lesser quality cases were not included in these current studies, so no values for those cases are shown in Tables 4.2 and 4.3.

For one case [El Cobre Tailings Dam] Olson (2001) did not employ his "kinetics" analysis method, and he also did not calculate a value of $S_{r,yield}$. The value of S_r for this case is shown within triangular brackets in Table 4.3, and it represents a very conservative (low) $S_{r,resid/geom}$ value.

Values of S_r were back-calculated by Wang (2003) for the nine highest quality field performance case histories using the "ZIF" method (see Section 2.3.7), which largely correctly incorporated momentum effects, and the resulting values of post-liquefaction strengths are listed in Tables 4.2 and 4.3 with no parentheses. Values of S_r listed with parentheses in Tables 4.2 and 4.3 are those for most of the 22 additional "secondary" cases with lesser quality data for which Wang did not perform the full ZIF analyses, and instead adopted values based on judgmental averaging of values developed by other previous investigators. These are probably not strongly systematically biased, but they are less likely to be fully accurate and reliable. Several of Wang's "secondary" cases were not included in these current studies, and so values for those are not shown in Tables 4.2 and 4.3.

The modified values shown in Table 4.3 then represent the best available basis for cross-comparison of back-calculated values of S_r that incorporate momentum effects for the cases of Classes A and C.

The value of S_r from Seed and Harder (1990) shown for the Fort Peck dam case history is notably low compared to the other three investigation teams. That is because the runout distance was very large for this case, and Seed and Harder underestimated the multiplier (ξ) in Equation 4-1 that would provide a good estimate of S_r with approximate inclusion of momentum effects for this case. (Better values of ξ as a function of runout indices are developed next in these current studies, as presented and described in Section 4.4 which follows.)

The value of Olson and Stark (2002) for the Shibecha-Cho Embankment case history is notably low compared to the results of the other investigation teams. This is because, as was discussed and illustrated previously in Section 4.2.3, the Shibecha-Cho failure was a strongly incrementally progressive failure, retrogressing backwards in successive slices towards the eventual back heel. (An even more complete explanation of the analyses of this incrementally progressive failure is presented in Appendix A, Section A.12). Olson correctly recognized that this was an incrementally progressive failure, and attempted to account for this retrogressive progression by performing his "kinetics" analysis by tracking only the initial (front-most) failure slice. This was not successful, as he was only able to track and analyze momentum, forces, and post-liquefaction shear strength, for the first (initial) small "slice" nearest to the front face. This neglected most of the overall failure mass, and most of the momentum, and it resulted in significant underestimation of S_r for this case.

Wang and Kramer (2003, 2008) appear to have selected high averaged values of S_r for the two La Marquesa Dam failures (upstream side and downstream side failures). These were developed by averaging of values developed by multiple previous investigators, and they were affected by high values developed by Seed and Harder (1990) as was discussed previously in Section 2.3.8.1(b).

Wang and Kramer calculated a somewhat lower S_r value, based on their ZIF analysis method, for the Calaveras Dam case history than the values back-calculated by Olson and Stark (2002) and by these current studies. Olson and Stark employed their kinetics method, and these current studies employed the incremental momentum approach. All three of these analysis methods explicitly incorporate momentum effects, and it must be suspected that the differences here are the result of differing modeling and parameter details in the three different sets of analyses. The Calaveras case history results are not employed in development of correlations for forward prediction of S_r in these current studies because, as described in Chapter 3, Section 3.3.2, the combination of still-consolidating cohesive-dominated hydraulic fill zones at the time of the failure, and unpredictable ageing effects occurring in variably cohesive/non-cohesive hydraulic fills over the eight decades that followed, make it impossible to reconcile modern site investigation results (and recent penetration resistance data) with the original field failure performance observed.

For the remainder of the 14 Class A and C cases, values of S_r are judged to be in generally good agreement among the four investigation teams represented in Tables 4.2 and 4.3, especially given the differences between analytical approaches and modeling details employed by the different investigation teams.

There are approximations and judgments required in each of these analyses, and overall agreement among the 14 cases comprising Classes A and C is judged to be good to excellent.

There is, of course, a preference here for the values developed by the more difficult, more detailed and more flexible incremental momentum method which better addresses some of the details of these cases and appears likely to provide higher levels of reliability of back-calculated S_r values as well. The cross-comparisons of Table 4.3 are interpreted herein as reflecting a good level of support for the values back-calculated by this method.

4.4 Development of New Empirical Relationships for Back-Analyses of Case Histories for Assessment of S_r

The values back-calculated and presented in Section 4.3 for the 14 Class A and Class C field case histories back-analyzed by the incremental momentum method were next used to develop two sets of empirical relationships for (a) cross-checking the results of back-analyses of liquefaction flow failures for consistency, and (b) making back-estimates of S_r from other liquefaction failure case histories where lesser quality data and information are available. In the end, these new relationships also provide a basis for approximate checking of engineering analyses of expected liquefaction-induced displacements and deformations for large displacements cases, with likely useful applications for evaluations of interim reservoir restrictions for dams that require eventual seismic hazard mitigation.

4.4.1 Pre-Failure and Post-Failure Analyses Calibrated Based on Runout Characteristics

As noted in a number of previous sections, simple static limit equilibrium analyses can be performed to evaluate (1) the back-calculated value of the "apparent" pre-failure stress ($S_{r,yield}$) along liquefied portions of the eventual slide surface required to provide a calculated static Factor of Safety equal to 1.0 for pre-failure geometry, and (2) the "apparent" residual stress ($S_{r,resid/geom}$) required to provide a post-failure calculated static Factor of Safety equal to 1.0 for the final, residual post-failure geometry. $S_{r,yield}$ would, of course, over-estimate the actual post-liquefaction strength; otherwise the failure would not have occurred. And $S_{r,resid/geom}$ would underestimate the actual post-liquefaction strength, as it does not account for momentum effects as the travelling failure mass must be brought back to rest. These values of $S_{r,yield}$ and $S_{r,resid/geom}$ would therefore "bracket" the actual value of S_r for any given case history.

Further discussion of this is now warranted.

For cases in which "flow" or slide displacements are very small, there would be relatively little difference between $S_{r,yield}$ and $S_{r,resid/geom}$, and momentum effects would also be small. In such cases, simply adding $S_{r,yield}$ plus $S_{r,resid/geom}$, and then dividing by two would provide a good estimate of S_r. This could be expressed as

$$S_r \approx \xi \bullet (S_{r,yield} + S_{r,resid/geom}) / 2 \qquad \text{[Eq. 4-2]}$$

where ξ can be taken as nearly 1.0.

At the other extreme, for cases in which runout distances were infinitely large, post-liquefaction strength would be essentially equal to zero, in which case S_r could be estimated as

$$S_r \approx \xi \bullet (S_{r,yield} + S_{r,resid/geom}) / 2 \qquad \text{[Eq. 4-3]}$$

where ξ can be taken as nearly equal to zero.

This reasoning then gives rise to the observation that the general form of Equations 4-1 through 4-3 can be improved by making the value of ξ a function of observed runout distance. Also, it is observed that ξ is bounded, and can have values of between 1.0 and zero. And that values of ξ can be expected to decrease with increases in runout distance.

Figure 4.6 shows best estimate values of post-liquefaction strength (S_r) back-calculated by the incremental momentum analyses for the 14 case histories of Classes A and C, plotted on the vertical axis, and on the horizontal axis it shows the averaged "before and after" values of ($S_{r,yield}$ + $S_{r,resid/geom}$) / 2 as calculated by Equation 4-1 with ξ assumed equal to 1.0. This "before and after" average is simply the average of $S_{r,yield}$ and $S_{r,resid/geom}$.

As shown in this figure, generally good fitting of a majority of the back-calculated data is achieved if the value of ξ is set a bit lower than 1.0, with most of the back-analyses being well-represented by values of ξ of between 0.6 to 1.0.

A fully general form of this relationship can then be expressed as

$$S_r \approx \xi \bullet (S_{r,yield} + S_{r,resid/geom}) / 2 \qquad \text{[Eq. 4-4]}$$

where ξ is a function of runout distance and overall failure mechanism characteristics.

Three of the 14 cases plotted in Figure 4.6 are cases in which incrementally progressive (retrogressive) failure initiation is thought to have affected back-calculated values of S_r, and it was necessary to develop a slightly modified version of Equation 4-4 for these types of cases. The initial value of $S_{r,yield}$ for these cases was calculated for (1) the initial (smaller) initial failure mass nearer the front face of the failure, and (2) for the eventual overall (entire) failure mass. These two values were then averaged to develop the "representative" overall value of $S_{r,yield}$ for purposes of the relationships modeled in Equation 4-4. This was then employed, along with $S_{r,resid/geom}$ from the eventual post-failure residual geometry (for the entire failure mass) in Equation 4-4 to develop the "before and after" averaged value of $(S_{r,yield} + S_{r,resid/geom}) / 2$ for these incrementally regressive cases. Additional analyses were then also performed for each of these three cases, but this time employing only the $S_{r,yield}$ value for the initial (smaller) initial failure slice and then the $S_{r,resid/geom}$ value for the overall residual post-failure condition of the overall failure mass, as with all of the other case histories (which were not significantly incrementally retrogressive).

The three cases to which this slightly modified calculation was applied were Case A.2 (Fort Peck Dam), Case A.3 (Uetsu Railway Embankment) and Case A.12 (Shibecha-Cho Embankment). For each of these cases, the values calculated based on only the $S_{r,yield}$ values calculated for the initial (smaller) initial failure slices are shown with dashed circles, and the values calculated using the averaged $S_{r,yield}$ values for the initial (smaller) initial slices and the larger (overall) failure mass are shown with solid circles. These latter values are judged to be the better and more representative values.

The Fort Peck Dam failure case history was modeled as being only slightly incrementally progressive/retrogressive (see Appendix A, Section A.2) and the differences here between the two approaches are minor, supporting both the interpretations here, and the modeling of the case as only slightly progressively retrogressive For the Uetsu and Shibecha Cho Embankment failure case histories, the differences were somewhat more significant, as would have been expected (see Appendix A, Sections A.3 and A.12, respectively).

The next step was then to invert Equation 4-4, using the actual values of S_r as calculated using the incremental momentum method, to develop case-specific values of ξ. These values of ξ for each of the 14 back-analyzed Class A and Class C case histories were then plotted against different measures of runout distance. The best relationship was found to be achieved by cross-correlation of ξ with "scaled runout distance", defined as the total distance travelled by the center of gravity of the overall failure mass divided by the initial slope height as measured from the toe of the failure to the top of the eventual back heel of the overall failure.

This is plotted for each of the 14 Class A and C case histories back-analyzed by the incremental momentum method in Figure 4.7. As shown in this figure, a relatively strong relationship between ξ and scaled runout resistance can be observed. It can also be seen that the value of ξ would approximately approach 1.0 for zero runout distance, as would be expected if

cyclic inertial effects were either zero or were neglected. It can also be seen that ξ appears to trend towards zero (as would theoretically be the case) for a runout ratio equal to infinity.

Figure 4.7 serves to demonstrate the good internal consistency between the back-calculated values of S_r for these 14 well-defined field case histories. It also represents a basis for evaluation of ξ as a function of runout distance, which in turn makes Equation 4-4 significantly more useful for empirical estimation of S_r.

A second set of empirical relationships were then developed by plotting "Initial Factor of Safety" vs. "Final Factor of Safety" for these 14 Class A and C cases, as shown in Figure 4.8. Initial factor of safety here is defined as the apparent static Factor of Safety calculated for pre-failure geometry with the strength of the of the liquefiable soils set equal to the best estimate value of actual S_r back-calculated using the full incremental momentum method. Similarly, the final factor of safety is the static value of FS calculated using this best estimate value of S_r from the incremental momentum back-analyses and assigning it to the liquefied soils in the post-failure (final) residual geometry configuration.

As shown in Figure 4.8, the values back-calculated for the 14 cases all occur within a reasonably well-defined range. Closer inspection of the individual cases (identified by number in the figure, and by name in the "key" in the upper right-hand corner of the figure) shows that cases with larger "scaled runout distance" have lower Initial FS values, and higher Final FS values. Figure 4.9 then repeats Figure 4.8, but this time each case history's "dot" is annotated (in parentheses) with the ratio representing scaled runout ratio (distance traveled by the center of gravity of the overall failure mass divided by the initial slope height from the toe to the top of the back heel of the failure). It be seen that the cases tend to move from the bottom right hand portion of the observed range, towards the top left portion of the figure, with increasing scaled runout distance.

The two relationships of (1) Figures 4.6 and 4.7 and (2) Figures 4.8 and 4.9 provide a systematic basis for understanding some of the interactions between the runout mechanics of liquefaction failures, and the post-liquefaction strengths and various calculated stability measures associated with these failures.

These relationships can then be used for several purposes:

1. They can be used as an internal check for consistency and reasonableness for back-analyses of S_r performed within a study such as this current one. There had not previously been any useful tools for that.

2. They can also be used to cross-check engineering analyses of expected deformations, and resulting displaced geometries, for forward analyses of engineering projects. As an example, it is not uncommon once a major dam has been studied and found likely to pose an unacceptable risk with regard to potential for liquefaction-induced failure, for the reservoir to be "restricted" to a constrained maximum elevation until repairs/mitigation can eventually be implemented. Reservoir restrictions imposed are usually the result of assessments of likely worst-case deformations, in order to ensure that these will not result

in uncontrolled release of the reservoir as long as the reservoir level is kept at or below the restricted level. High-order finite element and finite difference analyses are often brought to bear here. These analyses involve a number of choices and decisions with regard to modeling and parameters, and there are potential additional numerical difficulties associated with extreme mesh deformations as calculated deformations become large. The accuracy, and the acceptable conservatism, of such analyses can be difficult to verify. There are currently no widely accepted ways to reliably "check" the results of such analyses. Both of the relationships developed here (Figures 4.7 and 4.9) can be employed for that purpose.

3. Finally, these two sets of relationships can also be employed to help to extract reasonable back-analyzed or back-estimated values of S_r for liquefaction failure case histories of lesser overall quality, reliability, or documentation than the 14 cases of Classes A and C. These relationships are thus useful in back-analyses of a number of the 16 additional liquefaction failure case histories of Class B, as described in Appendix B and in Section 4.5 below.

4.5 Back-Analyses of the 16 Case Histories of Group B

4.5.1 Back-Analyses and Results

The 16 lesser quality liquefaction case histories of Group B were next back-analyzed. Details of individual analyses and assessments for each of these case histories are presented in Appendix B. The quality, quantity, reliability and level of documentation of data and information regarding various aspects of these Class B cases varied considerably. As a result, these cases were judged not to warrant the incremental momentum analyses applied to the Class A and C cases.

But it was not sufficient here to simply take the values back-calculated, or estimated, by previous investigators. One of the objectives of these current studies was to make the best achievable assessments of both the "best estimate" values of $\overline{S_r}$, $\overline{N_{1,60,CS}}$ and representative $\overline{\sigma'_{vo}}$ for each case history, and also the best possible estimates of uncertainty or variance for each of these three indices. Considerable effort was therefore also expended on back-analyses and back-assessments of these "lesser" cases.

This served to differentiate these current studies from all previous efforts. A number of previous studies had done a relatively good job, or at least applied a good deal of effort, to back-analyses of many of the Class A and C cases. But none of those studies had then continued on to devote significant and/or comprehensive efforts to independent evaluation (or re-evaluation) of the significantly larger number of Class B cases as well.

It is not possible to simply and concisely describe the ranges of approaches, judgments, etc. that were employed in back-assessments of the 16 additional cases. Engineers who are interested are encouraged to examine the case-by-case explanations and expositions presented in Appendix B, as the details of the judgments made in processing these cases can be important.

The values that resulted from these back-analyses and assessments generally carried larger values of uncertainty (and thus larger standard deviations) that was common for the Class A and

C cases. This often reflected significant uncertainties associated with lack of data, poor quality of data, poor documentation of data, etc. The values of standard deviations reported for each parameter are, for each case, the best estimates of this investigation team taking all uncertainties into account.

Table 4.4 presents a summary of the back-analysis results for the Class B cases, in the form of best estimate values of representative $\overline{S_r}$, $\overline{N_{1,60,CS}}$ and $\overline{\sigma'_{vo}}$ for each case. Four sets of values are shown, corresponding to the values recommended by each of four different investigation teams: (1) Seed and Harder (1990), (2) Olson and Stark (2002), (3) Wang and Kramer (2003, 2008) and (4) these current studies.

Table 4.5 then repeats the presentation of the back-analysis results for the Class B back-analyses, but the values shown in square parentheses for Olson and Stark (2002) again are modified values representing values calculated using Equation 4-1, with $\xi = 0.8$, and using the case-specific values of $S_{r,yield}$ and $S_{r,resid/geom}$ reported by Olson (2001). These replace the systematically biased (low) values estimated by Olson (2001) based on $S_{r,resid/geom}$., and they provide better estimates of S_r because they account (approximately) for momentum effects.

Similarly, the values shown in parentheses in Tables 4.4 and 4.5 for Wang and Kramer (2003, 2008) are values that they selected based on their averaging of selected values from other previous investigators, with no further analyses of their own, and so do not represent fully independent assessments of their own.

Generally good to excellent agreements among the several sets of values shown for the 16 Class B cases in Table 4.5 for most cases (after modifying the S_r values of Olson and Stark, 2002, based on their calculated $S_{r,yield}$ and $S_{r,resid/geom}$ values reported and Equation 4-1) appears to provide good support for the values developed in these current studies.

The value of S_r reported by Olson (2001) for the El Cobre Tailings Dam case history could not be modified to the value produced by Equation 4-1, because the necessary initial yield and post-failure residual geometry values of $S_{r,yield}$ and $S_{r,resid/geom}$ were not presented by Olson for that lone case. The value shown is that recommended by Olson and Stark, but as discussed in Appendix B, Section B.20, it appears to be estimated based on a very conservative back-calculation of $S_{r,resid/geom}$ and thus appears to be unreasonably low. The relationship of Figures 4.8 and 4.9 would suggest that this SS value would underestimate Sr for this case by a factor of approximately 2 to 3. Multiplying Olson's value of $S_{r,yield} = 40$ lbs/ft^2 by 2.5 would produce an estimate of Sr = 100 lbs/ft^2, in excellent agreement with the value of SS = 95 lbs/ft^2 back-calculated in these current studies.

Wang and Kramer (2003, 2008) appear to have unreasonably high values of S_r for two cases, the Hokkaido Tailings Dam failure and the Nerlerk Embankment Slides. They did not perform independent back-analyses of their own for these two cases; instead they averaged values from multiple previous investigations. As discussed previously in Chapter 2, Section 2.3.8.2(b), the Hokkaido Tailings Dam value employed by Kramer and Wang appears to be the result of an error. They averaged two values of S_r from previous investigations for this case, and one of these was a value of $S_r = 408$ lbs/ft^2 attributed to Ishihara, et al. (1990); but the actual value developed by Ishihara et al. (1990) for this case history is only $S_r = 137$ lbs/ft^2 . Using the (correct) lower

value would significantly lower the overall average. A similar, but more complicated set of apparent poor values led to an error in the value employed by Kramer and Wang for the Nerlerk Embankment Slides; readers are referred to the detailed discussion presented previously in Chapter 2, Section 2.3.8.2(b).

In these current studies, values of S_r back-calculated for the two Moshi-Koshi Tailings Dam failures (Dikes 1 and 2) were averaged (see Appendix B, Section B.25), because these were two very similar failures and it was judged that using them as two separate cases would over-emphasize their contribution to the regressions that will follow. Similarly, the three Nerlerk Embankment slides (Appendix B, Section B.26) were also averaged in these current studies, as they were also similar features and including them as three separate cases would over-emphasize their contribution to the regressions that will follow.

Finally it is noted that no cross-comparisons can be made for the values calculated in these current studies for two cases: the Sullivan Tailings case history and the Jamuna Bridge case history. This is because the other investigation teams listed in Tables 4.4 and 4.5 did not include these two more recent cases, which had not been available for their earlier studies. There have been previous back-analyses of these cases by other investigators, but those were not well documented and provide a relatively poor basis for cross-comparisons. See Appendix B, Sections B.28 and B.29 for details.

A second comparison of the results developed for the Class B cases can be made by plotting the results onto the figures and relationships previously presented in Figures 4.6 and 4.7.

Figure 4.10 repeats Figure 4.6, but this time the results of back-analyses of the 16 Class B cases have been added (with open triangles). For 8 of the Class B cases, no reliable post-failure geometry was available, so in some of the cases it was necessary to assume approximate values of the "After" value of $S_{r,resid/geom}$. These were, for the most part, cases wherein the post-failure displacements had been very large, often causing much of the failure mass to travel of down underwater slopes to such extent that they could not reliably be tracked. Low (but not quite zero) values of $S_{r,resid/geom}$ were assumed for most of these cases. These assumptions, and the bases for them, are presented in detail for each case in the corresponding sections of Appendix B. The uncertainties introduced by these assumptions are incorporated in the modeled values of uncertainty (or standard deviation) for each cases as listed in Tables 4.6 and 4.7.

Figure 4.11 then repeats Figure 4.7, but this time the results of back-analyses of the 16 Class B cases have been added (with open triangles). For 6 of the 16 Class B cases, it was not possible to make refined evaluations of the relative displacements in terms of runout ratios (center of failure mas travel distance divided by initial slope height defined as height from toe to back heel of the failure mass), so these cases could not be plotted in this framework. These were generally cases in which runout distances were very large, but they often involved (1) failures that travelled onto relatively steep offshore slopes where the slide masses did not quickly come to rest, (2) situations in which much of the failure mass travelled over a "lip" and then continued down a steeper slope, or (3) cases in which very soft surface sediments may have led to the very large continuing downslope displacements observed.

There is generally good consistency between the Class B cases, and the better-defined and better back-analyzed Class A and Class C cases, in both Figures 4.10 and 4.11, providing a useful additional check of internal consistency among the back-analyses and evaluations performed for the Class B cases.

4.6 Summary of Back-Analysis Results

The results of the back-analyses of all 30 cases (Classes A, B and C) as developed in these current studies (see Appendices A and B) are presented in Table 4.6. This table presents both the best-estimate mean values, and also the best estimate standard deviations, for each of the three indices that will next be used to develop predictive relationships for in situ S_r.

Only one other previous study has been carried forward far enough as to provide useful values for cross-comparison here, and that is the work of Wang (2003) and Kramer (2008).

Table 4.7 presents a comparison between the indices developed in these current studies and those developed by Wang (2003). The values for penetration resistance were subsequently changed to non-fines-corrected $N_{1,60}$ values by Kramer (2008) in his regressions to develop predictive relationships for S_r. The original fines-corrected $N_{1,60,CS}$ values are more appropriate for direct cross-comparisons, and so those will be used here as a cross-check on the two sets of studies.

As discussed previously in Section 2.3.7, the means and basis by which Wang (2003) and Kramer (2008) developed both their mean estimates and their estimates of standard deviation or variance of these means differed greatly from the approaches taken in these current studies. Their approaches did not fully incorporate the influence of uncertainties related to poor documentation of case history data and information, and poor quality of data and information, and so they subsequently applied judgmental weighting factors to down-weight the contributions of the less well-documented cases. That was prudent with regard to development of predictive relationships with good median fit (50% relationships), but it may not have fully characterized overall model uncertainty. The weighting factors (WF) employed by Kramer (2008) in performing regressions to develop predictive relationships are also listed in Table 4.7. These range from 1.0 for cases that are well-characterized and well-documented, to as low as 0.22 for cases with poor data and information quality.

In these current studies, the investigation team has preferred instead to put forth the best estimates of overall uncertainty of each parameter ($\overline{S_r}$, $\overline{N_{1,60,CS}}$ and $\overline{\sigma'_{vo}}$), including <u>all</u> factors (including paucity of data, poor quality data, poor information on pre-failure or post-failure geometries, uncertainty with regard to phreatic surface, poor documentation, etc.) As a result, the standard deviations shown for these current studies in Tables 4.6 and 4.7 incorporate all uncertainties as best that can be accomplished, and this results in natural "self-weighting" of each case in the probabilistic regressions that will follow in Chapter 5 as cases with higher uncertainties naturally exert less "pull" on the regressed relationships. This approach is preferred here, because (1) it does not require the engineering team to impose its judgment in the form of weighting factors, and (2) it permits the subsequent regressions to incorporate the best available characterizations of individual case history uncertainties in developing assessments of overall predictive model uncertainties. Because the cases are "self-weighting" with their total uncertainty estimates, the

additional weighting factors applied to all but one of the cases in these current studies are taken as WF = 1.0.

The single exception is the Calaveras Dam case history, which was reluctantly deleted from use in the regressions that will follow due to new information developed in the late 1990's that led the current investigation team to conclude that it was not possible to cross-relate the S_r values from the failure that occurred in 1918 with SPT data from more recent studies, given the variability of fines contents in some of the main hydraulic fill zones affecting the 1918 slope failure, and the variably cohesive nature of those fines, and the fact that portions of the dam's embankment fill were likely underconsolidated at the time of the failure under the still rising fill loads (see Appendix A, Section A.14). Because the Calaveras Dam case history is deleted from use in the regressions that will follow, the weighting factor assigned in Table 4.7 is WF = 0.

Both the approaches taken in these current studies, and those taken by Wang and Kramer, with regard to treatment of uncertainties should be considered valid alternatives. And so this just represents another set of differences in choices between the current engineering team and the efforts of Wang and Kramer (2003, 2008). In the end, the multiple, and potentially significant, differences in approaches taken by these two studies are a positive thing, as they permit two independent looks at a problem that is only moderately well constrained by data and thus subject to significant engineering judgment at multiple steps along the way.

Another difference between the studies of Wang and Kramer (2003, 2008) and these current studies was the vetting and selection of cases to include. As discussed in Chapter 3, Section 3.3.2, Wang and Kramer elected to include the Calaveras Dam failure case history, and the current investigation did not. Three additional cases included by Wang and Kramer, but deliberatively not included in these current studies, are the three cases listed in Table 4.7 as Class D. These are: (1) Snow River Bridge, (2) Kawagishi-cho Building, and (3) Koda Numa Embankment. Reasons for not including these three cases in the current studies were presented in Chapter 3, Section 3.3.3. Wang and Kramer also elected to employ the Moshi-Koshi Tailings Dam failures as two separate cases, while the current studies elected to combine and average them so that these two very similar cases would not exert inappropriately strong influence on the regressions that will follow.

These current studies include three cases that Wang and Kramer (2003, 2008) did not. The first of these is the Upper San Fernando Dam case history (see Appendix B, Section B.9). The other two cases are (1) Sullivan Tailings Dam, and (2) Jamuna Bridge (see Appendix B, Sections B.15 and B.16, respectively). These two newer cases had not been available to Wang and Kramer.

In the end, as shown in Table 4.7, each team elected to back-analyze and employ slightly different sets of case histories in their studies. Of at least equal importance, each of the two teams employed different analytical approaches, and engineering judgments, in the back-analyses of the cases selected. Many of the cases were common to both studies. A significant number of these have largely similar values in Table 4.7, but a number of them do not. It is therefore interesting to see how these values eventually lead to recommendations with regard to relationships for evaluation of in situ S_r, as are developed and discussed next in Chapter 5, and how the recommendations developed by each of the two investigations compare with each other. It is also interesting to see how they compare with other previous, and in some cases widely-used, recommendations by others as well.

Several important features of the values presented in Table 4.6 should be noted. The values developed for these current studies are the only set of values developed by an engineering team that (1) developed their own best estimate values for all of the cases studied and used in developing correlations, (2) employed back-analysis and assessment methods for all cases that accounted for momentum effects, and (3) developed best estimates of overall uncertainty or variance for each case based on their own assessments and back-analyses.

This does not mean that the current investigation team were not fully cognizant of previous studies, and previous recommendations; but the current team then developed their own best estimates armed with this information. Two former investigation teams had performed reasonably good back-analyses of 9 or 10 "well documented" case histories employing back-analysis methods the were targeted specifically at inclusion of momentum effects, but each of those teams then either (1) used simpler back-analysis methods for the less well documented cases (which outnumbered the well documented cases by factors of approximately 2), or (2) they developed values for the less well documented cases based on considering multiple values developed by previous investigations, without performing their own independent analyses and assessments. And because those less well documented case histories outnumbered the well documented cases by factors of approximately 2 to 1 in each of those previous studies, those cases were important contributors to the predictive relationships then developed and proposed.

Another important distinction is the level of effort invested in back-analyses of the 13 well documented Class A cases in these current studies, employing new analysis methods that can largely correctly incorporate, and explore, effects of (1) incrementally progressive (retrogressive) failure, (2) changing conditions (e.g. locally changing failure surface conditions, geometry, etc.), and (3) changes in hydroplaning or sliding on soft sediments, etc. as failure progresses.

A third distinction is the effort made to develop overall best estimates of all key parameter uncertainties, including both variance in the data sets available, as well as quality of data, quality of documentation, field information regarding phreatic surfaces at the time of failure, etc.

And finally, the values presented in Table 4.6 are the first comprehensive set of back-analysis results to have benefitted from internal cross-checking based on new empirical relationships developed earlier in this chapter specifically for characterization of the types of behaviors intrinsic in the suites of failure case histories studied and back-analyzed in these types of studies.

Table 4.1: Selected Methods for Back-Analyses of Liquefaction Failure case Histories for Purposes of Assessing Post-Liquefaction Residual Strength

Group A: Methods that explicitly address momentum effects:
A-1. Incremental momentum analysis method (Current studies). A-2. Kinetics analysis method (Olson and Stark; 2001, 2002). A-3. Zero inertial factor (ZIF) method (Wang, 2003; Kramer, 2008).
Group B: Methods that implicitly or approximately address momentum effects:
B-1. Displacement-calibrated pre-failure/post-failure analyses (Current studies). B-2. Pre-failure/post-failure analyses (Seed & Harder, 1990).
Group C: Methods that may or may not suitably incorporate momentum effects:
C-1. Adoption of the results of back-analyses from previous investigators.
Group D: Methods that do not incorporate momentum effects:
D-1. Back-analyses of pre-failure geometries with an assumed static factor of safety equal to 1.0. D-2. Back-analyses of post-failure geometries with an assumed static factor of safety equal to 1.0.

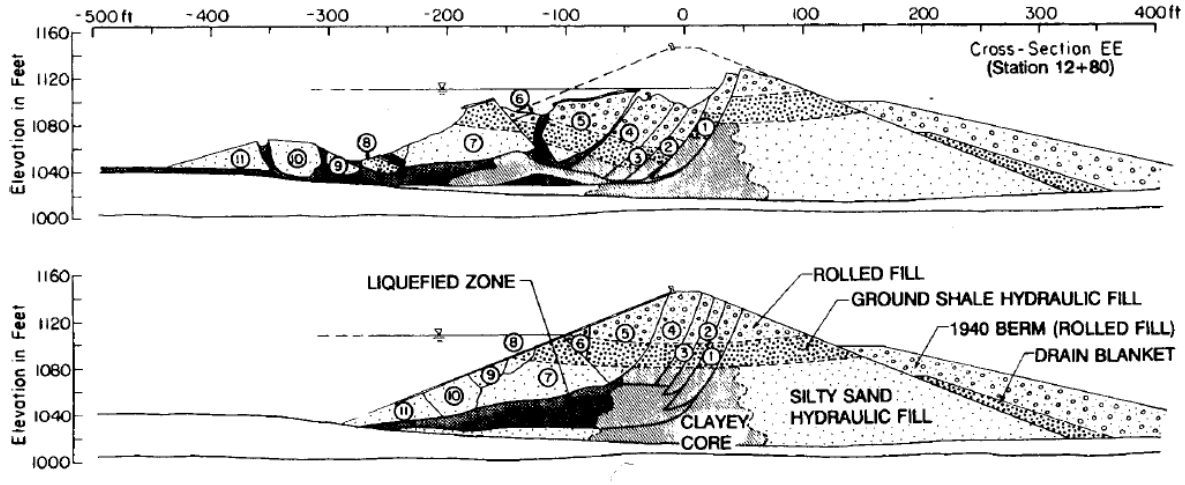

Figure 4.1: Pre-failure and post-failure cross-section of the Lower San Fernando Dam (Castro et al., 1992)

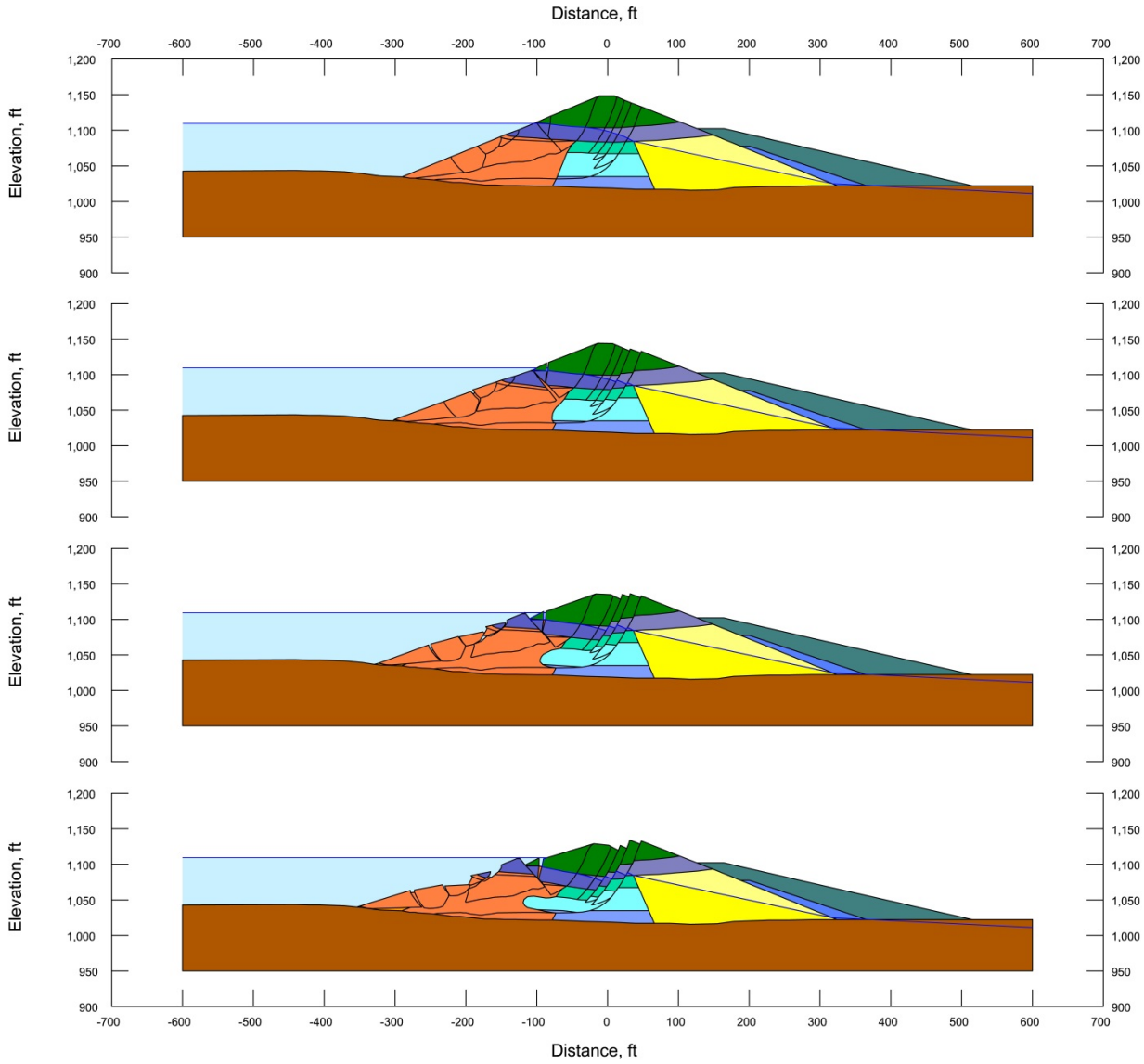

Figure 4.2: Incremental cross-sections used to model and back-analyze the liquefaction-induced upstream slide of the Lower San Fernando Dam (showing the first four cross-sections).

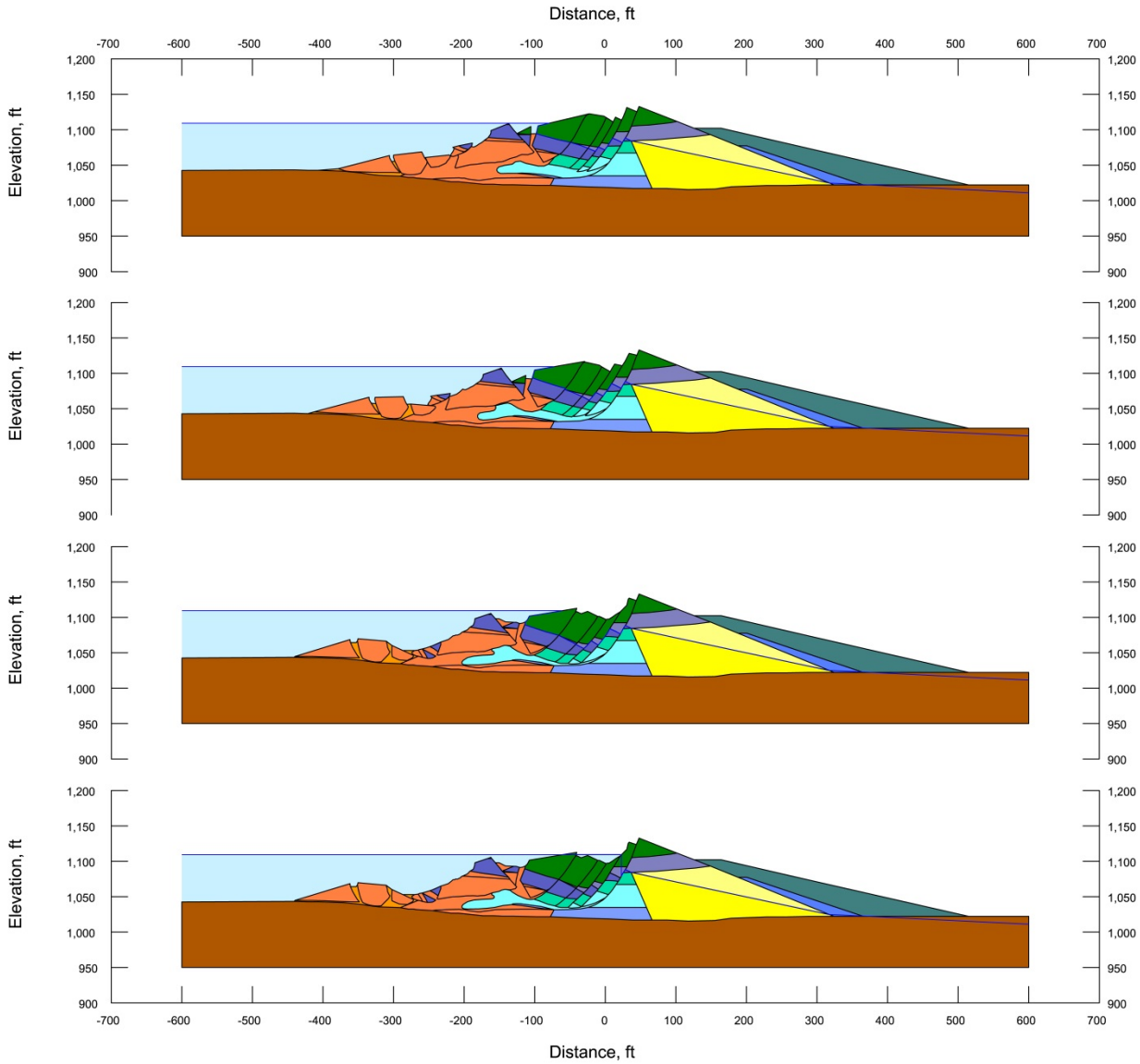

Figure 4.2 (Continued): Incremental cross-sections used to model and back-analyze the liquefaction-induced upstream slide of the Lower San Fernando Dam (showing the final four cross-sections).

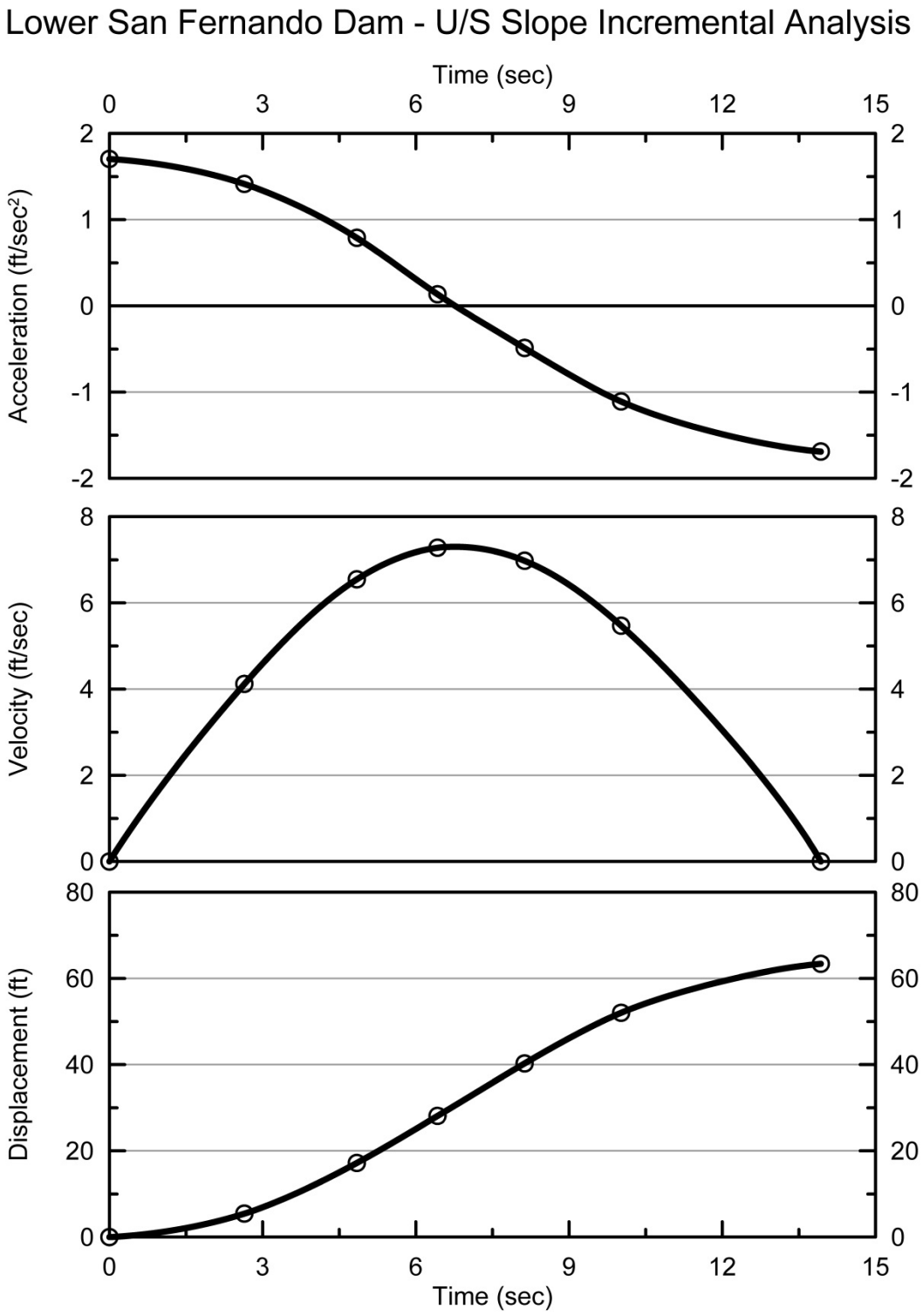

Figure 4.3: Calculated evolution of (1) acceleration vs. time, (2) velocity vs. time, and (3) dis-placement vs. time of the center of gravity of the overall failure mass of the Lower San Fernando Dam based on the progression scenario illustrated in Figure 4.2.

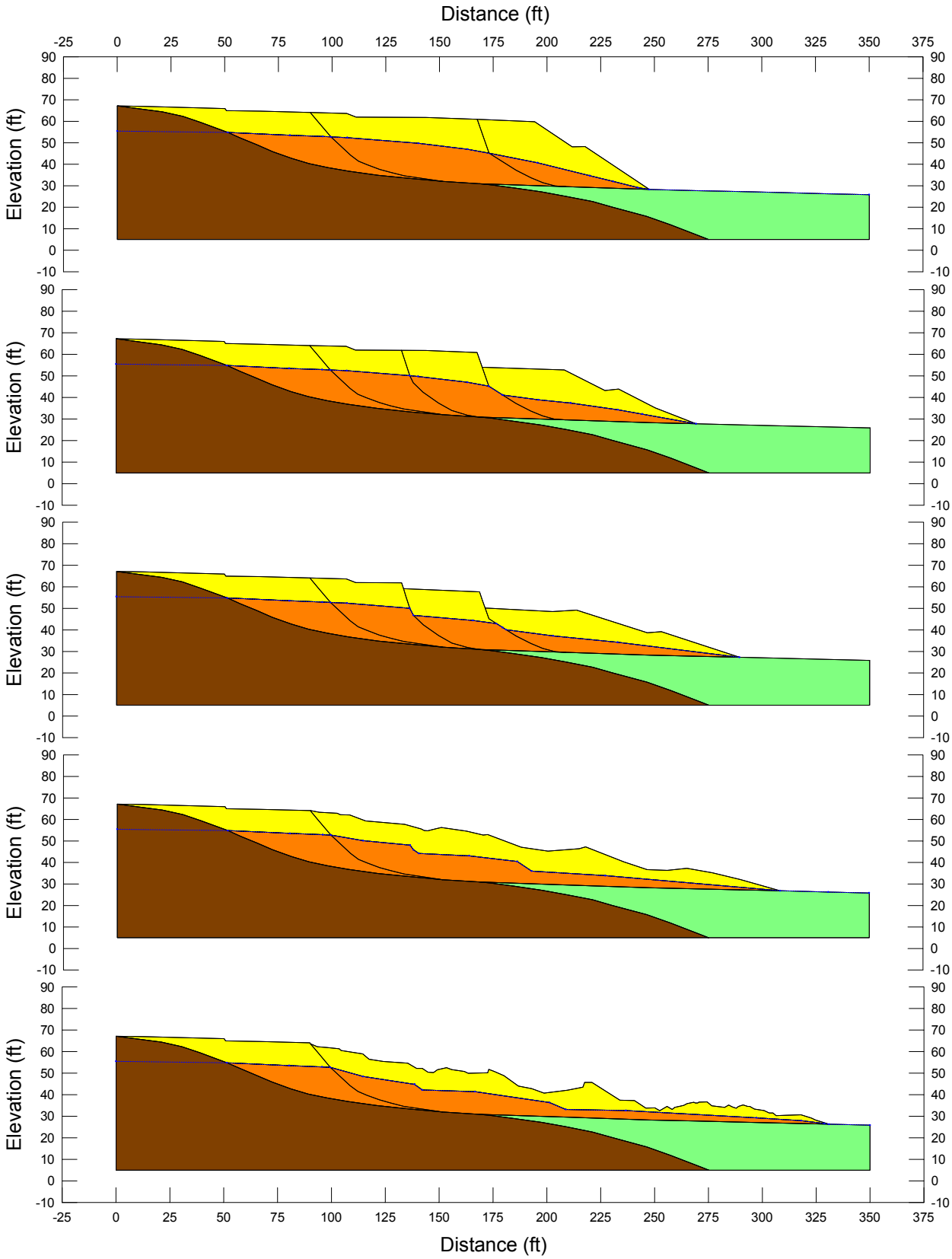

Figure 4.4: Incremental cross-sections used to model and back-analyze the liquefaction-induced failure of the Shibecha-Cho Embankment.

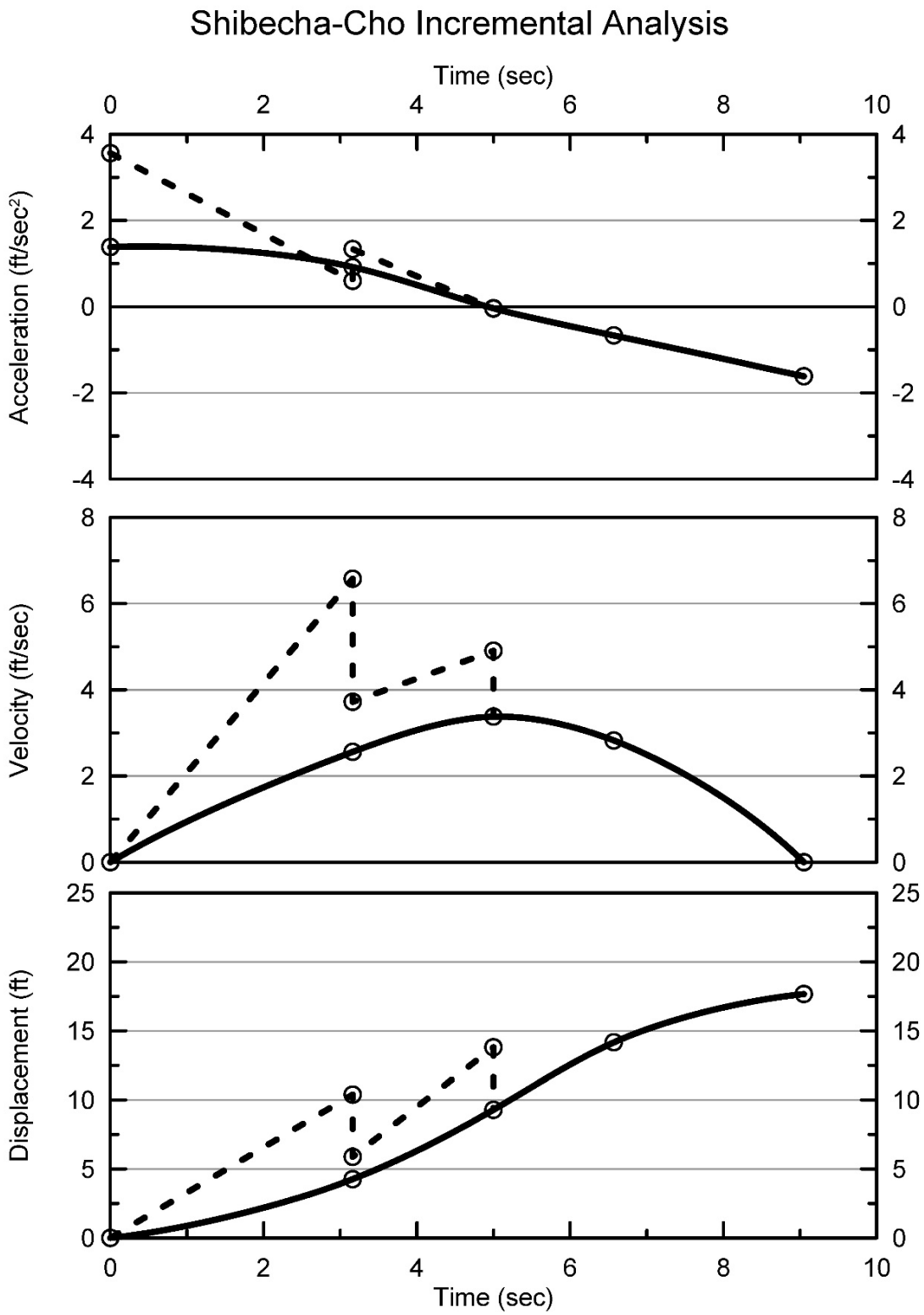

Figure 4.5: Calculated evolution of (1) acceleration vs. time, (2) velocity vs. time, and (3) displacement vs. time of the center of gravity of the overall failure mass of the Shibecha-Cho Embankment fill (solid line), and of incremental partial failure masses (dashed lines), based on the failure progression shown in Figure 4.4.

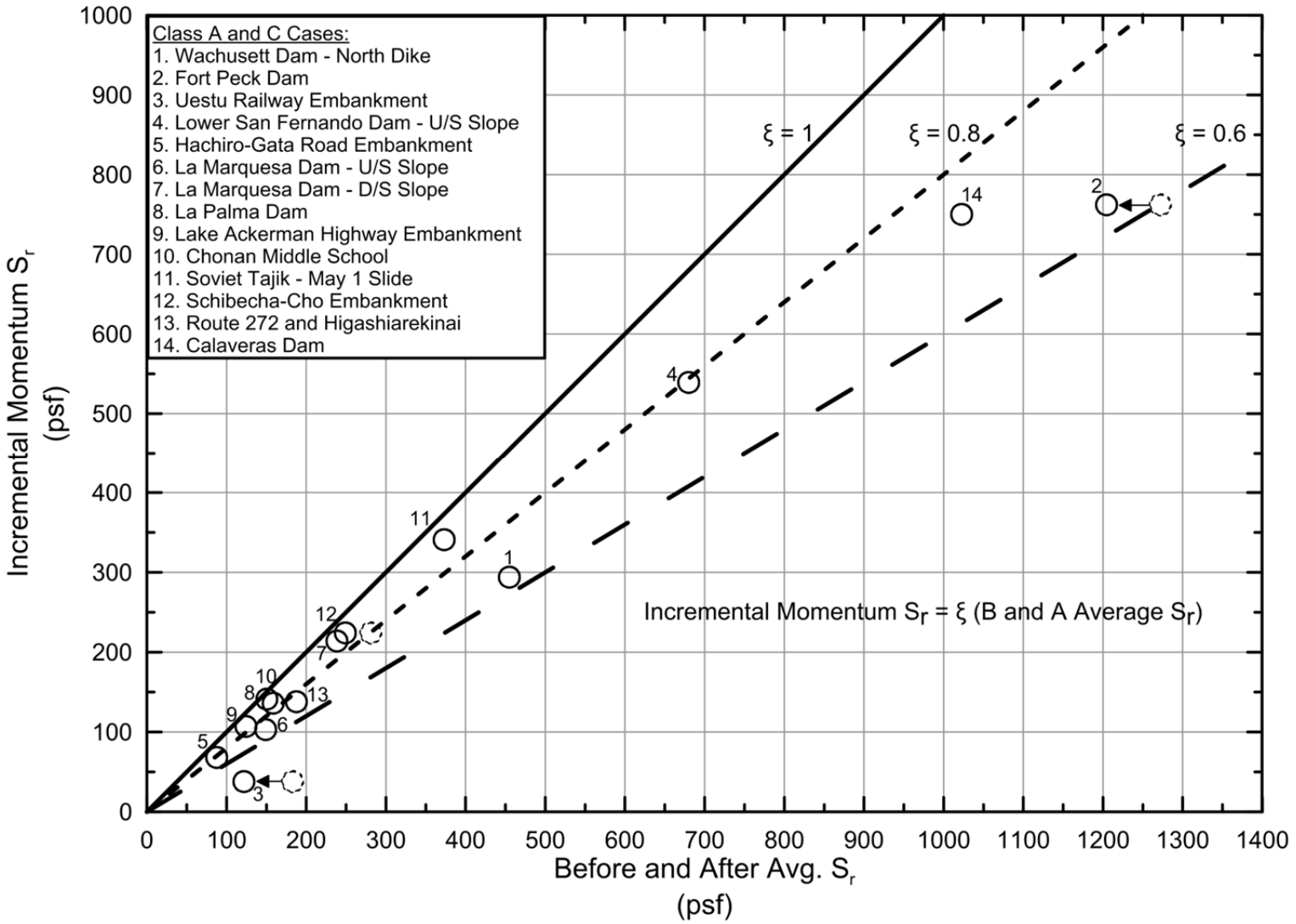

Figure 4.6: Plot of the results of back-analyses of the 14 Class A and C case histories, showing (1) the value of post-liquefaction strength S_r back-calculated by the incremental inertial method vs. (2) "before and after average S_r" which is the average of $S_{r,yield}$ and $S_{r,resid/geom}$ [taken as $(S_{r,yield} + S_{r,resid/geom})/2$].

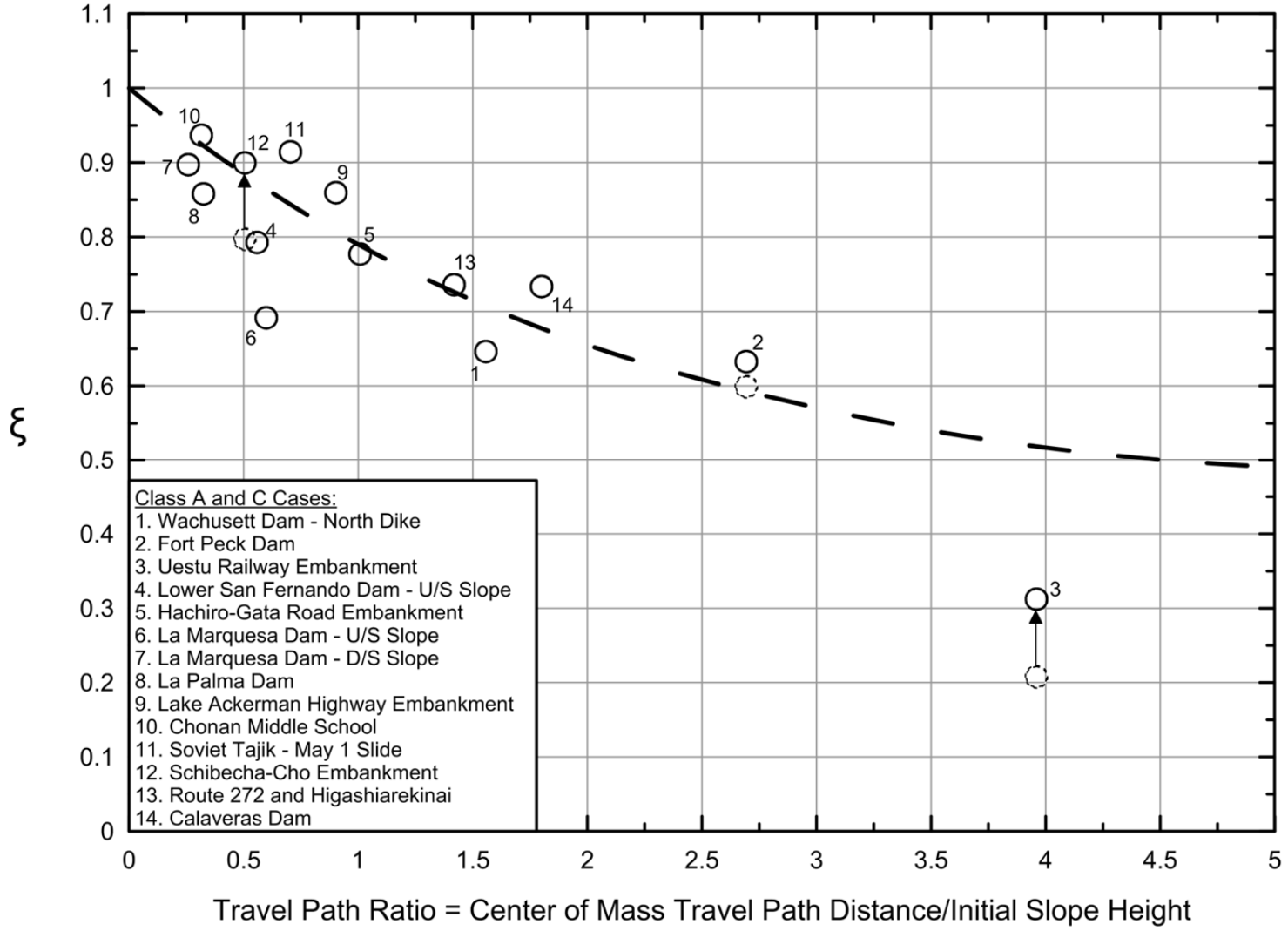

Figure 4.7: The empirical scaling parameter ξ for Equation 4-4, as a function of scaled runout distance.

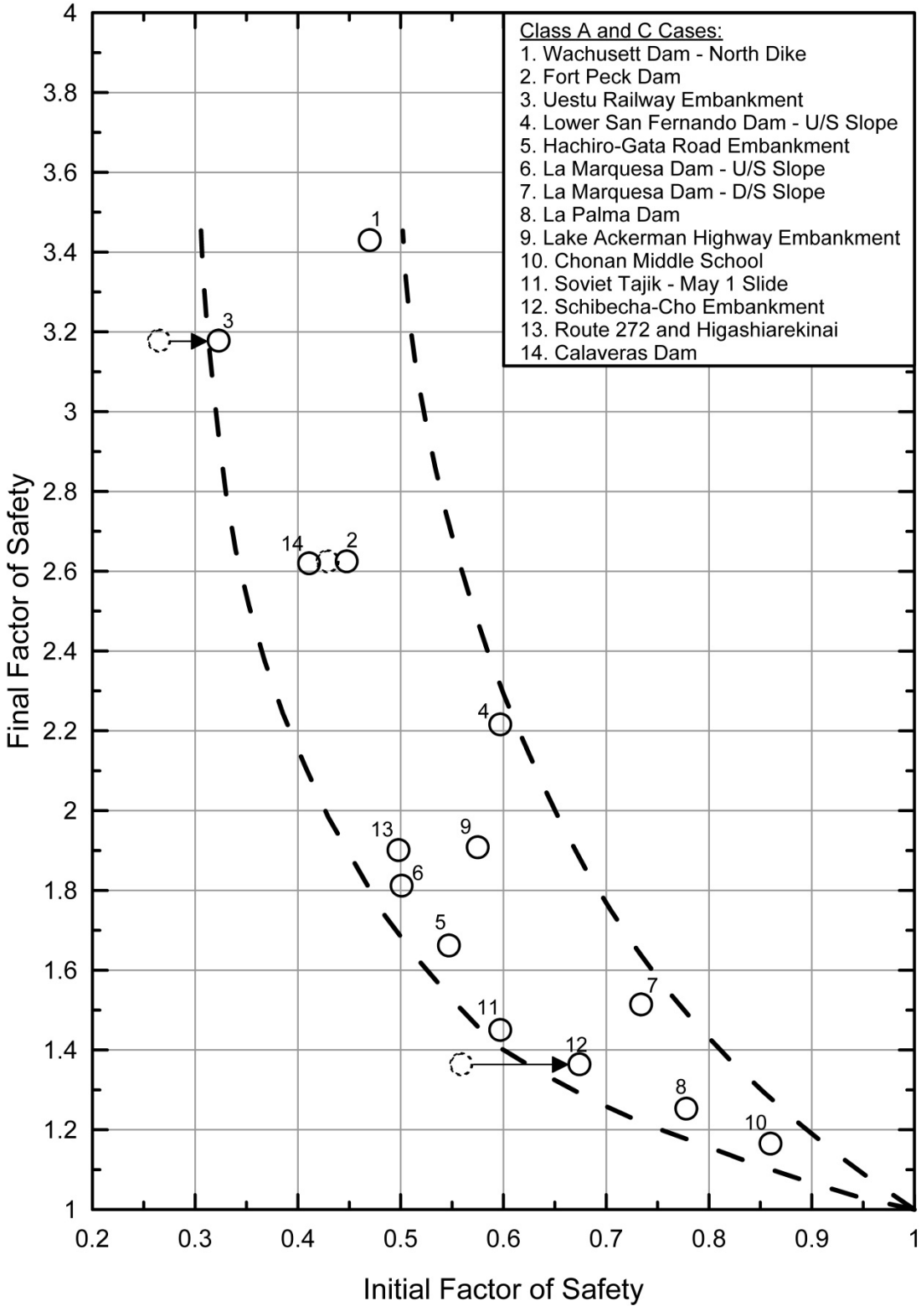

Figure 4.8: Plot of values of pre-failure FS_{liq} vs. post-failure FS_{liq} for the 14 back-analyzed liquefaction failure case histories of Classes A and C.

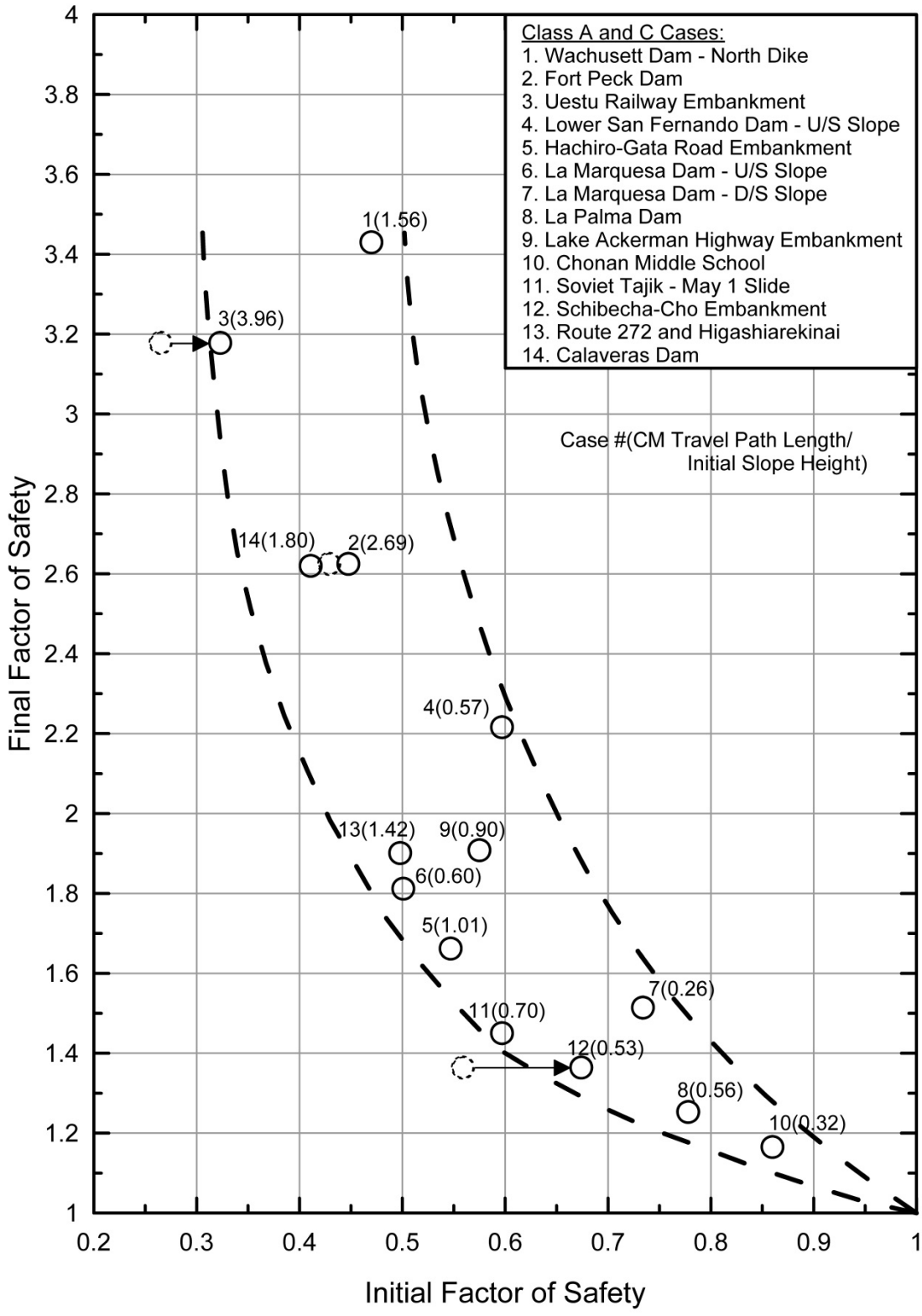

Figure 4.9: Figure 4.8 repeated, this time with the back-analyzed failure case histories annotated (in parentheses) with scaled runout distance ratio (travel distance of the center of gravity of the overall failure mass divided by the initial slope height as measured from the toe to the back heel of the failure)

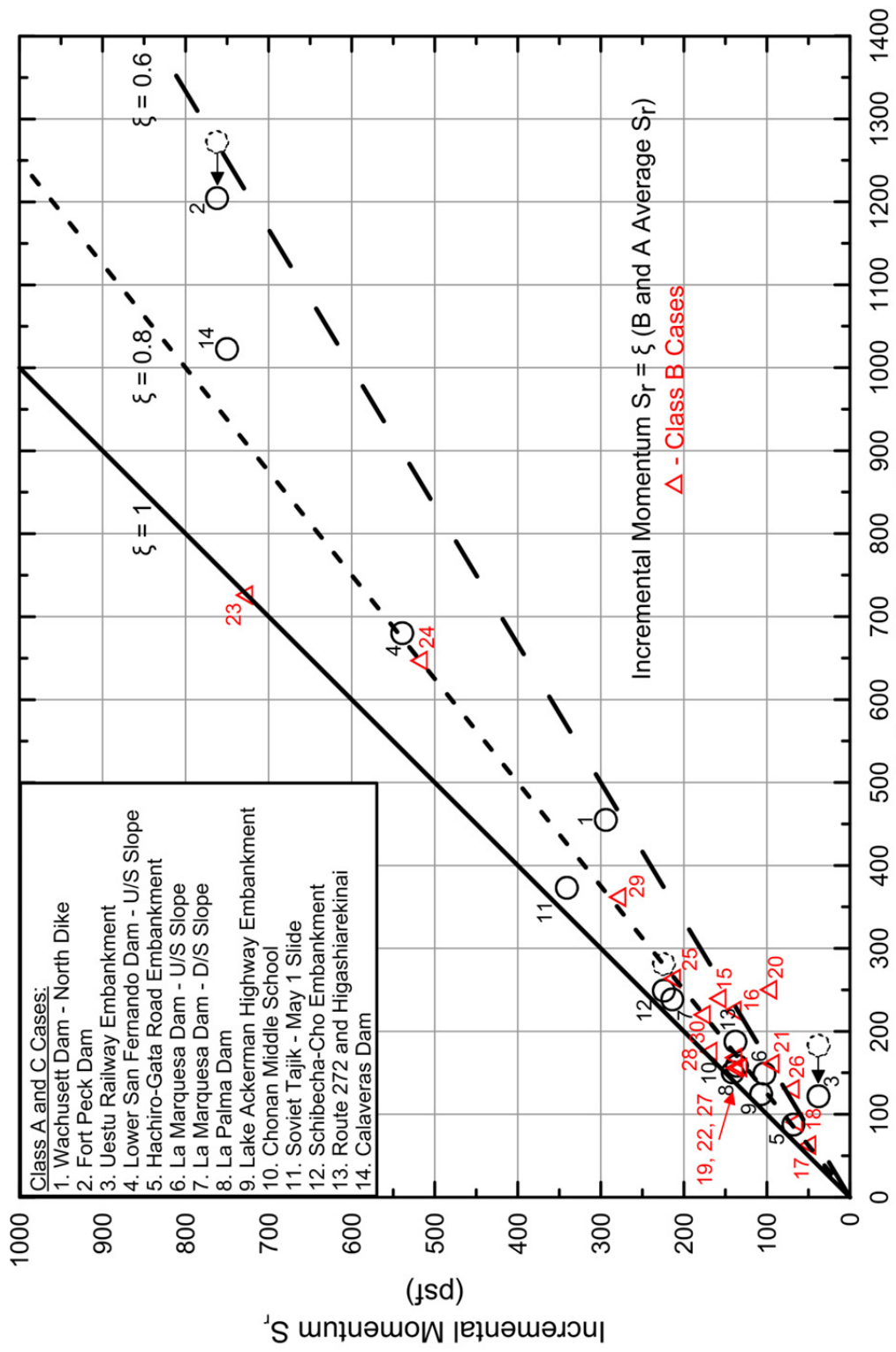

Figure 4.10: Figure 4.6 repeated, this time adding the back-analyzed Class B failure case histories (red triangles).

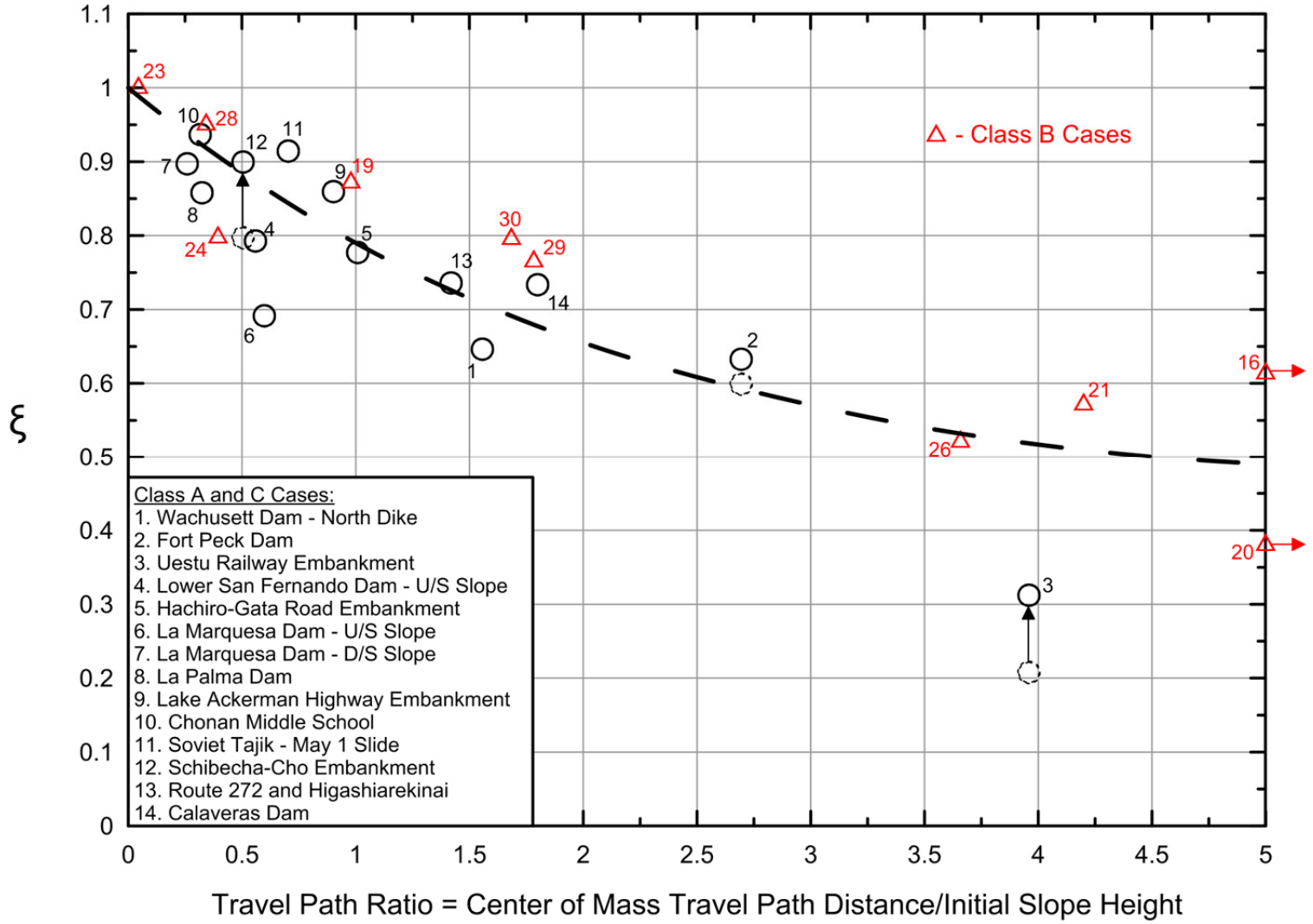

Figure 4.11: Figure 4.7 repeated, showing the empirical scaling parameter ξ for Equation 4-4, as a function of scaled runout distance this time adding the back-analyzed Class B failure case histories (red triangles).

Table 4.2: Back-analysis results for the well-defined liquefaction case histories of Classes A and C, and cross-comparisons with (1) Seed and Harder (1990), (2) Olson and Stark (2002) and (3) Wang and Kramer (2003, 2008).

Group	Case	Seed and Harder (1990)		Olson and Stark (2002)				Wang (2003) + Kramer (2008)				This Study			
		S_r (psf)	$N_{1,60,CS}$	S_u(Liq) (psf)	S_u(Liq)/σ'_{vo}	σ'_{vo} (psf)	$N_{1,60}$ (1)	$\bar{S}_r$ (psf) (2)	$\bar{S}_r/\bar{\sigma}'_{vo}$	$\bar{\sigma}'_{vo}$ (psf) (3)	$\bar{N}_{1,60,CS}$	$\bar{S}_r$ (psf)	$\bar{S}_r/\bar{\sigma}'_{vo}$	$\bar{\sigma}'_{vo}$ (psf)	$\bar{N}_{1,60,CS}$
A	Wachusett Dam - North Dike			334	0.106	3158	7	348	0.136	2559	7.3	294	0.094	3142	7.5
	Fort Peck Dam	350	10	570	0.078	7341	8.5	671.6	0.091	7380	15.8	762	0.105	7258	12.5
	Uetsu Railway Embankment	40	3	36	0.027	1280	3	43.7	0.048	910	2.9	38	0.026	1448	3
	Lower San Fernando Dam - U/S Slope	400	13.5	390	0.120	3482	11.5	484.7	0.133	3644	14.5	539	0.170	3174	13.5
	Hachiro-Gata Road Embankment			42	0.062	670	4.4	65	0.164	396	5.7	68	0.101	673	7
	La Marquesa Dam - U/S Slope	200	6	65	0.070	911	4.5	(185.1)	0.110	1683	6.5	103	0.105	981	6.5
	La Marquesa Dam - D/S Slope	400	11	111	0.110	1000	9	(343.5)	0.186	1847	9.9	214	0.176	1215	10.5
	La Palma Dam	200	4	100	0.120	789	3.5	(193.3)	0.123	1572	4.2	136	0.177	767	5
	Lake Ackerman Highway Embankment			82	0.076	1076	3	98	0.114	860	4.8	107	0.118	909	3.5
	Chonan Middle School			100	0.091	1119	5.2	(178.7)	0.091	1964	6.4	141	0.137	1032	6.5
	Soviet Tajik - May 1 Slide			175	0.082	2170	7.6	(334.3)	0.082	4077	8.9	341	0.179	1907	10.5
	Shibecha-Cho Embankement			117	0.086	1351	5.6	208.9	0.200	1045	5.6	224	0.158	1416	7.5
	Route 272 at Higashiarekinai			100	0.097	1030	6.3	130.5	0.125	1044	8.5	138	0.107	1285	8
B	Zeeland - Vlietepolder			115	0.048	2396	7.5	(226.0)	0.048	4708	8.5				
	Sheffield Dam	75	6	75	0.053	1429	5	(100.0)	0.072	1389	8.2				
	Helsinki Harbor			32	0.060	522	6	(53.2)	0.060	887	5.9				
	Solfatara Canal Dike	50	4	50	0.080	624	4	(77.1)	0.063	1224	4.9				
	Lake Merced Bank	100	6	144	0.108	1372	7.5	(139.5)	0.106	1316	5.9				
	El Cobre Tailings Dam			40	0.020	1946	0	(195.2)	0.020	9760	6.8				
	Metoki Road Embankment			38	0.043	875	2.6	(116.8)	0.044	2655	2				
	Hokkaido Tailings Dam			100	0.073	1376	1.1	(250.6)	0.074	3386	5.1				
	Upper San Fernando Dam - D/S Slope	600	15												
	Tar Island Dyke			251	0.058	4300	7	(364.2)	0.058	6279	8.9				
	Mochi-Koshi Tailings Dam, Dikes 1 and 2	250	5	75	0.060	1251	2.7	(158.9)	0.091	1746	8.9				
				113	0.104	1090	2.7	(233.6)	0.081	2884	10				
	Nerlerk Embankment, Slides 1 ,2 and 3			52	0.086	616	8.7	(178.5)	0.124	1440	11.4				
				36	0.060	650	7.2								
				31	0.034	925	7.2								
	Asele Road Embankment			132	0.104	1251	7	(163.6)	0.104	1573	11				
	Nalband Railway Embankment			119	0.109	1101	9.2	(139.9)	0.109	1283	6.3				
	Sullivan Tailings														
	Jamuna Bridge														
C	Calaveras Dam	650	12	721	0.112	6422	8	636.9	0.099	6433	10.5	749	0.106	7097	15

Notes : (1) No fines content correction utilized in Olson and Stark (2002).
(2) Where noted in parentheses, S_r values are for secondary cases in Wang (2003) and were not fully reanalyzed.
(3) σ'_{vo} not explicitly reported in Wang (2003) or Kramer (2008). Values shown were back calculated from reportedS_r and S_r/σ'_{vo}.

Table 4.3: Back-analysis results for the well-defined liquefaction case histories of Classes A and C, and cross-comparisons with (1) Seed and Harder (1990), (2) Olson and Stark (2002) [modified], and (3) Wang and Kramer (2003, 2008).

Group	Case	Seed and Harder (1990)		Olson and Stark (2002)				Wang (2003) + Kramer (2008)				This Study			
		S_r (psf)	$N_{1,60,CS}$	S_u(Liq) (psf) [1]	S_u(Liq)/σ'_{vo}	σ'_{vo} (psf)	$N_{1,60}$ [2]	$\bar{S}_r$ (psf) [3]	$\bar{S}_r$/ $\bar{\sigma}'_{vo}$	$\bar{\sigma}'_{vo}$ (psf) [4]	$\bar{N}_{1,60,CS}$	$\bar{S}_r$ (psf)	$\bar{S}_r$/ $\bar{\sigma}'_{vo}$	$\bar{\sigma}'_{vo}$ (psf)	$\bar{N}_{1,60,CS}$
A	Wachusett Dam - North Dike			334	0.106	3158	7	348	0.136	2559	7.3	294	0.094	3142	7.5
	Fort Peck Dam	350	10	570	0.078	7341	8.5	671.6	0.091	7380	15.8	762	0.105	7258	12.5
	Uetsu Railway Embankment	40	3	36	0.027	1280	3	43.7	0.048	910	2.9	38	0.026	1448	3
	Lower San Fernando Dam - U/S Slope	400	13.5	390	0.120	3482	11.5	484.7	0.133	3644	14.5	539	0.170	3174	13.5
	Hachiro-Gata Road Embankment			42	0.062	670	4.4	65	0.164	396	5.7	68	0.101	673	7
	La Marquesa Dam - U/S Slope	200	6	[104]	0.114	911	4.5	(185.1)	0.110	1683	6.5	103	0.105	981	6.5
	La Marquesa Dam - D/S Slope	400	11	[152]	0.152	1000	9	(343.5)	0.186	1847	9.9	214	0.176	1215	10.5
	La Palma Dam	200	4	[125]	0.158	789	3.5	(193.3)	0.123	1572	4.2	136	0.177	767	5
	Lake Ackerman Highway Embankment			82	0.076	1076	3	98	0.114	860	4.8	107	0.118	909	3.5
	Chonan Middle School			[142]	0.127	1119	5.2	(178.7)	0.091	1964	6.4	141	0.137	1032	6.5
	Soviet Tajik - May 1 Slide			[334]	0.154	2170	7.6	(334.3)	0.082	4077	8.9	341	0.179	1907	10.5
	Shibecha-Cho Embankement			117	0.086	1351	5.6	208.9	0.200	1045	5.6	224	0.158	1416	7.5
	Route 272 at Higashiarekinai			100	0.097	1030	6.3	130.5	0.125	1044	8.5	138	0.107	1285	8
B	Zeeland - Vlietepolder			[180]	0.075	2396	7.5	(226.0)	0.048	4708	8.5				
	Sheffield Dam	75	6	[159]	0.111	1429	5	(100.0)	0.072	1389	8.2				
	Helsinki Harbor			[44]	0.084	522	6	(53.2)	0.060	887	5.9				
	Solfatara Canal Dike	50	4	[71]	0.114	624	4	(77.1)	0.063	1224	4.9				
	Lake Merced Bank	100	6	[205]	0.149	1372	7.5	(139.5)	0.106	1316	5.9				
	El Cobre Tailings Dam			<40>	0.020	1946	0	(195.2)	0.020	9760	6.8				
	Metoki Road Embankment			[90]	0.103	875	2.6	(116.8)	0.044	2655	2				
	Hokkaido Tailings Dam			[138]	0.100	1376	1.1	(250.6)	0.074	3386	5.1				
	Upper San Fernando Dam - D/S Slope	600	15												
	Tar Island Dyke			[401]	0.093	4300	7	(364.2)	0.058	6279	8.9				
	Mochi-Koshi Tailings Dam, Dikes 1 and 2	250	5	[207]	0.165	1251	2.7	(158.9)	0.091	1746	8.9				
				[180]	0.165	1090	2.7	(233.6)	0.081	2884	10				
	Nerlerk Embankment, Slides 1 ,2 and 3			[44]	0.071	616	8.7	(178.5)	0.124	1440	11.4				
				[50]	0.077	650	7.2								
				[52]	0.056	925	7.2								
	Asele Road Embankment			[192]	0.153	1251	7	(163.6)	0.104	1573	11.0				
	Nalband Railway Embankment			[121]	0.110	1101	9.2	(139.9)	0.109	1283	6.3				
	Sullivan Tailings														
	Jamuna Bridge														
C	Calaveras Dam	650	12	721	0.112	6422	8	636.9	0.0993	6433	10.5	749	0.106	7097	15

Notes : (1) Where noted in brackets, S_u(Liq) and S_u(Liq)/σ'_{vo} for Olson (2001) reinterpreted using reported values of Su Yield and S_u Residual in Olson (2001) and the equation S_u(Liq) = 0.8 (S_u Yield + S_u Residual)/2. Reinterpretation of S_u(Liq) performed for cases not calculated using the Kinetic procedure in Olson (2001). Where noted in triangular brackets, no S_u Yield value reported in Olson (2001).

(2) No fines content correction utilized in Olson and Stark (2002).

(3) Where noted in parentheses, S_r values are for secondary cases in Wang (2003) and were not fully reanalyzed.

(4) σ'_{vo} not explicitly reported in Wang (2003) or Kramer (2008). Values shown were back calculated from reported S_r and S_r/σ'_{vo}.

Table 4.4: Back-analysis results for the less well-defined liquefaction case histories of Class B, and cross-comparisons with (1) Seed and Harder (1990), (2) Olson and Stark (2002) and (3) Wang and Kramer (2003, 2008).

Group	Case	Seed and Harder (1990)		Olson and Stark (2002)				Wang (2003) + Kramer (2008)				This Study			
		S_r (psf)	$N_{1,60,CS}$	S_u(Liq) (psf)	S_u(Liq)/σ'_{vo}	σ'_{vo} (psf)	$N_{1,60}$ (1)	$\bar{S}_r$ (psf) (2)	$\bar{S}_r/\bar{\sigma}'_{vo}$	$\bar{\sigma}'$vo (psf) (3)	$\bar{N}_{1,60,CS}$	$\bar{S}_r$ (psf)	$\bar{S}_r/\bar{\sigma}'_{vo}$	$\bar{\sigma}'_{vo}$ (psf)	$\bar{N}_{1,60,CS}$
A	Wachusett Dam - North Dike			334	0.106	3158	7	348	0.136	2559	7.3				
	Fort Peck Dam	350	10	570	0.078	7341	8.5	671.6	0.091	7380	15.8				
	Uetsu Railway Embankment	40	3	36	0.027	1280	3	43.7	0.048	910	2.9				
	Lower San Fernando Dam - U/S Slope	400	13.5	390	0.120	3482	11.5	484.7	0.133	3644	14.5				
	Hachiro-Gata Road Embankment			42	0.062	670	4.4	65	0.164	396	5.7				
	La Marquesa Dam - U/S Slope	200	6	65	0.07	911	4.5	(185.1)	0.110	1683	6.5				
	La Marquesa Dam - D/S Slope	400	11	111	0.11	1000	9	(343.5)	0.186	1847	9.9				
	La Palma Dam	200	4	100	0.12	789	3.5	(193.3)	0.123	1572	4.2				
	Lake Ackerman Highway Embankment			82	0.076	1076	3	98	0.114	860	4.8				
	Chonan Middle School			100	0.09	1119	5.2	(178.7)	0.091	1964	6.4				
	Soviet Tajik - May 1 Slide			175	0.08	2170	7.6	(334.3)	0.082	4077	8.9				
	Shibecha-Cho Embankement			117	0.086	1351	5.6	208.9	0.200	1045	5.6				
	Route 272 at Higashiarekinai			100	0.097	1030	6.3	130.5	0.125	1044	8.5				
B	Zeeland - Vlietepolder			115	0.05	2396	7.5	(226.0)	0.048	4708	8.5	156	0.063	2488	8
	Sheffield Dam	75	6	75	0.05	1429	5	(100.0)	0.072	1389	8.2	138	0.106	1308	7
	Helsinki Harbor			32	0.06	522	6	(53.2)	0.060	887	5.9	48	0.057	846	6
	Solfatara Canal Dike	50	4	50	0.08	624	4	(77.1)	0.063	1224	4.9	64	0.096	669	4.5
	Lake Merced Bank	100	6	144	0.11	1372	7.5	(139.5)	0.106	1316	5.9	136	0.163	834	8.5
	El Cobre Tailings Dam			40	0.020	1946	0	(195.2)	0.020	9760	6.8	95	0.046	2075	2
	Metoki Road Embankment			38	0.04	875	2.6	(116.8)	0.044	2655	2	92	0.106	871	2.5
	Hokkaido Tailings Dam			100	0.07	1376	1.1	(250.6)	0.074	3386	5.1	131	0.109	1203	4
	Upper San Fernando Dam - D/S Slope	600	15									726	0.231	3138	15
	Tar Island Dyke			251	0.06	4300	7	(364.2)	0.058	6279	8.9	516	0.123	4197	11
	Mochi-Koshi Tailings Dam, Dikes 1 and 2	250	5	75	0.06	1251	2.7	(158.9)	0.091	1746	8.9	211	0.138	1532	6
				113	0.10	1090	2.7	(233.6)	0.081	2884	10				
	Nerlerk Embankment, Slides 1 ,2 and 3			52	0.09	616	8.7	(178.5)	0.124	1440	11.4	68	0.058	1171	7.5
				36	0.06	650	7.2								
				31	0.03	925	7.2								
	Asele Road Embankment			132	0.10	1251	7	(163.6)	0.104	1573	11.0	137	0.132	1037	9.5
	Nalband Railway Embankment			119	0.11	1101	9.2	(139.9)	0.109	1283	6.3	167	0.138	1209	7.5
	Sullivan Tailings											277	0.114	2422	9.5
	Jamuna Bridge											175	0.125	1404	10.5
C	Calaveras Dam	650	12	721	0.112	6422	8	636.9	0.0993	6433	10.5				

Notes : (1) No fines content correction utilized in Olson and Stark (2002).
(2) Where noted in parentheses, $S_{u,r}$ values are for secondary cases in Wang (2003) and were not fully reanalyzed.
(3) σ'_{vo} not explicitly reported in Wang (2003) or Kramer (2008). Values shown were back calculated from reported S_r and S_r/σ'_{vo}.

Table 4.5: Back-analysis results for the less well-defined liquefaction case histories of Class B, and cross-comparisons with (1) Seed and Harder (1990), (2) Olson and Stark (2002) [modified], and (3) Wang and Kramer (2003, 2008).

Group	Case	Seed and Harder (1990)		Olson and Stark (2002)				Wang (2003) + Kramer (2008)				This Study			
		S_r (psf)	$N_{1,60,CS}$	$S_u(Liq)$ (psf) [1]	$S_u(Liq)/\sigma'_{vo}$	σ'_{vo} (psf)	$N_{1,60}$ [2]	$\bar{S}_r$ (psf) [3]	$\bar{S}_r/\bar{\sigma}'_{vo}$	$\bar{\sigma}'_{vo}$ (psf) [4]	$\bar{N}_{1,60,CS}$	$\bar{S}_r$ (psf)	$\bar{S}_r/\bar{\sigma}'_{vo}$	$\bar{\sigma}'_{vo}$ (psf)	$\bar{N}_{1,60,CS}$
A	Wachusett Dam - North Dike			334	0.106	3158	7	348	0.136	2559	7.3				
	Fort Peck Dam	350	10	570	0.078	7341	8.5	671.6	0.091	7380	15.8				
	Uetsu Railway Embankment	40	3	36	0.027	1280	3	43.7	0.048	910	2.9				
	Lower San Fernando Dam - U/S Slope	400	13.5	390	0.120	3482	11.5	484.7	0.133	3644	14.5				
	Hachiro-Gata Road Embankment			42	0.062	670	4.4	65	0.164	396	5.7				
	La Marquesa Dam - U/S Slope	200	6	[104]	0.114	911	4.5	(185.1)	0.110	1683	6.5				
	La Marquesa Dam - D/S Slope	400	11	[152]	0.152	1000	9	(343.5)	0.186	1847	9.9				
	La Palma Dam	200	4	[125]	0.158	789	3.5	(193.3)	0.123	1572	4.2				
	Lake Ackerman Highway Embankment			82	0.076	1076	3	98	0.114	860	4.8				
	Chonan Middle School			[142]	0.127	1119	5.2	(178.7)	0.091	1964	6.4				
	Soviet Tajik - May 1 Slide			[334]	0.154	2170	7.6	(334.3)	0.082	4077	8.9				
	Shibecha-Cho Embankement			117	0.086	1351	5.6	208.9	0.200	1045	5.6				
	Route 272 at Higashiarekinai			100	0.097	1030	6.3	130.5	0.125	1044	8.5				
B	Zeeland - Vlietepolder			[180]	0.075	2396	7.5	(226.0)	0.048	4708	8.5	156	0.063	2488	8
	Sheffield Dam	75	6	[159]	0.111	1429	5	(100.0)	0.072	1389	8.2	138	0.106	1308	7
	Helsinki Harbor			[44]	0.084	522	6	(53.2)	0.060	887	5.9	48	0.057	846	6
	Solfatara Canal Dike	50	4	[71]	0.114	624	4	(77.1)	0.063	1224	4.9	64	0.096	669	4.5
	Lake Merced Bank	100	6	[205]	0.149	1372	7.5	(139.5)	0.106	1316	5.9	136	0.163	834	8.5
	El Cobre Tailings Dam			<40>	0.020	1946	0	(195.2)	0.020	9760	6.8	95	0.046	2075	2
	Metoki Road Embankment			[90]	0.103	875	2.6	(116.8)	0.044	2655	2	92	0.106	871	2.5
	Hokkaido Tailings Dam			[138]	0.100	1376	1.1	(250.6)	0.074	3386	5.1	131	0.109	1203	4
	Upper San Fernando Dam - D/S Slope	600	15									726	0.231	3138	15
	Tar Island Dyke			[401]	0.093	4300	7	(364.2)	0.058	6279	8.9	516	0.123	4197	11
	Mochi-Koshi Tailings Dam, Dikes 1 and 2	250	5	[207]	0.165	1251	2.7	(158.9)	0.091	1746	8.9	211	0.138	1532	6
				[180]	0.165	1090	2.7	(233.6)	0.081	2884	10				
	Nerlerk Embankment, Slides 1 ,2 and 3			[44]	0.071	616	8.7	(178.5)	0.1239	1440	11.4	68	0.058	1171	7.5
				[50]	0.077	650	7.2								
				[52]	0.056	925	7.2								
	Asele Road Embankment			[192]	0.153	1251	7	(163.6)	0.104	1573	11	137	0.132	1037	9.5
	Nalband Railway Embankment			[121]	0.110	1101	9.2	(139.9)	0.109	1283	6.3	167	0.138	1209	7.5
	Sullivan Tailings											277	0.114	2422	9.5
	Jamuna Bridge											175	0.125	1404	10.5
C	Calaveras Dam	650	12	721	0.112	6422	8	636.9	0.099	6433	10.5				

Notes : (1) Where noted in brackets, $S_u(Liq)$ and $S_u(Liq)/\sigma'_{vo}$ for Olson (2001) reinterpreted using reported values of Su Yield and S_u Residual in Olson (2001) and the equation $S_u(Liq) = 0.8 (S_u$ Yield + S_u Residual)/2. Reinterpretation of $S_u(Liq)$ performed for cases not calculated using the Kinetic procedure in Olson (2001). Where noted in triangular brackets, no S_u Yield value reported in Olson (2001).

(2) No fines content correction utilized in Olson and Stark (2002).

(3) Where noted in parentheses, $S_{u,r}$ values are for secondary cases in Wang (2003) and were not fully reanalyzed.

(4) σ'_{vo} not explicitly reported in Wang (2003) or Kramer (2008). Values shown were back calculated from reported S_r and S_r/σ'_{vo}.

Table 4.6: Back-analysis results for liquefaction case histories of Class A, Class B, and Class C, and cross-comparisons with (1) Seed and Harder (1990), (2) Olson and Stark (2002) [modified], and (3) Wang and Kramer (2003, 2008).

Group	Case	Seed and Harder (1990)		Olson and Stark (2002)				Wang (2003) + Kramer (2008)				This Study			
		S_r (psf)	$N_{1,60,CS}$	$S_u(Liq)$ (psf) [1]	$S_u(Liq)/\sigma'_{vo}$	σ'_{vo} (psf)	$N_{1,60}$ [2]	$\bar{S}_r$ (psf) [3]	$\bar{S}_r/\ \bar{\sigma}'_{vo}$	$\bar{\sigma}'_{vo}$ (psf) [4]	$\bar{N}_{1,60,CS}$	$\bar{S}_r$ (psf)	$\bar{S}_r/\ \bar{\sigma}'_{vo}$	$\bar{\sigma}'_{vo}$ (psf)	$\bar{N}_{1,60,CS}$
A	Wachusett Dam - North Dike			334	0.106	3158	7	348	0.136	2559	7.3	294	0.094	3142	7.5
	Fort Peck Dam	350	10	570	0.078	7341	8.5	671.6	0.091	7380	15.8	762	0.105	7258	12.5
	Uetsu Railway Embankment	40	3	36	0.027	1280	3	43.7	0.048	910	2.9	38	0.026	1448	3
	Lower San Fernando Dam - U/S Slope	400	13.5	390	0.120	3482	11.5	484.7	0.133	3644	14.5	539	0.170	3174	13.5
	Hachiro-Gata Road Embankment			42	0.062	670	4.4	65	0.164	396	5.7	68	0.101	673	7
	La Marquesa Dam - U/S Slope	200	6	[104]	0.114	911	4.5	(185.1)	0.110	1683	6.5	103	0.105	981	6.5
	La Marquesa Dam - D/S Slope	400	11	[152]	0.152	1000	9	(343.5)	0.186	1847	9.9	214	0.176	1215	10.5
	La Palma Dam	200	4	[125]	0.158	789	3.5	(193.3)	0.123	1572	4.2	136	0.177	767	5
	Lake Ackerman Highway Embankment			82	0.076	1076	3	98	0.114	860	4.8	107	0.118	909	3.5
	Chonan Middle School			[142]	0.127	1119	5.2	(178.7)	0.091	1964	6.4	141	0.137	1032	6.5
	Soviet Tajik - May 1 Slide			[334]	0.154	2170	7.6	(334.3)	0.082	4077	8.9	341	0.179	1907	10.5
	Shibecha-Cho Embankement			117	0.086	1351	5.6	208.9	0.200	1045	5.6	224	0.158	1416	7.5
	Route 272 at Higashiarekinai			100	0.097	1030	6.3	130.5	0.125	1044	8.5	138	0.107	1285	8
B	Zeeland - Vlietepolder			[180]	0.075	2396	7.5	(226.0)	0.048	4708	8.5	156	0.063	2488	8
	Sheffield Dam	75	6	[159]	0.111	1429	5	(100.0)	0.072	1389	8.2	138	0.106	1308	7
	Helsinki Harbor			[44]	0.084	522	6	(53.2)	0.060	887	5.9	48	0.057	846	6
	Solfatara Canal Dike	50	4	[71]	0.114	624	4	(77.1)	0.063	1224	4.9	64	0.096	669	4.5
	Lake Merced Bank	100	6	[205]	0.149	1372	7.5	(139.5)	0.106	1316	5.9	136	0.163	834	8.5
	El Cobre Tailings Dam			<40>	0.020	1946	0	(195.2)	0.020	9760	6.8	95	0.046	2075	2
	Metoki Road Embankment			[90]	0.103	875	2.6	(116.8)	0.044	2655	2	92	0.106	871	2.5
	Hokkaido Tailings Dam			[138]	0.100	1376	1.1	(250.6)	0.074	3386	5.1	131	0.109	1203	4
	Upper San Fernando Dam - D/S Slope	600	15									726	0.231	3138	15
	Tar Island Dyke			[401]	0.093	4300	7	(364.2)	0.058	6279	8.9	516	0.123	4197	11
	Mochi-Koshi Tailings Dam, Dikes 1 and 2	250	5	[207]	0.165	1251	2.7	(158.9)	0.091	1746	8.9	211	0.138	1532	6
				[180]	0.165	1090	2.7	(233.6)	0.081	2884	10				
	Nerlerk Embankment, Slides 1 ,2 and 3			[44]	0.071	616	8.7	(178.5)	0.1239	1440	11.4	68	0.058	1171	7.5
				[50]	0.077	650	7.2								
				[52]	0.056	925	7.2								
	Asele Road Embankment			[192]	0.153	1251	7	(163.6)	0.104	1573	11	137	0.132	1037	9.5
	Nalband Railway Embankment			[121]	0.110	1101	9.2	(139.9)	0.109	1283	6.3	167	0.138	1209	7.5
	Sullivan Tailings											277	0.114	2422	9.5
	Jamuna Bridge											175	0.125	1404	10.5
C	Calaveras Dam	650	12	721	0.112	6422	8	636.9	0.099	6433	10.5	749	0.106	7097	15

Notes : (1) Where noted in brackets, $S_u(Liq)$ and $S_u(Liq)/\sigma'_{vo}$ for Olson (2001) reinterpreted using reported values of Su Yield and S_u Residual in Olson (2001) and the equation $S_u(Liq) = 0.8\ (S_u$ Yield + S_u Residual)/2. Reinterpretation of $S_u(Liq)$ performed for cases not calculated using the Kinetic procedure in Olson (2001). Where noted in triangular brackets, no S_u Yield value reported in Olson (2001).

(2) No fines content correction utilized in Olson and Stark (2002).

(3) Where noted in parentheses, $S_{u,r}$ values are for secondary cases in Wang (2003) and were not fully reanalyzed.

(4) σ'_{vo} not explicitly reported in Wang (2003) or Kramer (2008). Values shown were back calculated from reported S_r and S_r/σ'_{vo}.

Table 4.7: Summary of the back-calculated values of this study for (1) post-liquefaction strength, (2) representative initial vertical effective stress, and (3) penetration resistance, with inclusion of uncertainties.

Group	Case	This Study					
		$\bar{S}_r$ (psf)	$\sigma_{\bar{S}}$	$\bar{\sigma}'_{vo}$ (psf)	$\sigma_{\bar{\sigma}}$	$\bar{N}_{1,60,CS}$	$\sigma_{\bar{N}}$
A	Wachusett Dam - North Dike	294	31	3142	132	7.5	1.6
	Fort Peck Dam	762	118	7258	687	12.5	2.7
	Uetsu Railway Embankment	38	8	1448	116	3	0.8
	Lower San Fernando Dam - U/S Slope	539	47	3174	281	13.5	1.8
	Hachiro-Gata Road Embankment	68	12	673	41	7	1.2
	La Marquesa Dam - U/S Slope	103	33	981	134	6.5	1.8
	La Marquesa Dam - D/S Slope	214	57	1215	103	10.5	2.2
	La Palma Dam	136	23	767	42	5	1.2
	Lake Ackerman Highway Embankment	107	19	909	61	3.5	0.7
	Chonan Middle School	141	35	1032	82	6.5	2.1
	Soviet Tajik - May 1 Slide	341	57	1907	177	10.5	2.7
	Shibecha-Cho Embankement	224	37	1416	95	7.5	1.7
	Route 272 at Higashiarekinai	138	17	1285	104	8	1.6
B	Zeeland - Vlietepolder	156	37	2488	431	8	2.1
	Sheffield Dam	138	23	1308	71	7	2.3
	Helsinki Harbor	48	14	846	105	6	2.0
	Solfatara Canal Dike	64	22	669	59	4.5	1.5
	Lake Merced Bank	136	21	834	102	8.5	2.2
	El Cobre Tailings Dam	95	31	2075	183	2	1.0
	Metoki Road Embankment	92	20	871	85	2.5	0.9
	Hokkaido Tailings Dam	131	45	1203	191	4	1.1
	Upper San Fernando Dam - D/S Slope	726	138	3138	278	15	1.8
	Tar Island Dyke	516	119	4197	484	11	2.3
	Mochi-Koshi Tailings Dam, Dikes 1 and 2	211	38	1532	165	6	1.7
	Nerlerk Embankment, Slides 1 ,2 and 3	68	19	1171	129	7.5	1.8
	Asele Road Embankment	137	27	1037	77	9.5	2.0
	Nalband Railway Embankment	167	15	1209	94	7.5	2.5
	Sullivan Tailings	277	24	2422	142	9.5	2.4
	Jamuna Bridge	175	22	1404	210	10.5	2.5
C	Calaveras	749		7097		15	

Table 4.8: Comparison between the back-calculated values of this study and those developed by Wang (2003) for (1) post-liquefaction strength, (2) representative initial vertical effective stress, and (3) penetration resistance, with inclusion of uncertainties and case history weighting factors.

Group	Case	Wang (2003) + Kramer (2008)							This Study						
		$\bar{S}_r$ (psf) [1]	$\sigma_{\bar{S}}$	$\bar{\sigma}'_{vo}$ (psf) [2]	$\sigma_{\bar{\sigma}}$	$\bar{N}_{1,60,CS}$	$\sigma_{\bar{N}}$	WF	$\bar{S}_r$ (psf)	$\sigma_{\bar{S}}$	$\bar{\sigma}'_{vo}$ (psf)	$\sigma_{\bar{\sigma}}$	$\bar{N}_{1,60,CS}$	$\sigma_{\bar{N}}$	WF
A	Wachusett Dam - North Dike	348	74.8	2559	(-)	7.3	1.9	1.00	294	31	3142	132	7.5	1.6	1.00
	Fort Peck Dam	671.6	130.2	7380	(-)	15.8	0.9	0.85	762	118	7258	687	12.5	2.7	1.00
	Uetsu Railway Embankment	43.7	24.8	910	(-)	2.9	4.2	0.55	38	8	1448	116	3	0.8	1.00
	Lower San Fernando Dam - U/S Slope	484.7	111.0	3644	(-)	14.5	1.1	1.00	539	47	3174	281	13.5	1.8	1.00
	Hachiro-Gata Road Embankment	65	24.7	396	(-)	5.7	2.8	0.55	68	12	673	41	7	1.2	1.00
	La Marquesa Dam - U/S Slope	(185.1)	82.1	1683	(-)	6.5	2.8	0.76	103	33	981	134	6.5	1.8	1.00
	La Marquesa Dam - D/S Slope	(343.5)	113.8	1847	(-)	9.9	3.0	0.72	214	57	1215	103	10.5	2.2	1.00
	La Palma Dam	(193.3)	86.3	1572	(-)	4.2	1.8	0.80	136	23	767	42	5	1.2	1.00
	Lake Ackerman Highway Embankment	98	20.4	860	(-)	4.8	1.2	1.00	107	19	909	61	3.5	0.7	1.00
	Chonan Middle School	(178.7)	32.0	1964	(-)	6.4	6.9	0.74	141	35	1032	82	6.5	2.1	1.00
	Soviet Tajik - May 1 Slide	(334.3)	110.9	4077	(-)	8.9	5.7	0.22	341	57	1907	177	10.5	2.7	1.00
	Shibecha-Cho Embankement	208.9	38.6	1045	(-)	5.6	2.2	0.70	224	37	1416	95	7.5	1.7	1.00
	Route 272 at Higashiarekinai	130.5	33.5	1044	(-)	8.5	2.6	0.70	138	17	1285	104	8	1.6	1.00
B	Zeeland - Vlietepolder	(226.0)	75.0	4708	(-)	8.5	5.5	0.39	156	37	2488	431	8	2.1	1.00
	Sheffield Dam	(100.0)	29.8	1389	(-)	8.2	6.8	0.37	138	23	1308	71	7	2.3	1.00
	Helsinki Harbor	(53.2)	19.0	887	(-)	5.9	8.0	0.39	48	14	846	105	6	2.0	1.00
	Solfatara Canal Dike	(77.1)	25.6	1224	(-)	4.9	6.9	0.42	64	22	669	59	4.5	1.5	1.00
	Lake Merced Bank	(139.5)	41.4	1316	(-)	5.9	8.0	0.39	136	21	834	102	8.5	2.2	1.00
	El Cobre Tailings Dam	(195.2)	64.8	9760	(-)	6.8	0.9	0.60	95	31	2075	183	2	1.0	1.00
	Metoki Road Embankment	(116.8)	53.7	2655	(-)	2.0	1.5	0.39	92	20	871	85	2.5	0.9	1.00
	Hokkaido Tailings Dam	(250.6)	71.9	3386	(-)	5.1	1.4	0.31	131	45	1203	191	4	1.1	1.00
	Upper San Fernando Dam - D/S Slope								726	138	3138	278	15	1.8	1.00
	Tar Island Dyke	(364.2)	115.6	6279	(-)	8.9	9.7	0.32	516	119	4197	484	11	2.3	1.00
	Mochi-Koshi Tailings Dam, Dikes 1 and 2	(158.9)	47.7	1746	(-)	8.9	0.6	0.34	211	38	1532	165	6	1.7	1.00
		(233.6)	78.0	2884	(-)	10.0	1.3	0.67							
	Nerlerk Embankment, Slides 1 ,2 and 3	(178.5)	32.1	1440	(-)	11.4	7.7	0.41	68	19	1171	129	7.5	1.8	1.00
	Asele Road Embankment	(163.6)	54.6	1573	(-)	11.0	10.7	0.20	137	27	1037	77	9.5	2.0	1.00
	Nalband Railway Embankment	(139.9)	40.2	1283	(-)	6.3	5.6	0.51	167	15	1209	94	7.5	2.5	1.00
	Sullivan Tailings								277	24	2422	142	9.5	2.4	1.00
	Jamuna Bridge								175	22	1404	210	10.5	2.5	1.00
C	Calaveras Dam	636.9	223.1	6433	(-)	10.5	9.7	0.55	749		7097		15		0.00
D	Snow River Bridge Fill	(50.1)	16.6	2088	(-)	8.5	9.0	0.50							
	Kawagashi-cho Building	(123.5)	56.7	1388	(-)	4.3	1.2	0.50	`						
	Koda Numa Embankment	(48.0)	15.9	1067	(-)	3.6	4.1	0.44							

Notes : (1) Where noted in parentheses, $S_{u,r}$ values are for secondary cases in Wang (2003) and were not fully reanalyzed.
(2) σ'_{vo} not explicitly reported in Wang (2003) or Kramer (2008). Values shown were back calculated from reported S_r and S_r/σ'_{vo}.

Chapter Five

Development of Relationships for Evaluation of Post-Liquefaction Strength

5.1 Introduction

Chapter 4 presented back-analyses of field liquefaction case histories to develop indices for subsequent use here in the development of empirically-based correlations for engineering assessment of in situ post-liquefaction strengths (S_r) as a function of both (1) penetration resistance and (2) initial effective vertical stress. The indices from the individual case histories were internally cross-checked based on a series of calibrated empirical relationships and guidelines that were dependent upon failure mechanics and runout characteristics, etc. They were also checked against available values from other investigators who employed back-analysis methods that incorporated the effects of momentum and inertia. And they were also cross-checked against additional back-analyses performed by other investigators who employed methods that did not incorporate momentum effects, but for which the apparent resulting biases can now be at least approximately estimated.

The result is an unprecedented data set of reasonably well-constrained values of (1) back-calculated representative post-liquefaction strengths (S_r), (2) representative penetration resistances, and (3) representative initial effective vertical stresses on portions of the failure planes judged to have liquefied. Estimates of variance, or uncertainty, in each of these three indices were also developed for each of the 29 case histories back-analyzed in these current studies.

In Chapter 5, this hard-earned data set will now be used to develop improved predictive relationships for assessment of in situ post-liquefaction strength (S_r).

5.2 Non-Probabilistic Regressions

The first step was to perform non-probabilistic (or deterministic) regressions by the least squares method to investigate functional equational forms, and associated shapes of model fitting surfaces, to determine a promising basic equational form for subsequent fully probabilistic regressions to be performed by the Maximum Likelihood Method. These subsequent probabilistic regressions will incorporate all key sources of uncertainty, and will also permit modeling of heteroskedacity (variance of uncertainty across the domain of interest).

For this first step, the representative median values of $\overline{S_r}$, $\overline{N_{1,60,CS}}$ and $\overline{\sigma'_{vo}}$ for all 29 cases were assembled, as shown in Table 5.1. These mean values are assumed to also represent median values as all three indices are approximated as having normal distributions.

For these deterministic least squares regressions, the median values of Table 5.1 were taken as deterministic "best estimates", with no associated probabilistic likelihood. No weighting factors were assigned to the different cases, as the purpose of the exercise was only to determine promising potential (or candidate) equational forms for subsequent use in fully probabilistic regressions. This

permitted the performance of large numbers of nonlinear least squares regressions, using a large number of candidate equational forms.

A large number of candidate equational forms were regressed, and the most promising candidate form of equation was judged to be

$$S_r = \exp\left(\theta_1 \cdot N_{1,60,CS} + \theta_2 \cdot \sigma_v'^{\theta_3}\right) \qquad \text{[Eq. 5-1]}$$

The result of the regression with this equational form was found to be the equation

$$S_r = \exp\left(0.1625 \cdot N_{1,60,CS} + 4.004 \cdot \sigma_v'^{0.120}\right) \qquad \text{[Eq. 5-2]}$$

with $R^2 = 0.911$

In this equation:

S_r = Post-liquefaction shear strength [lbs/ft^2]

$N_{1,60,CS}$ = Overburden and equipment and procedurally corrected SPT penetration resistance with fines adjustment [blows/ft]

σ_v' = Initial vertical effective stress [atmospheres].

Figure 5.1(a) shows the shape of the resulting predictive fitting surface for this relationship, as a multi-colored surface in three-dimensional space with $\overline{S_r}$ plotted on the vertical axis, and $\overline{N_{1,60,CS}}$ and $\overline{\sigma'_{vo}}$ plotted on the two horizontal axes. Residuals for each field case history are plotted, but in the upper figure's oblique view only the residuals above the multi-colored surface can be seen. Figure 5.1(b) shows the residuals for all 29 field case histories, plotted relative to a "flattened" best-fit surface. The residuals in Figure 5.1(b) are shown at exaggerated vertical scale for clarity; residuals are vertically exaggerated by a factor of 5 in this figure.

The curved surface shown in Figure 5.1(a) simultaneously reflects the influences of both penetration resistance and initial effective vertical stress on post-liquefaction strength (S_r). The calculated R^2 value of $R^2 = 0.911$ indicates an excellent level of "fit" for the data set. Examination of the residuals shows no significant patterning or systematic skew, suggesting that the regression (and the equational form) have successfully characterized most of the available information.

Figure 5.2(a) shows the best-fit Equation 5-2 plotted as $\overline{S_r}$ vs. $\overline{N_{1,60,CS}}$, with the different curves labeled with the initial effective vertical stress $\overline{\sigma'_{vo}}$ (in units of atmospheres). Also plotted in this figure are the values back-calculated for each of the 29 liquefaction failure case histories (from Table 5.1), with case history data points "binned" by ranges of effective vertical stress as indicated in the key in the upper left-hand corner of the figure, and with solid symbols indicating cases of cyclic initiation of liquefaction and open symbols indicating static initiation of

liquefaction, and with larger symbols indicating case histories with larger initial effective vertical stresses.

Figure 5.2(b) also shows the best-fit Equation 5-2, but this time plotted in terms of post-liquefaction strength ratio ($\overline{S_r}/\overline{\sigma'_{vo}}$) vs. $\overline{N_{1,60,CS}}$, with the different curves again labeled with the initial effective vertical stress $\overline{\sigma'_{vo}}$ (in units of atmospheres), and the values back-calculated for the 29 liquefaction case histories again binned and labeled as in Figure 5.2(a). There is more apparent scatter in this figure, but in the end the same data points are presented, and the curved lines shown reflect the same relationship from Equation 5-2 and Figure 5.1.

The relationship of Equation 5-2 (and Figures 5.1 and 5.2) provides an R-square value of $R^2 = 0.911$, indicating a better level of "fit" for this data set and this relationship than has been achieved in previous studies by any regression employing 20 or more field case histories. This does not mean that this is the recommended final relationship, however, as this regression does not yet incorporate the best available information regarding the estimated uncertainties associated with the indices of $\overline{S_r}$, $\overline{N_{1,60,CS}}$ and $\overline{\sigma'_{vo}}$ for each of the 29 liquefaction field case histories. Instead, this is simply the opening step, and it serves mainly to show the promise of the data set and of the equational form selected at this stage.

5.3 Probabilistic Regressions by the Maximum Likelihood Method

Having thus ascertained and established an initially promising functional form for regression, the next step was to incorporate the full available information regarding variance and uncertainties, and to develop fully probabilistically based relationships between post-liquefaction strength and both (1) penetration resistance and (2) effective vertical stress.

The approach here was to employ the Maximum Likelihood Method, a Bayesian procedure which can (1) model all key sources of variance or uncertainty, and (2) model heteroskedastic variation of model error or variance over the problem domain of interest. This Bayesian procedure can be employed in a manner that is largely analogous to least squares regression, but with better ability to accommodate and model both parameter uncertainty and overall model uncertainty (Moss, 2009; Moss, 2011).

Table 5.2 shows the input variables for each of the 29 liquefaction field case histories as evaluated in Chapters 3 and 4, and Appendices A and B. Normal distributions were assumed for (1) mean post-liquefaction strength $\overline{S_r}$, (2) mean fines-corrected penetration resistance $\overline{N_{1,60,CS}}$, and (3) mean initial effective vertical stress $\overline{\sigma'_{vo}}$ for the portions of the field failure surfaces along which liquefaction was judged to have occurred in each of the case histories. Variances in these means were also evaluated, and these are also shown in Table 5.2. These variances, expressed as standard deviations of the respective means, were directly incorporated in these probabilistic regressions. It is important to note that the standard deviations listed are not standard deviations of the values of each of the respective indices for each case (e.g. individual $N_{1,60,CS}$ values); instead they are standard deviations of the <u>means</u> of these indices for each individual case.

Because the values listed in Table 5.2 include the engineering team's assessments of all sources of uncertainty or variance, no additional (judgmental) weighting factors were applied to each case history to further account for apparent data quality, or level of documentation, etc. The relative "weighting" of the information/data for each case history was thus a natural function of the variances in the three principal indices (or means) for each case, with cases that have higher variances or higher standard deviations having a somewhat lesser controlling impact on the regressed relationships developed than cases with lower variances or standard deviations.

A functional form similar to the one already shown to be effective in the deterministic regressions of Section 5.2 was then implemented in a Bayesian regression by the Maximum Likelihood method.

The results are a set of three-dimensional surfaces of different probabilities of exceedance of S_r, where the median values of S_r (50% probability of exceedance) are treated as essentially equivalent to the linear least squares regression trend relationship. The functional form employed here was unchanged from the deterministic regression, and the results are in the form of:

$$P \cong \Phi\left(\frac{g - S_r}{\Theta_\varepsilon}\right) \qquad \text{[Eq. 5-3]}$$

where

$P = probability$

$\Phi = cummulative\ standard\ normal\ distribution$

$g = functional\ form = exp\left(\theta_1 \cdot N_{1,60,CS} + \theta_2 \cdot \sigma_v'^{\theta_3}\right)$

$S_r = post - liquefaction\ residual\ strength\ [lbs/ft^2]$

$\theta_\varepsilon = error\ term$

Solving for the dependent variable can be accomplished by rearranging the equation:

$$S_r \cong g + \theta_\varepsilon \cdot \Phi^{-1}(P) \qquad \text{[Eq. 5-4]}$$

where $\Phi^{-1} = the\ inverse\ cummulative\ standard\ normal\ distribution$,

and P = probability of exceedance.

The predictive equation that results from this analysis then becomes:

$$S_r = exp\left(\theta_1 \cdot N_{1,60,CS} + \theta_2 \cdot \sigma_v'^{\theta_3}\right) + \theta_\epsilon \cdot \Phi^{-1}(P) \qquad \text{[Eq. 5-5]}$$

where θ_ε is the error term.

Setting P = 0.50 produces a median curve that is very similar, but not quite identical, to the deterministic predictive relationship of Equation 5-2. Evaluating for other probabilities of

exceedance will provide an estimate of the model uncertainty as captured by the Bayesian regression. The error term is a standard normal variate with zero mean and a standard deviation that equals the median value found in the Bayesian regression over the range of blow counts and effective stresses in the database.

The best-fit error term distribution was determined based on these mapped trends, and using the overall median uncertainty found in the Bayesian regression as the target value.

The overall resulting best-fit relationship was then determined to be

$$S_r = exp\left(0.1407 \cdot N_{1,60,CS} + 4.2399 \cdot \sigma_v'^{0.120}\right) + \Phi(\theta_\epsilon) \qquad \text{[Eq. 5-6(a)]}$$

where

$$\theta_\epsilon = N_{1,60,CS}{}^{1.45} + 0.2 * N_{1,60,CS} \cdot \sigma_v'^{2.48} + 41.13 \qquad \text{[Eq. 5-6(b)]}$$

and

S_r = Post-liquefaction strength [lbs/ft^2]

$N_{1,60,CS}$ = Overburden and equipment and procedurally corrected SPT penetration resistance with fines adjustment [blows/ft]

σ_v' = Initial vertical effective stress [atmospheres].

and these can be combined into spreadsheet format as

$$S_r = exp\left(0.1407 \cdot N_{1,60,CS} + 4.2399 \cdot \sigma_v'^{0.120}\right) + NORMINV(\mathrm{P}, 0, \theta_\epsilon) \qquad \text{[Eq. 5-7]}$$

Figure 5.3(a) illustrates the resulting median (50th percentile) predictive fitting surface for this relationship, as a multi-colored surface in three-dimensional space with $\overline{S_r}$ plotted on the vertical axis, and $\overline{N_{1,60,CS}}$ and $\overline{\sigma'_{vo}}$ plotted on the two horizontal axes. Residuals for each field case history are plotted, but in his upper figure's oblique view only the residuals above the multi-colored surface can be seen. Figure 5.3(b) shows the median residuals for all 29 field case histories, plotted relative to the "flattened" best-fit median (50th percentile) surface from Figure 5.3(a).

The variance or error term of Equation 5-6(b) is heteroskedastic, meaning that the variance in estimated values of S_r varies over the domain of interest as a function of both $\overline{N_{1,60,CS}}$ and $\overline{\sigma'_{vo}}$. This variance increases with increases in both $\overline{N_{1,60,CS}}$ and $\overline{\sigma'_{vo}}$ as will be discussed later, and as illustrated in Figure 5.5.

Figure 5.4(a) shows the median (50th percentile) predictive relationship of Equation 5-6, this time plotted as curves of post-liquefaction strength S_r vs. $\overline{\sigma'_{vo}}$, with the different curves again labeled with the initial effective vertical stress $\overline{\sigma'_{vo}}$ (in units of atmospheres), and the values back-calculated for the 29 liquefaction case histories are again binned and labeled as in Figure 5.2(a).

Figure 5.4(b) shows the median (50th percentile) predictive relationship of Equation 5-6, this time plotted as curves of post-liquefaction strength ratio S_r/σ'_{vo} vs. $\overline{\sigma'_{vo}}$, with the different curves again labeled with the initial effective vertical stress $\overline{\sigma'_{vo}}$ (in units of atmospheres), and the values back-calculated for the 29 liquefaction case histories again binned and labeled as in Figure 5.2(a).

A second important attribute of the Bayesian regression by the Maximum Likelihood Method is the ability to model all sources of variance or uncertainty, and the resulting modeling of the distribution of variance (the error term) as a function of $N_{1,60,CS}$ and σ'_v that can be achieved.

Figure 5.5 shows the distribution of standard deviation of post-liquefaction strength (σ_{Sr}) as a function of $N_{1,60,CS}$ and σ'_v resulting from the probabilistic Bayesian regression, as quantified in Equation 5-6(b). Standard deviation of S_r increases with both (1) increase in $N_{1,60,CS}$ and (2) increase in σ'_v, but comparison of Figure 5.5 with Figure 5.3(a) shows that these increases are not fully directly proportional to the similar increases in S_r with increases in both $N_{1,60,CS}$ and σ'_v. This reflects (1) the differing variances associated with the parameters developed from each of the case histories, (2) the relative paucity of data (or the availability of data) over different portions of the problem domain, (3) variability in residuals from the mean for each case history, and (4) resulting variability or uncertainty in the best estimate values of S_r for different areas of the domain of Figures 5.5 and 5.3.

A further examination of the means by which the Bayesian regression deals with variance and uncertainty can be achieved by examining the effects of either (1) including the Upper San Fernando Dam case history in these regressions, or (2) deleting this case history and regressing only the other 28 case histories.

One of the differences between the relationships developed or proposed by (1) Olson and Stark (2002) and (2) Wang and Kramer (2003, 2008) vs. those of (3) Seed and Harder (1990) and (4) these current studies, was the inclusion of the "non-failure" liquefaction case history for the Upper San Fernando Dam in the 1990 studies and in these current studies. It was the unanimous advice of the informal expert advisory panel that this was a suitable case to include, but the potential sensitivity of the resulting relationship to this decision then warrants examination. Figure 5.6 shows a comparison between the median (50th percentile) values of S_r from the probabilistic regression of Figures 5.3 and 5.5 (and Equation 5-6) as shown with the black lines vs. the 50th percentile probabilistic regressions results (also by the Maximum Likelihood Method) performed with the Upper San Fernando Dam case history deleted, as shown by the red lines. As shown in this figure, deletion of this case did not make a very significant difference. This was due in large part to the relatively high levels of uncertainty, or variance (standard deviation), assigned to the Upper San Fernando Dam case history, so that it did not exert strong control over the regressed fitting surfaces in its local neighborhood. It is the judgment of this engineering team

that the data and information from the Upper San Fernando Dam case history is both valid and useful, and that the probabilistically regressed relationship with this case included (as expressed in Equation 5-6) is to be preferred.

The relationship of Equation 5-6 is fully probabilistic, and values for any percentile of non-exceedance can be generated. It is the recommendation of this engineering team that 33rd percentile values (33% of values would be expected to be lower) represent a suitable level of conservatism for typical design applications. This represents a nearly mean-minus-one-half-standard-deviation level (more precisely, a mean minus 0.44 sigma level), and there is strong tradition for the use of this sort of "one third" level of enveloping (or similar) in geotechnical practice, and engineers are familiar with this and tend to and have good experience with this level of conservatism for shear strengths.

For larger projects, or projects of special importance, a fully probabilistic (or risk-based) analysis can be performed using the full range of values of S_r and their associated probabilities as can be developed using the full form of Equation 5-6.

The recommended simplified "deterministic" values of S_r for routine design are then the 33rd percentile values, and these can be calculated by a simplified version of Equation 5-6 as

$$S_r(33rd\ Percentile) = exp\left(0.1407 \cdot N_{1,60,CS} + 4.2399 \cdot {\sigma_v'}^{0.120}\right) - 0.43991\left({N_{1,60,CS}}^{1.45} + 0.2 * N_{1,60,CS} \cdot {\sigma_v'}^{2.48} + 41.13\right)$$

[Eq. 5-9]

Figure 5.7 repeats Figure 5.4(a), showing the median (50th percentile) predictive relationship of Equation 5-6 plotted as curves of post-liquefaction strength S_r vs. $\overline{\sigma'_{vo}}$, with the different curves again labeled with the initial effective vertical stress $\overline{\sigma'_{vo}}$ (in units of atmospheres), and the values back-calculated for the 29 liquefaction case histories again binned and labeled as in Figure 5.4(a). The red lines added to Figure 5.7 then show the 33rd percentile values calculated by Equation 5-9. This serves to illustrate the differences between the 50th percentile and the 33rd percentile values of S_r, and it also shows the relative juxtaposition of the recommended "simplified, deterministic" (33rd percentile) values relative to the "best-estimate" (median, or 50th percentile) values of each of the 29 back-analyzed individual field case histories.

Figures 5.8(a) and 5.8(b) then present the recommended deterministic relationship of Equation 5-9 (which is also the 33rd percentile probabilistic relationship of Equation 5-6) in two formats; showing S_r and $S_r/\sigma_{v,i}'$ as functions of penetration resistance and initial effective vertical stress.

The probabilistic and deterministic relationships of Equations 5-6 and 5-9, respectively, are based on a data set from field case histories that is confined to cases of large-displacement liquefaction failures with values of $N_{1,60,CS}$ of less than or equal to 15 blows/foot, and to cases with maximum values of initial effective stress (σ'_{vo}) of less than approximately 7 atmospheres, and "representative" values of initial effective stress ($\overline{\sigma'_{vo}}$) of less than four atmospheres.

It must be anticipated, however, that these relationships are likely to be extrapolated to higher levels of both $N_{1,60,CS}$ and σ'_{vo}, because there are currently no viable alternatives for projects with larger ranges of stresses. This is not, however, an unbounded problem.

Figure 5.9 show extrapolation of the 33rd percentile values of S_r from Equation 5-6 extended to higher $N_{1,60,CS}$ values and to higher effective stresses. Also shown in this figure are two dashed lines that delineate a shaded region that represents an approximate zone within which "drained friction cut-off" is likely to occur. Dilatant soils bifurcate narrowly, producing narrowly confined shear bands or "failure surfaces". That means that molecules of water have to travel only small distances to enter into the dilating zones in order to satisfy the "demand" created by dilatant reduction in pore pressures (below pre-failure phreatic conditions) during the rapid shearing or "failure". In the field, it is not safe to count on reduced (or even negative) pore pressures being fully maintained for any significant period of time, given these short distances that fluids must travel to begin to satisfy dilatant demand, especially in the cohesionless sandy and silty soils which are prone to classic liquefaction, and for which the relationships developed here for evaluation of S_r are intended to be applied.

Accordingly, at any given location, the post-liquefaction strength should be taken as the lower of either (a) the "undrained" post-liquefaction strength (S_r) which includes effects of localized void redistribution in otherwise globally undrained soil strata, or (b) the fully drained residual strength. The fully undrained residual shear strength $S_{r,drained}$ can be approximated as

$$S_{r,drained} \approx \sigma'_{n,o} \bullet \tan \text{Ø}' \qquad \text{[Eq. 5-10]}$$

where $\sigma'_{n,o}$ = initial (and current) effective stress normal to the failure plane, and Ø′ is a residual effective friction angle.

For cohesionless soils, and for silty soils of low plasticity, the residual (non-dilatant) effective friction angle can be taken as approximately 28° to 31°. The upper bound of the "drained frictional cut-off" range shown in Figure 5.9 is established by assuming that vertical effective stress is approximately equal to the normal effective stress on failure surfaces that are horizontal (e.g. basal failure surfaces for lateral translational failures, or the "bellies" of rotational failure surfaces). This then leads to an approximate upper bound drained frictional cut-off at

$$S_{r,drained} \approx \sigma'_{n,o} \bullet \tan \text{Ø}' \approx \sigma'_{v,o} \bullet \tan 30° \approx \sigma'_{v,o} \bullet 0.577 \qquad \text{[Eq. 5-11]}$$

And so the approximate upper bound of the drained frictional cut-off range in Figure 5.9 is shown at a ratio of $S_r/P \approx 0.577$.

For the steeply inclined (or even vertical) back heel of a failure surface, the effective normal effective stress can be very roughly approximated as being equal to the coefficient of at-rest lateral earth pressure (K_o) times the effective vertical stress, and for most problems of interest with regard to potential liquefaction failures the soils can be expected not to be very heavily overconsolidated, and K_o can be very roughly approximated as $K_o \approx 0.5$.

For very steeply inclined (or vertical) failure surfaces, the drained frictional cutoff strength can then be approximated as

$$S_{r,drained} \approx \sigma'_{n,o} \bullet K_o \bullet \tan \text{Ø}' \approx \sigma'_{v,o} \bullet 0.5 \bullet \tan 30° \approx \sigma'_{v,o} \bullet 0.5 \bullet 0.577 \approx \sigma'_{v,o} \bullet 0.29$$

[Eq. 5-12]

And so the lower bound of the approximate drained frictional cut-off range shown in Figure 5.9 is shown at $S_r/P \approx 0.29$.

Of course, engineers will need to more closely calculate the actual expected drained frictional cut-off strengths at each location on potential failure surfaces based on project-specific details.

Figure 5.9 then shows (approximately) the likely range of potential extrapolation of the 33rd percentile S_r relationships developed here. In this figure, it can be seen that (a) the drained frictional cut-off occurs at higher values of $N_{1,60,CS}$ for soils at higher initial effective stresses; in agreement with basic laws of soil mechanics and critical state principles. For soils with low initial effective vertical stresses (e.g. ~ 0.1 atmospheres), the value of $N_{1,60,CS}$ at which the drained frictional cut-off comes into effect can be as low as $N_{1,60,CS} \approx$ 10 or 11 blows/foot on very steeply inclined failure surfaces. Conversely, at very high effective stresses (e.g. ~ 8 atmospheres), the value of $N_{1,60,CS}$ at which the drained frictional cut-off comes into effect can be as high as $N_{1,60,CS} \approx$ 28 to 30 blows/foot on essentially horizontal failure surfaces.

The relationships shown in Figure 5.9 are approximate guides, but they are in good general agreement with both basic soil mechanics and with the principles of critical state soil mechanics.

They serve to illustrate the limits of the ranges over which values of S_r are likely to be needed by engineers. They also serve to illuminate an additional issue; the lack of large-displacement liquefaction field failure case histories for soils with high $N_{1,60,CS}$ values. For soils with $N_{1,60,CS}$ values of greater than about 15 to 20 blows/foot, the soils would behave sufficiently dilatantly that behavior would be limited by fully drained frictional "cut-off" strengths except at very high initial effective overburden stresses. There are relatively few large geotechnical structures or systems where very high effective vertical stresses are critical, and it must be hoped that there are even fewer that have not been well-engineered. As a result, there have been significantly less opportunities for "triggering" of large-displacement liquefaction-induced failures for soils with higher values of $N_{1,60,CS}$.

Values in this range will continue to be of interest, however, for a limited number of critical applications. The most apparent of these are large structures (e.g. major earth dams), and these are of course usually very critical structures with regard to public safety. Another example is bearing capacity, and tip settlements, for piles or piers bearing at depth. And so it must be expected that the relationships of Equation 5-6 will be extrapolated to higher ranges of $N_{1,60,CS}$ and to higher ranges of initial effective vertical stress.

Finally, it should be noted that it is routinely over a range of $N_{1,60,CS} \approx$ 10 to 22 blows/foot that engineers are usually most concerned. For lower blowcount materials ($N_{1,60,CS} <$ 10

blows/foot), post-liquefaction strength is usually insufficient, and mitigation of likely consequences of liquefaction is often required. For higher blowcounts ($N_{1,60,CS}$ > 22 blows/foot) post-liquefaction strengths are often sufficient (for all but the highest vertical effective stress situations). And so it is over this range ($N_{1,60,CS} \approx$ 10 to 22 blows/foot) that these relationships are expected to be most important, and to affect most projects.

5.4 Comparisons with Selected Previous Relationships for Evaluation of Post-Liquefaction Strength (S_r)

5.4.1 Wang (2003) and Kramer (2008)

Kramer (2008) extended the work of Wang (2003), and he performed regressions to develop both probabilistic and recommended simplified deterministic predictive relationships for in situ post-liquefaction strength (S_r). The work of Wang and Kramer (2003, 2008) is the only fully comprehensive study available for direct comparison with these current studies.

As discussed previously in Section 2.3.7, Kramer and Wang made very different choices with regard to selection of approaches at nearly every step of the way than those choices made by this current investigation team. They also made a number of very different judgments in implementing their selected approaches.

Table 4.7 presented a direct comparison between their table of values as employed in the probabilistic regressions of Kramer (2008), and the values employed in these current studies (as repeated in Table 5.1). As shown in Table 4.7, there are some significant differences in the case histories selected for inclusion by each of the two investigation teams, and the values back-calculated from some of the case histories common to both data sets also differ significantly for some of the cases. But the differences between the two studies run deeper than that. Wang and Kramer made different choices and judgments than the current investigation team at multiple steps along the way. Their approaches and choices and judgments represent differences in engineering opinions, and both studies conform to acceptable standards. So the pronounced differences at virtually every step along the way present a valuable opportunity to cross-compare the results developed by two very different studies and approaches.

An abridged (partial) overview of significant differences between the two studies is as follows:

1. Wang and Kramer employed the Calaveras Dam failure case history, as they were not yet aware of the new investigations (Olivia Chen Consultants, 2003) that showed the hydraulic fill materials to be more variably clayey and cohesive than had previously been suspected. The current engineering team, with concurrence of the advisory panel, judged that it would not be possible to cross-correlate the modern SPT and BPT performed many decades after the slope failure of 1918, given nearly a century of ongoing consolidation and ageing effects in these complicated and challenging soils, and it was also the unanimous consensus of the informal group of expert advisors that this case should not be included in the regressions for S_r. So the current studies did not employ the Calaveras Dam case history in our regressions.

2. The current studies do include the back-analyzed "non-failure" (small displacement) case of the Upper San Fernando Dam, and the regressions of Kramer (2008) do not. This does not have a very significant influence on the relationships developed in these current studies, however, as shown in Figure 5.6.

3. Wang and Kramer included three other case histories that were deliberatively not included in these current studies. These were (1) Snow River Bridge Fill, (2) Kawagishi-Cho Building, and (3) Koda Numa Embankment. Reasons for deleting these cases for the current studies are presented in Chapter 3, Sections 3.3.3.1 through 3.3.3.3.

4. These current studies include two newer case histories that had not been available to Wang (2003). These were (1) Sullivan Tailings and (2) Jamuna Bridge.

5. Wang and Kramer included the Moshi-Koshi Tailings Dam failures as two separate cases, while the current studies "averaged" them together so that these two very similar failures would not overly impact the overall correlations developed.

In the end, Wang (2003) and Kramer (2008) employed 31 case histories, and the current studies employed 29 case histories.

Different approaches were taken to the back-analyses of the field performance case histories.

6. Wang (2003) employed the Zero Inertial Factor (ZIF) method to incorporate momentum effects in back-analyses of the 9 best-documented case histories. These appear to have provided reasonably good to excellent results; matching up fairly well with the incremental momentum analyses performed for these same case histories in these current studies.

7. Wang (2003) then developed estimates of parameters for the remaining 22 less well documented case histories, designated as the "secondary" case histories, based on the back-analyses of multiple previous investigators, without performing any additional analyses of his own. Multiple values were collected from previous investigations, and these were then generally averaged. This left a bit more than two-thirds (22 out of 31) of the cases at least partially dependent upon the judgments and analysis choices of others. Chapter 2, Section 2.3.8, discusses a number of apparent errors and moderate biases that occurred here. Especially notable cases where Wang's values of S_r values differed by more than +/− 50% from the S_r values employed in these current studies are: (1,2) the two La Marquesa Dam cases (Upstream slope failure, and Downstream slope failure), where Wang's selected values of S_r were significantly higher than those of this current study (probably due to inclusion of significant allowance for cyclic inertial effects in the previous back-analyses by de Alba, et al, 1987), (3) Hokaido Tailings dam where Wang's value of S_r is approximately twice as high as the S_r values back-calculated by either Olson (2001) or in these current studies, and (4) the Nerlerk Embankment offshore slides where Wang's selected values are slightly more than twice as high as the values used by either Olson (2001) or in these current studies. Overall, there was a moderate tendency for Wang's selected values of S_r to be biased slightly to the high side (see Chapter 2, Section 2.3.8)

Larger problems occurred due to the approach used to infer initial effective vertical stress, and the values of $\sigma'_{v,i}$ adopted by Wang for at least nine of the secondary case histories are unreasonably high (see Section 2.3.8.1(b) – (iii)). These excessively high values of $\sigma'_{v,i}$ served to "stretch" the $\sigma'_{v,i}$ axis in the regressions that were performed, and resulted in somewhat conservative under-prediction of S_r by the eventual regressed predictive relationship, especially at high initial effective stresses in the final predictive relationship developed. The two sets of apparent errors in parameters from the "secondary" case histories were thus (a) unconservatively biased (overall) values of S_r, and (b) conservatively biased (Overall) values of $\sigma'_{v,i}$. These two sets of biases offset each to some extent, but the errors in $\sigma'_{v,i}$ were the stronger influence and the overall resulting (regressed) relationship appears to have been moderately conservatively biased as a result.

8. These current studies employed the incremental momentum method to incorporate momentum effects in the back-analyses of the 13 best-documented case histories. Results compared well with Wang (2003) for the 9 cases Wang analyzed with the ZIF method.

9. These current studies then made independent (new) assessments in back-analyzing the remaining 16 less well documented case histories, while fully cognizant of the back-analyses and assessments of previous investigators.

10. Kramer (2008) and thus also Kramer and Wang (2016) elected to employ non-fines-corrected $N_{1,60}$ values rather than $N_{1,60,CS}$ values as the basis for their regressions and predictive relationships. These current studies elected instead to use fines-corrected $N_{1,60,CS\ values}$. The field case history database is comprised largely of cases involving silty sands and sandy silts, and it appears to the current investigation team that fines corrections are potentially important. Kramer based his decision to switch to $N_{1,60}$ (from Wang's initial 2003 assessments of $N_{1,60,CS}$) based on the observation that $N_{1,60}$ gave a similar degree of model "fit" as measured in terms of dispersion or variance. The current investigation team did not find that fully compelling, given that so many of the cases had significant fines corrections. Due perhaps in part to different processing and back-analyses of the case histories, including new procedures and both internal cross-checks and external cross-checks, the current investigation team achieved an $N_{1,60,CS}$-based predictive relationship with a significantly smaller overall dispersion than the predictive relationship of Kramer and Wang (2015).

Very different approaches were also taken with regard to evaluation of uncertainties in all parameters, and in the incorporation of these uncertainties in the probabilistic regressions performed by the two investigation teams.

11. Wang (2003) used Monte Carlo simulations to assess parameter uncertainty for the 9 best-documented case histories, but this primarily served only to help to quantify variability of parameters (especially S_r) already established by engineering judgments made with regard to modeling of variability in geometry, failure surfaces, phreatic conditions and properties of non-liquefied soils. The Monte Carlo modeling simply reflected these judgments. These current studies performed back-analyses of the 13 best-documented case histories using the incremental momentum method, and preferred to employ parameter sensitivity studies and

engineering judgment directly in the development of characterizations of variability (e.g. standard deviations) of back-calculated indices from the case histories.

12. For their 22 "secondary" case histories, Wang's estimates of variability (e.g. standard deviations) were based on the back-analyses performed by multiple previous investigators, but it is unclear how judgments were made with regard to interpretations of these previous analyses to develop variance estimates for the indices of interest. In these current studies, new back-analyses were performed for all 16 of the less well documented case histories (the 16 Class B case histories), and these results, with sensitivity studies by means of parameter and geometry variations, as well as consideration of previous back-analyses by other investigators, were jointly used to develop estimates of variability (expressed as estimated standard deviations) of the three key indices from each case history.

13. Another significant difference between the two studies was the manner in which variance or uncertainty was evaluated and modeled in general, for all cases. Wang (2003) and Kramer (2008) generally preferred to perform as formal as possible an assessment of variability of the data available (e.g. variability of actual reported penetration resistance values), but they did not directly incorporate additional uncertainties associated with poor quality of data or information, or poor quality of documentation, into these estimates. Instead, they subsequently applied judgmental "weighting factors" to each of their 31 cases to reflect these additional uncertainties. That was likely largely effective with regard to development of good estimates of the median predictive relationship for S_r, but it may not have been ideal with regard to evaluation of overall predictive model uncertainties. The current engineering team preferred instead to incorporate uncertainties associated with poor quality data, poor documentation, transforming non-standard penetration resistances to equivalent SPT values, etc., into combined (overall) estimates of variance (standard deviations) for each of the three principal indices. In these current studies, estimated variances in all back-analyzed parameters included all of these sources of uncertainty, so no additional weighting factors were then applied to the individual case histories.

14. Kramer (2008) developed estimates of predictive model uncertainty by two different methods: Maximum Likelihood Estimation (MLE) and First-Order, Second Moment (FOSM). The MLE estimates of variance developed were judged to be excessively large, and were discarded. So the FOSM-based estimates of variance or model uncertainty are the basis for his overall probabilistic model uncertainty. The uncertainties (standard deviations) developed by this approach also appear to be large, as illustrated in Figure 5.12(b), and this will be discussed further a bit later. These current studies employed the Bayesian Maximum Likelihood Estimation method as a basis for development of estimates of model uncertainties, and the results are somewhat smaller values of variance or standard deviation for S_r across most of the problem domain, as illustrated in Figure 5.12(a). This may be due in part to the different overall treatments of uncertainty in the back-analysis data set, and it also likely due to the level of effort and care expended in performing and cross-checking the individual back-analysis results for <u>all</u> of the case histories studied.

15. Kramer (2008) studied a suite of lateral spreading case histories, and concluded that his regressed relationship warranted revision in order to ensure that post-liquefaction strengths

for very low initial effective overburden stresses would not be under-predicted. He intervened, and fixed the value one of his parameters (Θ_4) in performing his final regressions. That appears to have been a valid approach to fixing the problem of excessively low predicted S_r values at low $\sigma'_{v,i}$. In these current studies, the shape and position of the regressed predictive surface for S_r was judged to be suitable at low effective initial overburden stresses without this type of additional manipulation.

16. Kramer (2008) selected the 40th percentile values of post-liquefaction strength (S_r) as the recommended "deterministic" values for routine projects. This was based on his observation that all of the best-documented field case histories produced S_r values that plotted above the probabilistic 40th percentile value. These current studies preferred to assume that the probabilistic regressions performed had largely correctly characterized overall predictive accuracy, and that a more traditional 33rd percentile value would be appropriate for more simplistic "deterministic" values. This, too, will be discussed further.

The two investigation teams of (1) Wang and Kramer (2003, 2008, 2015) and (2) these current studies, took different approaches at virtually every step or decision point. These were largely all valid approaches, and reasonable judgments, given the state of knowledge and information available at the time, and so it is interesting now to cross-compare the overall results of these two studies.

Kramer (2008) selected the 40th percentile values of post-liquefaction strength (S_r) as the recommended "deterministic" values for routine projects. Figure 5.10 presents these 40th percentile values, based on the probabilistically regressed predictive relationship that he developed based on the first-order second moment (FOSM) method.

In these current studies, 33rd percentile values are recommended as "deterministic" values for routine design, and Figure 5.11 compares Kramer's recommended 40th percentile values (red lines) vs. the 33rd percentile values (black lines) recommended in these current studies. The level of approximate agreement between these two sets of recommended values is surprisingly good. Especially given the very different steps, procedures, assumptions, and judgments that went into the development of each set of values shown. And the differences can now be explained and understood.

A better comparison is achieved by slightly modifying the curves of Kramer and Wang (2015) by adding an approximate adjustment for fines so that both relationships can (approximately) be compared on an $N_{1,60,CS}$ basis. The average fines correction made for the 30 case histories back-analyzed in these current case histories was $\Delta N_{fines} \approx 1.3$ blows/ft, and the fines correction employed in these current studies progressively increased fines corrections as $N_{1,60}$ values increase, in addition to increasing them with increased fine content. Accordingly, an approximate adjustment was made by adding $\Delta N_{fines} \approx +0.5$ blows/ft to the relationship of Kramer and Wang at $N_{1,60} = 0$, and $\Delta N_{fines} \approx +2.0$ blows/ft at $N_{1,60} = 15$ blows/ft, so that an average correction of approximately +1.2 blows/ft is inferred over the range of the actual case histories. This was applied as a linear correction, so slightly increasing corrections continue to be added at $N_{1,60}$ values higher than 15 blows/ft.

Figure 5.12 repeats Figure 5.11, this time with this modest adjustment of the relationship of Kramer and Wang (2015) to an approximate a clean-sand-corrected basis. This is then the best (nearly direct) comparison of the two relationships.

As discussed in Chapter 2, there are three issues that principally affect the relationship of Kramer and Wang, and these can be seen in this comparative figure. These are as follow.

1. The first of these is the suite of errors made by Wang in estimation of $\sigma'_{v,i}$ for a significant number of his 22 secondary case histories due to the procedure that he employed here. As discussed in Section 2.3.8.1(b)-(iii), and illustrated in Table 2.3, many of the values of $\sigma'_{v,i}$ are clearly too high, and some of them are physically impossible. As shown in Figure 2.3, this appears to result in an <u>average</u> overestimation of $\sigma'_{v,i}$ by a factor of approximately 1.57. This has the effect of "stretching" the $\sigma'_{v,i}$ axis, and results in (over-conservative) under-prediction of S_r for real values of $\sigma'_{v,i}$. This causes the resulting predicted S_r values to be over-conservative, and to drop below those of this current study, especially at increasing $\sigma'_{v,i}$.

2. The second issue was problems with Wang's selections of values of S_r for some of the secondary case histories. These were more subtle issues, and they appear to have affected a lesser number of cases, and to lesser degree (see Section 2.3.8.1(b)-(ii). Most of these led to somewhat unconservative over-estimates of S_r for the individual cases affected. This tended to introduce a source of unconservative bias, but because of the lesser degree, and the lesser number of cases, it did not fully offset the over-conservatism due to the overestimation of numerous values of $\sigma'_{v,i}$. So the overall correlation remained overly-conservative.

3. Kramer (2008) noticed that the predicted values of S_r appeared to be too low at low $\sigma'_{v,i}$, and so he performed a study of lateral spreading case histories, and established a fixed value of Θ_4 to raise up S_r values for low $\sigma'_{v,i}$ based on an estimated lower bound for S_r at low $\sigma'_{v,i}$. He then used this as a basis for modifying his regression by fixing the value of one of his parameters (Θ_4) in his regressions. Because the suite of field case histories present in the liquefaction flow failure case history database was internally correlated in terms of lower $\sigma'_{v,i}$ cases also tending to be lower $N_{1,60}$ cases, this had the effect of also increasing S_r values at low $N_{1,60}$.

All three of these effects can be seen in Figure 5.12. The relationship of Kramer and Wang (2015) falls away below the relationship developed in these current studies at progressively higher values of $N_{1,60,CS}$ (and also $\sigma'_{v,i}$) due to the over-conservatism introduced by the errors in $\sigma'_{v,i}$ values out-weighing the errors in S_r values. At low $N_{1,60}$ (and at low $\sigma'_{v,i}$) the "fix" applied by Kramer (2008) suitably raises up the predicted S_r values, and both relationships agree well here. This "fix" also appears to result in higher predicted values of S_r, however, at low $N_{1,60,CS}$ but <u>higher</u> $\sigma'_{v,i}$; a range that was not analytically considered in the lateral spreading case history study that led to this fixing of (Θ_4). Because the case histories data set is internally correlated, with cases having lower N-values being correlated to some extent with cases that have lower $\sigma'_{v,i}$ values, the effect of imposing a fixed value of Θ_4 to slightly raise up predicted values of S_r at low $\sigma'_{v,i}$ may also have inadvertently slightly "tilted" the overall relationship; further lowering predicted values of S_r at higher N-values.

Overall, however, these two sets of results (and "deterministic" recommendations) would appear to largely represent what passes for "consensus" for these types of challenging geotechnical

issues, especially across the ranges of the available field case history data, and at blowcounts of $N_{1,60,CS} \leq 16$ blows/ft., if the over-conservative errors in selection of $\sigma'_{v,i}$ values made by Wang (2003) for at least 13 of the secondary case histories are taken into account.

Figure 5.13 shows the two different surfaces representing the estimated values of variance, expressed as standard deviation of S_r developed based on the probabilistic regressions of (a) these current studies, and (b) Kramer (2008). The standard deviations of Kramer are very similar to those of these current studies in the lower front corner, where both $N_{1,60,CS}$ and initial effective vertical stress are relatively low, but they increase more rapidly with increasing $N_{1,60,CS}$ and with increasing effective vertical stress. This has some ramifications for (a) the selection of recommended exceedance levels for the simplified "deterministic" relationships developed for the two different relationships, and (b) for the levels of conservatism that will be associated with more comprehensive use of the two fully probabilistic relationships (for all exceedance levels) on more complex and/or higher risk projects to which risk-based methods may be applied.

Kramer recommended setting his simplified "deterministic" relationship for S_r at the 40th percentile, based on the observation that all of the 9 well characterized field case histories exceeded this value. The current studies selected instead the 33rd percentile value, based on the assumption that the field case history data set had been properly characterized in its entirety, and that the use of this more traditional value of level of conservatism would be more familiar and would be better understood and thus better employed by working engineers.

Figure 5.14 shows a comparison between Kramer's 33rd percentile values (red lines) vs. the 33rd percentile values (black lines) recommended in these current studies. These "equal risk" based lines show that the relationship developed by Kramer and Wang drops away from the relationship developed in these current studies at higher $N_{1,60,CS}$ values when equal levels of non-exceedance are targeted. That has ramifications for fully risk-based engineering analyses for major projects.

Figure 5.15 then shows the recommended "deterministic" relationship (40th percentile) of Kramer (2008), this time expressed in terms of strength ratio (S_r/P) format, extrapolated to higher $N_{1,60,CS}$ values (red lines) and the recommended "deterministic" relationship (33rd percentile) of these current studies also extrapolated. This figure also shows the range of likely fully drained frictional cut-off as presented previously in Figure 5.9. This shows even more clearly how the relationship developed in these current studies rises more quickly at $N_{1,60,CS}$ values greater than about 10 to 15 blows/ft, and it also shows how the range of interest is limited by the likely range of drained frictional cut-off. (It should be noted that it is usually values at and near the top of the drained frictional cut-off range, corresponding to largely horizontal failure surfaces in the field, that are of principal interest for most engineering projects).

Overall, agreement between the relationships developed by Wang and Kramer (2003, 2008) and by these current studies is judged to be reassuringly good, if allowance is made for the excessively high representative $\sigma'_{v,i}$ values that Wang (2003) selected for at least 12 of his "secondary" (Class B) case histories; and the consequent degree of excessive conservatism (especially at high penetration resistances and initial effective overburden stresses) that resulted.

5.4.2 Olson and Stark (2002)

Figure 5.16 shows the recommended relationship between S_r/P and $N_{1,60}$ proposed by Olson and Stark (2002). Figure 5.17 then shows this relationship super-imposed (red lines) on the 33rd percentile relationship developed in these current studies. The relationship of Olson and Stark modeled the post-liquefaction strength ratio (S_r/P) as being independent of initial effective overburden stress, and so it was to be expected that their recommended relationship would be conservative for very low initial effective overburden stresses, and unconservative for very high initial effective overburden stresses. In addition, because 23 of their 33 liquefaction case histories were back-analyzed in a manner that produced values of $S_{r,resid/geom}$, instead of values of S_r that incorporated momentum effects, 23 of their case histories systematically underestimated S_r, and likely by factors of approximately 1.2 to 3.4, as discussed previously in Section 2.3.6. The other 10 cases were back-analyzed by their kinetics method, which did specifically incorporate momentum effects, and this appears to have produced generally good back-calculated values of S_r for those cases. Overall, however, it would be expected that their relationship would be significantly conservatively biased by the 23 cases for which S_r was systematically (and significantly) underestimated.

This is what Figure 5.17 shows. Allowing for the fact that their horizontal axis is $N_{1,60}$ rather than fines-adjusted $N_{1,60,CS}$, their recommended range of S_r/P values appears to be generally suitable at initial effective vertical stresses of approximately 1 to 4 atmospheres, and for $N_{1,60}$ values of less than about 10 to 12 blows per foot. At higher values of penetration resistance, their relationship lacks upward curvature, and would provide increasingly over-conservative values. And this over-conservatism would also be greater at lower effective overburden stresses. Their relationship fails to capture the "upwards curvature" inherent in the S_r values for any given level of effective overburden stress, and it also fails to capture the partial dependence of S_r/P on effective vertical stress.

5.4.3 Idriss and Boulanger (2008)

Figures 5.18 and 5.19 show the recommended relationships of Idriss and Boulanger (2008) for evaluation of post-liquefaction strength ratio (S_r/P) as a function of penetration resistance. Figure 5.18 shows the relationship of Idriss and Boulanger for residual strength ratio (S_r/P). Figure 5.19 then shows the relationship of Idriss and Boulanger (red lines) for residual strength ratio (S_r/P) from Figure 5.18 superimposed on the 33rd percentile relationship developed in these current studies (black lines). It is the lower of the two diverging lines in Figure 5.18 and 5.19 that represents Idriss and Boulanger's recommended relationship for field situations (in which void redistribution effects can occur). As shown in these figures, the relationship of Idriss and Boulanger (2008) fails to capture the dependence of S_r/P on effective vertical stress. It provides reasonable values of S_r/P for $N_{1,60,CS}$ values of less than about 12 blows/ft and for effective stresses of between about 0.5 to 2 atmospheres. In this same range of $N_{1,60,CS}$ values of less than about 12 blows/ft, the relationship is unconservative higher effective stresses. At lower effective stresses the relationship is overly conservative. In this same range of $N_{1,60,CS}$ values of less than about 12 blows/ft, the relationship is unconservative higher effective stresses. But at higher $N_{1,60,CS}$ values and higher effective overburden stresses the relationship of Idriss and Boulanger becomes increasingly conservative, and progressively matches up well with higher effective stress ranges

while being increasingly over-conservative for lower effective stresses. The "upper" dashed red line of the two diverging dashed lines in Figure 5.19 is a theoretical relationship, based on laboratory testing (see Section 2.3.10), and it is recommended only for cases in which void redistribution is not expected to occur. This upper dashed line is therefore not applicable to field conditions as considered in these current studies and no comparison is appropriate here.

Figure 5.20 shows the recommended relationship of Idriss and Boulanger (2008) for S_r as a function of penetration resistance (S_r). Figure 5.21 shows this relationship of Idriss and Boulanger (red lines) superimposed on the 33rd percentile relationship developed in these current studies black lines). This relationship also fails to capture the dependence of S_r on initial effective vertical stress. The relationship appears to be suitable for initial effective overburden stresses of approximately 1 atmosphere, and the upward curvature out to blowcounts as high as 16 blows per foot appears to continue to be generally appropriate for this level of effective overburden stress. This relationship would generally be increasingly overconservative for effective overburden stresses significantly greater than 1 atmosphere, and it would be unconservative for effective overburden stresses significantly lower than 1 atmosphere.

5.4.4 Seed and Harder (1990)

Figure 5.22 shows the relationship recommended by Seed and Harder (1990). Figure 5.23 shows this relationship (red lines) superimposed on the 33rd percentile relationship developed in these current studies (black lines). The relationship proposed by Seed and Harder (1990) is the oldest of the previously proposed relationships considered here, and it too fails to capture the partial dependency of S_r on effective vertical stress. This relationship is often employed based on an interpretation of S_r as being one-third of the way up from the bottom boundary curve towards the top boundary curve. The relationship of Seed and Harder (1990), taken at this "one-third" level, is fairly similar to the relationship of Idriss and Boulanger (2008) shown previously in Figures 5.20 and 5.21, and it has similar strengths and weaknesses. It too fails to capture the partial dependence of S_r on effective vertical stress. An approximate one-third interpretation appears to provide reasonable values of S_r for effective overburden stresses of approximately 1 to 2 atmospheres, and for $N_{1,60,CS}$ values of less than about 16 to 18 blows per foot. And it would be over-conservative for higher initial effective vertical stresses, and if extrapolated to values of $N_{1,60,CS}$ greater than about 17 blows per foot it would be unconservative for effective stresses less than about 2 atmospheres.

5.5 Remaining Uncertainty and Overall Conservatism

The new relationships developed herein appear to fit well with the previous relationships developed and presented by others, especially when the underlying bases of those previous relationships are closely examined with regard to (1) the strengths and drawbacks of the back-analyses of case histories performed to develop the data upon which the previous predictive relationships were developed, and (2) the strengths and drawbacks of the basic forms and assumptions upon which the previous relationships were based.

The new relationships are also based upon an internally consistent, and cross-checked, suite of back-analysis results from a large suite of field case histories.

But there remain three principal sets of uncertainties, and potential sources of systematic conservatism or unconservatism, in the new relationships. And these warrant further discussion.

5.5.1 Monotonic vs. Cyclically-Induced Values of Post-Liquefaction Strength (S_r)

A question that arises is whether cyclically-induced soil liquefaction will produce a greater amount of void redistribution, or a greater amount of inter-layer mixing, than monotonically-induced (or "static") liquefaction failures, and whether this might lead to systematically lower values of post-liquefaction strength (S_r) for cyclic cases than for monotonic cases.

In examining the database of case histories, there are eight cases that are purely monotonically-induced liquefaction failures, and these are plotted in all figures in this chapter with open symbols, while cyclically-induced failures are plotted with closed (solid) symbols. There are not enough monotonic cases available as to perform a separate regression for these cases, but by inspection it does not appear that there is a strong systematic bias between S_r values for monotonic and cyclic cases. Two of the static cases with higher $N_{1,60,CS}$ values plot towards the upper portion of Figure 5.4(a), potentially giving the impression that monotonically-induced failures might produce higher values of S_r, but closer inspection shows (1) that these cases also have higher values of $\sigma'_{v,o}$ which explain the higher Sr values, and (2) additional monotonically-induced liquefaction cases with lower $N_{1,60,CS}$ values occur lower on the figure, where they mix well with cyclically-induced cases.

Overall, the current field case history database does not appear to support the use of systematically higher values of S_r for monotonically-induced liquefaction failures.

5.5.2 Effects of Cyclic Inertial Forces

The back-analyses performed in these current studies, and in most previous studies, did not directly incorporate the potential effects of cyclic inertial forces on the deformations and displacements observed, and on the values of post-liquefaction strength back-calculated as best explaining these displacements. The question thus arises as to whether the back-calculated values of Sr may be systematically biased conservatively, as the cyclic "driving" shear forces associated with cyclic lurching have not been included.

Table 5.3 lists the case histories back-analyzed in these current studies. In this table, the cases have been sub-divided into four sub-sets based on liquefaction triggering mechanism and on the mechanisms that then produced the observed resulting deformations and displacements.

Group 1 is comprised of ten cases in which liquefaction was monotonically (or "statically") induced, and in which there were no cyclic inertial forces.

Group 2 is comprised of four cases in which liquefaction was "triggered" by cyclic loading, but in which there were again no significant cyclic inertial forces acting to contribute towards the displacements that ensued. The first two of these cases are (1) the Lower San Fernando Dam upstream slope failure, and (2) the two Moshi-Koshi Tailings Dam dike failures. In both of these cases, liquefaction was triggered by seismic (earthquake) loading, but there was then a delay before the ensuing large displacement slope failures occurred. These delays have been attributed to time required for pore pressure re-distribution (and for satisfaction of local dilation in the denser starter dikes of the Lower San Fernando Dam) such that a sufficient amount of liquefied material lost enough strength that the large failures could proceed. The delays of multiple hours were observed by witnesses in the case of the Moshi-Koshi dikes. In the case of the Lower San Fernando dam, the delay was only a matter of several tens of seconds, and it was recorded on an unusual strong motion instrument on the dam's crest which recorded multi-directional seismic movements due to strong shaking on a rounded glass ball, with time marks (tics) for timing during the earthquake, and then, subsequently, produced a largely linear record as the instrument was tipped by the subsequent large scale landslide in which it participated. Both of these cases thus experienced their large displacements in the absence of any significant strong shaking.

Group 3 is comprised of eight case histories which experienced liquefaction, and liquefaction-induced large displacements, during earthquakes. These eight cases all experienced only moderate levels of strong shaking (peak ground accelerations on level ground of less than approximately 0.2 g), and many of them experienced relatively short durations of shaking in small magnitude seismic events. These moderate levels of shaking, and of duration, would not have contributed significantly to the observed displacements, and these are cases in which the observed deformations and displacements are primarily due to static (gravity-induced) driving shear forces.

Group 4 is comprised of eight cases in which strong levels of seismic shaking occurred, and often with significant duration. These are thus cases in which cyclic inertial forces may have contributed meaningfully to the observed displacements. Two of these cases; the Shibecha-Cho Embankment Failure and the El Cobre Tailings Dam failure are marked with three asterisks. These two cases experienced catastrophic flow failures with very large displacements; displacements so large that cyclic inertial forces were unlikely to have contributed significantly.

It is then the remaining six cases of Group 4 in which cyclic inertial forces may have contributed at a potentially significant level to the observed displacements. It was not possible to incorporate cyclic inertial forces in the analyses performed in these current studies, nor in any of the previous studies by others, with good accuracy and reliability. Neglect of cyclic inertial forces may have caused the back-calculated values of S_r to be somewhat conservative (low) for these six cases.

Consideration was given to performing fully nonlinear time-domain finite element or finite difference analyses in order to simultaneously model both gravity-induced driving shear forces and cyclic lurching forces. Challenges here would include: (1) The inherent difficulties and challenges involved in performing fully nonlinear seismic response analyses in at least a two-dimensional context, and with ongoing changes in material strengths and stiffnesses as the events proceed, and (2) numerical issues associated with very large (and strongly localized) displacements. It was judged that this is difficult to accomplish, and that the reliability of these

types of calculations is not yet consistently high. It may be hoped that future investigators may pursue this further.

Overall, having back-analyzed all of the case histories, it is the judgment of this investigation team that conservative bias due to neglect of cyclic inertial forces for this suite of field case histories is likely to have had relatively little impact on the predictive relationships developed.

5.5.3 Potential Case History Sampling Bias

A third issue is the question of potential sampling bias with regard to the use of the selected suite of large displacement liquefaction failure case histories. The issue here is not whether the current investigation team, or previous investigators, introduced bias in their selection of case histories to back-analyze or employ in development of predictive relationships. Instead, the issue is whether the cases themselves have "self-selected" themselves in a systematically biased manner by exhibiting large displacements, while other, similar, situations and conditions did not produce observed failures and so did not become available for the database.

There is no good way to fully reliably address this question, nor to accurately quantify the potential bias that might result. And so it must be noted that if this bias exists, then the currently available predictive relationships (including the new relationships developed and presented herein) would be somewhat conservative as a result.

Table 5.1: Values of (1) representative post-liquefaction strength, (2) representative penetration resistance, and (3) initial effective vertical effective stress for each of the 29 back-analyzed liquefaction case histories as employed in the deterministic least squares regressions.

Group	Case	This Study		
		$\bar{S}_r$ (psf)	$\bar{\sigma}'_{vo}$ (psf)	$\bar{N}_{1,60,CS}$
A	Wachusett Dam - North Dike	294	3142	7.5
	Fort Peck Dam	762	7258	12.5
	Uetsu Railway Embankment	38	1448	3
	Lower San Fernando Dam - U/S Slope	539	3174	13.5
	Hachiro-Gata Road Embankment	68	673	7
	La Marquesa Dam - U/S Slope	103	981	6.5
	La Marquesa Dam - D/S Slope	214	1215	10.5
	La Palma Dam	136	767	5
	Lake Ackerman Highway Embankment	107	909	3.5
	Chonan Middle School	141	1032	6.5
	Soviet Tajik - May 1 Slide	341	1907	10.5
	Shibecha-Cho Embankement	224	1416	7.5
	Route 272 at Higashiarekinai	138	1285	8
B	Zeeland - Vlietepolder	156	2488	8
	Sheffield Dam	138	1308	7
	Helsinki Harbor	48	846	6
	Solfatara Canal Dike	64	669	4.5
	Lake Merced Bank	136	834	8.5
	El Cobre Tailings Dam	95	2075	2
	Metoki Road Embankment	92	871	2.5
	Hokkaido Tailings Dam	131	1203	4
	Upper San Fernando Dam - D/S Slope	726	3138	15
	Tar Island Dyke	516	4197	11
	Mochi-Koshi Tailings Dam, Dikes 1 and 2	211	1532	6
	Nerlerk Embankment, Slides 1 ,2 and 3	68	1171	7.5
	Asele Road Embankment	137	1037	9.5
	Nalband Railway Embankment	167	1209	7.5
	Sullivan Tailings	277	2422	9.5
	Jamuna Bridge	175	1404	10.5

Table 5.2: Values of (1) median post-liquefaction strength, (2) median penetration resistance, and (3) median effective vertical effective stress for each of the 29 back-analyzed liquefaction case histories, and standard deviations for each of these, as employed in the fully probabilistic maximum likelihood regressions.

Group	Case	This Study					
		$\bar{S}_r$ (psf)	$\sigma_{\bar{S}}$	$\bar{\sigma}'_{vo}$ (psf)	$\sigma_{\bar{\sigma}}$	$\bar{N}_{1,60,CS}$	$\sigma_{\bar{N}}$
A	Wachusett Dam - North Dike	294	31	3142	132	7.5	1.6
	Fort Peck Dam	762	118	7258	687	12.5	2.7
	Uetsu Railway Embankment	38	8	1448	116	3	0.8
	Lower San Fernando Dam - U/S Slope	539	47	3174	281	13.5	1.8
	Hachiro-Gata Road Embankment	68	12	673	41	7	1.2
	La Marquesa Dam - U/S Slope	103	33	981	134	6.5	1.8
	La Marquesa Dam - D/S Slope	214	57	1215	103	10.5	2.2
	La Palma Dam	136	23	767	42	5	1.2
	Lake Ackerman Highway Embankment	107	19	909	61	3.5	0.7
	Chonan Middle School	141	35	1032	82	6.5	2.1
	Soviet Tajik - May 1 Slide	341	57	1907	177	10.5	2.7
	Shibecha-Cho Embankement	224	37	1416	95	7.5	1.7
	Route 272 at Higashiarekinai	138	17	1285	104	8	1.6
B	Zeeland - Vlietepolder	156	37	2488	431	8	2.1
	Sheffield Dam	138	23	1308	71	7	2.3
	Helsinki Harbor	48	14	846	105	6	2.0
	Solfatara Canal Dike	64	22	669	59	4.5	1.5
	Lake Merced Bank	136	21	834	102	8.5	2.2
	El Cobre Tailings Dam	95	31	2075	183	2	1.0
	Metoki Road Embankment	92	20	871	85	2.5	0.9
	Hokkaido Tailings Dam	131	45	1203	191	4	1.1
	Upper San Fernando Dam - D/S Slope	726	138	3138	278	15	1.8
	Tar Island Dyke	516	119	4197	484	11	2.3
	Mochi-Koshi Tailings Dam, Dikes 1 and 2	211	38	1532	165	6	1.7
	Nerlerk Embankment, Slides 1 ,2 and 3	68	19	1171	129	7.5	1.8
	Asele Road Embankment	137	27	1037	77	9.5	2.0
	Nalband Railway Embankment	167	15	1209	94	7.5	2.5
	Sullivan Tailings	277	24	2422	142	9.5	2.4
	Jamuna Bridge	175	22	1404	210	10.5	2.5

Table 5.3: Classification of Failure Case Histories with Regard to Potential Effects of Cyclic Inertial Forces on Observed Displacements

Group 1. Static/Monotonic Failures: - Wachusett Dam U/S Slope Failure - Fort Peck Dam U/S Slope Failure - Zeeland-Vietepolder Offshore Slope Failure - Sheffield Dam Slope Failure - Helsinki Harbor Slope Failure - Tar Island Dike Slope Failure - Nerlerk Embankment Slides No's. 1, 2 and 3 - Sullivan Tailings Impoundment Slope Failure - Jamuna Bridge - Calaveras Dam Slope Failure
Group 2. Cyclically-Induced Liquefaction, but "Static" Failures: - Lower San Fernando Dam U/S Slope Failure* - Moshi-Koshi Tailings Dam, Dikes 1 and 2* - Lake Ackerman Highway Embankment Failure** - Asele Road Embankment**
Group 3: Cyclically-Induced Liquefaction, and Low to Moderate Cyclic Inertial Forces: - Uetsu Railway Embankment - Hachiro Gata Roadway Embankment - Chonan Middle School - Soviet Tajik, May 1 Slide - Solfatera Canal Dike - Lake Merced Bank - Metoki Roadway Embankment - Hokaido Tailings Dam
Group 4: Cyclically-Induced Liquefaction and Strong and Sustained Cyclic Inertial Forces: - La Marquesa Dam Upstream Slope Failure - La Marquesa Dam Downstream Slope Failure - La Palma Dam Upstream Slope Failure - Shibecha-Cho Embankment Failure*** - Route 272 Embankment Failure - El Cobre Tailings Dam Failure*** - Nalband Railway Embankment Failure - Upper San Fernando Dam Downstream Slope Displacement****

*Seismically-induced soil liquefaction triggering, but subsequent slope failure after strong shaking had ceased.
**Liquefaction triggered by vibratory vehicles, no strong cyclic inertial forces.
***Very large runout displacements, significantly exceeding cyclic inertial deformations.
****Cyclic inertial forces were considered in these current studies.

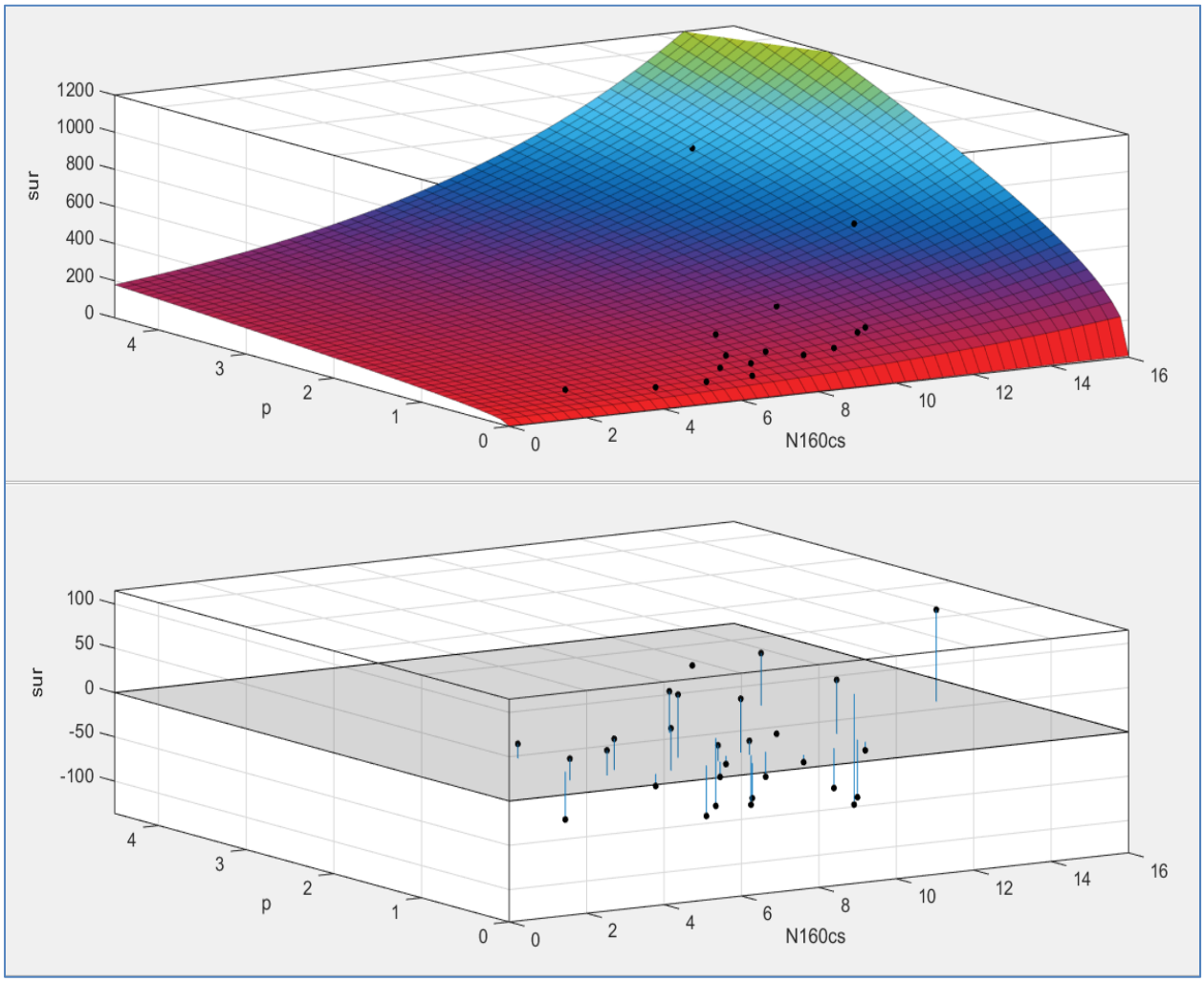

Figure 5.1: Results of deterministic least squares regression showing (a) the relationship for post-liquefaction strength ($\overline{S_r}$) as a function of both $\overline{N_{1,60,CS}}$ and $\overline{\sigma'_{vo}}$, and (b) residuals from the deterministic least squares regression in terms of predicted vs. observed $\overline{S_r}$ for each of the 29 liquefaction field case histories. [Note: Residuals in the lower figure are vertically exaggerated by a factor of 5 for clarity.]

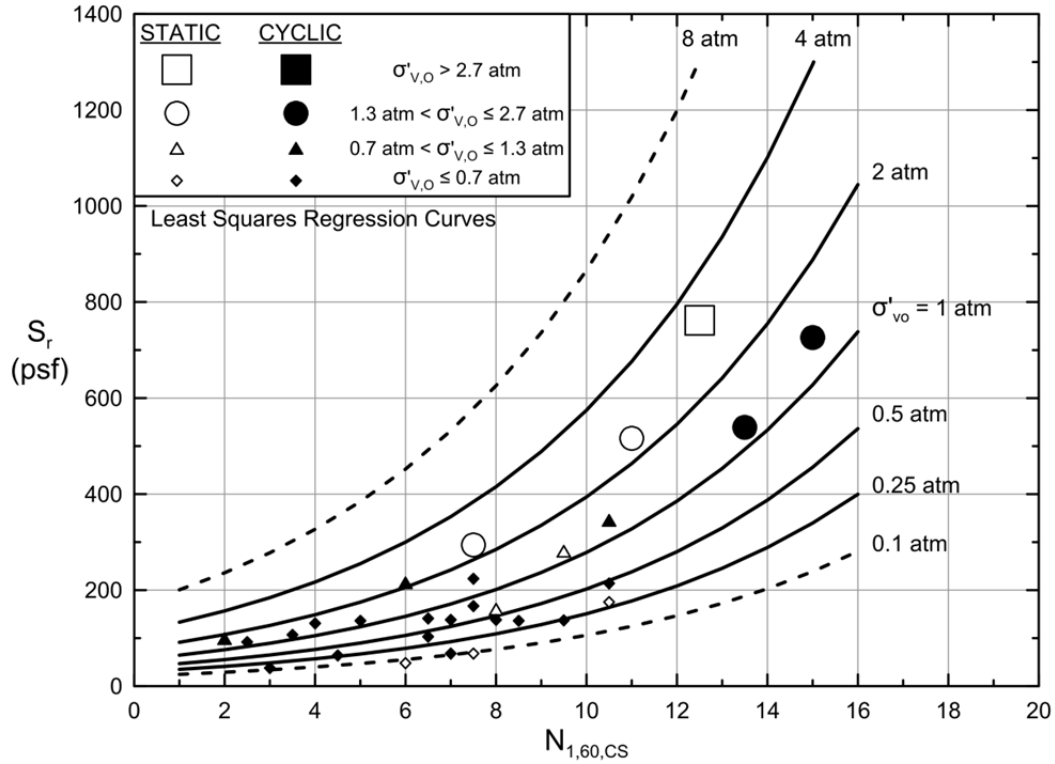

Figure 5.2(a): Results of deterministic regression showing post-liquefaction strength (S_r) as a function of both penetration resistance and initial effective vertical stress.

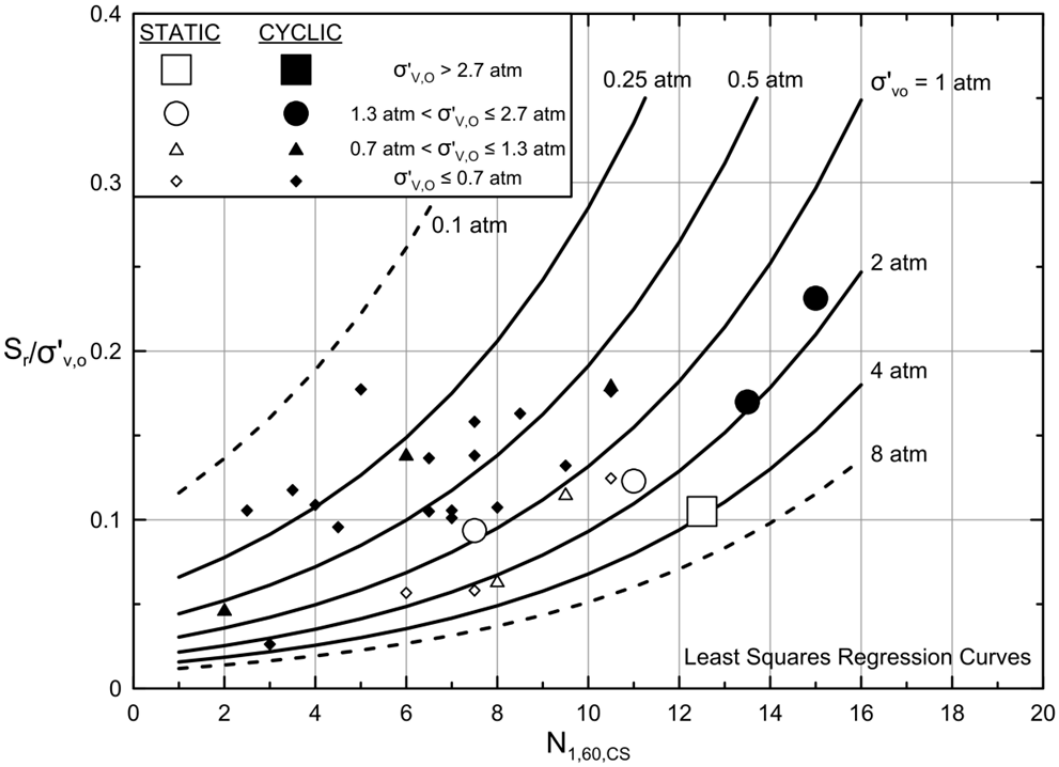

Figure 5.2(b): Results of deterministic regression showing post-liquefaction strength ratio (S_r/P) as a function of both penetration resistance and initial effective vertical stress.

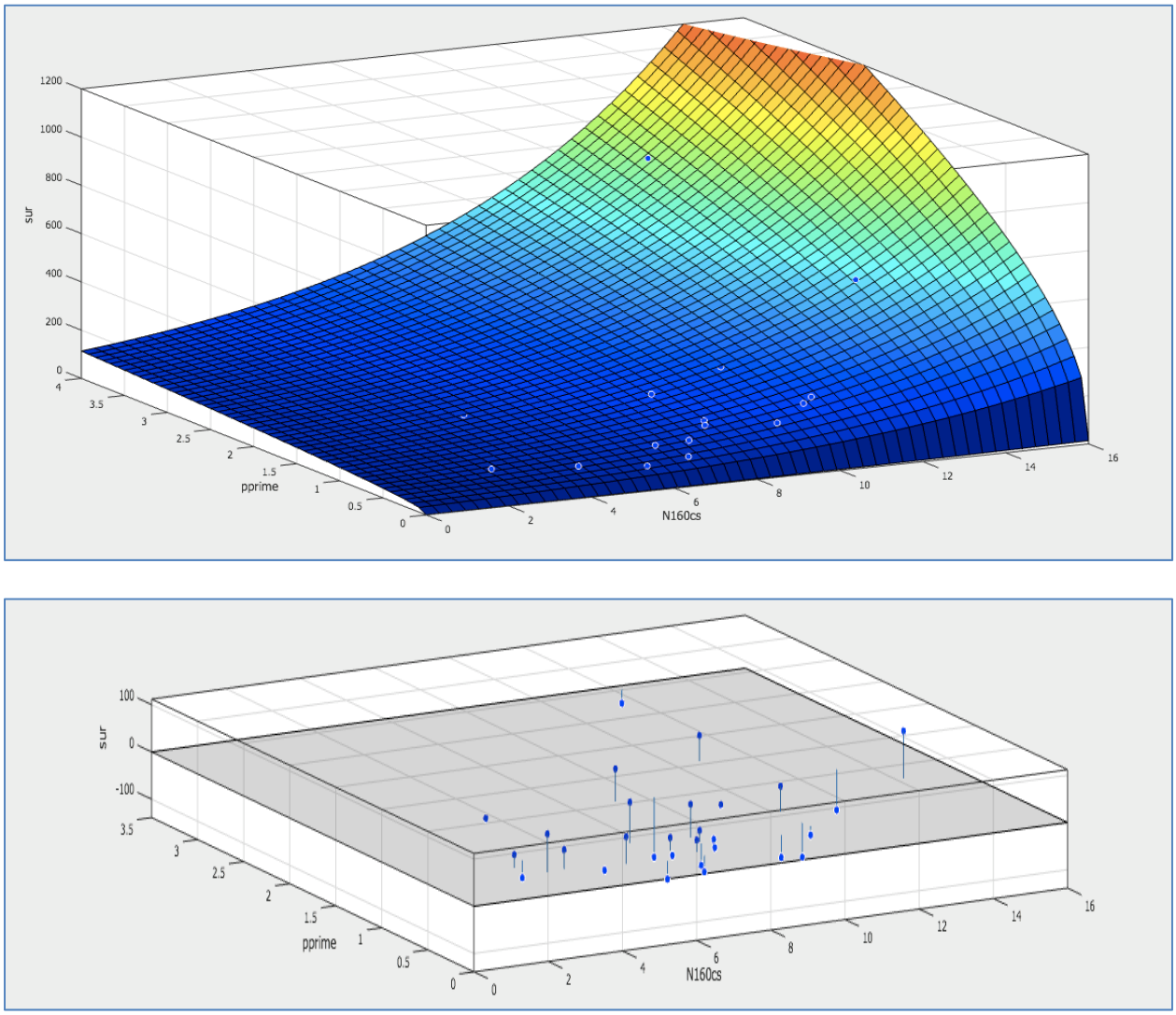

Figure 5.3: Results of probabilistic maximum likelihood regression showing (a) the relationship for post-liquefaction strength ($\overline{S_r}$) as a function of both $\overline{N_{1,60,CS}}$ and $\overline{\sigma'_{vo}}$, and (b) residuals from the deterministic least squares regression in terms of predicted vs. observed $\overline{S_r}$ for each of the 29 liquefaction field case histories. [Note: Residuals in the lower figure are vertically exaggerated by a factor of 2 for clarity.]

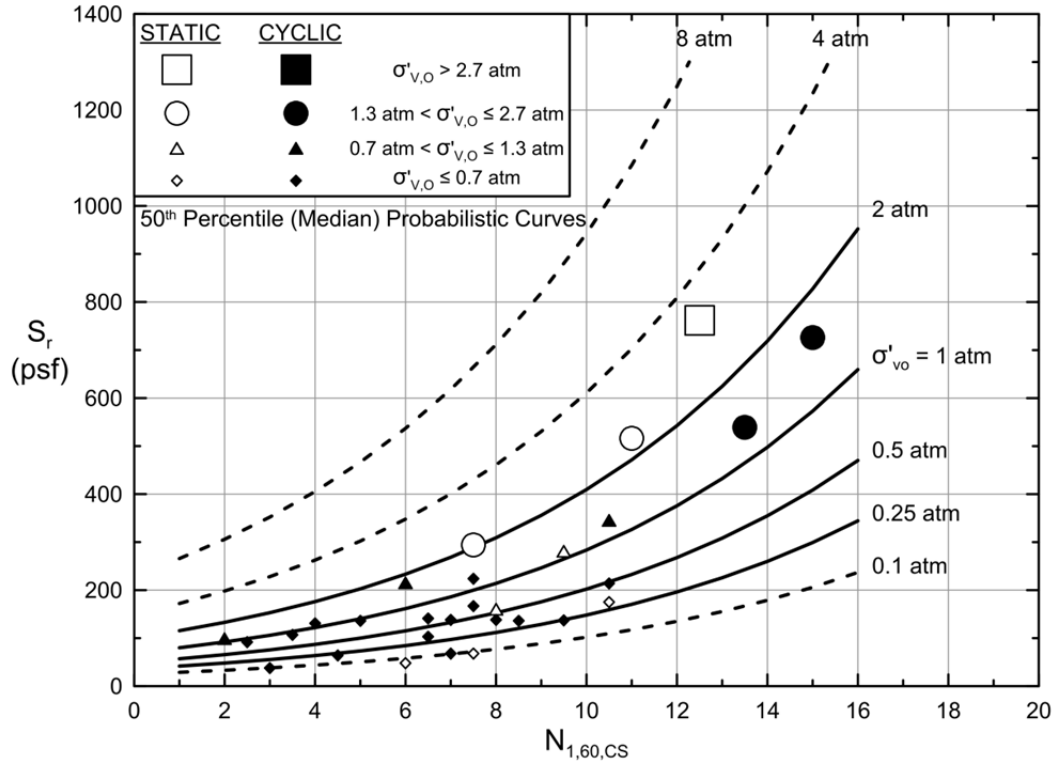

Figure 5.4(a): Results of probabilistic regression showing median values of S_r as a function of both penetration resistance and initial effective vertical stress.

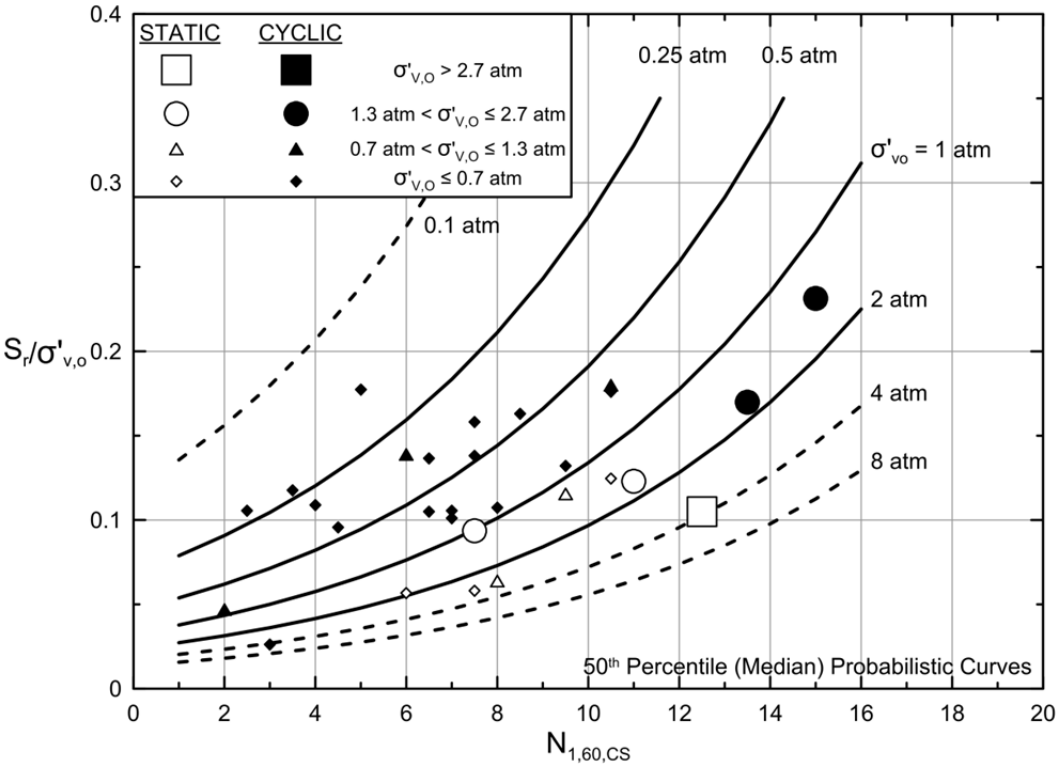

Figure 5.4(b): Results of probabilistic regression showing median values of S_r/P as a function of both penetration resistance and initial effective vertical stress.

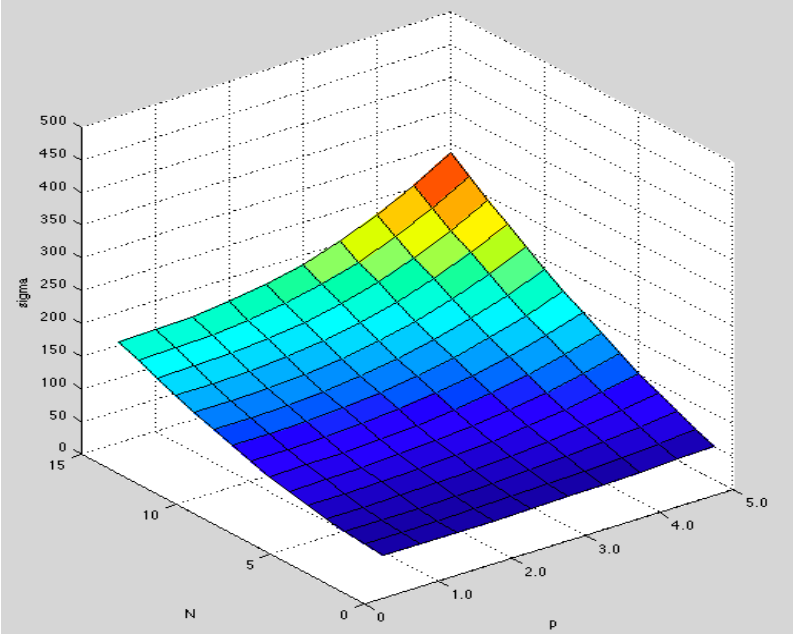

Figure 5.5: Three-dimensional surface showing values of standard deviation in S_r as a function of (1) $N_{1,60,CS}$ and (2) initial effective vertical effective stress based on the probabilistic maximum likelihood method regression analyses.

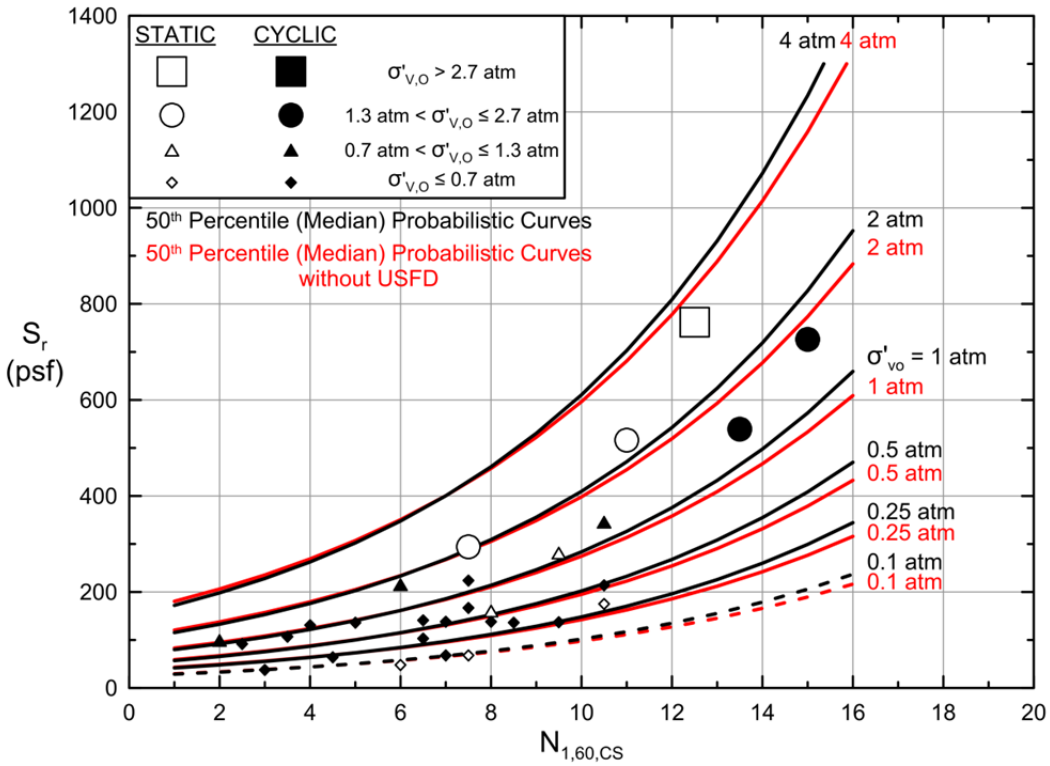

Figure 5.6: Figure 5.4(a) repeated (black lines) also showing the results of a probabilistic regression performed with the data point from the Upper San Fernando Dam case history deleted (red lines).

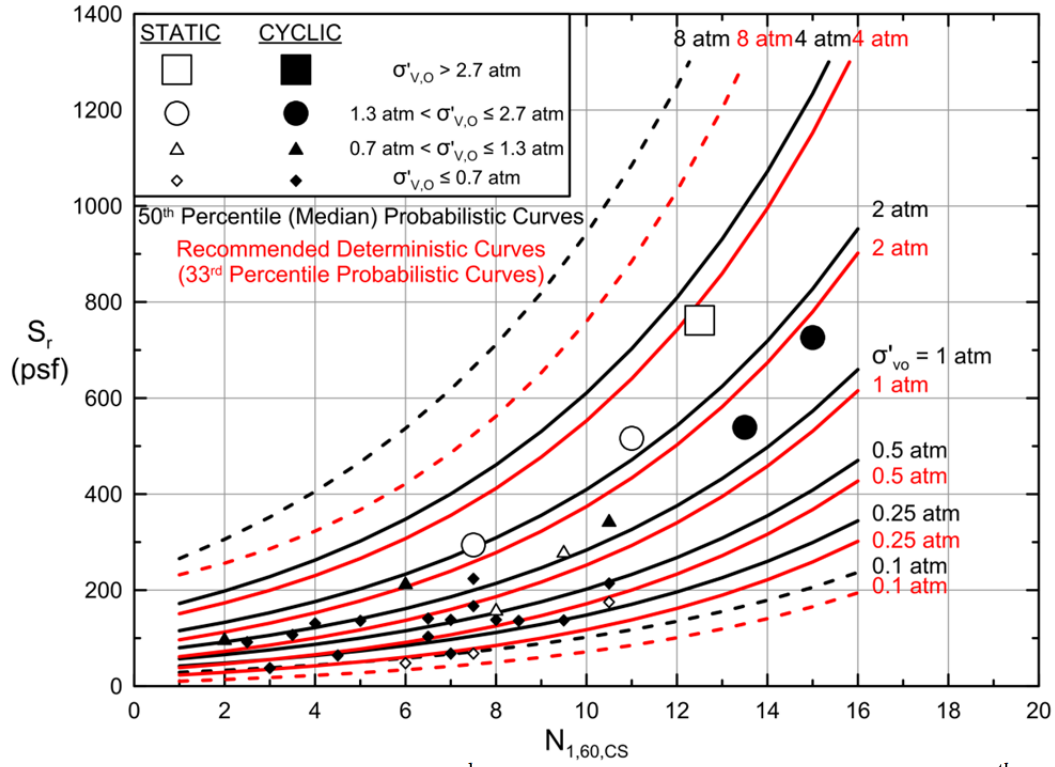

Figure 5.7(a): Comparison between 33rd percentile values of S_r (red lines) and 50th percentile values of S_r (black lines) from the probabilistic relationship of Equation 5-6.

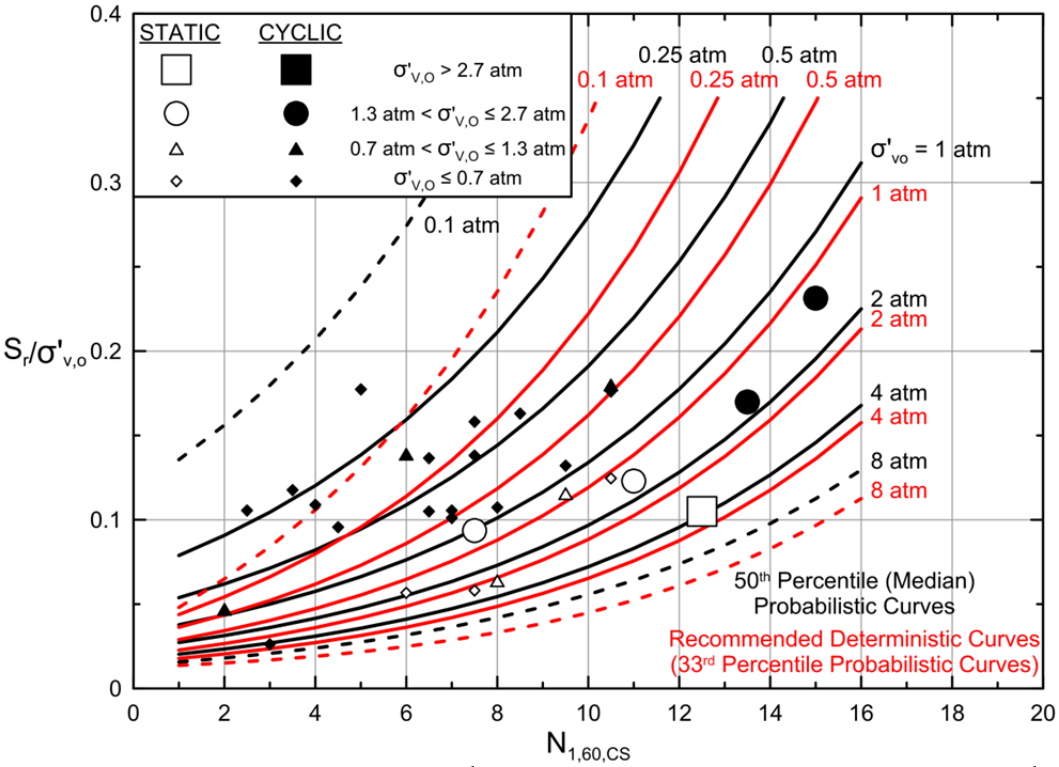

Figure 5.7(b): Comparison between 33rd percentile values of S_r/P (red lines) and 50th percentile values of S_r/P (black lines) from the probabilistic relationship of Equation 5-6.

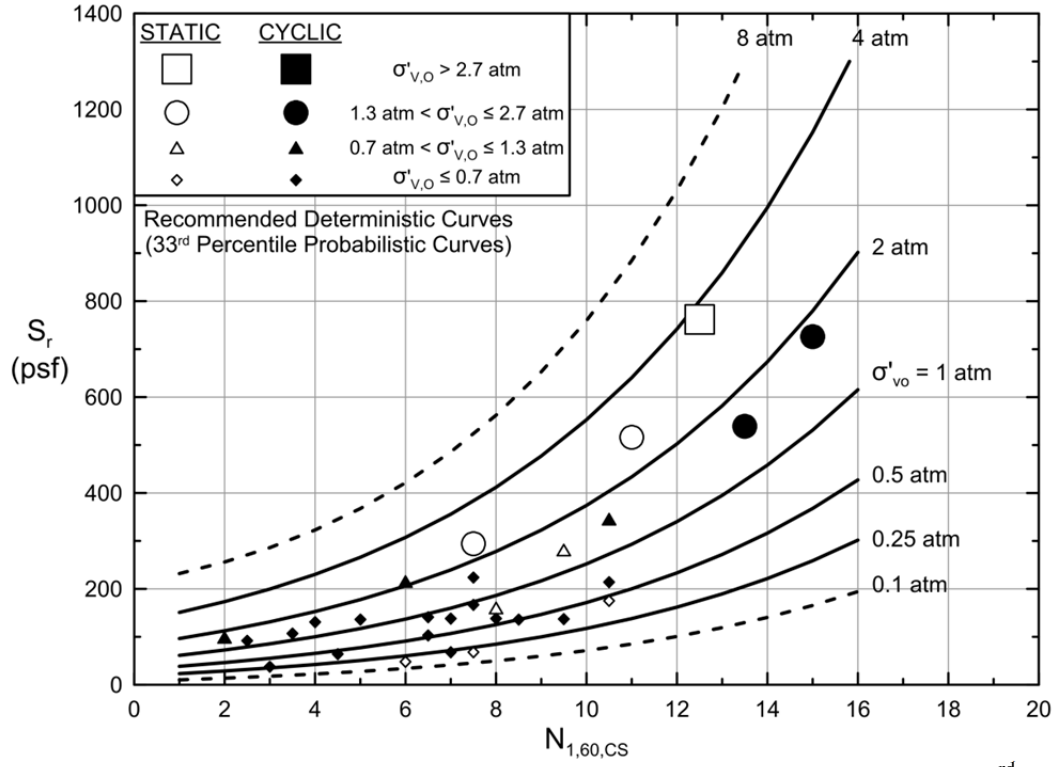

Figure 5.8(a): Recommended deterministic relationship (Equation 5-9); also the 33rd percentile values of S_r/P from the probabilistic relationship of Equation 5-6.

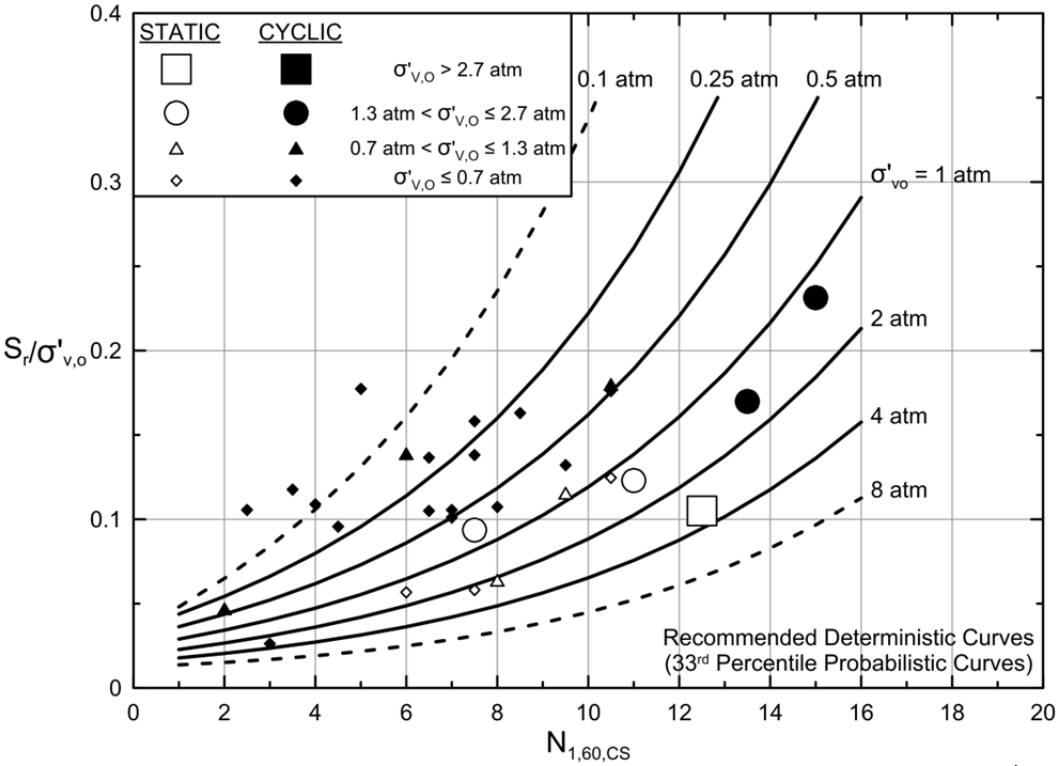

Figure 5.8(b): Recommended deterministic relationship (Equation 5-9); also the 33rd percentile values of S_r/P from the probabilistic relationship of Equation 5-6.

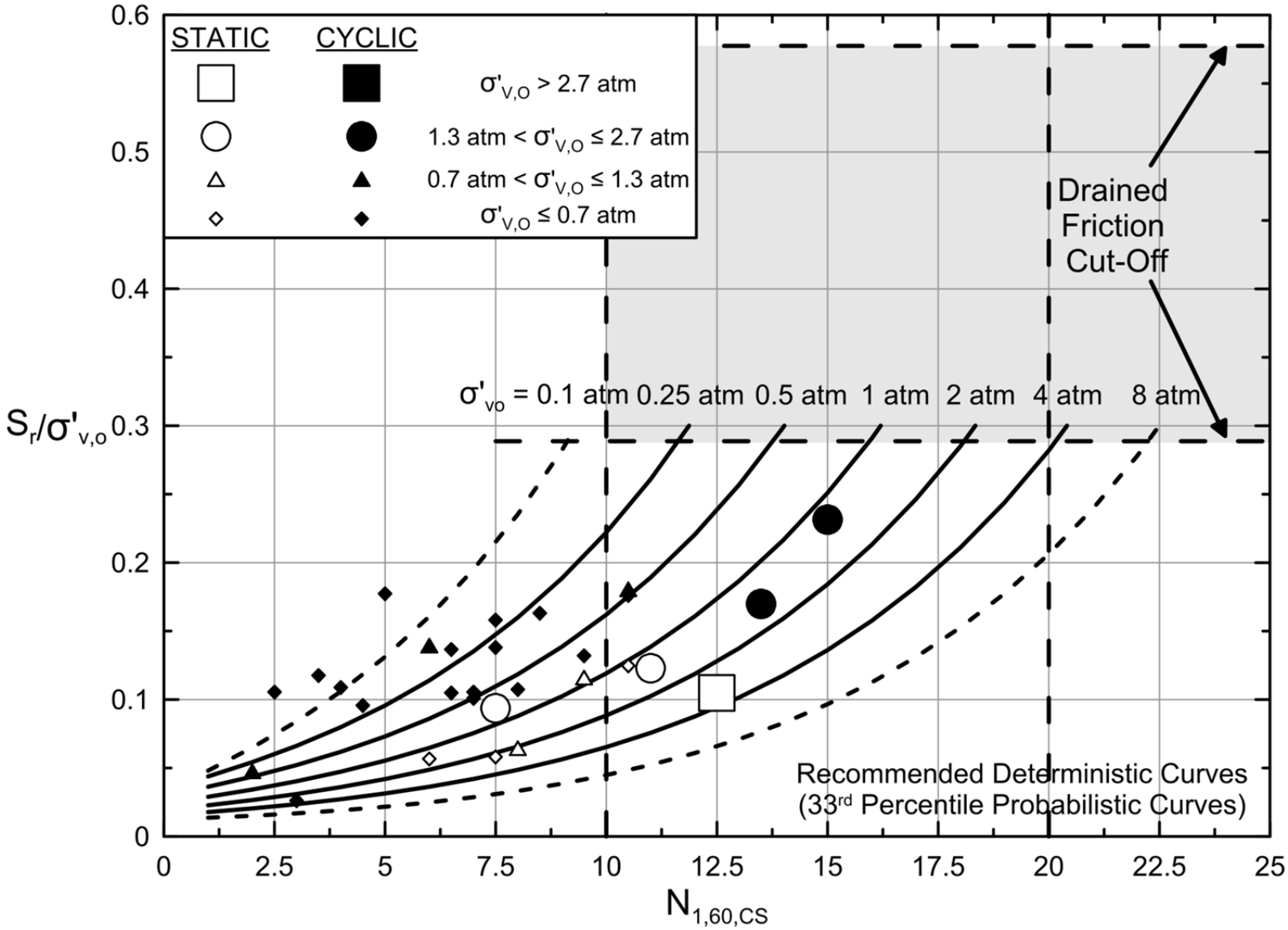

Figure 5.9: Extended view of 33rd percentile values of S_r/P from the probabilistic relationship of Equation 5-6, showing the approximate range of "fully drained cut-off" (shaded region).

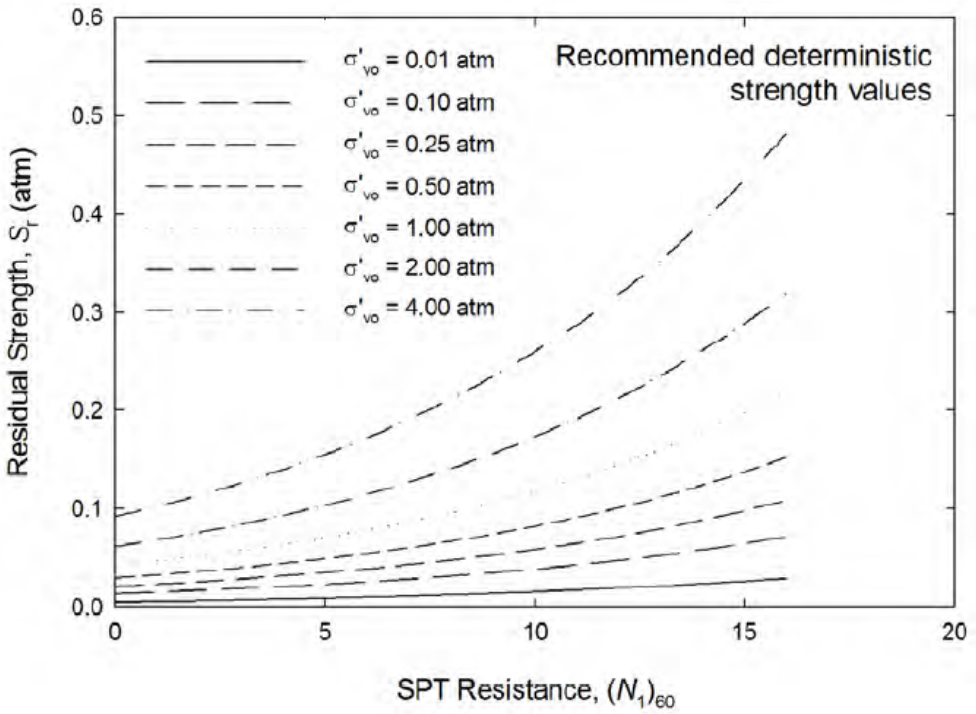

Figure 5.10: Recommended deterministic relationship of Kramer (2008) showing 40th percentile values of S_r as a function of (a) $N_{1,60,CS}$ and (b) initial effective vertical stress.

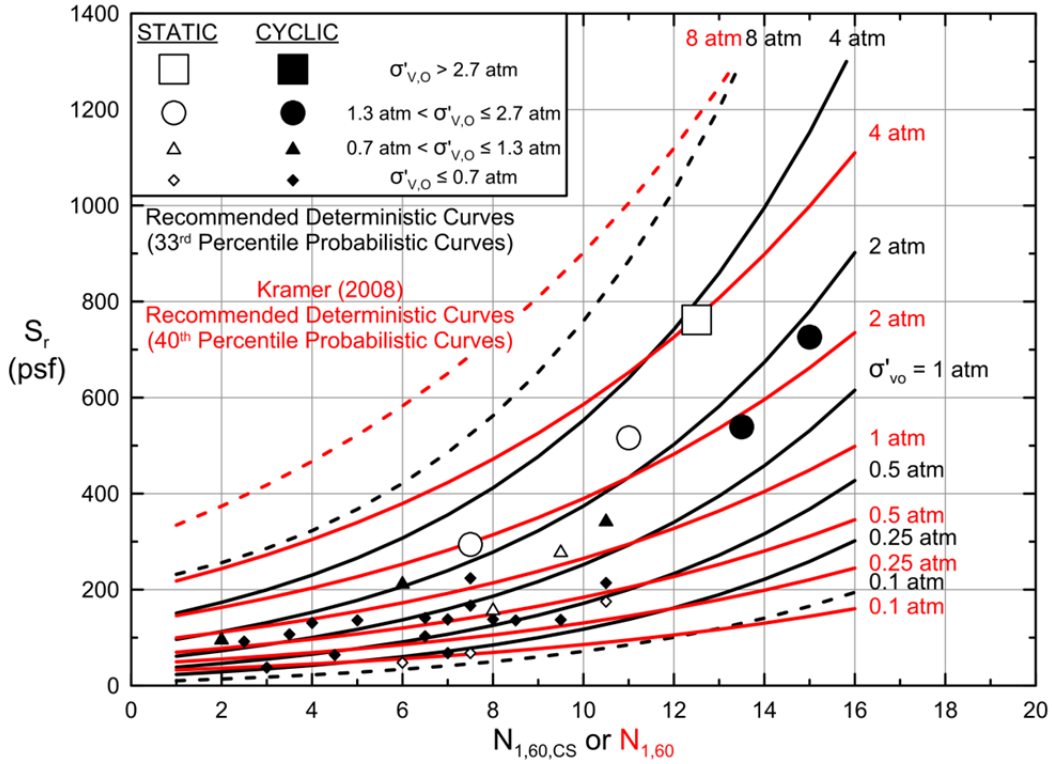

Figure 5.11: Comparison between the recommended deterministic relationship of these current studies from Figure 5.8(a) [33rd percentile; black lines] and the recommended deterministic relationship [40th percentile; red lines] of Kramer (2008).

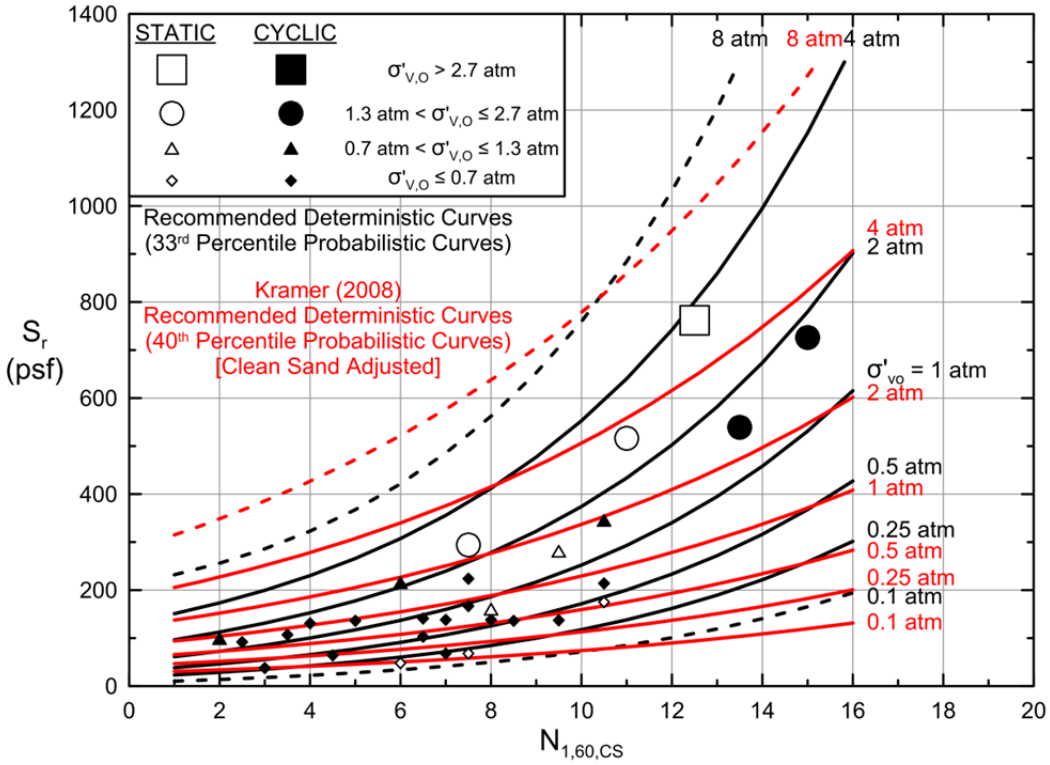

Figure 5.12: Comparison between the recommended deterministic relationship of these current studies from Figure 5.8(a) [33rd percentile; black lines] and the recommended deterministic relationship of Kramer (2008) [40th percentile; red lines, with approximate fines correction to clean sand basis].

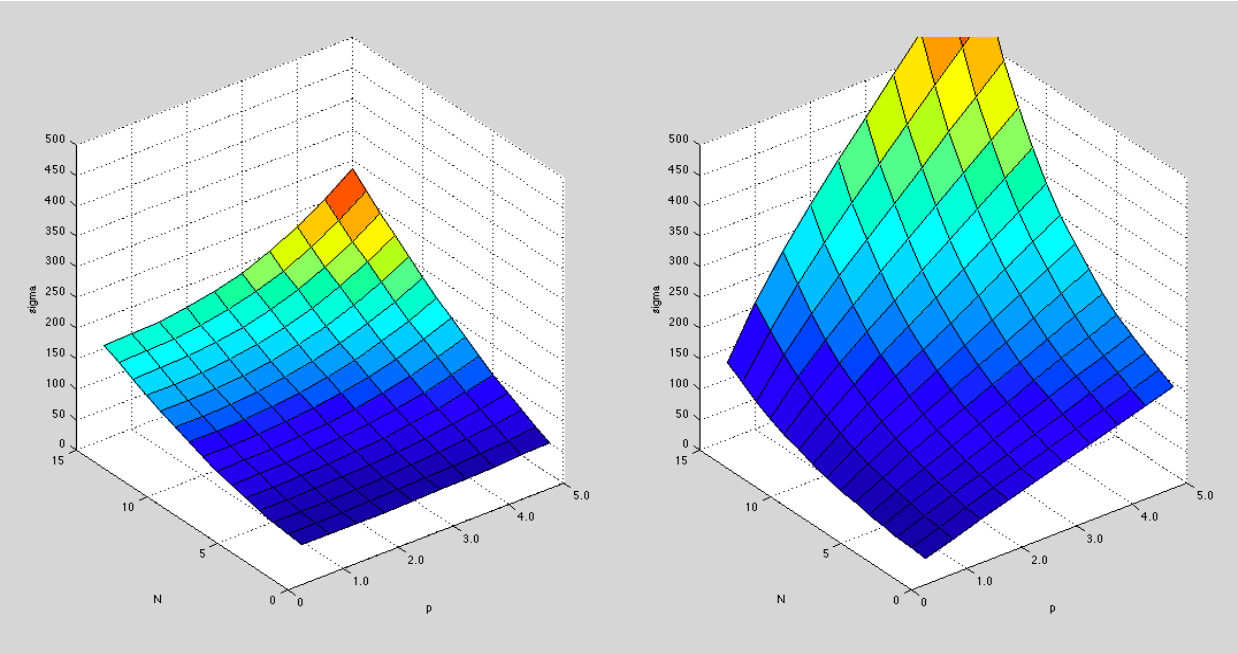

Figure 5.13: Surfaces showing standard deviation of S_r as a function of $N_{1,60,CS}$ and initial effective vertical stress from the probabilistic relationships developed (a) in these current studies, and (b) by Kramer (2008).

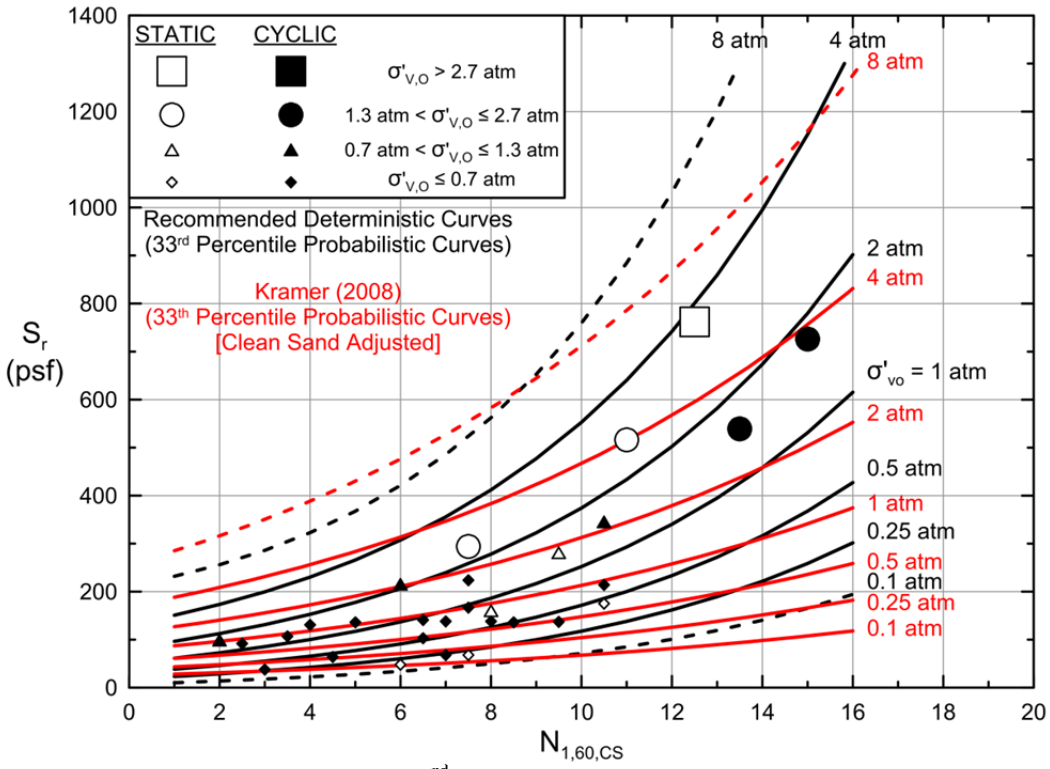

Figure 5.14: Comparison between 33rd percentile values of S_r from these current studies [black lines] and 33rd percentile values from Kramer (2008) [red lines, with approximate fines correction to clean sand basis].

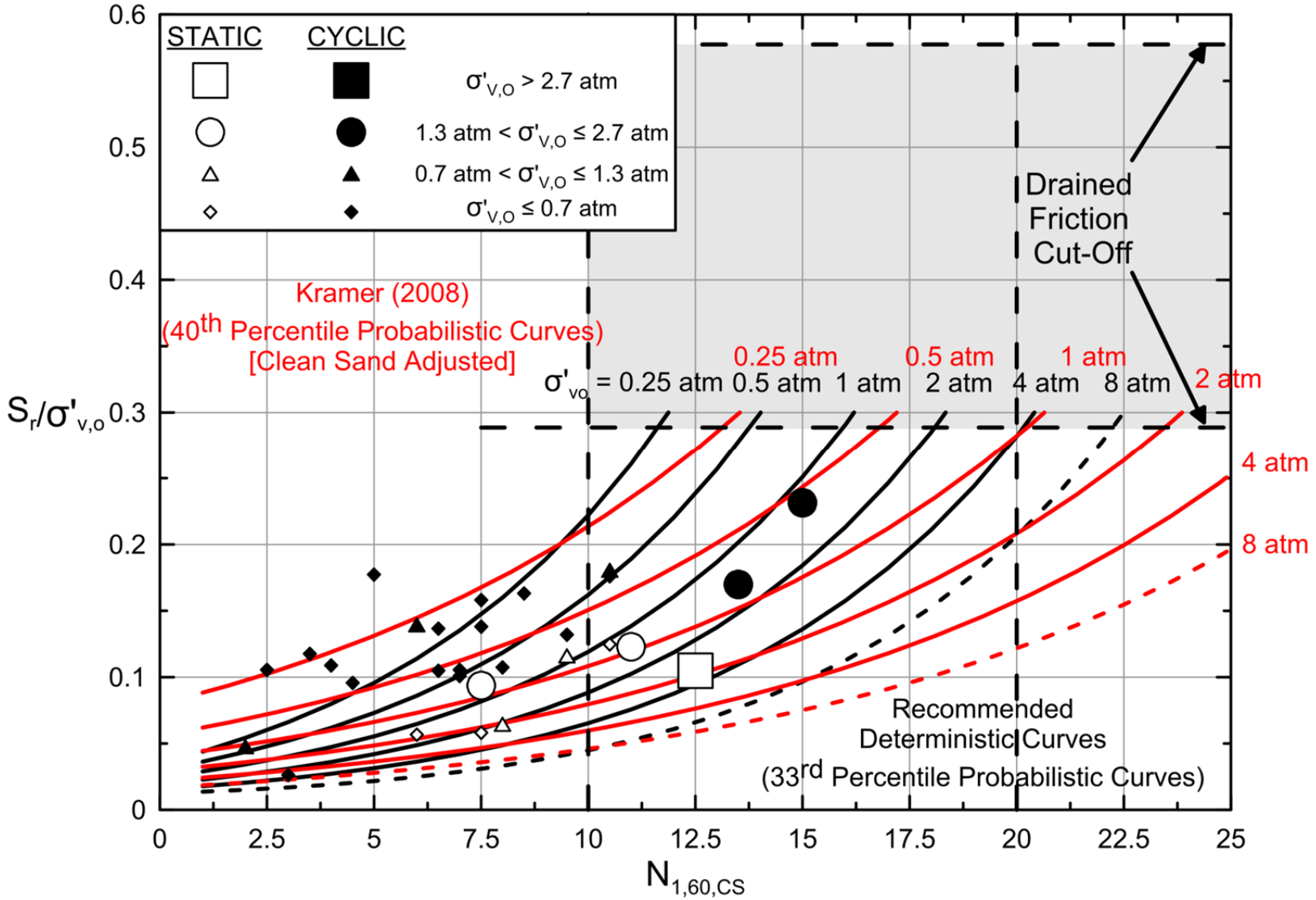

Figure 5.15: Comparison between the recommended deterministic relationships developed in these current studies [33rd percentile; black lines] and the recommended deterministic relationship of Kramer (2008) [40th percentile; red lines], extended to higher $N_{1,60,CS}$ values.

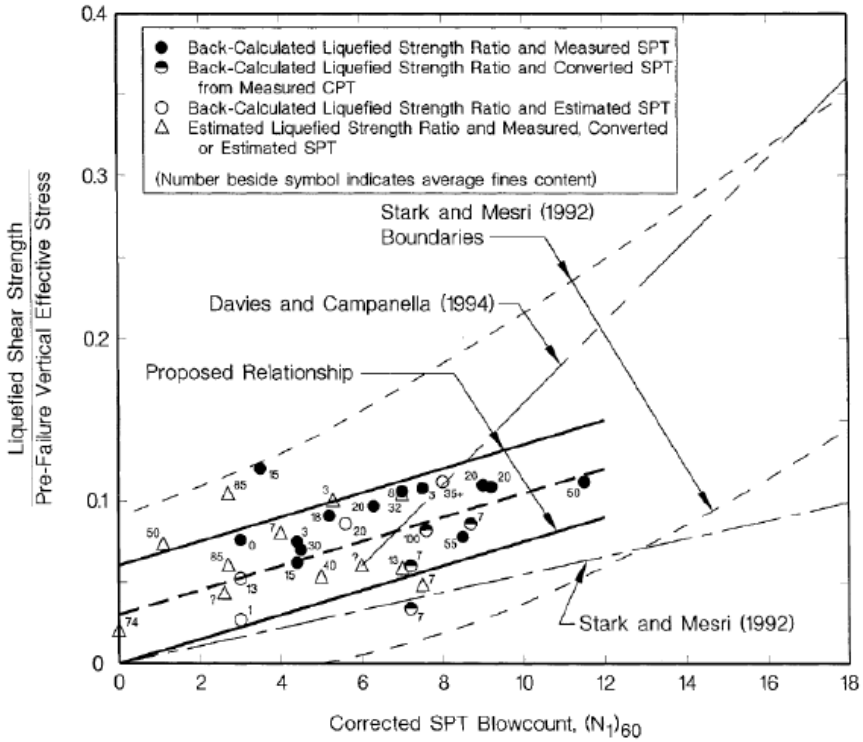

Figure 5.16: Recommended relationship between post-liquefaction strength ratio (S_r/P) and penetration resistance of Olson and Stark (2002).

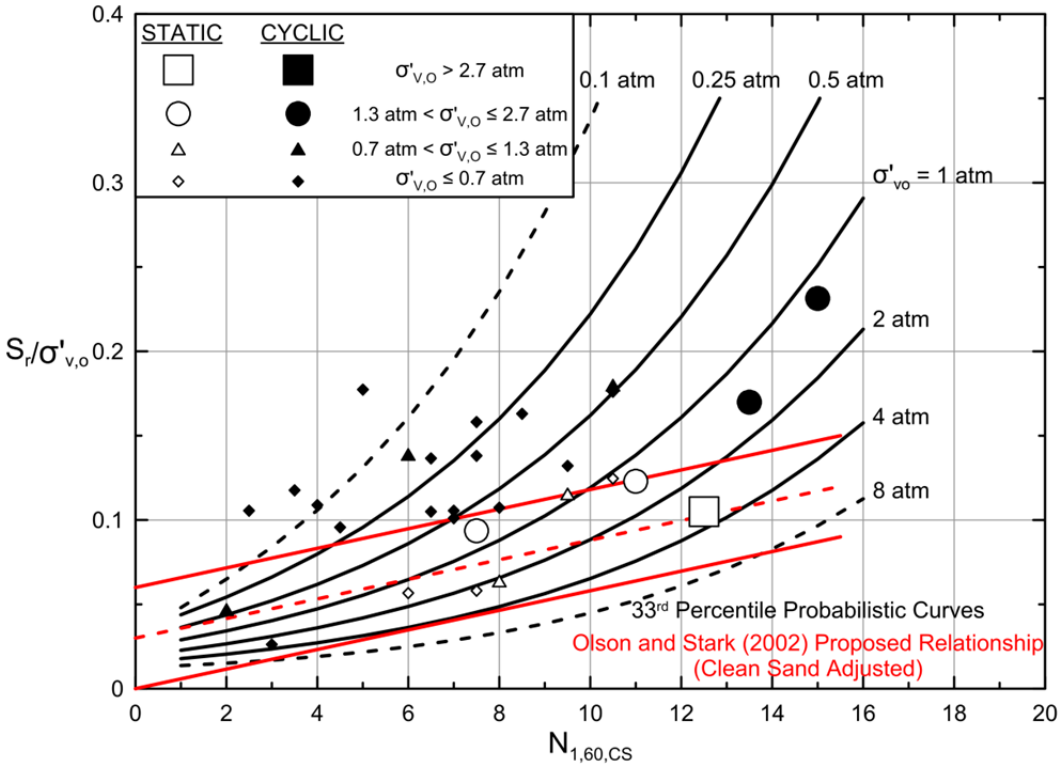

Figure 5.17: Comparison between the relationship of Olson and Stark (2002), and the recommended deterministic (33rd percentile) values of S_r based on these current studies.

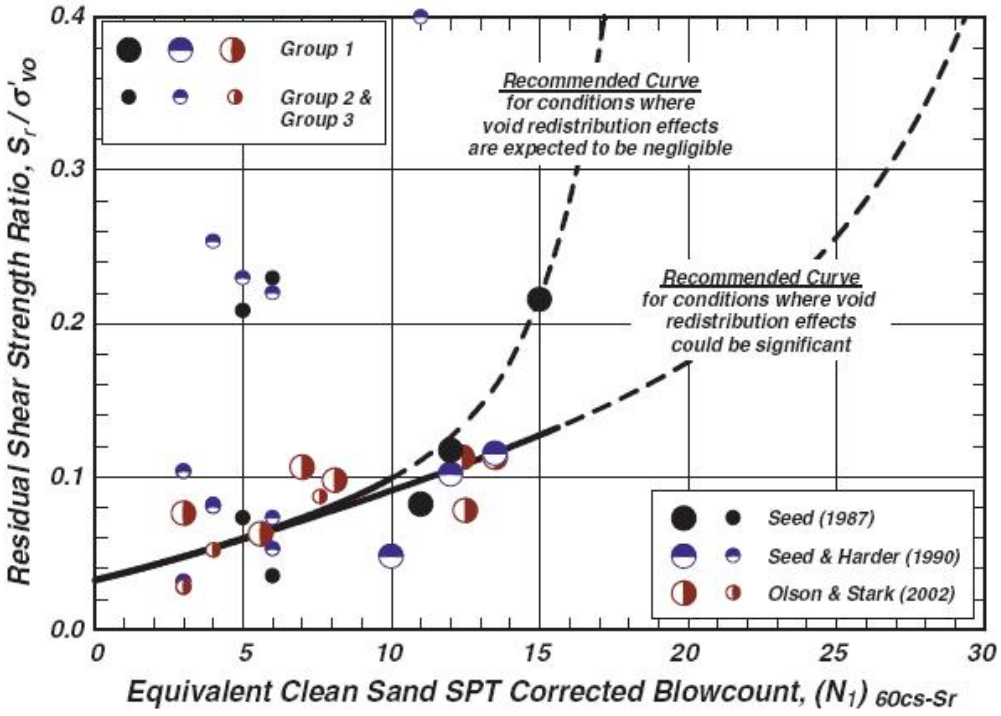

Figure 5.18: Recommended relationships between S_r/P and penetration resistance by Idriss and Boulanger (2008)

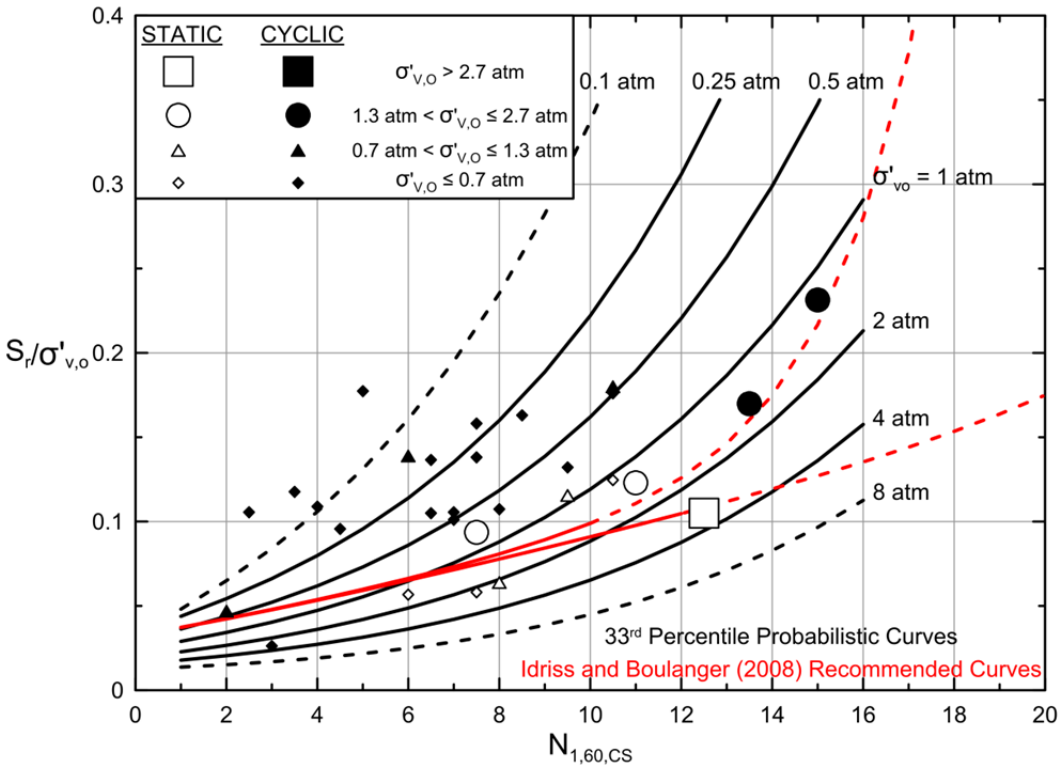

Figure 5.19: Comparison between the recommended relationships of Idriss and Boulanger (2008) from Figure 5.13 (red lines) with the recommended 33rd percentile relationship recommended in these current studies (black lines).

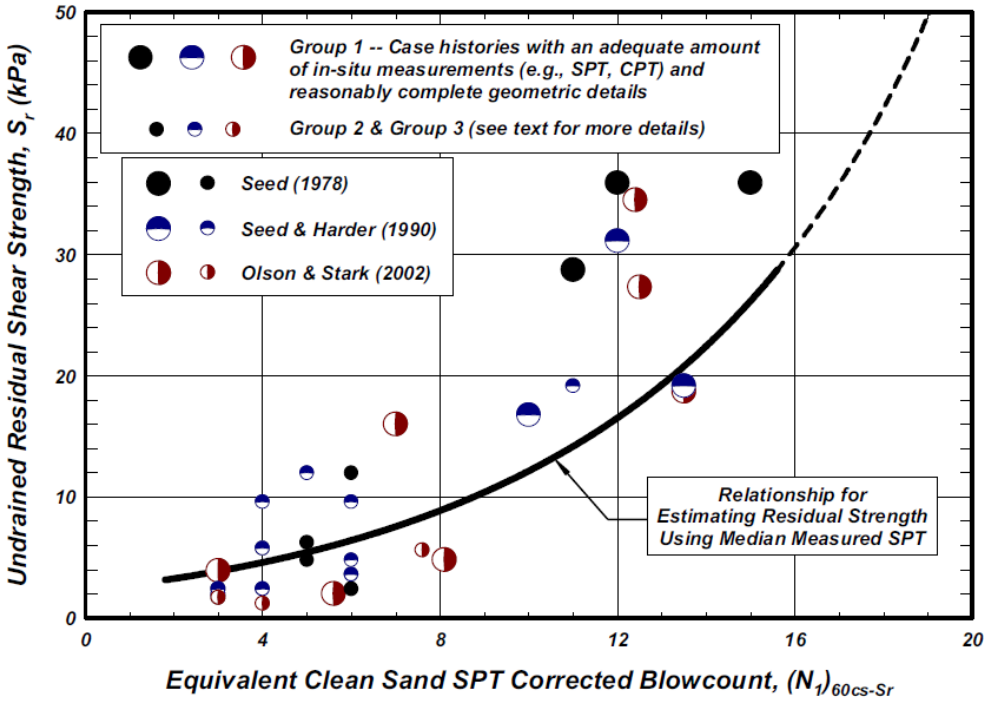

Figure 5.20: Recommended relationships between S_r and penetration resistance by Idriss and Boulanger (2008)

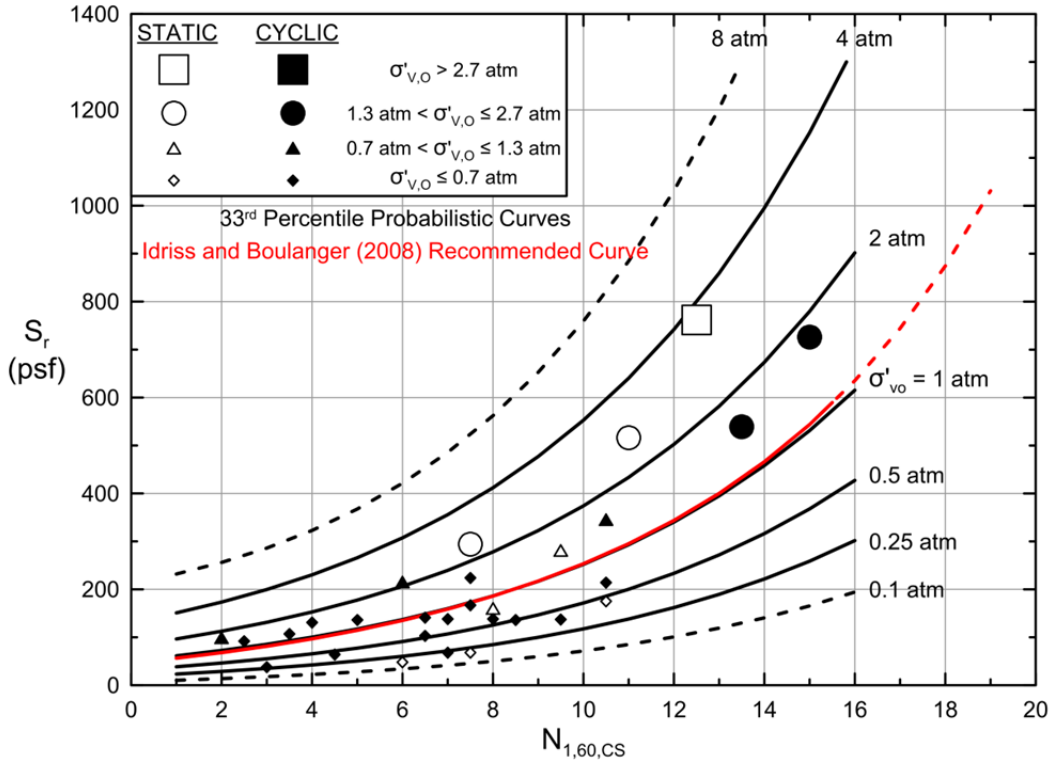

Figure 5.21: Comparison between the recommended relationship of Idriss and Boulanger (2008) from Figure 5.15 (red lines) with the recommended 33rd percentile relationship recommended in these current studies (black lines).

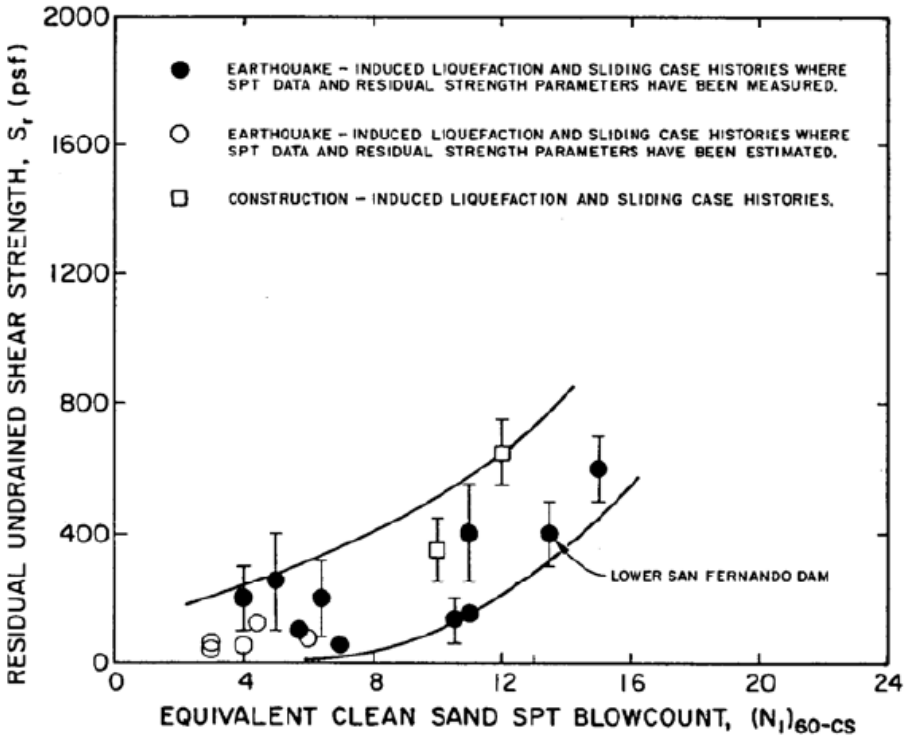

Figure 5.22: Recommended relationship between Sr and penetration resistance of Seed and Harder (1990).

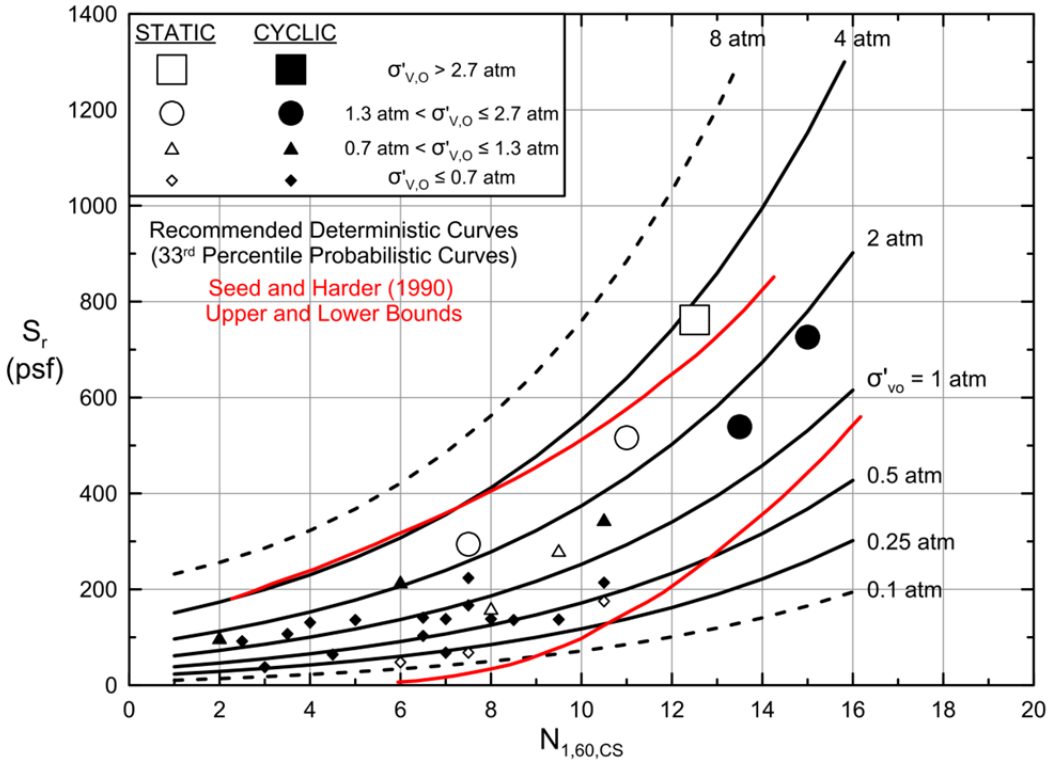

Figure 5.23: Comparison between the recommended relationship of Seed and Harder (1990) from Figure 5.17 (red lines) with the recommended 33rd percentile relationship recommended in these current studies (black lines).

Chapter Six

Summary and Conclusions

6.1 Summary and Findings

The issue of evaluation of in situ post-liquefaction strengths has grown rapidly in importance over the past three decades, as engineers have increasingly been called upon to provide more refined evaluations of projected seismic performance both for risk evaluation studies and for project design.

The topic of assessment of post-liquefaction strengths has sometimes been fraught with disagreement, and a number of different recommendations have been developed by different teams of experts and researchers over the past three decades.

These current studies began with a technical review of previous efforts. That proved to be a valuable exercise. Evaluation of previous work, and recommendations, with emphasis on strengths and drawbacks of prior efforts, led to some important insights. It turns out that a number of previous efforts had developed important lessons, and in some cases important pieces of the overall puzzle. They also served to provide ideas and to inspire elements of these current studies. And they provided lessons with regard to mistakes to avoid.

These current studies have focused on the development of empirical methods for evaluation of in situ post-liquefaction strengths, largely because of issues and challenges involved in application of laboratory-based testing approaches to evaluation of post-liquefaction strengths for full-scale field conditions.

A suite of full-scale liquefaction failure case histories were reviewed, vetted and selected for back-analyses. New methods were developed for performing these back-analyses, including methods that more accurately and reliably deal with momentum effects in liquefaction failures that experience large displacements. These new methods also appear to provide the first set of tools able to reasonably back-analyze large displacement slope failures that develop incrementally, on a slice by slice basis, retrogressing back towards the eventual back heel. And these new methods also provide increased ability to model changing conditions as slide movements progress from start to finish; which is important in back-analyses of many of the liquefaction failure case histories employed in these types of studies.

A suite of additional empirical relationships were developed specifically for cross-comparison of the results of back-analyses of large displacement liquefaction failures. These provided both a framework and a basis for cross-comparison of results of back-analyses of liquefaction failure case histories; both within this current study and with results from previous studies by others.

In the end, a suite of back-analysis results of unprecedented reliability were developed, based on (1) improved back-analysis procedures, (2) internal cross-checking within the framework of the new empirical relationships developed, and (3) external cross-checking against the results obtained by previous investigations, with an informed understanding of the strengths and drawbacks of the back-analysis methods and assumptions employed in those previous studies.

The resulting hard-earned back-analyzed field case history database was then used, in the context of probabilistic regressions that incorporated the best available evaluations of uncertainties, to perform probabilistic regressions by the maximum likelihood estimation method, in order to develop new predictive relationships for engineering evaluation of post-liquefaction strength as a function of both (1) corrected SPT penetration resistance, and (2) initial in situ effective vertical stress.

These new empirical relationships were then compared with previous relationships and recommendations. Here, again, with understanding of the strengths and drawbacks of the procedures by which the previous relationships were developed, and of the back-analyses that provided the parameters for those earlier efforts, a coherent overall pattern emerged and the juxtaposition of the different values of post-liquefaction strengths provided by different proposed relationships can now be better understood.

The new predictive relationships developed in these current studies agree well with the recent recommendations of Wang (2003) and Kramer (2008) who executed a similar overall effort, but with significant differences in approaches, and judgments, at essentially every step of the way. Some elements of their work are poorly documented, and thus difficult to check and verify. And there are a number of errors in their processing of a number of their "secondary" field case histories. These errors tend to bias their predictive relationships in a slightly conservative manner. But with appropriate allowance for this moderate conservative bias, the level of agreement between their findings with the results of these current studies is generally very good.

Similarly, the levels of agreement of the current studies with the recommendations of (1) Seed and Harder (1990), Olson and Stark (2002) and Idriss and Boulanger (2008) are also found to be reasonably good, but only over specific ranges of (1) initial in situ effective vertical stress, and (2) corrected SPT penetration resistance. In other ranges, these previous relationships can now be shown to be either conservative, or unconservative, and often to a significant degree. Moreover, the reasons for good agreement over specific ranges, and poorer agreement over other ranges, can now be understood.

The new predictive relationships for engineering evaluation of post-liquefaction strength are presented in a fully probabilistic form, and can be used for fully probabilistic risk studies and design of high-level projects. These are then "simplified" to develop deterministic recommendations that are likely to be more broadly applicable to more routine projects.

These new relationships offer potentially significant advantages over previously available recommendations and relationships. They are based on back-analyses, and regressions, which provide insight into the underlying forms of the relationships between post-liquefaction strengths and both (1) penetration resistance and (2) effective vertical stress, over the ranges of conditions

well-represented in the 30 full-scale field liquefaction case histories back-analyzed. Because they provide insight as to the underlying forms of these relationships, they provide a better basis for extrapolation to higher ranges of penetration resistance, and to higher ranges of effective stress, than do previous recommendations. The back-analyzed field case history database provides fair to good coverage for values of $N_{1,60,CS}$ up to approximately 15 blows per foot, and for representative effective overburden stresses of up to approximately 4 atmospheres. The range of principal engineering interest, however, is usually $N_{1,60,CS} \approx 10$ to 22 blows per foot as it is over that range that field behavior, and project performance, often transitions from unacceptable to acceptable. Similarly, for major earth and rockfill dams (and their foundations), ranges of effective overburden stress considerably larger than 4 atmospheres are often of critical importance.

In addition to the development of improved relationships for engineering evaluation of post-liquefactions strengths, the suite of new empirical relationships developed for use in cross-checking of back-analyses of liquefaction failure case histories will likely also have applications with regard to checking of forward engineering calculations and analyses of expected performance of actual engineering projects, including high-level analyses involving fully nonlinear finite element or finite difference analyses for critical and/or high risk projects involving soil liquefaction hazard.

Finally, it should be noted that the relationships developed and presented herein do not fully resolve all issues. As discussed in Section 5.6, the currently available suite of reasonably well characterized large displacement liquefaction failure case histories has limits with regard to the ranges of condition covered, and also with regard to the overall number of reliable case histories available. The 30 case histories back-analyzed in these current studies reflect failures that have occurred over slightly more than the past century (the earliest failure case history used in these current studies was the 1889 slope failure at Vietepolder, in Zeeland Province, the Netherlands). It must be assumed that suitable failures will continue to occur, further augmenting this failure case history database. But it is not possible simply to await further data. Accordingly, it is necessary to make best possible use of the data (and failure case histories) currently available.

It that regard, it is noted that the current suite of case histories include failures induced both by (1) monotonic loading, and (2) by cyclic loading. There are some potentially good arguments that can be made regarding the possibility that cyclic loading might result in greater amounts of void redistribution, and might thus produce lower post-liquefaction strengths than failures induced by monotonic loading; but the current failure case history data base does not provide good support for this.

Similarly, the back-analyses performed in these current studies, and in most previous studies, do not account for the effects of cyclic lurching as contributing to the overall liquefaction-induced displacements observed. A singular exception here is the Upper San Fernando Dam case history, but the treatment of cyclic lurching forces in back-analysis of this case in these current studies is deliberatively conservative given the uncertainties involved. As discussed in Section 5.5, it does not appear likely that cyclic lurching forces would contribute significantly to the displacements observed in most of the liquefaction failure case histories back-analyzed and then used in these current studies to develop the predictive relationships that result. Two main reasons for this are: (1) nine of the thirty case histories back-analyzed in these current studies were

statically (monotonically) triggered failures, and three more were cyclically-induced, but with essentially no significant cyclic lurching forces to drive large displacements, and (2) few of the remaining eighteen cyclically-induced liquefaction failures had strong enough cyclic lurching forces of sufficient duration (enough strong cycles) as to contribute significantly to the observed large displacements. Nonetheless, it is possible that the back-analyses of some of the liquefaction failure case histories may have conservatively underestimated, to some extent, the values of post-liquefaction for a limited number of the case histories due to inability to accurately assess cyclic lurching effects for cases in which statically driven displacements are very large.

A second source of potential conservatism, also discussed in Section 5.5, is the likelihood that the liquefaction-induced failure case histories back-analyzed in these current studies may represent some degree of "self-selection" as cases in which failures occurred, and these may represent some degree of conservatism with regard to enveloping of only "failure" case histories while not also capturing and considering near-failure situations in which similar conditions were present but failures did not occur. This is an issue that cannot be conclusively resolved at present, and the corollary potential for some undetermined degree of conservative bias in forward estimation of expected post-liquefaction strengths must simply be accepted for now.

For these two sets of reasons, it appears likely that the post-liquefaction strength assessment relationships developed and presented herein would likely be potentially biased in a somewhat conservative manner. Such bias appears unavoidable at this juncture, given the available data, and it is noted that (1) some degree of conservatism is to be preferred rather than an expected unconservative bias, and (2) the new relationships presented herein appear to provide for somewhat higher values of post-liquefaction strength (S_r) than do previously available relationships over most ranges of (a) penetration resistance, and (b) initial effective stress.

Overall, the relationships developed and presented herein appear to provide a flexibly adaptable set of tools suitable for engineering evaluation of post-liquefaction strengths on either a fully probabilistic or a more simplified deterministic basis. The underlying forms of the relationships developed are intended to optimize their extrapolation to ranges of higher penetration resistances, and higher effective stress ranges, than are currently represented in the available case history database. Given the lack of current alternatives, it must be expected that these relationships will be extrapolated for use in those ranges.

REFERENCES

Alarcon-Guzman, A., Leonards, G.A., and Chameau, J.L. (1988). “Undrained monotonic and cyclic strength of sands.” Journal of Geotechnical Engineering, ASCE, 114(10), 1089-1109.

Andresen, A. and Bjerrum, L. (1968). “Slides in subaqueous slopes in loose sand and silt.” Norwegian Geotechnical Institute Publication No. 81, 1-9.

Arulanandan, K., Seed, H.B., Yogachandran, C., Muraleetharan, K.K., Seed, R.B., and Kabilamany, K. (1993). “Centrifuge study on volume changes and dynamic stability of earth dams.” Journal of Geotechnical Engineering, ASCE, 119(11), 1717-1731.

Baziar, M.H. and Dobry, R. (1995). “Residual strength and large-deformation potential of loose silty sands.” Journal of Geotechnical Engineering, ASCE, 121(12), 896-906.

Been, K., Conlin, B. H., Crooks, J. H. A., Fitzpatrick, S. W., Jefferies, M. G., Rogers, B. T., & Shinde, S. (1987). “Back analysis of the Nerlerk berm liquefaction slides: Discussion.” Canadian Geotechnical Journal, 24(1), 170-179.

Been, K., Jefferies, M.G., and Hachey, J. (1991). “The critical state of sands.” Geotechnique, Volume 41, Number 3, pp. 365-381.

Bennett, M.J. (1989). “Liquefaction analysis of the 1971 ground failure at the San Fernando Valley Juvenile Hall, California.” Bulletin of Association of Engineering Geologists, 26(2), 209-226.

Bjerrum, L. (1971). “Subaqueous slope failures in Norwegian fjords.” Publication 88, Norwegian Geotechnical Institute, Oslo.

Boulanger, R. W., and Truman, S. P. (1996). "Void redistribution in sand under post-earthquake loading." Canadian Geotechnical Journal, 33, 829-834

Bray, J.D. and Rathje, E.M. (1998). “Earthquake-induced displacements of solid-waste landfills.” Journal of Geotechnical and Geoenvironmental Engineering, ASCE 124(3):242-253.

Bray, J. D., and Travasarou, T. (2007). “Simplified procedure for estimating earthquake-induced deviatoric slope displacements.” Journal of Geotechnical and Geoenvironmental Engineering, ASCE, 133(4), 381-392.

Bryant, S.M., Duncan, J.M., and Seed, H.B. (1983). “Application of tailings dam flow analyses to field conditions.” Report No. UCB/GT/83-03, Dept. of Civil Engineering, Univ. of California, Berkeley, CA.

Butler, J.J. (1997). “Analysis of Energy Measurement Methods of SPT Driving Systems”, M.S. Thesis in Civil Engineering, Utah State University, Logan, UT.

California Dept. of Water Resources [CDWR] - (1975) “Final Geologic Report on Perris Dam and Lake Part I Foundation Conditions, Grouting, and Instrumentation” Project Geology Report C-94, October 1975

California Dept. of Water Resources [CDWR] - (1998) Perris Dam Foundation Study, Results of Phase I Geologic Investigations, Project Geology Section Report No. 58-11-15, May 1998

Casagrande, A. (1940). “Characteristics of cohesionless soils affecting the stability of slopes and earth fills.” Contributions to Soil Mechanics, 1925-1940, Boston Society of Civil Engineers, October, (Originally published in the Journal of the Boston Society of Civil Engineers, January, 1936), 257-276.

Casagrande, A. (1965). “Second Terzaghi Lecture: the role of "calculated risk" in earthwork and foundation engineering.” Journal of the Soil Mechanics and Foundations Division, ASCE, 91(SM4), 1-40.

Casagrande, A. (1976). “Liquefaction and cyclic deformation of sands: a critical review.” Harvard Soil Mechanics Series No. 88, Harvard University Cambridge, MA.

Castro, G. (1969). “Liquefaction of sands.” Ph.D. Thesis, Harvard University, Cambridge, Massachusetts.

Castro, G. (1995). “Empirical methods in liquefaction evaluation.” Proc., First Annual Leonardo Zeevaert International Conference, Vol. 1, 1-41.

Castro, G. and Poulos, S.J. (1977). “Factors affecting liquefaction and cyclic mobility.” Journal of Geotechnical Engineering Division, ASCE, 103(GT6), 501-516.

Castro, G., Poulos, S.J., and Leathers, F.D. (1985). “Re-examination of slide of Lower San Fernando Dam.” Journal of Geotechnical Engineering, ASCE, 111(9), 1093-1106.

Castro, G., Keller, T.O., and Boynton, S.S. (1989). “Re-evaluation of the Lower San Fernando Dam: Report 1, an investigation of the February 9, 1971 slide.” U.S. Army Corps of Engineers Contract Report GL-89-2, Vols. 1 and 2, U.S. Army Corps of Engineers Waterways Experiment Station, Vicksburg, Mississippi.

Castro, G., Seed, R.B., Keller, T.O., and Seed, H.B. (1992). “Steady-state strength analysis of Lower San Fernando Dam slide.” Journal of Geotechnical Engineering, ASCE, 118(3), 406-427.

Cetin, K. O. (2000). "Reliability-Based Assessment of Seismic Soil Liquefaction Initiation Hazard." Dissertation in partial fulfillment for the degree of doctor of philosophy, University of California, Berkeley.

Cetin, K. O., Seed, R. B., Der Kiureghian, A., Tokimatsu, K., Harder Jr, L. F., Kayen, R. E., & Moss, R. E. (2004). Standard penetration test-based probabilistic and deterministic assessment of seismic soil liquefaction potential. Journal of Geotechnical and Geoenvironmental Engineering, 130(12), 1314-1340.

Cleary, A.J. (1914). "The Calaveras dam, California, the highest earth dam." Engineering News, 72(14), 692-695.

Davies, M.P., Dawson, B.D., and Chin, B.G. (1998). "Static liquefaction slump mine tailings – a case history." Proceedings 51st Canadian Geotechnical Conference, Vol. 1,123-131.

Davis, A.P. Jr., Poulos, S.J., and Castro, G. (1988). "Strengths backfigured from liquefaction case histories." Proc., 2nd Int. Conf. on Case Histories in Geotechnical Engineering, June 1- 5, St. Louis, MO, 1693-1701.

De Alba, P.A., Seed, H.B., Retamal, E., and Seed, R.B. (1987). "Residual strength of sand from dam failures in the Chilean earthquake of March 3, 1985." Earthquake Engineering Research Center Report No. UCB/EERC-87-11, University of California, Berkeley, CA.

De Alba, P.A., Seed, H.B., Retamal, E., and Seed, R.B. (1988). "Analyses of dam failures in 1985 Chilean earthquake." Journal of Geotechnical Engineering, ASCE, 114(12), 1414-1434.

Deger, T. T. (2014). "Overburden stress normalization and rod length corrections for the standard penetration test (SPT)." Doctoral Dissertation, University of California.

Dennis, N.D. (1988). "Influence of specimen preparation techniques and testing procedures on undrained steady state shear strength." Advanced Triaxial Testing of Soil and Rock, ASTM STP 977, R.T. Donaghe, R.C. Chaney, and M.L. Silver, eds., American Society for Testing and Materials, Philadelphia, 642-654.

Dobry, R. and Alvarez, L. (1967). "Seismic failures of Chilean tailings dams." Journal of the Soil Mechanics and Foundations Division, ASCE, 93(SM6), 237-260.

Duke, C. M., Johnson, K. E., Larson, L.E., and Egman, D.C. (1972). "Effects of Site Classification and Distance on Instrumental Indices in the San Fernando Earthquake." Report, UCLA Eng. 7247, School of Engineering, UCLA.

Ekström, A., & Olofsson, T. (1985). "Water and frost-stability risks for embankments of fine-grained soils." In From Proceedings of the Symposium on Failures in Earthworks, organized by the Institution of Civil Engineers, held in London, March 6-7, 1985.

Engineering News Record (1925). "What happened to municipal utilities at Santa Barbara." Engineering News Record, 95(4), 146-149.

Faris, A. T. (2004). "Probabilistic models for engineering assessment of liquefaction-induced lateral spreading displacements." Doctoral dissertation, University of California, Berkeley.

Fear, C.E. and Robertson, P.K. (1995). “Estimating the undrained strength of sand: a theoretical framework.” Canadian Geotechnical Journal, 32(4), 859-870.

Fiegel, G.F. and Kutter, B.L. (1994). “Liquefaction induced lateral spreading of mildly sloping ground.” Journal of Geotechnical Engineering, ASCE, 120(12), 2236-2243.

Gilboy, G. (1942). Discussion of “Fort Peck slide.” by T.A. Middlebrooks, Transactions of the American Society of Civil Engineers, 107, 723-764.

Gillette, D.R. (2010). “On the use of empirical correlations for estimating the residual undrained shear strength of liquefied soil in dam foundations.” Fifth International Conference on Recent Advances in Geotechnical Earthquake Engineering and Soil Dynamics, San Diego, California, May.

Gu, W.H., Morgenstern, N.R., and Robertson, P.K. (1993). “Progressive failure of Lower San Fernando Dam.” Journal of Geotechnical Engineering, ASCE, 119(2), 333-349.

GZA GeoEnvironmental, Inc. (1991). “Wachusett Dam – Clinton, Massachusetts – North Dike Stability.” Stage I Report, Volume II, Report to the Commonwealth of Massachusetts, Metropolitan District Commission, Boston, Massachusetts.

Haley & Aldrich, Inc. (1984a). “Report on Phase II Investigation, Wachusett Reservoir Dam, Clinton, Massachusetts.” Prepared for the Commonwealth of Massachusetts, Metropolitan District Commission, Boston, Massachusetts, February.

Haley & Aldrich, Inc. (1984b). “Report on Phase II Investigation, Wachusett Reservoir, North Dike, South Dike, Clinton, Massachusetts.” Prepared for the Commonwealth of Massachusetts, Metropolitan District Commission, Boston, Massachusetts, February.

Harder, L. F. Jr. (1988). "Use of Penetration Tests to Determine the Cyclic Loading Resistance of Gravelly Soils During Earthquake Shaking." Ph.D. Thesis, University of California, Berkeley.

Hazen, A. (1918). “A study of the slip in the Calaveras Dam.” Engineering News-Record, 81(26), 1158-1164.

Hazen, A. (1920). “Hydraulic-fill dams.” Transactions of the American Society of Civil Engineers, Paper No. 1458, 1713-1821 (including discussions).

Hazen, A. and Metcalf, L. (1918). “Middle section of upstream side of Calaveras dam slips into reservoir.” Engineering News-Record, 80(14), 679-681.

Holtz, W.G. and Gibbs, H.J. (1979). Discussion of “SPT and relative density in coarse sand.” Journal of the Geotechnical Engineering Division, ASCE, 105(GT3), 439-441.

Hryciw, R.D., Vitton, S., and Thomann, T.G. (1990). “Liquefaction and flow failure during seismic exploration.” Journal of Geotechnical Engineering, ASCE, 116(12), 1881-1899.

Hynes-Griffin, M.E., Franklin, A.G. (1984). “Rationalizing the seismic coefficient method.” Misc. Paper No. GL-84-13, U.S. Army Engr. WES, Vicksburg, MS

Idriss, I. M. (1998). “Evaluation of liquefaction potential, consequences and mitigation—An update.” Presentation Notes, Vancouver Geotechnical Society Meeting, Vancouver, Canada.

Idriss, I.M. and Boulanger, R.W. (2008). “Soil liquefaction during earthquakes.” EERI Monograph 12, Earthquake Engineering Research Institute, Oakland, California, 262 p.

Inada (1982). “Methods of in situ soil investigations.” Japanese Society of Soil Mechanics and Foundation Engineering, 217 p.

Ishihara, K. (1984). “Post-earthquake failure of a tailings dam due to liquefaction of the pond deposit.” Proc., Inter. Conf. on Case Histories in Geotechnical Engineering, Rolla, Missouri, May 6-11, Vol. 3, 1129-1143.

Ishihara, K. (1985). “Stability of natural deposits during earthquakes.” Proc., 11th International Conference on Soil Mechanics and Foundation Engineering, San Francisco, CA, Vol. 1, 321-376.

Ishihara, K. (1993). “Liquefaction and flow failure during earthquakes.” Geotechnique, 43(3), 351-415.

Ishihara, K., Yasuda, S., and Yoshida, Y. (1990). “Liquefaction-induced flow failure of embankments and residual strength of silty sands.” Soils and Foundations, 30(3), 69-80.

Ishihara, K., Okusa, S., Oyagi, N., and Ischuk, A. (1990). “Liquefaction-induced flow slide in the collapsible loess deposit in Soviet Tajik.” Soils and Foundations, 30(4), 73-89.

Iverson, R.M. and LaHusen, R.G. (1993). “Friction in debris flows: inferences from largescale flume experiments.” Proc., Hydraulic Engineering ’93, 1993 Conf. of the Hydraulics Division of the American Society of Civil Engineers, Vol. 2, 1604-1609.

Iverson, R.M., Reid, M.E., and LaHusen, R.G. (1997). “Debris-flow mobilization from landslides.” Annual Review of Earth Planetary Science, 25, 85-138.

Jefferies, M.G., Been, K., and Hachey, J.E. (1990). “Influence of scale on the constitutive behavior of sand.” Proceedings of the 43rd Canadian Geotechnical Engineering Conference, Laval University, Quebec, Vol. 1, p. 263-273.

Jefferies, M., & Been, K. (2006). “Soil liquefaction: a critical state approach.” CRC Press.

Jibson, R.W., Harp E.L., and Michael, J.A. (1998). “A method for producing digital probabilistic seismic landslide hazard maps: an example from the Los Angeles, California, Area.” USGS Open-File Report, 98–113.

Jitno, H. (1995). “Liquefaction induced deformation of earth structures.” Ph.D. Thesis, Civil Engineering Dept., Univ. of British Columbia, Vancouver, B.C.

Jitno, H. and Byrne, P.M. (1995). “Predicted and observed liquefaction response of Mochikoshi tailings dam.” Proc., 1st International Conf. on Earthquake Geotechnical Engineering, Nov. 14-16, Tokyo, Japan, Vol. 2, 1085-1090.

Kawasumi, H. (1968). “General report on the Niigata Earthquake of 1964.” Tokyo Electrical Engineering College Press, Tokyo, Japan.

Kokusho, T. (1999). “Water film in liquefied sand and its effect on lateral spread.” Journal of Geotechnical and Geoenvironmental Engineering, 125(10), 817-826.

Konrad, J.M. (1991). “The Nerlerk berm case history: some consideration for the design of hydraulic sand fills.” Canadian Geotechnical Journal, 28, 601-612.

Konrad, J.M. and Watts, B.D. (1995). “Undrained shear strength for liquefaction flow failure analysis.” Canadian Geotechnical Journal, 32, 783-794.

Koppejan, A.W., van Wamelen, B.M., and Weinberg, L.J.H. (1948). “Coastal flow slides in the Dutch province of Zeeland.” Proc., 2nd International Conf. Of Soil Mechanics and Foundation Engineering, Rotterdam, Netherlands, June 21-30, 89-96.

Kramer, S.L. (1996). Geotechnical Earthquake Engineering. Prentice Hall, New Jersey, 653 p.

Kramer, S. L. (2008). Evaluation of liquefaction hazards in Washington State (No. WA-RD 668.1). Washington State Department of Transportation, Office of Research and Library Services.

Kramer, S.L. (2015). Personal communication, August 7, 2015.

Kramer, S.L. and Wang, C.H. (2015). “Empirical Model for Estimation of the Residual Strength of Liquefied Soil.” Journal of Geotechnical and Geoenvironmental Engineering, ASCE, 04015038(15).

Kulasingam, R., Malvick, E. J., Boulanger, R. W., and Kutter, B. L. (2004). "Strength loss and localization at silt interlayers in slopes of liquefied sand." Journal of Geotechnical and Geoenvironmental Engineering, ASCE, 130(11), 1192-1202.

Kulhawy, F.H. and Mayne, P.W. (1990). “Manual on estimating soil properties for foundation design.” Electric Power Research Institute EL-6800, Project 1493-6, August, 400 pp.

Kulhawy, F.H. and Mayne, P.W. (1991). “Relative density, SPT, and CPT interrelationships.” 1st International Symposium on Calibration Chamber Testing, June 28-29, Potsdam, New York, 197-211.

Lade, P.V. (1993). “Initiation of static instability in the submarine Nerlerk berm.” Canadian Geotechnical Journal, 30, 895-904.

Lee, K.L., Seed, H.B., Idriss, I.M., and Makdisi, F.I. (1975). “Properties of soil in the San Fernando hydraulic fill dams.” Journal of the Geotechnical Engineering Division, ASCE, 101(GT8), 801-821.

Lewis, M.R., Arango, I., McHood, M.D. (2009). “Site characterization philosophy and liquefaction evaluation of aged sands.” Bechtel Technology Journal, Bechtel Corporation, Vol. 2, No. 1.

Liao, S.C., and Whitman, R.V. (1986). “Overburden correction factors for SPT in sand.” Journal of Geotechnical Engineering, ASCE, 112(3), 373-377.

Ligtenberg-Mak, C.E., Krajicek, P.V.F.S., and Kuiter, C. (1990). “Geological study of flow slide sensitive sediments.” Proc., 6th International Congress, International Association of Engineering Geology, Amsterdam, Vol. 1, 691-695.

Liu, H., & Qiao, T. (1984). “Liquefaction potential of saturated sand deposits underlying foundation of structure.” In Proceedings of the 8th World Conference on Earthquake Engineering, San Francisco, Calif., 21-28.

Lucia, P.C. (1981). “Review of experiences with flow failures of tailings dams and waste impoundments.” Ph.D. Thesis, University of California, Berkeley, Calif.

Makdisi, F. I., and Seed, H. B. (1978). “Simplified procedure for estimating dam and embankment earthquake-induced deformations.” Journal of the Geotechnical Engineering Division, 104(7), 849-867.

Malvick, E. J., Kutter, B. .L., Boulanger, R. W., & Kulasingam, R. (2006). “Shear localization due to liquefaction-induced void redistribution in a layered infinite slope.” Journal of Geotechnical and Geoenvironmental Engineering, 132(10), 1293–1303.

Marcuson, W.F., III. (1979). “Visit to Japan to observe damage which occurred during the Near Izu Oshima earthquakes January 14 and 15, 1978.” Miscellaneous Paper GL-79-20, U.S. Army Corps of Engineers Waterways Experiment Station, Vicksburg, MS.

Marcuson, W.F., III, and Krinitzsky, E.L. (1976). “Dynamic analysis of Fort Peck dam.” Technical Report S-76-1, U.S. Army Engineer Waterways Experiment Station, Vicksburg, MS, March.

Marcuson, W.F., III, Ballard, R.F., Jr., and Cooper, S.S. (1978). “Comparison of penetration resistance values to in situ shear wave velocities.” Proc., 2nd International Conf. on Microzonation for Safer Construction – Research and Application, San Francisco, CA Nov., 26 – Dec. 1, Vol. 2, 1013-1023.

Marcuson, W.F., III, Ballard, R.F., Jr., and Ledbetter, R.H. (1979). “Liquefaction failure of tailings dams resulting from the Near Izu Oshima earthquake, 14 and 15 January, 1978.” Proc. 6th Pan-American Conf. on Soil Mechanics and Foundation Engineering, Lima Peru, Vol. 2, 69-80.

McRoberts, E.C. and Sladen, J.A. (1992). “Observations on static and cyclic sandliquefaction methodologies.” Canadian Geotechnical Journal, 29, 650-665.

Mesri, G., Feng, T.W., and Benak, J.M. (1990). “Postdensification penetration resistance of clean sands.” Journal of Geotechnical Engineering, ASCE, 116(7), 1095-1115.

Meyerhof, G.G. (1957). “Discussion on sand density by spoon penetration.” Proc., 4th Intl. Conf. on Soil Mechanics and Foundation Engineering, Vol. 3, 110.

Meyerhof, G.G. (1957). Discussion of “Research on determining the density of sands by spoon penetration testing.” by H.J. Gibbs and W.G. Holtz, Proc., International Conf. on Soil Mechanics and Foundation Engineering, Vol. 3, 110.

Meyerhof, G.G. (1971). “The mechanism of flow slides in cohesive soils.” Geotechnique, 1, 41-49.

Middlebrooks, T.A. (1942). “Fort Peck slide.” Transactions of the American Society of Civil Engineers, 107, 723-764.

Mishima, S. and Kimura, H. (1970). “Characteristics of landslides and embankment failures during the Tokachioki earthquake.” Soils and Foundations, 10(2), 39-51.

Mitchell, D.E. (1984). “Liquefaction slides in hydraulically placed sands.” Proc., 4th International Symposium on Landslides, Toronto, Ontario, Vol. 1, 141-146.

Mittal, H.K. and Hardy, R.M. (1977). “Geotechnical aspects of a tar sand tailings dyke.” Proc., Conference on Geotechnical Practice for Disposal of Solid Waste Materials, ASCE Specialty Conference of the Geotechnical Engineering Division, Vol. 1, 327-347.

Miura, K., Yoshida, N., and Wakamatsu, K. (1995). “Damage to fill embankment during the 1993 Kushiro-oki earthquake.” Proc., 1st International Conf. on Earthquake Geotechnical Engineering, Nov. 14-16, Tokyo, Japan, Vol. 2, 1057-1062.

Miura, K., Yoshida, N., Nishimura, M., and Wakamatsu, K. (1998). “Stability analysis of the fill embankment damaged by recent two major earthquakes in Hokkaido, Japan.” Proc., 1998 Geotechnical Earthquake Engineering and Soil Dynamics Specialty Conference, ASCE Geo-Institute Geotechnical Special Publication No. 75, Vol. 2, August 3-6, Seattle, Washington, 926-937.

Mori, S. (1993). “Reconnaissance report on the liquefaction aspects of the Kushiro-oki earthquake, January 15, 1993.” Proc., 28th Japan National Conf. on Soil Mechanics and Foundation Engineering, 1091-1094.

Morrill, B.J. (1972). “Seismoscope Results – San Fernando Earthquake of 9 February 1971.” Chapter 3 of California Institute of Technology Report EERL, 72-02, 72-124.
Moss, R. E. S. (2009). “Reduced Uncertainty of Ground Motion Prediction Equations through Bayesian Variance Analysis.” PEER Report No. 2009/105, November.

Moss, R. E. S. (2011). "Reduced Sigma of Ground Motion Prediction Equations through Uncertainty Propagation.” Bulletin of Seismological Society of America, 101(1).

National Research Council (1985). “Liquefaction of soils during earthquakes.” Report No. CETS-EE-001, Committee on Earthquake Engineering, National Academy Press, Washington, D.C.

Newmark, N. (1965). “Effects of earthquakes on dams and embankments.” Geotechnique, 15(2), 139-160.

Norris, G., Siddharthan, R., Zafir, Z., and Madhu, R. (1997). “Liquefaction and residual strength of sands from drained triaxial tests.” Journal of Geotechnical and Geoenvironmental Engineering, ASCE, 123(3), 220-228.

Nunn, H. (1925). “Municipal problems of Santa Barbara.” Bulletin, Seismological Society of America, 15(4), 308-319.

Ohya, S., Iwasaki, T., and Wakamatsu, M. (1985). “Comparative study of various penetration tests in ground that underwent liquefaction during the 1983 Nihon-Kai-Chubu and 1964 Niigata earthquakes.” Proc., Workshop on In-Situ Testing Methods for Evaluation of Soil Liquefaction Susceptibility, San Francisco, California, Vol. 1, 56-88.

Okusa, S. and Anma, S. (1980). “Slope failures and tailings dam damage in the 1978 Izu-Ohshima-Kinkai earthquake.” Engineering Geology, 16, 195-224.

Okusa, S., Anma, S., and Maikuma, H. (1980). “Liquefaction of mine tailings in the 1978 Izu-Ohshima-Kinkai earthquake, central Japan.” Proc., 7th World Conf. on Earthquake Engineering, Sept. 8-13, Istanbul, Turkey, Vol. 3, 89-96.

Okusa, S., Anma, S., and Maikuma, M. (1984). “The propagation of liquefaction pressure and delayed failure of a tailings dam dike in the 1978 Izu-Oshima-Kinkai earthquake.” Proc., 8th World Conf. on Earthquake Engineering, July 21-28, San Francisco, CA, Vol. 1, 389-396.

Olivia Chen Consultants, Inc. (2003). “Report on the Seismic Stability of Calaveras Dam”, report prepared for the San Francisco Public Utilities Commission, Utilities Engineering Bureau.

Olson, S.M. (2001). “Liquefaction analysis of level and sloping ground using field case histories and penetration resistance.” Ph.D. thesis, University of Illinois at Urbana-Champaign, Urbana, Illinois.

Olson, S.M. and Johnson, C.I. (2008). “Analyzing liquefaction-induced lateral spreads using strength ratios.” Journal of Geotechnical and Geoenvironmental Engineering, ASCE, 134(8), 1035-1049.

Olson, S.M., Stark, T.D., Walton, W.H., and Castro, G. (2000). “Static liquefaction flow failure of the North Dike of Wachusett Dam.” Journal of Geotechnical and Geoenvironmental Engineering, ASCE, 126(12), 1184-1193.

Olson, S.M. and Stark, T.D. (2001). “Liquefaction analysis of Lower San Fernando Dam using strength ratios." Paper No. 4.05, Proc., 4th International Conf. on Recent Advances in Geotechnical Earthquake Engineering and Soil Dynamics, March 26-31, San Diego, CA.

Olson, S.M. and Stark, T.D. (2002). “Liquefied strength ratio from liquefaction flow failure case histories,” Canadian Geotechnical Journal, 39(5), 629-647.

Pillai, V.S. and Salgado, F.M. (1994). “Post-liquefaction stability and deformation analysis of Duncan Dam.” Candian Geotechnical Journal, 31, 967-978.

Plewes, H.D., O’Neil, G.D., McRoberts, E.C., and Chan, W.K. (1989), “Liquefaction considerations for Suncor tailings pond.” Proc., Dam Safety Seminar, Edmonton, Alberta, Sept., Vol 1, 61-89.

Popescu, R., Prevost, J.H., and Deodatis, G. (1997). “Effects of spatial variability on soil liquefaction: some design recommendations.” Geotechnique, 47(5), 1019-1036.

Poulos, S.J. (1981). “The steady state of deformation.” Journal of Geotechnical Engineering Division, ASCE, 17(GT5), 553-562.

Poulos, S.J. (1988). “Liquefaction and related phenomena.” in Advanced Dam Engineering for Design, Construction, and Rehabilitation, R.B. Jansen, ed., Van Nostrand Reinhold, New York, 292-320.

Poulos, S.J., Castro, G. and France, W. (1985). “Liquefaction evaluation procedure.” Journal of Geotechnical Engineering, ASCE, 111(6), 772-792.

Poulos, S.J., Robinsky, E.I., and Keller, T.O. (1985). “Liquefaction resistance of thickened tailings.” Journal of Geotechnical Engineering, ASCE, 111(12), 1380-1394.

Poulos, S.J. Castro, G., and France, W. (1988). Closure to discussion of “Liquefaction evaluation procedure.” Journal of Geotechnical Engineering, ASCE, 114(2), 251-259.

Riemer, M.F. and Seed, R.B. (1992). “Observed effects of testing conditions on the residual strength of loose, saturated sands at large strains.” Proc., 4th Japan-U.S. Workshop on Earthquake Resistant Design of Lifeline Facilities and Countermeasures for Soil Liquefaction, Tech. Rpt. No. NCEER-92-0019, M. Hamada and T.D. O’Rourke, eds., Vol. 1, 223-237.

Riemer, M.F. and Seed, R.B. (1997). “Factors affecting apparent position of steady-state line. Journal of Geotechnical and Geoenvironmental Engineering, ASCE, 123(3), 281-288.

Robertson, P.K. (2010). “Evaluation of flow liquefaction and liquefied strength using cone penetration test.” Journal of Geotechnical and Geoenvironmental Engineering, ASCE, 136(6), 842-853.

Robertson, P.K. (2014). Personal communication.

Robertson, P.K. and Campanella, R.G. (1983). “Interpretation of cone penetration tests. Part I: sand.” Canadian Geotechnical Journal, 20(4), 718-733.

Robertson, P.K., and Wride (Fear), C.E. (1998). “Evaluating cyclic liquefaction potential using the cone penetrometer test.” Canadian Geotechnical Journal, 35(3), 442-459.

Rogers, B.T., Been, K., Hardy, M.D., Johnson, G.J., and Hachey, J.E. (1990). “Re-analysis of Nerlerk B-67 berm failures.” Proc., 43rd Canadian Geotechnical Conf. - Prediction of Performance in Geotechnique, Quebec, Canada, Vol. 1, 227-237.

Ross, G.A. (1968). “Case studies of soil stability problems resulting from earthquakes.” Ph.D. Thesis, University of California, Berkeley, Calif. Saito, K. and Ine, N. (1993). Private communication to K. Miura, reported in Miura et al. (1998).

Saito, K. and Ine, N. (1993). Private communication to K. Miura, reported in Miura et al. (1998).

Sasaki, Y., Oshiki, H., and Nishikawa, J. (1994). “Embankment failure caused by the Kushiro-Oki earthquake of January 15, 1993.” Proc., 13th International Conf. on Soil Mechanics and Foundation Engineering, New Delhi, India, Vol. 1, 61-68.

Sasaki, Y., Tamura, K., Yamamoto, M., and Ohbayashi, J. (1995). “Soil improvement work for river embankment damaged by the 1993 Kushiro-Oki earthquake.” Proc., Earthquake Geotechnical Engineering, Nov. 14-16, Tokyo, Japan, Vol. 1, 43-48.

Schmertmann, J.H. (1987). Discussion of “Time-dependent strength in freshly deposited or densified sand.” by J.K. Mitchell and Z.V. Solymar, Journal of Geotechnical Engineering, ASCE, 113(2), 173-175.

Schofield, A.N. and Wroth, C.P. (1968). Critical State Soil Mechanics. McGraw-Hill, London.

Scott, R. F. (1972). “The calculation of horizontal accelerations from seismoscope records.” Paper presented at a Seismological Society of America Conference in Hawaii.

Seed, H.B. (1968). “Landslides during earthquakes due to soil liquefaction.” Journal of the Soil Mechanics and Foundation Division, ASCE, 94(SM5), 1055-1122.

Seed, H.B. (1979). “Considerations in the earthquake-resistant design of earth and rockfill dams.” Geotechnique, 29(3), 215-263.

Seed, H.B. (1987). “Design problems in soil liquefaction.” Journal of Geotechnical Engineering Division, ASCE, 113(8), 827-845.

Seed, H.B. and Lee, K.L. (1966). “Liquefaction of saturated sands during cyclic loading,” Journal of the Soil Mechanics and Foundations Division, ASCE, SM6(11), 105-134.

Seed, H. B. and Martin, G. R. (1966). “The seismic coefficient in earth dam design.” Journal of the Soil Mechanics and Foundations Division, 92(3), 25-58.

Seed, H.B. and Idriss, I.M. (1971). “Simplified procedure for evaluating soil liquefaction potential.” Journal of the Soil Mechanics and Foundation Division, ASCE, 97(SM9), 1249-1273.

Seed, H.B., Lee, K.L., and Idriss, I.M. (1969). “Analysis of Sheffield Dam failure.” Journal of the Soil Mechanics and Foundations Division, ASCE, 95(SM6), 1453-1490.

Seed, H.B., Lee, K.L., Idriss, I.M., and Makdisi, F. (1973). “Analysis of the slides in the San Fernando Dams during the earthquake of Feb. 9, 1971.” Earthquake Engineering Research Center 73-2, University of California, Berkeley, Calif.

Seed, H.B., Lee, K.L., Idriss, I.M., and Makdisi, F. (1975). “Dynamic analysis of the slide in the Lower San Fernando Dam during the earthquake of February 9, 1971.” Journal of the Geotechnical Engineering Division, ASCE, 101(GT9), 889-911.

Seed, H.B., Tokimatsu, K., Harder, L.F., and Chung, R. (1984). “The influence of SPT procedures on soil liquefaction resistance evaluations.” Report No. UCB/EERC-84/15, Earthquake Engineering Research Center, Univ. of California, Berkeley, CA, October.

Seed, H.B., Tokimatsu, K., Harder, L.F., and Chung, R. (1985). “Influence of SPT procedures in soil liquefaction resistance evaluations.” Journal of Geotechnical Engineering Division, ASCE, 111(12), 861-878.

Seed, H.B., Seed, R.B., Harder, L.F., and Jong, H.-L. (1989). “Re-evaluation of the Lower San Fernando Dam: Report 2, examination of the post-earthquake slide of February 9, 1971.” U.S. Army Corps of Engineers Contract Report GL-89-2, U.S. Army Corps of Engineers Waterways Experiment Station, Vicksburg, Mississippi.

Seed, R. B., Cetin, K. O., Moss, R. E., Kammerer, A. M., Wu, J., Pestana, J. M., Reimer, M.F., Sancio, R. B., Bray, J.D., Kayen, R.E., and Faris, A. (2003). “Recent advances in soil liquefaction engineering: a unified and consistent framework.” In Proceedings of the 26th Annual ASCE Los Angeles Geotechnical Spring Seminar: Long Beach, CA.

Seed, R.B. and Harder, L.F. Jr. (1990). “SPT-based analysis of cyclic pore pressure generation and undrained residual strength.” Proc. H.Bolton Seed Memorial Symposium, Bi- Tech Publishing Ltd., Vol. 2, 351-376.

Silvis, F. and de Groot, M.B. (1995). “Flow slides in the Netherlands: experience and engineering practice.” Canadian Geotechnical Journal, 32, 1086-1092.

Skempton, A.W. (1986). “Standard penetration test procedures and the effects in sand of overburden pressure, relative density, particle size, ageing, and overconsolidation.” Geotechnique, 36, 425-447.

Sladen, J.A., D'Hollander, R.D., and Krahn, J. (1985). “The liquefaction of sands, a collapse surface approach.” Canadian Geotechnical Journal, 22, 564-578.

Sladen, J.A., D'Hollander, R.D., Krahn, J., and Mitchell, D.E. (1985). “Back analysis of the Nerlerk berm liquefaction slides.” Canadian Geotechnical Journal, 22, 579-588.

Sladen, J.A., D'Hollander, R.D., Krahn, J., and Mitchell, D.E. (1987). “Back analysis of the Nerlerk berm liquefaction slides: Reply.” Canadian Geotechnical Journal, 24, 179-185.

Sladen, J.A. and Hewitt, K.J. (1989). “Influence of placement method on the in situ density of hydraulic sand fills.” Canadian Geotechnical Journal, 26, 453-466.

Spencer, E. (1967). “A method of analysis of the stability of embankments assuming parallel inter-slice forces.” Geotechnique, 17(1), 11-26.

Stark, T.D. and Mesri, G. (1992). “Undrained shear strength of liquefied sands for stability analysis.” Journal of Geotechnical Engineering, ASCE, 118(11), 1727-1747.

Stark, T.D., Olson, S.M., Kramer, S.L., and Youd, T.L. (1998). “Shear strength of liquefied soils.” Proc., Workshop on Post-Liquefaction Shear Strength of Granular Soils, April 17-18, 1997, University of Illinois at Urbana-Champaign, Urbana, Illinois, 288 p. (Available only on the World Wide Web at http://mae.ce.uiuc.edu)

Sully, J.P., Fernandez, A., and Zalzman, S. (1995). “Backanalysis of deformations for case histories involving flow-type failures.” Proc., 3rd International Conf. on Recent Advances in Geotechnical Earthquake Engineering and Soil Dynamics, April 2-7, St. Louis, MO, Vol. 1, 499-502.

Terzaghi, K., Peck, R.B., and Mesri, G. (1996). Soil Mechanics in Engineering Practice, Third Edition. John Wiley & Sons, Inc., New York, 549 p.

Tokimatsu, K. and Seed, H.B. (1987). “Evaluation of settlements in sands due to earthquake shaking.” Journal of Geotechnical Engineering, ASCE, 113(8), 861-878.

U.S. Army Corps of Engineers. (1939). “Report on the slide of a portion of the upstream face of the Fort Peck Dam, Fort Peck, Montana.” United States Government Printing Office, Washington, D.C.

U.S. Army Corps of Engineers. (1949). “Report on investigation of failure of Sheffield Dam, Santa Barbara, California.” Office of the District Engineer, Los Angeles, California, June.

Vaid, Y.P. and Chern, J.C. (1985). “Cyclic and monotonic undrained response of saturated sands.” in Advances in the Art of Testing Soils under Cyclic Conditions, V.Khosla, ed., ASCE, New York, 120-147.

Vaid, Y.P., Chung, E.F.K., and Kuerbis, R.H. (1990). “Stress path and steady state,” Canadian Geotechnical Journal, 27(1), 1-7.

Vaid, Y.P. and Thomas, J. (1995). “Liquefaction and post-liquefaction behavior of sand.” Journal of Geotechnical Engineering, ASCE, 121(2), 163-173.

Vaid, Y.P., Sivathayalam, S., and Stedman, D. (1999). “Influence of specimen reconstituting method on the undrained response of sand,” Geotechnical Testing Journal, ASTM, 22(3), 187-195.

Vasquez-Herrera, A. and Dobry, R. (1989). “Re-evaluation of the Lower San Fernando Dam: Report 3, the behavior of undrained contractive sand and its effect on seismic liquefaction flow failures of earth structures.” U.S. Army Corps of Engineers Contract Report GL-89-2, U.S. Army Corps of Engineers Waterways Experiment Station, Vicksburg, Mississippi.

Verdugo, R. (1992). “Characterization of sandy soil behavior under large deformation.” Ph.D. Thesis, Dept. of Civil Engineering, University of Tokyo, Japan.

Verdugo, R. and Ishihara, K. (1996): "The steady state of sandy soils," Soils and Foundations, Vol. 36, No. 2, pp. 81-92.

Von Thun, J. L. (1979). “Analysis of dynamic compaction foundation treatment requirements, Stage 1, Jackson Lake Dam.” Technical memorandum No. TM-JL-230-26, Bureau of Reclamation, Engineering and Research Center, Division of Dam and Waterway Design, Embankment Dams Branch.

Wang, C. (2003). Prediction of the residual strength of liquefied soils. (Doctoral Dissertation, University of Washington).

Willis, B. (1925). “A study of the Santa Barbara earthquake of June 29, 1925.” Bulletin, Seismological Society of America, 15(4), 255-278.

Wride (Fear), C.E. (1996). “In situ testing for liquefaction evaluation of sandy soils.” Ph.D. Thesis, University of Alberta, Edmonton, Alberta.

Wride (Fear), C.E., McRoberts, E.C., and Robertson, P.K. (1999). “Reconsideration of case histories for estimating undrained shear strength in sandy soils.” Canadian Geotechnical Journal, 36, 907-933.

Wu, J. (2003). "Liquefaction Triggering and Post Liquefaction Deformations of Monterey 0/30 Sand Under Uni-Directional Cyclic Simple Shear Loading." Dissertation in partial fulfillment for the degree of doctor of philosophy, University of California, Berkeley.

Yamada, G. (1966). “Damage to earth structures and foundations by the Niigata earthquake June 16, 1964, in JNR.” Soils and Foundations, 6(1), 1-13.

Yamauro, J.A. and Convert, K. M. (2001). “Monotonic and cyclic liquefaction of very loose sands with high silt content.” Journal of Geotechnical and Geoenvironmental Engineering, 127(4), 314-324.

Yashima, A., Oka, F., Konrad, J.M., Uzuoka, R., and Taguchi, Y. (1997). “Analysis of a progressive flow failure in an embankment of compacted till.” Proc., Deformation and Progressive Failure in Geomechanics, Vol. 1, 599-604.

Yasuda, S. et al. (1993). “Mechanical properties of soil where ground failure occurred during the Kushiro-oki earthquake.” Proc., 22nd JSCE Earthquake Engineering Symposium, 395-398.

Yegian, M.K., Ghahraman, V.G., and Harutinunyan, R.N. (1994). “Liquefaction and embankment failure case histories, 1988 Armenia earthquake.” Journal of Geotechnical Engineering, ASCE, 120(3), 581-596.

Yoshimine, M. and Ishihara, K. (1998). “Flow potential of sand during liquefaction.” Soils and Foundations, 38(3), 189-198.

Yoshimine, M., Robertson, P.K., and Wride (Fear), C.E. (1999). “Undrained shear strength of clean sands to trigger flow liquefaction.” Canadian Geotechnical Journal, 36(5), 891-906.

Yoshimine, M., Robertson, P.K. and Wride, C.E. (2001). “Undrained shear strength of clean sands to trigger flow liquefaction: Reply to discussion.” Canadian Geotechnical Journal, 38(3), 654-657.

Youd, T.L. (1995). “Liquefaction-induced lateral ground displacement.” Proc., 3rd International Conf. on Recent Advances in Geotechnical Earthquake Engineering and Soil Dynamics, April 2-7, St. Louis, MO, Vol. 2, 911-925.

Youd, T.L. and I.M. Idriss (1997). “Summary report.” Proc., NCEER Workshop on Evaluation of Liquefaction Resistance of Soils, NCEER-97-0022, 1-40.

Youd, T.L., I. M. Idriss, Ronald D. Andrus, Ignacio Arango, Gonzalo Castro, John T. Christian, Richardo Dobry, W. D. Liam Finn, Leslie F. Harder Jr., Mary Ellen Hynes, Kenji Ishihara, Joseph P. Koester, Sam S. C. Liao, William F. Marcuson III, Geoffrey R. Martin, James K. Mitchell, Yoshiharu Moriwaki, Maurice S. Power, Peter K. Robertson, Raymond B. Seed, and Kenneth H. Stokoe II. (2001). "Liquefaction Resistance of Soils: Summary Report from the 1996 NCEER and 1998 NCEER/NSF Workshops on Evaluation of Liquefaction Resistance of Soils." Journal of Geotechnical and Geoenvironmental Engineering, 124(10).

Youd, T. L., Hansen, C. M., and Bartlett, S. F. (2002). "Revised Multilinear Regression Equations for Prediction of Lateral Spread Displacement", Journal of Geotechnical and Geoenvironmental Engineering, Vol. 128, No. 12, pp. 1007-1017.

Appendix A:

Back-Analyses of Class A and Class C Liquefaction Failure Case Histories

Class A Case Histories:

A.1: Wachussett Dam (1907)

A.2: Fort Peck Dam (1938)

A.3: Uetsu Railway Embankment (1964)

A.4: Lower San Fernando Dam (1971)

A.5: Hachiro-Gata Road Embankment (1983)

A.6: La Marquesa Dam – U/S Slope (1985)

A.7: La Marquesa Dam – D/S Slope (1985)

A.8: La Palma Dam (1985)

A.9: Lake Ackerman Highway Embankment (1987)

A.10: Chonan Middle School (1987)

A.11: Soviet Tajikistan May 1 Slope Failure (1989)

A.12: Shibecha-Cho Embankment (1993)

A.13: Route 272 Embankment (1993)

Class C Case History:

A.14: Calaveras Dam (1918)

A.1 North Dike of Wachusett Dam (Massachusetts, USA; 1907)

A.1.1 Brief Summary of Case History Characteristics

Name of Structure	Wachusett Dam
Location of Structure	Massachusetts, USA
Type of Structure	Poorly compacted earthen dam
Date of Failure	April 11, 1907
Nature of Failure	Non-seismic, during initial reservoir filling
Approx. Maximum Slope Height	88 ft.

A.1.2 Introduction and Description of Failure

The best description and summary of field data regarding the failure of the North Dike of Wachusett Dam is presented by Olson et al. (2000), and the description here is based largely on Olson et al. (2000) and Olson (2001). GZA GeoEnvironmental (1991) performed geotechnical studies of the dam to investigate seismic stability of the North Dike, and Haley & Aldrich (1984a,b) also performed geotechnical studies of the North Dike.

Construction of the dike began in 1898 with the excavation of cut-off trenches in the foundation. Backfilling of these cut-of trenches occurred in 1902 and 1902. These cut-off trenches were not involved in the failure. Construction of the main dike embankment began in 1902, and fill placement for the North Dike was completed in 1904, approximately three years prior to the slope failure.

A slope failure occurred on the upstream side of the North Dike embankment on April 11, 1907, during initial filling of the reservoir. Figures A.1.1 and A.1.2 show pre-failure and post-failure cross-sections through the failure zone (Olson et al, 2000). The failure was centered over the former river channel, at the location of the maximum height embankment section where the dam reached a height of approximately 24.4 m (80 ft). The reservoir had risen to an elevation approximately 40 feet below the crest of the embankment when the failure occurred. The zone of likely "jetting" shown in Figure A.1.2 refers to "jetting" that was performed during the post-failure slope repair to try to inter-mix (and knit) the repair fill and the slope scarp. This "jetting" occurred after the failure, and is not pertinent to the back-analyses of the failure.

Olson et al. postulate that the cause of the failure was reduction in effective stress along the base of the failure mass due to increasing buoyancy as the reservoir filled, while there was a commensurate (but lesser) reduction in driving shear stresses along this failure surface as much of the embankment fill remained above the reservoir level. It is suggested here that a more likely cause would have been wetting-induced "collapse" of the very loose, cohesionless soils comprising the upstream shell. As discussed a bit later, saturation (wetting) was employed to "compact" the similar downstream shell fill materials, and this was observed to produce volumetric reductions of approximately 6% to 12% as each lift was saturated. No similar "saturation" was applied during placement of lifts of the upstream shell, and so there

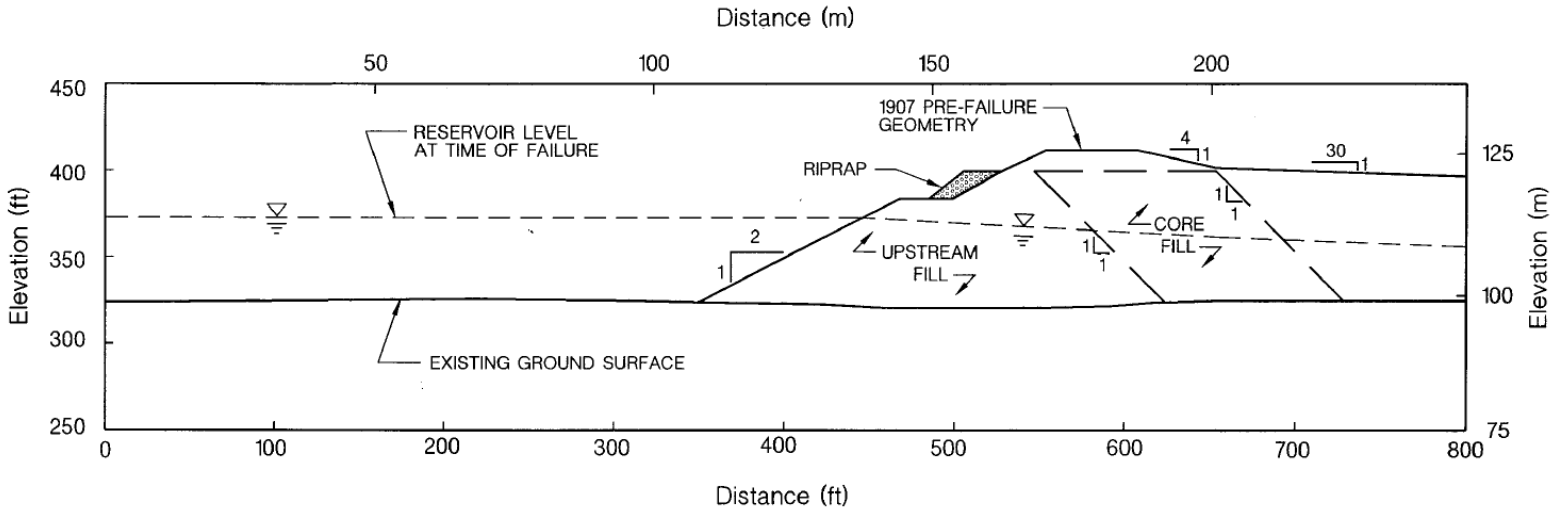

Figure A.1.1: Pre-failure cross-section of the North Dike of Wachusett Dam at Station 23+20 (from Olson et. al, 2000).

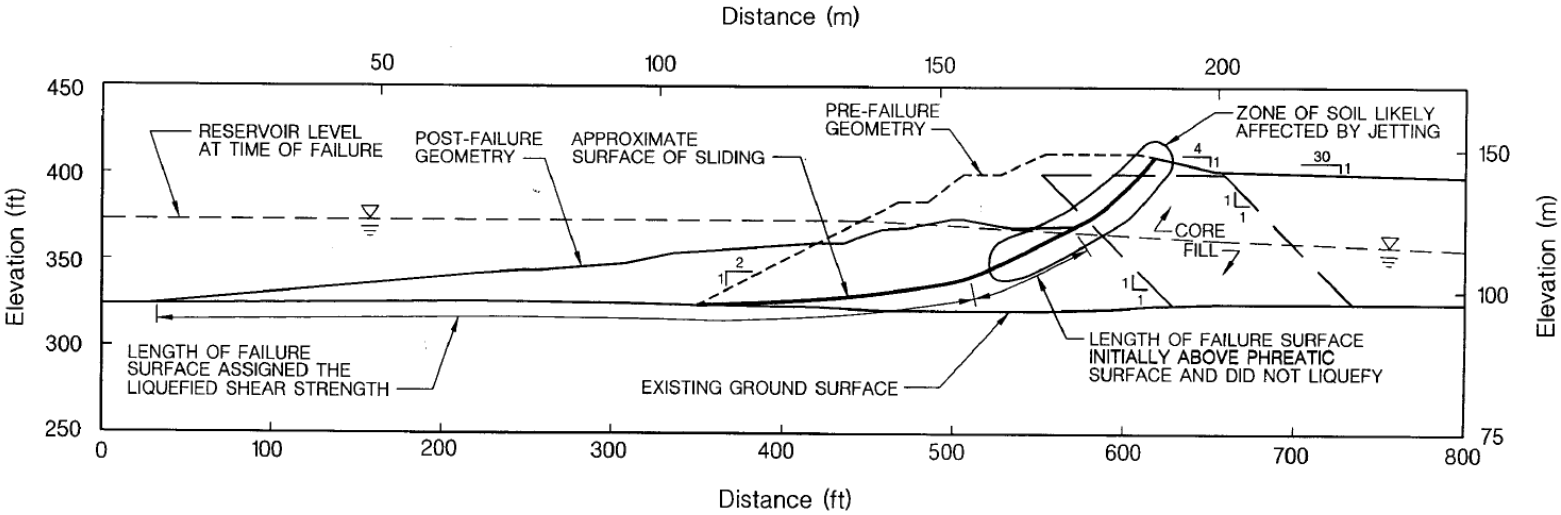

Figure A.1.2: Post-failure cross-section of the North Dike of Wachusett Dam at Station 23+20, showing the approximate location of the apparent sliding surface (from Olson et. al, 2000).

is a high likelihood that significant wetting-collapse would have occurred as the reservoir was filled for the first time. Regardless of the actual details of the triggering of the failure, the ensuing flow-type failure can be safely judged to have been initiated "statically", with no cyclic or dynamic triggering forces. As shown in Figures A.1.1 and A.1.2, movements of the failure mass into the reservoir were large.

The failed zone of the Dike was rebuilt in 1907, and the reservoir was re-filled without incident.

Foundation soils beneath the dike are comprised mainly of dense to very dense sands, gravels and non-plastic silts. A large portion of the fill soils for the embankment's shell zones consisted of fine sands, which were spoils from the excavation of the cut-off trenches into these foundation soils. Materials for the core were also stripped from the reservoir, and consisted of sandy silt to silty sand.

As shown in Figure A.1.1, the core was approximately 100 feet in width, with slopes of 1:1 towards the upstream direction on both the upstream and downstream sides of the core zone. The core soils were placed in lifts of approximately 6 inches, and were rolled by horse drawn carts. No direct measurements of the resulting unit weights of the core materials were made during construction, but more recent investigations indicate that current unit weights are on the order of 120 to 130 lbs/ft^3.

The downstream shell consists of sand to silty sand, with some gravel. As shown in Figure A.1.1, the downstream face has a slope of 4:1 near the crest, but the rest of the downstream face is sloped at 30:1 towards Coachlace Pond. The downstream shell soils were reportedly placed in approximately 7 to 8 foot lifts, and were "compacted" by flooding with water. Approximately 6 to 12 inches of settlement was observed following saturation of each lift. Further details of the downstream shell zone are not pertinent to these current analyses, as the downstream shell zone was not involved in the failure.

The upstream shell also consists of sand to silty sand with some gravel. Fines contents were low, typically on the order of approximately 5% to 10%, though some soils had somewhat higher fractions of largely non-plastic fines. Unlike the downstream shell, the upstream shell received neither compaction nor flooding with water during construction. As a result, the upstream shell was in a very loose condition, and likely prone to some degree of volumetric "collapse" upon initial wetting during the first filling of the reservoir. The slope of the upstream face was relatively steep at 4:1, with a bench near the crest, and with riprap on the upstream face above this bench.

A.1.3 Initial Yield Stress Analyses

Figure A.1.3(a) shows the cross-section used for back-analyses of the post-liquefaction initial yield strength $S_{r,yield}$ that would be required within the liquefied upstream shell materials to produce a calculated Factor of Safety equal to 1.0. This is not the actual post-liquefaction strength, but it proves to be useful in developing a number of charts and relationships for these overall studies.

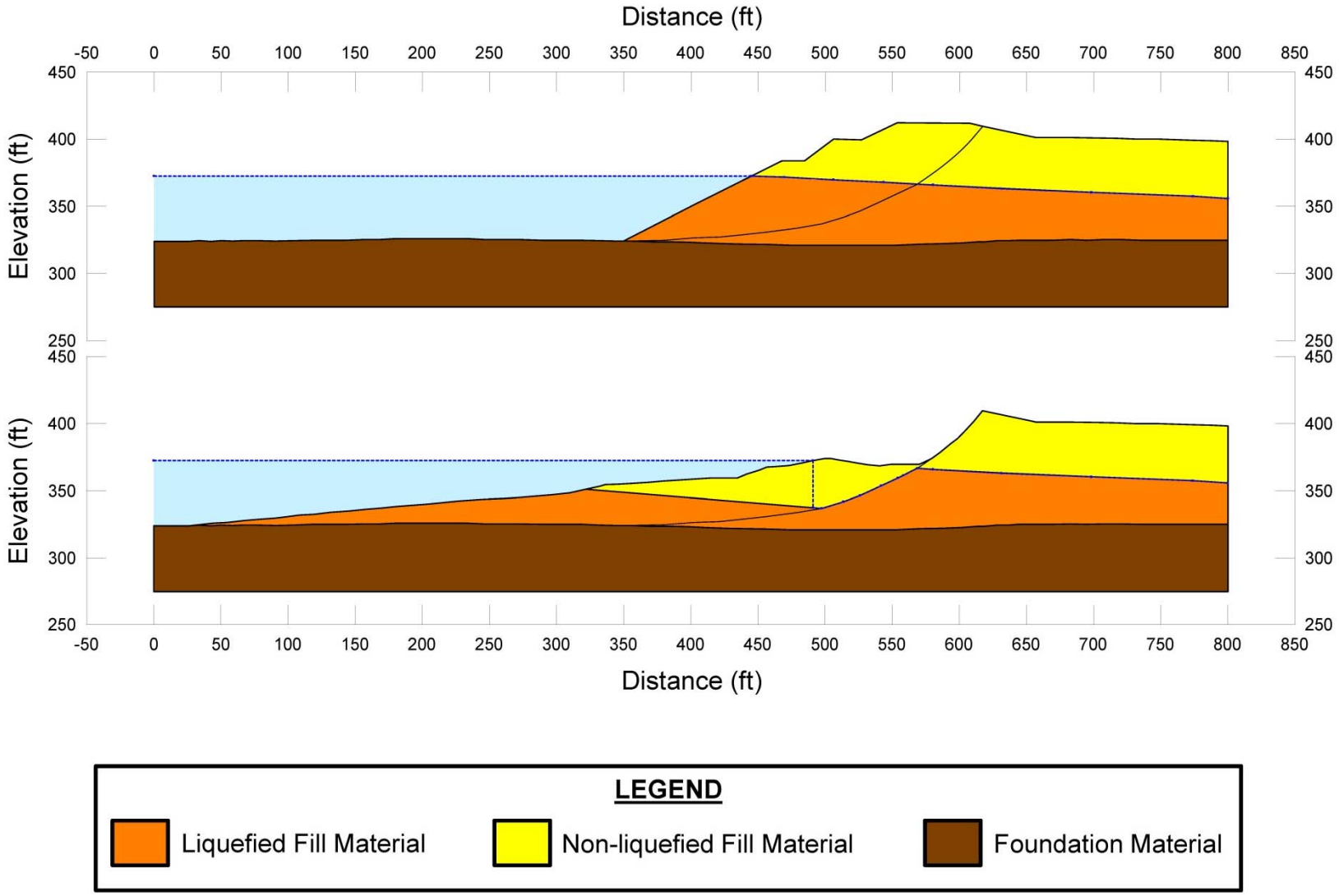

Figure A.1.3: Wachusett Dam at Station 23+20: (a) Pre-failure geometry and best-estimate failure surface for initial yield stress analyses, and (b) post-failure geometry and best-estimate failure surface for post-failure residual geometry analyses.

Figure A.1.3(a) also shows the best estimate failure surface. The failure surface is relatively well constrained at the back heel by the observable failure scarp. The precise location of the failure surface at the base of the failure is uncertain, but the most critical failure surfaces in terms of lowest Factor of Safety for a giver value of strength within the liquefied shell fill materials are those that go right to the bottom of the fill. The potential depths are then constrained by the very dense foundation soils. Additional analyses were performed, varying this failure surface; the shape at the lower back heel was varied, and the failure surface was allowed to occur at various elevations slightly above the base of the shell fill. These variations were performed to evaluate sensitivity of the resulting calculated values of $S_{r,yield}$.

Shear strength of the non-saturated, loose sand to silty shell and crest fill materials was modeled as frictional, with Ø′ = 30°. Unit weights of non-saturated shell and crest fills were taken as 111 lbs/ft^3. Shear strength of the moderately compacted, non-saturated sandy silt to silty sand of the upper "core" zone through which part of the failure surface passes was modeled with Ø′ = 30°. A unit weight of 111 lbs/ft^3 was modeled for these non-saturated "core" materials. The saturated unit weight of the liquefied silty sands was modeled as 123 lbs/ft^3.

The saturated portions of the upstream shell were considered to be potentially liquefiable, and shear strengths of portions of potential failure surfaces were modeled with post-liquefaction yield strength $S_{r,yield}$. $S_{r,yield}$ was modeled as uniform along any potential failure surface, and the calculation of the value of $S_{r,yield}$ was the primary objective of these analyses.

Permeabilities of the upstream shell zone were relatively high, and permeabilities of the siltier core zone are lower than those of the upstream shell. Accordingly, it is assumed that the phreatic surface on the upstream side of the core equilibrate relatively rapidly with reservoir elevation increase during the first filling in 1907. The phreatic surface within the core zone, and further downstream during this first reservoir filling cannot be estimated with similar confidence, but this is not important because the failure occurred to the upstream side of the potentially saturated portions of the core.

For the best estimate geometry, conditions, and failure surface described above and shown in Figure A.1.3, the resulting value of post-liquefaction yield strength was found to be $S_{r,yield}$ = 829 lbs/ft^2. Sensitivity analyses were then performed, varying the details and location (at depth) of the failure surface, unit weights, and friction angles for the non-liquefied upper crest and non-liquefied upper core zones. These analyses suggested that there was little likelihood that this failure would have proceeded in an incrementally progressive manner, and so this failure was modeled only as a monolithic event, with the full eventual sliding mass beginning to move largely coherently at the inception of failure. The resulting range of values of $S_{r,yield}$ for combinations of modeling assumptions and details considered to be reasonable was found to be $S_{r,yield} \approx$ 752 to 909 lbs/ft^2.

Olson (2001) also performed back-analyses to determine $S_{r,yield}$. Failure surfaces analyzed were similar. Olson reported values of $S_{r,yield} \approx$ 37.6 to 41.9 kPa (784 to 875 lbs/ft^2).

A.1.4 Residual Strength Analyses Based on Residual Geometry

The calculation of the "apparent" post-liquefaction strength ($S_{r,resid/geom}$) required to produce a calculated Factor of Safety equal to 1.0 based on residual geometry is illustrated in Figure A.1.4. This figure shows the phreatic surface, and the failure surface, used to calculate the best-estimate value of $S_{r,resid/geom}$, based on the best estimate modeling parameters as described in the previous section. An additional detail here is the shear strength modeled at the base of the portion of the upstream toe of the embankment that traveled out into the reservoir. This was the first filling of the reservoir, so there were no loose reservoir sediments accumulated yet at the upstream toe. There may have been some hydroplaning, however, as the embankment materials moved rapidly into the reservoir. The incremental inertial analyses presented in Section A.1.5 that follows indicate that the maximum velocity was on the order of approximately 14.3 ft/sec, and the velocity during most of the run-in was lower. As discussed, it is not possible to fully accurately determine the degree of hydroplaning that would have occurred. The best estimate analysis of $S_{r,resid/geom}$ was performed assuming that shear strength at the base of the embankment materials that entered into the reservoir was 100% of $S_{r,resid/geom}$. The resulting best estimate calculated value of "apparent" post-liquefaction strength based on post-failure residual geometry was $S_{r,resid/geom} \approx 81$ lbs/ft^2.

Variations were then made in parameters, and in location of the pre-failure phreatic surface, as was described in the preceding section in order to evaluate uncertainty or variability. Varying degrees of potential hydroplaning were also modeled, with the average shear strength at the base of the portion of the failure mass that entered the reservoir being modeled as varying from a low of 20% of $S_{r,resid/geom}$ to a high of 100% of $S_{r,resid/geom}$. Considering ranges of variations in modeling details and parameters considered to be reasonable, the resulting likely range of post-liquefaction strength required to provide a calculated Factor of Safety equal to 1.0 based on residual geometry was considered to be $S_{r,resid/geom} \approx 71$ to 87 lbs/ft^2.

Olson (2001) also calculated post-liquefaction strength required to produce a calculated Factor of Safety equal to 1.0 based on residual geometry, and reported a best estimate value of $S_{r,resid/geom} \approx 3.8$ kPA (79 lbs/ft^2). No range was reported.

A.1.5 Incremental Momentum Back-Analyses and Overall Estimates of S_r

Incremental inertial back-analyses were performed using the same sets of properties and geometries (including failure surfaces and phreatic surfaces) as described in the previous sections.

Figure A.1.5 shows the best-estimate progressive incremental inertial analysis, showing the five stages of geometry evolution modeled as the failure proceeds. Figure A.1.6 shows the associated calculations of (1) acceleration vs. time, (2) velocity vs. time, and (3) displacement of the overall center of gravity vs. time. The resulting best estimate value of post-liquefaction strength was $S_r = 294$ lbs/ft^2.

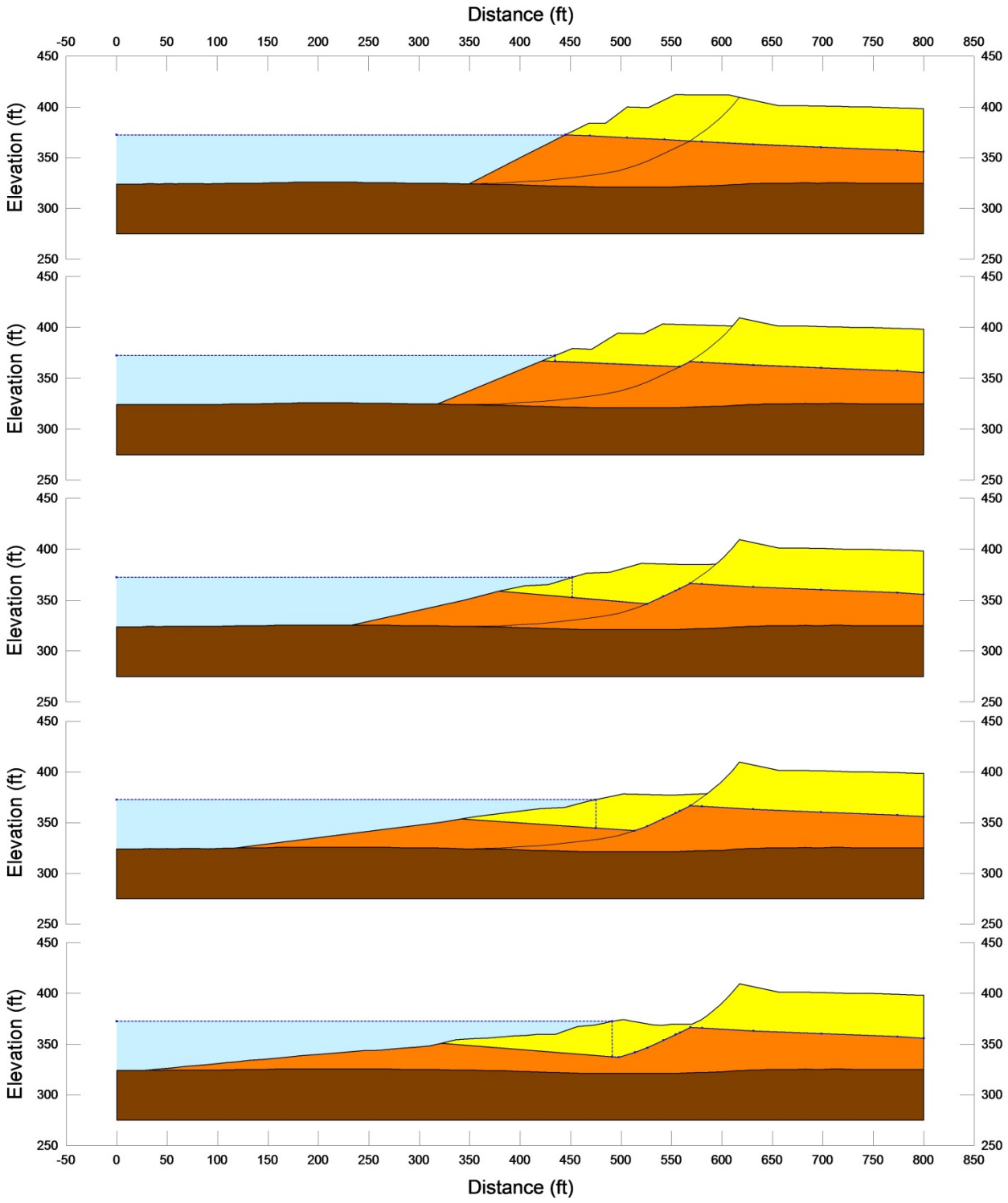

Figure A.1.5: Incremental inertial analysis of the failure of the North Dike of the Wachusett Dam, showing progressive evolution of cross-section geometry modeled

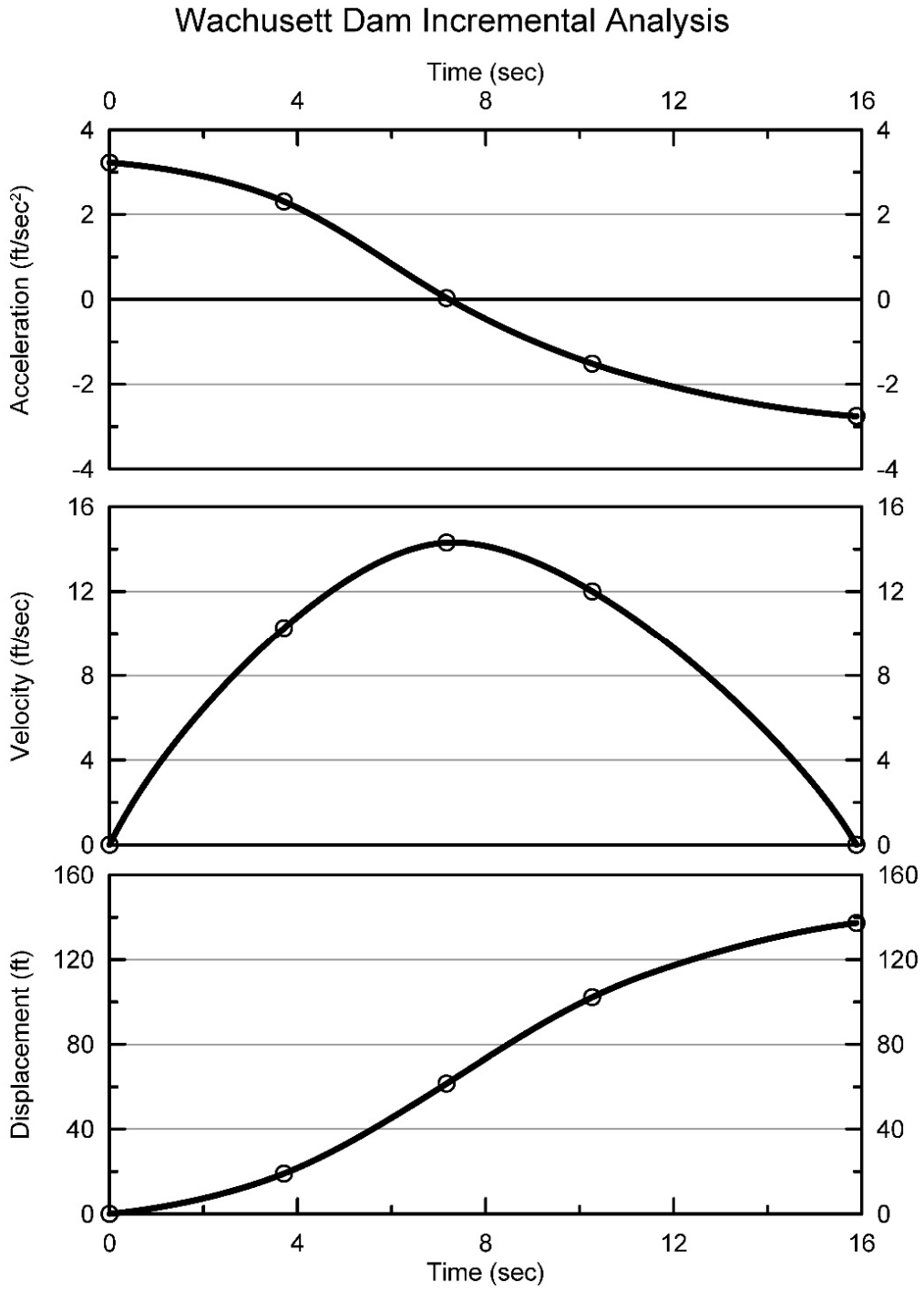

Figure A.1.6: Incremental inertial analysis of the failure of the North Dike of the Wachusett Dam, showing progressive evolution of: (1) acceleration vs. time, (2) velocity vs. time, and (3) displacement vs. time of the overall center of gravity of the failure mass

The main sources of uncertainty, or variability, in back-calculated values of S_r were (1) frictional strengths of the non-liquefied embankment fill materials, (2) degree of potential hydroplaning as the failure mass entered into the reservoir, (3) the precise location and shape of the failure plane at depth, and (4) unit weights.

Based on all analyses performed, and the considerations discussed, the overall best estimate value of post-liquefaction strength for the failure of the North Dike of Wachusett Dam was judged to be $S_r \approx 294$ lbs/ft^2, with a likely range of $S_r \approx 236$ to 360 lbs/ft^2. Based on the factors contributing to uncertainty or variance for this case history, it was the judgment of the investigation team that this range represented approximately ± 2 standard deviations. This range of variance is not symmetrical about the best estimate value, so minor further adjustments were made to produce a representative estimate of S_r suitable for regression analyses.

Overall, based on an assumed normal distribution, it was judged that the (mean and median) best estimate of post-liquefaction strength for this case history is

$$\overline{S_r} = 294 \text{ lbs/ft}^2$$

and that the best estimate of standard deviation of mean overall post-liquefaction strength is

$$\sigma_{\overline{S}} = 31 \text{ lbs/ft}^2$$

Wachusett Dam was more recently developed as a case history than most of the other cases considered in these studies, and it has not been back-analyzed by many investigators. Olson (2001) and Olson and Stark (2002) present one set of results, and Wang (2003) and Kramer (2008) present a second set of results. Interestingly, both the Olson/Stark and Wang/Kramer efforts specifically account analytically for momentum effects. Olson (2001) and Olson and Stark (2002), reported a best estimate value of $S_r = 16.0$ kPa (335 lbs/ft^2), based on their inertial displacement analyses that considered kinetics, and a range of $S_r = 10.4$ to 19.1 kPa (217 to 400 lbs/ft^2). Wang (2003) and Wang and Kramer (2008) employed their zero inertial force (ZIF) method to incorporate inertial effects in their back-analyses of this failure, and they developed estimates of both mean $\overline{S_r} = 348.0$ lbs/ft^2 as well as the associated standard deviation $\sigma_{\overline{S}} = 74.8$ lbs/ft^2. The details of their analyses, and the cross-sections and failure mass assumptions employed, are not presented and so cannot be checked.

This is an unusually well-defined case history, and these three sets of back-analyses that analytically incorporate momentum effects are all in good agreement.

A.1.6 Evaluation of Initial Effective Vertical Stress

Average initial (pre-failure) effective vertical stress was assessed for the liquefied zones of each of the failure surface shown in Figure A.1.3. Additional sensitivity analyses were then performed for reasonable ranges of variations in (1) the location of the phreatic surface, (2) unit weights, and (3) the precise location of the overall failure surface in order to evaluate uncertainty or variance.

The resulting best estimate of average pre-failure effective stress within the liquefied materials controlling the failure was then $\sigma_{vo}' \approx 3{,}142$ lbs/ft^2, with a reasonable range of $\sigma_{vo}' \approx$ 2,886 to 3,414 lbs/ft^2. This range is slightly non-symmetric about the median value, and this range was judged by the engineering team to represent approximately ± 2 standard deviations. Overall, the best characterization of initial (pre-failure) average effective vertical stress was then taken to be represented by a mean value of

$$\overline{\sigma'_{vo}} \approx 3{,}142 \text{ lbs/ft}^2$$

and with a standard deviation of

$$\sigma_{\bar{\sigma}} \approx 132 \text{ lbs/ft}^2$$

An estimate of representative σ_{vo}' was also calculated by Olson and Stark (2001, 2002) and these are shown in Table A.1.1(c). Olson (2001) and Olson and Stark (2002) report average initial effective vertical stresses of approximately $\sigma_{vo}' \approx 3{,}158$ lbs/ft^2. Average initial vertical effective stresses were not directly reported by Wang (2003) and Kramer (2008), but they were published more recently in the publication by Kramer and Wang (2015). As discussed in Section 2.3.8.1(a), the approach taken by Wang (2003) to evaluation of σ_{vo}' for his nine "primary" case histories (this is one of those nine) is not clearly explained, and it is also poorly documented. Wang's value of $\sigma_{vo}' = 2{,}558$ lbs/ft^2 is in fair agreement with the values of Olson (2001) and these current studies, but this is not considered a very rigorous check here. Agreement between Olson's independently back-calculated value, and the value developed in these current studies, is excellent.

A.1.7 Evaluation of $N_{1,60,CS}$

The field investigations reported by GZA Environmental (1991) and by Haley & Aldrich (1984a,b) included six SPT borings at the reconstructed failure section at Station 23+20. These are shown in Figure A.1.7. All of the borings were advanced by rotary wash boring, and a donut hammer with rope and cathead was used to drive the SPT samplers. It is assumed that the SPT hammer energy ration was approximately 45%. Thirty of the SPT's were performed in the upstream shell materials involved in the 1907 flow failure. Thirteen of these were performed near to the apparent shear failure surface, and these are shown with open circles in Figure A.1.7. A source of uncertainty, therefore, is how to weight the SPT blowcounts apparently "near" the failure surface vs. the rest of the SPT blowcounts in the upstream shell material. In these current studies, equal weighting was given to the thirteen blowcounts near the failure zone vs. the full ensemble of blowcounts in the upstream shell materials (assuming that variation is random, and that blowcounts might be distributed differently at nearby locations).

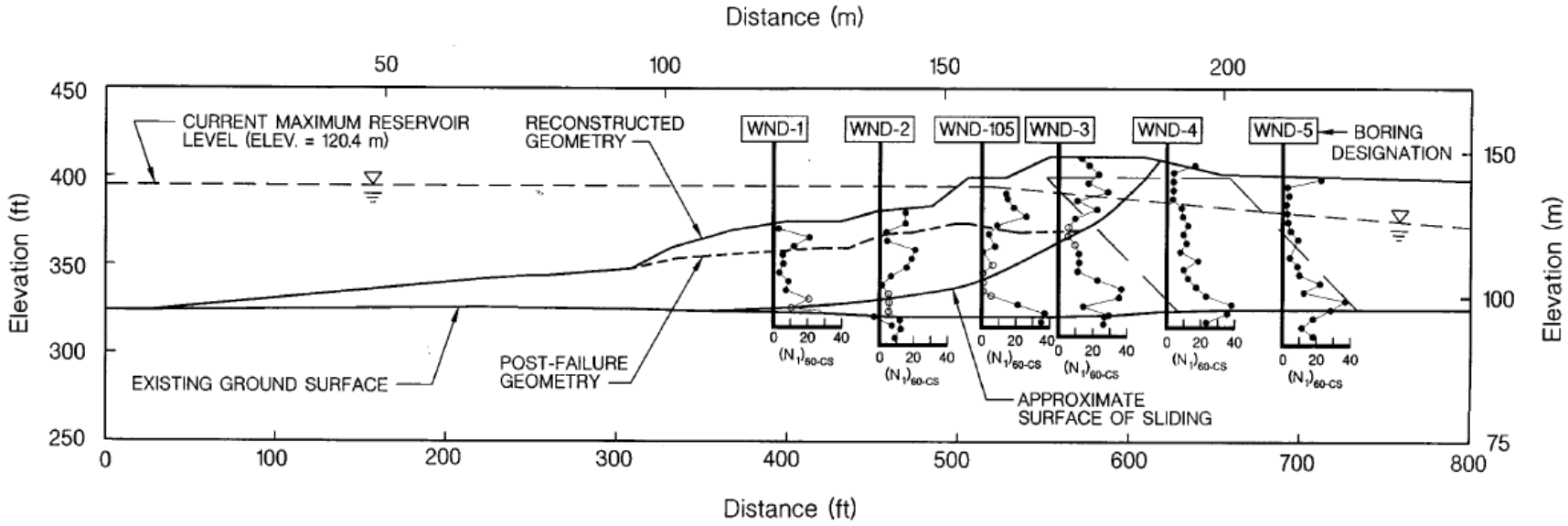

Figure A.1.7: Reconstructed cross-section of the North Dike of Wachusett Dam showing the locations and results of recent standard penetration tests (from Olson et al., 2001).

Corrections for effective overburden stress (C_N) were made using the relationships proposed by Deger (2014), as presented and discussed in Section C.1.1. Corrections for fines content were made using the relationship proposed by Cetin et al. (2004), and a representative fines content of approximately 5% to 10%; resulting in a null to minor fines adjustment. The resulting median $N_{1,60,CS}$ value for the thirteen SPT tests near to the failure surface was found to be approximately 8 blows/ft, and the median value for the full ensemble of SPT blowcounts (including the thirteen near the failure surface) was found to be approximately 7.5 blows/ft. The resulting best estimate median $\overline{N_{1,60,CS}}$ value for these current studies is then taken as $\overline{N_{1,60,CS}} \approx$ 7.5 blows/ft. Variance of $\overline{N_{1,60,CS}}$ was estimated primarily on the basis of the perceived uncertainties associated with the (1) the use of blowcounts from within the failure zone, (2) likely increases in blowcounts over time since the failure (the fill had been only recently placed at the time of the failure)the perceived high level of variability among the SPT data available. It appears unlikely that jetting of the interface between the failure scarp and the repair fill would have adversely affected these SPT data. Considering all of these, the representation of uncertainty in the representative median value of $\overline{N_{1,60,CS}}$ was taken as $\sigma_{\overline{N}} \approx 1.7$ blows/ft.

Table A.1.1(b) shows values of representative $N_{1,60}$ or $N_{1,60,CS}$ values developed by two other teams of investigators, and variance or standard deviations in these representative values if available. Olson and Stark (2001, 2002) developed an estimated representative value of $N_{1,60}$ = 7 blows/ft, but for this case history they proposed no range. Wang (2003) and Kramer (2008) jointly developed a representative value of $\overline{N_{1,60,CS}}$ = 7.3 blows/ft, and their estimated standard deviation of that overall mean value for this case history was $\sigma_{\overline{N}}$ = 1.8 blows/ft. Details of the development of this interpretation by Wang and Kramer are not presented. Overall agreement between the three independent assessments of representative $\overline{N_{1,60,CS}}$ values is excellent, and variance or uncertainty in $\overline{N_{1,60,CS}}$ appears to be relatively low.

A.1.8 Additional Indices from the Back-Analyses

A number of additional results, and indices, can be extracted from the analyses performed. Some of these are useful in developing some of the over-arching relationships and figures presented in the main text of this report. These values are presented in Table A.1.2.

Table A.1.1: Representative values for the North Dike of Wachusett Dam case history of: (a) post-liquefaction strength (S_r), (b) initial vertical effective stress (σ_{vo}'), and (c) $N_{1,60,CS}$ developed by various investigation teams, and estimates of variance in each of these indices when available.

(a) Post-Liquefaction Strength:	
Olson (2001) and Olson and Stark (2002)	S_r = 335 psf, and range = 217 to 399 psf
Wang (2003) and Kramer (2008)	$\overline{S_r}$ = 348.0 psf, and $\sigma_{\overline{S}}$ = 74.8 psf
This Study	$\overline{S_r}$ = 294 psf and $\sigma_{\overline{S}}$ = 31 psf
(b) Representative $N_{1,60}$ or $N_{1,60,CS}$ Value:	
Olson (2001) and Olson and Stark (2002)	$N_{1,60}$ = 7 bpf
Wang (2003) and Kramer (2008)	$\overline{N_{1,60,CS}}$ = 7.3 bpf, and $\sigma_{\overline{N}}$ = 1.9 bpf
This Study	$\overline{N_{1,60,CS}}$ = 7.5 bpf, and $\sigma_{\overline{N}}$ = 1.6 bpf
(c) Representative Initial Vertical Effective Stress:	
Olson (2001) and Olson and Stark (2002)	$\sigma_{vo}' \approx$ 3,158 psf, with no range provided.
Wang (2003) and Kramer (2008)	Value of $\sigma_{vo}' \approx$ 2,558 psf is poorly documented, and so is considered useful only as an approximate comparison. (See Section 2.3.8.1, and Table 2.3.)
This Study	$\overline{\sigma'_{vo}}$ = 3,142 psf, and $\sigma_{\overline{\sigma}}$ = 132 psf

Table A.1.2: Additional results and indices from the analyses of the North Dike of Wachusett Dam failure case history.

Maximum distance traveled by the center of gravity of the overall failure mass	137.3 ft.
Initial post-liquefaction Factor of Safety prior to displacement initiation, and based on best estimate value of S_r	FS = 0.47
Final post-liquefaction Factor of Safety at final (residual) post-failure geometry, and based on best estimate value of S_r	FS = 3.43

A.2 Fort Peck Dam (Montana, USA; 1938)

A.2.1 Brief Summary of Case History Characteristics

Name of Structure	Fort Peck Dam
Location of Structure	Montana, USA; Missouri River
Type of Structure	Hydraulic Fill Dam
Date of Failure	September 22, 1938
Nature of Failure	Static, During Construction
Approx. Maximum Slope Height	196 ft.

A.2.2 Introduction

The Fort Peck Dam embankment failed during construction on September 22, 1938. This failure was well-investigated, and details of the initial failure, investigations of that failure, and the repair (reconstruction) operations are well documented by the U.S Army Corps of Engineers (1939), Middlebrooks (1942), Casagrande (1965, 1976), Marcuson and Krinitsky (1976), and Marcuson et al. (1978). This case has also been studied by numerous teams investigating post-liquefaction strengths, as will be discussed in the Sections that follow.

The dam is located on the Missouri River, in northeastern Montana. The dam is a hydraulic fill structure, with a maximum height of 250 ft. (76.3 m) above the original river bed, and a crest length of approximately 10,580 ft. There is an additional dike, extending west of the main dam, with a crest length of approximately 10,450 ft. The main dam was constructed by traditional hydraulic fill methods; with starter dikes, and with dredged materials being deposited from both the upstream and downstream sides to develop relatively cohesionless "shells" and a central "puddle core" of finer materials near the center.

Dredging operations began on October 13, 1934. Nearly four years later, on the morning of September 22, 1938, hydraulic fill placement of the dam embankment section was nearing full design crest height. The reservoir was also partially filled, and at the time of failure was on the lower third of the upstream face of the dam. On the morning of September 22, settlements of as much as 1.5 feet were noted at the top of the upstream face near the right abutment (east abutment). At about 1:15 in the afternoon, a major slide occurred in the upstream slope at the right abutment, as shown in Figures A.2.1 through A.2.4.

Casagrande (1965) summarized observations of the failure as it occurred: "The movement began by a bulging out of the western portion of the affected upstream slope with simultaneous subsidence of the core pool. Then a transverse crack developed at the western end which widened rapidly into a deep gap while the moving portion of the slope started to swing in a rotational movement as if hinged at the abutment. Through this gap the core pool drained with enormous speed. The western portion which was moving out faster and further, broke into several large blocks and came to rest in the fan-shaped pattern seen in the aerial photographs."

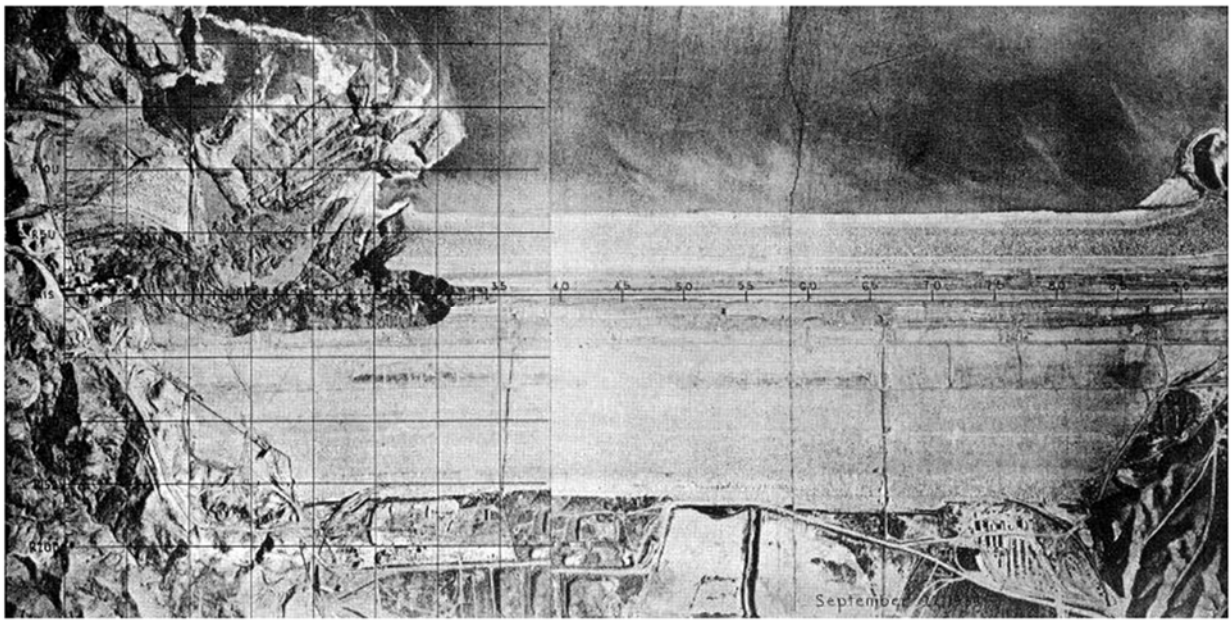

Figure A.2.1: Aerial view of post failure geometry. (U.S. Army Corps of Engineers, 1939)

Figure A.2.2: Enlarged aerial photo from Figure A.2.1 showing failure at the east end of the dam. (from http://www.midrivers.com/~rafter/lake/)

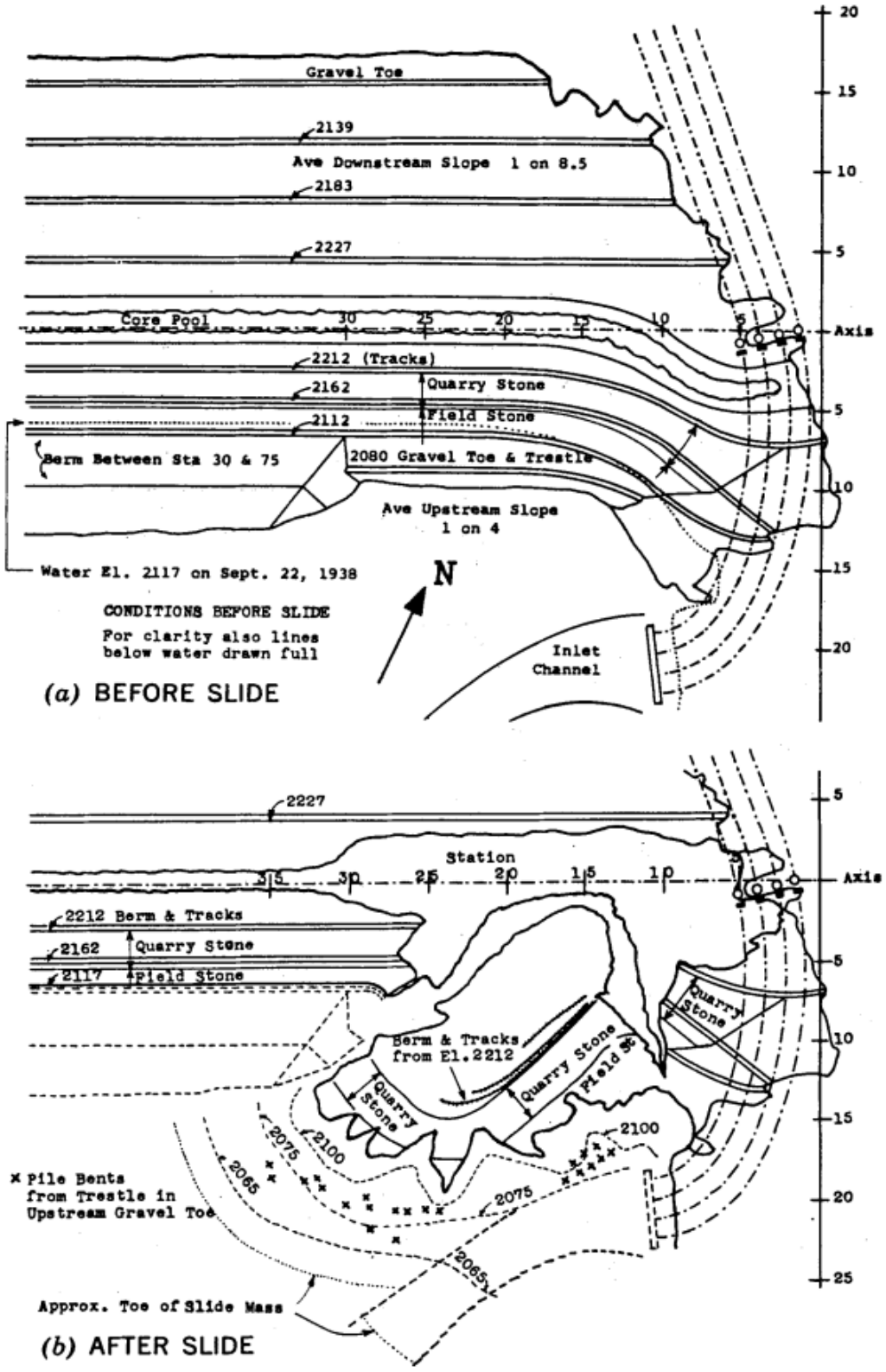

Figure A.2.3: (a) Pre-failure and (b) post-failure plan views of the east end of Fort Peck Dam, showing locations of identifiable elements and structures that can be tracked from inception of failure to final resting position. (Casagrande, 1965)

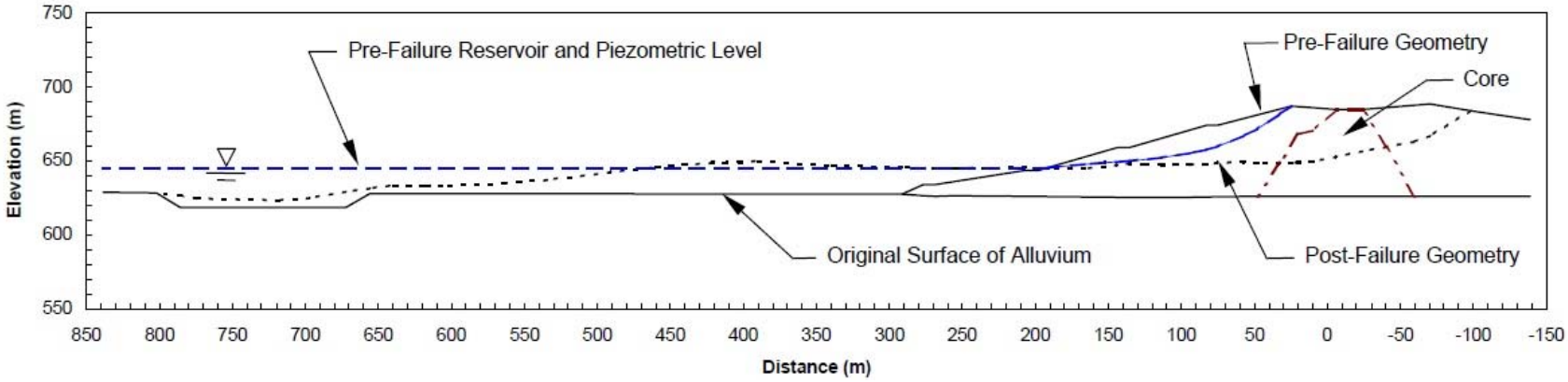

Figure A.2.4: Pre-failure and post-failure cross-section geometry of Fort Peck Dam. (from Olson, 2001; after Middlebrooks, 1942 and Casagrande, 1965)

Casagrande also summarized his initial observations upon visiting the site; noting that large, intact blocks of the embankment travelled "like floating islands in a mass of thoroughly disturbed materials". He also noted that the materials between the intact blocks was "dangerously quick", and that numerous sand boils were still actively discharging both sand and water ten days after the failure.

Following the initial investigations, a debate arose as to the actual cause of the failure. This debate can largely be tracked in Middlebrooks (1942) and in the associated follow-on Discussions in the ASCE Journal. A Board of Consultants was formed to determine the cause of this failure, and their majority conclusion was that the failure had been triggered by sliding along weak, nearly horizontal beds of Bearpaw Shale within the upper foundation. A few Board members had dissenting opinions, and felt that the initial movement may have been initiated by slippage along the shale beds, but that this, in turn, had triggered liquefaction of the overlying loose, saturated embankment shell and core materials (Gilboy, 1942; Casagrande, 1965). Gilboy summarized the expert panel minority view nicely as "liquefaction was triggered by shear failure in the shale, and the great magnitude of the failure was principally due to liquefaction."

Soil liquefaction was not very well understood at the time of the failure, and this debate was in part a product of the era; and so the majority opinion of the original Board of Consultants was that the shale beds were the principal culprits. Casagrande (1965) went on to better justify the alternate view that this was a liquefaction-induced flow failure, and his arguments and data were eventually compelling. As a result, this failure has been one of the most studied case histories for purposes of engineering evaluation of post-liquefaction strengths.

A.2.3 Geology and Site Conditions

Fort Peck Dam was constructed by hydraulic fill placement of local river sands and other alluvial soils (Casagrande, 1965). Most of the surficial clay deposits were removed prior to placement of base cutoff sheet piles and embankment fill. The remaining foundation alluvial deposits consist of alternating and interbedded layers of gravels, sands and clays, as can be seen in Figure A.2.5, which has an exaggerated vertical scale. Also shown in Figure A.2.5 is the contact between the site's alluvium and the underlying Bearpaw clay-shale deposit, which consists of layers of shale interbedded with thin layers of bentonite (Casagrande, 1965; Marcuson and Krinitzsky, 1976).

An extensive site investigation was performed at the Fort Peck Dam site as part of the static and seismic stability studies reported in Marcuson and Krinitzsky (1976). Figure A.2.6 shows a cross-section of the repaired and completed dam, and the locations of a number of the SPT borings performed as part of these studies. A number of rotary wash borings with SPT measurements were performed, and these will be discussed in more detail in the Sections that follow. Figure A.2.6 also shows the zonation developed by the USACE at station 42+00, based on these borings as well as previous cross-sections from the original failure investigations. This mid-1970's site investigation also included a limited number of Dutch cone soundings, but only one of the soundings penetrated into the sandy hydraulic fill materials of the dam shells.

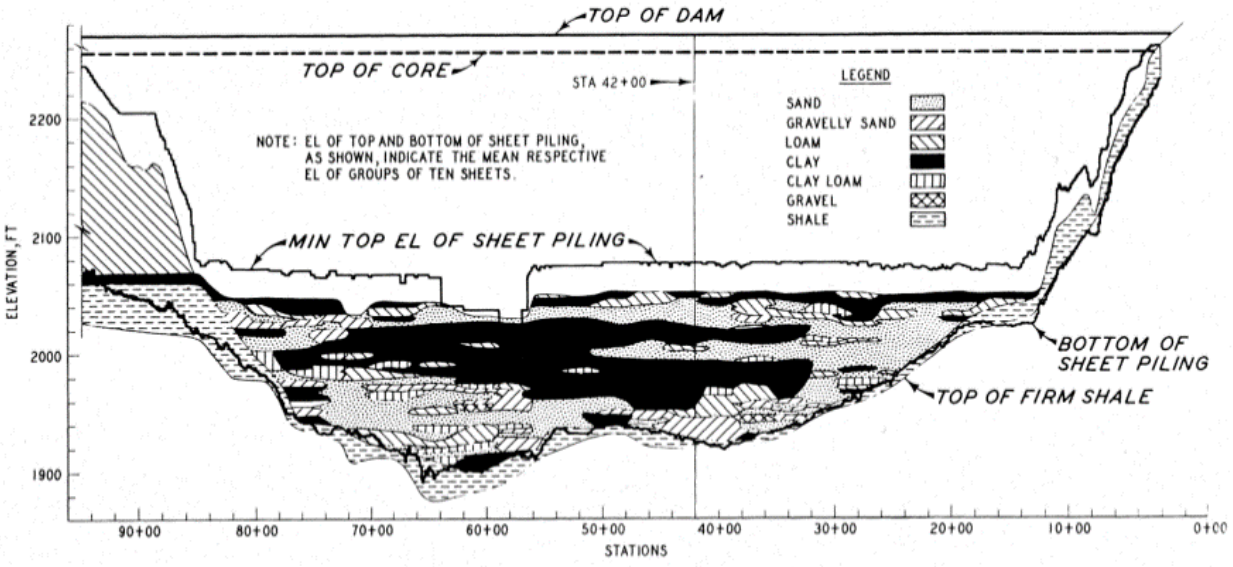

Figure A.2.5: Foundation site conditions at Fort Peck Dam. (Marcuson and Krinitzsky, 1976).

A.2.4 Evaluation of Representative Post-Liquefaction Residual Strength

A.2.4(a) Initial Yield Stress Analyses

The pre-failure and post-failure cross-sections utilized for back analyses were based in large part on the cross-sections presented in Casagrande (1965), as presented in Figure A.2.7. Figure A.2.8(a) shows the pre-failure cross-section geometry modelled as the best estimate case. This figure also shows the best estimate failure surface for these initial yield stress analyses. Initial yield stress ($S_{r,yield}$) is defined as the theoretical post-liquefaction strength within liquefiable materials on the eventual failure surface that would be necessary to develop a calculated Factor of Safety equal to 1.0 for the pre-failure geometry.

The unit weights of the hydraulic fill materials at the time of failure above and below the phreatic surface were estimated considering the recent time since placement, the nature of the hydraulic fill materials that comprised the dam, the values used by other investigators, and data developed by available field studies. Conventional Mohr-Coulomb type shear strength parameters were estimated for non-liquefied soils on a similar basis. Table A.2.1 summarizes the best estimate material properties employed for these analyses. Additional analyses were performed, varying these properties, to investigate sensitivity of resulting calculated post-liquefaction residual strengths.

The principal stratigraphy shown in Figure A.2.8(a) is separated into three main layers: (1) the foundation strata, (2) the liquefied hydraulic fill zones, and (3) non-liquefied hydraulic fill. The location of the interface between the foundation strata and liquefied embankment soils is primarily based on the results of SPT tests and the geologic cross section presented in Marcuson and Krinitzsky (1976) at station 42+00. The interface between the liquefied and non-liquefied

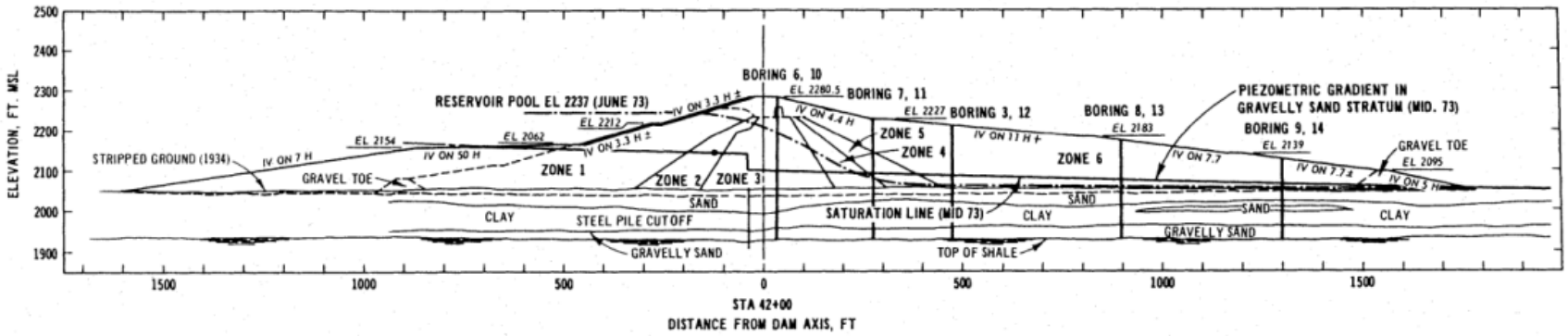

Zone	Elevation (ft)	Average D_{10} (mm)	Average Clay Content (%)
1 and 6	Below 2100	> 0.1	< 3
1 and 6	2100 – 2180	> 0.1	< 5
1 and 6	Above 2180	> 0.05	< 8
2 and 5	Below 2255	> 0.005	< 10
3	Below 2200	< 0.005	> 10 & < 30
3	Above 2200	< 0.01	< 30
4	Below 2255	Same as Zone 3 or Zone 5	
Sand Plugs	Below 2180	< 0.1	< 20
Above Sand Plugs	2180 - 2255	< 0.01	< 30

Figure A.2.6: Fort Peck Dam cross-section at Station 42+00. (Marcuson and Krinitzsky, 1976).

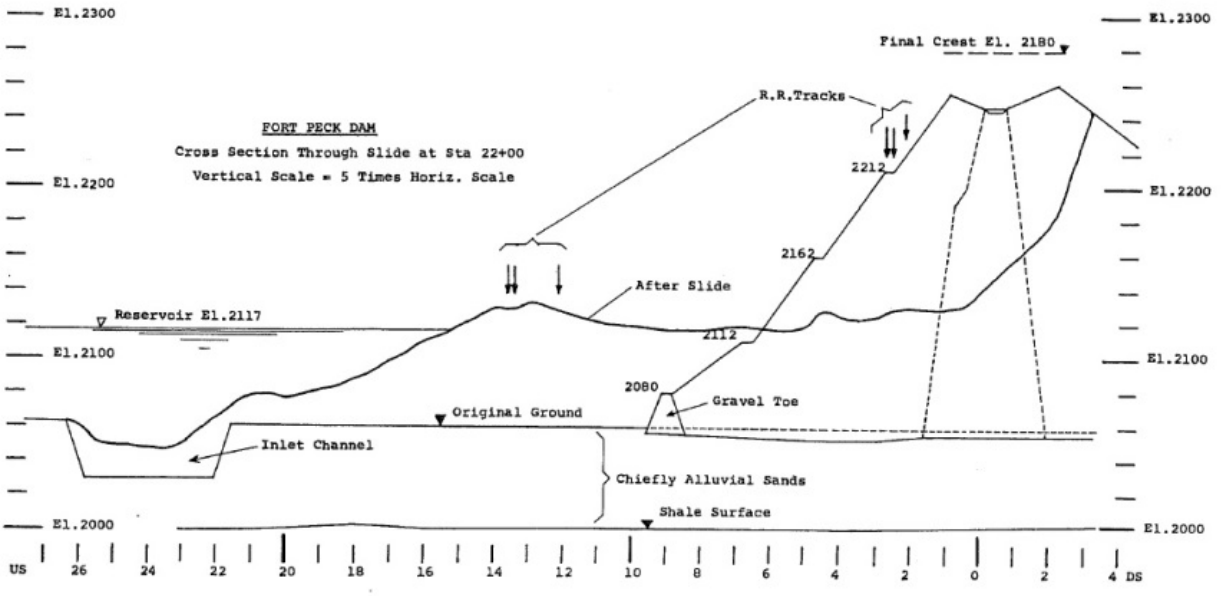

Figure A.2.7: Pre-failure and post-failure geometry of Fort Peck Dam at Station 22+00, with significant vertical scale exaggeration. (Casagrande, 1965).

Table A.2.1: Best estimate material properties for back-analyses of the failure.

Material	Unit Wt.	Mohr-Coulomb Strength Properties	
		Cohesion	Phi
Foundation	125 pcf	c′ = 0	Ø′ = 35°
Liquefied Hydraulic Fill	122 pcf	S_r = Back-Analyzed	Ø′ = 0
Non-Liquefied Hydraulic Fill	115 pcf	c′ = 0	Ø′ = 30

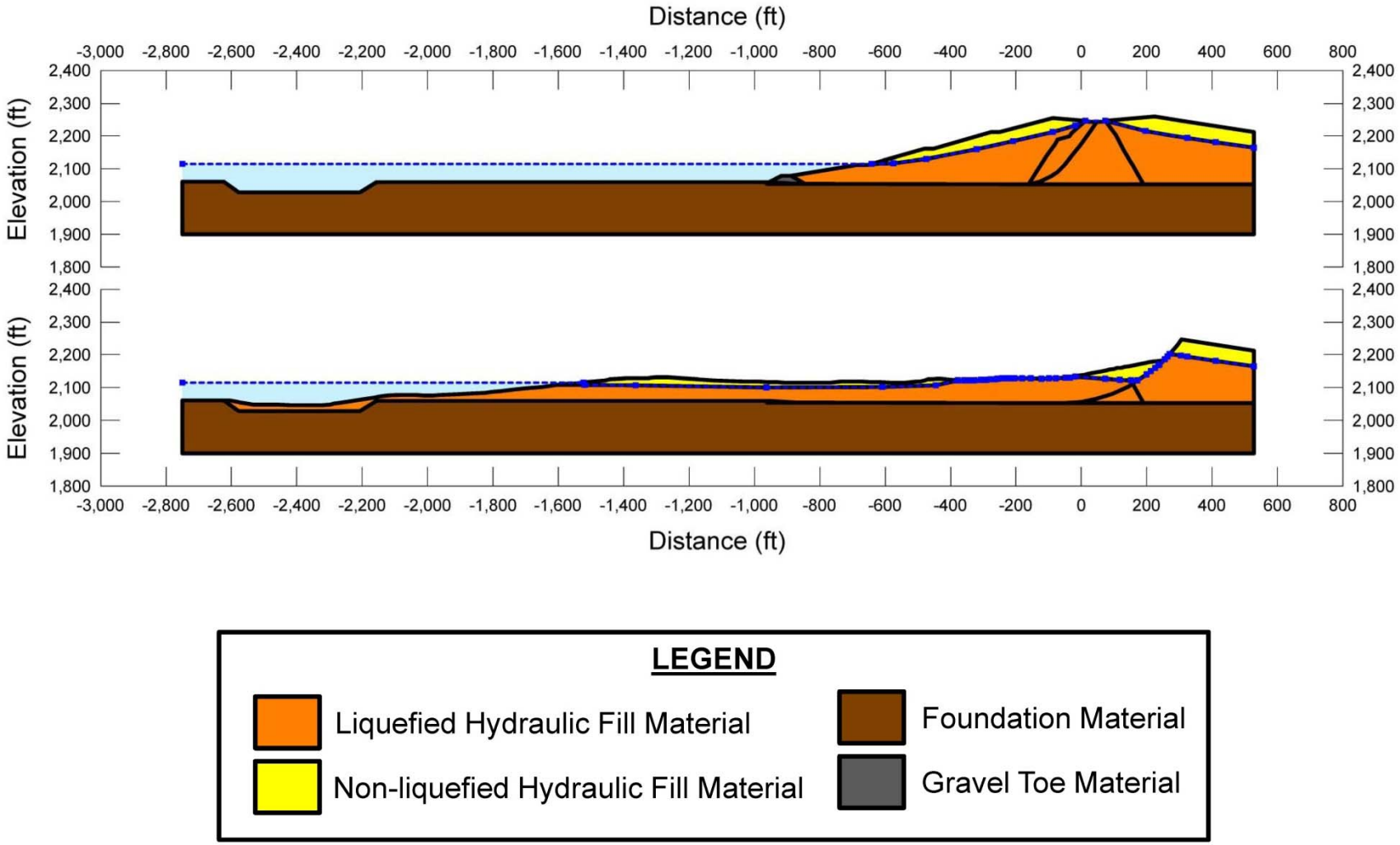

Figure A.2.8: Fort Peck Dam: (a) Pre-failure geometry and best-estimate failure surface for initial yield stress analyses, and (b) post-failure geometry and best-estimate failure surface for post-failure residual geometry analyses.

hydraulic fill material is based on the assumed phreatic surfaces on the upstream and downstream sides of the rising embankment fill. The locations of these phreatic surfaces are based on knowledge of the water level within the reservoir and the approximate elevation of the puddle core pool where material was actively being hydraulically placed at the time of the failure. With the control points at the upstream toe and the crest known, a phreatic surface was assumed in the relatively recently placed hydraulic fill. Resulting calculated post-liquefaction strengths were found not to be very sensitive to the phreatic surface modelled here, as the principal failure occurred at depth.

Conditions within the central "puddle core" and transition zones are complicated, and represent a challenge with regard to back-analyses of the post-liquefaction strength of the hydraulic fill materials of the upstream shell. Hydraulic fill was deposited from rail lines along the upstream and downstream edges of the rising fill, and was contained within starter dykes at the upstream and downstream sides. As a result, coarser materials tended to settle nearer the upstream and downstream faces, while finer soils tended to settle more slowly, and thus to propagate towards the center of the rising dam. The intent was to construct an embankment with a naturally transitioning gradation from coarser, free draining sandy shells towards a more clayey "puddle core".

In actuality, the result was more randomly variable and poorly controlled, with layers and lenses of coarser and finer soils interlayered together in a complex manner. Nine of the SPT borings from the 1976 stability studies provide the best available basis for characterization of the hydraulic fill materials comprising the dam. These 1976 stability studies were focused mainly on the potentially "liquefiable" coarser sands and silty sands of the shell zones, and only two of these nine borings penetrated the central "puddle core" and/or the adjacent "transition" zones. These two borings are presented in Figures A.2.9 and A.2.10. Boring No. 6 (shown in Figure A.2.9) was performed through the center of the "puddle core", as shown in the cross-section of Figure A.2.6. A second boring (Boring No. 10) was co-located at the same central core location, but it was performed for installation of a piezometer and was not carried to full depth and was not performed or logged as an SPT boring. Boring No. 7 (shown in Figure A.2.10) was performed through the downstream edge of the downstream side "transition" zone, as also shown in the cross-section of Figure A.2.6. Close examination of Borings No's. 6 and 7 show that layers and lenses of relatively clean sandy soils, with variable silt and clay content, extend right through the central "puddle core", while clayey and silty layers can also extend away from the central puddle core zone and across the adjacent "transition" zones and likely into the "shells".

As shown in Figures A.2.8(a) and A.2.8(b), the main failure surface passes through the lower portion of the central puddle core region as well as both the upstream and downstream transition regions. The apparent initial (smaller) failure surface nearer to the face of the dam passes through the upper portions of the central puddle core zone as well. Modeling of conditions, and shear strengths, across the central "puddle core" and "transition" embankment region is thus an important issue in back-analyses of the 1938 slope failure. Different approaches have been taken by different investigation teams and analysts. In these current studies, it was considered that some fraction of the sandier materials in the central "puddle core" were likely to perform as potentially liquefiable hydraulic fill soils, and that conditions were even more "mixed" in the even more variable adjacent transition zones. As a best estimate case,

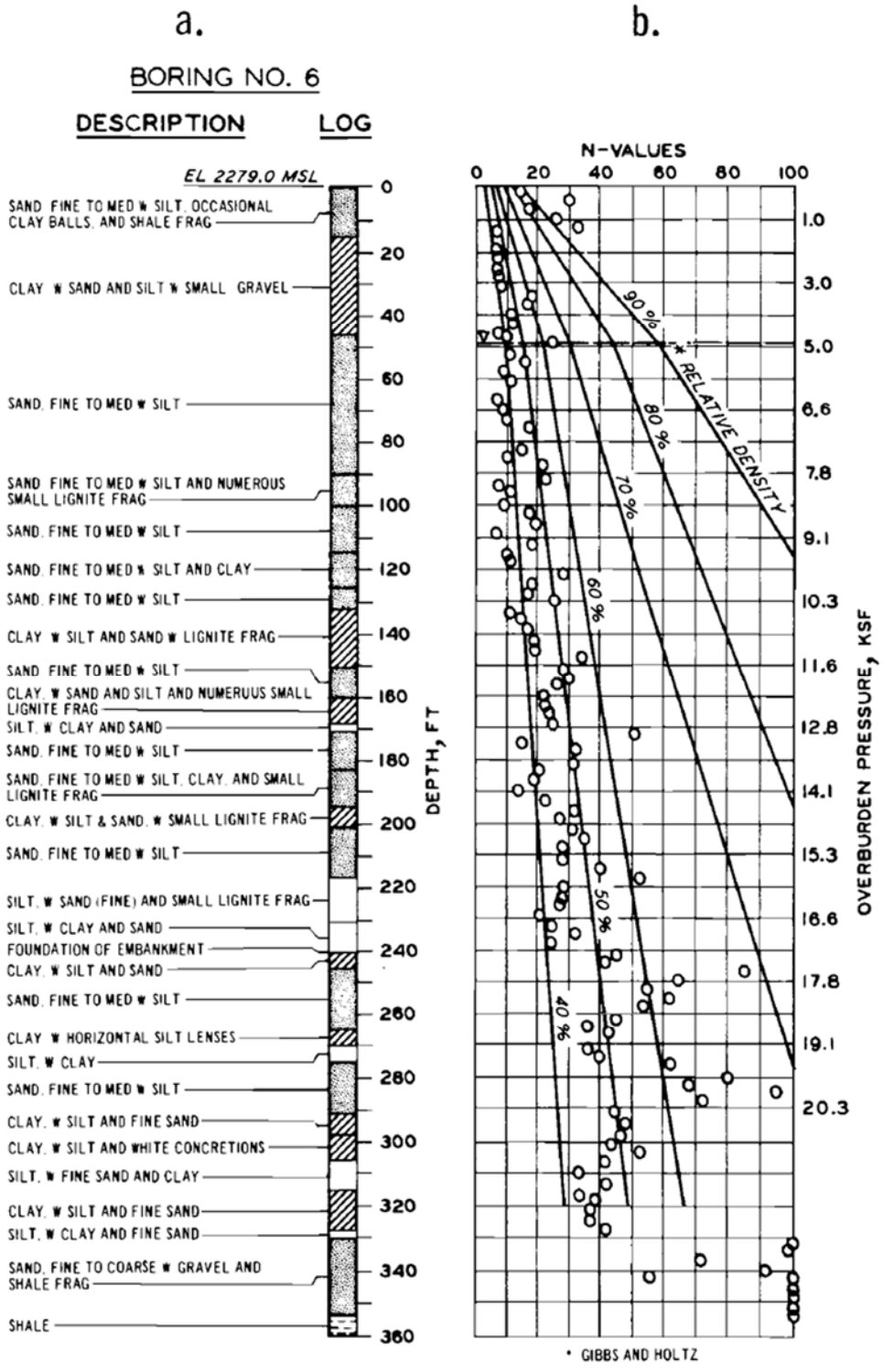

Figure A.2.9: Boring No. 6 through the central puddle core zone of Fort Peck Dam. (Marcuson and Krinitzsky, 1976)

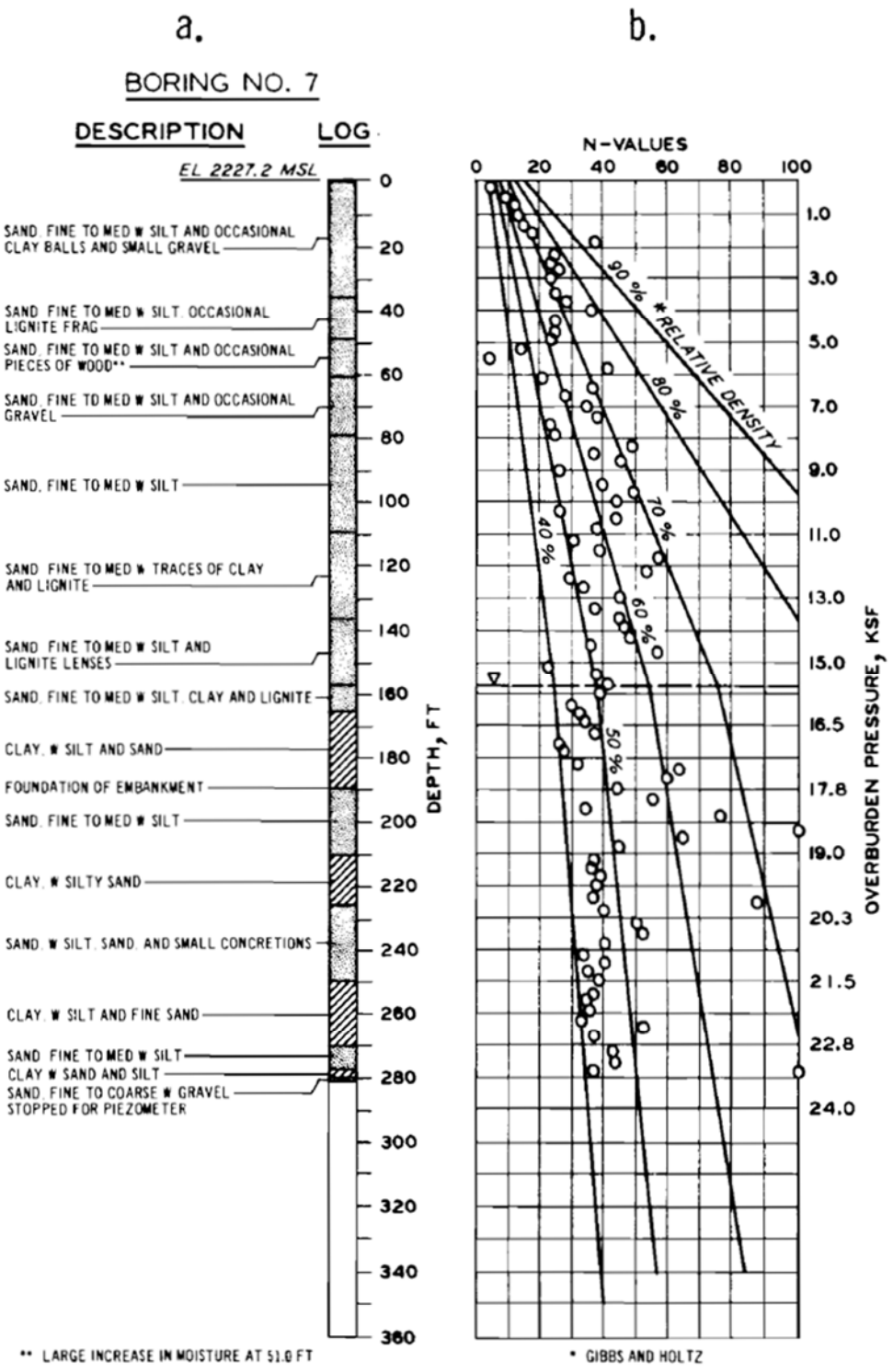

Figure A.2.10: Boring No. 7 through the upstream transition zone of Fort Peck Dam. (Marcuson and Krinitzsky, 1976)

it was considered that a considerable majority of the failure surface passing through the central "puddle core" zone shown in Figures A.2.5 through A.2.7 would pass through soils that would behave as clay-dominated materials with regard to undrained shear strength, and that only a small fraction of any potential failure surface would pass through soils that would behave as classically "liquefiable" sandy and silty soils. Similarly, it was assumed that a majority (but not all) of the transition zones would be best modeled as being comprised of soils likely to behave in a more classically "liquefiable" manner.

In this current study, the central puddle core zone materials were modeled as "clayey" soils with undrained residual strength $S_{u,r}$, and the adjacent transition zones were modeled as being comprised of potentially liquefiable hydraulic fill materials with post-liquefaction strength S_r. It is clear that cohesive, clayey soils occur into the transition zones, and that more cohesionless soils extend into the core zone, and this simplified modeling is intended to accomplish some "averaging" across this complicated region.

The lowest of the central puddle core and transition fill materials had been in place for a bit less than four years when the 1938 slope failure occurred. As a result, it was assumed that these primarily clayey soils in the central region of the embankment were likely underconsolidated to varying degrees. It is also noted, however, that largely horizontal layers and lenses of coarser, more free-draining sandy and silty soils would have helped to promote lateral drainage and would have accelerated consolidation of the more clayey materials to some degree. It is difficult to make a precise estimate of the undrained shear strength, and especially the large-strain undrained residual shear strength, of the clayey soils in this central embankment region. More recent testing data is of little assistance here, as multiple decades had passed and these soils had consolidated and gained strength over that period. As a best estimate scenario, it was assumed that these partially under consolidated soils would have an S_u/P ratio of approximately 0.1 to 0.18, and that they would also have significant sensitivity due to their loose (underconsolidated) condition. Sensitivity ratios of approximately 3 to 5 were assumed for these soils which were not likely flocculated (as they were freshwater deposited), but which were likely strongly contractive when sheared. This leads to a residual strength ratio in the range of $S_{u,r}/P \approx 0.02$ to 0.06 for these clayey soils. A value of $S_{u,r}/P$ of 0.04 was taken as the best estimate case, and additional analyses were performed exploring the likely range (upper and lower bounds) with $S_{u,r}/P = 0.02$ and $S_{u,r}/P = 0.06$ to study the sensitivity of calculated post-liquefaction strengths to these modeled conditions in the central embankment region.

Olson (2001), and Olson and Stark (2002) made a slightly different set of modeling assumptions. They also modeled shear strength across the lower portion of the central "puddle core" as being clay-dominated, with an average shear strength of $S_u \approx 4.8$ kPa (~100.3 lbs/ft^2), regardless of depth or effective overburden stress. They do not explain this choice. Most other investigators do not even describe how they modeled shear strengths across this region, so this is often a "black box" within back-analyses for this particular case history.

Based on the best estimate analysis of the failure scenario shown in Figure A.2.8(a), the resulting best estimate value of average initial yield stress (the value of post-liquefaction $S_{r,yield}$ required to produce a calculated Factor of Safety equal to 1.0 for pre-failure geometry) within the liquefiable hydraulic fill was found to be $S_{r,yield} \approx 2{,}370$ lbs/ft^2 for the smaller initial failure

surface shown in Figure A.2.8(a) and $S_{r,yield} \approx 2{,}100$ lbs/ft^2 when the final failure surface shown in Figure A.2.8(b) is imposed on the initial geometry . The representative value was then taken as intermediate between these two at $S_{r,yield} \approx 2{,}235$ lbs/ft^2. Failure surfaces were varied to evaluate sensitivity to modelling assumptions and details. Shear strengths across the central embankment were also varied, as discussed above, to evaluate sensitivity to modelling assumptions and details. Strengths of the non-liquefied embankment soils were also varied. Resulting values of representative $S_{r,yield}$ for variations considered reasonable were on the order of $S_{r,yield} \approx 2{,}023$ to $2{,}468$ lbs/ft^2. Initial yield stress is not intended to represent the operative post-liquefaction strength that controlled the full field failure that occurred, but it is useful in calibrating and checking the more rigorous analyses that will follow, and in development of relationships useful in evaluation of other back-analysis case histories.

Stark and Olson also calculated initial yield stress ($S_{r,yield}$), and they reported a best estimate value of $S_{r,yield} = 82.9$ kPa ($1{,}731$ lbs/ft^2), with a range of $S_{r,yield} = 69.9$ to 89.6 kPa ($1{,}441$ to $1{,}871$ lbs/ft^2), in generally good agreement with the values calculated in these current studies.

A.2.4(b) Residual Strength Analyses Based on Residual Geometry

Similar "static" stability analyses were performed to evaluate the "apparent" shear strength within the liquefiable hydraulic fill (S_r) that would result in a calculated Factor of Safety equal to 1.0 for the post-failure residual geometry of Figure A.2.8(b). Assumptions and modeling details were largely the same as described in the previous Section A.2.4(a), and sensitivity analyses with varying combinations of modeling and parameter details were performed here as well.

An additional modeling detail that affects these analyses is the possible occurrence of hydroplaning as the toe of the embankment failure mass enters rapidly into the reservoir, or the possibility of the failure mass being borne along upon weak reservoir sediments of even lower strength than the liquefied embankment materials as the toe of the embankment failure mass enters rapidly into the reservoir. As this was the first filling of the reservoir, it is assumed that there were not yet any significant deposits of loose, weak reservoir sediments accumulated. The question of hydroplaning is a more interesting one. The incremental momentum and displacement analyses described in Section A.2.4(c), which follows, show that peak translational velocities were momentarily as high as approximately 30 feet per second and more at the toe; a rate at which some degree of hydroplaning could occur (see Section 4.2.1). Scale model experiments for soil masses entering into water indicate, however, that hydroplaning seldom occurs over a distance beneath the base of materials entering the reservoir of more than about ten times the thickness of the entering soil thickness (see Section 4.2.1). In these studies, it was assumed that hydroplaning had negligible effect on the residual condition, because the shear strengths at the base of the forward tip of the materials that entered farthest into the reservoir were not modeled as contributing to overall stability of the larger failure mass farther upslope. Hydroplaning will be discussed again in the incremental momentum and displacements analyses described in Section A.2.4(c), which follows.

The full length of the potential failure plane at the base of the residual slide mass was not used to calculate $S_{r,resid/geom}$ because if the extended extreme toe section of the displaced slide mass developed significant resistance to translation, then the failure plane would have risen upwards to daylight through the very thin residual deposits of material at the final toe. Accordingly, the failure surface was assumed to "daylight" as a downstream station of approximately -1,800 feet in Figure A.2.8(b).

Based on the modeling conditions and assumptions described above, the resulting best estimate value of the post-liquefaction shear strength required for FS = 1.0 with residual geometry is $S_{r,resid/geom} \approx 174$ lbs/ft^2. The approximate range, based on reasonable variations in parameters and modeling details, is $S_{r,resid/geom} \approx 150$ to 202 lbs/ft^2.

Olson (2001) also calculated $S_{r,resid/geom}$ for this case history, and reports a best estimate value of $S_{r,resid/geom} \approx 3.8$ kPa (79 lbs/ft^2), and a range of $S_{r,resid/geom} \approx 0.7$ to 15.1 kPa (15 to 315 lbs/ft^2). These values are in good agreement with the values calculated by the current studies, except that Olson's lower bound is much lower. Olson's lower bound value appears to be very low, and insufficient details are presented so this cannot be examined in further detail.

Overall, it was judged that there was good agreement between the two sets of analyses, despite differences in analysis and modeling details and choices made by the two investigation teams.

A.2.4(c) Incremental Momentum and Displacement Analyses and Overall Evaluation of Post-Liquefaction Strength

Full incremental momentum and displacement analyses were performed using similar modeling assumptions and details as described in the preceding Sections. Figure A.2.11 shows the best estimate case analysis. It is difficult to see in detail, owing to the scale of the overall problem and the very large lateral displacements that accrue. But it is useful to see the progression of the increments in a single consecutive sequence. This figure is then repeated in six enlarged increment figures in Figure A.2.12 so that more detail can be seen. In these enlarged figures, the progressive locations of the overall center of mass of the active failure mass are also shown.

The modeled stratigraphy, phreatic surface, and failure progression can be seen in Figures A.2.11 and A.2.12. Figure A.2.13 then shows (1) acceleration vs. time, (2) velocity vs. time and (3) displacement vs. time for the center of gravity of the failure mass of Figures A.2.11 and A.2.12.

A total of six cross-sections were used for the progression of the failure mass, due to the very large displacements that accrue, and also due to the potential complexity of this progression. Based on eye witness reports, as well as the post-failure geometry observed, the initial failure surface (first time step) passes through the front edge of the modeled puddle core. By the second step, the failure surface is then modeled to progress to the larger assumed eventual maximum

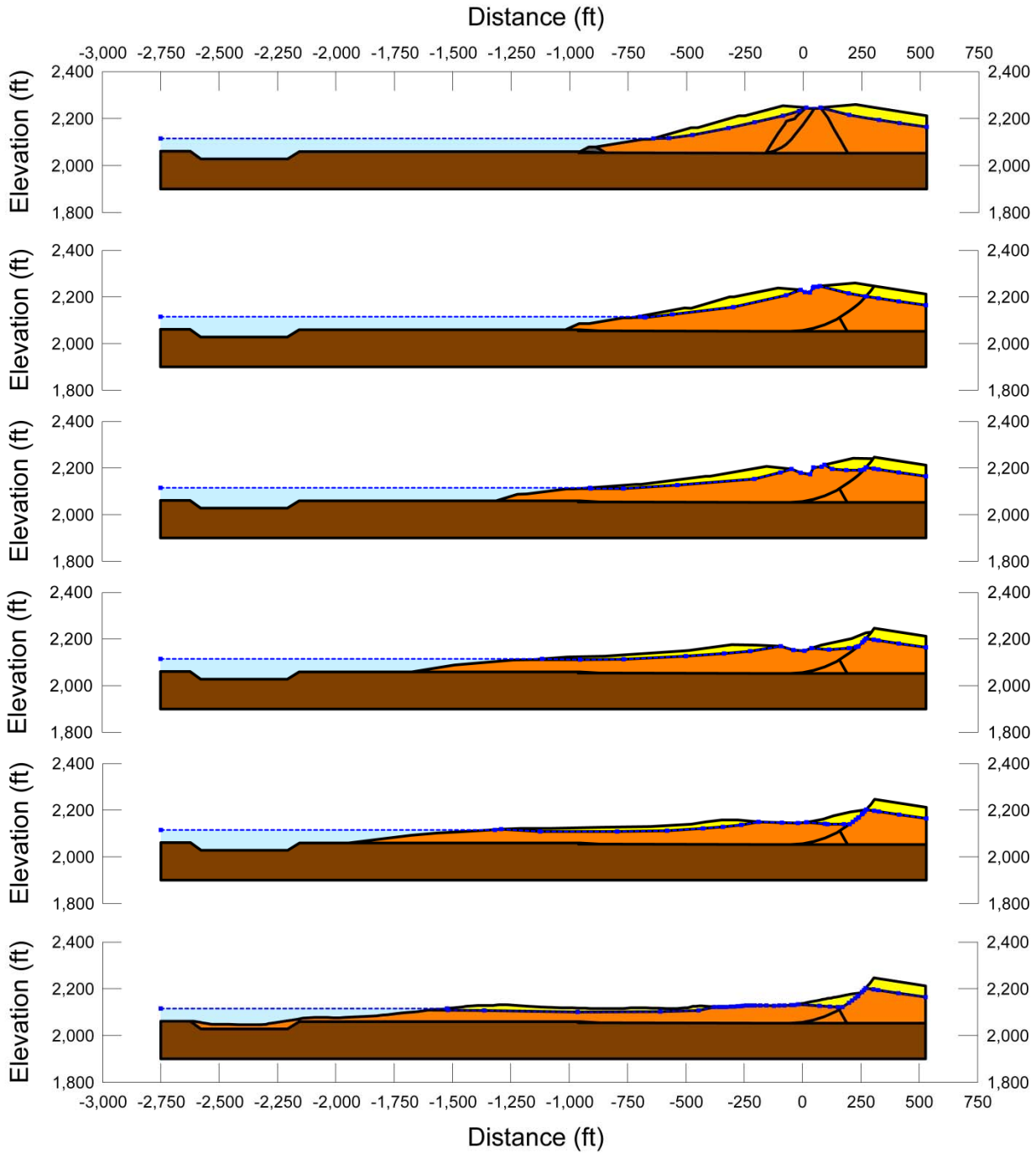

Figure A.2.11: Incremental displacement stages for the incremental momentum and displacement analyses for the best estimate scenario for Fort Peck Dam.

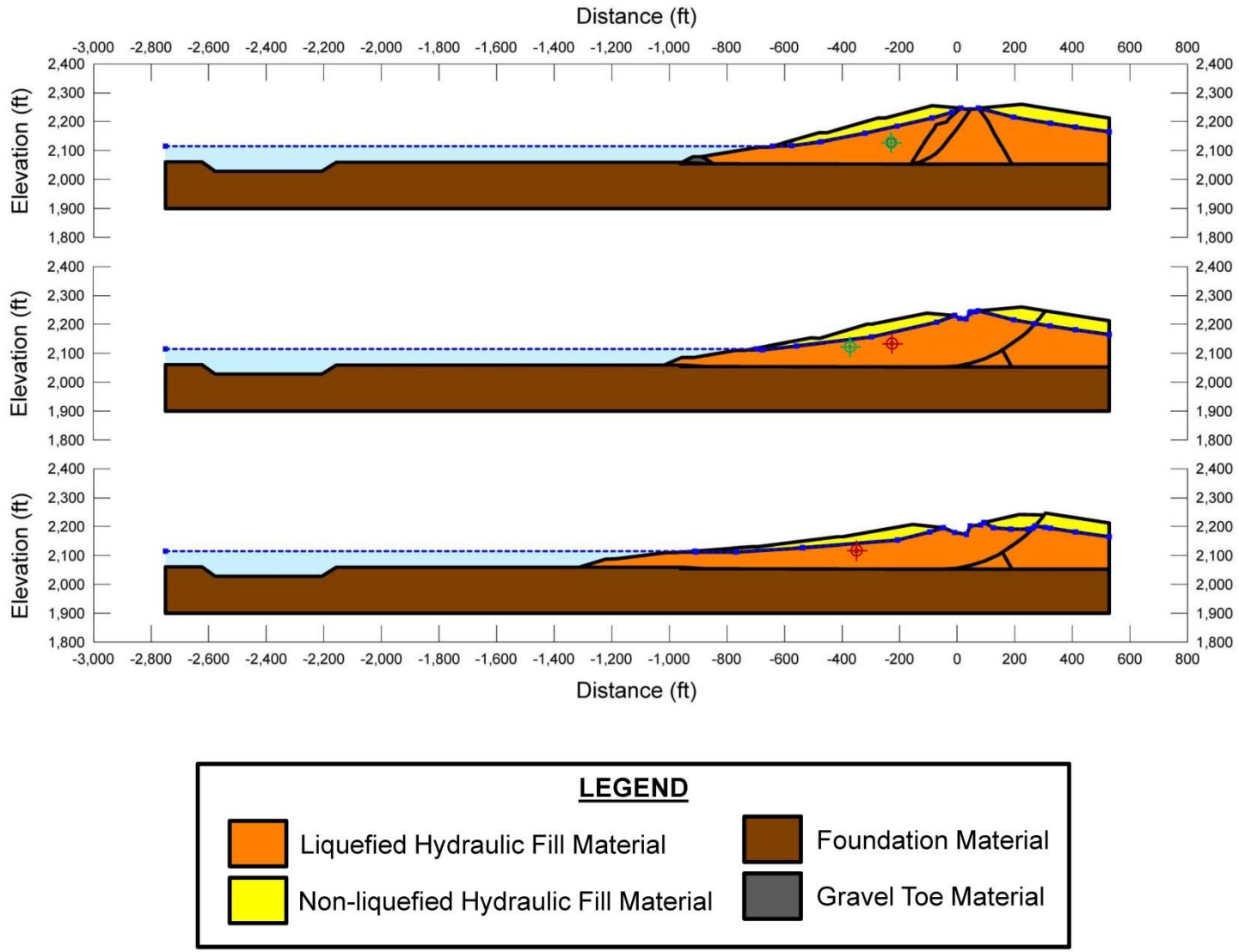

Figure A.2.12: Enlarged view of the incremental displacement stages for the incremental momentum and displacement analyses of Fort Peck Dam from Figure A.2.12 (first three incremental stages).

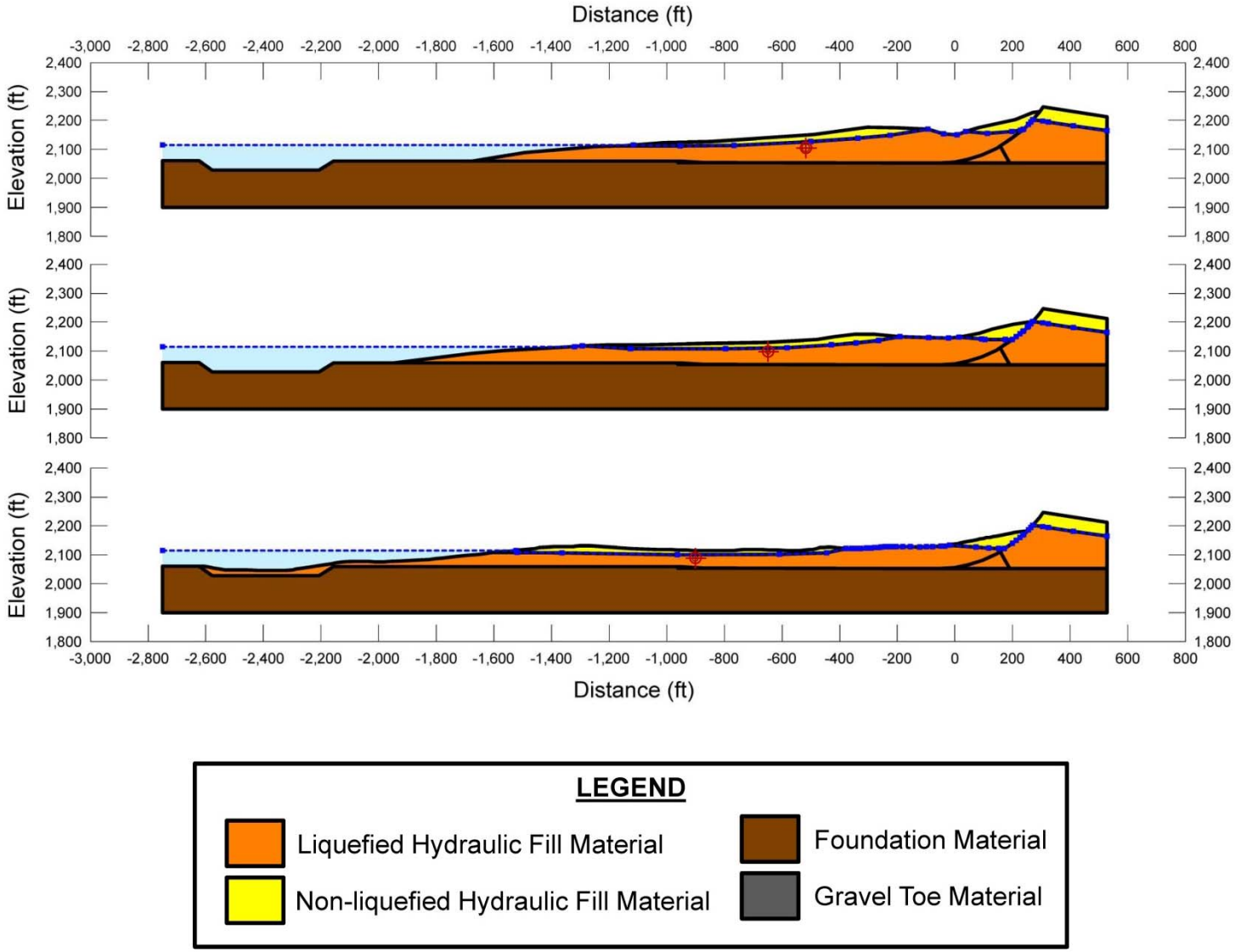

Figure A.2.12 (cont'd): Enlarged view of the incremental displacement stages for the incremental momentum and displacement analyses of Fort Peck Dam from Figure A.2.11 (additional three stages to completion).

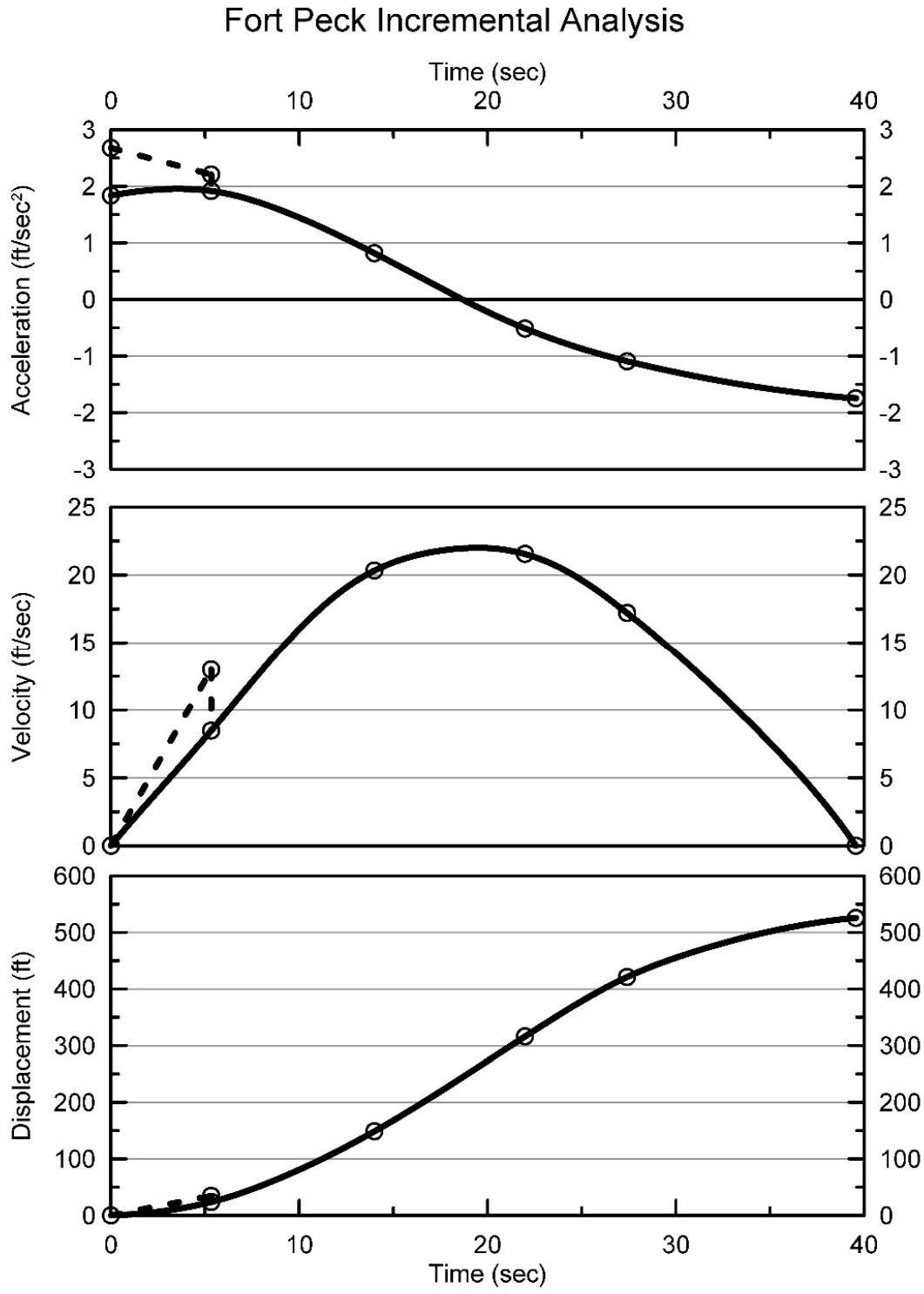

Figure A.2.13: Calculated development of (1) acceleration vs. time, (2) velocity vs. time and (3) displacement vs. time for the incremental momentum and displacement analyses of Figures A.2.11 and A.2.12.

failure surface. This is a slightly progressive development of failure, and it serves to provide for the separation observed at the "crest" section of the residual geometry.

This can be seen most clearly in the enlarged sequence of evolving cross-sections of Figure A.2.12. In this enlarged figure, centers of gravity have been added to the figure. The green cross-hairs of the first cross section are the initial position of the center of gravity delineated by the initial failure surface passing near to the front of the upstream crest. In the second figure, this initial failure mass has progressed, and the center of gravity has moved towards the reservoir. At this second stage, the failure of the eventual overall larger full failure mass along the most downstream back heel scarp begins to move. The red cross-hairs show the location of the new (combined) centers of gravity of the initial failure mass and the incremental additional mass. In the subsequent figures (stages), this center of gravity of the overall failure mass then moves towards the reservoir as the overall failure mass translates and elongates towards the upstream side.

Shear strengths for the "clayey" soils within the central puddle core zone are modeled with $S_{u,r}/P = 0.04$, and the shear strength assigned to the adjacent "transition" zones was the post-liquefaction strength S_r. Post-liquefaction strength (S_r) in the liquefied hydraulic fill soils of the shell and transition zones was iteratively adjusted until a value was found such that the final overall displacement agreed with the observed field displacement.

The failure occurred during first filling of the reservoir, so there were no significant accumulations of soft, weak reservoir sediments. The velocities calculated suggest that some degree of hydroplaning may have occurred as the toe of the embankment entered rapidly into the reservoir (see Section 4.2.1 of the main report). But the assumption that entrapment of fluids beneath the advancing front would occur over a lateral dimension of less than 10 times the thickness of the entering soils, coupled with the relatively flat pre-failure slope of the toe and increasing thinning of the toe failure "tip", suggest that hydroplaning would have likely been localized near to the advancing tip. For the best estimate case illustrated in Figures A.2.11 through A.2.13, it was assumed that hydroplaning would reduce the shear strength (S_r) at the base of the portion of the overall failure mass that entered into the reservoir and eventually moved farther upstream that lateral Station -1,800 feet in Figures A.2.11 and A.2.12 because embankment soils that eventually traveled farther upstream than this continued to thin and spread far beyond the more nearly coherent toe of the remainder of the failure mass. Even if hydroplaning had not occurred beneath these extreme toe materials, it would not have been possible for these extremely thin toe failure materials to provide significant resistance to movements of the failure materials farther to the right (farther upstream), and the failure surface would have "daylighted" upwards to the surface at about downstream Station -1,800 feet. So negligible shear strength was modeled for materials that passed farther downstream than lateral Station -1,800 feet from the crest centerline.

The resulting back-calculated post-liquefaction strength of the liquefied hydraulic fill that was calculated based on this particular combination of "best estimate" conditions is $S_r = 762$ lbs/ft^2.

A number of variations in parameters were analyzed to investigate variability and sensitivity with regard to calculated post-liquefaction strengths. The shear strengths of the

cohesive clayey soils in the central puddle core Zone C were modeled with strengths ratios as low as $S_{u,r}/P = 0.02$, and as high as 0.06. Friction angles in the non-liquefied soils above the phreatic surface were increased and decreased by 3°. The maximum average reduction in average shear strength at the base of the portion of the embankment failure mass that entered into the reservoir due to potential hydroplaning was taken as 90%, and the lateral distance upstream of the advancing toe was increased to nearly twice the best estimate scenario, and reduced to zero. Unit weights were varied up and down by several ponds per cubic foot.

Based on combinations of modeled conditions considered to be reasonable, the range of calculated values of representative S_r was found to be $S_r \approx 575$ to 929 lbs/ft^2. It was the judgment of this engineering team that this represented a range corresponding to approximately +/− 1.5 standard deviations. This range was nearly symmetric about the best estimate value of 762 lbs/ft^2, so no significant further adjustments were necessary. Overall, based on an assumed normal distribution, the best estimate (median) value of post-liquefaction strength from these studies was judged to be

$$\overline{S}_r = 762 \text{ lbs/ft}^2$$

with a standard deviation of

$$\sigma_{\overline{S}} = 118 \text{ lbs/ft}^2$$

The best previous studies for cross-comparisons here are those of Davis et al. (1988), Olson (2001) and Wang (2003), all of whom specifically performed analyses incorporating dynamic inertial effects. As shown in Table A.2.2, the results calculated here are just slightly higher than the other investigation teams in this group. The details of Wang's analyses are not presented, but it is noted that his results agree well with this current study. The full details of Davis' analyses are also not presented, but his value is in reasonably good agreement as well. The studies of Davis et al. and of Olson and Stark did not consider hydroplaning and so may be somewhat conservative.

Additional investigators have also analyzed this case, including Lucia (1981), Bryant et al. (1983), Seed (1987), Seed and Harder (1990), and others. The estimated S_R values from these previous studies range from approximately 240 to 599 lbs/ft^2, and serve to demonstrate the considerable variability in previous estimates made. Many of these earlier analyses employed conservative simplified approaches, and it is to be expected that their results would provide generally lower values of S_r.

A.2.5 Evaluation of Representative SPT Penetration Resistance

As part of the seismic stability analyses of Fort Peck Dam in the study reported by Marcuson and Krinitzsky (1976), a total of nine investigative SPT borings were drilled in the dam's crown and downstream slope. It is assumed that these SPT borings provide data largely representative of the upstream side failure zone due to the approximate symmetry of hydraulic fill placement operations prior to the 1938 slope failure. But the upstream face was much flatter in slope than the downsteam face, so that the distance from the line of upstream side hydraulic

Table A.2.2: Representative values for the Fort Peck Dam case history of: (a) post-liquefaction strength (S_r), (b) initial vertical effective stress (σ_{vo}'), and (c) $N_{1,60,CS}$ developed by various investigation teams, and estimates of variance in each of these indices when available.

(a) Post-Liquefaction Strength:	
Olson (2001) and Olson and Stark (2002)	S_r = 570 psf, and range = 63 to 211 psf
Wang (2003) and Kramer (2008)	$\overline{S_r}$ = 671.5 psf, and $\sigma_{\overline{S}}$ = 130.1 psf
Davis et al. (1988)	S_r = 701 psf
This Study	$\overline{S_r}$ = 762 psf, and $\sigma_{\overline{S}}$ = 118 psf
(b) Representative $N_{1,60,CS}$ or $N_{1,60}$ Value:	
Olson (2001) and Olson and Stark (2002)	$N_{1,60}$ = 8.5 bpf, and range = 4 to 14 bpf
Wang (2003) and Kramer (2008)	$\overline{N_{1,60,CS}}$ = 15.8 bpf, and $\sigma_{\overline{S}}$ = 0.9 bpf
Poulos (1988)	$N_{1,60}$ = 5.3 blows/ft
This Study	$\overline{N_{1,60,CS}}$ = 13.5 bpf, and $\sigma_{\overline{N}}$ = 2.7 bpf
(c) Representative Initial Vertical Effective Stress:	
Olson (2001) and Olson and Stark (2002)	σ_{vo}' = 7,341 psf, with no range provided.
Wang (2003) and Kramer (2008)	Value of $\sigma_{vo}' \approx$ 7,466 psf is not well documented, and so is considered useful only as an approximate comparison. (See Section 2.3.8.1, and Table 2.3.)
This Study	$\overline{\sigma'_{vo}}$ = 7,258 psf, and $\sigma_{\overline{\sigma}}$ = 687 psf

fill spigots depositing material to the center of the final crest was significantly greater than for the downstream side spigots, so perfect symmetry did not occur.

These investigation borings were performed by the rotary wash method, and SPT were performed at fairly regular intervals. The results of the SPT were filtered to exclude the results from tests performed outside the zone where liquefaction was assumed to have potentially occurred, and also for tests where clay dominated the material tested in an individual test. The remaining tests were corrected to $N_{1,60,CS}$ values based on the corrections and adjustments for equipment, test procedure, rod length, effective overburden stress, and fines content as per Cetin et al. (2004), and with the effective overburden stress correction (C_N) of Deger (2014).

The resulting corrected SPT data were then binned into sets based on lateral station along the dam's axis and relative distance from the dam's centerline. Materials tended to have higher fines contents near the dam's centerline (beneath the crest), and lower fines contents farther out towards the faces. $N_{1,60}$ blowcounts uncorrected for fines, on the other hand, tended to increase a bit with distance from the centerline.

Borings 1 through 5, plus 8 and 9, were judged to be most likely representative of $N_{1,60,CS}$ values for the sandy hydraulic fill materials of the downstream side shell zone. These were examined to eliminate the few SPT performed in potentially clayey samples. A small number of very high $N_{1,60}$ values (2% of the total number of SPT) were also deleted based on the

assumption of gravel having potentially biased the results. The remaining SPT $N_{1,60}$ values were then binned jointly for these 7 borings, and both median and mean $N_{1,60}$ values were determined. The mean value was determined to be 13.7 blows/ft., and the median value was determined to be 13.3 blows/ foot. The representative $N_{1,60}$ value was taken to be the median value of $N_{1,60}$ = 13.3 blows/ft. Because the shell materials generally had low fines contents of between 0% to 10%, fines adjustments per Cetin et al. would increase this representative value by a factor of between 1.00 to 1.08. A factor of 1.04 was applied, and the estimated representative value of fines adjusted penetration resistance was then $N_{1,60,CS} \approx 13.8$ blows/foot.

A single boring (B-7) provided SPT N-values for soils within the downstream transition zone. Similar processing was performed for this boring, including elimination of SPT performed in clayey soils, deletion of spuriously high values (there were none of these), determination of the mean and median values of $N_{1,60}$, and application of fines adjustments. $N_{1,60}$ values were somewhat lower in this transition zone, with a mean of 12.6 blows/ft and a median of 12.5 blows/ft. The median value was taken as representative. Fines adjustments were higher in the finer soils encountered in the transition zone, and based on typical reported fines contents of between 10% to 30%, the representative value of fines adjusted penetration resistance was $N_{1,60,CS} \approx 14.8$ blows/ft. This value was considered along with the value of 13.8 blows/foot for the sandier shell zones calculated above. Based on approximate weighted averages based on contribution of the downstream shell and the transition zones to the overall failure surface, the representative penetration resistance was taken to be $N_{1,60,CS}$ = 13.9 blows/ft.

An additional adjustment was then made to account for likely "ageing" effects over the roughly four decades that elapsed between the date of the failure and the performance of SPT tests in the 1970's. It is known that both cyclic resistance to triggering of liquefaction, and also penetration resistances, increase somewhat over time since placement or since deposition. Quantification of this with regard to SPT penetration resistance is difficult however. There is some research available regarding increases in both SPT N-values and in CPT tip resistances over time, due in large part to the relatively common use of CPT to evaluate ground improvement by means of densification using vibro-densification, deep dynamic compaction, blasting, etc. (e.g.: Skempton, 1986; Schmertmann, 1987; Lewis et al., 2009; etc.). Skempton (1986) proposes an equation for estimation of increase in SPT N-values over time, but this should be considered highly approximate. Over a period from 1 year after placement to 40 years after placement, Skempton's relationship predicts an increase in N-values of approximately 37%, but this should be considered very approximate. Kulhawy and Mayne (1990) propose an alternate relationship, logarithmically linear over time, and this would predict an increase in N-values of approximately 8% over a period from 1 year after placement to 40 years after placement. It is clear that <u>some</u> adjustment should be made here; otherwise the "representative" $N_{1,60,CS}$ value based on the 1970's SPT data would overestimate the representative value at the time of the failure. Values of between 5 to 40 % were considered here. For conservatism in developing relationships between $N_{1,60,CS}$ vs S_r, an adjustment nearer to the low side was made here. In the end an adjustment of 10% was adopted. The representative blowcount of 13.9 blows/ft from the 1970's SPT data was then reduced by a factor of $1/1.10$ to a final best estimate of $\overline{N_{1,60,CS}} \approx 12.6$ blows/ft.

Only one other failure case history back-analyzed by these current studies had similar potential ageing effects, and that was the Wachusett Dam embankment failure. That failure

occurred in 1907, and modern SPT investigations were finally performed seven decades later. As described in Section A.1.1, the representative $N_{1,60,CS}$ value for that case (without correction for ageing effects) was found to be $\overline{N_{1,60,CS}} \approx 8.2$ blows/ft, and a similar adjustment of approximately 10% was then made for ageing effects to produce a final estimate of $\overline{N_{1,60,CS}} \approx 7.5$ blows/ft for the fine sand shell materials of the Wachsett Dam which had been loosely placed in thick lifts. Only two case histories among the thirty case histories back-analyzed warranted adjustments for "ageing" effects, and the adjustments applied were relatively minor. These had relatively little effect on the overall predictive correlations eventually developed based on the back-analyses of the full 30 case histories.

Uncertainty, or variance in the overall average or representative $N_{1,60,CS}$ value was not so much a function of variance in individual contributing N-values. Instead it was a function of (1) perceived differences in localized $N_{1,60,CS}$ values at different locations that did not appear to be consistently correlated with distance from the core, (2) uncertainty with regard to the use of downstream side SPT data to represent upstream side conditions, especially given the non-symmetric geometry of the wider upstream vs. downstream shells, and (3) passage of time (approximately four decades) from the occurrence of the slope failure to the performance of the field SPT investigations of the 1970's. Overall, it was judged that the penetration resistance of the potentially liquefiable hydraulic fill materials of the downstream shell and the transition zones would be suitably modeled with a normal distribution with mean (and median) $N_{1,60,CS}$ = 12.5 blows/ft, and with a standard deviation of $\sigma_{\overline{N}}$ = 1.7 blows/ft.

As shown in Table A.2.2(c), Olson and Stark developed a somewhat lower estimate of $N_{1,60}$ = 8.5 of blows/ft, and range = 4 to 14 blows/ft. Their $N_{1,60}$ values were not adjusted for fines, and so were lower than the fines-adjusted $N_{1,60,CS}$ values of the other studies. Kramer and Wang developed slightly higher estimates of $\overline{N_{1,60,CS}}$ = 15.8 blows/ft, with a lower standard deviation of $\sigma_{\overline{S}}$ = 0.9 blows/ft. They made no adjustment for ageing effects, and their estimate of standard deviation for this case was driven primarily by the variance within the large suite of SPT N-values available, and did not include the factors in the preceding paragraph above and so likely underestimated uncertainty to some degree. Poulos (1988) working with Davis et al. (1988) proposed a best estimate value of 5.3 blows/ft, but this was lower than the values proposed by any other investigators, and it was not intended to represent a mean or median estimate as Poulos took the "representative" value to be a less than median value within the range of blowcounts available based on the observation that failure would tend to pass through the weaker soils within the failure zones. Accordingly, his estimate is not directly comparable with the others and would be expected to be lower. Each of these investigation teams explain the general approach taken, but do not provide much detail with regard to fine points that might have affected their assessments here.

Overall, it is clear that there is significant uncertainty associated with estimation of representative $N_{1,60,CS}$ for this case history. The values of this current study fall fairly centrally within the ranges of values proposed by previous investigators, and appear to be reasonably well supported given the different approaches taken by the previous investigation teams.

A.2.6 Evaluation of Representative Initial Effective Vertical Stress

The overall best estimate value of the average initial effective vertical effective stress on portions of the eventual failure surface that pass through liquefiable materials was calculated to be $\sigma_{vo}' = 7{,}258$ lbs/ft^2, with a range of $\sigma_{vo}' = 6{,}548$ to $7{,}992$ lbs/ft^2 based on variations in parameters, unit weights and phreatic conditions considered to be reasonable. This was judged to represent a variance of approximately +/- 1 standard deviation, and this range was not fully symmetric about the best estimate value so some minor additional adjustment was made to develop the best characterization of

$$\overline{\sigma'_{vo}} = 7{,}258 \text{ lbs/ft}^2$$

and

$$\sigma_{\bar{\sigma}} = 687 \text{ lbs/ft}^2$$

Values for comparison are shown in Table A.2.2. Olson (2001) calculated an average initial vertical effective stress of $\sigma_{vo}' = 7{,}341$ lbs/ft^2, with no range provided. This agrees very closely with the value developed in these current studies. Average initial vertical effective stresses were not directly reported by Wang (2003) and Kramer (2008), but they were published more recently in the publication by Kramer and Wang (2015). As discussed in Section 2.3.8.1(a), the approach taken by Wang (2003) to evaluation of σ_{vo}' for his nine "primary" case histories (this is one of those nine) is not clearly explained, and it is also poorly documented. Wang's value of $\sigma_{vo}' = 7{,}466$ lbs/ft^2 also agrees very closely with the value developed in these current studies. Agreement between the values of (1) Olson and Stark (2001, 2002), (2) Wang and Kramer (2003, 2008) and (3) these current studies is excellent.

A.2.7 Additional Indices from the Back-Analyses

A number of additional results, and indices, can be extracted from the analyses performed. Some of these are useful in developing some of the over-arching relationships and figures presented in the main text of this report. These values are presented in Table A.2.3 below.

Table A.2.3: Additional results and indices from the back-analyses of the Fort Peck Dam embankment failure case history.

Maximum distance traveled by the center of gravity of the overall failure mass	528 ft.
Initial post-liquefaction Factor of Safety prior to displacement initiation, and based on best estimate value of S_r	FS = 0.43
Final post-liquefaction Factor of Safety at final (residual) post-failure geometry, and based on best estimate value of S_r	FS = 2.63

A.3 Uetsu Line Railway Embankment (Niigata, Japan; 1964)

A.3.1 Brief Summary of Case History Characteristics

Name of Structure	Uetsu Railway Embankment
Location of Structure	Niigata, Japan
Type of Structure	Relatively symmetric railway embankment
Date of Failure	June 16, 1964
Nature of Failure	Seismic, During the 1964 Niigata Earthquake (M_W = 7.5)
Approx. Maximum Slope Height	31 ft.

A.3.2 Introduction and Description of Failure

The Uetsu Line railway embankment failed during the Niigata Earthquake of June 16, 1964 (M_W = 7.5), and was initially investigated by Yamada (1966). Peak ground accelerations in the vicinity of the failure were estimated to be on the order of 0.2 g.

Figure A.3.1 shows a cross-section of the failure section, showing pre-failure and post-failure geometry (Yamada, 1966). Figure A.3.2(a) shows the interpreted pre-failure cross-section modeled in these studies, and Figure A.3.2(b) shows the post-failure cross-section modeled in these studies. These are based on the cross-section of Figure A.3.1, and they are shown at true (not exaggerated) vertical scale. The embankment crossed a relatively level valley and the slope of the ground adjacent to the railway embankment was on the order of only 1° to 2°. The final (residual, post-failure) slope of the liquefied embankment material that ran out to a distance of approximately 100 meters (~ 330 feet) beyond the initial embankment toe was estimated have been on the order of about 4°

The railway embankment was constructed from poorly compacted or uncompacted clean, loose, fine sand fill. Fines contents were less than 5%. The embankment at the failure location was founded atop a peat layer, as shown in Figure A.3.1, and this was in turn underlain by clays and sands. The liquefied embankment material that ran out past the original toe spread out thinly over the top of the upper (peat) foundation soils, without wrinkling or bulging the underlying soils, indicating that the strength of the liquefied embankment soils was apparently lower than that of the upper foundation soils. The phreatic surface at the time of the failure was not known, and it was inferred to have been at or near to the base of the embankment. Given the fine sands, some degree of capillary rise may have contributed to some minor additional saturation above the phreatic surface.

A.3.3 Initial Yield Strength Analyses

Figure A.3.2(a) shows the cross-section used in these studies for the best estimate case back-analyses performed to determine the initial yield stress, defined as the value of the post-

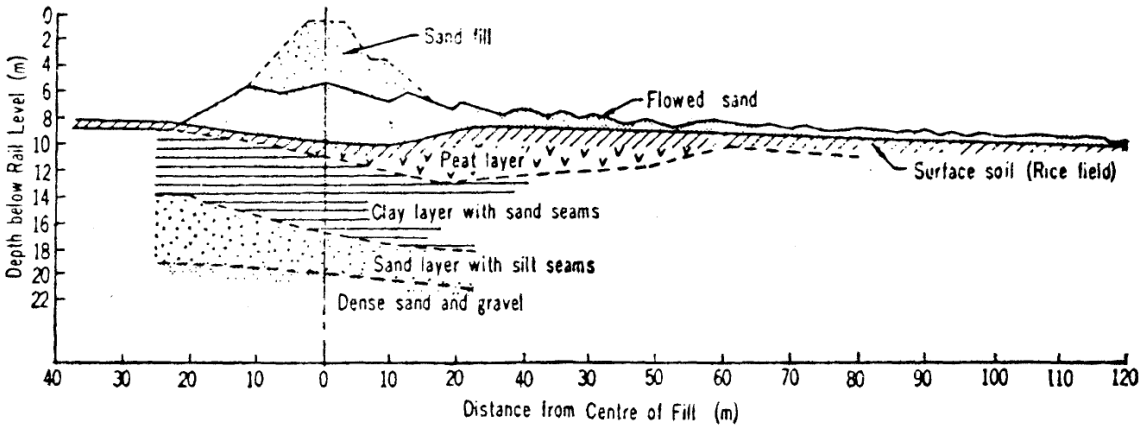

Figure A.3.1: Cross-section of the Uetsu Line railway embankment showing pre-failure and post-failure geometries (from Yamada, 1966)

liquefaction strength $S_{r,yield}$ within the liquefiable saturated lower embankment fill required to produce a calculated Factor of Safety equal to 1.0 for pre-failure geometry.

Based on an eyewitness description, it appears that this failure initiated near the face of the slope and then progressed as an incrementally progressive failure that retrogressed towards the back heel in a series of steps or slices. Based on an assumed phreatic surface that passes approximately through the mid-height of the slope, and exits at the toe, a search was made for the most critical static failure surface assuming liquefaction had been "triggered" in all potentially liquefiable embankment materials below the phreatic surface. This exercise showed that the most critical potential failure surfaces for this set of assumptions would have been for a failure initially closer to the slope face than the final rear scarp shown in Figure A.3.1 and A.3.3(b).

Figure A.3.2(a) shows most critical of the failure surfaces analyzed (the failure surface requiring the highest value of $S_{r,yield}$ to produce a calculated Factor of Safety of 1.0). Non-saturated embankment sand materials above the phreatic surface were modeled with $Ø' \approx 28°$, and a unit weight of $\gamma_m \approx 114$ lbs/ft^3. Materials below the phreatic surface were considered to liquefy, down to the base of the embankment, and were assigned an undrained post-liquefaction yield strength of $S_{r,yield}$ that was constant along any given failure surface, and a unit weight of $\gamma_s \approx 118$ lbs/ft^3. Results for the most critical initial yield surface shown in Figure A.3.2(a) were $S_{r,yield} = 355$ lbs/ft^2. In these analyses, it was assumed that failure at the toe occurred within the base of the liquefiable embankment fill.

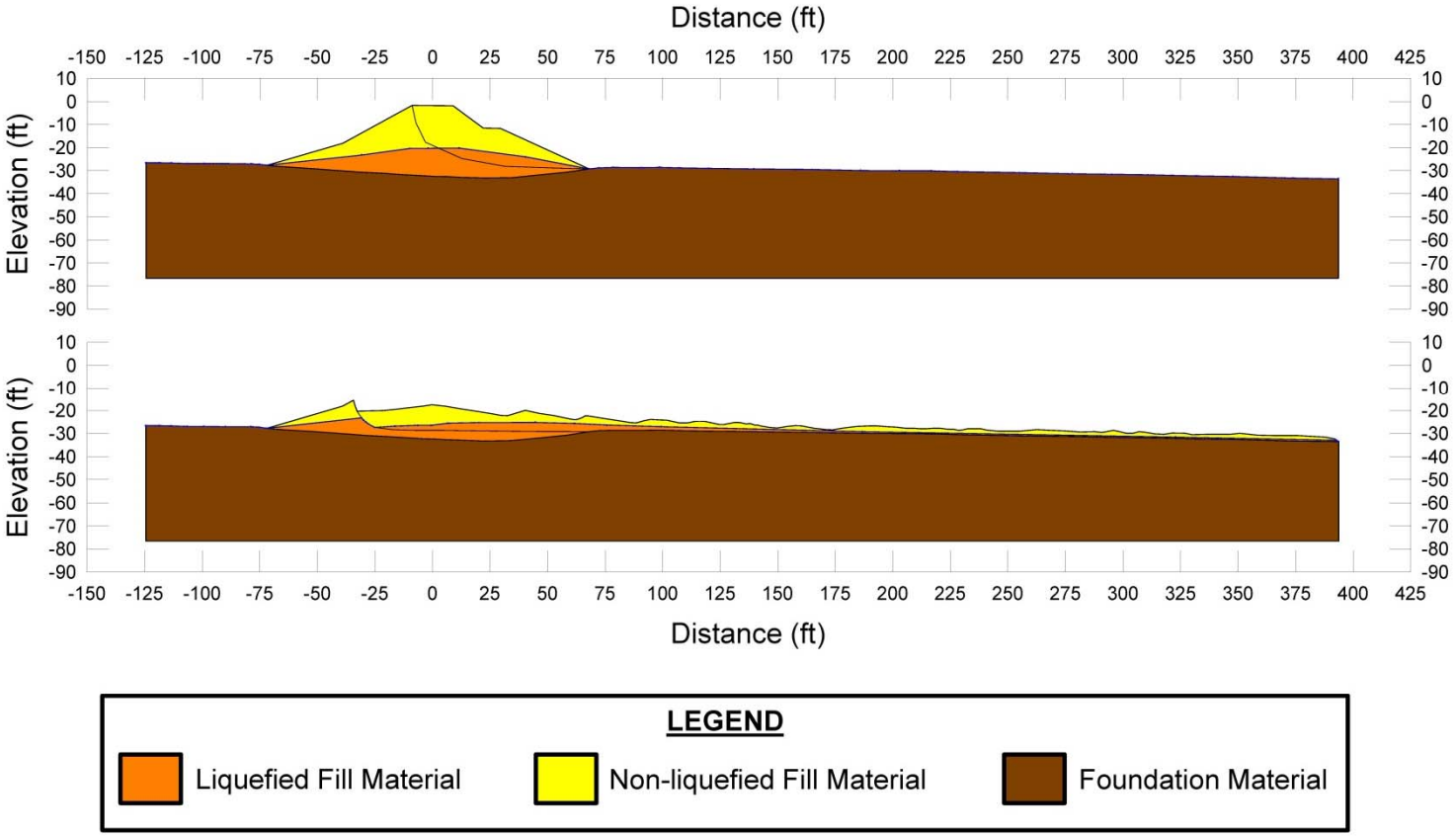

Figure A.3.2: Uetsu Railway Embankment: (a) Pre-failure geometry and best-estimate failure surface for initial yield stress analyses, and (b) post-failure geometry and best-estimate failure surface for post-failure residual geometry analyses.

Parameters and geometry were then varied to examine potential variability. The location of the phreatic surface was varied, raising it by up to 0.75 m at the center of the base of the embankment, and lowering it by up to a similar distance. Unit weights were also varied over the ranges considered likely, and the friction angle of non-liquefied material above the phreatic surface was varied from 27° to 30°. Searches were made for the most critical initial failure surface for each combination of assumptions and parameters modeled. Variability was found to be relatively small, and the resulting range of values of $S_{r,yield}$ for combinations of modeling assumptions and details considered to be reasonable was found to be $S_{r,yield} \approx 317$ to 408 lbs/ft^2.

Olson (2001) also performed back-analyses to determine $S_{r,yield}$. Failure surfaces analyzed were generally similar, but varied in close detail. Olson reported a best estimate value of $S_{r,yield} \approx 10.9$ kPa (228 lbs/ft^2), and a range of $S_{r,yield} \approx 10.0$ to 11.9 kPa (209 to 249 lbs/ft^2).

A.3.4 Residual Strength Analyses Based on Residual Geometry

The calculation of the "apparent" post-liquefaction strength ($S_{r,resid/geom}$) required to produce a calculated Factor of Safety equal to 1.0 based on residual geometry is illustrated in Figure A.3.2(b). This figure shows the phreatic surface, and the failure surface, used to calculate the best-estimate value of $S_{r,resid/geom} \approx 11$ lbs/ft^2. Variations were then made in parameters, and in location of the pre-failure phreatic surface, as was described in the preceding section in order to evaluate uncertainty or variability, except that all analyses assumed that the failure surface defining the boundaries of the base of the failure mass as it traveled out past the original toe failed at the interface between the embankment fill and the underlying natural soil. Considering ranges of variations in modeling details and parameters considered to be reasonable, the resulting likely range of post-liquefaction strength required to provide a calculated Factor of Safety equal to 1.0 based on residual geometry was considered to be $S_{r,resid/geom} \approx 7$ to 26 lbs/ft^2.

Olson (2001) also calculated post-liquefaction strength required to produce a calculated Factor of Safety equal to 1.0 based on residual geometry, and reported a best estimate value of $S_{r,resid/geom} \approx 0.6$ kPa (13 lbs/ft^2), with a range of $S_{r,resid/geom} \approx 0.3$ to 1.9 kPa (6 to 40 lbs/ft^2).

A.3.5 Incremental Inertial Back-Analyses and Overall Estimates of S_r

Incremental inertial back-analyses were performed using the same sets of properties and geometries (including failure surfaces and phreatic surfaces) as described in the previous sections. Strengths at the toe, both beneath the original embankment toe, and beneath the toe section as it translated outwards over the peaty marsh deposits, were modeled as 100% of S_r for the liquefiable embankment fill for the case illustrated in Figures A.3.3 and A.3.4. This was, again, based on the observed field geometry after failure which suggested that the base of the liquefied fill had lower strength that the underlying upper foundation soils.

Figure A.3.3 shows the best-estimate progressive incremental inertial analysis, showing the 7 stages of geometry evolution modeled as the failure proceeds. Figure A.3.4 shows the associated calculations of (1) acceleration vs. time, (2) velocity vs. time, and (3) displacement of

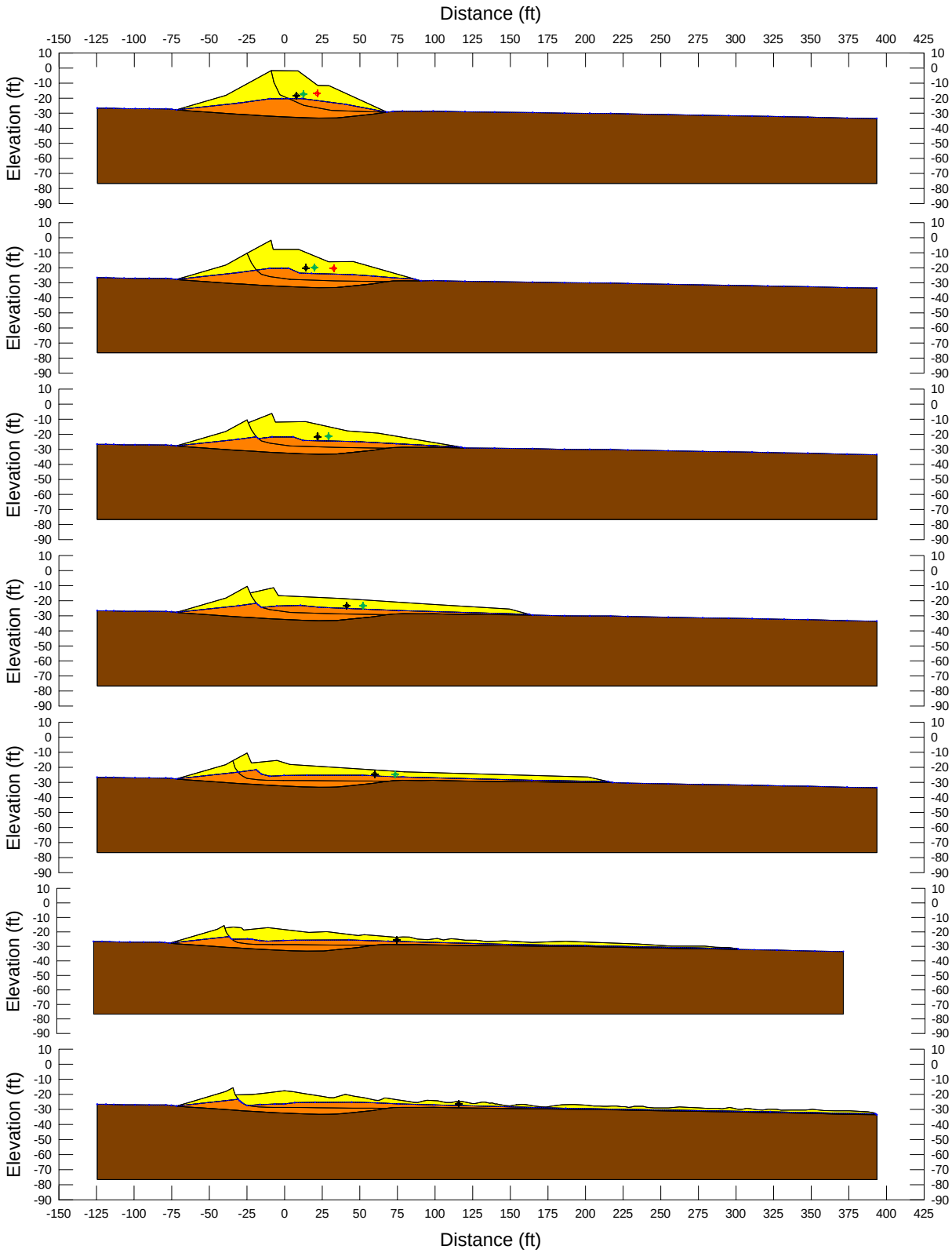

Figure A.3.3: Incremental inertial analysis of the failure of the Uetsu Line Railway Embankment, showing progressive evolution of cross-section geometry modeled

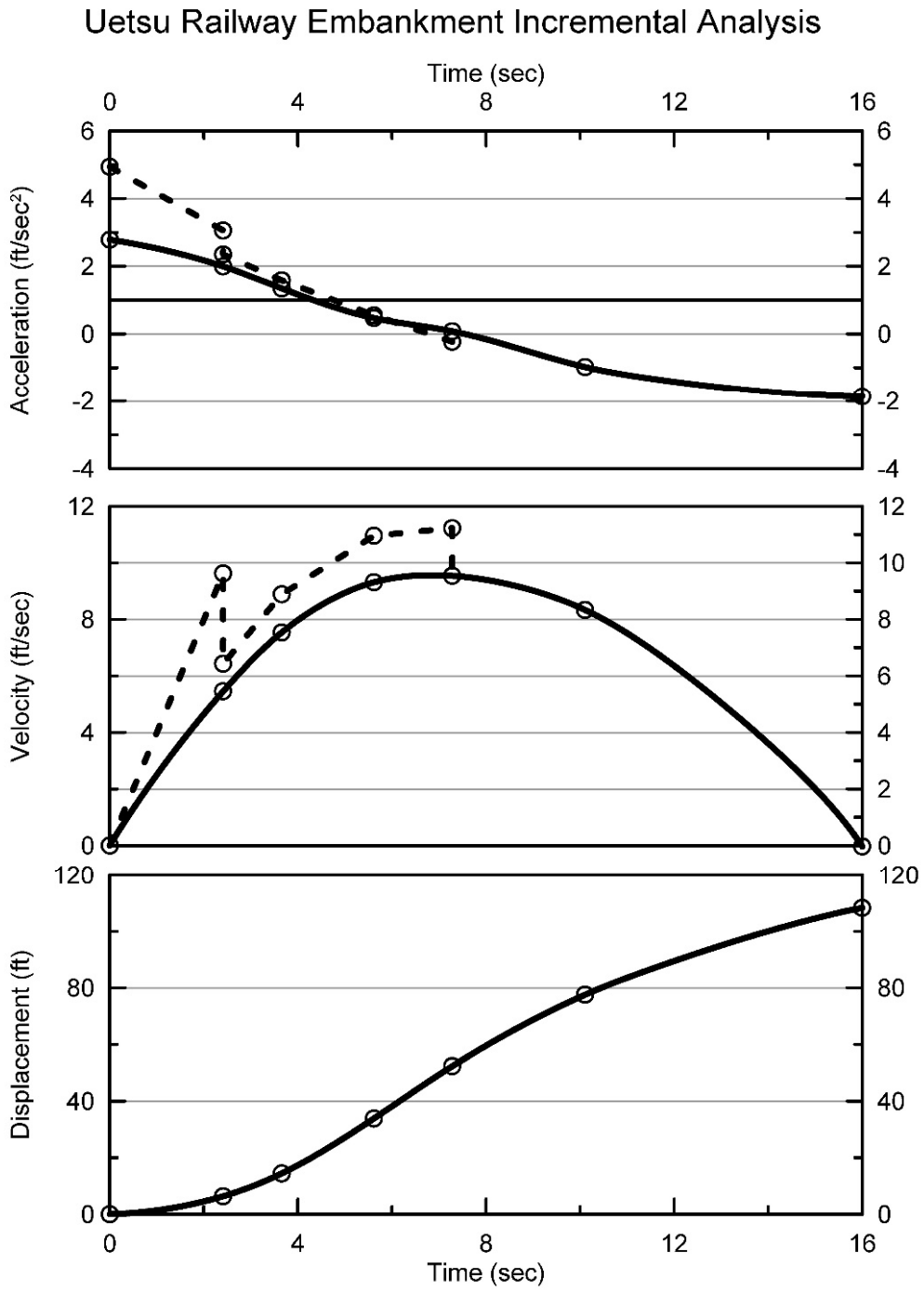

Figure A.3.4: Incremental inertial analysis of the failure of the Uetsu Line Railway Embankment, showing progressive evolution of: (1) acceleration vs. time, (2) velocity vs. time, and (3) displacement vs. time of the overall center of gravity of the failure mass

the overall center of gravity vs. time. For the geometry and phreatic surface shown in Figure A. 3.3, the best estimate value of post-liquefaction strength was $S_r = 38$ lbs/ft^2.

Failure may have been initiated as an incrementally regressive failure retrogressing in successive "slices" back towards the eventual final rear heel scarp, but given the catastrophically large run out distance, it was assumed that these very loose materials essentially liquefied all at once, or nearly so, and the best case analysis shown in Figures A.3.3 and A.3.4 assumes that failure of successive slices initiates rapidly once the slice in front of each successive begins to displace.

The main sources of uncertainty, or variability, in back-calculated values of S_r were (1) the location of the phreatic surface, (2) the rate at which the failure retrogressed progressively towards the back heel in a series of "slices", and the discretization and timing of potentially successive slice initiation, (3) unit weights, (4) frictional strength of the non-saturated upper embankment fill materials, and (5) the precise location of the overall failure surface.

The analysis shown in Figures A.3.3 and A.3.4 neglects cyclic inertial forces, and so may represent a slightly conservative assessment of actual post-liquefaction strength mobilized, but this minor conservatism was neglected.

Based on all analyses performed, and the considerations discussed herein, the overall best estimate value of post-liquefaction strength for the Uetsu Line Railway Embankment failure was judged to be $S_r \approx 38$ lbs/ft^2, with a likely range of $S_r \approx 23$ to 55 lbs/ft^2. Based on the factors contributing to uncertainty or variance for this case history, it was the judgment of the investigation team that this range represented approximately +/− 2 standard deviations. This range of variance is not symmetrical about the best estimate value, so minor further adjustments were made to produce a representative estimate of S_r suitable for regression analyses.

Overall, based on an assumed normal distribution, it was judged that the (mean and median) best estimate of post-liquefaction strength for this case history is

$$\overline{S_r} = 38 \text{ lbs/ft}^2$$

and that the best estimate of standard deviation of mean overall post-liquefaction strength is

$$\sigma_{\overline{S}} = 8 \text{ lbs/ft}^2$$

Estimates of S_r were also reported by several other investigation teams, and two sets of these are shown in Table A. 3.1(a). Olson (2001) and Wang (2003) both performed back-analyses specifically targeting analytical treatment of inertial effects. Olson (2001) and Olson and Stark (2002), reported a best estimate value of $S_r = 1.7$ kPa (35.5 lbs/ft^2), based on their inertial displacement analyses that considered kinetics. Wang (2003) and Wang and Kramer (2008) employed their zero inertial force (ZIF) method to incorporate inertial effects in their back-analyses of this failure, and they also developed estimates of both mean $\overline{S_r} = 43.5$ lbs/ft^2 as well as the associated standard deviation $\sigma_{\overline{S}} = 24.8$ lbs/ft^2. The details of these analyses, and the cross-sections and failure mass assumptions employed, are not presented and so cannot be

checked. But this is yet another case history in which the "ZIF" calculations of Wang (2003), which account for inertial effects, produces S_r values in very good agreement with the results of these current studies.

A.3.6 Evaluation of Initial Effective Vertical Stress

Average initial (pre-failure) effective vertical stress was assessed for the liquefied zones of each of the two failure surfaces (initial and final) shown in Figure A.3.3(a) and (b). The best estimate of the overall average initial vertical effective stress was then taken as the average of these two averages. Reasonable variations were then made in (1) the location of the phreatic surface, (2) unit weights, and (3) the precise location of the overall failure surface.

The resulting best estimate of average pre-failure effective stress within the liquefied materials controlling the failure was then $\sigma_{vo}' \approx 1{,}448$ lbs/ft^2, with a reasonable range of $\sigma_{vo}' \approx$ 1,687 to 1,223 lbs/ft^2. This range is slightly non-symmetric about the median value, and this range was judged by the engineering team to represent approximately +/− 2 standard deviations. Overall, the best characterization of initial (pre-failure) average effective vertical stress was then taken to be represented by a mean value of

$$\overline{\sigma'_{vo}} \approx 1{,}448 \text{ lbs/ft}^2$$

and with a standard deviation of

$$\sigma_{\bar{\sigma}} \approx 116 \text{ lbs/ft}^2$$

Estimates of σ_{vo}' were also reported by other investigation teams, and two sets of these are shown in Table A.3.1(c). Olson (2001) and Olson and Stark (2002) reported an average pre-failure effective vertical stress of $\sigma_{vo}' = 61.3$ kPa (1,280 lbs/ft^2), in generally good agreement with these current studies. Olson and Stark appear to have developed a slightly lower value of σ_{vo}' due to analysis of a slightly shallower failure surface. Average initial vertical effective stresses were not directly reported by Wang (2003) and Kramer (2008), but they were published more recently in the publication by Kramer and Wang (2015). As discussed in Section 2.3.8.1(a), the approach taken by Wang (2003) to evaluation of σ_{vo}' for his nine "primary" case histories (this is one of those nine) is not clearly explained, and it is also poorly documented. Wang's value of $\sigma_{vo}' = 916$ lbs/ft^2 is significantly lower than the values of Olson (2001) and these current studies, but this is not considered a very rigorous check here and the source of differences between Wang's value and those of Olson (2001) and these current studies cannot be back-tracked. Agreement between Olson's independently back-calculated value, and the value developed in these current studies, is considered good.

A.3.7 Evaluation of $N_{1,60,CS}$

As only Swedish cone soundings were performed within the liquefiable embankment fill materials, inferring equivalent SPT penetration resistances was a challenge. Conversion of these

Swedish cone data to equivalent SPT N-values was made using the relationship recommended by Ishihara et al. (1990). There is considerable uncertainty in this relationship, and this is therefore a significant contributor to uncertainty or variability with respect to the median $\overline{N_{1,60,CS}}$ value representative of this material. Corrections for effective overburden stress (C_N) were made using the relationships proposed by Deger (2014), as presented and discussed in Section 4.1.1. Corrections for fines content were made using the relationship propose by Cetin et al. (2004), and a representative fines content of approximately 20%. The resulting best estimate median $N_{1,60,CS}$ value for these current studies is $\overline{N_{1,60,CS}} \approx 3$ blows/ft. Variance of $\overline{N_{1,60,CS}}$ was estimated primarily on the basis of the perceived uncertainty associated with conversion for Swedish cone penetration resistances to equivalent SPT penetration resistances, and was taken as being represented by a standard deviation of $\sigma_{\overline{N}} \approx 0.8$ blows/ft.

Table A.3.1(b) shows values of representative $N_{1,60}$ or $N_{1,60,CS}$ values developed by two other teams of investigators, and variance or standard deviations in these representative values. Olson and Stark (2001, 2002) developed an estimated representative value of $N_{1,60} = 5.6$ blows/ft, and an estimated range of representative values of $N_{1,60} \approx 2.9$ to 10.7 blows/ft, but did not quantify variance or standard deviation in probabilistic terms. This value is a bit lower than the $N_{1,60,CS}$ value from these current studies because it is uncorrected for fines, and so is not an $N_{1,60,CS}$ value. If a similar fines correction were to be made, the resulting $N_{1,60,CS}$ value of Olson and Stark would be in closer agreement with these current studies. Wang (2003) and Kramer (2008) jointly developed a representative value of $\overline{N_{1,60,CS}} = 5.6$ blows/ft, and their estimated standard deviation of that overall mean value for this case history was $\sigma_{\overline{N}} = 2.2$ blows/ft. Details of the development of this interpretation by Wang and Kramer are not presented, so it is not known why their $\overline{N_{1,60,CS}}$ value is a bit lower than the corresponding value developed in these current studies. As relationships between $N_{1,60,CS}$ and S_r have relatively low slopes, this difference is relatively modest with regard to impact on subsequent development of SPT-based predictive relationships for evaluation of S_r.

A.3.8 Additional Indices from the Back-Analyses

A number of additional results, and indices, can be extracted from the analyses performed. Some of these are useful in developing some of the over-arching relationships and figures presented in the main text of this report. These values are presented in Table A. 3.2;

Table A.3.1: Representative values for the Uetsu Railway Embankment case history of: (a) post-liquefaction strength (S_r), (b) initial vertical effective stress (σ_{vo}'), and (c) $N_{1,60,CS}$ developed by various investigation teams, and estimates of variance in each of these indices when available.

(a) Post-Liquefaction Strength:	
Olson (2001) and Olson and Stark (2002)	S_r = 35.5 psf
Wang (2003) and Kramer (2008)	$\overline{S_r}$ = 43.5 psf, and $\sigma_{\overline{S}}$ = 24.8 psf
This Study	$\overline{S_r}$ = 38 psf and $\sigma_{\overline{S}}$ = 8 psf
(b) Representative $N_{1,60}$ or $N_{1,60,CS}$ Value:	
Olson (2001) and Olso and Stark (2002)	$N_{1,60}$ = 3 bpf
Wang (2003) and Kramer (2008)	$\overline{N_{1,60,CS}}$ = 2.9 bpf, and $\sigma_{\overline{N}}$ = 4.2 bpf
This Study	$\overline{N_{1,60,CS}}$ = 3 bpf, and $\sigma_{\overline{N}}$ = 0.8 bpf
(c) Representative Initial Vertical Effective Stress:	
Olson (2001) and Olson and Stark (2002)	Not reported, but can be inferred from reported S_r/P ratio to be $\overline{\sigma'_{vo}} \approx$ 1,280 psf. Likely range is not provided.
Wang (2003) and Kramer (2008)	Value of $\sigma_{vo}' \approx$ 916 psf is poorly documented, and is considered useful only as an approximate comparison (see Section 2.3.8.1, and Table 2.3.)
This Study	$\overline{\sigma'_{vo}}$ = 1,448 psf, and $\sigma_{\overline{\sigma}}$ = 116 psf

Table A.3.2: Additional results and indices from the analyses of the Uetsu Railway Embankment failure case history.

Maximum distance traveled by the center of gravity of the overall failure mass	108 ft.
Initial post-liquefaction Factor of Safety prior to displacement initiation, and based on best estimate value of S_r	FS = 0.27
Final post-liquefaction Factor of Safety at final (residual) post-failure geometry, and based on best estimate value of S_r	FS = 3.18

A.4 Lower San Fernando Dam (California, USA; 1971)

A.4.1 Brief Summary of Case History Characteristics

Name of Structure	Lower San Fernando Dam
Location of Structure	California, USA
Type of Structure	Hydraulic fill dam
Date of Failure	April 11, 1907
Nature of Failure	Seismic, During 1971 San Fernando Earthquake (M_W = 6.7)
Approx. Maximum Slope Height	141 ft.

A.4.2 Introduction and Description of Failure

The Lower San Fernando Dam (also known as the Lower Van Norman Dam, as it was part of the Van Norman Dam complex) suffered a liquefaction-induced landside on its upstream side as a result of the San Fernando Earthquake of February 9, 1971. Soil liquefaction occurred within the hydraulic fill materials of the upstream side, and the ensuing slide carried a large portion of the embankment, including the crest and most of the upstream side of the dam, back into the reservoir. The toe of the failure mass travelled laterally approximately 150 feet into the reservoir. Crest loss was significant, and perilously little freeboard remained at the lip of the slide scarp to contain the reservoir. Approximately 80,000 people were evacuated from the area downstream while the reservoir was safely lowered over the next three days after the earthquake.

This was a well-studied failure, with significant field investigations immediately after the earthquake, and it has been much investigated and studied since. Seed et al. (1973, 1975) and Lee et al. (1975) documented immediate post-earthquake investigations and studies. Additional studies have subsequently been performed by multiple investigators (e.g. Seed, 1979; Castro et al., 1989; Seed et al., 1989, etc.) as this well-documented case history has been used to develop and calibrate new analytical approaches and methods. This is the best-studied and best-documented liquefaction failure case history among the cases considered, and back-analyzed, for these current studies. The level of detail available regarding displacements internally within the embankment dam poses special opportunities with regard to the types of back-analyses performed for these current studies, but it also poses special challenges as very detailed knowledge of internal geometry (within the displaced embankment mass) is available for checking against the displacements analytically modeled.

Figure 4.1 shows two cross-sections through the dam. As part of the post-earthquake investigations, two large trenches were excavated completely through the dam, permitting a thorough inspection and study of the displaced materials. Figure 4.1(a) is a post-failure cross-section showing the displaced positions of a number of recognizable and relatively intact “blocks” of the embankment, and the Figure 4.1(b) shows a re-construction of the pre-failure geometry with these blocks returned to their pre-earthquake locations. These figures show clearly that the failure was the result of liquefaction-induced loss of strength of sandy and silty hydraulic fill materials

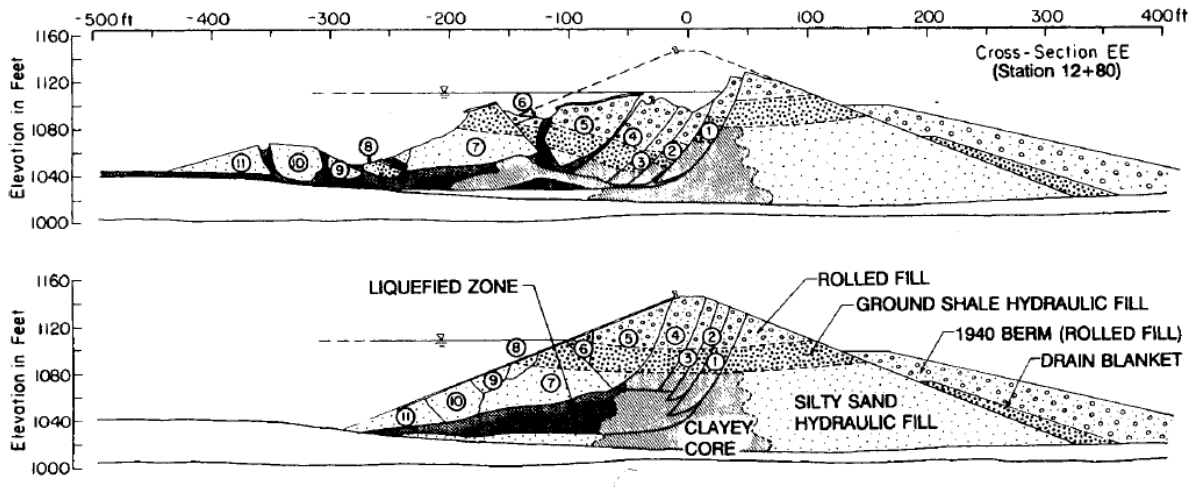

Figure A.4.1: Pre-failure and post-failure cross-sections of the Lower San Fernando Dam (from Castro et al., 1992; after Seed et al., 1973, 1975)

within the lower portions of the upstream hydraulic fill zone, with the overlying embankment materials being carried out (or "floated" outwards) as semi-intact blocks atop these underlying liquefied soils.

Construction of the dam began in 1912. Foundation soils consist primarily of stiff clays, with layers of sands and gravels. The foundation sands and gravels are denser than the overlying hydraulic fill, and these foundation units were not involved in the eventual upstream slope failure.

Initial embankment construction was performed by the hydraulic fill method, with starter dikes along the upstream and downstream toes, and deposition at the toes so that finer soils would travel towards the center of the rising dam and form a clayey "puddled" core. The upstream and downstream shells were raised symmetrically, and both sides were raised in a similar manner and from the same borrow sources. In this manner the initial embankment was eventually comprised of primarily sandy and silty "shells", with a more clayey central "core". Variability of excavated and hydraulically deposited materials, and variability of hydraulic deposition in terms of rate, and in terms of periodic pauses to relocate the pipes through which the materials were being transported and placed, resulted in significant localized variations in material gradation over very small distances, both vertically and laterally within the hydraulic fill embankment. The hydraulic fill zones of the upstream and downstream "shells" were basically striated, or varved, deposits comprised of layers of silts and sands and silty sands with varying fines contents, and these materials periodically penetrated well into the puddled "core" zone, which was otherwise generally comprised mainly of more clayey soils (often clays to sandy clays).

Soils within the lower hydraulic fill zone that liquefied during the earthquake were comprised primarily of variably silty and sandy soils, sometimes with trace amounts of fine gravels. Fines contents varied between approximately 5% to 90%, and most of the fines were low to medium plasticity silts (ML). Figure 2.8 (in Chapter 2 of this report) is a photograph showing the side of one of the two post-earthquake investigation trenches through the failed zone, and it shows these variably layered sandy and silty hydraulic fill materials.

In 1916 the crest was raised by hydraulically placing ground up shale at the crest of the hydraulic fill embankment. This ground shale varied in thickness between approximately 15 to 20 feet. Between 1916 to 1930 several additional layers of rolled earth fill (placed and rolled in layers) were placed atop the ground shale to further raise the crest.

A thin drainage blanket was placed on the downstream face of the hydraulic fill in 1929 to 1930, and a downstream side stability berm was placed over this drainage blanket in 1940.

A.4.3 Initial Yield Stress Analyses

Figure A.4.2(a) shows the cross-section used for back-analyses of the post-liquefaction initial yield strength $S_{r,yield}$ that would theoretically be required within the liquefied upstream shell materials to produce a calculated Factor of Safety equal to 1.0. This is not the actual post-liquefaction strength, but it proves to be useful in developing a number of charts and relationships for these overall studies.

Figure A.4.2(a) also shows the best estimate failure surface. This is well-constrained by the post-earthquake investigations and analyses, and by the excellent internal cross-section data available from those critical initial post-failure field studies.

An important question often raised in previous back-analyses is whether (1) the entire slide was initiated largely monolithically, and then dis-aggregated into distinct blocks and slices as it travelled, or (2) the slide initiated progressively, initiating first with the slice nearest the front face, and then retrogressing back towards the eventual back heel of the overall feature as each new slice became unbraced by the partial departure of the slice in front of it. The incremental momentum analyses presented next in Section A.4.4 answer this question, as they found that the final resting positions of the identifiable slices and blocks could not be reasonably achieved unless the slide initiated largely monolithically and then disaggregated as it travelled.

As a result, it is the overall basal failure surface that is analyzed for purposes of back-evaluation of $S_{r,yield}$.

Shear strengths of non-liquefied materials are a potentially significant issue here. The shear strengths of the upper ground shale and of the overlying rolled fill materials were modeled with drained shear strengths, with best estimate values of $Ø' = 30$ and 32°, respectively. In parameter sensitivity analyses that followed, this was then varied by ± 3° for the ground shale and ± 5° for the rolled fill. Some shear strength data were available for the clayey "puddle core" zone, and some information on liquidity index as well. To account for the increase in strength in the clayey materials the puddle core zone was split into three zones for the upper middle and lower depth zones. Based on liquidity index based assumption of moderate sensitivity and the results of one lab vane shear test in the puddle core material, shear strength within the "approximate" puddle core zone were modeled as undrained cohesive residual strengths with S_u= 550, 630, and 705 lbs/ft^2 for the upper, middle, and lower zones, respectively. These correspond to residual values of $S_u/P \approx 0.07$, as will be discussed in more detail in Section A.4.5. In parameter sensitivity analyses that followed, these assumed undrained cohesive residual strengths were varied by ± 20%.

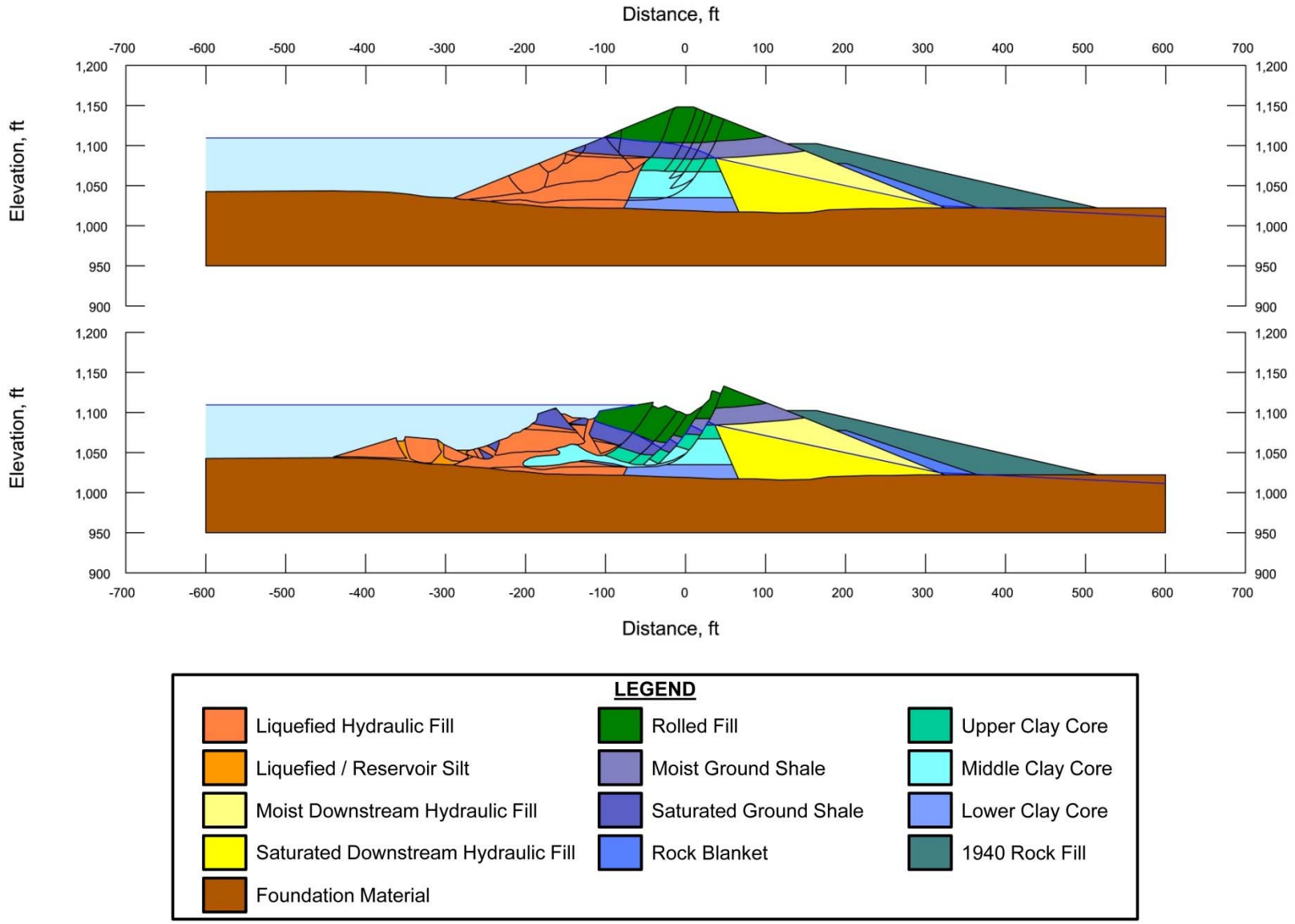

Figure A.4.2: Lower San Fernando Dam: (a) Pre-failure geometry and best-estimate failure surface for initial yield stress analyses, and (b) post-failure geometry and best-estimate failure surface for post-failure residual geometry analyses.

Shear strength of the liquefied hydraulic fill materials of the lower portions of the upstream "shell" zone were taken as $S_{r,yield}$, and the back-analyses were then performed to determine $S_{r,yield}$.

Saturated unit weights of the ground shale fill was modeled as γ_s = 126 lbs/ft^3, and non-saturated unit weights were modeled as γ_m = 118 lbs/ft^3. The unit weights of the non-saturated rolled crest fills were modeled as γ_m = 124 lbs/ft^3. An average saturated unit weight of γ_s = 120 lbs/ft^3 was modeled for the clayey "core" zone materials. The average saturated unit weight of the liquefiable sandy and silty hydraulic fill zones in the upstream "shell" zones were modeled as γ_s = 123 lbs/ft^3. These unit weights were then varied, typically by +/- 3 to 5 lbs/ft^3, in subsequent parameter sensitivity studies.

For the best estimate geometry, conditions, and failure surface described above and shown in Figure A.4.2(a), the resulting value of post-liquefaction yield strength was found to be $S_{r,yield}$ = 1,281 lbs/ft^2. Sensitivity analyses were then performed, varying the details and location (at depth) of the failure surface near the base of the upstream hydraulic fill zone, unit weights, and friction angles for the non-liquefied upper crest and non-liquefied upper core zones. The incremental momentum analyses that follow in Section A.4.5 suggested that there was little likelihood that this failure would have proceeded in an incrementally progressive manner, and so this failure was modeled only as a monolithic event, with the full eventual sliding mass beginning to move largely coherently at the inception of failure. The resulting range of values of $S_{r,yield}$ for combinations of modeling assumptions and details considered to be reasonable was found to be $S_{r,yield} \approx$ 1,207 to 1,358 lbs/ft^2.

Olson (2001) did not perform back-analyses to determine $S_{r,yield}$.for this case, so no direct comparisons from previous studies are available.

A.4.4 Residual Strength Analyses Based on Residual Geometry

The calculation of the "apparent" post-liquefaction strength ($S_{r,resid/geom}$) required to produce a calculated Factor of Safety equal to 1.0 based on residual geometry is illustrated in Figure A.4.2(b). This is not the actual post-liquefaction strength, because it neglects momentum effects and thus underestimates the actual value of post-liquefaction S_r, but $S_{r,resid/geom}$ is a useful index for development of a number of relationships in these overall studies. Figure A.4.2(b) shows the post-failure residual geometry, and the failure surface, used to calculate the best-estimate value of $S_{r,resid/geom}$, based on the best estimate modeling parameters as described in the previous section.

An additional detail here is the shear strength modeled at the base of the portion of the upstream toe of the embankment that traveled out into the reservoir. It is known that weak reservoir sediments were in place at the upstream toe prior to the failure, so there may have been some sliding atop these sediments as the toe of the failure mass entered into the reservoir, or the failure mass may have "plowed" through these weaker sediments in which case strengths at the base of the toe of the slide mass entering the reservoir may have been essentially the full liquefied strength of the upstream hydraulic fill materials (S_r). Similarly, there may have been some hydroplaning as the toe of the embankment materials moved rapidly into the reservoir. The incremental inertial analyses presented in Section A.4.5 that follows indicate that the maximum velocity was on the order of approximately 7 to 8 ft/sec, and that the velocity during most of the

run-in was lower, though the peak velocity at the toe may have briefly been a bit higher than this as the toe also "spread" as it translated laterally. As discussed previously in Section 4.2.2, it is not possible to fully accurately determine the degree of hydroplaning that would have occurred. The observed post-failure residual geometry suggests that the extreme toe of the failure mass did not fully separate itself from the rest of the failure as the overall mass came to rest, but it does appear to have partially separated (or "stretched out") to some degree, suggesting some lower strengths at the base of the materials entering into the reservoir (see Figures A.4.1 and A.4.2(b)).

Taking into account all of these uncertainties, the combined effects of (1) potential hydroplaning, and (2) potential sliding atop weaker reservoir sediments as the toe of the slide mass entered the reservoir were jointly modeled with an assumption that the best estimate strength at the base of the portion of the slide mass entering the reservoir was equal to 50% of the strength (S_r) of the liquefied upstream hydraulic fill materials. Parameter sensitivity studies were then performed, varying this over the range of 25% to 75% of S_r.

The best estimate analysis of $S_{r,resid/geom}$ was performed assuming that shear strength at the base of the embankment materials that entered into the reservoir was 50% of $S_{r,resid/geom}$. The resulting best estimate calculated value of "apparent" post-liquefaction strength based on post-failure residual geometry was $S_{r,resid/geom} \approx 79$ lbs/ft^2.

Variations were then made in parameters, as was described in the preceding section, in order to evaluate uncertainty or variability. Varying degrees of potential hydroplaning were also modeled, with the average shear strength at the base of the portion of the failure mass that entered the reservoir being modeled as varying from a low of 25% of $S_{r,resid/geom}$ to a high of 75% of $S_{r,resid/geom}$. Considering ranges of variations in modeling details and parameters considered to be reasonable, the resulting likely range of post-liquefaction strength required to provide a calculated Factor of Safety equal to 1.0 based on residual geometry was considered to be $S_{r,resid/geom} \approx 36$ to 121 lbs/ft^2.

Olson (2001) also calculated post-liquefaction strength required to produce a calculated Factor of Safety equal to 1.0 based on residual geometry, and reported a best estimate value of $S_{r,resid/geom} \approx 4.8$ kPa (100 lbs/ft^2), with an estimated range of 4.3 to 12.2 kPa (89 to 255 lbs/ft^2).

A.4.5 Incremental Momentum Back-Analyses and Overall Estimates of S_r

Incremental momentum back-analyses were performed using the same sets of properties and geometries (including failure surfaces, and modeling of conditions beneath the portions of the toe of the failure mass that entered into the reservoir) as described in the previous sections.

Shear strengths of the central "clayey" core zone were modeled based on (1) peak $S_u/P \approx$ 0.20 to 0.27 based on Plasticity Index, and $S_u/P \approx 0.24$ based on pocket torvane data (Figure A.4.3) from the similar hydraulically placed "puddle core" materials of the adjacent Upper San Fernando Dam (See Appendix B, Section B.9), and on (2) sensitivity ≈ 3.4 based on liquidity index and on sensitivity from a laboratory vane shear test on clayey materials from the clayey core zone of the Lower San Fernando dam performed and reported by Castro et al. (1989). Taken together, these values led to the values of post-liquefaction (large strain) strength of these central "clayey" core

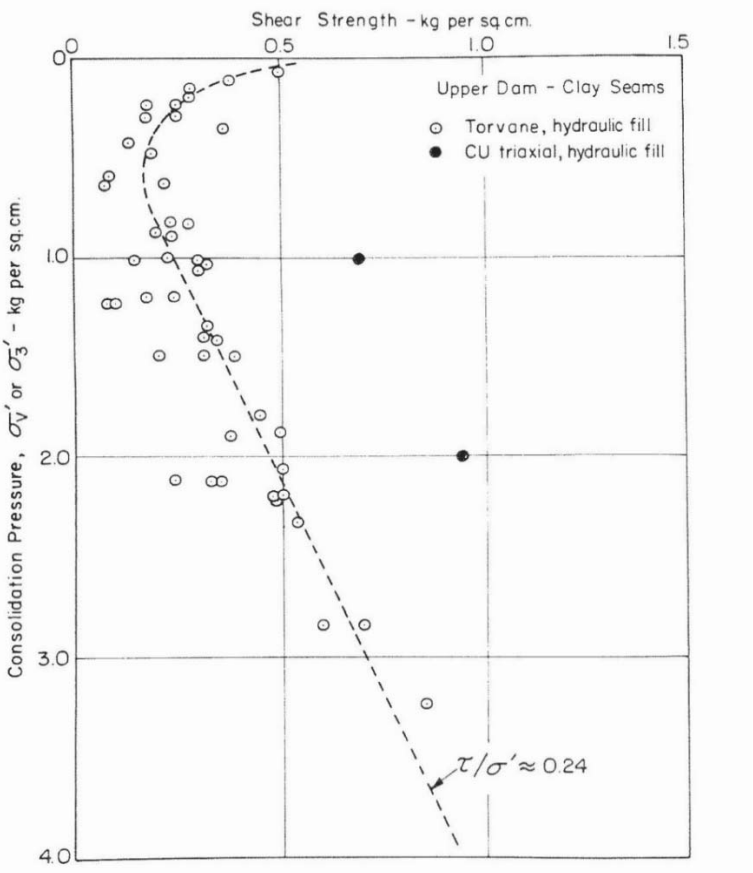

Figure A.4.3: In situ shear strengths of clayey central "puddle core" materials from the Upper San Fernando Dam based on torvane data.

materials modeled in these current analyses of $S_u/P \approx 0.24 \div 3.4 = 0.07$. Accordingly, shear strengths in the clayey central "puddle core" materials were modeled based on $S_u/P = 0.07$. For parameter sensitivity studies, this was subsequently varied by +/- 20%.

Figure 4.2 (in Chapter 4 of the main report text) shows the best-estimate progressive incremental inertial analysis for this case history, showing the seven stages of geometry evolution modeled as the failure proceeds. Figure 4.3 (in Chapter 4) shows the associated calculations of (1) acceleration vs. time, (2) velocity vs. time, and (3) displacement of the overall center of gravity vs. time. Figure A.4.4 (here) repeats Figure 4.2, at larger scale for clarity, as this is a large slide feature with many interesting details. The resulting overall best estimate value of post-liquefaction strength based on these incremental momentum analyses is $S_r = 539$ lbs/ft^2.

Appendix C, Section C.2, presents a series of successive composite views of (1) incremental displacements of the center of gravity of the overall failure mass (in graphical cross-sections), (2) incremental evolution of displacing geometry (with internal cross-section details), and (3) incremental evolution of (a) acceleration vs. time, (b) velocity vs. time, and (c) displacement vs. time of the overall center of gravity of the failure mass. These combined (or

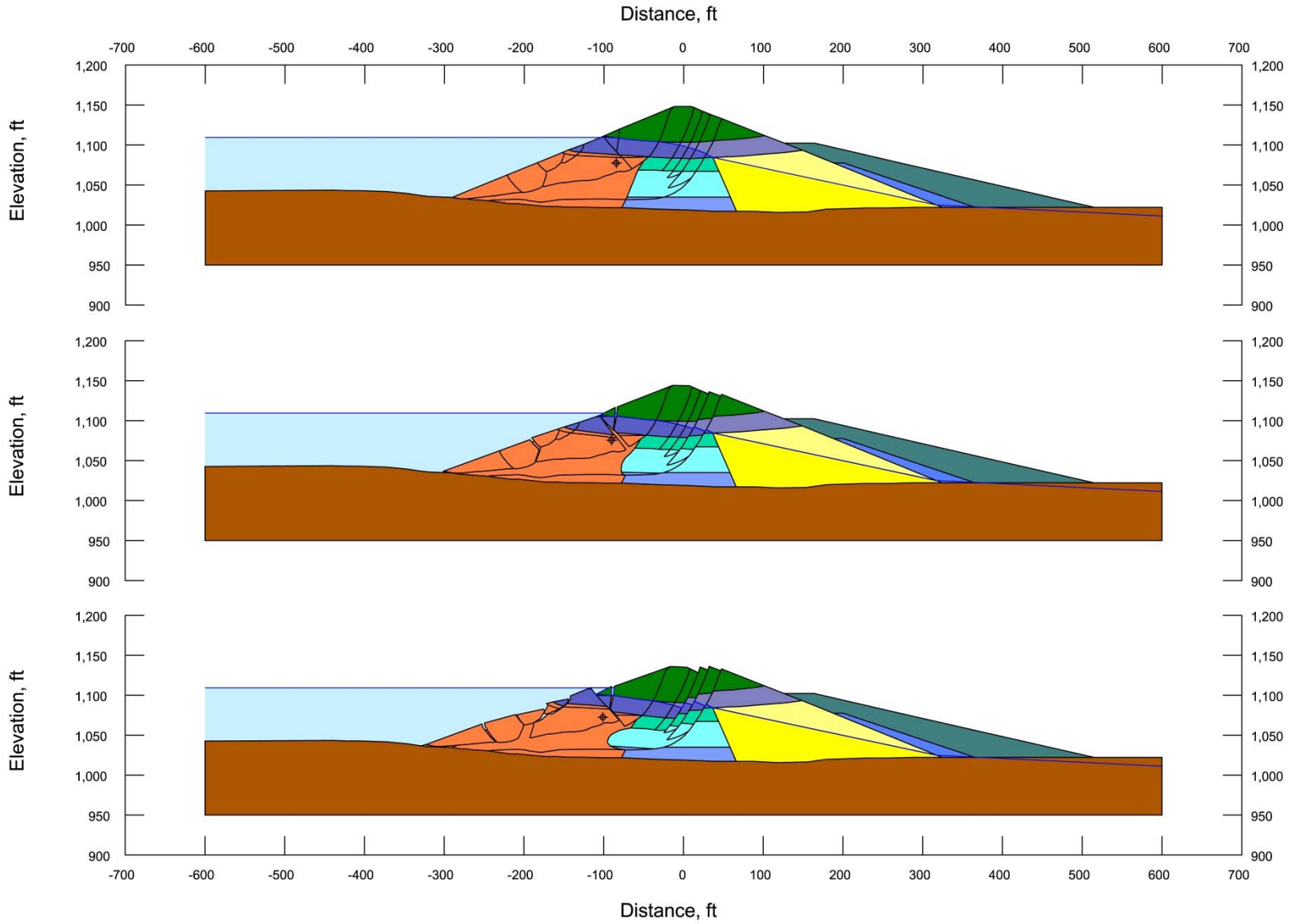

Figure A.4.4: Incremental inertial analysis of the failure of the upstream side of the Lower San Fernando Dam, showing progressive evolution of cross-section geometry as modeled for the best-estimate case.

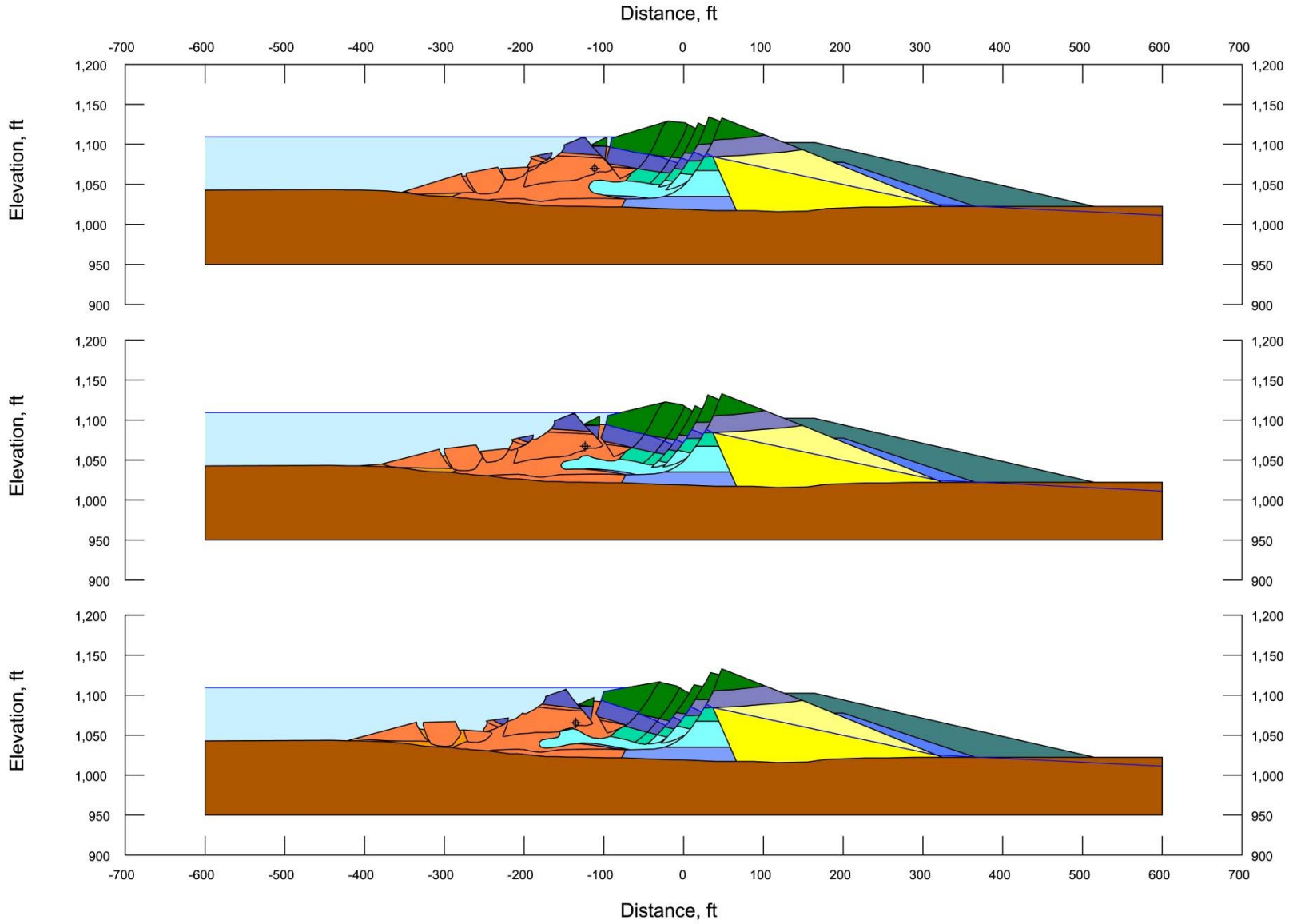

Figure A.4.4(cont'd): Incremental inertial analysis of the failure of the upstream side of the Lower San Fernando Dam, showing progressive evolution of cross-section geometry as modeled for the best-estimate case.

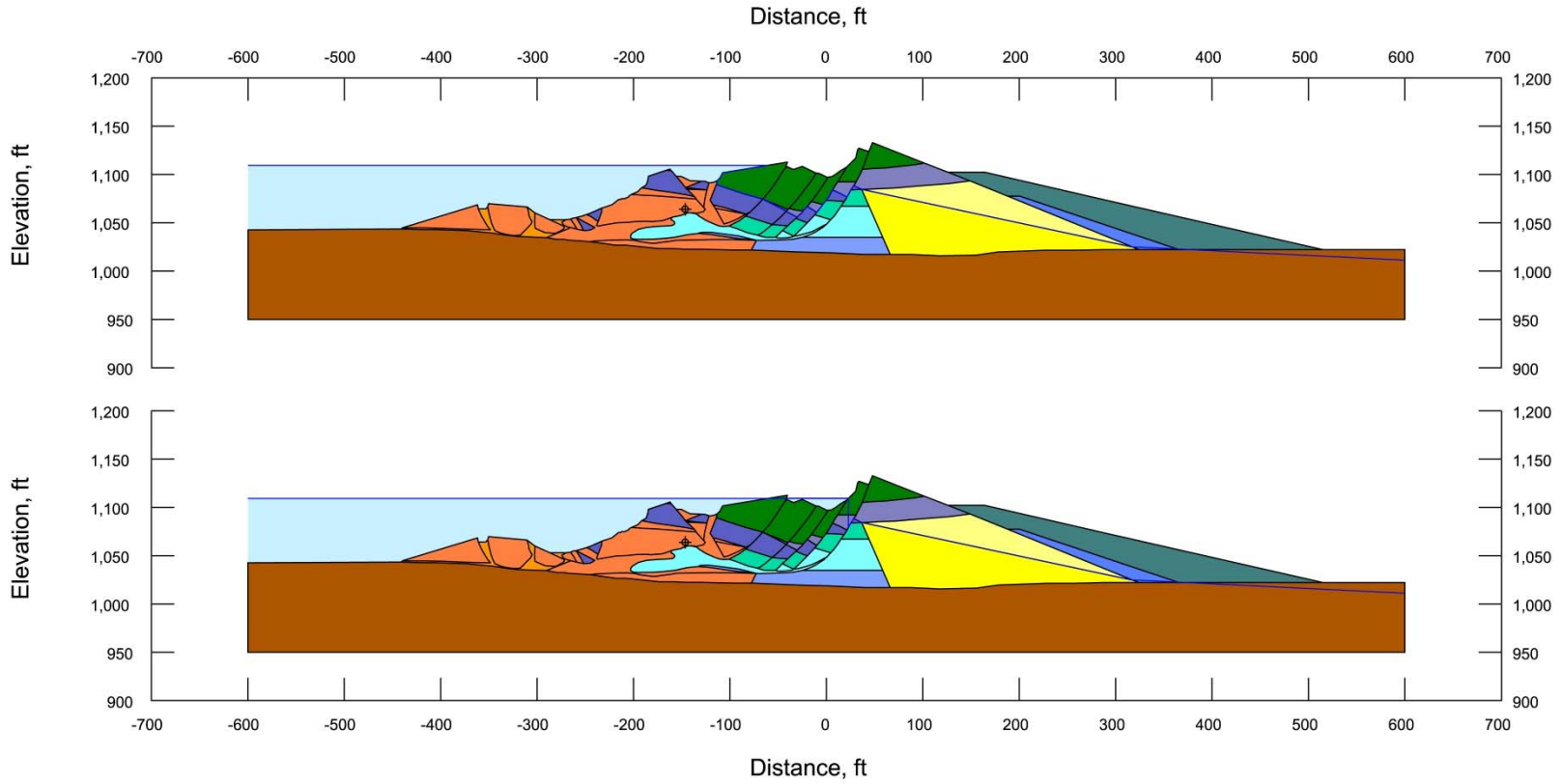

Figure A.4.4(cont'd): Incremental inertial analysis of the failure of the upstream side of the Lower San Fernando Dam, showing progressive evolution of cross-section geometry as modeled for the best-estimate case.

"composite") views in Appendix C can be "clicked" forward and backwards in either pdf views with Adobe, or in PowerPoint or similar, like a choppy movie or simulation, and this can be usefully informative.

The main sources of uncertainty, or variability, in back-calculated values of S_r were: (1) frictional strengths of the non-liquefied embankment fill materials, (2) shear strengths within the clayey "core" zone, (3) potential effects of hydroplaning and/or sliding atop weaker reservoir sediments as the failure mass entered into the reservoir, (4) the precise location and shape of the failure plane at depth near the base of the upstream hydraulic fill "shell", and (5) unit weights.

The exact edges of the "clayey" central core zone are poorly defined, and they are highly irregular due to the stratification resulting from the variability, and the "pauses", in the hydraulic deposition process. This results in silty and sandy "stringers" or strata extending into the clayey core zone, and clayey stringer extending out into the sandy and silty "shell" zones. Shear strengths of the clayey materials (based on $S_u/P \approx 0.07$) do not differ greatly from those of the hydraulic fill in this vicinity ($S_r/P \approx 0.12$), but they do differ somewhat. For the best estimate case, the edges of the zone modeled as "clayey" material are as shown in Figures A.4.2 and A.4.4.

Based on all analyses performed, and the considerations discussed, the overall best estimate value of post-liquefaction strength for the failure of the upstream slope of the Lower San Fernando Dam was judged to be $S_r \approx 539$ lbs/ft^2, with a likely range of $S_r \approx 447$ to 635 lbs/ft^2. Based on the factors contributing to uncertainty or variance for this case history, it was the judgment of the investigation team that this range represented approximately ± 2 standard deviations. This range of variance is not symmetrical about the best estimate value, so minor further adjustments were made to produce a representative estimate of S_r suitable for regression analyses.

Overall, based on an assumed normal distribution, it was judged that the (mean and median) best estimate of post-liquefaction strength for this case history is

$$\bar{S}_r = 539 \text{ lbs/ft}^2$$

and that the best estimate of standard deviation of mean overall post-liquefaction strength is

$$\sigma_{\bar{S}} = 47 \text{ lbs/ft}^2$$

The Lower San Fernando Dam case history has been either back-analyzed, or used in development of correlations and relationships, by a number of previous investigators. Table A.4.1 presents back-calculated values of S_r from these current studies, as well as from four previous investigations that specifically attempted to account for momentum effects.

Seed and Harder (1990) attempted to account for momentum effects by taking S_r as approximately intermediate (a bit lower than exactly intermediate) between back-calculated values of $S_{r,yield}$ and $S_{r,resid/geom}$, producing and estimated value of $S_r \approx 400$ lbs/ft^2. Based on the apparent large displacements, they may have leaned that estimate a bit to the low side (a bit closer towards $S_{r,resid/geom}$), resulting in a slight underestimation of S_r (see Chapter 4, especially the discussion of Equation 4.2 and Figure 4.7, and the plotting of the Lower San Fernando Dam case history in

Figure 4.7). Olson (2001) and Olson and Stark (2002), reported a best estimate value of S_r = 18.7 kPa (390 lbs/ft^2), based on their inertial displacement analyses that considered kinetics, and a range of S_r = 15.8 to 21.8 kPa (330 to 455 lbs/ft^2). Wang (2003) and Wang and Kramer (2008) employed their zero inertial force (ZIF) method to incorporate inertial effects in their back-analyses of this failure, and they developed estimates of both mean $\overline{S_r}$= 484.7 lbs/ft^2 as well as the associated standard deviation $\sigma_{\overline{S}}$ = 111.0 lbs/ft^2. The details of their analyses, and the cross-sections and failure mass assumptions employed, are not presented and so cannot be checked. Davis et al. (1988) calculated $S_r \approx$ 510 lbs/ft^2, reportedly based on analyses that specifically included momentum effects, but again the details are not clearly presented. The best estimate value of Olson and Stark (2001, 2002) of S_r = 390 lbs/ft^2 is close to that of Seed and Harder (1990), but both values appear to be low. Seed and Harder appear to have taken a low fraction of the average between $S_{r,yield}$ and $S_{r,resid/geom}$ based on the large runout distance observed. Olson and Stark appear to have potentially selected a poor shape for the polynomial path along which their center of gravity slid in their "kinetics" analysis, as shown in Chapter 2, Figure 2.21, and this may have caused some underestimation of S_r. Wang and Kramer (2003, 2008), Davis et al.(1988), and these current studies all provide slightly higher values of back-calculated S_r, and the Sr values developed in these three studies are in generally good agreement.

This is an unusually well-defined case history, and the three sets of back-analyses presented in Table A.4.1 that specifically analytically incorporated inertial effects are all in reasonably good agreement, given the differences in approaches taken in the different back-analyses and the complex challenges involved in back-analyses for this case history as conditions change continuously as the failure progresses, and potential issues including hydroplaning and sliding atop soft reservoir sediments arise.

Additional values of S_r were back-calculated by multiple additional investigators, but some of these evaluations were often not well documented as to their basis and details. Poulos (1988) calculated $S_r \approx$ 500 to 1,000 lbs/ft^2, reportedly incorporating momentum effects, but the details of this evaluation are not clearly presented. Castro et al. (1992) proposed a range of $S_r \approx$ 400 to 500 lbs/ft^2, also based on analyses that at least approximately accounted for momentum effects.

A.4.6 Evaluation of Initial Effective Vertical Stress

Average initial (pre-failure) effective vertical stress was assessed for the liquefied zones of the failure surface shown in Figure A.4.4. Additional sensitivity analyses were then performed for reasonable ranges of variations in (1) the location of the phreatic surface, (2) unit weights, and (3) the precise location of the overall failure surface in order to evaluate uncertainty or variance.

The resulting best estimate of average pre-failure effective stress within the liquefied materials controlling the failure is $\sigma_{vo}' \approx$ 3,174 lbs/ft^2, with a reasonable range of $\sigma_{vo}' \approx$ 2,614 to 3,738 lbs/ft^2. This range is slightly non-symmetric about the median value, and this range was judged by the engineering team to represent approximately ± 2 standard deviations. Overall, the best characterization of initial (pre-failure) average effective vertical stress was then taken to be represented by a mean value of

$$\overline{\sigma'_{vo}} = 3{,}174 \text{ lbs/ft}^2$$

and with a standard deviation of

$$\sigma_{\bar{\sigma}} = 281 \text{ lbs/ft}^2$$

Estimates of σ_{vo}' were also reported by Olson and Stark and by Wang and Kramer, and these are shown in Table A.1.1(c). Olson (2001) and Olson and Stark (2002) report an average initial vertical effective stress on the order of approximately $\sigma_{vo}' = 166.7$ kPa (3,482 lbs/ft^2). Average initial effective overburden stresses were not directly reported by Wang (2003) and Kramer (2008), but they were published more recently in the publication by Kramer and Wang (2015). As discussed in Section 2.3.8.1(a), the approach taken by Wang (2003) to evaluation of σ_{vo}' for his nine "primary" case histories (this is one of those nine) is not clearly explained, and it is also poorly documented. Wang's value of $\sigma_{vo}' = 3{,}538$ lbs/ft^2 is in good agreement with the values of Olson (2001) and these current studies, but this is not considered a very rigorous check here. Overall, agreement between these three teams of investigators is good for this case history.

A.4.7 Evaluation of $N_{1,60,CS}$

The Lower San Fernando Dam upstream slope failure has been a well-investigated case history. Figure A.4.5 shows a plan view of the borings performed after the failure as part of the 1971 investigation (Seed et al., 1973). Because of the massive upstream slope failure, only two rows of borings (with SPT) on the downstream side provided data pertinent to the sandy and silty hydraulic fill "shell" zones. As a result, analyses of the upstream side slope failure have been based largely on the assumption of symmetry of materials and depositional characteristics of the upstream and downstream shell zones as the hydraulic fill dam was constructed.

Figure A.4.6 shows a compilation of the SPT $N_{1,60}$ values developed and reported by Seed et al., 1988) based on those SPT borings. The hydraulic fill of the shell zones was encountered at elevations of between approximately +1,004 to +1,076 feet in the seven SPT borings that penetrated the downstream hydraulic fill "shell" zone. It was judged that the downstream hydraulic fill could be sub-divided into four zones by elevation as shown, and mean and median values are calculated and presented for each of these four sub-zones. These post-earthquake downstream $N_{1,60}$ values were then subsequently further modified to develop estimates of pre-earthquake representative values for the upstream side hydraulic fill within which the actual failure occurred. Details of the processing of the original N-values to develop $N_{1,60}$ values are presented in Seed et al. (1988), and so are the additional adjustments made to develop estimates of pre-earthquake $N_{1,60}$ values for the upstream side hydraulic fill zones.

Figure A.4.7 shows a plan view of the additional borings performed in the subsequent 1985 further investigations of this failure (Castro et al., 1989). By 1985 the dam had been largely re-configured, and only four of the mud-filled rotary wash SPT borings penetrated into the downstream hydraulic fill "shell" zone. Figure A.4.8 shows a summary of the $N_{1,60,CS}$ values from these four additional borings. Hydraulic fill shell zone materials were encountered at elevations of between approximately +998 to +1,076 feet in these borings. It was again judged that the hydraulic fill of the shell zone could be sub-divided into four sub-zones by elevation, based on the

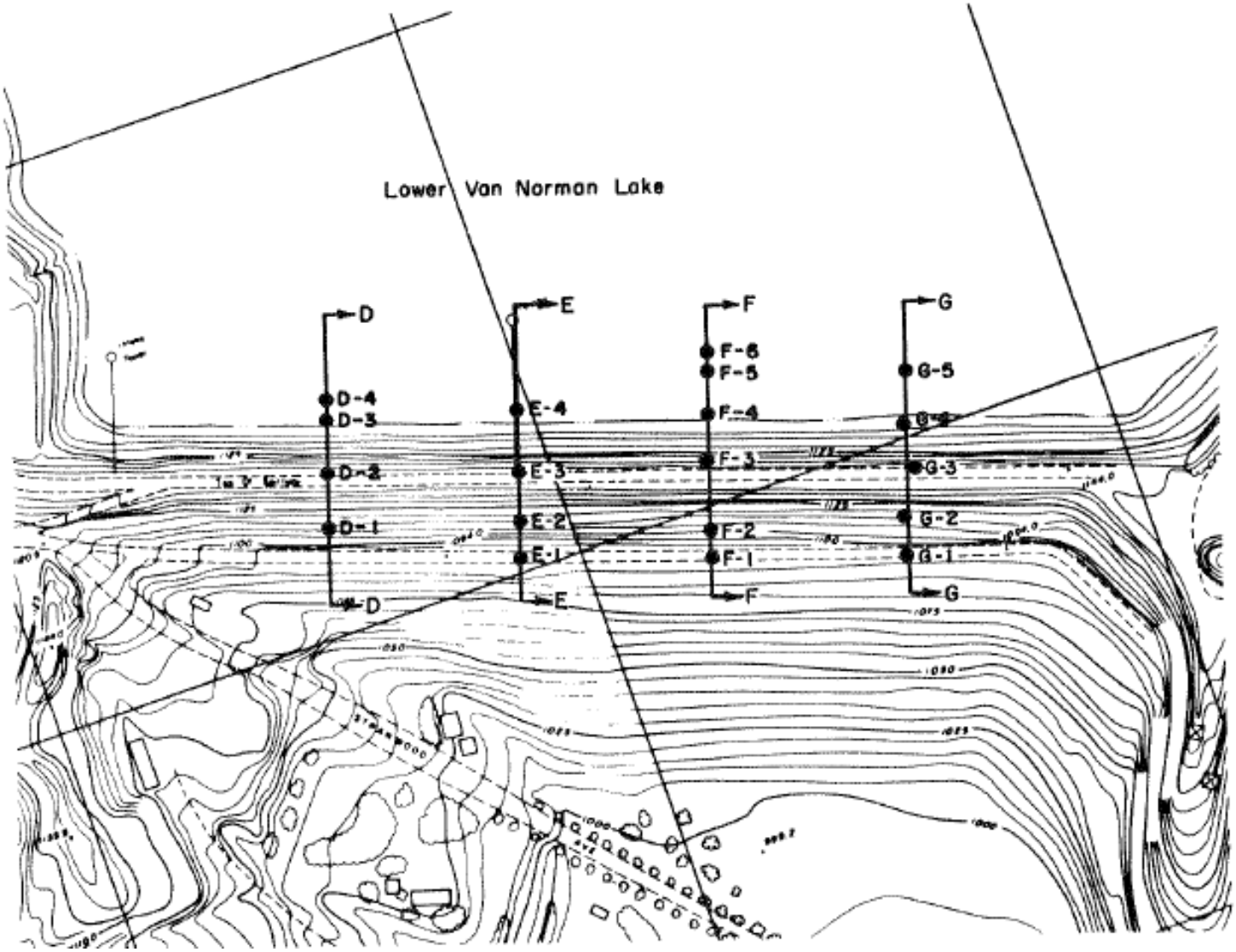

Figure A.4.5: Plan viiew of the Lower San Fernando Dam showing the locations of post-failure SPT borings performed for the 1971 investigation (Seed et al., 1973).

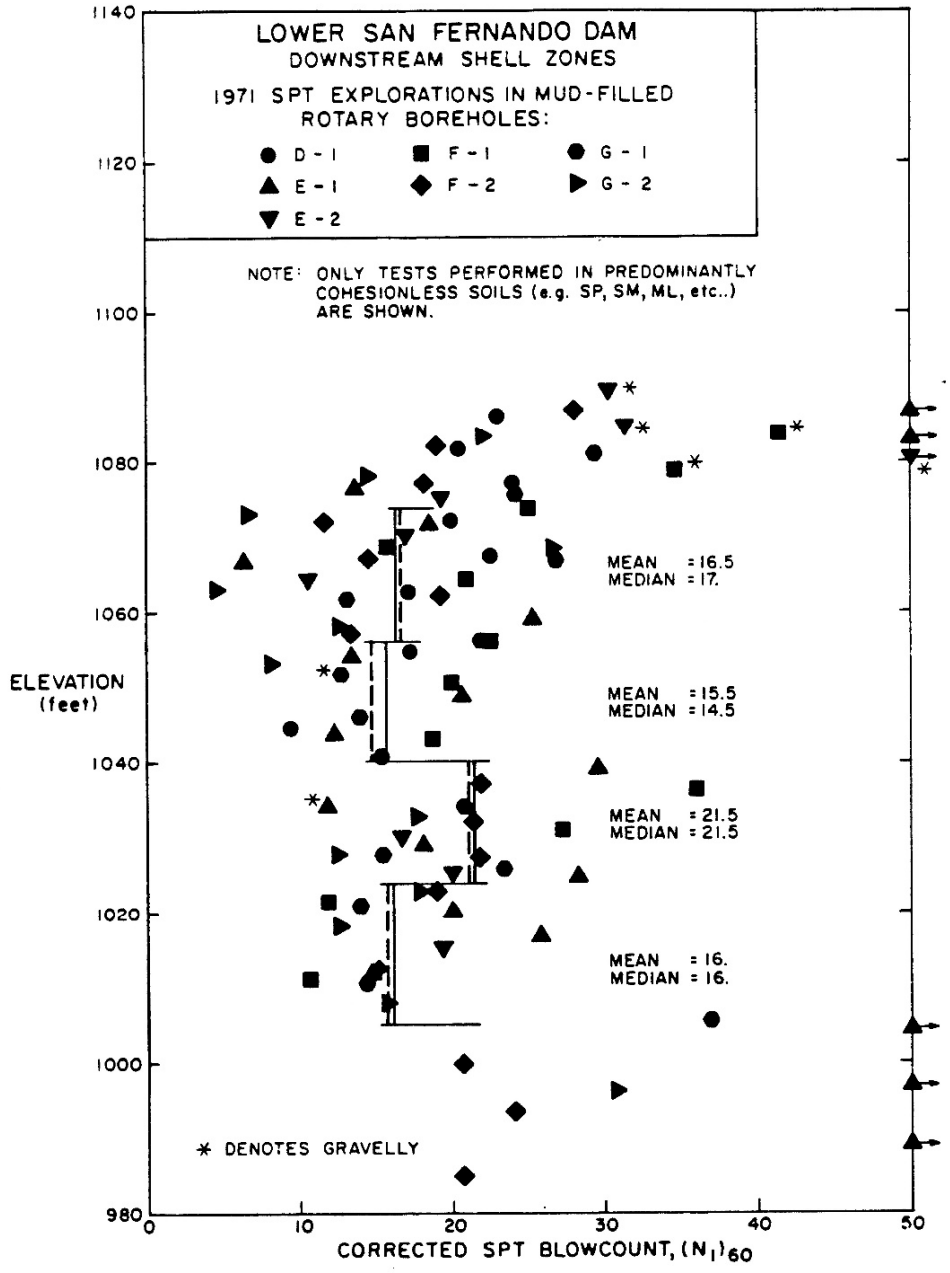

Fig. 4-5 ANALYSES OF SPT DATA FOR COHESIONLESS SOILS IN DOWNSTREAM SHELL - 1971 INVESTIGATION

Figure A.4.6: Summary of overburden and energy and equipment corrected $N_{1,60}$ values as developed and compiled in the 1971 investigation (Seed et al., 1973).

SPT data. These zones are shown, and the median and mean values of $N_{1,60,CS}$ developed for each sub-zone are shown in Figure A.4.8. The corrections for energy, equipment and procedures employed to develop these values are presented by Seed et al., 1988. Once again, additional corrections were made to the post-earthquake values measured pre-earthquake conditions in the upstream side hydraulic fill shell zone. These corrections have already been made, and the values shown in Figure A.4.8 are the estimated pre-earthquake values for representation of the upstream shell hydraulic fill zone.

Both the 1971 and the 1986 investigations developed characterizations of the hydraulic fill shell zones that involved largely similar sub-divisions of the shell zones into four sub-layers (by elevation) based on N1,60,CS values, and both developed fairly similar characterizations of each of these four sub-layers. From top to bottom, the second sub-layer (Elev. ~ 1,040 to 1,057 feet) and the fourth and deepest sub-layer (Elev. ~ 1,005 to 1,022 feet) have notably lower $N_{1,60,CS}$ values than the other two, and these are the strata that are suspected to be the principal culprits in the failure that developed (especially the lowest stratum).

Figure A.4.4.9 shows a compilation of six CPT probes that were passed through the downstream hydraulic fill shell zone as part of the 1985 investigation (Olson, 2001). These show the same pattern, again showing four relatively distinct sub-layers, with the second and fourth sub-layers having lower normalized CPT tip resistances than the other two.

In these current studies, all SPT data obtained in both the 1971 and the 1985 investigations were re-evaluated and re-processed. Figure A.4.10 shows the SPT data from the 11 SPT borings that penetrated into the upstream hydraulic fill shell zone. Energy and equipment and procedural corrections differed for the 1971 and the 1985 field investigations. All corrections applied to measured N-values to develop $N_{1,60,CS}$ values were made according to the procedures and relationships presented in Appendix C, Section C.1. Figure A.4.10 shows the resulting corrected $N_{1,60,CS}$ values.

The resulting corrected blowcounts from Figure A.4.10 were then further examined and processed. The inexplicably high blowcounts ($N_{1,60,CS}$ > 50 blows/ft) were clearly separated from the remainder of the data, and these high values were deleted as "spurious" (likely due to gravel interference). SPT test data and boring logs were carefully reviewed at the apparent base of the downstream side hydraulic fill shell zone. Individual SPT that had been logged as occurring in "foundation" soils were also deleted. In addition, all SPT performed in soils logged as primarily cohesive (CH, CL or SC with high field-estimated fines contents) were also deleted. The remaining SPT data are then presented in Figure A.4.11.

The values on $N_{1,60,CS}$ presented in Figure A.4.11 have been further adjusted to use the post-earthquake downstream side hydraulic fill shell SPT data to develop estimates of the pre-earthquake upstream side SPT $N_{1,60,CS}$ values. Both the 1971 and the 1985 investigations had made two corrections here. Post-earthquake $N_{1,60}$ (or $N_{1,60,CS}$) values were reduced by 2 blows/ft to account for the effects of post-earthquake densification (minus an allowance for disturbance). The same adjustment was made in these current studies. Both the 1971 and 1985 investigations also further reduced the downstream side $N_{1,60}$ or $N_{1,60,CS}$ values by an additional 1 blow/ft to account for the increased effective overburden stress on the (less buoyant) downstream side. That same adjustment was also made in these current studies. Accordingly, the SPT $N_{1,60,CS}$ values

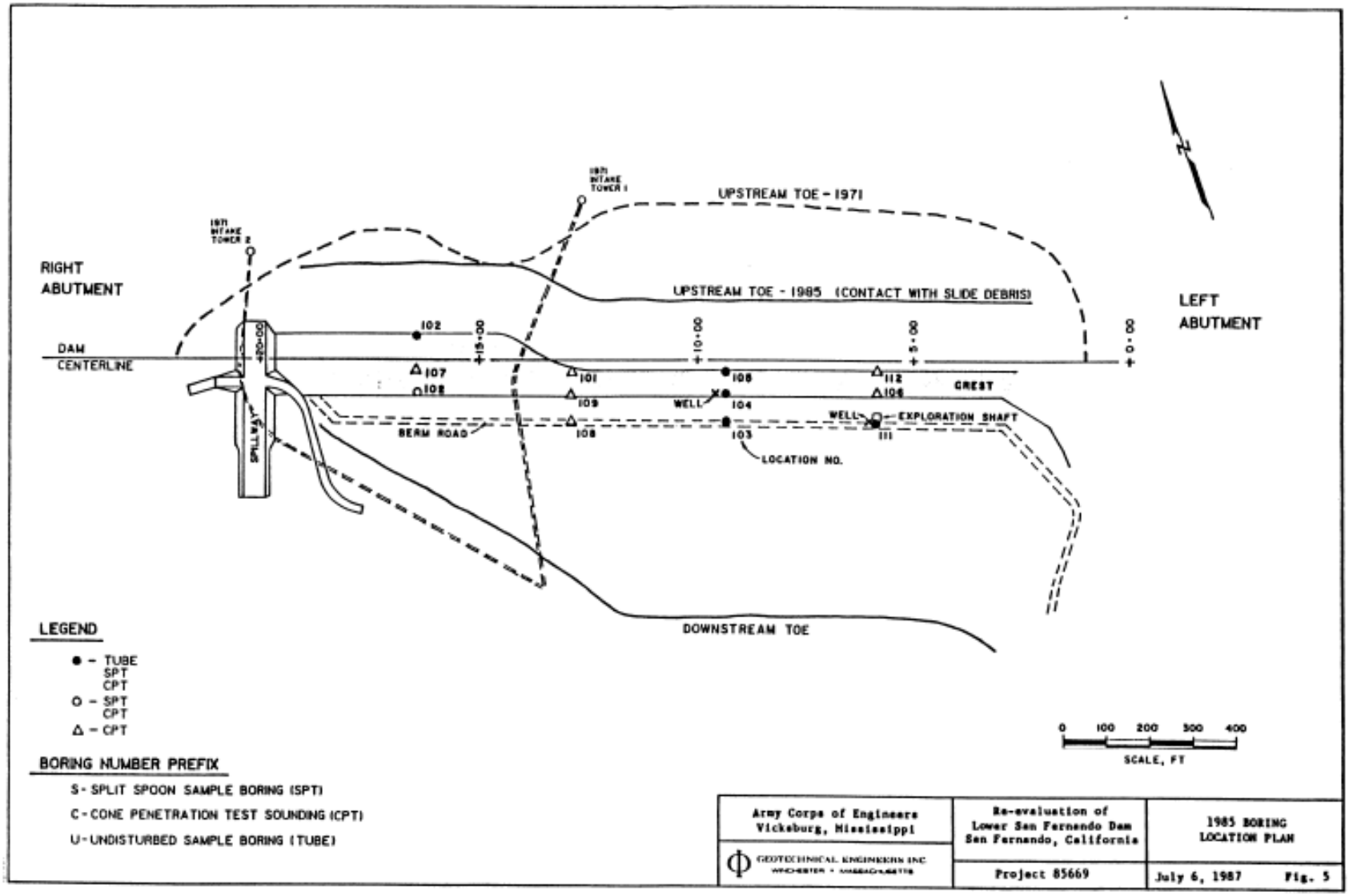

Figure A.4.7: Plan view showing the locations of additional SPT borings performed as part of the 1985 investigation (Castro et al., 1989).

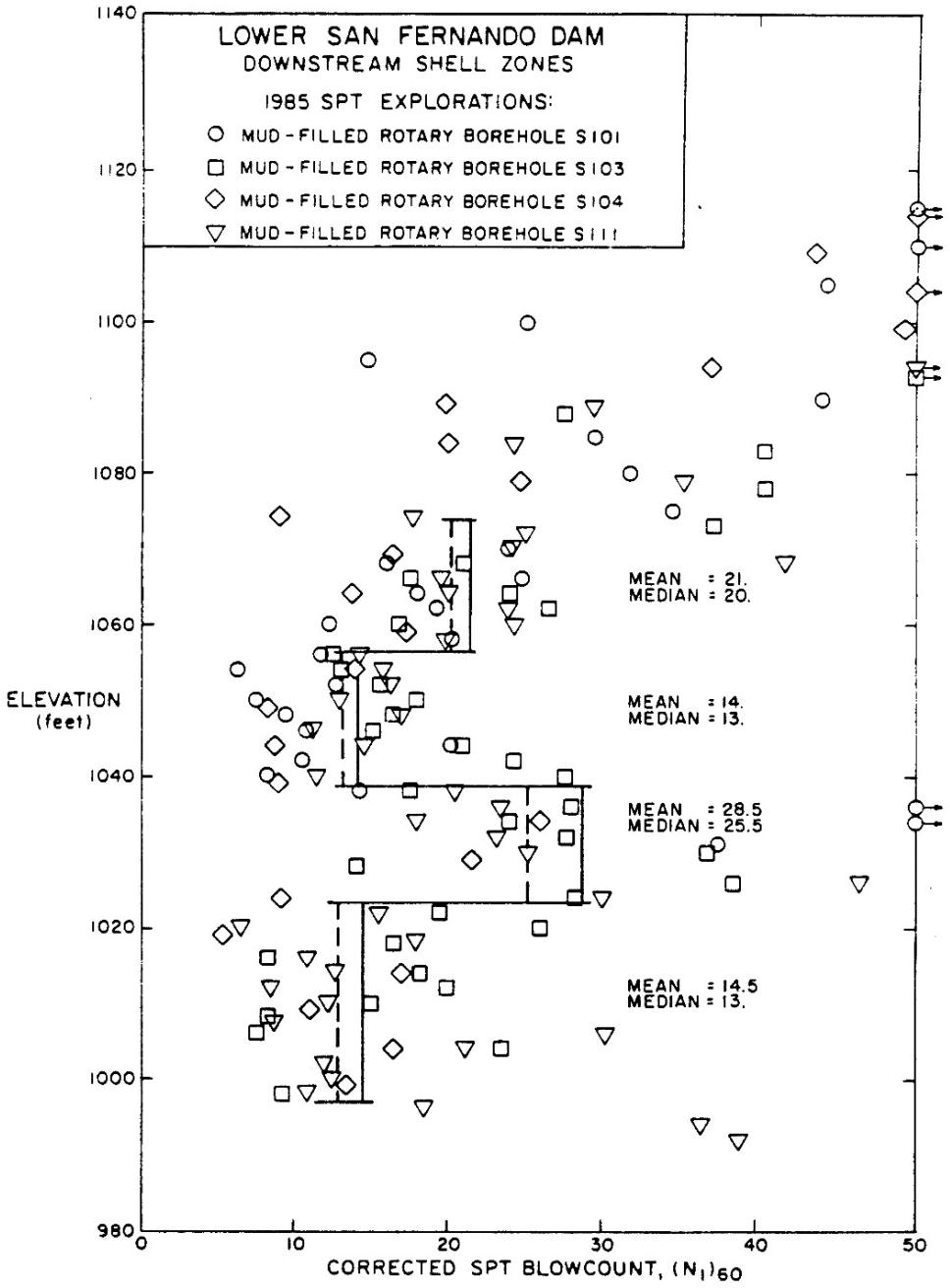

Fig. 4-8 ANALYSES OF SPT DATA FOR BORINGS IN DOWNSTREAM SHELL IN 1985 INVESTIGATION

Figure A.4.8: Summary of overburden and energy and equipment corrected $N_{1,6,CS}$ values as developed and compiled in the 1985 investigation (Seed et al., 1988).

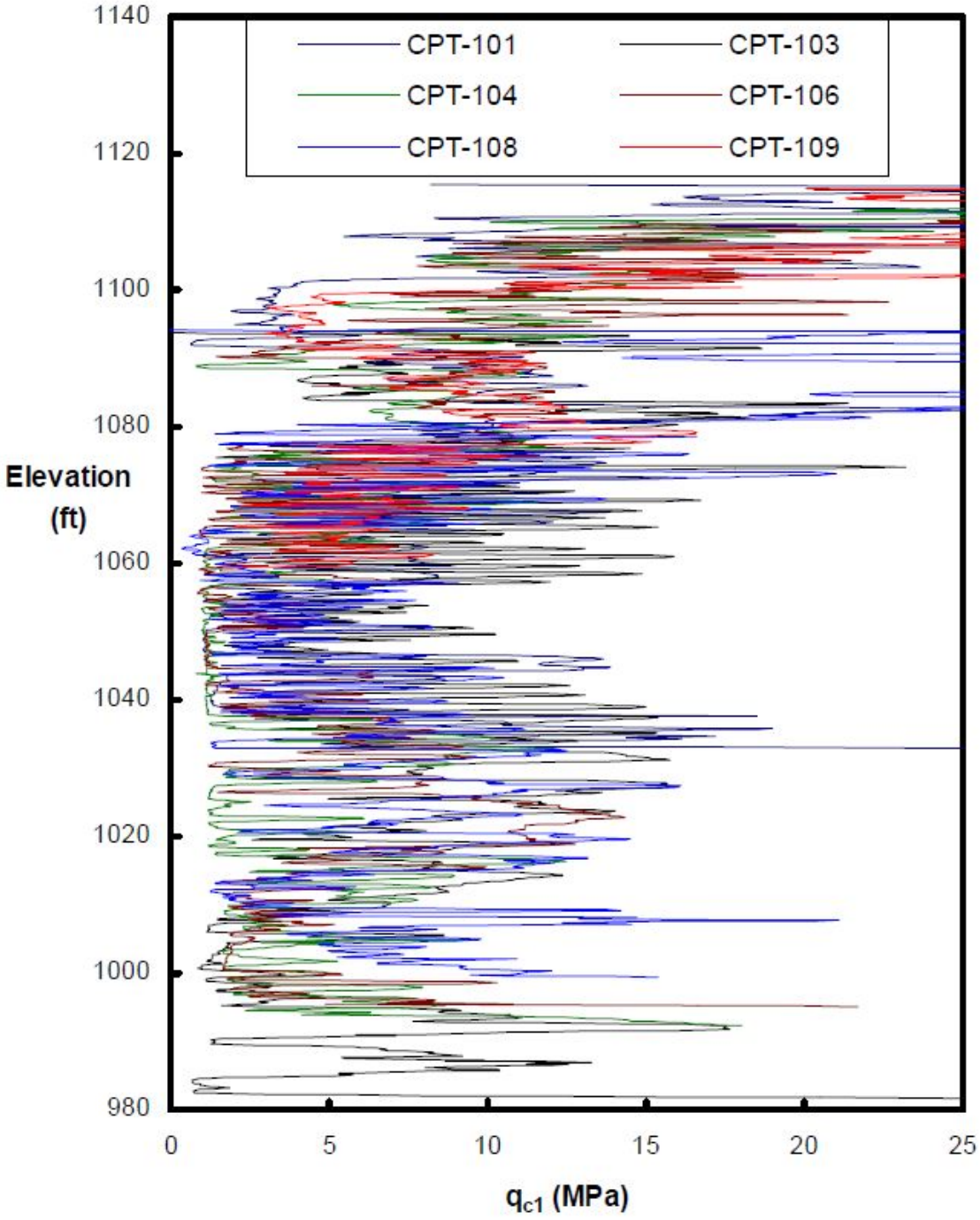

Figure A.4.9: Summary of corrected CPT tip resistance qc1 (MPa) performed through the downstream hydraulic fill "shell" zones as part of the 1985 investigations (Olson, 2001).

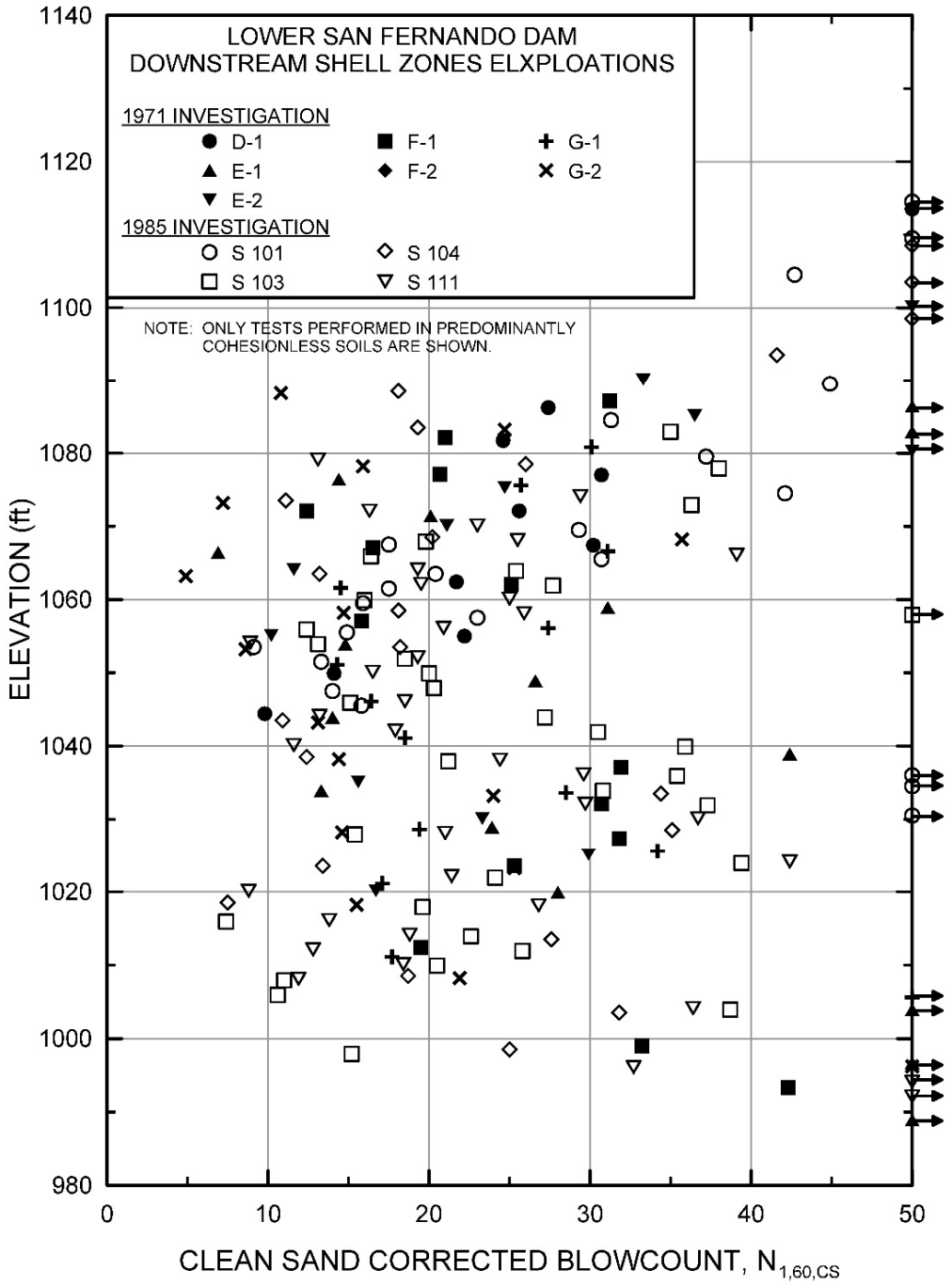

Figure A.4.10: Summary of available data from SPT borings that penetrated through the downstream hydraulic fill zones showing corrected $N_{1,60,CS}$ values as developed for these current studies.

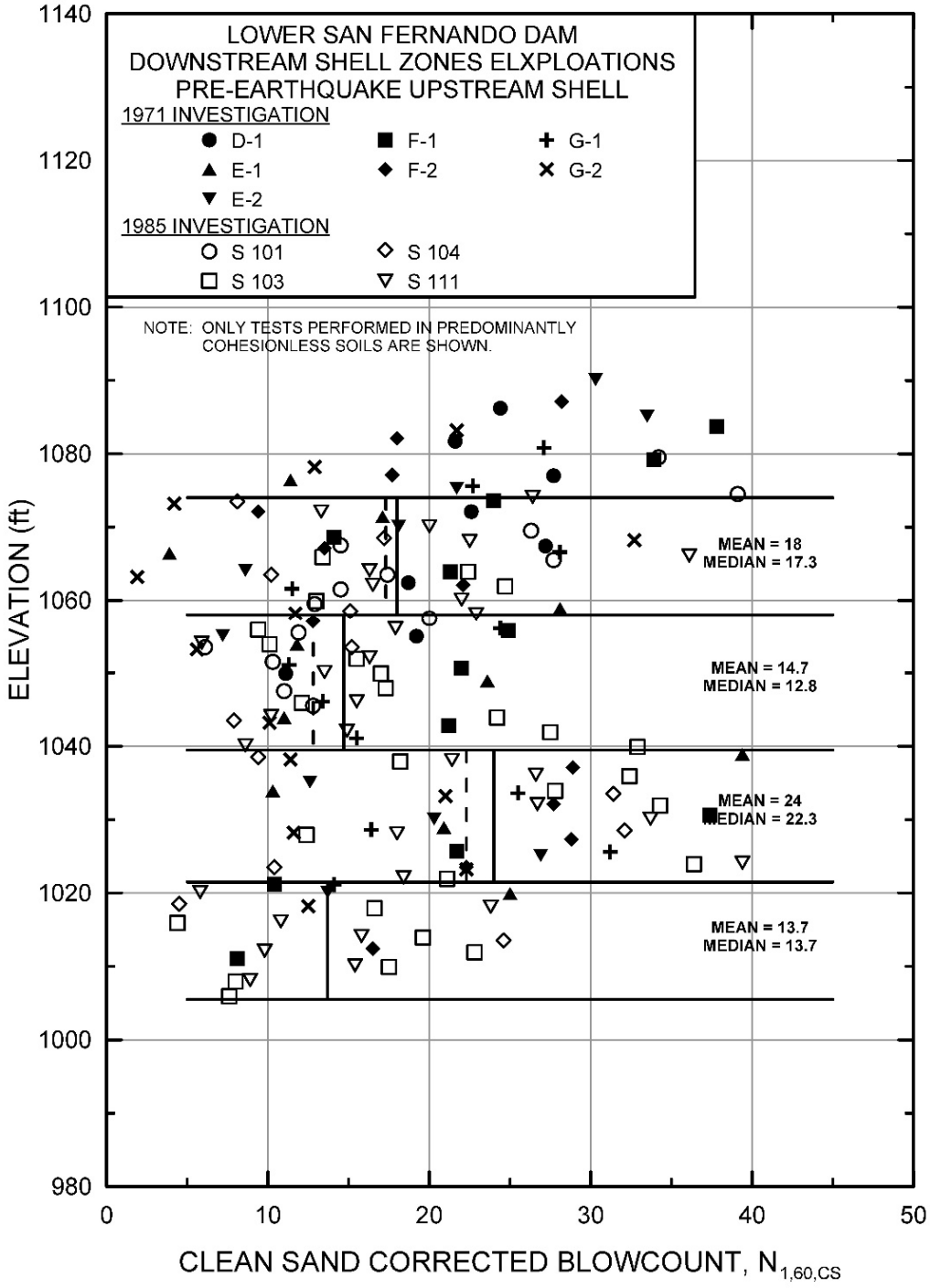

Figure A.4.11: Summary of available SPT data borings that penetrated through the downstream hydraulic fill zones showing corrected $N_{1,60,CS}$ values as adjusted to represent best-estimate values for the upstream side hydraulic fill pre-earthquake conditions.

carried forward from Figure A.4.10 were each reduced by 3 blows/ft before being re-plotted in Figure A.4.11.

Figure A.4.11 thus shows the best-estimate $N_{1,60,CS}$ characterization for pre-earthquake conditions within the upstream hydraulic fill shell zone. The resulting characterization is very similar to that which resulted previously from the 1971 and the 1985 investigations, and the hydraulic fill shell zone is again characterized as four sub-zones (by elevation) based on the $N_{1,60,CS}$ data. Mean and median values of $N_{1,60,CS}$ are shown for each sub-stratum. Once again, it is the second and the fourth sub-layers that have the lowest $N_{1,60,CS}$ values and that are thus the zones of principal interest. The fourth sub-layer (the deepest) is the zone within which a majority of the upstream failure occurred.

The mean and median $N_{1,60,CS}$ values of sub-layers No's. 2 and 4 are:

Sub-Layer No. 2: Mean $N_{1,60,CS}$ = 14.7 blows/ft and Median $N_{1,60,CS}$ = 12.8 blows/ft.

Sub-Layer No. 4: Mean $N_{1,60,CS}$ = 13.7 blows/ft and Median $N_{1,60,CS}$ = 13.7 blows/ft.

Based on these data, and an assumed Normal distribution, the values selected for characterization of the mean $N_{1,60,CS}$ value for the upstream hydraulic fill in the failure zone, and for the standard deviation of this mean, for the pre-earthquake conditions in the upstream side hydraulic fill shell zone were

$$\overline{N_{1,60,CS}} = 13.5 \text{ blows/ft} \quad \text{and} \quad \sigma_{\overline{N}} = 1.8 \text{ blows/ft.}$$

Table A.4.1(b) shows values of representative $N_{1,60}$ or $N_{1,60,CS}$ values developed by two other teams of investigators, and variance or standard deviations in these representative values if available. Seed and Harder (1990) recommended a representative value of $N_{1,60,CS}$ = 13.5 blows/ft. Olson and Stark (2001, 2002) developed an estimated representative value of $N_{1,60}$ = 11.5 blows/ft, with a range of 5 to 15 blows/ft.. This value of Olson and Stark includes no fines adjustment, and that would cause it to be lower than the corresponding $N_{1,60,CS}$ value in these silty sand and sandy silts. Wang (2003) and Kramer (2008) jointly developed a representative value of $\overline{N_{1,60,CS}}$ = 14.5 blows/ft, and their estimated standard deviation of that overall mean value for this case history was $\sigma_{\overline{N}}$ = 1.1 blows/ft. Overall agreement between the three independent assessments of representative $\overline{N_{1,60,CS}}$ values is excellent, with allowance for the lack of a fines adjustment by Olson and Stark, and variance or uncertainty in $\overline{N_{1,60,CS}}$ appears to be relatively low.

A.4.8 Additional Indices from the Back-Analyses

A number of additional results, and indices, can be extracted from the analyses performed. Some of these are useful in developing some of the over-arching relationships and figures presented in the main text of this report. These values are presented in Table A.4.2.

Table A.4.1: Representative values for the Lower San Fernando Dam upstream slope failure case history of: (a) post-liquefaction strength (S_r), (b) initial vertical effective stress (σ_{vo}'), and (c) $N_{1,60,CS}$ developed by various investigation teams, and estimates of variance in each of these indices when available.

(a) Post-Liquefaction Strength:	
Davis et al. (1988)	$S_r \approx 510$ psf
Seed and Harder (1990)	$S_r \approx 400$ psf
Olson (2001) and Olson and Stark (2002)	$S_r = 390$ psf, and range = 330 to 454 psf
Wang (2003) and Kramer (2008)	$\overline{S_r} = 484.7$ psf, and $\sigma_{\overline{S}} = 111.0$ psf
This Study	$\overline{S_r} = 539$ psf and $\sigma_{\overline{S}} = 47$ psf
(b) Representative $N_{1,60}$ or $N_{1,60,CS}$ Value:	
Seed and Harder (1990)	$N_{1,60,CS} \approx 13.5$ bpf
Olson (2001) and Olson and Stark (2002)	$N_{1,60} = 11.5$ bpf, range = 5 to 15 bpf
Wang (2003) and Kramer (2008)	$\overline{N_{1,60,CS}} = 14.5$ bpf, and $\sigma_{\overline{N}} = 1.1$ bpf
This Study	$\overline{N_{1,60,CS}} = 13.5$ bpf, and $\sigma_{\overline{N}} = 1.8$ bpf
(c) Representative Initial Vertical Effective Stress:	
Olson (2001) and Olson and Stark (2002)	$\sigma_{vo}' \approx 3{,}482$ psf. Likely range is not provided.
Wang (2003) and Kramer (2008)	Value of $\sigma_{vo}' \approx 3{,}538$ psf is not well documented, and so is considered useful only as an approximate comparison. (See Section 2.3.8.1, and Table 2.3.)
This Study	$\overline{\sigma'_{vo}} = 3{,}174$ psf, and $\sigma_{\overline{\sigma}} = 281$ psf

Table A.4.2: Additional results and indices from the analyses of the Lower San Fernando Dam upstream slope failure case history.

Maximum distance traveled by the center of gravity of the overall failure mass	63.4 ft.
Initial post-liquefaction Factor of Safety prior to displacement initiation, and based on best estimate value of S_r	FS = 0.60
Final post-liquefaction Factor of Safety at final (residual) post-failure geometry, and based on best estimate value of S_r	FS = 2.22

A.5 Hachiro-Gata Roadway Embankment (Akita, Japan; 1983)

A.5.1 Brief Summary of Case History Characteristics

Name of Structure	Hachiro-Gata Embankment
Location of Structure	Akita, Japan
Type of Structure	Roadway Embankment
Date of Failure	May 26, 1983
Nature of Failure	Seismic, During 1983 Nihon-Kai-Chubu Earthquake (M_L = 7.7)
Approx. Maximum Slope Height	12.7 ft.

A.5.2 Introduction and Description of Failure

The Hachiro-Gata Roadway Embankment failed during Nihon-Kai-Chubu Earthquake of May 26, 1983 (M_L = 7.7), and was investigated by Ohya et al. (1985). Ohya et al. reported a measured peak ground acceleration of 0.168g in the nearby town of Akita.

Figure A.5.1 shows a cross-section through the failure. The roadway approach embankment, which crossed a shallow lake (Hachirogata Lake), was comprised of loose fine sand fill, and it was underlain by layers of medium dense to dense sand and soft clay.

After the failure, an SPT boring and other in situ tests were performed at the toe of the roadway embankment slope, and these are shown in Figure A.5.2 (from Ohya et al., 1985). Results of lab test performed on samples collected during the site investigation are summarized in Figure A.5.3 (from Ohya et al., 1985). These penetration and laboratory tests reasonably well constrain the key ground conditions at the base of the failure. Construction details are not reported, and it is assumed that the sandy fill was locally sourced, and that it received minimal compaction effort.

Close inspection of the penetration tests shown in Figure A.5.2 shows that the transition from fill to underlying native soils appears to be relatively clearly demarcated by a transition from very low SPT blowcounts within the upper fill to slightly higher penetration resistances in the immediately underlying denser sand. The geometry of the back heel of the final failure surface not as well constrained because the roadway embankment slumped in both directions causing a vertical drop of the roadway and extensional spreading toward each slope. This appears to have been a relatively symmetric failure, and the down-dropped central graben section settled and also pulled apart laterally to some extent. However, a reasonable heel that exits near the center of the roadway can be assumed for the back-analyses. As a result, the approximate location of the overall bounding failure surface is relatively well constrained for this case by this heel scarp, and by the transition to firmer materials at the base of the liquefiable fill. Only the left side of the embankment is analyzed, as the post-failure geometry is better defined on that side. Ohya et al. reported an approximate phreatic surface, which should be fairly well constrained due to the embankment's location within a lake, as shown in Figure A.5.1.

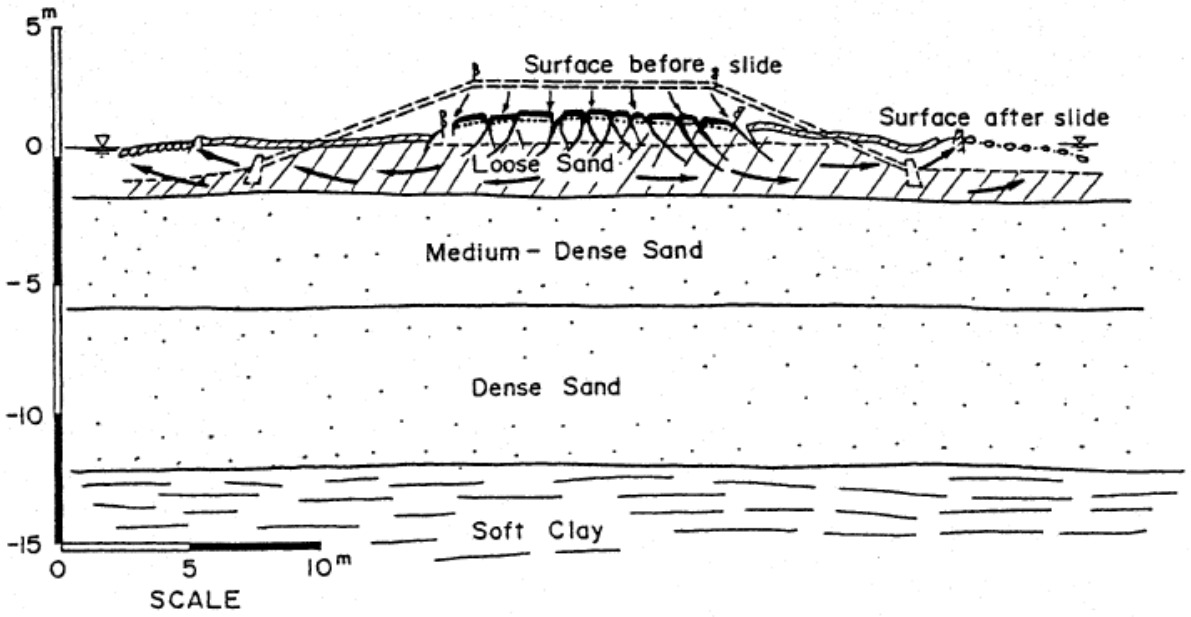

Figure A.5.1: Cross-section through the Hachiro-Gata Roadway Embankment showing pre-failure and post-failure geometry (from Ohya et al, 1985).

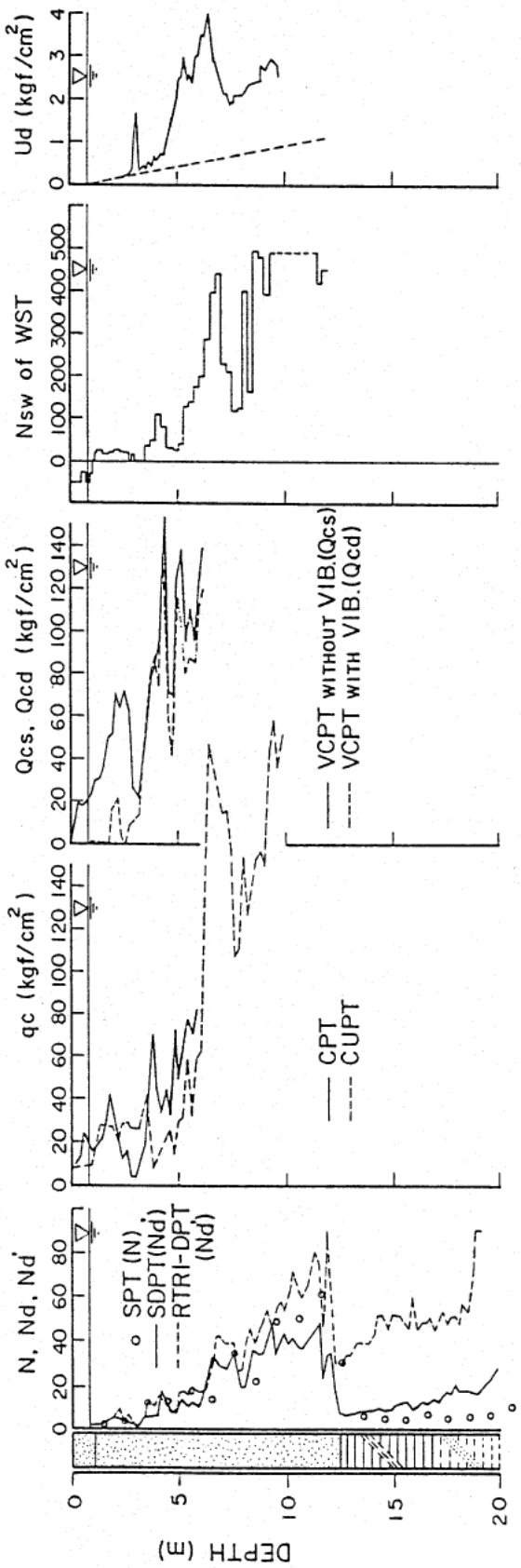

Figure A.5.2: Summary of penetration test results at the Hachiro-Gata Roadway Embankment (from Ohya et al, 1985).

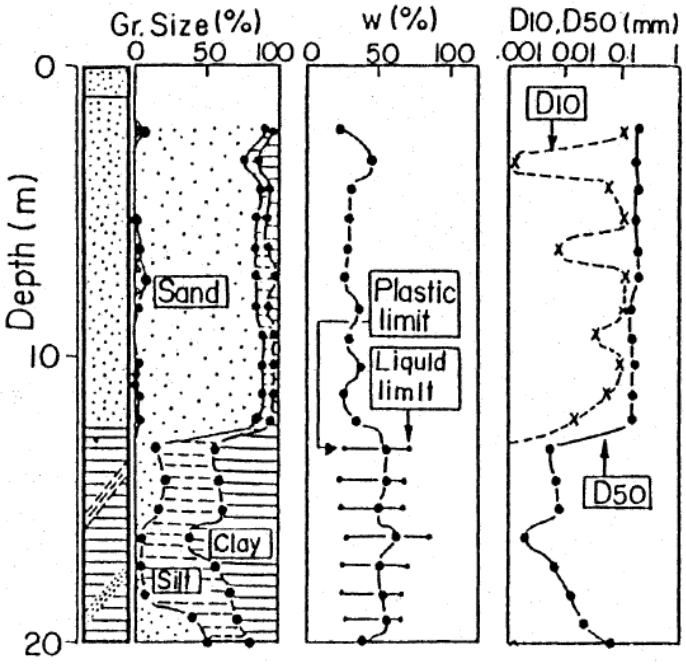

Figure A.5.3: Summary of laboratory tests performed on samples collected during the investigation at the Hachiro-Gata Roadway Embankment (from Ohya et al, 1985).

A.5.3 Initial Yield Strength Analysis

The post failure geometry shown in Figure A.5.1 provides insight as to the potential location of the critical failure surface. While this embankment failed almost symmetrically toward both slopes, the failure toward the left side of figure A.5.1 was chosen to be analyzed as the post failure geometry is better defined on that side.

The precise location of the initial failure surface at the base of the failure is uncertain, however given the geometry of the failure and the reported stratigraphy the location was fairly well constrained. Based on an assumed phreatic surface that passes approximately through the lower third of the embankment, a search was made for the most critical static failure surface assuming liquefaction had been "triggered" in all potentially liquefiable materials below the phreatic surface. This exercise showed that the most critical potential failure surfaces for this set of assumptions would result in a failure surface exiting near the toe of the slope and reaching to the bottom of the assumed liquefiable layer. The location of the heel of the failure surface is unknown, however the most critical surface was found to exit hear the middle to the roadway embankment as shown in Figure A.5.4(a). This result coincides well with the almost symmetrical sliding on each side of the roadway embankment as seen in the post failure geometry. These analyses neglected seismic inertial forces (which were moderate), however, and they also did not account for potentially progressive development of triggering of liquefaction within the slope.

Loose fine sand materials above the phreatic surface were modeled with Ø´ ≈ 30°, and a unit weight of $\gamma_m \approx 115$ lbs/ft^3. Materials below the phreatic surface were considered to liquefy, down to the base of the failure surfaces analyzed, and were assigned an undrained post-liquefaction yield strength of $S_{r,yield}$ that was constant along any given failure surface, and a unit weight of $\gamma_s \approx 122$ lbs/ft^3.

The resulting best-estimated value of $S_{r,yield}$ for the most critical initial failure surface was $S_{r,yield} = 135$ lbs/ft^2.

Parameters and geometry were then varied to examine potentially variability. The location of the phreatic surface was varied, raising it by up to 0.5 m (1.5 ft.) across the embankment, and lowering it by up to a similar distance. Unit weights were also varied over the ranges considered likely, and the friction angle of non-liquefied material above the phreatic surface was varied from 28° to 36°. The resulting range of values of $S_{r,yield}$ for the most critical initial failure surface was $S_{r,yield} \approx 96$ to 179 lbs/ft^2.

Olson (2001) also performed back-analyses to determine $S_{r,yield}$. Failure surfaces analyzed were similar, but did not extend to the bottom of the loose sand layer. Instead, Olson preferred failure surfaces that remained at some small elevation above the base of the liquefiable stratum. Olson reported values of $S_{r,yield} \approx 4.3$ to 5.3 kPa (90 to 111 lbs/ft^2).

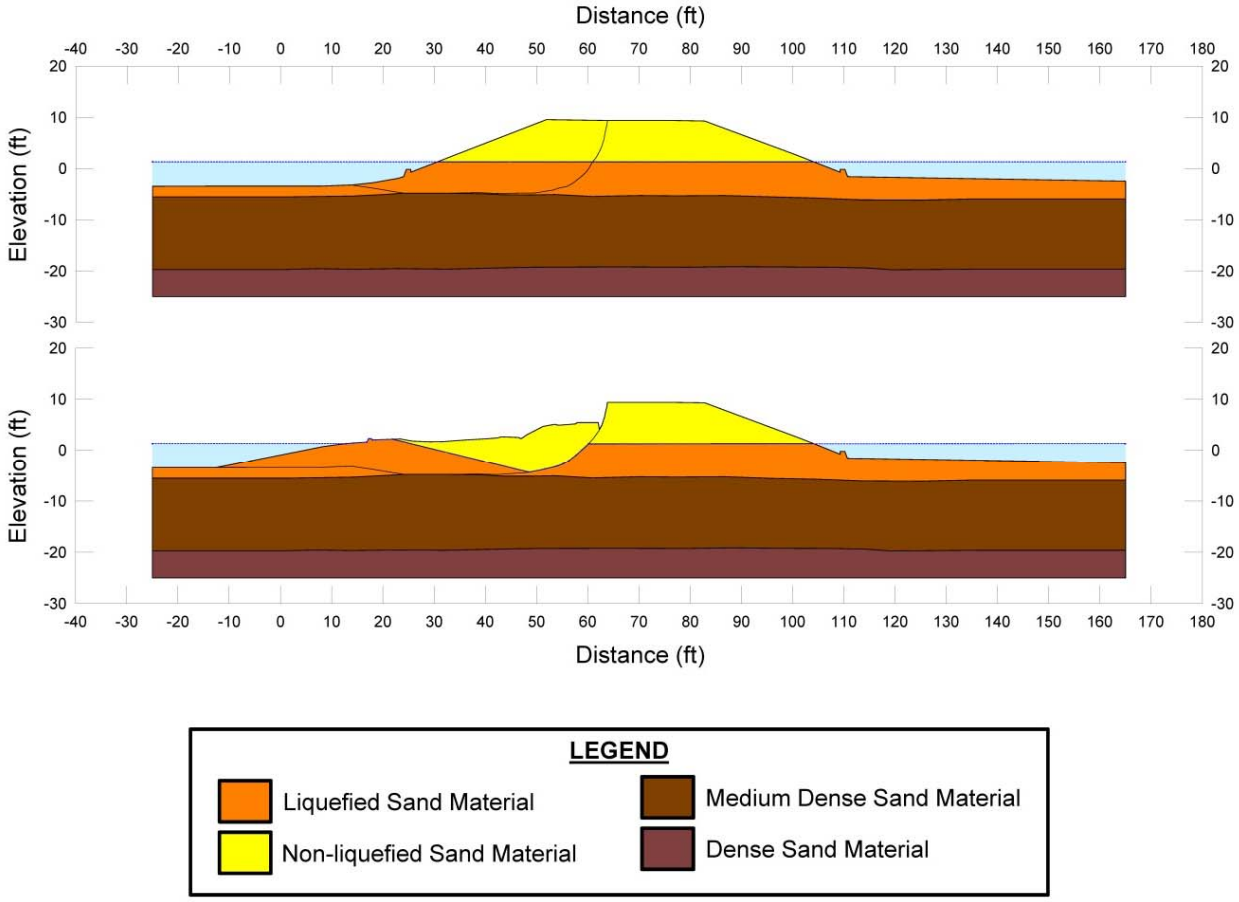

Figure A.5.4: Hachiro-Gata Roadway Embankment cross-sections showing (a) pre-failure geometry of the Hachiro-Gata embankment and the failure surfaces used for calculation of post-liquefaction initial yield strength $S_{r,yield}$, and (b) post-failure residual geometry and the failure surface used to calculate $S_{r,resid/geom}$.

A.5.4 Residual Strength Analysis Based on Residual Geometry

The calculation of the "apparent" post-liquefaction strength ($S_{r,resid/geom}$) required to produce a calculated Factor of Safety equal to 1.0 based on residual geometry is illustrated in Figure A.5.4(b).

An additional detail here is the shear strength modeled at the base of the portion of the toe of the embankment that traveled out into the lake. The incremental inertial analyses presented in Section A.1.4 that follows indicate that the maximum velocity was on the order of approximately 3.1 ft/sec, and the velocity during most of the run-in was lower. It is not possible to fully accurately determine the degree of hydroplaning that would have occurred or the strength of the sediments on the lake bottom. The best estimate analysis of $S_{r,resid/geom}$ was performed assuming that hydroplaning effects were negligible for this case, and that shear strength at the base of the embankment materials that entered into the reservoir was 100% of $S_{r,resid/geom}$.

This figure shows the phreatic surface, and the failure surface, used to calculate the best-estimate value of $S_{r,resid/geom} \approx 40$ lbs/ft^2. To capture uncertainty or variability, the strengths of the soil at the toe as the embankment material entered the lake was varied to have a strength as low as 50% of $S_{r,resid/geom}$ beneath the portion of the slide mass entering into the lake. Variations were also made in parameters, and in location of the pre-failure phreatic surface, as were described in the preceding section. The resulting likely range of post-liquefaction strength required to provide a calculated Factor of Safety equal to 1.0 based on residual geometry was considered to be $S_{r,resid/geom} \approx 16$ to 58 lbs/ft^2.

Olson (2001) also calculated post-liquefaction strength required to produce a calculated Factor of Safety equal to 1.0 based on residual geometry, and reported a range of $S_{r,resid/geom} \approx 1.1$ to 1.6 kPa (23 to 33 lbs/ft^2), in good agreement with the values calculated in these current studies.

A.5.5 Incremental Inertial Back-Analyses and Overall Estimates of S_r

Incremental inertial back-analyses were performed using the same sets of properties and geometries (including failure surfaces and phreatic surfaces) as described in the previous sections.

Figure A.5.5 shows the best-estimate progressive incremental inertial analysis, showing the five stages of geometry evolution modeled as the failure proceeds. Figure A.5.6 shows the associated calculations of (1) acceleration vs. time, (2) velocity vs. time, and (3) displacement of vs. time for the overall center of gravity. For the geometry and phreatic surface shown in Figure A.5.5, the best estimate value of post-liquefaction strength was $S_r = 68$ lbs/ft^2.

The main sources of uncertainty, or variability, in back-calculated values of S_r were (1) strengths of the materials outside the initial embankment toe as the failure mass entered the lake, (2) unit weights, (3) strengths within the non-liquefied materials, (4) the precise location of the overall failure surface, and (5) the location of the phreatic surface.

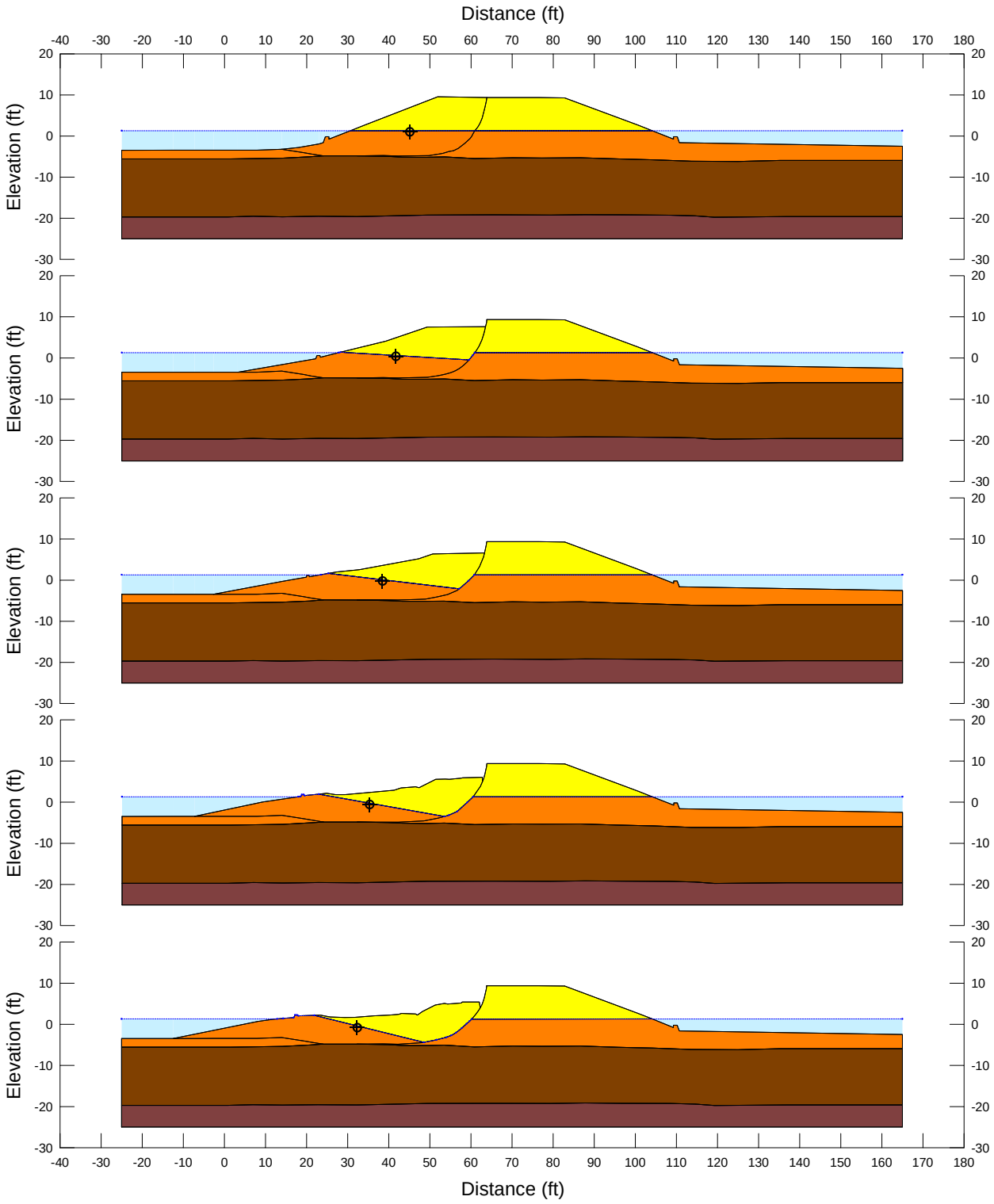

Figure A.5.5: Incremental inertial analysis of the failure of the Hachiro-Gata embankment, showing the progressive evolution of cross-section geometry modeled.

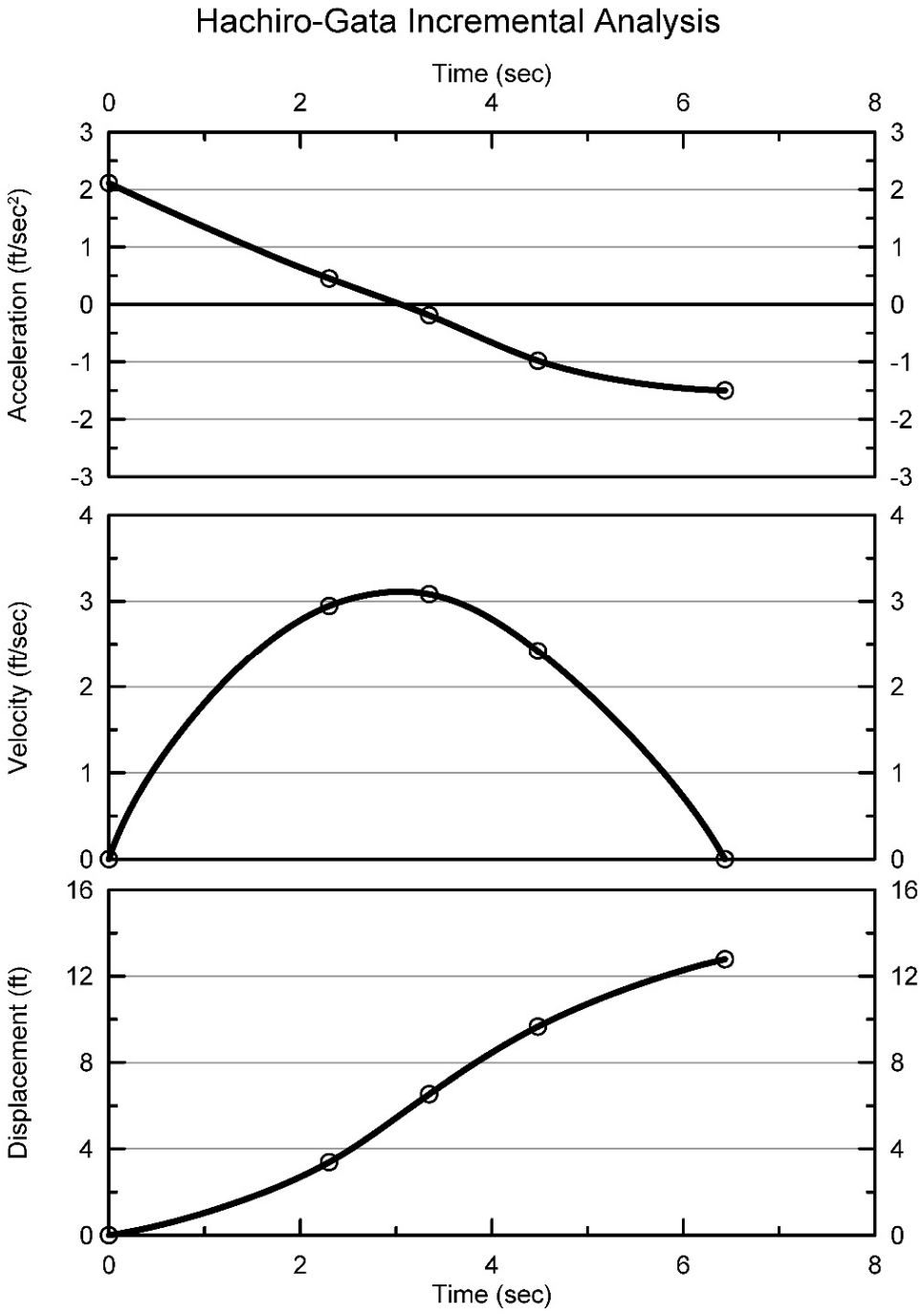

Figure A.5.6: Incremental inertial analysis of the failure of the Route 272 embankment, showing progressive evolution of: (1) acceleration vs. time, (2) velocity vs. time, and (3) displacement vs. time of the overall center of gravity.

The analysis shown in Figure A.5.5 neglects cyclic inertial forces, and so may represent a slightly conservative assessment of actual post-liquefaction strength mobilized.

Based on all analyses performed, and the considerations discussed herein, the overall best estimate value of post-liquefaction strength for the Route 272 embankment failure was judged to be $S_r \approx 68$ lbs/ft^2, with a likely range of $S_r \approx 45$ to 93 lbs/ft^2. Based on the factors contributing to uncertainty or variance for this case history, it was the judgment of the investigation team that this range represented approximately +/− 2 standard deviations. This range of variance is not quite symmetrical about the best estimate value, so minor further adjustments were made to produce a representative estimate of S_r suitable for regression analyses.

Overall, based on an assumed normal distribution, it was judged that the (mean and median) best estimate of post-liquefaction strength for this case history is

$$S_r = 68 \text{ lbs/ft}^2 \text{ (3.26 kPa)}$$

and that the best estimate of standard deviation of mean overall post-liquefaction strength is

$$\sigma_{\bar{S}} = 12 \text{ lbs/ft}^2 \text{ (0.57 kPa)}$$

Estimates of S_r were also reported by several other investigation teams, and these are shown in Table A.5.1(a). Olson (2001) and Olson and Stark (2002), reported a best estimate value of $S_r = 2.0$ kPa (42 lbs/ft^2), based on their inertial displacement analyses that considered kinetics, and a range of $S_r = 1.0$ to 3.2 kPa (21 to 69 lbs/ft^2). Wang (2003) and Wang and Kramer (2008) employed their zero inertial force (ZIF) method to incorporate inertial effects in their back-analyses of this failure, and they also developed estimates of both mean $\overline{S_r} = 65$ lbs/ft^2 as well as the associated standard deviation $\sigma_{\bar{S}} = 24.7$ lbs/ft^2. These other studies each employed different approaches, and different sets of modeling and analysis assumptions. Given these differences in approaches and modeling/analysis judgments, the overall agreement among these three investigations is very good.

A.5.6 Evaluation of Initial Effective Vertical Stress

Average initial (pre-failure) effective vertical stress was assessed for the liquefied zones of the failure surface shown in Figure A.5.4(a). Reasonable variations were then made in (1) the location of the phreatic surface, (2) unit weights, and (3) the precise location of the overall failure surface.

The resulting best estimate of average pre-failure effective stress within the liquefied materials controlling the failure was then $\sigma_{vo}' \approx 673$ lbs/ft^2, with a reasonable range of $\sigma_{vo}' \approx 594$ to 758 lbs/ft^2. This range is slightly non-symmetric about the median value, and this range was judged by the engineering team to represent approximately +/− 2 standard deviations. Overall, the best characterization of initial (pre-failure) average effective vertical stress was then taken to be represented by a mean and median value of

$$\overline{\sigma'_{vo}} \approx 673 \text{ lbs/ft}^2 \text{ (32.2 kPa)}$$

with a standard deviation of

$$\sigma_{\bar{\sigma}} \approx 41 \text{ lbs/ft}^2 \text{ (1.96 kPa)}$$

Estimates of σ_{vo}' were also reported by other investigation teams, and these are shown in Table A.13.1(c). Olson (2001) and Olson and Stark (2002) report an average initial vertical effective stress on the order of approximately $\sigma_{vo}' \approx 670$ lbs/ft^2, in excellent agreement with these current studies. Average initial vertical effective stresses were not directly reported by Wang (2003) and Kramer (2008), but they were published more recently in the publication by Kramer and Wang (2015). As discussed in Section 2.3.8.1(a), the approach taken by Wang (2003) to evaluation of σ_{vo}' for his nine "primary" case histories (this is one of those nine) is not clearly explained, and it is also poorly documented. Wang's value of $\sigma_{vo}' = 398$ lbs/ft^2 is significantly lower than the values developed by Olson (2001) and by these current studies. Wang (2003) presents no detailed cross-section for his analyses, so it is not possible to know why his estimated value of σ_{vo}' appears to be so much lower. Agreement between the values calculated by Olson (2001) and these current studies is excellent.

Table A.5.1: Representative values for the Hachiro-Gata Roadway Embankment case history of: (a) post-liquefaction strength (S_r), (b) initial vertical effective stress (σ_{vo}'), and (c) $N_{1,60,CS}$ developed by various investigation teams, and estimates of variance in each of these indices when available.

(a) Post-Liquefaction Strength:	
Olson (2001) and Olson and Stark (2002)	$S_r = 42$ psf, and range = 21 to 69 psf
Wang (2003) and Kramer (2008)	$\overline{S_r} = 65$ psf, and $\sigma_{\bar{S}} = 24.7$ psf
This Study	$\overline{S_r} = 68$ psf, and $\sigma_{\bar{S}} = 12$ psf
(b) Representative $N_{1,60}$ or $N_{1,60,CS}$ Value:	
Olson (2001) and Olson and Stark (2002)	$N_{1,60} = 4.4$ bpf, and range = 3.1 to 5.8 bpf
Wang (2003) and Kramer (2008)	$\overline{N_{1,60,CS}} = 5.7$ bpf, and $\sigma_{\bar{N}} = 2.8$ bpf
This Study	$\overline{N_{1,60,CS}} = 7$ bpf, and $\sigma_{\bar{N}} = 1.2$ bpf
(c) Representative Initial Vertical Effective Stress:	
Olson (2001) and Olson and Stark (2002)	$\sigma_{vo}' = 670$ psf, range is not provided.
Wang (2003) and Kramer (2008)	Value of $\sigma_{vo}' \approx 398$ psf is poorly documented, and so is considered useful only as an approximate comparison. (See Section 2.3.8.1, and Table 2.3.)
This Study	$\overline{\sigma'_{vo}} = 673$ psf, and $\sigma_{\bar{\sigma}} = 41$ psf

A.5.7 Evaluation of $N_{1,60,CS}$

As shown in Figure A.5.2, only 2 SPT were performed within the liquefiable upper stratum. As a result, lack of numbers of SPT tests is a significant contributor to uncertainty or variability with respect to the median or mean $N_{1,60,CS}$ value representative of this material. Ohya et al. (1985) reported an energy ratio of approximately 68%, and this current study assumes the same. Corrections for effective overburden stress (C_N) were made using the relationships proposed by Deger (2014), as presented and discussed in Appendix C, Section C.1. Corrections for SPT equipment and procedural details, and for fines content, were made based on Cetin et al. The resulting median $\overline{N_{1,60,CS}}$ value was 6.8 blows/ft.

Variance of $\overline{N_{1,60,CS}}$ within this limited data set was used to calculate the associated variance in the mean (and thus approximately the median) value of $\overline{N_{1,60,CS}}$, but this under-estimated the actual variance or uncertainty. Addition factors significantly affecting variance or uncertainty in the median representative $\overline{N_{1,60,CS}}$ value were (1) lack of numbers of SPT data, and (2) uncertainty as to actual SPT equipment and procedural details. Overall, it was the judgment of the investigation team that SPT penetration resistance could be suitably represented with a representative (median) value of $\overline{N_{1,60,CS}}$ = 6.8 blows/ft., and with a standard deviation of the median/representative value of approximately $\sigma_{\overline{N}}$ = 1.6 blows/ft.

Table A.5.1(b) shows values of representative $N_{1,60}$ or $N_{1,60,CS}$ values developed by other investigators, and variance or standard deviations in these representative values when available. Olson and Stark (2001, 2002) developed an estimated representative value of $N_{1,60}$ = 4.4 blows/ft, and an estimated range of representative values of $N_{1,60} \approx$ 3.1 to 5.8 blows/ft, but did not quantify variance or standard deviation in probabilistic terms. They applied no fines correction. Wang (2003) and Kramer (2008) jointly developed a representative value of $\overline{N_{1,60,CS}}$ = 5.7 blows/ft, and their estimated standard deviation of that overall mean value for this case history was $\sigma_{\overline{N}}$ = 2.8 blows/ft. The representative $N_{1,60}$ value of Olson and Stark is about 2 to 2.5 blows/ft lower than the other two sets of values in the table, in part because Olson and Stark did not make a fines correction, which would have served to increase their $N_{1,60}$ values as they became $N_{1,60,CS}$ values in these silty sands.

The investigation teams whose results are presented in Table A.5.1(c) each employed slightly different approaches with regard to corrections for effective overburden stress, fines content, and SPT equipment and procedural details. Given this, the agreement with the value employed in this current study is good. Wride, McRoberts and Robertson (1999) developed a somewhat lower estimate of representative $N_{1,60,CS}$ for this case history, but their approach targeted determination of a more nearly lower bound value, and so is this lower value is to be expected and it is not directly comparable with the other values shown.

A.5.8 Other Results and Indices

A number of additional results, and indices, can be extracted from the analyses performed. Some of these are useful in developing some of the over-arching relationships and figures presented in the main text of this report. These values are presented in Table A.5.2;

Table A.5.2: Additional results and indices from the analyses of the Hachiro-Gata Roadway Embankment failure case history.

Maximum distance traveled by the center of gravity of the overall failure mass	12.8 ft.
Initial post-liquefaction Factor of Safety prior to displacement initiation, and based on best estimate value of S_r	FS = 0.55
Final post-liquefaction Factor of Safety at final (residual) post-failure geometry, and based on best estimate value of S_r	FS = 1.66

A.6 La Marquesa Dam Upstream Slope (Chile; 1985)

A.6.1 Brief Summary of Case History Characteristics

Name of Structure	La Marquesa Dam, Upstream Slope
Location of Structure	Chile
Type of Structure	Zoned Earthen Dam
Date of Failure	March 3, 1985
Nature of Failure	Seismic, During 1985 Central Chilean Earthquake (M_S = 7.8)
Approx. Maximum Slope Height	29.2 ft. (U/S side)

A.6.2 Introduction and Description of Failure

The La Marquesa Dam suffered liquefaction-induced slope failures on both its upstream side and its downstream side as a result of the Central Chilean earthquake of March 3, 1985 (M_S = 7.8). This Appendix Section A.6 will deal primarily with the upstream side failure, though both failures are somewhat interactive with each other, and the subsequent Appendix Section A.7 will then deal primarily with the downstream side failure.

The dam is located near the Chilean coast, approximately 65 km west of Santiago. Peak horizontal ground surface accelerations recorded in the general vicinity of the dam during the earthquake were on the order of approximately 0.43 to 0.65 g.

As shown in Figure A.6.1, the dam suffered liquefaction-induced failures on both the upstream and downstream sides. Displacements were somewhat larger on the upstream side, where the upstream toe foundation soils appeared to have been partially excavated producing a slightly higher slope on the upstream side than on the downstream side. Upstream side displacements were approximately 12 feet vertically at the crest, and approximately 53 feet horizontally at the toe. The downstream side maximum displacements were approximately 9 feet vertically at the crest, and approximately 24 feet horizontally at the toe.

A.6.3 Geology and Site Conditions

Figure A.6.1 shows conditions both before and after the failure (from De Alba et al., 1987). Borings performed before the earthquake, and additional borings performed after the event, showed the dam foundation to consist of a relatively thin layer of silty sand, which was underlain by thicker deposits of sandy clay and clayey sand. The deeper sandy clay and clayey sand materials had higher fines contents, higher plasticity indices, and higher blowcounts and do not appear to have been involved in the two slope failures. It is within the relatively thin, upper (silty sand) foundation stratum that the liquefaction-induced sliding appears to have occurred; though it should be noted that failure through the lower portions of the embankment shells cannot be fully ruled out. This upper foundation stratum of silty sand had estimated fines contents of approxi-

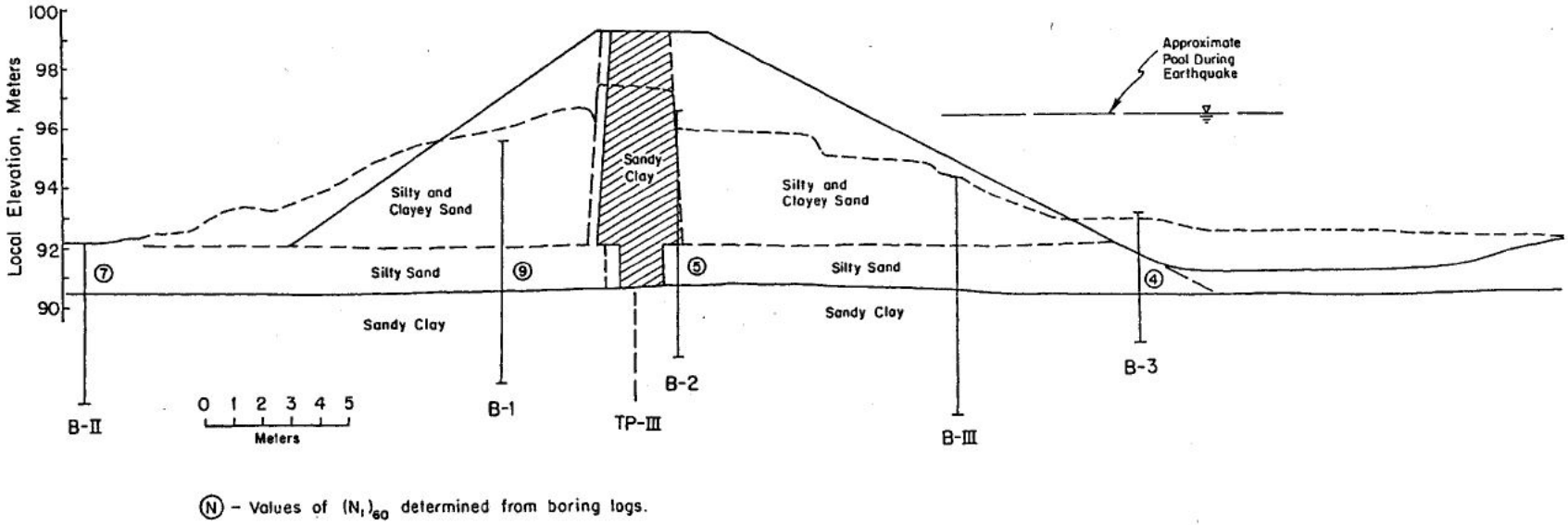

Figure A.6.1: Pre-failure and post-failure cross-sections of the La Marquesa Dam (from de Alba et. al, 1987).

mately 20% to 30% beneath the dam, and these soils appear to have been very loose, with very low SPT blowcounts.

Because of the presence of the relatively pervious upper silty sand stratum, a key trench was excavated to extend the central sandy clay core through this upper foundation stratum and this key trench was back-filled with compacted sandy clay core material in order to "key" the core into the lower, less pervious foundation soils.

The embankment fill materials were locally excavated from the valley floor, and from the abutments. The core zone was constructed using the more plastic sandy clays, and the shells were constructed using silty and clayey sands. Details of embankment compaction are not clear, but the embankment fill materials appear to have been very loosely placed, exhibiting SPT $N_{1,60,CS}$ values essentially equal to those of the loose and highly liquefiable underlying materials of the upper (silty sand) foundation stratum.

A.6.4 Initial Yield Stress Analyses

Figures A.6.2(a) and A.6.3(a)shows the cross-sections used for back-analyses of the post-liquefaction initial yield strength $S_{r,yield}$ that would be required within the liquefied upstream shell materials to produce a calculated Factor of Safety equal to 1.0. This is not the actual post-liquefaction strength, but it proves to be useful in developing a number of charts and relationships for these overall studies.

There are two different sets of potential failure surfaces in these two figures, and these correspond to "Scenario A" and "Scenario B". The central core section of the dam suffered some loss of height, as shown in Figures A.6.1 and A.6.6, and it spread a bit as well becoming a bit wider near its base. As shown in Figure A.6.6, a longitudinal crack occurred roughly along the centerline of the crest, and there was some lateral opening (separation) across the crack as well as some shear displacement across this crest crack. There were significantly greater vertical displacements of the two adjacent shell zones, leaving the core (even with its slightly reduced height) protruding upwards like a horst between the two adjacent down-dropped shell zones.

There were two sets of potential failure mechanisms that could potentially explain these features, and the overall observed post-failure geometries of Figures A.6.1 and A.6.6. The first (Scenario A) involves sliding primarily along the interface between the core zone and the adjacent shell zones, as shown in Figure A.6.2, with some lateral bulging of the core as the level of confinement provided by the adjacent shells reduced somewhat. The second (Scenario B) involves shearing through the lower portions of the core zone, producing both the observed crest settlements of the top of the core zone and also the minor lateral increase in core width, as illustrated in Figure A.6.3. This second Scenario B also serves to directly explain the observed crest crack, and provides a useful explanation for the observed differential vertical displacements across this longitudinal crest crack as well. Overall, it was judged that Scenario B provided a better overall explanation of the observed movements, but that Scenario A could not be completely discounted. Accordingly, both scenarios were modeled and analyzed.

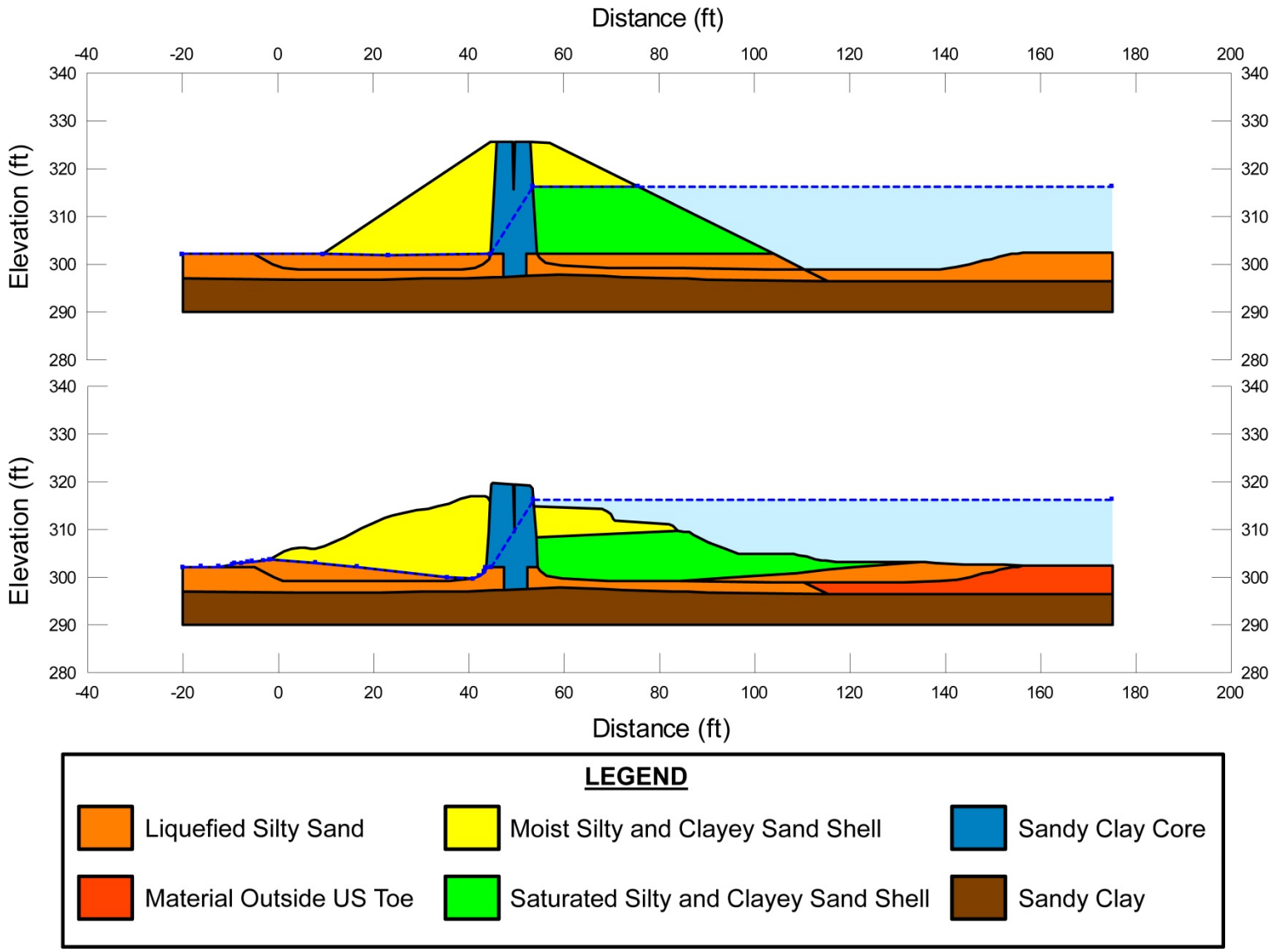

Figure A.6.2: La Marquesa Dam: (a) pre-failure geometry and Scenario A failure surface for initial yield stress analyses, and (b) post-failure geometry and Scenario A failure surface for post-failure residual geometry analyses.

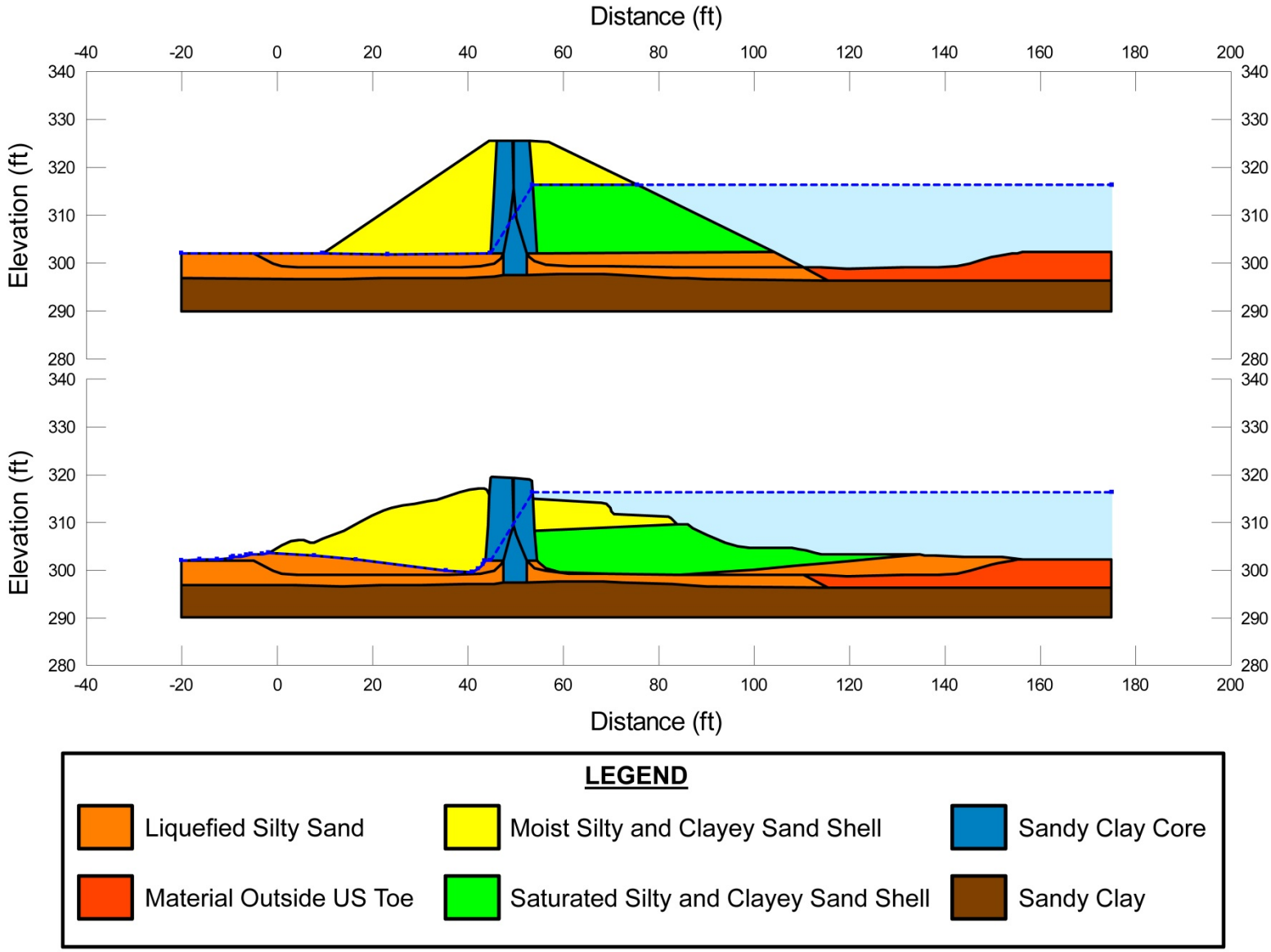

Figure A.6.3: La Marquesa Dam: (a) pre-failure geometry and Scenario B failure surface for initial yield stress analyses, and (b) post-failure geometry and Scenario B failure surface for post-failure residual geometry analyses.

There was no clear differentiation between the SPT blowcounts in the embankment shell zones and those of the underlying upper silty sand foundation stratum, so the embankment shell zone materials (which were of similar provenance) appear to have been placed in a very loose condition.

Shear strengths of non-saturated silty sand materials (above the phreatic surface) in the shell zones were modeled as frictional, with a best estimate value of Ø′ = 30 °. This was then varied between 26 to 34° in subsequent sensitivity analyses. Shear strengths within the saturated silty sands of both the lower upstream shell and the upper foundation stratum were modeled as S_r, and these current back-analyses were performed in order to determine this value. Shear strengths in the clayey sand core zone were modeled as cohesive, with residual (large displacement) values of $S_{u,r}/P \approx 0.09$ based on very limited data and information. This was then varied between 0.06 and 0.12 in subsequent sensitivity studies. Shears strengths along interfaces between the core and shell zones were considered to be controlled by the lesser of the two available shear strengths. Shear strengths of the nearly vertical cracks/shears at the upper portions of the central core zone (within the core) for Scenario B were modeled as negligible, in part because neither the upstream portion of the embankment nor the downstream portion of the embankment could usefully help to support the other when both were displacing vertically downwards.

Unit weights for the non-saturated shell zones were modeled as $\gamma_m = 120$ lbs/ft^3, and the saturated silty sands of the lower upstream shell and the upper foundation stratum were modeled as $\gamma_s = 125$ lbs/ft^3. These were varied by +/- 5 lbs/ft^3 in subsequent sensitivity studies. Unit weights of the silty clay core materials were modeled as $\gamma_s = 120$ lbs/ft^3 +/- 5 lbs/ft^3.

Based on the cross-sections shown in Figures A.6.2(a) and A.6.3(a), and the properties and parameters described above, the best-estimate value of $S_{r,yield}$ for Scenario A (Figure A.6.2(a)) was 240 lbs/ft^2, and the best-estimate value for Scenario B (Figure A.6.3(a)) was 254 lbs/ft^2. It was judged that Scenario B was more likely to have occurred than Scenario A, because it appears to better explain the overall observed post-failure geometry and cross-section and geometry details. Accordingly, a weighted average value of $S_{r,yield} = 249$ lbs/ft^2 was then selected as the overall best estimate value.

Parameters were next varied, as described previously, and alternate potential failure surfaces were also examined for both Scenarios A and B, including failure surfaces passing within the saturated lower portions of the upstream side embankment shell zone. The two sets of results were again weighted, favoring Scenario B, and the best overall estimate value was $S_{r,yield} \approx 253$ lbs/ft^2, and it was judged that a reasonable range was $S_{r,yield} \approx 227$ to 274 lbs/ft^2.

Olson (2001) was the only other investigator who also performed back-analyses to determine $S_{r,yield}$. Failure surfaces analyzed differed somewhat, and so did some of the parameters and other modeling assumptions. Olson reported a best estimate value of $S_{r,yield} \approx 9.3$ kPa (194 lbs/ft^2) , and a range of $S_{r,yield} \approx 6.7$ to 13.4 kPa (140 to 279 lbs/ft^2).

A.6.5 Residual Strength Analyses Based on Residual Geometry

The calculation of the "apparent" post-liquefaction strength ($S_{r,resid/geom}$) required to produce a calculated Factor of Safety equal to 1.0 based on residual geometry is illustrated in Figures A.6.2(b) and A.6.3(b), again representing Scenarios A and B. Modeling parameters and details are as previously described in the preceding sections.

Based on the cross-sections shown in Figures A.6.2(b) and A.6.3(b), and the properties and parameters described above, the best-estimate value of $S_{r,resid/geom}$ for Scenario A (Figure A.6.2(b)) was 38 lbs/ft^2, and the best-estimate value for Scenario B (Figure A.6.3(b)) was 55 lbs/ft^2. It was again judged that Scenario B was more likely to have occurred than Scenario A, because it appears to better explain the overall observed post-failure geometry and cross-section and geometry details. Accordingly, a weighted average value of $S_{r,resid/geom}$ = 49 lbs/ft^2 was then selected as the overall best estimate value.

Parameters were next varied, as described previously, and alternate potential failure surfaces were also examined for both Scenarios A and B, including failure surfaces passing within the saturated lower portions of the upstream side embankment shell zone. Again weighting the results in favor of Scenario B, it was judged that a reasonable range was $S_{r,resid/geom} \approx$ 32 to 68 lbs/ft^2.

Olson (2001) also performed back-analyses to determine $S_{r,yield}$. Failure surfaces analyzed again differed somewhat, and so did some of the parameters and other modeling assumptions. Olson reported a best estimate value of $S_{r,resid/geom} \approx$ 3.1 kPa (65 lbs/ft^2) , and a range of $S_{r,resid/geom} \approx$ 1.9 to 4.3 kPa (40 to 90 lbs/ft^2).

A.6.6 Incremental Momentum Back-Analyses and Overall Estimates of S_r

Incremental inertial back-analyses were performed using the same sets of properties and geometries (including failure surfaces and phreatic surfaces) as described in the previous sections. Two sets of analyses were again performed, for Scenario A and Scenario B.

Figure A.6.4 shows the best-estimate progressive incremental inertial analysis for Scenario A, showing the five stages of geometry evolution modeled as the failure proceeds. The resulting best estimate value of post-liquefaction strength for Scenario A was S_r = 91 lbs/ft^2.

Figure A.6.5 shows the best-estimate progressive incremental inertial analysis for Scenario B, showing the five stages of geometry evolution modeled as the failure proceeds. Figure A.6.6 shows the associated calculations of (1) acceleration vs. time, (2) velocity vs. time, and (3) displacement of the overall center of gravity vs. time for Scenario B. The resulting best estimate value of post-liquefaction strength was S_r = 106 lbs/ft^2.

Because Scenario B is judged to better explain the full details of the observed field failure, the overall best estimate of post-liquefaction strength based on these incremental momentum back-analyses was weighted in favor of Scenario B (and Figures A.6.5 and A.6.6), and the resulting overall best estimate value is S_r = 101 lbs/ft^2.

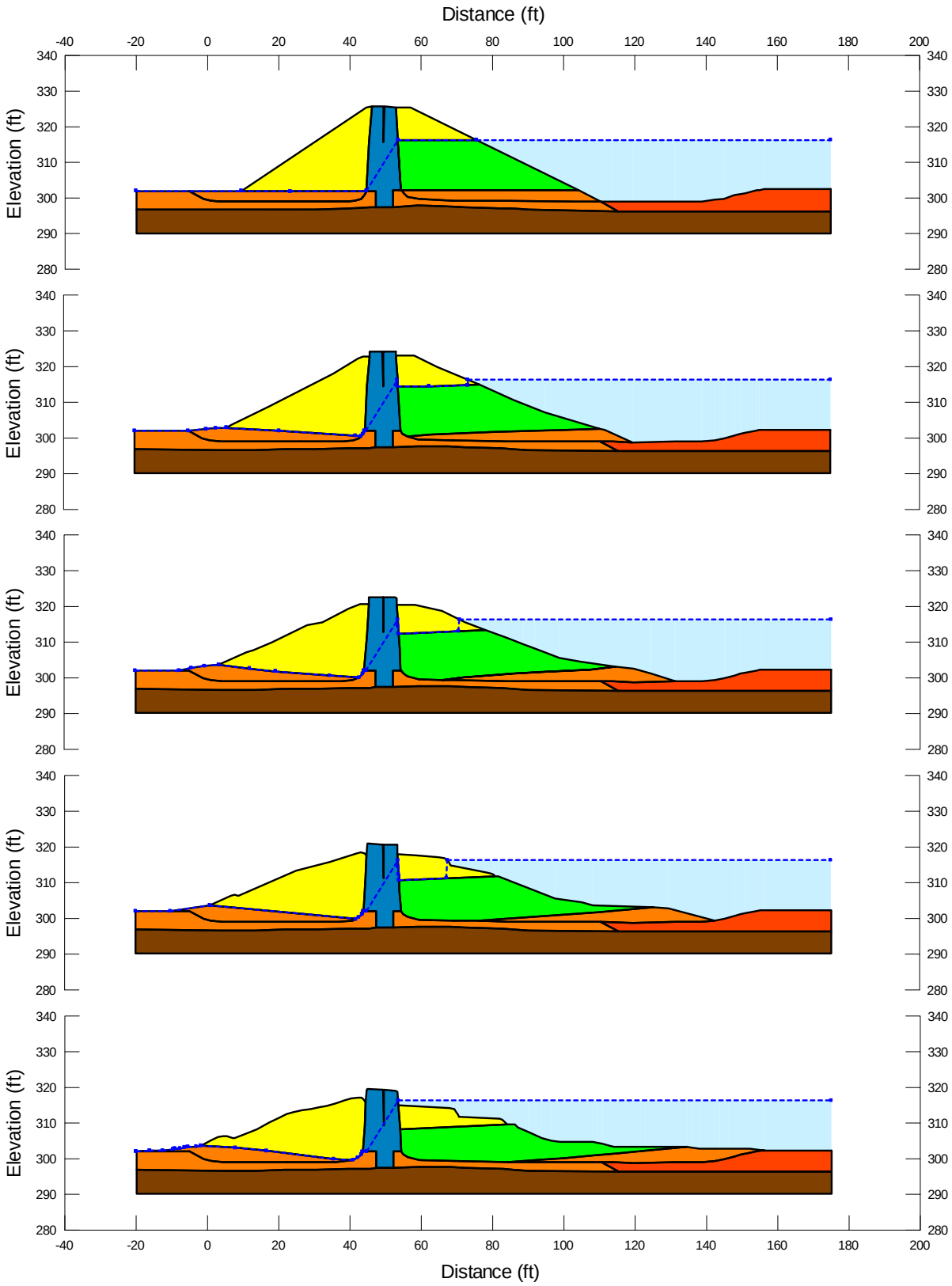

Figure A.6.4: Incremental momentum analysis of the failure of the La Marquesa Dam, showing progressive evolution of cross-section geometry modeled (for Scenario A).

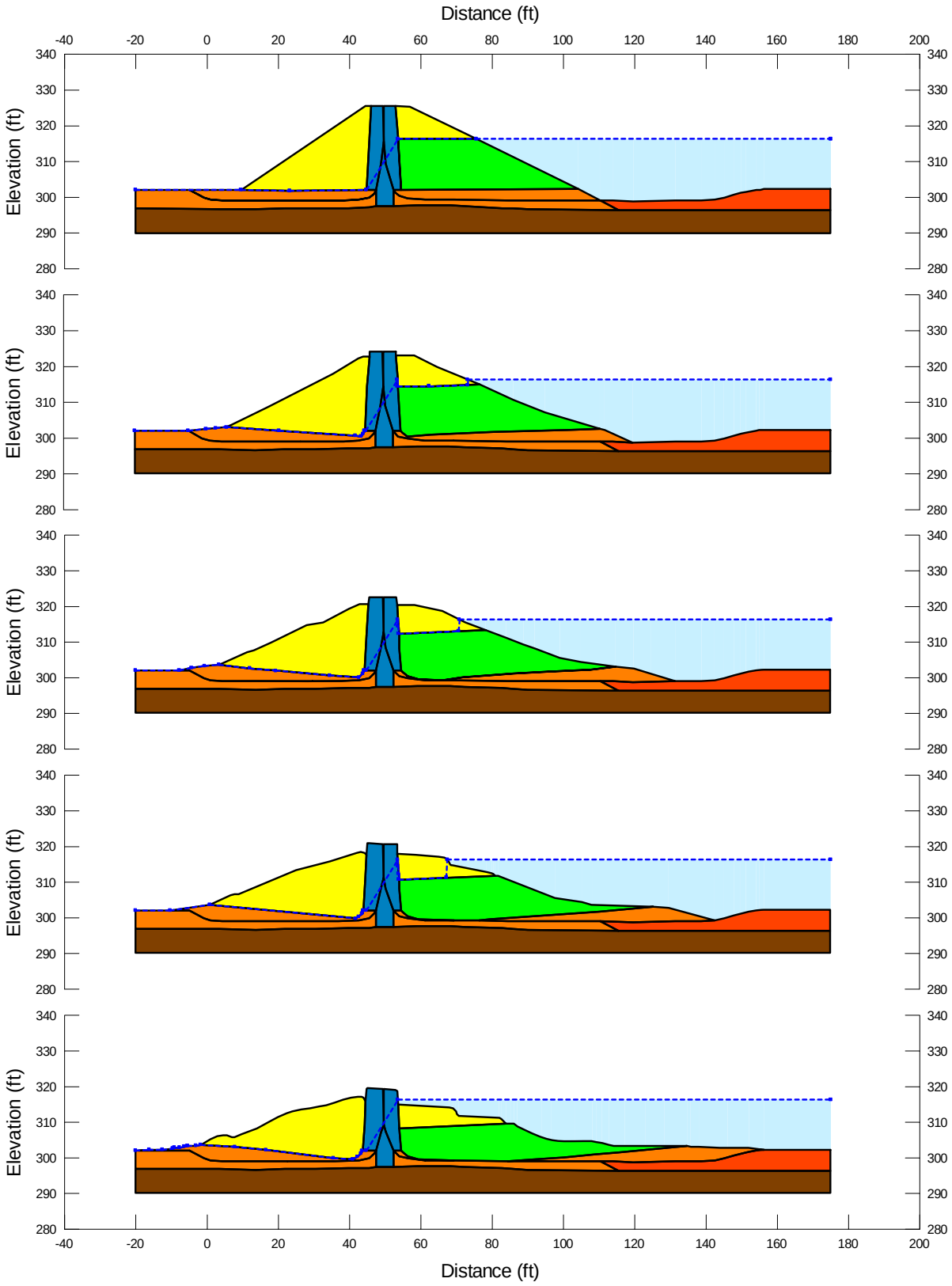

Figure A.6.5: Incremental momentum analysis of the failure of the La Marquesa Dam, showing progressive evolution of cross-section geometry modeled (for Scenario B).

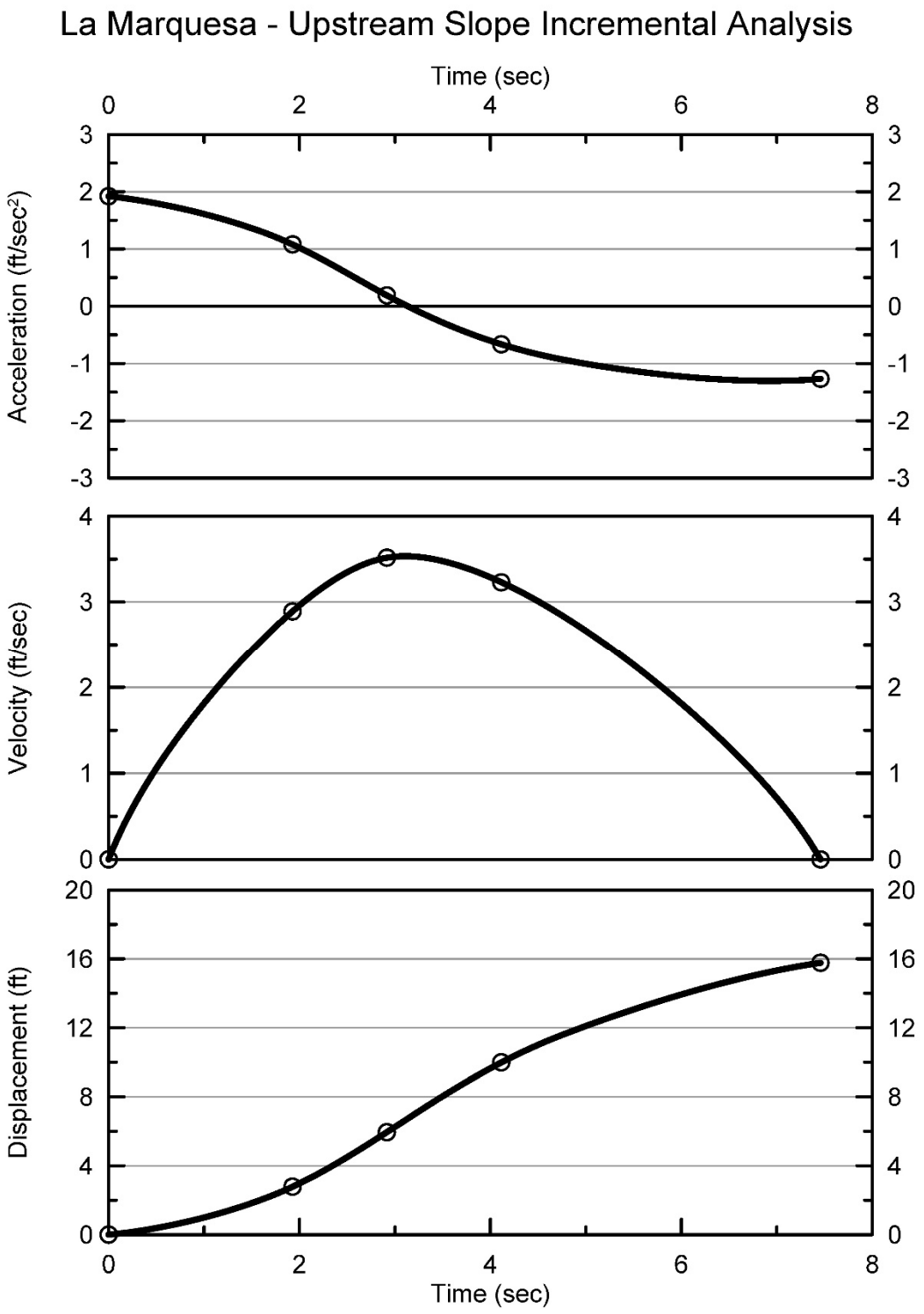

Figure A.6.6: Incremental momentum analysis of the upstream side slope failure of the La Marquesa Dam, showing progressive evolution of: (1) acceleration vs. time, (2) velocity vs. time, and (3) displacement vs. time of the overall center of gravity of the failure mass (for Scenario B).

Parameter sensitivity analyses, including modeling of additional potential failure surfaces considered to be "reasonable/feasible" were then performed to investigate the overall range of post-liquefactions strength values. This range was found to be S_r = 54 to 153 lbs/ft^2. This was judged to represent approximately +/- 1.5 standard deviations. This range of variance is not symmetrical about the best estimate value, so minor further adjustments were made to produce a representative estimate of S_r suitable for regression analyses.

Overall, based on an assumed normal distribution, it was judged that the (mean and median) best estimate of post-liquefaction strength for this case history is

$$\bar{S}_r = 103 \text{ lbs/ft}^2$$

and that the best estimate of standard deviation of mean overall post-liquefaction strength is

$$\sigma_{\bar{S}} = 33 \text{ lbs/ft}^2$$

The La Marquesa Dam upstream slope failure case history has been back-analyzed by a number of previous investigators, but not with back-analysis methods that reasonably accurately incorporate momentum effects. Seed and Harder (1990) reported a value of $S_r \approx 200$ lbs/ft^2, but their back-analyses included a judgmental addition to S_r to account for cyclic inertial effects. Olson (2001) and Olson and Stark (2002) did not apply their "kinetics" method to this case, and so they did not independently develop an estimate of S_r that incorporated momentum effects. Similarly, Wang (2003) and Wang and Kramer (2008) did not employ their zero inertial force (ZIF) method to incorporate inertial effects in back-analyses of this failure, and so they also did not independently develop an estimate of S_r that incorporated momentum effects.

Approximate comparisons can be made to Olson and Stark's (2001, 2002) values of back-calculated values of $S_{r,yield}$ and $S_{r,resid/geom}$ by means of Equation 4.2, as shown in Tables 4.3 and 4.6, but this is not a very rigorous comparison. As shown in Tables 4.3 and 4.6, the resulting inferred value of S_r for $\xi = 0.8$ would be $S_r \approx 104$ lbs/ft^2, in excellent agreement with these current studies. This is the value shown in Table A.6.1.

It appears that the values calculated in these current studies are the first set of back-calculated values of post-liquefaction S_r based on analysis methods that directly incorporate momentum effects.

Finally, it should be noted that this case history is one in which (1) a liquefaction-induced slope failure produced moderate displacements and deformations, and (2) levels and duration of strong shaking were high. This is thus a case in which it may be hypothesized that the values back-calculated in these current studies, even with incorporation of momentum effects, may conservatively underestimate the actual values of S_r to some extent due to the failure to also incorporate cyclic inertial effects during strong shaking. It is not (yet) analytically possible to reliably quantify this additional potential conservatism. Seed and Harder (1990) made a judgmental increase in estimated S_r to account for these cyclic inertial effects, but in these current studies this additional adjustment is not being made.

A.6.7 Evaluation of Initial Effective Vertical Stress

Average initial (pre-failure) effective vertical stress was assessed for the liquefied zones of each of the failure surfaces shown in Figures A.6.2(a) and A.6.3(a). Additional sensitivity analyses were then performed for reasonable ranges of variations in (1) the location of the phreatic surface, (2) unit weights, and (3) the precise location of the overall failure surface in order to evaluate uncertainty or variance.

The resulting best estimate of average pre-failure effective stress within the liquefied materials controlling the failure was then $\sigma_{vo}' \approx 981$ lbs/ft^2, with a reasonable range of $\sigma_{vo}' \approx 771$ to 1,253 lbs/ft^2. This range is slightly non-symmetric about the median value, and this range was judged by the engineering team to represent approximately ± 2 standard deviations. Overall, the best characterization of initial (pre-failure) average effective vertical stress was then taken to be represented by a mean value of

$$\overline{\sigma'_{vo}} \approx 981 \text{ lbs/ft}^2$$

and with a standard deviation of

$$\sigma_{\bar{\sigma}} \approx 134 \text{ lbs/ft}^2$$

An estimate of σ_{vo}' was also calculated by Olson and Stark (2001, 2002) and this is shown in Table A.1.1(c). They reported a weighted average mean value of $\sigma_{vo}' \approx 960$ lbs/ft^2, in excellent agreement with these current studies. Average initial vertical effective stresses were not directly reported by Wang (2003) and Kramer (2008), but they were published more recently in the publication by Kramer and Wang (2015). As discussed in Section 2.3.8.1(b)-(iii), Wang (2003) did not perform any independent analyses to assess σ_{vo}' for his 22 "secondary" cases, and this is one of those cases. Instead, he compiled values of S_r from multiple previous investigators, and averaged these for a best estimate. He also compiled multiple values of S_r/σ_{vo}' from previous investigators, and averaged these for a best estimate. He then used these two best-estimate values of S_r and S_r/σ_{vo}' to infer a resulting representative value of σ_{vo}'. As described in Section 2.3.8.1(b)-(iii), the resulting averaged values of S_r and S_r/σ_{vo}' were incompatible with each other for a number of Wang's "secondary" case histories, and this process produced unreasonable, and in some cases physically infeasible, values of σ_{vo}' for a number of case histories. Accordingly, Wang's value of $\sigma_{vo}' = 1{,}682$ lbs/ft^2 is not considered a useful check here. Agreement between Olson's value, which is well-documented, and the value developed in these current studies, is excellent.

A.6.8 Evaluation of $N_{1,60,CS}$

Figure A.6.6 shows the locations of post-failure SPT borings and SPT tests performed to investigate the failure. Based on the available data and information, it appears most likely that the upstream and downstream slope failures both occurred due to liquefaction-induced sliding within the silty sand upper foundation stratum immediately underlying the dam embankment. Only a

limited number of SPT tests are available within this material, so the paucity of useful penetration data is a major source of uncertainty here.

Based on the 2 SPT tests in these upper foundation silty sands on the upstream side, and re-processing these using the relationships and procedures presented in Appendix C, Section C.1, the best estimate mean value of $N_{1,60,CS}$ for the upstream side upper foundation silty sands was found to be $\overline{N_{1,60,CS}} \approx 6.5$ blows/ft. Variance of $\overline{N_{1,60,CS}}$ was estimated primarily on the basis of the perceived uncertainties associated with the (1) the limited number of blowcounts from within the failure zone, and (2) the somewhat higher average values of $N_{1,60,CS}$ in these same upper foundation silty sands on the downstream side. Considering these, the representation of uncertainty in the representative median value of $\overline{N_{1,60,CS}}$ was taken as $\sigma_{\overline{N}} \approx 1.8$ blows/ft.

Table A.1.1(b) shows values of representative $N_{1,60}$ or $N_{1,60,CS}$ values developed by two other teams of investigators, and variance or standard deviations in these representative values if available. Olson and Stark (2001, 2002) developed an estimated representative value of $N_{1,60}$ = 4.5 blows/ft for the upstream side, but for this case history they proposed no range. Wang (2003) and Kramer (2008) jointly developed a representative value of $\overline{N_{1,60,CS}}$ = 6.5 blows/ft, and their estimated standard deviation of that overall mean value for this case history was $\sigma_{\overline{N}}$ = 2.8 blows/ft. Details of the development of this interpretation by Wang and Kramer are not presented. Olson and Stark (2001, 2002) made no fines adjustments, so theirs is an $N_{1,60}$ value rather than an $N_{1,60,CS}$ value. Their value would increase if it was to be adjusted for fines in these silty sand materials. Overall agreement between the three independent assessments of representative $\overline{N_{1,60,CS}}$ values is excellent, and variance or uncertainty in $\overline{N_{1,60,CS}}$ appears to be moderate.

A.6.9 Additional Indices from the Back-Analyses

A number of additional results, and indices, can be extracted from the analyses performed. Some of these are useful in developing some of the over-arching relationships and figures presented in the main text of this report. These values are presented in Table A.6.2.

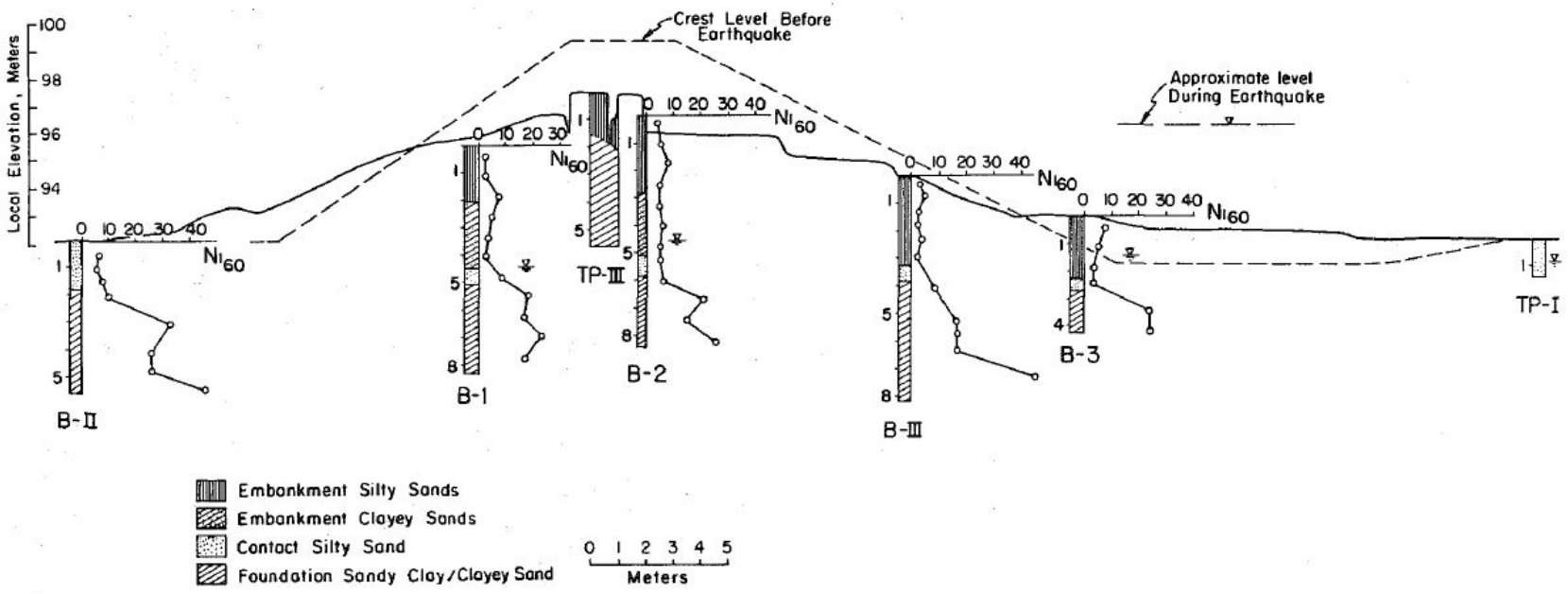

Figure A.6.6: Post-failure cross-section of La Marquesa Dam showing the locations and results of standard penetration tests (de Alba et al., 1987).

Table A.6.1: Representative values for the La Marquesa Dam upstream slope failure case history of: (a) post-liquefaction strength (S_r), (b) initial vertical effective stress (σ_{vo}'), and (c) $N_{1,60,CS}$ developed by various investigation teams, and estimates of variance in each of these indices when available.

(a) Post-Liquefaction Strength:	
Seed and Harder (1990	$S_r \approx 200$ psf[1]
Olson (2001) and Olson and Stark (2002)	$S_r \approx 104$ psf[2]
Wang (2003) and Kramer (2008)	N/A
This Study	$\overline{S_r} = 103$ psf and $\sigma_{\overline{S}} = 31$ psf
(b) Representative $N_{1,60}$ or $N_{1,60,CS}$ Value:	
Olson (2001) and Olson and Stark (2002)	$N_{1,60} = 4.5$ bpf
Wang (2003) and Kramer (2008)	$\overline{N_{1,60,CS}} = 6.5$ bpf, and $\sigma_{\overline{N}} = 2.8$ bpf
This Study	$\overline{N_{1,60,CS}} = 6.5$ bpf, and $\sigma_{\overline{N}} = 1.8$ bpf
(c) Representative Initial Vertical Effective Stress:	
Olson (2001) and Olson and Stark (2002)	Average $\sigma_{vo}' \approx 960$ psf, with no range provided.
Wang (2003) and Kramer (2008)	Value of $\sigma_{vo}' \approx 1{,}682$ psf is poorly based, and so is not very useful as a basis for comparison. (See Section 2.3.8.1(b) and Table 2.3)
This Study	$\overline{\sigma'_{vo}} = 981$ psf, and $\sigma_{\overline{\sigma}} = 134$ psf

[1] This value of S_r was increased to judgmentally incorporate cyclic inertial effects.
[2] See Section A.6.6 for an explanation of this value as presented.

Table A.6.2: Additional results and indices from the analyses of the La Marquesa Dam upstream slope failure case history.

Maximum distance traveled by the center of gravity of the overall failure mass	15.8 ft.
Initial post-liquefaction Factor of Safety prior to displacement initiation, and based on best estimate value of S_r	FS = 0.50
Final post-liquefaction Factor of Safety at final (residual) post-failure geometry, and based on best estimate value of S_r	FS = 1.81

A.7 La Marquesa Dam Downstream Slope (Chile; 1985)

A.7.1 Brief Summary of Case History Characteristics

Name of Structure	La Marquesa Dam, Downstream Slope
Location of Structure	Chile
Type of Structure	Zoned Earthen Dam
Date of Failure	March 3, 1985
Nature of Failure	Seismic, During 1985 Central Chilean Earthquake (M_S = 7.8)
Approx. Maximum Slope Height	26 ft. (D/S side)

A.7.2 Introduction and Description of Failure

The La Marquesa Dam suffered liquefaction-induced slope failures on both its upstream side and its downstream side as a result of the Central Chilean earthquake of March 3, 1985 (M_S = 7.8). This Appendix, Section A.7, will deal primarily with the upstream side failure, though both failures are somewhat interactive with each other. The previous Appendix Section A.6 dealt primarily with the upstream side slope failure, but it also presented a large amount of information, discussion, and figures pertinent to both the upstream and downstream slope failures, and an effort will be made to minimize repetition here.

A.7.3 Initial Yield Stress Analyses

Appendix A.6, Figures A.6.2(a) and A.6.3(a) show the cross-sections used for back-analyses of the post-liquefaction initial yield strength $S_{r,yield}$ that would be required within the liquefied upstream and downstream shell materials to produce a calculated Factor of Safety equal to 1.0. This is not the actual post-liquefaction strength, but it proves to be useful in developing a number of charts and relationships for these overall studies.

As described previously in Appendix A.6, there are two different sets of potential failure surfaces in these two figures, and these correspond to “Scenario A” and “Scenario B”. The central core section of the dam suffered some loss of height, as shown in Figures A.6.1 and A.6.6, and it spread a bit as well becoming a bit wider near its base. As shown in Figure A.6.6, a longitudinal crack occurred roughly along the centerline of the crest, and there was some lateral opening (separation) as well as some shear displacement across this crest crack. There were significantly greater vertical displacements of the two adjacent shell zones, leaving the core (even with its slightly reduced height) protruding upwards like a horst between the two adjacent down-dropped shell zones.

There were two sets of potential failure mechanisms that could potentially explain these features, and the overall observed post-failure geometries of Figures A.6.1 and A.6.6. The first (Scenario A) involves sliding primarily along the interface between the core zone and the adjacent

shell zones, as shown in Figure A.6.2, with some lateral bulging of the core as the level of confinement provided by the adjacent shells reduced somewhat. The second (Scenario B) involves shearing through the lower portions of the core zone, producing both the observed crest settlements of the top of the core zone and also the minor lateral increase in core width. This second Scenario B also serves to directly explain the observed crest crack, and provides a useful explanation for the observed differential vertical displacements across this longitudinal crest crack as well. It was judged that Scenario B provided a better overall explanation of the observed movements, but that Scenario A could not be completely discounted. Accordingly, both scenarios were modeled and analyzed. Modeling of strengths and unit eights, etc. was described previously in Appendix A.6.

Based on the cross-sections shown in Figures A.6.2(a) and A.6.3(a), and the properties and parameters described previously, the best-estimate value of $S_{r,yield}$ for the downstream side failure for Scenario A (Figure A.6.2(a)) was 303 lbs/ft^2, and the best-estimate value for Scenario B (Figure A.6.3(a)) was 324 lbs/ft^2. It was judged that Scenario B was more likely to have occurred than Scenario A, because it appears to better explain the overall observed post-failure geometry and cross-section and geometry details. Accordingly, a weighted average value of $S_{r,yield}$ = 317 lbs/ft^2 was then selected as the overall best estimate value.

Parameters were next varied, as described previously, and alternate potential failure surfaces were also examined for both Scenarios A and B, including failure surfaces passing within the saturated lower portions of the upstream side embankment shell zone. Again weighting the results in favor of Scenario B, it was judged that a reasonable range was $S_{r,yield} \approx$ 245 to 394 lbs/ft^2.

Olson (2001) was the only other investigator who also performed back-analyses to determine $S_{r,yield}$. Failure surfaces analyzed differed somewhat, and so did some of the parameters and other modeling assumptions. Olson reported a best estimate value of $S_{r,yield} \approx$ 12.9 kPa (269 lbs/ft^2) , and a range of $S_{r,yield} \approx$ 7.7 to 15.6 kPa (161 to 326 lbs/ft^2).

A.7.4 Residual Strength Analyses Based on Residual Geometry

The calculation of the "apparent" post-liquefaction strength ($S_{r,resid/geom}$) required to produce a calculated Factor of Safety equal to 1.0 based on residual geometry is illustrated in the previous Appendix A.6, Figures A.6.2(b) and A.6.3(b), again representing Scenarios A and B. Modeling parameters and details are as previously described in the preceding sections.

Based on the cross-sections shown in Figures A.6.2(b) and A.6.3(b), and the properties and parameters described above, the best-estimate value of $S_{r,resid/geom}$ for failure on the downstream side based on Scenario A (Figure A.6.2(b)) was 151 lbs/ft^2, and the best-estimate value for Scenario B (Figure A.6.3(b)) was 165 lbs/ft^2. It was again judged that Scenario B was more likely to have occurred than Scenario A, because it appears to better explain the overall observed post-failure geometry and cross-section and geometry details. Accordingly, a weighted average value of $S_{r,resid/geom}$ = 160 lbs/ft^2 was then selected as the overall best estimate value.

Parameters were next varied, as described previously, and alternate potential failure surfaces were also examined for both Scenarios A and B, including failure surfaces passing within

the saturated lower portions of the upstream side embankment shell zone. Again weighting the results in favor of Scenario B, it was judged that a reasonable range was $S_{r,resid/geom} \approx 109$ to 214 lbs/ft^2.

Olson (2001) also performed back-analyses to determine $S_{r,yield}$. Failure surfaces analyzed again differed somewhat, and so did some of the parameters and other modeling assumptions. Olson reported a best estimate value of $S_{r,resid/geom} \approx 5.3$ kPa (111 lbs/ft^2) , and a range of $S_{r,resid/geom} \approx 2.2$ to 9.8 kPa (46 to 205 lbs/ft^2).

A.7.5 Incremental Momentum Back-Analyses and Overall Estimates of S_r

Incremental inertial back-analyses were performed using the same sets of properties and geometries (including failure surfaces and phreatic surfaces) as described in the previous sections. Two sets of analyses were again performed, for Scenario A and Scenario B.

Appendix A.6, Figures A.6.4 through A.6.7 show the best-estimate progressive incremental inertial analysis for Scenarios A and B, showing the five stages of geometry evolution modeled as the failure proceeds. The resulting best estimate value of post-liquefaction strength for Scenario A was $S_r = 203$ lbs/ft^2, and the best estimate for Scenario B was $S_r = 215$ lbs/ft^2.

Because Scenario B is judged to better explain the full details of the observed field failure, the overall best estimate value of post-liquefaction strength based on these incremental momentum back-analyses was weighted in favor of Scenario B (and Figures A.6.6 and A.6.6, and the resulting overall best estimate value is $S_r = 211$ lbs/ft^2.

Parameter sensitivity analyses, including modeling of additional potential failure surfaces considered to be "reasonable/feasible" were then performed to investigate the overall range of post-liquefactions strength values. This range was found to be $S_r = 129$ to 299 lbs/ft^2. This was judged to represent approximately +/- 1.5 standard deviations. This range of variance is not symmetrical about the best estimate value, so minor further adjustments were made to produce a representative estimate of S_r suitable for regression analyses.

Overall, based on an assumed normal distribution, it was judged that the (mean and median) best estimate of post-liquefaction strength for this downstream failure case history was judged to be

$$\overline{S_r} = 214 \text{ lbs/ft}^2$$

and that the best estimate of standard deviation of mean overall post-liquefaction strength is

$$\sigma_{\overline{S}} = 57 \text{ lbs/ft}^2$$

The La Marquesa Dam upstream slope failure case history has been back-analyzed by a number of previous investigators, but not with back-analysis methods that reasonably accurately incorporate momentum effects. Seed and Harder (1990) reported a value of $S_r \approx 400$ lbs/ft^2, based

on analyses that only approximately accounted for momentum effects, and their reported value included an additional increase in S_r to attempt on a judgmental basis to incorporate cyclic inertial effects. Olson (2001) and Olson and Stark (2002) did not apply their "kinetics" method to this case, and so they did not independently develop an estimate of S_r that incorporated momentum effects. Similarly, Wang (2003) and Wang and Kramer (2008) did not employ their zero inertial force (ZIF) method to incorporate inertial effects in back-analyses of this failure, and so they also did not independently develop an estimate of S_r that incorporated momentum effects.

Approximate comparisons can be made to Olson and Stark's (2001, 2002) values of back-calculated values of $S_{r,yield}$ and $S_{r,resid/geom}$ by means of Equation 4.2, as shown in Tables 4.3 and 4.6, but this is not a very rigorous comparison. As shown in Tables 4.3 and 4.6, the resulting inferred value of S_r for $\xi = 0.8$ would be $S_r \approx 152$ lbs/ft^2, in fairly good agreement with these current studies. A slightly higher value of ξ might be justified by the runout characteristics of this case (see Chapter 4, and Equation 4-1).

A higher value of $S_r = 400$ lbs/ft^2 was developed by Seed and Harder (1990), but that value had a large allowance for cyclic inertial forces, and the current authors now feel that was an over-estimate.

It appears that the values calculated in these current studies are the first set of back-calculated values of post-liquefaction S_r based on analysis methods that formally incorporate momentum effects.

Finally, it should be noted that this case history is one in which (1) a liquefaction-induced slope failure produced moderate displacements and deformations, and (2) levels and duration of strong shaking were high. This is thus a case in which it may be hypothesized that the values back-calculated in these current studies, even with incorporation of momentum effects, may conservatively underestimate the actual values of S_r due to the failure to also incorporate cyclic inertial effects during strong shaking. It is not (yet) analytically possible to reliably quantify this additional potential conservatism. Seed and Harder (1990) had increased their back-estimated value of Sr to judgmentally incorporate incremental inertia effects, but the current engineering team have chosen not to make this type of further adjustment here.

A.7.6 Evaluation of Initial Effective Vertical Stress

Average initial (pre-failure) effective vertical stress was assessed for the liquefied zones of each of the failure surfaces shown in Figures A.6.2(a) and A.6.3(a) of Appendix A.6. Additional sensitivity analyses were then performed for reasonable ranges of variations in (1) the location of the phreatic surface, (2) unit weights, and (3) the precise location of the overall failure surface in order to evaluate uncertainty or variance.

The resulting best estimate of average pre-failure effective stress within the liquefied materials controlling the failure was then $\sigma_{vo}' \approx 1{,}215$ lbs/ft^2, with a reasonable range of $\sigma_{vo}' \approx$ 1,011 to 1,423 lbs/ft^2. This range is slightly non-symmetric about the median value, and this range was judged by the engineering team to represent approximately ± 2 standard deviations. Overall,

the best characterization of initial (pre-failure) average effective vertical stress was then taken to be represented by a mean value of

$$\overline{\sigma'_{vo}} \approx 1{,}215 \text{ lbs/ft}^2$$

and with a standard deviation of

$$\sigma_{\bar{\sigma}} \approx 103 \text{ lbs/ft}^2$$

An estimate of σ_{vo}' was also calculated by Olson and Stark (2001, 2002) and this is shown in Table A.1.1(c). They reported a weighted average mean value of $\sigma_{vo}' \approx 1{,}073$ lbs/ft^2, in good general agreement with these current studies. Average initial vertical effective stresses were not directly reported by Wang (2003) and Kramer (2008), but they were published more recently in the publication by Kramer and Wang (2015). As discussed in Section 2.3.8.1(b)-(iii), Wang (2003) did not perform any independent analyses to assess σ_{vo}' for his 22 "secondary" cases, and this is one of those cases. Instead, he compiled values of S_r from multiple previous investigators, and averaged these for a best estimate. He also compiled multiple values of S_r/σ_{vo}' from previous investigators, and averaged these for a best estimate. He then used these two best-estimate values of S_r and S_r/σ_{vo}' to infer a resulting representative value of σ_{vo}'. As described in Section 2.3.8.1(b)-(iii), the resulting averaged values of S_r and S_r/σ_{vo}' were incompatible with each other for a number of Wang's "secondary" case histories, and this process produced unreasonable, and in some cases physically infeasible, values of σ_{vo}' for a number of case histories. Accordingly, Wang's value of $\sigma_{vo}' = 1{,}850$ lbs/ft^2 is not considered a useful check here. Agreement between Olson's value, which is well-documented, and the value developed in these current studies is very good, especially considering Olson's apparent propensity to often model and analyze slightly shallower failure surfaces than those considered best estimates in this current study.

A.7.7 Evaluation of $N_{1,60,CS}$

Figure A.6.6 of Appendix A.6 showed the locations of post-failure SPT borings and SPT tests performed to investigate the failure. Based on the available data and information, it appears most likely that the upstream and downstream slope failures both occurred due to liquefaction-induced sliding within the silty sand upper foundation stratum immediately underlying the dam embankment. Only a limited number of SPT tests are available within this material, so the paucity of useful penetration data is a major source of uncertainty here.

Based on the six SPT tests in these upper foundation silty sands on the upstream side, and re-processed using the relationships and procedures presented in Appendix C, Section C.1, the best estimate mean value of $N_{1,60,CS}$ for the downstream side upper foundation silty sands was found to be $\overline{N_{1,60,CS}} \approx 10.5$ blows/ft. Variance of $\overline{N_{1,60,CS}}$ was estimated primarily on the basis of the perceived uncertainties associated with the (1) the limited number of blowcounts from within the failure zone, and (2) the somewhat higher average values of $N_{1,60,CS}$ in these same upper foundation silty sands on the downstream side. Considering these, the representation of uncertainty in the representative median value of $\overline{N_{1,60,CS}}$ was taken as $\sigma_{\bar{N}} \approx 2.2$ blows/ft.

Table A.1.1(b) shows values of representative $N_{1,60}$ or $N_{1,60,CS}$ values developed by two other teams of investigators, and variance or standard deviations in these representative values if available. Olson and Stark (2001, 2002) developed an estimated representative value of $N_{1,60}$ = 9.0 blows/ft for the upstream side, but for this case history they proposed no range. Wang (2003) and Kramer (2008) jointly developed a representative value of $\overline{N_{1,60,CS}}$ = 9.9 blows/ft, and their estimated standard deviation of that overall mean value for this case history was $\sigma_{\overline{N}}$ = 3.0 blows/ft. Details of the development of this interpretation by Wang and Kramer are not presented. Olson and Stark (2001, 2002) made no fines adjustments, so theirs is an $N_{1,60}$ value rather than an $N_{1,60,CS}$ value. Their value would increase if it was to be adjusted for fines in these silty sand materials. Overall agreement between the three independent assessments of representative $\overline{N_{1,60,CS}}$ values is excellent, and variance or uncertainty in $\overline{N_{1,60,CS}}$ appears to be moderate.

A.7.8 Additional Indices from the Back-Analyses

A number of additional results, and indices, can be extracted from the analyses performed. Some of these are useful in developing some of the over-arching relationships and figures presented in the main text of this report. These values are presented in Table A.7.2.

Table A.7.1: Representative values for the La Marquesa Dam downstream slope failure case history of: (a) post-liquefaction strength (S_r), (b) initial vertical effective stress (σ_{vo}'), and (c) $N_{1,60,CS}$ developed by various investigation teams, and estimates of variance in each of these indices when available.

(a) Post-Liquefaction Strength:	
Seed and Harder (1990)	$S_r \approx 400$ psf[1]
Olson (2001) and Olson and Stark (2002)	$S_r \approx 152$ psf[2]
Wang (2003) and Kramer (2008)	N/A
This Study	$\overline{S_r} = 214$ psf and $\sigma_{\overline{S}} = 57$ psf
(b) Representative $N_{1,60}$ or $N_{1,60,CS}$ Value:	
Olson (2001) and Olson and Stark (2002)	$N_{1,60} = 9.0$ bpf
Wang (2003) and Kramer (2008)	$\overline{N_{1,60,CS}} = 9.9$ bpf, and $\sigma_{\overline{N}} = 3.0$ bpf
This Study	$\overline{N_{1,60,CS}} = 10.5$ bpf, and $\sigma_{\overline{N}} = 2.2$ bpf
(c) Representative Initial Vertical Effective Stress:	
Olson (2001) and Olson and Stark (2002)	Average $\sigma_{vo}' \approx 1{,}063$ psf, no range provided.
Wang (2003) and Kramer (2008)	Value of $\sigma_{vo}' \approx 1{,}850$ psf is poorly based, and so is not very useful as a basis for comparison. (See Section 2.3.8.1(b) and Table 2.3)
This Study	$\overline{\sigma'_{vo}} = 1{,}215$ psf, and $\sigma_{\overline{\sigma}} = 103$ psf

[1] This value of S_r was increased to judgmentally incorporate cyclic inertial effects.
[2] See Section A.7.5 for an explanation of this value as presented.

Table A.7.2: Additional results and indices from the analyses of the a Marquesa Dam upstream slope failure case history.

Maximum distance traveled by the center of gravity of the overall failure mass	6.1 ft.
Initial post-liquefaction Factor of Safety prior to displacement initiation, and based on best estimate value of S_r	FS = 0.73
Final post-liquefaction Factor of Safety at final (residual) post-failure geometry, and based on best estimate value of S_r	FS = 1.51

A.8 La Palma Dam Upstream Slope (Chile; 1985)

A.8.1 Brief Summary of Case History Characteristics

Name of Structure	La Palma Dam, Upstream Slope
Location of Structure	Chile
Type of Structure	Zoned Earthen Dam
Date of Failure	March 3, 1985
Nature of Failure	Seismic, During 1985 Central Chilean Earthquake (M_S = 7.8)
Approx. Maximum Slope Height	25.6 ft. (U/S side)

A.8.2 Introduction and Description of Failure

The La Palma Dam suffered a liquefaction-induced slope failure its upstream side and its side as a result of the Central Chilean earthquake of March 3, 1985 (M_S = 7.8).

The dam is located near the Chilean coast, approximately 75 km northwest of Santiago, and approximately 55 km north of the La Marquesa Dam which was discussed in Appendices A.7 and A.8. Peak horizontal ground surface accelerations recorded in the general vicinity of the dam during the earthquake were on the order of approximately 0.43 to 0.65 g.

As shown in Figure A.8.1 (from de Alba et al, 1987), the dam suffered liquefaction-induced failure on the upstream side. Maximum displacements were approximately 6 to 8 feet vertically at the crest and upper face, and approximately 17 feet horizontally at the toe.

A.8.3 Geology and Site Conditions

Figure A.8.1 shows conditions both before and after the failure. Borings performed before the earthquake, and additional borings performed after the event, showed the dam foundation to consist primarily of sandy clays and clayey sands, but with shallow surficial deposits of silty sand and sandy silt underlying the upstream two-thirds of the dam. Of particular interest is the relatively thin layer of silty sand (Layer "2" in Figure A.8.1), as it is primarily within this stratum that liquefaction-induced sliding appears to have occurred. This liquefiable stratum extends from beneath the upstream toe to a point approximately mid-way between the dam's centerline and the downstream toe, but liquefaction appears to have occurred only beneath the upstream side of the dam because on the downstream side this layer was not saturated. The deeper underlying foundation soils were not very much better materials, in terms of material character and SPT penetration resistances, but they were generally somewhat better materials, and it was the judgment of the field investigation that the sliding had occurred primarily within the relatively thin silty sand stratum beneath the upstream side dam embankment shell zone.

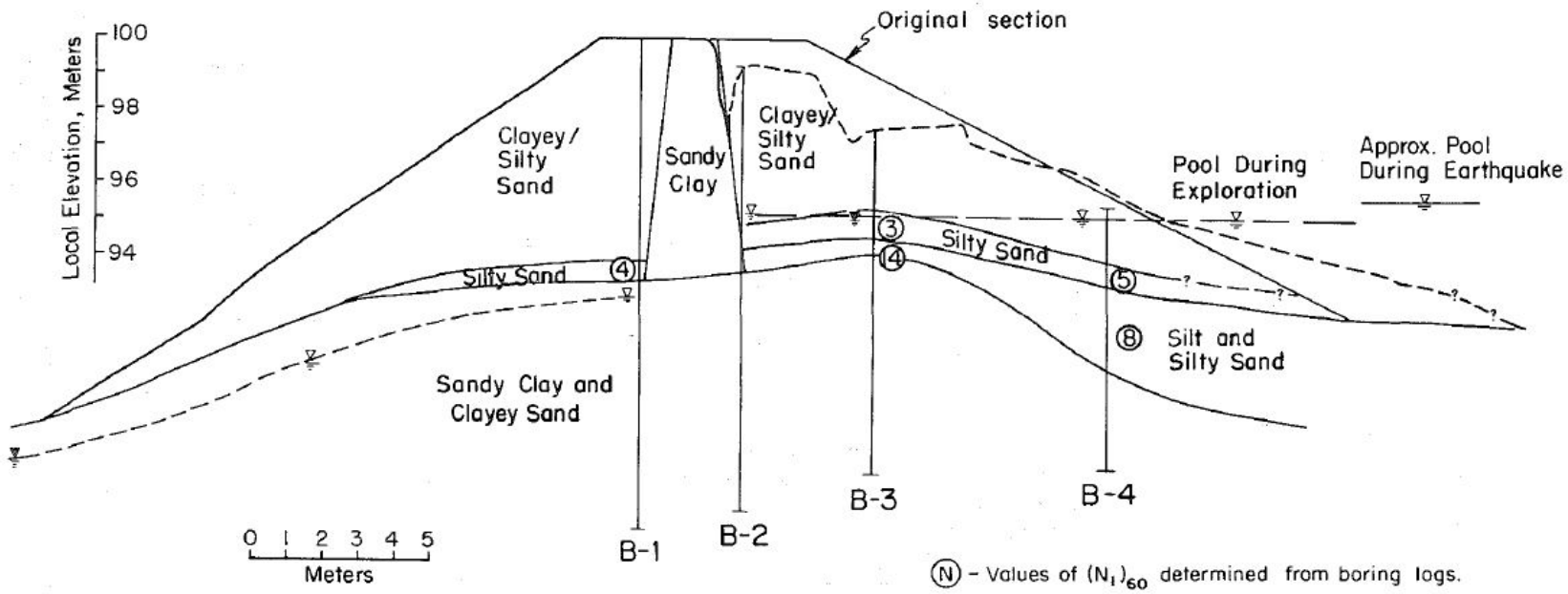

Figure A.8.1: Pre-failure and post-failure cross-sections of the La Palma Dam (from de Alba et. al, 1987).

The dam embankment was constructed with materials excavated locally from the reservoir floor and the abutments, and consisted primarily of clayey sands and silty sands in the upstream and downstream shell zones, and of sandy clay in the central core zone. A key trench was excavated through the upper silty sand and silt upper foundation strata beneath the core, and this was backfilled with sandy clay fill to create a key trench to key into the deeper sandy clay and clayey sand foundation units at slightly greater depth. Details of embankment fill placement and compaction are not clear, but based on a suite of four post-failure SPT borings, it appears that the embankment fill materials were moderately compacted.

A.8.4 Initial Yield Stress Analyses

Figure A.8.2 shows the cross-sections used for back-analyses of the pre-failure and post-failure conditions associated with calculation of (1) initial yield strength ($S_{r,yield}$) and (2) post-liquefaction residual strength based on final residual geometry ($S_{r,resid/geom}$). Figure A.8.2(a) shows the cross section used for calculation of the value of $S_{r,yield}$ that would be required within the liquefied upstream shell materials to produce a calculated Factor of Safety equal to 1.0. This is not the actual post-liquefaction strength, but it proves to be useful in developing a number of charts and relationships for these overall studies.

Shear strengths of non-saturated silty sand and clayey sand materials in the embankment shells (above the phreatic surface), and above the thin stratum of silty sand foundation material within which the liquefaction-induced sliding appears to have occurred, were modeled as frictional, with a best estimate value of Ø´ = 33 °. This was then varied between 30 to 36° in subsequent sensitivity analyses. Shear strengths in the clayey sand core zone were modeled as cohesive, with residual (large displacement) values of $S_{u,r}/P \approx 0.09$ based on very limited data and information. This was then varied between 0.06 and 0.12 in subsequent sensitivity studies. Shear strengths within the relatively thin stratum of silty sand beneath the base of the upstream shell were modeled with post-liquefaction strength $S_{r,yield}$, and these back-analyses were performed in order to determine this value. Shear strengths in the remaining foundation soils beneath the upper silty sand foundation stratum were not modeled as these did not participate in the failure observed.

Unit weights for the non-saturated shell zones were modeled as $\gamma_m = 120$ lbs/ft^3, and the saturated silty sands of the lower upstream shell and the upper foundation stratum were modeled as $\gamma_s = 125$ lbs/ft^3. These were varied by +/- 5 lbs/ft^3 in subsequent sensitivity studies. Unit weights of the silty clay core materials were modeled as $\gamma_s = 120$ lbs/ft^3 +/- 5 lbs/ft^3.

Based on the cross-section shown in Figures A.8.2(a), and the properties and parameters described above, the best-estimate value of $S_{r,yield}$ was 201 lbs/ft^2. Parameters were next varied, as described above, and the details as to precise depth and shape of the failure surface were also varied, to perform parametric sensitivity analyses. Based on ranges of properties and failure surfaces considered reasonable, the likely range of $S_{r,yield}$ was found to be $S_{r,yield} \approx 165$ to 238 lbs/ft^2.

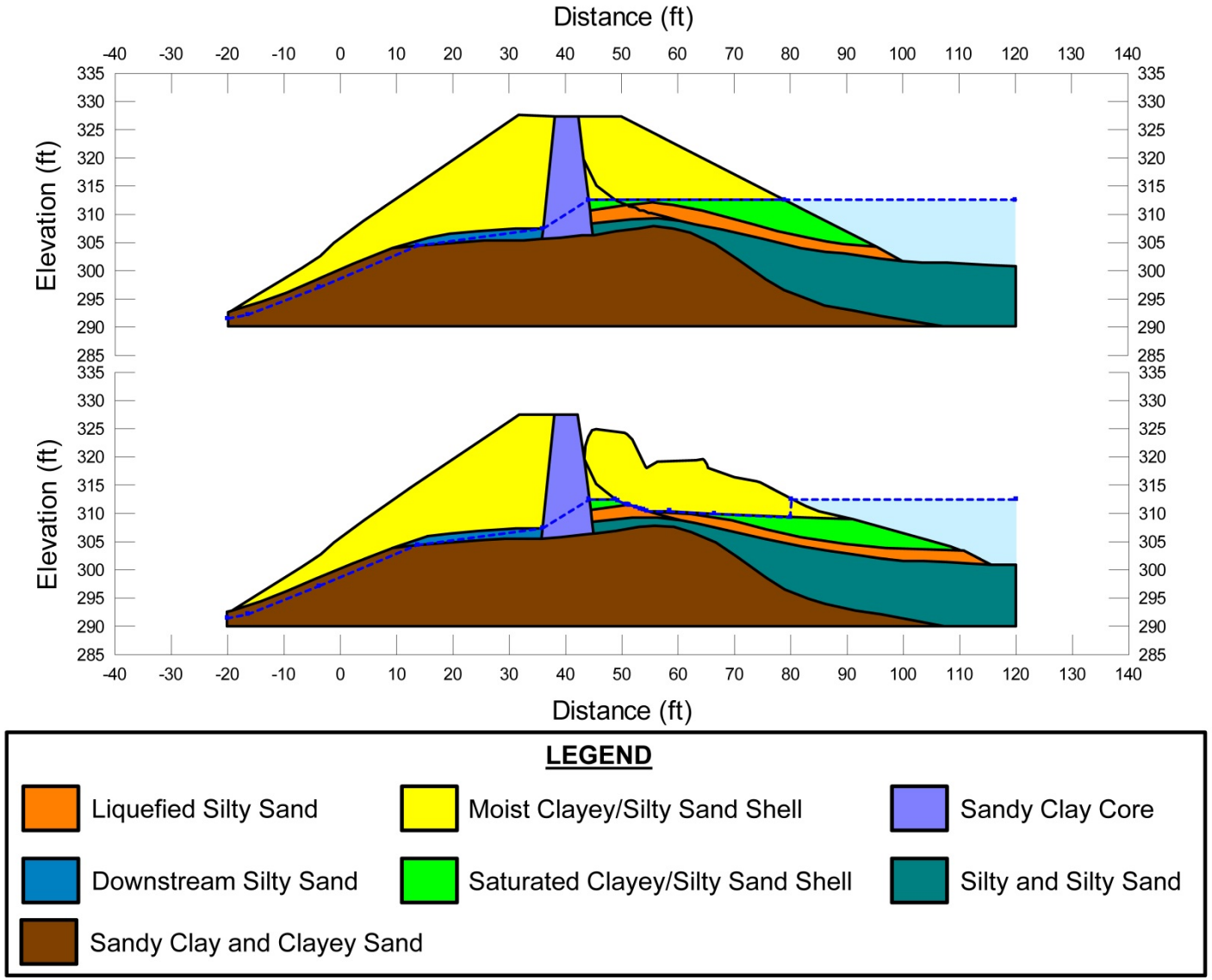

Figure A.8.2: La Palma Dam: (a) pre-failure geometry and failure surface for initial yield stress analyses, and (b) post-failure geometry and failure surface for post-failure residual geometry analyses.

Olson (2001) was the only other investigator who also performed and reported back-analyses to determine $S_{r,yield}$. Failure surfaces analyzed differed somewhat, and so did some of the parameters and other modeling assumptions. Olson reported a best estimate value of $S_{r,yield} \approx$ 10.1 kPa (211 lbs/ft^2) , and a range of $S_{r,yield} \approx$ 9.1 to 12.2 kPa (190 to 255 lbs/ft^2), in excellent agreement with these current studies.

A.8.5 Residual Strength Analyses Based on Residual Geometry

The calculation of the "apparent" post-liquefaction strength ($S_{r,resid/geom}$) required to produce a calculated Factor of Safety equal to 1.0 based on residual geometry is illustrated in Figure A.8.2(b). Modeling parameters and details are as previously described in the preceding sections. The resulting best-estimate value of $S_{r,resid/geom}$ was found to be $S_{r,resid/geom} = 84$ lbs/ft^2.

Parameters were next varied, as described previously, and alternate potential failure surfaces were also examined. Based on these parametric sensitivity analyses, it was judged that a reasonable range was $S_{r,resid/geom} \approx 68$ to 105 lbs/ft^2.

Olson (2001) also performed back-analyses to determine $S_{r,resid/geom}$. Failure surfaces analyzed differed slightly, and so did some of the parameters and other modeling assumptions. Olson reported a best estimate value of $S_{r,resid/geom} \approx$ 4.8 kPa (100 lbs/ft^2) , and a range of $S_{r,resid/geom} \approx$ 2.4 to 7.9 kPa (50 to 165 lbs/ft^2), in generally good agreement with these current studies.

A.8.6 Incremental Momentum Back-Analyses and Overall Estimates of S_r

Incremental inertial back-analyses were performed using the same sets of properties and geometries (including failure surfaces and phreatic surfaces) as described in the previous sections. Figure A.8.3 shows the best-estimate progressive incremental inertial analysis for Scenario A, showing the five stages of geometry evolution modeled as the failure proceeds, and Figure A.8.4 shows the associated best estimate calculations of (1) acceleration vs. time, (2) velocity vs. time, and (3) displacement of the overall center of gravity vs. time. The resulting best estimate value of post-liquefaction strength was $S_r = 136$ lbs/ft^2.

Parameter sensitivity analyses, including modeling of additional potential failure surfaces considered to be "reasonable/feasible" were then performed to investigate the overall range of post-liquefactions strength values. This range was found to be $S_r = 103$ to 172 lbs/ft^2. This was judged to represent approximately +/- 1.5 standard deviations. This range was nearly symmetric about the best estimate value of 136 lbs/ft^2, so no significant further adjustments were necessary.

Overall, based on an assumed normal distribution, it was judged that the (mean and median) best estimate of post-liquefaction strength for this case history is

$$\overline{S_r} = 136 \text{ lbs/ft}^2$$

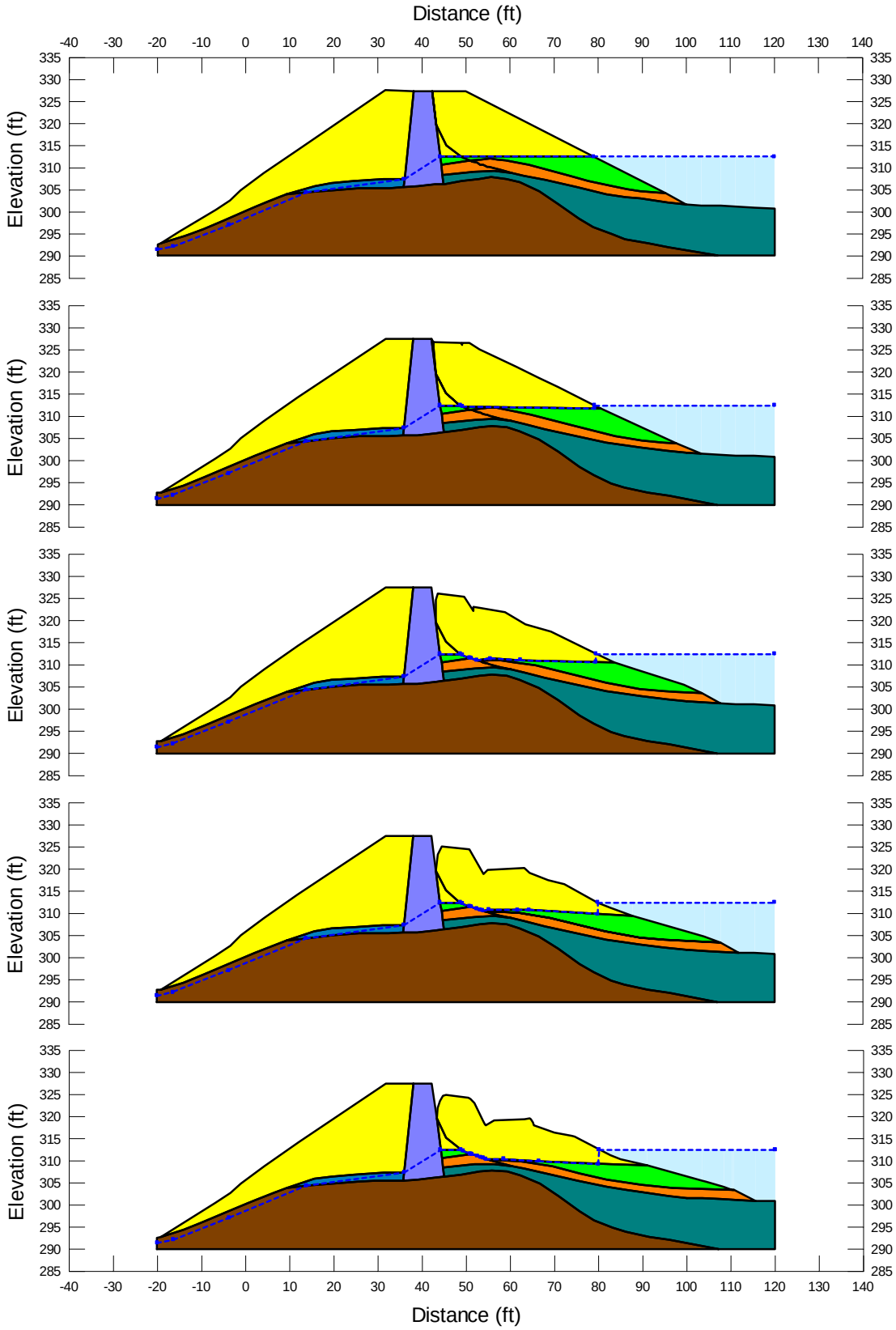

Figure A.8.3: Incremental inertial analysis of the failure of the La Palma Dam, showing progressive evolution of cross-section geometry modeled.

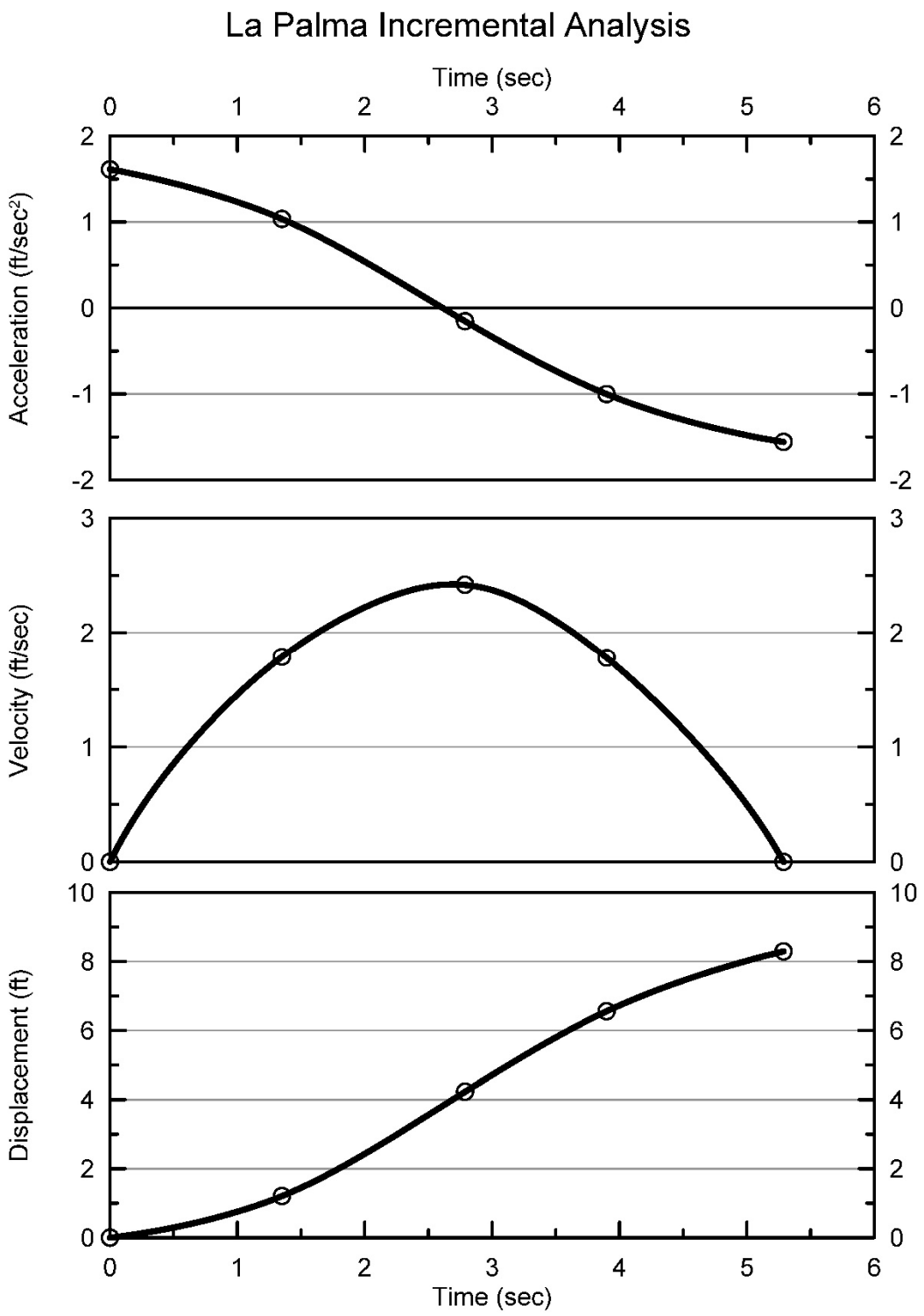

Figure A.8.4: Incremental inertial analysis of the failure of the Upstream Slope of La Palma Dam, showing progressive evolution of: (1) acceleration vs. time, (2) velocity vs. time, and (3) displacement vs. time of the overall center of gravity of the failure mass.

and that the best estimate of standard deviation of mean overall post-liquefaction strength is

$$\sigma_{\bar{S}} = 33 \text{ lbs/ft}^2$$

The La Palma Dam upstream slope failure case history has been back-analyzed by a number of previous investigators, but not with back-analysis methods that reasonably accurately incorporate momentum effects. Seed and Harder (1990) reported a value of $S_r \approx 200$ lbs/ft^2, butu this value was judgmentally increased to incorporate cyclic inertial effects. Olson (2001) and Olson and Stark (2002) did not apply their "kinetics" method to this case, and so they did not independently develop an estimate of S_r that incorporated momentum effects. Olson did, however, calculate values of $S_{r,yield}$ and $S_{r,resid/geom}$ (see Sections A.8.3 and A.8.4) for this case, Only the left side of the embankment is analyzed, as the postimate of S_r. Based on Equation 4-1 (see Chapter 4), a better estimate for S_r based on calculations performed by Olson (2001) would be $S_r \approx 0.8 \text{ x } [S_{r,yield} + S_{r,resid/geom}] / 2 \approx 0.8 \text{ x } [10.1 \text{ kPa} + 4.8 \text{ kPa}] /2 \approx 6.0$ kPa (125 lbs/ft^2), and this value is more directly comparable with the values of this current study, and so it is the value presented in Table A.8.1(a). This agrees very well with these current studies. Similarly, Wang (2003) and Wang and Kramer (2008) did not employ their zero inertial force (ZIF) method to incorporate inertial effects in back-analyses of this failure, and so they also did not independently develop an estimate of S_r that incorporated momentum effects.

Approximate comparisons can be made to Olson and Stark's (2001, 2002) values of back-calculated values of $S_{r,yield}$ and $S_{r,resid/geom}$ by means of Equation 4.2, as shown in Tables 4.3 and 4.6, but this is not a very rigorous comparison.

It appears that the values calculated in these current studies are the first set of back-calculated values of post-liquefaction S_r for the La Palma Dam upstream slope failure to be based on analysis methods that incorporate momentum effects.

Finally, it should be noted that this case history is one in which (1) a liquefaction-induced slope failure produced moderate displacements and deformations, and (2) levels and duration of strong shaking were high. This is thus a case in which it may be hypothesized that the values back-calculated in these current studies, even with incorporation of momentum effects, may conservatively underestimate the actual values of S_r due to the failure to also incorporate cyclic inertial effects during strong shaking. It is not (yet) analytically possible to reliably quantify this additional potential conservatism. Seed and Harder (1990) had increased their back-estimated value of S_r to attempt to judgmentally incorporate cyclic inertial effects. The current engineering team has elected not to make that further adjustment in these current studies.

A.8.7 Evaluation of Initial Effective Vertical Stress

Average initial (pre-failure) effective vertical stress was assessed for the liquefied zones of the failure surfaces analyzed in the preceding Sections A.8.4 through A.8.6. Sensitivity analyses were performed for reasonable ranges of variations in (1) the location of the phreatic surface, (2) unit weights, and (3) the precise location of the overall failure surface in order to evaluate uncertainty or variance.

The resulting best estimate of average pre-failure effective stress within the liquefied materials along the failure was then $\sigma_{vo}' \approx 767$ lbs/ft^2, with a reasonable range of $\sigma_{vo}' \approx 684$ to 852 lbs/ft^2. This range is slightly non-symmetric about the median value, and this range was judged by the engineering team to represent approximately ± 2 standard deviations. Overall, the best characterization of initial (pre-failure) average effective vertical stress was then taken to be represented by a mean value of

$$\overline{\sigma'_{vo}} \approx 767 \text{ lbs/ft}^2$$

and a standard deviation of

$$\sigma_{\bar{\sigma}} \approx 42 \text{ lbs/ft}^2$$

An estimate of σ_{VO}' was also calculated by Olson and Stark (2001, 2002) and this is shown in Table A.8.1(c). They reported a weighted average mean value of $\sigma_{vo}' \approx 789$ lbs/ft^2, in excellent agreement with these current studies. Average initial vertical effective stresses were not directly reported by Wang (2003) and Kramer (2008), but they were published more recently in the publication by Kramer and Wang (2015). As discussed in Section 2.3.8.1(b)-(iii), Wang (2003) did not perform any independent analyses to assess σ_{vo}' for his 22 "secondary" cases, and this is one of those cases. Instead, he compiled values of S_r from multiple previous investigators, and averaged these for a best estimate. He also compiled multiple values of S_r/σ_{vo}' from previous investigators, and averaged these for a best estimate. He then used these two best-estimate values of S_r and S_r/σ_{vo}' to infer a resulting representative value of σ_{vo}'. As described in Section 2.3.8.1(b)-(iii), the resulting averaged values of S_r and S_r/σ_{vo}' were incompatible with each other for a number of Wang's "secondary" case histories, and this process produced unreasonable, and in some cases physically infeasible, values of σ_{vo}' for a number of case histories. Accordingly, Wang's value of $\sigma_{vo}' = 1{,}577$ is not considered a useful check here. Agreement between Olson's value, which is well-documented, and the value developed in these current studies is excellent.

A.8.8 Evaluation of $N_{1,60,CS}$

Figure A.8.5 shows the locations of post-failure SPT borings, and the results of the SPT tests performed to investigate the failure. Based on the field investigation, it appears that the upstream slope failure occurred due to liquefaction-induced sliding within the silty sand upper foundation stratum immediately underlying the dam embankment. Only a limited number of SPT tests are available within this material, so the paucity of useful penetration data is a major source of uncertainty here.

Based on the 3 SPT tests in these upper foundation silty sands on the upstream side, after re-processing these using the relationships and procedures presented in Appendix C, Section C.1, the best estimate mean value of $N_{1,60,CS}$ for the upstream side upper foundation silty sands was found to be $\overline{N_{1,60,CS}} \approx 5$ blows/ft. Variance of $\overline{N_{1,60,CS}}$ was estimated primarily on the basis

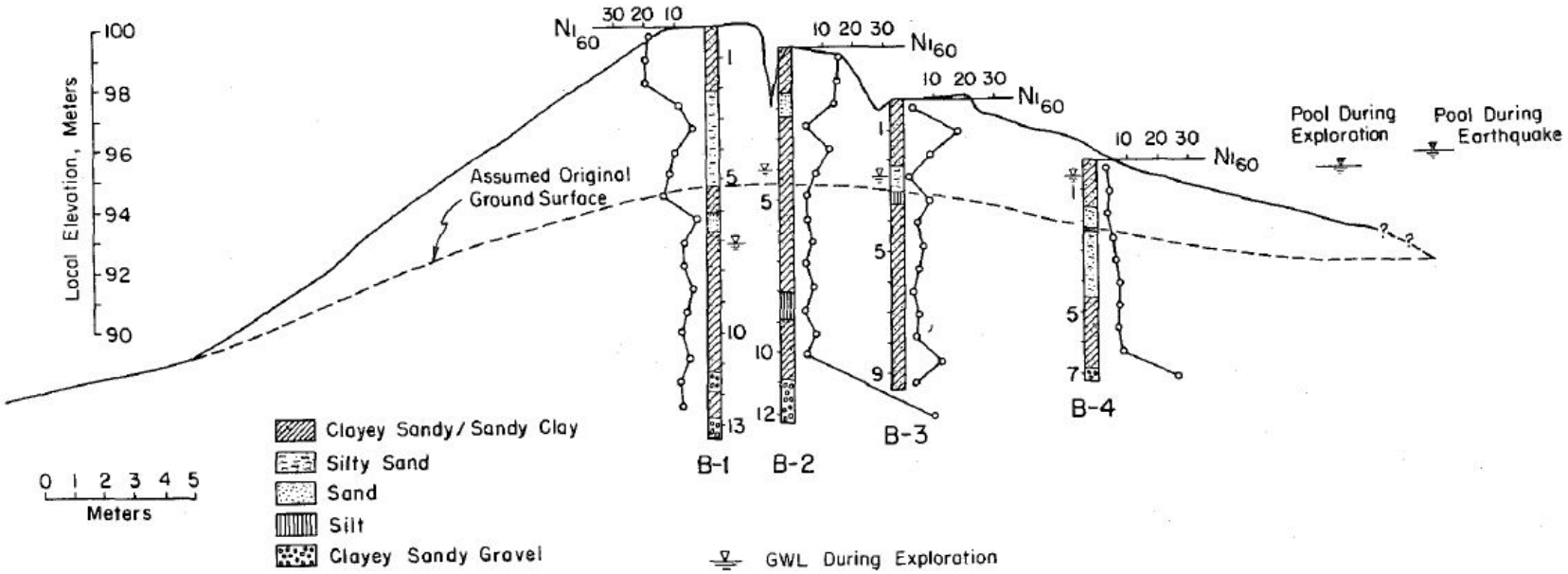

Figure A.8.5: Post-failure cross-section of La Palma Dam showing the locations and results of standard penetration tests (de Alba et al., 1987).

of the perceived uncertainties associated with the limited number of blowcounts from within the failure zone. Considering this, and the observed variance among the few available data, the representation of uncertainty in the representative median value of $\overline{N_{1,60,CS}}$, based on an assumed normal distribution, was taken as $\sigma_{\overline{N}} \approx 1.2$ blows/ft.

Table A.8.1(b) shows values of representative $N_{1,60}$ or $N_{1,60,CS}$ values developed by three other teams of investigators, and variance or standard deviations in these representative values if available. Olson and Stark (2001, 2002) developed an estimated representative value of $N_{1,60}$ = 4 blows/ft, but for this case history they proposed no range. Wang (2003) and Kramer (2008) jointly developed a representative value of $\overline{N_{1,60,CS}}$ = 4.2 blows/ft, and their estimated standard deviation of that overall mean value for this case history was $\sigma_{\overline{N}}$ = 1.8 blows/ft. Olson and Stark (2001, 2002) made no fines adjustments, so theirs is an $N_{1,60}$ value rather than an $N_{1,60,CS}$ value. Their value would increase if it was to be adjusted for fines in these silty sand materials. Overall agreement between the three independent assessments of representative $\overline{N_{1,60,CS}}$ values is excellent, and variance or uncertainty in $\overline{N_{1,60,CS}}$ appears to be relatively low.

A.8.9 Additional Indices from the Back-Analyses

A number of additional results, and indices, can be extracted from the analyses performed. Some of these are useful in developing some of the over-arching relationships and figures presented in the main text of this report. These values are presented in Table A.8.2.

Table A.8.1: Representative values for the La Palma Dam upstream slope failure case history of: (a) post-liquefaction strength (S_r), (b) initial vertical effective stress (σ_{vo}'), and (c) $N_{1,60,CS}$ developed by various investigation teams, and estimates of variance in each of these indices when available.

(a) Post-Liquefaction Strength:	
Seed and Harder (1990	$S_r \approx 200$ psf[1]
Olson (2001) and Olson and Stark (2002)	$S_r \approx 124$ psf[2]
Wang (2003) and Kramer (2008)	N/A
This Study	$\overline{S_r} = 136$ psf and $\sigma_{\overline{S}} = 231$ psf
(b) Representative $N_{1,60}$ or $N_{1,60,CS}$ Value:	
Seed and Harder (1990)	$N_{1,60,CS} = 4$ bpf
Olson (2001) and Olson and Stark (2002)	$N_{1,60} = 3.5$ bpf
Wang (2003) and Kramer (2008)	$\overline{N_{1,60,CS}} = 4.2$ bpf, and $\sigma_{\overline{N}} = 1.8$ bpf
This Study	$\overline{N_{1,60,CS}} = 5$ bpf, and $\sigma_{\overline{N}} = 1.2$ bpf
(c) Representative Initial Vertical Effective Stress:	
Olson (2001) and Olson and Stark (2002)	Average $\sigma_{vo}' \approx 789$ psf, with no range provided.
Wang (2003) and Kramer (2008)	Value of $\sigma_{vo}' \approx 1{,}577$ psf is poorly based, and so is not very useful as a basis for comparison. (See Section 2.3.8.1(b) and Table 2.3)
This Study	$\overline{\sigma'_{vo}} = 767$ psf, and $\sigma_{\overline{\sigma}} = 42$ psf

[1] This value of S_r was increased to judgmentally incorporate cyclic inertial effects.
[2] See Section A.8.6 for an explanation of this value as presented.

Table A.8.2: Additional results and indices from the analyses of the La Palma Dam upstream slope failure case history.

Maximum distance traveled by the center of gravity of the overall failure mass	8.3 ft.
Initial post-liquefaction Factor of Safety prior to displacement initiation, and based on best estimate value of S_r	FS = 0.78
Final post-liquefaction Factor of Safety at final (residual) post-failure geometry, and based on best estimate value of S_r	FS = 1.25

A.9 Lake Ackerman Highway Embankment (Michigan, USA; 1987)

A.9.1 Brief Summary of Case History Characteristics

Name of Structure	Lake Ackerman Highway Embankment
Location of Structure	Michigan, USA
Type of Structure	Elevated Highway Embankment Fill
Date of Failure	July 24, 1987
Nature of Failure	Cyclic, due to excitation by large geophysical exploration shakers
Approx. Maximum Slope Height	25.6 ft.

A.9.2 Introduction and Description of Failure

The liquefaction-induced flow failure of a section of Highway 24 in Michigan's upper peninsula was highly unusual inasmuch as the failure was triggered by shaking from a line of six massive (22-ton) trucks producing coordinated shaking for purposes of deep geophysical investigations (a seismic refraction survey). The six trucks also provided some extra weight (mass) loading the embankment, but it was primarily the strong vibratory shaking that triggered the failure.

Figure A.9.1 is a plan view of the highway embankment showing (a) the locations of the six trucks, and (b) the approximate extent of the failure. Figure A.9.2 presents a photograph taken after the failure, showing (a) the slope failure, and (b) four of the six shaking trucks (one is upright, and the other three are overturned at the left edge this photograph).

The drivers of the trucks all survived, and they provided useful eyewitness observations.

This failure was investigated by Hryciw et al. (1990). The highway embankment was constructed over the northern edge of Lake Ackerman, as shown in Figure A.9.1, in the mid-1950's. Approximately 1.2 m of weak lakebed peaty soils were removed prior to placement of the embankment fill. The embankment fill materials was a clean, medium to fine sand with subrounded particles that was borrowed from nearby road cuts. Figure A.2.3 shows the gradation of this material.

Figure A.9.4 shows a reconstructed cross-section through the failure zone (Hryciw et al., 1990), showing the excavation of lakebed peats and muds, and the pre-failure and post-failure embankment cross-sections.

The embankment fill sand was initially end-dumped into the lake, resulting in a very loose and saturates fine sand fill. Fill subsequently placed above the lake water level was reportedly moderately compacted, but the method of compaction was not described. It is the loose, saturated, end-dumped materials that are of primary interest for these back-analyses. The

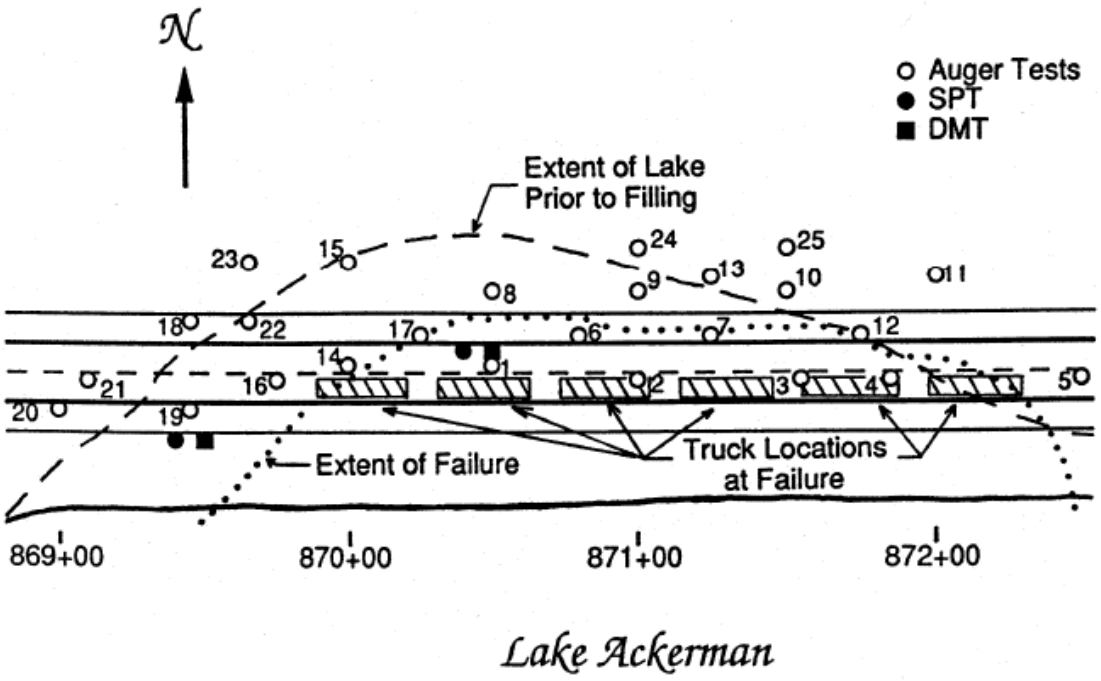

Figure A.9.1: Plan view of the Lake Ackerman slope failure showing (a) the extent of the failure, and (b) the locations of the six geophysical investigation trucks prior to the failure (Hryciw et al., 1990).

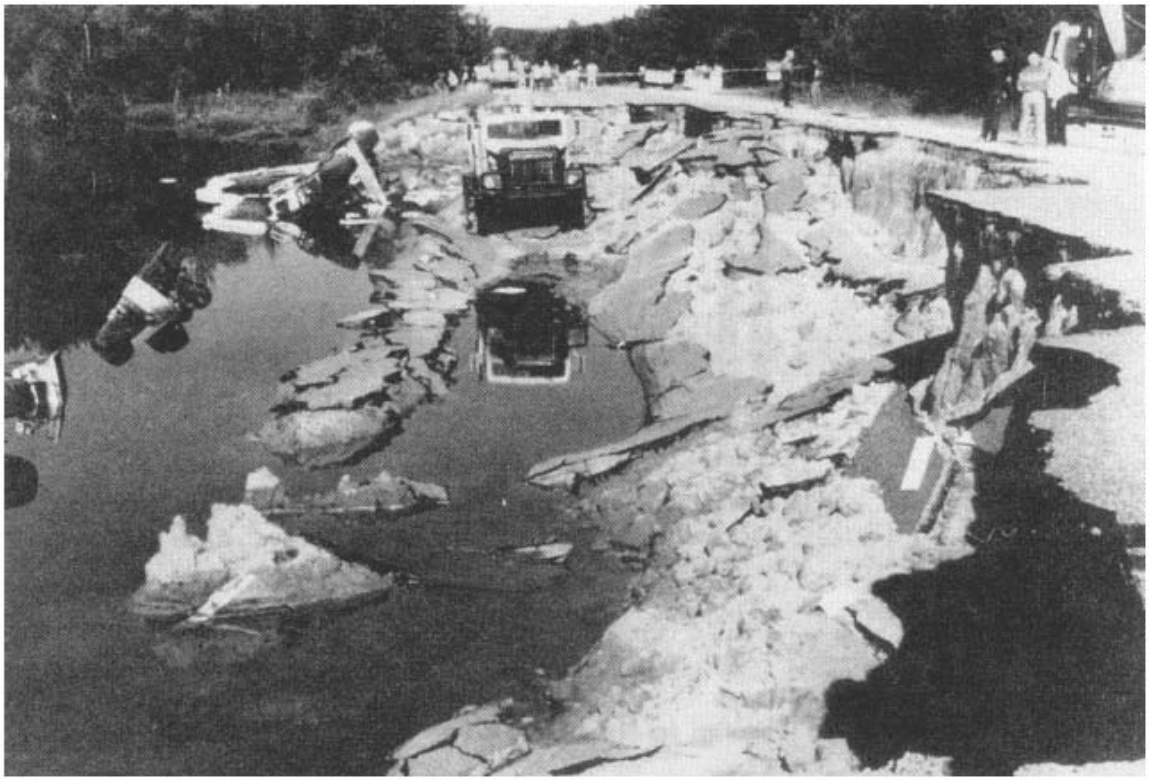

Figure A.9.2: Photograph showing the failed embankment (looking towards the west), showing crest loss and the positions of four of the large geophysical exploration trucks. (Hryciw et al., 1990).

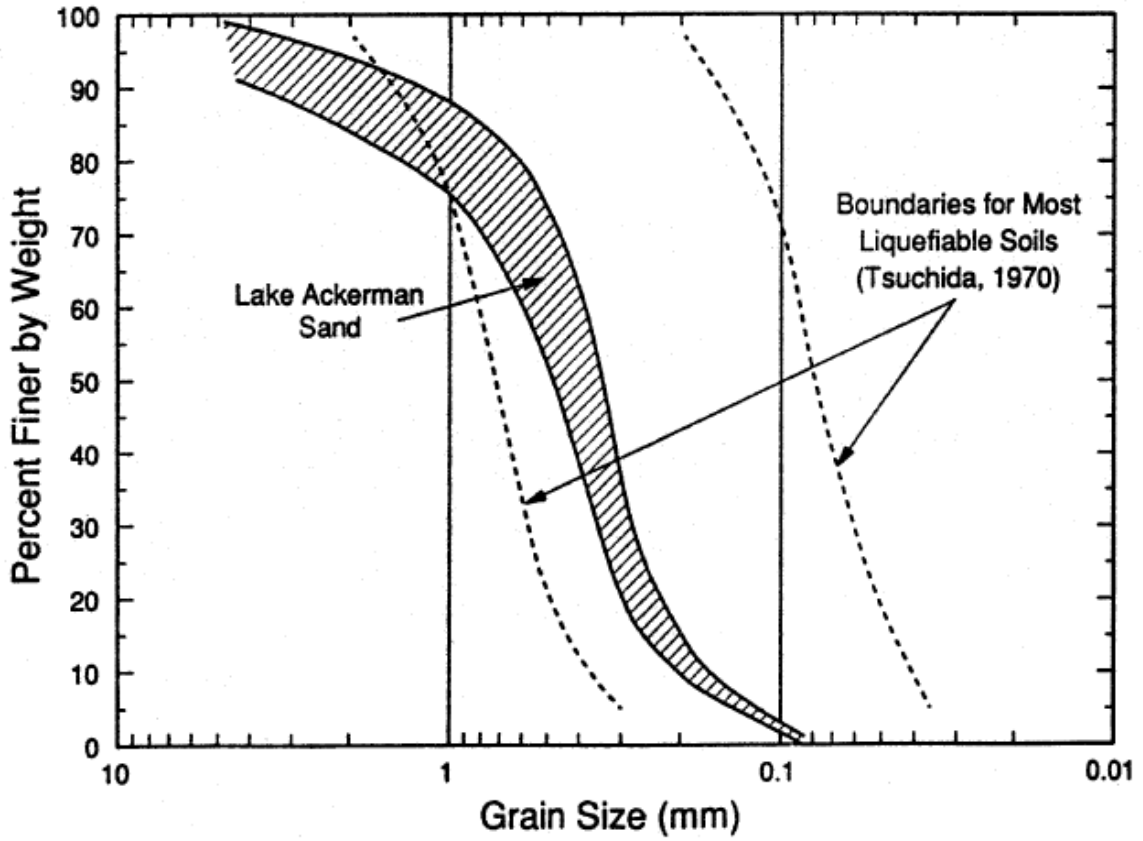

Figure A.9.3: Grain size distribution of the sand used for the Lake Ackerman Highway embankment fill (Hryciw et al., 1990)

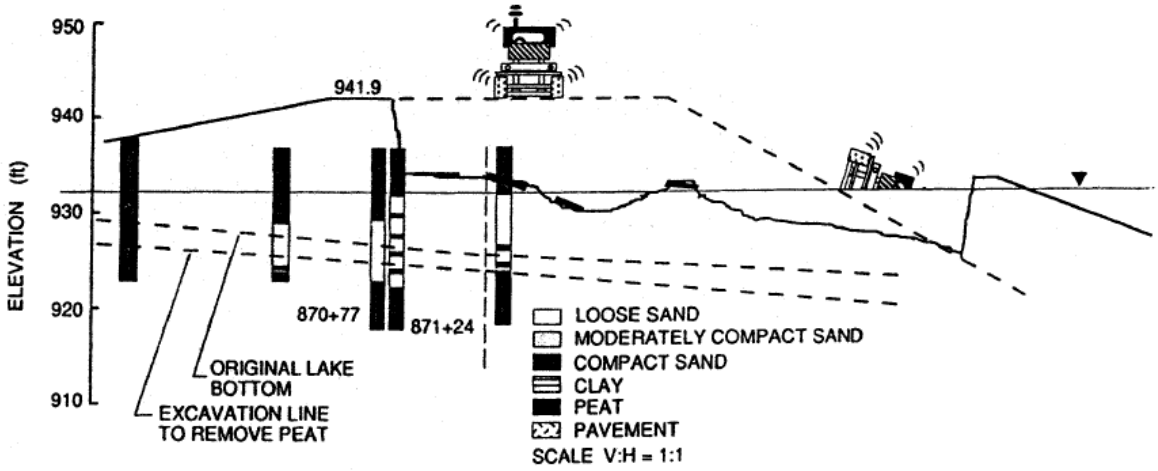

Figure A.9.4: Reconstructed pre-failure and post-failure cross sections (Hriciw et al., 1990)

unit weight of this sand was approximately 19.3 kN/m^3, and Hryciw et al. (1990) estimated the relative density to be as low as approximately 0%.

The presence of the six large trucks, nose-to-tail in a line, added weight to the top of the embankment, but is felt that the shaking of these six trucks (which could produce high frequency, synchronized shaking at controlled frequencies) was the main cause of the failure. Hryciw at al. (1990) estimated that these trucks produced a high frequency cyclic stress ratio of approximately CSR = 0.12 in the loose, saturated sands at the base of the embankment fill, and this agrees well with studies by Sully et al. (1995). This would have be amply sufficient to trigger liquefaction in these soils.

A.9.3 Initial Yield Strength Analysis

Figure A.9.5 shows the reconstructed pre-failure and post-failure cross-sections used in these current studies. These is based on the cross-sections developed by Hryciw et al. (1990) from Figure A.9.4, and also on the pre-failure and post-failure cross-sections developed and analyzed by Olson (2001). It is similar to Olson's cross-section, except for details regarding the failure surfaces analyzed. Olson's cross-sections were developed by extending the apparent slope of the lakebed to the toe of the failure zone, and by extending the apparent slope of the embankment fill as well. This current investigation team checked these extrapolations, and they appear to be reasonable.

Figure A.9.5(a) shows the pre-failure cross-section used to back-calculate the value of "apparent" initial post-liquefaction yield strength ($S_{r,yield}$) defined as the value that would be required to produce a calculated value of static Factor of Safety equal to 1.0 for pre-failure geometry and conditions assuming that the liquefiable soils have liquefied.

Shear strength of the non-saturated embankment zones above the phreatic surface was modeled as frictional, with a best estimate value of $Ø'_{residual}$ = 30°, based on DMT test results (Hryciw et al, 1990). Shear strength of the loose, saturated embankment zones below the phreatic surface was modeled as "liquefied", with the post-liquefaction strength ($S_{r,yield}$) to be back-calculated. Lakebed soils left in place beneath the embankment fill were assumed to have higher shear strengths than the liquefied strength of the very loose lower embankment fill.

Unit weights of the embankment fill were taken as γ_m = 115 lbs/ft^3 above the phreatic surface, and γ_s = 122.7 lbs/ft^3 below the phreatic surface. The weights of the six geophysical exploration trucks were distributed as a pair of line loads (two parallel sets of wheels) along the alignment.

Figure A.9.5(a) shows the best estimate of the most critical initial failure for this case. It is not known with certitude whether this was a monolithically initiated failure, or a failure that was incrementally progressive, initiating in successive slices retrogressively back to the eventual overall back heel of the failure. Analyses of the initial post-liquefaction cross-section showed that the preferred (most critical) initial failure surfaces would be surfaces deeply plunging towards the base of the liquefiable lower sand fill, and that they would tend to at least approach towards the eventual back heel. So if there was some incremental progression/retrogression, it

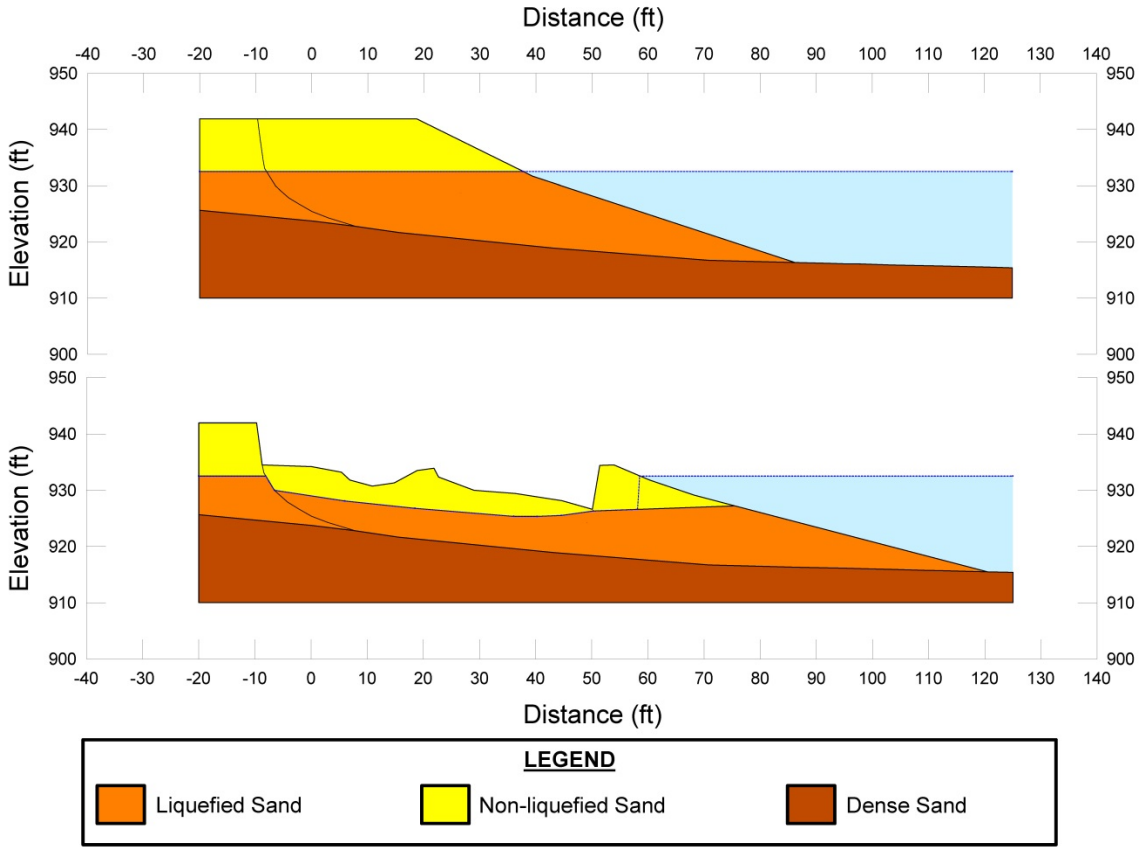

Figure A.9.5: Pre-failure and post-failure cross-sections used for back-calculation of initial post-liquefaction yield strength ($S_{r,yield}$) and of post-liquefaction residual strength based on final, residual geometry ($S_{r,resid/geom}$).

would likely have been relatively minor. Accordingly, the best estimate failure mechanism for this case is taken as a monolithically initiating failure that then articulates (or "breaks up") as it travels outwards into the lake.

For the best estimate failure surface shown in Figure A.9.5(a), the back-calculated value of $S_{r,yield}$ is 193 lbs/ft^2. Parameter and assumption sensitivity studies were next performed, varying the location of the initial yield surface (including allowing for partial incremental initiation and then retrogression to the back heel), and varying unit weights and the friction angle of the non-saturated upper embankment fill. For the ranges of conditions considered to be reasonable, the range of resulting values back-calculated was $S_{r,yield}$ = 174 to 205 lbs/ft^2.

Figure A.9.6 shows the pre-failure cross-section used by Olson (2001) to back-calculate $S_{r,yield}$. It also shows a number of the potential failure surfaces that he analyzed. Olson had concluded that because several of the large geophysical investigation trucks had all toppled towards the lake that the initial failure surface had likely had its rear scarp either closely at or to the lake side of the line of trucks. The current investigation team were aware of this assumption, but concluded that this evidence was inconclusive and that the trucks could have toppled in that direction as a result of a monolithically initiated failure that subsequently broke up and stretched

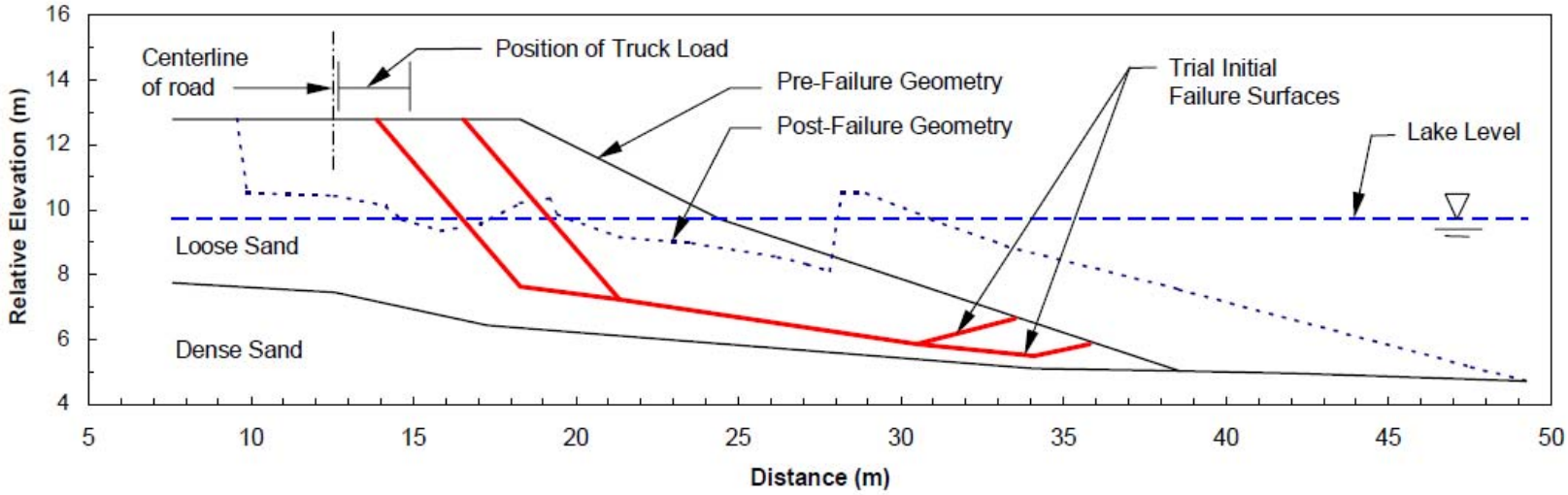

Figure A.9.6: Pre-failure cross-section and trial failure surfaces examined by Olson for purposes of assessing $S_{r,yield}$ (figure from Olson, 2001).

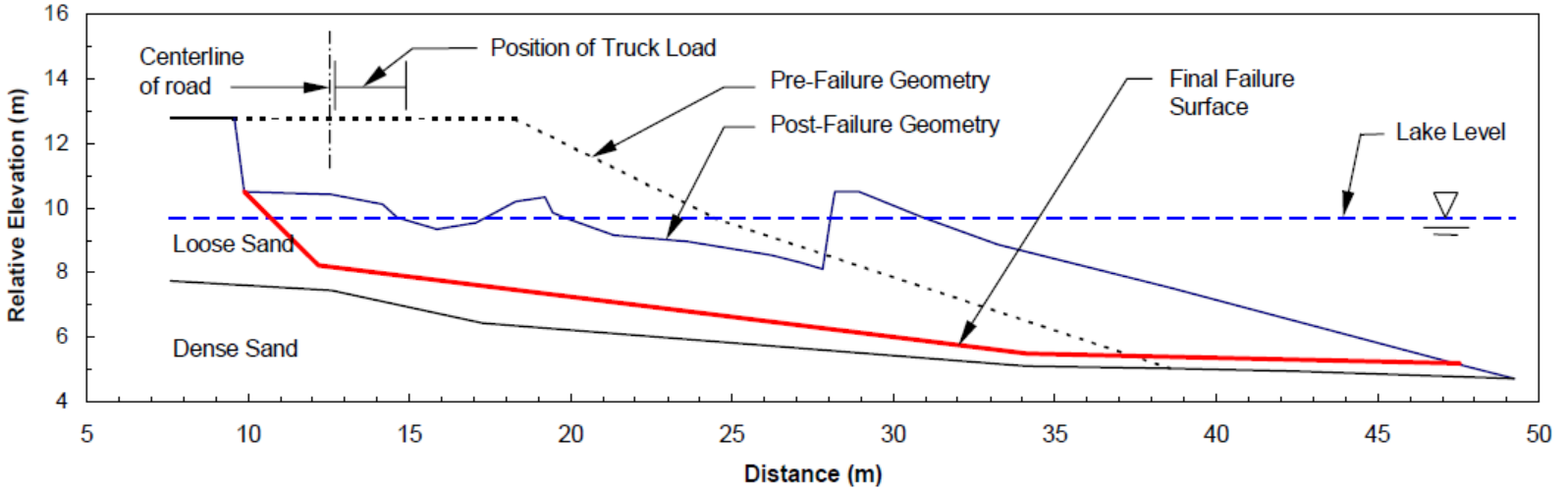

Figure A.9.7: Post-failure cross-section and trial failure surface used by Olson for back-calculation of $S_{r,resid/geom}$ (figure from Olson, 2001).

out as it travelled. Olson also tended to favor slightly shallower failure surfaces than the current investigation team. For this case history, that led Olson (2001) to estimate a slightly smaller initial $S_{r,yield}$ value of 10.1 kPa (211 lbs/ft^2), with a range of 8.6 kPa (180 lbs/ft^2) to 10.5 kPa (219 lbs/ft^2).

A.9.4 Residual Strength Analysis Based on Residual Geometry

The calculation of the "apparent" post-liquefaction strength ($S_{r,resid/geom}$) required to produce a calculated Factor of Safety equal to 1.0 based on residual geometry is illustrated in Figure A.9.5(b). This figure shows the phreatic surface, and the failure surface, used to calculate the best-estimate value of $S_{r,resid/geom}$. The relatively low velocities of this failure (see Section A.9.5) made it unlikely that any significant hydroplaning occurred as the toe of the failure mass entered into the reservoir. It was less easy to determine whether or not the failure mass may have been partially borne along atop weaker reservoir sediments. For the best estimate case it was assumed that strengths at the base of the portion of the failure mass that entered into the reservoir were 90% of the value of the post-liquefaction strength (S_r) of the overlying embankment fill. For the best estimate case, the resulting back-calculated value of $S_{r,resid/geom}$ was 56 lbs/ft^2. This was then varied from 50% to 100% in subsequent parameter sensitivity analyses. Variations were then made in parameters, and in location of the pre-failure phreatic surface, as was described in the preceding section in order to evaluate uncertainty or variability. The resulting likely range of post-liquefaction strength required to provide a calculated Factor of Safety equal to 1.0 based on residual geometry was considered to be $S_{r,resid/geom} \approx$ 46 to 65 lbs/ft^2.

Olson (2001) also calculated post-liquefaction strength required to produce a calculated Factor of Safety equal to 1.0 based on residual geometry, using the cross-section shown in Figure A.9.7, and reported a range of $S_{r,resid/geom} \approx$ 3.4 kPa (71 lbs/ft^2), with a range of 2.9 to 4.8 kPa (61 to 100 lbs/ft^2), in good agreement with the values calculated in these current studies.

A.9.5 Incremental Momentum Back-Analyses and Overall Estimates of S_r

Incremental inertial back-analyses were performed using the same sets of properties and geometries (including failure surfaces and phreatic surfaces) as described in the previous sections. Figure A.9.8 shows the best-estimate progressive incremental inertial analysis, showing the 5 stages of geometry evolution modeled as the failure proceeds. Figure A.9.9 repeats this figure, at larger scale for clarity, and it also shows the progressive locations of the center of gravity of the overall failure mass. Figure A.9.10 shows the associated calculations of: (1) acceleration vs. time, (2) velocity vs. time, and (3) displacement vs. time of the overall center of gravity. For the geometry and conditions shown in Figures A.9.8 through A.9.10, including assumption of shear strength equal to fully 100% of the liquefied strength S_r at the base of the portion of the toe of the embankment that entered into the reservoir, the best estimate value of post-liquefaction strength was S_r = 107 lbs/ft^2.

The main sources of uncertainty, or variability, in back-calculated values of S_r were (1) the precise location of the failure surface, (2) whether or not the failure initiated largely mono-

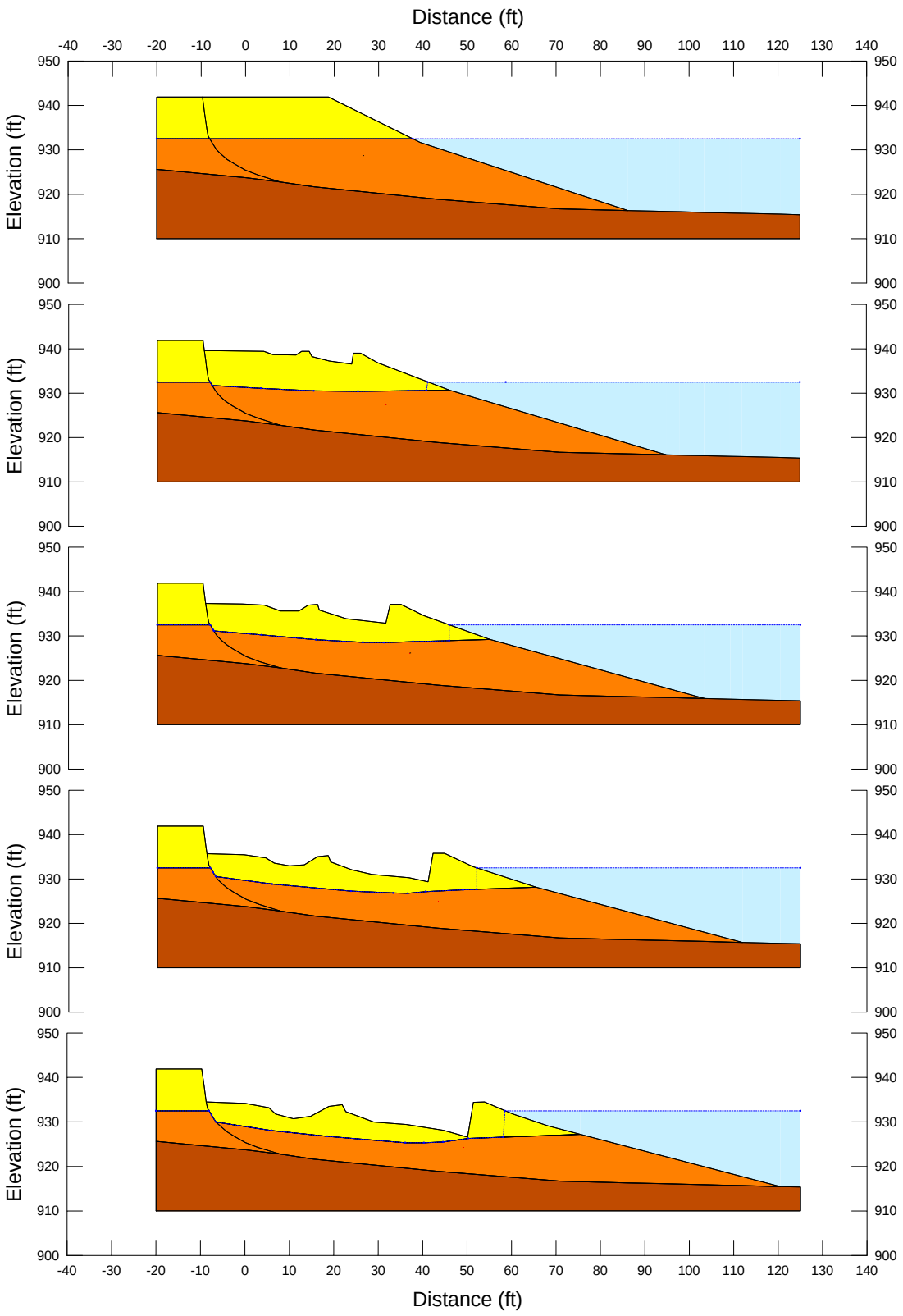

Figure A.9.8: Incremental inertial analysis of the failure of the Lake Ackerman Highway Embankment failure.

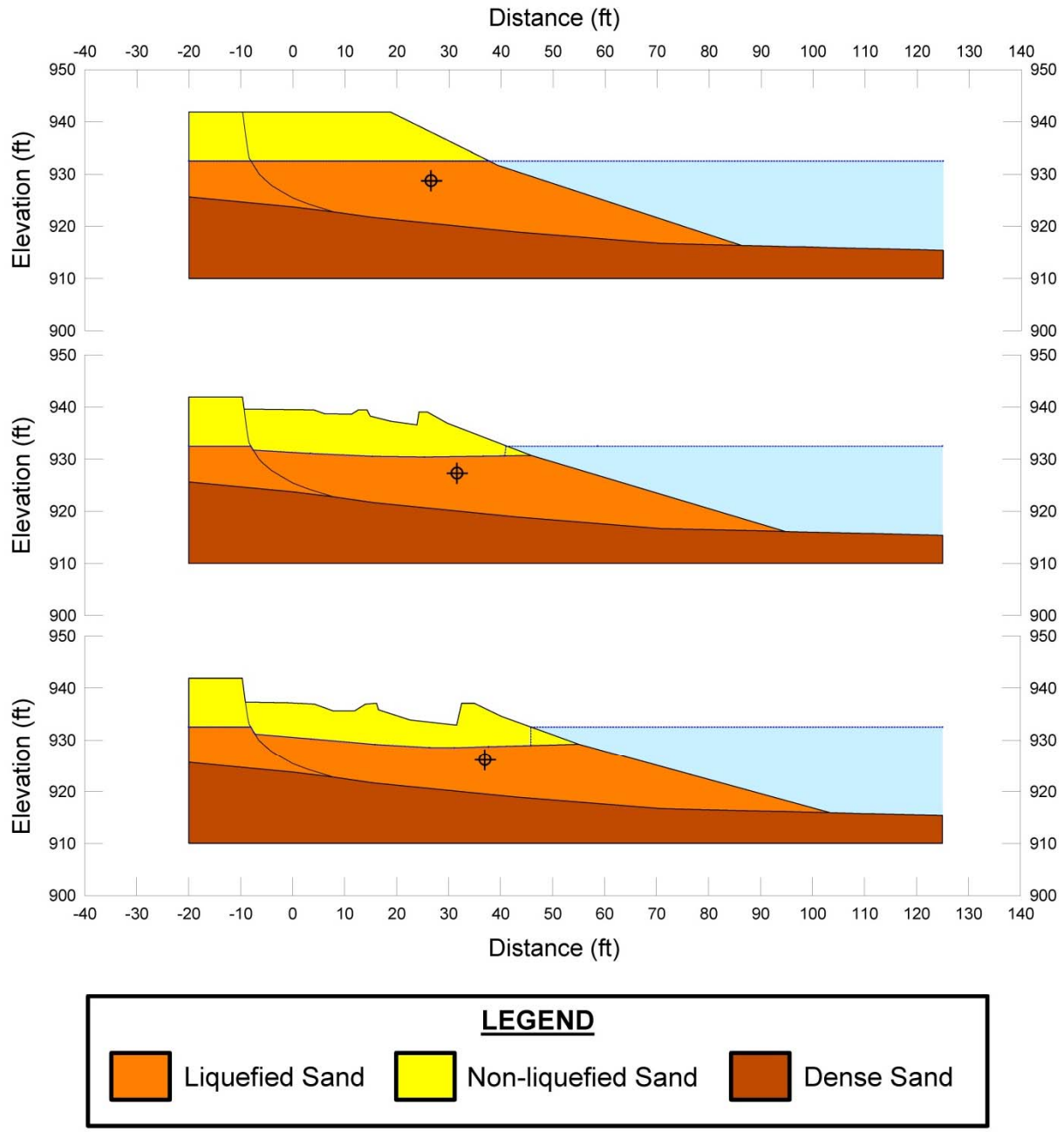

Figure A.9.9: Figure A.9.8 repeated, at larger scale, now also showing the progressive locations of the center of gravity of the overall failure mass.

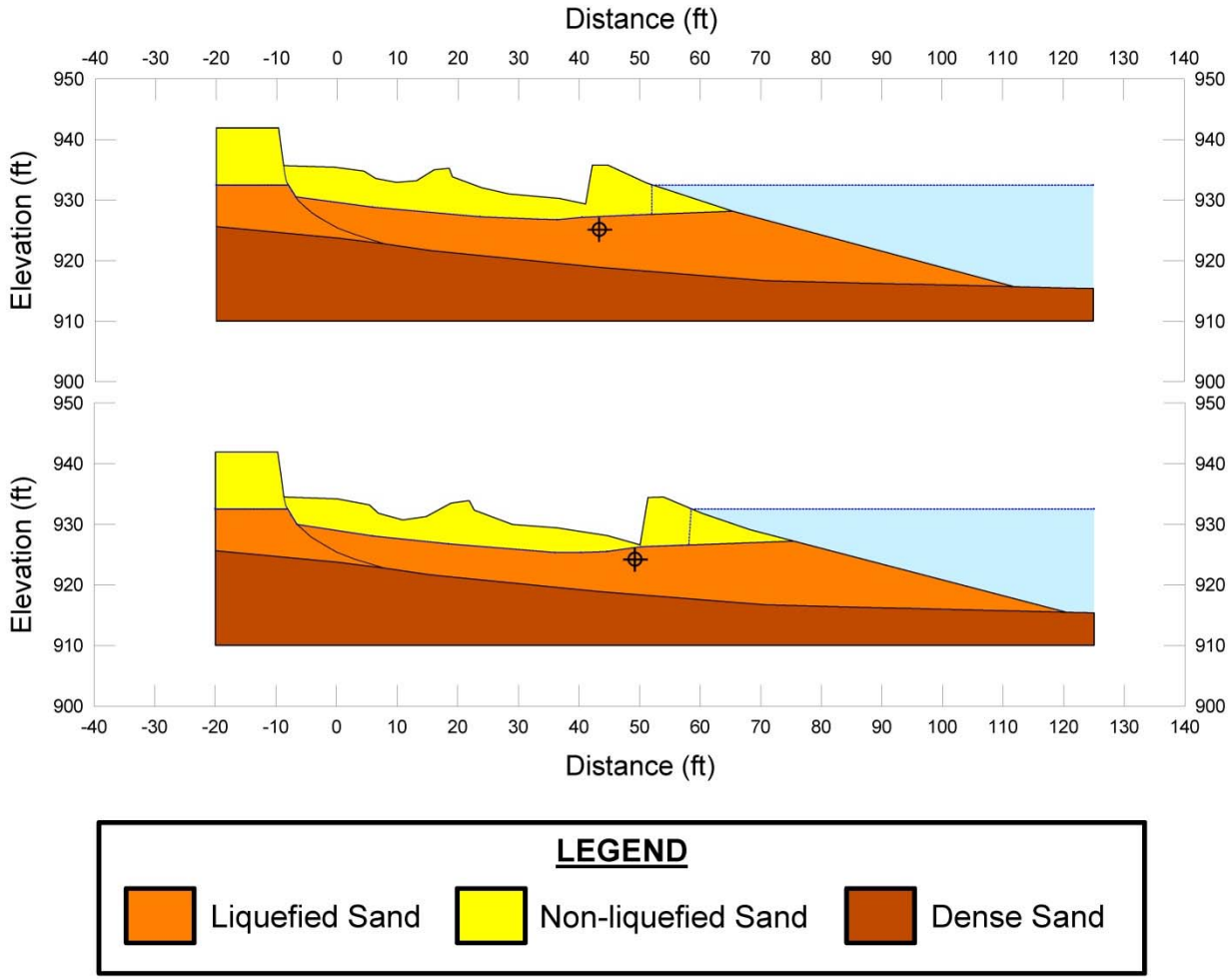

Figure A.9.9 (cont'd): Figure A.19.8 repeated, at larger scale, now also showing the progressive locations of the center of gravity of the overall failure mass.

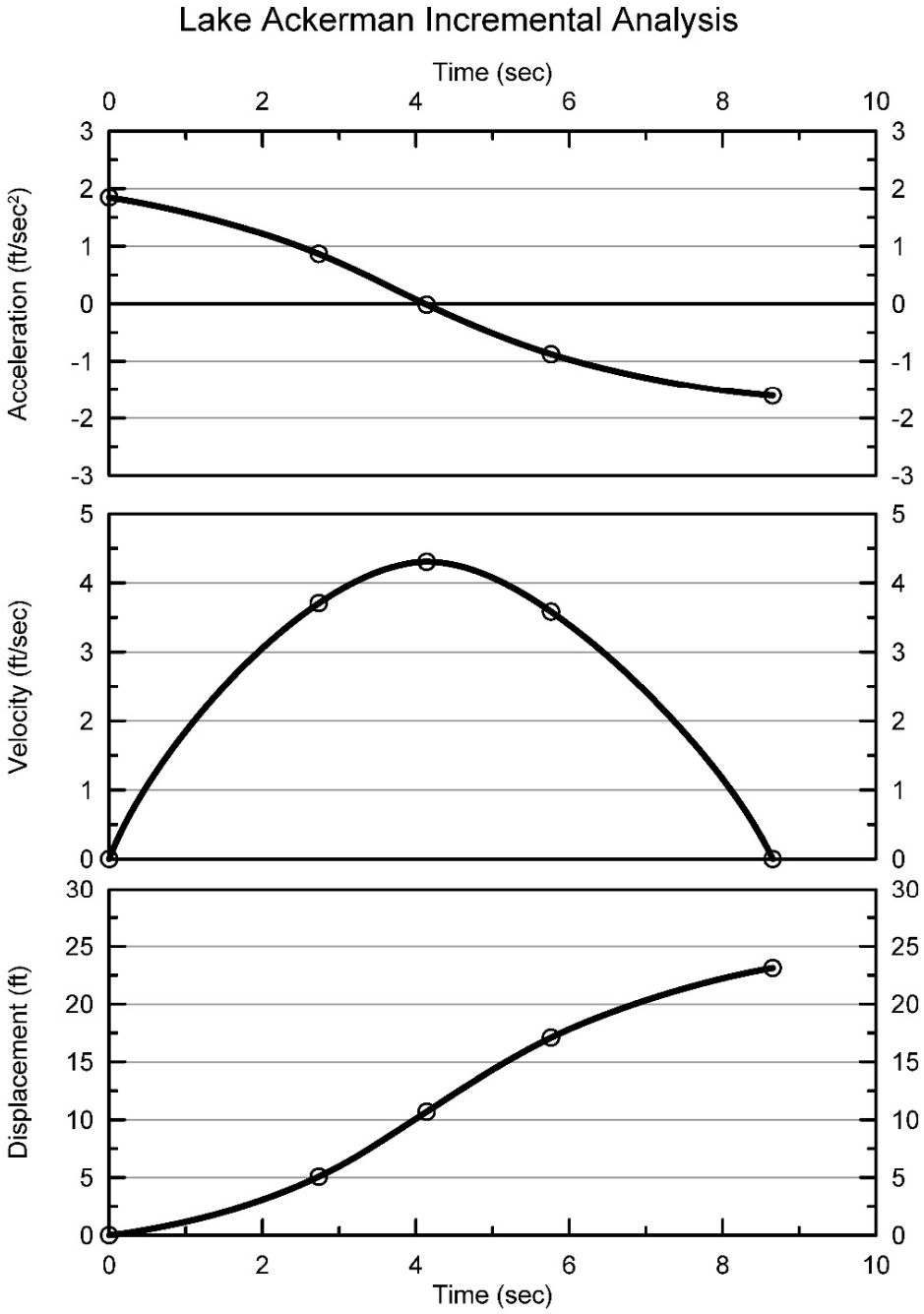

Figure A.9.10: Incremental inertial analysis of the failure of the Lake Ackerman Highway Embankment failure, showing progressive evolution of: (1) acceleration vs. time, (2) velocity vs. time, and (3) displacement vs. time of the overall center of gravity of the failure mass.

lithically or retrogressed progressively towards the back heel, (3) unit weights, and (4) strength within the non- liquefied materials at the top of the back heel scarp. Parameter sensitivity studies were next performed, varying these parameters and modeling assumptions over the ranges considered reasonable.

Based on all analyses performed, and the considerations discussed herein, the overall best estimate value of post-liquefaction strength for the Lake Ackerman Highway Embankment failure was judged to be $S_r \approx 107$ lbs/ft^2, with a likely range of $S_r \approx 74$ to 150 lbs/ft^2. Based on the factors contributing to uncertainty or variance for this case history, it was the judgment of the investigation team that this range represented approximately +/− 2 standard deviations. This range of variance is not quite symmetrical about the best estimate value, so minor further adjustments were made to produce a representative estimate of S_r suitable for regression analyses.

Overall, based on an assumed normal distribution, it was judged that the (mean and median) best estimate of post-liquefaction strength for this case history is

$$S_r = 107 \text{ lbs/ft}^2$$

and that the best estimate of standard deviation of mean overall post-liquefaction strength is

$$\sigma_{\bar{S}} = 19 \text{ lbs/ft}^2$$

Estimates of S_r were also reported by several other investigation teams, and two sets of these are shown in Table A.9.1(a). Olson (2001) and Olson and Stark (2002), reported a best estimate value of $S_r = 3.9$ kPa (81 lbs/ft^2), based on their inertial displacement analyses that considered kinetics, and a range of $S_r = 3.4$ to 4.7 kPa (71 to 98 lbs/ft^2). Wang (2003) and Wang and Kramer (2008) employed their zero inertial force (ZIF) method to incorporate inertial effects in their back-analyses of this failure, and they also developed estimates of both mean $\bar{S}_r = 98$ lbs/ft^2 as well as the associated standard deviation $\sigma_{\bar{S}} = 20.4$ lbs/ft^2. As discussed previously, Olson favored a slightly shallower failure surface for this case history, and that may have caused him to slightly underestimate S_r. The three studies represented in Table A.9.1(a) each employed different approaches, and different sets of modeling and analysis assumptions. Given this, overall agreement among these three investigations is very good.

A.9.6 Evaluation of Initial Effective Vertical Stress

Average initial (pre-failure) effective vertical stress was assessed for the liquefied zones of the failure surface shown in Figure A.9.8(a). Reasonable variations were then made in (1) unit weights, and (2) the precise location of the overall failure surface.

The resulting best estimate of average pre-failure effective vertical stress within the liquefied materials controlling the failure was then $\sigma_{vo}' \approx 909$ lbs/ft^2, with a reasonable range of

$\sigma_{vo}' \approx 787$ to 1,031 lbs/ft^2. This range is slightly non-symmetric abut the median value, and this range was judged by the engineering team to represent approximately +/− 2 standard deviations. Overall, the best characterization of initial (pre-failure) average effective vertical stress was then taken to be represented by a mean and median value of

$$\sigma_{vo}' \approx 909 \text{ lbs/ft}^2 \text{ (43.5 kPa)}$$

with a standard deviation of

$$\sigma_{\sigma o}' \approx 61 \text{ lbs/ft}^2 \text{ (2.9 kPa)}$$

Estimates of σ_{vo}' were also reported by other investigation teams, and two sets of these are shown in Table A.13.1(c). Average initial vertical effective stresses were reported by Olson (2001) and Olson and Stark (2002) as $\sigma_{vo}' = 1{,}075$ lbs/ft^2. Average initial vertical effective stresses were not directly reported by Wang (2003) and Kramer (2008), but they were published more recently in the publication by Kramer and Wang (2015). As discussed in Section 2.3.8.1(a), the approach taken by Wang (2003) to evaluation of σ_{vo}' for his nine "primary" case histories (this is one of those nine) is not clearly explained, and it is also poorly documented. Wang's value of $\sigma_{vo}' = 838$ lbs/ft^2 is in fairly good agreement with the value developed in these current studies, but this is not considered a very rigorous check here. Given the differences in assumptions and in failure surfaces modeled, overall, agreement among these three studies is acceptable here.

A.9.7 Evaluation of $N_{1,60,CS}$

SPT borings were performed after the failure, and the $N_{1,60}$ values varied between 1 to 7 blows/ft in the loosely dumped sand fill at elevations below the lake surface elevation (Hryciw et al., 1990). Hryciw et al. selected a representative value of $N_{1,60} = 3$ blows/ft, and Olson did the same. These were also $N_{1,60,CS}$ values because the fines adjustment was equal to zero in these clean fine sands. Wang (2002) and Kramer (2008) performed an independent evaluation, and developed a best estimate value of average $\overline{N_{1,60,CS}} = 4.8$ blows/ft, and a standard deviation of $\sigma_{\overline{N}} = 1.2$ blows/foot. An independent evaluation was also performed for these current studies, using the corrections and factors discussed in Appendix C, Section C.1, and the resulting characterization of the mean and median value of penetration resistance is $\overline{N_{1,60,CS}} = 3.5$ blows/ft, with a standard deviation of the value of this mean of $\sigma_{\overline{N}} = 0.7$ blows/ft. These values are all listed in Table A.9.1(b). Agreement among the three independent teams is very good here.

A.9.8 Other Results and Indices

A number of additional results, and indices, can be extracted from the analyses performed. Some of these are useful in developing some of the over-arching relationships and figures presented in the main text of this report. These values are presented in Table A.9.2.

Table A.9.1: Representative values for the Lake Ackerman Highway Embankment case history of: (a) post-liquefaction strength (S_r), (b) initial vertical effective stress (σ_{vo}'), and (c) $N_{1,60,CS}$ developed by various investigation teams, and estimates of variance in each of these indices when available.

(a) Post-Liquefaction Strength:	
Olson (2001) and Olson and Stark (2002)	S_r = 82 psf, and range = 71 to 98 psf
Wang (2003) and Kramer (2008)	$\overline{S_r}$ = 98 psf, and $\sigma_{\overline{S}}$ = 20.4 psf
This Study	$\overline{S_r}$ = 107 psf, and $\sigma_{\overline{S}}$ = 19 psf
(b) Representative $N_{1,60}$ or $N_{1,60,CS}$ Value:	
Olson (2001) and Olson and Stark (2002)	$N_{1,60}$ = 3 bpf, and range = 1 to 7 bpf
Wang (2003) and Kramer (2008)	$\overline{N_{1,60,CS}}$ = 4.8 bpf, and $\sigma_{\overline{N}}$ = 1.2 bpf
This Study	$\overline{N_{1,60,CS}}$ = 3.5 bpf, and $\sigma_{\overline{N}}$ = 0.7 bpf
(c) Representative Initial Vertical Effective Stress:	
Olson (2001) and Olson and Stark (2002)	σ_{vo}' = 1,076 psf, likely range is not provided.
Wang (2003) and Kramer (2008)	Value of $\sigma_{vo}' \approx$ 838 psf is poorly documented, and so is considered useful only as an approximate comparison. (See Section 2.3.8.1, and Table 2.3.)
This Study	$\overline{\sigma'_{vo}}$ = 909 psf, and $\sigma_{\overline{\sigma}}$ = 61 psf

Table A.9.2: Additional results and indices from the analyses of the Lake Ackerman Highway Embankment failure case history.

Maximum distance traveled by the center of gravity of the overall failure mass	23.1 ft.
Initial post-liquefaction Factor of Safety prior to displacement initiation, and based on best estimate value of S_r	FS = 0.58
Final post-liquefaction Factor of Safety at final (residual) post-failure geometry, and based on best estimate value of S_r	FS = 1.91

A.10 Chonan Middle School (Chiba, Japan; 1987)

A.10.1 Brief Summary of Case History Characteristics

Name of Structure	Chonan Middle School
Location of Structure	Chiba, Japan
Type of Structure	Embankment Fill
Date of Failure	December 17, 1987
Nature of Failure	Seismic, During 1987 Chiba-Toho-Oki Earthquake (M = 6.7)
Approx. Maximum Slope Height	19.3 ft.

A.10.2 Introduction and Description of Failure

The slope of the embankment fill at Chonan Middle School failed during the Chiba-Toho-Oki Earthquake of December 17, 1987 (M = 6.7), and was investigated by Ishihara et al. (1990). The estimated peak ground acceleration at the site was approximately 0.12 g (Olson, 2001).

Figure A.10.1 (from Ishihara et al., 1991) shows a plan view of the Chonan Middle School site and Figure A.10.2 shows a cross section through the failure. Areas where fill material that was excavated from the surrounding hilltops was placed are shown on Figure A.10.1. Fill placement occurred in approximately 1960 and the fill was reportedly placed loosely with no compaction effort (Ishihara, 1993).

Following the failure, Swedish cone penetration tests were performed in the area of the failed slope. Results of these tests are presented in Figure A.10.2. Weak layers can be seen in the results of the Swedish cone tests, and these can be used to infer a reasonable estimate of the likely failure surface. Ishihara et al. (1990) present a reasonable interpretation of a failure surface for the post failure geometry and this is reproduced in Figure A.10.3. Considering the results of the Swedish cone tests and the geometry at the heel and toe of the failure, a failure surface similar to that presented by Ishihara et al. (1990) can be assumed for purposes of back-analyses, and it can be considered to be reasonably well constrained.

Prior to the construction of a building on the school site, four SPT borings had been performed. Only one of these is reported in the available literature, and the location of the boring (Boring B) is shown in Figure A.10.1 to be within the area of fill placement. Figure A.10.4 shows the results of this SPT boring.

A difficulty encountered in performing back-analyses of this failure is that the post-failure volume of the failed slope materials shown in Figure A.10.1 is approximately 17% smaller than the pre-failure volume. This is accommodated in the back-analyses that follow, by progressively changing the overall volume of the slide mass as the failure develops. Analyses

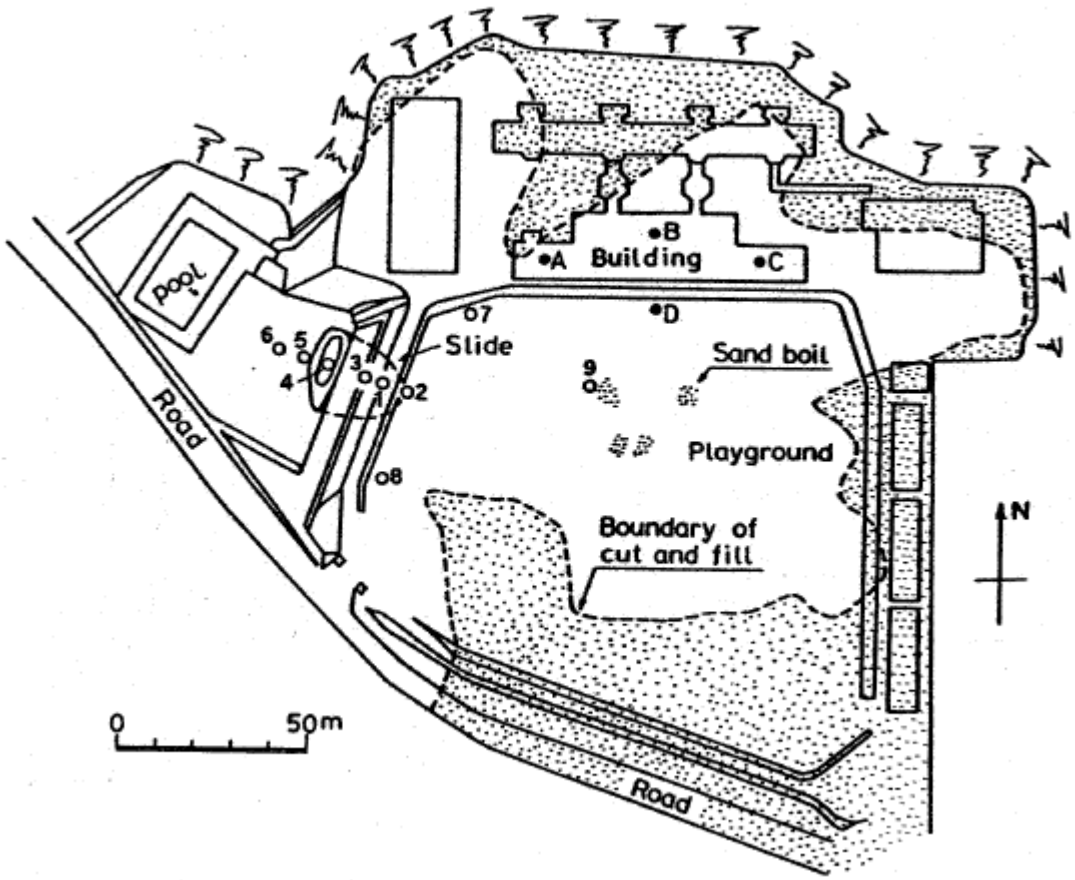

Figure A.10.1: Plan view of the Chonan Middle School site showing the location of the slope failure, locations of penetration tests, and the approximate limits of fill (from Ishihara et al., 1990).

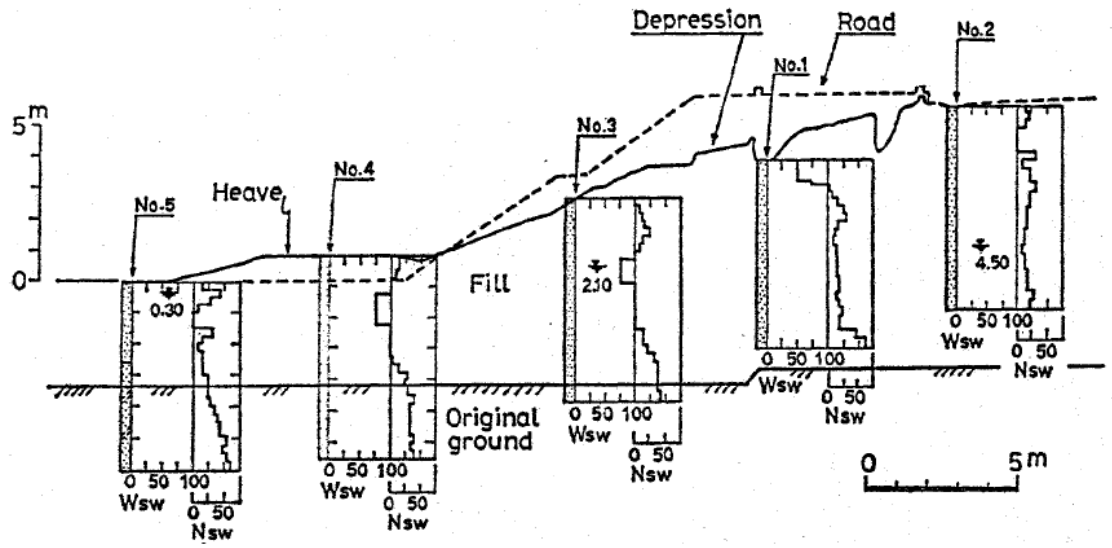

Figure A.10.2: Cross-section of the slope failure at the Chonan Middle School site showing the results of Swedish cone penetration tests and the pre- and post-failure geometry (from Ishihara et al., 1990).

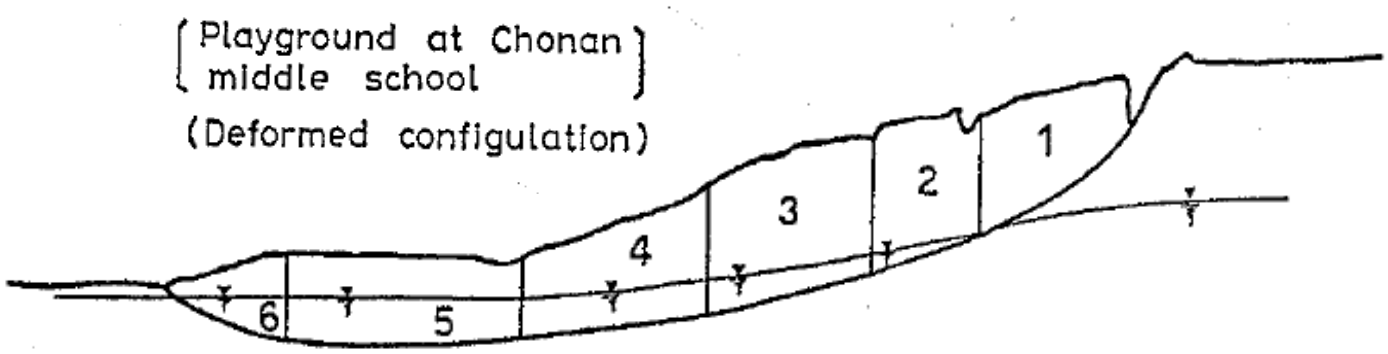

Figure A.10.3: Interpretation of the failure surface and phreatic surface for a limit equilibrium stability analysis of the post failure geometry performed by Ishihara et al. (1990).

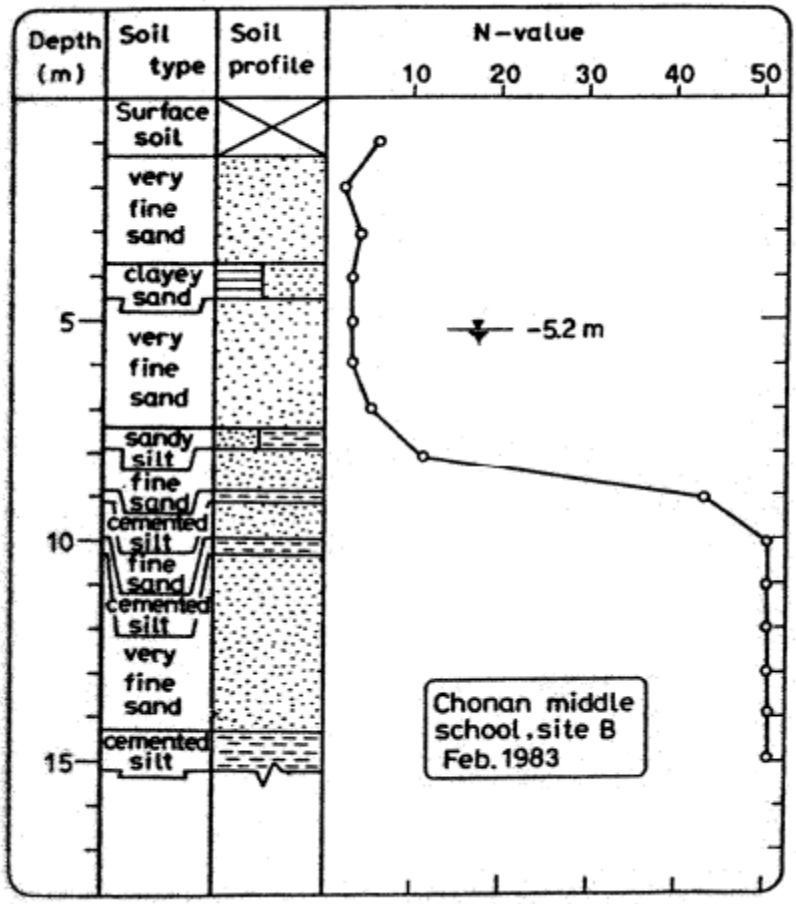

Figure A.10.4: Log of Boring B performed in February of 1983 at the Chonan Middle School site prior to the construction of a school building (from Ishihara, 1993).

performed with different approaches to this variation in slide mass (including using just the initial slide mass without changing it to eventually match the post-failure volume of Figure A.10.1) showed that this volume discrepancy has only a moderate effect on uncertainty, or variance, in back-calculated post-liquefaction strengths for this case history.

A.10.3 Initial Yield Strength Analysis

Figure A.10.5(a) shows the cross-section used in these studies for the best estimate case back-analyses to determine the initial yield stress, defined as the best estimate value of post-liquefaction $S_{r,yield}$ within the liquefiable hydraulic fill required to produce a calculated Factor of Safety equal to 1.0 for pre-failure geometry.

The precise location of the initial failure surface at the base of the failure is uncertain. However, given the geometry of the failure and the reported stratigraphy, the location was fairly well constrained. The best estimate location of the phreatic surface used in the back-analyses

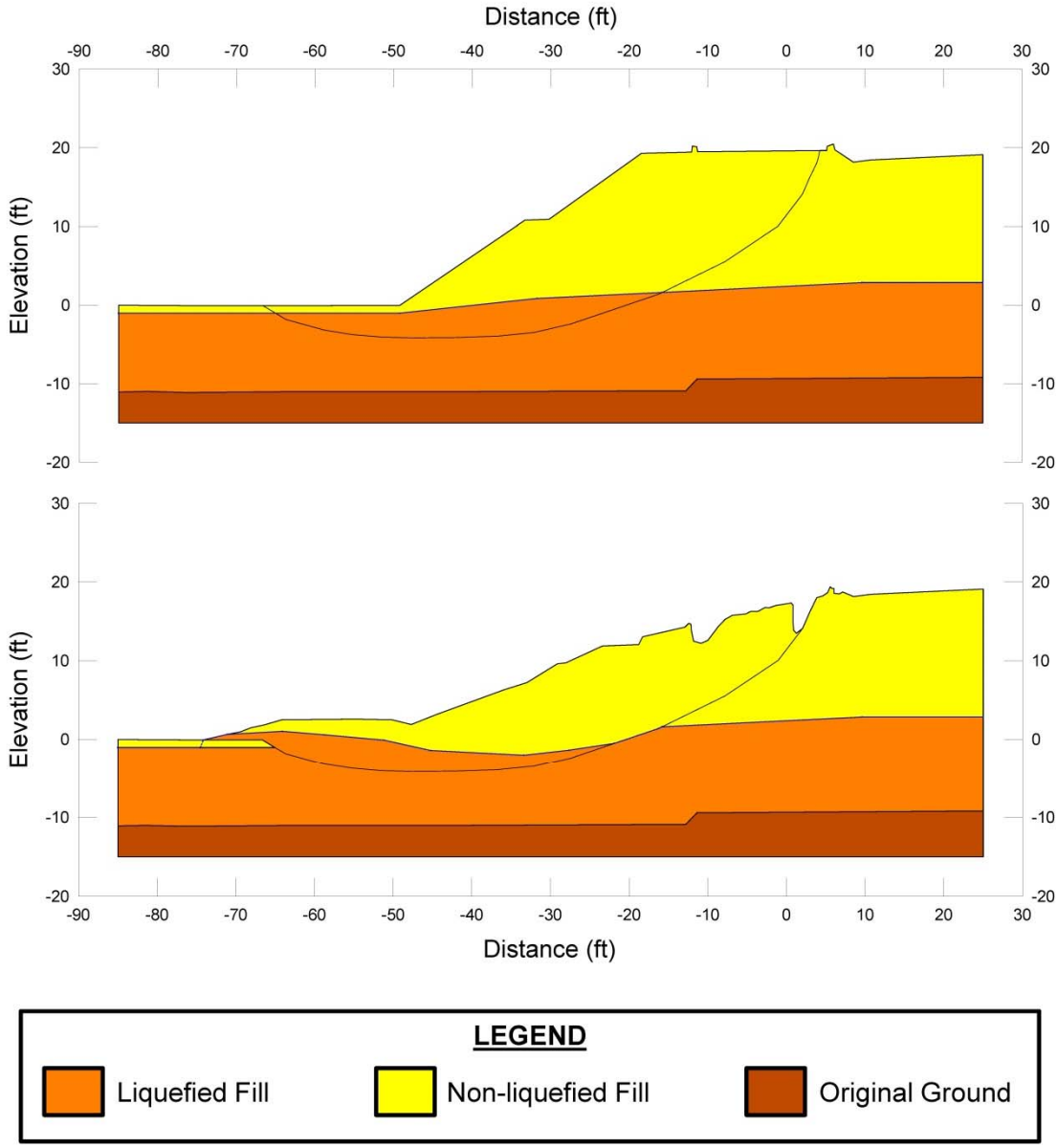

Figure A.10.5: Chonan Middle School cross-sections showing (a) pre-failure geometry of the fill slope and the failure surface used for calculation of post-liquefaction initial yield strength $S_{r,yield}$, and (b) post-failure residual geometry and the failure surface used to calculate $S_{r,resid/geom}$.

was developed considering the reported depths where ground water was encountered during the post-failure investigation reported in Ishihara et al. (1990). The location of the phreatic surface within the fill embankment corresponds well to the location that ground water was encountered during the 1983 investigation for the school building located in the middle of the fill shown in Figure A.10.4.

A search was made for the most critical static failure surface assuming that liquefaction had been "triggered" in all potentially liquefiable materials below the phreatic surface, while constraining the location the failure surface near the toe to match the approximate zone of lower penetration resistance from the Swedish cone tests. Following some minor refinement to the failure surface to better match a surface that would articulate the failed mass as observed, the "best estimate" failure surface is shown in Figure A.10.5(a). This resulting failure surface is in good agreement with the failure surface used for back-analyses performed by Ishihara et al. (1990). Those earlier analyses neglected seismic inertial forces, however, and they also did not account for likely progressive development of triggering of liquefaction within the slope.

Loose fine sand materials above the phreatic surface were modeled with Ø´ ≈ 30°, and a unit weight of $\gamma_m \approx 115$ lbs/ft^3. Materials below the phreatic surface were considered to liquefy, down to the base of the failure surfaces analyzed, and were assigned an undrained post-liquefaction yield strength of $S_{r,yield}$ that was constant along any given failure surface, and a unit weight of $\gamma_s \approx 120$ lbs/ft^3.

The resulting best-estimate value of $S_{r,yield}$ for the most critical initial failure surface was $S_{r,yield} = 199$ lbs/ft^2.

Parameters and geometry were then varied to examine potentially variability. The location of the phreatic surface was varied, raising it by up to 0.5 m (1.5 ft.) across the embankment, and lowering it by up to a similar distance. Unit weights were also varied over the ranges considered likely, and the friction angle of non-liquefied material above the phreatic surface was varied from 28° to 35°. The resulting range of values of $S_{r,yield}$ for the most critical initial failure surface was $S_{r,yield} \approx 165$ to 240 lbs/ft^2.

Olson (2001) also performed back-analyses to determine $S_{r,yield}$. Failure surfaces analyzed were similar, but there were some differences in the details of modeling of the phreatic surface and the failure surface. Olson reported values of $S_{r,yield} \approx 12.0$ to 12.9 kPa (251 to 269 lbs/ft^2), with a best estimate value of 12.2 kPa (255 lbs/ft^2).

A.10.4 Residual Strength Analysis Based on Residual Geometry

The calculation of the "apparent" post-liquefaction strength ($S_{r,resid/geom}$) required to produce a calculated Factor of Safety equal to 1.0 based on residual geometry is illustrated in Figure A.10.5(b).

This figure shows the phreatic surface, and the failure surface, used to calculate the best-estimate value of $S_{r,resid/geom} \approx 102$ lbs/ft^2. Variations were made in parameters, and in location

of the pre-failure phreatic surface, as was described in the preceding section. The resulting likely range of post-liquefaction strength required to provide a calculated Factor of Safety equal to 1.0 based on residual geometry was considered to be $S_{r,resid/geom} \approx 86$ to 125 lbs/ft^2.

Olson (2001) also calculated post-liquefaction strength required to produce a calculated Factor of Safety equal to 1.0 based on residual geometry, and reported a best estimate value of $S_{r,resid/geom} \approx 4.8$ kPa (100 lbs/ft^2), with a range of $S_{r,resid/geom} \approx 3.8$ to 6.0 kPa (79 to 125 lbs/ft^2).

A.10.5 Incremental Inertial Back-Analyses and Overall Estimates of S_r

Incremental inertial back-analyses were performed using the same sets of properties and geometries (including failure surfaces and phreatic surfaces) as described in the previous sections.

Figure A.10.6 shows the best-estimate progressive incremental inertial analysis, showing the 5 stages of geometry evolution modeled as the failure proceeds. Figure A.10.7 shows the associated calculations of (1) acceleration vs. time, (2) velocity vs. time, and (3) displacement of the overall center of gravity vs. time. For the geometry and phreatic surface shown in Figure A.10.5, the best estimate value of post-liquefaction strength was $S_r = 141$ lbs/ft^2.

The main sources of uncertainty, or variability, in back-calculated values of S_r were (1) the precise location of the overall failure surface, (2) unit weights, (3) strength within the non-liquefied materials, and (4) the location of the phreatic surface.

The analysis shown in Figure A.10.6 neglects cyclic inertial forces, and so may represent a slightly conservative assessment of actual post-liquefaction strength mobilized.

Based on all analyses performed, and the considerations discussed herein, the overall best estimate value of post-liquefaction strength for the Chonan Middle School slope failure was judged to be $S_r \approx 141$ lbs/ft^2, with a likely range of $S_r \approx 91$ to 196 lbs/ft^2. Based on the factors contributing to uncertainty or variance for this case history, it was the judgment of the investigation team that this range represented approximately +/− 1.5 standard deviations. This range of variance is not quite symmetrical about the best estimate value, so minor further adjustments were made to produce a representative estimate of S_r suitable for regression analyses.

Overall, based on an assumed normal distribution, it was judged that the (mean and median) best estimate of post-liquefaction strength for this case history is

$$S_r = 141 \text{ lbs/ft}^2 \text{ (6.75 kPa)}$$

and that the best estimate of standard deviation of mean overall post-liquefaction strength is

$$\sigma_{\bar{S}} = 35 \text{ lbs/ft}^2 \text{ (1.68 kPa)}$$

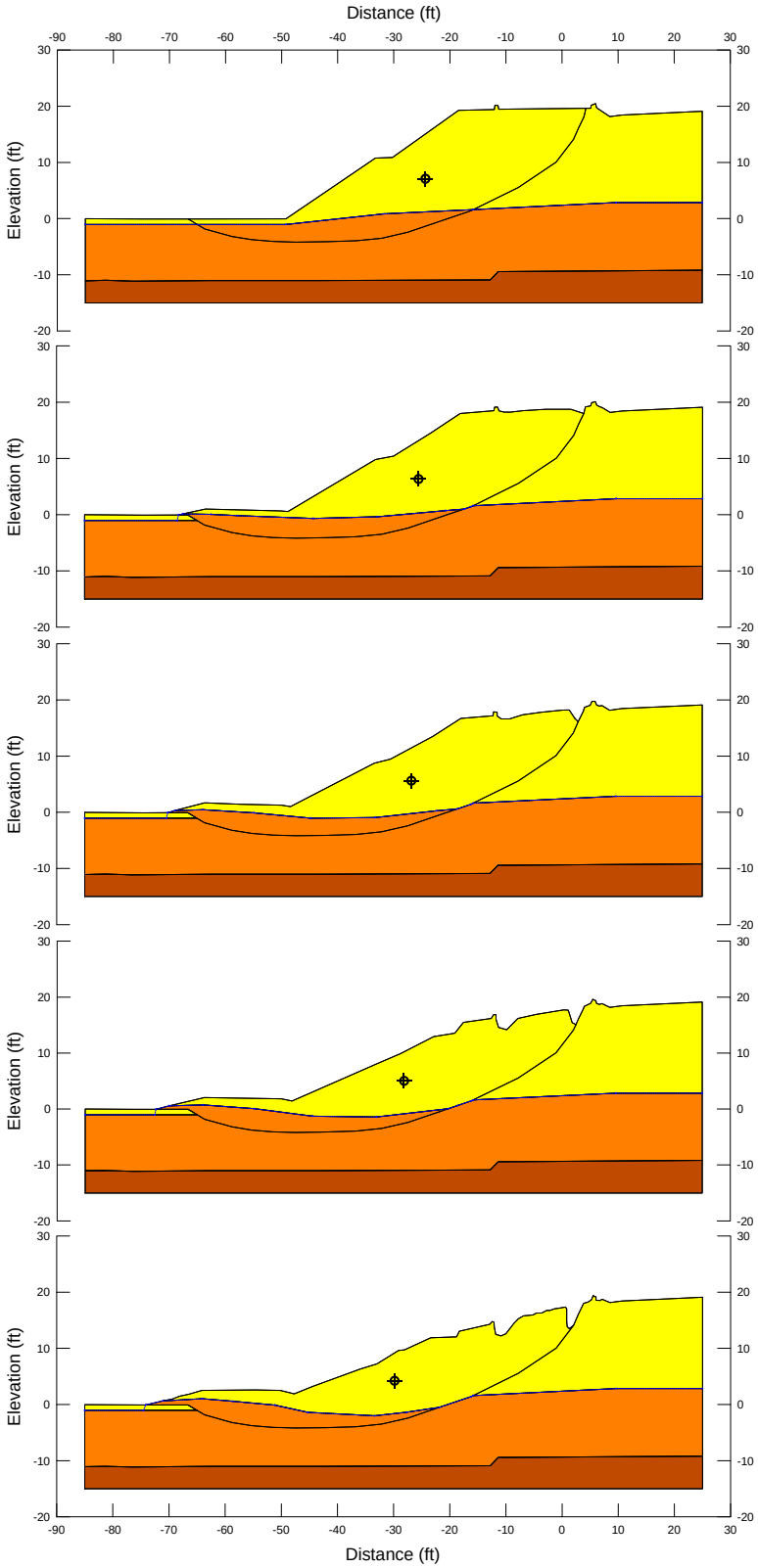

Figure A.10.6: Incremental inertial analysis of the failure of the fill slope at Chonan Middle School, showing progressive evolution of cross-section geometry modeled.

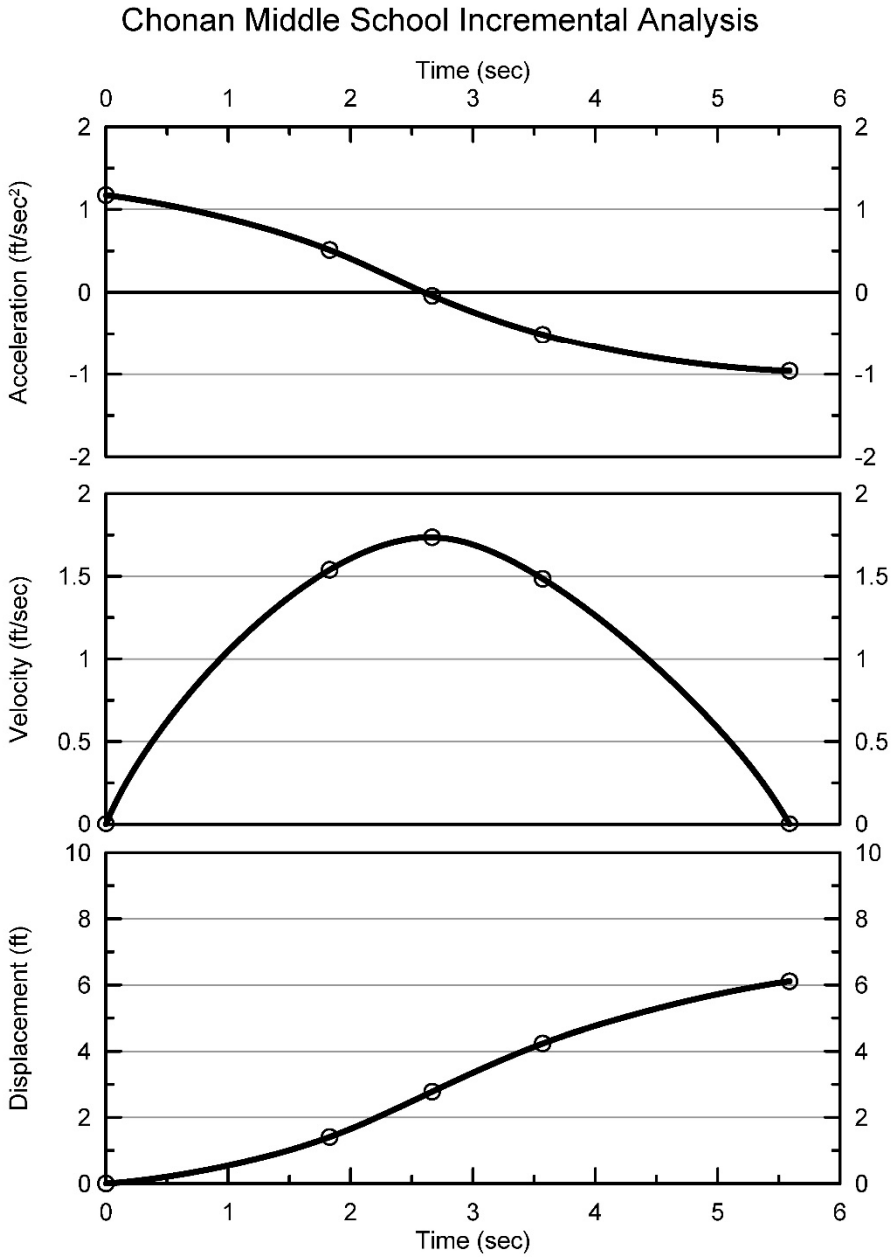

Figure A.10.7: Incremental inertial analysis of the failure of the fill slope a Chonan Middle School showing progressive evolution of: (1) acceleration vs. time, (2) velocity vs. time, and (3) displacement of the overall center of gravity vs. time

Estimates of S_r were also reported by several other investigation teams, and these are shown in Table A.10.1(a). Olson (2001) and Olson and Stark (2002), reported a best estimate value of S_r = 4.8 kPa (100 lbs/ft^2), but this was not based on their "kinetics" analyses that considered momentum effects. Instead, it was based on assessment of post-liquefaction residual geometry and it neglected momentum effects. As a result, it will be an overly conservative estimate (the value will be much too low). Olson also calculated $S_{r,yield}$ and $S_{r,resid/geom}$ (see Sections A.11.3 and A.11.4) for this case, however, and those two values can be convolved to provide a better estimate of S_r. Based on Equation 4-1 (see Chapter 4), a better estimate for S_r based on calculations performed by Olson (2001) would be $S_r \approx 0.8 \times [S_{r,yield} + S_{r,resid/geom}] / 2 \approx$ 0.8 x [12.2 kPa + 4.8 kPa] /2 ≈ 6.8 kPa (142 lbs/ft^2), and this value is more directly comparable with the values of this current study, and so it is the value presented in Table A.10.1(a). Wang (2003) and Kramer (2008) developed estimates of both mean $\overline{S}_r$ = 178.7 lbs/ft^2 as well as the associated standard deviation $\sigma_{\overline{S}}$ = 32.0 lbs/ft^2. Given the differences in approaches among the three studies, overall agreement among these investigations is very good.

A.10.6 Evaluation of Initial Effective Vertical Stress

Average initial (pre-failure) effective vertical stress was assessed for the liquefied zones of the failure surface shown in Figure A.10.5(a). Reasonable variations were then made in (1) the location of the phreatic surface, (2) unit weights, and (3) the precise location of the overall failure surface.

The resulting best estimate of average pre-failure effective stress within the liquefied materials controlling the failure was then $\sigma_{vo}' \approx$ 1,032 lbs/ft^2, with a reasonable range of $\sigma_{vo}' \approx$ 911 to 1,157 lbs/ft^2. This range is slightly non-symmetric about the median value, and this range was judged by the engineering team to represent approximately +/− 1.5 standard deviations. Overall, the best characterization of initial (pre-failure) average effective vertical stress was then taken to be represented by a mean and median value of

$$\sigma_{vo}' \approx 1{,}032 \text{ lbs/ft}^2 \text{ (49.4 kPa)}$$

with a standard deviation of

$$\sigma_{\sigma o'} \approx 82 \text{ lbs/ft}^2 \text{ (3.93 kPa)}$$

Estimates of σ_{vo}' were also reported by other investigation teams, and these are shown in Table A.10.1(c). Olson (2001) and Olson and Stark (2002) report an average initial vertical effective stress on the order of approximately $\sigma_{vo}' \approx$ 1,119 lbs/ft^2. Average initial vertical effective stresses were not directly reported by Wang (2003) and Kramer (2008), but they were published more recently in the publication by Kramer and Wang (2015). As discussed in Section 2.3.8.1(b)-(iii), Wang (2003) did not perform any independent analyses to assess σ_{vo}' for his 22 "secondary" cases, and this is one of those cases. Instead, he compiled values of S_r from multiple previous investigators, and averaged these for a best estimate. He also compiled multiple values of S_r/σ_{vo}' from previous investigators, and averaged these for a best estimate. He then used these two best-estimate values of S_r and S_r/σ_{vo}' to infer a resulting representative value

of σ_{vo}'. As described in Section 2.3.8.1(b)-(iii), the resulting averaged values of S_r and S_r/σ_{vo}' were incompatible with each other for a number of Wang's "secondary" case histories, and this process produced unreasonable, and in some cases physically infeasible, values of σ_{vo}' for a number of case histories. Accordingly, Wang's value of σ_{vo}' = 1,964 lbs/ft^2 is not considered a useful check here. Agreement between the value calculated by Olson (2001) and the value calculated in these current studies is very good.

A.10.7 Evaluation of $N_{1,60,CS}$

Shown in Figure A.10.4 from Ishihara (1993), only one boring in available literature with SPT tests performed in the fill material at Chonan Middle School. As a result, lack of numbers of SPT data is a significant contributor to uncertainty or variability with respect to the median or mean $N_{1,60,CS}$ value representative of this material. Olson (2001) utilized an energy ratio of approximately 68%, and current study does the same. Corrections for effective overburden stress (C_N) were made using the relationships proposed by Deger (2014), as presented and discussed in Appendix C, Section C.1.1. Corrections for SPT equipment and procedural details, and for fines content, were made based on Cetin et al. (2004) as also presented and explained in Section C.1.1. The resulting representative $N_{1,60}$ value was between 5 and 5.5 blows/ft. Based on the reported fines content of 18% (Ishihara, 1993), the representative (median) $\overline{N_{1,60,CS}}$ value was determined to be 6.5 blows/ft.

Variance of $\overline{N_{1,60,CS}}$, was only partially determined by variation of $N_{1,60,CS}$ values within this limited data set. Additional factors significantly affecting variance or uncertainty in the median representative $\overline{N_{1,60,CS}}$ value were (1) lack of numbers of SPT data, and (2) uncertainty as to actual SPT equipment and procedural details. Overall, it was the judgment of the investigation team that SPT penetration resistance could be suitably represented with a representative (median) value of $\overline{N_{1,60,CS}}$ = 6.5 blows/ft., and with a standard deviation of the median/representative value of approximately $\sigma_{\overline{N}}$ = 2.1 blows/ft.

Table A.10.1(b) shows values of representative $N_{1,60}$ or $N_{1,60,CS}$ values developed by selected other investigators, and variance or standard deviations in these representative values when available. Olson and Stark (2001, 2002) developed an estimated representative value of $N_{1,60}$ = 5.2 blows/ft, and an estimated range of representative values of $N_{1,60} \approx$ 2.6 to 8.8 blows/ft, but did not quantify variance or standard deviation in probabilistic terms. Wang (2003) and Kramer (2008) jointly developed a representative value of $\overline{N_{1,60,CS}}$ = 6.4 blows/ft, and their estimated standard deviation of that overall mean value for this case history was $\sigma_{\overline{N}}$ = 6.9 blows/ft. This standard deviation is larger than the mean value itself, and this is an artifact of the rigidly defined methodology employed by Wang (2003) to develop estimates of $\sigma_{\overline{N}}$. The representative $N_{1,60}$ value of Olson and Stark is about 1 to 1.5 blows/ft lower than the other two sets of values in the table, largely because Olson and Stark did not make a fines correction, which would have served to increase their $N_{1,60}$ values as they became $N_{1,60,CS}$ values in these silty sands. With any reasonable fines correction agreement between their value and the other values would be very good. Overall, the agreement all three sets of values shown in Table A.10.1(b) is very good.

A.10.8 Other Results and Indices

A number of additional results, and indices, can be extracted from the analyses performed. Some of these are useful in developing some of the over-arching relationships and figures presented in the main text of this report. These values are presented in Table A.10.2.

Table A.10.1: Representative values for the Chonan Middle School case history of: (a) post-liquefaction strength (S_r), (b) initial vertical effective stress (σ_{vo}'), and (c) $N_{1,60,CS}$ developed by various investigation teams, and estimates of variance in each of these indices when available.

(a) Post-Liquefaction Strength:	
Olson (2001) and Olson and Stark (2002)	$S_r \approx 142$ psf*
Wang (2003) and Kramer (2008)	$\overline{S_r} = 178.7$ psf, and $\sigma_{\overline{S}} = 32.0$ psf
This Study	$\overline{S_r} = 141$ psf, and $\sigma_{\overline{S}} = 35$ psf
(b) Representative $N_{1,60}$ or $N_{1,60,CS}$ Value:	
Olson (2001) and Olson and Stark (2002)	$N_{1,60} = 5.2$ bpf, and range = 2.6 to 8.8 bpf
Wang (2003) and Kramer (2008)	$\overline{N_{1,60,CS}} = 6.4$ bpf, and $\sigma_{\overline{N}} = 6.9$ bpf
This Study	$\overline{N_{1,60,CS}} = 6.5$ bpf, and $\sigma_{\overline{N}} = 2.1$ bpf
(c) Representative Initial Vertical Effective Stress:	
Olson (2001) and Olson and Stark (2002)	$\sigma_{vo}' = 1{,}119$ psf. Likely range is not provided.
Wang (2003) and Kramer (2008)	Value of $\sigma_{vo}' \approx 1{,}968$ psf is poorly based, and so is not very useful as a basis for comparison. (See Section 2.3.8.1(b) and Table 2.3)
This Study	$\overline{\sigma'_{vo}} = 1{,}032$ psf, and $\sigma_{\overline{\sigma}} = 82$ psf

* Olson (2001) did not employ his "kinetics" back-analysis approach to this case. See the text of Section A.10.5 for an explanation of the value of $S_r \approx 142$ psf attributed here.

Table A.10.2: Additional results and indices from the analyses of the Chonan Middle School failure case history.

Maximum distance traveled by the center of gravity of the overall failure mass	6.1 ft.
Initial post-liquefaction Factor of Safety prior to displacement initiation, and based on best estimate value of S_r	FS = 0.86
Final post-liquefaction Factor of Safety at final (residual) post-failure geometry, and based on best estimate value of S_r	FS = 1.17

A.11 Soviet Tajik May 1 Slope Failure (Tajikistan Republic; 1989)

A.11.1 Brief Summary of Case History Characteristics

Name of Structure	Soviet Tajikistan Slope
Location of Structure	Tajikistan Republic
Type of Structure	Natural Loess Slope
Date of Failure	January 23, 1989
Nature of Failure	Seismic, During the 1989 Soviet Tajik Earthquake (M_L = 5.5)
Approx. Maximum Slope Height	96.8 ft.

A.11.2 Introduction and Description of Failure

The Soviet Tajik Earthquake of January 23, 1989 (M_L = 5.5) produced a number of flow slides in the Gissar area of Tajikistan, USSR. As shown in Figure A.11.1, the Gissar area lies along the Iliakckin Fault, which produced the earthquake. Shaking duration was short (approximately 4 to 5 seconds) and as shown in Figure A.11.1, levels of peak acceleration recorded were relatively low.

Ishihara et al. (1990) describe a series of flow slides that occurred in loessial bluffs overlooking the Gissar area. One of these slides developed into a mud flowslide that travelled approximately 2 km, killing approximately 220 villagers. Another slide, which experienced more limited displacements and deformations, will be studied here.

The "May 1" slide occurred in a loessial hillside overlooking the village of May 1. Figure A.11.2 shows a cross-section through this feature showing the pre-failure and post-failure conditions. This figure is from Olson (2001), and is based on Ishihara et al. (1990), except that the phreatic surfaces shown are inferred by Olson.

This is an interesting case history in several regards. The materials responsible for the failure are fine loessial silts, and they were very loose; at water contents that approximately equaled or exceeded their liquid limits. As a result they were prone to collapse. Earthquake shaking was not very strong, and it was also of short duration, but it was sufficient to "trigger" or initiate this failure. After failure, the materials were not likely subject to much additional shaking, so this was likely a "cyclically initiated" failure that then "flowed" under largely static loading conditions. After initiation of failure, the failure mass travelled only a limited distance, and came to rest with a "pressure ridge" (or bulge) at the toe.

The silt materials responsible were reportedly 100% fines, with approximately 15% clay content based on a hydrometer test (Ishihara et al., 1990). The loess material in the region is reported by Ishihara et al. (1990) to plot near the A-line with a plasticity index of generally PI = 10%.

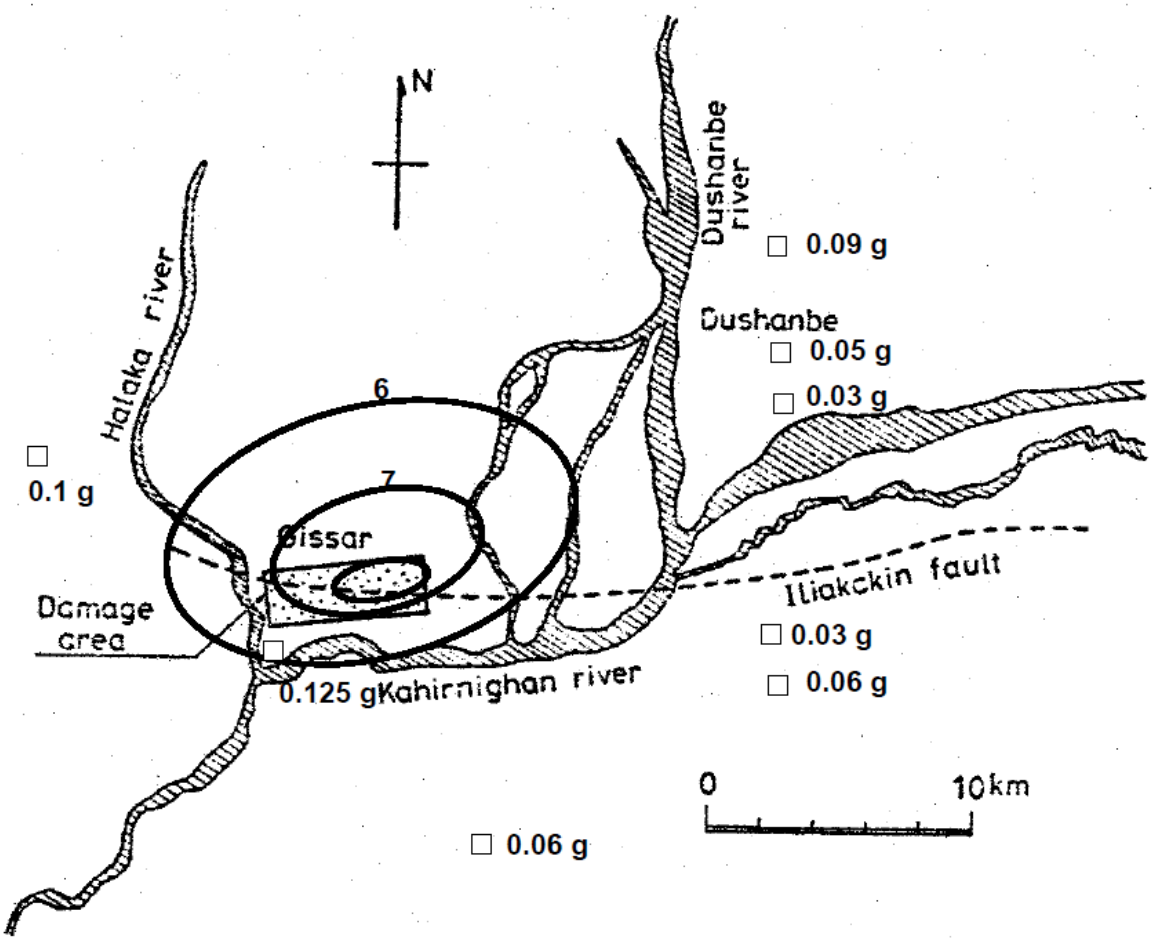

Figure A.11.1: Map of the Gissar area showing the location of the Iliakckin Fault, the damage zone, contours of estimated damage intensity, and recorded peak ground surface accelerations.

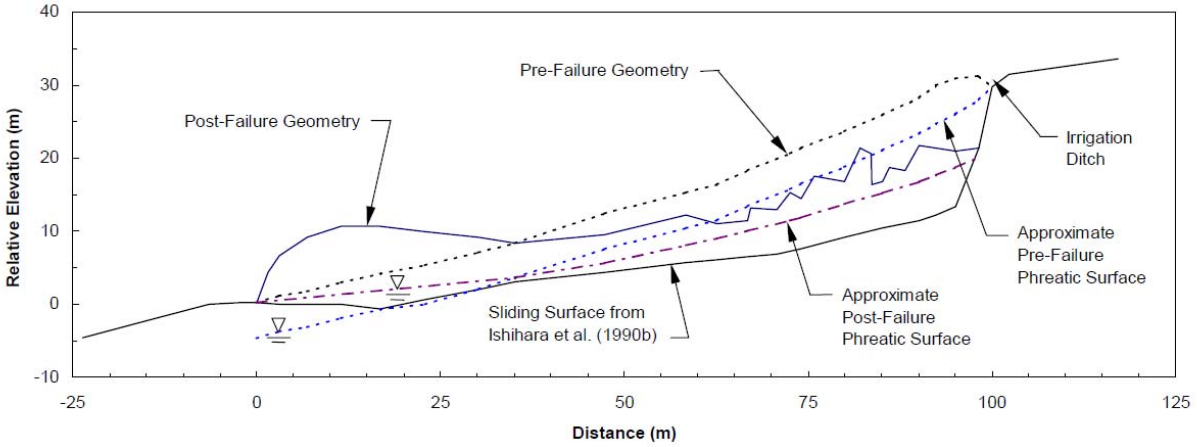

Figure A.11.2: Pre-failure and post-failure cross-sections of the Soviet Tajik May 1 slide (figure from Olson, 2002, after Ishihara et al, 1990)

Constraint as to the likely location of the basal slip surface was conditioned in part on the water content and liquidity indices of the loessial soils. The water contents varied significantly as a function of ground conditions and local irrigation efforts. As shown in Figure A.11.2 (pre-failure cross-section) there was an unlined irrigation ditch present near the crest of the slope. This resulted in elevated water levels within the slope. Ishihara et al. (1990) discuss the likely pre-failure water levels, and also the likelihood that the phreatic surface changed after the failure.

Ishihara et al. also suggested that the depth of cracking in the loess plays a significant role in its saturation, and in the distribution of differing water contents. Ishihara et al. indicated that the depth of cracking in the loess extended to depths of approximately 15 to 25 m. They also estimated that the pre-failure phreatic surface was located at a depth of approximately 5 m. prior to the failure, but without specificity as to the lateral location to which this assessment corresponds. Ishihara et al. state that the water content increases from a value near to the Plastic Limit at the phreatic surface (at a depth of approximately 5 m.) to water contents higher than the Liquid Limit at depths of between 7 to 17 m. In this range (depth ≈ 7 to 17 m.) with a liquidity index greater than 100%, these silty materials would be expected to be prone to collapse and flow. At slightly greater depths of between approximately 15 to 20m., the permeability of the loess decreases by approximately 4 to 5 orders of magnitude, largely preventing infiltration of water. It is inferred that these deeper loess materials would also be significantly denser and stronger, and that they were not involved in the failure except for their influence on the overlying phreatic conditions.

A.11.3 Initial Yield Strength Analyses

Figure A.11.3(a) shows the cross-section used in these studies for the best estimate case back-analyses to determine the initial yield stress, defined as the best estimate value of post-liquefaction $S_{r,yield}$ within the liquefiable hydraulic fill required to produce a calculated Factor of Safety equal to 1.0 for pre-failure geometry).

Based on the post-failure cross-section, it is assumed that this failure initiated as a monolithic failure, with the collapsible loessial silts that had in situ water contents at or greater than their liquid limits liquefying with the short initial shaking. A key issue here with regard to back-calculated strengths is the location of the phreatic surface at and near to the toe of the failure. Figure A.11.3(a) shows the best estimate cross-section in this regard, and this detail was then varied as part of parameter sensitivity studies.

Silty loess materials above the phreatic surface were modeled with Ø′ ≈ 32°, and a unit weight of $\gamma_m \approx 105$ lbs/ft^3. Silty loess materials below the phreatic surface were considered to liquefy, down to the base of the failure surfaces analyzed, and were assigned an undrained post-liquefaction yield strength of $S_{r,yield}$ that was constant along any given failure surface, and a unit weight of $\gamma_s \approx 118$ lbs/ft^3. Results for the best estimate conditions shown in Figure A.12.3 were $S_{r,yield} = 580$ lbs/ft^2.

The location of the phreatic surface was reasonably well constrained at the top of the slope by the presence of the operating irrigation ditch at the head of the failure scarp. The

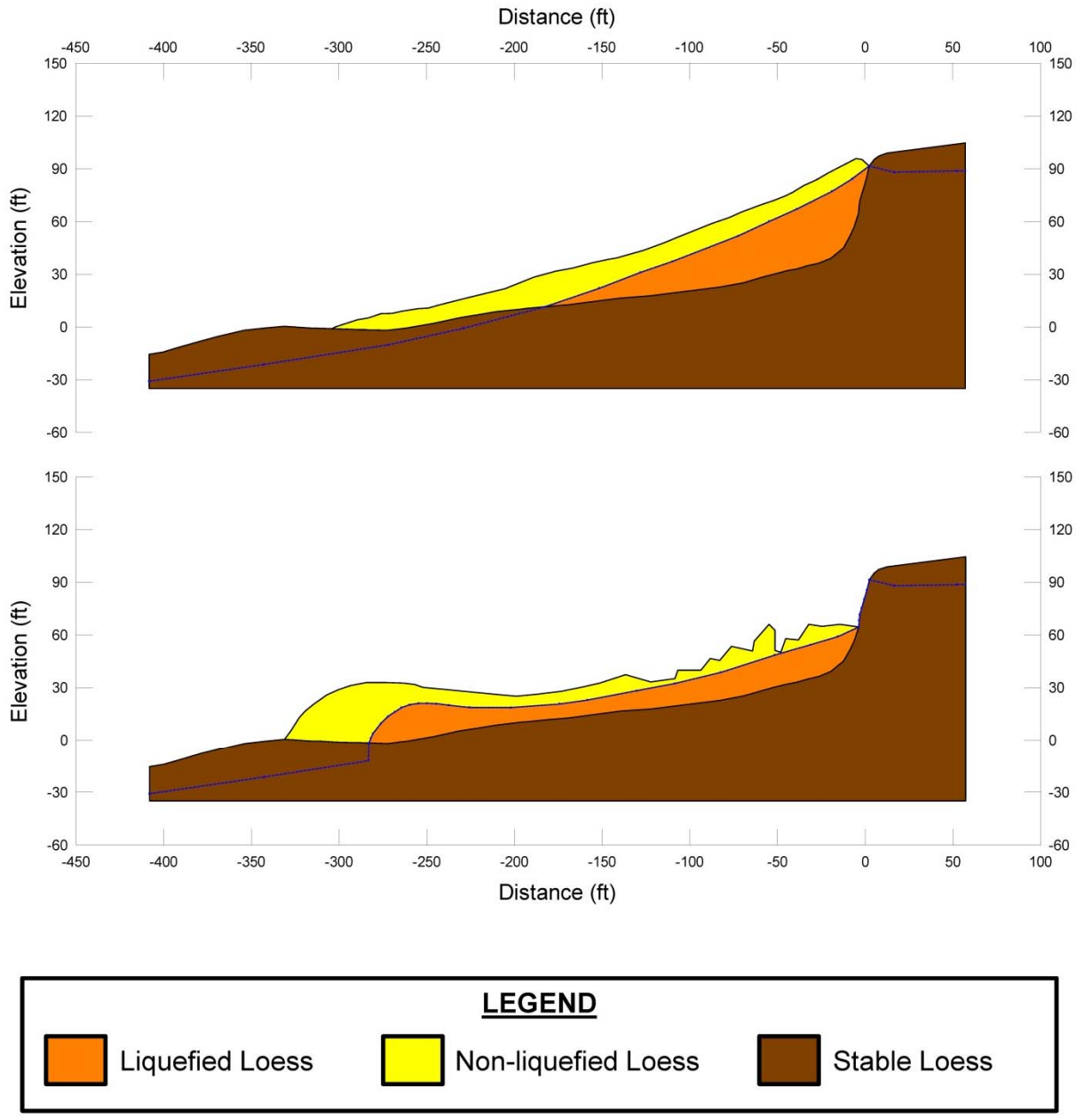

Figure A.11.3 Pre-failure geometry showing failure surfaces used for initial yield stress analyses, and (b) post-failure geometry and best-estimate failure surface for post-failure residual geometry analyses.

phreatic surface within the slope was considered to be approximately 5 m (16 ft) beneath the surface based on a general observation by Ishihara et al. (1990) of depth to ground water in the Gissar area. Due to the assumed location of the phreatic surface having a basis in only a general observation of the area, it was found that variations in the details of the phreatic surface at the toe of the slope, where a soil buttress formed during the failure, were a significant source of variance or uncertainty.

Parameters and geometry were then varied to examine parameter sensitivity. The phreatic surface was varied, raising it by up to 1.5 m (5 ft.) at about the mid-point of the failure surface, and lowering it by up to a similar distance. Lesser variations in the phreatic surface were applied at the back heel and at the toe. Unit weights were also varied over the ranges considered likely (+/- 5 pcf for the saturated loessial silts), and the friction angle of non-liquefied material above the phreatic surface was varied from 30° to 35°. Searches were made for the most critical initial failure surface for each combination of assumptions and parameters modeled. The resulting range of values of $S_{r,yield}$ for combinations of modeling assumptions and details considered to be reasonable was found to be $S_{r,yield} \approx 545$ to 613 lbs/ft^2.

Olson (2001) also performed back-analyses to determine $S_{r,yield}$. Failure surfaces analyzed were similar, but there were some differences in the details of modeling of the phreatic surface and the failure surface. Olson reported values of $S_{r,yield} \approx 30.4$ to 32.3 kPa (635 to 675 lbs/ft^2), with a best estimate value of 31.6 kPa (660 lbs/ft^2).

A.11.4 Residual Strength Analyses Based on Residual Geometry

The calculation of the "apparent" post-liquefaction strength ($S_{r,resid/geom}$) required to produce a calculated Factor of Safety equal to 1.0 based on residual geometry is illustrated in Figure A.11.3(b). This figure shows the phreatic surface, and the failure surface, used to calculate the best-estimate value of $S_{r,resid/geom} \approx 166$ lbs/ft^2.

Variations were then made in parameters and assumptions, as for the analyses of yield strength as described in the preceding Section A.11.3. Variations were made to all key parameters and to the locations of the post-failure phreatic surface (extrapolated through failure, but not including subsequent drainage and redistribution of pore pressures, and of the failure surface. Considering ranges of variations in modeling details and parameters judged to be reasonable, the resulting likely range of post-liquefaction strength required to provide a calculated Factor of Safety equal to 1.0 based on residual geometry was considered to be $S_{r,resid/geom} \approx 128$ to 206 lbs/ft^2.

Olson (2001) also calculated post-liquefaction strength required to produce a calculated Factor of Safety equal to 1.0 based on residual geometry, and reported a best estimate value of $S_{r,resid/geom} \approx 8.4$ kPa (175 lbs/ft^2), with a range of $S_{r,resid/geom} \approx 2.9$ to 15.6 kPa (61 to 326 lbs/ft^2).

A.11.5 Incremental Momentum Back-Analyses and Overall Estimates of S_r

Incremental inertial back-analyses were performed using the same sets of properties and geometries (including failure surfaces and phreatic surfaces) as described in the previous sections. Strengths at the toe were assumed to be controlled by the post-liquefaction strength Sr, as it was assumed that the underlying materials had higher strengths based on the post-failure geometry observed.

Figure A.11.4 shows the best-estimate progressive incremental inertial analysis, showing the 5 stages of geometry evolution modeled as the failure proceeds. Figure A.11.5 shows the associated calculations of (1) acceleration vs. time, (2) velocity vs. time, and (3) displacement vs. time of the overall center of gravity. For the geometry and phreatic surface shown in Figure A.11.4, the best estimate value of post-liquefaction strength was S_r = 341 lbs/ft^2.

The main sources of uncertainty, or variability, in back-calculated values of S_r were (1) the location of the phreatic surface, especially at and near the toe, (2) details of the failure surface near the toe, and (3) unit weights. Considering ranges of variations in modeling details and parameters judged to be reasonable, the resulting likely range of post-liquefaction strength was considered to be $S_r \approx$ 260 to 421 lbs/ft^2.

The analysis shown in Figures A.11.4 and A.11.5 neglects cyclic inertial forces, but this is not expected to significantly affect the assessment of actual post-liquefaction strength mobilized for this somewhat unusual case, because cyclic inertial forces appear to have been moderate to minimal during the actual failure movements.

Based on all analyses performed, and the considerations discussed herein, the overall best estimate value of post-liquefaction strength for the Soviet Tajik May 1 slope failure was judged to be $S_r \approx$ 341 lbs/ft^2, with a likely range of $S_r \approx$ 431 to 260 lbs/ft^2. Based on the factors contributing to uncertainty or variance for this case history, it was the judgment of the investigation team that this range represented approximately +/− 1.5 standard deviations. This range of variance is not symmetrical about the best estimate value, so minor further adjustments were made to produce a representative estimate of S_r suitable for regression analyses.

Overall, based on an assumed normal distribution, it was judged that the (mean and median) best estimate of post-liquefaction strength for this case history is

$$\overline{S_r} = 341 \text{ lbs/ft}^2$$

and that the best estimate of standard deviation of mean overall post-liquefaction strength is

$$\sigma_{\overline{S}} = 57 \text{ lbs/ft}^2$$

Estimates of S_r were also reported by several other investigation teams, and two sets of these are shown in Table A.11.1(a). Olson (2001) and Olson and Stark (2002), reported a best estimate value of S_r = 8.4 kPa (178 lbs/ft^2), but this was not based on their "kinetics" analyses that considered momentum effects. Instead, it was based on assessment of the post-liquefaction

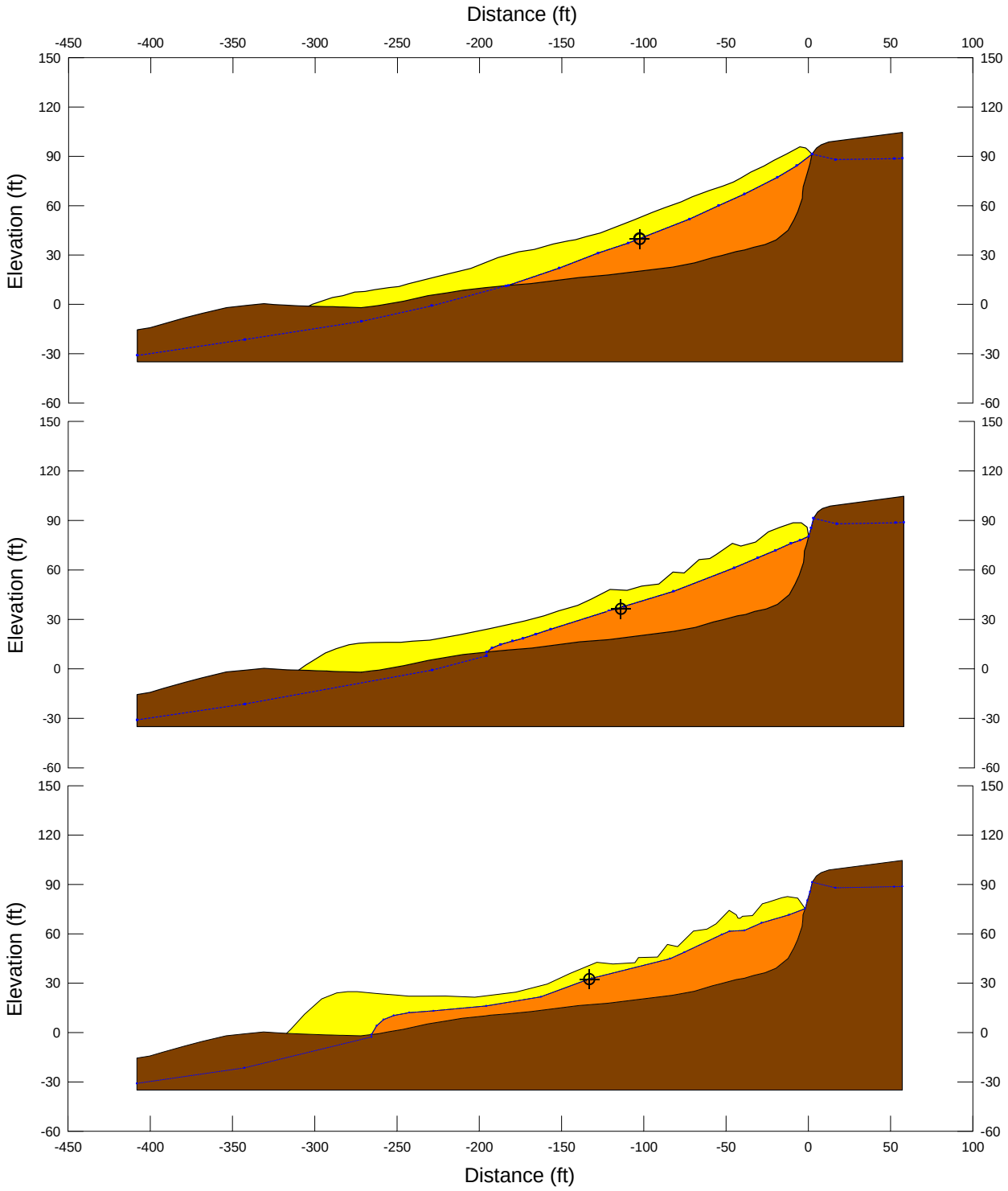

Figure A.11.4(a): Incremental inertial analysis of the failure of the Soviet Tajikistan slope failure, showing the progressive evolution of cross-section geometry modeled (first three cross-sections).

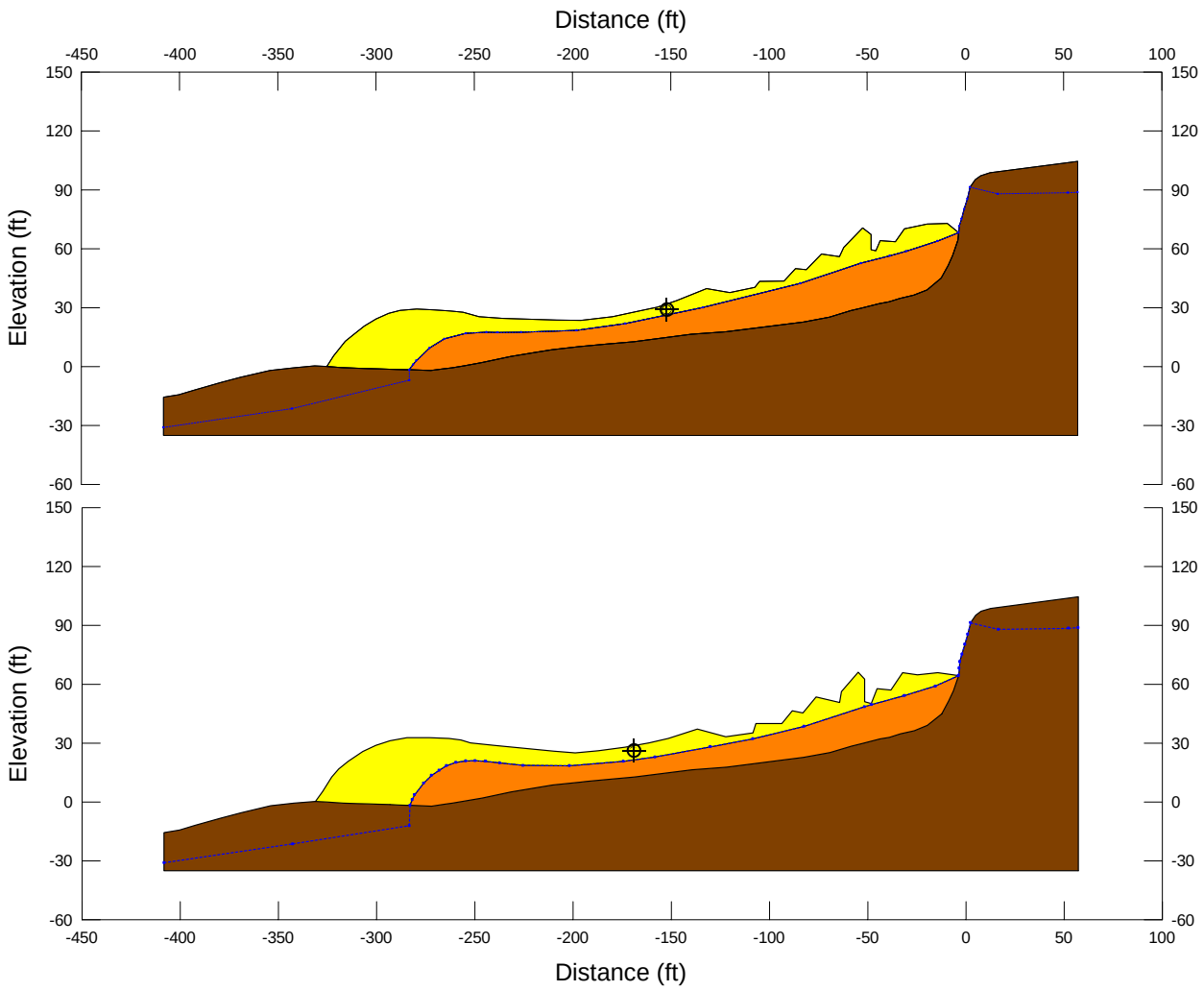

Figure A.11.4(b): Incremental inertial analysis of the failure of the Soviet Tajikistan slope failure, showing the progressive evolution of cross-section geometry modeled (final two cross-sections).

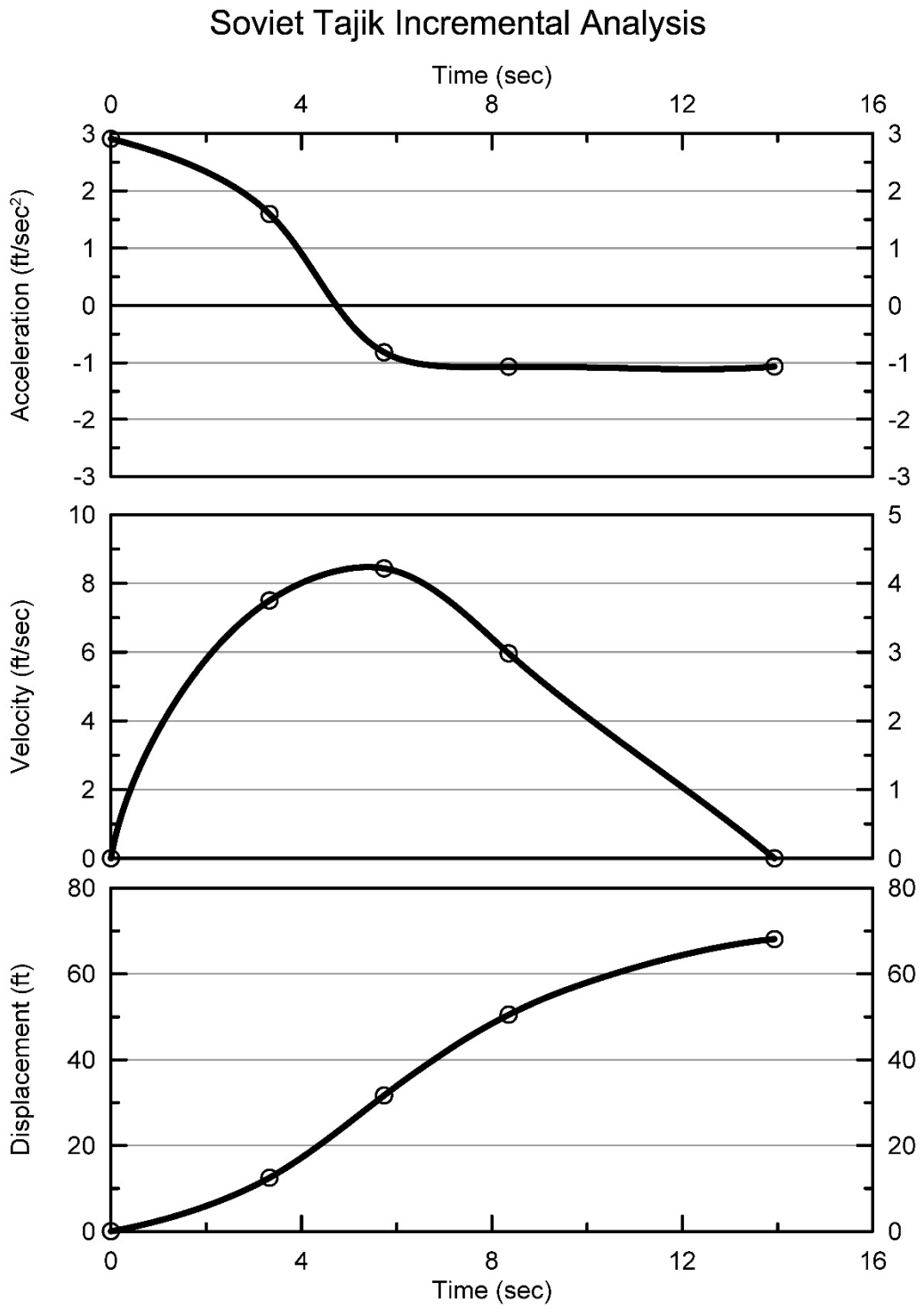

Figure A.11.5: Incremental inertial analysis of the failure of the Soviet Tajik slope failure, showing progressive evolution of: (1) acceleration vs. time, (2) velocity vs. time, and (3) displacement vs. time of the center of gravity of the overall failure mass.

residual geometry and it neglected momentum effects. As a result, it will be an overly conservative estimate (the value will be much too low). Olson also calculated $S_{r,yield}$ and $S_{r,resid/geom}$ (see Sections A.11.3 and A.11.4) for this case, however, and those two values can be convolved to provide a better estimate of S_r. Based on Equation 4-1, a better estimate for S_r can be developed based on the back-calculations of $S_{r,yield}$ and $S_{r,resid/geom}$ performed by Olson (2001) as $S_r \approx [S_{r,yield} + S_{r,resid/geom}] \times 0.8 \approx [31.6 \text{ kPa} + 8.4 \text{ kPa}] \times 0.8 \approx 16.0 \text{ kPa}$ (334 lbs/ft^2), and this value is more directly comparable with the values of this current study. Accordingly, the value listed in Table A.11.1 for Olson and Stark is $S_r \approx 334$ lbs/ft^2, and this agrees well with these current studies.

Wang (2003) and Wang and Kramer (2008) did not employ their zero inertial force (ZIF) method to incorporate inertial effects in their back-analyses of this failure; instead they developed their estimates of both mean $\overline{S_r} = 334$ lbs/ft^2 as well as the associated standard deviation $\sigma_{\overline{S}} = 111$ lbs/ft^2 based on evaluation and consideration of back-analyses performed by other teams of previous investigators. It is not possible to fully back-check these choices and judgments. What is remarkable, is the level of agreement between these three disparate teams of investigators, as the best estimate values of Sr for (1) Olson and Stark, (2) Wang and Kramer, and (3) these current studies are Sr = 334 lbs/ft^2, 334 lbs/ft^2 and 341 lbs/ft^2, respectively. Olson and Stark provide no range or estimate of variance. Wang and Kramer estimate that $\sigma_{\overline{S}} = 111$ lbs/ft^2, and the value developed in these current studies is $\sigma_{\overline{S}} = 57$ lbs/ft^2. Overall, agreement between the three investigation teams is excellent here.

A.11.6 Evaluation of Initial Effective Vertical Stress

Average initial (pre-failure) effective vertical stress was assessed for the liquefied zones of each of the initial failure surface shown in Figure A.11.4(a). The resulting best estimate of average pre-failure effective stress within the liquefied materials controlling the failure was then $\sigma_{vo}' \approx 1{,}907$ lbs/ft^2, with a reasonable range of $\sigma_{vo}' \approx 2{,}263$ to $1{,}555$ lbs/ft^2. This range is slightly non-symmetric about the median value, and this range was judged by the engineering team to represent approximately +/− 2 standard deviations. Overall, the best characterization of initial (pre-failure) average effective vertical stress was then taken to be represented by a mean value of

$$\overline{\sigma'_{vo}} \approx 1{,}907 \text{ lbs/ft}^2$$

and with a standard deviation of

$$\sigma_{\overline{\sigma}} \approx 177 \text{ lbs/ft}^2$$

Estimates of σ_{vo}' were also reported by other investigation teams, and two sets of these are shown in Table A.11.1(c). Olson (2001) calculated an average initial effective vertical stress of $\sigma_{vo}' = 106$ kPa (2,214 lbs/ft^2). Average initial vertical effective stresses were not directly reported by Wang (2003) and Kramer (2008), but they were published more recently in the publication by Kramer and Wang (2015). As discussed in Section 2.3.8.1(b)-(iii), Wang (2003)

did not perform any independent analyses to assess σ_{vo}' for his 22 "secondary" cases, and this is one of those cases. Instead, he compiled values of S_r from multiple previous investigators, and averaged these for a best estimate. He also compiled multiple values of S_r/σ_{vo}' from previous investigators, and averaged these for a best estimate. He then used these two best-estimate values of S_r and S_r/σ_{vo}' to infer a resulting representative value of σ_{vo}'. As described in Section 2.3.8.1(b)-(iii), the resulting averaged values of S_r and S_r/σ_{vo}' were incompatible with each other for a number of Wang's "secondary" case histories, and this process produced unreasonable, and in some cases physically infeasible, values of σ_{vo}' for a number of case histories. Accordingly, Wang's value of σ_{vo}' = 4,122 lbs/ft^2 is not considered a useful check here. Agreement between the values of (1) Olson and Stark (2001, 2002) and (2) these current studies is very good.

A.11.7 Evaluation of $N_{1,60,CS}$

Only very limited data and information was available as a basis for evaluation of representative penetration resistances for the silty loessial soils. As a result, this is a case history in which back-calculated values of S_r and σ_{vo}' are well constrained, but there is large uncertainty regarding $N_{1,60,CS}$.

No SPT data are available for this case history. Instead, a portable cone penetrometer was used to evaluate penetration resistance (Ishihara et al, 1990). The penetration tests were performed from the bottom of a crack in the post-slide failure zone, and extended downwards to the approximate depth of the apparent sliding surface. At that depth, the value of qc1 ranged from approximately 1.1 to 2.4 MPa. Olson (2001) selected a "representative" value of 1.9 MPa, and the current investigation team did the same. Using $q_{c1}/N_{1,60} \approx 2.5$, the current investigation team estimated $N_{1,60} \approx 7.6$ blows/ft. This was further adjusted for fines content (FC = 100%, all silt) as per Appendix C, Section C.1, to develop a best estimate value of $\overline{N_{1,60,CS}} \approx 10.5$ blows/ft. A significant range of uncertainty was then inferred due to (1) paucity of data, and (2) uncertainty regarding transformation of q_{c1} to $N_{1,60}$ for the portable CPT. Overall, the assessment of the current investigation team was that penetration resistance would be characterized as

$\overline{N_{1,60,CS}}$= 10.5 blows/ft, and $\sigma_{\overline{N}}$ = 2.7 blows/ft.

Values were also developed by other investigation teams, and two sets of these are presented in Table A.11.1(b). Olson and Stark (2001, 2002) employed values of $N_{1,60}$ = 7.6 blows/ft, with a range of 4.4 to 9.6 blows/ft. Wang and Kramer (2003, 2008) selected values of $\overline{N_{1,60,CS}}$ = 8.9 blows/ft, and $\sigma_{\overline{N}}$ = 5.7 blows/ft. The value of Olson and Stark is somewhat lower than those of (1) Wang and Kramer, and (2) these current studies because Olson and Stark did not make a fines adjustment, so theirs is an $N_{1,60}$ value rather than an $N_{1,60,CS}$ value. Given that the loessial soils of interest here are entirely silts, the fines adjustment by any recent approach would raise their value to an $N_{1,60,CS}$ value equal to or higher than those of (1) Wang and Kramer, or (2) these current studies. Overall, agreement between the three investigation teams is very good here.

A.11.8 Additional Indices from the Back-Analyses

A number of additional results, and indices, can be extracted from the analyses performed. Some of these are useful in developing some of the over-arching relationships and figures presented in the main text of this report. These values are presented in Table A.11.2.

Table A.11.1: Representative values for the Soviet Tajik May 1 slope failure case history of: (a) post-liquefaction strength (S_r), (b) initial vertical effective stress (σ_{vo}'), and (c) $N_{1,60,CS}$ developed by various investigation teams, and estimates of variance in each of these indices when available.

(a) Post-Liquefaction Strength:	
Olson (2001) and Olson and Stark (2002)*	$S_r \approx 334$ psf*
Wang (2003) and Kramer (2008)	$\overline{S_r} = 334$ psf, and $\sigma_{\overline{S}} = 111$ psf
This Study	$\overline{S_r} = 341$ psf and $\sigma_{\overline{S}} = 57$ psf
(b) Representative $N_{1,60}$ or $N_{1,60,CS}$ Value:	
Olson (2001) and Olson and Stark (2002)	$N_{1,60} = 7.6$ bpf, and range = 4.4 to 9.6 bpf
Wang (2003) and Kramer (2008)	$\overline{N_{1,60,CS}} = 8.9$ bpf, and $\sigma_{\overline{N}} = 5.7$ bpf
This Study	$\overline{N_{1,60,CS}} = 10.5$ bpf, and $\sigma_{\overline{N}} = 2.7$ bpf
(c) Representative Initial Vertical Effective Stress:	
Olson (2001) and Olson and Stark (2002)	$\sigma'_{vo} = 2{,}270$ psf, with no range given.
Wang (2003) and Kramer (2008)	Value of $\sigma_{vo}' \approx 4{,}122$ psf is poorly based, and so is not useful as a basis for comparison. (See Section 2.3.8.1(b) and Table 2.3)
This Study	$\overline{\sigma'_{vo}} = 1{,}907$ psf, and $\sigma_{\overline{\sigma}} = 177$ psf

* Olson (2001) did not employ his "kinetics" back-analysis approach to this case. See the text of Section A.11.5 for an explanation of the value and so his residual geometry based value of Sr ≈ 334 psf attributed here.

Table A.11.2: Additional results and indices from the analyses of the Soviet Tajik May 1 Slope failure case history.

Maximum distance traveled by the center of gravity of the overall failure mass	68.1 ft.
Initial post-liquefaction Factor of Safety prior to displacement initiation, and based on best estimate value of S_r	FS = 0.60
Final post-liquefaction Factor of Safety at final (residual) post-failure geometry, and based on best estimate value of S_r	FS = 1.45

A.12 Shibecha-Cho Embankment (Hokkaido, Japan; 1993)

A.12.1 Brief Summary of Case History Characteristics

Name of Structure	Shibecha-Cho Embankment
Location of Structure	Hokkaido, Japan
Type of Structure	Side Hill Structural Fill Pad
Date of Failure	September 22, 1933
Nature of Failure	Seismic, During the 1993 Kushiro-Oki Earthquake (M_L = 7.8)
Approx. Maximum Slope Height	33.7 ft.

A.12.2 Introduction and Description of Failure

The Shibecha-Cho Embankment failed during Kushiro-Oki Earthquake of January 15, 1993 (M_L = 7.8), and was initially investigated by Miura et al. (1995, 1998). Miura et al. estimated that the peak ground acceleration at this site was approximately 0.38 g.

Figure A.12.1 shows a plan view of the large embankment fill, and the resort development which was developed atop this fill platform. The embankment was constructed of fill taken from cut and fill operations on the adjacent slopes. Figure A.12.1 shows the locations in plan view of four cross-sections developed with pre-failure and post-failure geometries, and Figure A.12.2 shows these four cross-sections. Movements were only minor to moderate at cross-sections A, C and D, and it was judged here that these cross-sections were not suitable for the types of back-analyses performed in these current studies to evaluate post-liquefaction strengths because the scales of these movements could likely be explained to some significant degree by cyclic lurching displacements, so that accurate calculation of fully developed post-liquefaction S_r would be difficult. Cross-section B, on the other hand, experienced a flow-type of failure with large displacements, and it is this cross-section that will be analyzed here.

Post-failure geotechnical investigation was performed mainly by means of Swedish cone soundings, and the locations of these soundings are shown in Figure A.12.2 (from Miura et al., 1995). These soundings reasonably well constrain the key ground conditions at the base of the failure, especially beneath the main body of the failure zone and at the rear heel, as there is a relatively distinct increase in penetration resistance at the interface between the base of the fill and the "harder" underlying native soils. Figures A.12.3(a) and A.12.3(b) show the interpretations of cross-section geometry and stratigraphy for the pre-failure and post-failure cross-section at cross-section B made by Olson (2001). These are reasonable interpretations, and the topographic and stratigraphic interpretations employed in these current studies were in good agreement with these interpretations of Olson for the "best estimate" analyses performed here, although some alternate modeling of additional potential failure surfaces was performed for these current studies.

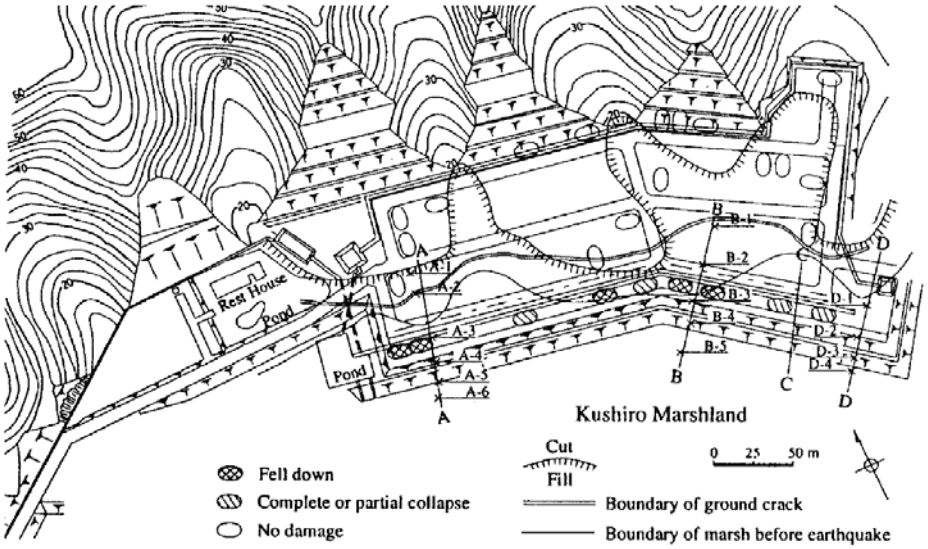

Figure A.12.1: Plan view of the Shibecha-Cho Embankment fill and the resort development atop the fill, showing the locations of four post-failure cross-sections (from Miura et al., 1998)

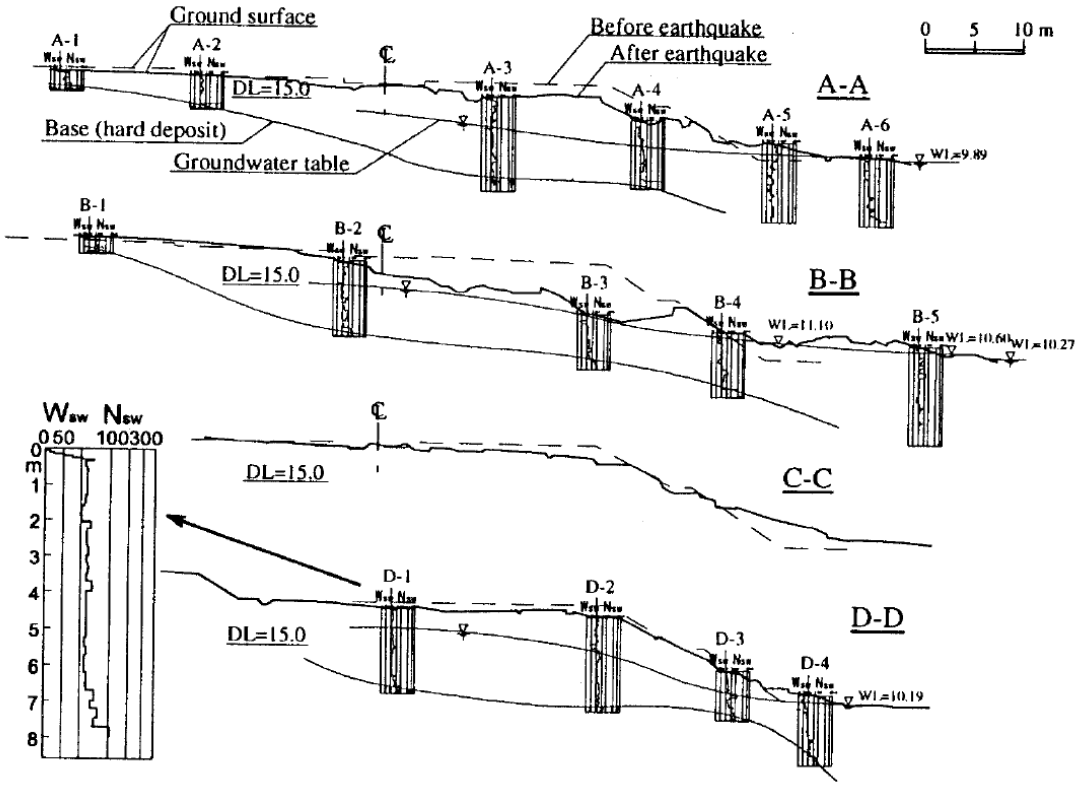

Figure A.12.2: Cross-sections A-A, B-B, C-C and D-D from Figure A.12.1 above (from Miura et al, 1998)

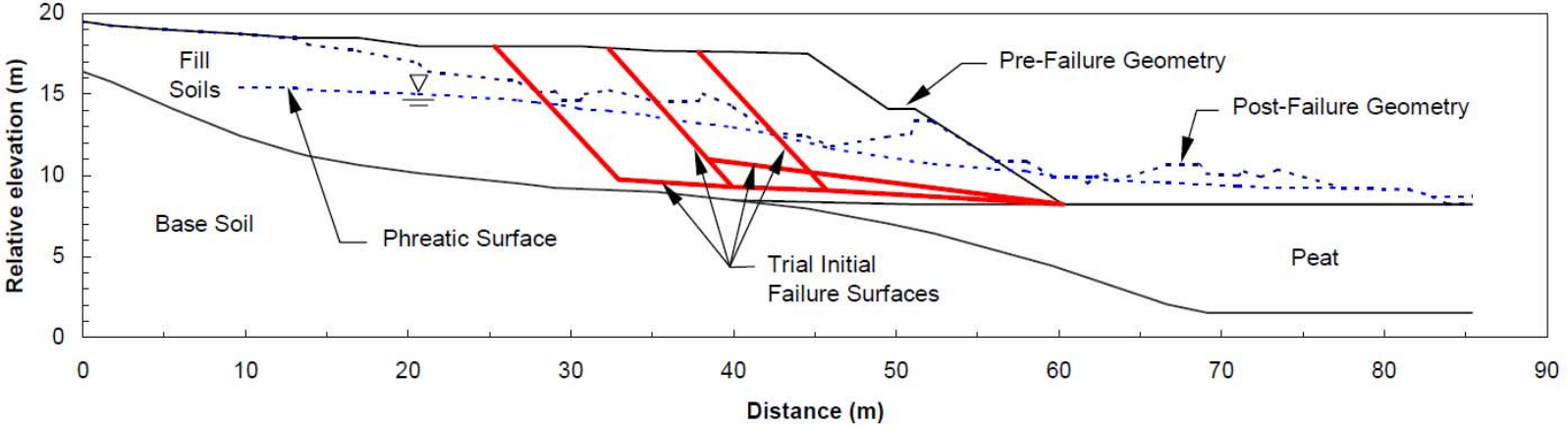

Figure A.12.3(a): Pre-failure geometry of the Shibecha-Cho Embankment showing failure surfaces used by Olson (2001) for calculation of post-liquefaction initial yield strength $S_{r,yield}$ (Figure from Olson, 2001).

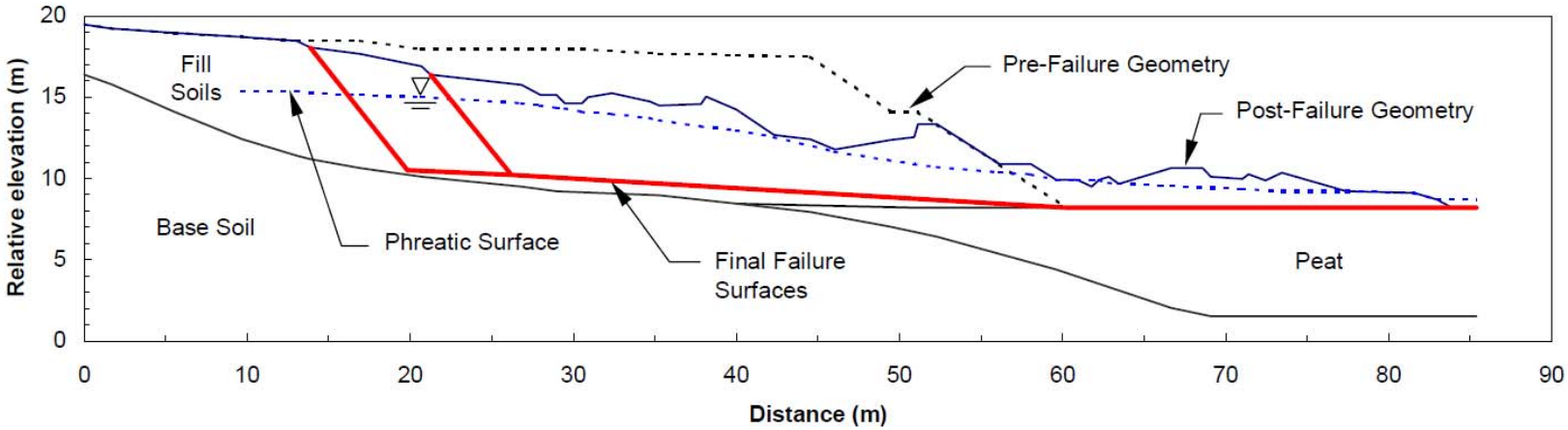

Figure A.12.3(b): Pre-failure geometry of the Shibecha-Cho Embankment showing failure surfaces used by Olson (2001) for calculation of post-liquefaction initial yield strength $S_{r,resid/geom}$ (Figure from Olson, 2001).

The embankment fill was comprised of the same volcanic silty sand ash deposits as the adjacent and underlying materials comprising the natural hills. This material had a fines content that varied between approximately 12% to 33%, with a representative value of approximately 20% (Yasuda et al, 1993; Saito et al., 1993 and Mori, 1993), but some of these gradations are taken from sampled boil ejecta and may have segregated somewhat during transport and ejection. The embankment fill was placed without formal, controlled engineering compaction and so was only lightly and variably compacted by random construction traffic.

As shown in Figure A.12.3(a), a unit of peaty marsh deposits (the adjacent Kushiro Marshland) occurs beneath the toe of the pre-failure embankment, and this peat extends farther out from the toe. An uncertainty in performing of back-analyses of this case history is whether or not the failure extended into the peaty marsh deposits beneath the embankment toe, and also as the toe of the embankment translated outwards further onto the peats during the failure. Lack of reported upwards bulging beyond the toe suggests that the failure did not extend into the peaty deposits at the toe. But there are other possibilities, and this will be discussed further.

Another uncertainty is the location of the phreatic surface at the time of the failure.

A.12.3 Initial Yield Strength Analyses

Figure A.12.4(a) shows the cross-section used in these studies for the best estimate case back-analyses to determine the initial yield stress, defined as the best estimate value of post-liquefaction $S_{r,yield}$ within the liquefiable hydraulic fill required to produce a calculated Factor of Safety equal to 1.0 for pre-failure geometry).

It is not known whether this failure initiated as a monolithic failure, or as an incrementally progressive failure that retrogressed towards the back heel in progressive slices. Based on an assumed phreatic surface that passes approximately through the mid-height of the slope, and exits at the toe, a search was made for the most critical static failure surface assuming liquefaction had been "triggered" in all potentially liquefiable embankment materials below the phreatic surface. This exercise showed that the most critical potential failure surfaces for this set of assumptions would have been for a failure initially closer to the slope face than the final rear scarp shown in Figure A.12.1.

Figure A.12.4(a) shows two potential failure surfaces analyzed. The rear-most surface is the eventual "final" underlying (or bounding) failure surface, which is reasonably well constrained by the data available. The other failure surface is the surface that was found to be a more critical initial yield surface (requiring a higher value of post-liquefaction yield strength in order to produce a calculated static Factor of Safety = 1.0). Silty sand embankment fill materials above the phreatic surface were modeled with $Ø' \approx 35°$, and a unit weight of $\gamma_m \approx 90$ lbs/ft^3. Materials below the phreatic surface were considered to liquefy, down to the base of the failure surfaces analyzed, and were assigned an undrained post-liquefaction yield strength of $S_{r,yield}$ that was constant along any given failure surface, and a unit weight of $\gamma_s \approx 95$ lbs/ft^3. Results for the most critical initial yield surface (near to the front face of the embankment) were $S_{r,yield} = 415$ lbs/ft^2.

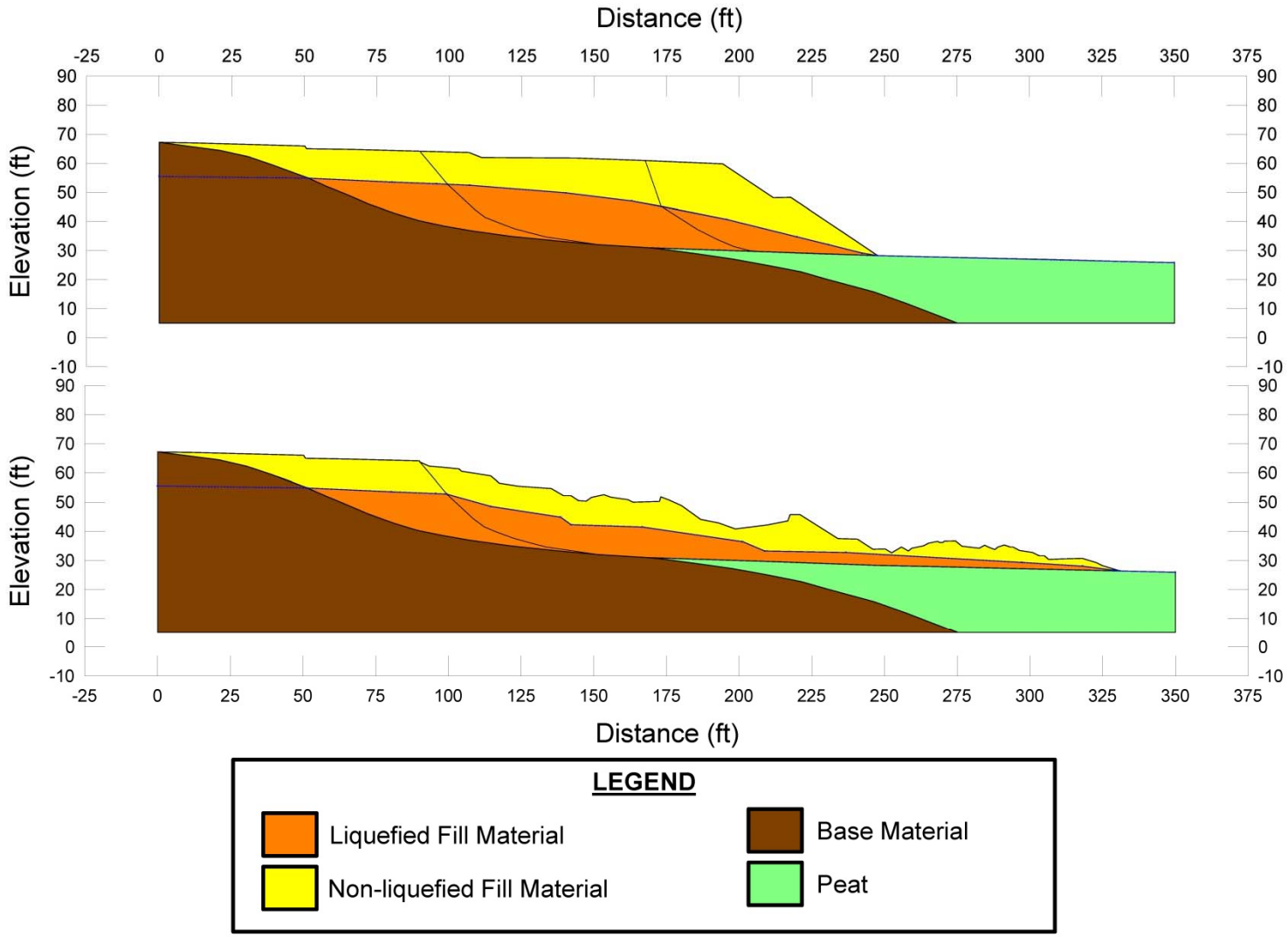

Figure A.12.4(a): Shibecha-Cho Embankment: Pre-failure geometry showing failure surfaces used for initial yield stress analyses, and (b) post-failure geometry and best-estimate failure surface for post-failure residual geometry analyses.

Parameters and geometry were then varied to examine potentially variability. The location of the phreatic surface was varied, raising it by up to 1.5 m (5 ft.) at the back heel of the final failure surface, and lowering it by up to a similar distance. The phreatic surface was considered to exit at or near the toe of the slope, based on the observed failure (and post-failure geometry), while the location of the phreatic surface within the embankment was varied. Unit weights were also varied over the ranges considered likely, and the friction angle of non-liquefied material above the phreatic surface was varied from 30° to 37°. Searches were made for the most critical initial failure surface for each combination of assumptions and parameters modeled. The resulting range of values of $S_{r,yield}$ for combinations of modeling assumptions and details considered to be reasonable was found to be $S_{r,yield} \approx 367$ to 467 lbs/ft^2.

Olson (2001) also performed back-analyses to determine $S_{r,yield}$. Failure surfaces analyzed were similar, but did not appear to include surfaces extending fully back to the rear heel of the eventual "final" yield surface for the evaluation of $S_{r,\,yield}$. Olson reported values of $S_{r,yield} \approx 14.8$ to 18.7 kPa (309 to 391 lbs/ft^2).

A.12.4 Residual Strength Analyses Based on Residual Geometry

The calculation of the "apparent" post-liquefaction strength ($S_{r,resid/geom}$) required to produce a calculated Factor of Safety equal to 1.0 based on residual geometry is illustrated in Figure A.12.4(b). This figure shows the phreatic surface, and the failure surface, used to calculate the best-estimate value of $S_{r,resid/geom} \approx 147$ lbs/ft^2. Variations were then made in parameters. One key parameter being the strength in the underlying peaty marsh deposits outside the toe. Strength outside the toe was varied, with the minimum toe strength assumption being that shear strength within the underlying peaty marsh deposits was less than that of the liquefied embankment fill, and a minimum shear strength of 50% of that of the calculated initial yield strength of the overlying embankment fill was employed. This case was judged to be of low likelihood, however, based on the lack of (a) observed compression wrinkles in the peaty marsh deposits just beyond the toe, and (b) lack of vertical heave in this same area. The upper bound toe strength condition assumed at the base of the toe section was the full post-liquefaction strength (S_r) of the liquefied embankment fill, and this was also the best estimate case. Variations were also made to other parameters and to the location of the pre-failure phreatic surface, as was described in the preceding section in order to evaluate uncertainty or variability, except that all analyses assumed that the failure surface defining the boundaries of the eventual full failure mass controlled $S_{r,resid/geom}$. Considering ranges of variations in modeling details and parameters considered to be reasonable, the resulting likely range of post-liquefaction strength required to provide a calculated Factor of Safety equal to 1.0 based on residual geometry was considered to be $S_{r,resid/geom} \approx 126$ to 172 lbs/ft^2.

Olson (2001) also calculated post-liquefaction strength required to produce a calculated Factor of Safety equal to 1.0 based on residual geometry, and reported a best estimate value of $S_{r,resid/geom} \approx 5.0$ kPa (104 lbs/ft^2), with a range of $S_{r,resid/geom} \approx 4.1$ to 6.2 kPa (86 to 130lbs/ft^2).

A.12.5 Incremental Momentum Back-Analyses and Overall Estimates of S_r

Incremental inertial back-analyses were performed using the same sets of properties and geometries (including failure surfaces and phreatic surfaces) as described in the previous sections. Strengths at the toe, both beneath the original embankment toe, and beneath the toe section as it translated outwards over the peaty marsh deposits, were modeled as 100% of S_r for the liquefiable embankment fill for the case illustrated in Figures A.12.5 and A.12.6.

Figure A.12.5 shows the best-estimate progressive incremental inertial analysis, showing the 5 stages of geometry evolution modeled as the failure proceeds. Figure A.12.6 shows the associated calculations of (1) acceleration vs. time, (2) velocity vs. time, and (3) displacement of the overall center of gravity vs. time. For the geometry and phreatic surface shown in Figure A.13.3, the best estimate value of post-liquefaction strength was $S_r = 224$ lbs/ft^2.

Based on the initial yield strength analyses described previously, and the observed pre- and post-failure field geometry, failure was modeled as proceeding in a progressive series of slices retrogressing back towards the back heel. This required some judicious juggling of progressively changing overall failure surface mass, momentum and velocity as successive slices began to join in the failure. The incremental inertial analyses for this case history are a bit more approximate than for most other cases as a result.

The main sources of uncertainty, or variability, in back-calculated values of S_r were (1) the location of the phreatic surface, (2) whether or not the failure initiated largely monolithically or retrogressed progressively towards the back heel in a series of "slices", and the discretization and timing of successive slice initiation, (3) unit weights, (4) whether the failure surface at and near the toe the ran along within the base of the liquefiable embankment fill or passed into the underling peaty marsh deposits, and (5) the precise location of the overall failure surface.

The analysis shown in Figures A.12.5 and A.12.6 neglects cyclic inertial forces, and so may represent a slightly conservative assessment of actual post-liquefaction strength mobilized, but this minor conservatism was neglected.

Based on all analyses performed, and the considerations discussed herein, the overall best estimate value of post-liquefaction strength for the Shibecha-Cho Embankment failure was judged to be $S_r \approx 224$ lbs/ft^2, with a likely range of $S_r \approx 166$ to 277 lbs/ft^2. Based on the factors contributing to uncertainty or variance for this case history, it was the judgment of the investigation team that this range represented approximately +/− 1.5 standard deviations. This range of variance is not symmetrical about the best estimate value, so minor further adjustments were made to produce a representative estimate of S_r suitable for regression analyses.

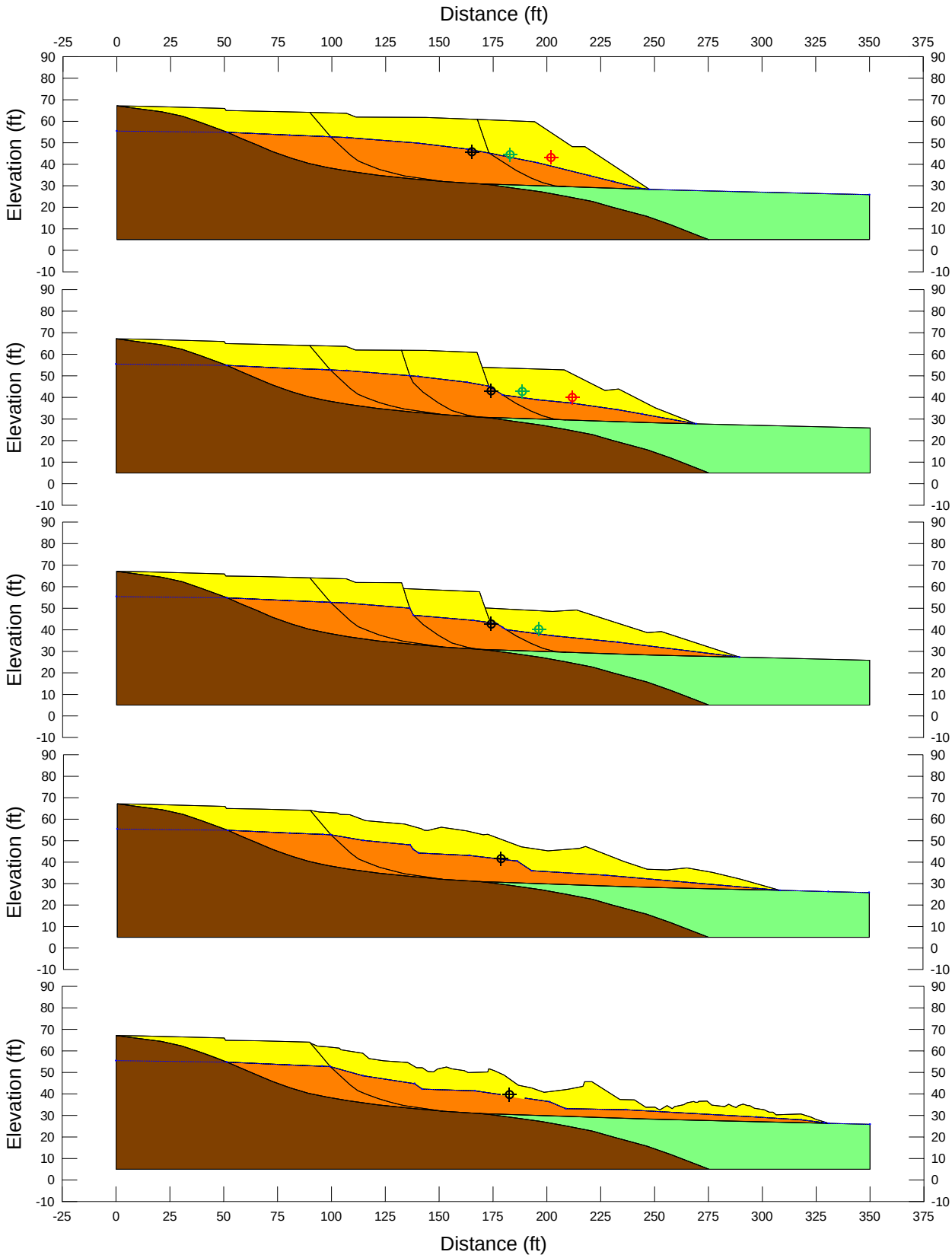

Figure A.12.5: Incremental inertial analysis of the failure of the Shibecha-Cho Embankment, showing progressive evolution of cross-section geometry modeled

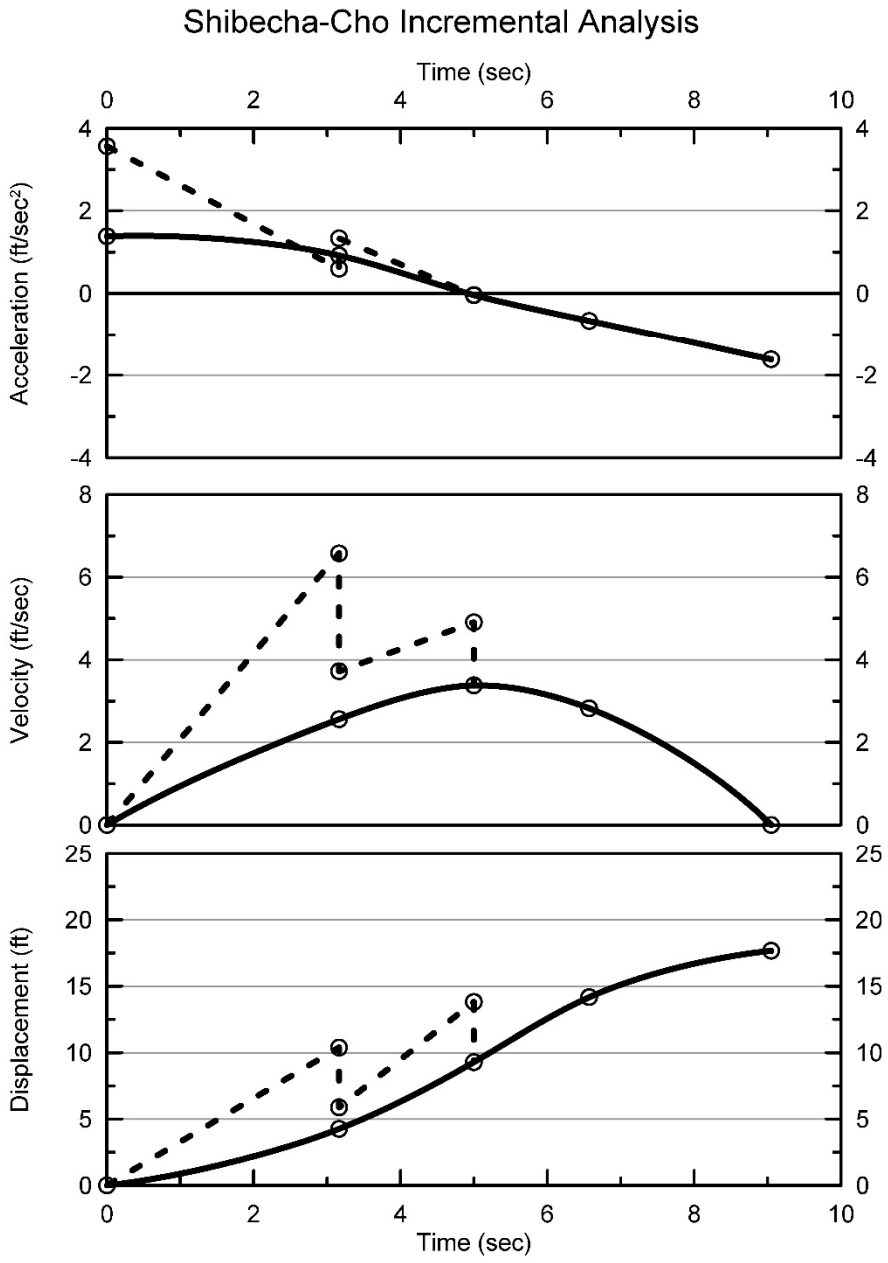

Figure A.12.6: Incremental inertial analysis of the failure of the Shibecha-Cho Embank--ment, showing progressive evolution of: (1) acceleration vs. time, (2) velocity vs. time, and (3) displacement vs. time of the overall center of gravity of the failure mass

Overall, based on an assumed normal distribution, it was judged that the (mean and median) best estimate of post-liquefaction strength for this case history is

$$\overline{S_r} = 224 \text{ lbs/ft}^2$$

and that the best estimate of standard deviation of mean overall post-liquefaction strength is

$$\sigma_{\overline{S}} = 37 \text{ lbs/ft}^2$$

Estimates of S_r were also reported by several other investigation teams, and these are shown in Table A.13.1(a). Olson (2001), and Olson and Stark (2002), reported a best estimate value of S_r = 5.6 kPa (117 lbs/ft^2), based on their inertial displacement analyses that considered kinetics, and a range of S_r = 3.9 to 8.3 kPa (81 to 174 lbs/ft^2). Their kinetics analysis, however, only tracked the movements of the centroid of a failure mass corresponding to a smaller "initial" toe failure, rather than the overall eventual failure mass. It appears that this resulted in a conservative underestimate of S_r. Wang (2003) and Wang and Kramer (2008) employed their zero inertial force (ZIF) method to incorporate inertial effects in their back-analyses of this failure, and they also developed estimates of both mean $\overline{S_r}$ = 208.9 lbs/ft^2 as well as the associated standard deviation $\sigma_{\overline{S}}$ = 38.6 lbs/ft^2. The details of these analyses, and the cross-sections and failure mass assumptions employed, are not presented and so cannot be checked. But this is yet another case history in which the "ZIF" calculations of Wang (2003), which account for inertial effects, produced S_r values in very good agreement with the results of these current studies.

A.12.6 Evaluation of Initial Effective Vertical Stress

Average initial (pre-failure) effective vertical stress was assessed for the liquefied zones of each of the two failure surfaces shown in Figure A.12.4(a). The best estimate of the overall average initial vertical effective stress was then taken as the average of these two averages. Reasonable variations were then made in (1) the location of the phreatic surface, (2) unit weights, and (3) the precise location of the overall failure surface.

The resulting best estimate of average pre-failure effective stress within the liquefied materials controlling the failure was then $\sigma_{vo}' \approx$ 1,416 lbs/ft^2, with a reasonable range of $\sigma_{vo}' \approx$ 1,234 to 1,614 lbs/ft^2. This range is slightly non-symmetric about the median value, and this range was judged by the engineering team to represent approximately +/− 2 standard deviations. Overall, the best characterization of initial (pre-failure) average effective vertical stress was then taken to be represented by a mean value of

$$\overline{\sigma'_{vo}} \approx 1{,}416 \text{ lbs/ft}^2$$

and with a standard deviation of

$$\sigma_{\overline{\sigma}} \approx 95 \text{ lbs/ft}^2$$

Estimates of σ_{vo}' were also reported by other investigation teams, and two sets of these are shown in Table A.12.1(c). Olson (2001) and Olson and Stark (2002) reported a value of $\overline{\sigma'_{vo}}$ = 1,351 lbs/ft^2, in good agreement with these current studies. Average initial vertical effective stresses were not directly reported by Wang (2003) and Kramer (2008), but they were published more recently in the publication by Kramer and Wang (2015). As discussed in Section 2.3.8.1(a), the approach taken by Wang (2003) to evaluation of σ_{vo}' for his nine "primary" case histories (this is one of those nine) is not clearly explained, and it is also poorly documented. Wang's value of σ_{vo}' = 1,048 lbs/ft^2 is somewhat lower than the values of Olson (2001) and these current studies, but this is not considered a very rigorous check here. Wang (2003) presents no detailed cross-section for his analyses, so it is not possible to know why his estimated value of σ_{vo}' is lower than the values calculated (1) by Olson (2001) and (2) in these current studies.

A.12.7 Evaluation of $N_{1,60,CS}$

As only Swedish cone data were performed within the liquefiable embankment fill materials. Conversion of these to equivalent SPT N-values was made using the relationship recommended by Ishihara et al. (1990). There is considerable uncertainty in this relationship, and this is a significant contributor to uncertainty or variability with respect to the median $\overline{N_{1,60,CS}}$ value representative of this material. Corrections for effective overburden stress (C_N) were made using the relationships proposed by Deger (2014), as presented and discussed in Section C.1.1. Corrections for fines content were made using the relationship propose by Cetin et al. (2004), and a representative fines content of approximately 20%. The resulting best estimate median $N_{1,60,CS}$ value for these current studies is $\overline{N_{1,60,CS}} \approx 7.5$ blows/ft. Variance of $\overline{N_{1,60,CS}}$ was estimated primarily on the basis of the perceived uncertainty associated with conversion for Swedish cone penetration resistances to equivalent SPT penetration resistances, and was taken as being represented by a standard deviation of $\sigma_{\overline{N}} \approx 1.7$ blows/ft.

Table A.12.1(b) shows values of representative $N_{1,60}$ or $N_{1,60,CS}$ values developed by two other teams of investigators, and variance or standard deviations in these representative values. Olson and Stark (2001, 2002) developed an estimated representative value of $N_{1,60}$ = 5.6 blows/ft, and an estimated range of representative values of $N_{1,60} \approx 2.9$ to 10.7 blows/ft, but did not quantify variance or standard deviation in probabilistic terms. This value is a bit lower than the $N_{1,60,CS}$ value from these current studies because it is uncorrected for fines, and so is not an $N_{1,60,CS}$ value. If a similar fines correction were to be made, the resulting $N_{1,60,CS}$ value of Olson and Stark would be in closer agreement with these current studies. Wang (2003) and Kramer (2008) jointly developed a representative value of $\overline{N_{1,60,CS}}$ = 5.6 blows/ft, and their estimated standard deviation of that overall mean value for this case history was $\sigma_{\overline{N}}$ = 2.2 blows/ft. Details of the development of this interpretation by Wang and Kramer are not presented, so it is not known why their $N_{1,60,CS}$(Bar) value is a bit lower than the corresponding value developed in these current studies. As relationships between $N_{1,60,CS}$ and S_r have relatively low slopes, this difference is relatively modest with regard to impact on subsequent development of SPT-based predictive relationships for evaluation of S_r.

A.12.8 Additional Indices from the Back-Analyses

A number of additional results, and indices, can be extracted from the analyses performed. Some of these are useful in developing some of the over-arching relationships and figures presented in the main text of this report. These values are presented in Table A.12.2.

Table A.12.1: Representative values for the Shibecha-Cho Embankment case history of: (a) post-liquefaction strength (S_r), (b) initial vertical effective stress (σ_{vo}'), and (c) $N_{1,60,CS}$ developed by various investigation teams, and estimates of variance in each of these indices when available.

(a) Post-Liquefaction Strength:	
Olson (2001) and Olson and Stark (2002)	S_r = 117 psf, and range = 81 to 174 psf
Wang (2003) and Kramer (2008)	$\overline{S_r}$ = 208.9 psf, and $\sigma_{\bar{S}}$ = 38.6 psf
This Study	$\overline{S_r}$ = 214 psf and $\sigma_{\bar{S}}$ = 37 psf
(b) Representative $N_{1,60}$ or $N_{1,60,CS}$ Value:	
Olson (2001) and Olson and Stark (2002)	$N_{1,60}$ = 6.3 bpf, and range = 2.4 to 10.0 bpf
Wang (2003) and Kramer (2008)	$\overline{N_{1,60,CS}}$ = 8.5 bpf, and $\sigma_{\bar{N}}$ = 2.6 bpf
This Study	$\overline{N_{1,60,CS}}$ = 8.1 bpf, and $\sigma_{\bar{N}}$ = 1.6 bpf
(c) Representative Initial Vertical Effective Stress:	
Olson (2001) and Olson and Stark (2002)	σ'_{vo} = 1,351 psf, likely range is not provided.
Wang (2003) and Kramer (2008)	Value of $\sigma_{vo}' \approx$ 2,558 psf is poorly documented, and so is considered useful only as an approximate comparison. (See Section 2.3.8.1, and Table 2.3.)
This Study	$\overline{\sigma'_{vo}}$ = 1,285 psf, and $\sigma_{\bar{\sigma}}$ = 104 psf

Table A.12.2: Additional results and indices from the analyses of the Shibecha-Cho Embankment failure case history.

Maximum distance traveled by the center of gravity of the overall failure mass	17.9 ft.
Initial post-liquefaction Factor of Safety prior to displacement initiation, and based on best estimate value of S_r	FS = 0.79
Final post-liquefaction Factor of Safety at final (residual) post-failure geometry, and based on best estimate value of S_r	FS = 1.36

A.13 Route 272 Embankment (Higashiarekinai, Japan; 1993)

A.13.1 Brief Summary of Case History Characteristics

Name of Structure	Route 272 Embankment
Location of Structure	Higashiarekinai, Japan
Type of Structure	Sidehill Highway Embankment
Date of Failure	September 22, 1933
Nature of Failure	Seismic, During 1993 Kushiro-Oki Earthquake (M_L = 7.8)
Approx. Maximum Slope Height	26 ft.

A.13.2 Introduction and Description of Failure

The Route 272 Highway Embankment failed during Kushiro-Oki Earthquake of January 15, 1993 (M_L = 7.8), and was investigated by Sasaki et al. (1994). Sasaki et al. developed an event-specific acceleration attenuation relationship for the Kushiro-Oki Earthquake, and estimated that the peak ground acceleration at this site was approximately 0.38 g.

Figure A.13.1 shows a cross-section through the failure. The highway embankment was a sidehill fill underlain by pumice bearing volcanic sands and silts, and by partially pumice tuff.

After the failure, two SPT borings were performed and these are shown in Figure A.13.1 (from Sasaki et al., 1994). These two borings reasonably well constrain the key ground conditions at the base of the failure. Construction details are not reported, and it is assumed that the sandy fill was locally sourced, and that it received minimal compaction effort. This embankment is not far from the Shibecha-Cho Embankment discussed previously in Section A.12, and fill material is assumed to have been locally available volcanic sands and silty sands.

Close inspection of the two borings shown in Figure A.13.1 shows that the transition from fill to underlying native soils appears to be relatively clearly demarcated by a transition from very low SPT blowcounts within the fill to slightly higher penetration resistances in the immediately underlying pumice bearing volcanic sand. The back heel of the final failure surface is also well constrained. As a result, the approximate location of the overall bounding failure surface is relatively well constrained for this case by the clear heel scarp, and by the transition to firmer materials at the base of the liquefiable fill. The location of the phreatic surface at the time of the earthquake was not so well constrained, but potential variability with regard to location of the phreatic surface was at least reasonably bounded.

A difficulty encountered in performing back-analyses of this failure is that the post-failure volume of the failed slope materials shown in Figure A.13.1 is approximately 27% larger than the pre-failure volume. This is accommodated in the back-analyses that follow, and it is found that this volume discrepancy has only a moderate effect on uncertainty, or variance, in back-calculated post-liquefaction strengths for this case history.

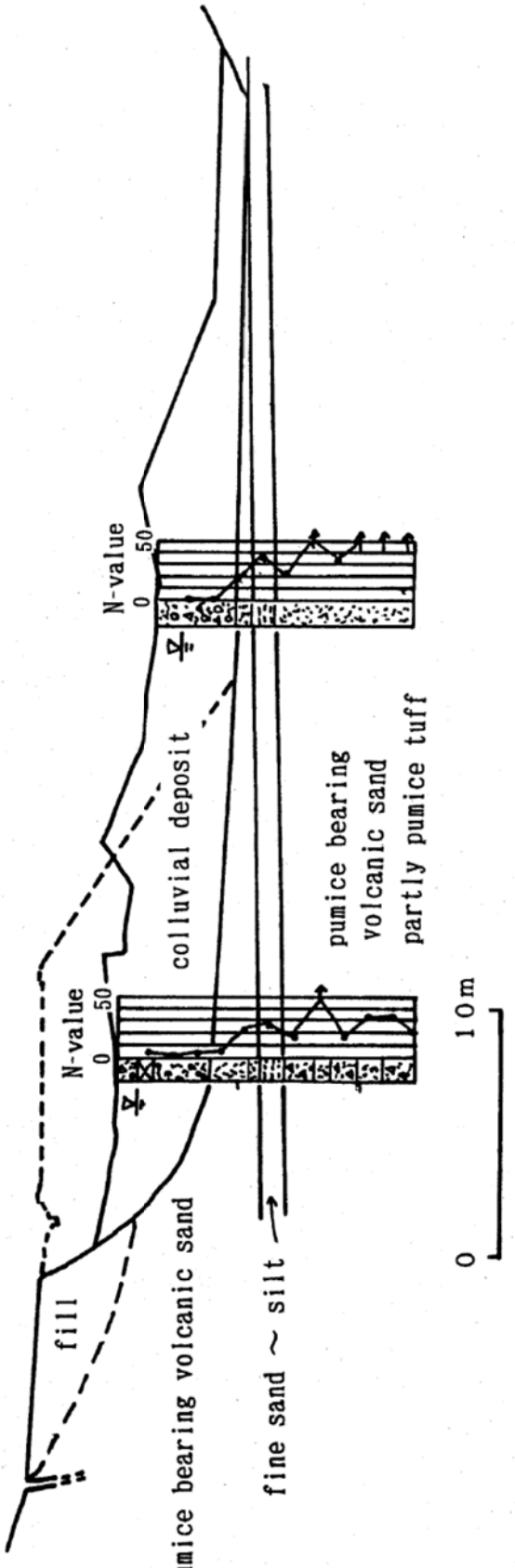

Figure A.13.1: Cross-section through the Route 272 Highway Embankment showing pre-failure and post-failure geometry and the available SPT boring logs (from Sasaki et al., 1994)

A.13.3 Initial Yield Strength Analysis

It is not known whether this failure initiated as a monolithic failure, or as an incrementally progressive failure that retrogressed towards the back heel in progressive slices. Based on an assumed phreatic surface that passes approximately through the mid-height of the slope, and exits at the toe, a search was made for the most critical static failure surface assuming liquefaction had been "triggered" in all potentially liquefiable materials below the phreatic surface. This exercise showed that the most critical potential failure surfaces for this set of assumptions would have been for a failure initially closer to the slope face than the final rear scarp shown in Figure A.13.1. These analyses neglected seismic inertial forces, however, and they also did not account for likely progressive development of triggering of liquefaction within the slope.

The post-failure geometry shown in Figure A.13.1 is suggestive, on the other hand, of a more monolithic failure, possibly articulating itself into sub-sections as it progressed.

Figure A.13.2(a) shows two potential failure surfaces analyzed. The rear-most surface is the eventual "final" underlying (or bounding) failure surface, which is reasonably well constrained by the data provided by Sasaki et al. (1994). The other failure surface is the surface that was found to be the most critical initial yield surface (requiring the highest value of post-liquefaction yield strength in order to produce a calculated static Factor of Safety = 1.0). Silty sand materials above the phreatic surface were modeled with $Ø' \approx 32°$, and a unit weight of $\gamma_m \approx 103$ lbs/ft^3. Materials below the phreatic surface were considered to liquefy, down to the base of the failure surfaces analyzed, and were assigned an undrained post-liquefaction yield strength of $S_{r,yield}$ that was constant along any given failure surface, and a unit weight of $\gamma_s \approx 108$ lbs/ft^3.

The resulting best-estimated value of $S_{r,yield}$ for the most critical initial (smaller) failure surface was $S_{r,yield} = 374$ lbs/ft^2, and the best-estimated value for the eventual "final" larger failure surface was $S_{r,yield} = 307$ lbs/ft^2.

Parameters and geometry were then varied to examine potentially variability. The location of the phreatic surface was varied, raising it by up to 1.5 m (5 ft.) at the back heel of the final failure surface, and lowering it by up to a similar distance. The phreatic surface was considered to exit at or near the toe of the slope, based on the observed failure (and post-failure geometry). Unit weights were also varied over the ranges considered likely, and the friction angle of non-liquefied material above the phreatic surface was varied from 28° to 36°. The resulting range of values of $S_{r,yield}$ for the most critical initial failure surface was $S_{r,yield} \approx 360$ to 391 lbs/ft^2, and the best-estimated range for the eventual "final" larger failure surface (which would be pertinent if the failure initiated monolithically) was $S_{r,yield} \approx 286$ to 319 lbs/ft^2.

Given the uncertainty as to whether or not this failure was initiated largely monolithically, or was progressively retrogressive towards the back heel, the overall best estimate value of post-liquefaction initial yield strength was developed by considering both sets of possible mechanisms and then taking a middle position with regard to the median value, and then considering the full range of variability for both mechanisms, again averaged for the two

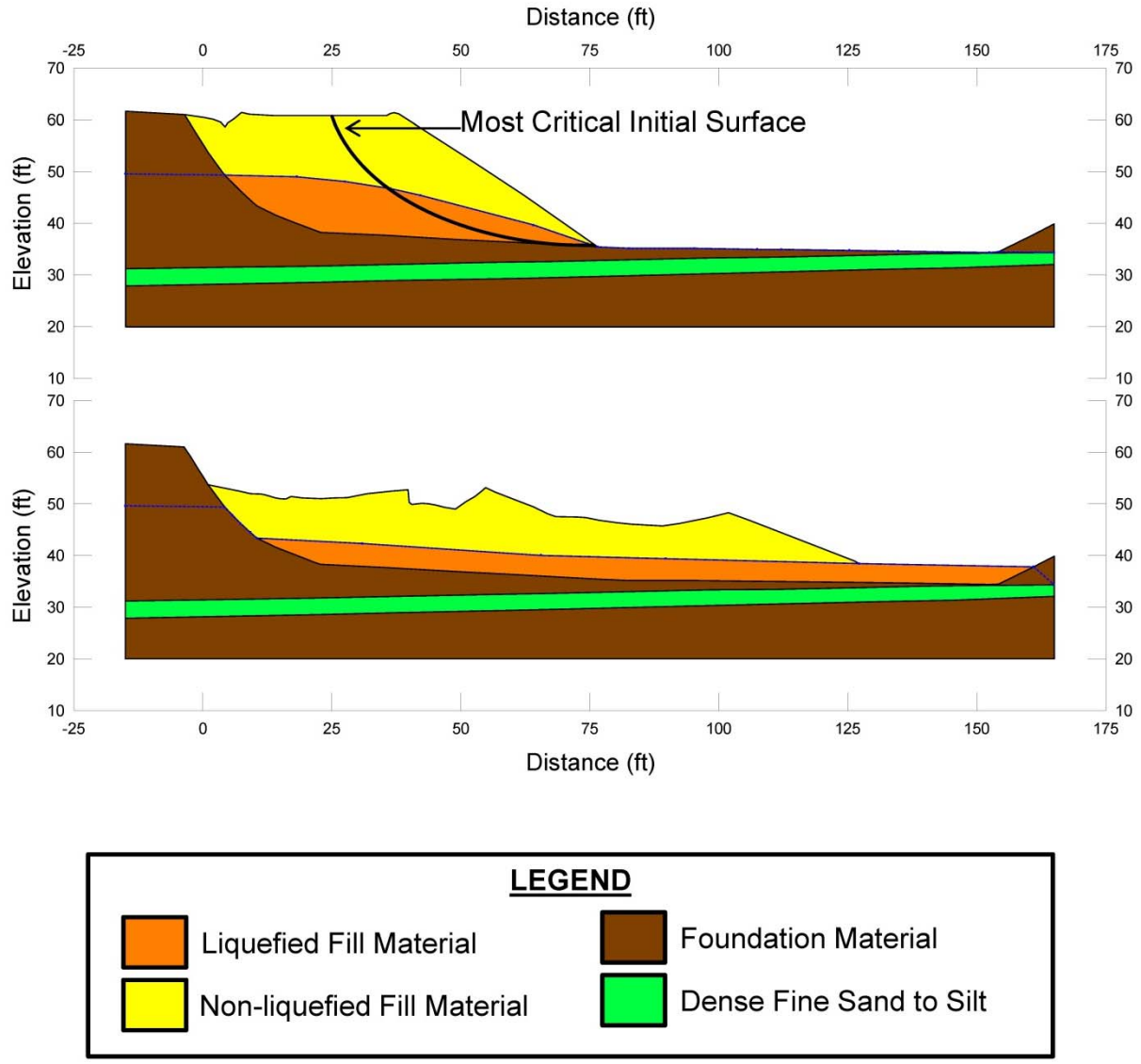

Figure A.13.2: Route 272 Embankment cross-sections showing (a) pre-failure geometry of the embankment and the failure surfaces used for calculation of post-liquefaction initial yield strength $S_{r,yield}$, and (b) post-failure residual geometry and the failure surface used to calculate $S_{r,resid/geom}$.

potential failure surfaces. The resulting best estimate (median) value was found to be on the order of $S_{r,yield} \approx 341$ lbs/ft^2, with a likely range of $S_{r,yield} \approx 302$ to 380 lbs/ft^2.

Olson (2001) also performed back-analyses to determine $S_{r,yield}$. Failure surfaces analyzed were similar, but did not appear to include surfaces extending fully back to the rear heel of the eventual "final" yield surface. Olson reported values of $S_{r,yield} \approx 13.0$ to 13.4 kPa (272 to 280 lbs/ft^2).

A.13.4 Residual Strength Analysis Based on Residual Geometry

The calculation of the "apparent" post-liquefaction strength ($S_{r,resid/geom}$) required to produce a calculated Factor of Safety equal to 1.0 based on residual geometry is illustrated in Figure A.13.2(b). This figure shows the phreatic surface, and the failure surface, used to calculate the best-estimate value of $S_{r,resid/geom} \approx 69$ lbs/ft^2. Variations were then made in parameters, and in location of the pre-failure phreatic surface, as was described in the preceding section in order to evaluate uncertainty or variability. The resulting likely range of post-liquefaction strength required to provide a calculated Factor of Safety equal to 1.0 based on residual geometry was considered to be $S_{r,resid/geom} \approx 65$ to 74 lbs/ft^2.

Olson (2001) also calculated post-liquefaction strength required to produce a calculated Factor of Safety equal to 1.0 based on residual geometry, and reported a range of $S_{r,resid/geom} \approx 2.9$ to 3.0 kPa (61 to 63 lbs/ft^2), in good agreement with the values calculated in these current studies.

A.13.5 Incremental Momentum Back-Analyses and Overall Estimates of S_r

Incremental inertial back-analyses were performed using the same sets of properties and geometries (including failure surfaces and phreatic surfaces) as described in the previous sections. Overall volume of the failure mass was subtly increased progressively throughout the increments because, as discussed previously, the post-failure geometry shown in Figure A.13.1 (Sasaki et al., 1994) shows an increase in the volume of the failure mass of approximately 27% from pre-failure to post-failure geometry. This anomalous volume discrepancy was progressively shared relatively equally from inception of failure to cessation of movements in the incremental inertial analyses.

Figure A.13.3 shows the best-estimate progressive incremental inertial analysis, showing the 5 stages of geometry evolution modeled as the failure proceeds. Figure A.13.4 shows the associated calculations of (1) acceleration vs. time, (2) velocity vs. time, and (3) displacement of the overall center of gravity vs. time. For the geometry and phreatic surface shown in Figure A.13.3, and the monolithic initiation of failure modeled in Figures A.13.3 through A.13.5, the best estimate value of post-liquefaction strength was $S_r = 138$ lbs/ft^2.

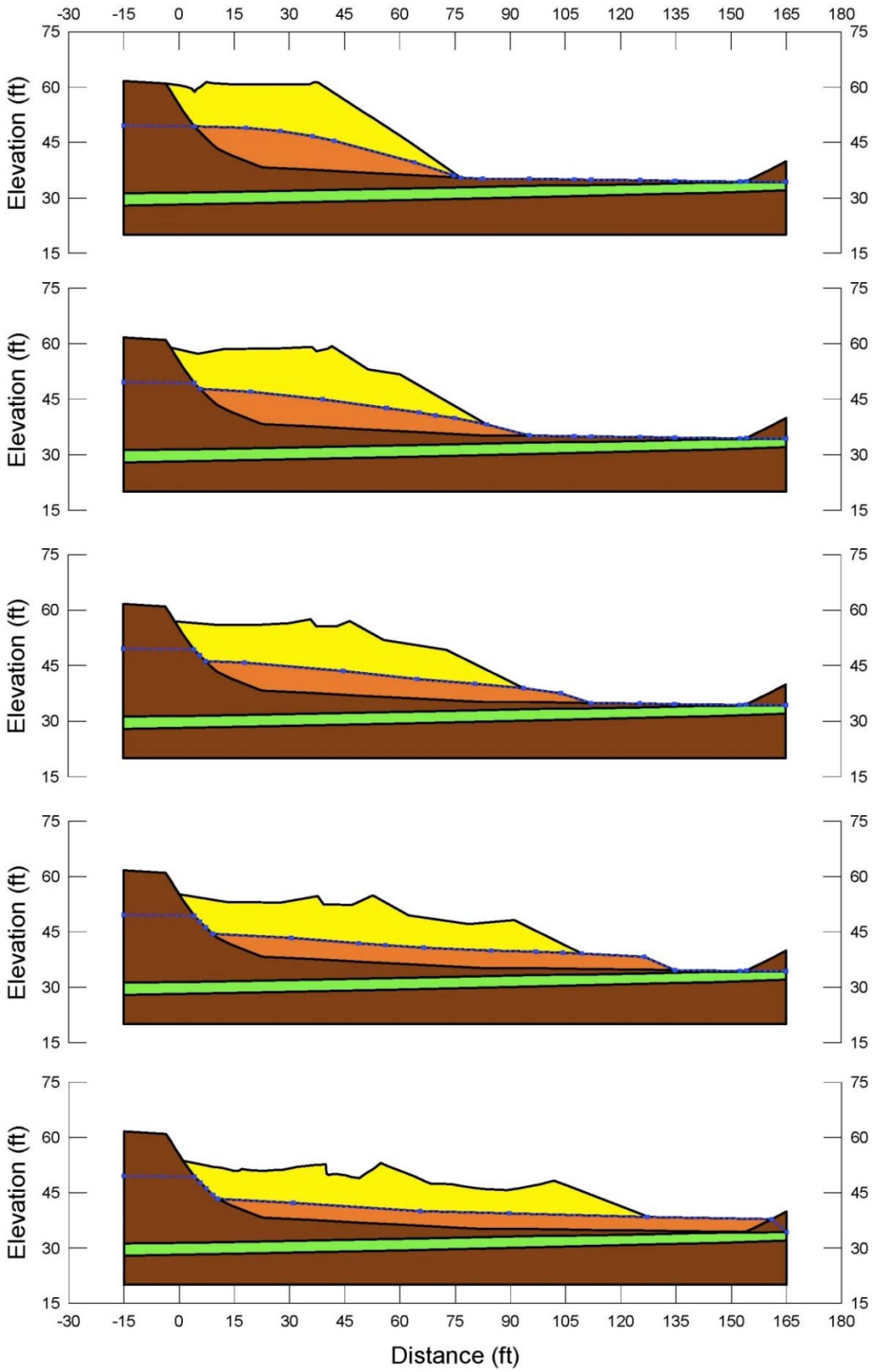

Figure A.13.3: Incremental inertial analysis of the failure of the Route 272 Embankment, showing progressive evolution of cross-section geometry modeled

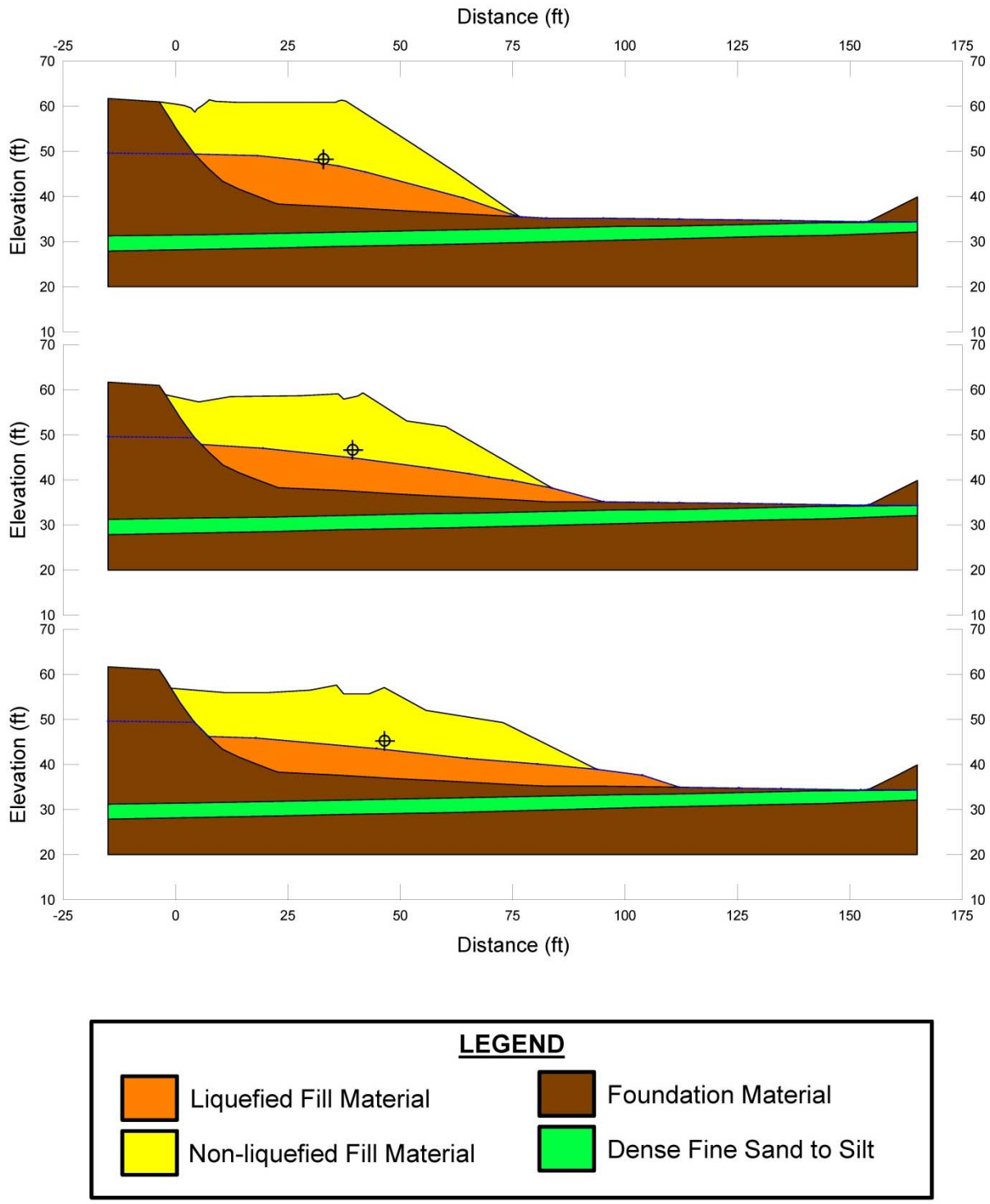

Figure A.13.4: Figure A.13.3 repeated, at larger scale, now also showing the progressive locations of the center of gravity of the overall failure mass.

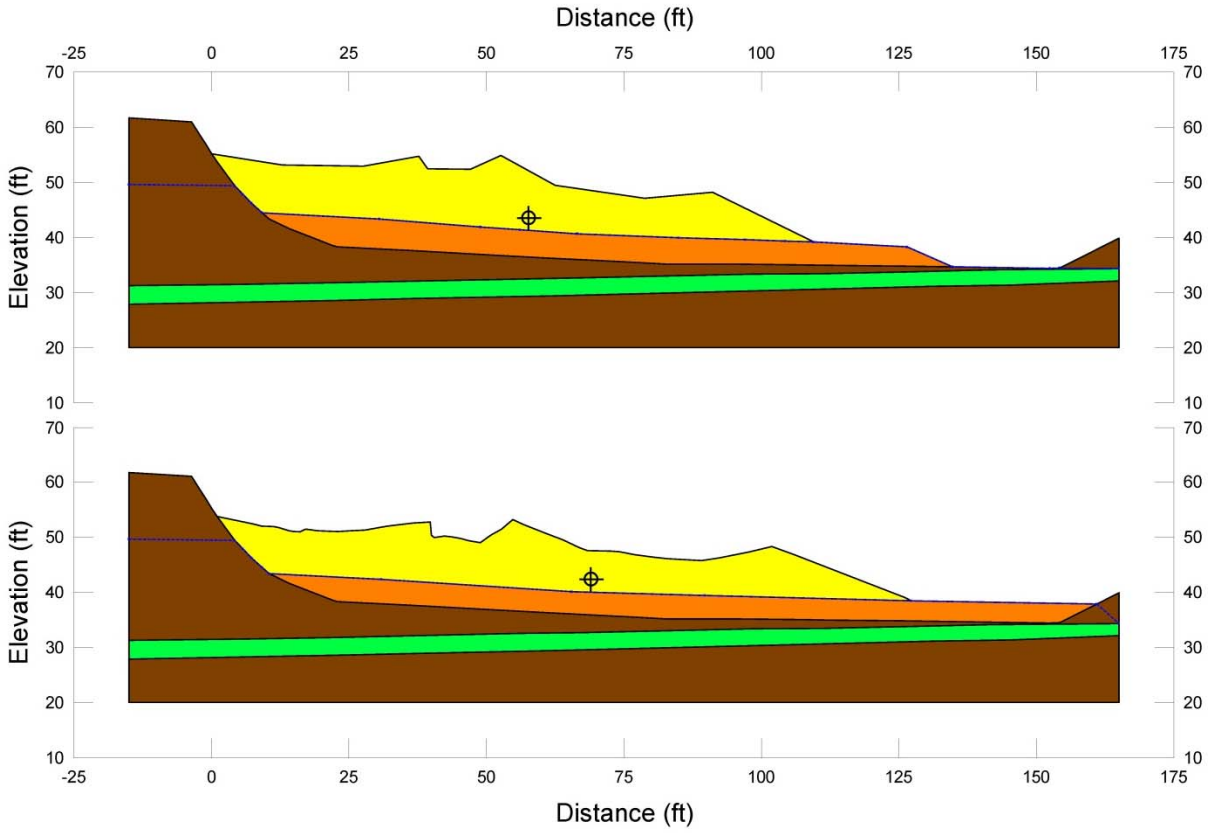

Figure A.13.4 (Cont'd): Figure A.13.3 repeated, at larger scale, now also showing the progressive locations of the center of gravity of the overall failure mass.

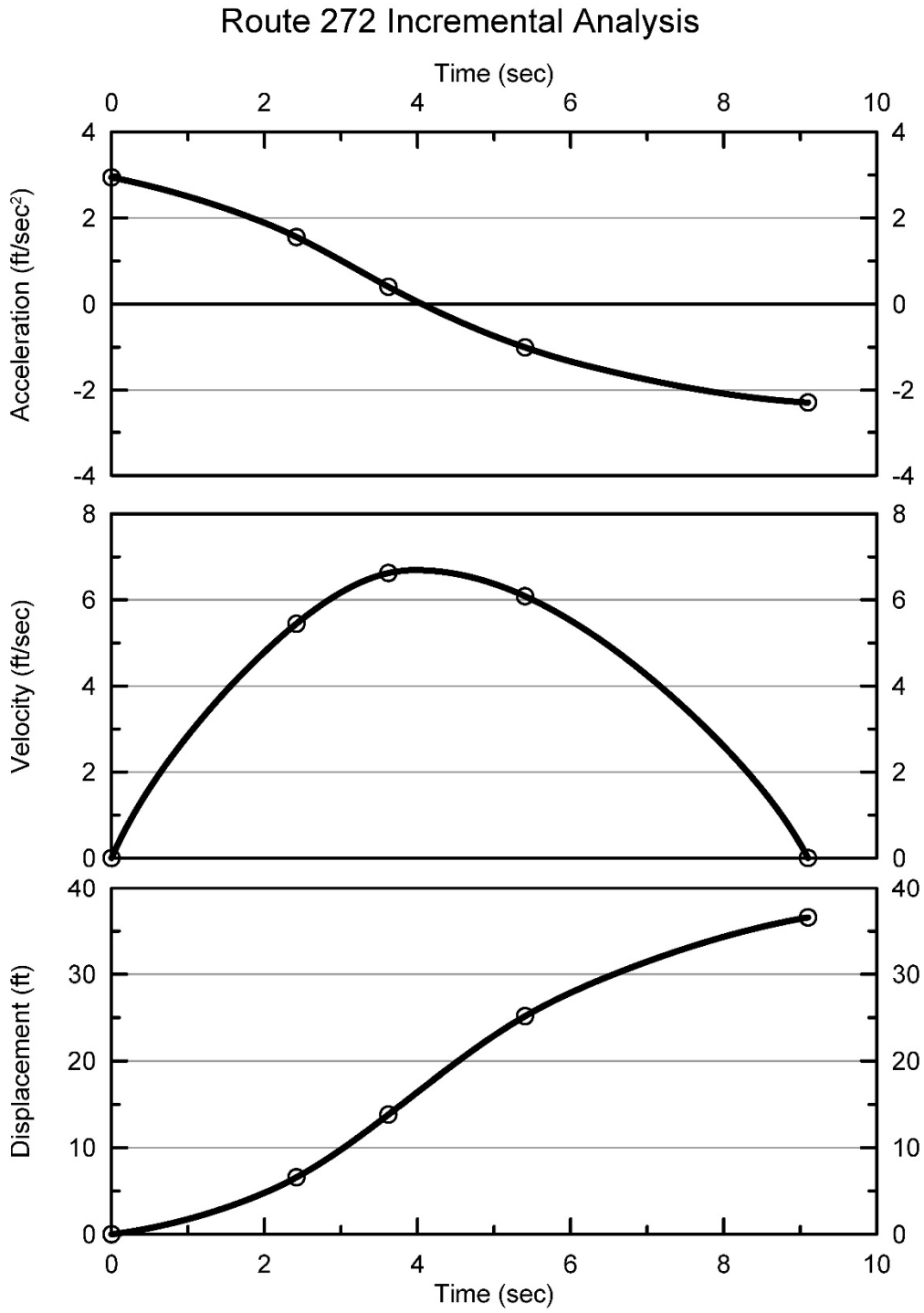

Figure A.13.5: Incremental inertial analysis of the failure of the Route 272 Embankment, showing progressive evolution of: (1) acceleration vs. time, (2) velocity vs. time, and (3) displacement of the overall center of gravity vs. time

The main sources of uncertainty, or variability, in back-calculated values of S_r were (1) the location of the phreatic surface, (2) whether or not the failure initiated largely monolithically or retrogressed progressively towards the back heel, (3) unit weights, (4) strength within the non-liquefied materials at the top of the back heel scarp, and (5) the precise location of the overall failure surface.

Because the location of the overall final failure surface was relatively well constrained in this case history, the two main sources of uncertainty, or variability, were (1) the location of the phreatic surface, and (2) the question as to whether the actual failure initiated largely monolithically, or progressed retrogressively towards the back heel.

The analysis shown in Figures A.13.3 through A.13.5 neglects cyclic inertial forces, and so may represent a slightly conservative assessment of actual post-liquefaction strength mobilized. Incremental inertial back-analyses assuming that failure initiates with a failure surface similar to the forward-most initial failure surface shown in Figure A.13.2(a) and then retrogresses back towards the eventual back heel scarp develop somewhat lower overall calculated values of S_r, with the amount of decrease being dependent upon the rate at which subsequent progression of retrogressive failure towards the back heel initiates. It is not feasible to produce the final post-failure geometry actually documented in the field by Sasaki et al. (1994) if an initial yield surface from the forward section of the eventual failure mass is allowed to "run out" too very far before a subsequent second failure extending further rearwards towards the eventual final back heel of the failure initiates. There may have been only a single monolithic inception of failure, or there may have been multiple retrogressive initiations (two or more). But the additional analyses performed suggest that retrogressive progressive failures would have reduced the S_r values from those calculated based on the largely monolithic failure shown in Figures A.13.3 and A.13.4 by on the order of approximately 5 to 12%. It was then judged that the best-estimate value of post-liquefaction strength would have been intermediate between a monolithic initiation of failure and a progressively retrogressive initiation.

Based on all analyses performed, and the considerations discussed herein, the overall best estimate value of post-liquefaction strength for the Route 272 Embankment failure was judged to be $S_r \approx 138$ lbs/ft^2, with a likely range of $S_r \approx 107$ to 175 lbs/ft^2. Based on the factors contributing to uncertainty or variance for this case history, it was the judgment of the investigation team that this range represented approximately +/− 2 standard deviations. This range of variance is not quite symmetrical about the best estimate value, so minor further adjustments were made to produce a representative estimate of S_r suitable for regression analyses.

Overall, based on an assumed normal distribution, it was judged that the (mean and median) best estimate of post-liquefaction strength for this case history is

$$S_r = 138 \text{ lbs/ft}^2 \text{ (6.61 kPa)}$$

and that the best estimate of standard deviation of mean overall post-liquefaction strength is

$$\sigma_{\bar{S}} = 17 \text{ lbs/ft}^2 \text{ (0.81 kPa)}$$

Estimates of S_r were also reported by several other investigation teams, and these are shown in Table A.13.1(a). Olson (2001) and Olson and Stark (2002), reported a best estimate value of S_r = 4.8 kPa (100 lbs/ft^2), based on their inertial displacement analyses that considered kinetics, and a range of S_r = 3.0 to 5.7 kPa (63 to 119 lbs/ft^2). Wang (2003) and Wang and Kramer (2008) employed their zero inertial force (ZIF) method to incorporate inertial effects in their back-analyses of this failure, and they also developed estimates of both mean $\overline{S_r}$ = 130.5 lbs/ft^2 as well as the associated standard deviation $\sigma_{\overline{S}}$ = 33.5 lbs/ft^2. These other studies each employed different approaches, and different sets of modeling and analysis assumptions. Given this, overall agreement among these investigations is very good.

A.13.6 Evaluation of Initial Effective Vertical Stress

Average initial (pre-failure) effective vertical stress was assessed for the liquefied zones of each of the two failure surfaces shown in Figure A.13.2(a). The best estimate of the overall average initial vertical effective stress was then taken as the average of these two averages. Reasonable variations were then made in (1) the location of the phreatic surface, (2) unit weights, and (3) the precise location of the overall failure surface.

The resulting best estimate of average pre-failure effective stress within the liquefied materials controlling the failure was then $\sigma_{vo}' \approx$ 1,285 lbs/ft^2, with a reasonable range of $\sigma_{vo}' \approx$ 1097 to 1512 lbs/ft^2. This range is slightly non-symmetric about the median value, and this range was judged by the engineering team to represent approximately +/− 2 standard deviations. Overall, the best characterization of initial (pre-failure) average effective vertical stress was then taken to be represented by a mean and median value of

$$\sigma_{vo}' \approx 1{,}285 \text{ lbs/ft}^2 \text{ (61.5 kPa)}$$

with a standard deviation of

$$\sigma_{\sigma o'} \approx 104 \text{ lbs/ft}^2 \text{ (4.98 kPa)}$$

Estimates of σ_{vo}' were also reported by other investigation teams, and these are shown in Table A.13.1(c). Average initial vertical effective stresses were reported by Olson (2001) and Olson and Stark (2002) as σ_{vo}' = 1,030 lbs/ft^2. Average initial vertical effective stresses were not directly reported by Wang (2003) and Kramer (2008), but they were published more recently in the publication by Kramer and Wang (2015). As discussed in Section 2.3.8.1(a), the approach taken by Wang (2003) to evaluation of σ_{vo}' for his nine "primary" case histories (this is one of those nine) is not clearly explained, and it is also poorly documented. Wang's value of σ_{vo}' = 1,043 lbs/ft^2 is in good agreement with the value of Olson (2003), and in fair agreement with the value developed in these current studies. Overall, agreement among these three studies is acceptable here.

A.13.7 Evaluation of $N_{1,60,CS}$

As shown in Figure A.13.1, only 5 SPT were performed within the liquefiable upper stratum. As a result, lack of numbers of SPT data is a significant contributor to uncertainty or variability with respect to the median or mean value representative of this material. Seed et al. (1985) and Ishihara (1993) assumed an energy ratio of approximately 72%, and current study does the same. Corrections for effective overburden stress (C_N) were made using the relationships proposed by Deger (2014), as presented and discussed in Section C.1.1. Corrections for SPT equipment and procedural details, and for fines content, were made based on Cetin et al. The resulting median $\overline{N_{1,60,CS}}$ value was 8.1 blows/ft.

Variance of $N_{1,60,CS}$ within this limited data set was used to calculate the associated variance in the mean (and thus approximately the median) value of $\overline{N_{1,60,CS}}$, but this under-estimated the actual variance or uncertainty. Additional factors significantly affecting variance or uncertainty in the median representative $\overline{N_{1,60,CS}}$ value were (1) lack of numbers of SPT data, and (2) uncertainty as to actual SPT equipment and procedural details. Overall, it was the judgment of the investigation team that SPT penetration resistance could be suitably represented with a representative (median) value of $\overline{N_{1,60,CS}}$ = 8.1 blows/ft., and with a standard deviation of the median/representative value of approximately $\sigma_{\overline{N}}$ = 1.6 blows/ft.

Table A.13.1(b) shows values of representative $N_{1,60}$ or $N_{1,60,CS}$ values developed by other investigators, and variance or standard deviations in these representative values when available. Olson and Stark (2001, 2002) developed an estimated representative value of $N_{1,60}$ = 6.3 blows/ft, and an estimated range of representative values of $N_{1,60} \approx$ 2.4 to 10 blows/ft, but did not quantify variance or standard deviation in probabilistic terms. Wang (2003) and Kramer (2008) jointly developed a representative value of $\overline{N_{1,60,CS}}$ = 8.5 blows/ft, and their estimated standard deviation of that overall mean value for this case history was $\sigma_{\overline{N}}$ = 2.6 blows/ft. The representative $N_{1,60}$ value of Olson and Stark is about 2 to 2.5 blows/ft lower than the other two sets of values in the table, in part because Olson and Stark did not make a fines correction, which would have served to increase their $N_{1,60}$ values as they became $N_{1,60,CS}$ values in these silty sands.

The investigation teams whose results are presented in Table A.13.1(c) each employed slightly different approaches with regard to corrections for effective overburden stress, fines content, and SPT equipment and procedural details. Given this, the agreement with the value employed in this current study is good. Wride, McRoberts and Robertson (1999) developed a somewhat lower estimate of representative $N_{1,60,CS}$ for this case history, but their approach targeted determination of a more nearly lower bound value, and so is this lower value is to be expected and is not directly comparable with the others shown.

A.13.8 Other Results and Indices

A number of additional results, and indices, can be extracted from the analyses performed. Some of these are useful in developing some of the over-arching relationships and figures presented in the main text of this report. These values are presented in Table A.13.2.

Table A.13.1: Representative values for the Route 272 Highway Embankment case history of: (a) post-liquefaction strength (S_r), (b) initial vertical effective stress (σ_{vo}'), and (c) $N_{1,60,CS}$ developed by various investigation teams, and estimates of variance in each of these indices when available.

(a) Post-Liquefaction Strength:	
Olson (2001) and Olson and Stark (2002)	S_r = 100 psf, and range = 63 to 211 psf
Wang (2003) and Kramer (2008)	$\overline{S_r}$ = 130.5 psf, and $\sigma_{\overline{S}}$ = 33.5 psf
This Study	$\overline{S_r}$ = 138 psf, and $\sigma_{\overline{S}}$ = 17 psf
(b) Representative $N_{1,60}$ or $N_{1,60,CS}$ Value:	
Olson (2001) and Olson and Stark (2002)	$N_{1,60}$ = 6.3 bpf, and range = 2.4 to 10.0 bpf
Wang (2003) and Kramer (2008)	$\overline{N_{1,60,CS}}$ = 8.5 bpf, and $\sigma_{\overline{N}}$ = 2.6 bpf
This Study	$\overline{N_{1,60,CS}}$ = 8.0 bpf, and $\sigma_{\overline{N}}$ = 1.6 bpf
(c) Representative Initial Vertical Effective Stress:	
Olson (2001) and Olson and Stark (2002)	σ_{vo}' = 1,030 psf, likely range is not provided.
Wang (2003) and Kramer (2008)	Value of $\sigma_{vo}' \approx$ 1,043 psf is poorly documented, and so is considered useful only as an approximate comparison. (See Section 2.3.8.1, and Table 2.3.)
This Study	$\overline{\sigma'_{vo}}$ = 1,285 psf, and $\sigma_{\overline{\sigma}}$ = 104 psf

Table A.13.2: Additional results and indices from the analyses of the Route 272 Highway Embankment failure case history.

Maximum distance traveled by the center of gravity of the overall failure mass	36.6 ft.
Initial post-liquefaction Factor of Safety prior to displacement initiation, and based on best estimate value of S_r	FS = 0.50
Final post-liquefaction Factor of Safety at final (residual) post-failure geometry, and based on best estimate value of S_r	FS = 1.90

A.14 Calaveras Dam (California, USA, 1918)

A.14.1 Brief Summary of Case History Characteristics

Name of Structure	Calaveras Dam
Location of Structure	San Francisco Bay Area, California, USA
Type of Structure	Hydraulic Fill Dam
Date of Failure	March 24, 1918
Nature of Failure	Static, During Construction
Approx. Maximum Slope Height	201 ft.

A.14.2 Introduction

The Calaveras Dam embankment failed during construction on March 24, 1918, suffering a massive flowslide on its upstream side. The dam was being constructed by the ponded hydraulic fill method, and was nearing completion at the time of the failure. The nearly completed embankment had a maximum crest height of approximately 200 feet at the tallest section, and the reservoir was partially filled, with a reservoir surface elevation of approximately 75 feet above the base of the lowest point of the embankment; approximately 35 to 40% of the way up towards the still uncompleted dam crest.

Figure A.14.1 shows a photograph of the failure, with the failure mass having moved upstream (towards the upper right hand corner of the photograph). Figure A.14.2 shows a complicated set of super-imposed cross-sections (Hazen, 1920). The lower portion of the cross-section shows the post-failure cross-section geometry. The dashed lines (which can be difficult to see) show the pre-failure geometry, and the remainder of the figure shows the final cross-section after reconstruction and then completion of the dam. Figure A.14.3 shows pre-failure and post-failure cross-sections as interpreted by Olson (2001) based on Hazen (1920) and the information available in 2001. This interpretation is essentially identical to the cross-sections employed in these current studies.

This failure was well investigated for its time, and Hazen (1918) and Hazen (1920) provide good descriptions of the failure, and of the construction of the dam up to the time of the failure.

There had been partial movements on the upstream side of the dam for at least nine months prior to the eventual failure. On June 18, 1917 horizontal displacements of approximately 0.5 m had been measured at one location on the upstream face, and additional horizontal movements of approximately 0.15 m occurred over the next day, eventually opening a crack along approximately 650 feet of the upstream side concrete facing. Fill placement was stopped, and the movements quickly ceased. So fill placement resumed. Two additional, similar, incidents of observed movements and temporary stoppage of fill placement then occurred prior to the eventual failure. Finally, on the day before the failure, approximately 4 feet of horizontal movement has been measured on the upstream face.

Figure A.14.1: Oblique aerial photograph of the March 24, 1918 upstream slope failure (the failure mass moved towards the upper right hand corner of this photograph). [Photo from Hazen, 1920 (with arrow and notation from Olson, 2001)]

The failure itself was observed by witnesses. According to Hazen (1918): "The men who saw the dam go state that at first the whole mass seemed to move forward as a unit. Afterward it seemed to separate, and the parts that were farthest back stopped, while those that were further advanced continued to move forward… The material was carried forward on a good lubricant, and that lubricant first became used up or expelled near the center of the dam and left the higher parts of the dam on solid bottom while there was still lubricant to carry forward the lower and more advanced portions."

This was thus a slide that was monotonically initiated, and it then subsequently elongated as it travelled upstream into the partially filled reservoir.

Soil liquefaction was not well understood at the time of the failure, and Hazen (1918) and others were surprised that the failure mass was "hard and solid" soon after the failure when test piles were driven to qualitatively asses the consistency and apparent density of the massively displaced slide mass. It was initially suspected that clayey materials from the puddled core might have been present as horizontal lenses extending well into the upstream shell zone, and that these weak clay strata might have been responsible for the observed failure. Post-failure investigations were unable, however, to find any significant amounts of clay-dominated strata within the displaced failure mass.

As a result, Hazen (1920) suggested instead that: "As water pressure increased, the pressure on the edges is reduced and the friction resistance of the material becomes less. If the

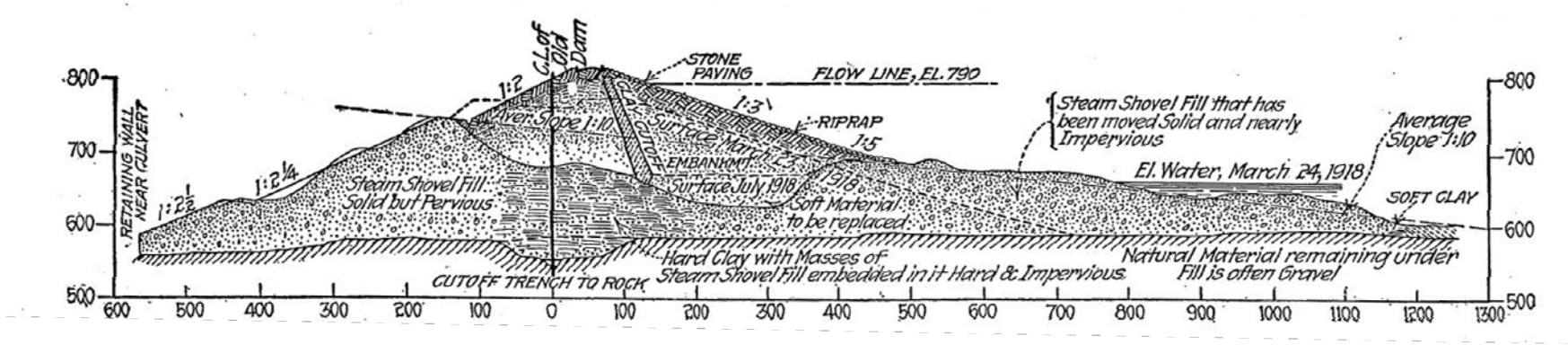

Fig. A.14.2: Cross-section from Hazen, 1920 showing both pre-failure and post-failure conditions, as well as the re-constructed and completed dam.

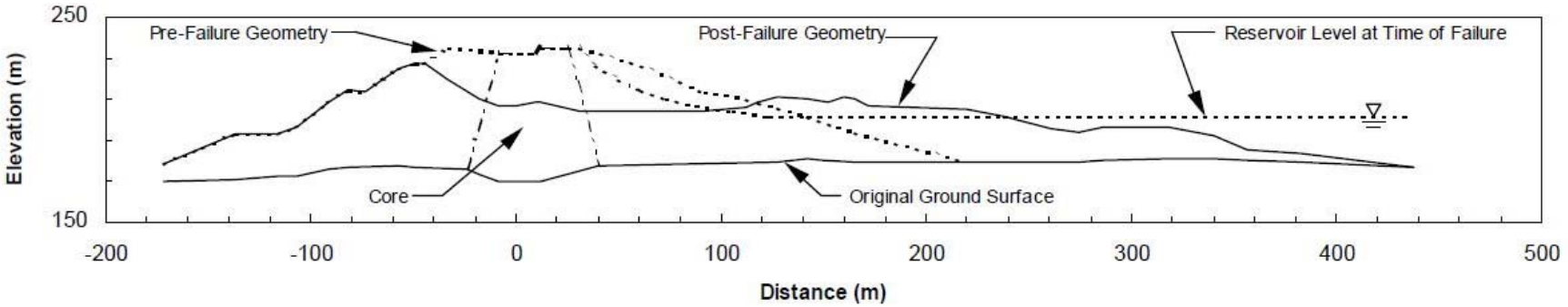

Fig. A.14.3: Pre-failure and post-failure cross-sections as interpreted by Olson (2001) based on Hazen (1918).

pressure of the water is great enough to carry all the load, it will have the effect of holding the particles apart and of producing a condition that is practically equivalent to that of quicksand. A sharp blow, as with a foot, however liquefies a certain volume and makes quicksand…. The condition of quicksand lasts only for a few seconds until the surplus water can find its way out. When this happens the grains again come to solid bearings and stability is restored. During the few seconds after the sand is struck, however, it is almost liquid, and is capable of moving or flowing or of transmitting pressure in the same measure as a liquid…. The conditions that control stability or lack of stability in quicksand may also control the stability or lack of stability in dams…. It may be that after the first movement there was some readjustment of the material in the toe which resulted in producing temporarily this condition of quicksand, and which destroyed for a moment the stability of the material and facilitated the movement that took place."

That was a brilliantly insightful early description of the mechanisms involved in this type of liquefaction-induced flow failure, and it stands as one of the earliest useful engineering descriptions of soil liquefaction and resulting stability failure.

A.14.3 Geology and Site Conditions

The base of the dam appears to have been constructed with little or no excavation of existing foundation materials. The valley floor and side slopes were covered with weathered colluvium, and with alluvium sourced from the weathered colluvium. Relatively clean gravelly fill was placed both by sluicing and by steam shovels to initially level the deepest portions of the foundation prior to construction of the main embankment. The gravel used was locally available material from the existing creek bed, and had few fines. Neither these gravels, nor the underlying foundation soils, appear to have been involved in the eventual failure.

The dam was being constructed by the hydraulic fill method, with starter dikes on the upstream and downstream sides to contain the arriving hydraulic fill. Figure A.14.4 gives a good idea of the complexity of the evolving internal geometry as the embankment was raised. Hydraulic fill was simultaneously deposited from pipes on both the upstream and downstream edges of the dam, so that coarser materials would settle out and form "shell" zones while finer materials would travel towards the center of the pool (and thus the center of the rising embankment) producing a clayey "puddled core". The hydraulic fill material was excavated from the surrounding hills, and consisted of variably weathered sandstone materials that were easily broken down by excavation and transport. Gradation, and clay content, were variable within these weathered materials. As a result, the hydraulic material actually emplaced was also highly variable as to gradation and fines content. Fines tended to be low to moderate plasticity CL materials (Olivia Chen Consultants, 2003).

The materials placed as starter dikes were also excavated from the surrounding hillsides, and had the same general characteristics. The starter dikes were unusually thick, as illustrated in Figure A.14.4, and these were placed primarily by steam shovels. This steam shovel fill of the "starter dikes" was placed in large lifts of approximately 4 to 6 feet, and was not compacted.

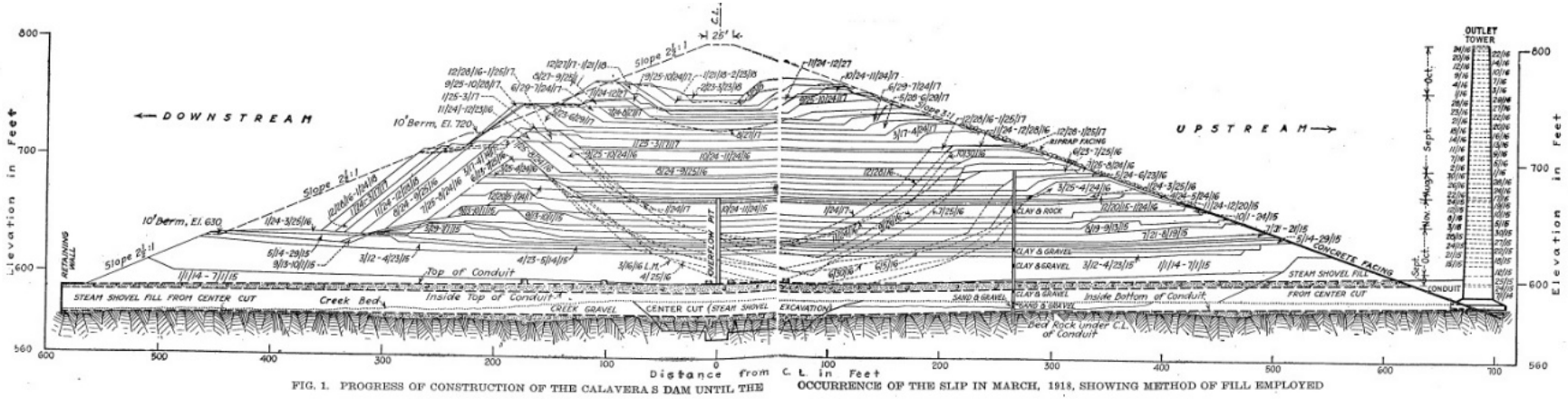

FIG. 1. PROGRESS OF CONSTRUCTION OF THE CALAVERAS DAM UNTIL THE OCCURRENCE OF THE SLIP IN MARCH, 1918, SHOWING METHOD OF FILL EMPLOYED

Fig. A.14.4: Cross-section by Hazen (1920) showing the progressive evolution of the Calaveras Dam embankment as a series of starter dikes and hydraulic fill beaches and puddled core ponds were used to raise the embankment up to the time of the failure on March 24, 1918.

Subsequent modern investigations were performed from 2000 to 2003 (Olivia Chen Consultants, 2003) to assess seismic stability of the repaired and completed dam, and these newer studies served to usefully further characterize the materials and approximate zonation within the dam, as will be discussed further. These more recent seismic studies concluded that the dam was seismically unsafe, and this resulted in emptying of the reservoir and removal of the dam. As this is being written, an entirely new dam is currently under construction so that this important reservoir can be re-established.

The modern (2000 to 2003) investigations provided significantly improved insight regarding the nature and character of the materials comprising the main embankment, including (a) the starter dikes, (b) the original hydraulic fill shells, and (c) the central "puddled" clayey core. Figures A.14.5(a) and (b) show the pre-failure and post-failure cross-sections, respectively, as analyzed in these current studies. No internal stratigraphy or zonation is shown in these figures, and this will be discussed further.

Figure A.14.6 shows the internal zonation developed by Olivia Chen Consultants (2003) for the recent seismic stability investigations. Multiple zones and sub-zones were employed to characterize the highly variable conditions within this complex embankment. Table A.14.1 presents summaries of estimated equivalent SPT $N_{1,60,CS}$ values for the principal zones shown in Figure A.14.6, as developed in the 2002-2003 studies.

Most of the embankment shell materials, including both hydraulically placed fill and also fill placed (largely uncompacted) with steam shovels, were comprised of weathered and fractured sandstone excavated from local hillsides. These materials were weathered and friable, and the resulting fill materials were broadly well-graded, with highly variable fines contents ranging from only a few percent fines to as much as 90% fines, and with relatively random variations in fines content locally within even the multiple zones shown in Figure A.14.6 and in Table A.14.1. Fines tended to be low to moderate plasticity CL materials. These "shell" materials also had significant gravel and cobble contents, also highly variable, and maximum particle sizes were often up to approximately 8-inches or greater, with gravel or coarser contents of between 15% to 60% and more being relatively common. The central "core" materials tended to have higher fines contents, but there were layers and stringers of cleaner material that appeared to penetrate into what was characterized as the puddled core zone.

To deal with these very broadly graded, and highly variable, materials the principal characterizations of seismic soil liquefaction potential were developed by means of (1) large diameter Becker Penetrometer tests (BPT), and (b) "short interval" SPT in which blowcounts were measured per each inch of penetration so that corrections could be made for apparent interference from larger particles (gravels and cobbles). Special steps were taken to deal with significant casing adhesion/friction on the Becker Penetrometer tests as the penetrometer passed through these broadly well-graded and variably cohesive to non-cohesive materials.

As a result of these recent investigations, it was the conclusion of this current investigation team, with unanimous concurrence from the informal advisory panel, that (1) the soils were more randomly variable than had been previously understood, (2) there were (variably) higher fines contents in many of the "shell" materials including both the hydraulically

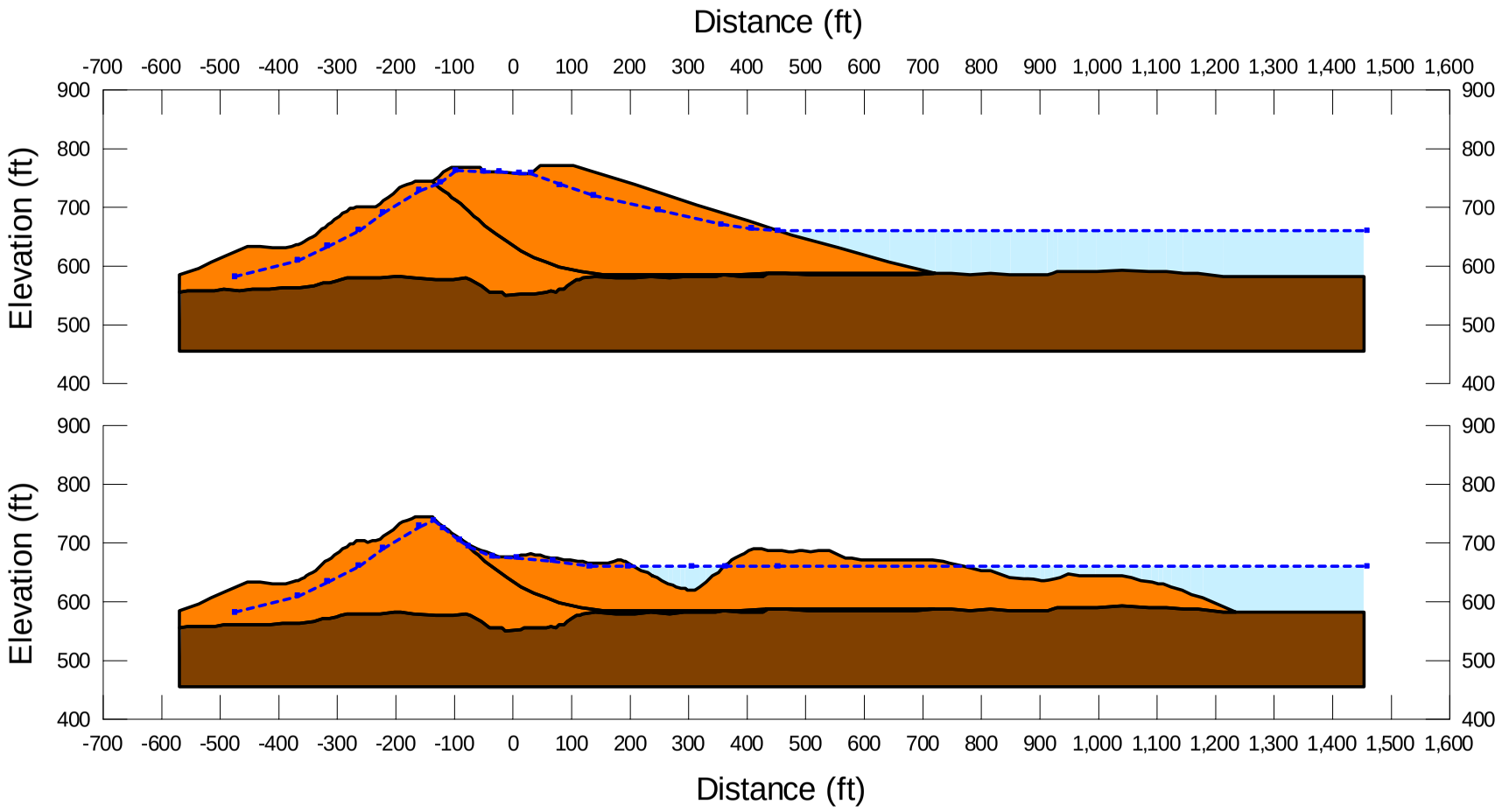

Figure A.14.5: Pre-failure and post-failure cross-sections of Calaveras Dam as analyzed in these current studies.

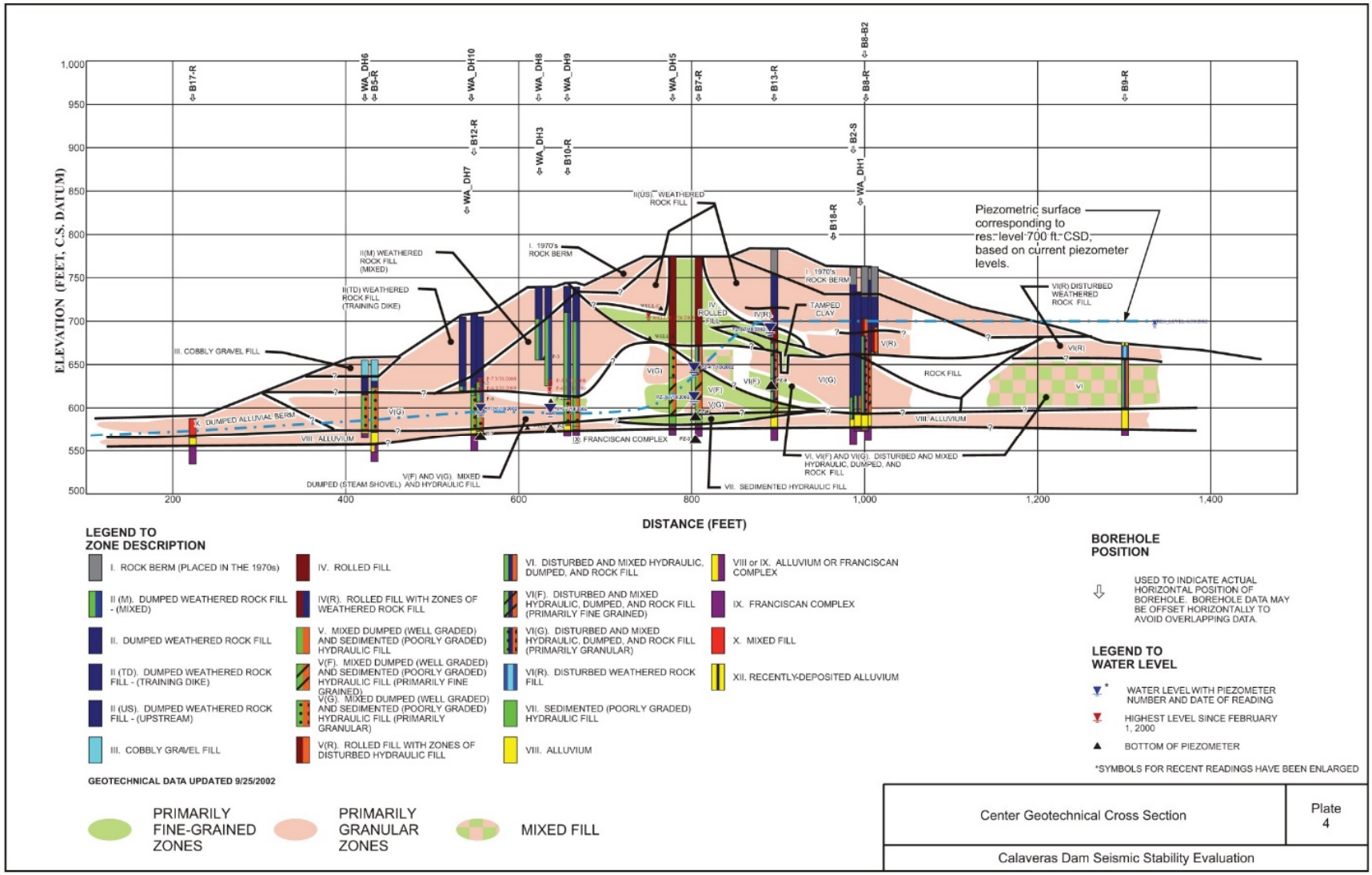

Fig. A.14.6: Cross-section developed by Olivia Chen Consultants (2003) for seismic stability analyses of Calaveras Dam.

Table A.14.1: Characterizations of equivalent (and representative) $N_{1,60,CS}$ values for zones within the reconstructed Calaveras Dam (Olivia Chen Consultants, 2003).

Table 2: Selection of Representative $(N_1)_{60,CS}$ Values for Embankment and Foundation Zones and Subzones, Calaveras Dam and Foundation

Zone	Zone Description	Subzone	30th Percentile $(N_1)_{60}$ SPT	30th Percentile $(N_1)_{60}$ BPT	50th Percentile $(N_1)_{60}$ SPT	50th Percentile $(N_1)_{60}$ BPT	Representative Fines Content	ΔN_{CS} (for fines)
I	Rock Berm (Placed In The 1970s)		N/D	22	N/D	29	15 (F)	N/A
II	Dumped Weathered Rock Fill	II(M) II(TD) II(US)	17 9 23	19 (B) 8 21	21 12 22	23 8 20	14 7 10	1.5 1 1
III	Cobbly Gravel Fill		/ND	7	N/D	8	20 (F)	1.5
IV	Rolled Fill	IV IV(R)	17 24	23 (L) 12 (L)	22 (L) 32 (L)	25 16	48 12 (F)	N/A 1
V	Mixed Dumped and Sedimented Hydraulic Fill	V V(F) V(G)	13 12 17	19 17 17	16 17 20	23 23 22	20 15 (F) 19	1.5 1.5 1.5
V(R)	Mixed Hydraulic and Rolled Fill		21	14 (L)	24	18	15 (F)	1.5
VI	Disturbed and Mixed Hydraulic, Dumped, and Rock Fill	VI VI(F) VI(G)-Res VI(G)-Emb VI(R)	10 11 7 27 12 (L)	N/D 22 (L) N/D 22 N/D	17 18 8 40 12 (L)	N/D 36 (L) N/D 31 N/D	11 59 11 11 15	1 N/A 1 1 1.5
VII	Sedimented Hydraulic Fill		10	N/D	13	N/D	62	N/A
VIII	Base Alluvium		19	20	30	26	8	1
X	Mixed Fill		12	17	13	26	19 (F)	1.5
XI	Rocky Colluvium		32	36	34	43	N/D	0

(L): Limited penetration data available
(B): Based on data at bottom of zone
(F): Calibrated field-estimated fines contents were also considered
N/A: Not Applicable (High CL content)
N/D: Not Determined

placed materials and those placed by steam shovels, and (3) it would not be possible to suitably infer equivalent penetration resistance for conditions as they existed at the time of the 1918 slope failure in these complex materials that would provide a suitable basis for the current development of correlations between penetration resistance and post-liquefaction strength. Issues here include the observation that some portions of the "shell" zones were actually fines dominated, and that it would be exceedingly difficult to infer strengths in materials that would have been underconsolidated at the time of the failure, and that would also require very significant adjustments in penetrations resistances measured in the 2000 – 2003 studies in order to develop suitable characterizations compatible with conditions associated with a failure that had occurred eight decades prior.

Accordingly, with great reluctance, it was determined that this classic case history would not be employed in development of predictive correlations in these current studies.

That does not mean that this case history is not of value to these current studies, however, and so this case is the single "Class C" case in these current studies.

This case history provides an excellent opportunity to perform both incremental momentum analyses, as well as more simplistic $S_{r,yield}$ and $S_{r,resid/geom}$ analyses, and by doing so to develop useful information and back-analysis results that can be employed in development of relationships for characterization of post-liquefaction strengths as a function of failure and runout characteristics.

The recent (2000 - 2003) studies confirmed previous assessments that the materials comprising the uncompacted steam shovel fill forming the starter dikes, and those comprising the hydraulic fill "shell" zones, were generally similar with regard to material types and variability of materials, and that they were also generally similar in density. As a result, the upstream shell zones comprised of steam shovel fill and those comprised of hydraulic fill will be treated as essentially similar materials in these current studies.

The central puddled core materials would have been underconsolidated at the time of the 1918 failure, and it is difficult to estimate exactly what their strength characteristics would have been. They would have been mainly cohesive dominated materials, with CL fines, and they would have had high liquidity indices. Accordingly they would have (a) had relatively low ratios of Su/P, and (b) they would also have been sensitive and so would have suffered strength reduction when sheared to large strains.

Fortunately, as this case history will not be sued in development of correlations between penetration resistance and post-liquefaction strength (S_r), it is not necessary to closely characterize these puddled "core" materials here. Instead, these materials will not be differentiated from the adjacent "shell" materials (including both hydraulically placed materials and materials loosely placed by steam shovels, and the entire length of the apparent failure surface will simply be characterized by an undrained strength "S_r". As shown in Figure A.14.5, the phreatic surface created jointly by the "pond" atop the rising hydraulic fill and by the partially filled reservoir led to a situation in which essentially all of the failure surface was saturated.

A.14.4 Evaluation of Representative Post-Liquefaction Residual Strength

A.14.4(a) Initial Yield Stress Analyses

The pre-failure and post-failure cross-sections utilized for back analyses were based in large part on the cross-sections presented by Hazen (1918), and these are shown in Figure A.14.7. Figure A.14.7(a) shows the pre-failure cross-section geometry modeled as the best estimate case. This figure also shows the best estimate failure surface for these initial yield stress analyses. Initial yield stress ($S_{r,yield}$) is defined as the theoretical post-liquefaction strength within liquefiable materials on the eventual failure surface that would be necessary to develop a calculated Factor of Safety equal to 1.0 for the pre-failure geometry.

The unit weights of the hydraulic fill materials at the time of failure above and below the phreatic surface were estimated considering the recent time since placement, the nature of the hydraulic fill materials that comprised the dam, the values used by other investigators, and data developed by available field studies. Unit weights for saturated embankment materials were taken as $\gamma_s \approx 128$ lbs/ft^3. Because all materials involved in the stability analyses were saturated, this is the only unit weight required.

Similarly, as discussed in the previous section, all materials along the eventual failure surface were assigned a strength of $S_{r,yield}$.

The location of the failure surface was well-constrained by the observed field failure and by the post-failure investigations.

Based on these conditions and geometry, the best-estimate value of $S_{r,yield}$ was found to be $S_{r,yield} = 1{,}790$ lbs/ft^2. Parameter sensitivity studies were then performed, including varying the unit weights of the materials (and also varying the distribution of unit weights, employing slightly lower unit weights in the "core" zone and slightly higher unit weights in the "shell" zone). Sensitivity studies also analyzed a suite of slightly different failure surfaces, but these variations in details of the failure surface were minor. Based on these sensitivity studies, a reasonable range of back-calculated values was judged to be $S_{r,yield} \approx 1{,}445$ to 21,33 lbs/ft^2.

Olson (2001) also calculated values of $S_{r,yield}$ in his studies, but his values were targeted specifically at the materials of the "shell" zones and so they are directly comparable.

A.14.4(b) Residual Strength Analyses Based on Residual Geometry

Similar "static" stability analyses were performed to evaluate the "apparent" shear strength within the liquefiable hydraulic fill (S_r) that would result in a calculated Factor of Safety equal to 1.0 for the post-failure residual geometry of Figure A.14.7(b). Assumptions and modeling details were largely the same as described in the previous Section A.14.7(a), and sensitivity analyses with varying combinations of modeling and parameter details were performed here as well.

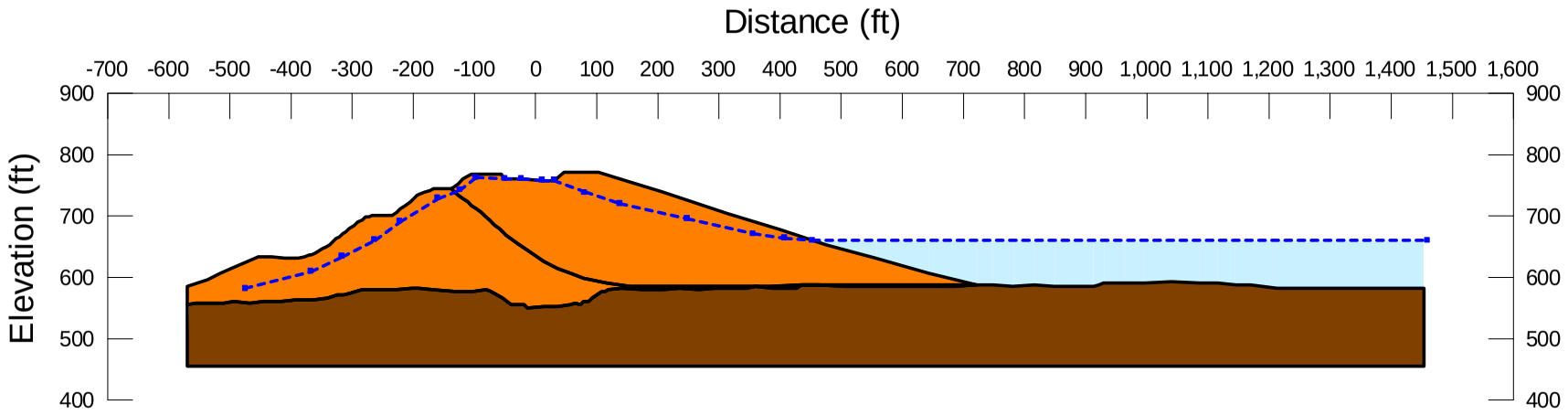

Figure A.14.7(a): Pre-failure cross-section of Calaveras dam used for evaluation of $S_{r,yield}$.

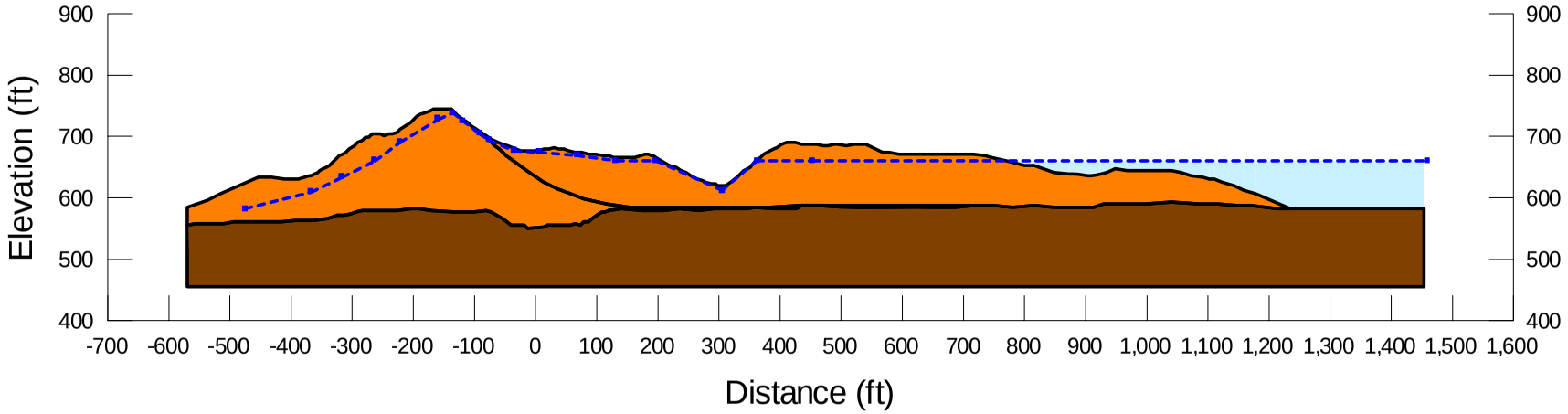

Figure A.14.7(b): Post-failure cross-section of Calaveras dam used for evaluation of $S_{r,,resid/geom}$.

Based on the modeling conditions and assumptions described above, the resulting best estimate value of the post-liquefaction shear strength required for FS = 1.0 with residual geometry is $S_{r,resid/geom} \approx 255$ lbs/ft^2. The approximate range, based on reasonable variations in parameters and modeling details, is $S_{r,resid/geom} \approx 207$ to 313 lbs/ft^2.

Olson (2001) also calculated $S_{r,resid/geom}$ for this case history, but because his values specifically targeted the "shell" zone materials, they are not directly comparable here.

A.14.4(c) Incremental Momentum and Displacement Analyses and Overall Evaluation of Post-Liquefaction strength

Full incremental momentum and displacement analyses were performed using similar modeling assumptions and details as described in the preceding Sections. Figures A.14.8 and A.14.9 show the best estimate case analysis. The modeled geometric failure progression can be seen in Figure A.14.9. A total of eight cross-sections were modeled for this large-displacement case. Figure A.14.10 then shows the associated plots of (1) acceleration vs. time, (2) velocity vs. time and (3) displacement vs. time for the center of gravity of the failure mass.

The resulting best estimate value of post-liquefaction strength for this case was $S_r = 749$ lbs/ft^2. Based on sensitivity analyses, a reasonable range of Sr was judged to be $S_r \approx 622$ to 900 lbs/ft^2.

A.14.5 Evaluation of Representative Penetration Resistance

No significant effort was expended to develop a well-refined characterization of representative penetration resistance for this case history because, as discussed previously in Section A.14.3, it will not be feasible to attempt to cross-correlate penetration resistance in materials that were underconsolidated (and sometimes fines dominated) at the time of the 1918 with penetration resistances measured eight decades later.

Accordingly, as a proxy, the penetration resistance assigned for this case will be the value developed by the 2000 to 2003 studies of Olivia Chen Consultants for the zones considered, as an ensemble, to best represent the zones that controlled the 1918 failure. This value is judged to be $N_{1,60,CS} \approx 15$ blows/ft.

It should be noted that this value is similar to values employed in a number of previous studies, which did employ this case history in development of correlations between Sr and $N_{1,60,CS}$ or similar. If this penetration was to be used in such an effort, it would be necessary to make significant adjustments for both ageing and consolidation effects over the past eight decades, and to employ a number far lower than 15 blows/ft.

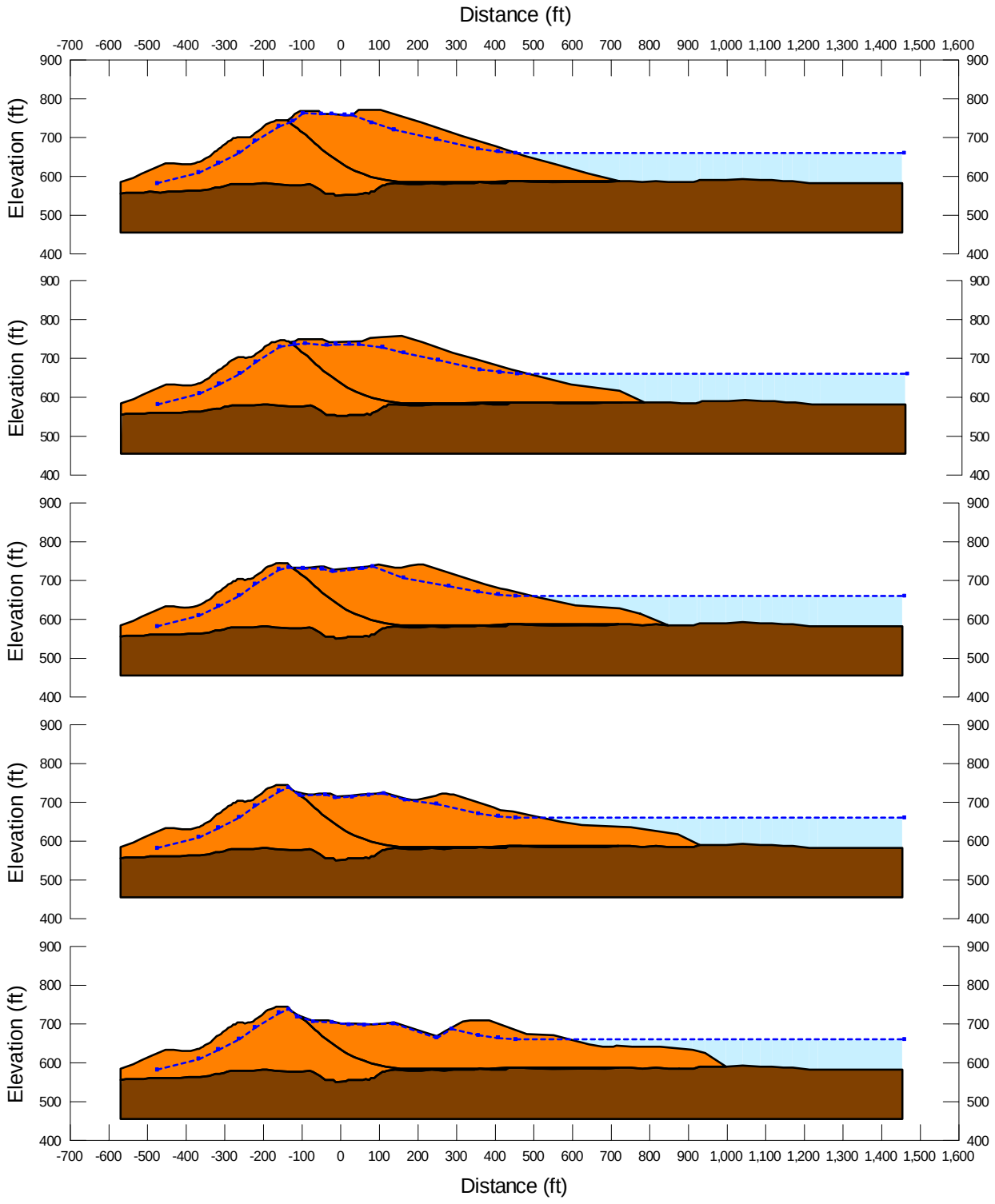

Figure A.14.8: Incremental inertial analysis of the failure of the Calaveras Dam, showing the progressive evolution of cross-section geometry modeled (first five of eight cross-sections).

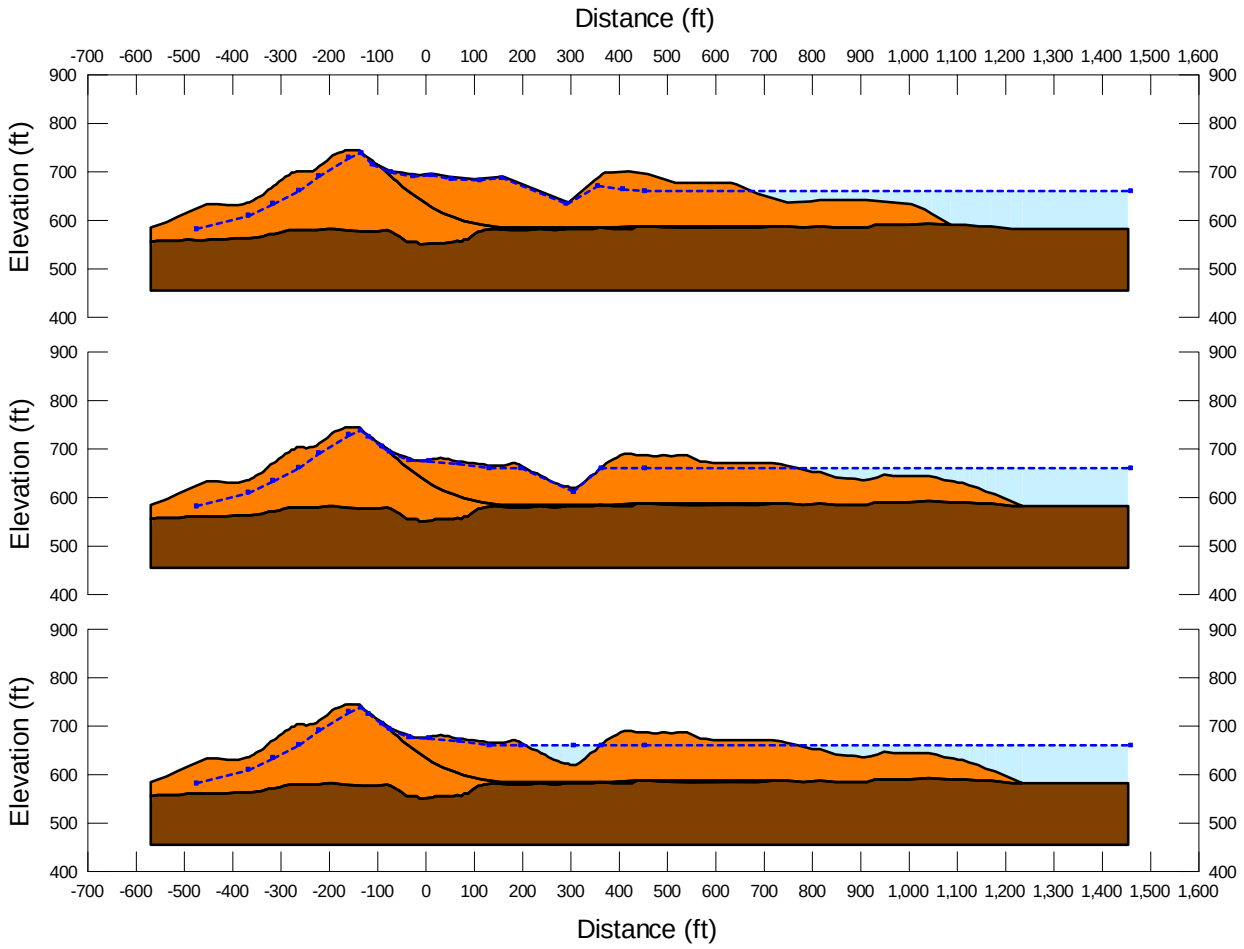

Figure A.14.8(cont'd): Incremental inertial analysis of the failure of the Calaveras Dam, showing the progressive evolution of cross-section geometry modeled (last three of eight cross-sections).

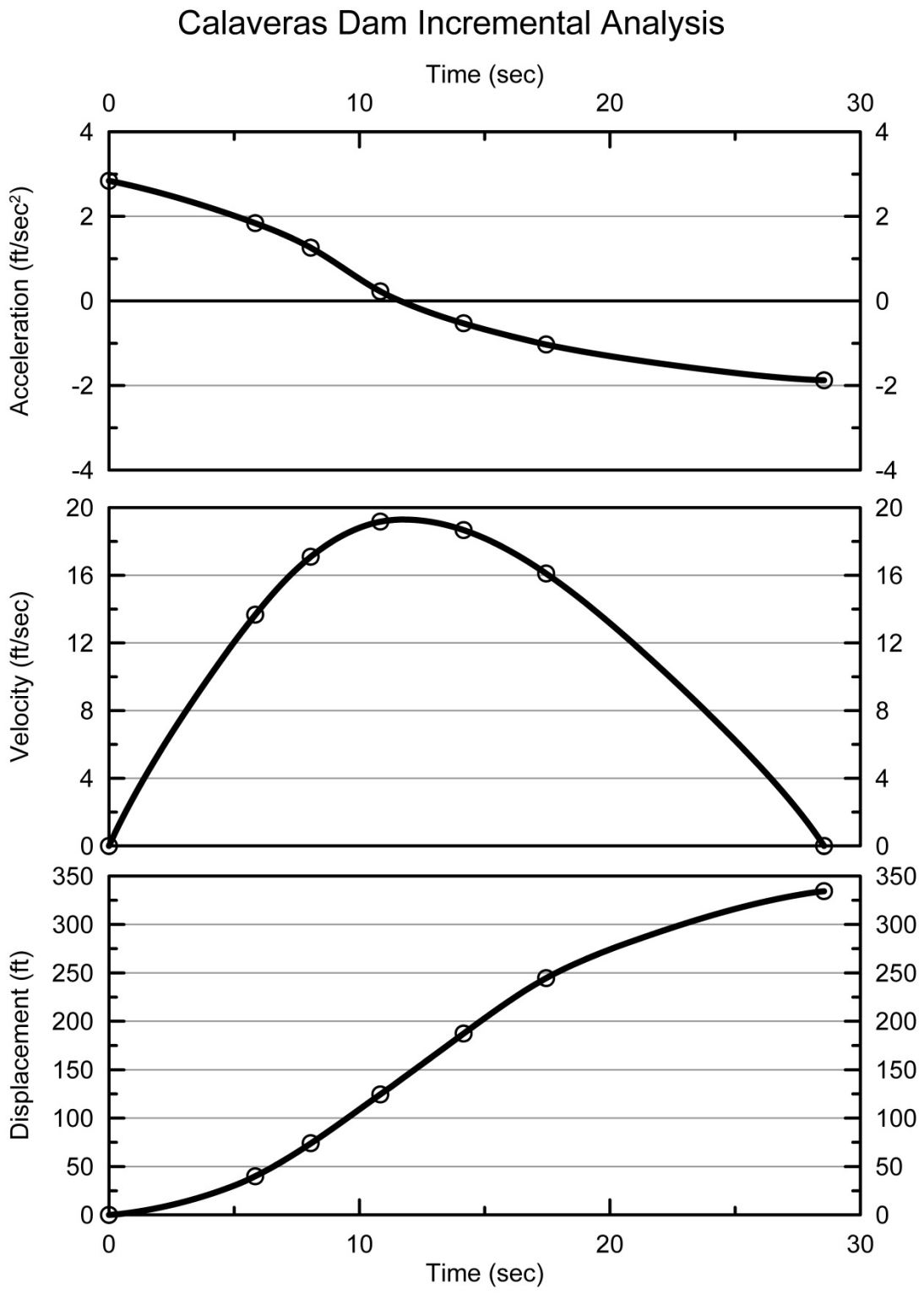

Fig. A.14.9: Incremental inertial analysis of the failure of the Upstream Slope of Calaveras Dam, showing progressive evolution of: (1) acceleration vs. time, (2) velocity vs. time, and (3) displacement vs. time of the overall center of gravity of the failure mass.

A.14.6 Evaluation of Representative Initial Effective Vertical Stress

The overall best estimate value of the average initial effective vertical effective stress on the eventual failure surface was calculated to be $\sigma_{vo}' = 7{,}097$ lbs/ft^2, with a range of $\sigma_{vo}' \approx 5{,}500$ to 8,650 lbs/ft^2.

Olson (2001) also calculated initial effective vertical stresses, but his values specifically targeted the "shell" zone materials, and so they are not directly comparable here.

Wang (2003) also calculated initial vertical stresses for this case, and his value was $\sigma_{\mathbf{vo}}' =$ 6,433 lbs/ft^2, in generally good agreement with these current studies.

A.14.7 Additional Indices from the Back-Analyses

A number of additional results, and indices, can be extracted from the analyses performed. Some of these are useful in developing some of the over-arching relationships and figures presented in the main text of this report. These values are presented in Table A.14.1 below.

Table A.14.1: Additional results and indices from the analyses of the Calaveras Dam embankment failure case history.

Maximum distance traveled by the center of gravity of the overall failure mass	334 ft.
Initial post-liquefaction Factor of Safety prior to displacement initiation, and based on best estimate value of S_r	FS = 0.41
Final post-liquefaction Factor of Safety at final (residual) post-failure geometry, and based on best estimate value of S_r	FS = 2.62

Appendix B:

Back-Analyses of Class B Liquefaction Failure Case Histories

Class B Case Histories:

B.1: Zeeland-Vlieteploder (1889)

B.2: Sheffield Dam (1925)

B.3: Helsinki Harbor (1936)

B.4: Solfatara Canal Dike (1940)

B.5: Lake Merced Bank (1957)

B.6: El Cobre Tailings Dam (1965)

B.7: Metoki Road Embankment (1968)

B.8: Hokkaido Tailings Dam (1968)

B.9: Upper San Fernando Dam – D/S Slope (1971)

B.10: Tar Island Dyke (1974)

B.11: Mochi-Koshi Tailings Dam, Dikes 1 and 2 (1978)

B.12: Nerlerk Embankment, Slides 1, 2 and 3 (1983)

B.13: Nalband Railway Embankment (1988)

B.14: Sullivan Tailings (1991)

B.15: Jamuna Bridge (1994)

B.1 Zeeland - Vlietepolder (Netherlands; 1889)

B.1.1 Brief Summary of Case History Characteristics

Name of Structure	Zeeland - Vlietepolder
Location of Structure	Zeeland Province, Netherlands
Type of Structure	Delta Bank
Date of Failure	September 11, 1889
Nature of Failure	Static, During 1889 Low Tide
Approx. Maximum Slope Height	9.5 ft.

B.1.2 Introduction and Description of Failure

The Dutch Province of Zeeland is in the southwest corner of Holland, fronting the North Sea, and immediately north of Belgium, as shown in Figure B.1.1. This is a very active deltaic area, with deposition of sediments from several large rivers (including the Rhine, Meuse and Scheldt rivers). The rapid deltaic deposition produces large numbers of coastal failures, and Silvis and de Groot (1995) state that several hundreds of coastal slope failures have been reported in this region over the past two centuries.

Most of these failures have occurred primarily in relatively uniformly graded, fine deltaic sands and silty sands, and liquefaction is suspected to be the common causative mechanism. Failures appear to be related to localized over-steepening of coastal and offshore slopes, and these failures are routinely also associated with very low tides suggesting that tidal drawdown and resulting reversal of seepage flow back towards the sea may also contribute to the initiation of many of these slides.

Most of these coastal slides occur mainly below the surface of the sea, and so it is difficult to determine both pre-failure and post-failure cross-section geometries with any confidence. Pre-failure geometries can only reliably be determined if a coastal bathymetric survey was undertaken shortly before the failure, and a concerted effort would be required to ascertain the post-failure geometry at depth of the runout slide mass. As a result, it has not been possible to perform well-constrained back-analyses of most of these failures.

A singular exception was the slide that occurred on September 11, 1889 in a coastal area known as Vlietepolder. Figure B.1.2 shows the pre-failure and post-failure cross-sections for this slide feature (Koppejan et al., 1948). The pre-failure cross section is available because the pre-failure survey was recent enough as to provide a reliable geometry, and the post-failure cross-section was determined shortly after the failure before potentially significant erosion by currents or tides. This slide involved approximately 940,000 m^3 of material, and nearly 60,000 m^3 of land area above the low water mark was lost. Observations made during this failure, and experience with multiple previous failures in this region, suggest that this was a retrogressively progressive failure, and the analyses performed as part of these current studies suggest this as well.

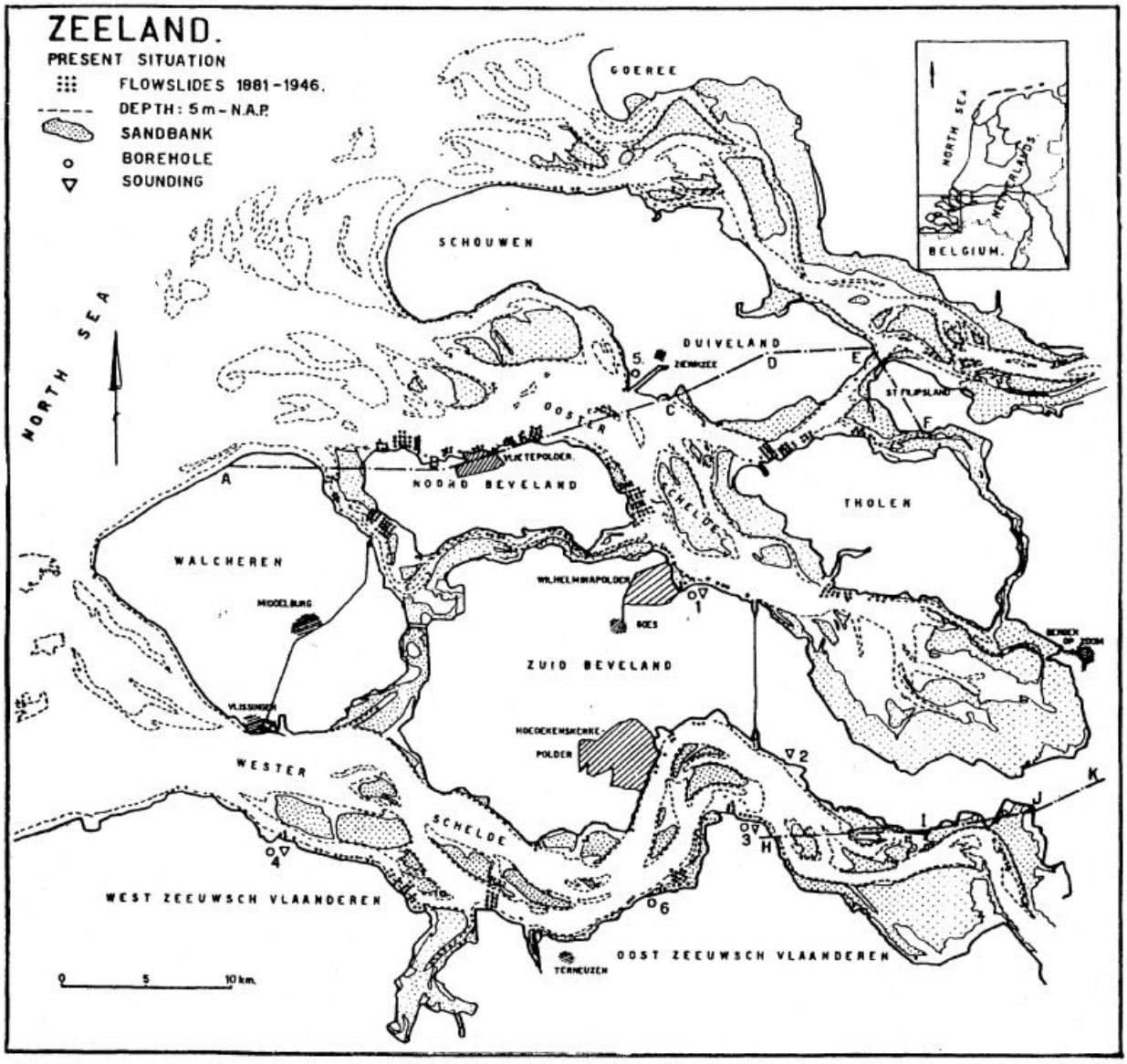

Figure B.1.1: Map of the Zeeland region showing locations of a number of flow slides that occurred between 1881 to 1946 (Koppejan, 1948).

B.1.3 Geology and Site Conditions

The coastal and offshore soils of the Zeeland region are comprised primarily of deltaic deposits from Rhine, Meuse and Scheldt rivers. The uppermost (most recent) deposits are the Holocene age Dunkirk and Calais deposits, and it is within these deposits that the failure occurred. Both the Dunkirk and Calais deposits are comprised mainly of uniformly graded fine sands to clayey sands, deposited primarily as sandy tidal channel sediments with a loose structure (Koppejan et al., 1948), though occasional deposits of peats and clays also occur. These loose sandy soils are notoriously susceptible to liquefaction-induced coastal slides. These Holocene deposits are underlain by Pleistocene deposits of the Twente and Tegelen formations.

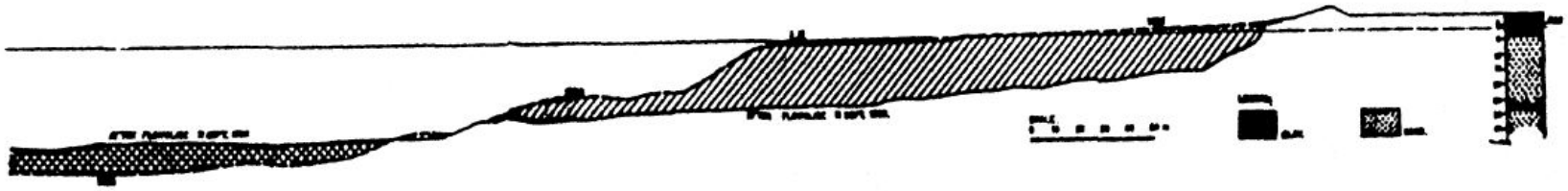

Figure B.1.2: Pre-failure and post-failure cross-sections for the Vlietepolder coastal failure of September 11, 1889 (Koppejan et al., 1948).

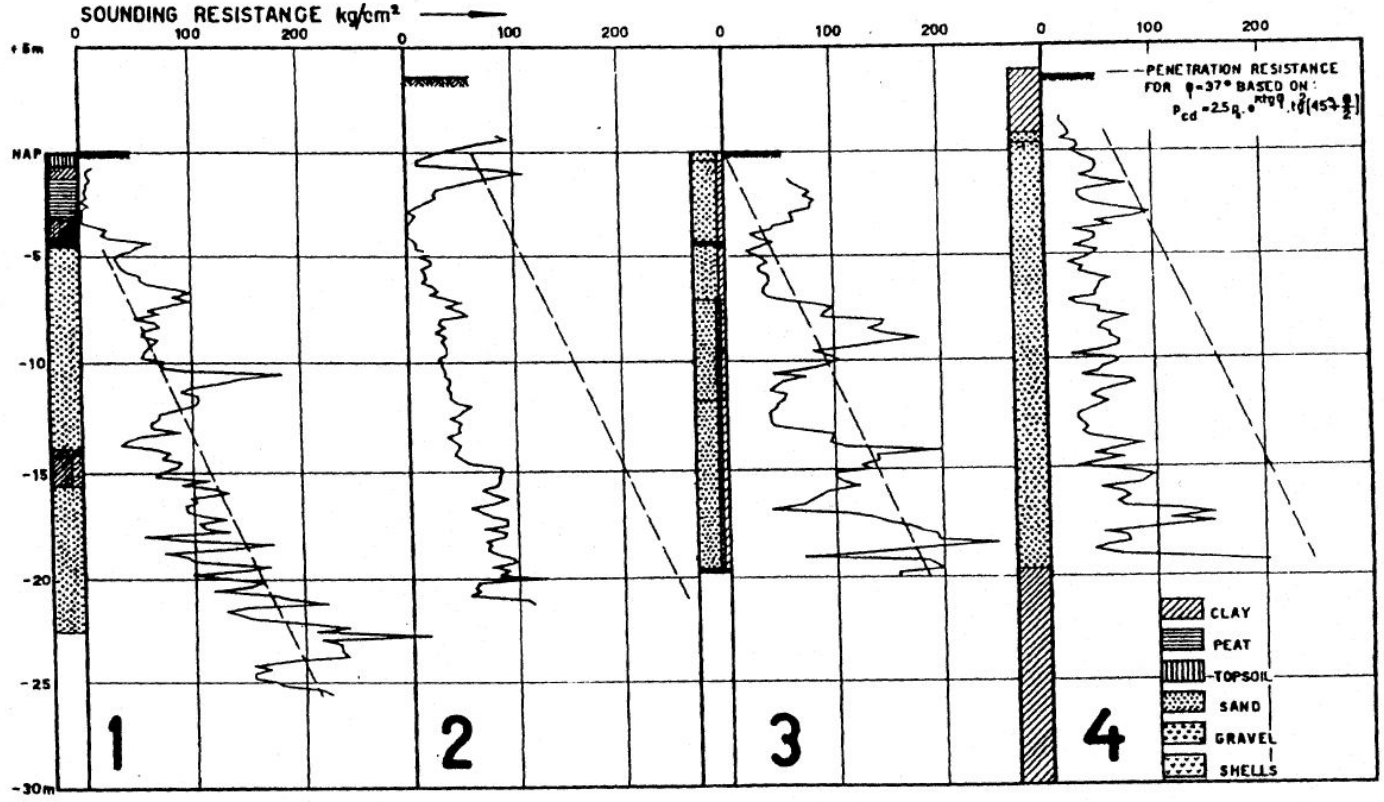

Figure B.1.3: Logs of four mechanical CPT soundings from the Zeeland region (Koppejan et al., 1948).

The Twente formation consists primarily of fine grained aeolian sands and medium grained glaciofluvial sands, and the Tegelen formation consists of generally coarser fluvial sands and gravels, and these older formations are usually denser than the younger Holocene deposits (Silvis and de Groot, 1995). Of the approximately 700 flow slides identified by Ligtenberg-Mak et al. (1990), approximately 75% occurred primarily in Dunkirk channel deposits, 14% in Calais channel deposits, and 1% in older Pleistocene sands.

Figure B.1.3 presents the logs of four mechanical cone penetration soundings from Koppejan et al. (1948). The numbers of the logs correspond to locations shown in Figure B.1.1. None of these soundings were performed at the site of the coastal slope failure of September 11, 1889, but these are considered indicative of the general conditions of the younger Holocene deposits of this region. Conversions to equivalent modern CPT tip resistances are challenging, but Olson (2001) estimated equivalent (and overburden corrected) CPT q_{c1} values for these four soundings, and estimated an average value of $q_{c1} \approx 3.0$ MPa, with lower and upper bounds of approximately 1.7 MPa and 4.4 MPa, respectively. No potentially useful values of SPT blowcounts are known to be available in this region.

B.1.4 Initial Yield Stress Analyses

Figure B.1.4 shows the cross-section used for back-analyses of the post-liquefaction initial yield strength $S_{r,yield}$ that would be required within the liquefied soils to produce a calculated Factor of Safety equal to 1.0. This is not the actual post-liquefaction strength, but it proves to be useful in developing estimates of post-liquefaction strength (S_r) for this case history.

Unit weights of the non-saturated sands and silty sands above the phreatic surface were modeled with a unit weight of $\gamma_m \approx 112$ lbs/ft^3, and this was then varied over a range of 110 to 115 lbs/ft^3 for parameter sensitivity studies. Unit weights of the saturated sands and silty sands below the phreatic surface were modeled with a unit weight of $\gamma_s \approx 117$ lbs/ft^3, and this was then varied over a range of 115 to 120 lbs/ft^3 for parameter sensitivity studies. The friction angle of the non-saturated materials above the phreatic surface was modeled with $Ø' \approx 30°$, and a range of $Ø' \approx 28°$ to 32°.

The available information suggests that this was an incrementally retrogressive failure, and the analyses performed here support this. A number of "initial" potential failure slices were analyzed, and the solid line in Figure B.13.4(a) shows the most critical of these (with the lowest post-liquefaction Factor of Safety). The back-calculated value of $S_{r,yield}$ for this failure surface is $S_{r,yield} = 480$ lbs/ft^2 based on the best estimate soil parameters from above. Additional initial potential failure surfaces were also analyzed, including wedge-like surfaces as well as rotational surfaces, and parameters were varied as described above. Initial failures near the toe of the main slope (as illustrated in Figure B.1.4(a)) dominated the possible initial failure surfaces based on criticality. For these types of initial failure surfaces, the best estimate of the most critical failure surface produced the value of $S_{r,yield} = 430$ lbs/ft^2, and additional analyses of the likely ranges of parameters and potential initial failure surfaces produced a range of approximately $S_{r,yield} = 347$ to 507 lbs/ft^2.

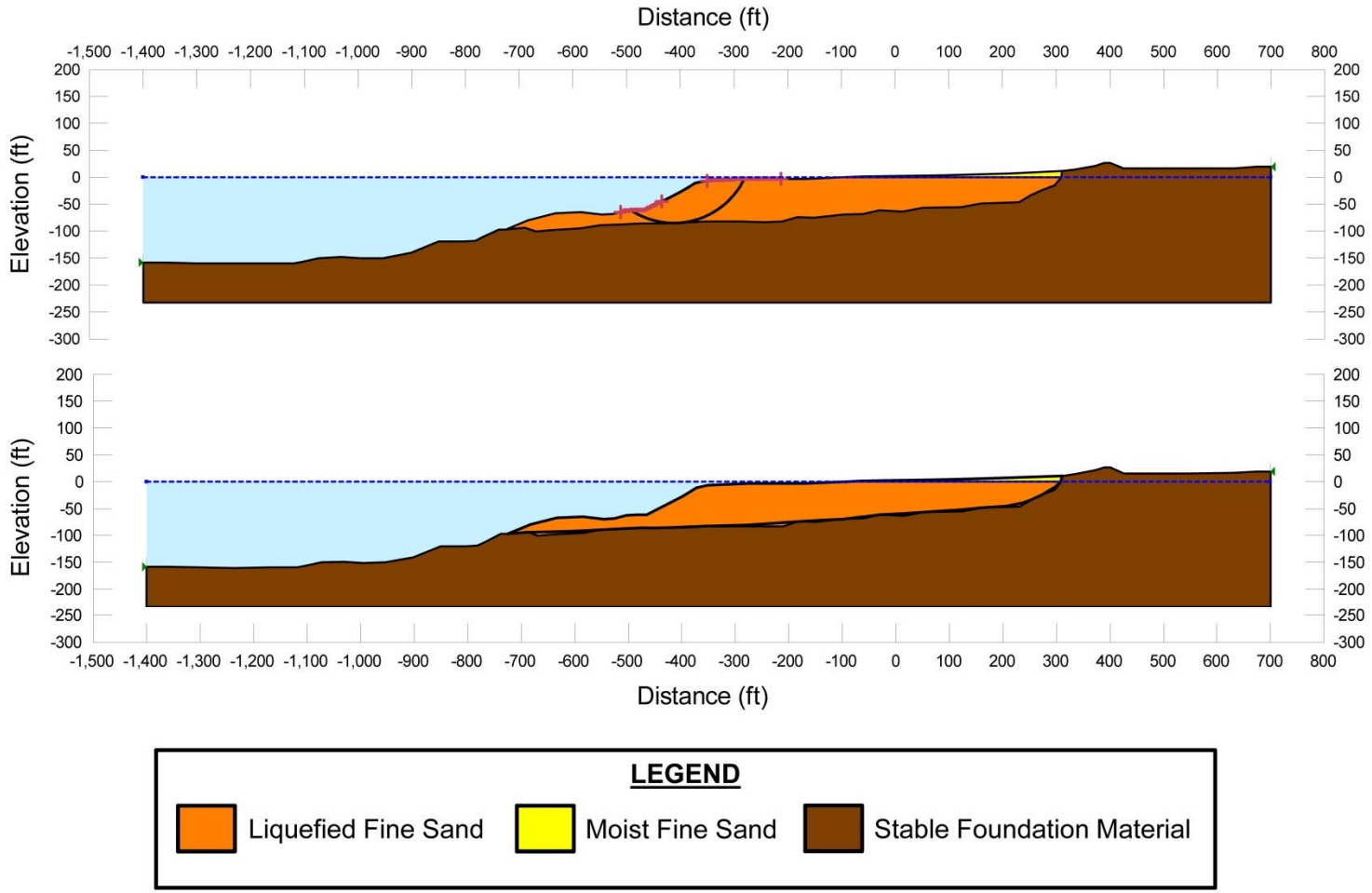

Figure B.1.4: Cross-sections used to perform back-analyses to determine $S_{r,yield}$ for the Zeeland - Vlietepolder slide of September 11, 1889.

Figure B.1.4(b) shows the best estimate of the final (overall) failure surface when retrogressive sliding had progressed fully to the eventual rear-most scarp. For this failure surface, back-analyses produced a best estimate of $S_{r,yield}$ = 248 lbs/ft^2, and a range of approximately $S_{r,yield}$ = 213 to 289 lbs/ft^2. This is not considered likely to represent the actual "yield" value, because it is expected that this was an incrementally progressive retrogressive failure.

The best overall estimate of $S_{r,yield}$ for this case was then by averaging the $S_{r,yield}$ values for smaller initial yield slices with the Sr,yield values for the overall final) slide scarp. Given the geometry of the cross-section, a 2:1 weighted average was used here where

$$S_{r,yield} = [\ 2 \times S_{r,yield}\ (\text{smaller initial yield surface}) + S_{r,yield}\ (\text{final overall failure scarp})] / 3$$

Based on the range of variations in properties and parameters, and a range of potential failure mechanisms and associated feasible failure surfaces, the resulting best estimate overall of "representative" $S_{r,yield}$ was found to be $S_{r,yield}$ = 369 lbs/ft^2, with a range of $S_{r,yield} \approx$ 302 to 434 lbs/ft^2.

Olson (2001) also performed back-analyses to estimate $S_{r,yield}$. He analyzed a suite of rotational potential failure surfaces generally similar to those shown in Figure B.1.4(a), and his best estimate of $S_{r,yield}$ was 16.1 kPa (336 lbs/ft^2), with a range of 15.0 to 16.8 kPa (313 to 350 lbs/ft^2).

B.1.5 Residual Strength Analyses Based on Residual Geometry

It was not possible to perform rigorous and reliable back-analyses to determine the value of $S_{r,resid/geom}$ required to produce a calculated Factor of Safety equal to 1.0 based on residual geometry. This case is one of six cases (out of the 29 cases back-analyzed as part of these current studies) where the slide mass "went over a lip" and then traveled down a steeper slope, and the ensuing displacements either (1) could not be reliably tracked, or (2) could not be reliably back-analyzed. Both situations apply in this current case because the post-failure geometry of the failure mass runout is largely undefined. The cross-section provided by Koppejan et al. (1948), as presented in Figure B.1.2, shows only a portion of the failure mass runout. A majority of the displaced failure mass is unaccounted for and will occur to the left of the figure. This is a significant source of uncertainty for this case history.

In these current studies, it was assumed that $S_{r,resid/geom}$ would have at least been higher than zero. Values of $S_{r,resid/geom}$ back-calculated from the reasonably well-documented Class A case histories were next examined, and for the range of effective overburden stress and $N_{1,60,CS}$ values for this current case an approximate range of $S_{r,resid/geom} \approx$ 70 to 170 lbs/ft^2 was conservatively assumed, based on analyses of other Class A and B case histories. This range of values was selected to be slightly conservatively biased (a conservative bias of approximately 10% reduction of best estimates of $S_{r,resid/geom}$ was targeted here), so that any resulting error in evaluation of overall S_r would also be slightly conservative (nominally by approximately 5% or so).

It is interesting to note that this range of $S_{r,resid/geom} \approx 70$ to 170 lbs/ft^2 agrees fairly well with the range developed by Olson (2001), based on alternate approaches, as described below.

Based on what he acknowledged to be the "incomplete" post-failure geometry of Figure B.1.2, Olson assumed an infinite slope with a top and base slope of 4°, and a best estimate thickness of the final runout materials of 8.5 m. (and a range of thicknesses of 7 to 10 m.), and calculated $S_{r,resid/geom} \approx 5.5$ kPa (115 lbs/ft^2), with a range of $S_{r,resid/geom} \approx 4.5$ to 6.5 kPa (94 to 136 lbs/ft^2). Olson's range is somewhat narrower than the range (70 to 170 lbs/ft^2) used in these current studies, but the two ranges are "centered" at approximately the same values, despite the different approaches and assumptions employed.

B.1.6 Overall Estimates of S_r

Overall estimates of S_r for this Class B case history were made based on the pre-failure geometry, the partial post-failure geometry, and the approximate runout features and characteristics, and the values of $S_{r,yield}$ and $S_{r,resid/geom}$ as calculated and/or estimated in the preceding sections.

Runout characteristics for this case cannot be accurately assessed due to the incomplete post-failure cross section as reported. Runout distance, and runout ratio, appear to be "large", but the failure mass travelled out over a "lip" at the toe of the slide scarp, and then down what may at least initially been a steeper slope.

Runout ratio (defined as runout distance traveled by the center of gravity of the overall failure mass divided by the initial slope height from toe to back heel of the failure) was taken to be at least medium to large. This allowed Equation 4-4, and Figures 4.7 and 4.11 to serve as one basis for estimation of post-liquefaction strength S_r. Using the ranges of $S_{r,yield}$ and $S_{r,resid/geom}$ from Sections B.13.4 and B.13.5, and assuming that $\xi \approx 0.4$ to 0.65 for this large runout case, with 0.525 as the best estimate, provided a best estimate value of $S_r \approx 128$ lbs/ft^2 and an estimated range of $S_r \approx 74$ to 196 lbs/ft^2. A second basis for estimation of S_r was the use of the relationship of Figure 4.9, and the range of values of $S_{r,yield}$ from Section B.5.4. Based on the large runout distance, values of initial (pre-failure displacement) Factor of Safety were taken as approximately 0.4 to 0.6, and this produced a best estimate value of $S_r \approx 185$ lbs/ft^2 and an estimated range of $S_r \approx 121$ to 260 lbs/ft^2. No similar use was made of Figure 4.9 in conjunction with the ranges of $S_{r,resid/geom}$ estimated in Section B.4.5 because these estimates of $S_{r,resid/geom}$ were considered to be very approximate.

The estimates by each of the two methods above were then averaged together, and this produced a best estimate value of $S_r \approx 156$ lbs/ft^2 and an estimated range of $S_r \approx 74$ to 260 lbs/ft^2. These estimates of variance are non-symmetric about the best estimated mean value, and the range was judged to represent approximately +/- 2.5 standard deviations, so further adjustments were then necessary.

Overall, based on an assumed normal distribution, it was judged that the (mean and median) best estimate of post-liquefaction strength for this case history is

$$\overline{S_r} = 156 \text{ lbs/ft}^2$$

and that the best estimate of standard deviation of mean overall post-liquefaction strength is

$$\sigma_{\overline{S}} = 37 \text{ lbs/ft}^2$$

Olson (2001) and Olson and Stark (2002) did not apply their "kinetics" method to this case, and so they did not independently develop an estimate of S_r that incorporated momentum effects. Instead they simply used their value of $S_{r,resid/geom}$ as a conservative approximation of S_r for this less well-defined case, and used S_r = 5.5 kPa (115 lbs/ft^2), with a range of 4.5 to 6.5 kPa (105 to 155 lbs/ft^2) in developing their predictive relationship. Because these values are based on residual post-failure geometry with an assumed Factor of Safety equal to 1.0, they do not include momentum effects and so they will be too low.

A better basis for comparison would be to taek Olson's back-calculated values of Sr,yield and Sr,resid/geom, and then use Equation 4-1 which estimates Sr as

$$S_r \approx \xi \bullet (S_{r,yield} + S_{r,resid/geom}) / 2 \qquad \text{[Eq. 4-1, repeated]}$$

with $\xi \approx 0.8$ as a first-order approximation. The result would then be an estimated value of $S_r \approx$ 180 lbs/ft^2, in reasonably good agreement with these current studies.

Similarly, Wang (2003) and Wang and Kramer (2008) did not employ their zero inertial force (ZIF) method to incorporate inertial effects in back-analyses of this failure. Instead they selected their value of S_r based on selection and then averaging of back-analyses results of several previous investigators. For this case Wang (2003) selected only a "modified" value based on Olson's values of $S_{r,yield}$ and $S_{r,resid/geom}$, but with a value of ξ = 1.0 (rather than 0.8). That would tend to moderately over-estimate the actual value of S_r for this case. The resulting value would be $S_r \approx$ 180 lbs/ft^2, as listed in Tables 4.3 and 4.6.

B.1.7 Evaluation of Initial Effective Vertical Stress

Average initial (pre-failure) effective vertical stress was assessed for the liquefied portion of the overall (final scarp) failure surface in Figure B.13.4. Parameters and sensitivity analyses were as described previously in Section B.13.4. Additional analyses were then performed for alternate potential failure surfaces, including failure surfaces initial slices of a retrogressive incremental failure eventually extending back to the apparent back heel of the final failure. Depths of failure surfaces were varied, and both rotational and translational (wedge-like) failure surfaces were considered. When an initial (smaller) slice of a retrogressive failure was analyzed, the resulting average value of σ_{vo}' was then averaged with the value of the overall (Final slide scarp), and this averaged value of the two failure surfaces was taken as "representative" here. This produced a moderately large, but finite, range of estimated values of average pre-failure effective stress within the liquefied materials controlling the failure.

The resulting best estimate of average pre-failure effective stress within the liquefied materials controlling the failure was then $\sigma_{vo}' \approx 2{,}471$ lbs/ft^2, with a reasonable range of $\sigma_{vo}' \approx$ 1,626 to 3,350 lbs/ft^2. This range is slightly non-symmetric about the median value, and this range was judged by the engineering team to represent approximately ± 2 standard deviations. Overall, the best characterization of initial (pre-failure) average effective vertical stress was then taken to be represented by a mean value of

$$\overline{\sigma'_{vo}} \approx 2{,}488 \text{ lbs/ft}^2$$

and with a standard deviation of

$$\sigma_{\bar{\sigma}} \approx 431 \text{ lbs/ft}^2$$

An estimate of σ_{vo}' was also calculated by Olson and Stark (2001, 2002). They reported a weighted average mean value of $\sigma_{vo}' \approx 115$ kPa (2,401 lbs/ft^2), and a range of 57 to 172 kPa (1,190 to3,592 lbs/ft^2), in excellent agreement with these current studies. Average initial vertical effective stresses were not directly reported by Wang (2003) and Kramer (2008), but they were published more recently in the publication by Kramer and Wang (2015). As discussed in Section 2.3.8.1(b)-(iii), Wang (2003) did not perform any independent analyses to assess σ_{vo}' for his 22 "secondary" cases, and this is one of those cases. Instead, he compiled values of S_r from multiple previous investigators, and averaged these for a best estimate. He also compiled multiple values of S_r/σ_{vo}' from previous investigators, and averaged these for a best estimate. He then used these two best-estimate values of S_r and S_r/σ_{vo}' to infer a resulting representative value of σ_{vo}'. As described in Section 2.3.8.1(b)-(iii), the resulting averaged values of S_r and of S_r/σ_{vo}' were incompatible with each other for a number of Wang's "secondary" case histories, and this process produced unreasonable, and in some cases physically infeasible, values of σ_{vo}' for a number of case histories. Wang's value of $\sigma_{vo}' = 4{,}708$ is clearly physically infeasible for this case, based on the cross-section, and so it is not considered a useful check here. Agreement between Olson's value, which is well-documented, and the values developed in these current studies is excellent.

B.1.8 Evaluation of $N_{1,60,CS}$

As explained previously in Section B.1.3, there were no published standard penetration test data for this failure case history, and no site specific penetration data of any kind. As a result, there is considerable uncertainty with regard to selection of representative $N_{1,60,CS}$ values for this case history.

Olson (2001) and Olson and Stark (2002) reprocessed the four logs of mechanical cone soundings from Figure B.1.2, and estimated an average value of $q_{c1} \approx 3.0$ MPa, with lower and upper bounds of approximately 1.7 MPa and 4.4 MPa, respectively. These conversions to equivalent modern CPT values are challenging. They then further converted these estimated CPT tip resistances to estimated SPT $N_{1,60}$ values, producing a best estimate representative value of $N_{1,60} = 7.5$ blows/ft, and a range of 4.2 to 10.9 blows/ft. These are $N_{1,60}$ values, and they

include no fines adjustment. Given the low to moderate reported clayey fines content of the sediments, fines adjustment to $N_{1,60,CS}$ values would be expected to increase these values.

Wang (2003) and Kramer (2008) selected a slightly higher fines adjusted value of $\overline{N_{1,60,CS}}$ ≈ 8.5 blows/ft., and a very high standard deviation of $\sigma_{\overline{N}}$ ≈ 5.5 blows/ft. Precise details are not presented, but it is noted here that a high standard deviation is potentially justified based on the overall uncertainties involved. This high standard deviation would produce negative values of $N_{1,60,CS}$ at a mean minus 1.55 standard deviations level, and at a mean plus two standard deviations level would produce a value of $N_{1,60,CS}$ ≈ 19.5 blows/ft, which would appear to be high for the materials as described and as they performed. These upper and lower values (even the low probability negative values) are not mathematically problematic in the framework of the regressions subsequently performed by Kramer (2008) to develop predictive correlations, but this standard deviation is somewhat larger than the one employed in these current studies.

In these current studies, the principal overall uncertainties were considered to be: (1) use of the sparse available mechanical cone penetration logs/data from four sites not located or near to the actual site of the failure, and with four different tip resistance profiles and signatures, (2) conversion of (now historic) mechanical cone data to equivalent modern CPT tip resistances, and (3) conversion of CPT tip resistances to equivalent SPT $N_{1,60,CS}$ values. Overall uncertainties (and variance or standard deviation of the mean value) with regard to resulting values of $N_{1,60,CS}$ will necessarily be high. Advice was sought from Robertson (2014) regarding interpretation of the mechanical cone tip resistances and conversion to equivalent modern CPT tip resistances. Several methods were taken to estimate conversion of the resulting CPT tip resistances to equivalent SPT $N_{1,60,CS}$ values, with adjustments as necessary to the SPT fines corrections being employed in these current studies. Considering the ranges of values produced, and the overall uncertainties, an overall best estimate value of $\overline{N_{1,60,CS}}$ ≈ 8 blows/ft. was selected, with a standard deviation of this mean of $\sigma_{\overline{N}}$ ≈ 2.1 blows/ft.

Overall agreement with regard to characterization of $N_{1,60,CS}$ (and $N_{1,60}$) among these two previous studies, and the current study, is considered to be very good for this case, with the exception of characterization of variance (or standard deviation) of the mean value of $\overline{N_{1,60,CS}}$.

B.2 Sheffield Dam (California, USA; 1925)

B.2.1 Brief Summary of Case History Characteristics

Name of Structure	Sheffield Dam
Location of Structure	California, USA
Type of Structure	Zoned Embankment Dam
Date of Failure	June 29, 1925
Nature of Failure	Seismic, During 1925 Santa Barbara Earthquake (M_L = 6.3)
Approx. Maximum Slope Height	25 ft.

B.2.2 Introduction and Description of Failure

The Sheffield Dam suffered a catastrophic liquefaction-induced translational failure during the 1925 Santa Barbara earthquake (M_L = 6.3). The epicenter of the earthquake was located approximately seven miles northwest of the dam, and Seed et al. (1969) estimated the peak ground surface acceleration at the dam at approximately 0.15g. There were no local ground motion records obtained. Local witnesses reported that shaking lasted approximately 15 to 18 seconds, but there is no instrumental confirmation of either this estimated level or duration of shaking.

Figure B.2.1 shows the approximate pre-failure cross-section and reservoir water level (Seed et al., 1969). At the time of the failure, the reservoir surface was approximately halfway up the concrete-lined upstream face of the dam.

Figure B.2.2 shows a photograph of the dam shortly after the failure (Engineering News Record, 1925), and Figure B.2.3 shows a plan view of the approximate post-failure configuration (Engineering News Record, 1925).

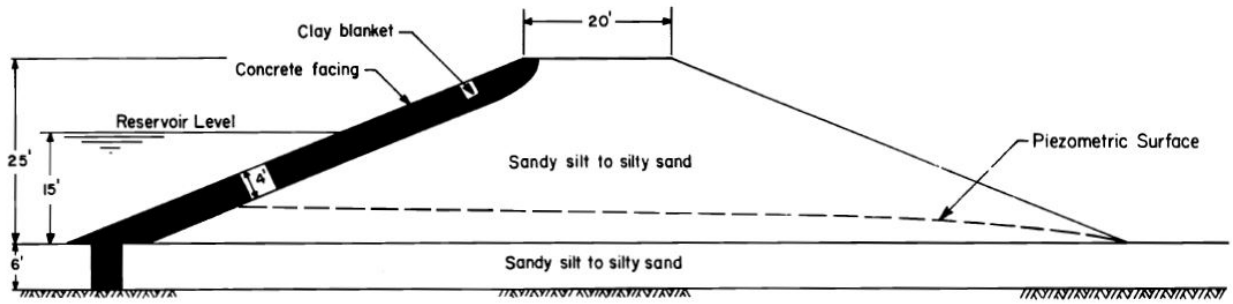

Figure B.2.1: Cross-section through the original embankment of the Sheffield Dam (Seed et al., 1969).

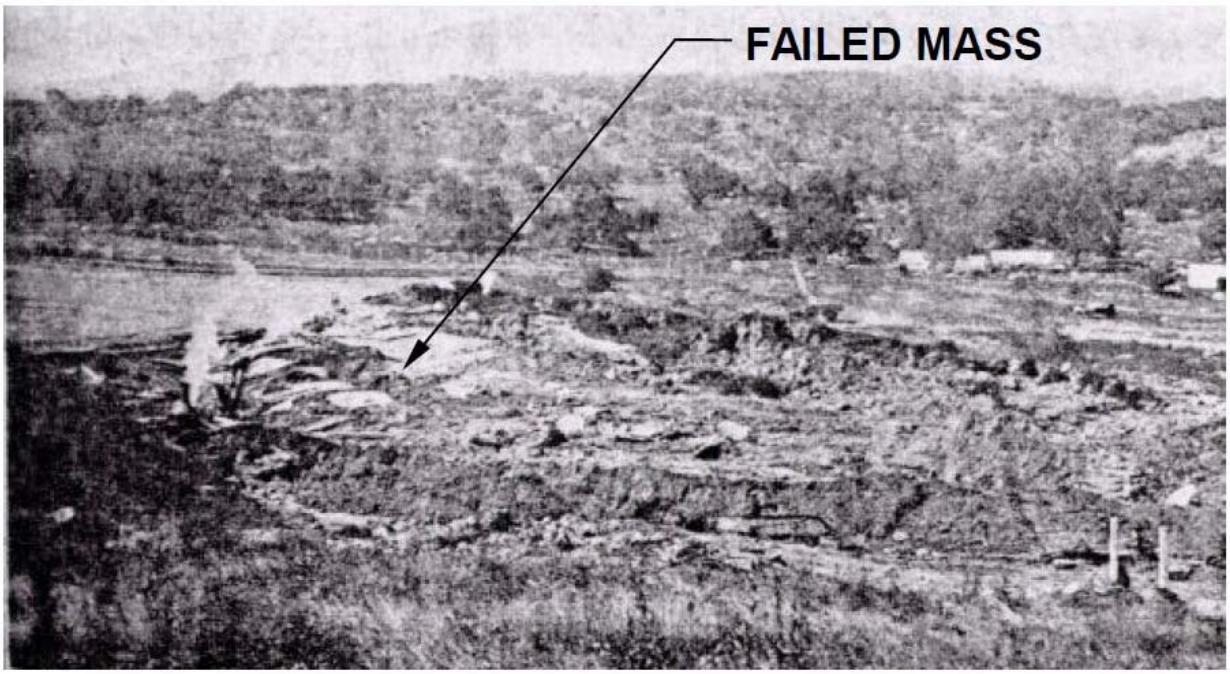

Figure B.2.2: Post-failure photograph of the Sheffield Dam (Photo from Engineering News Record, 1925).

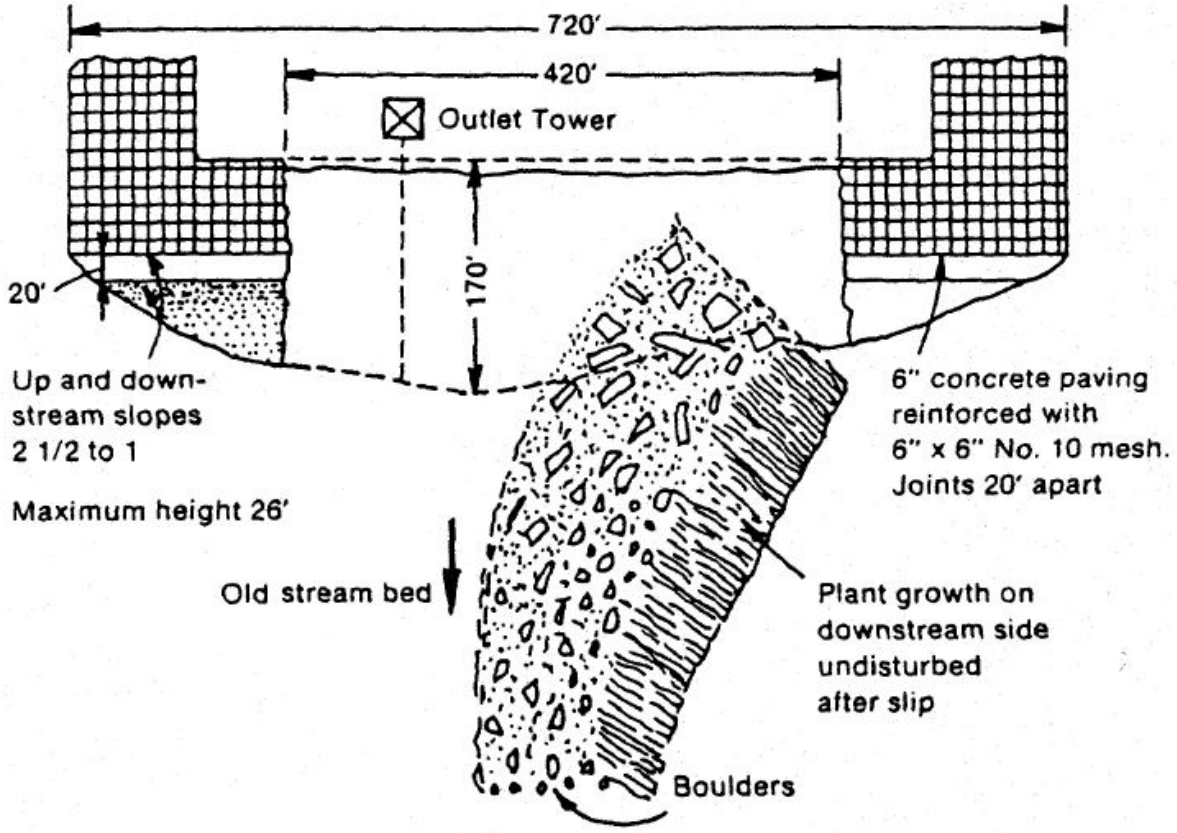

Figure B.2.3: Plan view showing post-failure conditions (Engineering News Record, 1925).

There were no eyewitnesses to the failure, but a number of engineers examined the dam after the failure had occurred. It appeared that the failure had occurred as a largely translational failure, with the failure surface located approximately at the base of the earthen embankment, and with the primary slippage occurring in either the lower embankment soils or the upper foundation soils immediately below. A section of the embankment dam approximately 530 feet in length had traveled a maximum distance of approximately 200 feet, and much of it remained largely intact during these movements. As this failure mass traveled, it rotated in a counter-clockwise direction, reaching the final position shown in Figures B.2.2 and B.2.3.

Although both the Wachusett Dam and Calaveras Dam liquefaction failures had previously occurred, soil liquefaction was still not generally well understood in 1925, so it is interesting to note that Willis (1925) surmised: "The foundations of the dam had become saturated and the rise of water as the ground was shaken formed a liquid layer of sand under the dam, on which it floated out, swinging about as if on a hinge." This was an apt description of the failure.

B.2.3 Geology and Site Conditions

The dam had been constructed in 1917 to serve as a reservoir for the Santa Barbara Municipal Water Department. The earthen dam embankment had a maximum crest height of approximately 25 feet, and a crest length of approximately 220 feet. After the failure, the dam was reconstructed with a more conservative cross-section.

The original (pre-failure) dam embankment was constructed across a ravine in recent alluvial terrace deposits. The U.S. Army Corps of Engineers (1949) studied the dam, and determined that there had been no stripping of these alluvial terrace deposits beneath the footprint of the original dam. Because the reconstruction of the dam after the failure had included stripping of these upper foundation materials beneath the reconstructed footprint, the USACE performed a suite of five borings closely adjacent to (and downstream) of the reconstructed dam in order to characterize the likely conditions beneath the original dam. The alluvial terrace deposits were found to consist primarily of loose silty sand, with fines contents of approximately 33% to 48%. Atterberg Limits tests subsequently performed by Seed et al. (1969) found the silt fines to be low plasticity silts with PI ≈ 4%, and LL ≈ 24%. In-situ density tests of these silty sands indicated dry unit weights of $\gamma_d \approx 89.7$ lbs/ft^3 in the upper one to three feet or so, and significantly higher unit weights of $\gamma_d \approx 101.1$ lbs/ft^3 at greater depths. Seed et al. (1969) determined the maximum dry density by the Standard Proctor Compaction Test (ASTM D698) for these silty sands to by $\gamma_{d,max} \approx 118.0$ lbs/ft^3, indicating that the very loose upper several feet of foundation material were at an equivalent Relative Compaction of approximately RC = 76% (Std. Proctor). These were very loose silty sands and sandy silts, and it is within this relatively thin veneer of loose, saturated, upper foundation soils that the liquefaction-induced failure and slippage appears to have occurred.

The original dam embankment was constructed of these same silty sands and sandy silts, excavated (borrowed) from within the reservoir footprint. The embankment fill was placed in lifts, but was compacted only by means of routing of light construction vehicles over the

evolving fill; there was no formal compaction, and no useful vibratory compaction was employed. As a result, these embankment materials were also loose, saturated silty sands and sandy silts, and so it is also possible that the failure occurred in part due to liquefaction of the loose, saturated silty sands and sandy silts at the base of the embankment fill. It is unlikely, however, that this lightly rolled fill was actually looser than the top veneer of the underlying foundation soils, and so it has generally been assumed (e.g. Seed et al., 1969; Seed and Harder, 1990; Olson, 2001, etc.) that the failure was due to liquefaction-induced loss of strength of the very loose upper foundation soils immediately beneath the embankment. These current studies will also take this view.

The original embankment had an upstream side facing consisting of a concrete facing 6-inches in thickness, underlain by a clay blanket approximately 3.5 feet in thickness. This served to constrain the flow through the embankment. There were no data upon which to base estimates of the phreatic surface through the dam at the time of the failure. The phreatic surface shown in Figure B.2.1 was based on judgment, and a similar phreatic surface is assumed in these current studies. Back-analyses of this failure case history are not very sensitive to minor changes in this assumed phreatic surface, so long as the upper foundation soils are modeled as saturated.

B.2.4 Initial Yield Stress Analyses

Figure B.2.4 shows the cross-section used for back-analyses of the post-liquefaction initial yield strength $S_{r,yield}$ that would be required within the liquefied upstream shell materials to produce a calculated Factor of Safety equal to 1.0. This is not the actual post-liquefaction strength, but it proves to be useful in developing estimates of post-liquefaction strength (S_r) for this case history.

As explained in the preceding sections, failure is assumed to have occurred primarily due to liquefaction of the very loose silty sands of the upper few feet of the foundation soils immediately underlying the embankment fill.

Unit weights of the non-saturated embankment silty sands above the phreatic surface were modeled with a unit weight of $\gamma_m \approx 115$ lbs/ft^3, and this was then varied over a range of 112 to 118 lbs/ft^3 for parameter sensitivity studies. Unit weights of the saturated silty embankment sands below the phreatic surface were modeled with a unit weight of $\gamma_s \approx 120$ lbs/ft^3, and this was then varied over a range of 117 to 123 lbs/ft^3 for parameter sensitivity studies. The friction angle of the loose silty sands above the phreatic surface was modeled with $Ø' \approx 30°$, and a range of $Ø' \approx 28°$ to 33°.

A number of potential failure surfaces were analyzed, including (1) monolithic sliding along the full base of the entire embankment, and (2) smaller initial failures nearer to the downstream side, followed by (assumed) retrogressive propagation of the failure back towards the upstream side. These back-analyses showed that it was likely that this had been a retrogressive failure, initiating with a failure slice or wedge on the downstream side and then progressing, on a slice by slice basis, eventually back to the reservoir side. The depth that the failure surface penetrates into the foundation soils was also varied during the sensitivity studies.

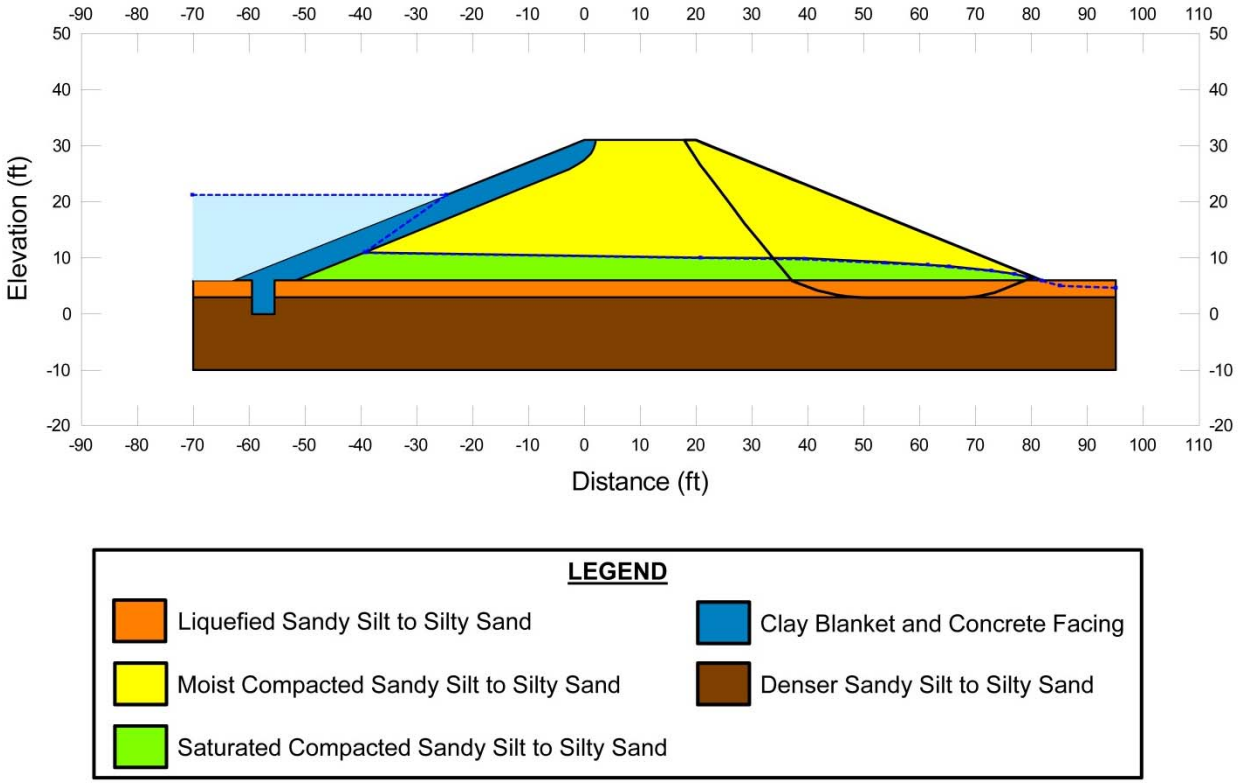

Figure B.2.4: Cross-section of Sheffield Dam used to back-calculate $S_{r,yield}$, showing the most critical initial failure surface.

Seed et al. (1969) had concluded that the entire base of the dam had liquefied, and that the reservoir pressures against the concrete-lined upstream face had then had pushed the dam downstream. These current studies found that to be unlikely, at least in the simplified manner described. Instead this appears likely to have been an incrementally retrogressive slide, initiated by liquefaction along the full base of the embankment, but with the first failure slices initiating nearer the downstream side. The failure then likely progressed incrementally back towards the upstream side, where reservoir pressures against the increasingly unbraced upstream face eventually produced a breach. The photograph and plan view of Figures B.2.2 and 2.2.3 are inconclusive here, suggesting some degree of de-aggregation of the slide mass but shedding no conclusive light on the question as to whether (1) the slide mass de-aggregated (incrementally) before the failure reached the reservoir side, or (2) the slide mass initiated movements monolithically and then de-aggregated as it traveled.

If the slide had initiated monolithically, then the post-liquefaction initial yield strength would have been the lateral force applied by the reservoir to the upstream face divided by the area of the base of the embankment. This would produce a calculated value of $S_{r,yield} \approx 51$ lbs/ft^2.

Initial failure of smaller slide features nearer to the downstream face (as the beginning stage of a retrogressive failure) appears more likely, based on these back-analyses, and the most critical potential failure surface of this type is shown in Figure B.2.4. Based on the parameters described above, this failure surface results in a best estimate value of $S_{r,yield}$ = 345 lbs/ft^2, with a range of $S_{r,yield} \approx$ 299 to 370 lbs/ft^2.

Olson also performed back-analyses to estimate $S_{r,yield}$. He also assumed that the failure was retrogressive, and that an initial failure slice initiated first near the downstream side. His assumed initial failure surfaces were wedge-like failures similar to the failure shown in Figure B.2.4, except that (1) he assumed that the very loose upper foundation soils extended to slightly greater depths (approximately 7 feet below the base of the embankment), and (2) his toe failures exited farther downstream of the toe of the embankment. Olson's back-calculated best estimate of $S_{r,yield}$ was 15.4 kPa (321 lbs/ft^2), with a range of 12.7 to 18.0 kPa (265 to 376 lbs/ft^2). These appear to be in excellent agreement with the values back-calculated in these current studies.

B.2.5 Residual Strength Analyses Based on Residual Geometry

It was not possible to perform rigorous and reliable back-analyses to determine the value of $S_{r,resid/geom}$ required to produce a calculated Factor of Safety equal to 1.0 based on residual geometry because the post-failure residual geometry could not be suitably reliably determined based on the available information and data. The reported post-failure conditions, and the available photographs (e.g. Figure B.2.1) clearly show that the post-liquefaction strength was greater than zero, but they do not provide a basis for very refined estimates. This is a principal source of uncertainty for this case history.

Olson (2001) attempted to estimate the slopes and thicknesses of the post-failure residual embankment geometry based on available photographs, and then performed a simplified infinite slope analysis (for assumed residual, static conditions). The approximate slope angle used was not stated, nor the soil thicknesses, but the result was a reported best-estimate value of $S_{r,resid/geom}$ = 4.0 kPa (84 lbs/ft^2), with no range given.

In these current studies, it was assumed that $S_{r,resid/geom}$ would have at least been higher than zero. Values of $S_{r,resid/geom}$ back-calculated from the reasonably well-documented Class A case histories were examined for insight as to "expected" ranges of post-liquefaction strengths, and for the range of effective overburden stress and $N_{1,60,CS}$ values for this current case an approximate range of $S_{r,resid/geom} \approx 70$ to 140 lbs/ft^2 was conservatively assumed, based on analyses of other Class A and B case histories. This range of values was selected to be slightly conservatively biased (a conservative bias of approximately 20% reduction of best estimates of $S_{r,resid/geom}$ was targeted here), so that any resulting error in evaluation of overall S_r would also be slightly conservative (nominally by approximately 10% or so). It is interesting to note that the mid-range value here would be 105 lbs/ft^2, in fairly good agreement of with the value of $S_{r,resid/geom}$ calculated and reported by Olson (2001) as described in the preceding paragraph.

B.2.6 Overall Estimates of S_r

Overall estimates of S_r for this Class B case history were made based on the observed geometry and runout features and characteristics, and the values of $S_{r,yield}$ and $S_{r,resid/geom}$ as calculated or estimated in the two preceding sections.

Runout characteristics for this case include a runout distance travelled by the center of gravity of the overall failure mass of D ≈ 125 feet, and a slope height (from toe to top of the back scarp) of H = 25 feet, producing a runout ratio of D/H ≈ 6. This led to a best estimate of $\xi \approx 0.5$ with a likely range of $\xi \approx 0.4$ to 0.6. Based on the relationship of Equation 4-4 and Figure 4.11, and best estimate values (and ranges) of $S_{r,yield}$ and $S_{r,resid/geom}$ from the preceding Sections B.6.4 and B.6.5, this produces and an overall best estimate of $S_r \approx 112$ lbs/ft^2, and a range of $S_r \approx 74$ to 153 lbs/ft^2. Based on the relationship of Figure 4.9, and the values of $S_{r,yield}$ from Section B.2.4, a second (less precise) estimate of the value of S_r was estimated based on pre-displacement FS ≈ 0.3 to 0.5, which produced estimates of $S_r \approx 105$ to 204 lbs/ft^2. Variance in values of back-calculated $S_{r,yield}$ and $S_{r,resid/geom}$ from these current studies were then also considered, and so were values back-calculated or estimated by previous investigators. Values from previous investigators were given little weight here, however, and these were simply examined largely to ensure that previous studies were understood and that the current engineering team had made suitable accommodation for potential uncertainty or variance.

Overall, based on an assumed normal distribution, it was judged that the (mean and median) best estimate of post-liquefaction strength for this case history is

$$\overline{S_r} = 138 \text{ lbs/ft}^2$$

and that the best estimate of standard deviation of mean overall post-liquefaction strength is

$$\sigma_{\overline{S}} = 23 \text{ lbs/ft}^2$$

Seed (1987) had reported a value of $S_r = 50$ lbs/ft^2 based on a simplified analysis of monolithic sliding along the full base of the dam pushed by lateral forces from the reservoir against the upstream face. That appears to have been an overconservative analysis, and it was adjusted upwards by Seed and Harder (1990) who reported a value of $S_r \approx 75$ lbs/ft^2, with a range of 50 to 100 lbs/ft^2, for this case. But theirs was still a deliberately conservative estimate for a case that they considered to be poorly constrained by the available data and information. Olson (2001) and Olson and Stark (2002) did not apply their "kinetics" method to this case, and so they did not independently develop an estimate of S_r that incorporated momentum effects. Instead, as described previously in Section B.2.5, they attempted to estimate the slopes and thicknesses of the post-failure residual embankment geometry based on available photographs, and then performed a simplified infinite slope analysis (for assumed residual, static conditions). They did not state the approximate slope angle they used, nor the soil thicknesses, but they reported a best-estimate value of $S_{r,resid/geom} = 4.0$ kPa (84 lbs/ft^2), which they judged to support the values of Seed and Harder (1990), and they then adopted the range of Seed and Harder. Similarly, Wang (2003) and Wang and Kramer (2008) did not employ their zero inertial force (ZIF) method to incorporate inertial effects in back-analyses of this failure. Instead they selected their value of S_r

based on examination of values from back-analyses by several previous investigators, and in the end selected $\overline{S_r}$ = 100.0 lbs/ft^2, and a standard deviation of $\sigma_{\overline{S}}$ = 29.8 lbs/ft^2. This may have been influenced significantly by the deliberately conservative (low) estimates of Seed and Harder (1990), which were repeated by Olson and Stark (2001, 2002) and thus entered twice into their suite of previous values considered.

Agreement between the values used in these three previous studies, and the values developed and employed in these current studies, is not very good unless one delves into the background (genesis) of the values used in the three preceding studies cited here. The current engineering team feel that the new values presented herein serve to correct the previous conservatism of Seed (1987) and of Seed and Harder (1990) for this challenging case history, and the (also low) values of Olson and Stark (2001, 2002) and Kramer and Wang (2003, 2008) which had been affected by the initial low estimates of Seed and Harder (1990) and of Seed (1987).

B.2.7 Evaluation of Initial Effective Vertical Stress

Average initial (pre-failure) effective vertical stress was assessed for the liquefied portion of the failure surface shown in Figure B.2.4). Parameters and sensitivity analyses were as described previously in Section B.2.4. Values of initial effective vertical stress were also calculated for assumed liquefaction across the full base of the embankment, but due to approximate symmetry, the resulting average initial vertical stresses did not differ significantly from those calculated for the liquefied portions of the failure plane of Figure B.2.4.

The resulting best estimate of average pre-failure effective stress within the liquefied materials controlling the failure was then $\sigma_{vo}' \approx$ 1,301 lbs/ft^2, with a reasonable range of $\sigma_{vo}' \approx$ 1,166 to 1,450 lbs/ft^2. This range is slightly non-symmetric about the median value, and this range was judged by the engineering team to represent approximately ± 2 standard deviations. Overall, the best characterization of initial (pre-failure) average effective vertical stress was then taken to be represented by a mean value of

$$\overline{\sigma'_{vo}} \approx 1{,}308 \text{ lbs/ft}^2$$

and with a standard deviation of

$$\sigma_{\overline{\sigma}} \approx 71 \text{ lbs/ft}^2$$

An estimate of σ_{vo}' was also calculated by Olson and Stark (2001, 2002). They reported a weighted average mean value of $\sigma_{vo}' \approx$ 68.4 kPa (1,428 lbs/ft^2), in excellent agreement with these current studies. Average initial vertical effective stresses were not directly reported by Wang (2003) and Kramer (2008), but they were published more recently in the publication by Kramer and Wang (2015). As discussed in Section 2.3.8.1(b)-(iii), Wang (2003) did not perform any independent analyses to assess σ_{vo}' for his 22 "secondary" cases, and this is one of those cases. Instead, he compiled values of S_r from multiple previous investigators, and averaged

these for a best estimate. He also compiled multiple values of S_r / σ_{vo}' from previous investigators, and averaged these for a best estimate. He then used these two best-estimate values of S_r and S_r/σ_{vo}' to infer a resulting representative value of $\sigma_{vo}' = 1{,}389$ lbs/ft^2. This is in excellent agreement with the values of (1) Olson (2001) and (2) these current studies.

B.2.8 Evaluation of $N_{1,60,CS}$

As described in Section B.2.3, there were no penetration test data available for the silty sands of the upper foundation immediately underlying the dam embankment within which the failure appears to have occurred. In situ density tests, and a Standard Proctor compaction test (D698) had indicated that the uppermost one to three feet of these soils existed at an equivalent relative compaction of RC = 76%.

Based on this relative compaction of 76% (Standard Proctor), and the correlations of Holtz and Gibbs (1979) and of Robertson and Campanella (1983), Olson (2001) estimated that the corresponding in situ relative density was approximately 20 to 40%. Then, based on this estimated range of relative density, he estimated an approximate value of $N_{1,60}$ on the order of 4 to 6 blows/ft.

Seed (1987) and Seed and Harder (1990) had employed similar processes and chains of logic, and had developed estimates of fines corrected $N_{1,60,CS}$ = 8 blows/ft. and 6 blows/ft., respectively.

In these current studies, this same approach is employed, and the characterization of penetration resistance is represented by a best estimate mean value of $\overline{N_{1,60,CS}} \approx 7$ blows/ft., and an estimated standard deviation of this mean of $\sigma_{\overline{N}} \approx 2.3$ blows/ft.

Wang (2003) and Kramer (2008) jointly developed a representative value of $\overline{N_{1,60,CS}} = 8.2$ blows/ft, and their estimated standard deviation of that overall mean value for this case history was $\sigma_{\overline{N}} = 6.8$ blows/ft. Details of the development of this interpretation by Wang and Kramer are not presented, but the very large variance (or standard deviation) in $\overline{N_{1,60,CS}}$ appears to have been an artifact of the procedures used to estimate such variances for poorly defined cases.

Overall agreement between these three independent assessments of representative $\overline{N_{1,60,CS}}$ values is judged to be very good, excepting the very large standard deviation ascribed by Wang and Kramer which reflects what they view to be large uncertainties with respect to the selection of a representative value of $N_{1,60,CS}$ for this case.

B.3 Helsinki Harbor (Finland; 1936)

B.3.1 Brief Summary of Case History Characteristics

Name of Structure	Helsinki Harbor
Location of Structure	Helsinki, Finland
Type of Structure	Harbor
Date of Failure	November 30, 1936
Nature of Failure	Static, During Fill Placement
Approx. Maximum Slope Height	19 ft.

B.3.2 Introduction and Description of Failure

A statically-induced liquefaction flow failure occurred on November 30, 1936 during construction of an engineered fill to serve as an extension of a section of the southern section of Helsinki Harbor. Figure B.3.1 shows both a plan view of this failure, and at the left-hand side of the figure it also shows the pre-failure and post-failure cross-sections through approximately the centerline of the feature.

The harbor extension was being created by placing sandy hydraulic fill into an outer confining berm that had been created by placement of blasted rock. The outer berm was not yet complete when hydraulic fill placement began, with an open "gap" in the rockfill dike, as shown in Figure B.3.1.

Figure B.3.1 shows pre-failure conditions at the time of the failure of November 30. During the night preceding the failure, a small slide (or slump) had occurred in the hydraulic sand fill adjacent to the opening in the rock dike. Filling was re-started the next day, and after only a few loads of additional sand had been placed a large flow failure occurred which carried approximately 6,000 m^3 of the hydraulic sand fill out through the gap in the rock dike and into the harbor (Andreson and Bjerrum, 1968). Detailed investigations after the failure showed that approximately 2 to 3 m of hydraulic sand fill remained in place over the foundation marine clays, and that the foundation clays were not disturbed and had not participated in the failure. This was thus a flow slide in the hydraulic sand fill, likely triggered by local over-steepening, that progressively retrogressed (and spread) until a large portion of the sand fill had become involved and had been carried out into the harbor.

B.3.3 Geology and Site Conditions

The soils of the Helsinki Harbor region are primarily deltaic and estuarine silty sands and clays. Fortunately, the clays that underlay the sandy hydraulic fill were not involved in this failure, so it is only necessary to characterize the silty sands of the hydraulic fill itself.

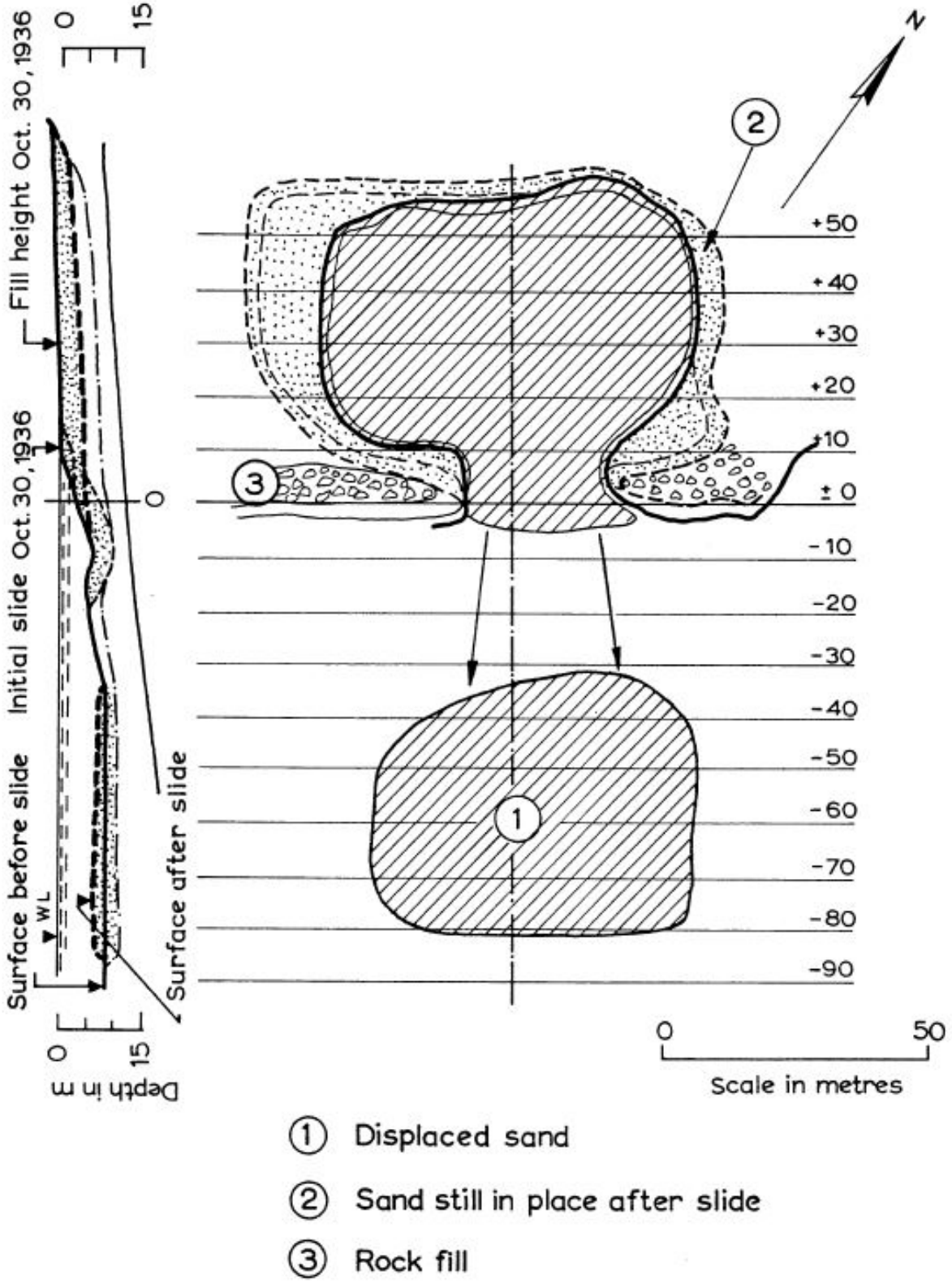

Figure B.3.1: Plan view, and pre-failure and post-failure cross-sections, of the Helsinki Harbor flow slide of November 30, 1936 (Figure from Andreson and Bjerrum, 1968).

The hydraulic fill is known to have been obtained from a nearby borrow source, and so it is generally assumed that the sandy fill was comprised of locally available deltaic deposits, and likely consisted of fine sands with variable fines content. This fill was hydraulically placed, and without compaction. Unfortunately, there is no further information or data available regarding the sandy hydraulic fill, and so gradation, fines contents, etc. are not known. The hydraulic fill would have been a loose, saturated sandy material, but there were no penetration test data or other useful data to provide a useful basis for quantitative assessment of penetration resistances.

B.3.4 Initial Yield Stress Analyses

Figure B.3.2 shows the cross-sections used for back-analyses of the post-liquefaction initial yield strength $S_{r,yield}$ that would be required within the foundation and embankment materials of the north dike section to produce a calculated Factor of Safety equal to 1.0. This is not the actual post-liquefaction strength, but it proves to be useful in developing estimates of post-liquefaction strength (S_r) for this case history.

This failure is known to have been an incrementally progressive retrogressive failure, initiated by a small failure near to the opening in the rock dike, and then retrogressing in a slice by slice progression to the eventual full failure scarp. Accordingly, both smaller (initiating) failures and also the overall (final) failure scarp will be analyzed with regard to values of $S_{r,yield}$.

Unit weights of saturated hydraulic sand fill materials were modeled with a unit weight of $\gamma_m \approx 113$ lbs/ft^3, and this was then varied over a range of 111 to 115 lbs/ft^3 for parameter sensitivity studies. Unit weights of the non-saturated sands and silty sands above the phreatic surface were modeled with a unit weight of $\gamma_s \approx 118$ lbs/ft^3, and this was then varied over a range of 116 to 120 lbs/ft^3 for parameter sensitivity studies. The friction angle of the non-saturated hydraulic fill materials above the phreatic surface was modeled with $Ø' \approx 30°$, and a range of $Ø' \approx 28°$ to 32°.

Both rotational and wedge-like potential failure surfaces were analyzed, and the failure surface shown in Figure B.3.2(a) is the most critical potential "initiating" failure surface found. The value of $S_{r,yield}$ associated with this failure surface, based on best estimate soils parameters, is $S_{r,yield} = 104$ lbs/ft^2. Additional potential failure surface were analyzed, and parameters were varied over the ranges described above. The best overall characterization of localized "initiating" likely critical potential failure surfaces produced a best estimate value of $S_{r,yield} = 104$ lbs/ft^2, and a range of $S_{r,yield} = 88$ to 121 lbs/ft^2.

Figure B.3.2(b) illustrates the back-analysis of $S_{r,yield}$ for the overall (final) eventual failure scarp. Failure surface geometry and unit weights were varied, and the overall best estimate was found to be $S_{r,yield} = 60$ lbs/ft^2, with a range of $S_{r,yield} = 51$ to 71 lbs/ft^2.

Olson (2001) also calculated values of $S_{r,yield}$ for this case history. He analyzed rotational potential failure surfaces similar to the one shown in Figure B.2.2, and including failures that transgressed slightly into the underlying harbor clays. His reported best estimate of $S_{r,yield}$ was $S_{r,yield} = 3.8$ kPa (79 lbs/ft^2), with a range of 2.2 to 4.4 kPa (46 to 92 lbs/ft^2). This was in good

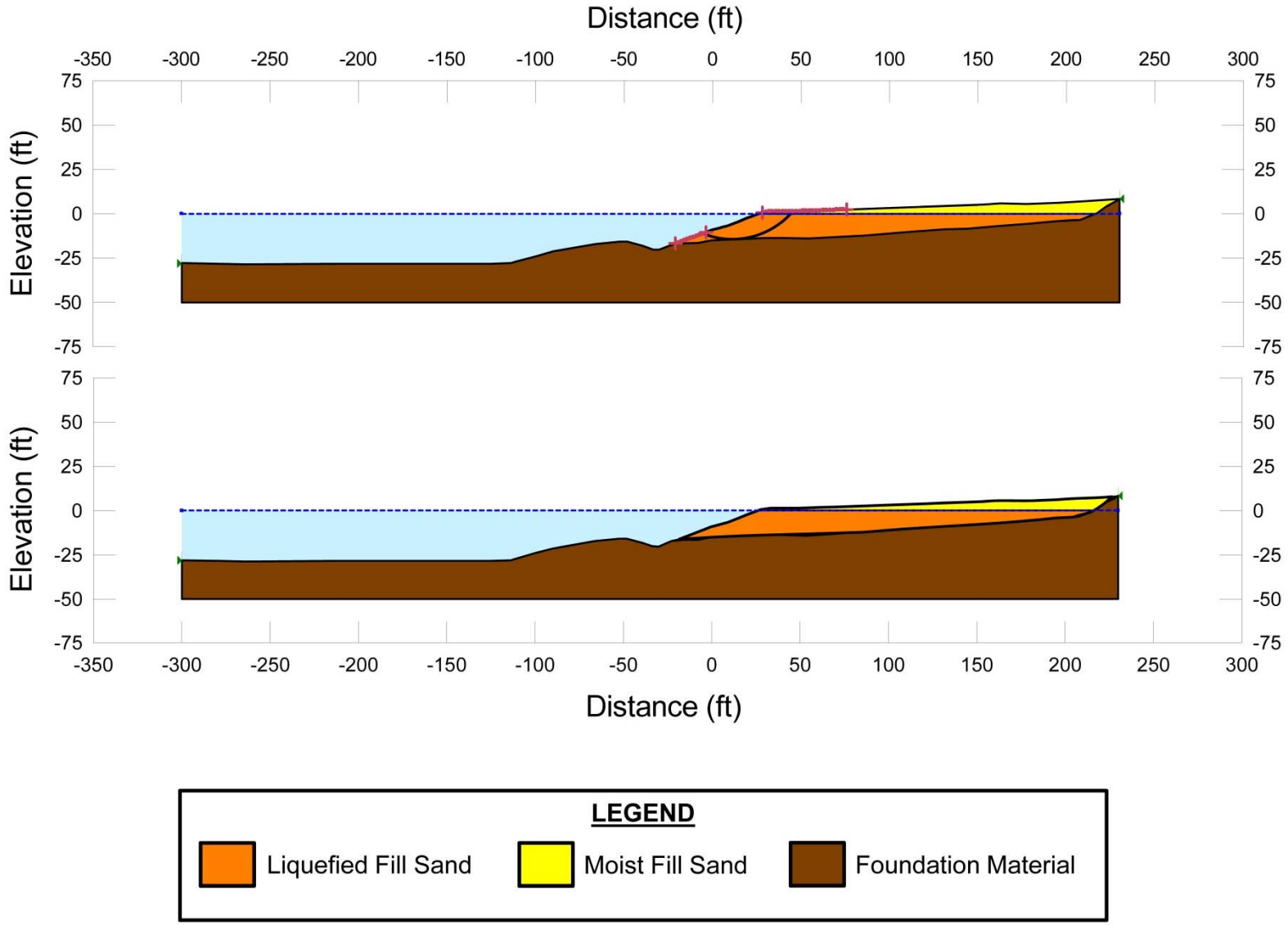

Figure B.3.2: Cross-sections used for back-analyses of $S_{r,yield}$ for the Helsinki Harbor liquefaction flow failure.

agreement with the values calculated for the smaller "initiating" failures in these current studies as described above.

Overall estimates of "representative" $S_{r,yield}$ for purposes of evaluation of overall S_r were then developed by weighted averaging, employing a 3:1 weighting factor (for this strongly retrogressive failure) as

$$S_{r,yield} = [\ 3 \times S_{r,yield}\ (\text{smaller initial yield surface}) + S_{r,yield}\ (\text{final overall failure scarp})] / 4$$

Based on the range of variations in properties and parameters, and a range of potential failure mechanisms and associated feasible failure surfaces, the resulting best estimate overall of "representative" $S_{r,yield}$ was found to be $S_{r,yield} = 93$ lbs/ft^2, with a range of $S_{r,yield} \approx 79$ to 109 lbs/ft^2.

B.3.5 Residual Strength Analyses Based on Residual Geometry

Back-analyses were also performed to evaluate the "apparent" post-liquefaction strength ($S_{r,resid/geom}$) required to produce a calculated Factor of Safety equal to 1.0 based on residual geometry. This is not a direct measure of post-liquefaction strength (S_r), as it neglects momentum effects and would underestimate S_r, but it is useful for overall evaluation of S_r for this case history.

Figure B.3.1 shows the post-failure cross-section geometry, both for the remaining hydraulic fill that remained in place within the partially confined filling basin, and also the hydraulic fill materials that flowed out through the opening in the rock dike and into the harbor. The average slope of the post-failure top of the hydraulic fill that traveled out into the harbor was reported to be approximately 4° to 5° (Andreson and Bjerrum, 1968). This is not the apparent slope shown in Figure B.3.1, but it is assumed that this slope is largely correct as reported and that the slope shown in the figure may be somewhat approximate in this regard.

Olson took this view, and employed an infinite slope analysis under static conditions, with slopes of 4° to 5° simultaneously modelled at both the top and the base of the failure mass, and with a modeled thickness of failure mass hydraulic fill materials reportedly taken from Figure B.3.1 (but the thickness selected was not stated), and he calculated and reported a best estimate of $S_{r,resid/geom} = 1.55$ kPa (32 lbs/ft^2), with a range of $S_{r,resid/geom} = 1.1$ to 2.0 kPa (23 to 42 lbs/ft^2).

In these current studies, a similar approach was taken, producing a best estimate value of $S_{r,resid/geom} \approx 45$ lbs/ft^2, and a range of $S_{r,resid/geom} \approx 30$ to 60 lbs/ft^2, with top and base slopes of 4° to 5°, and with failure mass thicknesses of 8 to 10 feet.

B.3.6 Overall Estimates of S_r

Overall estimates of S_r for this Class B case history were made based on the pre-failure geometry, the partial post-failure geometry, and the approximate runout features and

characteristics, and the values of $S_{r,yield}$ and $S_{r,resid/geom}$ as calculated and/or estimated in the preceding sections.

Runout distance of the center of mass of the overall failure was approximately D ≈ 300 feet, and the initial failure slope height was H = 26 feet. This produces a runout ratio (defined as runout distance traveled by the center of gravity of the overall failure mass divided by the initial slope height from toe to back heel of the failure) of D/H = 11.5. This allows Equation 4-4, and Figures 4.7 and 4.11 to serve as one basis for estimation of post-liquefaction strength S_r. Using the ranges of $S_{r,yield}$ and $S_{r,resid/geom}$ from Sections B.13.4 and B.13.5, and assuming that $\xi \approx 0.45$ to 0.65 for this large runout case, with 0.525 as the best estimate, provided a best estimate value of $S_r \approx 38$ lbs/ft^2 and an estimated range of $S_r \approx 31$ to 55 lbs/ft^2. A second basis for estimation of S_r was the use of the relationship of Figure 4.9, and the range of values of $S_{r,yield}$ from Section B.5.4. Based on the large runout distance, values of initial (pre-failure displacement) Factor of Safety were taken as approximately 0.4 to 0.6, and this produced a best estimate value of $S_r \approx 46$ lbs/ft^2 and an estimated range of $S_r \approx 37$ to 56 lbs/ft^2. No similar use was made of Figure 4.9 in conjunction with the ranges of $S_{r,resid/geom}$ estimated in Section B.4.5 because these estimates of $S_{r,resid/geom}$ were considered to be very approximate.

The estimates by each of the two methods above were then averaged together, and this produced a best estimate value of $S_r \approx 42$ lbs/ft^2 and an estimated range of $S_r \approx 31$ to 65 lbs/ft^2. These estimates of variance are non-symmetric about the best estimated mean value, and the range was judged to represent approximately +/- 1.5 standard deviations, so further adjustments were then necessary.

Overall, based on an assumed normal distribution, it was judged that the (mean and median) best estimate of post-liquefaction strength for this case history is

$$\overline{S_r} = 48 \text{ lbs/ft}^2$$

and that the best estimate of standard deviation of mean overall post-liquefaction strength is

$$\sigma_{\overline{S}} = 14 \text{ lbs/ft}^2$$

Olson (2001) and Olson and Stark (2002) did not apply their "kinetics" method to this case, and so they did not independently develop an estimate of S_r that incorporated momentum effects. Instead they simply used their value of $S_{r,resid/geom}$ as a conservative approximation of S_r for this less well-defined case, and used $S_r = 1.55$ kPa (33 lbs/ft^2), with a range of 1.1 to 2.0 kPa (23 to 42 lbs/ft^2) in developing their predictive relationship. Because these values are based on residual post-failure geometry with an assumed Factor of Safety equal to 1.0, they do not include momentum effects and so they will be too low.

A better estimate can be obtained by using the values of Sr,yield and Sr,resid/geom back-calculated by Olson (2001), and then combining these using Equation 4-1, and a first-order estimate of $\xi \approx 0.8$. This would produce an estimate of $S_r \approx 44$ lbs/ft^2, as shown in Tables 4.3 and 4.6. This would agree very closely with the best-estimate value developed in these current studies.

Similarly, Wang (2003) and Wang and Kramer (2008) did not employ their zero inertial force (ZIF) method to incorporate inertial effects in back-analyses of this failure. Instead they selected their value of S_r based on examination of back-analyses of several previous investigators, and averaged these to develop their selected $\overline{S_r}$ = 53.2 lbs/ft^2, and a (very high) standard deviation of $\sigma_{\overline{S}}$ = 19.0 lbs/ft^2. Their values are also in very good agreement with the values determined in these current studies.

B.3.7 Evaluation of Initial Effective Vertical Stress

This was a somewhat unusual failure case history because the observed failure was so strongly retrogressive; spreading from a small, localized initial failure to eventually encompass a significantly larger overall feature.

Average initial (pre-failure) effective vertical stress was assessed for the liquefied portion of the overall (final scarp) failure surface in Figure B.3.1. Parameters and sensitivity analyses were as described previously in Section B. 3.4. Additional analyses were then performed for alternate potential failure surfaces, including failure surfaces representing initial (smaller) slices of a retrogressive incremental failure eventually extending back to the apparent back heel of the final failure. The values of σ_{vo}' calculated for smaller (initial) failure slices were then averaged together with the values calculated for the overall (final) slide scarp, and these averaged value of the two failure surfaces was taken as "representative" here. This produced a moderately large, but finite, range of estimated values of average pre-failure effective stress within the liquefied materials controlling the failure.

The resulting best estimate of average pre-failure effective stress within the liquefied materials controlling the failure was then $\sigma_{vo}' \approx 842$ lbs/ft^2, with a reasonable range of $\sigma_{vo}' \approx 556$ to 1136 lbs/ft^2. This range is slightly non-symmetric about the median value, and this range was judged by the engineering team to represent approximately ± 2 standard deviations. Overall, the best characterization of initial (pre-failure) average effective vertical stress was then taken to be represented by a mean value of

$$\overline{\sigma'_{vo}} \approx 846 \text{ lbs/ft}^2$$

and a standard deviation of

$$\sigma_{\overline{\sigma}} \approx 105 \text{ lbs/ft}^2$$

The relatively large variance (and standard deviation) here is due in large part to the uncertainties associated with the averaging of smaller initial failure slices with the overall (final) failure scarp.

An estimate of σ_{vo}' was also calculated by Olson and Stark (2001, 2002). They reported a best estimate of $\sigma_{vo}' \approx 25$ kPa (522 lbs/ft^2), with a range of 20.1 to 29.9 kPa (420 to 624 lbs/ft^2). These values are somewhat lower than the values calculated and used in these current studies, and it is not clear why their values are so low. Average initial vertical effective stresses were not directly reported by Wang (2003) and Kramer (2008), but they were published

more recently in the publication by Kramer and Wang (2015). As discussed in Section 2.3.8.1(b)-(iii), Wang (2003) did not perform any independent analyses to assess σ_{vo}' for his 22 "secondary" cases, and this is one of those cases. Instead, he compiled values of S_r from multiple previous investigators, and averaged these for a best estimate. He also compiled multiple values of S_r/σ_{vo}' from previous investigators, and averaged these for a best estimate. He then used these two best-estimate values of S_r and S_r/σ_{vo}' to infer a resulting representative value of σ_{vo}'. As described in Section 2.3.8.1(b)-(iii), the resulting averaged values of S_r and of S_r/σ_{vo}' were incompatible with each other for a number of Wang's "secondary" case histories, and this process produced unreasonable values of σ_{vo}' for a number of case histories. For this case history, however, Wang's resulting value of $\sigma_{vo}' \approx 887$ lbs/ft^2 is in excellent agreement with these current studies.

B.3.8 Evaluation of $N_{1,60,CS}$

As discussed previously in Section B.3.3 there were no penetration data of any type available for characterization of the hydraulic fill, and these was also only very limited information available regarding the nature of this sandy fill material.

Olson (2001) cites Sladen and Hewitt (1989) who indicated that hydraulic fills placed using a point source distribution typically have relative densities on the order of 40 to 50%. Based on this estimated range of relative density, and the correlations of Holtz and Gibbs (1979) and of Tokimatsu and Seed (1987), they then estimated an approximate representative value of $N_{1,60} \approx 6$ blows/ft. No range was given.

In this current study, the investigation team largely concurs, but adds a significant standard deviation to account for the multiple uncertainties here. The characterization of penetration resistance for these current studies is $\overline{N_{1,60,CS}} \approx 6$ blows/ft., with a standard deviation of $\sigma_{\overline{N}} \approx 2.0$ blows/ft.

Wang (2003) and Kramer (2008) selected a similar fines adjusted value of $\overline{N_{1,60,CS}} \approx 5.9$ blows/ft., and a very high standard deviation of $\sigma_{\overline{N}} \approx 8.0$ blows/ft. This very high standard deviation produces a value of $N_{1,60,CS}$ equal to zero at just the mean minus 0.73 standard deviations level, and at a mean plus two standard deviations the value would be approximately 21.9 blows/ft., which appears to be unreasonably high for the materials as described (and as they performed). This very high standard deviation in mean $N_{1,60,CS}$ is an artifact of the rigorously defined approach taken to evaluation of $N_{1,60,CS}$ in Wang's work, and it should be noted that neither the negative $N_{1,60,CS}$ values at mean minus more than 0.73 standard deviations, nor the very high values at mean plus more than about 2 standard deviations, likely had significant adverse impact on their overall predictive correlations. Uncertainty or variance was high, and the impact of this case history on the regressions that produced their predictive relationships was further reduced by their assigning a very low "Weighting Factor" of WF = 0.39 for this case.

Overall agreement with regard to characterization of $N_{1,60,CS}$ among these two previous studies, and the current study, is excellent for this case with the exception of characterization of variance (or standard deviation) of the mean value of $N_{1,60,CS}$.

B.4 Solfatara Canal Dike (Mexico; 1940)

B.4.1 Brief Summary of Case History Characteristics

Name of Structure	Solfatara Canal Dike
Location of Structure	Mexico
Type of Structure	Dike
Date of Failure	May 18, 1940
Nature of Failure	Seismic, During 1940 El Centro Earthquake (M_L = 7.1)
Approx. Maximum Slope Height	9.5 ft.

B.4.2 Introduction and Description of Failure

Approximately 60 miles of canal banks were heavily damaged or destroyed in an area extending from the southeastern portion of California's Imperial Valley south across the border into Mexico as a result of earthquake shaking following the El Centro Earthquake of May 18, 1940 (Ross, 1968). Failures along the Solfatara Canal in Mexico accounted for about 12 of the 60 miles that experienced significant damage.

The damage to the dikes on the north and south sides of the Solfatara Canal is described by Ross (1968) as consisting primarily of longitudinal fissures and crest settlement of up to 7 feet into the foundation soils. One section of north dike, approximately 1,000 feet in length, reportedly moved laterally approximately 75 feet according to first hand observations (as subsequently reported in Ross, 1968). An approximate pre-failure and post-failure cross section for this failure section was developed and presented by Ross (1968), based on eyewitness reports and existing photographs, and this is shown in Figure B.4.1. The locations of soil borings S-1 and S-2, which were performed as part of the 1967 investigation by Ross (summarized in Ross, 1968), are also shown in this figure.

B.4.3 Geology and Site Conditions

Figure B.4.2 presents an enlarged view of the boring logs from the 1967 investigation as presented in Ross (1968). The borings were performed using a 5-inch diameter hand auger with no casing or drilling fluid. Borings performed at this site were advanced until the shallower soils sloughed, collapsing the hole. Following collapse of the hole, a probe was pushed with the combined weight of 2 men, estimated at approximately 350 lbs., until refusal in order to provide an indication as to the resistance of the soils beneath the base of the hole.

Boring S.1 was performed in the south dike and is reported to have only encountered levee fill material, consisting of loose clean fine sand. An effort to retrieve samples from the borings using a 2.8-inch diameter piston sampler resulted in the recovery of one sample from Boring S.1 at a depth of 7.4 feet in what is believed to be levee fill material. Results from tests

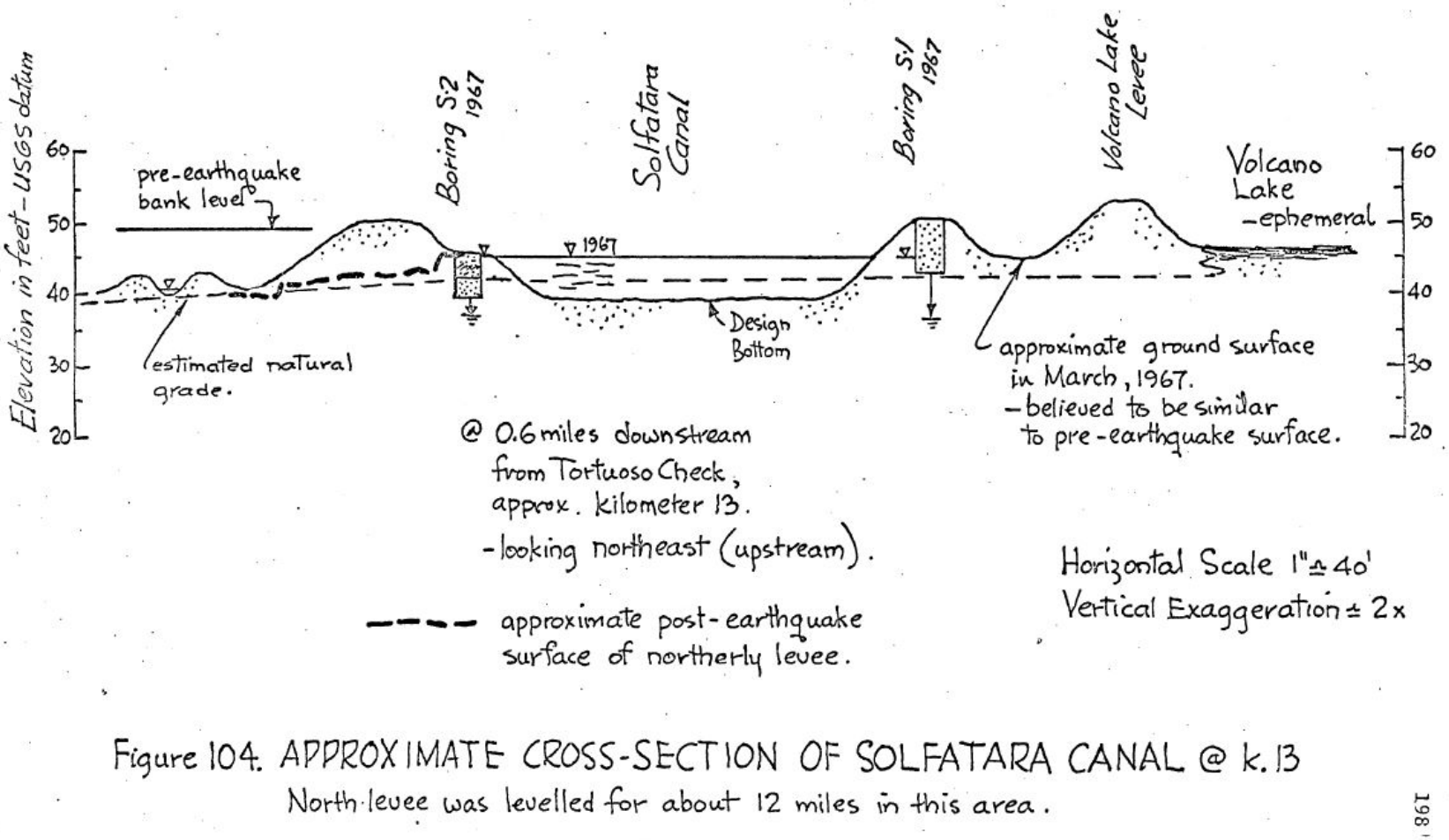

Figure 104. APPROXIMATE CROSS-SECTION OF SOLFATARA CANAL @ k. 13
North levee was levelled for about 12 miles in this area.

Figure B.4.1: Approximate cross-section showing both pre-failure and post-failure geometry of the Solfatara Canal at the 13 km canal marker (Figure from Ross, 1968)

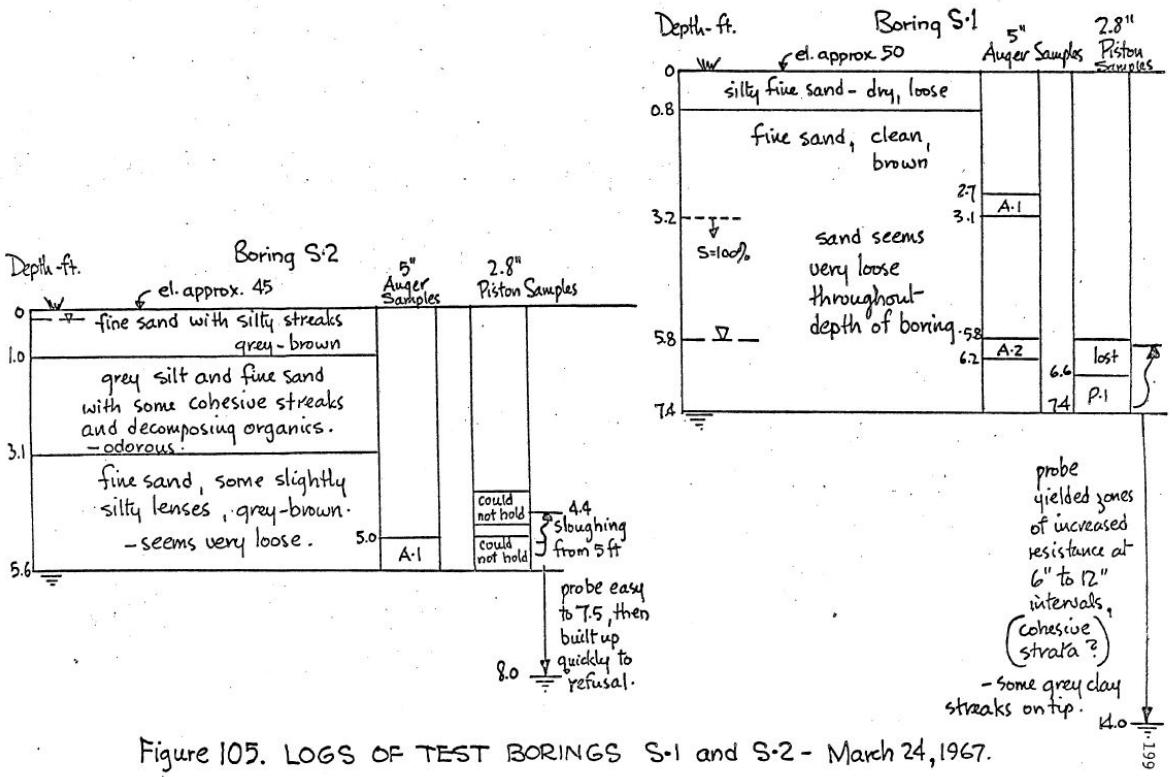

Figure B.4.2: Logs of Borings S-1 and S-2 from the Solfatara Canal at the 13 km canal marker (Figure from Ross, 1968)

performed on the material from this sample P.1 within the levee embankment indicated a relative density of $D_R \approx 32\%$.

Boring S-2 was performed from the top of a bench on the remaining crest of the north dike, which was just above the canal water level at the time of the 1967 investigation. The north levee was found to consist of organic soil in the upper 3 feet, underlain by what is described in Ross (1968) as likely native, very loose fine sand with some slightly silty lenses. The likelihood that these were native soils was based in significant part on the fact that a stratum of decomposing organics, likely from the lakebed of Volcano Lake, was encountered near the top of the boring, underlain by loose sands and silty sands. No sample was able to be recovered from Boring S-2. Three additional borings along this bench, for which logs were not reported, all yielded the same lack of recovery in these loose sands. However, probing beneath the bases of all borings in the north levee did indicate a loose sand layer extending to a depth of about 7.5 feet, below which probing resistance (penetration resistance) reportedly increased rapidly. Ross (1968) considered the sands encountered in these north levee borings to likely represent natural soils. These fine sands and silty sands were very loose, and this along with their saturated condition, was considered to be the reason that samples could not be recovered.

B.4.4 Initial Yield Stress Analyses

Figure B.4.3 shows the cross-section used for back-analyses of the post-liquefaction initial yield strength $S_{r,yield}$ that would be required within the foundation and embankment materials of the north dike section to produce a calculated Factor of Safety equal to 1.0. This is not the actual post-liquefaction strength, but it proves to be useful in developing estimates of post-liquefaction strength (S_r) for this case history.

There were two general sets of potential failure mechanisms that could potentially explain the observed features, and the overall (approximate) observed post-failure geometry of Figure B.4.1. The first involves sliding primarily along liquefied materials at (and within) the upper portions of the loose, saturated native sands and silty sands underlying the embankment fill. The second involves sliding primarily along liquefied materials at (and within) the lower portions of the loose, saturated sands and silty sands of the fill that comprised the levee embankment. Both sets of possibilities were considered in these current studies.

The failure surface shown in Figure B.4.3 is the best estimate of the most critical initial failure surface for this section. This would infer that the failure may have been incrementally progressive, retrogressing in a series of successive slices back towards the eventual back-heel of the overall failure feature. This would also infer that the loose native upper foundation sands and silty sands underlying the levee embankment fill were of critical importance.

Additional failure surfaces, and failure mechanisms, were also back-analyzed. These included failure surfaces encompassing essentially the entire failure mass as initiating monolithically (all at once), and failure surfaces confined to within only the upper (loose, saturated) silty sand levee embankment fill.

There appeared to be little basis for differentiation in basic properties between the embankment fill materials and the underlying native soils. Unit weights of the non-saturated sands and silty sands above the phreatic surface were modeled with a unit weight of $\gamma_m \approx 117$ lbs/ft^3, and this was then varied over a range of 114 to 120 lbs/ft^3 for parameter sensitivity studies. Unit weights of the saturated sands and silty sands below the phreatic surface were modeled with a unit weight of $\gamma_s \approx 122$ lbs/ft^3, and this was then varied over a range of 119 to 125 lbs/ft^3 for parameter sensitivity studies. The friction angle of the loose sands and silty above the phreatic surface was modeled with $Ø' \approx 30°$, and a range of $Ø' \approx 28°$ to 33°.

Based on the range of variations in properties and parameters, and a range of potential failure mechanisms and associated feasible failure surfaces, the resulting best estimate value of $S_{r,yield}$ was found to be $S_{r,yield} = 149$ lbs/ft^2, with a range of $S_{r,yield} \approx 119$ to 182 lbs/ft^2.

Olson (2001) also performed back-analyses to estimate $S_{r,yield}$. He stated that his assumed failure mechanism was liquefaction of the loose, saturated levee embankment fill, but his assumed failure surface extended beneath the levee embankment fill and was an initial rotational feature similar to the failure surface shown as the best estimate case in Figure B.4.3 with much of the shear failure occurring within what may have been loose foundation soils. This represents an "initial slice" not encompassing the entire eventual failure mass, and so implies the assumption of a progressively retrogressive failure by slices for this case. Olson then also back-

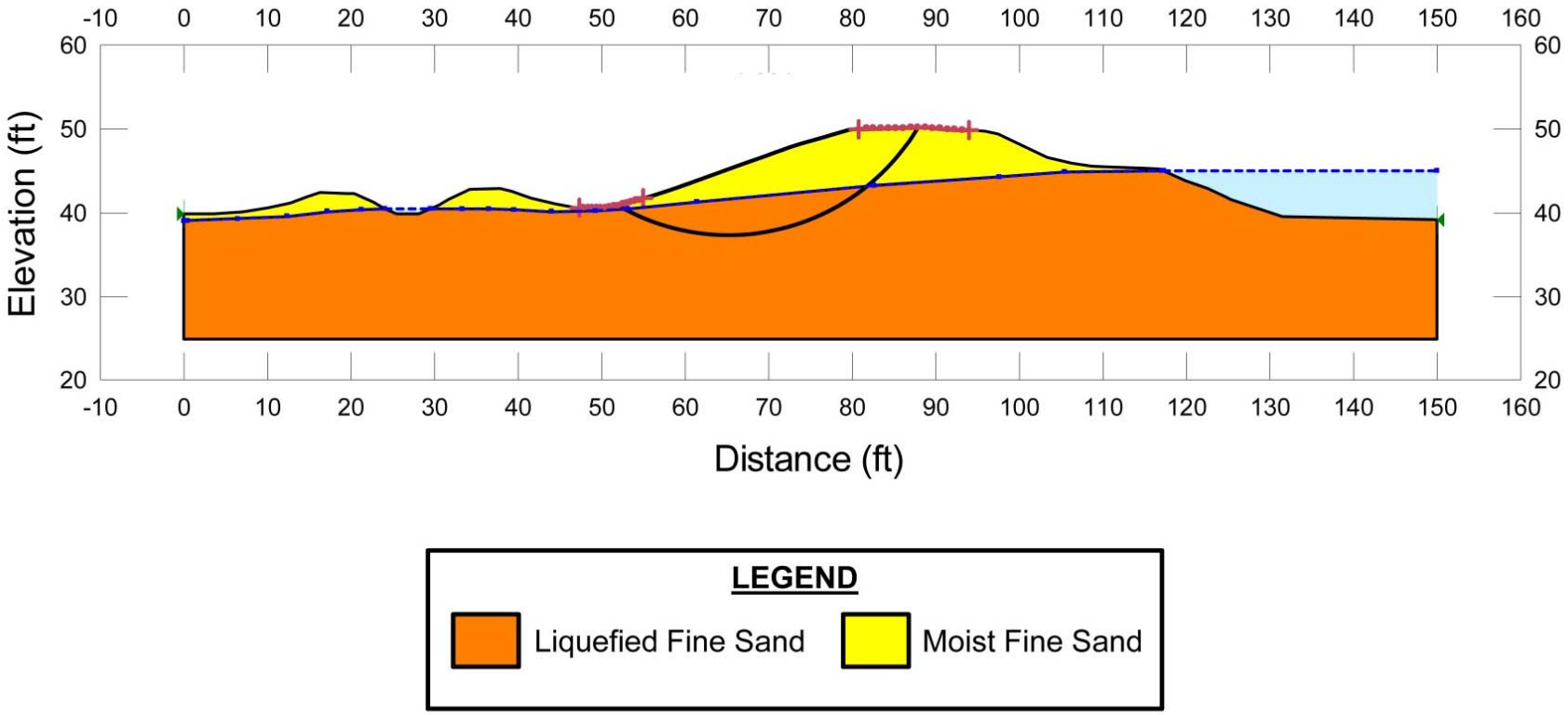

Figure B.4.3: Cross-section showing the pre-failure geometry and conditions for back-analyses of the initial yield strength ($S_{r,yield}$) for the failure section of the north dike of the Solfatara Canal.

analyzed additional potential failure surfaces and mechanisms, as with these current studies. Olson's best estimate of $S_{r,yield}$ was 6.0 kPa (125 lbs/ft^2), with a range of 3.9 to 6.75 kPa (81 to 141 lbs/ft^2).

B.4.5 Residual Strength Analyses Based on Residual Geometry

It was not possible to perform rigorous and reliable back-analyses to determine the value of $S_{r,resid/geom}$ required to produce a calculated Factor of Safety equal to 1.0 based on residual geometry because the post-failure residual geometry reported was not fully accurate or reliable. The reported post-failure cross-section shows that the post-liquefaction strength was greater than zero, but does not provide a basis for very refined estimates. This is a principal source of uncertainty for this case history.

The sketch presented in Figure B.5.1 shows the slope of the post-failure embankment to be as steep as 6.5°, but conservation of mass is not achieved with the post-failure cross-section as shown in this figure. The "probing" at the base of the boreholes suggested that the foundation soils became denser (or at least more difficult to penetrate) at a depth of approximately 7.5 feet beneath the bases of the borings, but this provides poor definition of the depth of potentially liquefiable materials. Assuming a range of residual slopes of 4° to 6°, and thicknesses of potentially liquefiable soils that extended up to as much as 0 to 8 feet below the dashed line in Figure B.5.1, infinite slope analyses provide potential estimates of $S_{r,resid/geom} \approx 25$ to 120 lbs/ft^2. Given the overall uncertainties here, the current investigation team selected a best estimate of $S_{r,resid/geom} \approx 70$ lbs/ft^2, with a large range of approximately 25 to 120 lbs/ft^2.

Olson was the other investigator to report a value of $S_{r,resid/geom}$. He assumed that the slope of the failed mass was the same as that of the natural grade, with a slope of approximately 4°. He spread the failure mass (removed from its initial position) over an assumed runout footprint, and estimated the average thickness of the runout failure mass to be approximately 1.8 m. He then performed an infinite slope analysis to estimate $S_{r,resid/geom} = 2.4$ kPa (50 lbs/ft^2). Olson noted that this was essentially the same as the value of post-liquefaction strength reported by Seed and Harder (1990). Seed and Harder reported a value of $S_r \approx 50$ lbs/ft^2 and a range of 25 to 75 lbs/ft^2. The values of Seed and Harder had, however, been targeted at conservative estimation of actual post-liquefaction strength (S_r), rather than $S_{r,resid/geom}$.

B.4.6 Overall Estimates of S_r

Overall estimates of S_r for this Class B case history were made based on the pre-failure geometry and the approximate runout features and characteristics, and the values of $S_{r,yield}$ and $S_{r,resid/geom}$ as calculated in the preceding sections.

Runout characteristics for this case cannot be fully accurately assessed due to the approximate nature of the post-failure cross section as reported. It was noted that runout ratio (runout distance traveled by the center of gravity of the overall failure mass divided by the initial slope height from toe to back heel of the failure) was large to very large. This allowed Equation

4-4, and Figures 4.7 and 4.11 to serve as one basis for estimation of post-liquefaction strength S_r. Using the ranges of $S_{r,yield}$ and $S_{r,resid/geom}$ from Sections B.4.4 and B.4.5, and assuming that $\xi \approx$ 0.45 to 0.65 for this large runout case, , with 0.55 as the best estimate, provided a best estimate value of $S_r \approx 60$ lbs/ft^2 and an estimated range of $S_r \approx 32$ to 98 lbs/ft^2. A second basis for estimation of S_r was the use of the relationship of Figure 4.9, and the range of values of $S_{r,yield}$ from Section B.4.4. A second estimate was made using Figure 4.9 in conjunction with the values of Sr,yield from Section B.4.4. Based on the large runout distance, values of initial (pre-failure displacement) Factor of Safety were taken as approximately 0.4 to 0.6, and when combined with the range of $S_{r,yield}$ from Section B.4.4, this produced a best estimate value of $S_r \approx 74$ lbs/ft^2 and an estimated range of $S_r \approx 48$ to 109 lbs/ft^2. No similar use was made of Figure 4.9 in conjunction with the ranges of $S_{r,resid/geom}$ estimated in Section B.4.5 because these estimates of $S_{r,resid/geom}$ were considered to be very approximate. These two sets of estimates of S_r, and of variance or standard deviation, were then averaged. The overall variance was then slightly non-symmetric about the best estimated mean value, so further adjustments were then necessary. Considering these ranges of estimated S_r, and their bases, the best estimate of post-liquefaction strength was then taken as $S_r \approx 64$ lbs/ft^2, with a range of 32 to 109 lbs/ft^2. This was then adjusted to provide a characterization compatible with the assumed normal distribution that would be employed in the regressions that would follow.

Overall, based on an assumed normal distribution, it was judged that the (mean and median) best estimate of post-liquefaction strength for this case history is

$$\overline{S_r} = 64 \text{ lbs/ft}^2$$

and that the best estimate of standard deviation of mean overall post-liquefaction strength is

$$\sigma_{\overline{S}} = 22 \text{ lbs/ft}^2$$

This represents a very large degree of uncertainty, or variance, and it is noted that approximately mean minus three standard deviations produces a value of S_r approximately equal to zero for this case history.

Seed and Harder (1990) reported a value of $S_r \approx 50$ lbs/ft^2 for this case, and a range of 25 to 75 lbs/ft2. Olson (2001) and Olson and Stark (2002) did not apply their "kinetics" method to this case, and so they did not independently develop an estimate of S_r that incorporated momentum effects. Instead they simply used their value of $S_{r,resid/geom}$ as a conservative approximation of S_r for this less well-defined case, and used $S_r = 2.4$ kPa (75lbs/ft^2) in developing their predictive relationship. Similarly, Wang (2003) and Wang and Kramer (2008) did not employ their zero inertial force (ZIF) method to incorporate inertial effects in back-analyses of this failure. Instead they selected their value of S_r based on examination of back-analyses of several previous investigators, and in the end selected $\overline{S_r} = 77.1$ lbs/ft^2, and a standard deviation of $\sigma_{\overline{S}} = 25.6$ lbs/ft^2. Despite these differing approaches taken to evaluation and/or selection of S_r, agreement between the values used in these three previous studies, and the values developed and employed in these current studies, is very good for this case history.

B.4.7 Evaluation of Initial Effective Vertical Stress

Average initial (pre-failure) effective vertical stress was assessed for the liquefied portion of the failure surface in Figure B.4.4. Parameters and sensitivity analyses were as described previously in Section B.4.4. Additional analyses were then performed for alternate potential failure surfaces, including failure surfaces representing the end result of retrogressive incremental failures extending back to the apparent back heel of the final failure. Depths of failure surfaces were varied, and both rotational and translational (wedge-like) failure surfaces were considered. This produced a moderately large, but finite, range of estimated values of average pre-failure effective stress within the liquefied materials controlling the failure.

The resulting best estimate of average pre-failure effective stress within the liquefied materials controlling the failure was then $\sigma_{vo}' \approx 669$ lbs/ft^2, with a reasonable range of $\sigma_{vo}' \approx 548$ to 784 lbs/ft^2. This range is slightly non-symmetric about the median value, and this range was judged by the engineering team to represent approximately ± 2 standard deviations. Overall, the best characterization of initial (pre-failure) average effective vertical stress was then taken to be represented by a mean value of

$$\overline{\sigma'_{vo}} \approx 669 \text{ lbs/ft}^2$$

and with a standard deviation of

$$\sigma_{\bar{\sigma}} \approx 59 \text{ lbs/ft}^2$$

An estimate of σ_{vo}' was also calculated by Olson and Stark (2001, 2002). They reported a weighted average mean value of $\sigma_{vo}' \approx 29.9$ kPa (624 lbs/ft^2), in excellent agreement with these current studies. Average initial vertical effective stresses were not directly reported by Wang (2003) and Kramer (2008), but they were published more recently in the publication by Kramer and Wang (2015). As discussed in Section 2.3.8.1(b)-(iii), Wang (2003) did not perform any independent analyses to assess σ_{vo}' for his 22 "secondary" cases, and this is one of those cases. Instead, he compiled values of S_r from multiple previous investigators, and averaged these for a best estimate. He also compiled multiple values of S_r / σ_{vo}' from previous investigators, and averaged these for a best estimate. He then used these two best-estimate values of S_r and S_r/σ_{vo}' to infer a resulting representative value of σ_{vo}'. As described in Section 2.3.8.1(b)-(iii), the resulting averaged values of S_r and S_r/σ_{vo}' were incompatible with each other for a number of Wang's "secondary" case histories, and this process produced unreasonable, and in some cases physically infeasible, values of σ_{vo}' for a number of case histories. Wang's value of $\sigma_{vo}' = 1{,}224$ lbs/ft^2 is clearly physically infeasible for this case, based on the cross-section, and so it is not considered a useful check here. Agreement between Olson's value, which is well-documented, and the value developed in these current studies is excellent.

B.4.8 Evaluation of $N_{1,60,CS}$

Section B.4.3 described the geology and materials involved in this case history, and explained that there were no formal penetration data for the materials involved in this failure.

This failure either occurred mainly within the lower portion of the loose sand and silty sand dike embankment fill, or in the upper portion of the immediately underlying loose foundation sands and silty sands.

The single piston sample obtained from Boring S-1 reportedly had a relative density of 32%, but the basis for this D_r is not clearly explained (the full details of evaluation of e_{max} and for e_{min} are not clearly presented). It is also not known with certainty whether this sample represented the embankment fill, or the underlying foundation soils.

Both the embankment sands and silty sands, and the underlying foundation sands and silty sands, were clearly very loose materials, based on the descriptions provided by Ross (1968) and the difficult of retrieving piston samples. Precise estimation of representative penetration resistance for these soils is, however, a significant source of uncertainty for this case history.

Olson (2001) used the reported relative density of $D_r \approx 32\%$, and a suite of relationships between relative density and penetration resistance, to develop an estimate of representative penetration resistance of $N_{1,60} \approx 4$ blows/ft., with a range of approximately 4 to 5 blows/ft. This was an $N_{1,60}$ value, as there was no correction for fines.

In these current studies, a best estimate value of $\overline{N_{1,60,CS}} \approx 4.5$ blows/ft. was selected to represent these loose sands and silty sands, and a proportionally large standard deviation of $\sigma_{\overline{N}} \approx 1.5$ blows/ft. was applied to represent the significant uncertainty here. Mean minus three standard deviations produces a value of zero.

Wang (2003) and Kramer (2008) selected a slightly higher value of $\overline{N_{1,60,CS}} \approx 4.9$ blows/ft., and a significantly higher value of $\sigma_{\overline{N}} \approx 6.9$ blows/ft. This very high standard deviation produces a value of $N_{1,60,CS}$ equal to zero at just the mean minus 0.71 standard deviations level, and at a mean plus two standard deviations the value would be approximately 18.7 blows/ft., which appears to be unreasonably high for the materials as described (and as they peformed). This very high standard deviation is an artifact of the rigorously defined approach taken to evaluation of $N_{1,60,CS}$ in Wang's work, and it should be noted that neither the negative $N_{1,60,CS}$ values at mean minus more than 0.71 standard deviations, nor the very high values at mean plus more than about 2 standard deviations, likely had significant impact on their overall predictive correlations. The basis for their selection of $\overline{N_{1,60,CS}} \approx 4.9$ blows/ft. is not presented.

Seed and Harder (1990) had selected a representative value of $N_{1,60,CS} = 4$ blows/ft.

Overall, the values of representative $N_{1,60}$ and $N_{1,60,CS}$ selected among these three previous studies, and the values selected in this current study, appear to be in generally good agreement, and variance or uncertainty appears to be relatively large.

B.5 Lake Merced Bank (California, USA; 1957)

B.5.1 Brief Summary of Case History Characteristics

Name of Structure	Lake Merced Bank
Location of Structure	California, USA
Type of Structure	Lakeside Bank and Fill
Date of Failure	March 22, 1957
Nature of Failure	Seismic, During 1957 San Francisco Earthquake (M_L = 5.3)
Approx. Maximum Slope Height	32.3 ft.

B.5.2 Introduction and Description of Failure

During the 1957 San Francisco Earthquake (M_L = 5.3), a series of small to moderate slope failures occurred around the edges of the southern end of Lake Merced, near San Francisco. Figure B.5.1 shows the locations of these five features. The largest of these, Slide 1, was investigated by Ross (1968) as part of a study of landslides and sloughs induced both near the Pacific coast as well as around the edges of Lake Merced. The 1957 earthquake was not a large event, but the south end of Lake Merced is located within approximately 3 km of the section of the San Andreas fault which ruptured during this moderate event.

Figure B.5.2 presents a cross-section through the failure (from Ross, 1968), showing the pre-failure and post-failure conditions. The failure appears to have been a liquefaction-induced slope failure, with sliding occurring primarily within loosely placed lake shore fill sands, but also potentially involving some of the underlying natural lakeshore deposits that were also loose and saturated. The post-failure geometry for Slide 2 was not determined in detail, so it is Slide 1 that will be analyzed in these current studies.

The actual shaking level that occurred at Lake Merced during this small magnitude event is unknown, as there were no local strong motion instruments in the area. Based on modern attenuation relationships, and a single instrument recording obtained at Golden Gate Park (approximately 11 km from the fault rupture) which recorded a peak horizontal acceleration of approximately 0.12g, it appears that the peak horizontal acceleration at Lake Merced would have been a bit higher than 0.12g, but with short duration and a limited number of significant cycles.

B.5.3 Geology and Site Conditions

The lakes occupies a trough that largely parallels the San Andreas fault, which was infilled with marine sediments during the Pleistocene. The uppermost materials in the lake area are primarily fine aeolian sands and silty sands blown across from the sand dunes to the west. These can be very loose. The uppermost lake bed deposits are primarily aeolian and fluvial fine sands and silty sands, with several layers of clays and some peats.

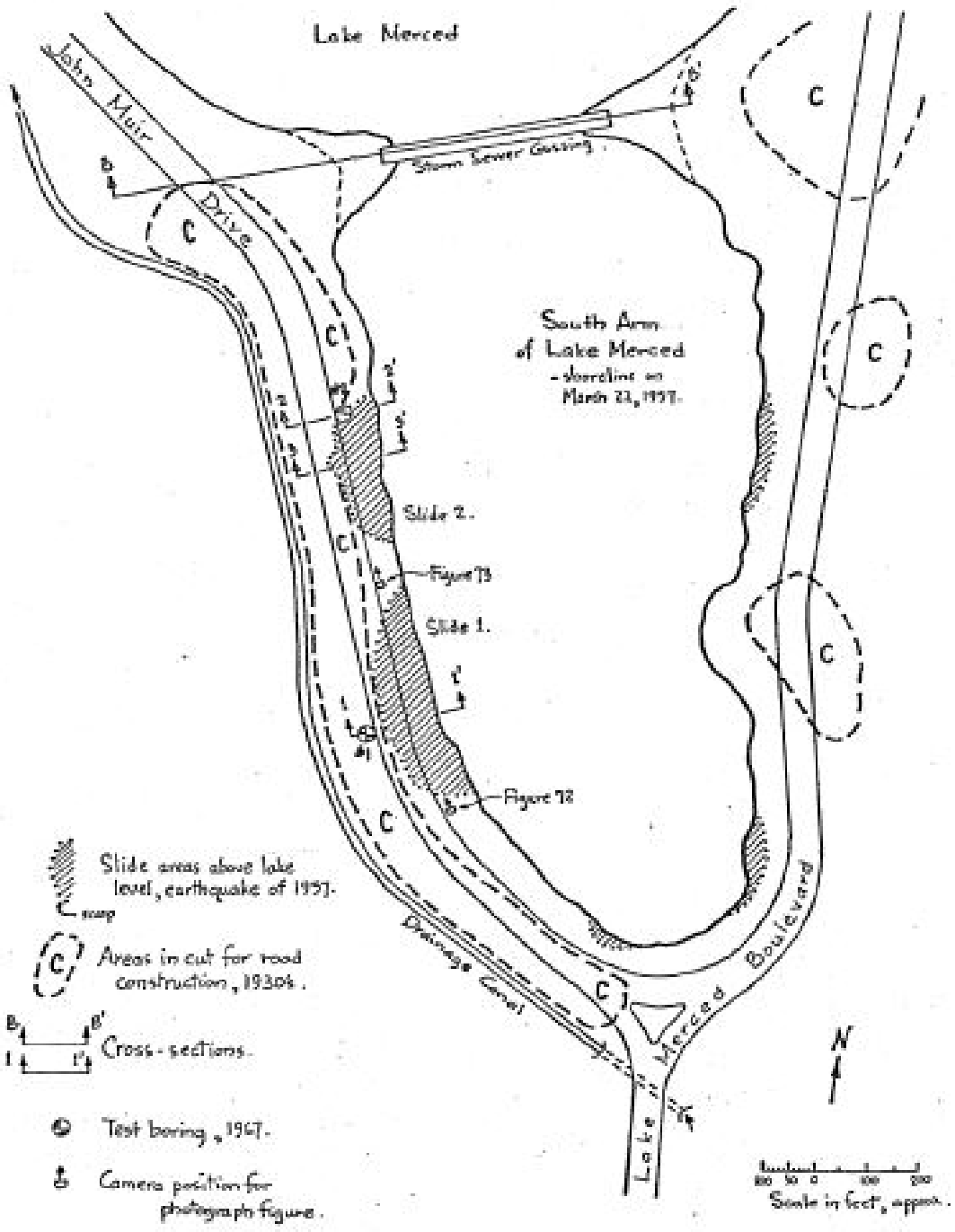

Figure B.5.1: Plan View of the south end of Lake Merced, showing the five edge failures, and the locations of Slides 1 and 2 and of the two borings performed to investigate them (Figure from Ross, 1968).

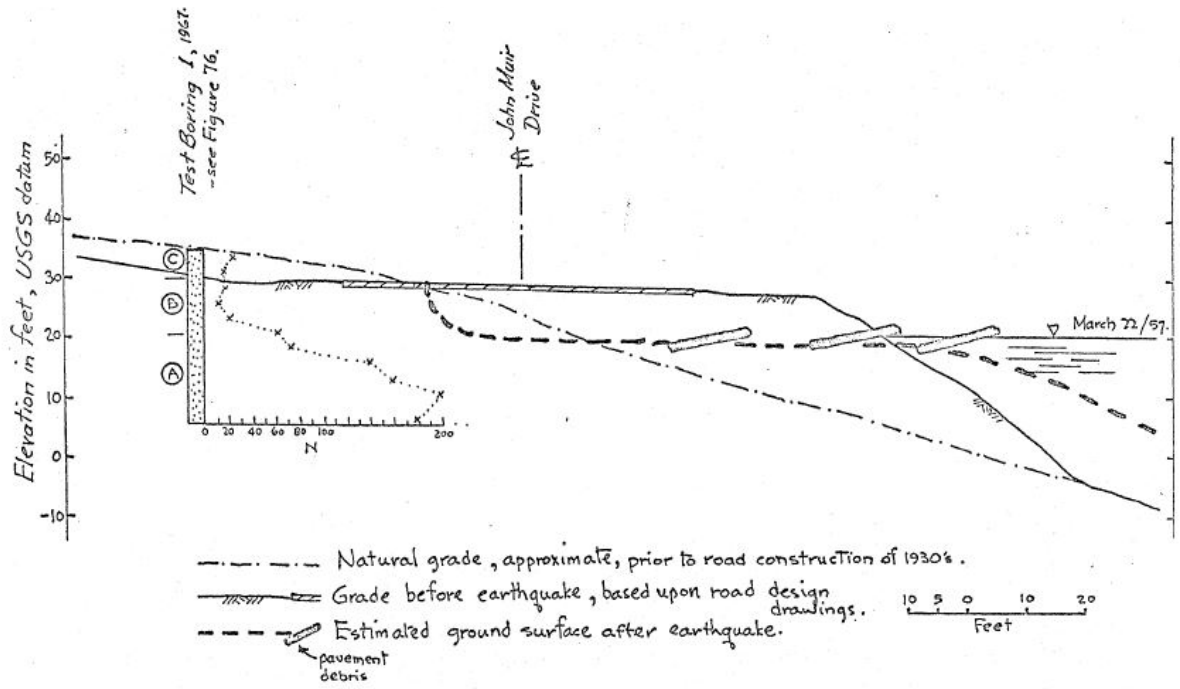

Figure B.5.2: Cross-section through Slide 1 showing the pre-failure and post-failure geometries and the location of Test Boring 1 and the SPT data from this test boring (Figure from Ross, 1968).

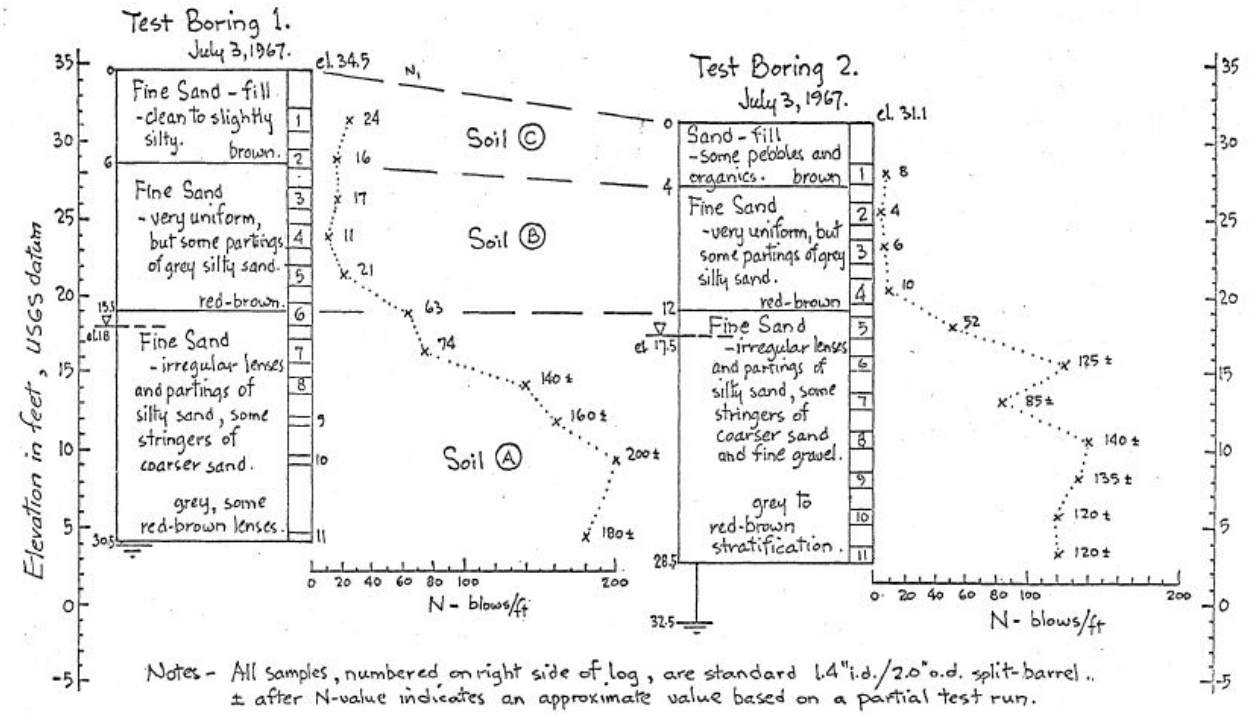

Figure B.5.3: Boring logs from Test Borings 1 and 2 showing soil types and also SPT results (Figure from Ross, 1968).

The current configuration of the west bank of Lake Merced is the result of cut and fill operations performed to create the existing lake shoreline. Figure B.5.1 shows dashed outlines of zones marked "C" indicating areas where borrow materials were excavated for use in road construction. Lakeshore fills were placed to create the necessary right of way for construction of John Muir Drive along the west shoreline. These excavated materials were fine sands and silty sands, and they were placed by end dumping to extend the shoreline into the lake. Compaction details are not known, and previous investigators have assumed that these soils were in a very loose condition. It should be noted, however, that the underlying natural soils were also in a very loose condition, and that liquefaction within only the natural soils underlying the fill would have been sufficient to explain the failure observed.

As shown in Figure B.5.1, two SPT borings were performed to investigate Slide 1 and Slide 2. These two borings were each located behind the rear heel scarps of the slides, and they both appear to have been performed either entirely in native ground, in which case they do not serve to also characterize the fill, or they may have encountered fill in their upper 4 to 6 feet.

Figure B.5.3 presents the logs of these two borings. The uppermost 4 to 6 feet of material encountered in these two borings was logged as "fill" (Soil C), and it was comprised of fine sands with some silt, and in Boring 2 also some pebbles and organics. If this characterization of the upper materials as "fill" is accurate, then as many as 3 SPT blowcounts were obtained in this fill and it was indeed a loosely dumped material.

The next material encountered in both borings is Soil B, and it appears to be very loose fine sand with some occasional silt. This material is logged as natural soil, and it has very low SPT blowcounts as well; characteristic of the local aeolian deposits and dune sands.

The deeper unit encountered (Soil C) was also primarily fine sand with some silt, but it was notably denser, with significantly higher SPT blowcounts.

Various investigators who have back-analyzed this case history have had differing views as to whether or not the uppermost material encountered in Test Borings 1 and 2 was actually fill, or whether there is no SPT data for the fill material so that approximate blowcounts have to be inferred based on assumptions regarding this loosely end dumped material. In either case, most previous investigators have assumed that a majority of the failure occurred due to liquefaction-induced sliding in the lower portion of the fill, and that the native materials played a lesser role.

In these current studies, it is recognized that both the end dumped fill, and the underlying native soils, are fine sands with some silt, and that both are likely to be very loose. Accordingly, a suite of potential failure surfaces, and mechanisms, was analyzed.

Characterization of the fill material can be based either simply on the assumption that it was loosely end dumped, or it can be based on the 3 SPT N-values logged by Ross (1968) as occurring in fill in the upper 4 to 6 feet of Test Borings 1 and 2. Characterization of the underlying uppermost native soil (Soil B) is more straightforward as multiple SPT N-values are available in Test Borings 1 and 2 within this material.

B.5.4 Initial Yield Stress Analyses

Figure B.5.4(a) shows the cross-section used for back-analyses of the post-liquefaction initial yield strength $S_{r,yield}$ that would be required within the liquefied upstream shell materials to produce a calculated Factor of Safety equal to 1.0. This is not the actual post-liquefaction strength, but it proves to be useful in developing estimates of post-liquefaction strength (S_r) for this case history.

There were two general sets of potential failure mechanisms that could potentially explain the observed features, and the overall observed post-failure geometry of Figure B.5.3. The first involves sliding primarily along liquefied materials at (and within) the upper portions of the loose, saturated natural aeolian sands underlying the fill. The second involves sliding along a slightly shallower failure surface within the lower portion of the loose, saturated sand fill. In either case, the failure surface appears to occur roughly sub-parallel to the existing slope face downslope of the toe of the fill. Failure surfaces were varied over a finite range, above and below the failure surface shown in Figure B.5.4(a), and a range of resulting values of $S_{r,yield}$ were back-calculated based on these failure surfaces.

Unit weights of the non-saturated sands above the phreatic surface were modeled with a unit weight of $\gamma_m \approx 105$ lbs/ft^3, and this was then varied over a range of 100 to 110 lbs/ft^3 for parameter sensitivity studies. Unit weights of the saturated sands below the phreatic surface were modeled with a unit weight of $\gamma_s \approx 110$ lbs/ft^3, and this was then varied over a range of 105 to 115 lbs/ft^3 for parameter sensitivity studies. The friction angle of the loose sands above the phreatic surface was modeled with $Ø' \approx 35°$, and a range of $Ø' \approx 32°$ to 38°.

The resulting best estimate value of $S_{r,yield}$ was found to be $S_{r,yield} = 190$ lbs/ft^2, with a range of $S_{r,yield} \approx 153$ to 236 lbs/ft^2.

Olson also performed back-analyses to estimate $S_{r,yield}$. His assumed failure surface was exactly parallel to the apparent slope face downstream of the toe of the fill, and he assumed that the failure occurred within the loose fill material (and not the underlying aeolian sands). He assumed that the drainage length at the toe was "very small", and assigned a drained frictional strength of $Ø' = 35°$ at the toe, but the length of the failure surface over which this was applied is not clearly explained. His most critical failure is a wedge-like failure with an initial back heel steeper than that shown in Figure B.5.4(a). This represents an "initial slice" not encompassing the entire eventual failure mass, and so implies the assumption of a progressively retrogressive "failure by slices" for this case. Olson's back-calculated best estimate of $S_{r,yield}$ was 17.7 kPa (369 lbs/ft^2), with a range of 15.7 to 18.1 kPa (328 to 380 lbs/ft^2).

B.5.5 Residual Strength Analyses Based on Residual Geometry

The calculation of the "apparent" post-liquefaction strength ($S_{r,resid/geom}$) required to produce a calculated Factor of Safety equal to 1.0 based on residual geometry is illustrated in Figure B.5.4(b). Modeling parameters and details are as described in the preceding section.

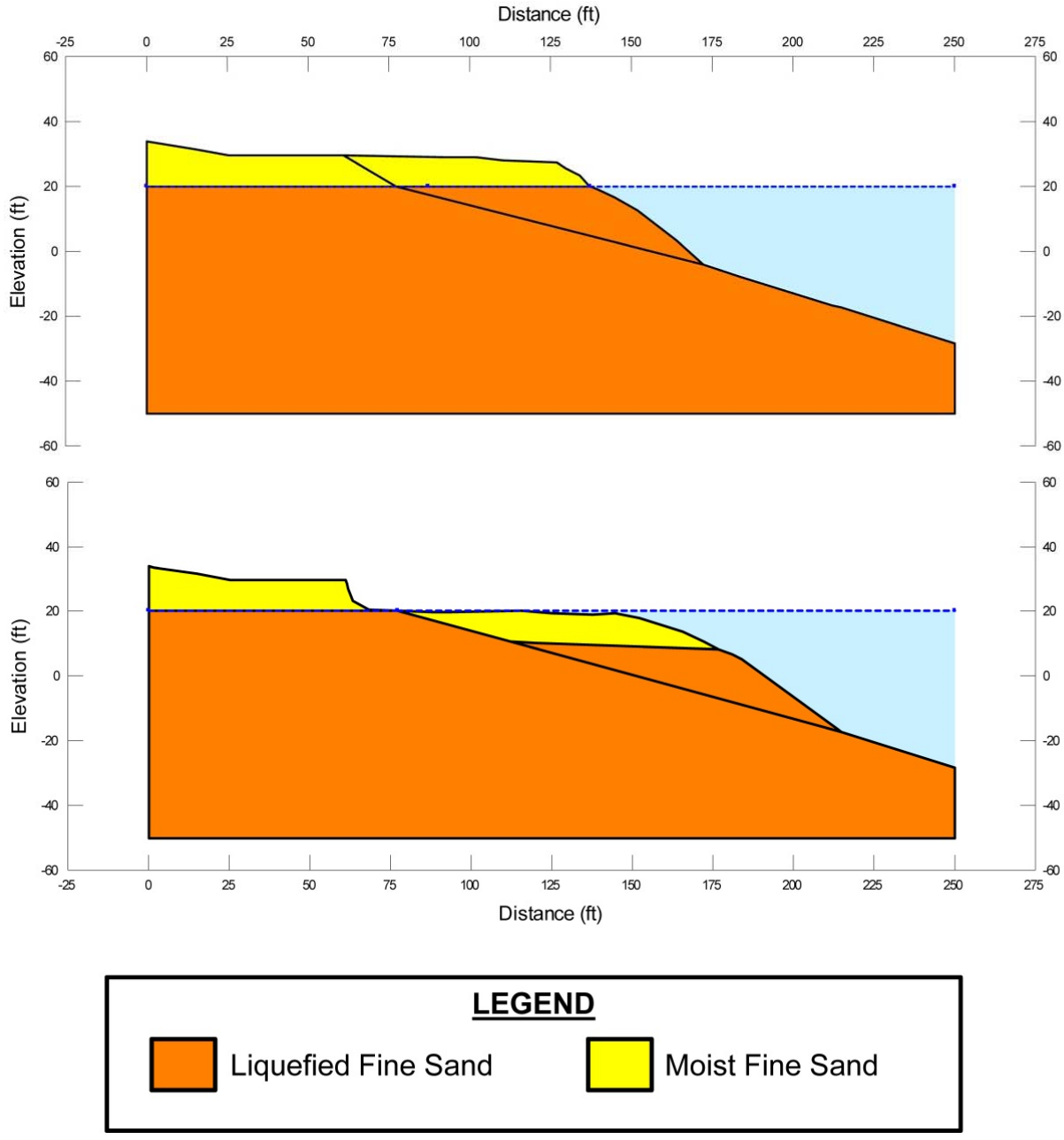

Figure B.5.4: Lake Merced Bank: (a) pre-failure geometry and best estimate failure surface for initial yield stress analyses, and (b) post-failure geometry and the best estimate failure surface for post-failure residual geometry analyses.

Based on the cross-sections shown in Figure B.5.4(b), and the properties and parameters described above, the best-estimate value of $S_{r,resid/geom}$ was $S_{r,resid/geom}$ = 122 lbs/ft^2. Parameters were next varied, as described previously, including analyses of alternate potential failure surfaces slightly above and below the failure surface shown in Figure B.5.4(b). Based on these analyses, it was judged that a reasonable range was $S_{r,resid/geom} \approx$ 101 to 147 lbs/ft^2.

Olson (2001) also back-calculated values of $S_{r,resid/geom}$. His best estimate failure surface was laid back slightly into the apparent underlying natural aeolian sand deposits, and is similar to the failure surface shown in Figure B.5.4 but is laid back even a bit farther into the natural soils near the back heel. He again reportedly assumed, however, that the fill materials largely controlled the failure. Olson's back-calculated best estimate of $S_{r,resid/geom}$ was 6.9 kPa (145 lbs/ft^2), with a range of 4.8 to 7.4 kPa (100 to 155 lbs/ft^2). He attributed the lower end of this range (4.8 kPa) to Seed (1987).

B.5.6 Overall Estimates of S_r

Overall estimates of S_r for this Class B case history were made based on the observed geometry and runout features and characteristics, and the values of $S_{r,yield}$ and $S_{r,resid/geom}$ as calculated in the preceding sections.

Runout characteristics for this case include a runout distance travelled by the center of gravity of the overall failure mass of D = 31.6 feet, and a slope height (from toe to top of the back scarp) of H = 32.3 feet, producing a runout ratio of D/H = 0.98. One set of estimates of Sr was made using the relationship of Equation 4-4 and Figure 4.11, and the resulting best estimate ranges of values of $S_{r,yield}$ and $S_{r,resid/geom}$ from the preceding Sections B.6.4 and B.6.5. Based on apparent runout characteristics, a range of $\xi \approx$ 0.65 to 0.95 was employed here, and this this led to best estimate of $S_r \approx$ 125 lbs/ft^2 and a range of $S_r \approx$ 83 to 182 lbs/ft^2. A second estimate was then made based on the relationship shown in Figure 4.9, and the range of values of $S_{r,yield}$ from Section B.5.4. Pre-failure Factors of Safety were estimated, based on runout, to be on the order of 0.55 to 0.8. This produced a resulting likely best estimate of $S_r \approx$ 128 lbs/ft^2, with a likely range of $S_r \approx$ 84 to 189 lbs/ft^2. Values estimated based on Equation 4-4 and Figure 4.11 were given some precedence over the estimates based on Figure 4.9. Variance in values of back-calculated $S_{r,yield}$ and $S_{r,resid/geom}$ from these current studies were then also considered, and so were values back-calculated or estimated by previous investigators. Values from previous investigators were given little weight here, however, and these were simply examined largely to ensure that previous studies were understood and that the current engineering team had made suitable accommodation for potential variability or variance.

Overall, based on an assumed normal distribution, it was judged that the (mean and median) best estimate of post-liquefaction strength for this case history is

$$\overline{S_r} = 136 \text{ lbs/ft}^2$$

and that the best estimate of standard deviation of mean overall post-liquefaction strength is

$\sigma_{\bar{S}} = 21$ lbs/ft^2

Seed and Harder (1990) reported a value of $S_r \approx 100$ lbs/ft^2 for this case. Olson (2001) and Olson and Stark (2002) did not apply their "kinetics" method to this case, and so they did not independently develop an estimate of S_r that incorporated momentum effects. Instead they simply used their value of $S_{r,resid/geom}$ as a conservative approximation of S_r for this less well-defined case, and used $S_r = 144$ lbs/ft^2 in developing their predictive relationship. Similarly, Wang (2003) and Wang and Kramer (2008) did not employ their zero inertial force (ZIF) method to incorporate inertial effects in back-analyses of this failure. Instead they selected their value of S_r based on examination of back-analyses of several previous investigators, and in the end selected $\overline{S_r} = 139.5$ lbs/ft^2, and a standard deviation of $\sigma_{\bar{S}} = 41.4$ lbs/ft^2. Despite these differing approaches taken to evaluation and/or selection of S_r, agreement between the values used in these three previous studies, and the values developed and employed in these current studies, is very good for this case history.

B.5.7 Evaluation of Initial Effective Vertical Stress

Average initial (pre-failure) effective vertical stress was assessed for the liquefied portion of the failure surface described in Section B.6.4 (and illustrated in Figure B.4.4). Parameters and sensitivity analyses were as described previously in Section B.6.4.

The resulting best estimate of average pre-failure effective stress within the liquefied materials controlling the failure was then $\sigma_{vo}' \approx 834$ lbs/ft^2, with a reasonable range of $\sigma_{vo}' \approx 630$ to 1,038 lbs/ft^2. This range is slightly non-symmetric about the median value, and this range was judged by the engineering team to represent approximately ± 2 standard deviations. Overall, the best characterization of initial (pre-failure) average effective vertical stress was then taken to be represented by a mean value of

$\overline{\sigma'_{vo}} \approx 834$ lbs/ft^2

and with a standard deviation of

$\sigma_{\bar{\sigma}} \approx 102$ lbs/ft^2

An estimate of σ_{vo}' was also calculated by Olson and Stark (2001, 2002). They reported a weighted average mean value of $\sigma_{vo}' \approx 1{,}157$ lbs/ft^2. This is larger than the value developed in these current studies, and the difference is largely due to the different failure surfaces assumed by the two investigation teams. Average initial vertical effective stresses were not directly reported by Wang (2003) and Kramer (2008), but they were published more recently in the publication by Kramer and Wang (2015). As discussed in Section 2.3.8.1(b)-(iii), Wang (2003) did not perform any independent analyses to assess σ_{vo}' for his 22 "secondary" cases, and this is one of those cases. Instead, he compiled values of S_r from multiple previous investigators, and averaged these for a best estimate. He also compiled multiple values of S_r/σ_{vo}' from previous investigators, and averaged these for a best estimate. He then used these two best-estimate values

of S_r and S_r/σ_{vo}' to infer a resulting representative value of σ_{vo}'. As described in Section 2.3.8.1(b)-(iii), the resulting averaged values of S_r and S_r/σ_{vo}' were incompatible with each other for a number of Wang's "secondary" case histories, and this process produced unreasonable, and in some cases physically infeasible, values of σ_{vo}' for a number of case histories. Wang's value of σ_{vo}' = 1,316 is in very good agreement with that of Olson. But because of differences in assumed failure planes, neither value is directly comparable to the values of σ_{vo}' developed in these current studies.

B.5.8 Evaluation of $N_{1,60,CS}$

Section B.5.3 described the geology and materials involved in this case history, and also presented the available SPT data. This failure either occurred mainly within the lower portion of the loosely end dumped sandy fill, or in the upper portion of the immediately underlying loose aeolian sands.

If the loose fill controlled the failure, then estimation of suitable $N_{1,60,CS}$ values can be developed by either of two approaches. Olson (2001) assumed that the failure was within this fill, and that Test Borings 1 and 2 had occurred behind the rear extent of the fill (as potentially suggested in Figure B.5.5) and so did not serve to characterize this loose fill material. Accordingly, he estimated equivalent approximate $N_{1,60,CS}$ values based on assumed loose conditions associated with end dumping and an absence of useful compaction. An alternate approach would be to assume that the two Test Borings are correctly logged as having penetrated into this loosely end dumped fill, and that the top several SPT values occur within this material as shown in Figures B.5.2 and B.5.3. As the SPT equipment and procedures were not well defined, this still leaves significant uncertainties as to the appropriate characterization of $N_{1,60,CS}$ for this loosely dumped fill.

If the underlying loose aeolian sands (and silty sands) controlled the failure, then the SPT data from Test Borings 1 and 2 are useful here, but there are again significant uncertainties due to the lack of well-defined SPT equipment and procedures.

In these current studies, all of these sets of possibilities were considered. In the end, it did not make a great deal of difference with regard to estimation of representative $N_{1,60,CS}$ values, as the values that the current engineering team would "infer" for the loosely end dumped fill would be very similar to the values apparently measured in the upper "fill" of Test Borings 1 and 2, and the $N_{1,60,CS}$ values of the (also loose) aeolian natural sands underlying the fill are also very similar.

The overall best estimate mean value of $N_{1,60,CS}$ for either the loosely dumped fill sands, or the underlying loose aeolian sands, or a combination of the two, was judged to be $\overline{N_{1,60,CS}} \approx 8.5$ blows/ft. Variance of $\overline{N_{1,60,CS}}$ was estimated primarily on the basis of the perceived uncertainties described previously, including uncertainties as to which of the two materials mainly controlled the failure, whether the Test Borings characterized the loose fill, and the details regarding the SPT equipment and procedures employed. Considering these, the representation of uncertainty in the representative median value of $\overline{N_{1,60,CS}}$ was taken as $\sigma_{\overline{N}} \approx 2.2$ blows/ft.

Olson and Stark (2001, 2002) developed an estimated representative value of $N_{1,60}$ = 7.5 blows/ft for this case history, and they presented no range. Wang (2003) and Kramer (2008) jointly developed a representative value of $\overline{N_{1,60,CS}}$ = 5.9 blows/ft, and their estimated standard deviation of that overall mean value for this case history was $\sigma_{\overline{N}}$ = 8.0 blows/ft. Details of the development of this interpretation by Wang and Kramer are not presented, but the apparently excessively large variance (or standard deviation) in $\overline{N_{1,60,CS}}$ appears to have been an artifact of the procedures used to estimate such variances for poorly defined cases.

Overall agreement between these three independent assessments of representative $\overline{N_{1,60,CS}}$ values is judged to be generally good, excepting the very large standard deviation ascribed by Wang and Kramer which would lead to negative values of $N_{1,60,CS}$ at a mean minus less than one standard deviation level. That does not necessarily adversely affect the mathematics of their regressions, however, and it is a useful representation of what they view to be large uncertainties with respect to a selection of a representative value of $N_{1,60,CS}$ for this case.

B.6 El Cobre Tailings Dam (Chile; 1965)

B.6.1 Brief Summary of Case History Characteristics

Name of Structure	El Cobre Tailings Dam
Location of Structure	El Cobre, Chile
Type of Structure	Tailings Dam
Date of Failure	March 28, 1965
Nature of Failure	Seismic, During 1965 Chile Earthquake (M_L = 7.4)
Approx. Maximum Slope Height	103 ft.

B.6.2 Introduction and Description of Failure

The Chile earthquake of March 28, 1965 (M_L = 7.4) produced catastrophic failures of multiple mine tailings dams and impoundments in central Chile (Dobry and Alvarez, 1967). Prominent among these failures were the failures of the El Cobre tailings dams, which released more than 2 x 10^6 tons of tailings into the valley downstream, destroying part of the town of El Cobre and resulting in more than 200 deaths.

The El Cobre tailings dams had begun impounding tailings in 1930, and the overall facility consisted of three dams: the Old Dam, the Small Dam, and the New Dam. When the 1965 earthquake occurred, the Old Dam was partially out of service and functioned only as an emergency dam, and the Small Dam was also out of service. The New Dam had recently begun operations in 1963, and was actively accepting tailings.

Both the Old Dam and the New Dam suffered liquefaction-induced failures. There was insufficient documentation of the failure of the New Dam as to represent a suitable basis for forensic back-analyses, and so it is the failure of the Old Dam that has been investigated and back-analyzed by multiple investigation teams, including these current studies.

Figure B.6.1 shows the pre-failure and post-failure cross-sections of the Old Dam, at exaggerated vertical scale (Dobry and Alvarez, 1967). There were no eyewitnesses to the failure of the Old Dam. The failure appears to have occurred almost entirely within the impounded tailings, and did not involve the underlying foundation materials.

Dobry and Alvarez (1967) reported: "The front slope of the southern corner of the Old Dam receded 65m, making the adjacent intermediate terrace disappear completely; the scarp produced was almost vertical…. All the fine and unconsolidated tailings flowed out, and from the upper part only a horseshoe-shaped shell was left, which bound(ed) the back and sides of the large central depression left by the material which had flowed out. The bottom of this central depression was formed by several almost horizontal terraces (2% slope toward the valley)….."

Figure B.6.3(a) shows the rim of horseshoe shaped top deck remaining after the failure, and the depressed central zone from which the liquefied tailings departed, and Figure B.6.3(b) shows the runout materials that flowed out from the impoundment. Runout of the liquefied

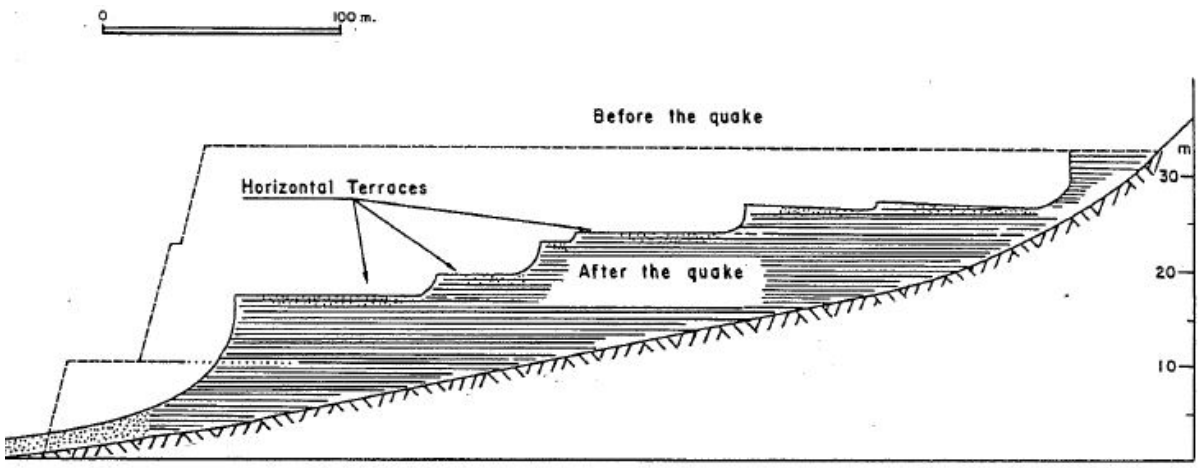

Figure B.6.1: Pre-failure and post-failure cross-sections (at 5:1 exaggerated vertical scale) of the El Cobre Tailings Dam "Old Dam" (Dobry and Alvarez, 1967).

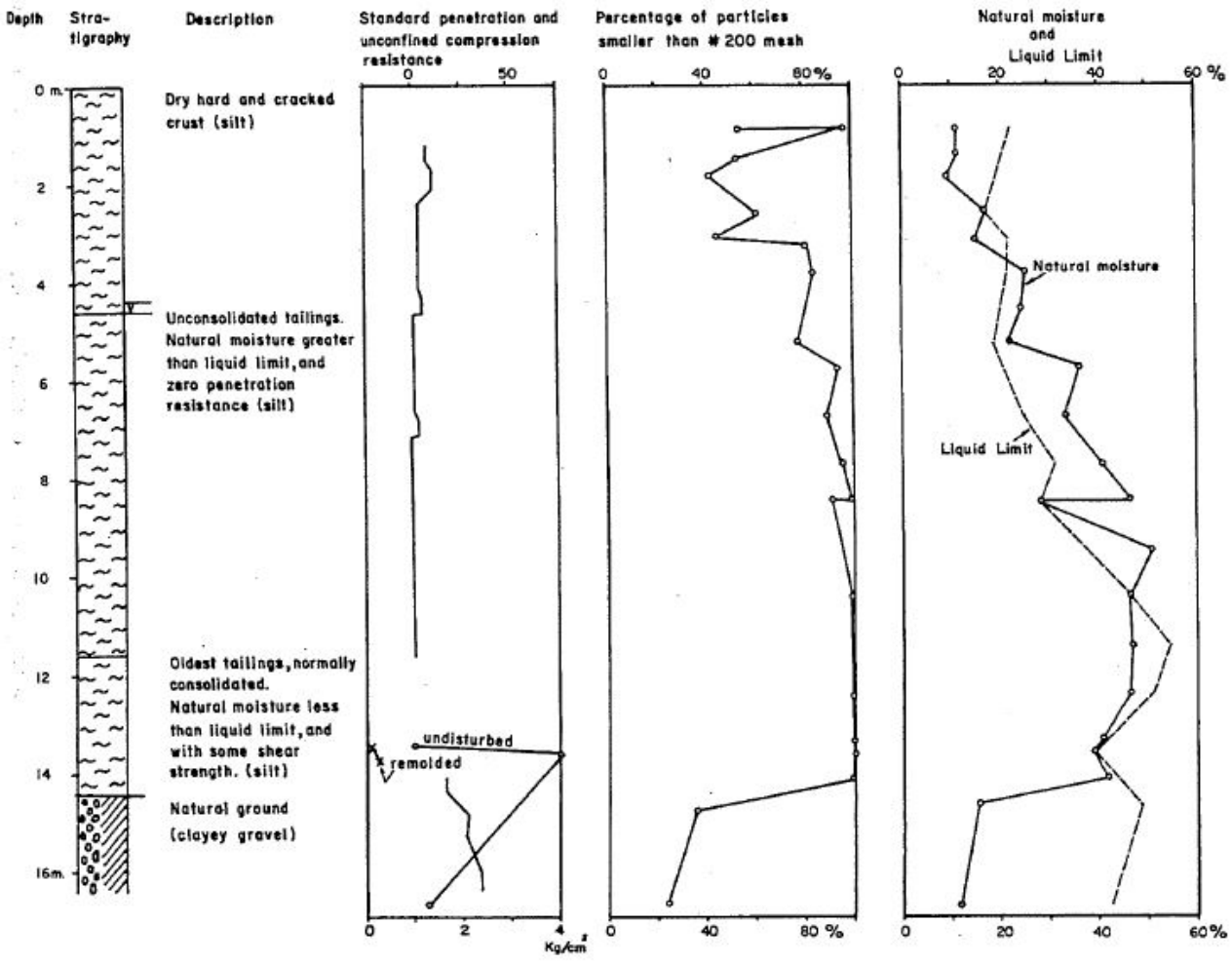

Figure B.6.2: Boring log, SPT results, fines contents, natural water contents and liquid limits in the tailings of the El Cobre "Small Dam" (Dobry and Alvarez, 1967).

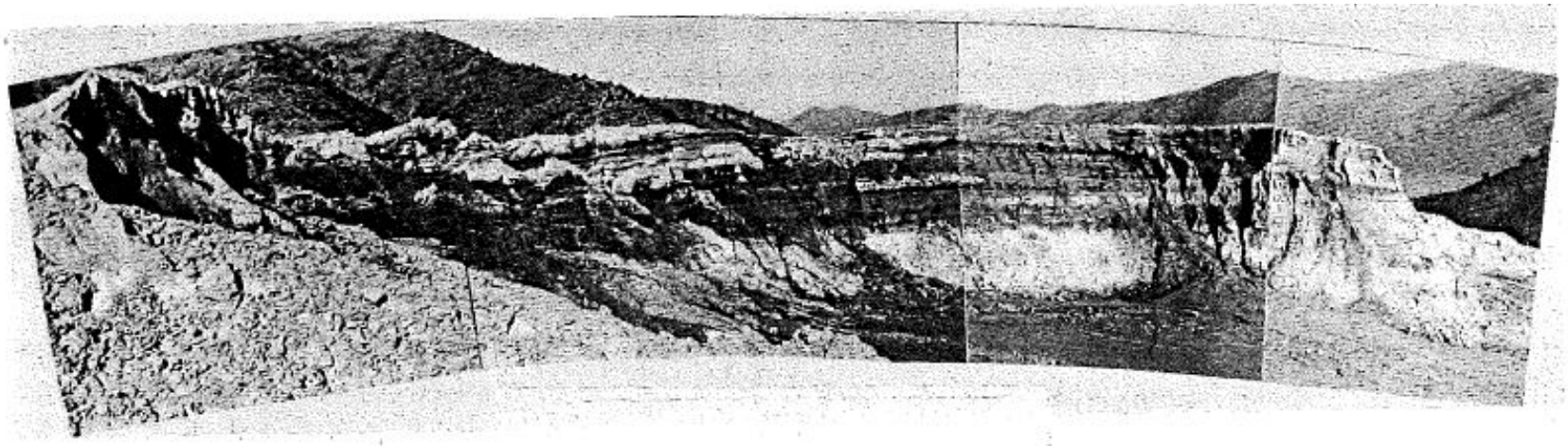

Figure B.6.3(a): Photograph showing post-failure conditions at the Old Dam; photo taken looking upstream towards the back edge and the "horseshoe shaped" scarp (Dobry and Alvarez, 1967).

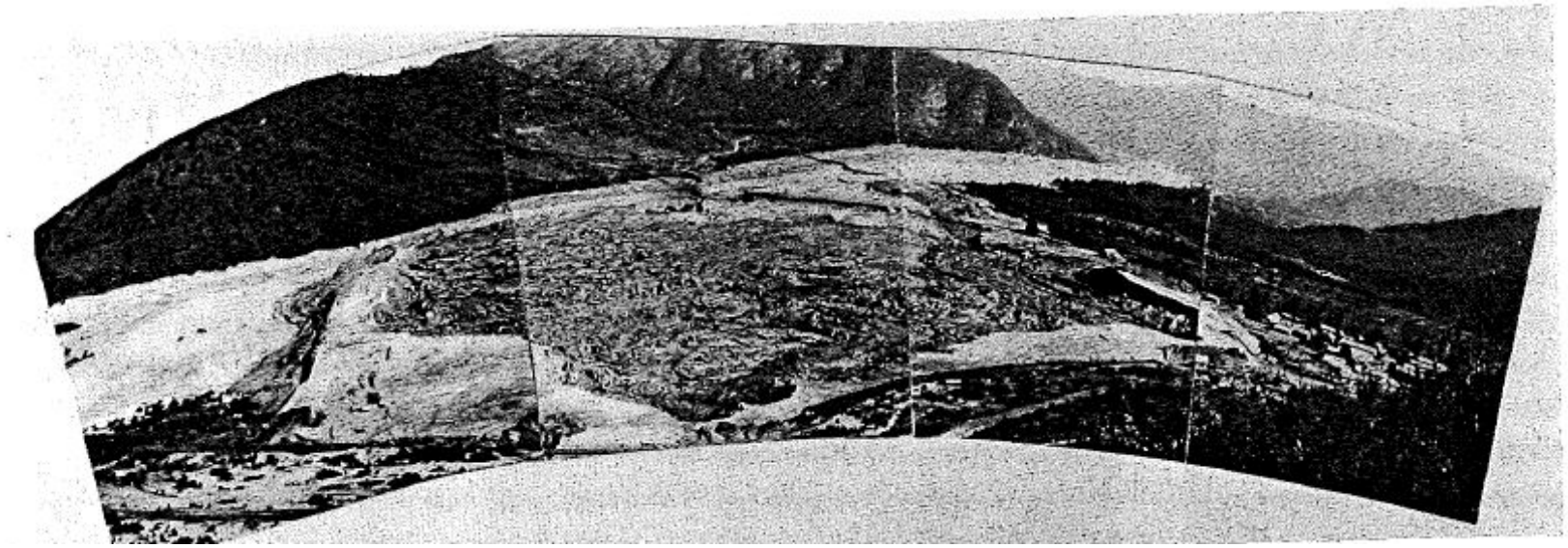

Figure B.6.3(b): Photograph of post-failure conditions at the Old Dam showing the liquefied tailings outflow mass (Dobry and Alvarez, 1967).

tailings traveled significant distances, and the runout materials immediately downstream of the toe of the failure were relatively thinly spread and had relatively low (nearly horizontal) post-failure surface slopes.

B.6.3 Geology and Site Conditions

Figure B.6.2 shows the log of an exploratory SPT boring performed in the Small Dam. The Small Dam and the Old Dam had been filled during the same general period, and with similar materials and similar placement methods, and so it is assumed that the results of this boring log are also generally representative of conditions in the Old Dam.

As shown in the boring log of Figure B.6.2, a relatively dry, desiccated crust was present at the top of the Small Dam, and it is assumed that a similar crust with a thickness of about 4 to 5 meters was also present at the top of the Old Dam. Beneath this desiccated upper crust, the next 7 meters were comprised of underconsolidated tailings, as evidenced by in situ water contents that were higher than the liquid limits of these materials, as shown in Figure B.6.2. Dobry and Alvarez (1967) suggest that a similar layer of underconsolidated tailings, approximately 10 m in thickness, underlay the desiccated upper crust in the Old Dam. The underlying deeper tailings were then more normally consolidated (or nearly normally consolidated), as evidenced by in situ water contents slightly lower than their liquid limits.

These normally consolidated tailings at the base of the impoundment were underlain by the natural foundation soils. These were comprised mainly of clayey gravels, likely of colluvial origin. These were firmer materials than the overlying tailings deposits, and were not involved in the failures that occurred. The phreatic surface within the impoundment was assumed to have been located at or near to the boundary between the desiccated upper crust and the underlying underconsolidated tailings.

Similar stratigraphy and conditions, including the location of the phreatic surface at or near to the boundary between the desiccated upper crust and the underlying underconsolidated tailings, was inferred by Alvarez and Dobry to have been likely present at the Old Dam as well.

The tailings impounded were comprised mainly of fine sandy silts, with fines contents generally of 90% or greater. Liquid limits varied with depth, and were generally between about 10% to 50%. A single boring with multiple SPT tests was performed in the tailings of the Small Dam, and the results are shown in Figure B.6.2.

B.6.4 Initial Yield Stress Analyses

Back-analyses for assessment of both $S_{r,yield}$ and $S_{r,resid/geom}$ were exceptionally difficult for this case history, due to the poorly defined post-failure geometry (especially downstream of the original toe of the Old Dam), and the nature of the apparent failure mechanism(s) involved.

Figures B.6.4(a) and (b), and Figure B.6.5, show examples of some of the analyses performed to attempt to obtain some understanding of the ranges of types of potential failure

mechanisms involved, and the associated values of initial yield strength ($S_{r,yield}$) for each mechanism that would be required within the foundation and embankment materials of the north dike section to produce a calculated Factor of Safety equal to 1.0. $S_{r,yield}$ is not the actual post-liquefaction strength, but it proves to be useful in developing estimates of post-liquefaction strength (S_r) for most of the failure case histories back-analyzed in these current studies.

Figure B.6.4(a) shows the most critical potential failure surface for the types of rotational failures, or semi-rotational and translational failures, that could have removed the buttressing provided at the downstream toe of the overall failure; requiring shearing through some portion of the initial starter dike.

Unit weights of the non-saturated tailings above the phreatic surface were modeled with a unit weight of $\gamma_m \approx 80$ lbs/ft^3, and this was then varied over a range of 76 to 84 lbs/ft^3 for parameter sensitivity studies. Unit weights of the saturated tailings below the phreatic surface were modeled with a unit weight of $\gamma_s \approx 85$ lbs/ft^3, and this was then varied over a range of 81 to 89 lbs/ft^3 for parameter sensitivity studies. The friction angle of the tailings above the phreatic surface was modeled with $Ø' \approx 29°$, and a range of $Ø' \approx 27°$ to 32°. The shell material of the starter dikes was assumed not to liquefy, and was modeled with a friction angle of $Ø' \approx 35°$, and a range of $Ø' \approx$ 32° to 38°. These types of moderate parameter variations proved to be of little significance, however, as the overall uncertainties were dominated by uncertainties as to mechanisms and sequence of failures, rather than variations in parameters of the non-liquefied soils for this case history.

For the failure surface shown in Figure B.6.4(a), the back-calculated value of $S_{r,yield}$ within the liquefied tailings was $S_{r,yield} = 643$ lbs/ft^2. This would not prove to be very useful, however, because (1) post-failure displacements were very large after this initial toe failure, (2) likely erosion as liquefied materials poured through the opening in the starter dike probably eroded and enlarged the hole and altered the eventual post-failure geometry, and (3) both higher and lower values of $S_{r,yield}$ were subsequently back-calculated for other elements of this likely retrogressive failure.

Figure B.6.4(b) shows an example back-analysis of the failure of the next section (the "first deck" behind the initial toe dike), with the entire deck modeled as failing monolithically. The back-calculated value for this is $S_{r,yield} = 331$ lbs/ft^2.

It is judged by the current engineering team to be unlikely that this entire "first deck" section moved out monolithically. Figure B.6.5 shows an example set of back-analyses of incrementally retrogressive failures sequentially initiating and eventually removing the materials of this "first deck" in a series of sequential (retrogressive) sub-failures. These are a more critical set of failure mechanisms, and they produce significantly higher values of $S_{r,yield}$. The values of $S_{r,yield}$ decrease towards the rear heel, partly due to slight thinning of the materials above the failure surface (which inclines at approximately 2° towards the valley), but the selected lateral thickness of each incremental slice has a significant effect on back-calculated values of $S_{r,yield}$, so the values shown should be considered to be only "illustrative" here. Eventually, the failure surface selected a new (and slightly higher elevation) preferred failure surface, and it "stepped up" to start a second deck section.

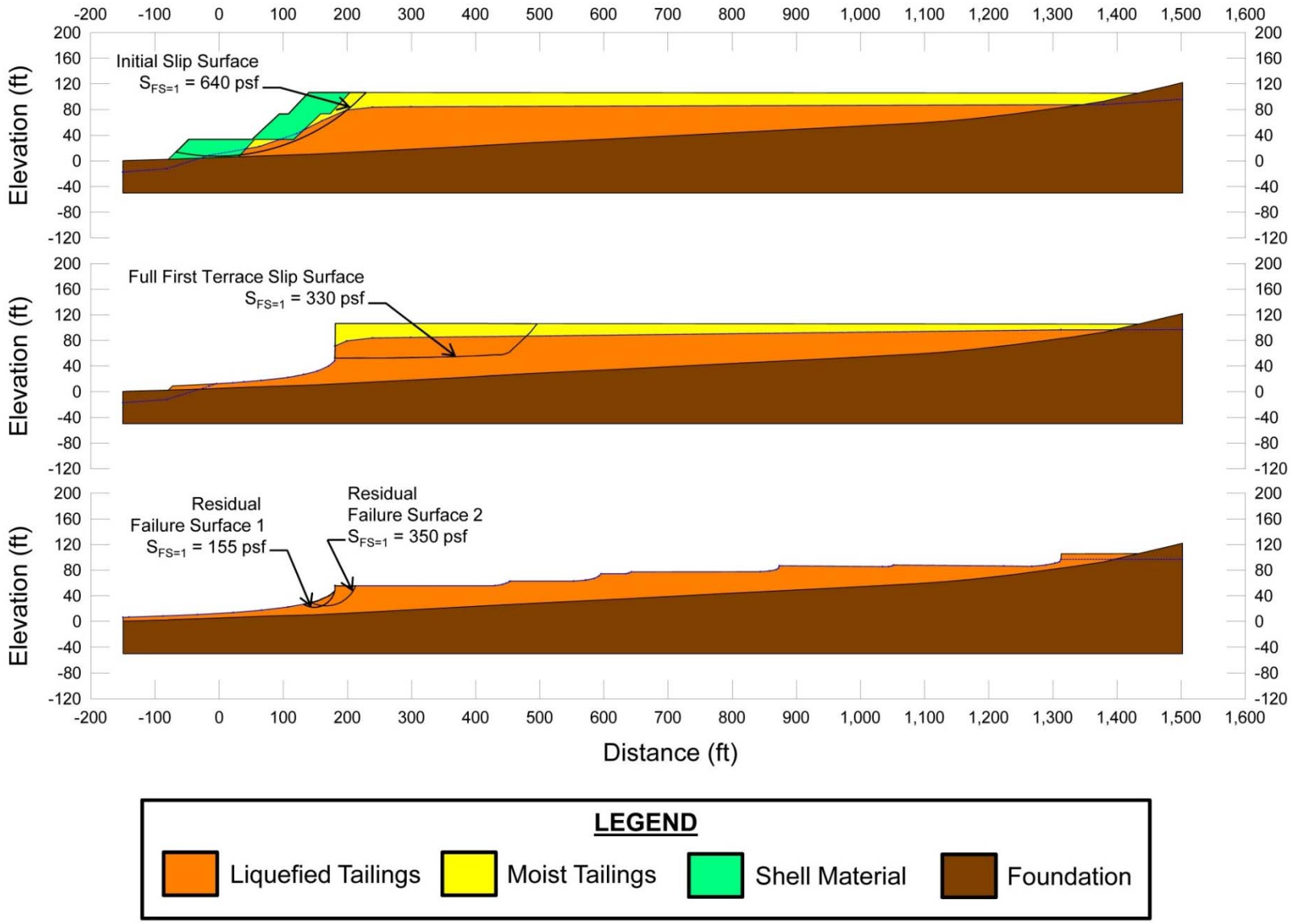

Figure B.6.4: Examples of some of the trial analyses performed to garner an understanding of the potential mechanics and potential strength characteristics of the Old Dam and its potential failure mechanisms.

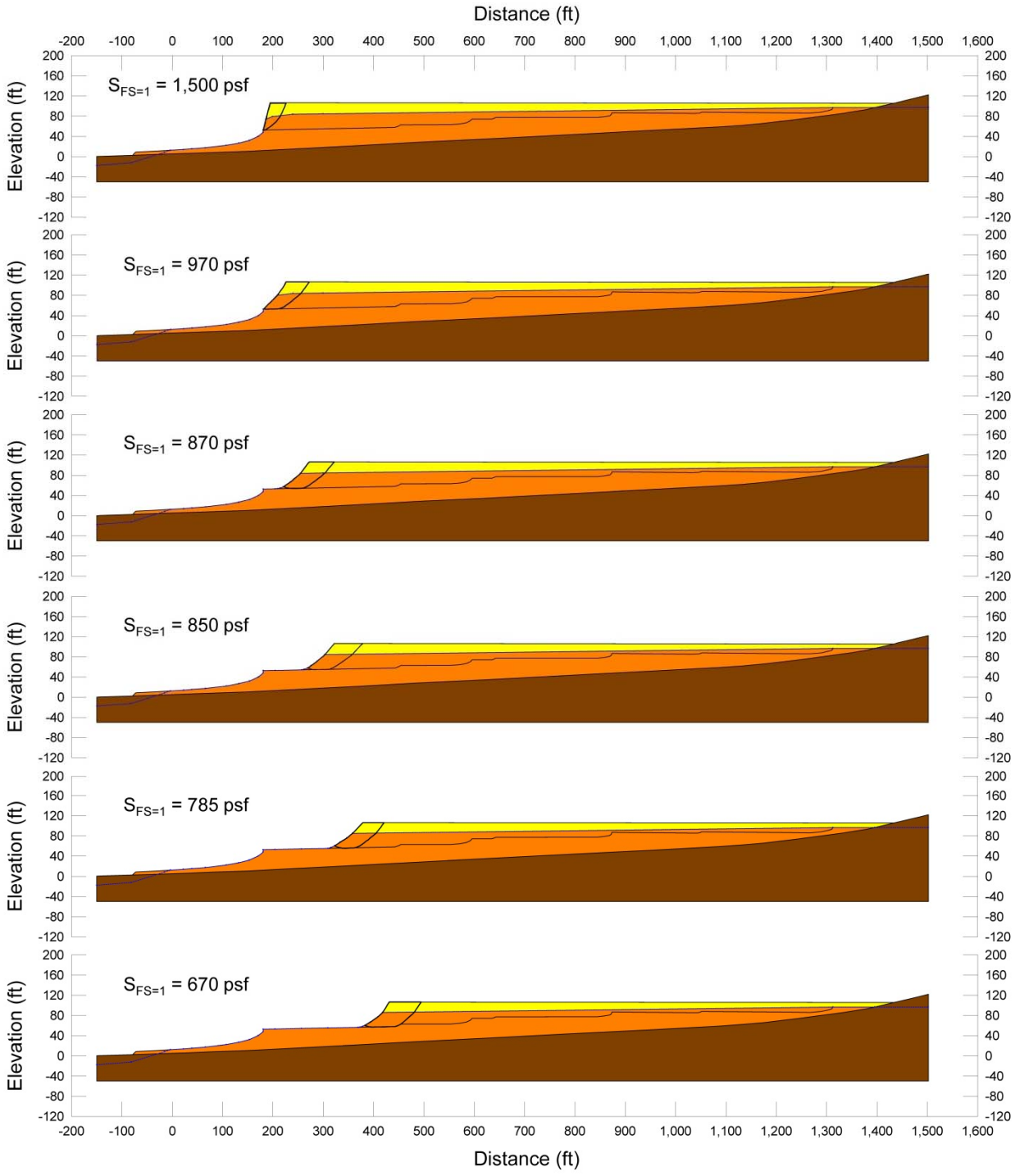

Figure B.6.5: Examples of some of the trial analyses of retrogressive failures of the "first deck" of the Old Dam, and associated values of $S_{r,yield}$.

This process appears to have been repeated, until the eventual final back-heel of the overall feature remained stable. Back-analysis of that eventual back-heel was not fruitful, because it appears likely that the failure "stepped up" into non-saturated materials that did not liquefy at this eventual back heel.

Other sets of similar analyses were performed, and these showed that values of $S_{r,yield}$ of on the order of $S_{r,yield} \approx 250$ to 950 lbs/ft^2 could be back-calculated for these types of retrogressive failures, with values generally decreasing towards the upper (back heel) region as failure progressed.

Due to the very large runout distance, and the large runout ratio, as well as the apparently relatively "clean" deck surfaces shown in Figure B.6.1, it is difficult to make a well-constrained quantitative assessment of a "representative" value of $S_{r,yield}$ for this complicated retrogressive failure. It is also difficult to develop consensus on how to "weight" the various potential values of $S_{r,yield}$ for the different mechanisms and different potential individual failure surfaces. Overall, the current investigation team developed a consensus view that representative values of $S_{r,yield}$ would be on the order of approximately 300 to 600 lbs/ft^2.

Olson (2001) did not develop a back-calculated value of $S_{r,yield}$ for this challenging case history, and so there are no values of $S_{r,yield}$ from previous investigations against which to compare this current range of estimated $S_{r,yield}$ values. This was the only one of his 33 back-analyzed case histories for which Olson did not develop an estimated value (or range of estimated values) of $S_{r,yield}$.

B.6.5 Residual Strength Analyses Based on Residual Geometry

It was not possible to perform rigorous and fully reliable back-analyses to determine the value of $S_{r,resid/geom}$ required to produce a calculated Factor of Safety equal to 1.0 based on residual geometry, because the post-failure residual geometry was insufficiently well defined. This is a significant source of uncertainty for this case history.

Olson (2001) assumed that the thickness of tailings runout shown at the left side of Figure B.6.1 was representative of the thickness of the entire failure mass in order to make what he termed a "crude estimate" of $S_{r,resid/geom}$. He assumed a thickness of 2 m., and an underlying slope of approximately 4° and a top slope of approximately 4°, and with assumed unit weights of 12.6 to 14.1 kNn/m^3 he used a simplified infinite slope analysis to calculate $S_{r,resid/geom} \approx 1.8$ to 2.0 kPa, (38 to 42 lbs/ft^2) with a best estimate of $S_{r,resid/geom} = 1.9$ kPa (40 lbs/ft^2).

In these current studies, several additional analyses were performed to attempt to further explore potential ranges of values of $S_{r,resid/geom}$.

Figure B.6.4(b) shows two potentially critical rotational failures at the toe of the final overall geometry, and the associated values of $S_{r,resid/geom}$. The overall tailings facility was strongly shaken, and it would seem likely that it liquefied at these locations, in which case these back-calculated values of $S_{r,resid/geom}$ would be valid. But it is also possible that liquefaction of

surrounding and overlying materials "shielded" the tailings at these toe locations, by preventing full cyclic shear stress transfer from overlying materials through softened (liquefied) materials, and that the materials associated with the potential failure surfaces of Figure B.6.4(b) therefore did not "trigger" or liquefy, and so did not achieve a post-liquefaction strength condition. The depths modeled for the two potentially critical failure surfaces shown in Figure B.6.4(b) are limited by the observation that the liquidity index, and thus the likely post-liquefaction strengths, of the materials at the very base of the tailings impoundment are more favorable (see Sections B.6.3 and B.6.8), so that the base of the tailings would have been somewhat stronger than the materials above them.

Additional efforts to evaluate potential values of $S_{r,resid/geom}$ were frustrated by lack of documentation. Conditions further downstream of the toe section shown in Figure B.6.1 are not quantifiably well documented. Aerial photos, and oblique photos, show that tailings flowed out to considerable distances, and they also show an irregular top surface of the flowed tailings that is not reflected in the cross-section of Figure B.6.1. This may reflect the "Several chunks of the upper dry crust were left on these terraces" reported by Dobry and Alvarez (1967).

It cannot be determined whether or not the materials controlling stability of the residual geometry of the "upper decks" liquefied (or "triggered"), and so it cannot be determined with certainty whether post-failure back-analyses of these would provide representative values of $S_{r,resid/geom}$ for this case.

Aerial photo evidence shows considerable flow of tailings extending far downstream of the original dam toe, but lack of quantified characterization of (1) the topography (top slopes) of this failure mass, and (2) the underlying basal contact slopes at the base of this flowed mass precludes reliable back-analyses of $S_{r,resid/geom}$ for these sections.

The back-calculated (approximate) value of $S_{r/resid/geom} \approx 40$ lbs/ft^2 proposed by Olson appears to be a likely lower bound estimate of $S_{r,resid/geom}$, but there appears to be no fully reliable basis for quantification of useful higher values.

The current investigation team concluded that a representative range of values of $S_{r,resid/geom}$ for this case would be estimated as $S_{r,resid/geom} \approx$ 40 to 60 lbs/ft^2, with the expectation that this would likely be somewhat conservatively biased.

B.6.6 Overall Estimates of S_r

Overall estimates of S_r for this Class B case history were very challenging, due to the very large runout and the poorly defined post-failure conditions downstream of the original toe of the dam. Estimates were made by a number of approaches, and then the current engineering team discussed and debated until a consensus was reached with regard to characterization of both the best estimate mean value of post liquefaction strength ($\overline{S_r}$) and also the standard deviation of this mean ($\sigma_{\overline{S}}$).

The toe of the runout mass extended more than 900 feet beyond the pre-failure toe of the embankment, and the center of gravity of the failure mass appears to have traveled more than 500 to 800 feet. The height of the failure can measured as approximately 105 feet from the original base of the failure at the original toe of the starter dike to the top of the eventual (final) heel scarp, or it can be measured as approximately 95 feet from the toe of the liquefied tailings behind the starter dike to the top of the eventual (final) heel scarp. In either case, the runout ratio is approximately 500/100 to 800/100 ≈ 5 to 8. Based on Figure 4.7, this would suggest a likely value of that $\xi \approx 0.4$ to 0.5 for this relatively large runout case. Based on the ranges of values of $S_{r,yield}$ ≈ 300 to 600 lbs/ft^2 and $S_{r,resid/geom} \approx$ 40 to 60 lbs/ft^2 from Section B.6.4 and B.6.5, respectively, and Equation 4-4, this would produce an estimated range of values of $S_r \approx$ 68 to 165 lbs/ft^2.

The current investigation team then further adjusted this approximate range based on their individual judgments of the available information, with each member weighing their own perceptions as to the apparent characteristics of the failure (including photographs, published descriptions, etc.), and the relative merits of the apparent ranges of values of $S_{r,yield}$ and $S_{r,resid/geom}$ as reported above and the basis upon which they were each developed. The team then developed a consensus overall characterization. It was generally agreed that the value of S_r was likely higher than the lower bound value of $S_{r,yield} \approx$ 40 lbs/ft^2 conservatively estimated by Olson (2001), but it was noted that the value may not have been much higher than this.

The result was a likely best estimate range of $S_r \approx$ 40 to 150 lbs/ft^2. This range was judged to represent approximately +/- 2 standard deviations, so the overall characterization of S_r for this case was then a best estimate of median post-liquefaction strength for this case history of

$$\overline{S_r} = 95 \text{ lbs/ft}^2$$

and a standard deviation of mean overall post-liquefaction strength is

$$\sigma_{\overline{S}} = 27 \text{ lbs/ft}^2$$

Olson (2001) and Olson and Stark (2002) did not apply their "kinetics" method to this case, and so they did not independently develop an estimate of S_r that incorporated momentum effects. Instead they simply used their value of $S_{r,resid/geom}$ (as described previously in Section B.6.5) as a conservative approximation of S_r, and used S_r = 1.8 to 2.0 kPa, (38 to 42 lbs/ft^2) with a best estimate of S_r = 1.9 kPa (40 lbs/ft^2).

Similarly, Wang (2003) and Wang and Kramer (2008) did not employ their zero inertial force (ZIF) method to incorporate inertial effects in back-analyses of this failure. Instead Wang's (2003) dissertation states that they selected their value of S_r based on examination of back-analyses of previous investigators, and in the end selected $\overline{S_r}$ = 195.2 lbs/ft^2, and a standard deviation of $\sigma_{\overline{S}}$ = 64.8 lbs/ft^2. Wang's approach to these "lesser" (or Class B) case histories was to obtain values from multiple previous investigations, and then to simply average them. For this case (El Cobre Tailings Dam), in Table 6-8 of his dissertation, he lists only one source and that is Olson (2001), and he lists Olson's value of S_r as 195 lbs/ft^2. That appears to be an error, as Olson's value was 40 lbs/ft^2. This may be a simple error, but it appears more likely that Wang recognized that Olson's value of $S_{r,resid/geom}$ would underestimate the actual value of S_r for this case, and that he either

performed his own assessment either of S_r or at least of $S_{r,yield}$, and then developed an independent estimate of overall S_r (but failed to document this work). Wang was regularly taking values of $S_{r,yield}$ and $S_{r,resid/geom}$ for other cases, and then averaging them to estimate S_r, and he may have done that here as well. In any case, his best estimate value of value of $\overline{S_r} = 195.2$ lbs/ft^2 does not appear to be necessarily unreasonable here.

Wang's approach to estimation of standard deviation of the mean value of S_r for the "Secondary" case histories was to place each case history into one of five categories based on the quality and reliability of the data available, and then to assign coefficients of variation of between 5% to 25% based on these assessments of data quality, quantity and reliability. An equational relationship was then applied to provide scaling of these assessments in a manner that provided approximate consistency with estimates of variance (and standard deviations) for the 10 "Primary" case histories that had been back-analyzed by the ZIF method.

B.6.7 Evaluation of Initial Effective Vertical Stress

Average initial (pre-failure) effective vertical stress was assessed for the liquefied portion of the overall (final scarp) failure surface in Figure B.6.5. Parameters and sensitivity analyses were as described previously in Section B.6.4.

The resulting best estimate of average pre-failure effective stress within the liquefied materials controlling the failure was then $\sigma_{vo}' \approx 2{,}061$ lbs/ft^2, with a reasonable range of $\sigma_{vo}' \approx$ 1,709 to 2,441 lbs/ft^2. This range is slightly non-symmetric about the median value, and this range was judged by the engineering team to represent approximately ± 2 standard deviations. Overall, the best characterization of initial (pre-failure) average effective vertical stress was then taken to be represented by a mean value of

$$\overline{\sigma'_{vo}} \approx 2{,}075 \text{ lbs/ft}^2$$

and with a standard deviation of

$$\sigma_{\bar{\sigma}} \approx 183 \text{ lbs/ft}^2$$

An estimate of σ_{vo}' was also calculated by Olson and Stark (2001, 2002). They reported a representative value of $\sigma_{vo}' \approx 82.6$ to 103.9 kPa (1,725 to 2,169 lbs/ft^2), in very good agreement with these current studies. Average initial vertical effective stresses were not directly reported by Wang (2003) and Kramer (2008), but they were published more recently in the publication by Kramer and Wang (2015). As discussed in Section 2.3.8.1(b)-(iii), Wang (2003) did not perform any independent analyses to assess σ_{vo}' for his 22 "secondary" cases, and this is one of those cases. Instead, he compiled values of S_r from multiple previous investigators, and averaged these for a best estimate. He also compiled multiple values of S_r/σ_{vo}' from previous investigators, and averaged these for a best estimate. He then used these two best-estimate values of S_r and S_r/σ_{vo}' to infer a resulting representative value of σ_{vo}'. As described in Section 2.3.8.1(b)-(iii), the resulting averaged values of S_r and S_r/σ_{vo}' were incompatible with each other for a number of

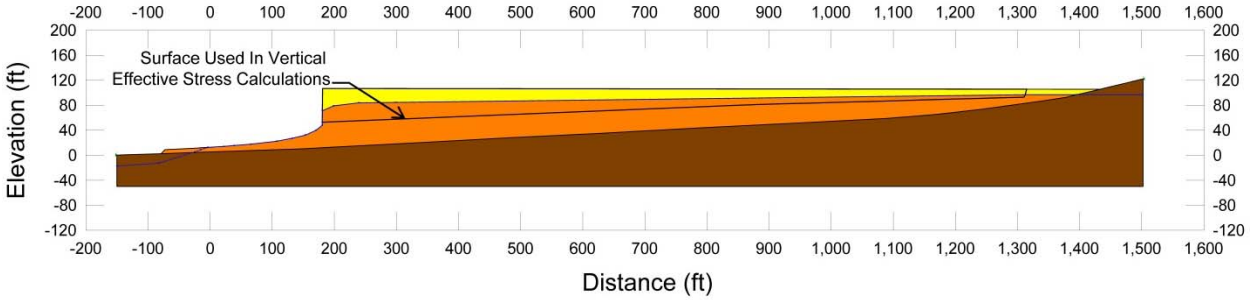

Figure B.6.6: Failure surface used for initial (pre-failure) vertical effective stress calculations.

Wang's "secondary" case histories, and this process produced unreasonable, and in some cases physically infeasible, values of σ_{vo}' for a number of case histories. Wang's value of σ_{vo}' = 9,760 lbs/ft^2 is clearly physically infeasible for this case, based on the cross-section, and so it is not considered a useful check here. Agreement between Olson's value, which is well-documented, and the values developed in these current studies is excellent.

B.6.8 Evaluation of $N_{1,60,CS}$

No SPT data are available from the tailings impounded in the Old Dam, but SPT data are available from a boring performed in the Small Dam, as shown in Figure B.6.2. Equipment and procedure details for these SPT are not known, which is a source of uncertainty here. An additional source of uncertainty here is the need to extrapolate SPT data from the tailings of the Small Dam to represent the tailings of the Old Dam. In addition, Olson (2001) speculated that large pore pressures generated by the SPT in these fines-dominated and very loose soils might have led to underestimation of penetration resistances, as Ishihara (1984) and Ishihara et al. (1990) had suggested for SPT performed in the tailings of the Moshi-Koshi Tailings Dam failure (see Appendix B, Section B.11).

As shown in Figure B.6.2, uncorrected blowcounts in the upper 4 meters of the tailings in the Small Dam were in the range of N = 3 to 12 blows/ft. Below this upper (desiccated) crust the underlying underconsolidated tailings had uncorrected blowcounts of either zero or one (most were reported as zero, only two were reported as one). It is difficult to know exactly what these values mean. A blowcount of zero can mean that the rod weight alone caused bearing failure of the sampler, or it can mean that the sampler was struck once and liquefaction occurred and the sampler sank with no second blow required. Usually that second situation is reported as a blowcount of "one".

The tailings at the base of the deposit appear to be less underconsolidated, and it appears that post-liquefaction strengths would be more favorable over the lowest portion of the tailings deposit (see Section B.6.3 and Figure B.6.2). Accordingly, failures were generally assumed not to penetrate into the lowest 1.5 meters of the tailings pile.

In either case, penetration resistance within the portion of the tailings deposit that was underconsolidated was clearly very low.

In these current studies, the representative penetration resistance for these very loose, silty tailings was taken as $\overline{N_{1,60,CS}}$ = 2 blows/ft, with a standard deviation of the value of this mean of $\sigma_{\overline{N}}$ = 1.0 blows/ft.

Olson (2001) and Olson and Stark (2002) did not make a fines adjustment, and so selected a value of $N_{1,60}$ (rather than $N_{1,60,CS}$) for this case history. Their selected value of representative penetration resistance was $N_{1,60}$ = 0 blows/ft.

Wang (2003) and Kramer (2008) made a fines adjustment based on the fines adjustment of Seed and Harder (1990), and selected a somewhat higher value of $\overline{N_{1,60,CS}}$ = 6.8 blows/ft, and a standard deviation of $\sigma_{\overline{N}}$ = 0.9 blows/foot. The full details of the basis for this selection are not reported. It appears likely that an uncorrected blowcount was selected as representative, and that effective overburden corrections then led to a value of $N_{1,60} \approx 1.8$ blows/ft. Based on the very high fines contents, they would then have added 5 blows per foot to develop a best estimate value of $\overline{N_{1,60,CS}}$ = 6.8 blows/ft.

B.7 Metoki Road Embankment (Japan; 1968)

B.7.1 Brief Summary of Case History Characteristics

Name of Structure	Metoki Road Embankment
Location of Structure	Metoki, Japan
Type of Structure	Roadway Embankment
Date of Failure	March 28, 1965
Nature of Failure	Seismic, During 1968 Tokachi-Oki Earthquake (M_w = 8.3)
Approx. Maximum Slope Height	16.4 ft.

B.7.2 Introduction and Description of Failure

A section of the roadway embankment near Metoki, Japan suffered a liquefaction-induced flow failure during the 1968 Tokoachi-Oki earthquake (M_w = 8.3), as reported by Ishihara et al. (1990). Figure B.7.1 shows a plan view of the post-failure conditions, with a temporary detour road in place to the rear of the slide scarp. Figure B.7.2 shows a cross-section of the embankment (at exaggerated vertical scale) along Section f-f', with the temporary detour road in place, and Figure B.7.3 shows an interpreted pre-failure cross-section (at true vertical scale) which will be discussed further.

The phreatic surface was at or near the ground surface at the toe of the embankment, and it is assumed that failure occurred due to seismically induced liquefaction of the loose silty sands of the upper foundations soils underlying the embankment. Maximum lateral displacements of the liquefied materials were on the order of approximately 35 to 40 m.

B.7.3 Geology and Site Conditions

Ishihara et al. (1990) stated that the roadway embankment was founded atop a layer of what they termed "soft" silty sand, and that this upper stratum of soft silty sand was underlain at depth by a "medium soft soil". No further descriptions of these two foundation units are given, so gradations, fines contents, etc. are not known. It is assumed (based on common local practice) that the roadway embankment was also comprised of these locally available silty sands, but there is no information available regarding compaction procedures, etc.

B.7.4 Initial Yield Stress Analyses

Figure B.7.3 shows the cross-section used for back-analyses of the post-liquefaction initial yield strength $S_{r,yield}$ that would be required within the foundation and embankment materials of the north dike section to produce a calculated Factor of Safety equal to 1.0. This is not the actual

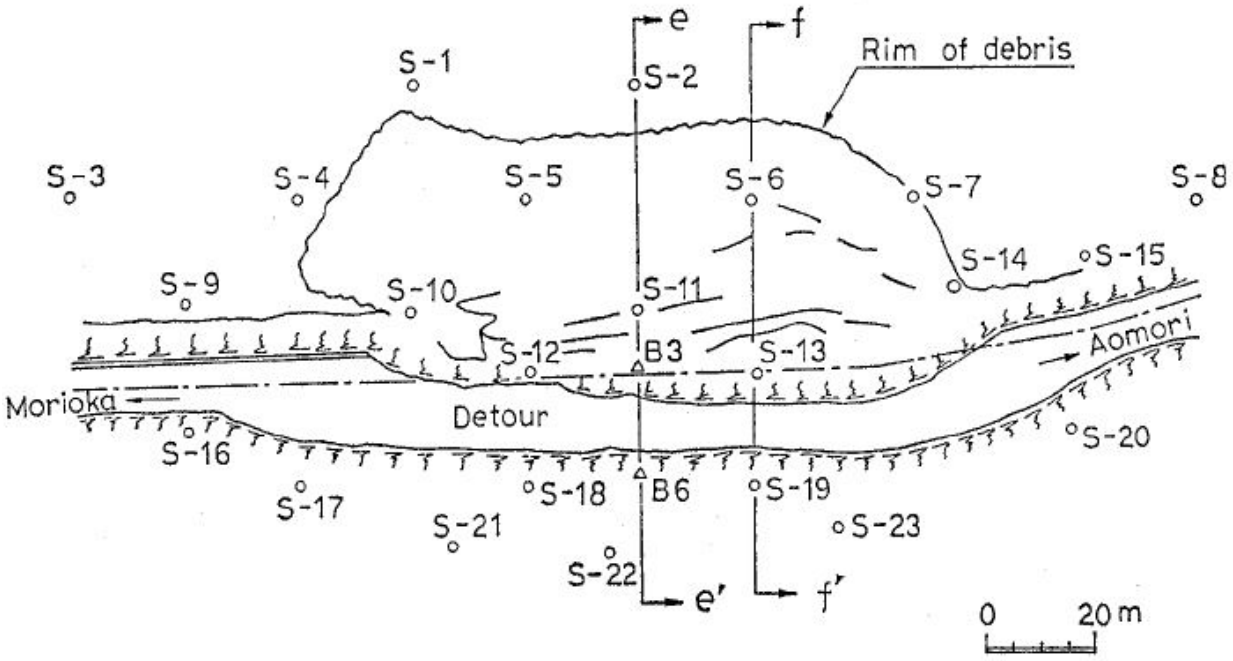

Figure B.7.1: Plan view of the failure of the roadway embankment near Metoki (from Ishihara et al., 1990)

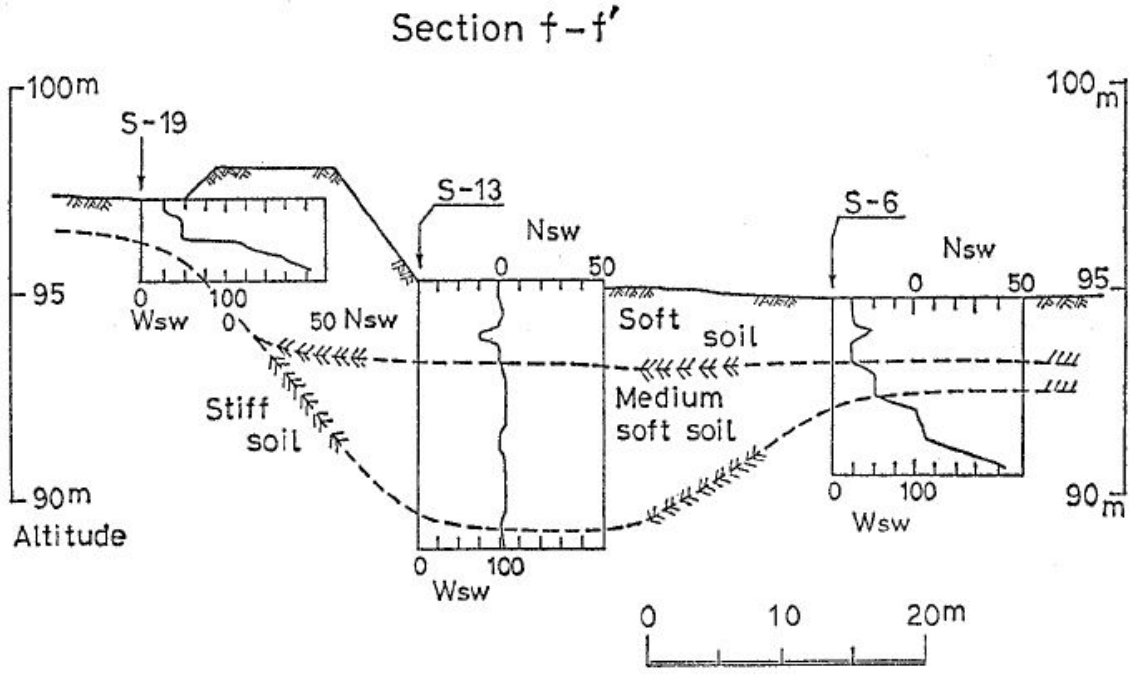

Figure B.7.2: Cross-section f-f' through the repaired Metoki roadway embankment (shown at exaggerated vertical scale), showing also three of the Swedish Cone soundings (Figure from Ishihara et al., 1990).

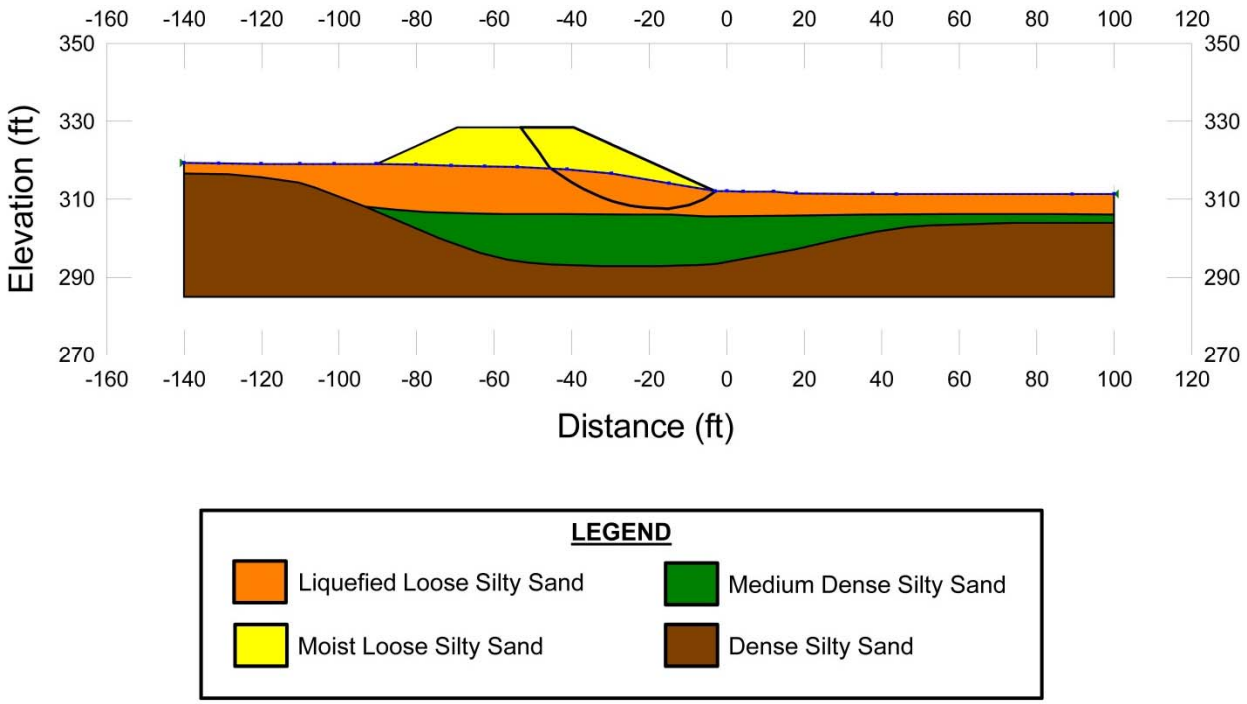

Figure B.7.3: Pre-failure cross-section of the Metoki roadway embankment used for back-analyses of $S_{r,yield}$.

post-liquefaction strength, but it proves to be useful in developing estimates of post-liquefaction strength (S_r) for this case history.

There were two general sets of potential failure mechanisms that could potentially explain the observed features: (1) the failure may have been incrementally retrogressive, initiating with a "slice" near to the front of the feature, and then retrogressing on a slice by slice basis back towards the eventual back heel, or (2) the entire slide may have initiated monolithically (all at once). Both sets of possibilities were analyzed, and multiple potential "initial" failure surfaces were analyzed for the incrementally retrogressive scenario. In all cases, failure was modeled as occurring within the loose, saturated silty sands immediately underlying the embankment fill.

Unit weights of the non-saturated sands and silty sands of the embankment fill above the phreatic surface were modeled with a unit weight of $\gamma_m \approx 110$ lbs/ft^3, and this was then varied over a range of $\gamma_m \approx 107$ to 113 lbs/ft^3 for parameter sensitivity studies. Unit weights of the saturated upper ("soft") foundation silty sands below the phreatic surface were modeled with a unit weight of $\gamma_s \approx 115$ lbs/ft^3, and this was then varied over a range of 112 to 118 lbs/ft^3 for parameter sensitivity studies. The friction angle of the embankment fill materials above the phreatic surface was modeled with $Ø' \approx 30°$, and a range of $Ø' \approx 28°$ to 32°.

Potential initial failure surfaces were modeled as either (1) wedge-like semi-translational features, or (2) rotational features. The rotational failure surface shown in Figure B.7.3 was the

most critical post-liquefaction potential failure surface found, though wedge-like failure surfaces in this same general vicinity were found to produce similar values of $S_{r,yield}$. Because this failure surface conforms only somewhat with the observed final rear slide scarp, it was judged likely that the failure had been essentially monolithically initiated with a failure surface similar to the one shown, or that it had initiated on a failure surface extending slightly farther back towards the rear heel (as the observed field rear slide scarp occurred farther to the left, nearer to the rear edge of the roadway platform of the embankment), or that it had retrogressed in two or more slices.

Based on a range of potential failure surfaces encompassing these possibilities, and the parameters (and parameter variations) described above, it was judged that the resulting best estimate value was $S_{r,yield}$ = 236 lbs/ft^2, with a range of $S_{r,yield} \approx$ 221 to 263 lbs/ft^2.

Olson (2001) also performed back-analyses to evaluate $S_{r,yield}$. He also analyzed both rotational and wedge-like failure surfaces, mainly exiting at approximately the middle third of the roadway platform atop the embankment. His best estimate value was $S_{r,yield}$ = 9.0 kPa (188 lbs/ft^2), with a range of $S_{r,yield} \approx$ 8.5 to 11.1 kPa (176 to 232 lbs/ft^2).

B.7.5 Residual Strength Analyses Based on Residual Geometry

It was not possible to perform rigorous and reliable back-analyses to determine the value of $S_{r,resid/geom}$ required to produce a calculated Factor of Safety equal to 1.0 based on residual geometry. This is a significant source of uncertainty for this case history.

Olson (2001) noted that Ishihara had reported that the original embankment flowed approximately 50 meters, as shown in Figure B.7.1. Based on conservation of mass, he estimated the average or representative thickness of the failed (flow) mass to be approximately 2.3 m. Taking the representative slope of the flow mass at residual geometry as being approximately 2° to 3°, and with a unit weight of 18.1 kN/m^3, he employed an infinite slope analysis to develop a simplified best estimate of $S_{r,resid/geom}$ = 1.8 kPa (38 lbs/ft^2) with a range of 1.4 to 2.2 kPa (29 to 46 lbs/ft^2).

In these current studies, it was assumed that $S_{r,resid/geom}$ would have at least been higher than zero, and likely higher than this simplified estimate of Olson based on approximate geometry and an infinite slope analysis. Values of $S_{r,resid/geom}$ back-calculated from the reasonably well-documented Class A case histories were next examined, and for the range of effective overburden stress and $N_{1,60,CS}$ values for this current case an approximate range of $S_{r,resid/geom} \approx$ 30 to 90 lbs/ft^2 was conservatively assumed, based on analyses of other Class A and B case histories. This range is slightly higher than Olson's simplified estimate, and so was not adjusted further. This range of values was selected to be slightly conservatively biased (a conservative bias of approximately 10% reduction of best estimates of $S_{r,resid/geom}$ was targeted here), so that any resulting error in evaluation of overall S_r would also be slightly conservative (nominally by approximately 5% or so).

B.7.6 Overall Estimates of S_r

Overall estimates of S_r for this Class B case history were made based on the pre-failure geometry and the approximate runout features and characteristics, and the values of $S_{r,yield}$ and $S_{r,resid/geom}$ as calculated and/or estimated in the preceding sections.

Runout characteristics for this case cannot be fully accurately assessed due to the approximate nature of the post-failure geometry as reported. Runout distance, and runout ratio, appear to be "large", and the runout ratio (defined as the distance travelled by the center of gravity of the failure mass divided by the initial slope height measured from the toe to the top back edge of the rear heel scarp) was estimated as approximately 70 feet / 16.4 feet ≈ 4.2.

This allowed Equation 4-4, and Figures 4.7 and 4.11 to serve as one basis for estimation of post-liquefaction strength S_r. Using the ranges of $S_{r,yield}$ and $S_{r,resid/geom}$ from Sections B.7.4 and B.7.5, respectively, and assuming that $\xi \approx 0.4$ to 0.6 for this large runout case (based on a runout ratio of approximately 4.2), Equation 4-4 provided a best estimate value of $S_r \approx 76$ lbs/ft^2 and an estimated range of $S_r \approx 50$ to 106 lbs/ft^2. A second basis for estimation of S_r was the use of the relationship of Figure 4.9, and the range of values of $S_{r,yield}$ from Section B.7.4. Based on the runout ratio of approximately 4.2, values of initial (pre-failure displacement) Factor of Safety were taken as approximately 0.35 to 0. 5, and multiplying these by the range of $S_{r,yield}$ values produced a best estimate value of $S_r \approx 101$ lbs/ft^2 and an estimated range of $S_r \approx 78$ to 132 lbs/ft^2. No similar use was made of Figure 4.9 in conjunction with the ranges of $S_{r,resid/geom}$ estimated in Section B.4.5 because these estimates of $S_{r,resid/geom}$ were considered to be very approximate.

The estimates by each of the two methods above were then averaged together, and this produced a best estimate value of $S_r \approx 89$ lbs/ft^2 and an estimated range of $S_r \approx 50$ to 132 lbs/ft^2. These estimates of variance are non-symmetric about the best estimated mean value, and the range was judged to represent approximately +/- 2 standard deviations, so further adjustments were then necessary.

Overall, based on an assumed normal distribution, it was judged that the (mean and median) best estimate of post-liquefaction strength for this case history is

$$\overline{S_r} = 92 \text{ lbs/ft}^2$$

and that the best estimate of standard deviation of mean overall post-liquefaction strength is

$$\sigma_{\overline{S}} = 20 \text{ lbs/ft}^2$$

Olson (2001) and Olson and Stark (2002) did not apply their "kinetics" method to this case, and so they did not independently develop an estimate of S_r that incorporated momentum effects. Instead they simply used their value of $S_{r,resid/geom}$ as a conservative approximation of S_r for this less well-defined case, and used $S_r = 1.8$ to 2.0 kPa (38 to 42 lbs/ft^2) in developing their predictive relationship. This was an unconservative assessment, because these are Sr,resid/geom values and they neglect momentum effects.

A better estimate of S_r that approximately incorporates momentum effects, and a better basis for comparison with these current studies, can be obtained by employing their best estimate values of $S_{r,yield}$ = 188 lbs/ft^2 and $S_{r,resid/geom}$ = 38 lbs/ft^2, and an assumed average value of $\xi \approx 0.8$ in Equation 4-4 as

$$S_r \approx 0.5 \times [188 \text{ lbs/ft}^2 + 38 \text{ lbs/ft}^2] \times 0.8 = 90 \text{ lbs/ft}^2$$

This value ($S_r \approx 90$ lbs/ft^2) agrees very closely with the best estimate value of $S_r \approx 92$ lbs/ft^2 developed in these current studies.

Wang (2003) developed his characterization of post-liquefaction strength for the "Secondary" case histories based on averaging of values from multiple previous investigators. For this particular case (Metoki Road) he lists only one previous back-calculated value of S_r = 113 lbs/ft^2, and attributes this to Olson (2001). As discussed in Section 2.3.8 and Chapter 4, this represents the use of Equation 4-4, and Olson's best estimate values of $S_{r,yield}$ = 188 lbs/ft^2 and $S_{r,resid/geom}$ = 38 lbs/ft^2, and an assumed average value of $\xi \approx 1.0$. Because ξ is assumed to be 1.0, this value is about 25% higher than the value calculated above using ξ = 0.8.

Overall, agreement between the three sets of values calculated by (1) Olson (2001) [after combining their best estimate values of $S_{r,yield}$ and $S_{r,resid/geom}$ using Equation 4-4 and ξ = 0.8], (2) Wang (2003) and Kramer (2008) [after combining their best estimate values of $S_{r,yield}$ and $S_{r,resid/geom}$ using Equation 4-4 and ξ = 1.0] and (3) these current studies, is generally very good to excellent.

An interesting additional value of S_r was back-estimated by Ishihara et al. (1990). This was reportedly a simplified estimate, but the basis for this value (details of the back-analysis and/or judgments made) were not documented, and so Wang (2003) did not include this estimate in his averaging of prior results for this case. Ishihara's value was S_r = 6.2 kPa (129 lbs/ft^2), and this is also in generally good agreement with the S_r values of the three other investigation teams discussed above.

B.7.7 Evaluation of Initial Effective Vertical Stress

Average initial (pre-failure) effective vertical stress was assessed for the liquefied portions of the failure surfaces for both rotational and wedge-like failures similar to the one shown in Figure B.7.3. Parameters and sensitivity analyses were as described previously in Section B.7.4. Additional analyses were then performed for alternate potential failure surfaces, including failure surfaces initial (smaller) slices of a retrogressive incremental failure eventually extending back to the apparent back heel of the final failure. Depths of failure surfaces were varied, and both rotational and translational (wedge-like) failure surfaces were considered.

The resulting best estimate of average pre-failure effective stress within the liquefied materials controlling the failure was then $\sigma_{vo}' \approx 868$ lbs/ft^2, with a reasonable range of $\sigma_{vo}' \approx 701$ to 1041 lbs/ft^2. This range is slightly non-symmetric about the median value, and this range was judged by the engineering team to represent approximately ± 2 standard deviations. Overall, the

best characterization of initial (pre-failure) average effective vertical stress was then taken to be represented by a mean value of

$$\overline{\sigma'_{vo}} \approx 871 \text{ lbs/ft}^2$$

and with a standard deviation of

$$\sigma_{\bar{\sigma}} \approx 85 \text{ lbs/ft}^2$$

An estimate of σ_{vo}' was also calculated by Olson and Stark (2001, 2002). They reported a weighted average mean value of $\sigma_{vo}' \approx 41.9$ kPa (875 lbs/ft^2), in excellent agreement with these current studies. Average initial vertical effective stresses were not directly reported by Wang (2003) and Kramer (2008), but they were published more recently in the publication by Kramer and Wang (2015). As discussed in Section 2.3.8.1(b)-(iii), Wang (2003) did not perform any independent analyses to assess σ_{vo}' for his 22 "secondary" cases, and this is one of those cases. Instead, he compiled values of S_r from multiple previous investigators, and averaged these for a best estimate. He also compiled multiple values of S_r/σ_{vo}' from previous investigators, and averaged these for a best estimate. He then used these two best-estimate values of S_r and S_r/σ_{vo}' to infer a resulting representative value of σ_{vo}'. As described in Section 2.3.8.1(b)-(iii), the resulting averaged values of S_r and S_r/σ_{vo}' were incompatible with each other for a number of Wang's "secondary" case histories, and this process produced unreasonable, and in some cases physically infeasible, values of σ_{vo}' for a number of case histories. Wang's value of $\sigma_{vo}' = 2{,}655$ lbs/ft^2 is clearly physically infeasible for this case, based on the cross-section, and so it is not considered a useful check here. Agreement between Olson's value, which is well-documented, and the values developed in these current studies is excellent.

B.7.8 Evaluation of $N_{1,60,CS}$

Twenty three Swedish cone penetration tests were conducted following the failure, but only three of these Swedish cone penetration tests were reported in Ishihara et al. (1990). These are superimposed on section f-f' in Figure B.7.2. Based on the results of those three cone soundings, and using the correlation of Inada (1982) to convert from Swedish cone tip resistances to equivalent SPT penetration resistances, $N_{1,60}$ is estimated to be approximately 1.5 to 2.5 blows/ft. Ishihara reported the material to be silty sand, but there is no further information as to the likely range of fines contents. Based on the description provided, a representative clean sand corrected blowcount of $N_{1,60,CS} = 3$ blows/ft was chosen for these current studies.

Olson (2001) and Olson and Stark (2002) made no correction for fines, and selected a "representative" uncorrected $N_{1,60}$ value of 2.6 blows/ft. for this case. Wang (2003) and Kramer (2008) selected a fines adjusted value of $\overline{N_{1,60,CS}} \approx 2.0$ blows/ft., and a proportionally high standard deviation of $\sigma_{\bar{N}} \approx 1.5$ blows/ft.

Overall agreement with regard to characterization of $N_{1,60}$ or $N_{1,60,CS}$ among these two previous studies, and the current study, is considered to be good for this case. with the exception of characterization of variance (or standard deviation) of the mean value of $N_{1,60,CS}$.

B.8 Hokkaido Tailings Dam (Japan; 1968)

B.8.1 Brief Summary of Case History Characteristics

Name of Structure	Hokkaido Tailings Dam
Location of Structure	Hokkaido, Japan
Type of Structure	Tailings Dam
Date of Failure	March 28, 1968
Nature of Failure	Seismic, During 1968 Tokachi-Oki Earthquake (M_w = 8.3)
Approx. Maximum Slope Height	24 ft.

B.8.2 Introduction and Description of Failure

A tailings dam near Hokkaido suffered a liquefaction-induced failure during the 1968 Tokachi-Oki Earthquake (M_w = 8.3), as reported by Ishihara et al. (1990). There are no local instrumental recordings, and shaking levels are not known.

Figure B.8.1 shows a plan view of the failure, and Figure B.8.2 presents pre-failure and post-failure cross-sections (Ishihara et al., 1990). As shown in Figure B.8.2, the failure involved a slope stability failure entirely within the impounded tailings, which flowed out over the top of the starter dike. Neither the confining starter dike nor the underlying foundation soils were involved. As shown in Figure B.8.1, the tailings flowed out to a distance extending approximately 170 meters downstream of the toe of the starter dike.

Tailings were being actively deposited at the time of the failure, and the phreatic surface shown in Figure B.8.2 was inferred by Ishihara et al. (1990).

B.8.3 Geology and Site Conditions

There is no information available regarding foundation conditions, or the nature and condition of materials comprising the starter dike. This is not problematic, because the failure was judged to have occurred entirely within the impounded tailings.

Ishihara et al. (1990) describe the tailings as silty sand, but no further information regarding gradation or fines content is provided. Ishihara et al. estimated the unit weight of the tailings to be on the order of 19.6 kN/m^3. Dutch cone penetration test soundings were performed after the failure, and the results of two of these soundings are presented in Figure B.8.3. With the exception of what may be a stiffer interim deck at a depth of approximately 1.6 meters, the tailings show very low (and relatively consistent) tip resistances over the upper 6 meters at the sites of these two soundings.

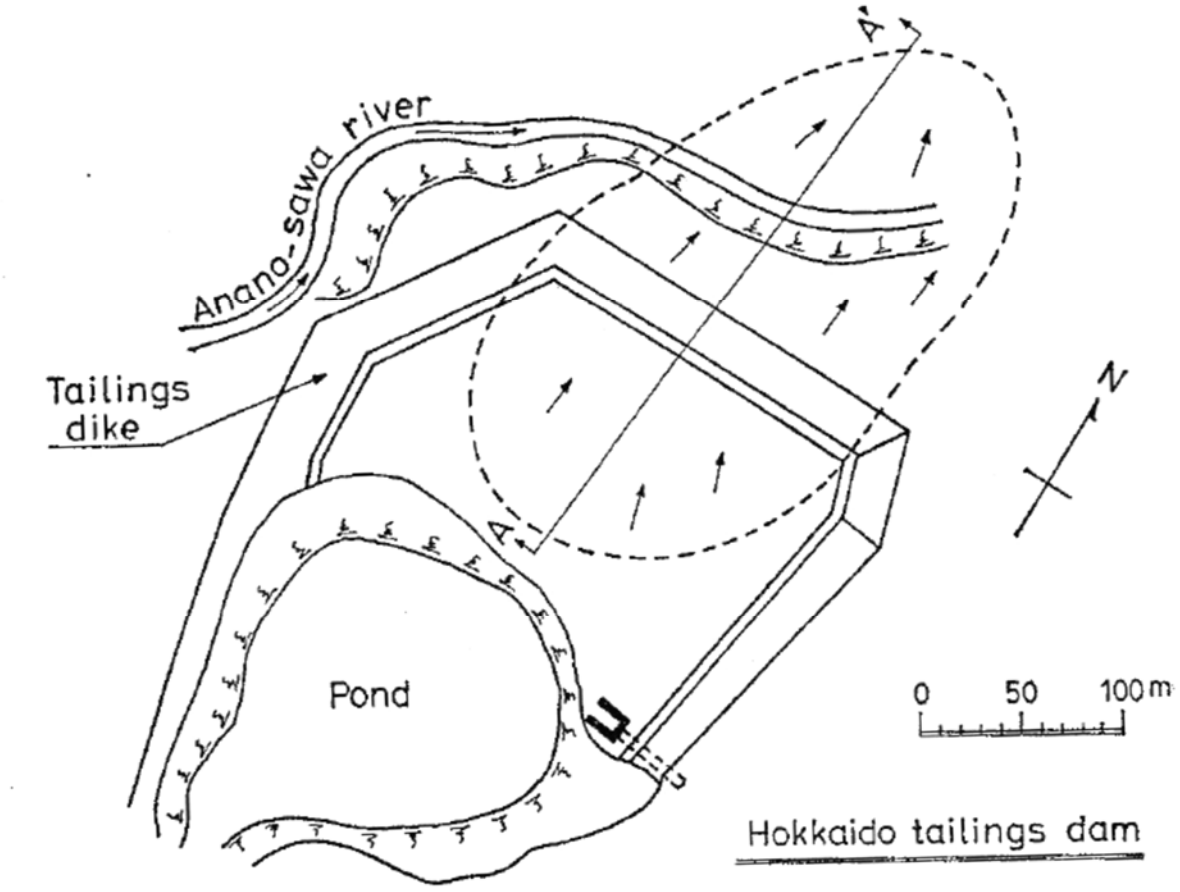

Figure B.8.1: Plan view of the Hokkaido tailings dam showing the approximate extent of the flow failure (figure from Ishihara et al., 1990).

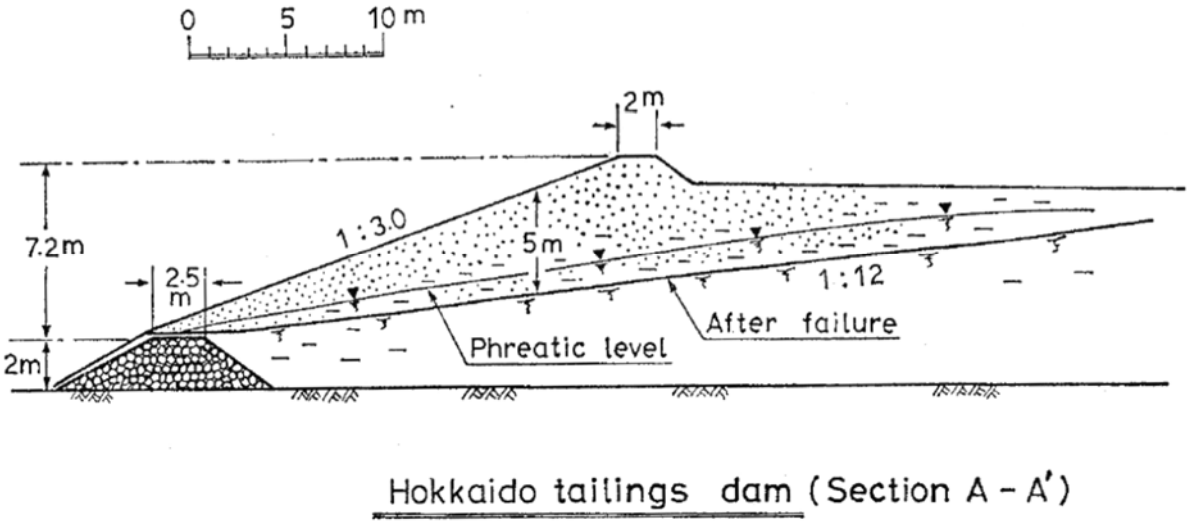

Figure B.8.2: Pre-failure and post-failure cross-sections at Section A-A' from Figure B.8.1 (figure from Ishihara et al., 1990).

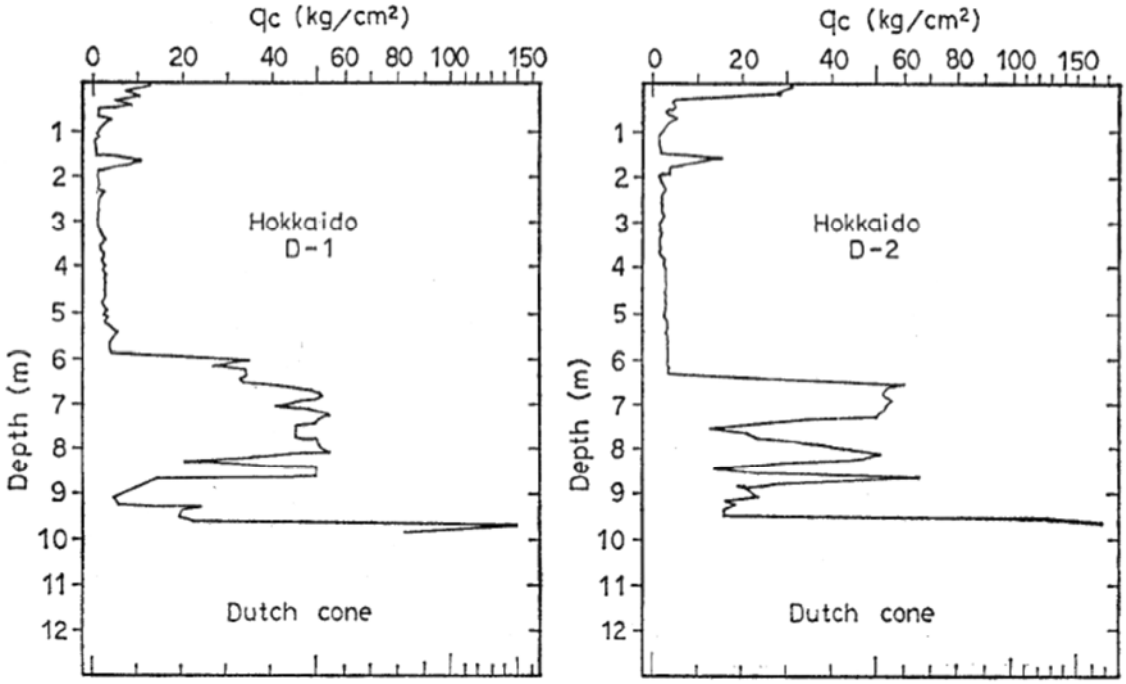

Figure B.8.3: Results of two Dutch cone penetration test soundings performed after the failure (figure from Ishihara et al., 1990).

B.8.4 Initial Yield Stress Analyses

Figure B.8.4(a) shows the cross-section used for back-analyses of the post-liquefaction initial yield strength $S_{r,yield}$ that would be required within the liquefied upstream shell materials to produce a calculated Factor of Safety equal to 1.0. This is not the actual post-liquefaction strength, but it proves to be useful in developing estimates of post-liquefaction strength (S_r) for this case history.

Unit weights of the non-saturated tailings above the phreatic surface were modeled with a unit weight of $\gamma_m \approx 118$ lbs/ft^3, and this was then varied over a range of 114 to 122 lbs/ft^3 for parameter sensitivity studies. Unit weights of the saturated tailings below the phreatic surface were modeled with a unit weight of $\gamma_s \approx 123$ lbs/ft^3, and this was then varied over a range of 119 to 127 lbs/ft^3 for parameter sensitivity studies. The friction angle of the tailings above the phreatic surface was modeled with $Ø' \approx 30°$, and a range of $Ø' \approx 28°$ to 33°.

There were no eyewitness reports, so it is not known with certainty whether this was an incrementally retrogressive failure, or a more monolithic failure in which most or all of the failure mass initiated its movements all at once.

A number of different potential failure surfaces were analyzed. These back-analyses showed that it was likely that this had been a retrogressive failure, initiating with a large initial failure slice or wedge that encompassed the interim crest lip section, and then retrogressing eventually back to the final back heel.

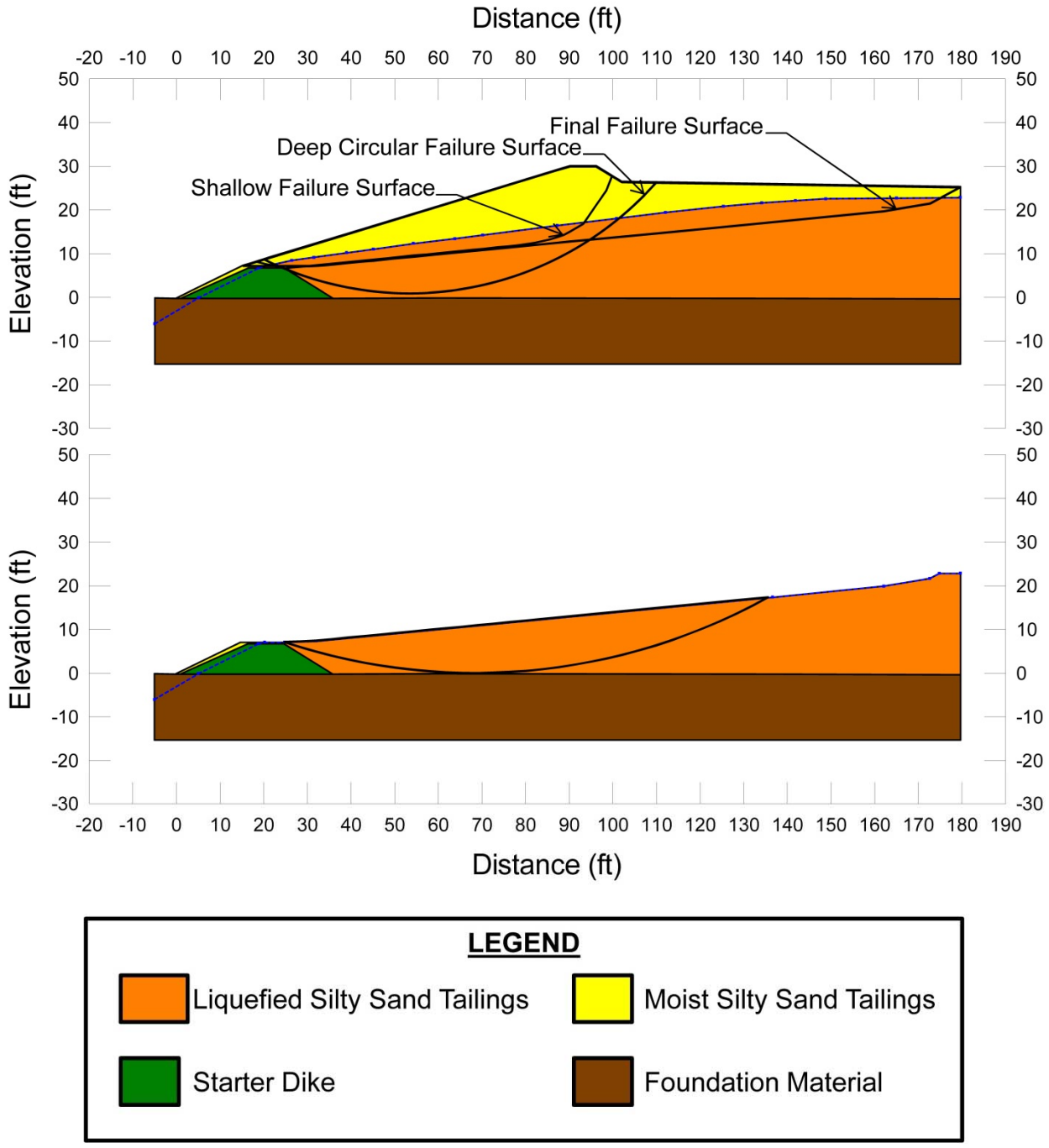

Figure B.8.4: Selected potential failure surfaces analyzed for evaluation of (a) $S_{r,yield}$ and (b) $S_{r,resid/geom}$ for the Hokkaido Tailings Dam

Figure B.8.4(a) shows a select subset of the potential failure surfaces analyzed for back-analyses of $S_{r,yield}$. Based on all of the analyses performed, the most likely failure mechanism was judged to be an initial failure surface similar to the "shallow" failure surface shown in Figure B.8.4(a), as the first stage of an incrementally retrogressive overall failure sequence. The shallow

failure surface shown in this figure is the most critical failure surface of this type, and the calculated best estimate for this surface is $S_{r,yield}$ = 351 lbs/ft^2. Based on parameter variations (parameter sensitivity studies), and moderate variations of failure surface geometries, the likely range is estimated as $S_{r,yield}$ = 306 to 409 lbs/ft^2 for this type of initial failure surface.

The "deep circular failure surface" shown in Figure B.8.4(a) is the most critical of a second set of potential initial failure surfaces passing beneath the final observed post-failure ground surface, and again representing the first stage of an incrementally retrogressive overall failure sequence. For this surface, the best estimate was $S_{r,yield}$ = 242 lbs/ft^2, with a range of $S_{r,yield}$ = 215 to 274 lbs/ft^2.

The third type of potential failure surface analyzed was a failure surface approximating the overall post-failure ground surface, and would reflect either the assumption that this defined the basal overall failure surface, or that it closely approximated at least the latest stages of an incrementally retrogressive failure. The back-calculated initial yield stress for this overall failure surface, and for a monolithically initiated overall failure along this surface, is $S_{r,yield}$ = 109 lbs/ft^2, with a range of $S_{r,yield}$ = 75 to 134 lbs/ft^2, but it was considered unlikely that the failure was monolithically initated.

Overall assessment of $S_{r,yield}$ for this case was based on weighted averages of the values of $S_{r,yield}$ back calculated for these three types of potential failure surfaces. The shallower initial failure surface near the downstream toe was considered the most likely, and was assigned a weighting factor of 2. The deeper rotational failure surface was assigned a weighting factor of 1. The failure surface representing an overall monolithically initiated failure along the observed post-failure ground surface was assigned a weighting factor of 0.5. Based on these estimates and associated weighting factors, and the back-calculated values from above, the overall best estimate was $S_{r,yield}$ = 254 lbs/ft^2, with a range of $S_{r,yield}$ = 221 to 293 lbs/ft^2.

Olson (2001) also performed back-analyses to estimate $S_{r,yield}$. He also assumed that the failure was retrogressive, and that an initial failure slice initiated first near the downstream side. His assumed initial failure surfaces were rotational failures similar to the "deep rotational" failure shown in Figure B.8.4(a), except that he constrained the base of these rotational failures over a range of elevations that did not pass more than about 0.5 meters below the elevation of the crest of the starter dike. These rotational failure surfaces did extend below the final post-failure surface of the tailings. A range of potential initial rotational failure surfaces were analyzed. Olson's back-calculated best estimate was $S_{r,yield} \approx$ 11.7 kPa (245 lbs/ft^2), with a range of 10.3 to 12.7 kPa (215 to 265 lbs/ft^2). These values were developed by a different set of procedures and judgments, but they are in very good agreement with the values back-calculated in these current studies.

B.8.5 Residual Strength Analyses Based on Residual Geometry

It was not possible to perform rigorous and reliable back-analyses to determine the value of $S_{r,resid/geom}$ required to produce a calculated Factor of Safety equal to 1.0 based on residual geometry. This case is one of six cases (out of the 29 cases back-analyzed as part of these current studies) where the slide mass "went over a lip" and then traveled down a steeper slope, and the

ensuing displacements either (1) could not be reliably tracked, or (2) could not be fully reliably back-analyzed. Both situations apply in this current case because the post-failure geometry of the failure mass runout is not well characterized.

Olson (2001) examined the plan view presented in Figure B.8.1, and assumed conservation of mass, concluding that the average thickness of the failed material downstream of the original dike was probably on the order of 2.5 to 3 meters. He then appears to have performed his simplified (infinite slope) analysis to determine his estimated values of $S_{r,resid/geom}$, but for this case history he does not indicate what slope angle(s) he assumed here either for the top slope or basal slope of the flowed tailings. He reports a best estimate value of $S_{r,resid/geom} \approx 4.8$ kPa (100 lbs/ft^2) for a thickness of 3 meters and a unit weight of 19.6 kN/m^3. His estimated range was $S_{r,resid/geom} \approx 4.1$ kPa (86 lbs/ft^2), which was based on a thickness of 2.5 m, to $S_{r,resid/geom} \approx 6.6$ kPa (125 lbs/ft^2), which was based on an assumed thickness of 4 meters as was used by Ishihara et al. (1990). These calculations would correspond to an assumed infinite slope angle of approximately 4.8° for the runout tailings downstream of the original dam toe, or it would represent the assumption that the observed post-failure slope of 1:12 ≈ 4.8° within the tailings impoundment represented a residual condition.

In these current studies, it was assumed that $S_{r,resid/geom}$ would have at least been higher than zero. Values of $S_{r,resid/geom}$ back-calculated from the reasonably well-documented Class A case histories were next examined, and for the range of effective overburden stress and $N_{1,60,CS}$ values for this current case an approximate range of $S_{r,resid/geom} \approx 30$ to 100 lbs/ft^2 was conservatively assumed, based on analyses of several of the Class A case histories. This range of values was selected to be slightly conservatively biased (a conservative bias of approximately 10% reduction of best estimates of $S_{r,resid/geom}$ was targeted here), so that any resulting error in evaluation of overall S_r would also be slightly conservative (nominally by approximately 5% or so).

Analyses were also performed of the residual slope left in place after the failure, as shown in Figure B.8.4(b). There is no certainty that the tailings below this residual top surface liquefied (or "triggered"), but there is no reason to expect that the relatively steep (1:12) post-failure slope surface shown in Figure B.8.2 would represent bedding planes arising from the hydraulic placement of tailings, and both the initial yield stress analyses performed by Olson (2001) and in these current studies showed that deeper rotational potential failure surfaces may have been the initial most critical failure surfaces for this case. If the deeper tailings did liquefy, then for the rotational failure surface illustrated in Figure B.8.2 the back-calculated value would be $S_{r,resid/geom} \approx 83$ lbs/ft^2. Similarly, if the deeper tailings did liquefy, then an infinite slope analysis of this post-failure slope surface can be performed as an approximation, with a tailings thickness of approximately 2 to 4 m. (6.6 to 13.1 ft.), a unit weight of approximately 19.6 kN/m3 (125 lbs/ft^3), and a slope angle of approximately 4.8° (1:12, H:V), producing values of $S_{r,resid/geom} \approx 69$ to 138 lbs/ft^2.

Overall, considering the estimates (1) made based on infinite slope analyses of assumed downstream (runout) geometry by Olson (2001), (2) similar infinite slope analyses made by Olson using the assumed representative post-failure tailings runout thickness of 6 m as proposed by Ishihara et al. (1990), (3) the rotational failure surface shown in Figure B.8.4(b), (4) approximate infinite slope analyses of the post-failure slope remaining within the tailings impoundment after

the event, and (5) values of $S_{r,resid/geom}$ back-calculated for better-defined post failure conditions from the Class A case histories, it was concluded that a best estimate value would be taken as $S_{r,resid/geom} \approx 70$ lbs/ft^2, with a range of $S_{r,resid/geom} \approx 30$ to 110 lbs/ft^2. It is interesting to note that these values are in good agreement with the values of $S_{r,resid/geom}$ developed by Olson (2001) despite the very different approaches and judgments made in develop the two sets of values.

B.8.6 Overall Estimates of S_r

Overall estimates of post-liquefaction strength S_r were made by two approaches. The first approach was to employ Equation 4-4, and Figure 4.11 as

$$S_r \approx \xi \bullet (S_{r,yield} + S_{r,resid/geom}) / 2$$

where ξ is a function of runout distance and overall failure mechanism characteristics.

Unfortunately, runout characteristics cannot be reliably characterized for this case history, because it is one of the six case histories back-analyzed in which the failure mass "went over a lip" and then down a steeper slope rather than coming to rest on a gentler basal slope as with most of the cases plotted in Figure 4.11. It is clear that runout distance is not small, but runout distance (and runout ratio) cannot be fully reliably quantified. The current engineering team therefore developed a consensus estimate that an appropriate range of values of ξ for this case would be on the order of $\xi \approx 0.45$ to 0.55. Using these values, and the values of $S_{r,yield}$ and $S_{r,resid/geom}$ presented previously in Sections B.8.4 and B.8.5, and the associated ranges of both $S_{r,yield}$ and $S_{r,resid/geom}$, this produced a best estimate of $S_r \approx 81$ lbs/ft^2, with a range of $S_r = 56$ to 111 lbs/ft^2.

The second approach was to employ the relationship presented in Figure 4.9, wherein pre-failure Factor of Safety can be approximately evaluated as a function of runout characteristics. Here again the difficulty was that the post-failure runout characteristics were not fully quantifiable because the failure mass went over a lip and then down a steeper slope. The engineering team developed a consensus estimate that the pre-failure range of Factor of Safety for this case would have been on the order of FS = 0.3 to 0.55. Multiplying these values by the values of $S_{r,yield}$ from Section B.8.4, produces a best estimate of $S_r \approx 95$ lbs/ft^2, with a range of $S_r = 66$ to 132lbs/ft^2.

Averaging the two sets of values developed by these two approaches then produced a best estimate of $S_r \approx 88$ lbs/ft^2, with a range of $S_r = 56$ to 111 lbs/ft^2. The variance was slightly non-symmetric about the best estimate, so this was slightly further adjusted to produce a characterization that could be modeled with a Normal distribution. The range was estimated to represent approximately +/- 1.5 standard deviations.

Overall, based on an assumed normal distribution, it was judged that the (mean and median) best estimate of post-liquefaction strength for this case history is

$$\overline{S_r} = 98 \text{ lbs/ft}^2$$

and that the best estimate of standard deviation of mean overall post-liquefaction strength is

$\sigma_{\bar{S}} = 25$ lbs/ft^2

Olson (2001) and Olson and Stark (2002) did not apply their "kinetics" method to this case, and so they did not independently develop an estimate of S_r that incorporated momentum effects. Instead, they took their value of $S_{r,resid/geom}$ as representing S_r. Their best estimate value was therefore $S_r = S_{r,resid/geom} = 100$ lbs/ft^2, with a range of 86 to 125 lbs/ft^2, as described previously in Section B.8.5.

A better estimate can be obtained by taking their back-calculated best estimate values of $S_{r,yield}$ and $S_{r,resid/geom}$ are using the simplified Equation 4.1 with a fixed $\xi = 0.8$, in which case the resulting estimate would be

$$S_r \approx \xi \bullet (S_{r,yield} + S_{r,resid/geom}) / 2 \approx (0.8) \bullet (245 \text{ lbs/ft}^2 + 100 \text{ lbs/ft}^2) / 2 \approx 138 \text{ lbs/ft}^2$$

Wang (2003) and Wang and Kramer (2008) did not employ their zero inertial force (ZIF) method to incorporate inertial effects in back-analyses of this failure. Instead they selected their value of S_r based on examination of values from back-analyses by several previous investigators. Wang (2001) selected two values for this case history as:

$S_r = 408$ lbs/ft^2 (Ishihara et al., 1990)

$S_r = 172$ lbs/ft^2 (Olson, 2001)

where Wang's value for "Olson, 2001" was taken as $S_r \approx (S_{r,yield} + S_{r,resid/geom}) / 2$, representing an implied value of $\xi = 1.0$, which would clearly over-estimate S_r for this case. The value of 408 lbs/ft^2 attributed to Ishihara et al. (1990) is mysterious, as the paper by Ishihara actually presents a value of $S_r = 0.67$ t/m^2 (137lbs/ft^2). So both of Wang's selected values appear to be in error, and they are unconservatively high. Averaging these together therefore produced a value that was also unconservatively too high.

B.8.7 Evaluation of Initial Effective Vertical Stress

The representative vertical effective stress for the Hokkaido Tailings Dam was determined by averaging the calculated vertical effective stress on the failure plane in the liquefied zone from the deep and final failure surfaces shown in Figure B.8.4(a). Parameter variations (unit weights) were then varied, and so to some extent were the depths of the potential failure surfaces of each type.

The resulting best estimate of average pre-failure effective stress within the liquefied materials controlling the failure was then $\sigma_{vo}' \approx 1{,}198$ lbs/ft^2, with a reasonable range of $\sigma_{vo}' \approx$ 916 to 1,489 lbs/ft^2. This range was judged by the engineering team to represent approximately ± 1.5 standard deviations. Overall, the best characterization of initial (pre-failure) average effective vertical stress was then taken to be represented by a mean value of

$$\overline{\sigma'_{vo}} \approx 1{,}203 \text{ lbs/ft}^2$$

and with a standard deviation of

$\sigma_{\bar{\sigma}} \approx 191$ lbs/ft^2

An estimate of σ_{vo}' was also calculated by Olson and Stark (2001, 2002). They reported a weighted average mean value of $\sigma_{vo}' \approx 65.9$ kPa (1,376 lbs/ft^2), in very good agreement with these current studies. Average initial vertical effective stresses were not directly reported by Wang (2003) and Kramer (2008), but they were published more recently in the publication by Kramer and Wang (2015). As discussed in Section 2.3.8.1(b)-(iii), Wang (2003) did not perform any independent analyses to assess σ_{vo}' for his 22 "secondary" cases, and this is one of those cases. Instead, he compiled values of S_r from multiple previous investigators, and averaged these for a best estimate. He also compiled multiple values of S_r/σ_{vo}' from previous investigators, and averaged these for a best estimate. He then used these two best-estimate values of S_r and S_r/σ_{vo}' to infer a resulting representative value of σ_{vo}'. As described in Section 2.3.8.1(b)-(iii), the resulting averaged values of S_r and S_r/σ_{vo}' were incompatible with each other for a number of Wang's "secondary" case histories, and this process produced unreasonable, and in some cases physically infeasible, values of σ_{vo}' for a number of case histories. Wang's value of $\sigma_{vo}' = 3{,}336$ lbs/ft^2 is clearly physically infeasible for this case, based on the cross-section, and so it is not considered a useful check here. Agreement between Olson's value, which is well-documented, and the values developed in these current studies is very good.

B.8.8 Evaluation of $N_{1,60,CS}$

Dutch cone soundings were performed after the failure (Ishihara et al, 1990). Only two soundings are published, and these are presented in Figure B.8.3. No standard penetrations tests were performed at this site.

Conversion of the Dutch cone tip resistances to equivalent SPT $N_{1,60,CS}$ values was an approximate exercise, but as the measures penetration resistances were very low the degree of uncertainty was acceptable here. In these current studies, the characterization of penetration resistance is represented by a best estimate mean value of $\overline{N_{1,60,CS}} \approx 4$ blows/ft., and an estimated standard deviation of this mean of $\sigma_{\bar{N}} \approx 1.1$ blows/ft.

Olson employed no fines adjustment, and developed a best estimate of $N_{1,60} = 1.1$ blows/ft, with a range of 1.0 to 1.2 blows/ft.

Wang (2003) and Kramer (2008) jointly developed a representative value of $\overline{N_{1,60,CS}} = 5.1$ blows/ft, and their estimated standard deviation of that overall mean value for this case history was $\sigma_{\bar{N}} = 1.4$ blows/ft. Details of the development of this interpretation by Wang and Kramer are not presented. Kramer and Wang (2105) subsequently converted to a non-fines-corrected representative value of $N_{1,60} = 1.1$ blows/ft, and they do not present their associated variance or standard deviation.

Overall agreement between these three independent assessments of representative $N_{1,60}$ and $N_{1,60,CS}$ values is judged to be very good, allowing for the differences between fines-corrected and non-fines corrected penetration resistance measures.

B.9 Upper San Fernando Dam (California, USA; 1971)

B.9.1 Brief Summary of Case History Characteristics

Name of Structure	Upper San Fernando Dam
Location of Structure	California, USA
Type of Structure	Hydraulic fill dam
Date of Failure	February 9, 1971
Nature of Failure	Seismic, During 1971 San Fernando Earthquake (M_W = 6.7)
Approx. Maximum Slope Height	67 ft.

B.9.2 Introduction and Description of Failure

The Lower San Fernando Dam (also known as the Lower Van Norman Dam, as it was part of the Van Norman Dam complex) suffered a liquefaction-induced landside on its upstream side as a result of the San Fernando Earthquake of February 9, 1971. The back-analysis of that slope failure case history was presented and discussed in Appendix B.4.

The Upper San Fernando Dam (or the Upper Van Norman Dam) also suffered liquefaction-induced damage, and displacements, during the 1971 San Fernando Earthquake. It is the Upper Dam that will be the subject of this Appendix section. The performance of the Upper Dam during the 1971 earthquake was well studied, though it has not received nearly as much attention from researchers as the Lower Dam. Seed et al. (1973, 1975) and Lee et al. (1975) documented immediate post-earthquake investigations and studies, and a number of researchers have studied and/or back-analyzed this dam since. It has not, however, been back-analyzed by many investigation teams for purposes of studying post-liquefaction strengths. Seed and Harder (1990) back-analyzed this dam performance case history for purposes of evaluation of post-liquefaction strengths, but Olson and Stark (2001, 2002) and Wang and Kramer (2003, 2008, 2015) did not. The informal panel of experts advising these current studies agreed unanimously that displacements for this case history were sufficient as to warrant inclusion of this case in these current studies, as fully developed post-liquefaction strength (S_r) would have been produced by the levels of shearing evidenced.

Figure B.9.1 presents a cross-section through the Upper San Fernando Dam after the 1971 earthquake, showing both the pre-earthquake and post-earthquake sections. The Upper dam, like the Lower dam, was also primarily constructed by means of hydraulic fill methods, with some rolled earth sections. Liquefaction occurred within at least some portions of the hydraulic fill on the downstream side of the dam. This loss of strength, likely coupled with cyclic inertial forces from the earthquake, produced moderate but not insignificant displacements of a large "slip mass" towards the downstream side. As shown in Figure B.9.1, the dam crest displaced approximately 5 feet toward the downstream direction, and settled approximately 3 feet. A complementary toe slippage feature was also observed, also shown in Figure B.9.1, with an associated lateral displacement of approximately 7 to 9 feet towards the downstream direction.

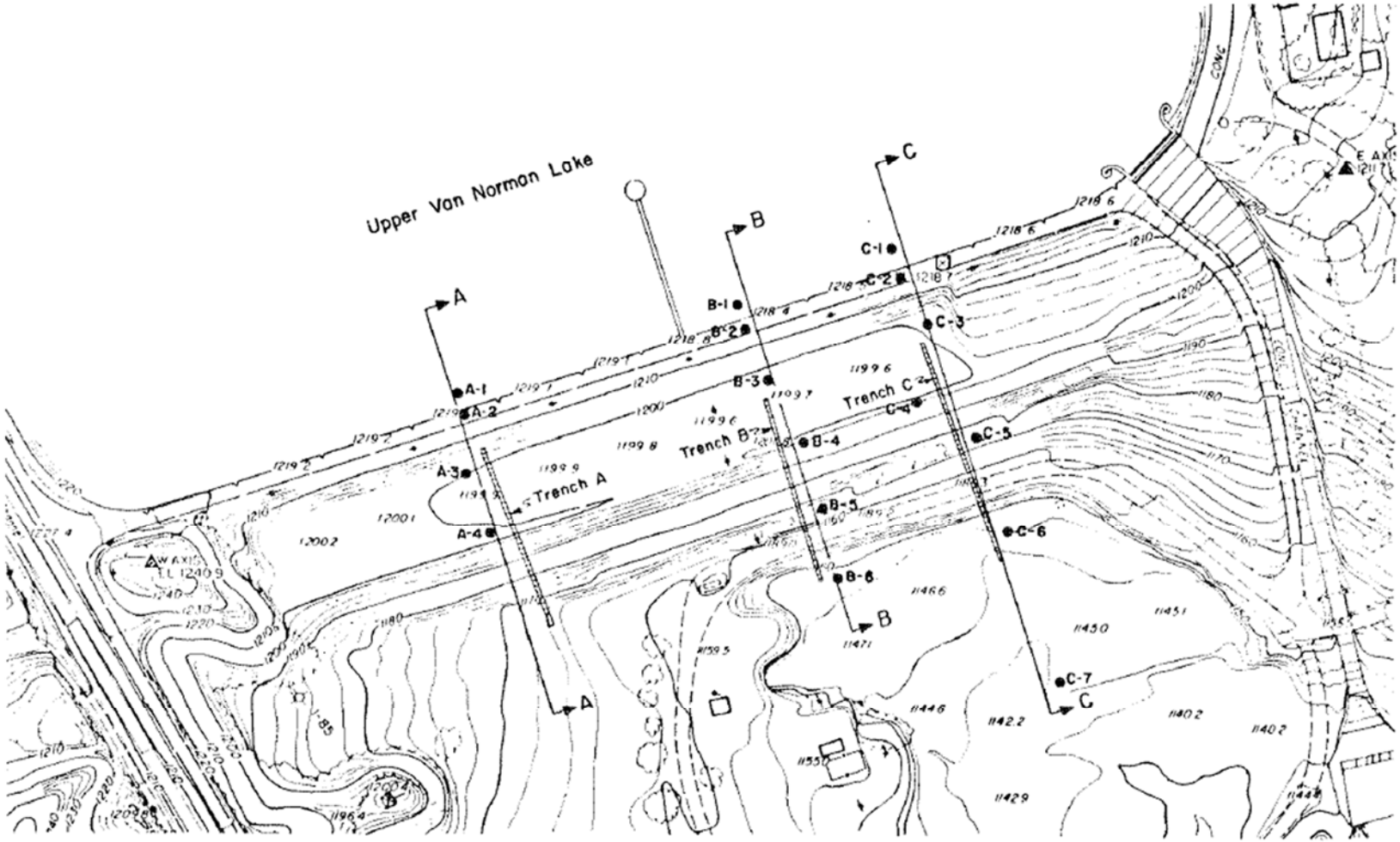

Figure B.9.1: Plan view of the Upper San Fernando Dam showing the locations of post-failure SPT borings performed for the 1971 investigation (Seed et al., 1973).

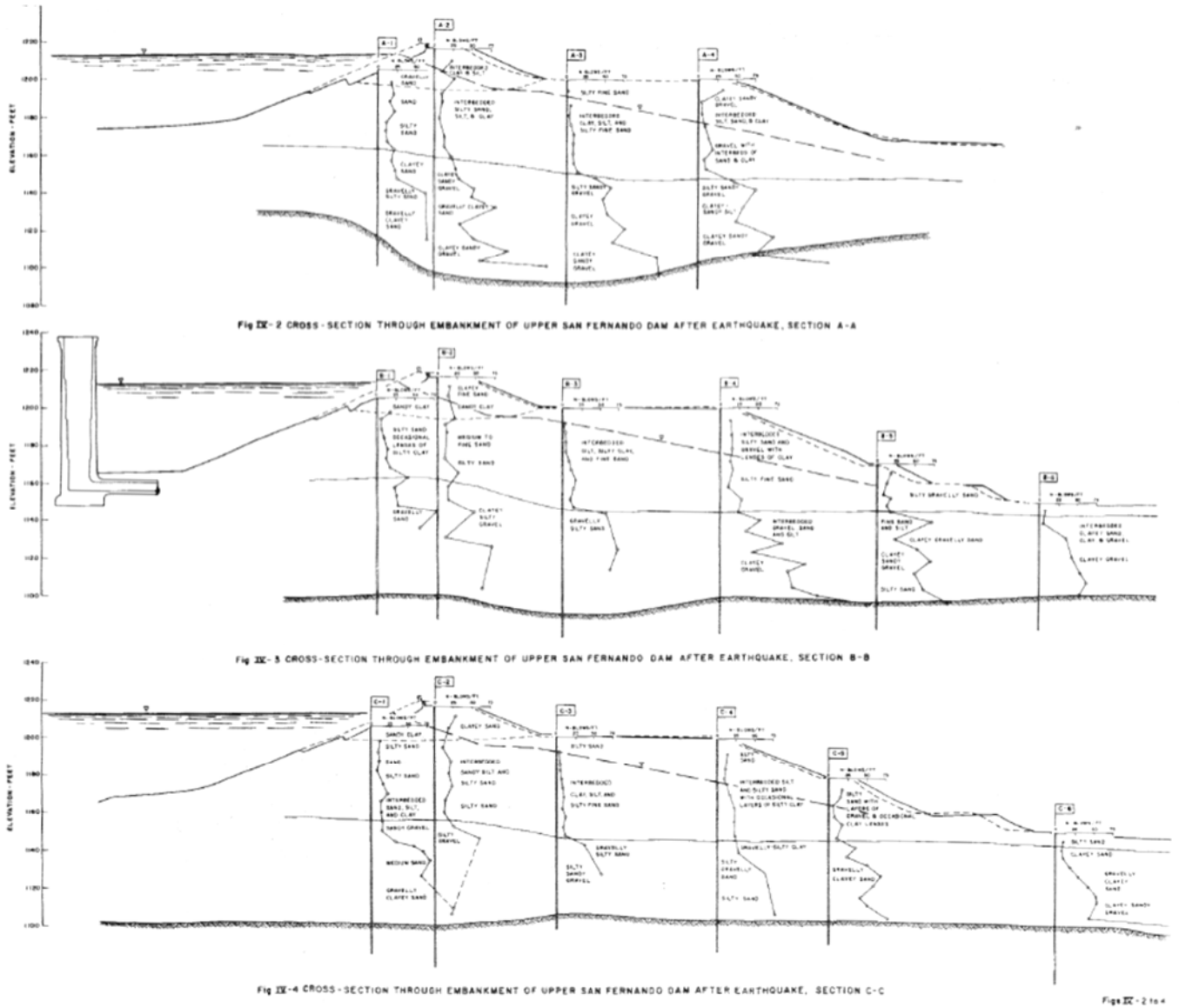

Figure B.9.2: Pre-failure and post-failure cross-sections of the Upper Fernando Dam from the 1971 investigation (Seed et al., 1973).

The downstream movements of the Upper Dam led to some cracking of the embankment, opening up some joints in the outlet conduit which passes through the embankment and leading to formation of a sinkhole along the line of the conduit. The deformations did not, however, result in a breach and release of the reservoir.

There were two seismoscopes at the Lower dam; one on the right abutment and one on the crest. These were not very modern instruments, and interpretation of the recordings was challenging. The crest instrument was carried into the reservoir by the upstream slope failure, but it was recovered and processed. It appeared to indicate that strong shaking had ceased before the upstream slide in the Lower dam was initiated. Morrill (1972) computed maximum spectral displacement for these two strong motion records, and also lists instrument characteristics including the natural period. Duke et al. (1972) computed the spectral accelerations of the two records, and assigned the following values of peak horizontal acceleration: Crest $a_{max} \approx 0.48g$ and abutment $a_{max} \approx 0.55g$. This suggests little amplification from abutment to crest for this event. Scott (1972) performed an additional interpretation of the crest record. Some uncertainties developed where the instrument reached its maximum travel and bumped against its support, and also where the pen ran briefly scale. Scott also concluded that the peak horizontal acceleration at the crest was likely on the order of $a_{max} \approx 0.55$ to $0.6g$, in good agreement with Duke et al.

B.9.3 Geology and Site Conditions

The Lower dam was constructed first, beginning in 1912, and construction of the Upper Dam began in 1921.

Both the Upper and Lower Dams were constructed primarily by means of hydraulic fill placement, and with similar materials and similar procedures. Hydraulic fill was placed simultaneously in a central puddled pool from starter dikes on both the upstream and downstream edges, producing “shells: on both the upstream and downstream sides comprised mainly of silty sands and sandy silts, and also a “puddled clay core”. Another construction method sometimes used when water was scarce was the “semi-hydraulic” procedure, in which the fill would be excavated from the borrow area by teams and Fresno scrapers or steam shovels, and then hauled to the dam, dumped into the pool, and then dispersed by hydraulic monitors operating from barges floating in the pool. Significant portions of the Upper Dam are believed to have been constructed by this semi-hydraulic method, although no detailed records or photographs appear to be available.

Seed et al. (1973) concluded that “Although standard hydraulic fill construction was used for the lower part of the Lower San Fernando Dam and the semi-hydraulic fill process was used for most of the fill at the Upper Dam, the results of drilling, sampling and trenching at both dams indicate no major difference in the type or quality of finished product obtained by either of the two methods.”

As with the Lower dam, additional rolled fill was placed atop the hydraulic fill of the Upper dam to further raise the crest section. The rolled fill was placed as “dry fill” (not hydraulic fill), and the materials were excavated by side hill borrow, spread in thin lifts, sprinkled and wagon-rolled. These materials were not well characterized in the post-failure investigations, but that has

little impact on the back-analyses performed as the strengths of these upper rolled fill materials are not significant because the apparent partially developed failure surface passes beneath these materials and does not shear them (see Figures B.9.2 through B.9.4).

The embankment of the Upper Dam is founded on deposits of "recent" alluvium, consisting of stiff clays and clayey gravels about 50 to 60 feet in thickness. These foundation deposits are not considered to be potentially liquefiable. Underlying the alluvium, and forming the abutments, are poorly cemented conglomeritic sandstone and coarse-grained sandstone of the Saugus Formation (Lower Pleistocene)-[Seed et al., 1973].

B.9.4 Initial Yield Stress Analyses

Back-analyses of the strength required for a static factor of safety equal to 1.0 were performed using the failure surface shown in Figure B.9.4. This is the best-estimate failure surface based on Figure B.9.3 (which is an enlarged view of Cross-Section B-B' from Figure B.9.2. This cross-section is slightly displaced, so the failure surface from Figure B.9.4 was imposed on the pre-earthquake cross-section geometry for this cross-section.

Shear strengths of the liquefied hydraulic fill along the failure surface were modeled as $S_{r,yield}$. Shear strengths of the clayey puddled core zone were modeled as increasing with increased effective overburden stress, based on laboratory testing of these soils as presented in Figure B.9.5.

Unit weights of the upper rolled fill above the phreatic surface were modeled as $\gamma_m = 126$ lbs/ft^3. For parametric sensitivity studies this was then varied over a range of $\gamma_m = 122$ to 130 lbs/ft^3. Unit weights of the upper rolled fill below the phreatic surface were modeled as $\gamma_s = 132$ lbs/ft^3. For parametric sensitivity studies this was then varied over a range of $\gamma_s = 128$ to 136 lbs/ft^3.

Unit weights of the sandy silt and silty sand hydraulic fill above the phreatic surface were modeled as $\gamma_m = 117$ lbs/ft^3. For parametric sensitivity studies this was then varied over a range of $\gamma_m = 112$ to 122 lbs/ft^3. Unit weights of the sandy silt and silty sand hydraulic fill below the phreatic surface were modeled as $\gamma_s = 123$ lbs/ft^3. For parametric sensitivity studies this was then varied over a range of $\gamma_s = 118$ to 128 lbs/ft^3.

Unit weights of the clayey puddled core both above and below the phreatic surface were modeled as $\gamma_m \approx \gamma_s \approx 116$ lbs/ft^3. For parametric sensitivity studies this was then varied over a range of $\gamma_m \approx \gamma_s \approx 112$ to 120 lbs/ft^3.

For these ranges of parameters, and for moderate variations in the vertical location of the failure plane (away from the upstream and downstream faces), the resulting best estimate value was $S_{r,yield} = 744$ lbs/ft^2, with a range of $S_{r,yield} = 602$ to 885 lbs/ft^2.

These back-analyses to evaluate $S_{r,yield}$ were performed only as an approximate check of the back-analyses described below in Section B.9.5. The differences between the two cross-

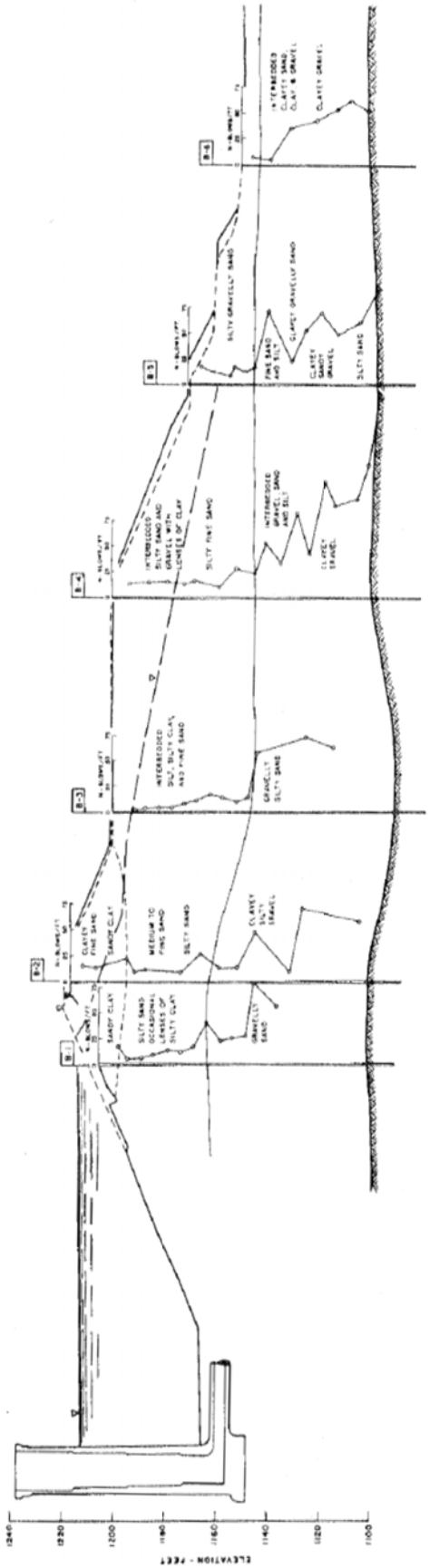

Fig IX-3 CROSS-SECTION THROUGH EMBANKMENT OF UPPER SAN FERNANDO DAM AFTER EARTHQUAKE, SECTION B-B

Figure B.9.3: Pre-failure and post-failure cross-sections of the Upper San Fernando Dam for Section B-B the 1971 investigation (Seed et al., 1973).

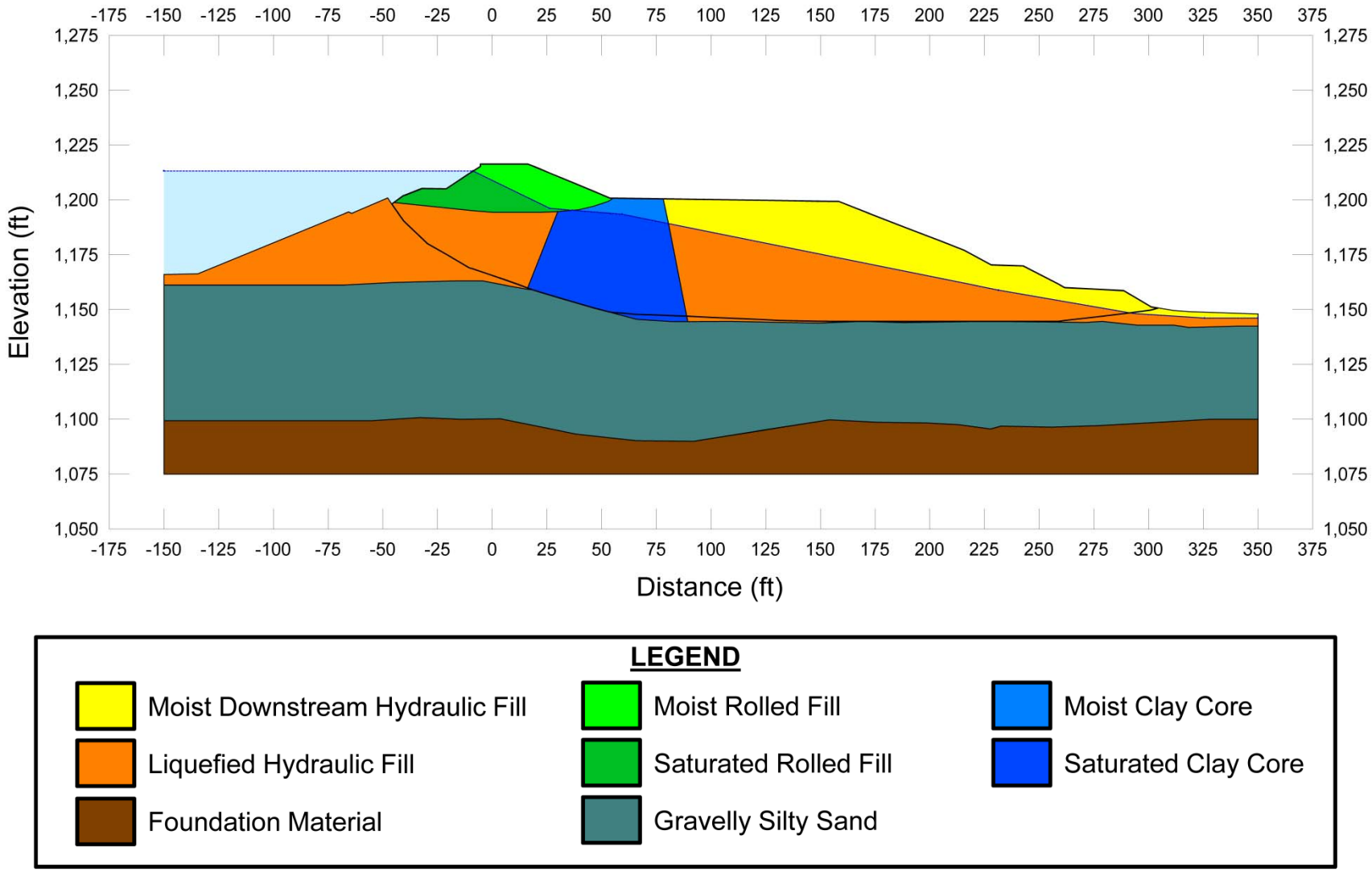

Figure B.9.4: Post-earthquake cross-section through the Upper San Fernando Dam showing potential failure surface analyzed.

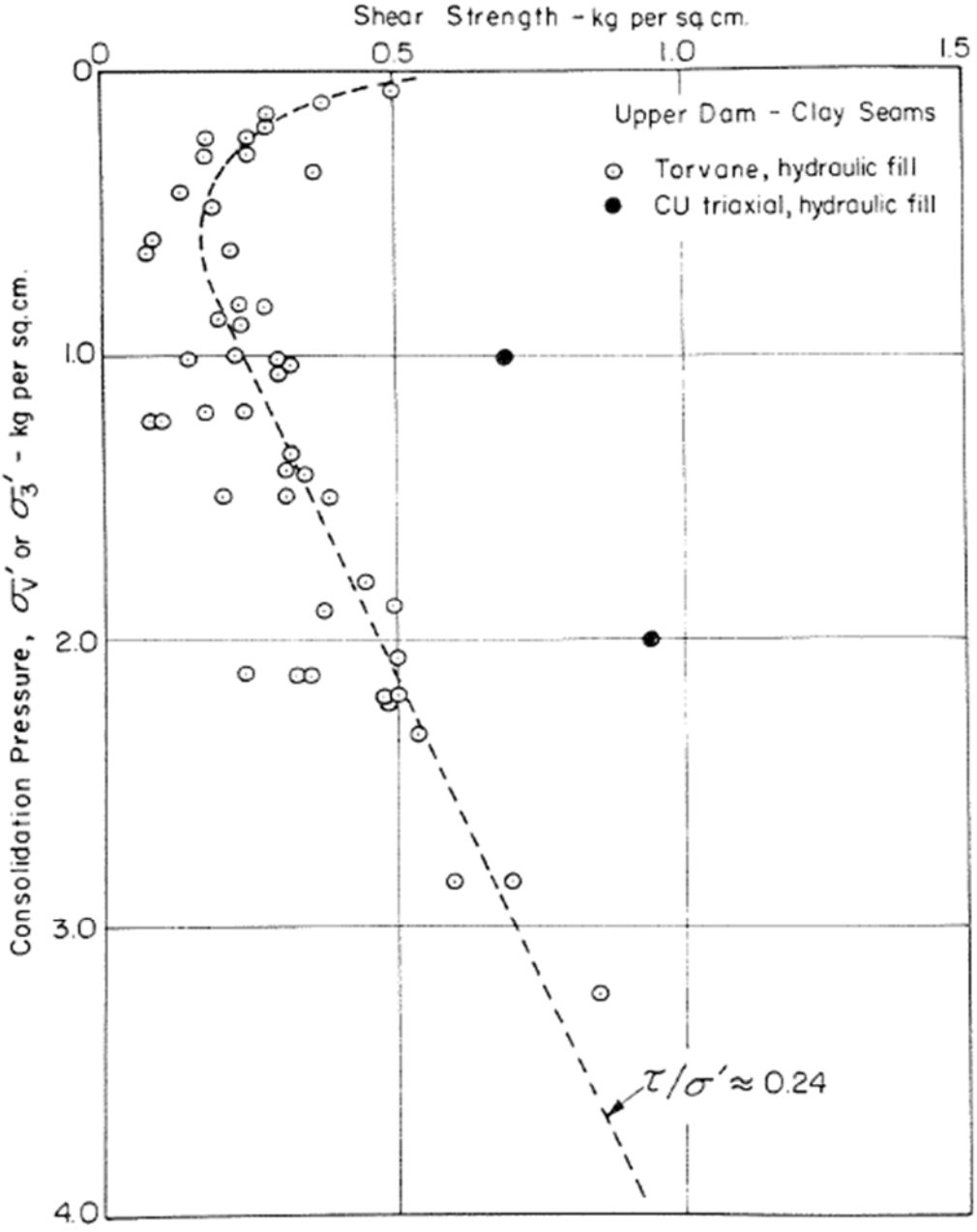

Figure B.9.5: In situ shear strengths of clayey central "puddle core" materials from the Upper San Fernando Dam based on torvane data. (Seed et al. 1973)

sections (pre-earthquake and post-earthquake) are relatively minor, and so these two sets of analyses are nearly redundant.

B.9.5 Residual Strength Analyses Based on Residual Geometry

Back-analyses were also performed to evaluate the value of $S_{r,resid/geom}$ required to provide a static factor of safety equal to 1.0 for post-failure (residual) geometry. The cross-section of Figure B.9.4 was employed here, and the failure surface shown in this figure was taken as the best estimate case. Model parameters were as described in the previous Section B.9.4.

For these ranges of parameters, and for moderate variations in the vertical location of the failure plane (away from the upstream and downstream faces), the resulting best estimate value was $S_{r,resid/geom}$ = 711 lbs/ft^2, with a range of $S_{r,resid/geom}$ = 577 to 848 lbs/ft^2.

B.9.6 Overall Estimates of S_r

A number if approaches were considered for evaluation of S_r. In all of the other liquefaction failure case histories back-analyzed as part of these studies, the failures experienced large displacements after initial liquefaction. This case history is different, because the total shear displacement offsets along the apparent failure surface were only on the order of approximately 5 to 9 feet. These were large enough to reliably reach a value of S_r, but the modest amount of displacement that occurred suggests that the post-liquefaction static Factor of Safety was equal to 1.0 or greater, and that the observed displacements were largely the result of additional cyclic lurching forces during the later stages of the earthquake (after significant liquefaction occurred along at least most or all of the apparent main failure surface).

There are a range of approaches available for calculating and/or estimating these types of displacements induced by cyclic (seismic) lurching. But none of these are of high precision, and it is difficult to make accurate and reliable predictions of cyclic displacements for this type of case wherein (1) liquefaction likely required some time to occur, so that some unknown portion of the seismic motions were expended before significant displacements began to occur, and (2) where overall cyclically-induced displacements are “moderate” (neither “small” nor “large” relative to the scale of the overall slope and the scale of the seismic motions applied.

Various types of simplified Newmark-type analyses are available (e.g. Seed and Martin, 1966; Makdisi and Seed, 1978; Hynes-Griffin and Franklin, 1984; etc.) Some of these can be enhanced by performing seismic response analyses of the overall Embankment, and then extracting from these the Mean Horizontal Equivalent Acceleration (MHEA) time history over the region of the eventual failure mass. This MHEA time history, coupled with pseudo-static stability analyses, can be used to directly integrate the exceedances of average driving shear stresses to develop estimates of overall resulting displacements (e.g. Jibson et al., 1998, Rathje and Bray, 1998; Bray and Travasarou, 2007; etc.).

All of these analytical approaches are sensitive to details of either (a) simplified estimation of MHEA, or (b) site response analyses for evaluation of MHEA time histories. As a result, estimates of displacements for a given set of strengths is relatively imprecise. As demonstrated by Olson and Johnson (2008), when these types of procedures are inverted, and used instead to estimate Sr, the results are highly imprecise as well.

These types of analytical methods are also sensitive to details of the input ground motion parameters (for the most simplified methods), or to actual input ground motion histories (for the more detailed analyses involving full site response analyses). Because the two seismometers at the Lower San Fernando Dam were very old instruments and did not produce good and reliable records of strong shaking), this adds significant further uncertainty.

And finally, a significant additional amount of uncertainty was associated with lack of knowledge as to how much for the input earthquake excitation for this relatively short Mw = 6.6 event was expended in "triggering: liquefaction before significant displacements began to occur. It would be only the remaining incoming strong pulses after significant triggering of liquefaction that would "drive: cyclic displacements for this marginal (moderate displacement) case.

A number of approaches were attempted, and a number of parametrizations of likely input motions, and it was found that for reasonable ranges of modeling details, and for reasonable approaches, a very wide range of uncertainty resulted.

It was also observed, however, that the embankment was certainly stable at the end of the earthquake. This meant that the problem was "bounded"; the static Factor of Safety for the post-earthquake geometry was certainly greater than or equal to 1.0.

It was then possible to make reasonably bounded estimates of S_r, noting that the displacements that accrues were "moderate" and that the levels of shaking and duration of shaking were likely sufficient to trigger liquefaction over much of the hydraulic fill on the downstream side, especially as cyclically-induced downstream shear displacements began to occur, but not with a great deal of energy to spare.

In order that any errors in estimation of S_r would be conservative, it was decided to deliberately target a slightly conservatively range of estimates of S_r here. In Section B.9.5, the best-estimate value of $S_{r,resid/geom}$ was $S_{r,resid/geom}$ = 711 lbs/ft^2, with a range of $S_{r,resid/geom}$ = 577 to 848 lbs/ft^2. It was decided by consensus that the best estimate of S_r would then be conservatively taken as 0.90 to 1.10 times $S_{r,resid/geom}$. This produced a resulting best estimate of $S_r \approx$ 711 lbs/ft^2, with a range of $S_r \approx$ 519 to 933 lbs/ft^2. These estimates of variance are non-symmetric about the best estimated mean value, and the range was conservatively judged to represent approximately +/- 1.5 standard deviations, so further adjustments were then necessary.

Overall, based on an assumed normal distribution, it was judged that the (mean and median) best estimate of post-liquefaction strength for this case history is

$$\overline{S_r} = 726 \text{ lbs/ft}^2$$

and that the best estimate of standard deviation of mean overall post-liquefaction strength is

$$\sigma_{\bar{S}} = 138 \text{ lbs/ft}^2$$

Only one previous investigation team had developed an independent estimate of Sr for this case history, and that was Seed and Harder (1990) who estimated $S_r \approx$ 500 to 700 lbs/ft^2. This was a bit lower than these current studies, but Seed and Harder had also deliberately cast this value in a conservative range given the uncertainties involved.

B.9.7 Evaluation of Initial Effective Vertical Stress

Average initial (pre-failure) effective vertical stress was assessed for the liquefied portion of the failure surface in Figure B.9.4. Parameters and sensitivity analyses were as described previously in Section B.9.4. Additional analyses were then performed for alternate potential failure surfaces, including failure surfaces representing the end result of retrogressive incremental failures extending back to the apparent back heel of the final failure. Depths of failure surfaces were varied, and both rotational and translational (wedge-like) failure surfaces were considered. This produced a moderately large, but finite, range of estimated values of average pre-failure effective stress within the liquefied materials controlling the failure.

The resulting best estimate of average pre-failure effective stress within the liquefied materials controlling the failure was then $\sigma_{vo}' \approx 3{,}129$ lbs/ft^2, with a reasonable range of $\sigma_{vo}' \approx$ 2,582 to 3,694 lbs/ft^2. This range is slightly non-symmetric about the median value, and this range was judged by the engineering team to represent approximately ± 2 standard deviations. Overall, the best characterization of initial (pre-failure) average effective vertical stress was then taken to be represented by a mean value of

$$\overline{\sigma'_{vo}} \approx 3{,}138 \text{ lbs/ft}^2$$

and with a standard deviation of

$$\sigma_{\bar{\sigma}} \approx 278 \text{ lbs/ft}^2$$

Olson (2001) and Olson and Stark (2002), in addition to Wang (2003) and Kramer (2008), did not consider this case history, therefore no comparison can be made to those studies. An estimate of vertical effective stress for the case was reported by Stark and Mesri (1992). They reported value of $\sigma_{vo}' \approx 2{,}975$ lbs/ft^2, in very good agreement with these current studies.

B.9.8 Evaluation of $N_{1,60,CS}$

As described in Section A.4.7, following the 1971 San Fernando Earthquake, and extensive investigation was performed on both the Lower and Upper San Fernando Dams. Figures B.9.1 and B.9.2 show a summary of boring locations and results of Standard Penetration Tests for the

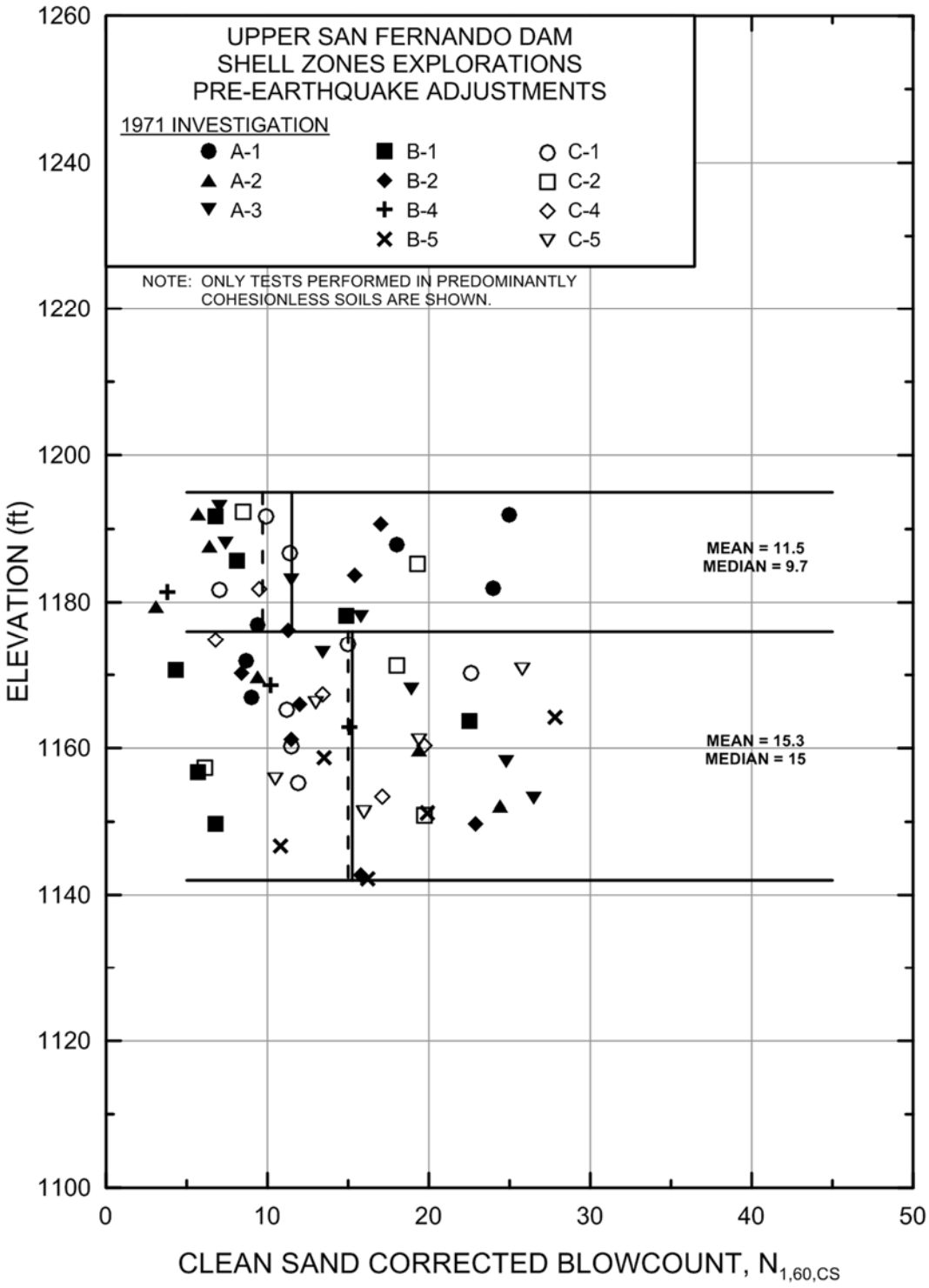

Figure B.9.6: Summary of available SPT data borings that penetrated through the downstream hydraulic fill zones showing corrected $N_{1,60,CS}$ values as adjusted to represent best-estimate values for the upstream side hydraulic fill pre-earthquake conditions.

1971 investigation. The blowcounts were corrected following the same procedures for of the 1971 borings, as were described previously in Section A.4.7 for the Lower San Fernando Dam. Figure B.9.6 shows a summary of the clean sand corrected 1971 SPTs performed in the silty sand and sandy silt hydraulic fill materials. The results were separated into elevation ranges of similar penetration resistances. From Elev. 1195 ft. to Elev. 1176 ft. the mean and median $N_{1,60,CS}$ values were calculated to be 11.5 and 9.7 blows/ft., respectively. From Elev. 1176 ft. to Elev. 1142 ft. the mean and median $N_{1,60,CS}$ values were calculated to be 15.3 and 15.0 blows/ft., respectively. While, the upper hydraulic fill material appears to have had a lower clean sand corrected representative blowcount than the lower material, the lower hydraulic fill material was judged to be the material of interest due to the deeper failure surface inferred form the observed displacements. Overall, the characterization of penetration resistance for these current studies was then taken as $\overline{N}_{1,60,CS} \approx 15$ blows/ft., with a standard deviation of $\sigma_{\overline{N}} \approx 1.8$ blows/ft.

Seed and Harder (1990) were the other investigation team to develop an estimate of representative $N_{1,60,CS}$ for this case. Their fines adjustments differed, and so did some of the other details of the processing and corrections of SPT N-values to develop values of $N_{1,60,CS}$. It appears that these factors largely balanced out, as their final representative value was also $N_{1,60,CS} \approx 15$ blows/ft.

B.10 Tar Island Dyke (Alberta, Canada; 1974)

B.10.1 Brief Summary of Case History Characteristics

Name of Structure	Tar Island Dyke
Location of Structure	Alberta, Canada
Type of Structure	Tailings Dyke
Date of Failure	August 23, 1974
Nature of Failure	Static liquefaction flow failure
Approx. Maximum Slope Height	46.2 ft.

B.10.2 Introduction and Description of Failure

The Tar Island Dyke is located in northern Alberta, Canada. The dyke serves to confine a tailings pond into which waste tailings consisting primarily of fine sands are place after bitumen has been removed from the locally mined tar sands deposits.

Four static liquefaction failures occurred between 1972 and 1974. All four failures occurred at the upstream side of the dyke, and there was no threat of potential tailings release. One of these four failures occurred on August 23, 1974, and it is this failure that had sufficient information available for back-analysis. Descriptions of the failure, and information on geometry, properties, and construction are provided by Mittal and Hardy (1977), Plewes et al. (1989) and Konrad and Watts (1995).

The dyke was constructed by modified upstream construction, with successive raises of the dyke embankment being placed partially atop recently deposited pond tailings, as shown in Figure B.10.1. The failure of August 23, 1974 produced only modest displacements, and resulted in a settlement of approximately 16 ft. of the upstream edge of the crest section of the recently raised dyke embankment. This settlement was nearly level, with just a slight slant downwards towards the upstream edge, and there was little or no lateral separation from the rest of the embankment section. There were a series of vertical cracks through the step over mat parallel to the crest of the dyke, but these did not open significantly. Figure B.10.1 shows an apparent rise in the elevation of the tailings at the left edge of the figure. This does not appear to be the result of "toe bulging" as the mass balance does not work out; the small settlement at the back heel cannot explain the apparent raise at this location.

The embankment section placed atop the recent tailings was called the step over mat. At the time of the failure, the step over mat was approximately 42 feet in height, and the width of the cell of the mat being placed was approximately 120 feet. Mittal and Hardy (1977) attributed the failure to three factors: (1) the adjacent tailings beach upon which the step over section was being placed had been raised by discharging tailings sand into approximately 20 feet of water, resulting in tailings placed below water with very low relative densities, (2) the average rate of raising the dyke during the three month period preceding the failure had been approximately three times faster than had previously been achieved at this site, and (3) the total height (42 feet) of the step-over mat was significantly more than had previously been achieved in a similar period.

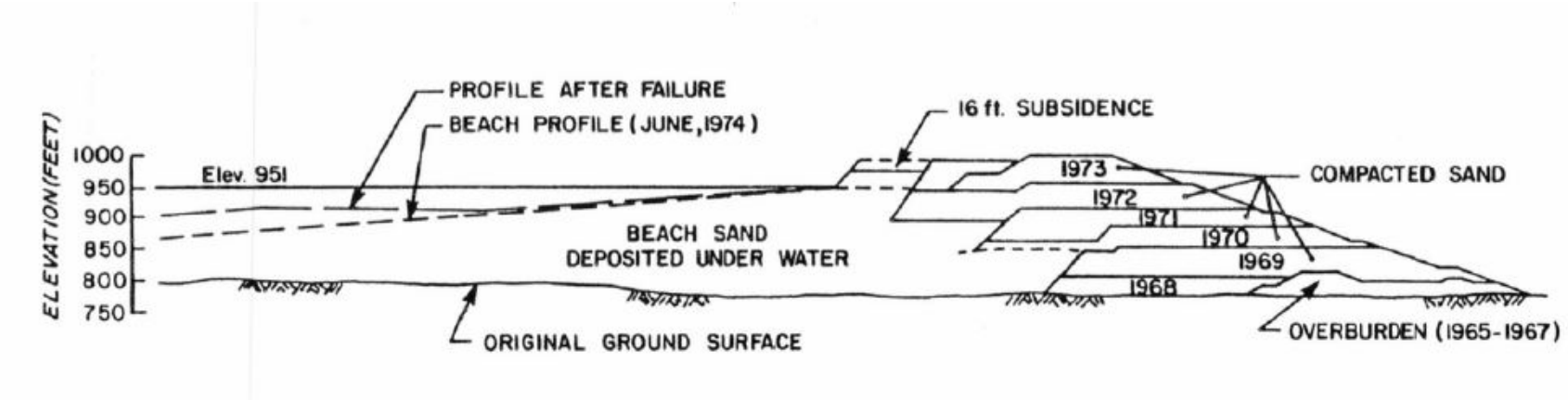

Figure B.10.1: Cross-section of Tar island Dyke showing the subsidence (failure) of August 23, 1974 (from Plewes et al., 1989)

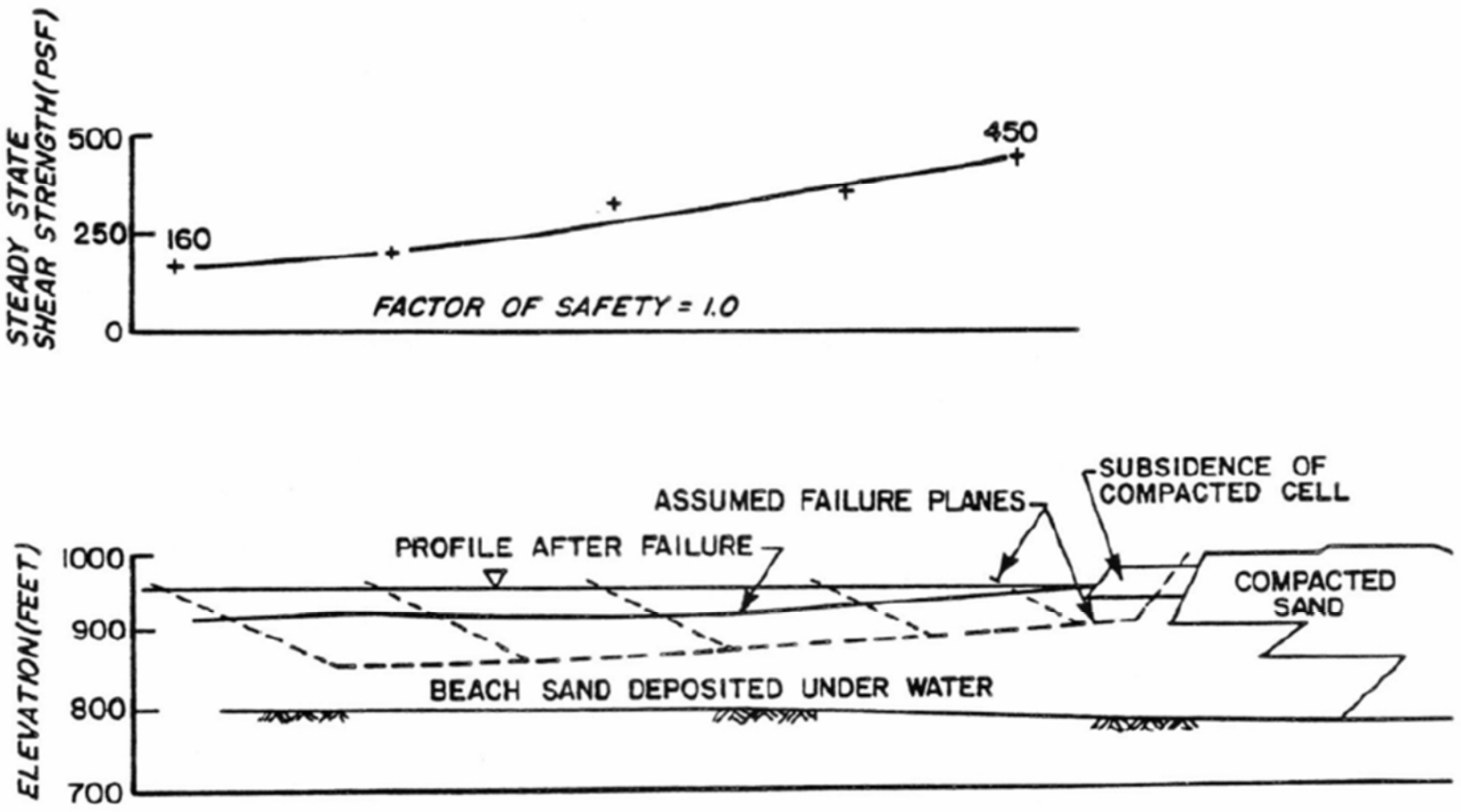

Figure B.10.2: Figure 8 from Plewes et al. (1989) showing potential failure surfaces considered and analyzed in their studies.

B.10.3 Geology and Site Conditions

The Tar Island Dyke was constructed by a "modified" upstream method. The initial starter dyke was placed and compacted as a normal embankment, using excavated "overburden" soils rather than tailings.

Subsequent raises of the dyke were then accomplished by placing sluiced tailings in cells, and compacting them with bulldozers. New tailings were then emplaced behind each successive embankment raise. The next embankment raise was then placed partially atop the underlying compacted embankment section, and partially atop the recently placed tailings. The materials used for these subsequent embankment raises were relatively clean sandy tailings, and these were sluiced into place in large cells and then compacted. It was recognized that this posed some risk of upstream side liquefaction failures, but it was concluded that the downstream side would be suitably stable as to prevent risk of tailings release so long as the overlap of compacted new embankment with the previous compacted embankment section was adequate. Early studies showed that this sluicing and compaction of the embankment fills achieved relative densities of approximately 70 to 75% in the compacted embankment materials (Mittal and Hardy, 1977).

Tailings were placed into the pond by overboarding from the upstream edge of the current embankment. Overboarded tailings deposited above the pond surface (beach deposits) achieved relative densities of on the order of approximately 40%, and overboarded tailings deposited below pond level (underwater deposits) achieved even lower relative densities on the order of approximately 30% (Mittal and Hardy, 1977). The tailings materials were fine, subangular quartz sands with fines contents typically on the order of about 10 to 15%, but this varied somewhat depending on material selection, transport and placement procedures (Mittal and Hardy, 1977; Plewes et al., 1989). These loose, fine tailings were potentially subject to liquefaction.

B.10.4 Initial Yield Stress Analyses

This has been a difficult case history for back-analyses, and it has not been tackled by many investigation teams. There have been a number of different positions taken with regard to likely failure mechanisms and details, and the field evidence is arguably inconclusive.

Mittal and Hardy (1977) stated "It appeared that a layer of beach sand about 15 feet (4.5m) thick below the mat liquefied and flowed out into the pond." That appears unlikely, as it would probably have produced a large lateral translation of the overlying step over mat.

Plewes et al. (1989) considered a number of potential failure surfaces passing through the beach sands (tailings) beneath and outboard of the step over mat, as shown in Figure B.10.2. They calculated values of $S_{r,yield}$ of between 8 kPa (160 lbs/ft^2) to 23 kPa (450 lbs/ft^2) for these trial surfaces. They also felt that because the overall displacements had been relatively small, these values of $S_{r,yield}$ would also represent reasonable estimates of S_r for this case.

Olson (2001) assumed that liquefaction was more likely in the most recently deposited layer of tailings (which were below water deposited beach sands), and that the previous layer of

tailings sands would have consolidated and aged a bit and so would be less susceptible. The upper (potential liquefaction) zone tailings had been placed recently (between April 1 to May 14, 1974). The resulting zone of tailings that they hypothesized to have potentially liquefied is shown by the shaded zone in Figure B.10.3. Olson did not show the actual full failure surfaces that he then analyzed. His verbal description is "Several failure surfaces passing through approximately the center of the zone of liquefaction were analyzed, as shown in Figure A.82 [Figure B.10.3], and values of yield shear strength were varied until a factor of safety was achieved." It is assumed that he meant until a factor of safety of 1.0 was achieved. The resulting best estimate value was $S_{r,yield}$ = 35.9 kPa (750 lbs/ft^2), with a range of $S_{r,yield}$ = 32.3 kPa (675 lbs/ft^2) to 38.6 kPa (806 lbs/ft^2). Lack of detail regarding the actual full failure surfaces analyzed makes this somewhat difficult to interpret.

Figure B.10.4(a) shows the cross-section used for back-analyses of the post-liquefaction initial yield strength $S_{r,yield}$ that would be required within the tailings materials of the typical section of the Tar Island Dyke tailings to produce a calculated Factor of Safety equal to 1.0 for static, pre-failure conditions. This is not the actual post-liquefaction strength, but it proves to be useful in developing estimates of post-liquefaction strength (S_r) for this case history.

In these current studies, a range of potential failure surfaces were considered. One mechanism considered involves smaller rotational or block-like failures that act more like punching/bearing failures of the underlying tailings. The other mechanism considered, is similar to the range of failure surfaces evaluated by Plewes et al. (1989). All of the failure surfaces evaluated were assumed, as Olson assumed, to penetrate into the tailings to a maximum depth approximately equal to the older deposits of tailings. Example failure surfaces for each of these types of mechanism are shown in Figure B.10.4(a)

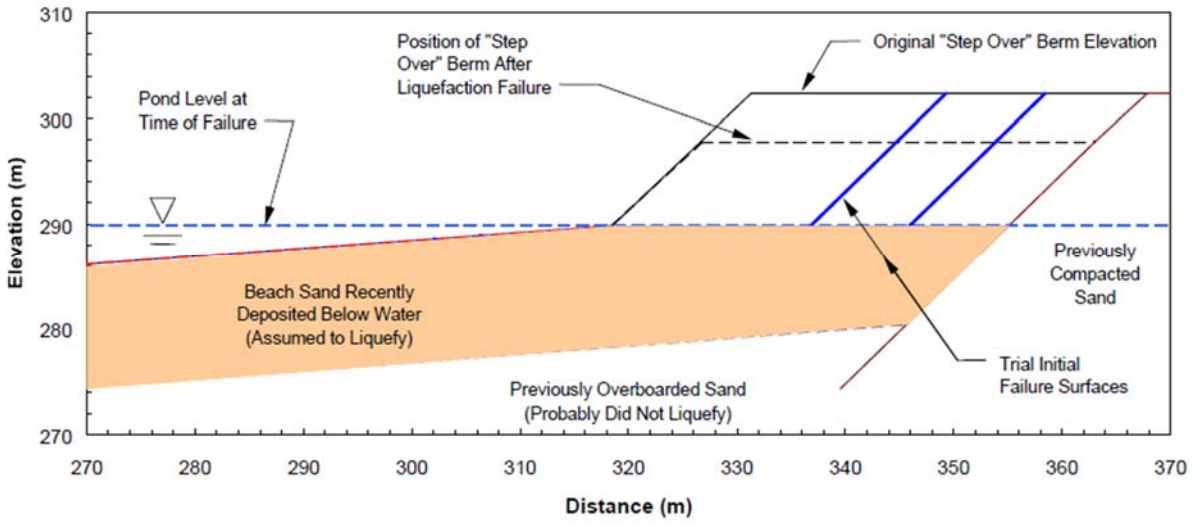

Figure B.10.3: Figure A.82 from Olson (2001) showing the assumed zone of potential liquefaction and the upper portions of example potential failure surfaces analyzed.

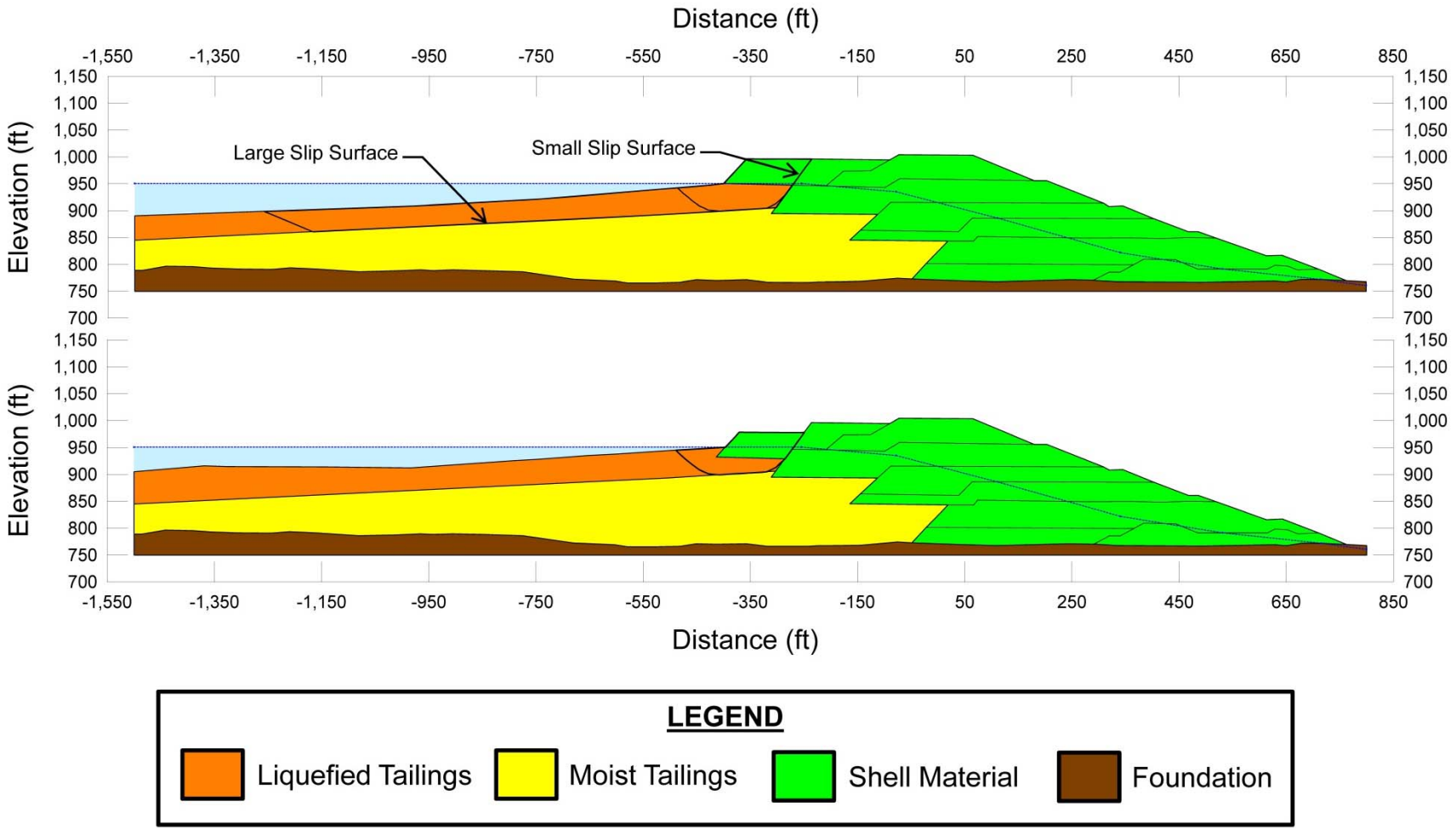

Figure B.10.4: Tar Island Dyke: (a) pre-failure geometry and trail failure surfaces for initial yield stress analyses, and (b) post-failure geometry and failure surface for post-failure residual geometry analyses.

Unit weights of the non-saturated compacted sand dyke fill above the phreatic surface were modeled with a unit weight of $\gamma_m \approx 120$ lbs/ft^3, and this was then varied over a range of $\gamma_m \approx 115$ to 125 lbs/ft^3 for parameter sensitivity studies. Unit weights of the saturated compacted sand dyke fill below the phreatic surface were modeled with a unit weight of $\gamma_s \approx 125$ lbs/ft^3, and this was then varied over a range of 120 to 130 lbs/ft^3 for parameter sensitivity studies. Unit weights of the saturated tailings below the phreatic surface were modeled with a unit weight of $\gamma_s \approx 115$ lbs/ft^3, and this was then varied over a range of 110 to 120 lbs/ft^3 for parameter sensitivity studies. The friction angle of the compacted sand dyke fill materials above the phreatic surface was modeled with $Ø' \approx 32°$, and a range of $Ø' \approx 29°$ to 35°.

Potential initial failure surfaces were modeled as either (1) wedge-like semi-translational features, or (2) semi-rotational/translational features, or (3) the potential monolithically initiated largely translational scenario with a failure mass extending far downslope.

A significant number of smaller punching failure surfaces were analyzed, corresponding to a scenario in which the dyke block punches nearly vertically into the recently placed tailings materials. Figure B.10.4(a) shows an initial failure surface that was the most critical potential initiating failure surface found (lowest post-liquefaction, pre-displacement Factor of Safety) but additional potential failure surfaces were also analyzed, including failure surfaces with more translational features. The resulting best estimate value of $S_{r,yield}$ for the smaller initial yield surface was found to be $S_{r,yield} = 911$ lbs/ft^2, with a likely range of $S_{r,yield} \approx 757$ to 1,067 lbs/ft^2.

For the case of the larger, more translational scenario similar to some of the larger Plewes et al. (1989) surfaces the best estimate value of $S_{r,yield}$ was found to be $S_{r,yield} = 336$ lbs/ft^2, with a range of $S_{r,yield} \approx 272$ to 403 lbs/ft^2.

Based on these analyses, it was judged that the punching mechanism corresponding to the smaller failure surfaces was a more likely failure mechanism. As such, the results from that analysis were weighted more heavily than the results from the larger, more translational, failure surfaces. The weighting factors utilized, expressed in terms of smaller surface to larger surface, was developed by consensus among the current analysis team and the weighting ratio was 7 to 3. Based on that weighting scheme, the range of variations in properties and parameters, and a range of potential failure mechanisms and feasible failure surfaces, the resulting best estimate of "representative" overall $S_{r,yield}$ was found to be $S_{r,yield} = 739$ lbs/ft^2, with a range of $S_{r,yield} \approx 612$ to 868 lbs/ft^2.

The resulting best estimate values and range of $S_{r,yield}$ are in very good agreement with those values developed by Olson (2001), as presented earlier in this section.

B.10.5 Residual Strength Analyses Based on Residual Geometry

Back-analysis were also performed to evaluate the "apparent" post-liquefaction strength ($S_{r,resid/geom}$) required to produce a calculated static Factor of Safety equal to 1.0 based on residual geometry. This is not a direct measure of post-liquefaction strength (S_r), as it neglects momentum effects and would underestimate S_r, but it is useful for overall evaluation of S_r for this case history.

Figure B.10.4(b) shows the post-failure cross-section geometry and an example assumed slip surface utilized in the residual geometry analyses. The slip surface shown is the most critical one (highest resulting value of $S_{r,resid/geom}$). Based on the post-failure cross-section, with additional potential failure surfaces examined in addition to the potential failure surface shown in Figure B.10.4(b), and the properties and parameters described above, a number of alternate potential failure surfaces were analyzed. Material parameters were also varied. Based on these analyses, it was judged that a best estimate value was $S_{r,resid/geom}$ = 452 lbs/ft^2, and a reasonable range was $S_{r,resid/geom} \approx$ 354 to 553 lbs/ft^2.

Olson (2001) performed a simplified infinite slope analysis to evaluate $S_{r,resid/geom}$. He analyzed a tailings slope with top and base slopes of approximately 4°, and an average thickness of approximately 9.1 m. The resulting best estimate value was then $S_{r,resid/geom}$ = 12 kPa (250 lbs/ft^2). Olson adopted the estimated range of Plewes et al. (1989) of $S_{r,resid/geom}$ = 7.7 to 21.6 kPa (160 to 450 lbs/ft^2) as his likely range.

B.10.6 Overall Estimates of S_r

Overall estimates of S_r for this Class B case history were made based on the pre-failure geometry, the partial post-failure geometry, the approximate runout features and characteristics, and the values of $S_{r,yield}$ and $S_{r,resid/geom}$ as calculated and/or estimated in the preceding sections.

Runout distance of the center of mass of the overall failure was approximately D = 18.2 feet, and the initial failure slope height was H = 46.2 feet. This produces a runout ratio (defined as runout distance traveled by the center of gravity of the overall failure mass divided by the initial slope height from toe to back heel of the failure) of D/H = 0.39. This allows Equation 4-4, and Figures 4.7 and 4.11, to serve as one basis for estimation of post-liquefaction strength S_r. Using the ranges of $S_{r,yield}$ and $S_{r,resid/geom}$ from Sections B.15.4 and B.15.5, and assuming that $\xi \approx 0.70$ to 0.95 for this runout ratio, with 0.825 as the best estimate, provided a best estimate value of $S_r \approx$ 492 lbs/ft^2 and an estimated range of $S_r \approx$ 338 to 675 lbs/ft^2. A second basis for estimation of S_r was the use of the relationship of Figure 4.9, and the range of values of $S_{r,yield}$ from Section B.10.4. Based on the runout ratio, values of initial (pre-failure displacement) Factor of Safety were taken as approximately 0.60 to 0.80, and this produced a best estimate value of $S_r \approx$ 517 lbs/ft^2 and an estimated range of $S_r \approx$ 367 to 694 lbs/ft^2. No similar use was made of Figure 4.9 in conjunction with the ranges of $S_{r,resid/geom}$ estimated in Section B.10.5.

The estimates by each of the two methods above were then averaged together, and this produced a best estimate value of $S_r \approx$ 505 lbs/ft^2 and an estimated range of $S_r \approx$ 338 to 694 lbs/ft^2. These estimates of variance are non-symmetric about the best estimated mean value, and the range was judged to represent approximately +/- 1.5 standard deviations, so further adjustments were then necessary.

Overall, taking into consideration the slightly asymmetric range of these results for S_r, it was judged that the (median) best estimate of post-liquefaction strength for this case history is

$$\overline{S_r} = 516 \text{ lbs/ft}^2$$

and that the best estimate of standard deviation of mean overall post-liquefaction strength is

$$\sigma_{\bar{S}} = 119 \text{ lbs/ft}^2$$

Olson (2001) and Olson and Stark (2002) did not apply their "kinetics" method to this case, and so they did not independently develop an estimate of S_r that incorporated momentum effects. Instead, they took their value of $S_{r,resid/geom}$ as representing S_r. Their best estimate value was therefore $S_r = S_{r,resid/geom} = 12$ kPa (250 lbs/ft^2), with a range of $S_r = S_{r,resid/geom} = 7.7$ to 21.6 kPa (160 to 450 lbs/ft^2), as described previously in Section B.8.5.

A better estimate can be obtained by taking their back-calculated best estimate values of $S_{r,yield}$ and $S_{r,resid/geom}$ are using the simplified Equation 4.1 with a fixed value of $\xi = 0.8$, in which case the resulting estimate would be

$$S_r \approx \xi \bullet (S_{r,yield} + S_{r,resid/geom}) / 2 \approx (0.8) \bullet (750 \text{ lbs/ft}^2 + 250 \text{ lbs/ft}^2) / 2 \approx 400 \text{ lbs/ft}^2$$

This is about 20% lower than the values developed in these current studies.

Wang (2003) and Wang and Kramer (2008) did not employ their zero inertial force (ZIF) method to incorporate inertial effects in back-analyses of this failure. Instead they selected their value of S_r based on examination of values from back-analyses by several previous investigators. Wang (2003) selected three values for this case history as:

$S_r = 305$ lbs/ft^2 (Plewes et al. (1989)

$S_r = 80$ lbs/ft^2 (Konrad and Watts, 1995)

$S_r = 500$ lbs/ft^2 (Olson, 2001)

where Wang's value for "Olson, 2001" was taken as $S_r \approx (S_{r,yield} + S_{r,resid/geom}) / 2$, representing an implied value of $\xi = 1.0$, which would clearly over-estimate S_r for this case. Averaging these three values from previous investigations together produced a value of $S_r \approx 346$ lbs/ft^2. The value of $S_r = 80$ lbs/ft^2 proposed by Konrad and Watts appears to be unreasonably low relative to the other two sets of values, and these current studies, so this overall average of Wang (2003) is likely somewhat low as well.

B.10.7 Evaluation of Initial Effective Vertical Stress

Average initial (pre-failure) effective vertical stress was assessed for the liquefied portions of the failure surfaces for both the smaller and larger rotational and wedge-like failures similar to both failure surfaces shown in Figure B.10.4(a). Failure surfaces, parameters and sensitivity analyses were as described previously in Section B.10.4. Depths of failure surfaces were varied slightly, and both rotational and translational (wedge-like) failure surfaces were considered. The same weighting factors utilized in the strength determination for each surface were also implemented for the evaluation of initial effective vertical stress.

The resulting best estimate of average pre-failure effective stress within the liquefied materials controlling the failure was then $\sigma_{vo}' \approx 4{,}180$ lbs/ft^2, with a reasonable range of $\sigma_{vo}' \approx$ 3,299 to 5,164 lbs/ft^2. This range is slightly non-symmetric about the median value, and this range was judged by the engineering team to represent approximately ± 2 standard deviations. Overall, the best characterization of initial (pre-failure) average effective vertical stress was then taken to be represented by a mean value of

$$\overline{\sigma'_{vo}} \approx 4{,}197 \text{ lbs/ft}^2$$

and with a standard deviation of

$$\sigma_{\bar{\sigma}} \approx 484 \text{ lbs/ft}^2$$

An estimate of σ_{vo}' was also calculated by Olson and Stark (2001, 2002). They reported a weighted average mean value of $\sigma_{vo}' \approx 205.9$ kPa (4,300 lbs/ft^2), in very good agreement with these current studies. Average initial vertical effective stresses were not directly reported by Wang (2003) and Kramer (2008), but they were published more recently in the publication by Kramer and Wang (2015). As discussed in Section 2.3.8.1(b)-(iii), Wang (2003) did not perform any independent analyses to assess σ_{vo}' for his 22 "secondary" cases, and this is one of those cases. Instead, he compiled values of S_r from multiple previous investigators, and averaged these for a best estimate. He also compiled multiple values of S_r/σ_{vo}' from previous investigators, and averaged these for a best estimate. He then used these two best-estimate values of S_r and S_r/σ_{vo}' to infer a resulting representative value of σ_{vo}'. As described in Section 2.3.8.1(b)-(iii), the resulting averaged values of S_r and S_r/σ_{vo}' were incompatible with each other for a number of Wang's "secondary" case histories, and this process produced unreasonable values for a number of case histories. Wang's value of $\sigma_{vo}' = 6{,}279$ lbs/ft^2 for this case is very high, and it is not considered a useful check here.

B.10.8 Evaluation of $N_{1,60,CS}$

Figure B.10.5 presents CPT and SPT data from the Tar Island site tailings reported by Mittal and Hardy (1977). Konrad and Watts (1995) reported an average $N_{1,60}$ value, conveyed to them through personal communications with H. Plewes, of $N_{1,60} = 7$ blows/ft with an average fines content of approximately 10 to 15%.

Boring 75-ND-4, which was drilled form the beach and appears to have encountered the more recently places tailings sands provides SPT data local to the failure. The precise drilling procedures, equipment and conditions are unknown. Assuming no energy correction (ER = 60%), and applying corrections for effective overburden stress, the approximate representative value of the upper sands of $N_{1,60} \approx 12$ blows/ft. The CPT, 74-DC-4, advanced in the same material, has a representative tip resistance of approximately 2 4 MPa, and this would produce equivalent $N_{1,60,CS}$ values in this same general range.

Incorporating all corrections and considering the sparseness and large degree of uncertainty of the data for this case history, characterization of penetration resistance for these current studies was then taken as $\overline{N_{1,60,CS}} \approx 11$ blows/ft., with a standard deviation of $\sigma_{\bar{N}} \approx 2.3$ blows/ft.

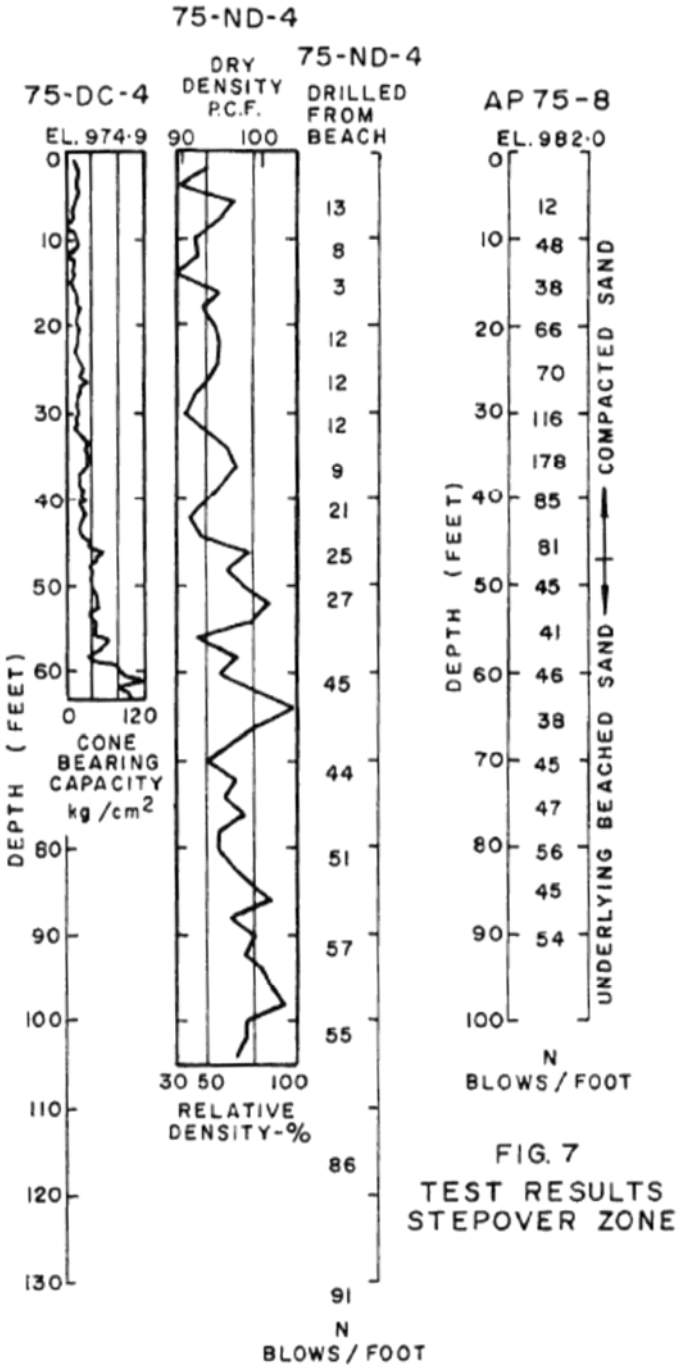

FIG. 6 TEST RESULTS BEACH SAND

FIG. 7 TEST RESULTS STEPOVER ZONE

Figure B.10.5: Figures 6 and 7 from Mittal and Hardy (1977) showing the results of field explorations performed at the Tar Island site.

B.11 Mochi-Koshi Tailings Dam (Japan; 1978)

B.11.1 Brief Summary of Case History Characteristics

Name of Structure	Mochi-Koshi Tailings Dam, Dikes 1 and 2
Location of Structure	Izu Peninsula, Japan
Type of Structure	Mine Tailings Dams
Date of Failure	January 14 and 15, 1978
Nature of Failure	Seismic: Dike 1 failed immediately following the 1978 Izu-Ohshima-Kinkai Earthquake (M_L = 7.0), and Dike 2 after large aftershock (M_L = 5.8)
Approx. Maximum Slope Height	Dam 1 = 46.9 ft., Dam 2 = 33.2 ft

B.11.2 Introduction and Description of Failure

A tailings impoundment consisting of three dams on the Izu Peninsula suffered a pair of liquefaction-induced failures during the 1978 Izu-Ohshima-Kinkai Earthquake (M_L = 7.0). Based on surveys of damage, a distribution of shaking density was created and an acceleration of approximately 250 gal. (0.25 g) was estimated at the Mochi-Koshi site (Ishihara, 1984).

The impoundment for gold mine tailings was created with the construction of three dams surrounding a natural bowl-like depression on a mountain top. To construct the impoundment, strongly weathered surface material was first stripped, and an underlying tuff formation was "exposed in a saw-teeth shape" providing a rough contact for the starter dam. Construction of the starter dikes occurred in 1964 by placement of local volcanic soils by means of bulldozers. The tailings, from gold mining operations along the Mochi-Koshi River, were pumped up to the imppoundment, raising them 600 m (1,970 ft.) through a series of pipes. The tailings material was placed at the site of either Dike 1 or Dike 2 by discharging toward the pond. The dikes were raised at a rate of approximately 2 m (6.6 ft.) per year by placing local volcanic soils using the upstream method (Ishihara, 1984).

Dike 1, the largest of the three dikes with a height of 28 m (92 ft.) and a width of 73 m (240 ft.), failed immediately following the main earthquake. Ishihara recounted an observer's testimony stating that the dam failed about 10 seconds following the shaking of the main earthquake. The observer recounted seeing the face of the dam swell, and the breach occurred in the upper part of the dam near the left abutment. A huge mass of slime is said to have followed the breach rushing down the valley to the Mochi-Koshi River. In total, approximately 80,000 m^3 (approximately 105,000 yd^3) of tailings were released from the dam. A bed of sediment and tailings, approximately 1.0 to 1.9 m (3.3 to 6.2 ft.) thick, remained in the Mochi-Koshi River (Ishihara, 1984).

Dike 2 failed approximately 5 hours and 20 minutes after a ML = 5.8 aftershock on the day following the main earthquake. That main aftershock occurred at 7:31 am, with an additional

aftershock at 7:36 am. Five to six cracks were observed in the face of Dike 2 parallel to the axis of the dam about an hour after the first large aftershock. The cracks were initially approximately 1 to 3 m (3.3 to 9.8 ft.) long and 5 mm (0.2 in.) in width. After about an additional hour these cracks had grown to about 5 m (16.4 ft.) long and 5 cm (2 in.) in width. Another observer onsite observed the central part of Dike 2 gradually sinking at about 1:00 pm that same day, eventually leading to a sudden release of tailings. The initial release of material coincided with a breach of about 20 m (66 ft.) of crest width. The breach of the crest was later enlarged to a width of about 65 m (213 ft.). In total, approximately 3,000 m^3 (approximately 4,000 yd^3) of material flowed down the valley reaching a maximum distance of 240 m (790 ft); (Ishihara, 1984).

Figure B.11.1 presents a plan view of the Mochi-Koshi tailings impoundment, showing the approximate extent of the two failures. Pre and post-failure cross sections for each dike were also reported, and are presented as Figure B.11.2.

Figures B.11.2(a) and (ba) show pre-failure and post-failure cross-sections through the two dike failures. The post-failure slope of Dike No. 1 was between 4° to 8°, and the failure appears to have passed mainly above the crest of the embankment dam comprised of volcanic soil. The

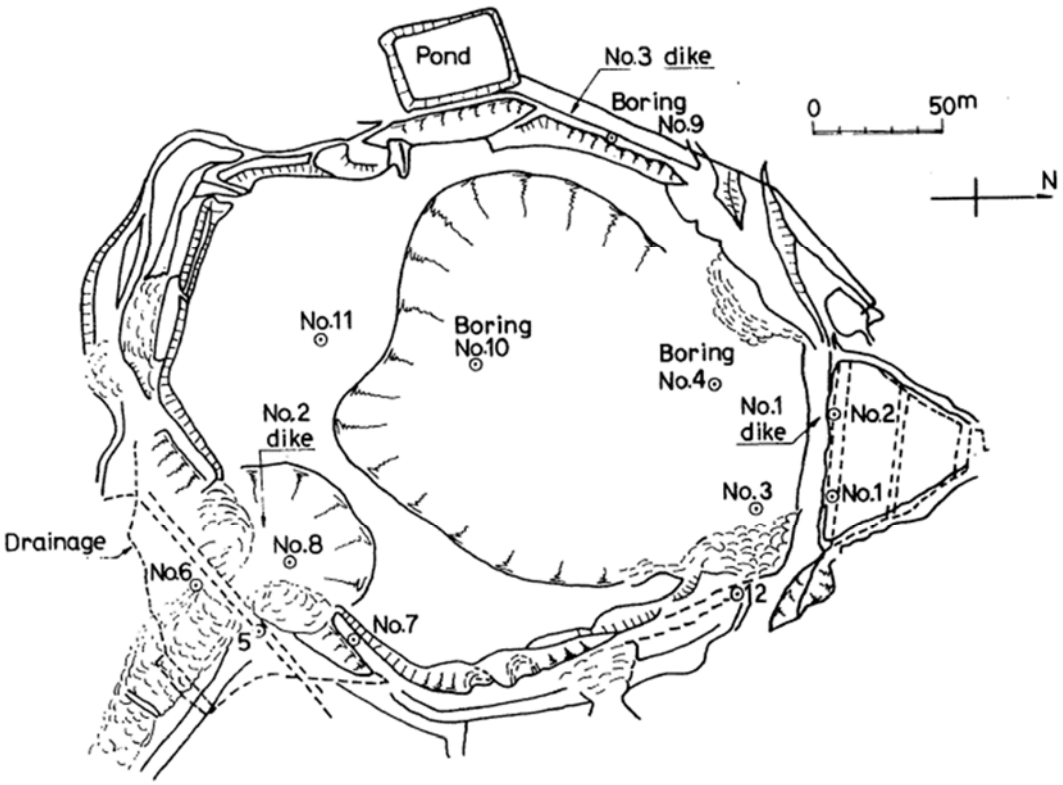

Figure B.11.1: Plan view of the Mochi-Koshi tailings dam showing the approximate extent of the flow failures and the locations of borings performed following the failure (figure from Ishihara, 1984).

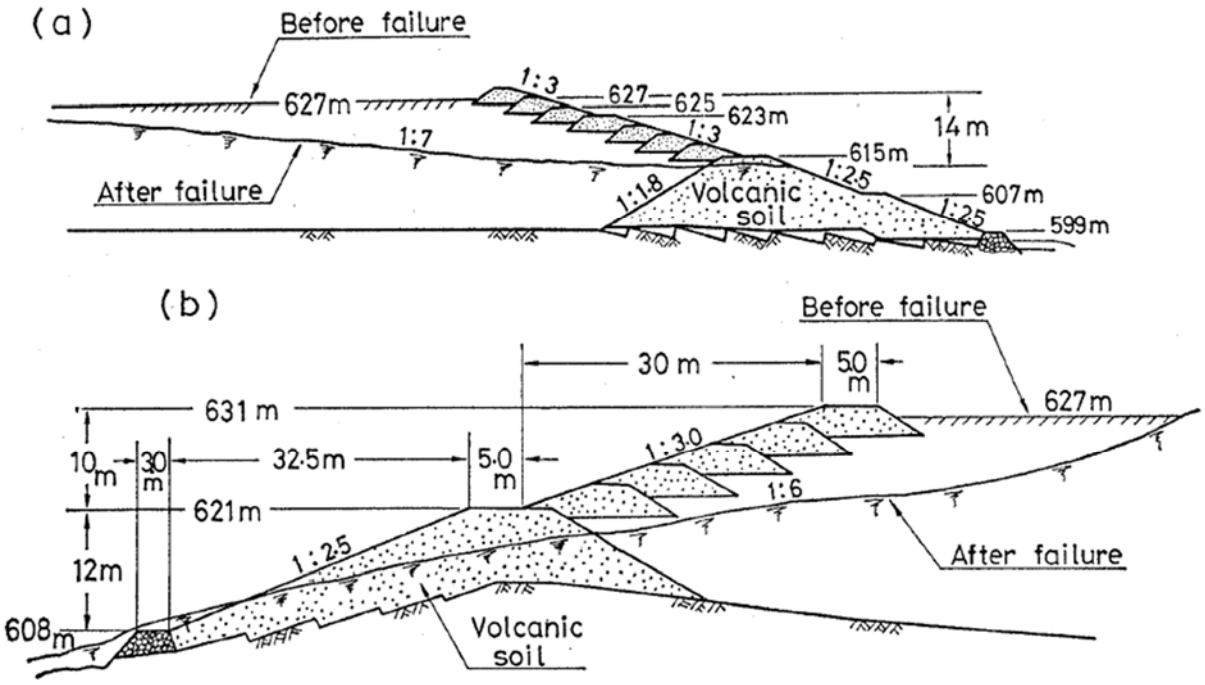

Figure B.11.2: Pre-failure and post-failure cross-sections of (a) Dike 1 and (b) Dike 2 at Mochi-Koshi. (figure from Ishihara et al., 1990)

post-failure slope of tailings at Dike No.2 was a bit steeper, averaging approximately 9° to 10°, and it varied somewhat from the toe to the back heel. The top of the initial retaining dam comprised of volcanic soil was lowered, but this may have been due to erosion by the tailings flowing out through the breach.

B.11.3 Geology and Site Conditions

As described in Section B.11.2, the tailings impoundment was constructed in a bowl-shaped mountain top. The weathered surface material was stripped to the underlying competent tuff formation. The three dams were constructed of local volcanic soils. Placement of the dam materials was first done using bulldozers for the starter dikes, with the subsequent raising of the dikes accomplished using the upstream method of placement (Ishihara, 1984).

Following the failures of the two dams, explorations were performed at the site to assist in the characterization of the material at the site. Based on Figure B.11.1, eleven borings appear to have been performed at the site, however only six boring logs were presented in Ishihara (1984). Those six boring logs will be discussed further in Section B.11.8, and they are reproduced here as Figures B.11.6 though B.11.8. A portable double tube cone penetrometer was also utilized to characterize the site.

These borings, as summarized by Ishihara, indicated that the tailings were comprised of fines silty sands and sandy silts. The silty sands were largely non-plastic, while the siltier materials had reported plasticity indices on the order of PI = 10%.. Penetration resistances in the tailings

corresponded to N-values on the order of zero to 7 blows/ft. The uppermost tailings were very loose, having a penetration resistance of nearly zero blows/ft. Ishihara (1984) suggested that some of the very low N-values were the result of liquefaction and disturbance. Penetration resistances were a bit higher in the deeper, consolidated tailings.

The containment dikes, placed using the upstream method, and assumed to have been tracked by bulldozers, had a penetration resistance of about 5 blows/ft. The bulldozer-placed starter dams were found to have a similar penetration resistance as the containment dikes (Ishihara, 1984).

The tailings were comprised of fine layers of sandy stilt and silty sand. The plasticity index, as reported in Ishihara (1984), for the silty sand was found to be approximately 10 and the sandy silt was found to be non-plastic. The sandy silt to silty sand tailings material was estimated by Ishihara et al. (1990) as having approximately 50% average fines content, though this varied considerably in sub-layers as depositional conditions varied.

The locations of the borings are shown in Figures 11.1. The logs of the six borings presented by Ishihara (1984) are reproduced in Figures B.11.6 through B.11.8.

.

B.11.4 Initial Yield Stress Analyses

Figures B.11.3(a) and Figure B.11.4(a) show the cross-sections of Dike 1 and Dike 2, respectively, used for back-analyses of the post-liquefaction initial yield strength $S_{r,yield}$ that would be required within the liquefied upstream shell materials to produce a calculated static Factor of Safety equal to 1.0. This is not the actual post-liquefaction strength, but it proves to be useful in developing estimates of post-liquefaction strength (S_r) for this case history.

Unit weights of the saturated tailings were modeled with a unit weight of $\gamma_s \approx 110$ lbs/ft^3, and this was then varied over a range of 105 to 115 lbs/ft^3 for parameter sensitivity studies. Unit weights of the non-saturated dike material above the phreatic surface were modeled with a unit weight of $\gamma_m \approx 118$ lbs/ft^3, and this was then varied over a range of 113 to 123 lbs/ft^3 for parameter sensitivity studies. Unit weights of the saturated tailings below the phreatic surface were modeled with a unit weight of $\gamma_s \approx 125$ lbs/ft^3, and this was then varied over a range of 120 to 130 lbs/ft^3 for parameter sensitivity studies. The friction angle of the dike material was modeled with $Ø' \approx 35°$, and a range of $Ø' \approx 33°$ to 37°.

The release of tailings from Dike 1 is described by Ishihara (1984) to have occurred very quickly. The failure at Dike 2 is described by Ishihara to have had an initial release with a subsequent breach widening and sloughing some time later. With the very loose nature of the tailings, once the containment dikes failed a retrogressive failure could progress very quickly. It is not known with certainty whether these were incrementally retrogressive failures, or a more monolithic failures in which most or all of the failure masses initiated their movements all at once. Therefore, both mechanisms were considered in the initial yield analyses.

Figure B.11.4(a) shows a select subset of the potential failure surfaces analyzed for back-analyses of $S_{r,yield}$ for Dike 1. Based on all of the analyses performed, the most likely failure

mechanism was judged to be an initial failure surface similar to the smaller circular failure surface shown in Figure B.11.4(a), as the first stage of an incrementally retrogressive overall failure sequence. The calculated best estimate for this surface is $S_{r,yield}$ = 617 lbs/ft^2. Based on parameter variations (parameter sensitivity studies), and moderate variations of failure surface geometries, the likely range is estimated as $S_{r,yield}$ = 489 to 742 lbs/ft^2 for this type of initial failure surface. The other mechanism for Dike 1 considered was a failure surface similar to the final failure surface shown in Figure B.11.4(a). For this monolithically initiated failure, the calculated best estimate for this surface is $S_{r,yield}$ = 158 lbs/ft^2, with a range of $S_{r,yield}$ = 131 to 189 lbs/ft^2 for this type of initial failure surface considering parameter and failure surface sensitivities described above.

Figure B.11.5(a) shows a select subset of the potential failure surfaces analyzed for back-analyses of $S_{r,yield}$ for Dike 2. Based on all of the analyses performed, the most likely failure mechanism was judged to be an initial failure surface similar to the smaller circular failure surface shown in Figure B.11.5(a), as the first stage of an incrementally retrogressive overall failure sequence. The calculated best estimate for this surface is $S_{r,yield}$ = 438 lbs/ft^2, with a range of $S_{r,yield}$ = 353 to 528 lbs/ft^2 for this type of initial failure surface, considering parameter and failure surface

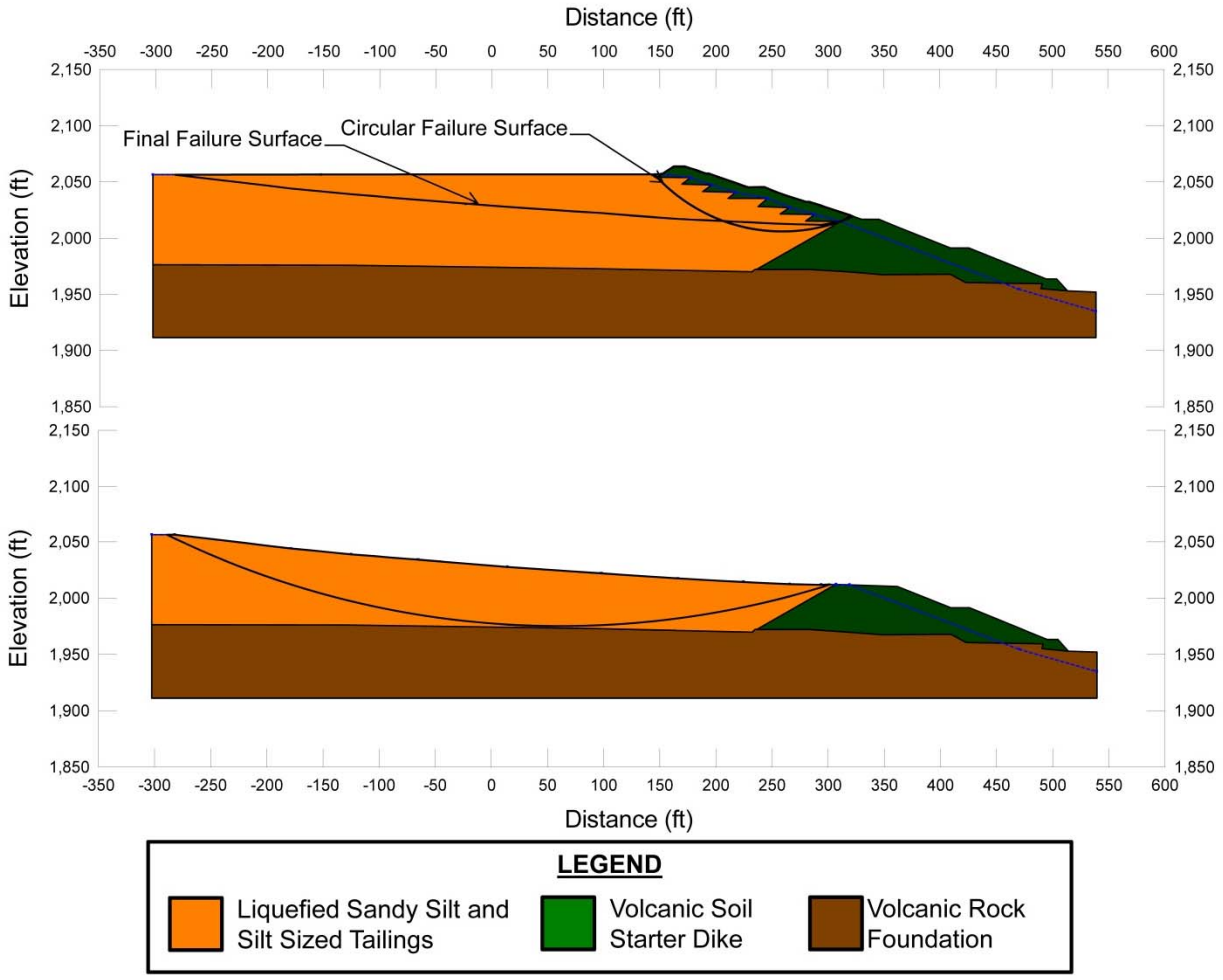

Figure B.11.4: Selected potential failure surfaces analyzed for evaluation of (a) $S_{r,yield}$ and (b) $S_{r,resid/geom}$ for the Mochi-Koshi Tailings Dam 1

variations as described above. The other mechanism for Dike 2 considered was a failure surface similar to the final failure surface shown in Figure B.11.5(a). For this monolithically initiated failure, the calculated best estimate for this surface is $S_{r,yield}$ = 219 lbs/ft^2, with a range of $S_{r,yield}$ = 172 to 269 lbs/ft^2 for this type of initial failure surface considering parameter and failure surface sensitivities described above. .

Overall assessment of $S_{r,yield}$ for this case was based on weighted averages of the two sets of values of $S_{r,yield}$ back-calculated for these two types of potential failure surfaces. The smaller initial failure surfaces near the dam faces were considered the most likely mechanisms for both dams, and were assigned a weighting factor of 4. The failure surfaces representing an overall monolithically initiated failure along the observed post-failure ground surface was assigned a weighting factor of 1. Based on these estimates and associated weighting factors, and the back-calculated values from above, the best estimate for Dike No. 1 was $S_{r,yield}$ = 548 lbs/ft^2, with a range of $S_{r,yield}$ = 443 to 659 lbs/ft^2. Similarly, the best estimate for Dike No. 2 was $S_{r,yield}$ = 394 lbs/ft^2, with a range of $S_{r,yield}$ = 317 to 476 lbs/ft^2.

The best estimates for both Dike 1 and Dike 2 were then averaged to determine an overall best estimate for this case history. The resulting overall best estimate was $S_{r,yield} \approx$ 477 lbs/ft^2, with a range of $S_{r,yield} \approx$ 385 to 574 lbs/ft^2.

Olson (2001) also performed back-analyses to estimate $S_{r,yield}$. He also assumed that the failures were retrogressive. His assumed initial failure surfaces were rotational failures similar to the "circular" failures shown in Figures B.11.4(a) and B.11.5(a). These rotational failure surfaces did extend below the final post-failure surface of the tailings. A range of potential initial rotational failure surfaces were analyzed. Olson's back-calculated best estimate for Dike 1 was $S_{r,yield} \approx$ 21.1 kPa (441 lbs/ft^2), with a range of 18.0 to 23.9 kPa (376 to 499 lbs/ft^2). His back-calculated best estimate for Dike 2 was $S_{r,yield} \approx$ 16.0 kPa (334 lbs/ft^2), with a range of 10.5 to 18.7 kPa (219 to 390 lbs/ft^2). Olson did not combine these; instead he elected to treat these as two separate case histories.

B.11.5 Residual Strength Analyses Based on Residual Geometry

It was not possible to perform rigorous and reliable back-analyses to determine the value of $S_{r,resid/geom}$ required to produce a calculated Factor of Safety equal to 1.0 based on residual geometry. This case is one of six cases (out of the 29 cases back-analyzed as part of these current studies) where the slide mass "went over a lip" and then traveled down a steeper slope, and the ensuing displacements either (1) could not be reliably tracked, or (2) could not be fully reliably back-analyzed. Both situations apply in this current case because the post-failure geometry of the failure mass runout is not well characterized.

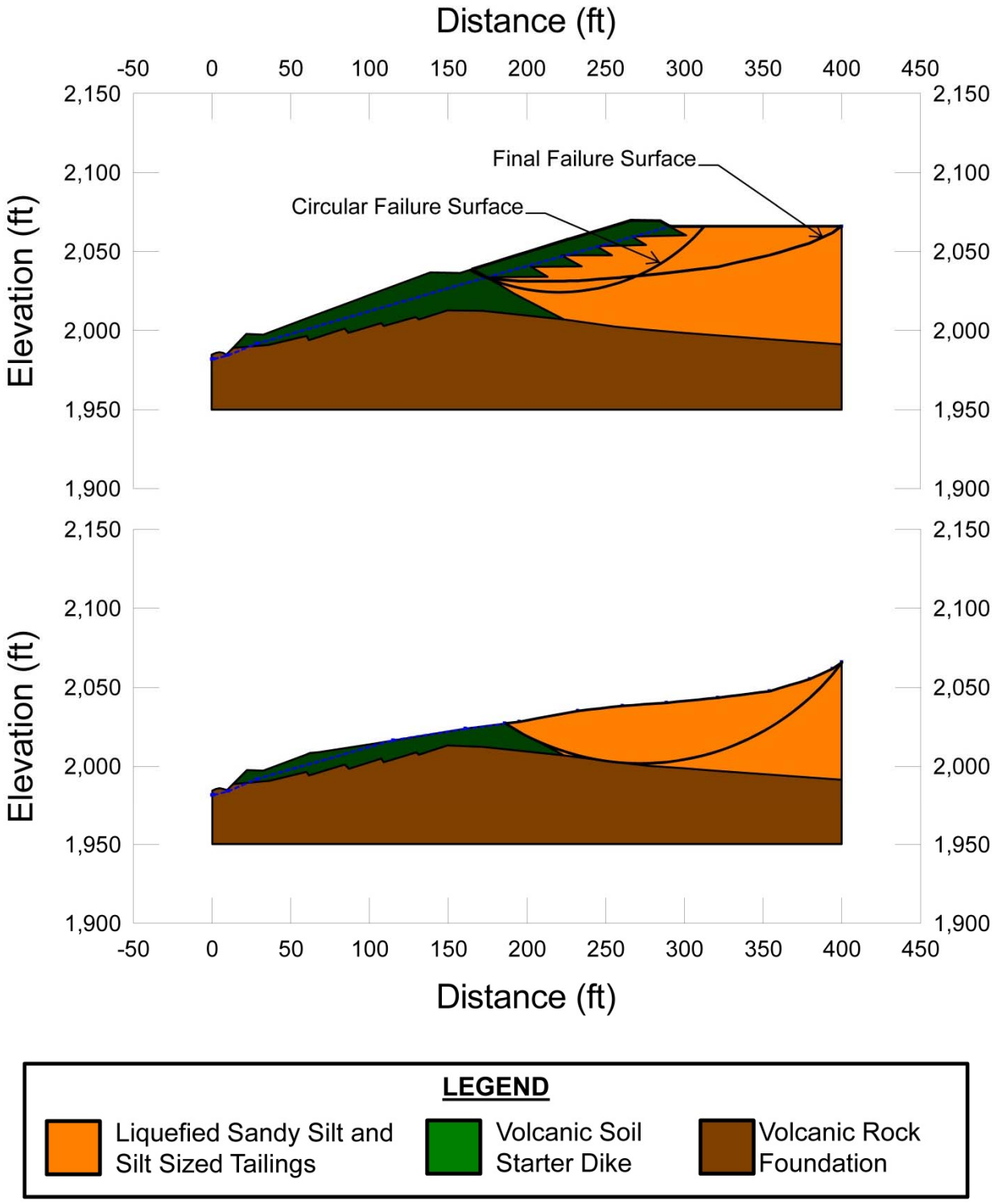

Figure B.11.5: Selected potential failure surfaces analyzed for evaluation of (a) $S_{r,yield}$ and (b) $S_{r,resid/geom}$ for the Mochi-Koshi Tailings Dam 2

Olson (2001) performed infinite slope analyses based on reported thicknesses of residual material that came to rest downslope. For Dike 1, Olson estimated a thickness of about 1.5 m (5 ft.) coming to rest at a slope of about 8 deg. Based on those parameters, Olson estimated a value of $S_{r,resid/geom} \approx 3.6$ kPa (75 lbs/ft^2). His estimated range was $S_{r,resid/geom} \approx 2.4$ kPa (50 lbs/ft^2), which was based on a thickness of 1.0 m (3.3 ft.), to $S_{r,resid/geom} \approx 7.2$ kPa (150 lbs/ft^2), based on a thickness of 1.9 m (6.2 ft.). For Dike 2, performing a similar set of analyses, Olson estimated a thickness of about 1.8 m (5.9 ft.) coming to arrest at a slope of about 10 deg. Based on those parameters, Olson estimated a $S_{r,resid/geom} \approx 5.8$ kPa (121 lbs/ft^2). His estimated range was $S_{r,resid/geom} \approx 4.8$ kPa (100 lbs/ft^2), which was based on a thickness of 1.6 m (5.2 ft.), to $S_{r,resid/geom} \approx 6.0$ kPa (125 lbs/ft^2), based on a thickness of 2.0 m (6.6 ft.).

Ishihara et al. (1990) performed similar infinite slope analyses, but instead considered a nominal thickness of about 6 m (20 ft) and residual slope of the tailings material remaining in the tailings impoundment. From these analyses, Ishihara et al. estimated a $S_{r,resid/geom} \approx 1.5$ t/m^2 (206 lbs/ft^2) for Dike 1 and $S_{r,resid/geom} \approx 1.75$ t/m^2 (357 lbs/ft^2) for Dike 2.

In these current studies, it was assumed that $S_{r,resid/geom}$ would have at least been higher than zero, and likely higher than this simplified estimate of Olson based on approximate geometry and an infinite slope analysis. Considering how uniform and low the penetration resistance was in the tailings material that remained in the impoundment following the failures, it was judged to be unlikely that the material that remained did not also liquefy. Analyses were also performed of the residual slopes left in place after the failure, as shown in Figure B.11.4(b) and Figure B.11.5(b). If the deeper tailings did liquefy, then for the rotational failure surface for Dike 1 illustrated in Figure B.11.4(b), the back-calculated value would be $S_{r,resid/geom} \approx 270$ lbs/ft^2, with a range of $S_{r,resid/geom} = 209$ to 334 lbs/ft^2., considering similar parameter and failure surface sensitivities as described in Section B.11.4. Performing similar analyses for Dike 2 resulted in a best estimated back-calculated value would be $S_{r,resid/geom} \approx 280$ lbs/ft^2, with a range of $S_{r,resid/geom} = 217$ to 344 lbs/ft^2.

In addition to the previously described analyses, comparisons were also made to similar Class A and B case histories where values of $S_{r,resid/geom}$ back-calculated from the reasonably well-documented. Considering the range of effective overburden stress and $N_{1,60,CS}$ values for this current case, an approximate range of $S_{r,resid/geom} \approx 90$ to 200 lbs/ft^2 was conservatively assumed, based on analyses of other Class A and B case histories.

Overall, considering the estimates (1) made based on infinite slope analyses of assumed downstream (runout) geometry by Olson (2001), (2) similar infinite slope analyses made by Olson using the assumed representative post-failure tailings runout thickness of 6 m as proposed by Ishihara et al. (1990), (3) the rotational failure surface shown in Figure B.8.4(b), (4) approximate infinite slope analyses of the post-failure slope remaining within the tailings impoundment after the event, and (5) values of $S_{r,resid/geom}$ back-calculated for better-defined post failure conditions from the Class A case histories, it was concluded that a best estimate value would be taken as $S_{r,resid/geom} \approx 225$ lbs/ft^2, with a range of $S_{r,resid/geom} \approx 150$ to 300 lbs/ft^2.

B.11.6 Overall Evaluation of S_r

Overall estimates of post-liquefaction strength S_r were made by two approaches. The first approach was to employ Equation 4-4, and Figure 4.11 as

$$S_r \approx \xi \bullet (S_{r,yield} + S_{r,resid/geom}) / 2$$

where ξ is a function of runout distance and overall failure mechanism characteristics.

Unfortunately, runout characteristics cannot be reliably characterized for this case history, because it is one of the six case histories back-analyzed in which the failure mass "went over a lip" and then down a steeper slope rather than coming to rest on a gentler basal slope as with most of the cases plotted in Figure 4.11. It is clear that runout distance is not small, but runout distance (and runout ratio) cannot be fully reliably quantified. The current engineering team therefore developed a consensus estimate that an appropriate range of values of ξ for this case would be on the order of $\xi \approx 0.45$ to 0.60. Using these values, and the values of $S_{r,yield}$ and $S_{r,resid/geom}$ presented previously in Sections B.11.4 and B.11.5, and the associated ranges of both $S_{r,yield}$ and $S_{r,resid/geom}$, this produced a best estimate of $S_r \approx 180$ lbs/ft^2, with a range of $S_r = 117$ to 256 lbs/ft^2.

The second approach was to employ the relationship presented in Figure 4.9, wherein pre-failure Factor of Safety can be approximately evaluated as a function of runout characteristics. Here again the difficulty was that the post-failure runout characteristics were not fully quantifiable because the failure mass went over a lip and then down a steeper slope. The engineering team developed a consensus estimate that the pre-failure range of Factor of Safety for this case would likely have been on the order of FS = 0.35 to 0.55. Multiplying these values by the values of $S_{r,yield}$ from Section B.8.4 produces a best estimate of $S_r \approx 207$ lbs/ft^2, with a range of $S_r = 130$ to 305 lbs/ft^2.

Averaging the two sets of values developed by these two approaches then produced a best estimate of $S_r \approx 194$ lbs/ft^2, with a range of $S_r = 117$ to 305 lbs/ft^2. The variance was slightly non-symmetric about the best estimate, so this was slightly further adjusted to produce a characterization that could be modeled with a Normal distribution. The range was estimated to represent approximately +/- 2.5 standard deviations.

Overall, based on an assumed normal distribution, it was judged that the (mean and median) best estimate of post-liquefaction strength for this case history is

$$\overline{S_r} = 211 \text{ lbs/ft}^2$$

and that the best estimate of standard deviation of mean overall post-liquefaction strength is

$$\sigma_{\overline{S}} = 38 \text{ lbs/ft}^2$$

Olson (2001) and Olson and Stark (2002) did not apply their "kinetics" method to this case, and so they did not independently develop an estimate of S_r that incorporated momentum effects. Instead, they took their value of $S_{r,resid/geom}$ as representing S_r. Their best estimate value for Dike 1 was $S_r = S_{r,resid/geom} = 75$ lbs/ft^2, with a range of 50 to 150 lbs/ft^2, as described previously in

Section B.11.5. For Dike 2 their best estimate was $S_{r,resid/geom}$ = 121 lbs/ft^2, with a range of 100 to 125 lbs/ft^2, also described previously in Section B.11.5. Considering the values estimated by Olson for $S_{r,yield}$ for Dike 1 and Dike 2 ($S_{r,yield}$ = 441 and 334 lbs/ft^2, respectively),and the values of $S_{r,resid/geom}$ for Dike 1 and Dike 2 ($S_{r,resid/geom}$ = 441 and 334 lbs/ft^2, respectively), and using the procedure outlined in Chapter 4, Equation 4-4 of this study would result in more reasonable estimates for residual strength. Using an value of $\xi = 0.8$, which is roughly an average value for this overall data set, the best estimate value of S_r for Dike 1 would be S_r = 206 lbs/ft^2 and the best estimate value of S_r for Dike 2 would be S_r = 182 lbs/ft^2. The average of these two values would then be $S_r \approx$ 194 lbs/ft^2, in excellent agreement with these current studies.

Wang (2003) and Wang and Kramer (2008) did not employ their zero inertial force (ZIF) method to incorporate inertial effects in back-analyses of this failure. Instead they selected their value of S_r based on examination of values from back-analyses by several previous investigators. The resulting estimates for Dike 1 and Dike 2 were S_r = 159 lbs/ft^2 and S_r = 234 lbs/ft^2, respectively. Averaging these two values produces $S_r \approx$ 197 lbs/ft^2, again in excellent agreement with these current studies. The standard deviations of S_r were also estimated by Kramer and Wang. For Dike 1 the estimated value was σ_S = 47.7 lbs/ft^2, and for Dike 2 σ_S = 78.0 lbs/ft^2.

Despite these differing approaches taken to evaluation and/or selection of S_r, agreement between the values developed in these previous studies, and the values developed and employed in these current studies, is very good for this case history.

B.11.7 Evaluation of Initial Effective Vertical Stress

The representative vertical effective stress for the Mochi-Koshi Tailings Dam dike failures was determined by averaging the calculated vertical effective stress on the failure plane in the liquefied zone from the smaller circular and final failure surfaces shown in Figures B.11.4(a) and B.11.5(a), using the same weighting factors employed for the evaluation of $S_{r,yield}$. Parameter variations (unit weights) were then varied, and so to some extent were variations of the depths of the potential failure surfaces of each type.

The resulting best estimate of average pre-failure effective stress within the liquefied materials controlling the failure of Dike 1 was then $\sigma_{vo}' \approx$ 1,599 lbs/ft^2, with a reasonable range of $\sigma_{vo}' \approx$ 1,249 to 1,961 lbs/ft^2. Similarly, for Dike 2, the best estimate of average pre-failure effective stress was then estimated to be $\sigma_{vo}' \approx$ 1,443 lbs/ft^2, with a reasonable range of $\sigma_{vo}' \approx$ 1,155 to 1,763 lbs/ft^2. Averaging the results from both dams, the overall best estimate was estimated to be $\sigma_{vo}' \approx$ 1,521 lbs/ft^2, with a reasonable range of $\sigma_{vo}' \approx$ 1,202 to 1,862 lbs/ft^2. This non-symmetric range was judged by the engineering team to represent approximately ± 2 standard deviations. Overall, assuming a normal distribution, the best characterization of initial (pre-failure) average effective vertical stress was then taken to be represented by a mean value of

$$\overline{\sigma'_{vo}} \approx 1{,}532 \text{ lbs/ft}^2$$

with a standard deviation of

$\sigma_{\bar{\sigma}} \approx 165$ lbs/ft^2

An estimate of σ_{vo}' was also calculated by Olson and Stark (2001, 2002). They reported a weighted average mean value of $\sigma_{vo}' \approx 59.9$ kPa (1,251 lbs/ft^2) for Dike 1 and $\sigma_{vo}' \approx 52.2$ kPa (1,090 lbs/ft^2) for Dike 2. These values are slightly lower than the values estimated from these studies, likely due to a slight difference in failure surfaces and assumed unit weights. Average initial vertical effective stresses were not directly reported by Wang (2003) and Kramer (2008), but they were published more recently in the publication by Kramer and Wang (2015). As discussed in Section 2.3.8.1(b)-(iii), Wang (2003) did not perform any independent analyses to assess σ_{vo}' for his 22 "secondary" cases, and this is one of those cases. Instead, he compiled values of S_r from multiple previous investigators, and averaged these for a best estimate. He also compiled multiple values of S_r/σ_{vo}' from previous investigators, and averaged these for a best estimate. He then used these two best-estimate values of S_r and S_r/σ_{vo}' to infer a resulting representative value of σ_{vo}'. As described in Section 2.3.8.1(b)-(iii), the resulting averaged values of S_r and S_r/σ_{vo}' were incompatible with each other for a number of Wang's "secondary" case histories, and this process produced unreasonable, and in some cases physically infeasible, values of σ_{vo}' for a number of case histories. Wang's values of $\sigma_{vo}' = 1{,}746$ lbs/ft^2 (Dike 1) and $\sigma_{vo}' = 2884$ lbs/ft^2 (Dike 2) appear physically unlikely, based on the cross-sections, and so they are not considered a useful check here.

B.11.8 Evaluation of $N_{1,60,CS}$

Following the failure of the two dams, explorations were performed at the site to assist in the characterization of the material at the site. Based on Figure B.11.1, 11 borings appear to have been performed at the site, however only six boring logs were shown in Ishihara (1984). Those six boring logs are reproduced here as Figures B.11.6 though B.11.8. A portable double tube cone penetrometer was also utilized to characterize the site. The results from two tests in the tailings material, as reported by Ishihara et al. (1990), are reproduced here as Figure B.11.9. While these test do show low penetration resistances in the tailings material, since there were a reasonable number of borings with measured blowcounts, they were not heavily relied upon for this study.

The results from the standard penetration tests performed at the site were evaluated. No energy correction (ER = 60%) was applied, and the other necessary corrections for fines and effective overburden stress were applied. After applying corrections, the representative median penetration resistance was determined to be $N_{1,60} \approx 3.7$ blows/ft. Assuming an average fines content of about 50%, a clean sand correction was also applied. In these current studies, the characterization of penetration resistance is represented by a best estimate mean value of $\overline{N_{1,60,CS}} \approx 6$ blows/ft., and an estimated standard deviation of this mean of $\sigma_{\overline{N}} \approx 1.7$ blows/ft.

Olson employed no fines adjustment, and developed a best estimate of $N_{1,60} = 2.7$ blows/ft, with a range of 0.0 to 6 blows/ft.

Wang (2003) and Kramer (2008) jointly developed a representative values of $\overline{N_{1,60,CS}} = 8.9$ blows/ft for Dam 1 and $\overline{N_{1,60,CS}} = 10.0$ blows/ft for Dam 2. Their estimated standard deviations of

that overall mean values for Dam 1 and Dam 2 were $\sigma_{\overline{N}}$ = 0.6 blows/ft and 1.3 blows/ft., respectively. Full details of the development of this interpretation by Wang and Kramer are not presented. Kramer and Wang (2015) subsequently converted to non-fines-corrected representative values of mean estimates of $N_{1,60}$ = 4 blows/ft and 5.2 blows/ft for Dam No. 1 and Dam No. 2, respectively.

Overall agreement between these three independent assessments of representative $N_{1,60}$ and $N_{1,60,CS}$ values is judged to be very good, allowing for the differences between fines-corrected and non-fines corrected penetration resistance measures. The values developed in these current studies are in the mid-range of he values developed by these other investigation teams.

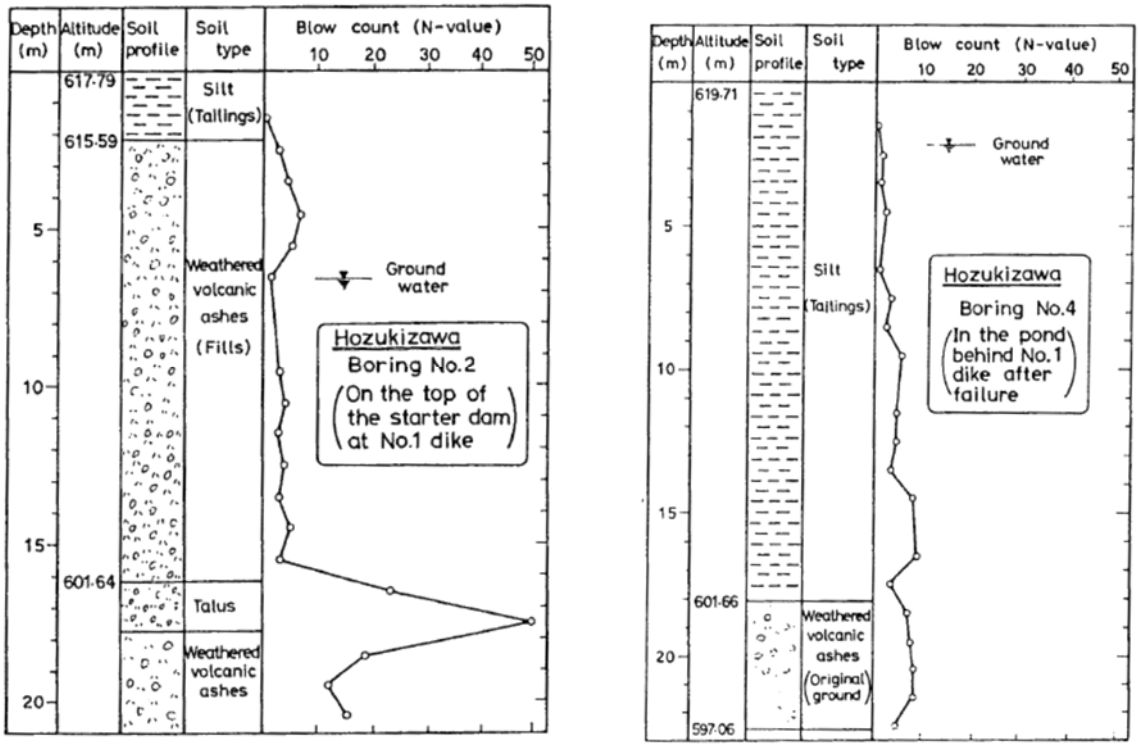

Figure B.11.6: Log of Borings No. 2 and 4 (reproduced from Ishihara, 1984)

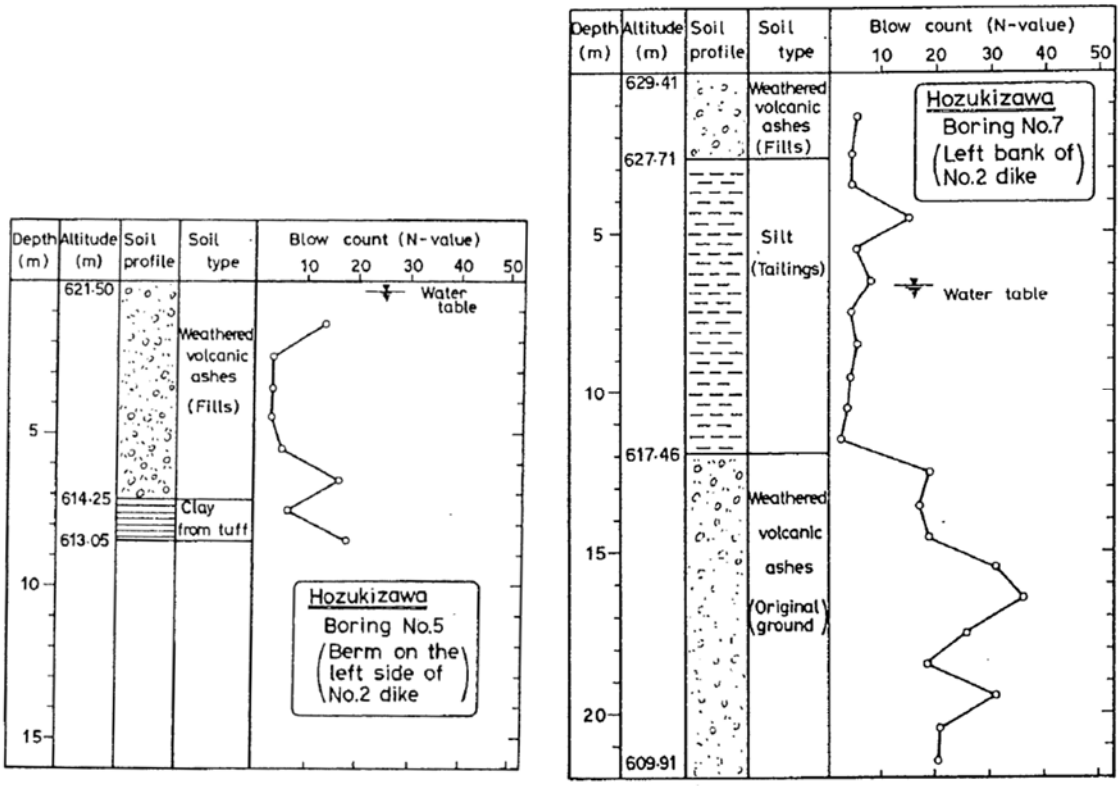

Figure B.11.7: Logs of Borings No. 5 and 7 (reproduced from Ishihara, 1984)

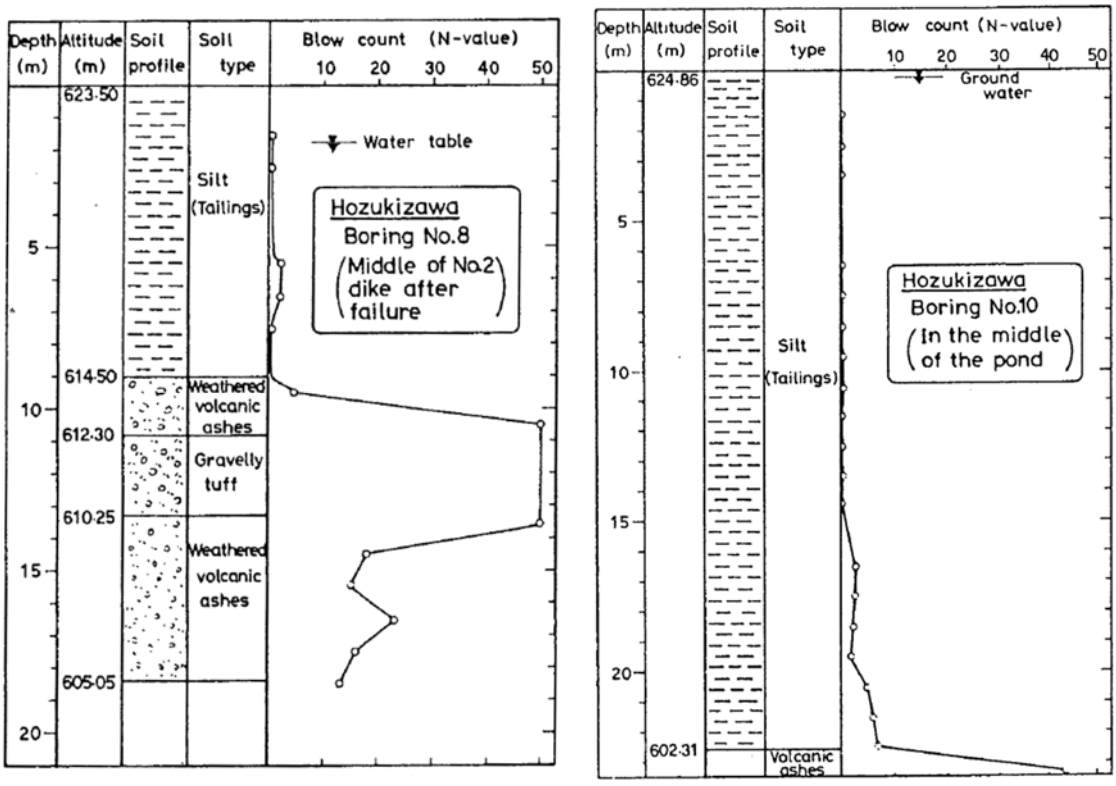

Figure B.11.8: Log of Borings No. 8 and 10 (reproduced from Ishihara, 1984)

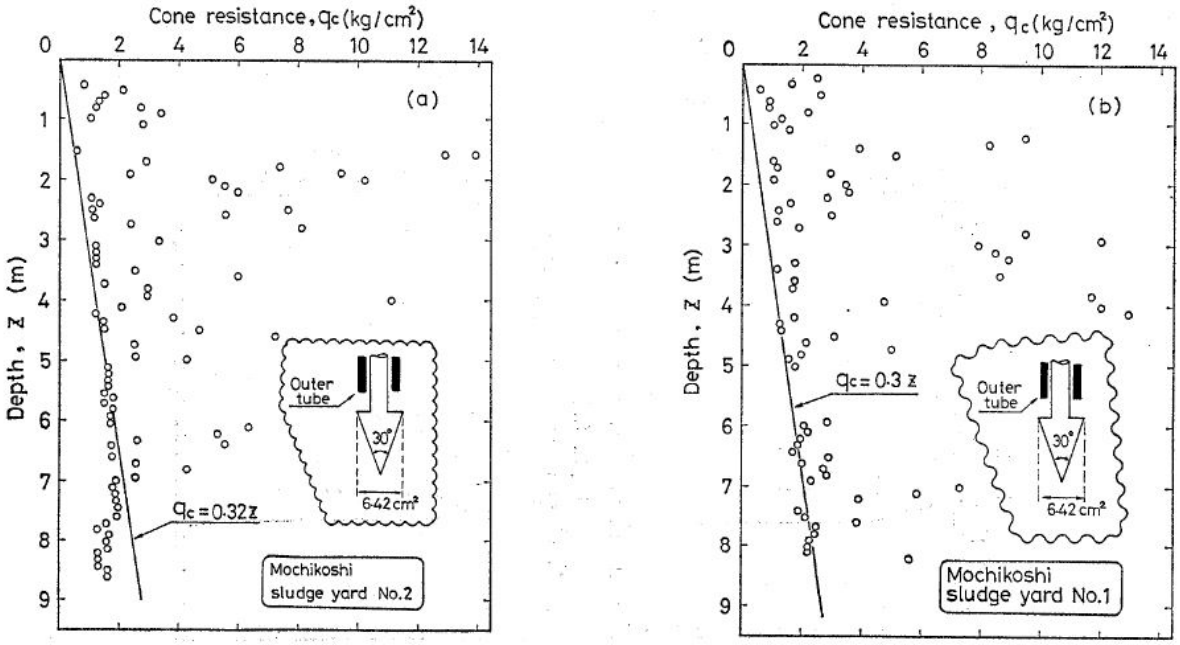

Fig. 4. Double-tube cone penetration test at Mochikoshi

Figure B.11.9: Results of two double-tube cone penetration test soundings performed after the failure (figure from Ishihara et al., 1990).

B.12 Nerlerk Embankment; Slides 1, 2 and 3 (Canada; 1983)

B.12.1 Brief Summary of Case History Characteristics

Name of Structure	Nerlerk Embankment; Slides 1, 2 and 3
Location of Structure	Beaufort Sea, Canada
Type of Structure	Hydraulic Fill Undersea Sand Berm
Dates of Failures	July 20, 25 and 28, 1983
Nature of Failure	Static, During Placement of Fill
Approx. Maximum Slope Height	Slide 1 = 67.5 ft, Slide 2 = 61.4 ft, Slide 3 = 67.8 ft

B.12.2 Introduction and Description of Failures

The Nerlerk undersea sand berm was an engineered, hydraulically placed sand mound created to provided a platform for hydrocarbon exploration in the Canadian Beaufort Sea. Figure B.12.1 shows the location of the berm, and the locations of seven additional berms.

Six undersea slope failures occurred during construction of the berm in 1982 and 1983. The first of these occurred in 1982, and was not reported in the open literature. The other five slope failures occurred between July 20 and August 4, 1983. Figure B.12.2 shows a plan view of the berm and the locations of these five failures. These five failures were well studied (e.g. Mitchell, 1984; Sladen et al., 1985 & 1987; Been at al., 1987; Sladen, 1989; Sladen and Hewitt, 1989; Rogers et al., 1990; and Konrad, 1991). All five failures were liquefaction-induced flow failures, and all five exhibited very large runout ratios.

A number of similar sand berm platforms had previously been constructed for the same purpose (e.g. Figure B.12.2), and the designers did not anticipate the problems that occurred at the Nerlerk platform.

Placement of sand commenced in 1982. Borrow materials were obtained from a site near Ukalerk, and were transported to the berm site and deposited by hopper dredges. Later in 1982, and into 1983, borrow materials were obtained from a site nearer to Nerlerk, and were deposited at the still undersea berm by point source discharge. This point discharge appeared to produce an even looser fill, and side slopes of the point discharged fill were typically on the order of 10:1, rather than the 5:1 slopes specified in the design. Construction was temporarily halted to make changes in the point discharge equipment.

Fill placement re-commenced in July of 1983. On July 20, 1983, bathymetric surveys indicated that a large slope failure had occurred on the north face of the still submerged berm, as shown in Figure B.12.2. Three additional slides then occurred in fairly rapid succession on July 25, July 28, August 4 and August 8, 1983. The locations of these additional slides are also shown in Figure B.12.2. Figure B.12.2 is taken from Sladen et al. (1985), and Rogers et al. (1990) disagreed with some of the locations and extents of the slides as depicted.

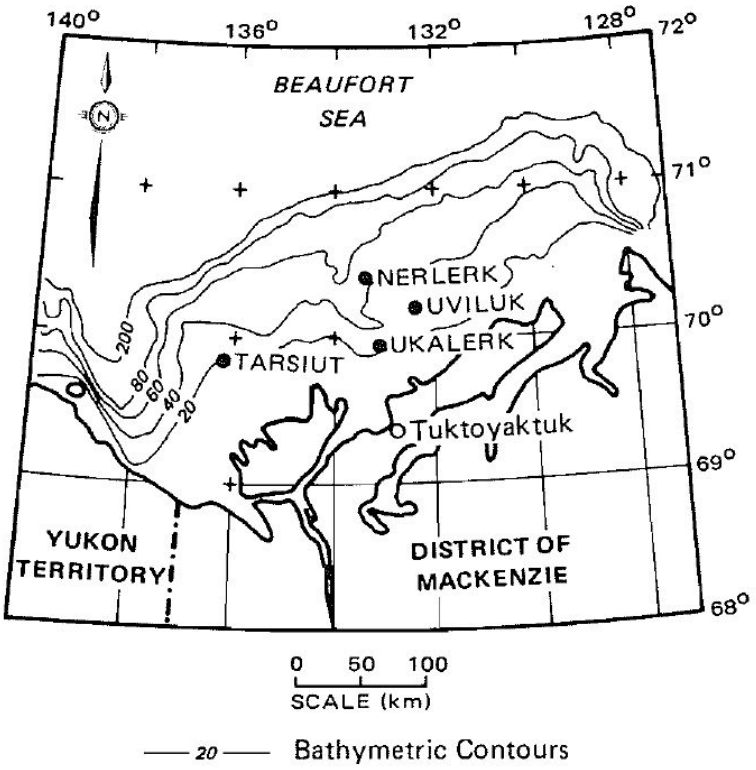

Figure B.12.1: Map of the of the region offshore of the Mackenzie and Yukon Districts of Canada, showing the locations of the Nerlerk Berm and three additional berm platforms, along with offshore bathymetric contours (Figure from Sladen et al., 1985).

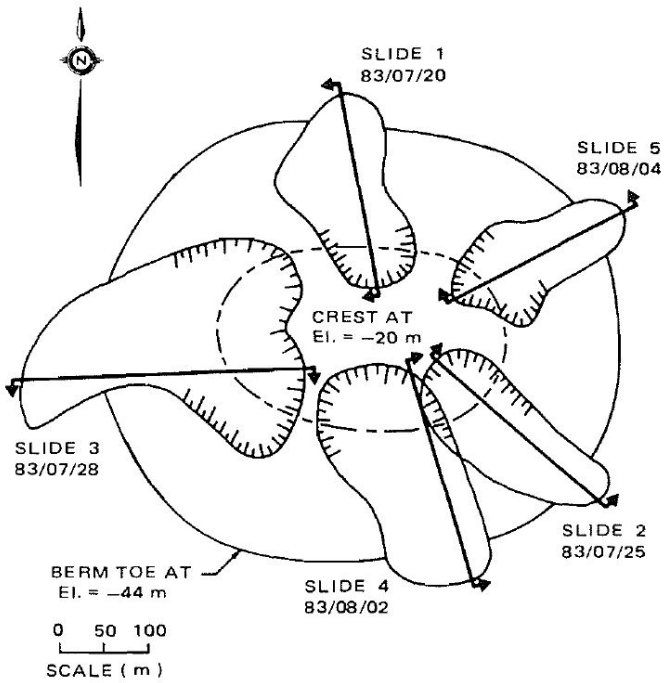

Figure B.12.2: Plan view of the Nerlerk Berm showing the five slope failures that occurred between July 20 and August 8, 1983 (Figure from Sladen et al., 1985).

Figure B.12.3 shows approximate pre-failure and post-failure cross-sections for the last five slope failures from Figure B.12.2. Slides 1, 2 and 3 were judged to have sufficiently well-defined pre-failure and post-failure geometries as to warrant back-analyses, and these are the three failures that were back-analyzed in these current studies. The cross-sections of Figure B.12.3 are based on bathymetric surveys, as all of the slides occurred underwater during fill placement. Figure B.12.4 shows the interpreted bathymetric morphology of Slide 4, illustrating the complicated and three-dimensional nature of these flow slides.

B.12.3 Geology and Site Conditions

Figure B.12.5 shows the approximate gradations of the Nerlerk and Ukalerk sands placed to construct the berm. Figure B.12.6 shows a cross-section through the partially completed berm at the end of the 1982 season, showing the face slopes and the distribution of the Nerlerk and Ukalerk sands at that time. The Nerlerk sands had a slightly higher silty fines content of on the order of 2% to 12%, while the Ukalerk Sands had a lower fines content of approximately 0 to 3% (Sladen et al., 1985).

It is generally assumed that the failures occurred primarily within the upper, very loose Nerlerk sand fill materials. Twenty six CPT tests were performed to assess the conditions of these two materials, and the results are presented and discussed in Section B.12.7.

The underyling foundation materials upon which the berm was placed consisted of approximately 1 to 2 meters of high plasticity clay, underlain by poorly graded sands with some traces of silt.

B.12.4 Initial Yield Stress Analyses

Figure B.12.7 shows the cross-section used for back-analyses of the post-liquefaction initial yield strength $S_{r,yield}$ that would be required within the foundation and embankment materials of the typical section of Slide 1 to produce a calculated Factor of Safety equal to 1.0. This is not the actual post-liquefaction strength, but it proves to be useful in developing estimates of post-liquefaction strength (S_r) for this case history.

There were two general sets of potential failure mechanisms that could potentially explain the observed features: (1) the failures may have been incrementally retrogressive, initiating with a small "slice" near to the front of the feature, and then retrogressing on a slice by slice basis back towards the eventual back heel, or (2) the entire slide may have initiated monolithically (all at once). Both sets of possibilities were analyzed, and multiple potential "initial" failure surfaces were analyzed for the incrementally retrogressive scenario. In all cases, failure was modeled as occurring within the Nerlerk sands with failure surface allowed to go only deep enough as to slide tangent to the Ukalerk sands.

Unit weights of the Nerlerk sands were modeled with a unit weight of $\gamma_s \approx 120$ lbs/ft^3, and this was then varied over a range of 115 to 125 lbs/ft^3 for parameter sensitivity studies.

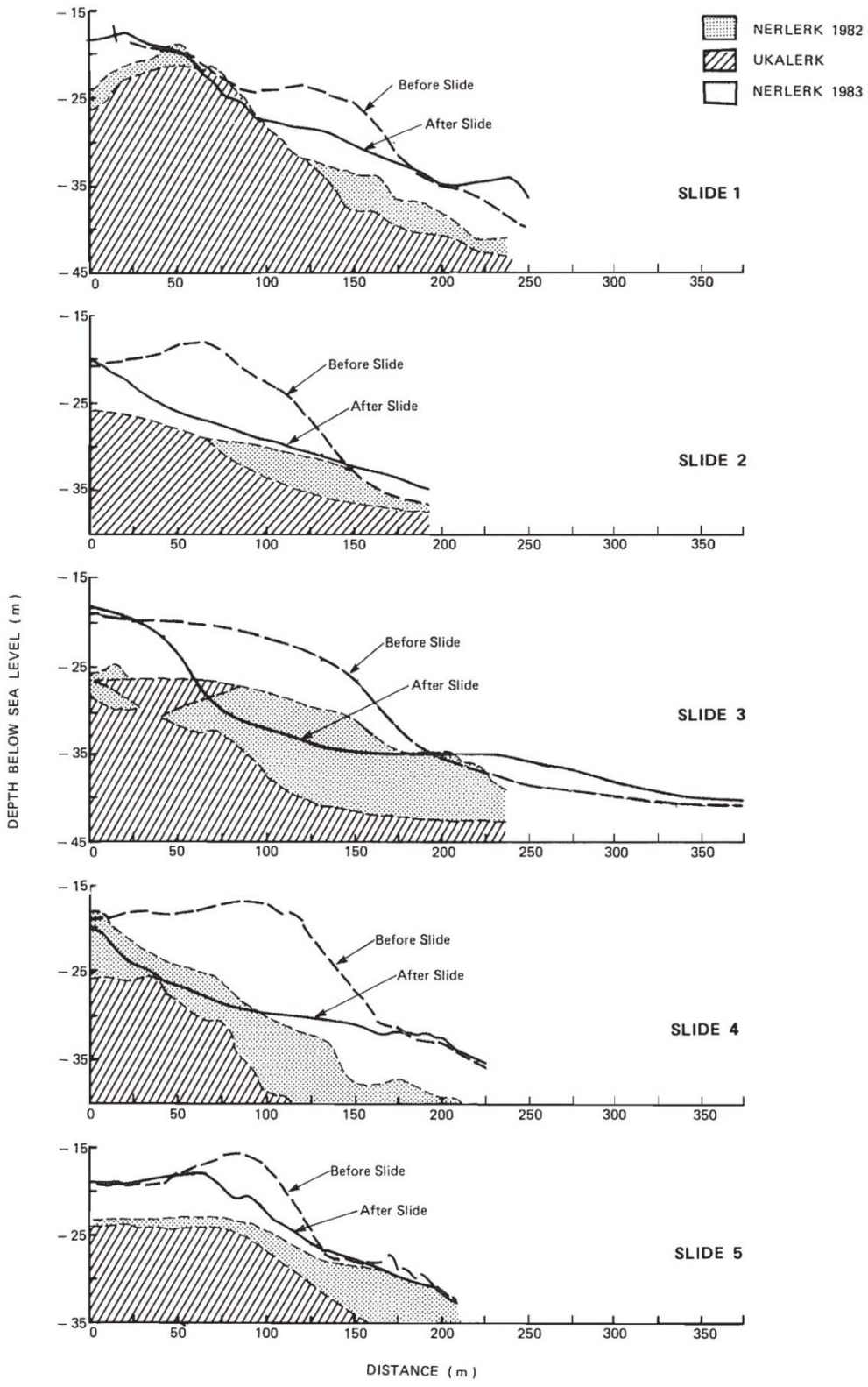

Figure B.12.3: Pre-failure and post-failure cross-sections of Slides 1 through 5 (from Sladen at al., 1985.

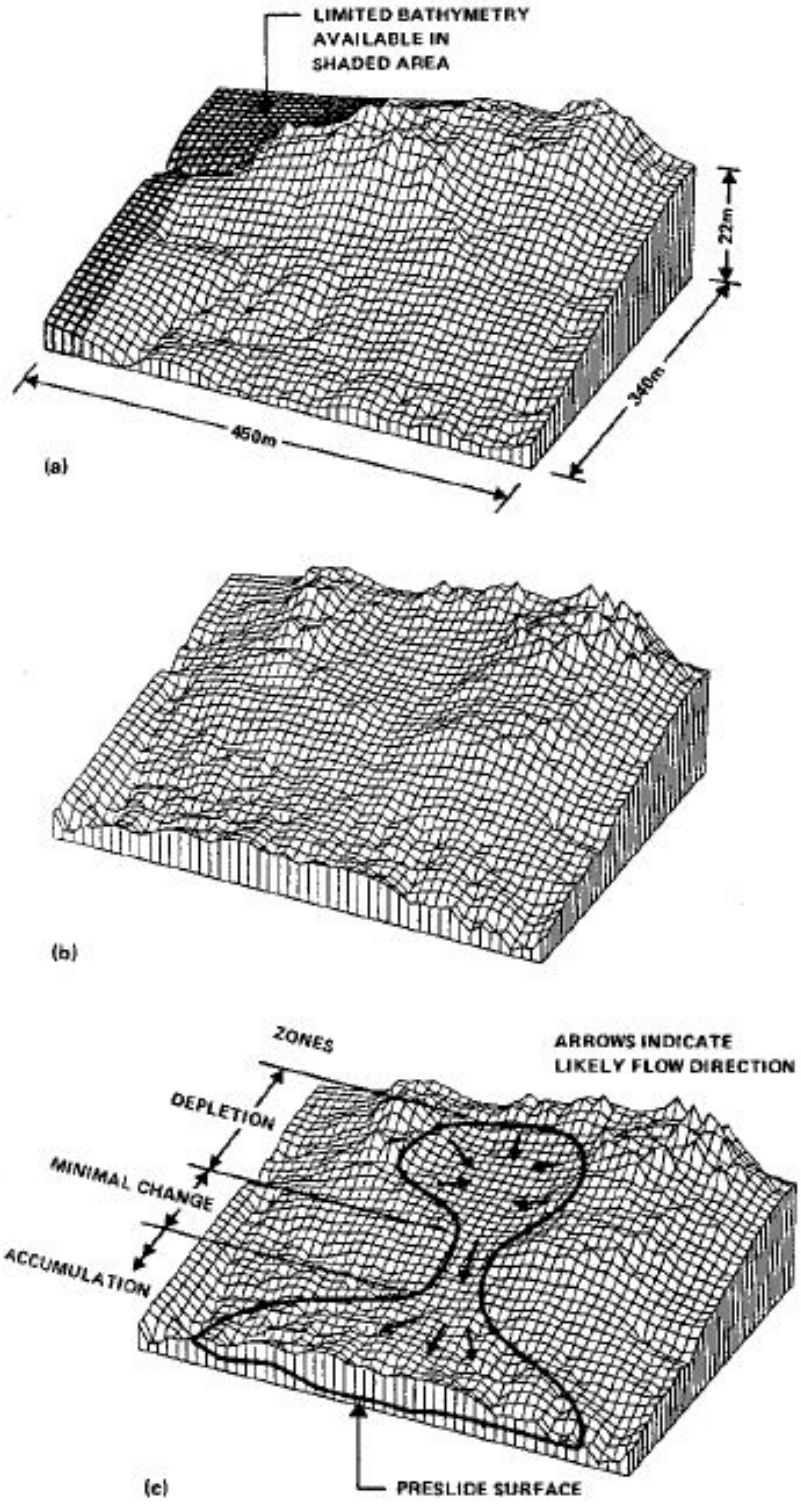

Figure B.12.4: Three-dimensional morphologies of Slide 4 based on detailed bathymetry; (a) pre -slide, (b) post-slide, and (c) interpretation of geomorphology based on (a) and (b). (Figure from Sladen et al., 1987).

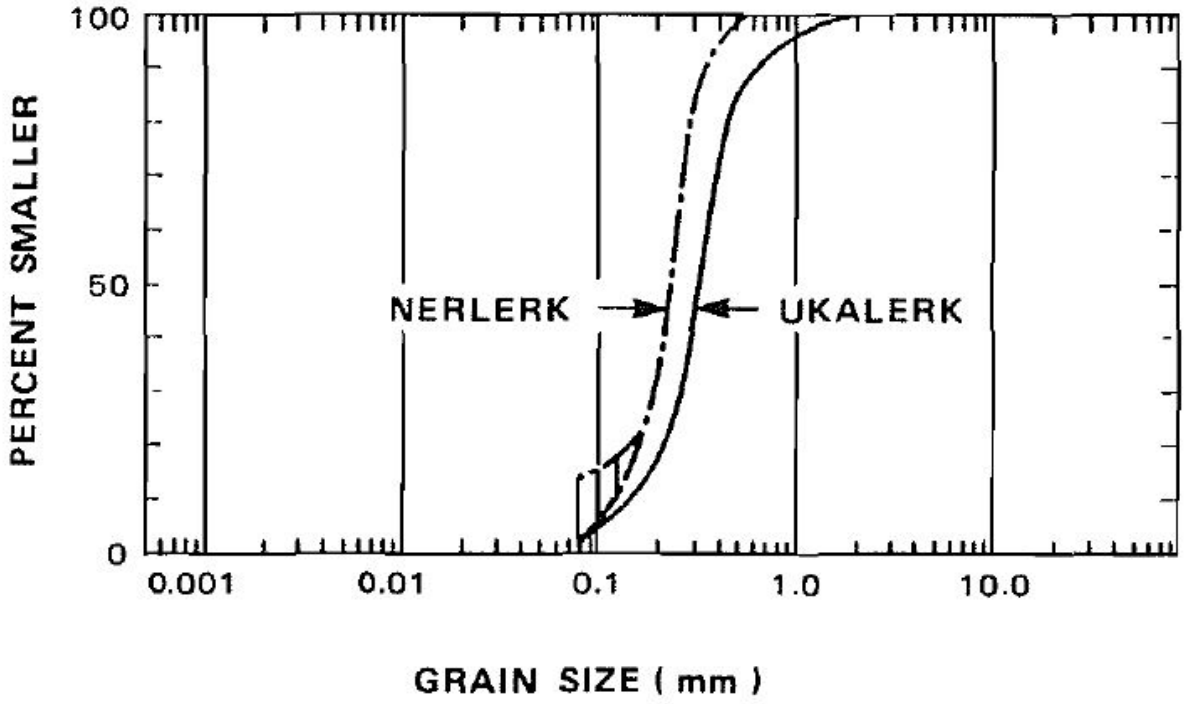

Figure B.12.5: Typical grain size distributions of the Ukalerk and Nerlerk sands (Sladen et al., 1985)

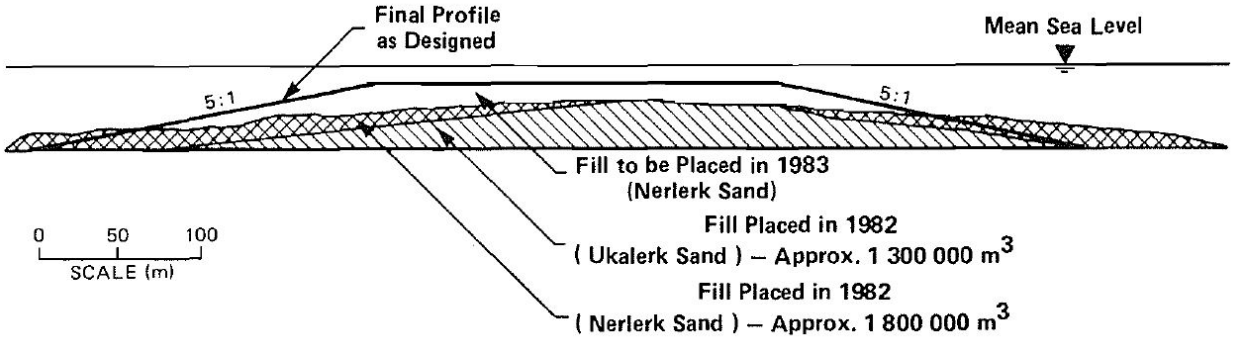

Figure B.12.6: Section through the Nerlerk berm showing distributions of materials types at the end of the 1982 construction season (Figure from Sladen et al., 1985)

Potential initial failure surfaces were modeled as either (1) wedge-like semi-translational features, or (2) semi-rotational/translational features, or (3) conforming essentially to the final observed overall failure scarp (the monolithically initiated scenario).

For the special case of the monolithically initiated scenario, involving initial failure on the eventual (final) observed overall failure scarp, the best estimate value of $S_{r,yield}$ was found to be $S_{r,yield} = 156$ lbs/ft^2, with a range of $S_{r,yield} \approx 115$ to 198 lbs/ft^2.

A significant number of smaller "initial" potential (first slice) failure surfaces were also analyzed, corresponding to a scenario in which the overall failure may have been retrogressive in nature. Figure B.12.7(a) shows a semi-rotational initial failure surface that was the most critical potential initiating failure surface found (lowest post-liquefaction Factor of Safety) but additional potential failure surfaces were also analyzed. The resulting best estimate value of $S_{r,yield}$ for smaller initial yield slices was found to be $S_{r,yield} = 67$ lbs/ft^2, with a likely range of $S_{r,yield} \approx 48$ to 88 lbs/ft^2.

In keeping with the tenets and protocols of these current studies, the values of $S_{r,yield}$ calculated for these potential "initial" slices were then averaged directly with the $S_{r,yield}$ values calculated for the monolithically initiated (eventual overall) failure surface as described above, and these averages values were taken as "representative" $S_{r,yield}$ values for incrementally retrogressive initiation scenarios. Both scenarios were taken as equally as likely and therefore the results were averaged with equal weighting. Based on the range of variations in properties and parameters, and a range of potential failure mechanisms and feasible failure surfaces, the resulting best estimate of "representative" overall $S_{r,yield}$ for Slide 1 was found to be $S_{r,yield} = 112$ lbs/ft^2, with a range of $S_{r,yield} \approx 82$ to 143 lbs/ft^2.

Additional were performed in a similar manner to determined $S_{r,yield}$ for Slide 2 and Slide 3. For Slide 2, example initial failure surfaces are shown on Figure B.12.8(a). The results from analyses assuming a monolithic mechanism produced a best estimate of $S_{r,yield} = 144$ lbs/ft^2, with a likely range of $S_{r,yield} \approx 105$ to 186 lbs/ft^2. A smaller "initial" failure surface assumption resulted in a best estimate of $S_{r,yield} = 201$ lbs/ft^2, with a likely range of $S_{r,yield} \approx 153$ to 253 lbs/ft^2. Equally weighting each mechanism, the resulting best estimate of "representative" overall $S_{r,yield}$ for Slide 2 was found to be $S_{r,yield} = 173$ lbs/ft^2, with a range of $S_{r,yield} \approx 129$ to 220 lbs/ft^2.

For Slide 3, example initial failure surfaces are shown on Figure B.12.9(a). The results from analyses assuming a monolithic mechanism produced a best estimate of $S_{r,yield} = 109$ lbs/ft^2, with a likely range of $S_{r,yield} \approx 86$ to 133 lbs/ft^2. A smaller "initial" failure surface assumption resulted in a best estimate of $S_{r,yield} = 236$ lbs/ft^2, with a likely range of $S_{r,yield} \approx 169$ to 295 lbs/ft^2. Equally weighting each mechanism, the resulting best estimate of "representative" overall $S_{r,yield}$ for Slide 2 was found to be $S_{r,yield} = 173$ lbs/ft^2, with a range of $S_{r,yield} \approx 128$ to 214 lbs/ft^2.

The results of all three slides were then averaged, as only a single set of indices will be used for the overall Nerlerk case history. This is because (1) the three slides are very similar, and so are the initial geometries and materials, and (2) it was desirable not to over-weight the contribution of this (three slide) case history to the eventual regressions that would subsequently be performed. Averaging the results of all three slides, it was judged that the overall best estimate of $S_{r,yield}$ for this case history is be $S_{r,yield} = 153$ lbs/ft^2, with a range of $S_{r,yield} \approx 113$ to 192 lbs/ft^2.

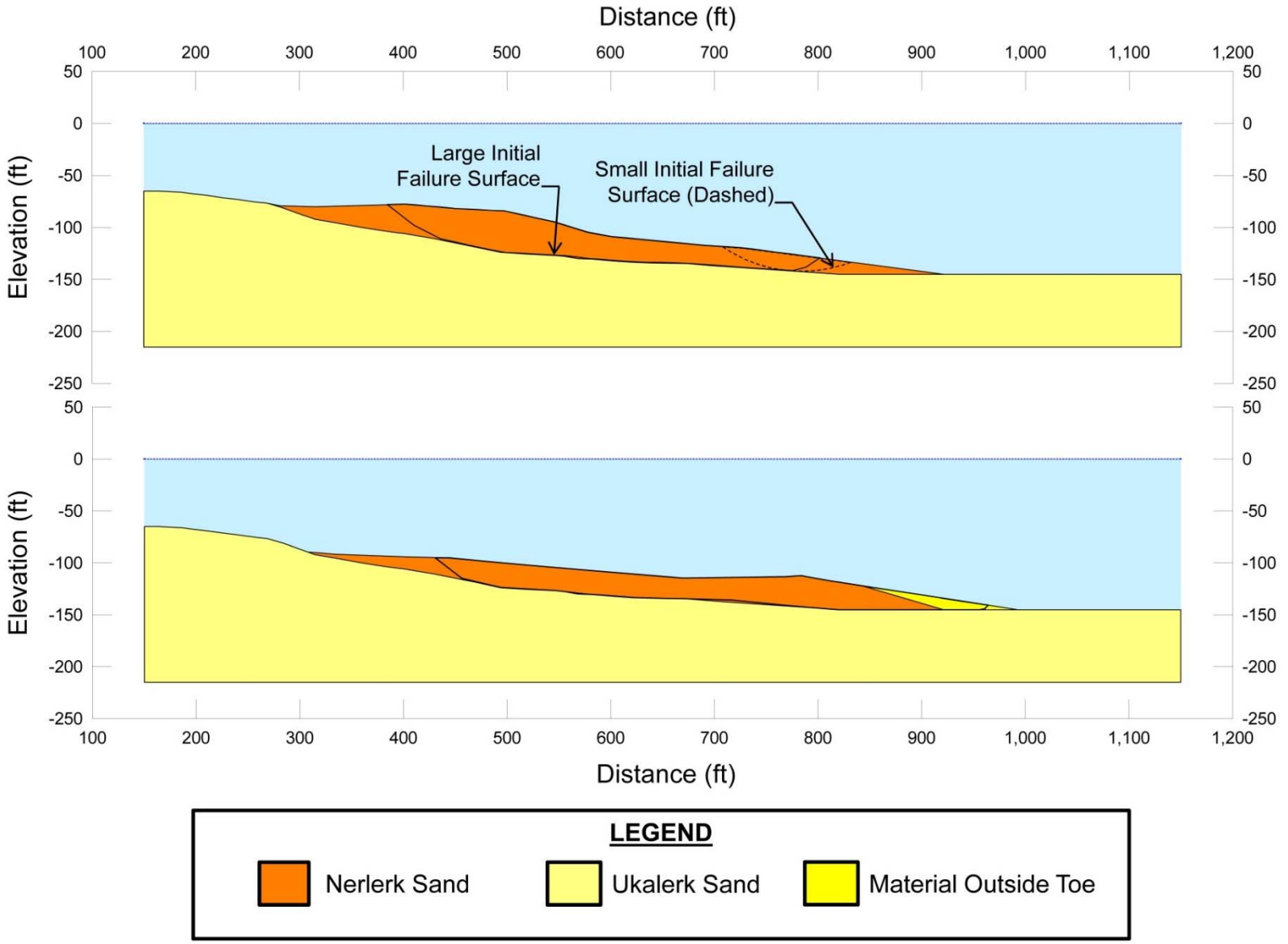

Figure B.12.7: Pre-failure and post-failure cross-sections used for back-analyses of Slide 1 of the Nerlerk Berm

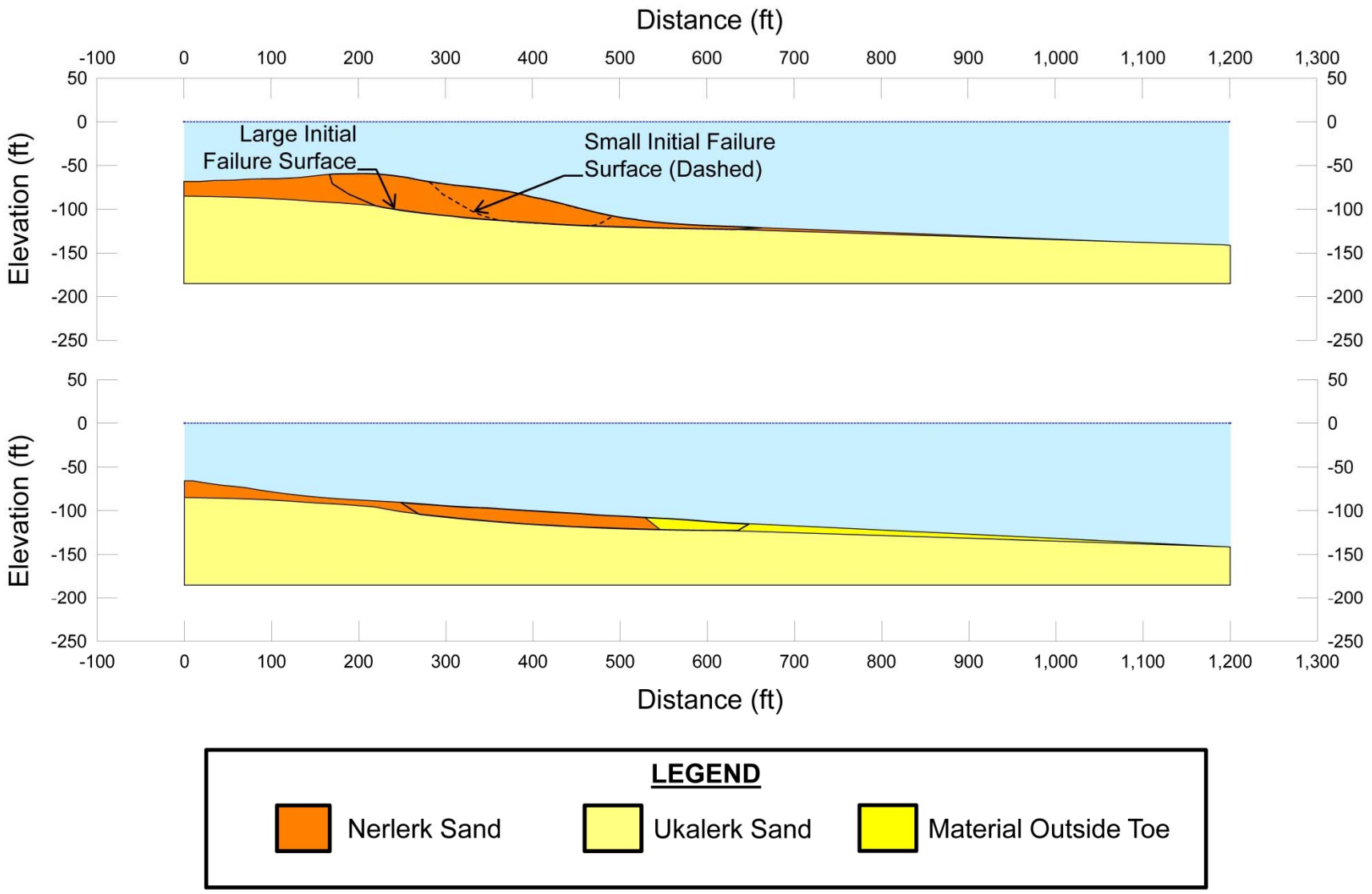

Figure B.12.8: Pre-failure and post-failure cross-sections used for back-analyses of Slide 2 of the Nerlerk Berm

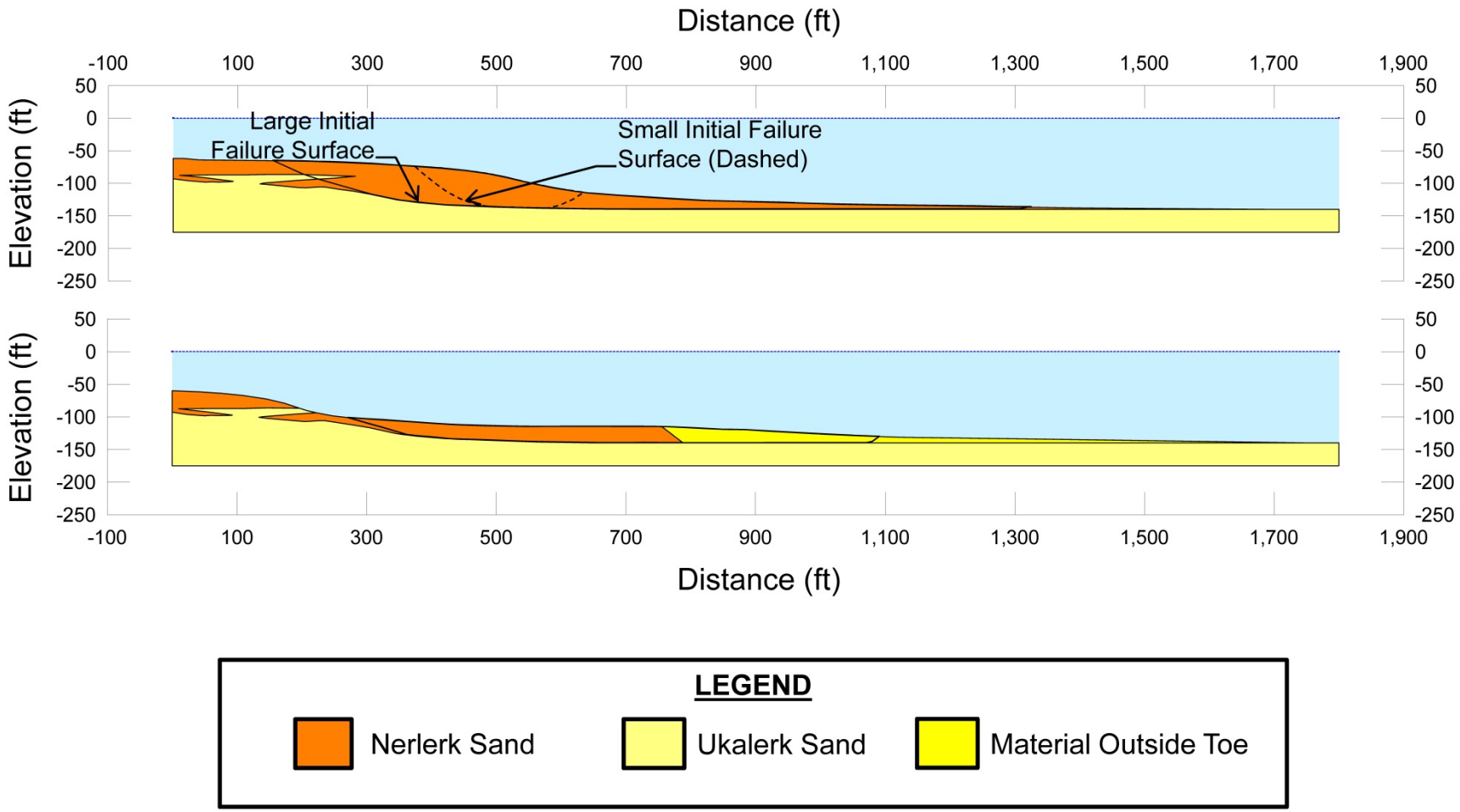

Figure B.12.9: Pre-failure and post-failure cross-sections used for back-analyses of Slide 3 of the Nerlerk Berm

Olson (2001) also performed back-analyses to evaluate $S_{r,yield}$ for each of the three Nerlerk slides considered in this study. He analyzed only wedge-type toe failures surfaces within the Nerlerk sand fill material. His resulting best estimate values of $S_{r,yield}$ for Slides 1, 2 and 3 are

Slide 1: $S_{r,yield}$ = 2.7 kPa (56 lbs/ft^2) with a range of 2.7 kPa (56 lbs/ft^2) to 4.0 kPa (84 lbs/ft^2)

Slide 2: $S_{r,yield}$ = 4.2 kPa (88 lbs/ft^2) with a range of 4.0 kPa (84 lbs/ft^2) to 4.8 kPa (100 lbs/ft^2)

Slide 3: $S_{r,yield}$ = 4.8 kPa (100 lbs/ft^2) with a range of 4.2 kPa (88 lbs/ft^2) to 5.7 kPa (84 lbs/ft^2)

Average = 3.9 kPa (81 lbs/ft^2)

These values are somewhat lower than the values calculated in these current studies because of the differences between the smaller toe wedges analyzed by Olson and the slightly larger rotational and rotational/translational toe failures analyzed in these current studies.

B.12.5 Residual Strength Analyses Based on Residual Geometry

The calculation of the "apparent" post-liquefaction strength ($S_{r,resid/geom}$) required to produce a calculated static Factor of Safety equal to 1.0 based on residual geometry for Slide 1 is illustrated in Figure B.12.7(b). This value of $S_{r,resid/geom}$ is not the post-liquefaction strength (S_r), as it neglects momentum effects and so underestimates Sr. It is, however, useful in evaluation of S_r.

Most modeling parameters and details are as described in the preceding section.

Occurring under the Beaufort Sea, these slides likely experienced some degree of the combined effects of (1) potential hydroplaning, and (2) potential sliding atop weaker seabed sediments as the toe of the slide mass traveled down slope outboard of the berm toe. These two effects were jointly modeled with an assumption that the best estimate of strength at the base of the portion of the slide mass sliding outside the original toe was equal to 50% of the post-liquefaction strength (S_r) of the liquefied Nerlerk sands. Parameter sensitivity studies were then performed, varying this over the range of 25% to 75% of S_r.

Based on the Slide 1 cross-sections shown in Figure B.12.7(b), and the properties and parameters described above, the best-estimate value of $S_{r,resid/geom}$ was $S_{r,resid/geom}$ = 86 lbs/ft^2. Parameters were next varied, as described previously, including analyses of alternate potential failure surfaces slightly above and below the failure surface shown in Figure B.12.7(b). Based on these analyses, it was judged that a reasonable range was $S_{r,resid/geom} \approx$ 66 to 108 lbs/ft^2.

Additional were performed in a similar manner to evaluate $S_{r,resid/geom}$ for Slides 2 and 3, using the cross-sections of Figures B.12.8(b) and B.12.9(b), respectively. For Slide 2, an example residual failure surface is shown on Figure B.12.8(b). The results from these analyses produced a best estimate of $S_{r,resid/geom} \approx$ 41 lbs/ft^2, with a likely range of $S_{r,resid/geom} \approx$ 26 to 58 lbs/ft^2.

For Slide 3, an example residual failure surface is shown on Figure B.12.9(b). The results from the analyses produced a best estimate of $S_{r,resid/geom}$ = 32 lbs/ft^2, with a likely range of $S_{r,resid/geom} \approx$ 23 to 44 lbs/ft^2.

The results of all three slides were then averaged, as only a single set of indices will be used for the overall Nerlerk case history. This is because (1) the three slides are very similar, and so are the initial geometries and materials, and (2) it was desirable not to over-weight the contribution of this (three slide) case history to the eventual regressions that would subsequently be performed. Averaging the results of all three slides, it was judged that the overall best estimate of $S_{r,resid/geom}$ = 53 lbs/ft^2, with a range of $S_{r,resid/geom} \approx$ 38 to 70 lbs/ft^2.

Olson (2001) also performed back-analyses to evaluate $S_{r,resid/geom}$ for each of the three Nerlerk slides considered in this study. He projected an estimate of runout geometry beyond the toe of the embankments, but does not then go on to show or clearly explain the failure surfaces he considered. His best estimate values of $S_{r,,resid/geom}$ for Slides 1, 2 and 3 are

Slide 1: $S_{r,resid/geom}$ = 2.5 kPa (52 lbs/ft^2) with no range given.

Slide 2: $S_{r,resid/geom}$ = 1.7 kPa (36 lbs/ft^2) with range ≈ 1.0 kPa (21 lbs/ft^2) to 2.4 kPa (84 lbs/ft^2)

Slide 3: $S_{r,resid/geom}$ = 1.5 kPa (31 lbs/ft^2) with range ≈ 1.2 kPa (25 lbs/ft^2) to 1.7 kPa (36 lbs/ft^2)

Average = 1.9 kPa (40 lbs/ft^2)

These values are only a bit lower than the values calculated in these current studies.

B.12.6 Overall Estimates of S_r

Overall estimates of S_r for this Class B case history were made based on the pre-failure geometry, the partial post-failure geometry, the approximate runout features and characteristics, and the values of $S_{r,yield}$ and $S_{r,resid/geom}$ as calculated and/or estimated in the preceding sections.

An average runout distance of the center of masses of the overall failures for Slides 1, 2 and 3 was approximately D = 240 feet, and the average initial failure slope height for the three slides was H = 65.6 feet. This produces a runout ratio (defined as runout distance traveled by the center of gravity of the overall failure mass divided by the initial slope height from toe to back heel of the failure) of D/H = 3.66. This allows Equation 4-4, and Figures 4.7 and 4.11, to serve as one basis for estimation of post-liquefaction strength S_r. Using the ranges of $S_{r,yield}$ and $S_{r,resid/geom}$ from Sections B.12.4 and B.12.5, and assuming that $\xi \approx 0.4$ to 0.65 for this long runout case, with 0.525 as the best estimate, provided a best estimate value of $S_r \approx$ 54 lbs/ft^2 and an estimated range of $S_r \approx$ 30 to 85 lbs/ft^2. A second basis for estimation of S_r was the use of the relationship of Figure 4.9, and the range of values of $S_{r,yield}$ from Section B.5.4. Based on the large runout distance, values of initial (pre-failure displacement) Factor of Safety were taken as approximately 0.35 to 0.55, and this produced a best estimate value of $S_r \approx$ 69 lbs/ft^2 and an estimated range of $S_r \approx$ 40 to

106 lbs/ft^2. No similar use was made of Figure 4.9 in conjunction with the ranges of $S_{r,resid/geom}$ estimated in Section B.12.5 because these estimates of $S_{r,resid/geom}$ were considered to be very approximate.

The estimates by each of the two methods above were then averaged together, and this produced a best estimate value of $S_r \approx 62$ lbs/ft^2 and an estimated range of $S_r \approx 30$ to 106 lbs/ft^2. These estimates of variance are non-symmetric about the best estimated mean value, and the range was judged to represent approximately +/- 2 standard deviations, so further adjustments were then necessary.

Overall, based on an assumed normal distribution, it was judged that the (mean and median) best estimate of post-liquefaction strength for this case history is

$$\overline{S_r} = 68 \text{ lbs/ft}^2$$

and that the best estimate of standard deviation of mean overall post-liquefaction strength is

$$\sigma_{\overline{S}} = 19 \text{ lbs/ft}^2$$

Olson (2001) and Olson and Stark (2002) did not apply their "kinetics" method to this case, and so they did not independently develop an estimate of S_r that incorporated momentum effects. Instead they simply used their value of $S_{r,resid/geom}$ as presented above in Section B.12.5 as a conservative approximation of S_r for this less well-defined case. Because these values are based on residual post-failure geometry with an assumed Factor of Safety equal to 1.0, they do not include momentum effects and so they will be too low.

A better estimate of S_r that approximately incorporates momentum effects, and a better basis for comparison with these current studies, can be obtained by employing Olson's best estimate averaged values of $S_{r,yield} = 81$ lbs/ft^2 and $S_{r,resid/geom} = 40$ lbs/ft^2, and an assumed average value of $\xi \approx 0.8$ in Equation 4-4 as

$$S_r \approx 0.5 \text{ x } [81 \text{ lbs/ft}^2 + 40 \text{ lbs/ft}^2] \text{ x } 0.8 = 48 \text{ lbs/ft}^2$$

This value ($S_r \approx 48$ lbs/ft^2) agrees reasonably well with the best estimate value of $S_r \approx 68$ lbs/ft^2 developed in these current studies, especially considering the uncertainties and the very different approaches taken by the two investigation teams.

Wang (2003) and Wang and Kramer (2008) did not employ their zero inertial force (ZIF) method to incorporate inertial effects in back-analyses of this failure. Instead they selected their value of S_r based on examination of back-analyses of several previous investigators, and in the end selected $\overline{S_r} = 178.5$ lbs/ft^2, and a standard deviation of $\sigma_{\overline{S}} = 32.1$ lbs/ft^2. Their best estimate appears to be unreasonably high, based on comparison with the values developed (1) by Olson (2110 and (2) these current studies. This appears to be the result of inadvertent double-counting of the high value of S_r proposed by Jeffries et al. (1990) in their averaging of four previous values, as described in Section 2.3.8.1(b)-(ii). The value of Jeffries et al. ($S_r = 308$ lbs/ft^2) was then adopted by Stark and Mesri (1992) who rounded it to 400 lbs/ft^2. That was not a second "independent" assessment.

Wang averaged both 408 lbs/ft^2 and 400 lbs/ft^2 as two of the four values from previous investigations to develop his resulting averaged value for this case.

Sladen et al. (1985) also performed back-analyses to develop estimates of S_r for this case, and averaging his values for Slides 1, 2 and 3 his resulting value would be S_r = 42 lbs/ft^2, in reasonable agreement with both Olson (2001) and these current studies.

B.12.7 Evaluation of Initial Effective Vertical Stress

Average initial (pre-failure) effective vertical stress was assessed for each of the three large final failure surfaces for Slides 1, 2 and 3 shown in Figures B.12.7(a) through B.12.9(a). Parameters and sensitivity analyses were as described previously in Section B.12.4. Additional analyses were then performed for alternate potential failure surfaces, including failure surfaces representing the end result of retrogressive incremental failures extending back to the apparent back heel of the final failure. Depths of failure surfaces were varied, and both rotational and translational (wedge-like) failure surfaces were considered. This produced a moderately large, but finite, range of estimated values of average pre-failure effective stress within the liquefied materials controlling the failure.

For failure Slide 1, the resulting best estimate of average pre-failure effective stress within the liquefied materials controlling the failure was then $\sigma_{vo}' \approx 1{,}066$ lbs/ft^2, with a reasonable range of $\sigma_{vo}' \approx 813$ to 1,326 lbs/ft^2.

For failure Slide 2, the resulting best estimate of average pre-failure effective stress within the liquefied materials controlling the failure was then $\sigma_{vo}' \approx 1{,}281$ lbs/ft^2, with a reasonable range of $\sigma_{vo}' \approx 1{,}026$ to 1,550 lbs/ft^2.

For failure Slide 3, the resulting best estimate of average pre-failure effective stress within the liquefied materials controlling the failure was then $\sigma_{vo}' \approx 1{,}148$ lbs/ft^2, with a reasonable range of $\sigma_{vo}' \approx 899$ to 1,411 lbs/ft^2.

Averaging the Results from Slides 1, 2 and 3, the resulting best estimate of average pre-failure effective stress within the liquefied materials controlling the failure was then $\sigma_{vo}' \approx 1{,}165$ lbs/ft^2, with a reasonable range of $\sigma_{vo}' \approx 913$ to 1,429 lbs/ft^2. This range is slightly non-symmetric about the median value, and this range was judged by the engineering team to represent approximately ± 2 standard deviations. Overall, the best characterization of initial (pre-failure) average effective vertical stress was then taken to be represented by a mean value of

$$\overline{\sigma'_{vo}} \approx 1{,}171 \text{ lbs/ft}^2$$

and with a standard deviation of

$$\sigma_{\overline{\sigma}} \approx 129 \text{ lbs/ft}^2$$

Estimates of σ_{vo}' were also back-calculated by Olson and Stark (2001, 2002). Averaging their best estimate values for Slides 1, 2 and 3 produces a resulting overall average value of $\sigma_{vo}' \approx$ 35.0 kPa (731 lbs/ft^2), which is somewhat lower than the value developed in these current studies. Average initial vertical effective stresses were not directly reported by Wang (2003) and Kramer (2008), but they were published more recently in the publication by Kramer and Wang (2015). As discussed in Section 2.3.8.1(b)-(iii), Wang (2003) did not perform any independent analyses to assess σ_{vo}' for his 22 "secondary" cases, and this is one of those cases. Instead, he compiled values of S_r from multiple previous investigators, and averaged these for a best estimate. He also compiled multiple values of S_r/σ_{vo}' from previous investigators, and averaged these for a best estimate. He then used these two best-estimate values of S_r and S_r/σ_{vo}' to infer a resulting representative value of σ_{vo}'. As described in Section 2.3.8.1(b)-(iii), the resulting averaged values of S_r and S_r/σ_{vo}' were incompatible with each other for a number of Wang's "secondary" case histories, and this process produced unreasonable values for a number of case histories. Wang's value of $\sigma_{vo}' = 1{,}440$ lbs/ft^2 for this case is somewhat higher than the values developed by Olson (2001) and by these current studies.

B.12.8 Evaluation of $N_{1,60,CS}$

Sladen et al. (1985) report that results from soil borings indicate that the fines content of the Nerlerk sands had a fines content of about 10%, while Rogers et al.(1990) reported an average of 3%. It is not reported if any SPTs were performed as a part of those investigations.

Sladen et al. (1985) reported that 26 CPTs were performed at the site in the both the pipeline-placed Nerlerk and hopper-placed Ukalerk sands. Figure B.10.10 presents separate summaries of the tip resistances for the Nerlerk and Ukalerk sands. These serve to confirm that the hopper-placed Ukalerk sands have a higher penetration resistance, confirming the more critical state of the Nerlerk sands.

Olson (2001) reports representative penetration resistances from the Nerlerk sands from 2 CPTs that are reported to be near to Slides 1 and 2. Olson assumed the penetration resistance from the CPT near Slide 2 was also representative of Slide 3. He determined a representative penetration resistance and range for Slide 1 to be $q_{c1} = 4.5$ MPa, with a range from 2.6 to 7.8 MPa. The assigned representative penetration resistance and range for Slides 2 and 3 to be $q_{c1} = 3.8$ MPa, with a range from 1.9 to 8.0 MPa. While the individual CPT soundings used to produce those estimates were not reported by Olson, the values appear to be consistent with the average CPT values in Nerlerk sands shown in Figure B.12.11. He also reported a range of fines contents from 2 to 12% for the Nerlerk sands.

For this study, it was determined that a representative qc1 value for the Nerlerk sands of qc1 ≈ 3.8, with a range of 3 to 4.5 MPa is appropriate. The ratio of $(q_c/Pa)/N_{60}$ was assumed to be approximately of 4 to 6. Based on the ranges of fines content reported form other studies, a fines content correction ranging from no correction to a slight correction was adopted. After applying the necessary corrections and conversions, the resulting best estimate mean value of $N_{1,60,CS}$ for the iron tailings was judged to be $\overline{N_{1,60,CS}} \approx 7.5$ blows/ft. Variance of $\overline{N_{1,60,CS}}$ was estimated

primarily on the range of results assumed in this and other studies. Considering these, the representation of uncertainty in the representative median value of $\overline{N_{1,60,CS}}$ was taken as $\sigma_{\overline{N}} \approx 2.5$ blows/ft.

Olson (2001) developed the following estimates of penetration resistances for Slides 1, 2 and 3:

Slide 1: $N_{1,60}$ = 8.7 bpf, with a range of 5 to 15 bpf

Slide 2: $N_{1,60}$ = 7.2 bpf, with a range of 3.5 to 15.3 bpf

Slide 3: $N_{1,60}$ = 7.2 bpf, with a range of 3.5 to 15.3 bpf

These are in good agreement with these current studies. Fines adjustments are essentially null for the Nerlerk sands.

Wang (2003) developed a significantly higher value of $N_{1,60,CS}$ = 11.4 bpf for this case. It is not clear what caused this value to be so much higher than the values of (1) Olson (2001) and (2) these current studies.

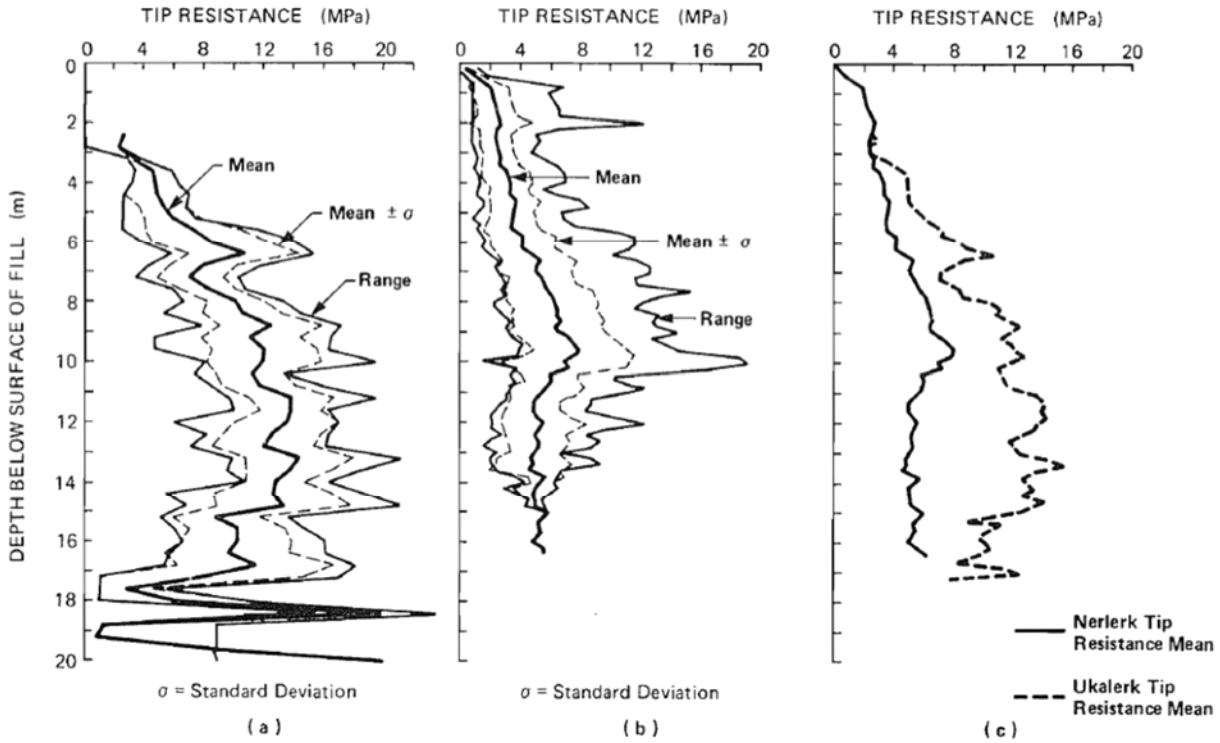

Figure B.12.10: Mean CPT tip resistances, and ranges, separated by material type (a) Ukalerk sand, (b) Nerlerk sand, (c) means of Ukalerk and Nerlerk sands (Figure from Sladen et al., 1985)

B.13 Asele Road Embankment (Sweden; 1983)

B.13.1 Brief Summary of Case History Characteristics

Name of Structure	Asele Road Embankment
Location of Structure	Sweden
Type of Structure	Earthen Embankment
Date of Failure	October 4, 1983
Nature of Failure	Cyclic, Road Pavement Repairs
Approx. Maximum Slope Height	29.2 ft.

B.13.2 Introduction and Description of Failure

Road No. 351 near Asele was constructed on a raised earthen embankment along the edges of two existing lakes, and the embankment would eventually be partially submerged due to the impoundment of a reservoir for a nearby hydropower facility. Figure B.13.1 shows a plan view site map. The embankment was constructed as prescribed using the "wet-fill" method, however it was constructed during the winter months, contrary to implied recommendations, allowing to embankment to potentially freeze during construction.

The Asele Road Embankment was completed and opened to traffic in August of 1978. Filling of the reservoir began five years later in August of 1983. When the water had risen to about 3 meters above the toe on September 18, 1983 longitudinal cracks along the embankment were noticed. By the time the water reached within about 2 meters of the road level, extensive damage had occurred, requiring the embankment road to be resurfaced. It was during this resurfacing effort, and specifically during the compaction of the subgrade by the use of a 3.6 ton vibratory roller drawn by a tractor on October 4, 1983, that a pair of liquefaction-induced slides of the embankment occurred. The tractor and vibratory roller were carried out by the larger of the two slide and travelled approximately 60 m laterally out into the reservoir (Ekstrom and Olofsson, 1985), and the operator perished. The failure occurred during the first pass of the large vibratory roller.

Figure B.13.1 presents a photograph (from Ekstrom and Olofsson, 1985) showing the scarp after the failure, and Figure B.13.2 shows a cross-section through the failed road embankment section (from Konrad and Watts, 1995, based on Ekstrom and Olofsson, 1985).

The failure was attributed by Ekstrom and Olofsson (1985) to cyclically initiated liquefaction of the loose embankment fill due to the shaking applied by the vibratory roller. Ekstrom and Olofsson attributed the loose nature of the fill material to the use of a "wet fill" method during winter months which reportedly left the fill susceptible to freezing, which in turn defeated efforts at compaction of the fill when the embankment was under construction.

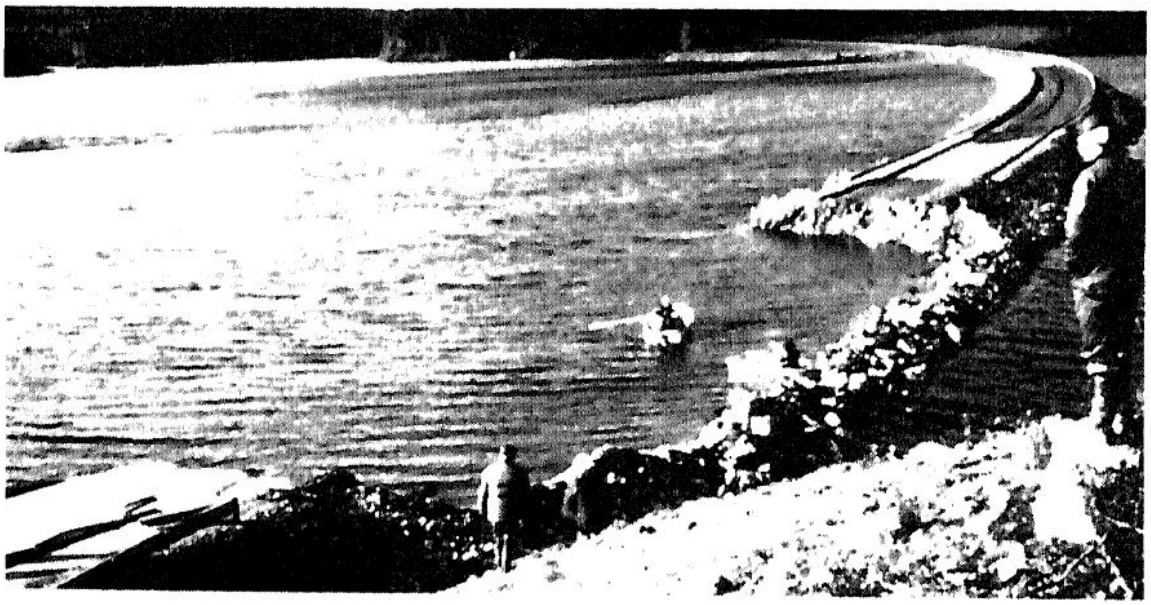

Fig. 1 View of the failure, October 4th 1983.

Figure B.13.1: Photograph of the Asele Road Embankment failure scarp and the remaining embankment on October 4, 1983 (Ekstrom and Olofsson, 1985).

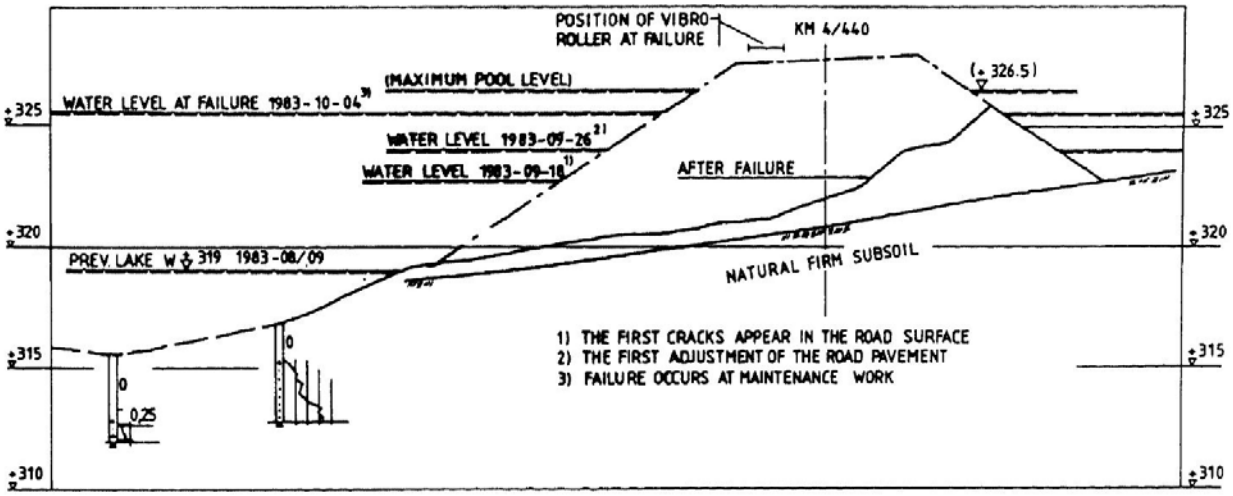

Figure B.13.2: Pre-failure and post-failure cross-sections of the Asele Road Embankment (Ekstrom and Olofsson, 1985).

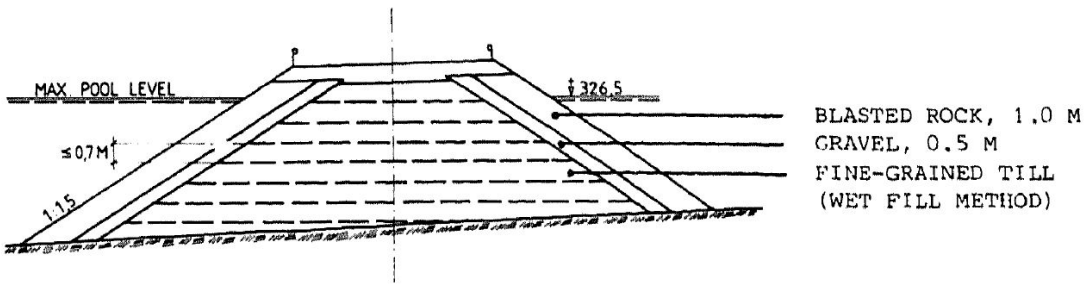

Fig. 4 Principal section for the construction of the embankment.

Figure B.13.3: Design cross-section for the Asele Road Embankment (Ekstrom and Olofsson, 1985).

B.13.3 Geology and Site Conditions

Figure B.13.3 shows the design cross-section for the Asele Road Embankment. The embankment was constructed with fine sandy till, with facings consisting of a layer of gravel overlain by coarser blasted rock. The foundation material consisted of what Ekstrom and Olofsson describe as natural firm (glacial) till. As shown in Figure B.13.2, the failure occurred within the loose, fine sandy till embankment. The water level at the time of the failure is reported in Ekstrom and Olofsson (1985) as being El +325.5 m., and this is also shown in Figure B.13.2.

The "fine-grained" till materials used for the main embankment fill were broadly well graded glacial till materials with maximum particle sizes of approximately ¾ inches, and fines contents of approximately 22% to 40% (Ekstrom and Olofsson, 1985). "Fine-grained" was a relative term here; distinguishing between the materials used to construct the main body of the embankment, and the coarser materials of the facings which were sized as slope face protection against wave erosion. The fines were silt dominated, and these soils are generally of a potentially liquefiable nature.

There were no published penetration test data for this failure case history, but Konrad and Watts (1995) reported a personal communication from Prof. Rainer Masarch, who conducted a post-failure investigation of the Asele Road Embankment. Prof. Masarch reported an average $N_{1,60}$ value of approximately 6 to 8 blows/ft., but the details of SPT equipment and procedures, and the corrections and adjustments made to produce these $N_{1,60}$ values, are not known.

B.13.4 Initial Yield Stress Analyses

Figure B.13.4 shows the cross-section used for back-analyses of the post-liquefaction initial yield strength $S_{r,yield}$ that would be required within the foundation and embankment materials of the north dike section to produce a calculated Factor of Safety equal to 1.0. This is not the

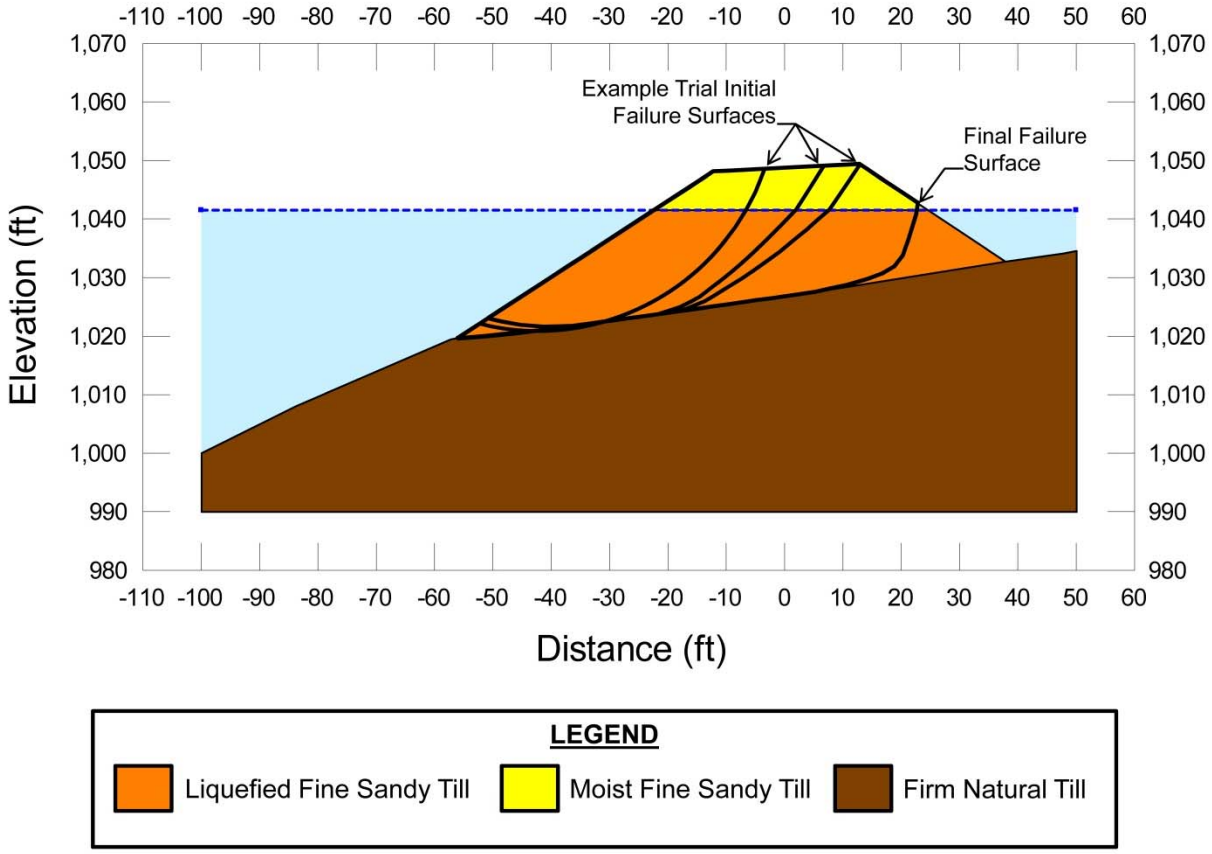

Figure B.13.4: Cross-section showing the pre-failure geometry and conditions for back-analyses of the initial yield strength ($S_{r,yield}$) for the failure section of the north dike of the Asele Road Embankment, showing examples of trial failure surfaces analyzed.

actual post-liquefaction strength, but it proves to be useful in developing estimates of post-liquefaction strength (S_r) for this case history.

The solid line in Figure B.13.4 shows the final back heel scarp of the slide. The dashed lines show a suite of potential initial failure surfaces analyzed for evaluation of $S_{r,yield}$. These are not a comprehensive representation, and additional potential failure surfaces were also analyzed here.

There were two general sets of potential failure mechanisms that could potentially explain the observed features: (1) the failure may have been incrementally retrogressive, initiating with a "slice" near to the front of the feature, and then retrogressing on a slice by slice basis towards the eventual back heel, or (2) the entire slide may have initiated monolithically (all at once). Both sets of possibilities were analyzed, and multiple potential "initial" failure surfaces were analyzed for the incrementally retrogressive scenario. In all cases, failure was modeled as occurring within the embankment fill. The phreatic surface was taken as the level of the lake at the time of the failure, and this was well-defined (as shown previously in Figure B.13.2.

Unit weights of the non-saturated sands and silty sands of the embankment fill above the phreatic surface were modeled with a unit weight of $\gamma_m \approx 115$ lbs/ft^3, and this was then varied over a range of 112 to 118 lbs/ft^3 for parameter sensitivity studies. Unit weights of the saturated sands and silty sands below the phreatic surface were modeled with a unit weight of $\gamma_s \approx 120$ lbs/ft^3, and this was then varied over a range of 117 to 123 lbs/ft^3 for parameter sensitivity studies. The friction angle of the embankment fill materials above the phreatic surface was modeled with Ø′ ≈ 30°, and a range of Ø′ ≈ 28° to 32°.

As shown in Figure B.13.4, potential initial failure surfaces were modeled as either (1) wedge-like semi-translational features, or (2) semi-rotational/translational features, or (3) conforming essentially to the final observed overall failure scarp (the monolithically initiated scenario).

For the special case of the monolithically initiated scenario, involving initial failure on the eventual (final) observed overall failure scarp, the best estimate value of $S_{r,yield}$ was found to be $S_{r,yield} = 193$ lbs/ft^2, with a range of $S_{r,yield} \approx 154$ to 233 lbs/ft^2.

It was, however, the opinion of this current engineering team that the failure may have been at least somewhat incrementally retrogressive. Accordingly, a significant number of smaller "initial" potential (first slice) failure surfaces were also analyzed. The resulting best estimate value of $S_{r,yield}$ for smaller initial yield slices was found to be $S_{r,yield} = 344$ lbs/ft^2, with a range of $S_{r,yield} \approx 263$ to 426 lbs/ft^2.

In keeping with the tenets and protocols of these current studies, the values of $S_{r,yield}$ calculated for these potential "initial" slices were then averaged directly with the $S_{r,yield}$ values calculated for the monolithically initiated (eventual overall) failure surface as described above, and these averages values were taken as "representative" $S_{r,yield}$ values for incrementally retrogressive initiation scenarios. The averaging here was weighted averaging, using 2:1 weighting as

$$S_{r,yield} = [\ 2 \times S_{r,yield}\ (\text{smaller initial yield surface}) + S_{r,yield}\ (\text{final overall failure scarp})] / 3$$

Based on the range of variations in properties and parameters, and a range of potential failure mechanisms and associated feasible failure surfaces, the resulting best estimate overall of "representative" $S_{r,yield}$ was found to be $S_{r,yield} = 294$ lbs/ft^2, with a range of $S_{r,yield} \approx 227$ to 362 lbs/ft^2.

Olson (2001) also performed back-analyses to estimate $S_{r,yield}$. He analyzed a suite of two-wedge potential failure surfaces representing assumption of an overall retrogressive failure. The "initial" failure surfaces that he analyzed encompassed approximately 50% to 70% of the eventual overall failure, and he did not then average the resulting values of $S_{r,yield}$ with those associated with the eventual (final) overall failure scarp. Olson's best estimate of $S_{r,yield}$ was 16.8 kPa (351 lbs/ft^2), with a range of 13.9 to 18.9 kPa (290 to 395 lbs/ft^2).

B.13.5 Residual Strength Analyses Based on Residual Geometry

It was not possible to perform rigorous and reliable back-analyses to determine the value of $S_{r,resid/geom}$ required to produce a calculated Factor of Safety equal to 1.0 based on residual geometry. This case is one of six cases (out of the 29 cases back-analyzed as part of these current studies) where the slide mass "went over a lip" and then traveled down a steeper slope, and the ensuing displacements either (1) could not be reliably tracked, or (2) could not be reliably back-analyzed. Both situations apply in this current case because the post-failure geometry of the failure mass runout is largely undefined. This is a significant source of uncertainty for this case history.

The large vibratory compactor had been rolling along at the forward edge of the level roadbed, just behind the lip of the pre-failure embankment. After the failure it was reported to have travelled laterally approximately 60 meters, in which case it would have ended up approximately 45 meters left of the pre-failure embankment toe shown in Figure B.13.4.

Konrad and Watts (1995) assumed that 60 meters at least approximately represented the distance of flow, and used the flow failure runout analysis method of Lucia (1981) to back-estimate an approximate value of $S_{r,resid/geom.} \approx$ 5 to 7.5 kPa (105 to 155 lbs/ft^2). Olson (2001) states that this back-calculation by the Lucia (1981) method produces shear strengths similar to those back-calculated by the simplified method, and so Olson adopts these values back-calculated by Konrad and Watts. The "simplified method" referred to by Olson is an infinite slope analysis of a stratum of uniform thickness, and is applied to post-liquefaction residual (final) geometry. The details of Olson's analyses using this approach are not presented.

The 60 meters of assumed slope displacement are not closely constrained by the available information. It is not clear that the heavy compactor would have experienced movements representative of those of the slope failure mass. The failure mass may have failed to transport the compactor the full distance, or the compactor may have traveled farther either by tumbling or due to its own momentum. These are, however, interesting points of comparison.

In these current studies, it was assumed that $S_{r,resid/geom}$ would have at least been higher than zero. Values of $S_{r,resid/geom}$ back-calculated from the reasonably well-documented Class A case histories were next examined, and for the range of effective overburden stress and $N_{1,60,CS}$ values for this current case an approximate range of $S_{r,resid/geom} \approx$ 101 to 162 lbs/ft^2 was conservatively assumed, based on analyses of other Class A and B case histories. This range of values was selected to be slightly conservatively biased (a conservative bias of approximately 10% reduction of best estimates of $S_{r,resid/geom}$ was targeted here), so that any resulting error in evaluation of overall S_r would also be slightly conservative (nominally by approximately 5% or so).

It is interesting to note that this range of $S_{r,resid/geom} \approx$ 101 to 162 lbs/ft^2 agrees fairly well with the ranges back-calculated by Konrad and Watts (1985) and also with the values apparently developed by Olson (2001), based on alternate approaches, as described above.

B.13.6 Overall Estimates of S_r

Overall estimates of S_r for this Class B case history were made based on the pre-failure geometry and the approximate runout features and characteristics, and the values of $S_{r,yield}$ and $S_{r,resid/geom}$ as calculated and/or estimated in the preceding sections.

Runout characteristics for this case cannot be accurately assessed due to the approximate nature of the post-failure cross section as reported. Runout distance, and runout ratio, appear to be "large", but the failure mass travelled out over a "lip" at the toe of the slide scarp, and then down what may have been a steeper slope.

Runout ratio (defined as runout distance traveled by the center of gravity of the overall failure mass divided by the initial slope height from toe to back heel of the failure) was taken to be at least medium to large. This allowed Equation 4-4, and Figures 4.7 and 4.11 to serve as one basis for estimation of post-liquefaction strength S_r. Using the ranges of $S_{r,yield}$ and $S_{r,resid/geom}$ from Sections B.13.4 and B.13.5, and assuming that $\xi \approx 0.35$ to 0.70 for this large runout case, with 0.525 as the best estimate, provided a best estimate value of $S_r \approx 112$lbs/ft^2 and an estimated range of $S_r \approx 57$ to 178 lbs/ft^2. A second basis for estimation of S_r was the use of the relationship of Figure 4.9, and the range of values of $S_{r,yield}$ from Section B.5.4. Based on the large runout distance, values of initial (pre-failure displacement) Factor of Safety were taken as approximately 0.35 to 0.6, and this produced a best estimate value of $S_r \approx 140$ lbs/ft^2 and an estimated range of $S_r \approx 79$ to 217 lbs/ft^2. No similar use was made of Figure 4.9 in conjunction with the ranges of $S_{r,resid/geom}$ estimated in Section B.4.5 because these estimates of $S_{r,resid/geom}$ were considered to be very approximate.

The estimates by each of the two methods above were then averaged together, and this produced a best estimate value of $S_r \approx 126$ lbs/ft^2 and an estimated range of $S_r \approx 57$ to 217 lbs/ft^2. These estimates of variance are non-symmetric about the best estimated mean value, and the range was judged to represent approximately +/- 3 standard deviations, so further adjustments were then necessary.

Overall, based on an assumed normal distribution, it was judged that the (mean and median) best estimate of post-liquefaction strength for this case history is

$$\bar{S}_r = 137 \text{ lbs/ft}^2$$

and that the best estimate of standard deviation of mean overall post-liquefaction strength is

$$\sigma_{\bar{S}} = 27 \text{ lbs/ft}^2$$

Olson (2001) and Olson and Stark (2002) did not apply their "kinetics" method to this case, and so they did not independently develop an estimate of S_r that incorporated momentum effects. Instead they simply used their value of $S_{r,resid/geom}$ as a conservative approximation of S_r for this less well-defined case, and used $S_r = 5$ to 7.5 kPa (105 to 155 lbs/ft^2). in developing their predictive relationship. As described previously in Section B.13.5, this was actually the value of S_r back-calculated by Konrad and Watts (1995) based on back-calculation by the method of Lucia (1981),

which was adopted by Olson (2001). Similarly, Wang (2003) and Wang and Kramer (2008) did not employ their zero inertial force (ZIF) method to incorporate inertial effects in back-analyses of this failure. Instead they selected their value of S_r based on examination of back-analyses of several previous investigators, and in the end selected $\overline{S_r} = 163.6$ lbs/ft^2, and a standard deviation of $\sigma_{\overline{S}} = 54.6$ lbs/ft^2. Despite these differing approaches taken to evaluation and/or selection of S_r, agreement between the values used in these two previous studies, and the values developed and employed in these current studies, is good for this case history.

B.13.7 Evaluation of Initial Effective Vertical Stress

Average initial (pre-failure) effective vertical stress was assessed for the liquefied portion of the overall (final scarp) failure surface in Figure B.13.4. Parameters and sensitivity analyses were as described previously in Section B.13.4. Additional analyses were then performed for alternate potential failure surfaces, including failure surfaces initial (smaller) slices of a retrogressive incremental failure eventually extending back to the apparent back heel of the final failure. Depths of failure surfaces were varied, and both rotational and translational (wedge-like) failure surfaces were considered. When an initial (smaller) slice of a retrogressive failure was analyzed, the resulting average value of σ_{vo}' was then averaged with the value of the overall (Final slide scarp), and this averaged value of the two failure surfaces was taken as "representative" here. This produced a moderately large, but finite, range of estimated values of average pre-failure effective stress within the liquefied materials controlling the failure.

The resulting best estimate of average pre-failure effective stress within the liquefied materials controlling the failure was then $\sigma_{vo}' \approx 1{,}037$ lbs/ft^2, with a reasonable range of $\sigma_{vo}' \approx$ 884 to 1,192 lbs/ft^2. This range is symmetric about the median value, and this range was judged by the engineering team to represent approximately ± 2 standard deviations. Overall, the best characterization of initial (pre-failure) average effective vertical stress was then taken to be represented by a mean value of

$$\overline{\sigma'_{vo}} \approx 1{,}037 \text{ lbs/ft}^2$$

and with a standard deviation of

$$\sigma_{\overline{\sigma}} \approx 77 \text{ lbs/ft}^2$$

An estimate of σ_{vo}' was also calculated by Olson and Stark (2001, 2002). They reported a weighted average mean value of $\sigma_{vo}' \approx 59.9$ kPa (1,251 lbs/ft^2), in relatively good agreement with these current studies. Average initial vertical effective stresses were not directly reported by Wang (2003) and Kramer (2008), but they were published more recently in the publication by Kramer and Wang (2015). As discussed in Section 2.3.8.1(b)-(iii), Wang (2003) did not perform any independent analyses to assess σ_{vo}' for his 22 "secondary" cases, and this is one of those cases. Instead, he compiled values of S_r from multiple previous investigators, and averaged these for a best estimate. He also compiled multiple values of S_r/σ_{vo}' from previous investigators, and averaged these for a best estimate. He then used these two best-estimate values of S_r and S_r/σ_{vo}'

to infer a resulting representative value of σ_{vo}'. As described in Section 2.3.8.1(b)-(iii), the resulting averaged values of S_r and S_r/σ_{vo}' were incompatible with each other for a number of Wang's "secondary" case histories, and this process produced unreasonable, and in some cases physically infeasible, values of σ_{vo}' for a number of case histories. Wang's value of σ_{vo}' = 1,573 lbs/ft^2 appears unlikely, based on the cross-section, and so it is not considered a useful check here.

B.13.8 Evaluation of $N_{1,60,CS}$

As explained previously in Section B.13.3, there were no published penetration test data for this failure case history, but Konrad and Watts (1995) reported a personal communication from Prof. Rainer Masarch, who conducted a post-failure investigation of the Asele Road Embankment. Prof. Masarch reported an average $N_{1,60}$ value of approximately 6 to 8 blows/ft., but the details of SPT equipment and procedures, and the corrections and adjustments made to produce these $N_{1,60}$ values, are not known. There was also no information presented as to how potential interference of gravel sized particles was dealt with in this glacial till fill material with a maximum screened particle size of approximately ¾ inches. As a result, there is considerable uncertainty with regard to selection of representative $N_{1,60,CS}$ values for this case history.

Olson (2001) and Olson and Stark (2002) took the middle of the reported range, and selected a "representative" $N_{1,60}$ value of 7 blows/ft., with no range given. This was an $N_{1,60}$ value, and reflected no fines adjustment. Given the relatively high reported silty fines content of the fill, fines adjustment to $N_{1,60,CS}$ values would be expected to increase this value.

Wang (2003) and Kramer (2008) selected a somewhat higher fines adjusted value of $\overline{N_{1,60,CS}} \approx 11.0$ blows/ft., and a very high standard deviation of $\sigma_{\overline{N}} \approx 10.7$ blows/ft. This very high standard deviation produces a value of $N_{1,60,CS}$ equal to zero at just the mean minus 1.03 standard deviations level, and at a mean plus two standard deviations the value would be approximately 32.4 blows/ft., which appears to be unreasonably high for the materials as described (and as they performed). This very high standard deviation in mean $N_{1,60,CS}$ is an artifact of the rigorously defined approach taken to evaluation of $N_{1,60,CS}$ in Wang's work, and it should be noted that neither the negative $N_{1,60,CS}$ values at mean minus more than 0.71 standard deviations, nor the very high values at mean plus more than about 2 standard deviations, likely had significant impact on their overall predictive correlations. Uncertainty or variance was high with regard to penetration resistance, and the impact of this case history on the regressions that produced their predictive relationships was further reduced by assigning a very low "Weighting Factor" of WF = 0.20 for this case.

In these current studies, the values reported by Konrad and Watts (1995) attributed to Prof. Masarch were taken as the best available data, but with consideration of the associated uncertainties and variance. In these current studies, a best estimate value of $\overline{N_{1,60,CS}} \approx 9.5$ was selected, with a standard deviation of $\sigma_{\overline{N}} \approx 2.0$ blows/ft.

Overall agreement with regard to characterization of $N_{1,60,CS}$ among these two previous studies, and the current study, is considered generally good for this case with the exception of characterization of variance (or standard deviation) of the mean value of $N_{1,60,CS}$.

B.14 Nalband Railway Embankment (Armenia; 1988)

B.14.1 Brief Summary of Case History Characteristics

Name of Structure	Nalband Railway Embankment
Location of Structure	Armenia
Type of Structure	Earthen Embankment
Date of Failure	December 7, 1988
Nature of Failure	Seismic, During 1988 Armenia Earthquake (M_S = 6.8)
Approx. Maximum Slope Height	20.5 ft.

B.14.2 Introduction and Description of Failure

The Nalband Railway Embankment experienced a liquefaction-induced ground and slope failure as a result of the Armenia earthquake of December 7, 1988 (M_S = 6.8) in the Northwest region of Armenia. A total more than 1,000 multistory buildings collapsed or were damaged beyond repair, and more than 40,000 casualties were attributed to the event. Areas where liquefaction was observed were investigated by researchers funded by the U.S. National Science Foundation. Liquefaction in the area was largely attributed to loose to medium dense gravelly sands (Yegian et al., 1994).

Figure B.14.1 presents a photo reproduced from Yegian et al. (1994) showing the damage attributed to liquefaction of the foundation soils at the Nalband Railway Embankment. Maximum observed displacements, as reported in Yegian et al. (1994), were approximately 3 meters vertically 2 meters horizontally.

The peak ground acceleration recorded at a strong motion station over 25 km away from the Nalband site was 0.2g. Peak ground accelerations between 0.5 to 1.0g were estimated closer to the Nalband site, based on damage observed in the area. Figure B.14.2 presents a plan view of the region, showing the location of the Nalband site, the location of the strong motion station, and the rupturing fault trace (Yegian et al., 1994).

B.14.3 Geology and Site Conditions

Figure B.14.3 shows a cross section of the failure as reported in Yegian et al. 1994.

Two borings (NB-1 and NB-2) were drilled following the event in the locations presented on the cross section presented in Figure B.14.3. Boring NB-1 was drilled through what appears to be the toe of the failure, and boring NB-2 was drilled adjacent to the heel of the failure outside of the apparent failure mass. Logs of these exploratory SPT borings as presented in Yegian et al. (1994) are reproduced as Figure B.14.5. Yegian et al. report that the phreatic surface was unusually high in the area of the failure due to the shape of the natural terrain, and found evidence of a

FIG. 13. Photograph of Failed Embankment at Railway Station in Nalband (Site 3) (Photo Courtesy of A. Karakhanian, 1989)

Figure B.14.1: Photo of the failure of the railway embankment near Nalband (from Yegian et al., 1994)

high phreatic surface in the area adjacent to the failed embankment. The embankment in this area was constructed of compacted sand fill over loosely dumped gravelly sand material, which was in turn underlain by naturally sloping volcanic tuff (Yegian et al., 1994).

B.14.4 Initial Yield Stress Analyses

Figure B.14.4 shows the cross-section used for back-analyses of the post-liquefaction initial yield strength $S_{r,yield}$ that would be required within the foundation and embankment materials of the north dike section to produce a calculated Factor of Safety equal to 1.0. This is not the actual post-liquefaction strength, but it proves to be useful in developing estimates of post-liquefaction strength (S_r) for this case history.

There were two general sets of potential failure mechanisms that could potentially explain the observed features: (1) the failure may have been incrementally retrogressive, initiating with a "slice" near to the front of the feature, and then retrogressing on a slice by slice basis back towards the eventual back heel, or (2) the entire slide may have initiated monolithically (all at once). Both

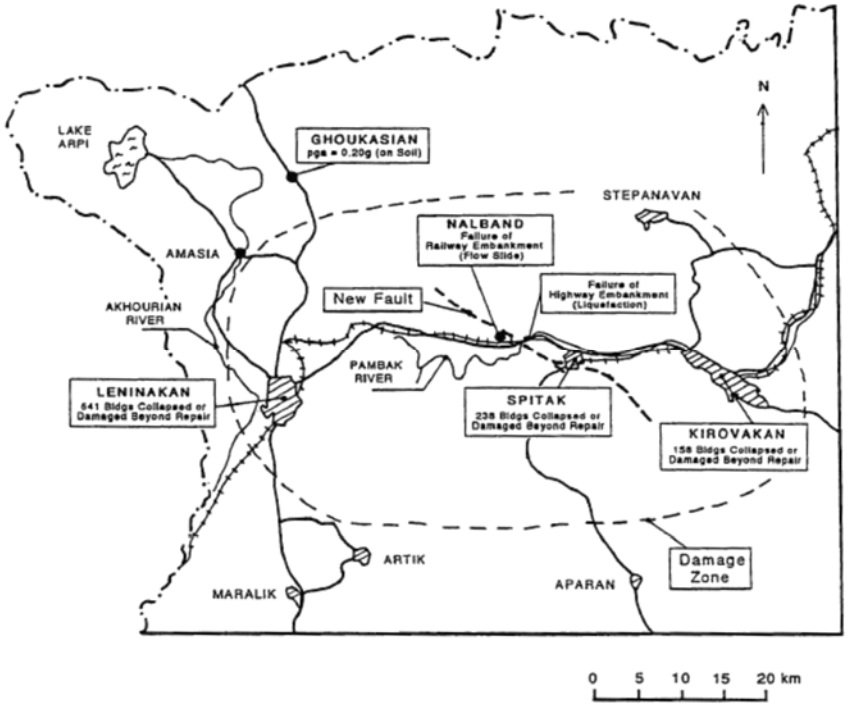

Figure B.14.2: Plan view of the failure of the region surrounding the Nalband Railway Embankment failure (from Yegian et al., 1994).

sets of possibilities were analyzed, and multiple potential "initial" failure surfaces were analyzed for the incrementally retrogressive scenario. In all cases, failure was modeled as occurring within the loose, saturated gravelly sand with silt immediately underlying the embankment fill.

Unit weights of the non-saturated compacted silty sand embankment fill above the phreatic surface were modeled with a unit weight of $\gamma_m \approx 128$ lbs/ft^3, and this was then varied over a range of $\gamma_m \approx 123$ to 133 lbs/ft^3 for parameter sensitivity studies. Unit weights of the saturated compacted silty sand below the phreatic surface were modeled with a unit weight of $\gamma_s \approx 133$ lbs/ft^3, and this was then varied over a range of 128 to 138 lbs/ft^3 for parameter sensitivity studies. The saturated foundation gravelly sand with silt below the phreatic surface were modeled with a unit weight of $\gamma_s \approx 125$ lbs/ft^3, and this was then varied over a range of 120 to 130 lbs/ft^3 for parameter sensitivity studies. The friction angle of the embankment fill materials above the phreatic surface was modeled with $Ø' \approx 33°$, and a range of $Ø' \approx 30°$ to 35°.

Potential initial failure surfaces were modeled as either (1) wedge-like semi-translational features, or (2) semi-rotational/translational features, or (3) conforming essentially to the final observed overall failure scarp (the monolithically initiated scenario).

For the special case of the monolithically initiated scenario, involving initial failure on the eventual (final) observed overall failure scarp, the best estimate value of $S_{r,yield}$ was found to be $S_{r,yield} = 172$ lbs/ft^2, with a range of $S_{r,yield} \approx 157$ to 187 lbs/ft^2.

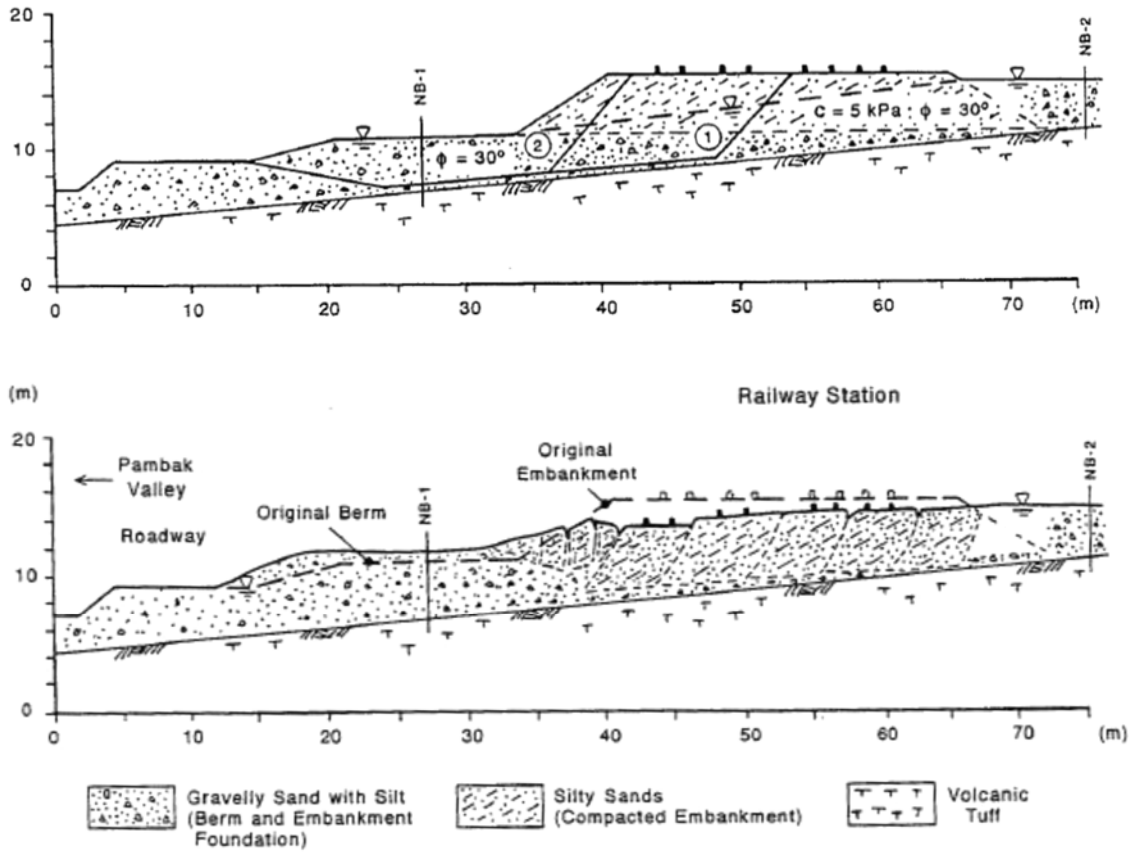

Figure B.14.3: Pre- and post-failure cross sections of the railway embankment failure near Nalband (from Yegian et al., 1994)

A significant number of smaller "initial" potential (first slice) failure surfaces were also analyzed, corresponding to a scenario in which the overall failure may have been retrogressive in nature. Figure B.14.3(a) shows a semi-rotational initial failure surface that was the most critical potential initiating failure surface found (lowest post-liquefaction Factor of Safety) but additional potential failure surfaces were also analyzed, including failure surfaces with their rear scarps set back further into the tailings impoundment. The resulting best estimate value of $S_{r,yield}$ for smaller initial yield slices was found to be $S_{r,yield} = 249$ lbs/ft^2, with a likely range of $S_{r,yield} \approx 231$ to 268 lbs/ft^2.

In keeping with the tenets and protocols of these current studies, the values of $S_{r,yield}$ calculated for these potential "initial" slices were then averaged directly with the $S_{r,yield}$ values calculated for the monolithically initiated (eventual overall) failure surface as described above, and these averages values were taken as "representative" $S_{r,yield}$ values for incrementally retrogressive initiation scenarios. Both scenarios were taken as equally as likely and therefore the results were averaged with equal weighting.

Based on the range of variations in properties and parameters, and a range of potential failure mechanisms and feasible failure surfaces, the resulting best estimate of "representative" overall $S_{r,yield}$ was found to be $S_{r,yield} = 211$ lbs/ft^2, with a range of $S_{r,yield} \approx 194$ to 228 lbs/ft^2.

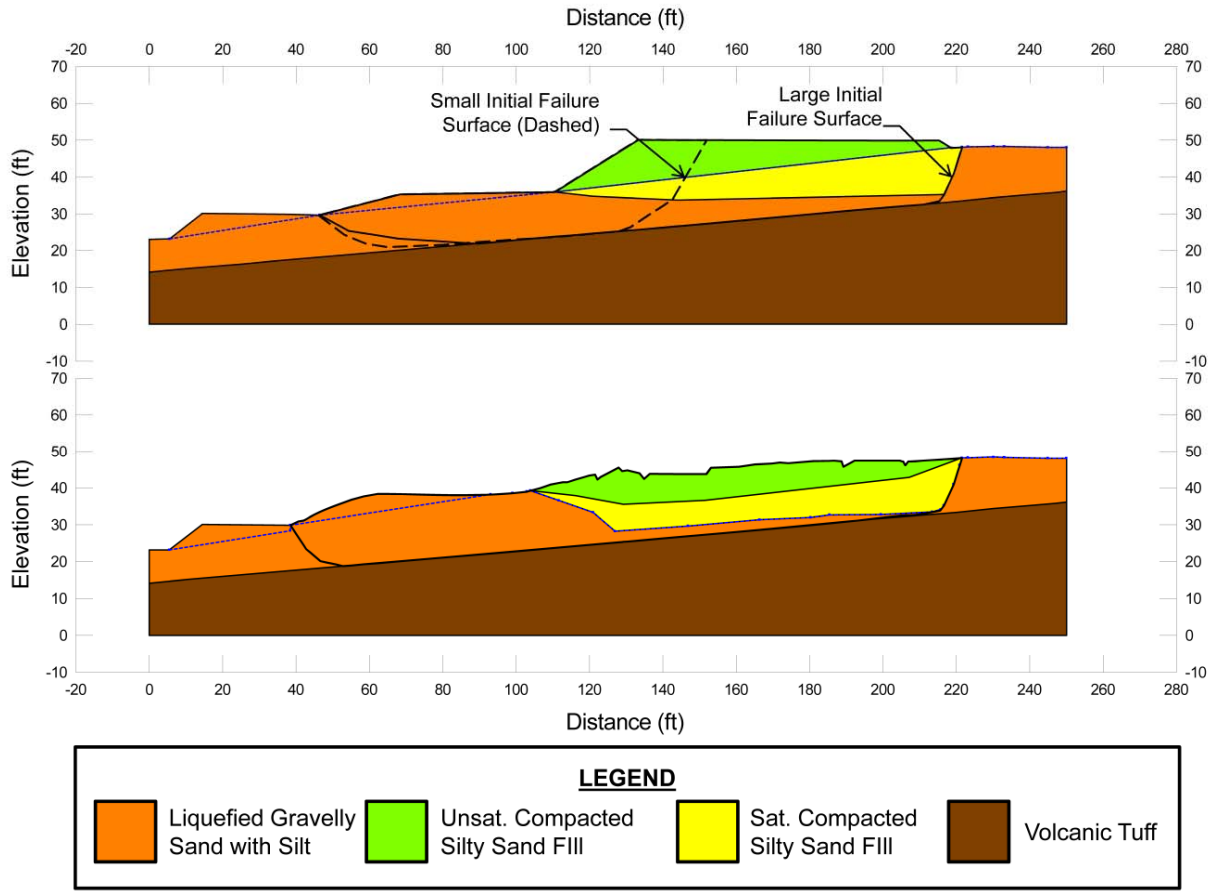

Figure B.14.4: Pre- and post-failure cross-sections of the Nalband Railway Embankment used for back-analyses of $S_{r,yield}$ and $S_{r,resid\ geom}$.

Olson (2001) also performed back-analyses to evaluate $S_{r,yield}$. He analyzed only block surfaces within the fill material that were tangent to the volcanic tuff foundation, similar to initial surfaces utilized in this study as presented in Figure B.14.4(a). His best estimate value was $S_{r,yield}$ = 8.9 kPa (186 lbs/ft^2), with a range of $S_{r,yield} \approx$ 8.6 to 9.6 kPa (180 to 200 lbs/ft^2).

B.14.5 Residual Strength Analyses Based on Residual Geometry

The calculation of the "apparent" post-liquefaction strength ($S_{r,resid/geom}$) required to produce a calculated Factor of Safety equal to 1.0 based on residual geometry is illustrated in Figure B.14.3(b). Modeling parameters and details are as described in the preceding section.

Based on the cross-sections shown in Figure B.14.3(b), and the properties and parameters described above, the best-estimate value of $S_{r,resid/geom}$ was $S_{r,resid/geom}$ = 138 lbs/ft^2. Parameters were next varied, as described previously, including analyses of alternate potential failure surfaces slightly above and below the failure surface shown in Figure B.5.4(b). Based on these analyses, it was judged that a reasonable range was $S_{r,resid/geom} \approx$ 128 to 149 lbs/ft^2.

Olson (2001) also back-calculated values of $S_{r,resid/geom}$. His best estimate failure surface was a block failure tangent to the volcanic tuff foundation, similar to final surface assumed in this study presented in Figure B.14.3(b). He again assumed, however, that the fill materials largely controlled the failure. Olson's back-calculated best estimate of $S_{r,resid/geom}$ was 5.7 kPa (119 lbs/ft^2), with a range of 5.3 to 6.2 kPa (111 to 129 lbs/ft^2).

B.14.6 Overall Estimates of S_r

Overall estimates of S_r for this Class B case history were made based on the pre-failure geometry, the partial post-failure geometry, the approximate runout features and characteristics, and the values of $S_{r,yield}$ and $S_{r,resid/geom}$ as calculated and/or estimated in the preceding sections.

Runout distance of the center of mass of the overall failure was approximately D = 7 feet, and the initial failure slope height was H = 20.5 feet. This produces a runout ratio (defined as runout distance traveled by the center of gravity of the overall failure mass divided by the initial slope height from toe to back heel of the failure) of D/H = 0.34. This allows Equation 4-4, and Figures 4.7 and 4.11, to serve as one basis for estimation of post-liquefaction strength S_r. Using the ranges of $S_{r,yield}$ and $S_{r,resid/geom}$ from Sections B.13.4 and B.13.5, and assuming that $\xi \approx 0.8$ to 0.99 for this short runout case, with 0.9 as the best estimate, provided a best estimate value of $S_r \approx$ 158 lbs/ft^2 and an estimated range of $S_r \approx$ 129 to 187 lbs/ft^2. A second basis for estimation of S_r was the use of the relationship of Figure 4.9, and the range of values of $S_{r,yield}$ from Section B.5.4. Based on the large runout distance, values of initial (pre-failure displacement) Factor of Safety were taken as approximately 0.7 to 0.9, and this produced a best estimate value of $S_r \approx$ 169 lbs/ft^2 and an estimated range of $S_r \approx$ 136 to 205 lbs/ft^2. No similar use was made of Figure 4.9 in conjunction with the ranges of $S_{r,resid/geom}$ estimated in Section B.4.5 because these estimates of $S_{r,resid/geom}$ were considered to be very approximate.

The estimates by each of the two methods above were then averaged together, and this produced a best estimate value of $S_r \approx$ 163 lbs/ft^2 and an estimated range of $S_r \approx$ 129 to 205 lbs/ft^2. These estimates of variance are non-symmetric about the best estimated mean value, and the range was judged to represent approximately +/- 2.5 standard deviations, so further adjustments were then necessary.

Overall, based on an assumed normal distribution, it was judged that the (mean and median) best estimate of post-liquefaction strength for this case history is

$$\overline{S_r} = 167 \text{ lbs/ft}^2$$

and that the best estimate of standard deviation of mean overall post-liquefaction strength is

$$\sigma_{\overline{S}} = 15 \text{ lbs/ft}^2$$

Olson (2001) and Olson and Stark (2002) did not apply their "kinetics" method to this case, and so they did not independently develop an estimate of S_r that incorporated momentum effects. Instead they simply used their value of $S_{r,resid/geom}$ as a conservative approximation of S_r for this

less well-defined case, and used S_r = 5.7 kPa (119 lbs/ft^2), with a range of 5.3 to 6.2 kPa (111 to 129 lbs/ft^2) in developing their predictive relationship. Because these values are based on residual post-failure geometry with an assumed Factor of Safety equal to 1.0, they do not include momentum effects and so they will be too low.

A better estimate of S_r that approximately incorporates momentum effects, and a better basis for comparison with these current studies, can be obtained by employing Olson's best estimate values of $S_{r,yield}$ = 186 lbs/ft^2 and $S_{r,resid/geom}$ = 119 lbs/ft^2, and an assumed average value of $\xi \approx 0.8$ in Equation 4-4 as

$$S_r \approx 0.5 \text{ x } [186 \text{ lbs/ft}^2 + 119 \text{ lbs/ft}^2] \text{ x } 0.8 = 122 \text{ lbs/ft}^2$$

This value ($S_r \approx$ 122 lbs/ft^2) agrees fairly well with the best estimate value of $S_r \approx$ 92 lbs/ft^2 developed in these current studies.

Similarly, Wang (2003) and Wang and Kramer (2008) did not employ their zero inertial force (ZIF) method to incorporate inertial effects in back-analyses of this failure. Instead they selected their value of S_r based on examination of back-analyses of several previous investigators, and in the end selected $\overline{S_r}$ = 140 lbs/ft^2, and a standard deviation of $\sigma_{\overline{S}}$ = 40.2lbs/ft^2. The best estimate was judged to be in fairly good agreement with the values developed in these current studies, but their standard deviation was significantly larger.

B.14.7 Evaluation of Initial Effective Vertical Stress

Average initial (pre-failure) effective vertical stress was assessed for the liquefied portion of the large final failure surface in Figure B.4.4. Parameters and sensitivity analyses were as described previously in Section B.14.4. Additional analyses were then performed for alternate potential failure surfaces, including failure surfaces representing the end result of retrogressive incremental failures extending back to the apparent back heel of the final failure. Depths of failure surfaces were varied, and both rotational and translational (wedge-like) failure surfaces were considered. This produced a moderately large, but finite, range of estimated values of average pre-failure effective stress within the liquefied materials controlling the failure.

The resulting best estimate of average pre-failure effective stress within the liquefied materials controlling the failure was then $\sigma_{vo}' \approx$ 1,201 lbs/ft^2, with a reasonable range of $\sigma_{vo}' \approx$ 1,021 to 1,397 lbs/ft^2. This range is slightly non-symmetric about the median value, and this range was judged by the engineering team to represent approximately ± 2 standard deviations. Overall, the best characterization of initial (pre-failure) average effective vertical stress was then taken to be represented by a mean value of

$$\overline{\sigma'_{vo}} \approx 1{,}209 \text{ lbs/ft}^2$$

and with a standard deviation of

$$\sigma_{\overline{\sigma}} \approx 94 \text{ lbs/ft}^2$$

An estimate of σ_{VO}' was also calculated by Olson and Stark (2001, 2002). They reported a weighted average mean value of $\sigma_{vo}' \approx 48.9$ kPa (1,021 lbs/ft^2), in good agreement with these current studies. Average initial vertical effective stresses were not directly reported by Wang (2003) and Kramer (2008), but they were published more recently in the publication by Kramer and Wang (2015). As discussed in Section 2.3.8.1(b)-(iii), Wang (2003) did not perform any independent analyses to assess σ_{vo}' for his 22 "secondary" cases, and this is one of those cases. Instead, he compiled values of S_r from multiple previous investigators, and averaged these for a best estimate. He also compiled multiple values of S_r/σ_{vo}' from previous investigators, and averaged these for a best estimate. He then used these two best-estimate values of S_r and S_r/σ_{vo}' to infer a resulting representative value of σ_{vo}'. As described in Section 2.3.8.1(b)-(iii), the resulting averaged values of S_r and S_r/σ_{vo}' were incompatible with each other for a number of Wang's "secondary" case histories, and this process produced unreasonable values for a number of case histories. Wang's value of $\sigma_{vo}' = 1{,}283$ lbs/ft^2 for this case, however, is in very good agreement with the value developed in these current studies. Overall, agreement between the values of (1) Olson (2001), (2) Wang (2003) and (3) these current studies is considered to be very good here.

B.14.8 Evaluation of $N_{1,60,CS}$

As discussed previously in Section B.14.3, there were two borings performed following the failure. The location of the borings and the logs of the borings can be seen in Figures B.14.3 and B.14.5, respectively. Only one of the explorations, boring NB-1 to approximately a depth of 9 ft. (3 m), was performed in the failed mass. There were two recorded blowcounts, with N values of 4 and 14 blows/ft., in the saturated gravelly sand with silt (Yegian et al., 1994).

In this current study, it is judged that the loose material in the upper part of the layer (N = 4 blows/ft.) is likely more representative of the material that controlled the failure. The higher blowcount (N = 14 blows/ft.) found near the lower part of the unit was judged to have likely been influenced by the gravels reported to be present in the material, and may also have been by the underlying very dense gravel and fractured tuff material. The precise drilling procedure, equipment and conditions are unknown. Assuming no energy correction (ER = 60%), after applying corrections the approximate representative value of $N_{1,60} \approx 6$ blows/ft is assumed. The effects of fines content of the silty gravelly sand were also considered. Incorporating all corrections and considering the sparseness and large degree of uncertainty of the data for this case history, characterization of penetration resistance for these current studies was then taken as $\overline{N_{1,60,CS}} \approx 7.5$ blows/ft., with a standard deviation of $\sigma_{\overline{N}} \approx 2.5$ blows/ft.

Olson (2001), in his assessment of the data from Yegian et al. (1994), also assumed an energy ratio of about 60%. However, Olson elected to incorporate a gravel content correction suggested by Terzaghi et al. (1996) for the average 20% gravel content in the material. He did not state what blowcount values were considered in his assessment. In the end, his selected representative penetration resistance was $N_{1,60} \approx 9.2$ blows/ft, with a range of 3.6 to 12.4 blows/ft.

Wang (2003) and Kramer (2008) also focused on the test (4 blows/ft.) in the upper part of the unit for the assessment of the representative penetration resistance, however, it appears that either no corrections were applied or the corrections were counteracting as the representative value of $N_{1,60} \approx 4$ blows/ft. was reported. A similar fines content correction was applied to produce an adjusted value of $\overline{N_{1,60,CS}} \approx 6.3$ blows/ft., and a high standard deviation of $\sigma_{\overline{N}} \approx 5.6$ blows/ft was selected.

Overall agreement with regard to characterization of $N_{1,60,CS}$ among these two previous studies, and the current study, is very good for this case with the exception of characterization of variance (or standard deviation) of the mean value of $N_{1,60,CS}$.

B.15 Sullivan Mine Tailings Dam (British Columbia, Canada; 1991)

B.15.1 Brief Summary of Case History Characteristics

Name of Structure	Sullivan Mine Tailings Dam
Location of Structure	Southeastern British Columbia, Canada
Type of Structure	Tailings Dam
Date of Failure	August 23, 1991
Nature of Failure	Static liquefaction flow failure during dyke raising
Approx. Maximum Slope Height	37.6 ft.

B.15.2 Introduction and Description of Failure

The Sullivan Mine is a base metal mine that was established in 1905 near Kimberly in southeastern British Colombia, Canada. Impoundments have been produced over the years to contain the mine tailings. Not much is known about the either the design or construction methods implemented before the early 1970's. There was, however, an embankment failure in 1948 leading to a release of about 1 million tons of iron tailings. Beginning in the early 1970's, each impoundment raise was engineered independently, using increasingly modern approaches (Jefferies and Been, 2006).

On August 23, 1991, a static liquefaction failure occurred during a 2.4 m raising of an impoundment dyke. The failure encompassed about 300 m of crest, and the toe of the failure moved laterally up to 45 m in the downstream direction. About 75,000 m^3 (100,000 yd^3) of tailings were involved in the failure. Before the failure, the dyke had reached a maximum height of 21 m (approx. 70 ft.). Slopes of the post-failure mass reportedly ranged from 1:10 (V:H) to 1:5. The failure is reported to have occurred quickly, and sand boils were observed immediately after the event and continued for hours, leading to the conclusion that the failure was due to static liquefaction (Jefferies and Been, 2006).

Construction methods of the dyke had been performed by the upstream placement method. During the raising of the dyke, engineers were concerned about pore pressures and were monitoring piezometers at the site. Pore pressures are reported to have been in general within a few feet of the ground surface and above the dyke toe. The last recordings before the failure were taken in mid-July. At that time, some piezometers were showing a declining trend in pore pressures. It was not reported as to how the timing of the recordings correlated to timing of the construction of lifts of the dyke (Jefferies and Been, 2006).

A picture of the failed mass is presented in Figure B.15.1 and pre- and post-failure cross sections reported by Jefferies and Been are shown in Figure B.15.2.

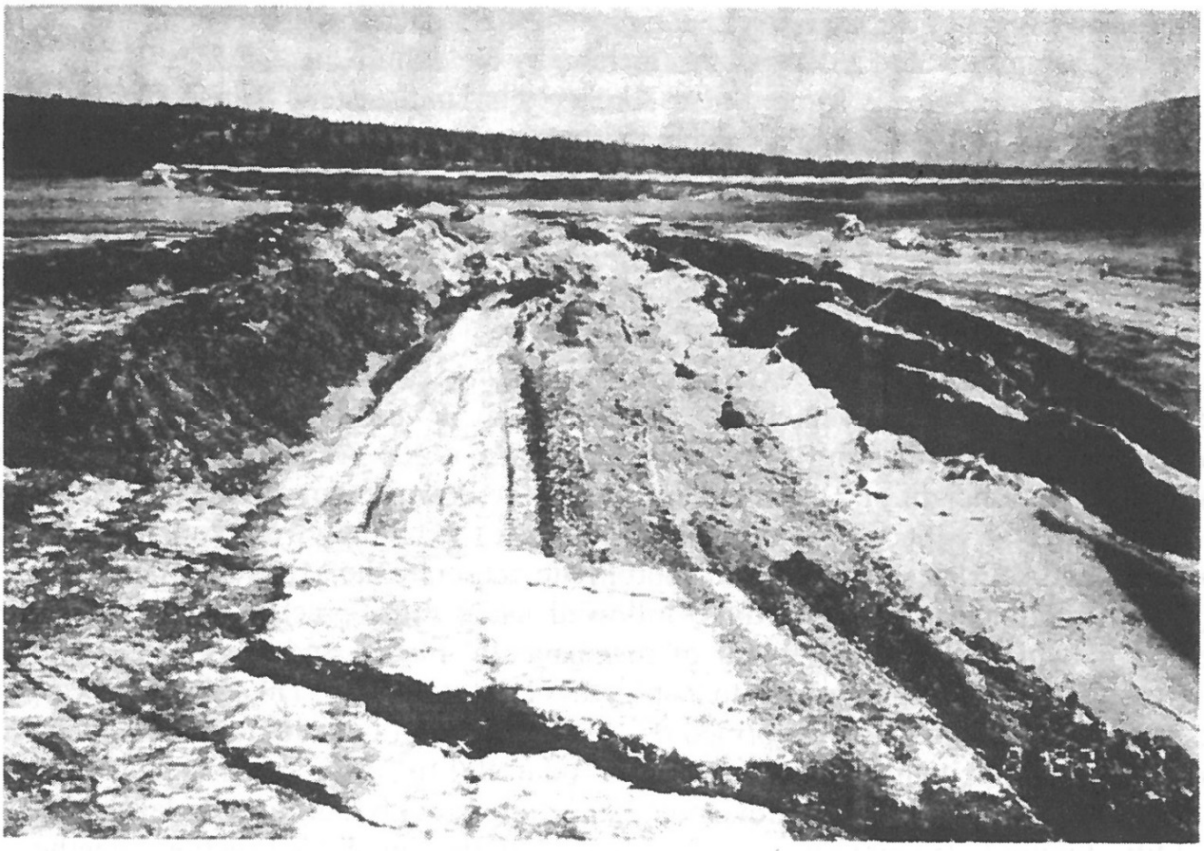

Figure B.15.1: Photograph showing the Sullivan Mine tailings dyke failure (from Jefferies and Been, 2006; originally from Davies, Dawson and Chin, 1998).

B.15.3 Geology and Site Conditions

Following the failure, 42 CPTs were advanced at the mine site. Of those 42 CPTs, 12 were advanced in the area of the failed mass. A sub-set of those explorations were reported by Jefferies and Been and are reproduced in figure B.15.4. The soils encountered in the explorations showed a wide range of materials. Dense sandy material was encountered in the areas of the containment dykes. Loose sandy silts were encountered in the area under the dykes and at the toe of the failure. The loose silts were underlain by dense till. (Jefferies and Been, 2006)

Jefferies and Been (2006) reported estimated bulk unit weights of the compacted fill and iron silt tailings as being 22.4 and 24.0 kN/m^3 (approximately 143 to 153 lbs/ft^3), respectively. The sandy silt iron tailings were also reported by Jefferies and Been to have a fines content of 50 percent or more (passing #200 sieve), and the silts were non-plastic.

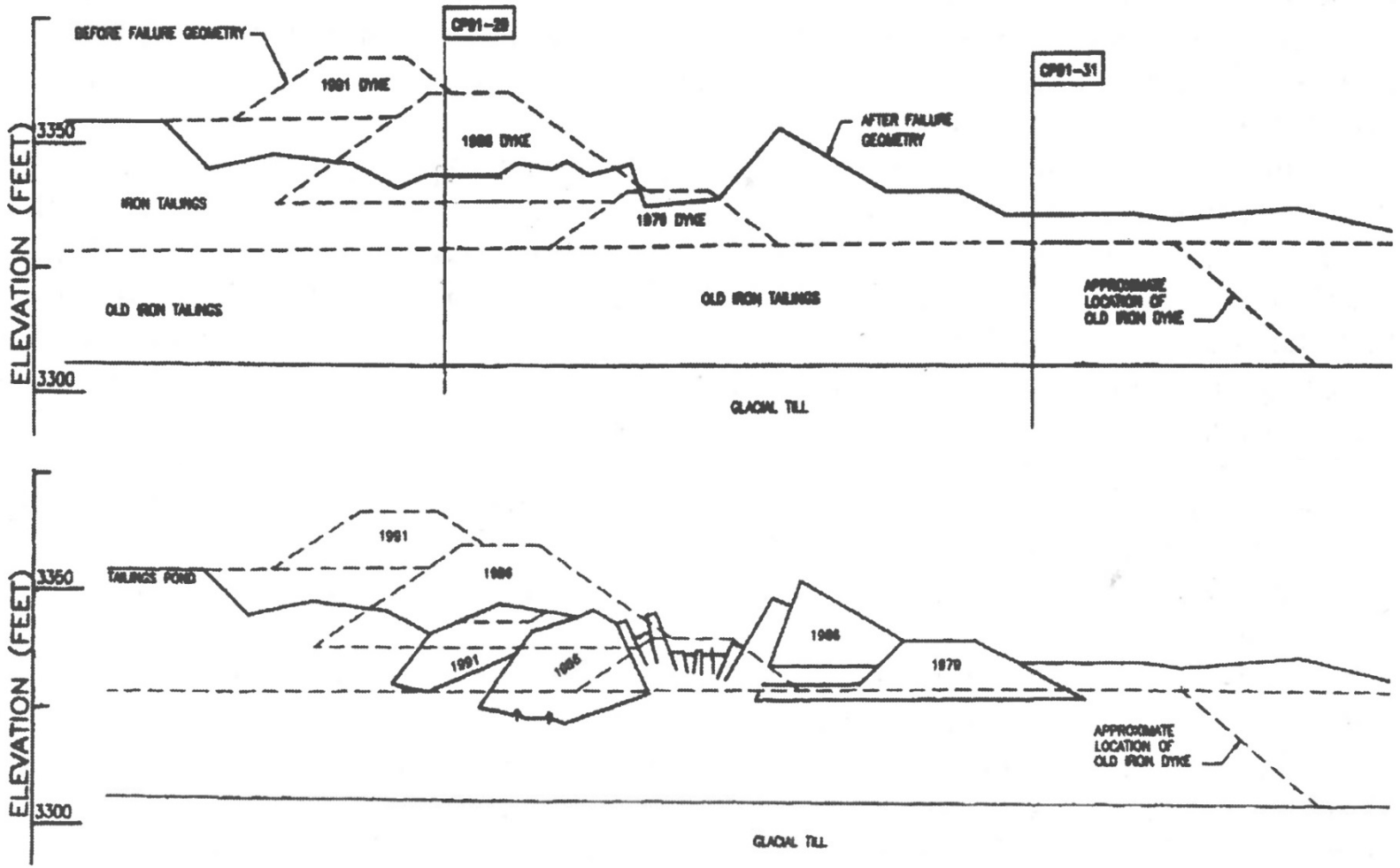

Figure B.15.2: Pre- and post-failure cross sections of the Sullivan Mine tailings dyke failure. Also shown is the location of CPTs CP91-29 and CP91-31 (from Jefferies and Been, 2006; originally from Davies, Dawson and Chin, 1998).

B.15.4 Initial Yield Stress Analyses

Figure B.15.3 shows the cross-section used for back-analyses of the post-liquefaction initial yield strength $S_{r,yield}$ that would be required within the tailings materials of the typical section of the Sullivan Mine tailings to produce a calculated Factor of Safety equal to 1.0 for static, pre-failure conditions. This is not the actual post-liquefaction strength, but it proves to be useful in developing estimates of post-liquefaction strength (S_r) for this case history.

Unit weights of the non-saturated compacted sand dyke fill above the phreatic surface were modeled with a unit weight of $\gamma_m \approx 130$ lbs/ft^3, and this was then varied over a range of $\gamma_m \approx 125$ to 135 lbs/ft^3 for parameter sensitivity studies. Unit weights of the saturated compacted sand dyke fill below the phreatic surface were modeled with a unit weight of $\gamma_s \approx 135$ lbs/ft^3, and this was then varied over a range of 130 to 140 lbs/ft^3 for parameter sensitivity studies. Unit weights of the moist iron tailings above the phreatic surface were modeled with a unit weight of $\gamma_m \approx 140$ lbs/ft^3, and this was then varied over a range of $\gamma_m \approx 135$ to 145 lbs/ft^3 for parameter sensitivity studies. Unit weights of the saturated iron tailings below the phreatic surface were modeled with a unit weight of $\gamma_s \approx 145$ lbs/ft^3, and this was then varied over a range of 140 to 145 lbs/ft^3 for parameter sensitivity studies. The friction angle of the compacted sand dyke fill materials above the phreatic surface was modeled with $Ø' \approx 35°$, and a range of $Ø' \approx 32°$ to 38°. The friction angle of the iron sandy silt tailings above the phreatic surface was modeled with $Ø' \approx 32°$, and a range of $Ø' \approx 29°$ to 35°.

Jefferies and Been (2006) interpreted the failure as starting with the translational movement of the embankment toe comprising the 1979 dyke and part of the 1986 dyke followed by movement of the remaining dyke sections. This description would lead to an initial failure surface that shears the 1986 dyke and exits pas the toe of the 1979 dyke. Another interpretation of the failure would include the initiating movements encompassing the entire mass at once, with the 1979 dyke and part of the 1986 dyke separating and translating further downstream as the failure progressed. Given the post failure geometry, both interpretations appear to be potentially valid. Potential initial failure surfaces were modeled as either (1) wedge-like semi-translational features, or (2) semi-rotational/translational features, or (3) conforming essentially to the final observed overall failure scarp (the monolithically initiated scenario).

For the special case of the monolithically initiated scenario, involving initial failure on the eventual (final) observed overall failure scarp, the best estimate value of $S_{r,yield}$ was found to be $S_{r,yield} = 611$ lbs/ft^2, with a range of $S_{r,yield} \approx 565$ to 680 lbs/ft^2.

A significant number of smaller "initial" potential (first slice) failure surfaces were also analyzed, corresponding to a scenario in which the overall failure may have been retrogressive in nature. Figure B.15.3.3(a) shows an initial failure surface that was the most critical potential initiating failure surface found (lowest post-liquefaction, pre-displacement Factor of Safety) but additional potential failure surfaces were also analyzed, including failure surfaces with more translational features. The resulting best estimate value of $S_{r,yield}$ for smaller initial yield slices was found to be $S_{r,yield} = 643$ lbs/ft^2, with a likely range of $S_{r,yield} \approx 601$ to 715 lbs/ft^2.

The results of the various trial slip surfaces, shown in Figure B.15.3, and utilizing the best estimate parameters reported above, resulted in only moderate variations in $S_{r,yield}$ values. As modeled, the more critical toe failures were more rotational in nature and were unlikely to produce the translational nature of the failure at the toe. The large failure surfaces encompassing the entire embankment, tended to produce failure surfaces more similar to that which could produce the movements observed. In keeping with the tenets and protocols of these current studies, the values of $S_{r,yield}$ calculated for these potential "initial" slices were then averaged directly with the $S_{r,yield}$ values calculated for the monolithically initiated (eventual overall) failure surface as described above, and these averages values were taken as "representative" $S_{r,yield}$ values for incrementally retrogressive initiation scenarios. Both scenarios were taken as equally as likely and therefore the results were averaged with equal weighting.

Based on the range of variations in properties and parameters, and a range of potential failure mechanisms and feasible failure surfaces, the resulting best estimate of "representative" overall $S_{r,yield}$ was found to be $S_{r,yield} = 627$ lbs/ft^2, with a range of $S_{r,yield} \approx 583$ to 698 lbs/ft^2.

Olson (2001) did not include this case history in his failure database and therefore did not perform back-analyses to evaluate $S_{r,yield}$.

B.15.5 Residual Strength Analyses Based on Residual Geometry

Back-analysis were also performed to evaluate the "apparent" post-liquefaction strength ($S_{r,resid/geom}$) required to produce a calculated static Factor of Safety equal to 1.0 based on residual geometry. This is not a direct measure of post-liquefaction strength (S_r), as it neglects momentum effects and would underestimate S_r, but it is useful for overall evaluation of S_r for this case history.

Figure B.15.3 (b) shows the post-failure cross-section geometry and example assumed range of slip surfaces utilized in the residual geometry analyses.

Based on the post-failure cross-section, with a failure surface corresponding to a location mid-way between the two potential failure surfaces shown in Figure B.15.4(b), and the properties and parameters described above, the best-estimate value of $S_{r,resid/geom}$ was $S_{r,resid/geom} = 124$ lbs/ft^2. Parameters were next varied, as described previously, and this included analyses of alternate potential failure surfaces. Based on these analyses, it was judged that a reasonable range was $S_{r,resid/geom} \approx 105$ to 146 lbs/ft^2.

There was no value of $S_{r,resid/geom}$ from Olson (2001) for this case history.

B.15.6 Overall Estimates of S_r

Overall estimates of S_r for this Class B case history were made based on the pre-failure geometry, the partial post-failure geometry, the approximate runout features and characteristics, and the values of $S_{r,yield}$ and $S_{r,resid/geom}$ as calculated and/or estimated in the preceding sections.

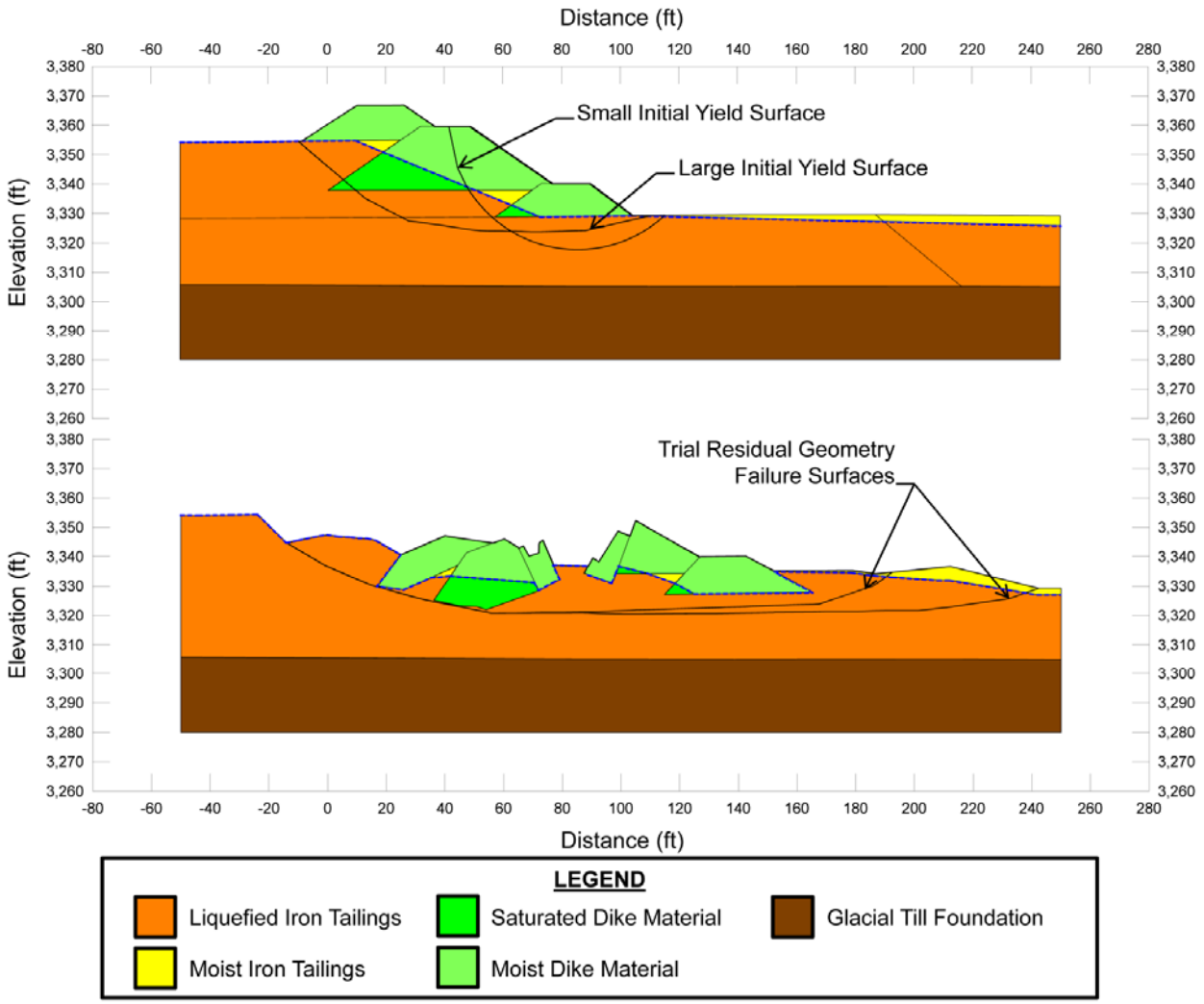

Figure B.15.3: Sullivan Mine Tailings Dyke: (a) pre-failure geometry and trail failure surfaces for initial yield stress analyses, and (b) post-failure geometry and failure surface for post-failure residual geometry analyses.

Runout distance of the center of mass of the overall failure was approximately D = 67 feet, and the initial failure slope height was H = 37.6 feet. This produces a runout ratio (defined as runout distance traveled by the center of gravity of the overall failure mass divided by the initial slope height from toe to back heel of the failure) of D/H = 1.78. This allows Equation 4-4, and Figures 4.7 and 4.11 to serve as one basis for estimation of post-liquefaction strength S_r. Using the ranges of $S_{r,yield}$ and $S_{r,resid/geom}$ from Sections B.15.4 and B.15.5, and assuming that $\xi \approx 0.60$ to 0.80 for this runout ratio, with 0.7 as the best estimate, provided a best estimate value of $S_r \approx 263$ lbs/ft^2 and an estimated range of $S_r \approx 206$ to 383 lbs/ft^2. A second basis for estimation of S_r was the use of the relationship of Figure 4.9, and the range of values of $S_{r,yield}$ from Section B.5.4. Based on the runout ratio, values of initial (pre-failure displacement) Factor of Safety were taken as approximately 0.3 to 0.5, and this produced a best estimate value of $S_r \approx 266$ lbs/ft^2 and an estimated range of $S_r \approx 204$ to 349 lbs/ft^2. No similar use was made of Figure 4.9 in conjunction with the ranges of $S_{r,resid/geom}$ estimated in Section B.4.5.

The estimates by each of the two methods above were then averaged together, and this produced a best estimate value of $S_r \approx 265$ lbs/ft^2 and an estimated range of $S_r \approx 204$ to 349 lbs/ft^2. These estimates of variance are non-symmetric about the best estimated mean value, and the range was judged to represent approximately +/- 3 standard deviations, so further adjustments were then necessary.

Overall, taking into consideration the largely asymmetric range of the results from assumed $S_{r,yield}$ slip surfaces, it was judged that the (median) best estimate of post-liquefaction strength for this case history is

$$\overline{S_r} = 277 \text{ lbs/ft}^2$$

and that the best estimate of standard deviation of mean overall post-liquefaction strength is

$$\sigma_{\overline{S}} = 24 \text{ lbs/ft}^2$$

Olson (2001) and Olson and Stark (2002), and Wang (2003) and Kramer (2008), did not consider this case history, therefore no comparison can be made to those studies. However, Jefferies and Been (2006) did estimate the residual strength as $S_r = 10$ kpa (approximately 200 lbs/ft^2) and a corresponding range of strength ratios of 0.07 to 0.13. Jefferies and Been report having estimated approximately the same residual strength from both a toe failure mechanism and also a retrogressive failure mechanism. It is unclear how momentum effects were taken into consideration, if the effects were at all. Robertson (2010) presents a best estimate strength ratio of 0.10 for this case history. As a comparison, the best estimate of strength ratio for this current study is

$$S_r/P = 277 \text{ lbs/ft}^2 / 2{,}422 \text{ lbs/ft}^2 = 0.11$$

which is in good agreement with the value back-calculated by Robertson (2010), and which at least falls within the range of Jefferies and Been (2006). Overall, agreement between the back-analysis

results of (1) Jeffries and Been (2006), (2) Robertson (2010) and (3) these current studies is very good.

B.15.7 Evaluation of Initial Effective Vertical Stress

Average initial (pre-failure) effective vertical stress was assessed for the liquefied portions of the failure surfaces for both rotational and wedge-like failures similar to the large failure surface shown in Figure B.15.3(a). Failure surfaces, parameters and sensitivity analyses were as described previously in Section B.15.4. Depths of failure surfaces were varied, and both rotational and translational (wedge-like) failure surfaces were considered.

The resulting best estimate of average pre-failure effective stress within the liquefied materials controlling the failure was then $\sigma_{vo}' \approx 2{,}413$ lbs/ft^2, with a reasonable range of $\sigma_{vo}' \approx$ 2,138 to 2,706 lbs/ft^2. This range is slightly non-symmetric about the median value, and this range was judged by the engineering team to represent approximately ± 2 standard deviations. Overall, the best characterization of initial (pre-failure) average effective vertical stress was then taken to be represented by a mean value of

$$\overline{\sigma'_{vo}} \approx 2{,}422 \text{ lbs/ft}^2$$

and with a standard deviation of

$$\sigma_{\bar{\sigma}} \approx 142 \text{ lbs/ft}^2$$

Olson (2001) and Olson and Stark (2002) in addition to Wang (2003) and Kramer (2008) did not consider this case history, therefore no comparison can be made to those studies. Jefferies and Been (2006) reported average initial vertical stresses of $\sigma'_{vo} \approx 80$ kpa (1,671 lbs/ft^2) for the initial toe failure and $\sigma'_{vo} \approx 140$ kpa (2,924 lbs/ft^2) for the final failure surface. The locations of these failure surfaces were not reported, however from the description of the failures they are assumed to be fairly similar to the initial failure surfaces used in this study. The stress corresponding to the final failure surface, which is the one most comparable to the surface used as representative of the initial vertical effective stress for this study, is about 500 lbs/ft^2 (27 percent) higher than the value back-calculated in these current studies.

B.15.8 Evaluation of $N_{1,60,CS}$

A total of 42 CPTs, 12 of which were in the vicinity of the failure, were performed on the Sullivan Mine following the failure. Six of the 12 CPTs in the vicinity of the failure were reported by Jefferies and Been (2006). Those six CPTs (three were pushed form the crest and three were pushed at the toe) were reported in Figure 15.4 (b). Figure 15.4 (a), shows CPT CP91-29, which was pushed through the failed mass. The processed data from CPT CP-91-29, as reported by Jefferies and Been, is reproduced as Figure 15.5. The fines content of the iron sandy silt tailings is reported as 50 percent or greater by Jefferies and Been. Figure 15.5 shows the interbedded nature of the iron tailings material, which is predicted to have a soil behavior type similar to that

of both sand to silty sand and silty sand to silt. Similarly, Robertson (2010) reports an I_c of 2.6, which corresponds to the boundary between sand and silt mixtures.

Figure B.15.2 shows the locations of CPT's CP91-29 and CP91-31 performed to investigate the failures. Based on the available data, Jefferies and Been (2006) reported a normalized penetration resistance Q_k = 10 to 14 and a fines content of 50 percent or greater. Robertson (2010), in his evaluation of residual strength case histories, also considered this case history. Robertson reported a representative of normalized tip resistance of Q_{tn} = 15, a clean sand corrected normalized tip resistance of $Q_{tn,cs}$ = 50, and a representative fines content of approximately 50 percent.

Based on the available data for the crest and toe CPTs reproduced in B.15.2, the representative q_c value for the tailings material encountered in the crest and toe CPTs range from about 2 to 4 MPa and 1 to 3 MPa, respectively. The ratio of $(q_c/Pa)/N_{60}$ for the tailings material was assumed to be in the range of 2 to 4. After applying the necessary corrections and conversions, resulting best estimate mean value of $N_{1,60,CS}$ for the iron tailings was judged to be $\overline{N_{1,60,CS}} \approx 9.5$ blows/ft. Variance of $\overline{N_{1,60,CS}}$ was estimated primarily on the range of results reported from the 6 CPTs. Considering these, the representation of uncertainty in the representative median value of $\overline{N_{1,60,CS}}$ was taken as $\sigma_{\overline{N}} \approx 2.5$ blows/ft.

Olson (2001) and Olson and Stark (2002) in addition to Wang (2003) and Kramer (2008) did not consider this case history, therefore no comparison can be made to those studies.

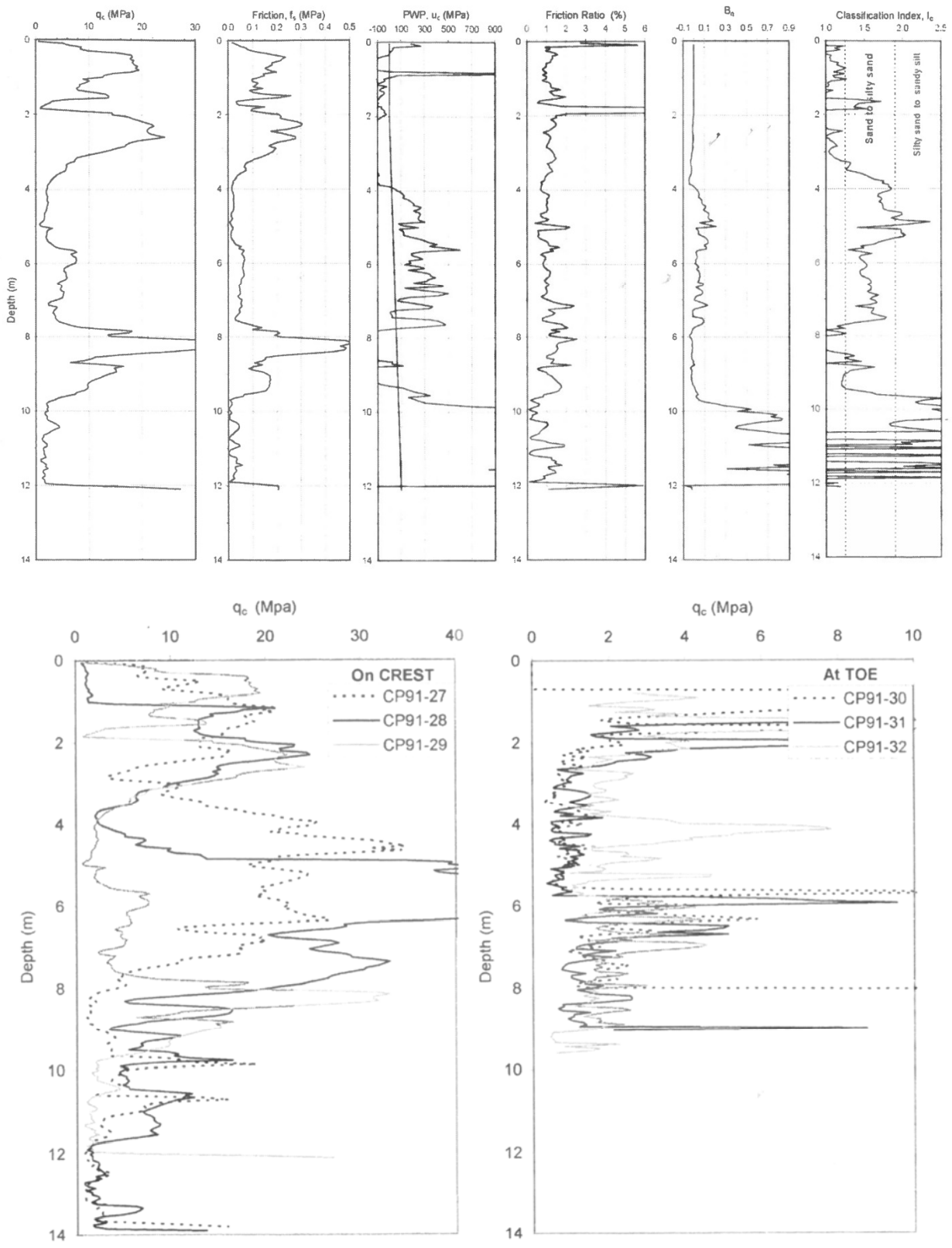

Figure B.15.4: Summary of (a) CPT CP91-29 and a (b) comparison of 6 CPTs, three from the crest and three from the toe (from Jefferies and Been, 2006).

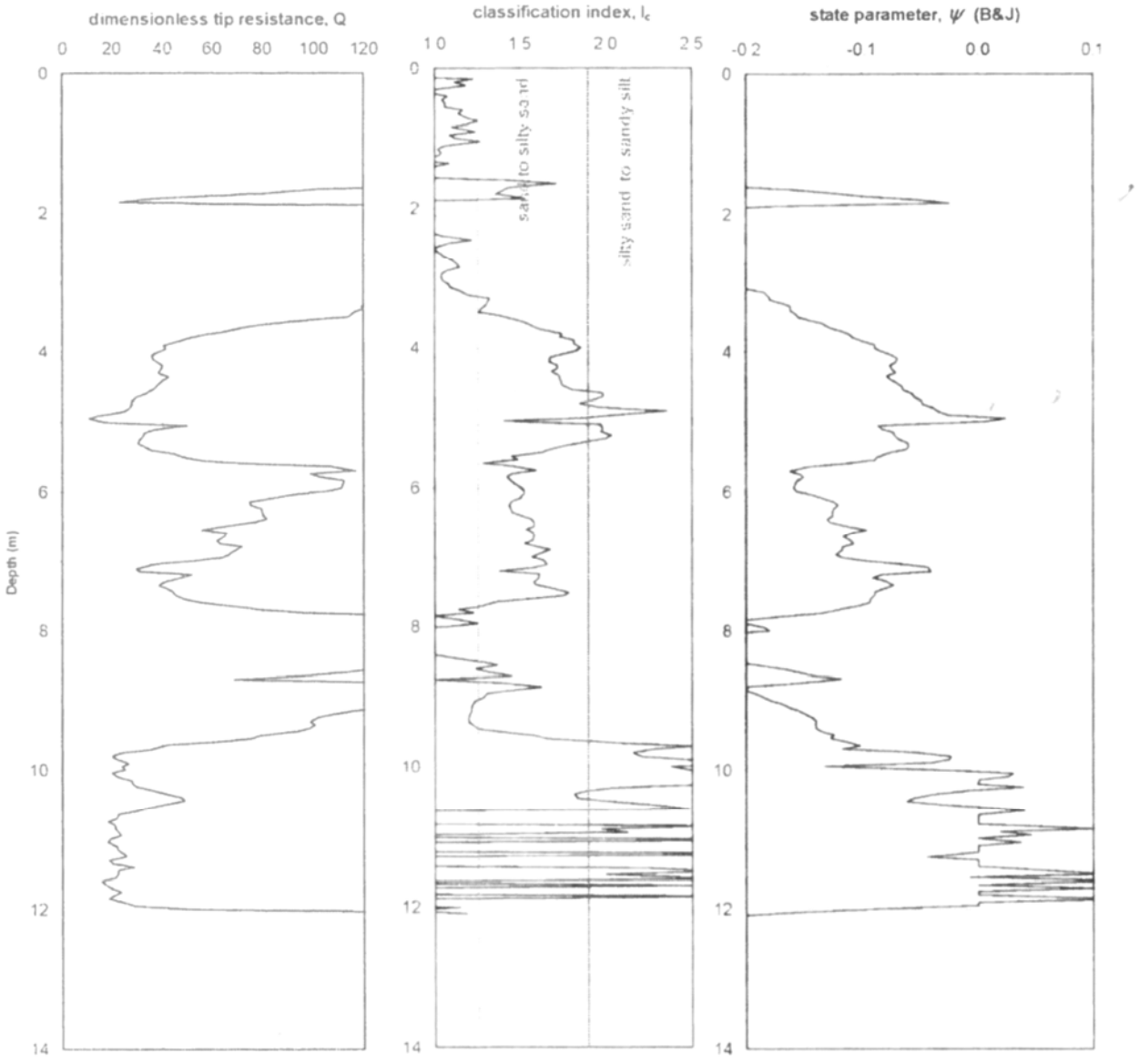

Figure B.15.5: Summary of the processed data from CPT CP91-29 as reported in Jefferies and Been (2006)

B.16 Jamuna Bridge (Bangladesh; 1994 to 1998)

B.16.1 Brief Summary of Case History Characteristics

Name of Structure	Jamuna Bridge, West Guide Bund
Location of Structure	Bangladesh
Type of Structure	Guide bund
Date of Failure	Between 1994 and 1998
Nature of Failure	More than 30 static liquefaction flow failures occurred during construction
Approx. Maximum Slope Height	64.5 ft.

B.16.2 Introduction and Description of Failure

The West Guide Bund of the Jamuna Bridge, located in Bangladesh along the Jamuna River, experienced over 30 submarine static liquefaction flow slides during construction. The Jamuna River, the fifth longest river in the world, is a braided river that typically shifts significantly during the flood seasons. Two constraining guide bunds were constructed between 1994 and 1996 on each side of the river to train the river to travel under the 4.8 km bridge corridor (Yoshimine et al., 1999; Jefferies and Been, 2006).

Figure B.16.1 shows a plan view of the western Jamuna guide bund, and Figure B.16.2 shows a typical cross section of a failure experienced in the western guide bund.

B.16.3 Geology and Site Conditions

The construction of the Guide Bund slopes occurred in very young sediments, less than 200 years of age, deposited by the Jamuna River. The flow slides occurred in normally consolidated fine to medium-grained micaceous sand, which were tested to have approximately 15 to 30% mica content by weight. The mean gran size of this material was tested to be approximately 0.1 - 0.2 mm, with 2% to 10% passing by weight the 0.06 mm sieve (Yoshimine et al., 1999).

The slopes of the Guide Bund were placed at slopes ranging from 1:3.5 (V:H) to 1.5. Flow slides of the West Guide Bund cane to rest at slopes ranging from about 1:8 to 1:20 (Yoshimine et al., 1999).

B.16.4 Initial Yield Stress Analyses

Figure B.16.3 shows the cross-section used for back-analyses of the post-liquefaction initial yield strength $S_{r,yield}$ that would be required within the foundation and embankment materials of the typical section of the West Guide Bund to produce a calculated Factor of Safety equal to

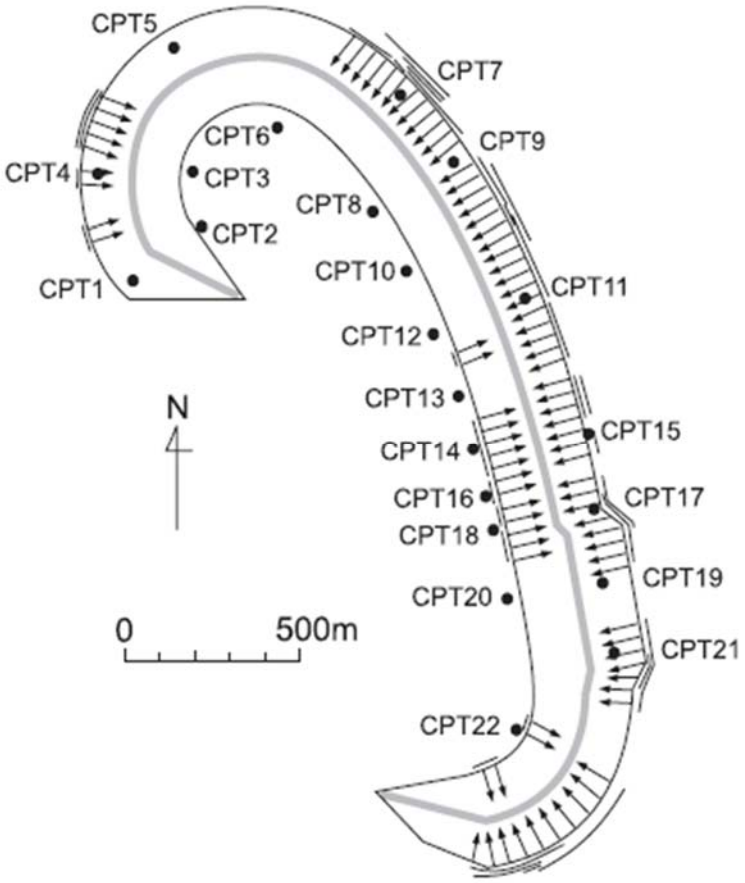

Figure B.16.1: Plan view of the West Guide Bind of the Jamuna Bridge, with arrows showing locations of failures and points noting locations of CPT's (from Yoshimine et al., 2001).

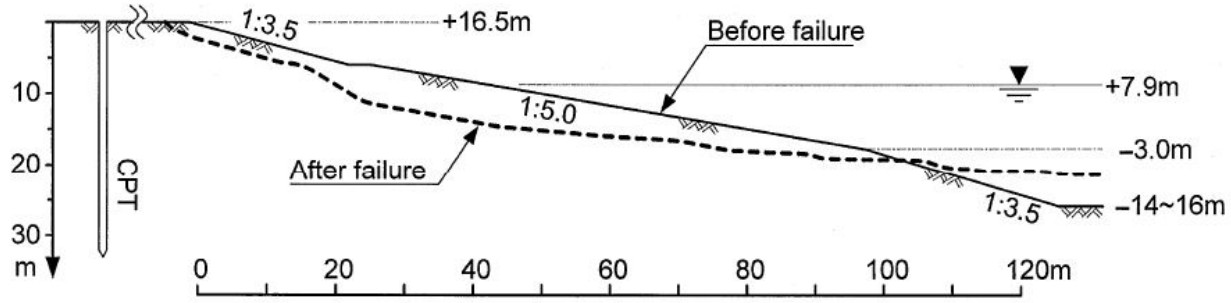

Figure B.16.2: Typical cross section of the West Guide Bind of the Jamuna Bridge with pre- and post-failure geometries depicted (from Yoshimine et al., 1999).

1.0. This is not the actual post-liquefaction strength, but it proves to be useful in developing estimates of post-liquefaction strength (S_r) for this case history.

There were two general sets of potential failure mechanisms that could potentially explain the observed features: (1) the failures may have been incrementally retrogressive, initiating with a "slice" near to the front of the feature, and then retrogressing on a slice by slice basis back towards the eventual back heel, or (2) the entire slide may have initiated monolithically (all at once). Both sets of possibilities were analyzed, and multiple potential "initial" failure surfaces were analyzed for the incrementally retrogressive scenario. In all cases, failure was modeled as occurring within the loose, saturated micaceous sands immediately underlying the Guide Bund fill.

Unit weights of the non-saturated compacted micaceous sand embankment fill above the phreatic surface were modeled with a unit weight of $\gamma_m \approx 115$ lbs/ft^3, and this was then varied over a range of $\gamma_m \approx 110$ to 120 lbs/ft^3 for parameter sensitivity studies. Unit weights of the saturated compacted sand below the phreatic surface were modeled with a unit weight of $\gamma_s \approx 120$ lbs/ft^3, and this was then varied over a range of 115 to 125 lbs/ft^3 for parameter sensitivity studies. The friction angle of the embankment micaceous sand materials above the phreatic surface was modeled with $Ø' \approx 28°$, and a range of $Ø' \approx 26°$ to 30°.

Potential initial failure surfaces were modeled as either (1) wedge-like semi-translational features, or (2) semi-rotational/translational features, or (3) conforming essentially to the final observed overall failure scarp (the monolithically initiated scenario).

The results of the various trial slip surfaces, shown in Figure B.16.3, and utilizing the best estimate parameters reported above, resulted in only moderate variations in $S_{r,yield}$ values. Based on a range of potential failure surfaces encompassing these possibilities, and the parameters (and parameter variations) described above, it was judged that the resulting best estimate value was $S_{r,yield} \approx 350$ lbs/ft^2, with a range of $S_{r,yield} \approx 321$ to 409 lbs/ft^2.

Olson (2001) did not include this case history in his failure database and therefore did not perform back-analyses to evaluate $S_{r,yield}$.

B.16.5 Residual Strength Analyses Based on Residual Geometry

Back-analysis were also performed to evaluate the "apparent" post-liquefaction strength ($S_{r,resid/geom}$) required to produce a calculated Factor of Safety equal to 1.0 based on residual geometry. This is not a direct measure of post-liquefaction strength (S_r), as it neglects momentum effects and would underestimate S_r, but it is useful for overall evaluation of Sr for this case history.

Figure B.16.3 (b) shows the post-failure cross-section geometry and example assumed slip surface utilized in the residual geometry analyses.

Based on the post-failure cross-section with the example assumed slip surface shown in Figure B.5.4(b), and the properties and parameters described above, the best-estimate value of $S_{r,resid/geom}$ was $S_{r,resid/geom} = 90$ lbs/ft^2. Parameters were next varied, as described previously, and

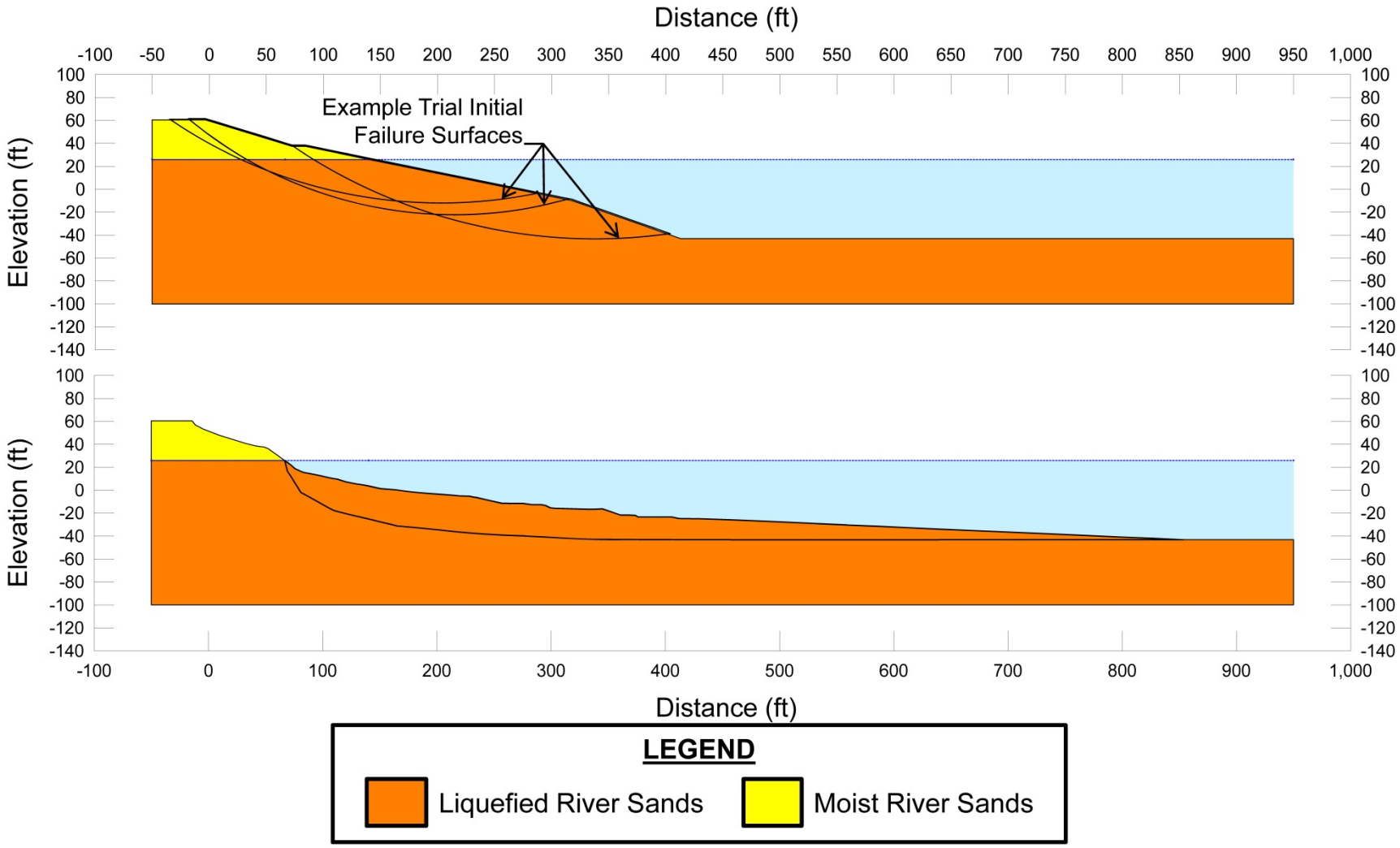

Figure B.16.3: Jamuna Bridge West Guide Bund: (a) pre-failure geometry and trail failure surfaces for initial yield stress analyses, and (b) post-failure geometry and Scenario A failure surface for post-failure residual geometry analyses.

this included analyses of alternate potential failure surfaces slightly above and below the failure surface shown in Figure B.5.4(b). Based on these analyses, it was judged that a reasonable range was $S_{r,resid/geom} \approx 76$ to 106 lbs/ft^2.

There was no value of $S_{r,resid/geom}$ from Olson (2001) for this case history.

B.16.6 Overall Estimates of S_r

Overall estimates of S_r for this Class B case history were made based on the pre-failure geometry, the partial post-failure geometry, and the approximate runout features and characteristics, and the values of $S_{r,yield}$ and $S_{r,resid/geom}$ as calculated and/or estimated in the preceding sections.

Runout distance of the center of mass of the overall failure was approximately D = 109 feet, and the initial failure slope height was H = 64.5 feet. This produces a runout ratio (defined as runout distance traveled by the center of gravity of the overall failure mass divided by the initial slope height from toe to back heel of the failure) of D/H = 1.69. This allows Equation 4-4, and Figures 4.7 and 4.11 to serve as one basis for estimation of post-liquefaction strength S_r. Using the ranges of $S_{r,yield}$ and $S_{r,resid/geom}$ from Sections B.13.4 and B.13.5, and assuming that $\xi \approx 0.58$ to 0.82 for this large runout case, with 0.7 as the best estimate, provided a best estimate value of $S_r \approx$ 154 lbs/ft^2 and an estimated range of $S_r \approx 128$ to 180 lbs/ft^2. A second basis for estimation of S_r was the use of the relationship of Figure 4.9, and the range of values of $S_{r,yield}$ from Section B.5.4. Based on the large runout distance, values of initial (pre-failure displacement) Factor of Safety were taken as approximately 0.4 to 0.55, and this produced a best estimate value of $S_r \approx 168$ lbs/ft^2 and an estimated range of $S_r \approx 140$ to 193 lbs/ft^2. No similar use was made of Figure 4.9 in conjunction with the ranges of $S_{r,resid/geom}$ estimated in Section B.4.5 because these estimates of $S_{r,resid/geom}$ were considered to be very approximate.

The estimates by each of the two methods above were then averaged together, and this produced a best estimate value of $S_r \approx 160$ lbs/ft^2 and an estimated range of $S_r \approx 115$ to 225 lbs/ft^2. These estimates of variance are non-symmetric about the best estimated mean value, and the range was judged to represent approximately +/- 2.5 standard deviations, so further adjustments were then necessary.

Overall, taking into consideration the largely asymmetric range of the results from assumed $S_{r,yield}$ slip surfaces, it was judged that the (median) best estimate of post-liquefaction strength for this case history is

$$\bar{S}_r = 175 \text{ lbs/ft}^2$$

and that the best estimate of standard deviation of mean overall post-liquefaction strength is

$$\sigma_{\bar{S}} = 22 \text{ lbs/ft}^2$$

Olson (2001) and Olson and Stark (2002), and Wang (2003) and Kramer (2008), did not consider this case history, therefore no comparison can be made to those studies. However, Yoshimine et al. (1999) did estimate the range of strength ratio for this case to be between 0.11 and 0.26. Robertson (2010) presents a best estimate strength ratio of 0.15 for this case history. As a comparison, the best estimate of strength ratio for this current study is

$$S_r/P = 175 \text{ lbs/ft}^2 / 1{,}404 \text{ lbs/ft}^2 = 0.12$$

which is in fairly good agreement with the value back-calculated by Robertson (2010), and which at least falls within the range of Yoshimine et al. (1999).

B.16.7 Evaluation of Initial Effective Vertical Stress

Average initial (pre-failure) effective vertical stress was assessed for the liquefied portions of the failure surfaces for both rotational and wedge-like failures similar to the one shown in Figure B.16.3. Failure surfaces, parameters and sensitivity analyses were as described previously in Section B.16.4. Depths of failure surfaces were varied, and both rotational and translational (wedge-like) failure surfaces were considered.

The resulting best estimate of average pre-failure effective stress within the liquefied materials controlling the failure was then $\sigma_{vo}' \approx 1{,}392$ lbs/ft^2, with a reasonable range of $\sigma_{vo}' \approx$ 984 to 1,824 lbs/ft^2. This range is slightly non-symmetric about the median value, and this range was judged by the engineering team to represent approximately ± 2 standard deviations. Overall, the best characterization of initial (pre-failure) average effective vertical stress was then taken to be represented by a mean value of

$$\overline{\sigma'_{vo}} \approx 1{,}404 \text{ lbs/ft}^2$$

and with a standard deviation of

$$\sigma_{\bar{\sigma}} \approx 210 \text{ lbs/ft}^2$$

Olson (2001) and Olson and Stark (2002) in addition to Wang (2003) and Kramer (2008) did not consider this case history, therefore no comparison can be made to those studies. Also no estimate of representative initial vertical effective stress was directly reported in Yoshimine et al. (1999).

B.16.8 Evaluation of $N_{1,60,CS}$

A total of 22 CPTs were performed on the shoulder of the West Guide Bund. The apparent representative fines content of the material was about 15% (Yoshimine et al., 1999).

Figure B.16.1 shows the locations of CPT tests performed to investigate the failures. A summary of these explorations can be seen in Figure B.16.4. Based on the available data and information, a representative range of normalized and fines corrected $(q_{c1N})_{CS}$, corrected using the

procedure recommended by Robertson and Wride (1998), as reported in Yoshimine et al. (1999), is approximately 50 to 65. Yoshimine suggested that the mean minus one sigma values would lie in a range of 40 to 65. The ratio of $(q_c/Pa)/N_{60}$ was assumed to be approximately of 5 to 6. The resulting best estimate mean value of $N_{1,60,CS}$ for the micaceous silty sands was thus found to be $\overline{N_{1,60,CS}} \approx 10.5$ blows/ft. Variance of $\overline{N_{1,60,CS}}$ was estimated primarily on the range of results reported from the 22 CPTs. Considering these, the representation of uncertainty in the representative median value of $\overline{N_{1,60,CS}}$ was taken as $\sigma_{\overline{N}} \approx 2.5$ blows/ft.

Olson (2001) and Olson and Stark (2002) in addition to Wang (2003) and Kramer (2008) did not consider this case history, therefore no comparison can be made to those studies. Representative $(q_{c1N})_{CS}$ was reported in Yoshimine et al. (1999) is 40 to 55, however that range appears to be intended to represent mean minus one sigma values. Robertson (2010) presents a representative normalized value of $Q_{tn,cs} = 57$ for this case history.

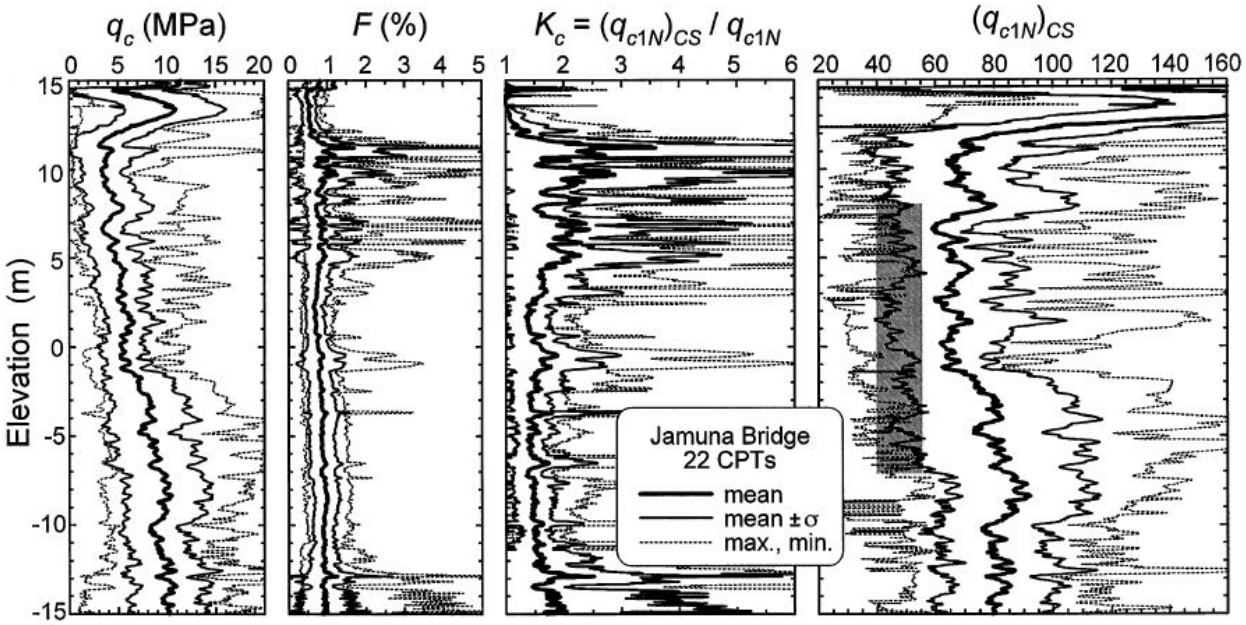

Figure B.16.4: Summary of 22 CPTs preformed at the West Guide Bund of the Jamuna Bridge as reported by Yoshimine et al. (1999).

Appendix C:

Incrementally Progressive Analyses in Simulation Format

C: Incrementally Progressive Analyses in Simulation Format

C.1: Lower San Fernando Dam (1971)

C. Incrementally Progressive Analyses in Simulation Format

C.1 Lower San Fernando Dam (California, USA; 1971)

The following pages present a comprehensive rendering of the incremental momentum analyses of the upstream slope failure of the Lower San Fernando Dam which occurred as a result of the 1971 San Fernando Earthquake. A full description of the back-analyses of this case history is presented in Appendix A, Section A.4.

In this current section, a number of the elements of the incremental momentum analyses that were performed as part of those back-analyses are combined into a composite set of images showing the following all on a single page:

1. Incremental evolution of cross-section geometry as the failure progresses.

2. Incremental evolution of the location of the position of the center of gravity of the overall failure mass as the failure progresses.

3. Incremental evolution of acceleration vs. time of the center of gravity of the overall failure mass as the failure progresses.

4. Incremental evolution of velocity vs. time of the center of gravity of the overall failure mass as the failure progresses.

5. Incremental evolution of displacement vs. time of the center of gravity of the overall failure mass as the failure progresses.

All five of these are displayed simultaneously, on a single sheet. Multiple sheets are presented, advancing with time as the failure progresses. As a result, it is possible for "viewers" to advance their screen view by clicking through these images in a manner that allows the sequence of images to be "played" like a choppy video or animation. This can provide useful insight as to how the various elements combine together to represent the scenario modeled.

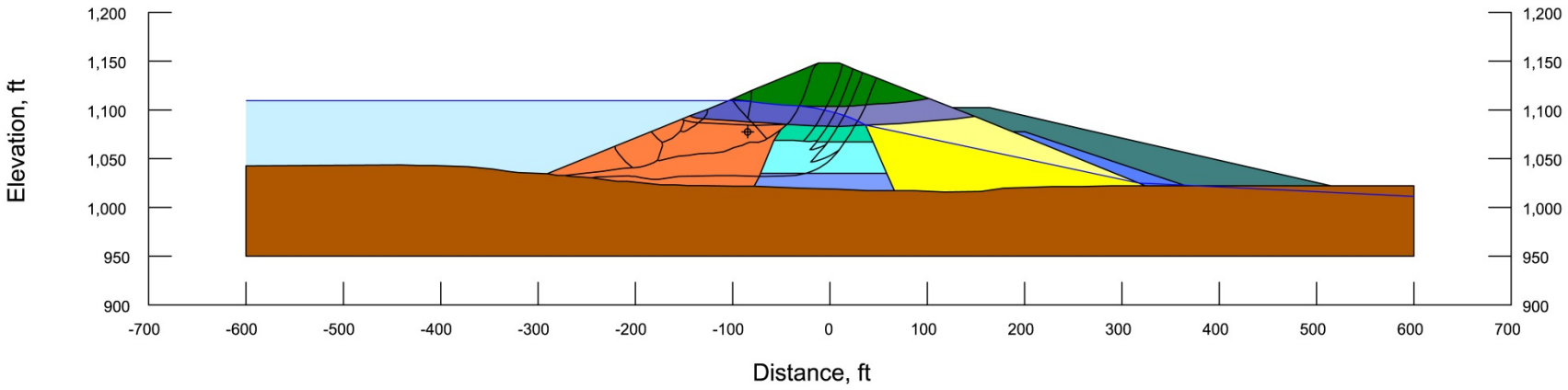
Elevation, ft
1,200
1,150
1,100
1,050
1,000
950
900
-700
-600
-500
-400
-300
-200
-100
0
100
200
300
400
500
600
700
Distance, ft

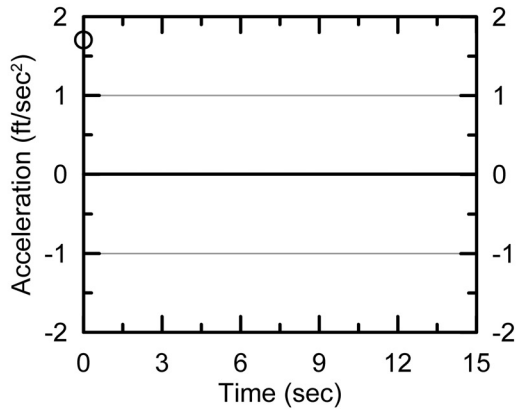
Acceleration (ft/sec²)
2
1
0
-1
-2
0
3
6
9
12
15
Time (sec)

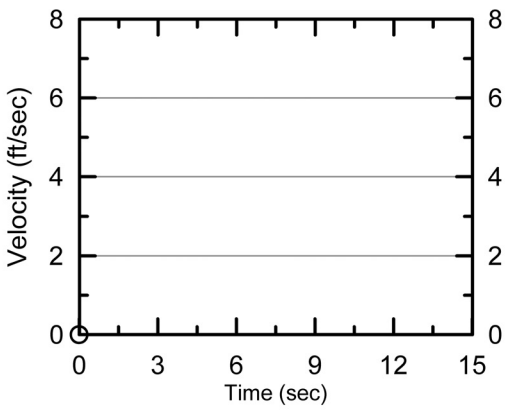
Velocity (ft/sec)
8
6
4
2
0
0
3
6
9
12
15
Time (sec)

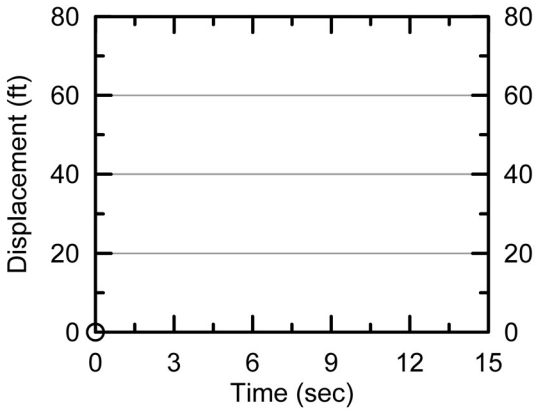
Displacement (ft)
80
60
40
20
0
0
3
6
9
12
15
Time (sec)

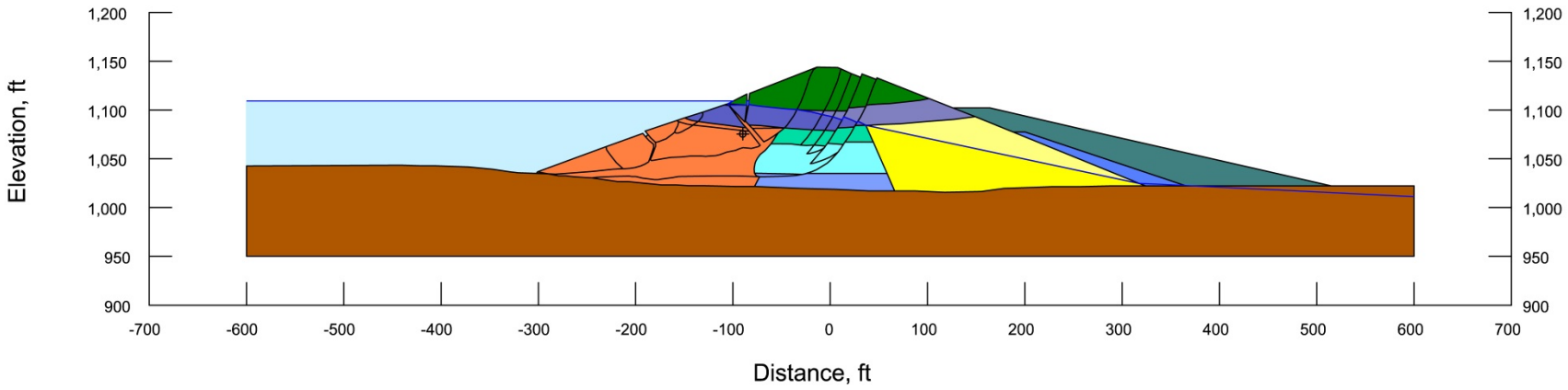
Elevation, ft
1,200
1,150
1,100
1,050
1,000
950
900
-700
-600
-500
-400
-300
-200
-100
0
100
200
300
400
500
600
700
Distance, ft

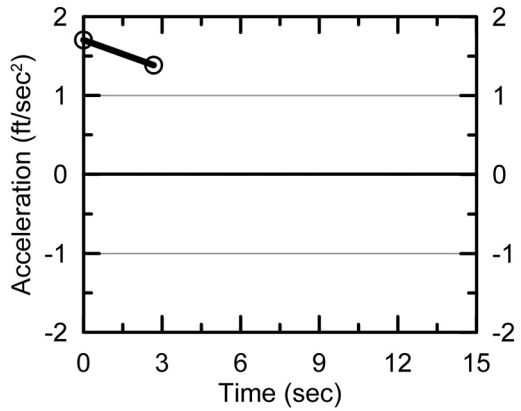
Acceleration (ft/sec²)
2
1
0
-1
-2
0
3
6
9
12
15
Time (sec)

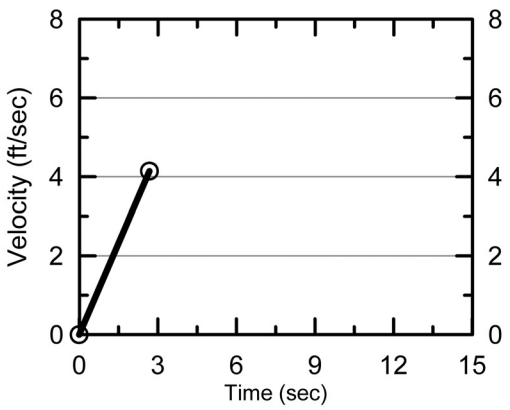
Velocity (ft/sec)
8
6
4
2
0
0
3
6
9
12
15
Time (sec)

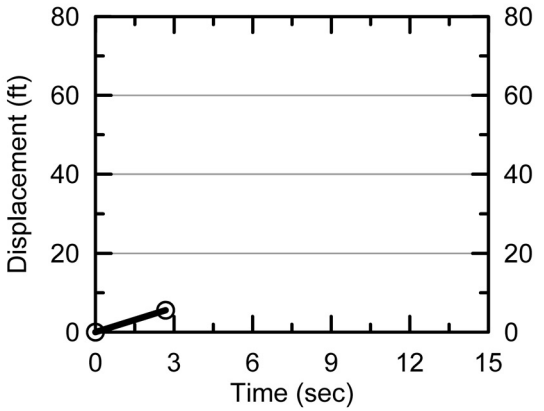
Displacement (ft)
80
60
40
20
0
0
3
6
9
12
15
Time (sec)

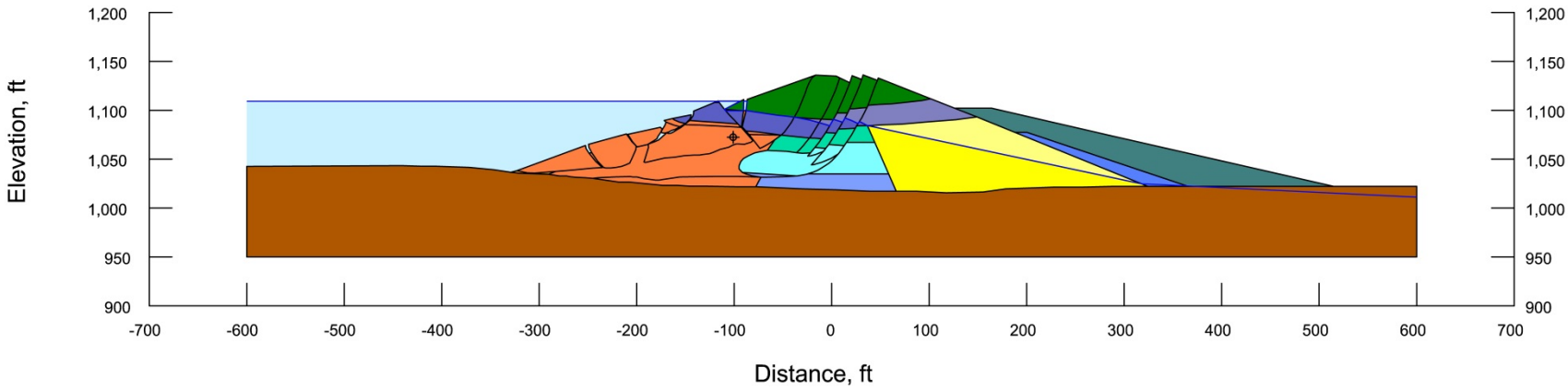
Elevation, ft
1,200
1,150
1,100
1,050
1,000
950
900
-700
-600
-500
-400
-300
-200
-100
0
100
200
300
400
500
600
700
Distance, ft

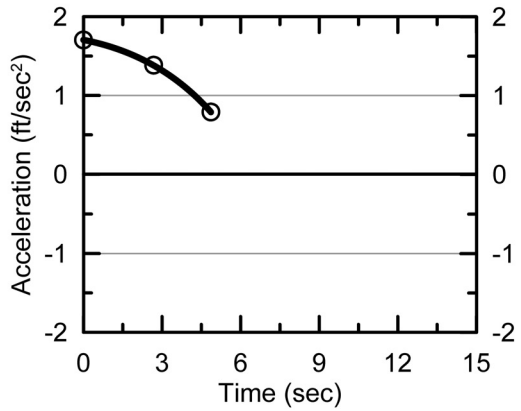
Acceleration (ft/sec²)
2
1
0
-1
-2
0
3
6
9
12
15
Time (sec)

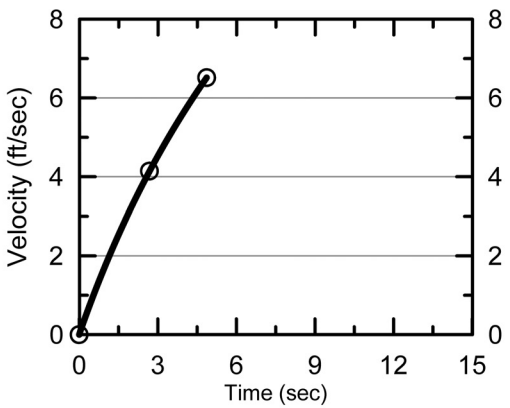
Velocity (ft/sec)
8
6
4
2
0
0
3
6
9
12
15
Time (sec)

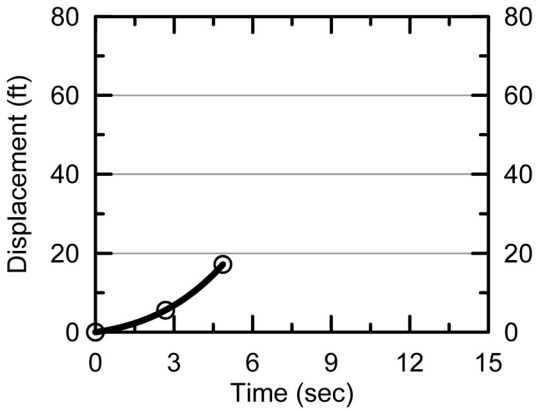
Displacement (ft)
80
60
40
20
0
0
3
6
9
12
15
Time (sec)

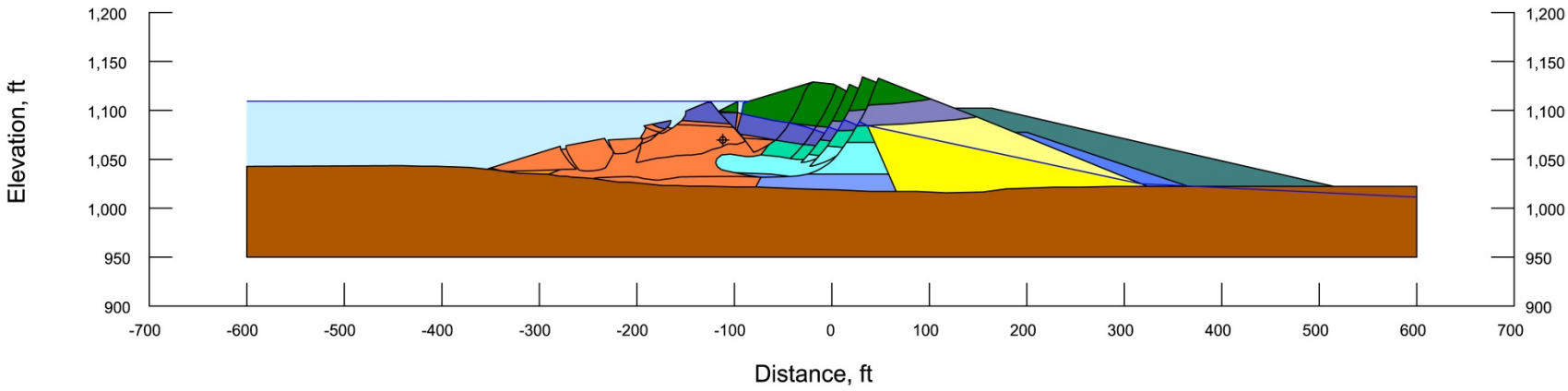
Elevation, ft
1,200
1,150
1,100
1,050
1,000
950
900
-700
-600
-500
-400
-300
-200
-100
0
100
200
300
400
500
600
700
Distance, ft

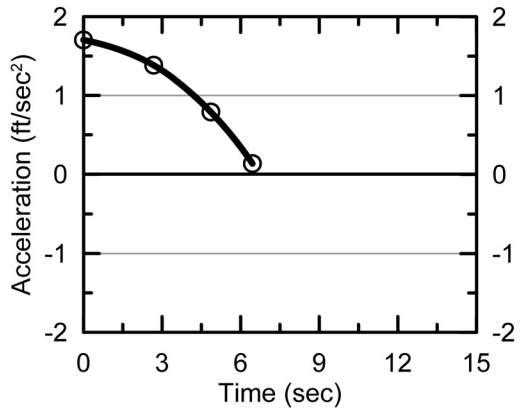
Acceleration (ft/sec²)
2
1
0
-1
-2
0
3
6
9
12
15
Time (sec)

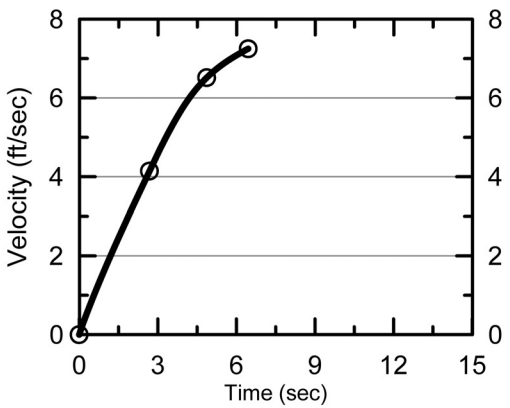
Velocity (ft/sec)
8
6
4
2
0
0
3
6
9
12
15
Time (sec)

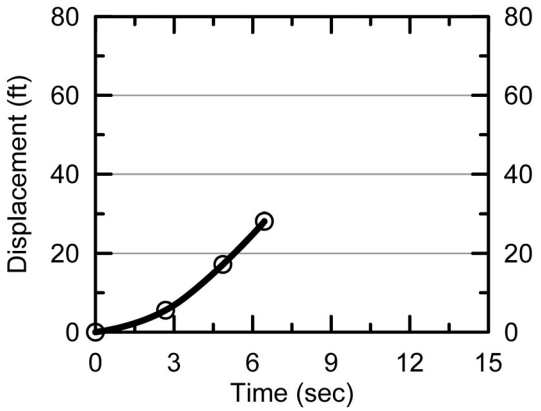
Displacement (ft)
80
60
40
20
0
0
3
6
9
12
15
Time (sec)

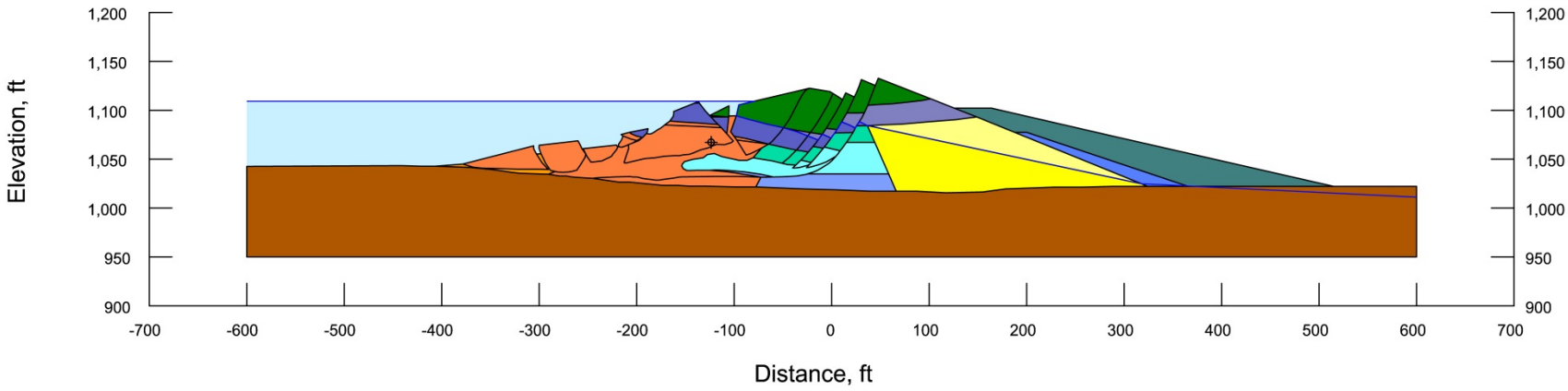
Elevation, ft
1,200
1,150
1,100
1,050
1,000
950
900
-700
-600
-500
-400
-300
-200
-100
0
100
200
300
400
500
600
700
Distance, ft

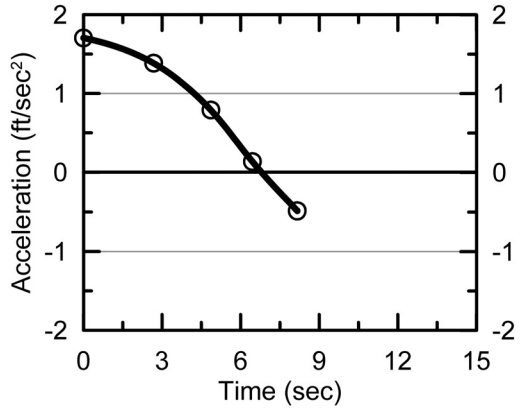
Acceleration (ft/sec²)
2
1
0
-1
-2
0
3
6
9
12
15
Time (sec)

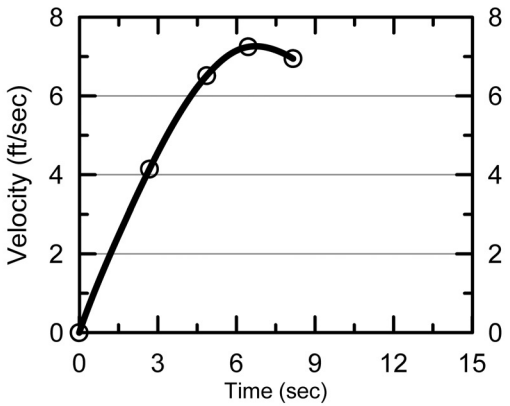
Velocity (ft/sec)
8
6
4
2
0
0
3
6
9
12
15
Time (sec)

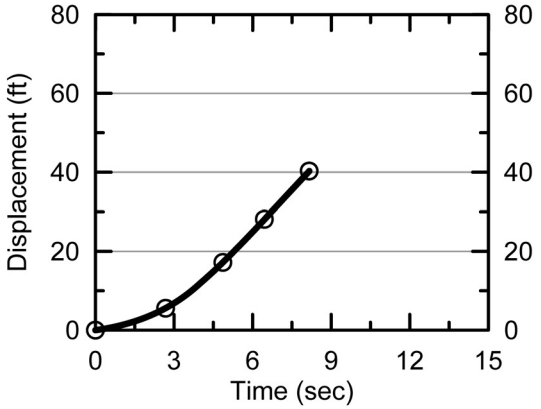
Displacement (ft)
80
60
40
20
0
0
3
6
9
12
15
Time (sec)

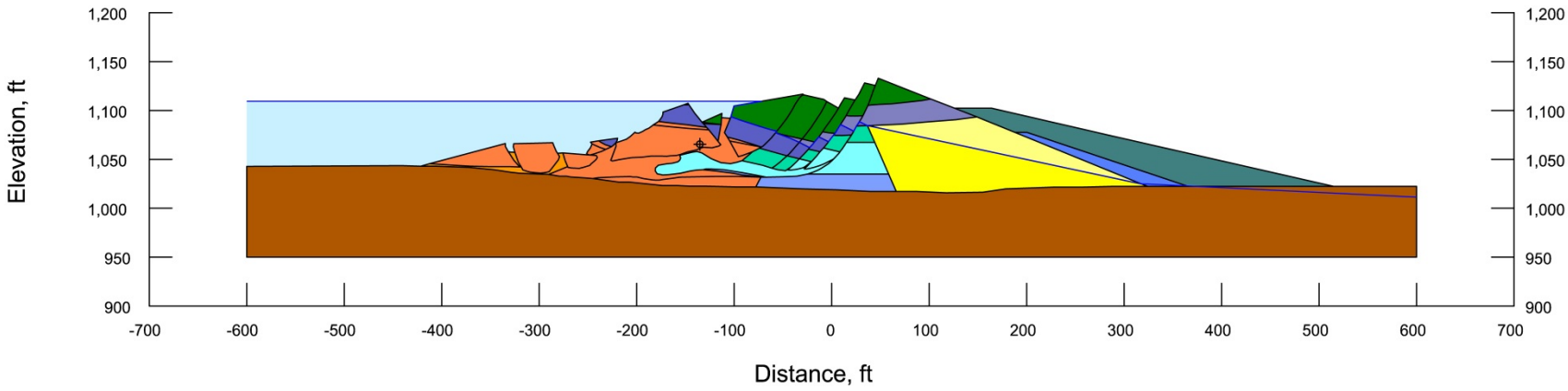
Elevation, ft
1,200
1,150
1,100
1,050
1,000
950
900
-700
-600
-500
-400
-300
-200
-100
0
100
200
300
400
500
600
700
Distance, ft

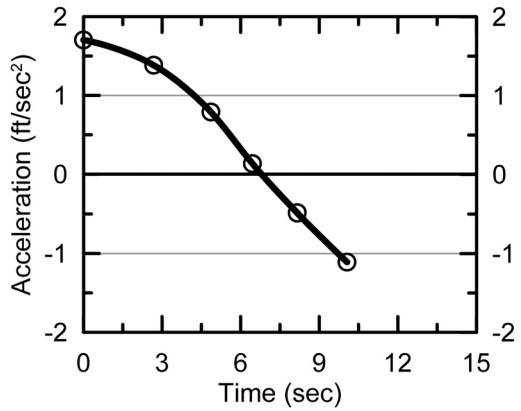
Acceleration (ft/sec²)
2
1
0
-1
-2
0
3
6
9
12
15
Time (sec)

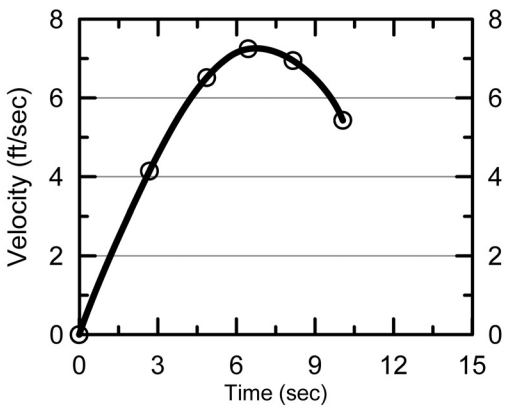
Velocity (ft/sec)
8
6
4
2
0
0
3
6
9
12
15
Time (sec)

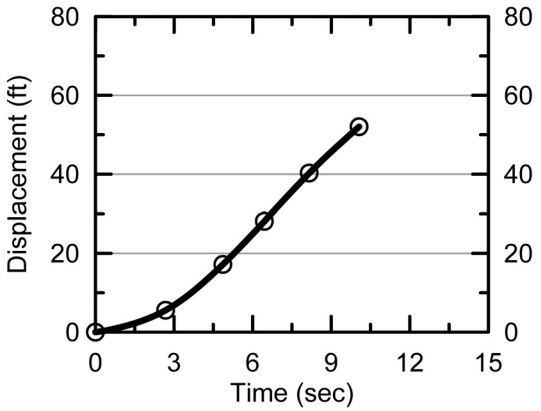
Displacement (ft)
80
60
40
20
0
0
3
6
9
12
15
Time (sec)

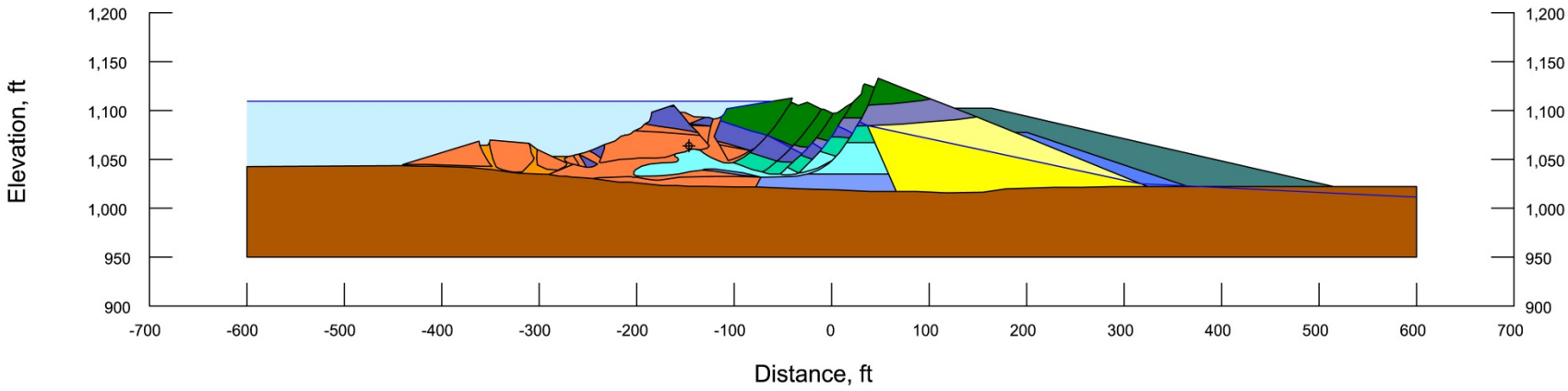
Elevation, ft
1,200
1,150
1,100
1,050
1,000
950
900
-700
-600
-500
-400
-300
-200
-100
0
100
200
300
400
500
600
700
Distance, ft

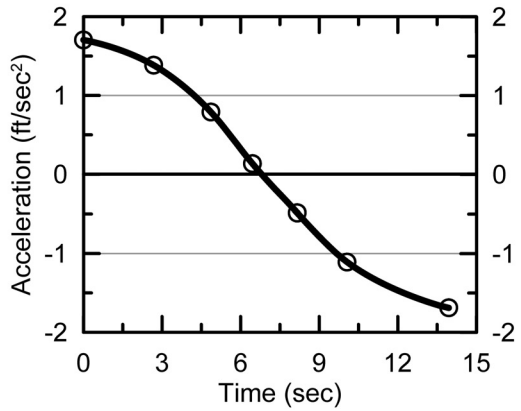
Acceleration (ft/sec²)
2
1
0
-1
-2
0
3
6
9
12
15
Time (sec)

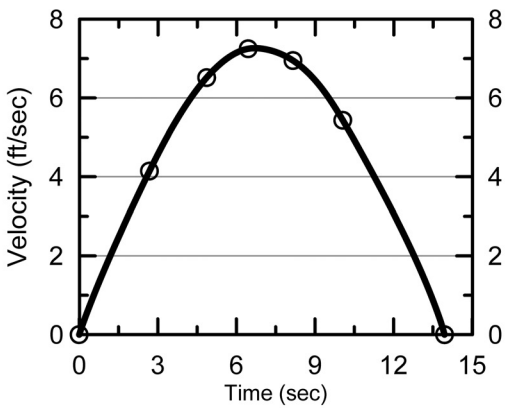
Velocity (ft/sec)
8
6
4
2
0
0
3
6
9
12
15
Time (sec)

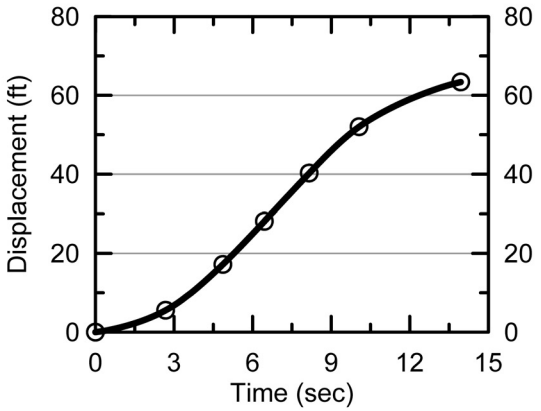
Displacement (ft)
80
60
40
20
0
0
3
6
9
12
15
Time (sec)

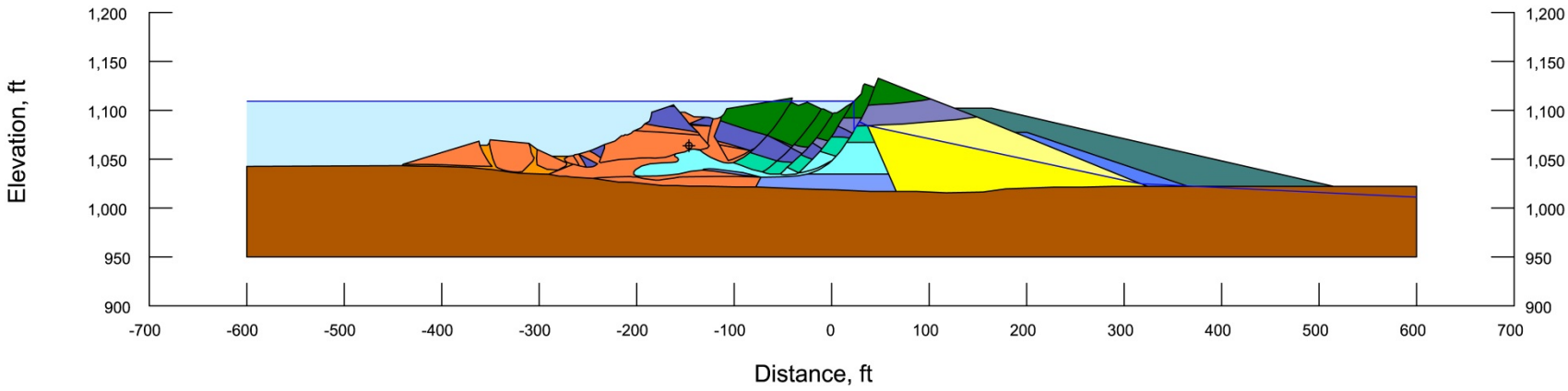
Elevation, ft
1,200
1,150
1,100
1,050
1,000
950
900
-700
-600
-500
-400
-300
-200
-100
0
100
200
300
400
500
600
700
Distance, ft

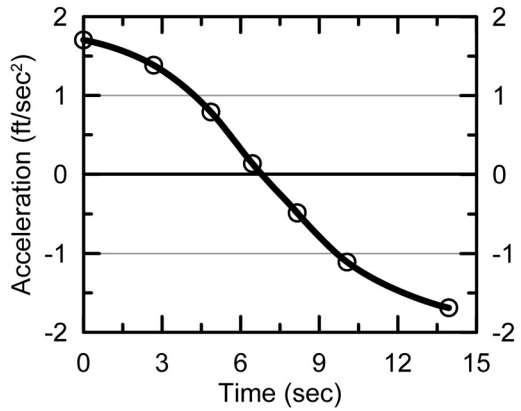
Acceleration (ft/sec²)
2
1
0
-1
-2
0
3
6
9
12
15
Time (sec)

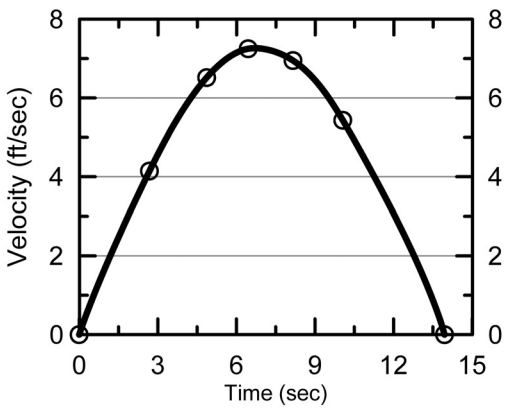
Velocity (ft/sec)
8
6
4
2
0
0
3
6
9
12
15
Time (sec)

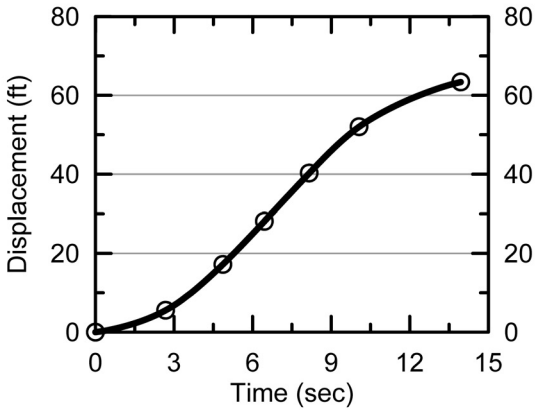
Displacement (ft)
80
60
40
20
0
0
3
6
9
12
15
Time (sec)